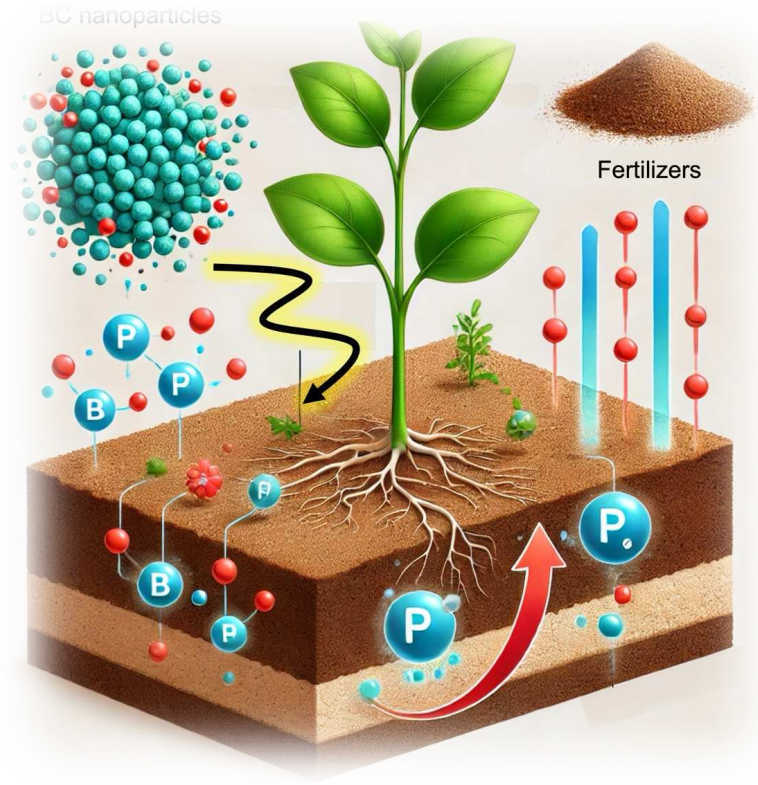
Universität Rostock Traditio et Innovatio

Institut für Chemie

INSTITUT FÜR PHYSIK

Advances in Phosphorus Binding: Computational Chemistry Insights into Reactive Molecular Systems



Kumulative Habilitationsschrift
zur Erlangung des akademischen Grades
doctor rerum naturalium habilitatus (Dr. rer. nat. habil.)
der Mathematisch-Naturwissenschaftlichen Fakultät
der Universität Rostock

vorgelegt von
Dr. Ashour Ahmed, geb. am 14 November 1983 in Sohag, Ägypten

Rostock, 2025

https://doi.org/10.18453/rosdok_id00005130



Dieses Werk ist lizenziert unter einer
Creative Commons Namensnennung - Nicht kommerziell - Keine Bearbeitungen 4.0 International Lizenz.

Gutachter:

" **Prof. Dr. Oliver Kühn**

Institute of Physics, University of Rostock, Rostock, Germany

" **PD. Dr. Daniel Tunega**

Institute of Soil Research, University of Natural Resources and Life Sciences, Vienna, Austria

" **Prof. Dr. James Kubicki**

Department of Earth, Environmental and Resource Sciences, University of Texas at El Paso, El Paso, Texas United States

Datum der Einreichung: 19.07.2024

Datum der Verteidigung: 30.01.2025

Abstract

Ever-improving molecular simulation techniques, coupled with advanced software and hardware, have become indispensable in chemistry and related fields, providing detailed insights into molecular geometries, thermodynamics, reaction kinetics, molecular dynamics, and spectroscopy, simulating pure phases, solutions, and interfaces. However, environmental chemistry, particularly soil biogeochemical processes, remains underexplored due to the complex heterogeneity of soil. My habilitation thesis addresses this gap by focusing on phosphorus (P) binding in soil and its availability, demonstrating the power of computational chemistry and molecular simulations. To tackle soil heterogeneity, we break down the P binding problem into separate problems, each connected to a well-defined model, revealing P binding to soil organic matter, metal ions, and mineral surfaces. Simulation results provide a comprehensive understanding of P binding, considering factors such as the type and species of P compounds, soil constituent quality and quantity, mineral surfaces, binding motifs, water, solution pH, initial P concentration, complexation versus precipitation, organic acids, central metal ions, and redox potential. Additionally, the thesis explores glyphosate interactions with soil constituents, clarifying its detection and binding mechanisms under various pH and redox conditions. The role of water in controlling P binding at mineral surfaces is examined, along with P binding mechanisms at low and high surface loadings. The thesis also discusses the role of organic matter (OM) in mobilizing bound P, considering different OM and P compounds and treatments. The design concept of smart fertilizers, their gradual dissolution, and P release under controlled conditions are introduced. By integrating molecular-level results, the thesis provides an overall picture of P binding in soil. It concludes with a discussion of challenges and necessary modifications to existing molecular modeling approaches, emphasizing the need to bridge the molecular and mesoscale levels. Addressing these challenges through joint advanced experimental and theoretical approaches and multidisciplinary efforts can enhance P availability in soils, improve soil fertility, protect water quality, and advance sustainable agricultural practices and environmental conservation.

Zusammenfassung

Ständig verbesserte molekulare Simulationstechniken, gepaart mit fortschrittlicher Software und Hardware, sind in der Chemie und verwandten Bereichen unverzichtbar geworden. Sie bieten detaillierte Einblicke in molekulare Geometrien, Thermodynamik, Reaktionskinetik, Molekulardynamik und Spektroskopie und ermöglichen die Simulation von reinen Phasen, Lösungen und Grenzflächen. Die Umweltchemie, insbesondere die biogeochemischen Prozesse im Boden, ist jedoch aufgrund der komplexen Heterogenität des Bodens noch nicht ausreichend erforscht. Meine Habilitationsschrift schließt diese Lücke, indem sie sich auf die Bindung von Phosphor (P) im Boden und dessen Verfügbarkeit konzentriert und die Leistungsfähigkeit der Computerchemie und molekularen Simulationen demonstriert. Um die Heterogenität des Bodens anzugehen, zerlegen wir das Problem der P-Bindung in separate Teilprobleme, die jeweils mit einem gut definierten Modell verbunden sind, und zeigen die P-Bindung an organische Bodensubstanz, Metallionen und Mineraloberflächen auf. Die Simulationsergebnisse liefern ein umfassendes Verständnis der P-Bindung unter Berücksichtigung von Faktoren wie der Art und Spezies der P-Verbindungen, der Qualität und Quantität der Bodenbestandteile, der Mineraloberflächen, der Bindungsmotive, des Wassers, des LösungspH-Werts, der anfänglichen P-Konzentration, der Komplexierung versus Fällung, organischer Säuren, zentraler Metallionen und des Redoxpotenzials. Darüber hinaus untersucht die Arbeit die Wechselwirkungen von Glyphosat mit Bodenbestandteilen und klärt dessen Nachweis- und Bindungsmechanismen unter verschiedenen pH- und Redoxbedingungen. Die Rolle des Wassers bei der Kontrolle der P-Bindung an Mineraloberflächen wird ebenso untersucht wie die P-Bindungsmechanismen bei niedriger und hoher Oberflächenbeladung. Die Arbeit erörtert auch die Rolle organischer Materie (OM) bei der Mobilisierung gebundenen P, wobei verschiedene OM- und P-Verbindungen sowie Behandlungen berücksichtigt werden. Es wird das Designkonzept intelligenter Düngemittel, deren allmähliche Auflösung und die P-Freisetzung unter kontrollierten Bedingungen eingeführt. Durch die Integration molekularer Ergebnisse vermittelt die Arbeit ein Gesamtbild der P-Bindung im Boden. Sie schließt mit einer Diskussion über Herausforderungen und notwendige Modifikationen bestehender molekularer Modellierungsansätze und betont die Notwendigkeit, die molekularen und mesoskaligen Ebenen zu verbinden. Die Bewältigung dieser Herausforderungen durch gemeinsame experimentelle und theoretische Ansätze sowie multidisziplinäre Anstrengungen kann die P-Verfügbarkeit im Boden verbessern, die Bodenfruchtbarkeit erhöhen, die Wasserqualität schützen und nachhaltige landwirtschaftliche Praktiken und den Umweltschutz vorantreiben.

Acknowledgments

First and foremost, "**Alhamdulillahi Rabbil-'alamin**", all praise belongs to **Allah**, the Lord of all that exists. O **Allah**, to You belong all praise and thanks in every moment, always and forever. All praise and thanks are due to You for granting me the ability to complete my habilitation and for Your countless blessings, guidance, and mercy that have sustained me throughout every moment of my life.

I would like to express my sincere appreciation to Prof. Oliver Kühn and Prof. Peter Leinweber for their invaluable mentorship and support throughout my PhD journey. I am deeply grateful for the nine years of collaboration that followed. My heartfelt thanks go to Prof. Kühn for hosting me as a senior researcher and junior group leader within the Molecular Quantum Dynamics Group. I am equally indebted to Prof. Leinweber for his exceptional leadership of the InnoSoilPhos project, which I was honored to contribute to. Your guidance and support have been truly invaluable to me.

I am also deeply grateful to Prof. Ralf Ludwig for hosting my habilitation at the Institute of Chemistry.

I am profoundly thankful to my master's supervisors, Dr. Mohamed Shibl and Prof. Rifaat Hilal, as well as each lecturer and demonstrator who taught me at Cairo University, Egypt. Your guidance has been instrumental in shaping my academic journey.

I extend my gratitude to all colleagues in the groups of Prof. Kühn and Prof. Leinweber, with special thanks to my former and current PhD students: Mr. Lorenz Dettmann, Dr. Prasanth Ganta, and Dr. Moyassar Meshhal. Gratitude also to the collaborators of the InnoSoilPhos project, particularly Dr. Peter Gros, Dr. Mohsen Morshedizad, Dr. Stella Gypser, Dr. Dirk Freese, Prof. Sabry Shaheen, and Prof. Jörg Rinklebe.

I must acknowledge the dearest people in my heart: my mother and father. No words or deeds can ever repay their endless love and sacrifices. I am profoundly grateful to my beloved wife for her unwavering support and boundless patience and for standing by me through every challenge. Her encouragement and sacrifices have been my greatest strength, providing me with the motivation and resilience needed to complete this journey. To my children, Mohammad, Ali, Hazem, and Mariam, thank you for your support, understanding, and the burdens you have shared with me. I am also grateful to my sister, brothers, and all my family members in Egypt for their constant encouragement and support.

Finally, I extend my gratitude to the BMBF and DFG for their financial support over the past nine years, which has been crucial for my extensive research on phosphorus.

My heartfelt thanks to everyone who has been part of this journey.

Contents

1 Introduction **1**
1.1 Motivation 1
1.2 P Problem and Experimental Efforts 4

2 Computational Chemistry and Computational Efforts **9**
2.1 Computational Chemistry 9
2.2 Computational Efforts 12

3 Toward Squaring the Circle **14**
3.1 Coping with the heterogeneity 14
3.2 P Binding at the Goethite-Water Interface 16
3.2.1 Binding Mechanism and Relevant Effects 16
3.2.2 IR Spectroscopy 21
3.2.3 Complexation versus Precipitation 24
3.2.4 High Surface Loading 26
3.2.5 Organic Phosphates 27
3.3 P Binding at Diaspore: Impact of Central Metal Ion 31
3.4 Complex Reactions and Redox Potential 33
3.5 Organic Matter Competition 37
3.6 Smart Fertilizers 42
3.7 Environmental Impact of Glyphosate 45
3.7.1 Glyphosate Interactions in Soil 46
3.7.2 Impact of Peptides and Metal Ions on Glyphosate Detection . . . 51

4 Summary and Conclusions **55**

Bibliography **59**

Appendices **77**

List of Abbreviations

CC Computational chemistry

QM Quantum mechanics

DFT Density functional theory

SE Semi-empirical methods

MM Molecular mechanics

MD Molecular dynamics

PBC Periodic boundary condition

NVT Constant particle number, temperature, and volume

GPW The hybrid Gaussian and plane-wave approach

PBE The Perdew–Burke–Ernzerhof DFT functional

B3LYP The Becke, three-parameter, Lee–Yang–Parr DFT functional

ECP Effective core potential

GTH Goedecker–Teter–Hutter pseudopotentials

BSSE Basis set superposition error

GD3 The empirical dispersion correction D3 by Grimme

CPCM Conductor-like polarizable continuum model

NMR Nuclear magnetic resonance

FTIR Fourier-transform infrared

IRST Infrared surface titration

UV Ultraviolet

XPS X-ray photo-electron spectroscopy

XANES X-ray absorption near-edge spectroscopy

EXAFS Extended X-ray absorption fine structure

Py-FIMS Pyrolysis field-ionization mass spectrometry

P Phosphorus

OP Orthophosphate

GP Glycerolphosphate

GLP Glyphosate

IHP Inositolhexaphosphate

BC Bone char

OM Organic matter

SOM Soil organic matter

DOM Dissolved organic matter

DOC Dissolved organic carbon

CIT Citric acid

IHP Histidine

M^{n+} Metal ion

M Monodentate (i.e., formation of one covalent/coordination bond)

B Bidentate (i.e., formation of two covalent/coordination bonds)

HBs Hydrogen bonds

PZC Point of zero charge

SSA Specific surface area

1 Introduction

1.1 Motivation

Understanding critical environmental processes, such as the chemical reactions that control the speciation, abundance, transformation, fate, and transport of pollutants and nutrients, requires molecular-level insight. This necessitates combining advanced experimental techniques, including sorption/desorption processes, kinetics, and characterization tools utilizing cutting-edge spectroscopic, microscopic, and molecular technologies. Incorporating computational molecular physics and chemistry into environmental science is promising for gaining this molecular-level insight. Molecular-level simulations have become indispensable tools in chemistry and related fields, benefiting from increasingly sophisticated numerical algorithms and computer hardware.

Despite their broad applications, molecular simulations of biogeochemical processes in soil have not received as much attention. This is surprising given their potential to provide molecular-level understanding. However, the inherent complexity of soil (a heterogeneous natural system containing various metal ions, reactive inorganic minerals, soil organic matter (SOM), soil solution, and gases, all of which vary spatially and temporally) presents significant challenges (Schulten and Schnitzer, 1993; Schulten and Leinweber, 2000; Leinweber et al., 1999; Schaumann and Thiele-Bruhn, 2011; Di Iorio et al., 2022). To address this, we have focused on developing relevant molecular models and introducing advanced molecular simulation techniques into environmental science, particularly soil chemistry and geochemistry. This multidisciplinary effort involves physics, chemistry, and soil science.

Our research focuses on applying advanced molecular modeling techniques to simulate the binding, sorption, and desorption processes of potential pollutants and nutrients at soil surfaces and interfaces. By investigating these chemical reactions and physical processes at the molecular level, we aim to develop more effective environmental strategies. We are dedicated to developing molecular models for SOM and examining the interactions and fate of common organic and inorganic contaminants and nutrients. A key emphasis is placed on understanding the binding dynamics and reaction mechanisms

of phosphorus (P)-containing compounds with soil constituents, particularly Fe- and Al-oxyhydroxides. We explore the effects of soil surface composition, spatial configuration, soil solution, ionic strength, and solution pH. Additionally, we strive to enhance phosphorus availability for plants and contribute to developing new, smart phosphorus fertilizers.

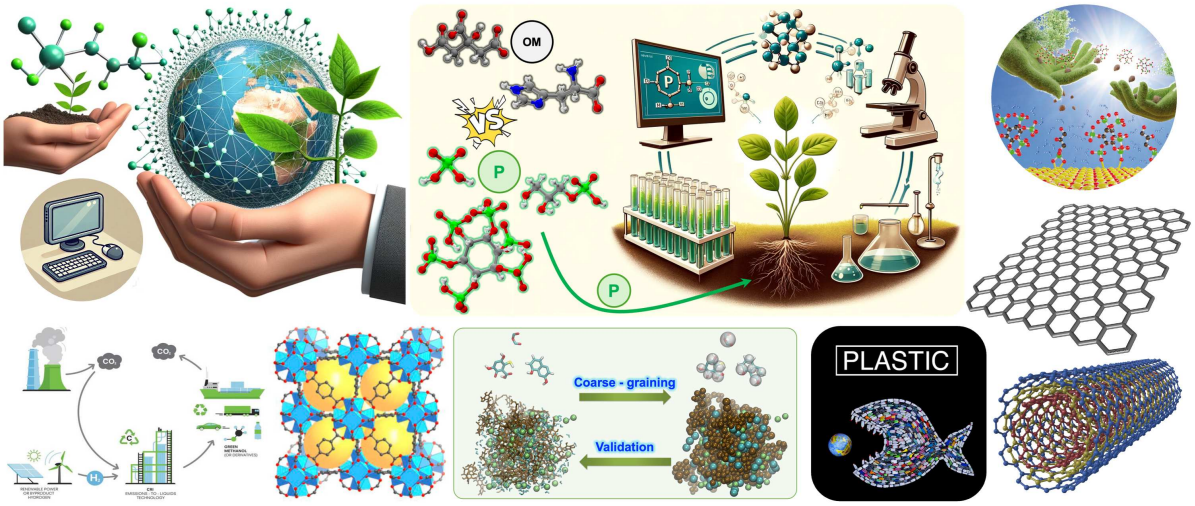


Figure 1.1: Graphical illustration of our research emphasis on leveraging computational chemistry to address critical environmental and sustainability challenges. This includes enhancing phosphorus mobility and availability to plants, understanding the fate of organic contaminants like micro- and nano-plastics and their capture using 2D materials, and converting CO_2 into valuable organic compounds.

In the context of P research, we have participated in the initiation of the collaborative multidisciplinary project "InnoSoilPhos", funded by the Federal Ministry of Education and Research (BMBF), which aims to find innovative solutions for sustainable soil P management. This project addresses the challenges posed by the limited P resource of rock phosphate and its implications for agriculture, water bodies, and ecological sustainability. The project involves seven institutions in Germany and operates on four scales: atomic and molecular, plot-to-field, field-to-catchment, and societal. Additionally, we are engaged in the second phase of the DFG SPP 1685 priority program "Ecosystem nutrition: Forest strategies for limited P resources", which aims to understand the processes controlling phosphorus acquisition and cycling. This program focuses on maintaining forest ecosystem stability under climate change, high nitrogen loading, and increased forest biomass export (Lang et al., 2016). This program includes over 20 research projects from numerous institutions in Germany and Switzerland, exploring various aspects of

the phosphorus issue, such as the bioaccessibility and bioavailability of subsoil phosphorus, the impact of nutrient inputs on organic phosphorus dynamics, and the mechanisms of phosphorus leaching and mobilization in forest ecosystems. Furthermore, we are part of the Leibniz Science-Campus Rostock "Phosphorus Research", which seeks to improve the efficient and sustainable use of P resources (Kruse et al., 2015; Edixhoven et al., 2013; Obersteiner et al., 2013).

An in-depth molecular-level understanding of P-related processes necessitates quantum chemical modeling approaches to complement experimental work (Ahmed et al., 2023; Osman et al., 2023; Ahmed et al., 2024). Within the InnoSoilPhos project and the SPP 1685 priority program, we focused on quantum chemical modeling of P in the soil matrix. Our objectives included developing computational strategies for describing P-related processes at mineral surfaces, identifying binding motifs and energies of different phosphates, and understanding the influence of organic compounds on P-mineral surface interactions. Additionally, we investigated interactions of glyphosate (GLP), a widely used herbicide linked to cancer, with soil constituents, examining the effects of metal ions and peptides on GLP detection in complex matrices. This comprehensive approach aims to enhance understanding of critical environmental processes and contribute to more effective and sustainable management practices.

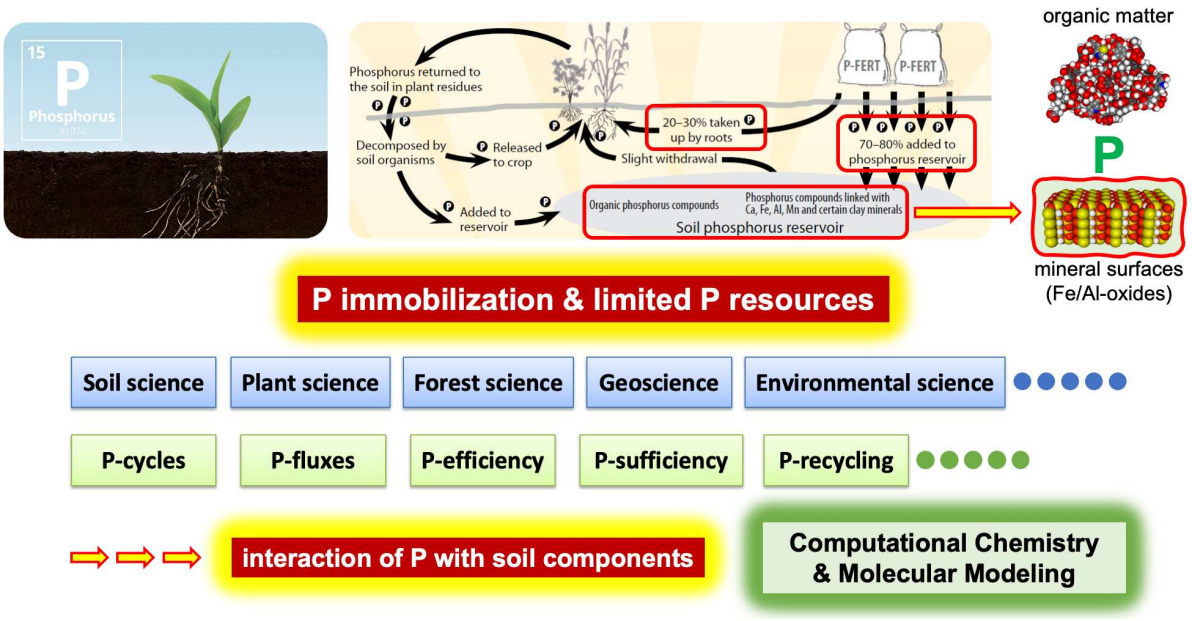


Figure 1.2: Graphical depiction illustrating the origins of the P problem (immobilization in soil and P-fixing minerals, and limited P resources) and the collaborative multidisciplinary efforts aimed at resolving it.

My habilitation thesis provides a concise overview of the P binding problem and the application of state-of-the-art molecular modeling techniques to address it. The focus is on recent advancements in understanding how phosphates bind to key soil constituents responsible for P-fixation, particularly Fe- and Al-oxyhydroxide mineral surfaces, with an emphasis on goethite and diaspore. The thesis highlights significant findings from atomistic simulations and advanced spectroscopic, microscopic, and molecular techniques that have enhanced our knowledge of P immobilization and cycling in soil systems. It demonstrates how molecular simulations complement and deepen the understanding of experimental results. After a general overview of the P issue and related experimental efforts in Chapter 1, the thesis introduces computational chemistry and computational efforts in Chapter 2, and discusses different model systems and molecular simulations in Chapter 3. Key topics include the effect of pH on P binding, IR spectra of phosphate-goethite complexes, complexation versus precipitation, high surface loading, organic phosphates, the impact of surface central metal ions, the influence of redox potential on P binding, organic matter competition, smart fertilizers, and the environmental impact of GLP. Eventually, the thesis presents a summary and conclusions in Chapter 4. Finally, the thesis showcases how advancements in molecular modeling and experimental techniques have provided a comprehensive understanding of the P binding problem, paving the way for more effective strategies in soil management and P-fertilizer development.

1.2 P Problem and Experimental Efforts

Soil is a crucial source of life on Earth, providing fiber, food, and fuel. It acts as a water filter, a growing medium, and a habitat for billions of organisms, while also supplying most antibiotics. The composition and quantity of soil constituents are key factors in controlling many critical environmental issues, including P availability and soil fertility (Lehmann et al., 2020). P is essential for all life forms, and its efficient use in fertilizers is crucial for meeting the food demands of a rapidly growing human population (Maciá, 2005). Phosphate rock is the primary source of P fertilizers, but a peak in phosphate rock production is projected for this century, raising concerns about future P scarcity and its potential impact on global food security (Cordell et al., 2009; Jupp et al., 2021).

To address the projected peak P scenario, substantial research efforts have been initiated to enhance the efficient and sustainable use of P resources, including its recovery and recycling (Cordell and White, 2011; Kruse et al., 2015; Jupp et al., 2021; Alam et al., 2021; Keyikoglu et al., 2022). The main objective is to understand the processes controlling P acquisition by arable crops, P cycling, and P inputs into waterways. These

processes are influenced by phosphate speciation. A meta-analysis of soil ^{31}P-NMR data by Menezes-Blackburn et al. (2018), based on 258 soil samples, revealed that inorganic P (OP) constitutes $57 \pm 7\%$ of total P stocks in soil, while organic P (monoester and diester) accounts for $33 \pm 2\%$ and $4 \pm 0\%$, respectively. Furthermore, the efficiency of P immobilization is largely controlled by its interactions with various soil constituents, including SOM (Gros et al., 2017), free metal ions (Gros et al., 2019; Urrutia et al., 2013), and soil minerals (Ahmed et al., 2023; Liu et al., 2022).

Among soil constituents, mineral surfaces such as Fe- and Al-(oxyhydr)oxides, calcium phosphates, silicates, and carbonates exhibit a strong affinity to bind phosphates (Liu et al., 2012; Okano et al., 2013; Minamisawa et al., 2022). In particular, Fe- and Al-(oxyhydr)oxides act as the main phosphate adsorbents in soils (Borggaard, 2001; Borggaard et al., 2004; Elzinga and Sparks, 2007; Zhong et al., 2007). The strong binding of phosphates to these oxides is due to the formation of stable inner-sphere surface complexes, where covalent bonds form between phosphates and oxide surfaces (Luengo et al., 2006; Kruse et al., 2015; Wang et al., 2016; Ahmed et al., 2023). Among these oxyhydroxides, goethite (α-FeOOH) is the most prevalent and reactive ferric iron (Fe(III)) form, making it crucial for P fixation in soils (Barrow, 1983; Arai and Sparks, 2001; Cornell and Schwertmann, 2003; Chitrakar et al., 2006; Arai and Sparks, 2007; Tsao et al., 2011). Goethite's high thermodynamic stability and widespread occurrence in both oxic and anoxic environments drive its significant susceptibility to P (Ofoegbu, 2019; Schwertmann, 1993; Cornell and Schwertmann, 2003). Consequently, considerable research efforts have been directed towards understanding the mechanisms underlying phosphate adsorption and binding to goethite surfaces, as will be introduced below.

The adsorption of phosphate on Fe- and Al-(oxyhydr)oxide surfaces is influenced by several factors, including solution pH, background electrolytes, initial P concentration, molecular structure of the phosphate and adsorbent, surface crystallinity and morphology, specific surface area (SSA), point of zero charge (PZC), and the presence of competing anions (Strauss et al., 1997b,a; Geelhoed et al., 1997, 1998; Gao and Mucci, 2001; Hongshao and Stanforth, 2001; Guppy et al., 2005; Yan et al., 2014; Ognalaga et al., 1994; Ruttenberg and Sulak, 2011; Gypser et al., 2018). For detailed insights, refer to Ahmed et al. (2023).

Solution pH plays a significant role in controlling phosphate adsorption on goethite (Arroyave et al., 2018; Boukemara et al., 2016; Chitrakar et al., 2006; Li and Stanforth, 2000; Rietra et al., 2001; Ahmed et al., 2020). This is because pH affects the surface charge and saturation degree of pedogenic oxides, which are highly phosphate-affine soil minerals, as well as the protonation state of phosphate species (Antelo et al., 2005;

Gao and Mucci, 2001). Most studies reported a decrease in adsorption capacity with increasing solution pH. At higher pH levels, repulsion between phosphate anions and the negatively charged surface sites increases, along with competition between phosphate anions and hydroxyl (OH^-) groups. Consequently, goethite exhibits high phosphate adsorption at pH levels below the PZC, where the surface has a positive net charge. As pH increases above the PZC, the surface charge becomes less positive and eventually negative, hindering further adsorption (Bowden et al., 1980). Additionally, Hiemstra and Van Riemsdijk (1996) and Strauss et al. (1997a) demonstrated that phosphate adsorption on goethite is accompanied by proton (H^+) adsorption.

The impact of background electrolyte nature and ionic strength on phosphate adsorption is well-documented in studies by Barrow et al. (1980), Rietra et al. (2001), Antelo et al. (2005), and Ahmed et al. (2020). Barrow et al. (1980) found that increasing NaCl concentration decreased phosphate adsorption at pH < 4 due to a reduction in the positive surface potential. Conversely, at pH > 4, higher NaCl concentrations led to stronger phosphate adsorption by making the surface potential less negative. This effect is more pronounced with higher phosphate concentrations (Geelhoed et al., 1997), as confirmed by Rietra et al. (2001) and Antelo et al. (2005). Recently, Ahmed et al. (2020) showed that using 0.01 M $CaCl_2$ significantly increased phosphate adsorption at pH 6, while 0.01 M KCl resulted in almost constant adsorption. This behavior is consistent with Arai and Sparks (2001), who observed a slight increase in P adsorption with higher NaCl ionic strength at pH > 7.5, but no significant change at pH 4-7.5. For $CaCl_2$, Barrow (1972) demonstrated that Ca^{2+} ions increase phosphate adsorption due to the electric potential developed at the soil surface, influenced by electrolyte concentration. Barrow and Shaw (1979) noted that changes in activity coefficient and concentration contribute to the complexity of the adsorption process. These findings suggest that electrolytes like Ca^{2+} can significantly impact phosphate adsorption by altering charge distribution and adsorption activity.

Initial P concentration plays a crucial role in adsorption, as demonstrated by Geelhoed et al. (1997), who showed varying P concentrations lead to different adsorption enhancements. This effect is evident across a broad range of conditions, including initial P concentrations (0.005-500 mM), SSA (17.2-132 m^2g^{-1}), PZC (6.3-9.7), background electrolytes (0.00-1.0 M), and adsorption times (0-168 h). Reported phosphate adsorption capacities range from 0.07 to 2.8 μmol P m^{-2}, with Li and Stanforth (2000) noting the highest values (5.6-46.1 μmol P m^{-2}) due to high initial P concentrations and surface phosphate precipitates. Excluding precipitates, capacities drop to 1.81-4.1 μmol P m^{-2}. High capacities were also observed by Chitrakar et al. (2006) (794.1 μmol P g^{-1}),

Boukemara et al. (2016) (5.6 μmol P m^{-2}), and Ganta et al. (2021) (7.64 μmol P m^{-2}).

Studies by Yan et al. (2014), Ganta et al. (2021), and Amadou et al. (2022) examined the adsorption behavior of inorganic and organic phosphates (orthophosphate (OP), glycerolphosphate (GP), and inositolhexaphosphate (IHP)) on well-defined mineral surfaces such as goethite, gibbsite, boehmite, α-Al_2O_3, and amorphous $Al(OH)_3$. Results indicated that adsorption affinity varied by mineral surface and phosphate type. GP showed the lowest affinity, while IHP had the highest on goethite and amorphous $Al(OH)_3$, with the order reversed on gibbsite and boehmite. For α-Al_2O_3, IHP had the lowest affinity, OP the highest, and GP intermediate. These findings highlight the influence of phosphate molecular structure and mineral surface type and crystallinity on adsorption. Yan et al. (2014) observed that P adsorption capacities (in μmol P g^{-1}) increased with decreasing mineral crystallinity, in the order of α-Al_2O_3 < boehmite < amorphous $Al(OH)_3$. This trend is supported by Wang et al. (2015b) and Gypser et al. (2018), emphasizing the significant impact of crystallinity and SSA on P adsorption.

Organic acids have a strong affinity for adsorption onto Fe- and Al-hydroxide surfaces, enabling them to compete with phosphates and increase phosphate mobility, potentially dissolving Al- and Fe-hydroxide surfaces. Johnson and Loeppert (2006) found that organic acids release adsorbed P from ferrihydrite, with efficiency increasing from oxalate = malonate = succinate < tartrate < malate < citrate. Geelhoed et al. (1998) observed that phosphate decreased citrate adsorption on goethite over a wide pH range, while citrate adsorption decreased phosphate adsorption only at low pH. Wang et al. (2015a,b, 2016) reported that humic acids significantly decrease P adsorption on goethite, hematite, and ferrihydrite. In a long-term desorption study, Gypser et al. (2019) found that P desorption from Fe- and Al-hydroxides increased in the order: $CaCl_2$ < $CaSO_4$ < humic acid < citric acid. Further, Gypser et al. (2021) showed that goethite exhibited the highest desorption, followed by gibbsite and ferrihydrite, when using organic and inorganic competitors. Despite significant research efforts, the specific mechanism for these competition reactions remains unclear.

At the molecular scale, Fourier-transform infrared (FTIR) spectroscopy has been widely used to investigate the binding motifs of adsorbed phosphate species on Fe-oxide surfaces (Chapman and Thirlwell, 1964; Tejedor-Tejedor and Anderson, 1990; Persson et al., 1996; Arai and Sparks, 2001; Lefèvre, 2004; Ahmed et al., 2019). Characteristic mid-infrared bands from symmetric and anti-symmetric P–O(H) vibrations can be detected based on the phosphate ion's symmetry, even at low concentrations. The IR spectrum can hint at phosphate binding motifs and mechanisms at mineral surfaces. However, difficulties such as different surface planes, multiple binding motifs, and vary-

ing experimental conditions can complicate FTIR assignments (Villalobos et al., 2009; Kubicki et al., 2012). For instance, Tejedor-Tejedor and Anderson (1990) assigned P binding motifs by P-O vibrational band positions, while Arai and Sparks (2001) focused on the number of P-O bands. Others, like Persson et al. (1996), identified monodentate binding motifs with different protonation states depending on pH.

Recently, Arroyave et al. (2018) used infrared surface titration (IRST) to explore phosphate surface speciation on goethite under various conditions. Advanced spectroscopic techniques such as P K-edge X-ray absorption near-edge structure (XANES) spectroscopy, extended X-ray absorption fine structure (EXAFS) spectroscopy, and liquid ^{31}P nuclear magnetic resonance (NMR) spectroscopy have also been used to study inorganic and organic P species adsorbed at mineral surfaces and in soil (Turner et al., 2003; Dougherty et al., 2005; McLaren et al., 2015; McLaren et al., 2020; Kruse and Leinweber, 2008; Andersson et al., 2016). ^{31}P NMR can differentiate between surface-adsorbed phosphate in inner-sphere complexes, phosphate in surface Al-phosphate precipitates, and precipitated phosphate from residual solution (Johnson et al., 2002; Kim and Kirkpatrick, 2004; Van Emmerik et al., 2007; Li et al., 2013). XANES and EXAFS are powerful tools for distinguishing between P adsorption and surface precipitation, and for analyzing bonding configurations at mineral/water interfaces, although EXAFS is limited in detecting protonation environment changes (Hesterberg et al., 1999; Khare et al., 2005, 2007; Abdala et al., 2015). These techniques have significantly contributed to identifying binding motifs of adsorbed phosphate species on Fe- and Al-(oxyhydr)oxide surfaces, as shown in studies by Parfitt and Atkinson (1976); Rahnemaie et al. (2007); Li et al. (2010); Kim et al. (2011); Krumina et al. (2016); Ahmed et al. (2019). However, further research is necessary to deepen our understanding of these complex processes.

To sum up this brief and selective overview, it should be noted that considerable experimental efforts do not always lead to an unequivocal understanding of the phosphate adsorption process. Given the multitude of influencing factors, it is not surprising that the exact nature of phosphate–goethite complexes remains debated. Computational chemistry can provide a complementary description and in-depth understanding of experimental findings. This thesis will demonstrate how computational chemistry systematically investigates possible molecular mechanisms and binding motifs for phosphate binding with soil mineral surfaces and other reactive soil constituents under various experimental conditions.

2 Computational Chemistry and Computational Efforts

2.1 Computational Chemistry

Computational chemistry (**CC**), grounded in the fundamental laws of Physics, offers insights into molecular geometries, thermodynamics, chemical reaction kinetics, molecular dynamics, and spectroscopic data. It can simulate pure phases, solutions, and interfaces, making it indispensable in fields like chemistry, biochemistry, chemical physics, and material science. Despite its broad applicability, environmental chemistry, particularly soil biogeochemical processes, has not been extensively explored due to the complexity of soil as a heterogeneous multi-component material and habitat. Developing molecular models and simulation techniques for this field requires a multi-disciplinary effort (Ahmed et al., 2012, 2014, 2015, 2023, 2024). **CC** holds promise for understanding P-related processes in soil at a molecular level, including phosphate sorption/desorption on mineral surfaces (Kwon and Kubicki, 2004). It can explore the effects of soil composition, spatial configuration, soil solution, ionic strength, and pH (Kubicki, 2016), and calculate relevant spectroscopic data (IR, UV, NMR, XPS, and XANES) for phosphate binding characterization (Cramer, 2004; Jensen, 2017).

My habilitation research encompassed a broad range of **CC** theories, each varying in accuracy and computational efficiency, from molecular mechanics (MM) to quantum mechanics (QM) through QM/MM hybrid approaches (Cramer, 2004; Jensen, 2017; Kubicki, 2016; Koch and Holthausen, 2008; Kmiecik et al., 2016; Senn and Thiel, 2009; Stewart, 2007; Elstner et al., 1998; Ahmed et al., 2023; Dettmann et al., 2024). At the simplest level, MM describes the energy of molecular systems using empirical potentials for bonded and non-bonded particles, involving three main resolution levels: all-atom, united-atom, and coarse-grained representations. In all-atom representation, each atom is treated as a particle (point charge) with implicit electrons. The united-atom representation groups atoms (e.g., CH_3) into a single particle or pseudo-atom, while the coarse-grained representation combines groups of atoms, functional groups, or molecules

into beads. Bonded interactions cover bonds, angles, and dihedral angles, whereas non-bonded interactions are primarily described by electrostatic and van der Waals potentials. A complete set of empirical potentials and parameters for a molecular system is known as a force field. MM methods can simulate millions of atoms at a moderate computational cost but cannot typically describe bond formation and dissociation.

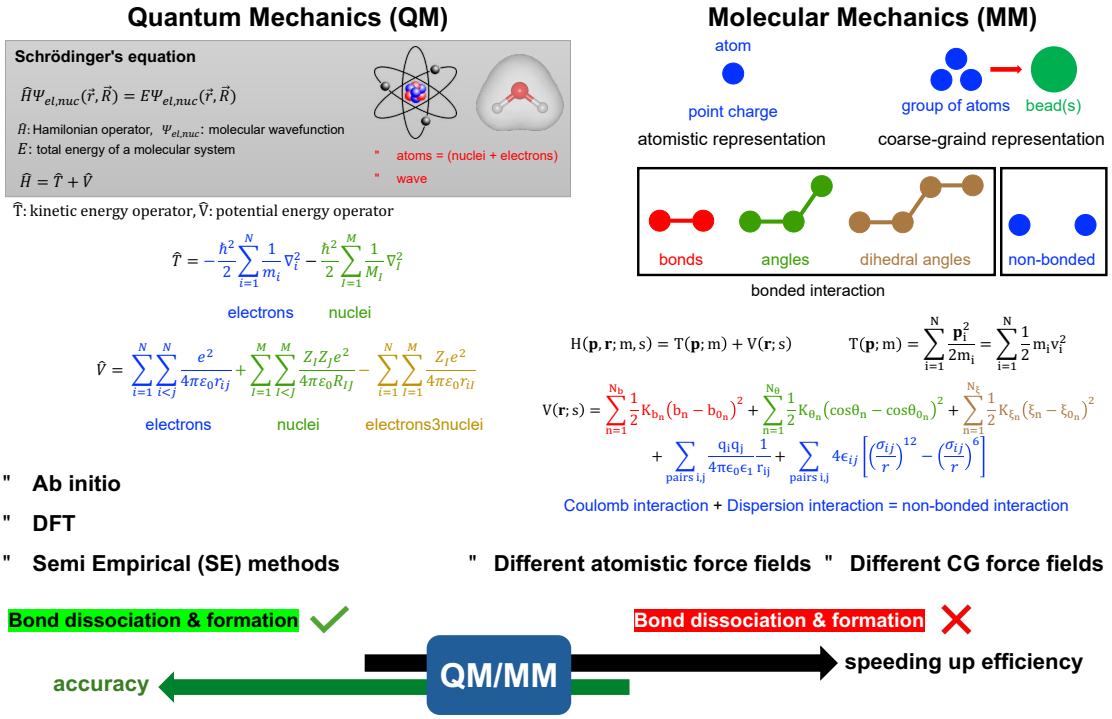


Figure 2.1: Graphical illustration of the representations of three major **CC** methods.

Alternatively, QM describes chemical bonds by explicitly treating nuclei and electrons through the Schrödinger equation, classified into ab initio, density functional theory (DFT), and semi-empirical (SE) methods (Cramer, 2004). Ab initio methods are computationally expensive and unsuitable for complex P-related problems beyond simple models. SE methods, using approximations and empirical parameters, are less costly and applicable to P-related problems involving a few hundred atoms. DFT, the most prominent method, balances efficiency and accuracy by calculating electron density through Kohn-Sham molecular orbitals. The quality of DFT results depends on the exchange-correlation functional used, with Becke, three-parameter, Lee–Yang–Parr (B3LYP) (Lee et al., 1988) and Perdew-Burke-Ernzerhof (PBE) (Perdew et al., 1996) being common choices for simulating phosphate-related processes. The basis set chosen to represent the electronic wave function also affects the simulation quality. Gaussian atom-centered and periodic plane-wave basis functions describe molecules and extended

systems (e.g., surfaces and crystals), respectively. Effective core potentials (ECP) or pseudo-potentials often simplify core orbital descriptions, focusing on valence orbitals (e.g., Goedecker–Teter–Hutter (GTH) pseudo-potentials used extensively in our work). Each basis set type has its advantages and limitations, and the Gaussian and plane-waves (GPW) method efficiently combines both (Lippert et al., 1997; VandeVondele et al., 2005; Kühne et al., 2020). Long-range van der Waals dispersion interactions, not covered by standard functionals, can be included through empirical corrections like GD3 (Grimme et al., 2011).

Despite DFT's advancements, practical calculations for larger systems (over a few hundred atoms) remain unfeasible. Hence, hybrid QM/MM methods combine QM (mostly DFT) for the reactive part and MM for the rest of the molecular system, e.g., the solvent. QM/MM schemes differ in their QM and MM linkage methods (e.g., electrostatic embedding used extensively in our work) as reviewed by Senn and Thiel (2009).

Regardless of the **CC** level of theory, various techniques can be applied to obtain a stable geometry or the so-called optimized structure, representing an energetic minimum on the potential energy surface. Most algorithms provide access only to local optimization, converging to the nearest local minimum. Normal mode coordinates can be introduced to obtain IR vibrational spectra. Statistical properties, considering the random motion of nuclei due to finite temperature, can be obtained using molecular dynamics (MD) (Marx and Hutter, 2009). By solving Newton's equations, a trajectory is generated, sampling the thermal ensemble at a given temperature, and the trajectory data can be used to obtain average geometries.

A simplification arises in implicit models, where solvent molecules are described as a classical dielectric medium polarized by the electron density in the reactive quantum region. One popular implicit solvation model is the conductor-like polarizable continuum model (CPCM) (Barone and Cossi, 1998; Cossi et al., 2003). Another important aspect is mimicking macroscopic systems like surfaces, where either finite clusters or periodic treatments can be used. For modeling surface-related processes in crystalline or amorphous materials, periodic boundary conditions (PBC) are standard. A well-defined unit cell is repeated in two dimensions to construct the surface, while slab models are used for interfacial processes, involving periodicity perpendicular to the surface.

For a comprehensive conclusion on the advantages and limitations of various **CC** techniques, refer to Ahmed et al. (2023). This review article highlights the strengths and weaknesses of different theories and methods, comparing stationary calculations versus MD simulations, cluster versus periodic calculations, vacuum versus solvation methods, and hybrid Gaussian/plane-wave basis sets versus individual ones.

2.2 Computational Efforts

CC, especially DFT has been applied in P research to understand phosphate binding to mineral surfaces. In an early investigation, Kubicki and co-workers studied phosphate binding to goethite and its pH dependence using an embedded-molecular-cluster approach (Kwon and Kubicki, 2004; Kubicki et al., 2007). Goethite was modeled as a small cluster with iron octahedra saturated with water molecules and OH^- groups, with a few explicit water molecules to mimic the surrounding solvent. By comparing experimental and calculated IR vibrational frequencies, they suggested that a diprotonated bidentate (**B**) complex forms at pH 4-6, a deprotonated **B** or monoprotonated monodentate (**M**) complex at pH 7.5-7.9, and a deprotonated **M** complex at pH 12.8. Calculated reaction energies indicated the monoprotonated **M** complex as the most abundant across the modeled pH range, with the diprotonated **B** complex favored at low pH (4-6).

Further studies explored the effects of surface charge distributions, phosphate speciation, competitive water, pH, and hydrogen bonds (HBs) on phosphate binding to the same small cluster (Rahnemaie et al., 2007; Acelas et al., 2013). Rahnemaie et al. (2007) found a deprotonated **B** complex more favorable at low P loading, while a monoprotonated **M** complex was more favorable at low pH and high P loading. In contrast, Acelas et al. (2013) found a mix of diprotonated **B** and **M** complexes at pH 4.2-5.7, and a mix of monoprotonated **B** and **M** complexes at pH 7.9.

Similar studies have investigated phosphate binding to boehmite (γ-AlOOH) (Li et al., 2010), corundum (α-Al_2O_3) (Li et al., 2013), γ-Al_2O_3 (Ren et al., 2012), aqueous uranium complexes (Kubicki et al., 2009), and ferrihydrite (Khare et al., 2007). Li et al. (2010) observed a mix of deprotonated and monoprotonated **B** complexes, with the deprotonated form more abundant. Li et al. (2013) found a mix of deprotonated and monoprotonated **B** complexes at pH 5, with the deprotonated **B** complex dominant at pH 9. These observations were made using cluster calculations, which may not be the most accurate approach for describing extended or periodic systems.

Kubicki et al. (2012) extended their investigations of phosphate-surface binding motifs by performing periodic DFT calculations, considering different goethite surface planes. They carried out stationary calculations and MD simulations for HPO_4^{2-} species and calculated IR vibrational frequencies for extracted molecular clusters to assign phosphate binding motifs. Their results predicted the formation of **M** complexes on the 001, 210, 101, and 100 surface planes, and **B** complexes on the 010, 101, and 100 surface planes. Similarly, Belelli et al. (2014) utilized periodic DFT calculations to investigate phosphate complexes on pure and Al-rich goethite surfaces. They examined bidentate binuclear

(**B**), bidentate mononuclear (**BM**), monodentate mononuclear (**M**), and monodentate binuclear (**MB**) complexes, including their monoprotonated and nonprotonated species, on the 110 planes of both pure and Al-rich goethite surfaces. Their findings indicated the potential formation of all examined complexes on both surface types. Analysis of calculated and experimental vibrational frequencies suggested a prevalence of protonated **BM** complexes at pH 3.1, **B** complexes within the pH range of 4.2-7.9, and protonated **B** complexes at pH 12.8.

Additionally, Weng et al. (2020) performed short MD simulations (3 ps) using periodic DFT calculations to study **M**, **B** (chemisorption), and outer-sphere (physisorption) configurations on the 100 goethite surface plane. They found that the chemisorbed **M** configuration was more abundant than the physisorbed configuration, accounting for 83% and 17% of the total adsorbed species, respectively, with a high binding/adsorption energy of -2.13 eV for the physisorbed configuration. These reported energies were based on the Maxwell-Boltzmann distribution weighting.

In a series of contributions, Ahmed et al. investigated the binding mechanisms of inorganic and organic P compounds to soil constituents, including mineral surfaces, free metal ions, and SOM (Gros et al., 2017, 2019; Ahmed et al., 2018a,b, 2019, 2020; Ganta et al., 2019, 2020b,a, 2021; Shaheen et al., 2022; Ahmed et al., 2024; Luo et al., 2024; Ahmed et al., 2023; Osman et al., 2023). These studies thoroughly explored the effects of surface morphology, surface saturation, central metal ion exchange, metal ion valency, SOM composition, water, pH, and redox potential on P binding. For most of these investigations, we utilized periodic calculations with considerably larger simulation boxes, incorporating bigger phosphate-mineral-water molecular models with explicit solvation using a water density of 1 g.cm^{-3}. These simulations utilized MD based on either QM, QM/MM, or MM in combination with the hybrid Gaussian and plane-wave approach for QM calculations, and included long-range dispersion corrections. The detailed findings from these investigations will be presented in the main Chapter, 3.

For a comprehensive overview of the **CC** efforts to understand phosphate binding to Fe- and Al-surfaces and phosphate-metal-humic complexes, refer to Ahmed et al. (2023). This review compiles data from relevant literature studies investigating the binding motifs of adsorbed phosphates on Al- and Fe-mineral surfaces using various levels of theory and molecular simulation techniques, including works by Kwon and Kubicki (2004); Kubicki et al. (2007); Li et al. (2010); Kubicki et al. (2012); Acelas et al. (2013); Belelli et al. (2014); Weng et al. (2020); Ahmed et al. (2019, 2020); Ganta et al. (2019, 2020b,a, 2021); Shaheen et al. (2022).

3 Toward Squaring the Circle

3.1 Coping with the heterogeneity

The fate of P in soil is governed by multiscale biogeochemical processes that span molecular to macroscopic length and time scales. Soil, as a highly complex and heterogeneous medium, presents numerous challenges for P-binding, influenced by a variety of factors discussed in Chapters 1-2. While broader-scope **CC** investigations at the molecular level are still emerging, their link to mesoscale and larger scales remains to be fully established. Simplified atomistic and molecular modeling approaches are critical initial steps in understanding P's environmental fate at microscopic and macroscopic scales.

Molecular simulations based on atomistic models provide fundamental insights into related chemical reactions, binding mechanisms, and relevant binding motifs that are otherwise inaccessible. However, modeling phosphate binding in soil must address the inherent heterogeneity of the medium. We adopted a practical approach by breaking down the problem into well-defined soil constituents (e.g., SOM, metal ions, mineral surfaces) and focusing on key factors such as surface chemistry, morphology, saturation, metal ion type and valency, SOM composition, water, pH, and redox potential. Combining data from these focused studies can construct a comprehensive molecular picture of P binding in soil. Validation through experiments, particularly those targeting controlled samples, is critical to the success of this bottom-up modeling approach. For instance, a set of SOM models covering the most abundant functional groups (more than 30 representative molecular systems) has been developed and validated against high-resolution mass spectrometry and XANES data (Ahmed et al., 2012, 2014, 2015; Gros et al., 2017). In the context of P-binding, interactions with SOM, free metal ions, and mineral surfaces under various pH conditions have been modeled and validated against experimental data (Gros et al., 2017, 2019; Ahmed et al., 2018a,b, 2019, 2020, 2023, 2024; Ganta et al., 2019, 2020a,b, 2021; Shaheen et al., 2022).

The following sections provide an illustrative overview of various molecular modeling approaches related to P binding to soil constituents. Section 3.2.1 discusses the effects of key factors such as solution pH, crystal surface planes (including surface morphology

and surface saturation), binding motifs, and the influence of water on phosphate binding at two goethite surface planes. Section 3.2.2 explores simulations of IR spectra as a tool to assign phosphate-goethite binding motifs. Section 3.2.3 offers a brief overview of the distinction between complexation and precipitation. Sections 3.2.4 and 3.2.5 highlight the effects of high surface loading and organic phosphates on phosphate binding, respectively. Section 3.3 discusses adsorption at the diaspore surface and the impact of surface central ion replacement on the phosphate binding process. Section 3.4 presents the combined effects of redox potential and pH on the binding process of phosphate with metal ions and SOM. Section 3.5 examines the presence of organic matter (OM) and its competition with different phosphates, including how this mobilizes phosphate. Section 3.6 introduces the concept and preliminary results regarding the design of smart fertilizers. Finally, Section 3.7 provides an overview of the environmental impact of GLP, including its interaction with soil constituents, its presence in water, and detection challenges.

Technically, PBC calculations were performed to simulate phosphate binding at mineral surfaces with explicit water in Sections 3.2.1-3.2.5, 3.3, and 3.5-3.6. In Sections 3.2.1-3.2.4, DFT calculations for various phosphate-goethite-water models were conducted at the GPW/PBE/GTH/GD3 level using the CP2K software package (VandeVondele et al., 2005; Hutter et al., 2014; Lippert et al., 1997; Perdew et al., 1996; Krack, 2005; VandeVondele and Hutter, 2007; Grimme et al., 2011; Kühne et al., 2020). Sections 3.2.1-3.2.4 focus on inorganic phosphate, while Sections 3.2.5 and 3.3 address larger organic phosphates, involving molecular models, each with over 1200 atoms. Therefore, hybrid QM/MM-based MD simulations were applied (Laino et al., 2006) in Sections 3.2.5 and 3.3, with the QM region at the same theory level as in Sections 3.2.1-3.2.4, and the MM region using CLAYFF and CHARMM force fields (Cygan et al., 2004; Vanommeslaeghe et al., 2009). In Section 3.4, cluster calculations with implicit solvent treatment were performed to investigate phosphate binding to metal ions and OM at the B3LYP/GD3/CPCM level using the Gaussian software package (Hehre et al., 1972; Lee et al., 1988; Cossi et al., 2003; Grimme et al., 2011; Frisch et al., 2016). In Sections 3.5-3.6, MM-based MD simulations were applied using CLAYFF and CHARMM force fields for molecular models, each with over 20,000 atoms (Cygan et al., 2004; Vanommeslaeghe et al., 2009). In Section 3.7, GLP interactions with free metal ions and SOM used the same cluster calculations as in Section 3.4, while GLP-goethite interactions employed DFT-based MD simulations at the same DFT level as the phosphate-mineral-water models in Sections 3.2-3.3. For more details on the molecular modeling approaches and computational setup in Chapter 3, refer to Gros et al. (2017, 2019); Ahmed et al. (2018a,b, 2019, 2020, 2023, 2024); Ganta et al. (2019, 2021); Shaheen et al. (2022).

3.2 P Binding at the Goethite-Water Interface

3.2.1 Binding Mechanism and Relevant Effects

To investigate the effects of solution pH, crystal surface planes (surface morphology and surface saturation), binding motifs, and water on phosphate adsorption at mineral surfaces, molecular modeling at the goethite-water interface was employed (Ahmed et al., 2020). Different models were created for six phosphate species (H_3PO_4, KH_2PO_4, K_2HPO_4, K_3PO_4, K_2HPO_4 + 10 KOH, and K_3PO_4 + 10 KOH), each adsorbed on 010 or 100 goethite surface planes. Water density was set at 1 g.cm^{-3} to simulate the adsorption medium, as shown in Fig. 3.1. The stability of the 010-surface (Xiu et al., 2016; Guo and Barnard, 2011) and the prevalence of the 100-surface (Rakovan et al., 1999; Cornell and Schwertmann, 2003; Paul et al., 2007; Kubicki et al., 2008, 2017) motivated this focus. These surfaces present different coordination environments for Fe atoms, facilitating the exploration of various binding motifs, illustrated in Fig. 3.1b and 3.1d. For each phosphate species, two models were constructed: monodentate (**M**) and bidentate (**B**), as depicted in Fig. 3.1f-h. This resulted in 24 phosphate-goethite-water models, with 6 **M** and 6 **B** motifs per surface plane. Both overall (phosphate-goethite-water) and individual interactions (phosphate-goethite, phosphate-water, goethite-water) were analyzed. For instance, the interaction energy (E_{int}) for the complexation reaction, phosphate (A) + goethite surface (B) $\rightarrow$ phosphate-goethite (A-B) complex, was calculated as follows:

$$E_{int} = E_{A-B\,complex} - (E_A + E_B) \tag{3.1}$$

where $E_{A-B\,complex}$, E_A, and E_B are the total electronic energies of the phosphate-goethite complex, phosphate, and goethite surface, respectively. The basis set superposition error (BSSE) was corrected using the counterpoise method (Boys and Bernardi, 1970).

For the 010-goethite surface plane, simulations indicate that the **M** binding motif is stable and predominant at extremely acidic and alkaline conditions (with H_3PO_4 and excess OH^-, respectively), as shown in Fig. 3.2. In intermediate pH ranges, without excess OH^-, the **B** binding motif becomes more stable. As pH increases from $H_2PO_4^-$ to PO_4^{3-}, the stability of both **M** and **B** phosphate complexes also increases. However, the presence of OH^- groups decreases the stability of these binding motifs, especially for HPO_4^{2-} and PO_4^{3-}. A similar trend is observed on the 100-goethite surface plane, aligning with experimental findings of decreased phosphate adsorption at high pH.

The simulations suggest that binding strength at the goethite surface follows the order: water < phosphate < OH^-. Thus, phosphate can replace water molecules at the goethite

surface, but OH^- can displace both phosphate and water, leading to reduced adsorption at high pH.

At high pH, the competition between phosphate and OH^- for interactions with the goethite surface results in a lower probability of **M** and **B** complex formation. This is due to the formation of more covalent bonds between OH^- groups and the goethite surface. To confirm the instability of these binding motifs, in particular the **B** motif, at high pH, short MD simulations (about 13 ps at 300 K) were performed for two **B** complexes (K_2HPO_4 and K_2HPO_4 + 10 KOH). The results showed that the **B** phosphate-goethite complex remained stable throughout the MD trajectory for K_2HPO_4 (see Fe–O distances in Fig. 3.3). In contrast, for K_2HPO_4 + 10 KOH, the **B** motif transformed into an **M** motif after about 2 ps due to the dissociation of one Fe–O bond (see Fig. 3.3).

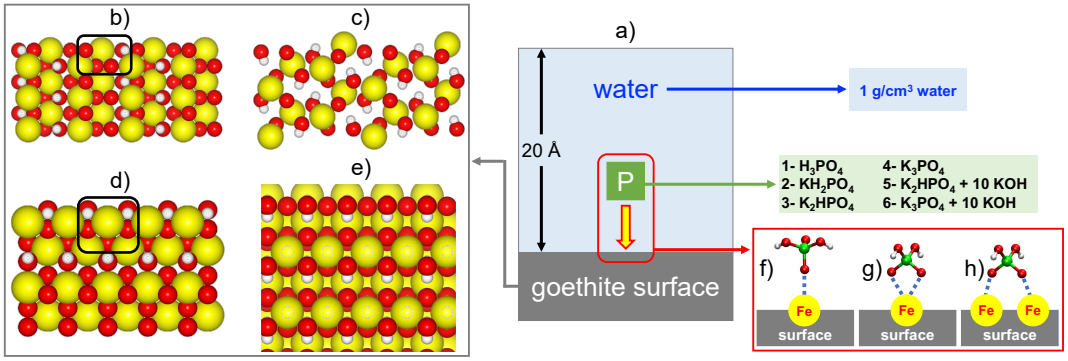


Figure 3.1: Molecular modeling of phosphate binding at the goethite-water interface. Schematic in a) shows the phosphate-goethite-water model. Side and top views of 010- (b, c) and 100-goethite surfaces (d, f) follow the Pnma space group, with different Fe atom coordination (4 for 010- and 5 for 100-goethite). Schematic binding motifs: **M** motif at 010- and 100-surfaces (f), (2O + 1Fe) **B** motif at 010-surface (g), and (2O + 2Fe) **B** motif at 100-surface (h). Atoms are H (white), O (red), P (green), and Fe (yellow). Simulations include phosphate species: H_3PO_4, KH_2PO_4, K_2HPO_4, K_3PO_4, K_2HPO_4 + 10 KOH, K_3PO_4 + 10 KOH. Binding motifs involve one covalent bond (**M**) or two covalent bonds (**B**) between phosphate O atoms and goethite Fe atoms.

Although phosphate binding at the 010- and 100-goethite surface planes shares similarities, significant differences arise due to surface morphology and saturation. The geometric configuration of the **B** binding motif differs notably between the surfaces. The shortest distance between adjacent surface Fe atoms is about 4.6 Å for the 010-surface and 3.0 Å for the 100-surface. Thus, the 010-surface favors forming the (2O + 1Fe) **B** motif (two phosphate O atoms and one surface Fe atom, see Fig. 3.1g), while the

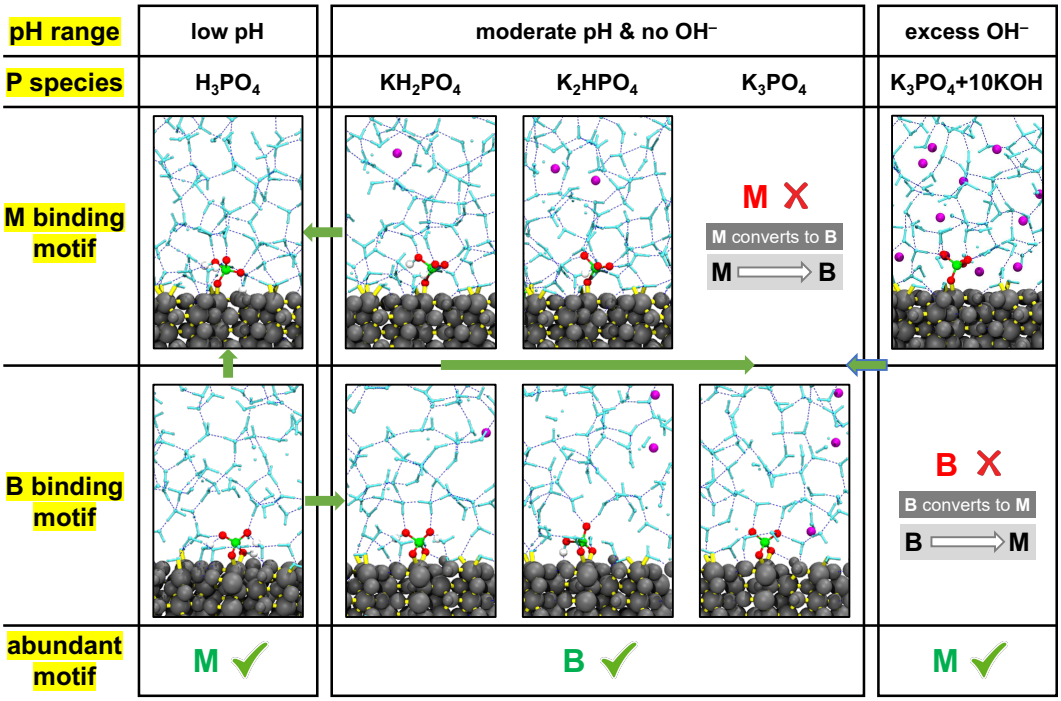


Figure 3.2: Geometry-optimized structures of phosphate-goethite-water complexes for different phosphate species at the 010 goethite surface. Each species shows two binding motifs: **M** and **B** (2O+1Fe). Goethite and water atoms are gray and cyan, respectively. Phosphate atoms are green (P), red (O), white (H), and purple (K). Covalent bonds with goethite atoms are yellow; HBs are blue. Arrows indicate increasing interaction energy and stability.

100-surface favors the (2O + 2Fe) **B** motif (two phosphate O atoms and two surface Fe atoms, see Fig. 3.1h). Moreover, **M** complexes, except for the H_3PO_4 case, are generally more stable on the 100-goethite surface compared to the 010-surface. This stability difference can be explained by surface saturation: each Fe atom on the 010-surface is coordinated by four O atoms, whereas on the 100-surface, each Fe atom is coordinated by five O atoms. Formation of the **M** binding motif results in Fe atoms achieving six coordination bonds on the 100-surface (full saturation) and five coordination bonds on the 010-surface. Thus, the **M** binding motif is more stable on the 100-goethite surface due to complete saturation.

Moreover, **B** complexes are stable and abundant on the 100-goethite surface in the presence of competing OH^- groups. At extremely low pH, both **M** and **B** complexes are more stable on the 010-goethite surface, with the **M** complex predominating on both surfaces. For the PO_4^{3-} case, the **B** complex is more stable on the 010-goethite surface

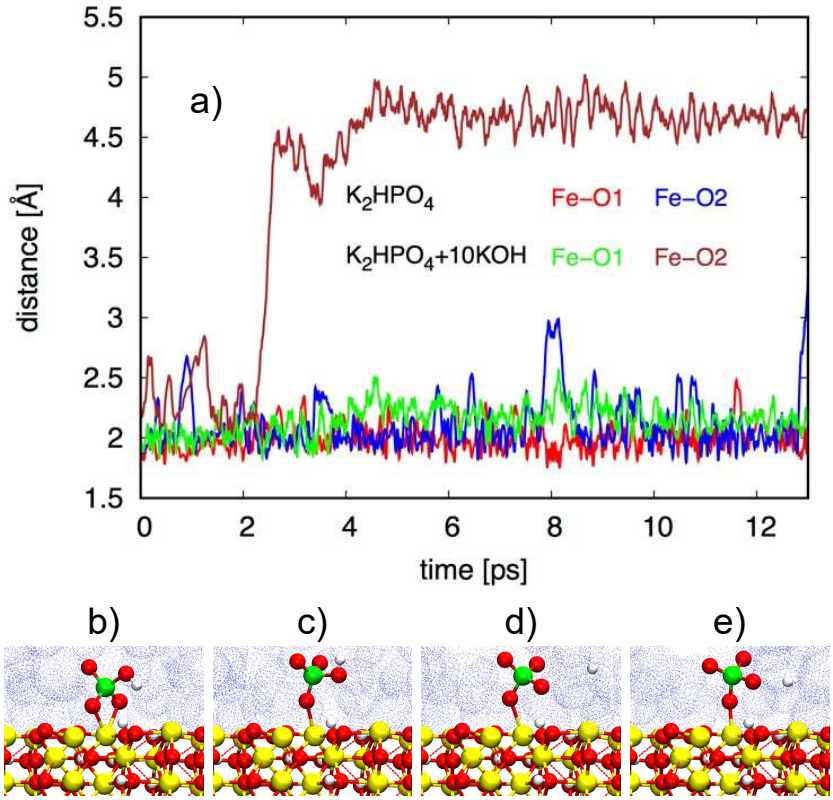


Figure 3.3: a) Intermolecular distances between phosphate O atoms (O1, O2) and surface Fe atom for the 2O+1Fe **B** motifs at the 010-goethite surface along the MD trajectory for K_2HPO_4 (red, blue) and K_2HPO_4 + 10 KOH (green, brown). In the latter, a **B** → **M** transformation occurs after 2 ps as the second Fe–O2 bond dissociates (brown). Snapshots (b–e) show this **B** → **M** transformation at high pH. Atoms: yellow (Fe), green (P), red (O), white (H), purple (K). Water molecules are represented as blue points. b–c) **B** → **M** transformation. c–d) Proton transfer from phosphate to water. d–e) Phosphate reorganization and proton re-approach.

than on the 100-goethite surface. These findings underscore the importance of surface plane type (saturation and morphology), binding motif (**M** or **B**), and pH in controlling phosphate binding. They can guide predictions of phosphate binding motifs on goethite surfaces under specific pH conditions and help identify the prevalent crystallographic planes if binding motifs are determined experimentally.

Water significantly influences phosphate adsorption at both goethite surface planes, forming covalent bonds with goethite Fe atoms and HBs with goethite O atoms. Some water molecules dissociate into protons (H^+) and hydroxyl (OH^-) groups, which then form covalent bonds with the surface atoms. This aligns with Hiemstra and Van Riems-

dijk (1996) and Strauss et al. (1997a), who observed proton adsorption at the goethite surface during phosphate adsorption. Protons are transferred from phosphate to water and the surface, making the solution more acidic.

The simulation results have been validated against pH-dependent phosphate adsorption experiments (Ahmed et al., 2020). These experiments revealed two stages: a slight increase in phosphate adsorption as the pH increased from 4 to 8, followed by a significant decrease from 8 to 12. Similar trends were observed in previous studies by Gao and Mucci (2001), Chitrakar et al. (2006), and Boukemara et al. (2016), aligning well with the molecular-level picture provided. This uncommon initial increase in adsorption occurs in the absence of competing ions when the goethite surface maintains a positive net charge below the PZC. When the surface charge changes significantly, a common decrease in adsorption is observed. This can be explained by considering the relevant phosphate species in sorption experiments: H_3PO_4 (pH 2), $H_2PO_4^-$ (pH 2.1–7.2), and HPO_4^{2-} (pH 7.2–12.4) on the 010-goethite surface, which show a decrease in phosphate adsorption with increasing pH. It is important to emphasize that such adsorption experiments are influenced by several factors, including SSA, surface coverage, purity, crystallinity of the goethite surface, and the presence of different crystal planes. Despite this complexity, both experimental results, particularly those without a buffer solution, and theoretical findings indicate that phosphate sorption decreases solution pH. This suggests that phosphate fertilization may contribute to soil acidification due to the acidity of phosphate fertilizers and the induced acidity from adsorbed phosphate on pedogenic oxides.

The outcome of this molecular modeling approach has been validated also by comparing bond distances with other calculations and experimental EXAFS data. The optimized geometries of phosphate-goethite complexes in the presence of water show Fe-P distances of 2.54-3.54 Å (Ahmed et al., 2020), consistent with predictions by Kwon and Kubicki (2004) (3.21-3.37 Å), Kubicki et al. (2012) (3.25-3.55 Å), and EXAFS measurements for colloidal phosphate-Fe complexes (3.05-3.39 Å) (Rose et al., 1997) and vivianite (3.19-3.43 Å) (Rose et al., 1996). The calculated Fe-P distances for the **M** binding motif at the 010-surface (3.02-3.41 Å), the **M** motif at the 100-surface (3.39-3.50 Å), and the **B** motif at the 100-surface (3.15-3.54 Å) closely match X-ray measurements (3.05-3.43 Å) compared to the **B** motif at the 010-surface (2.54–2.71 Å). Additionally, the calculated bond lengths for adsorbed water molecules on goethite (Fe-O_{H_2O}) at the 010- (1.87-2.06 Å) and 100- (2.01-2.09 Å) surfaces agree well with crystal truncation rod measurements (2.15 Å) (Ghose et al., 2010) and DFT calculations (2.04 Å) (Kubicki et al., 2008).

3.2.2 IR Spectroscopy

IR spectroscopy is a sensitive tool for probing chromophores and their chemical environments. Section 1.2 discusses various strategies for assigning IR spectral features to phosphate binding motifs at mineral surfaces, which can sometimes yield controversial conclusions. **CC** methods can address this by combining simulation results from different surface planes and binding motifs into an effective model, as real soil mineral particles have various crystal planes and imperfections (Rakovan et al., 1999; Cornell and Schwertmann, 2003; Catalano, 2011; Guo and Barnard, 2011). IR spectra were calculated for phosphate-goethite complexes on both 010- and 100-goethite surface planes, focusing on the prevalent $H_2PO_4^-$ species in common soils. The vibrational frequencies and IR intensities were computed for optimized **M** and **B** phosphate-goethite complexes at these planes (**M**@010, **B**@010, **M**@100, and **B**@100). The overall IR spectrum of the adsorbed phosphate was generated by considering all molecular vibrations of the phosphate-goethite complex and the goethite surface. Parallel to these simulations, phosphate adsorption kinetics experiments at pH 6.3 were conducted, and the adsorbed phosphate was characterized using FTIR spectroscopy. This combined approach helps reconcile the computational and experimental findings for a comprehensive understanding of phosphate binding.

To quantify phosphate contributions within the overall spectra, vibrational modes dominated by phosphate vibrations were analyzed to produce phosphate-related spectra (Fig. 3.4a-d). For the **M**@010 binding motif (Fig. 3.4a), not all spectral features originate from phosphate molecular vibrations; features 2 and 5 arise solely from goethite surface vibrations. While the **M**@010 spectrum includes contributions from both the phosphate–goethite complex and the goethite surface, features 1 and 6 are primarily due to phosphate vibrations. In the **B**@010 complex (Fig. 3.4b), phosphate vibrations dominate features 1 and 4. For the **M**@100 motif (Fig. 3.4c), goethite vibrations dominate the entire spectral range. In the **B**@100 complex (Fig. 3.4d), phosphate vibrations contribute significantly to all features, with feature 4 being solely due to phosphate modes. Feature 2, which appears as a shoulder in the phosphate spectrum, is prominent in the overall spectrum, while feature 3 shows the opposite behavior.

Overall, the calculated IR spectra and their assignment are strongly influenced by the type of binding motif in the phosphate–goethite complex and the specific goethite crystal surface plane. For detailed information on the assignment of the IR spectra for the different binding motifs, refer to Ahmed et al. (2019).

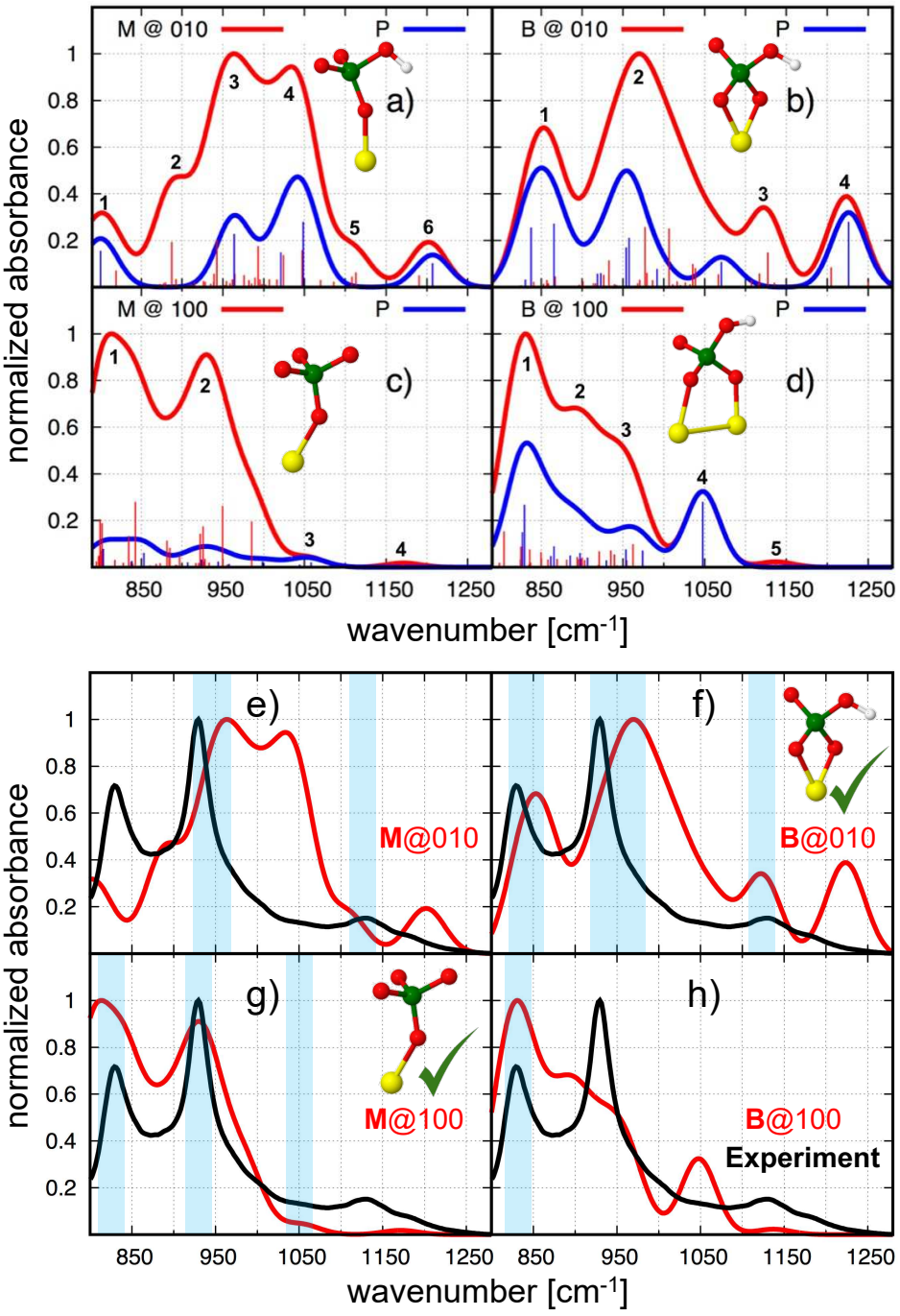


Figure 3.4: Upper panel: Calculated IR spectra (sticks and broadened with a half-width of 30 cm^{-1}) for adsorbed $H_2PO_4^-$ on goethite surfaces: **M**@010 (a), **B**@010 (b), **M**@100 (c), and **B**@100 (d). Red shows the overall spectrum (goethite and phosphate–goethite complexes), and blue shows phosphate–goethite contributions. Lower panel: Experimental IR spectrum (black) vs. calculated spectra (red) for **M**@010 (e), **B**@010 (f), **M**@100 (g), and **B**@100 (h). Fe-phosphate clusters are shown for visualization with atoms colored yellow (Fe), green (P), red (O), and white (H). Blue rectangles highlight the agreement between calculated and experimental spectra and "right symbols" refer to the best agreement.

The calculated spectra for adsorbed phosphate in both **M** and **B** binding motifs on the 010- and 100-goethite surface planes, compared with the experimental FTIR spectrum, are shown in Fig. 3.4e-h. The experimental spectrum features three main peaks (827, 927, and 1132 cm^{-1}) and a shoulder at 1050 cm^{-1}. According to the band number approach (Arai and Sparks, 2001), the experimental spectrum can be assigned to an **M** complex based on the three main peaks alone, while including the shoulder suggests a **B** complex. Tejedor-Tejedor and Anderson (1990) indicated that the 1132 cm^{-1} peak corresponds to a monoprotonated **B** motif, the 1050 cm^{-1} shoulder to a nonprotonated **B** and/or monoprotonated **M**, and the peaks at 827 and 927 cm^{-1} to the goethite surface rather than the phosphate-goethite complex (Tejedor-Tejedor and Anderson, 1990; Loring et al., 2009).

Our analysis indicates a strong match between theoretical and experimental IR spectra, particularly for the **B**@010 (Fig. 3.4f) and **M**@100 (Fig. 3.4g) complexes. This suggests that the 010-goethite surface is prevalent in samples where the **B** motif dominates, while the 100-plane is more common in samples where the **M** motif is abundant. This could explain discrepancies between experiments. Considering the first two experimental peaks, **M**@100 aligns better with the experiment (Fig. 3.4g), whereas the last peak fits better with the **B**@010 complex (Fig. 3.4f). The following conclusions can be drawn: 1. Peaks around 1132 and 1050 cm^{-1} likely correspond to **B**@010 and **M**@100 motifs, respectively; 2. The peak around 927 cm^{-1} could be attributed to **M**@010, **B**@010, and **M**@100 motifs; 3. The peak around 827 cm^{-1} may originate from all considered motifs; and 4. Interactions with goethite are most significant below 1000 cm^{-1}.

The analysis suggests that the overall spectrum likely includes contributions from various complexes in proportion to their presence on specific surface planes. To account for this, weighted averages of spectra from different motifs were calculated, producing combined overall spectra. As shown in Fig. 3.5, comparing these weighted average spectra with experimental data shows improved agreement as the **B**:**M** ratio increases from 1:9 to 9:1 for the 010-goethite surface (Fig. 3.5a). For the 100-surface, decreasing the **B**:**M** ratio improves agreement (Fig. 3.5b). This indicates the importance of both **B**@010 and **M**@100 binding motifs.

High proportions of the **M**@100 complex (Fig. 3.5b) align better with experimental data than high proportions of the **B**@010 complex (Fig. 3.5a). A mix of **B**@010 and **M**@100 complexes (Fig. 3.5c) improves agreement, especially for the first two features, while the **B**@010 complex is necessary for the feature around 1132 cm^{-1}. The best agreement (Fig. 3.5d) involves all binding motifs at both surface planes, suggesting that the **B** motif is most abundant at low phosphate loading, with a **B**:**M** ratio of 8:1. This

matches interaction energy calculations, indicating monoprotonated **B** motifs dominate with **M** motifs as a minor fraction. This theoretical assignment provides a benchmark for characterizing experimental IR data for adsorbed phosphate species at the goethite-water interface.

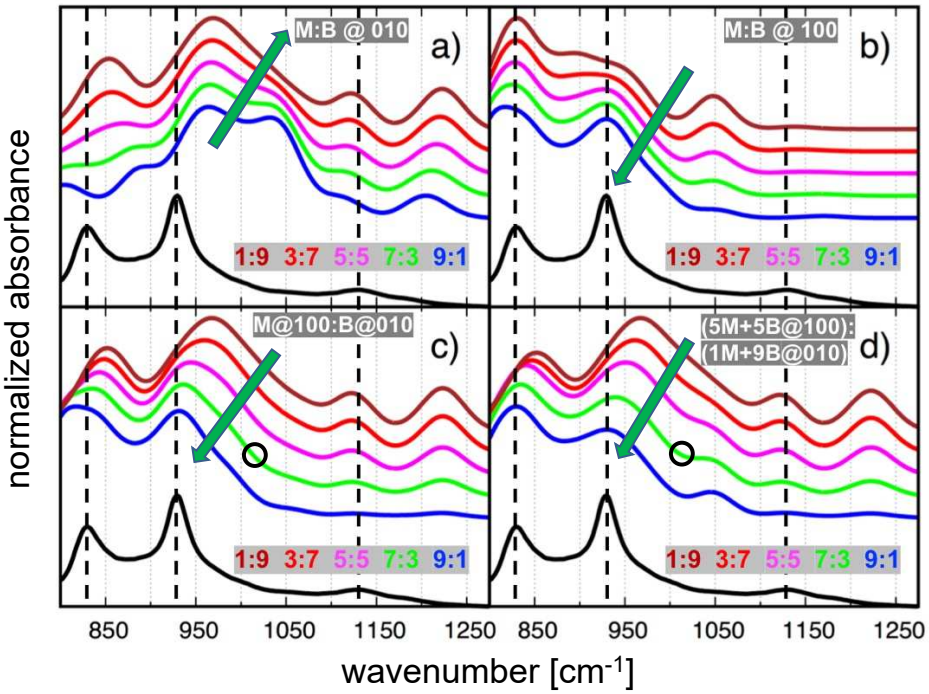


Figure 3.5: Overall experimental IR spectrum (in black) versus weighted average spectra that are obtained via different combinations of the calculated overall spectra with different proportions of **M**@010 and **B**@010 binding motifs (a), **M**@100 and **B**@100 binding motifs (b), **M**@100 and **B**@010 binding motifs (c), and 5**M**@100 + 5**B**@100 binding motifs and 1**M**@010 + 9**B**@010 binding motifs (d). Arrows are added to indicate to the direction of increasing the agreement level between the calculated and experimental spectra. Black circles refer to the best agreement.

3.2.3 Complexation versus Precipitation

Complexation, as discussed, involves the formation of a stable layer of phosphate ions on a mineral surface through direct chemical bonding with reactive sites. The resulting complexes can vary in coordination, forming **M**, **B**, or tridentate (**T**) bonds (binding motifs), depending on the specifics of the interaction. Complexation does not create a new solid phase but binds phosphate ions directly to the mineral surface, relying heavily on the surface properties of the mineral, including surface charge and functional groups.

In contrast, phosphate precipitation, as reported by Li and Stanforth (2000), occurs when dissolved phosphate ions chemically react with metal ions (e.g., Ca^{2+}, Fe^{3+}) to form an insoluble, stable crystalline solid phase that separates from the solution as distinct particles, such as calcium phosphate ($Ca_3(PO_4)_2$) or iron phosphate ($FePO_4$). This process is influenced by factors such as ion saturation, pH, and temperature, typically requiring supersaturation of ions. A schematic representation differentiating between surface complexation and precipitation is provided in Fig. 3.6.

In environmental contexts, precipitation is used in water treatment to remove phosphate, while complexation affects soil phosphate availability by adsorption on iron oxides. Understanding and distinguishing between these processes is essential for managing phosphate in natural and engineered systems, influencing nutrient availability, water quality, and soil chemistry.

To discriminate between precipitation and complexation at the molecular level, we modeled both the complexation reactions and the dissolution process of a single iron atom/ion (Fe^{3+}) from the goethite surface into the solution/water bulk. Subsequently, we modeled the binding of Fe^{3+} and other free metal ions (e.g., Ca^{2+}, Al^{3+}, Fe^{2+}) with phosphate ions as a critical step in precipitate formation (see Fig. 3.6). The results reveal that surface complexation reactions are dominant over precipitation reactions, with reaction energies ranging from -59 to -150 kcal.mol^{-1}. While precipitation reactions involving free metal ions can occur concurrently or after surface complexation, they are less energetically favorable. If free metal ions are present in the solution, their complexation with phosphate (precipitation) is spontaneous but still less favorable than surface complexation, with reaction energies as low as -107 kcal.mol^{-1}. Without free metal ions, the process requires the energetically costly detachment of Fe atoms/ions from the goethite surface (reaction energies around +109 kcal.mol^{-1}) before precipitation can take place, see Fig. 3.6.

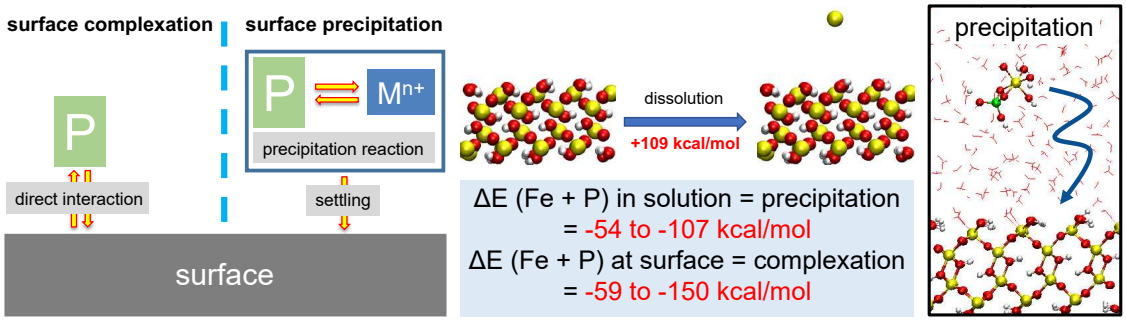


Figure 3.6: Schematic illustration differentiating surface complexation from precipitation, along with exemplary modeling and simulation results.

3.2.4 High Surface Loading

One of the most crucial factors influencing the phosphate binding mechanism at mineral surfaces is the surface loading or initial phosphate concentration. To thoroughly investigate this effect, we modeled several larger goethite surfaces with varying initial phosphate concentrations, ranging from a single phosphate ion to 20 phosphate ions adsorbed on the surface. Our goal was to explore the co-sorption process of phosphates and the successive addition of phosphate molecules to the goethite surface. We conducted these investigations for both **M** and **B** motifs at the 010 and 100 surface planes using stationary calculations of adsorbed $H_2PO_4^-$ species. The adsorption process was analyzed in terms of interaction energies, revealing the predominance of the **M** motif as the number of adsorbed phosphates increased.

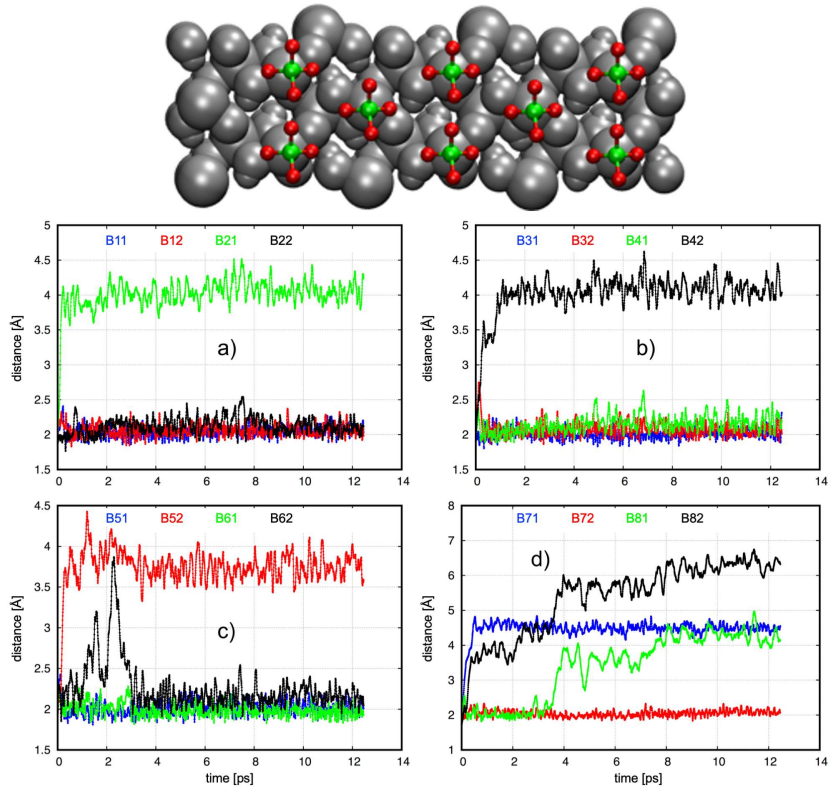


Figure 3.7: Top view of a model with 8 phosphate ions adsorbed on the 010 goethite surface (192 atoms). Phosphate atoms are green (P) and red (O), while surface atoms are gray. Water molecules are omitted for clarity. Calculated bond lengths between phosphate O atoms and goethite Fe atoms contributing to 8 **B** motifs along the MD trajectory. B11 and B12 are the bonds for the first **B** motif, B21 and B22 for the second, and so on, up to B81 and B82 for the eighth **B** motif.

To validate this finding, we also studied the dynamics of phosphate co-adsorption at high surface loadings on goethite/water interfaces. Specifically, we examined the co-adsorption of eight phosphate molecules on the 010 and 100 goethite surfaces in the presence of water (see Fig. 3.7). Initially, **B** binding motifs were used for all phosphates at the goethite-water interface. DFT-based MD simulations were conducted under conditions relevant to pH 4-6, where $H_2PO_4^-$ species are present. During these simulations, we observed the formation of HBs between phosphate and the surface, phosphate and water, and surface and water. Notably, we observed a transformation from **B** to **M** binding motifs over time (see Fig. 3.7). The simulation, which began with eight **B** motifs, ended with three **B** motifs, four **M** motifs, and one desorbed phosphate molecule. This shift indicates a predominance of **M** motifs at high phosphate concentrations, consistent with experimental findings, although the **B** motif remains significantly present.

3.2.5 Organic Phosphates

Achieving a molecular-level understanding of the differences between inorganic and organic phosphate binding at mineral-water interfaces is paramount in addressing the P binding issue. Currently, there is a significant gap in our knowledge regarding the mechanisms of organically bound phosphate binding at these interfaces, necessitating substantial research efforts. To bridge this gap, we investigated the binding mechanisms of glycerolphosphate (GP) and inositolhexaphosphate (IHP) at the goethite-water interface, focusing on the 010 and 100 surface planes and various binding motifs. Using QM/MM-based MD simulations, we meticulously analyzed the geometries and interactions of phosphate-goethite-water complexes. For comparison, we also simulated the adsorption of orthophosphate (OP) at the 100-goethite surface using the same methodology. For further details regarding the molecular modeling approach, refer to Ganta et al. (2020a, 2021).

For the 100-goethite surface plane, MD simulations revealed that OP and GP form stable **M** and **B** binding motifs (see Fig. 3.8). The **B** motif is more stable than the **M** motif for both OP and GP. However, OP binds more strongly than GP in the **B** motif, while the reverse is true for the **M** motif, underscoring the significance of binding type. OP exhibits higher interaction energy per bond in the **B** motif compared to the **M** motif, suggesting a preference for forming an additional covalent bond with goethite. This observation aligns with QM calculations and IR spectra in Sections 3.2.1-3.2.2, which indicate the prevalence of the **B** motif for OP on goethite surfaces.

For GP, the **B** motif has lower interaction energy per bond than the **M** motif due to strain from GP's polar organic moiety interacting with water molecules, making the **B** motif less stable. Previous studies by Xu et al. (2017) showed that GP adsorption induces a more negative charge on hematite compared to OP, straining the Fe-O_P bonds. Li et al. (2017) suggested that GP might not form a **B** motif due to steric hindrance. The dominant binding motif for GP (**M** or **B**) depends on environmental conditions and GP's interactions with its surroundings, typically forming a **B** motif at low phosphate loading and a **M** motif at high loading (Li et al., 2017; Sheals et al., 2002).

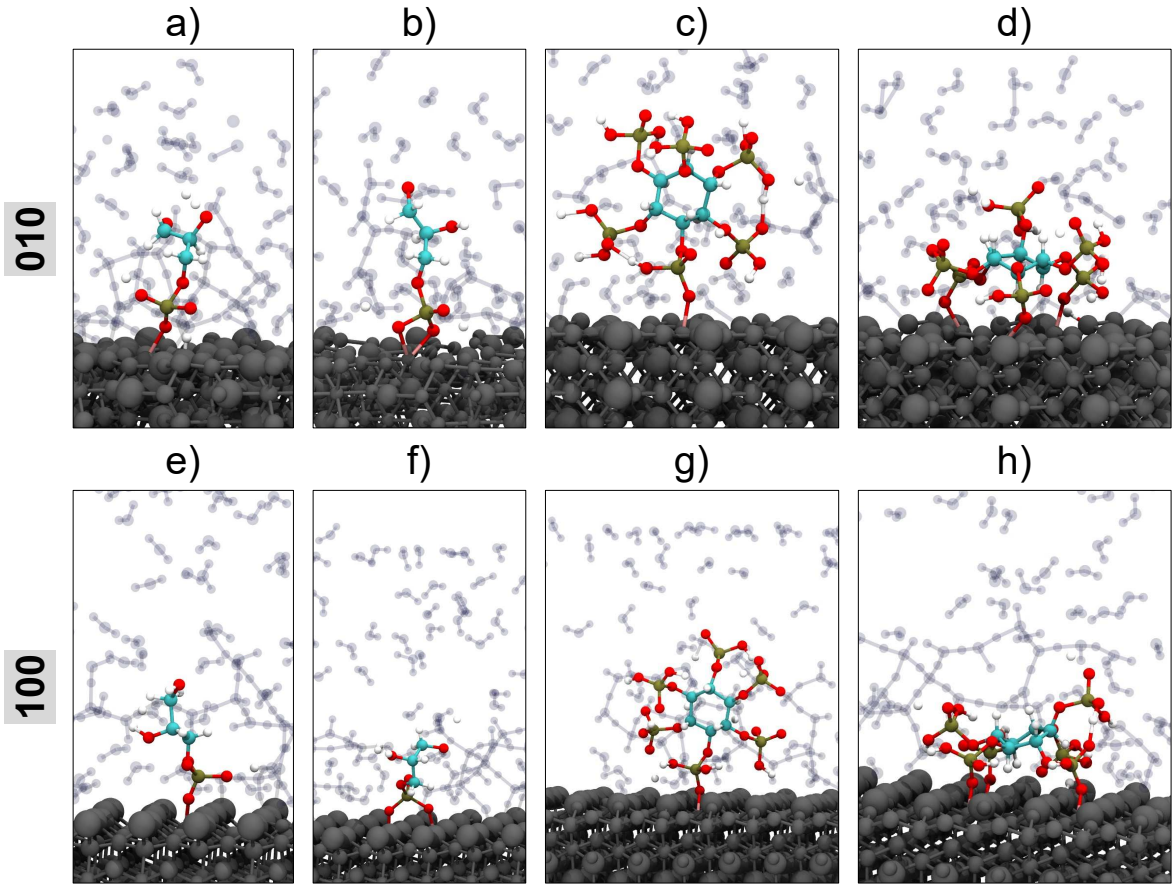


Figure 3.8: Snapshots of equilibrated adsorbed GP and IHP molecules on the goethite-water interfaces. At the 010 surface: **M** GP motif (a), **B** (2O+1Fe) GP motif (b), **M** IHP motif (c), and 3**M** IHP motif (d). At the 100 surface: **M** GP motif (e), **B** (2O+2Fe) GP motif (f), **M** IHP motif (g), and 3**M** IHP motif (h). H, O, P, and C atoms are shown in white, red, lime, and cyan, respectively. Goethite surface atoms are grey, and water molecules are transparent for clarity.

For IHP at the 100-goethite surface, MD simulations showed stable **M** and 3**M** binding motifs with multiple intramolecular HBs between adjacent phosphate groups (see Fig. 3.8). The interaction energy per bond for the 3**M** motif is lower than for the **M** motif due to steric hindrance from the large organic moiety of IHP. However, the total interaction energy of the 3**M** motif is significantly higher, indicating greater overall stability.

The binding strength at the 100-goethite surface follows the order: OP **M** < GP **M** < GP **B** < OP **B** < IHP **M** < IHP 3**M**. This order shows that IHP binds more strongly than OP and GP, regardless of the binding motif type. This suggests that IHP can replace adsorbed OP and GP, aligning with the findings by De Groot and Golterman (1993) that IHP can inhibit further OP adsorption. The number of phosphate groups is a key factor in controlling adsorption strength (Anderson and Arlidge, 1962), explaining the higher abundance of IHP compared to GP in forest soil colloid samples, as revealed by liquid-state NMR measurements (Missong et al., 2016). However, not all phosphate groups contribute to inner-sphere complexes with mineral surfaces, as IHP does not form a 4**M** motif. The binding strength order indicates that the IHP 3**M** motif has the highest interaction energy with the goethite surface, making it the dominant binding motif at low surface loading.

The 010-goethite surface exhibits similar binding motifs to those on the 100-goethite surface. GP forms stable **M** and **B** motifs, while IHP forms stable **M** and 3**M** motifs, as shown in Fig. 3.8. The binding strength follows the order: GP **M** < GP **B** < IHP **M** < IHP 3**M**, consistent across both surfaces. Notably, the less saturated 010-goethite surface binds GP and IHP more strongly than the more saturated 100-goethite surface, underscoring the significant role of surface morphology and saturation in phosphate binding.

In comparison and validation against experiments, our joint adsorption studies fitted to the Freundlich model revealed that the adsorption strength increases in the order GP < OP < IHP (Ganta et al., 2021). This finding is consistent with studies by Yan et al. (2014); Amadou et al. (2022); Ahmed et al. (2024), which demonstrated that GP has the lowest affinity and IHP the highest on goethite and amorphous $Al(OH)_3$ surfaces, highlighting the significant impact of molecular structure on adsorption, as discussed in Ahmed et al. (2023). Moreover, the experimental results showed that the binding strength of incoming phosphate molecules on surfaces already covered with existing phosphate molecules increases in the order IHP < GP < OP (Ganta et al., 2021; Ahmed et al., 2024). This suggests that IHP saturates the goethite surface more quickly than GP and OP, potentially explaining its prevalence in soil.

Combining both experimental and theoretical findings, we observed that the overall binding strength follows the order GP (**M**) < OP (**B**) < IHP (**M** + 3**M**). This indicates that GP likely forms **M** motifs, OP forms **B** motifs, and IHP forms both **M** and 3**M** motifs. Additionally, GP adsorption induces a more negative charge on goethite compared to OP, suggesting that GP prefers **M** motifs, resulting in lower interaction energy.

For both goethite surfaces, MD simulations revealed that interfacial water molecules significantly influence the interactions and binding mechanisms of phosphates (OP, GP, and IHP) with goethite. Some interfacial water molecules form covalent bonds with goethite Fe atoms, while others dissociate into protons (H^+) and hydroxyl (OH^-) groups, facilitating proton transfer. Additionally, water molecules form HBs with phosphates and the goethite surface. These HBs are characterized by their geometries along the trajectory (see Fig. 3.9), quantifying HB strength and related proton transfer processes (Guo et al., 2012; Ahmed et al., 2013). Most analyzed HBs in the phosphate-mineral-water systems are of moderate strength. Overall, water interactions with the goethite surface are stronger than those of the studied phosphates.

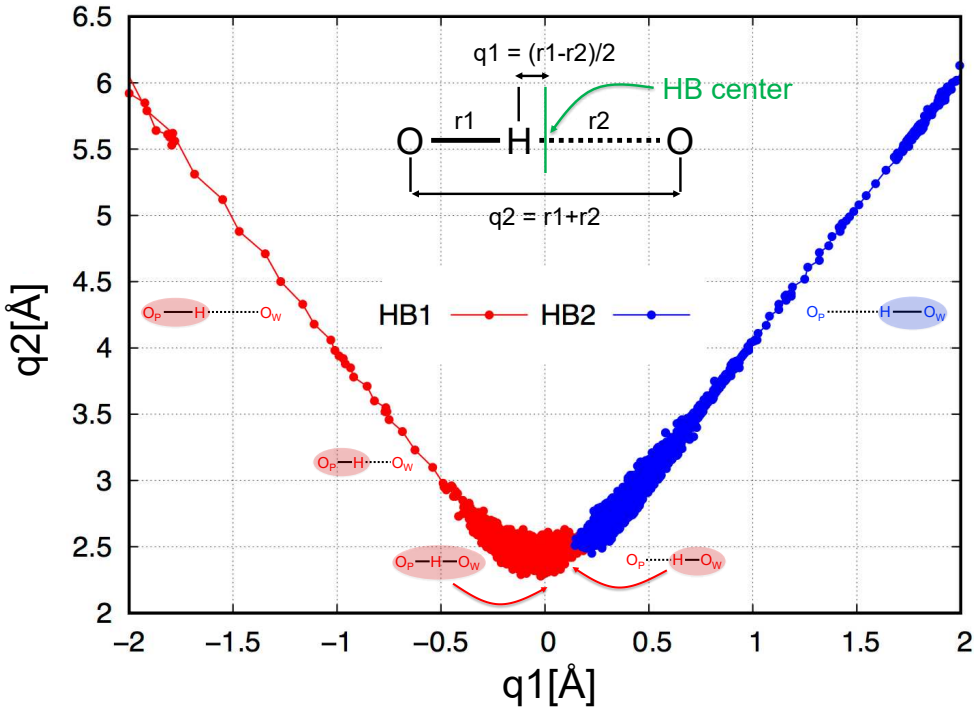


Figure 3.9: Representative examples of observed HBs (HB1 and HB2) along the MD simulations of the phosphate binding at the goethite-water interface. Here, q1 indicates the deviation of the H atom from the center of the HB, representing proton transfer, and q2 represents the O—O HB length, indicating the HB strength.

3.3 P Binding at Diaspore: Impact of Central Metal Ion

The central metal ion in mineral surfaces is a critical factor that shapes the nature and mechanism of phosphate binding (Ahmed et al., 2023). Minerals containing Fe^{3+} and Al^{3+} ions, particularly Fe(III)-oxides like goethite and hematite, as well as AlOOH-type minerals such as diaspore and boehmite, play a pivotal role in phosphate fixation (Borggaard et al., 2004; Elzinga and Sparks, 2007; Zhong et al., 2007). To understand the influence of the central metal ion on phosphate binding, we focused on diaspore (α-AlOOH), which is isomorphous with goethite but contains Al^{3+} instead of Fe^{3+}. Using the same setup, conditions, and techniques applied in Section 3.2.5, we investigated the binding mechanisms of GP and IHP at the diaspore-water interface, particularly on the 010- and 100-surface planes (Ganta et al., 2019, 2020b). This study aims to elucidate the role of central metal ions in phosphate binding, enhancing our understanding of P fixation in various soil constituents.

Our MD simulations revealed the formation of stable phosphate-diaspore binding motifs at the 010-diaspore surface plane, including **M** and **B** motifs for GP, and 2**M** and 3**M** motifs for IHP (see Fig. 3.10). For GP, the **B** motif is significantly more stable than the **M** motif, with interaction energy per bond for the **B** motif being 2.4 times higher. This increased stability is attributed to the additional bond and the transfer of two more protons from GP to the surface in the **B** motif.

For IHP, the 3**M** motif has a higher total interaction energy than the 2**M** motif but is lower per bond, suggesting strain in the third bond due to a mismatch between phosphate groups and Al sites. Consequently, IHP's **B** motif transforms into a 2**M** motif during MD simulation. IHP interacts more strongly with both the surface and water compared to GP. Despite similar interaction energies per bond for GP **B** and IHP 3**M** motifs, IHP forms more covalent bonds with the surface and HBs with water.

Water plays a crucial role in stabilizing these binding motifs and overall interactions via HBs and proton transfers. For GP, the **M** motif shows stronger water interaction and proton transfer than the **B** motif. For IHP, water interaction strength is similar for both 2**M** and 3**M** motifs. Across all models, water interaction with the diaspore surface is stronger than with the phosphates (GP and IHP).

Similar to the 010-diaspore surface plane, our MD simulations showed stable binding motifs for both GP and IHP at the 100 surface plane. GP forms **M** and **B** motifs, with a preference for the **B** motif, while IHP forms **M** and 2**M** motifs, favoring the 2**M** motif. IHP interacts more strongly than GP with water due to its larger water-accessible surface area. Both phosphates exhibit proton transfer to water and form strong HBs.

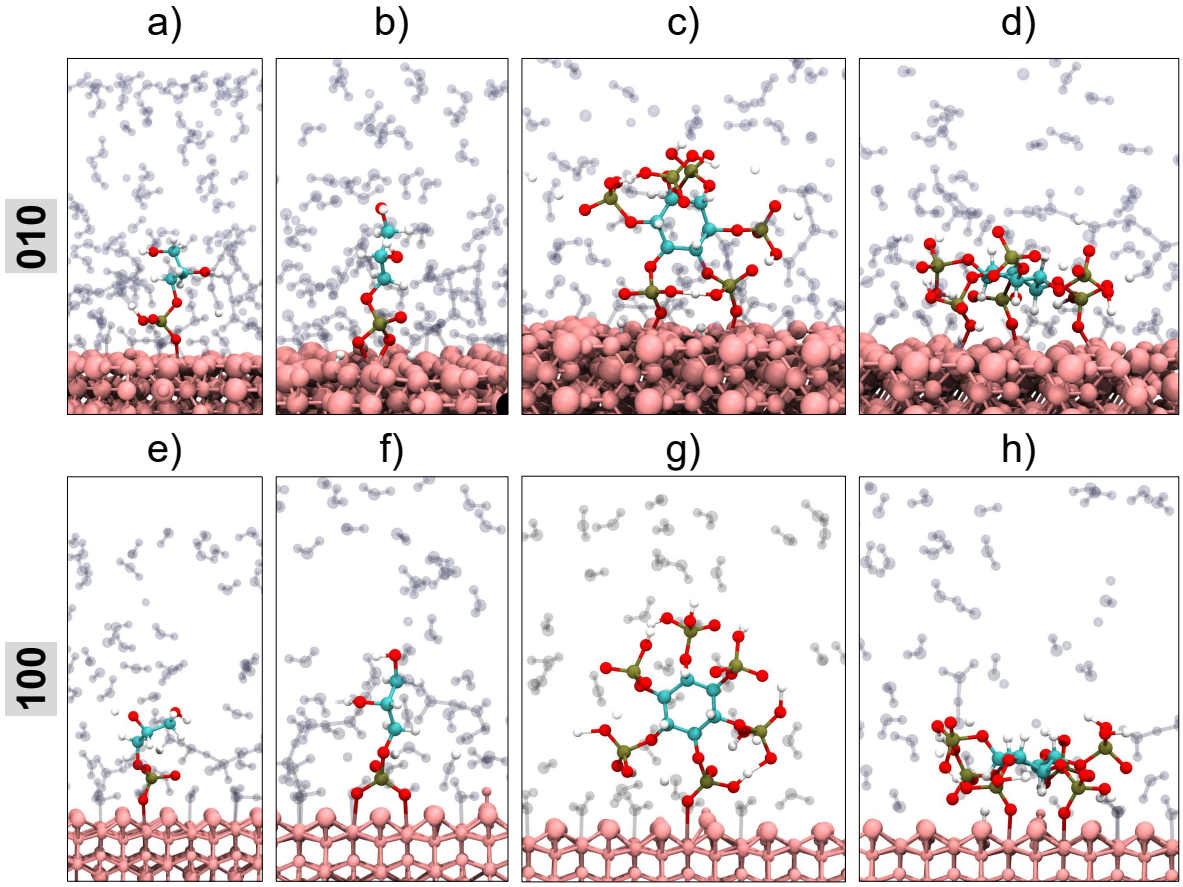


Figure 3.10: Snapshots of equilibrated adsorbed GP and IHP molecules on the diaspore-water interfaces. At the 010 surface: **M** GP motif (a), **B** (2O+1Fe) GP motif (b), 2**M** IHP motif (c), and 3**M** IHP motif (d). At the 100 surface: **M** GP motif (e), **B** (2O+2Fe) GP motif (f), **M** IHP motif (g), and 2**M** IHP motif (h). H, O, P, and C atoms are shown in white, red, lime, and cyan, respectively. Diaspore surface atoms are pink, and water molecules are transparent for clarity.

Comparing the binding at both the 010- and 100-diaspore surface planes reveals that the less saturated 010-surface binds GP and IHP more strongly than the 100-surface for all binding motifs, consistent with findings for goethite surfaces (see Section 3.2.5). The higher saturation of the 100-surface with more hydroxide groups results in more negative charges and lower electrostatic potential, leading to a lower affinity for phosphate and water binding than the 010-surface. Surface morphology also plays a crucial role in phosphate binding, resulting in different dominant binding motifs with varying stabilities for each surface plane. Particularly, the distribution and positioning of surface metal ions within both planes enable GP and IHP to form more stable covalent bonds with

the 010-surface than the 100-surface. IHP prefers the 3**M** motif on the 010-surface and the 2**M** motif on the 100-surface, while GP predominantly forms the **B** motif, especially on the 010-surface. Both diaspore surfaces, like goethite, bind IHP more strongly than GP, indicating a higher soil abundance of IHP (Anderson and Arlidge, 1962; Missong et al., 2016).

In conclusion, the binding behavior of phosphates on goethite and diaspore surfaces reveals intricate and significant patterns. For all **M** binding motifs, phosphates bind more strongly to goethite than to diaspore. On the other hand, for GP **B** binding motifs, goethite shows stronger binding on the 100-surface plane, while diaspore demonstrates stronger binding on the 010-surface plane. Notably, diaspore binds IHP more robustly than goethite for the 3**M** motifs on both surface planes. These findings highlight the crucial role of the molecular structure of both the phosphate and the adsorbent surface. This complexity is corroborated by various experimental studies, including those by Yan et al. (2014), Ganta et al. (2021), Amadou et al. (2022), Wang et al. (2015b), and Gypser et al. (2018). For more detailed insights, refer to Ahmed et al. (2023). This comprehensive understanding of binding mechanisms significantly enhances our knowledge of phosphate interactions, providing valuable guidance for future research and practical applications.

3.4 Complex Reactions and Redox Potential

Redox conditions are critical factors influencing phosphate binding in soil and aquatic systems (Shaheen et al., 2022; Ahmed et al., 2023). In soil samples, redox potential (E_h), a measure of a species' tendency to gain or lose electrons, can fluctuate over time (from minutes to days) and across different spatial scales (from microsites to landscapes) (Vepraskas et al., 1999; Gao et al., 2002; Fiedler et al., 2007). These fluctuations are driven by variables such as precipitation, infiltration, water-filled pore space, groundwater levels, microbial activity, and the quality and quantity of organic matter (Fiedler et al., 2007; Zimmer et al., 2016). For example, E_h may decrease when soil moisture replaces oxygen-containing gas in pore spaces due to precipitation or rising groundwater levels, affecting phosphorus binding and mobilization in soil (Baumann et al., 2020a). The impact of redox changes on key plant nutrients and soil pollutants has garnered significant attention (Frohne et al., 2011; El-Naggar et al., 2018; Baumann et al., 2020b), yet a detailed molecular-level understanding remains elusive.

To address this knowledge gap, we simulated the binding of OP with various metal ions (Ca^{2+}, Al^{3+}, Fe^{2+}, Fe^{3+}, Mn^{2+}, Mn^{3+}, Mn^{4+}) and dissolved organic matter in soil

solutions (Shaheen et al., 2022). We modeled the complexation reactions, considering two binding motifs (**M** and **B**), where phosphate oxygen atoms form one or two coordination bonds with the metal ion in an octahedral metal aqua-complex setup (see Fig. 3.11). The stability and binding strength of these M^{n+}-P complexes were characterized by calculating reaction energies and free energies (ΔE and ΔG) for phosphate species $H_2PO_4^-$ (pH 2.1-7.2) and HPO_4^{2-} (pH 7.2-12.4) (Powell et al., 2005). Additionally, we simulated the binding of phosphorus to organic matter molecules under various redox conditions, calculating the corresponding reaction energies and free energies as shown in equation 3.1. This comprehensive approach aims to elucidate the molecular mechanisms of phosphate binding under fluctuating redox conditions, providing deeper insights into nutrient and pollutant dynamics in soils.

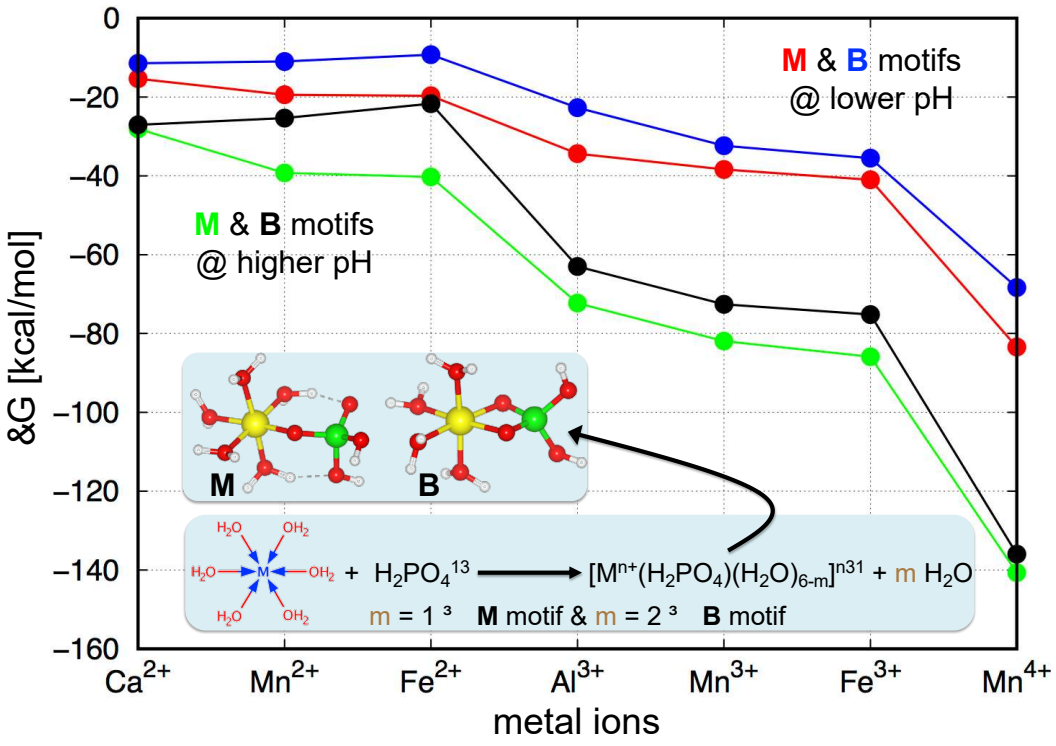


Figure 3.11: Calculated reaction free energies (ΔG) for complexation reactions between phosphate and various metal ions. Red and blue colors represent **M** and **B** binding motifs, respectively. Example geometries for **M** and **B** Fe^{3+}-P complexes are shown. H, O, P, and Fe atoms are visualized in white, red, green, and yellow, respectively. Dashed lines indicate HBs.

For the M^{n+}-$H_2PO_4^-$ complexation reactions, our calculated reaction free energies (ΔG) indicate that the chemical reactions between phosphate and each free metal ion

are spontaneous (see Fig. 3.11). The **M** complexes are more favored than the **B** ones across all metal ions, with stability increasing in the order of divalent < trivalent < tetravalent ions. Specifically, tetravalent Mn^{4+} and trivalent Mn^{3+} and Fe^{3+} ions bind phosphate significantly stronger than the corresponding divalent Mn^{2+} and Fe^{2+} ions. This suggests that phosphates can strongly bind to high oxidation state metal ions (e.g., Al^{3+}, Fe^{3+}, Mn^{3+}, and Mn^{4+}) and become potentially immobilized in the soil through complexation with their oxides.

Notably, phosphates bind more strongly to mineral surfaces than to free metal ions in soil solutions because mineral surfaces provide a range of binding sites that interact with phosphates through various chemical and physical mechanisms. For instance, the binding energies for M^{n+} complexation with $H_2PO_4^-$ are -20 and -41 kcal.mol^{-1} for Fe^{2+} and Fe^{3+}, respectively. However, interaction energies between adsorbed $H_2PO_4^-$ and goethite range from -59 to -150 kcal.mol^{-1}, depending on factors such as surface morphology, surface saturation, crystal plane, presence of water, and pH. This suggests that phosphate binding in soils is generally weaker under reducing conditions. Reductive dissolution mechanisms, including proton-promoted dissolution, ligand-promoted dissolution, microbial reduction, electrochemical reduction, and photochemical reduction, can release metal ions like Fe(II) into the solution. Consequently, applying reducing conditions to soil samples increases the availability of phosphorus in the solution by converting Fe^{3+}, Mn^{3+}, and Mn^{4+} to Fe^{2+} and Mn^{2+} (Han et al., 2020).

Our calculations reveal that phosphate binds significantly less strongly to organic matter (OM) compared to free metal ions and metal-oxide surfaces, as evidenced by substantially lower binding energies and free energies (see Fig. 3.12) (Shaheen et al., 2022; Ahmed et al., 2019, 2020; Ganta et al., 2019, 2020b,a, 2021). As a result, phosphate bound to dissolved organic carbon (DOC) or soil organic matter (SOM) is much more readily available than phosphate bound to metal ions and their oxides. Furthermore, aromatic DOC binds phosphate more strongly than aliphatic DOC, and phosphate exhibits stronger binding to oxidized forms of OM compared to reduced ones. This means that phosphate release is significantly higher under reducing conditions (lower E_h values) and lower under oxidizing conditions, emphasizing the pivotal role of redox chemistry in phosphorus mobilization in soils. This aligns with experimental findings, which demonstrate that aluminum-phosphate (Al-P) complexes are the most dominant, followed by iron-phosphate (Fe-P), calcium-phosphate (Ca-P), and organic-phosphate (organic-P) complexes (Shaheen et al., 2022). This order is determined by the binding strength and the relative abundance of soil constituents, particularly the concentrations of free metal ions in soil solutions, especially Fe^{3+} and Al^{3+}.

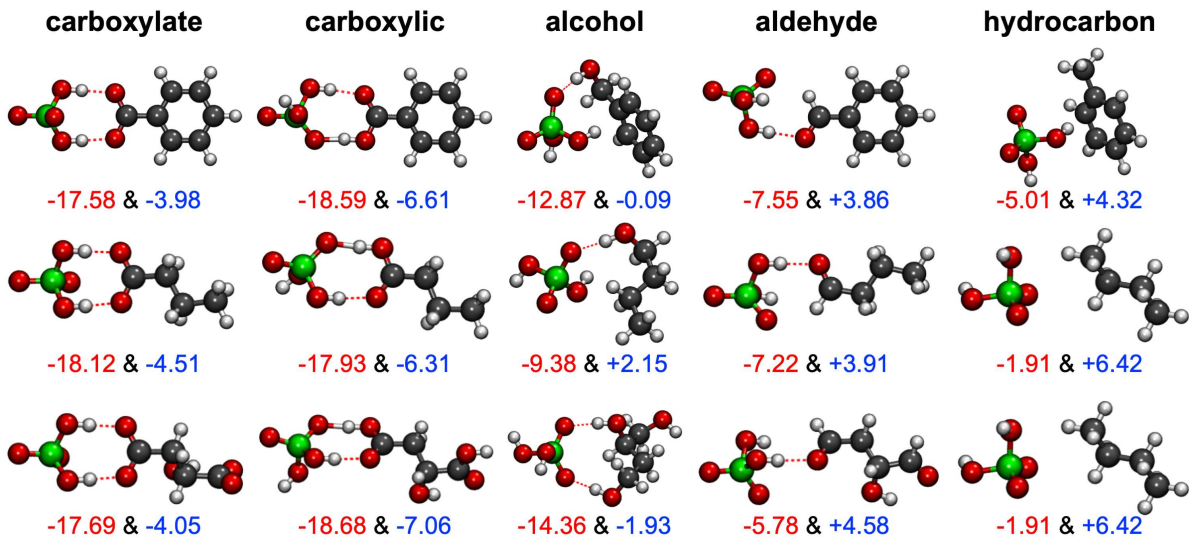


Figure 3.12: Optimized geometries for selected OM–P complexes formed between $H_2PO_4^-$ and modeled OM functional groups. Reaction/binding energy (ΔE_B) and corresponding free energy (ΔG_B) are shown in red and blue, respectively. H, O, P, and C atoms are visualized in white, red, green, and gray, respectively. Dashed red lines indicate HBs.

At higher pH levels, considering the HPO_4^{2-} species, metal ions can potentially precipitate through interactions with OH^- groups in the soil solution. Despite this, M^{n+}-P complexation reactions remain more favorable, with **M** complexes proving more stable than **B** complexes, and M^{n+}-P binding strength decreases under reducing conditions (see Fig. 3.11). M^{n+}-P complexes also exhibit stronger binding at higher pH levels than at lower pH levels. This aligns with findings from a microcosm experiment with controlled redox oscillations, confirming higher P release under reducing and acidic conditions and lower P release under oxidizing and alkaline conditions (Shaheen et al., 2022).

The effect of pH on P mobilization, however, varies among soil constituents. Molecular modeling indicates that P binds more strongly to organic compounds at lower pH than at higher pH (see ΔG_B for carboxylic and carboxylate groups in Fig. 3.12), and a similar trend is observed for metal oxide surfaces. This suggests a higher release of P under alkaline conditions when considering metal oxides and organic matter, highlighting the complex influence of pH on P binding and mobility. Altogether, these insights underscore the dynamic interplay among redox conditions, pH, and P availability, emphasizing the significant impact of redox chemistry and pH on nutrient cycling and soil fertility.

3.5 Organic Matter Competition

Organic matter (OM), particularly organic acids, plays a crucial role in P binding by adsorbing onto mineral surfaces and altering properties such as specific surface area, reactive OH groups, and surface charge. This, in turn, affects phosphate adsorption, impacting P mobility, bioavailability, and environmental behavior (Yan et al., 2014, 2016; Kaiser and Guggenberger, 2003). OM competes with phosphate for adsorption sites, enhancing phosphate mobility and promoting surface dissolution (Guppy et al., 2005). For instance, citrate reduces phosphate adsorption on goethite at low pH (Geelhoed et al., 1998), and organic acids effectively release adsorbed P from ferrihydrite, with efficiency increasing in the order oxalate $\approx$ malonate $\approx$ succinate $<$ tartrate $<$ malate $<$ citrate (Johnson and Loeppert, 2006). Humic acids also significantly decrease P adsorption by reducing the specific surface area and isoelectric point of iron oxides (Wang et al., 2015b,a, 2016). Recent studies confirm that organic and inorganic competitors increase P desorption from Fe- and Al-hydroxides (Gypser et al., 2019; Gypser and Freese, 2020; Gypser et al., 2021; Kubicki and Ohno, 2020).

Despite extensive research, the molecular-level competition mechanisms between phosphates and organic acids at mineral surfaces and in soils remain inadequately understood due to analytical limitations, soil complexity, and variations in mineral surface properties (Han et al., 2020; Ahmed et al., 2023). To address these challenges, we employed a comprehensive combined experimental-theoretical approach, integrating adsorption experiments and MD simulations, to investigate how OM influences P adsorption at the goethite-water interface (Ahmed et al., 2023, 2024). Our investigation focused on the impact of common soil OM compounds, citric acid (CIT) and histidine (HIS), on the adsorption of three distinct phosphates: OP, GP, and IHP. We examined the adsorption behavior of each phosphate on goethite under controlled conditions using three scenarios: P adsorption onto bare goethite, P adsorption onto goethite covered with OM, and co-adsorption of P and OM onto bare goethite.

To provide a detailed understanding of these interactions, we established an extensive molecular modeling approach involving several models simulating the adsorption and binding behavior of specific adsorbates (P and OM) at the goethite-water interface. These models included studying the adsorption of individual P and OM molecules, co-adsorption of P and OM, adsorption of a complete monolayer of each P and OM, and adsorption of P on goethite surfaces pre-covered with OM. Employing extensive MD simulations and relevant analyses, we uncovered the significant role of electrostatic environments and P-OM complexes in either enhancing or inhibiting P adsorption. These

findings offer new perspectives for sustainable soil fertility management. For a simplified picture of the molecular models involved in this study, refer to Fig. 3.13. For further details about the molecular modeling approach and computational specifics, refer to Ahmed et al. (2024).

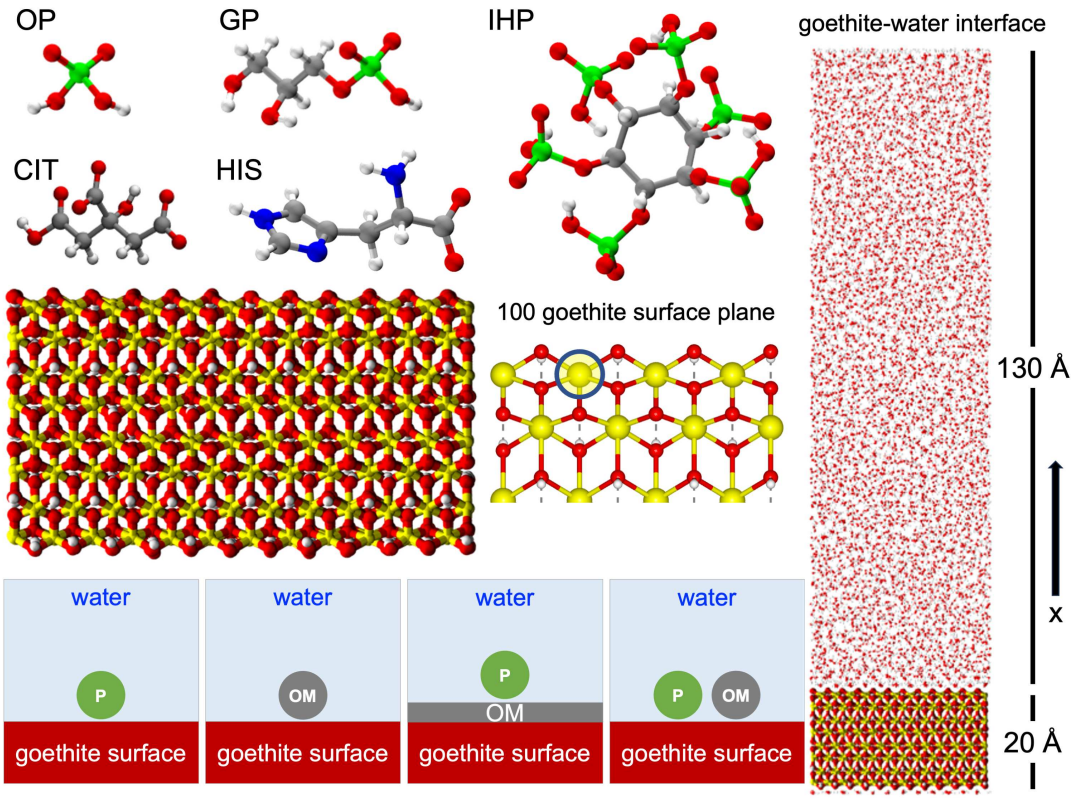


Figure 3.13: Illustration of the molecular modeling approach examining the OM impact on P binding at the goethite-water interface. It includes structures of P compounds (OP, GP, IHP) and OM compounds (CIT, HIS), side views of the 100-goethite surface plane, and highlights the coordination of surface Fe atoms (dashed lines denote HBs). Schematic representations of four scenarios are provided: P adsorption on bare goethite, OM adsorption on goethite, P adsorption on OM-covered goethite, and co-adsorption of P and OM. The goethite-water interface is also depicted. Atom colors: H (white), C (gray), N (blue), O (red), P (green), Fe (yellow).

Our experimental investigations revealed that the adsorption capacity of P on goethite surfaces follows the order: GP < OP < IHP. This trend remained consistent across all conditions, whether OM was present or absent, and regardless of whether OM was added simultaneously with P or used to pre-cover the goethite surface. OM significantly influ-

enced P adsorption, particularly affecting OP, with citric acid reducing its adsorption by 70%. IHP was less affected, showing only a 20% reduction, while GP adsorption decreased by 31% when the goethite surface was pre-covered with HIS. These findings highlight the critical role of the chemical structures of both P and OM in determining adsorption behavior and P mobility efficiency. When OM and P were co-adsorbed, the inhibition of P adsorption varied: OP co-adsorption with OM resulted in a 54% reduction, whereas IHP adsorption decreased by only 10%, showing no significant difference between CIT and HIS. Interestingly, GP co-adsorption with OM increased its adsorption capacity by 47% with CIT and 38% with HIS, suggesting that OM can either inhibit or enhance P adsorption depending on the specific P species and the nature of the OM. These results underscore the importance of applying OM to regulate P mobility and release.

Our MD simulations extensively characterized the goethite-water interface, revealing positively active sites on the goethite surface capable of binding anions like phosphates and carboxylates. The charge density distribution along the interface, including the Helmholtz layer, showed peaks for Fe^{3+}, O^{2-}, and OH^{-} of goethite, and $O^{\delta-}$ and $H^{\delta+}$ of water. A high density of water was observed at the surface, gradually decreasing to normal liquid density around 10 Å from the surface. In the absence or at low concentrations of P and OM, a positive electric potential at the goethite-water interface attracted anions from the bulk solution to the surface, facilitating the adsorption of phosphates and carboxylates.

We investigated the dynamic behavior of single P and OM (OP, GP, IHP, CIT, and HIS) binding at the goethite-water interface (see Fig. 3.14). MD simulations and extensive analysis revealed that OP and GP initially bind to the goethite surface but eventually diffuse into the water bulk, indicating weak binding affinity (Fig. 3.14a-d). In contrast, IHP and CIT maintain close contact with the surface throughout the simulation, suggesting strong binding affinity (Fig. 3.14e-h, m-p). HIS displayed intermediate behavior, remaining close to the surface for over half the simulation before diffusing between the surface and water bulk, indicating intermediate binding affinity (Fig. 3.14j-l). The calculated interaction energies indicate the binding strength of P and OM compounds with the goethite surface follows the order: GP (-0.5 $kcal.mol^{-1}$) < OP (-4.8) < HIS (-21.9) < CIT (-31.4) < IHP (-93.5). This hierarchy shows that IHP has the strongest binding to the goethite surface, likely due to its multi-phosphate structure providing multiple binding sites. OP binds more strongly than GP, which has the weakest interaction energy. These findings align with our QM/MM results (Ganta et al., 2021) and joint adsorption experiments, both indicating a similar order of P bind-

ing affinity: GP < OP < IHP. CIT's stronger binding compared to HIS is attributed to its multiple carboxyl groups, which can form multiple bonds with the surface.

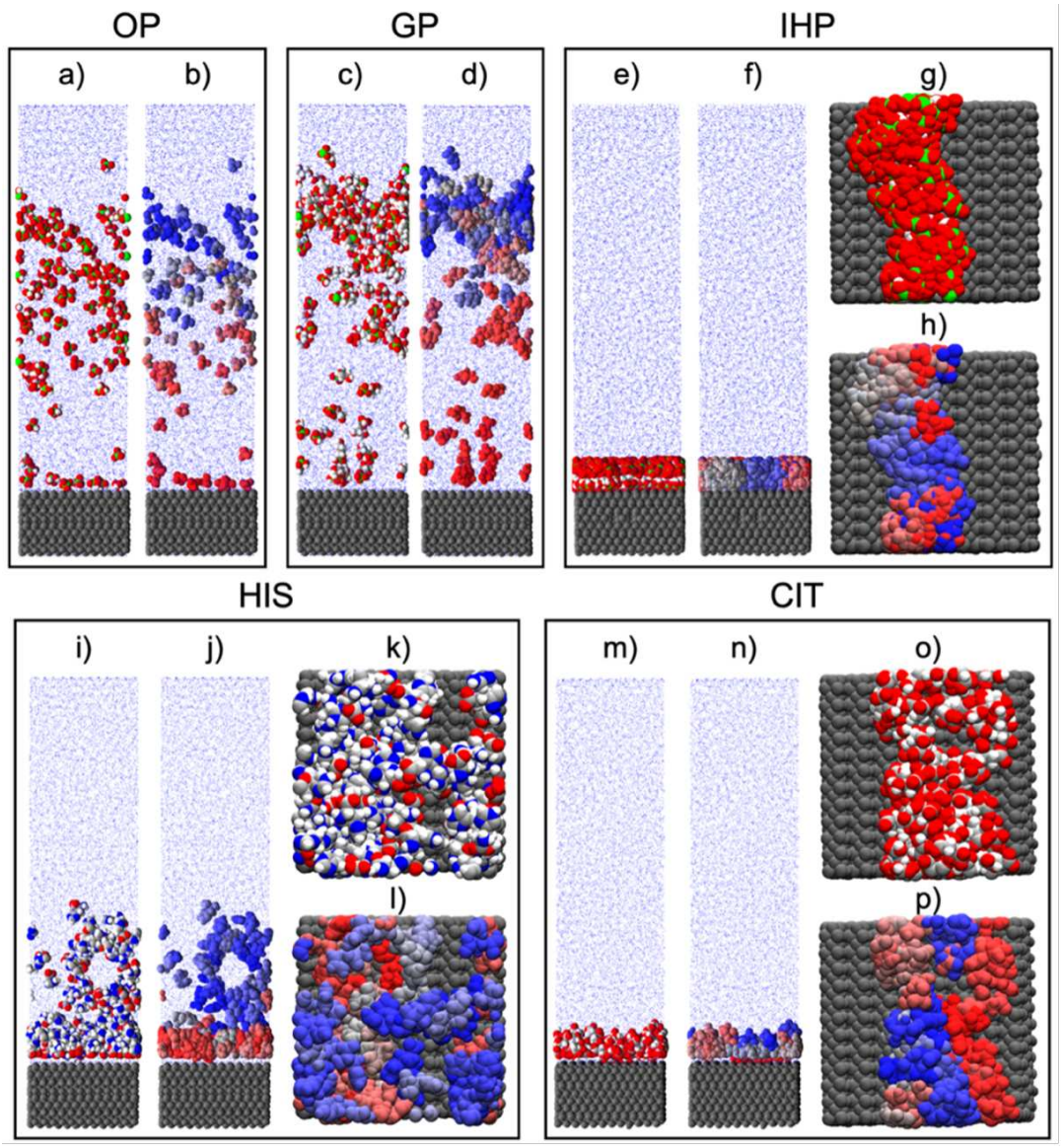


Figure 3.14: Overlays of snapshots captured at intervals during MD simulations of OP, GP, IHP, CIT, and HIS adsorption on the goethite surface. Side views are shown for OP ((a), (b)) and GP ((c), (d)), while both side and top views are provided for IHP ((e), (f), (g), (h)), HIS ((i), (j), (k), (l)), and CIT ((m), (n), (o), (p)). Each P and OM is represented in two styles. In the first style, color-coding of atoms: H (white), C (gray), N (blue), O (red), and P (green). In the second style ((b), (d), (f), (h), (j), (l), (p)), P and OM molecules transition from red (start: 0 ns) to blue (end: 20 ns), illustrating their dynamic behavior at the goethite surface.

To thoroughly investigate the impact of OM on P binding, we conducted MD simulations of goethite surfaces covered with a monolayer of either CIT or HIS, each comprising 38 molecules (Fig. 3.15). The results were striking: CIT molecules showed a much stronger adherence to the goethite surface compared to HIS. Specifically, 34-35 CIT molecules remained adsorbed, while only 3-4 diffused into the bulk water. In contrast, 28 HIS molecules remained adsorbed, with 10 diffusing into the bulk water. This pronounced affinity of CIT for the goethite surface is driven by powerful electrostatic interactions, leading to surface dissolution, a phenomenon also observed experimentally by Guppy et al. (2005), which enhances phosphate mobility. CIT and HIS can effectively displace OP and GP from the goethite surface, blocking active sites and promoting P desorption. CIT's superior adsorption capacity results in a stronger inhibitory effect. An unfavorable electric potential was observed at the covered goethite surface in both cases, further hindering anion adsorption. These insights align perfectly with experimental findings, elucidating CIT's potent inhibition of P binding to goethite. This effect is especially pronounced when the surface is pre-covered with OM, as demonstrated by CIT or HIS monolayers on the goethite surface (Fig. 3.15).

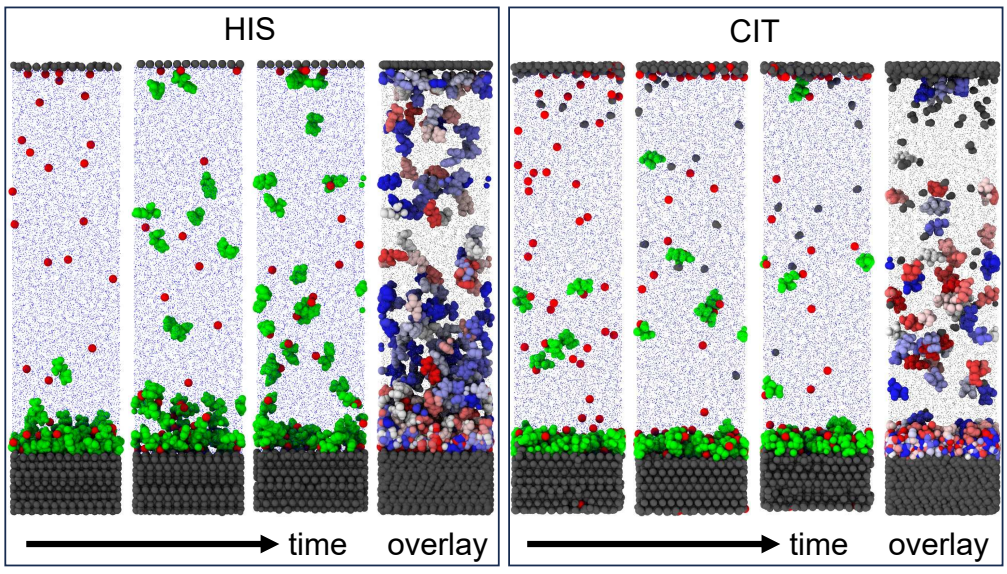


Figure 3.15: MD simulation snapshots showing monolayer adsorption of HIS (left 4 panels) and CIT (right 4 panels) at goethite. The first three panels for each case depict their arrangements: HIS and CIT are visualized in green, goethite in gray, Na^+ ions in red, and water in blue points. Overlays illustrate the overall dynamic behavior, with HIS and CIT transitioning from red (0 ns) to blue (20 ns) while goethite remains gray.

In contrast, our co-adsorption models with CIT or HIS and GP demonstrated that these complexes have a stronger affinity for the goethite surface than the bare GP adsorption. Notably, the GP-HIS complex exhibited even stronger binding to the goethite surface than the GP-CIT complex, resulting in enhanced GP adsorption in the presence of OM, especially HIS. This finding aligns well with experimental observations. Conversely, IHP displayed weaker binding in the presence of HIS during co-adsorption than when adsorbed alone. Ultimately, these results highlight the intricate and varying effects of OM on P binding, consistently corroborating the experimental data.

Our research provides critical insights into the molecular-level influence of OM on P binding at surfaces, impacting P mobility and soil fertility. Future research should explore OM variants with more carboxylate groups, aromatic OM, naturally occurring humic substances and the effects of electrolytes and ionic strength. Understanding inorganic anion roles, characterizing P and OM binding at the goethite-water interface, and assessing sequential adsorption will further enhance knowledge for sustainable soil fertility management and environmental conservation.

3.6 Smart Fertilizers

Smart fertilizers are advanced formulations designed to enhance nutrient delivery efficiency to plants by releasing nutrients in a controlled manner aligned with crop growth stages. This targeted release minimizes nutrient loss through leaching, volatilization, or runoff, thereby improving nutrient uptake and reducing environmental impact (Ghosh et al., 2024). The technologies employed include slow-release coatings, bio-based materials, and nutrient inhibitors, all designed to optimize fertilizer use, boost crop yields, and mitigate negative effects on soil health and water quality. Specifically, P smart fertilizers leverage innovative approaches such as nanotechnology, microbial inoculants, and chelating agents to enhance phosphorus use efficiency. These methods ensure a gradual release of phosphorus, improving its solubility and availability while preventing environmental losses, ultimately promoting sustainable agriculture and increasing crop yields.

In the realm of smart fertilizers, we have explored various innovative strategies to enhance nutrient efficiency. One approach focuses on understanding the competitive binding of phosphates and organic matter to reactive surfaces at the molecular level. Building on Section 3.5, we modeled and simulated the adsorption and desorption processes of various common P compounds across a range of concentrations. Additionally, we examined the co-adsorption and desorption of these P compounds in the presence

of different OM compounds, considering variables like concentrations, electrolyte backgrounds, ionic strengths, pH levels, and temperatures. This comprehensive approach has informed the development of more efficient and sustainable fertilization practices. In another direction, we are modeling phosphate-metal-humic complexes with various metal ions and organic molecular systems. This research aims to identify the most suitable metal ions and organic molecules to design new smart fertilizers, enhancing their effectiveness and sustainability.

A third focus area involves exploring the potential of bone char (BC), a sustainable by-product of the meat industry, as a smart P fertilizer. BC is an excellent phosphorus source, offering a slow-release nutrient that enhances P use efficiency in agricultural soils (Leinweber et al., 2019; Zimmer et al., 2019; Kruse et al., 2022). Its porous structure improves soil aeration and water retention, leading to better crop yields. Integrating BC with innovative technologies such as nanotechnology, microbial inoculants, and chelating agents amplifies its effectiveness, creating smart P fertilizers that meet crop nutrient demands while fostering long-term soil fertility and environmental health. Despite its promise, the molecular-level understanding of BC's role in advanced smart fertilizers remains largely unexplored. By delving into this area, we aim to unlock new insights that will advance sustainable agricultural practices.

In our research, we model BC primarily as hydroxyapatite, both in its crystalline forms and as non-crystalline nanoparticles, including bare BC and sulfur-modified BC (BCplus), with and without organic matter. Our approach involves two main strategies. Firstly, we investigate the dissolution of phosphates from BC, identifying the factors that influence this process. Various electrolyte solutions (e.g., NaCl, KCl, $CaCl_2$) with different ionic strengths (from 0.1 M to 1.0 M), and different inorganic oxyanions and organic matter compounds (e.g., KH_2PO_4, K_2HPO_4, K_2SO_4, K_2CO_3, KHCOO, KCH_3COO, KCH_3S, K_2SO_4 + KH_2PO_4, K_2SO_4 + KCH_3COO) are included in the simulation box. Secondly, we examine the adsorption of phosphate on both bare and sulfur-modified BC, as well as on BC coated with organic material. Our goal is to weaken phosphorus binding on BC surfaces to make it more accessible for plant uptake. A schematic illustration explaining our concept of phosphorus release from BC is depicted in Fig. 3.16.

For instance, our MD simulations demonstrated the effectiveness of organic acids such as formate (HCOO) and sulfur-containing compounds like sulfate (SO_4) and thiolate (e.g., CH_3S) in enhancing BC dissolution, thereby facilitating P release. Fig. 3.17 illustrates the overlay of snapshots depicting the BC dissolution process in water and in 1.0 M solutions of formate, sulfate, and methanethiolate. A 0.1 M KCl + 1.0 M formate solution showed significant efficacy in dissolving BC and releasing P, as shown

by the gradual dissolution dynamics in Fig. 3.18. Our results and ongoing research elucidate conditions that reduce P binding, facilitating its mobilization and availability for plant uptake. This applies to both adsorbed P in minerals and existing P within BC, representing a significant advancement in our understanding of nutrient dynamics at the molecular scale.

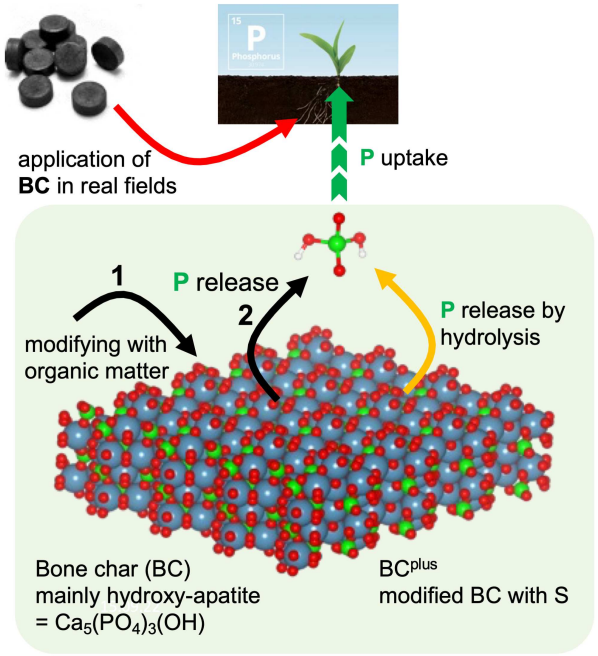


Figure 3.16: Schematic representation of the concept behind designing a smart fertilizer and the controlled dissolution and P release through the application of organic matter or other specific conditions.

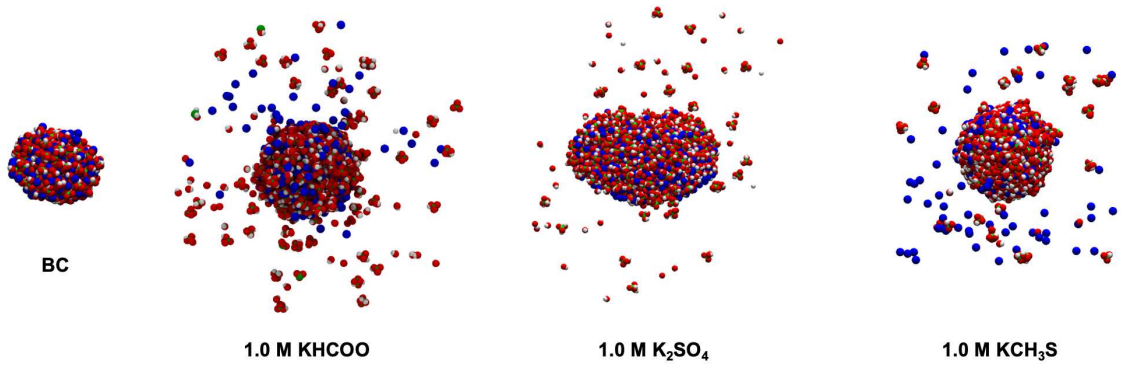


Figure 3.17: Overlay of snapshots along 20 ns MD simulations of the BC dissolution process in water, and a 1.0 M of formate, sulfate, methanethiolate. The atoms are colored green (P), red (O), white (H), and blue (Ca). Water is omitted for clarity.

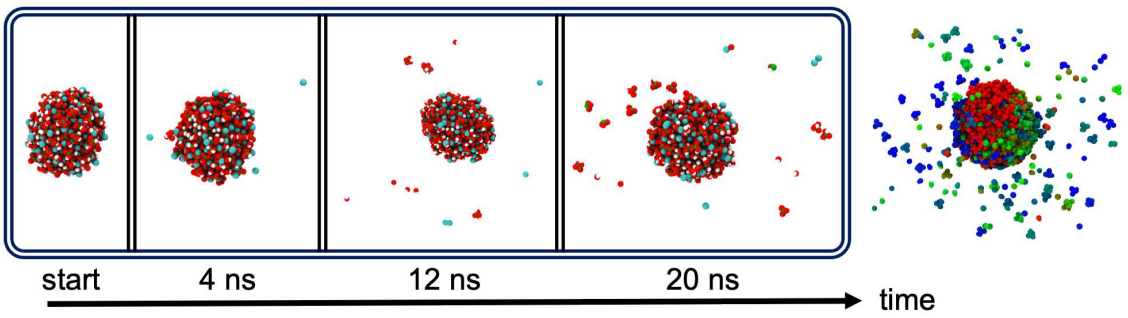


Figure 3.18: Snapshots and overlay of snapshots along 20 ns MD simulations of the BC dissolution process in a 0.1 M KCl + 1.0 M formate (HCOO). For the snapshots, the atoms are colored green (P), red (O), white (H), and cyan (Ca). For the overlay (right), atoms are colored from red (starting of the simulation: 0 ns) to blue (end of the simulation 20 ns). Water molecules are omitted for clarity.

3.7 Environmental Impact of Glyphosate

Glyphosate (GLP, N-(phosphonomethyl)glycine) is among the most extensively used herbicides worldwide, playing a pivotal role in modern agriculture by effectively controlling a wide array of weeds. Despite its widespread use, substantial concerns persist regarding its environmental fate and behavior. Contrary to the prevalent belief that GLP degrades swiftly or is strongly adsorbed by soil particles, evidence indicates that GLP can persist in soil for years post-application and can be detected in water at concentrations exceeding legal limits. This persistence and mobility prompt critical questions about its interactions with various soil constituents, such as soil organic matter (SOM), metal ions, and mineral surfaces.

Understanding the molecular-level interactions between GLP and soil components is essential for several reasons. Firstly, the binding mechanisms and stability of GLP with SOM, metal ions, and mineral surfaces dictate its environmental mobility, bioavailability, and potential for leaching into water bodies. Secondly, these interactions can significantly influence GLP's degradation pathways and its half-life in the environment. Thirdly, gaining insights into these mechanisms can aid in developing better strategies for mitigating GLP's environmental impact and enhancing its management in agricultural practices. Additionally, accurately detecting GLP in environmental samples is crucial for monitoring its presence and assessing its ecological impact. Standard detection methods, often involving derivatization with 9-fluorenylmethyloxycarbonyl chloride (FMOC-Cl), can be affected by interfering substances such as peptides and metal ions, leading to significant overestimations or underestimations of GLP concentrations and

complicating the assessment of its environmental levels.

To address these critical issues and elucidate the binding mechanisms, stability, and environmental behavior of GLP, we conducted an extensive investigation into the interactions of GLP with SOM, metal ions, and mineral surfaces using a combined experimental-theoretical approach. Furthermore, we examined the effects of metal ions and peptides on GLP detection to improve the accuracy of environmental monitoring methods. This research offers valuable insights into the environmental dynamics of GLP, contributing to more effective management practices and ensuring the protection of both environmental and human health.

3.7.1 Glyphosate Interactions in Soil

For the GLP-SOM interaction, our research involved batch sorption experiments with 23 meticulously characterized arable surface soils. We correlated the isotherm coefficients with various inorganic and organic soil parameters to gain deeper insights into the binding mechanisms. Additionally, we investigated the molecular-level interactions between GLP and a specially developed SOM test set (Gros et al., 2017). This test set, comprising over 30 molecules representing the most abundant functional groups in SOM, was created using extensive characterization and analysis of numerous soil samples through pyrolysis field-ionization mass spectrometry (Py-FIMS) and x-ray absorption near-edge spectroscopy (XANES) (Ahmed et al., 2012, 2014). Our approach enabled us to examine interactions on three levels: individual SOM functional groups (small organic molecules), SOM compound classes (or building blocks), and the entire SOM. Detailed information on the molecular modeling approach and methodology can be found in Gros et al. (2017).

Our findings revealed that binding strength, as indicated by Freundlich constants, is positively correlated with clay/silt content, organic carbon (C_{org}) content, and various SOM building blocks such as carbohydrates (CHYDR), phenols/lignin monomers (PHLM), lignin dimers (LDIM), lipids (LIPID), alkylaromatics (ALKY), non-amide nitrogen-containing compounds (NCOMP), amides (PEPTI), and sterols (STEROL). Quantum-chemical modeling showed that GLP binds more strongly to polar organic molecules than to non-polar ones. Furthermore, both the GLP phosphonic and carboxylic functional groups form HBs with polar SOM functional groups, with the phosphonic moiety being particularly critical in GLP-SOM interactions.

We further explored the interaction mechanisms between GLP and SOM building blocks, highlighting the roles of polarity, electron density, and attack sites of SOM

fragments in GLP-SOM binding (see Fig. 3.19). By combining the partial binding energies of GLP with SOM building blocks, we calculated the total binding energy of GLP to the entire SOM, taking into account the mass spectrometrically quantified compound classes for each soil sample. The strong positive correlation between these total binding energies and C_{org} values provides compelling new experimental-theoretical evidence of the critical role SOM plays in GLP binding and its environmental behavior.

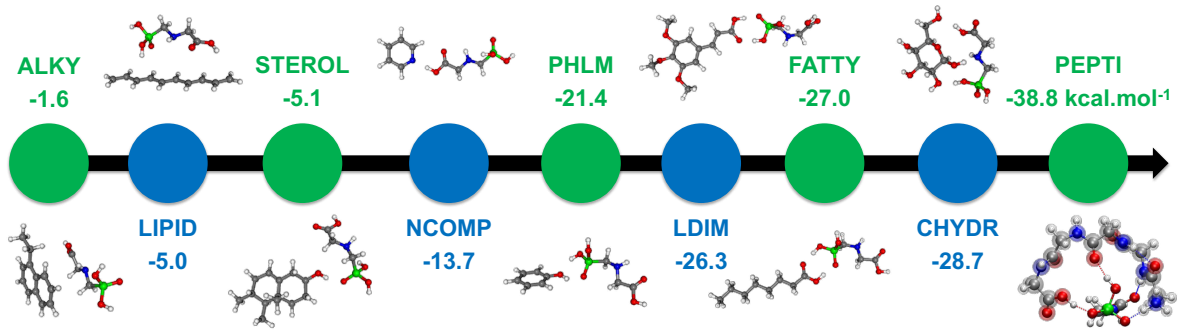


Figure 3.19: Schematic representation summarizes the GLP–SOM interaction and the binding order of GLP with the SOM compound classes. According to the Py-FIMS interpretation, SOM may include phenols + lignin monomers (PHLM), alkyl aromatics (ALKY), carbohydrates (CHYDR), heterocyclic nitrogen-containing compounds (NCOMP), peptides (PEPTI), lipids, alkanes, alkenes, bound fatty acids, and alkyl monoesters (LIPID), free fatty acids (FATTY), sterols (STEROL) and lignin dimers (LDIM).

For the GLP-metal interactions, we conducted an in-depth investigation of the complexation reactions between GLP and major free metal ions present in soil solutions, supplemented with experimental measurements. Our study focused on both divalent metal ions (Mg^{2+}, Ca^{2+}, Fe^{2+}, Mn^{2+}, Co^{2+}, Cu^{2+}, and Zn^{2+}) and trivalent metal ions (Al^{3+}, Fe^{3+}, and Cr^{3+}), examining the formation of various complexes with GLP. These complexes involved multiple binding motifs between the metal ions (M^{n+}) and the amino, carboxylic, and phosphonic groups of GLP (see Fig. 3.20). For each metal ion, we simulated three complexation reactions based on different M^{n+}:GLP stoichiometric ratios: 1 M^{n+} + 1 GLP $\rightarrow$ [M-GLP]$^{n+}$ complex, 1 M^{n+} + 2 GLP $\rightarrow$ [M-2GLP]$^{n+}$, and 1 M^{n+} + 3 GLP $\rightarrow$ [M-3GLP]$^{n+}$. In addition to modeling GLP in its neutral form (and zwitter ion), we also modeled GLP in its charged forms with charges of -1, -2, and -3.

The reaction energies and corresponding free energies for these reactions indicated that the most prevalent binding motif for GLP with free metal ions involved one covalent bond with the GLP carboxylic group and another with the GLP phosphonic group.

In the 1:1 M^{n+}:GLP reaction, the free metal ion completes its coordination by forming additional bonds with surrounding water molecules. Notably, the GLP amino group showed no tendency to participate in covalent bonding with the free metal ions. GLP also demonstrated a propensity to form complexes with multiple GLP molecules, with reaction-free energy increasing in the order of 1 M^{n+}:1 GLP < 1 M^{n+}:2 GLP < 1 M^{n+}:3 GLP. Additionally, trivalent metal ions exhibited stronger interactions with GLP compared to divalent ones. The binding order for GLP complexation with free metal ions across different binding motifs and M^{n+}:GLP stoichiometric ratios is illustrated in Fig. 3.20.

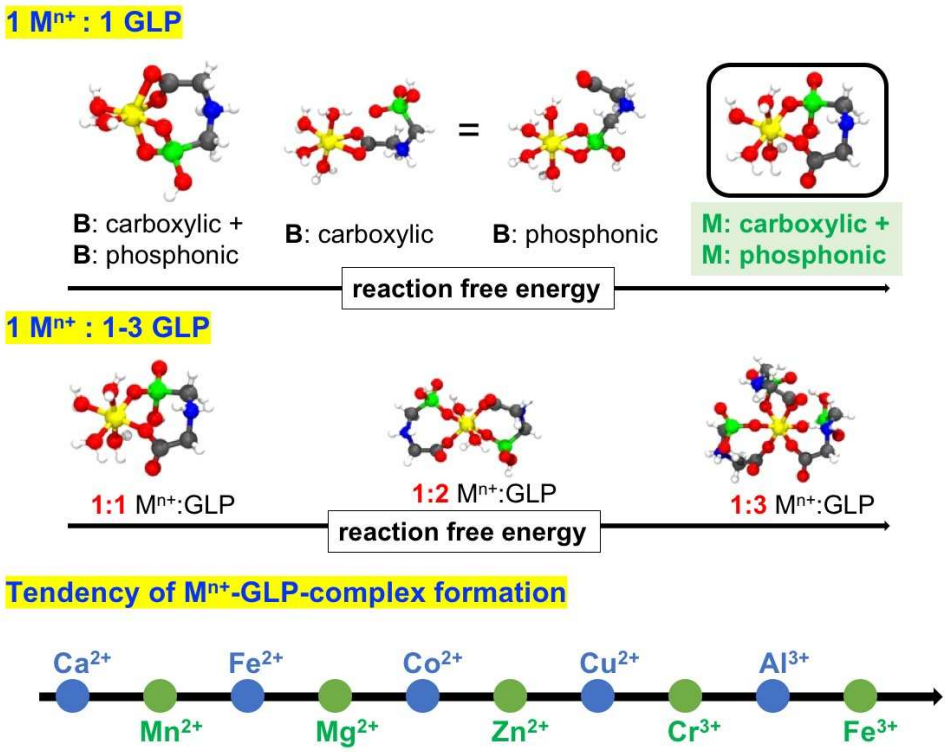


Figure 3.20: Schematic representation summarizes the GLP-metals-interaction and the order of the binding of GLP with the free metal ions.

For the GLP–mineral interactions, our research delved into the dynamics and mechanisms of GLP binding to various goethite surface planes at the molecular scale. Previous studies have not comprehensively explored the intermolecular and intramolecular HBs, the competition between GLP and water molecules for goethite adsorption sites, and the effects of solution pH and water. To address this gap, we investigated the mechanisms and dynamics of different GLP binding motifs on various goethite surface planes using periodic DFT-based MD simulations for the first time (Ahmed et al., 2018b). This study

considered the heterogeneity of goethite nanoparticles in real environmental systems by examining possible binding motifs for GLP on three goethite surface planes (010, 001, and 100) in the presence of water, focusing on **M** and **B** binding motifs (see Fig. 3.21).

The **B** motifs on the three surface planes exhibited distinct binding structures: at the 100 surface, two oxygen atoms of GLP bind to two surface iron atoms (2O + 2Fe); at the 001 surface, one oxygen atom of GLP binds to two iron atoms (1O + 2Fe); and at the 010 surface, two oxygen atoms of GLP bind to one iron atom (2O + 1Fe). The **B** binding motifs were found to be more stable than the **M** ones at the 010 and 001 surfaces, whereas, at the 100 surface plane, the **M** binding motif was stronger. Overall, the binding strength of GLP to goethite in the presence of water followed the order: **M** at 001 < **M** at 010 < **B** at 100 < **M** at 100 < **B** at 001 < **B** at 010. Additionally, MD simulations revealed that neither the GLP amino group nor the carboxylate group significantly contributed to surface complexation, aligning with previous studies. GLP demonstrated stability against dissociation of its C–N and C–P bonds, with calculated distances ranging from 1.46–1.49 Å and 1.83–1.85 Å, respectively, consistent with experimental data indicating high bond stability.

GLP forms dissociative complexes with goethite surfaces through deprotonation, transferring protons to surrounding water and the surface, which enhances interaction energies between GLP and goethite. Some transferred protons remain in contact with their original GLP donating oxygen atoms via HB formation, promoting the formation of **M** binding motifs over **B** motifs. Intramolecular HBs between GLP phosphonate and amino groups further confirm and explain experimental outcomes indicating predominant **M** complexation in the presence of these HBs.

The presence of water also shows strong interactions with goethite surfaces, forming **M** and **B** motifs between water O atoms and surface Fe atoms, dissociating at the surface, and forming intermolecular HBs. The study also simulated the effect of high pH on these interactions by examining the interaction between hydroxide ions (OH^-) and the goethite surface. The results indicate that the binding strength to the goethite surface increases in the order: H_2O < GLP < OH^-. This suggests that while GLP can replace H_2O at the goethite surface, OH^- can replace GLP. This finding explains the significant drop in GLP adsorption observed in experiments at high pH.

In summary, our simulation results provide a comprehensive molecular-level analysis of GLP interactions with SOM, metal ions, mineral surfaces, and water. The inclusion of water molecules in simulations was crucial for accurately depicting GLP binding, particularly at the goethite-water interface. Key findings reveal the intricate dynamics of GLP-SOM interactions, which govern GLP's environmental mobility, bioavailability, and

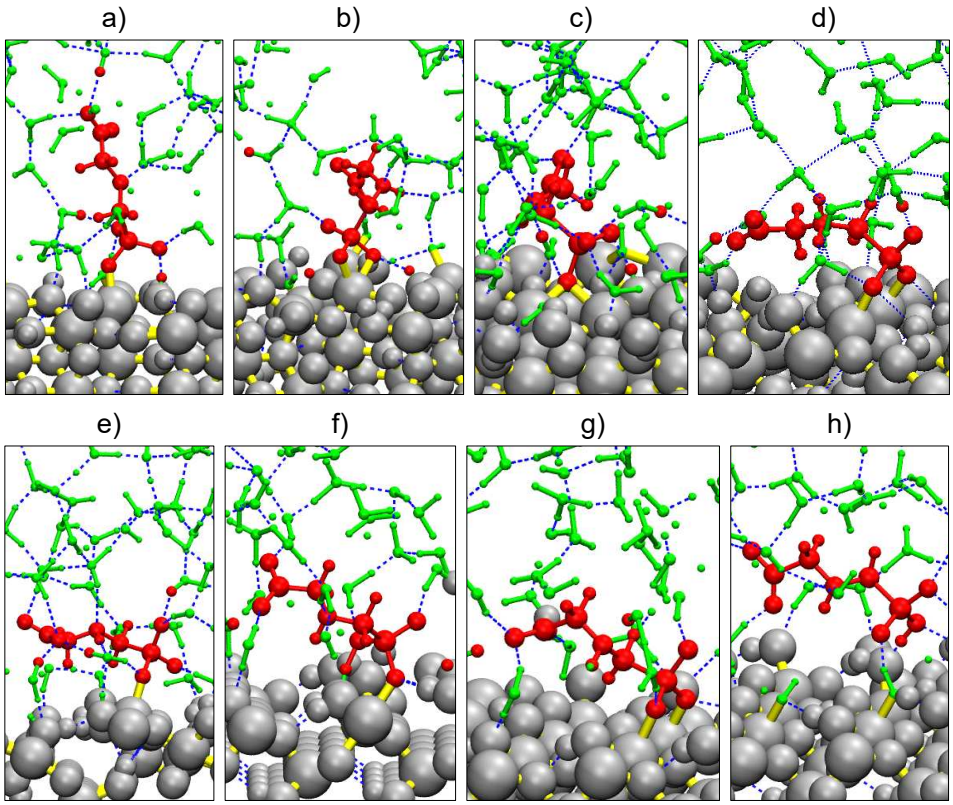


Figure 3.21: Snapshots of equilibrated GLP–goethite–water trajectories: a) **M** motif at the 010 surface plane (**M**@010), b) 2O+1Fe **B**@010, c) 1O+2Fe **B**@001, d) 2O+2Fe **B**@001, e) **M**@001, f) **M**@100, g) 2O+2Fe **B**@100, h) outer-sphere complex at the 100 surface. GLP, goethite, and water atoms are colored in red, silver, and green, respectively. Covalent bonds are shown in yellow, and HBs are in blue.

persistence. This understanding is essential for managing GLP's environmental impact and ensuring sustainable agricultural practices. Additionally, insights into GLP-metal interactions highlight the strength and binding motifs of these interactions, crucial for understanding GLP's environmental behavior. The results also emphasize the importance of surface planes, pH, and water presence in GLP-goethite interactions. Our results show that GLP binds strongly to all soil constituents, with binding strength increasing from SOM to free metal ions to metal oxides or mineral surfaces. Although GLP shows relatively lower binding to SOM, its interaction with HB-providing structures within SOM significantly affects its sorption.

Practical implications include the high complexation potential of inorganic components and organic matter, making it unlikely for GLP to remain free in soil solutions. Instead, GLP can leach through soil profiles in complex forms with SOM building blocks

or organic-mineral particles, explaining its unexpected presence in various environmental compartments. This study provides a comprehensive dataset for GLP sorption in untreated soils, supported by extensive soil characterization for physical and chemical properties. Overall, our findings provide insights into the molecular mechanisms of GLP interactions with soil constituents, which can aid in developing effective strategies for managing GLP's environmental presence and ensuring sustainable agricultural practices.

3.7.2 Impact of Peptides and Metal Ions on Glyphosate Detection

Our investigation into GLP-SOM interactions, particularly with peptides, revealed significant concerns about GLP detection in samples containing peptides (Gros et al., 2017). Typically, GLP detection in environmental samples involves derivatizing the target molecule with the chromophore FMOC-Cl. However, strong interactions with peptides can mask GLP, leading to underestimation. Conversely, FMOC-Cl is sensitive to all primary and secondary amines, potentially causing GLP overestimation. To address these issues, we used well-defined peptides like pentaglycine (PG) and albumin, as well as peptide mixtures like peptone, to quantify the interference on GLP detection (Ahmed et al., 2018a). By adding these peptides to the GLP derivatization solution at varying concentrations and determining UV extinction coefficients, we aimed to elucidate the nature of these interactions. Additionally, we performed quantum chemical modeling to study the interactions among GLP, FMOC-Cl, and peptides, as well as their absorption spectra.

Our analysis, bolstered by quantum chemical modeling, revealed strong interactions between GLP and PG in solution. Both GLP and peptides react similarly with FMOC-Cl, disrupting the GLP derivatization reaction (see Fig. 3.22). This creates two competing effects in environmental samples: peptides can lead to GLP overestimation, while GLP complexation with peptides can cause underestimation. The balance of these effects is unknown and could potentially neutralize each other.

The results showed strong interactions between GLP and PG, leading to underestimation at all studied concentrations. For albumin and peptone, we observed complex behaviors. High concentrations of albumin (16 mg/L) and peptone (32 mg/L) with low GLP concentrations resulted in significant GLP overestimation. Conversely, at high concentrations of both GLP (94.67 mmol/L) and peptides (32 mg/L), we noted GLP underestimation. These findings underscore the critical need for accurate detection methods for GLP in environmental samples, considering the strong interactions with peptides and the potential for both overestimation and underestimation. Our study

highlights the intricate dynamics of GLP-peptide interactions and their implications for environmental monitoring, emphasizing the importance of precise analytical methods in assessing GLP's environmental impact.

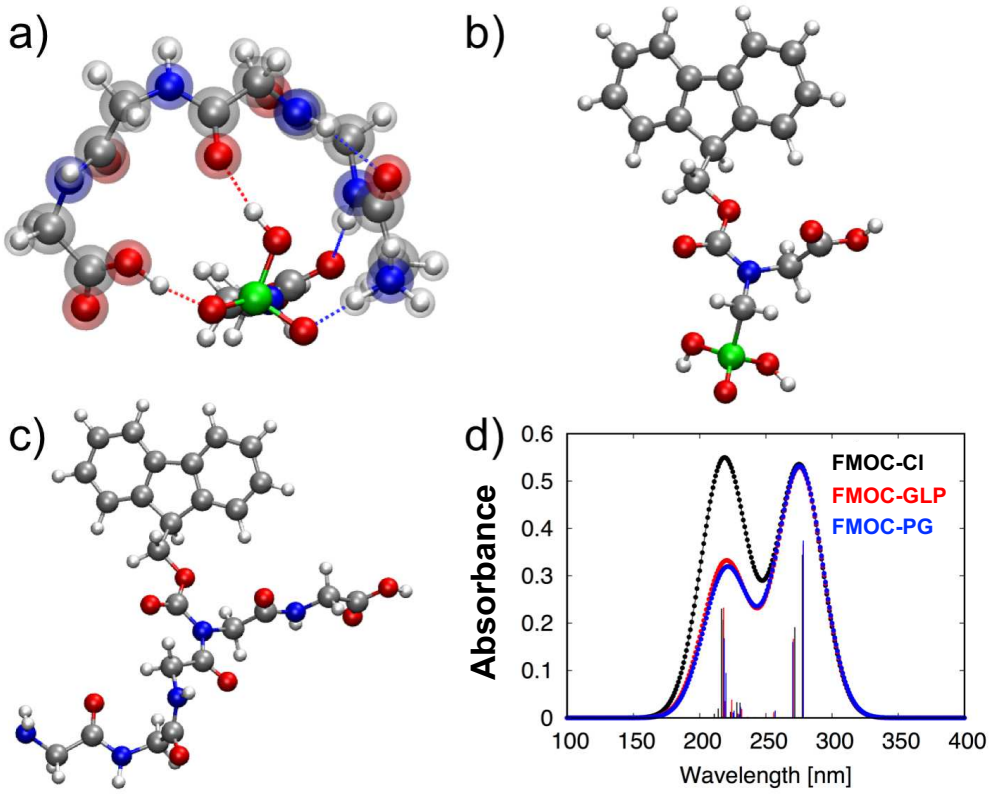


Figure 3.22: Optimized geometries of the GLP–PG a), FMOC–GLP b), and FMOC–PG complexes c) at the DFT/B3LYP/D3/6–311++G(d,p) level of theory and using the CPCM model. For the GLP–PG complex, PG atoms are surrounded by transparent spheres for better visualization of the complex formation. White, gray, blue, red, and green colors are corresponding to H, C, N, O, and P atoms, respectively. Panel d) contains the calculated UV spectra with their electronic transitions for FMOC-Cl and its complexes with GLP and PG at the TD-DFT/B3LYP/6–311++G(d,p)/CPCM level of theory.

Our investigation extended to the influence of metal ions on GLP detection using FMOC-Cl, employing both experimental and theoretical approaches akin to those used for peptides. We conducted photometric measurements of GLP recovery and quantum chemical modeling of reaction energies to study how metal ions inhibit GLP derivatization with FMOC-Cl. We prepared equimolar solutions of GLP and various metal ions (Mg^{2+}, Ca^{2+}, Fe^{2+}, Mn^{2+}, Co^{2+}, Cu^{2+}, Zn^{2+}, Cd^{2+}, Al^{3+}, and Fe^{3+}) and allowed them

to form M–GLP complexes before the derivatization process.

Our experimental results showed low GLP recovery in the presence of Cd^{2+} (19%), Co^{2+} (14%), Cu^{2+} (14%), Mn^{2+} (59%), and Zn^{2+} (20%), suggesting these metal ions form stronger complexes with GLP. In contrast, good recoveries (ranging from 94% to 108%) were observed with Mg^{2+}, Ca^{2+}, Fe^{2+}, Cd^{2+}, Al^{3+}, and Fe^{3+}. The low recoveries for Cd^{2+}, Co^{2+}, Cu^{2+}, Mn^{2+}, and Zn^{2+} suggest strong complex formation with GLP compared to other metals.

We performed quantum chemical modeling of the reaction process between M–GLP complexes and FMOC-Cl to resolve the apparent discrepancy with the generally stronger complexes formed by trivalent metal ions. The calculated reaction free energy (ΔG) indicated that while the reaction between M–GLP complexes and FMOC-Cl is spontaneous, it is less so than the M–GLP complexation reaction, except for Fe^{3+}. This suggests a decrease in the reactivity of FMOC-Cl towards M–GLP complexes compared to free GLP, providing a deeper understanding of the interactions between GLP and metal ions.

In general, M–GLP–FMOC complexes are stable, with the stability and spontaneity of the derivatization reaction increasing in the order: $Ca^{2+} \approx Mg^{2+}$ ($\sim$ -2 kcal/mol) < $Zn^{2+} \approx Mn^{2+} \approx Fe^{2+} \approx Cu^{2+} \approx Co^{2+}$ ($\sim$ -3 kcal/mol) < $Al^{3+} \approx Cr^{3+}$ ($\sim$ -11 kcal/mol) < Fe^{3+} ($\sim$ -32 kcal/mol). This implies that the derivatization reaction of FMOC-Cl with pure GLP and GLP complexes with trivalent metal ions like Fe^{3+} and Al^{3+} proceeds more readily than with GLP complexes involving divalent metal ions. Consequently, pure GLP and GLP complexes with trivalent metal ions are likely detected with higher recoveries than those with divalent metal ions.

This general trend is consistent with our experimental findings, though exceptions exist. Specifically, the low recovery of GLP in the presence of certain divalent metal ions can be attributed to several interacting factors: (i) a slow and incomplete reaction between the M-GLP complex and FMOC-Cl, (ii) potential formation of precipitates from the M-GLP complex, leading to decreased recovery, and (iii) changes in the UV peak position or a decrease in peak intensity due to interactions between some metals and the FMOC-Cl chromophore. These insights highlight the complexities involved in GLP detection in the presence of various metal ions and emphasize the need for careful consideration of these interactions in environmental analysis.

In conclusion, our study reveals that peptide type and concentration, as well as specific metal ions, significantly impact GLP detection in environmental samples using FMOC-Cl derivatization. Environmental matrices such as soil, water, vegetables, and fruits often contain elements that inhibit GLP derivatization, leading to potential underestimation of GLP levels, as demonstrated by low recoveries in a round-robin groundwater study

(Reichert et al., 2006). Our experimental and theoretical results confirm that adding EDTA before derivatization, rather than adjusting pH, ensures full GLP recovery. These findings highlight the need for more robust GLP detection methods in complex environmental matrices to ensure accurate monitoring and assessment of its environmental impact, thereby improving our understanding of GLP's behavior and persistence in the environment.

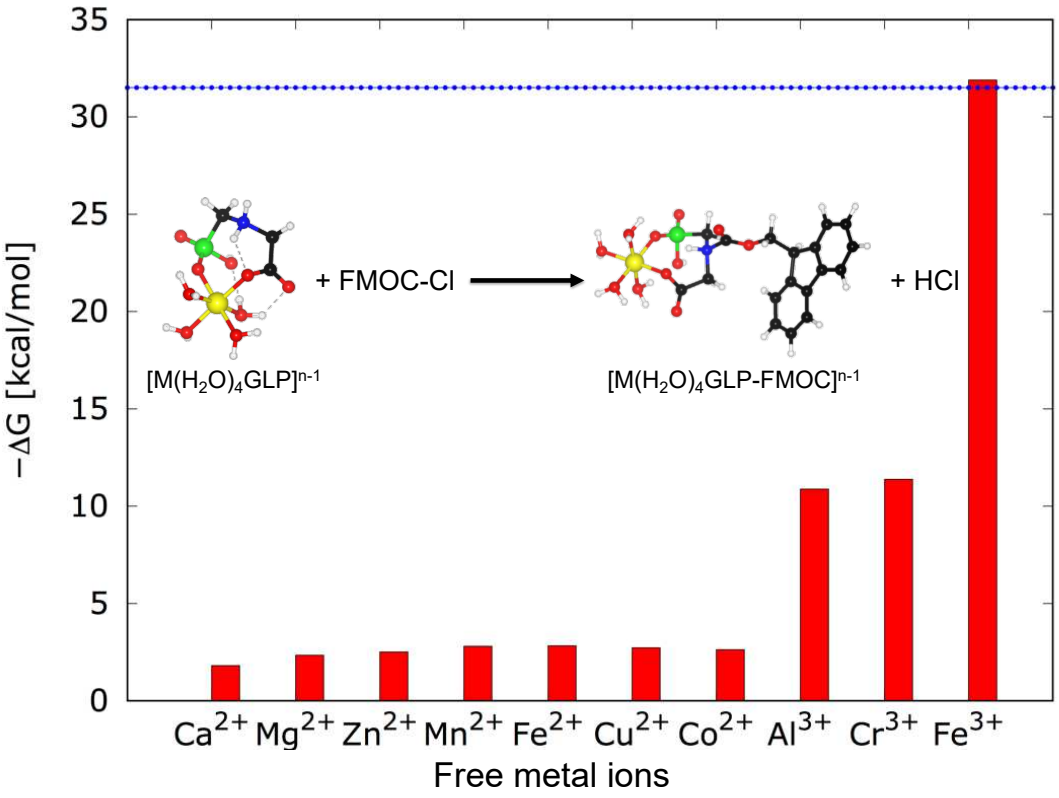


Figure 3.23: Calculated reaction free energies (ΔG) in kcal/mol for the derivatization reaction o FMOC-Cl with the metal–GLP complexes for different metal ions at the DFT/B3LYP/D3/6–311++G(d,p) level of theory. The blue line refers to the free energy of the derivatization reaction of FMOC-Cl with pure GLP. White, black, blue, red, green, and yellow colors correspond to H, C, N, O, P, and metal atoms, respectively.

4 Summary and Conclusions

Complementary to extensive experimental studies, my habilitation thesis underscores the powerful application of computational chemistry (**CC**) and molecular modeling to provide a molecular-level understanding of phosphorus (P) binding in soil, aiding the development of effective soil management practices. This work examines key factors controlling P binding processes and their strength, including the type and species of P-containing compounds, soil constituent quality and quantity, mineral surfaces and planes, surface morphology and saturation, binding motifs, water and electrolytes, solution pH, initial P concentration or surface loading, complexation versus precipitation, organic acids, central metal ions, and redox potential. Additionally, it highlights the concepts of smart fertilizers, particle dissolution, and P release under controlled conditions. The thesis also addresses glyphosate (GLP) interactions with soil constituents, resolving uncertainties regarding its detection.

In general, phosphate binds more strongly to metal ions and mineral surfaces than to organic matter (OM). For binding to OM, dispersion interactions and hydrogen bonds (HBs) are the main contributors. Conversely, phosphate binds to metal ions and mineral surfaces through inner-sphere complexes (covalent/coordination bonds) with significant contributions from both HBs and dispersion interactions. Therefore, P bound to soil organic matter (SOM) is expected to be more available and mobile compared to P bound to metal ions and mineral surfaces. This implies that phosphate binds more strongly to soils rich in pedogenic oxides. Furthermore, phosphate binding to soil constituents, especially metal ions and metal oxides, is weaker under reducing conditions (low E_h) compared to oxidizing conditions. Thus, more available P is anticipated under reducing conditions, such as during flooding.

Surface complexation is generally more dominant than precipitation on mineral surfaces. Although the precipitation of free metal ions with phosphate occurs spontaneously, it is less favorable than surface complexation. If free metal ions are present, precipitation can happen concurrently with or after surface complexation. In the absence of free metal ions, precipitation requires the energetically costly detachment of Fe atoms/ions from the goethite surface. Considering surface complexation, goethite (α-FeOOH)

generally binds phosphates more strongly than diaspore (α-AlOOH), especially for all **M** motifs. However, specific surface and adsorbate properties can make diaspore bind phosphates stronger. The surface morphology, particularly the positions of surface metal ions, influences the binding process and controls the motifs and their strength. Favorable alignment of surface metal positions with phosphate oxygen atoms enhances the formation of certain inner-sphere complexes, while misalignment can strain covalent bonds within phosphate-mineral complexes, sometimes leading to dissociation. For instance, orthophosphate (OP) favors forming the (2O + 1Fe) **B** binding motif at the 010-goethite surface plane and the (2O + 2Fe) **B** motif at the 100-surface plane.

Phosphate adsorption is significantly influenced by the type and number of phosphate groups in the interacting species. Phosphates with single phosphate groups, such as OP and glycerolphosphate (GP), can form stable **M** and **B** motifs, but the dominant motif varies based on surface loading, mineral surface nature, surface plane, and pH. More saturated surfaces generally exhibit weaker phosphate interactions. The polar organic moiety of GP interacts with surrounding water molecules, potentially hindering phosphate-mineral surface interactions and affecting binding motif stability. Phosphates with multiple phosphate groups, such as inositolhexaphosphate (IHP), bind to mineral surfaces through multiple groups, forming stable binding motifs like **M**, 2**M**, and 3**M**, with the latter two being dominant for IHP. IHP's intramolecular HBs between adjacent phosphate groups can induce strain and lead to dissociation of covalent bonds, destabilizing motifs like **B** and 4**M**. IHP binds more strongly to mineral surfaces than monophosphates (OP and GP), with binding strength increasing in the order GP < OP < IHP. The negative charge induced by phosphates at the surface also increases in this order, which may explain the decreasing binding strength of new incoming phosphate molecules in the order IHP < GP < OP on surfaces already covered with phosphate molecules.

Water plays a crucial role in phosphate binding at mineral surfaces through HB formation, surface dissociation producing H^+ and OH^- ions, proton transfer processes, and covalent/coordination bond formation. Proton transfer from phosphates to water can acidify the solution, indicating potential soil acidity from P-fertilization. Intermolecular HBs between phosphates (GP and IHP) and water molecules introduce strain into phosphate-mineral complexes, leading to binding motif instability, correlated with the water-accessible surface area of the phosphate species. The interaction energies follow the order: water < GP < OP < IHP. This suggests phosphates can replace water at these surfaces, with IHP replacing OP and GP, explaining IHP's abundance as organically bound phosphate in soil due to its stronger binding to mineral surfaces.

Our molecular modeling and simulations reveal the significant influence of pH on P binding and mobilization in soil. The effect varies among soil constituents. For free metal ions, P binding increases with rising pH, while for OM and mineral surfaces, P binding generally decreases with increasing pH. At mineral surfaces, an initial increase in phosphate adsorption is often followed by a significant drop, particularly at pH levels above the point of zero charge (PZC). These findings suggest that higher pH promotes P release from OM and metal oxides, whereas lower pH facilitates P release from free metal ions. Thus, P binding in soil is heavily influenced by the type and quantity of soil constituents and the solution pH.

pH significantly affects binding motifs at mineral surfaces. At very low and high pH, the **M** motif predominates for OP on goethite surface planes, while the **B** motif is more common at intermediate pH levels. Calculated IR spectra show a **B**:**M** ratio of 8:1, suggesting that comprehensive analyses, including multiple motifs, are necessary for accurate theory-experiment comparisons. For the P-goethite system, the best match with experimental spectra was achieved by considering both **B**@010 and **M**@100 motifs, with a higher proportion of **B**@010. This approach helps resolve debates on binding motifs and characterizing experimental IR spectra. Additionally, our simulations indicate that the **M** motif becomes more prevalent at high P surface loadings, though the **B** motif remains significantly present.

Our research provides valuable insights into the competition between OM, specifically citric acid (CIT)) and histidine (HIS), and P at the goethite-water interface. Through a combined experimental-theoretical approach, we revealed how P adsorption is influenced by the chemical structures of P and OM, treatment conditions, initial P concentrations, and electrostatic environments. We found that the binding strength of P and OM compounds with goethite follows the order: GP $<$ OP $<$ HIS $<$ CIT $<$ IHP, with IHP showing the strongest binding due to its multi-phosphate structure. Consequently, OM significantly inhibits OP adsorption, with CIT reducing it by 70% when pre-covered on the surface. GP adsorption varies with specific OM treatments, while IHP shows reduced adsorption primarily at higher P concentrations. CIT and HIS exhibit a higher affinity for goethite surfaces than OP and GP, effectively competing and replacing them. Conversely, OM's impact on IHP adsorption is minimal due to IHP's higher affinity for goethite. OM coverage blocks active sites and generates unfavorable electric potentials, reducing P binding. In the context of smart fertilizers, our findings demonstrated the effectiveness of organic acids like formate and sulfur-containing compounds such as sulfate and thiolate in enhancing bone char (BC) dissolution and facilitating P release. These findings could help develop strategies to enhance P availability, minimize leaching, and

mitigate the environmental impact of P fertilization. Managing OM in soils can control P mobility and bioavailability, improving soil fertility and protecting water quality.

Despite extensive research, significant challenges remain in understanding P adsorption and release dynamics. Future studies should explore OM variants with diverse functional groups, such as aliphatic and aromatic compounds with multiple carboxylate groups, and naturally occurring humic substances. Key areas for further investigation include the effects of electrolytes and ionic strength, understanding the role of inorganic anions, characterizing P and OM binding at the mineral-water interface, and assessing sequential adsorption by P and OM. Additionally, understanding how microbes and plants overcome strong P-mineral binding, binding mechanisms of other oxyanions at soil-reactive surfaces, temperature dependence of P binding, and simulating P-adsorption isotherms and kinetics, and modeling complex soil systems are crucial. Developing new smart P fertilizers from bio-available materials like bare and modified BC and phosphate-metal-humic complexes is vital. Addressing these issues will enhance our understanding of P binding, promote its mobilization and availability for plant uptake, and inform sustainable agricultural practices and environmental conservation. Integrating experimental and theoretical approaches will significantly advance effective soil fertility management.

The complexity of soil as a heterogeneous medium, composed of a mixture of organic and inorganic components of varying sizes, presents a formidable challenge. Molecular models must account for this complexity by focusing on a range of setups designed through chemical intuition. While this may not fully capture the statistical complexity of soil, **CC** has already significantly advanced our understanding of soil processes and their dependence on chemical conditions. The next step is to scale from microscopic to macroscopic molecular systems and connect to mesoscale diffusion processes by developing coarse-grained models capable of studying more complex processes in the soil environment. Suitable computational tools exist, and models based on lessons learned from atomistic and molecular-level simulations need to be developed. This approach will provide innovative insights into the molecular-level understanding of complex systems like soil, incorporating organic matter, minerals, and free metal ions.

In conclusion, by gathering insights from atomistic simulations, addressing key challenges, leveraging joint advanced experimental and theoretical approaches, and involving multidisciplinary efforts, we can enhance P availability in soils, minimize leaching, and mitigate the environmental impact of P fertilization. This will not only improve soil fertility but also protect water quality, advancing sustainable agricultural practices and environmental conservation.

Bibliography

Abdala, D. B., Northrup, P. A., Arai, Y., and Sparks, D. L. (2015). Surface loading effects on orthophosphate surface complexation at the goethite/water interface as examined by extended X-ray Absorption Fine Structure (EXAFS) spectroscopy. *J. Colloid Interface Sci.* 437, 297–303. doi:10.1016/j.jcis.2014.09.057

Acelas, N. Y., Mejia, S. M., Mondragón, F., and Flórez, E. (2013). Density functional theory characterization of phosphate and sulfate adsorption on Fe-(hydr)oxide: Reactivity, pH effect, estimation of Gibbs free energies, and topological analysis of hydrogen bonds. *Comput. Theor. Chem.* 1005, 16–24. doi:10.1016/j.comptc.2012.11.002

Ahmed, A. A., Gros, P., Kühn, O., and Leinweber, P. (2018a). Molecular level investigation of the role of peptide interactions in the glyphosate analytics. *Chemosphere* 196, 129–134

Ahmed, A. A., Gypser, S., Freese, D., Leinweber, P., and Kühn, O. (2020). Molecular level picture of the interplay between pH and phosphate binding at the goethite–water interface. *Phys. Chem. Chem. Phys.* 22, 26509–26524. doi:10.1039/D0CP04698A

Ahmed, A. A., Gypser, S., Leinweber, P., Freese, D., and Kühn, O. (2019). Infrared spectroscopic characterization of phosphate binding at the goethite–water interface. *Phys. Chem. Chem. Phys.* 21, 4421–4434

Ahmed, A. A., Kühn, O., Aziz, S. G., Hilal, R. H., and Leinweber, P. (2014). How soil organic matter composition controls hexachlorobenzene-soil-interactions: Adsorption isotherms and quantum chemical modeling. *Sci. Total Environ.* 476-477C, 98–106

Ahmed, A. A., Kühn, O., and Leinweber, P. (2012). Controlled experimental soil organic matter modification for study of organic pollutant interactions in soil. *Sci. Total Environ.* 441, 151–158

Ahmed, A. A., Kühn, O., Hilal, R. H., and Shibl, M. F. (2013). Structure and cooperativity of the hydrogen bonds in sodium dihydrogen triacetate. *Int. J. Quantum Chem.* 113, 1394–1400. doi:10.1002/qua.24328

Ahmed, A. A., Leinweber, P., and Kühn, O. (2018b). Unravelling the nature of glyphosate binding to goethite surfaces by *ab initio* molecular dynamics simulations. *Phys. Chem. Chem. Phys.* 20, 1531–1539

Ahmed, A. A., Leinweber, P., and Kühn, O. (2023). Advances in understanding the phosphate binding to soil constituents: A computational chemistry perspective. *Sci. Total Environ.* 887, 163692. doi:10.1016/j.scitotenv.2023.163692

Ahmed, A. A., Morshedizad, M., Kühn, O., and Leinweber, P. (2024). Deciphering competitive interactions: Phosphate and organic matter binding on goethite through experimental and theoretical insights. *Sci. Total Environ.* 940, 173510. doi:10.1016/j.scitotenv.2024.173510

Ahmed, A. A., Thiele-Bruhn, S., Aziz, S. G., Hilal, R. H., Elroby, S. A., Al-Youbi, A. O., et al. (2015). Interaction of polar and nonpolar organic pollutants with soil organic matter: Sorption experiments and molecular dynamics simulation. *Sci. Total Environ.* 508C, 276–287

Alam, M. M., Srinivasan, V., Mueller, A. V., and Gu, A. Z. (2021). Status and advances in technologies for phosphorus species detection and characterization in natural environment- A comprehensive review. *Talanta* 233, 122458. doi:10.1016/j.talanta.2021.122458

Amadou, I., Faucon, M.-P., and Houben, D. (2022). Role of soil minerals on organic phosphorus availability and phosphorus uptake by plants. *Geoderma* 428, 116125. doi:10.1016/j.geoderma.2022.116125

Anderson, G. and Arlidge, E. Z. (1962). The adsorption of inositol phosphates and glycerophosphate by soil clays, clay minerals, and hydrated sesquioxides in acid media. *J. Soil Sci.* 13, 216–224. doi:10.1111/j.1365-2389.1962.tb00699.x

Andersson, K. O., Tighe, M. K., Guppy, C. N., Milham, P. J., McLaren, T. I., Schefe, C. R., et al. (2016). XANES demonstrates the release of calcium phosphates from alkaline vertisols to moderately acidified solution. *Environ. Sci. Technol.* 50, 4229–4237. doi:10.1021/acs.est.5b04814

Antelo, J., Avena, M., Fiol, S., López, R., and Arce, F. (2005). Effects of pH and ionic strength on the adsorption of phosphate and arsenate at the goethite–water interface. *J. Colloid Interface Sci.* 285, 476–486. doi:10.1016/j.jcis.2004.12.032

Arai, Y. and Sparks, D. (2001). ATR–FTIR Spectroscopic Investigation on Phosphate Adsorption Mechanisms at the Ferrihydrite–Water Interface. *J. Colloid Interface Sci.* 241, 317–326. doi:10.1006/jcis.2001.7773

Arai, Y. and Sparks, D. (2007). Phosphate Reaction Dynamics in Soils and Soil Components: A Multiscale Approach. In *Advances in Agronomy* (Elsevier), vol. 94. 135–179. doi:10.1016/S0065-2113(06)94003-6

Arroyave, J. M., Puccia, V., Zanini, G. P., and Avena, M. J. (2018). Surface speciation of phosphate on goethite as seen by InfraRed Surface Titrations (IRST). *Spectrochim. Acta. A. Mol. Biomol. Spectrosc.* 199, 57–64. doi:10.1016/j.saa.2018.03.043

Barone, V. and Cossi, M. (1998). Quantum Calculation of Molecular Energies and Energy Gradients in Solution by a Conductor Solvent Model. *J. Phys. Chem. A* 102, 1995–2001. doi:10.1021/jp9716997

Barrow, N., Bowden, J., Posner, A., and Quirk, J. (1980). Describing the effects of electrolyte on adsorption of phosphate by a variable charge surface. *Soil Res.* 18, 395. doi:10.1071/SR9800395

Barrow, N. J. (1972). Influence of solution concentration of calcium on the adsorption of phosphate, sulfate, and molybdate by soils. *Soil Science* 113

Barrow, N. J. (1983). A mechanistic model for describing the sorption and desorption of phosphate by soil. *J. Soil Sci.* 34, 733–750. doi:10.1111/j.1365-2389.1983.tb01068.x

Barrow, N. J. and Shaw, T. C. (1979). Effects of ionic strength and nature of the cation on desorption of phosphate from soil. *Journal of Soil Science* 30, 53–65. doi:10.1111/j.1365-2389.1979.tb00964.x

Baumann, K., Nastah, S., Shaheen, S. M., Rinklebe, J., and Leinweber, P. (2020a). Phosphorus cycling and spring barley crop response to varying redox potential. *Vadose zone j.* 19. doi:10.1002/vzj2.20088

Baumann, K., Shaheen, S. M., Hu, Y., Gros, P., Heilmann, E., Morshedizad, M., et al. (2020b). Speciation and sorption of phosphorus in agricultural soil profiles of redoximorphic character. *Environ Geochem Health* 42, 3231–3246. doi:10.1007/s10653-020-00561-y

Belelli, P. G., Fuente, S. A., and Castellani, N. J. (2014). Phosphate adsorption on goethite and Al-rich goethite. *Comput. Mater. Sci.* 85, 59–66. doi:10.1016/j.commatsci.2013.12.030

Borggaard, O., Szilas, C., Gimsing, A., and Rasmussen, L. (2004). Estimation of soil phosphate adsorption capacity by means of a pedotransfer function. *Geoderma* 118, 55–61. doi:10.1016/S0016-7061(03)00183-6

Borggaard, O. K. (2001). *Soil chemistry in a pedological context* (Royal Veterinary and Agricultural University), 5. rev. ed edn. OCLC: 476766674

Boukemara, L., Boukhalfa, C., Reinert, L., and Duclaux, L. (2016). Characterization of Phosphate Adsorption on Goethite Macroscopic and Spectroscopic Analyses. *J. Mater. Environ. Sci.* 7, 2541–2550

Bowden, J., Nagarajah, S., Barrow, N., Posner, A., and Quirk, J. (1980). Describing the adsorption of phosphate, citrate and selenite on a variable-charge mineral surface. *Soil Res.* 18, 49. doi:10.1071/SR9800049

Boys, S. and Bernardi, F. (1970). The calculation of small molecular interactions by the differences of separate total energies. Some procedures with reduced errors. *Mol. Phys.* 19, 553–566. doi:10.1080/00268977000101561

Catalano, J. G. (2011). Weak interfacial water ordering on isostructural hematite and corundum (001) surfaces. *Geochim. Cosmochim. Acta* 75, 2062–2071. doi:10.1016/j.gca.2011.01.025

Chapman, A. and Thirlwell, L. (1964). Spectra of phosphorus compounds—I the infra-red spectra of orthophosphates. *Spectrochim. Acta* 20, 937–947. doi:10.1016/0371-1951(64)80094-1

Chitrakar, R., Tezuka, S., Sonoda, A., Sakane, K., Ooi, K., and Hirotsu, T. (2006). Phosphate adsorption on synthetic goethite and akaganeite. *J. Colloid Interface Sci.* 298, 602–608. doi:10.1016/j.jcis.2005.12.054

Cordell, D., Drangert, J.-O., and White, S. (2009). The story of phosphorus: Global food security and food for thought. *Glob. Environ. Change* 19, 292–305. doi:10.1016/j.gloenvcha.2008.10.009

Cordell, D. and White, S. (2011). Peak Phosphorus: Clarifying the Key Issues of a Vigorous Debate about Long-Term Phosphorus Security. *Sustainability* 3, 2027–2049. doi:10.3390/su3102027

Cornell, R. M. and Schwertmann, U. (2003). *The Iron Oxides: Structure, Properties, Reactions, Occurrences, and Uses* (Weinheim: Wiley-VCH), 2nd, completely rev. and extended ed edn.

Cossi, M., Rega, N., Scalmani, G., and Barone, V. (2003). Energies, structures, and electronic properties of molecules in solution with the C-PCM solvation model. *J. Comput. Chem.* 24, 669–681. doi:10.1002/jcc.10189

Cramer, C. J. (2004). *Essentials of Computational Chemistry: Theories and Models* (Chichester, West Sussex, England ; Hoboken, NJ: Wiley), 2nd ed edn.

Cygan, R. T., Liang, J.-J., and Kalinichev, A. G. (2004). Molecular Models of Hydroxide, Oxyhydroxide, and Clay Phases and the Development of a General Force Field. *J. Phys. Chem. B* 108, 1255–1266. doi:10.1021/jp0363287

De Groot, C. J. and Golterman, H. L. (1993). On the presence of organic phosphate in some Camargue sediments: Evidence for the importance of phytate. *Hydrobiologia* 252, 117–126. doi:10.1007/BF00000133

Dettmann, L. F., Kühn, O., and Ahmed, A. A. (2024). Martini-based coarse-grained soil organic matter model derived from atomistic simulations. *J. Chem. Theory Comput.* 20, 5291–5305. doi:10.1021/acs.jctc.4c00332

Di Iorio, E., Circelli, L., Angelico, R., Torrent, J., Tan, W., and Colombo, C. (2022). Environmental implications of interaction between humic substances and iron oxide nanoparticles: A review. *Chemosphere* 303, 135172. doi:10.1016/j.chemosphere.2022.135172

Dougherty, W. J., Smernik, R. J., and Chittleborough, D. J. (2005). Application of spin counting to the solid-state ^{31} p NMR analysis of pasture soils with varying phosphorus content. *Soil Sci. Soc. Am. J.* 69, 2058–2070. doi:10.2136/sssaj2005.0017

Edixhoven, J. D., Gupta, J., and Savenije, H. H. G. (2013). Recent revisions of phosphate rock reserves and resources: reassuring or misleading? an in-depth literature review of global estimates of phosphate rock reserves and resources. *Earth System Dynamics Discussions* 4, 1005–1034. doi:10.5194/esdd-4-1005-2013

El-Naggar, A., Shaheen, S. M., Ok, Y. S., and Rinklebe, J. (2018). Biochar affects the dissolved and colloidal concentrations of Cd, Cu, Ni, and Zn and their phytoavailability and potential mobility in a mining soil under dynamic redox-conditions. *Sci. Total Environ.* 624, 1059–1071. doi:10.1016/j.scitotenv.2017.12.190

Elstner, M., Porezag, D., Jungnickel, G., Elsner, J., Haugk, M., Frauenheim, T., et al. (1998). Self-consistent-charge density-functional tight-binding method for simulations of complex materials properties. *Phys. Rev. B* 58, 7260–7268. doi:10.1103/PhysRevB.58.7260

Elzinga, E. J. and Sparks, D. L. (2007). Phosphate adsorption onto hematite: An in situ ATR-FTIR investigation of the effects of pH and loading level on the mode of phosphate surface complexation. *Journal of Colloid and Interface Science* 308, 53–70. doi:10.1016/j.jcis.2006.12.061

Fiedler, S., Vepraskas, M. J., and Richardson, J. (2007). Soil Redox Potential: Importance, Field Measurements, and Observations. In *Advances in Agronomy* (Elsevier), vol. 94. 1–54. doi:10.1016/S0065-2113(06)94001-2

[Software] Frisch, M. J., Trucks, G. W., Schlegel, H. B., Scuseria, G. E., Robb, M. A., Cheeseman, J. R., et al. (2016). Gaussian Inc. Wallingford CT 2016

Frohne, T., Rinklebe, J., Diaz-Bone, R. A., and Du Laing, G. (2011). Controlled variation of redox conditions in a floodplain soil: Impact on metal mobilization and biomethylation of arsenic and antimony. *Geoderma* 160, 414–424. doi:10.1016/j.geoderma.2010.10.012

Ganta, P. B., Kühn, O., and Ahmed, A. A. (2019). QM/MM simulations of organic phosphorus adsorption at the diaspore–water interface. *Phys. Chem. Chem. Phys.* 21, 24316–24325

Ganta, P. B., Kühn, O., and Ahmed, A. A. (2020a). Ab Initio Molecular Dynamics Simulations of the Interaction between Organic Phosphates and Goethite. *Molecules* 26, 160. doi:10.3390/molecules26010160

Ganta, P. B., Kühn, O., and Ahmed, A. A. (2020b). QM/MM Molecular Dynamics Investigation of the Binding of Organic Phosphates to the 100 Diaspore Surface. *Front. For. Glob. Change* 3, 71

Ganta, P. B., Morshedizad, M., Kühn, O., Leinweber, P., and Ahmed, A. A. (2021). The Binding of Phosphorus Species at Goethite: A Joint Experimental and Theoretical Study. *Minerals* 11, 323. doi:10.3390/min11030323

Gao, S., Tanji, K. K., Scardaci, S. C., and Chow, A. T. (2002). Comparison of Redox Indicators in a Paddy Soil during Rice-Growing Season. *Soil Sci. Soc. Am. J.* 66, 805–817. doi:10.2136/sssaj2002.8050

Gao, Y. and Mucci, A. (2001). Acid base reactions, phosphate and arsenate complexation, and their competitive adsorption at the surface of goethite in 0.7 M NaCl solution. *Geochim. Cosmochim. Acta* 65, 2361–2378. doi:10.1016/S0016-7037(01)00589-0

Geelhoed, J. S., Hiemstra, T., and Van Riemsdijk, W. H. (1997). Phosphate and sulfate adsorption on goethite: Single anion and competitive adsorption. *Geochim. Cosmochim. Acta* 61, 2389–2396. doi:10.1016/S0016-7037(97)00096-3

Geelhoed, J. S., Hiemstra, T., and Van Riemsdijk, W. H. (1998). Competitive interaction between phosphate and citrate on goethite. *Environmental Science & Technology* 32, 2119–2123. doi:10.1021/es970908y

Ghose, S. K., Waychunas, G. A., Trainor, T. P., and Eng, P. J. (2010). Hydrated goethite (α-FeOOH) (100) interface structure: Ordered water and surface functional groups. *Geochim. Cosmochim. Acta* 74, 1943–1953. doi:10.1016/j.gca.2009.12.015

Ghosh, D., Sarkar, M. M., and Roy, S. (2024). Smart fertilizers: The prospect of slow release nanofertilizers in modern agricultural practices. In *Nanofertilizers for Sustainable Agroecosystems*, eds. K. A. Abd-Elsalam and M. A. Alghuthaymi (Springer Nature Switzerland). 343–372. doi:10.1007/978-3-031-41329-2_13. Series Title: Nanotechnology in the Life Sciences

Grimme, S., Ehrlich, S., and Goerigk, L. (2011). Effect of the damping function in dispersion corrected density functional theory. *J. Comput. Chem.* 32, 1456–1465. doi:10.1002/jcc.21759

Gros, P., Ahmed, A., Kühn, O., and Leinweber, P. (2017). Glyphosate binding in soil as revealed by sorption experiments and quantum-chemical modeling. *Sci. Total Environ.* 586, 527–535

Gros, P., Ahmed, A. A., Kühn, O., and Leinweber, P. (2019). Influence of metal ions on glyphosate detection by FMOC-Cl. *Environ. Monit. Assess.* 191, 244

Guo, H. and Barnard, A. S. (2011). Thermodynamic modelling of nanomorphologies of hematite and goethite. *J. Mater. Chem.* 21, 11566. doi:10.1039/c1jm10381d

Guo, J., Tolstoy, P. M., Koeppe, B., Golubev, N. S., Denisov, G. S., Smirnov, S. N., et al. (2012). Hydrogen Bond Geometries and Proton Tautomerism of Homoconjugated Anions of Carboxylic Acids Studied via H/D Isotope Effects on ^{13} C NMR Chemical Shifts. *J. Phys. Chem. A* 116, 11180–11188. doi:10.1021/jp304943h

Guppy, C. N., Menzies, N. W., Moody, P. W., and Blamey, F. P. C. (2005). Competitive sorption reactions between phosphorus and organic matter in soil: a review. *Soil Research* 43, 189. doi:10.1071/SR04049

Gypser, S. and Freese, D. (2020). Phosphorus release from vivianite and hydroxyapatite by organic and inorganic compounds. *Pedosphere* 30, 190–200. doi:10.1016/S1002-0160(20)60004-2

Gypser, S., Hirsch, F., Schleicher, A. M., and Freese, D. (2018). Impact of crystalline and amorphous iron- and aluminum hydroxides on mechanisms of phosphate adsorption and desorption. *J. Environ. Sci.* 70, 175–189. doi:10.1016/j.jes.2017.12.001

Gypser, S., Schütze, E., and Freese, D. (2019). Crystallization of single and binary iron- and aluminum hydroxides affect phosphorus desorption. *J. Plant Nutr. Soil Sci.* 182, 741–750. doi:10.1002/jpln.201700543

Gypser, S., Schütze, E., and Freese, D. (2021). Single and binary fe- and al-hydroxides affect potential phosphorus mobilization and transfer from pools of different availability. *Soil Systems* 5, 33. doi:10.3390/soilsystems5020033

Han, J., Kim, M., and Ro, H.-M. (2020). Factors modifying the structural configuration of oxyanions and organic acids adsorbed on iron (hydr)oxides in soils. a review. *Environ Chem Lett* 18, 631–662. doi:10.1007/s10311-020-00964-4

Hehre, W. J., Ditchfield, R., and Pople, J. A. (1972). Self—Consistent Molecular Orbital Methods. XII. Further Extensions of Gaussian—Type Basis Sets for Use in Molecular Orbital Studies of Organic Molecules. *J. Chem. Phys.* 56, 2257–2261. doi:10.1063/1.1677527

Hesterberg, D., Zhou, W., Hutchison, K. J., Beauchemin, S., and Sayers, D. E. (1999). XAFS study of adsorbed and mineral forms of phosphate. *J Synchrotron Rad* 6, 636–638. doi:10.1107/S0909049599000370

Hiemstra, T. and Van Riemsdijk, W. (1996). A Surface Structural Approach to Ion Adsorption: The Charge Distribution (CD) Model. *J. Colloid Interface Sci.* 179, 488–508. doi:10.1006/jcis.1996.0242

Hongshao, Z. and Stanforth, R. (2001). Competitive adsorption of phosphate and arsenate on goethite. *Environ. Sci. Technol.* 35, 4753–4757. doi:10.1021/es010890y

Hutter, J., Iannuzzi, M., Schiffmann, F., and VandeVondele, J. (2014). CP2K: Atomistic Simulations of Condensed Matter Systems. *Wiley Interdiscip. Rev. Comput. Mol. Sci.* 4, 15–25. doi:10.1002/wcms.1159

Jensen, F. (2017). *Introduction to Computational Chemistry* (John Wiley & Sons), third edition edn.

Johnson, B. B., Ivanov, A. V., Antzutkin, O. N., and Forsling, W. (2002). ^{31} p nuclear magnetic resonance study of the adsorption of phosphate and phenyl phosphates on -al $_2$ o $_3$. *Langmuir* 18, 1104–1111. doi:10.1021/la001537t

Johnson, S. E. and Loeppert, R. H. (2006). Role of Organic Acids in Phosphate Mobilization from Iron Oxide. *Soil Sci. Soc. Am. J.* 70, 222. doi:10.2136/sssaj2005.0012

Jupp, A. R., Beijer, S., Narain, G. C., Schipper, W., and Slootweg, J. C. (2021). Phosphorus recovery and recycling – closing the loop. *Chem. Soc. Rev.* 50, 87–101. doi:10.1039/D0CS01150A

Kaiser, K. and Guggenberger, G. (2003). Mineral surfaces and soil organic matter. *Eur. J. Soil Sci.* 54, 219–236. doi:10.1046/j.1365-2389.2003.00544.x

Keyikoglu, R., Khataee, A., and Yoon, Y. (2022). Layered double hydroxides for removing and recovering phosphate: Recent advances and future directions. *Adv. Colloid Interface Sci.* 300, 102598. doi:10.1016/j.cis.2021.102598

Khare, N., Hesterberg, D., and Martin, J. D. (2005). XANES investigation of phosphate sorption in single and binary systems of iron and aluminum oxide minerals. *Environ. Sci. Technol.* 39, 2152–2160

Khare, N., Martin, J. D., and Hesterberg, D. (2007). Phosphate bonding configuration on ferrihydrite based on molecular orbital calculations and XANES fingerprinting. *Geochim. Cosmochim. Acta* 71, 4405–4415

Kim, J., Li, W., Philips, B. L., and Grey, C. P. (2011). Phosphate adsorption on the iron oxyhydroxides goethite (α-FeOOH), akaganeite (β-FeOOH), and lepidocrocite (γ-FeOOH): A 31P NMR Study. *Energy Environ. Sci.* 4, 4298. doi:10.1039/c1ee02093e

Kim, Y. and Kirkpatrick, R. J. (2004). An investigation of phosphate adsorbed on aluminium oxyhydroxide and oxide phases by nuclear magnetic resonance: Phosphate adsorbed on aluminium phases. *European Journal of Soil Science* 55, 243–251. doi:10.1046/j.1365-2389.2004.00595.x

Kmiecik, S., Gront, D., Kolinski, M., Wieteska, L., Dawid, A. E., and Kolinski, A. (2016). Coarse-Grained Protein Models and Their Applications. *Chem. Rev.* 116, 7898–7936. doi:10.1021/acs.chemrev.6b00163

Koch, W. and Holthausen, M. C. (2008). *A Chemist's Guide to Density Functional Theory* (Weinheim: Wiley-VCH), 2nd ed., 5. reprint edn.

Krack, M. (2005). Pseudopotentials for H to Kr optimized for gradient-corrected exchange-correlation functionals. *Theor. Chem. Acc.* 114, 145–152. doi:10.1007/s00214-005-0655-y

Krumina, L., Kenney, J. P., Loring, J. S., and Persson, P. (2016). Desorption mechanisms of phosphate from ferrihydrite and goethite surfaces. *Chem. Geol.* 427, 54–64. doi:10.1016/j.chemgeo.2016.02.016

Kruse, J., Abraham, M., Amelung, W., Baum, C., Bol, R., Kühn, O., et al. (2015). Innovative methods in soil phosphorus research: A review. *J. Plant Nutr. Soil Sci.* 178, 43–88. doi:10.1002/jpln.201400327

Kruse, J. and Leinweber, P. (2008). Phosphorus in sequentially extracted fen peat soils: A k-edge x-ray absorption near-edge structure (XANES) spectroscopy study. *Z. Pflanzenernähr. Bodenk.* 171, 613–620. doi:10.1002/jpln.200700237

Kruse, J., Panten, K., and Siebers, N. (2022). The fate of phosphorus from bone char-based fertilizers in soil pools in a 5-year crop rotation. *Nutr. Cycling Agroecosyst.* 124, 263–277. doi:10.1007/s10705-022-10228-y

Kubicki, J. D. (ed.) (2016). *Molecular Modeling of Geochemical Reactions: An Introduction* (Chichester, West Sussex, United Kingdom: Wiley)

Kubicki, J. D., Halada, G. P., Jha, P., and Phillips, B. L. (2009). Quantum mechanical calculation of aqueuous uranium complexes: Carbonate, phosphate, organic and biomolecular species. *Chem. Cent. J.* 3, 10. doi:10.1186/1752-153X-3-10

Kubicki, J. D., Kwon, K. D., Paul, K. W., and Sparks, D. L. (2007). Surface complex structures modelled with quantum chemical calculations: Carbonate, phosphate, sulphate, arsenate and arsenite. *Eur. J. Soil Sci.* 58, 932–944. doi:10.1111/j.1365-2389.2007.00931.x

Kubicki, J. D. and Ohno, T. (2020). Integrating density functional theory modeling with experimental data to understand and predict sorption reactions: Exchange of salicylate for phosphate on goethite. *Soil Syst.* 4, 27. doi:10.3390/soilsystems4020027

Kubicki, J. D., Paul, K. W., Kabalan, L., Zhu, Q., Mrozik, M. K., Aryanpour, M., et al. (2012). ATR–FTIR and Density Functional Theory Study of the Structures, Energetics, and Vibrational Spectra of Phosphate Adsorbed onto Goethite. *Langmuir* 28, 14573–14587. doi:10.1021/la303111a

Kubicki, J. D., Paul, K. W., and Sparks, D. L. (2008). Periodic density functional theory calculations of bulk and the (010) surface of goethite. *Geochem. Trans.* 9, 4. doi:10.1186/1467-4866-9-4

Kubicki, J. D., Tunega, D., and Kraemer, S. (2017). A density functional theory investigation of oxalate and Fe(II) adsorption onto the (010) goethite surface with implications for ligand- and reduction-promoted dissolution. *Chem. Geol.* 464, 14–22. doi:10.1016/j.chemgeo.2016.08.010

Kwon, K. D. and Kubicki, J. D. (2004). Molecular Orbital Theory Study on Surface Complex Structures of Phosphates to Iron Hydroxides: Calculation of Vibrational Frequencies and Adsorption Energies. *Langmuir* 20, 9249–9254. doi:10.1021/la0487444

Kühne, T. D., Iannuzzi, M., Del Ben, M., Rybkin, V. V., Seewald, P., Stein, F., et al. (2020). CP2K: An electronic structure and molecular dynamics software package - Quickstep: Efficient and accurate electronic structure calculations. *J. Chem. Phys.* 152, 194103. doi:10.1063/5.0007045

Laino, T., Mohamed, F., Laio, A., and Parrinello, M. (2006). An Efficient Linear-Scaling Electrostatic Coupling for Treating Periodic Boundary Conditions in QM/MM Simulations. *J. Chem. Theory Comput.* 2, 1370–1378. doi:10.1021/ct6001169

Lang, F., Bauhus, J., Frossard, E., George, E., Kaiser, K., Kaupenjohann, M., et al. (2016). Phosphorus in forest ecosystems: New insights from an ecosystem nutrition perspective. *J. Plant Nutr. Soil Sci.* 179, 129–135. doi:10.1002/jpln.201500541

Lee, C., Yang, W., and Parr, R. G. (1988). Development of the Colle-Salvetti correlation-energy formula into a functional of the electron density. *Phys. Rev. B* 37, 785–789. doi:10.1103/PhysRevB.37.785

Lefèvre, G. (2004). In situ Fourier-transform infrared spectroscopy studies of inorganic ions adsorption on metal oxides and hydroxides. *Adv. Colloid Interface Sci.* 107, 109–123. doi:10.1016/j.cis.2003.11.002

Lehmann, J., Bossio, D. A., Kögel-Knabner, I., and Rillig, M. C. (2020). The concept and future prospects of soil health. *Nat. Rev. Earth Environ.* 1, 544–553. doi:10.1038/s43017-020-0080-8

Leinweber, P., Hagemann, P., Kebelmann, L., Kebelmann, K., and Morshedizad, M. (2019). Bone char as a novel phosphorus fertilizer. In *Phosphorus Recovery and Recycling*, eds. H. Ohtake and S. Tsuneda (Springer Singapore). 419–432. doi:10.1007/978-981-10-8031-9_29

Leinweber, P., Schulten, H.-R., and Jancke, H. (1999). New evidence for the molecular composition of soil organic matter in vertisols. *Soil Sci.* 164, 857–870

Li, H., Wan, B., Yan, Y., Zhang, Y., Cheng, W., and Feng, X. (2017). Adsorption of glycerophosphate on goethite: A macroscopic and infrared spectroscopic study. *J. Soil Sci. Plant Nutr.* 181, 557–565. doi:10.1002/jpln.201700517

Li, L. and Stanforth, R. (2000). Distinguishing Adsorption and Surface Precipitation of Phosphate on Goethite (α-FeOOH). *J. Colloid Interface Sci.* 230, 12–21. doi:10.1006/jcis.2000.7072

Li, W., Feng, J., Kwon, K. D., Kubicki, J. D., and Phillips, B. L. (2010). Surface Speciation of Phosphate on Boehmite (γ-AlOOH) Determined from NMR Spectroscopy. *Langmuir* 26, 4753–4761. doi:10.1021/la903484m

Li, W., Pierre-Louis, A.-M., Kwon, K. D., Kubicki, J. D., Strongin, D. R., and Phillips, B. L. (2013). Molecular level investigations of phosphate sorption on corundum (α-Al2O3) by 31P solid state NMR, ATR-FTIR and quantum chemical calculation. *Geochim. Cosmochim. Acta* 107, 252–266. doi:10.1016/j.gca.2013.01.007

Lippert, G., Hutter, J., and Parrinello, M. (1997). A hybrid Gaussian and plane wave density functional scheme. *Mol. Phys.* 92, 477–488. doi:10.1080/002689797170220

Liu, Q., Guo, L., Zhou, Y., Dai, Y., Feng, L., Zhou, J., et al. (2012). Phosphate adsorption on biogenetic calcium carbonate minerals: effect of a crystalline phase. *Desalination and Water Treatment* 47, 78–85. doi:10.1080/19443994.2012.696798

Liu, X., Tournassat, C., Grangeon, S., Kalinichev, A. G., Takahashi, Y., and Marques Fernandes, M. (2022). Molecular-level understanding of metal ion retention in clay-rich materials. *Nat. Rev. Earth Environ.* 3, 461–476. doi:10.1038/s43017-022-00301-z

Loring, J. S., Sandström, M. H., Norén, K., and Persson, P. (2009). Rethinking Arsenate Coordination at the Surface of Goethite. *Chem. - Eur. J.* 15, 5063–5072. doi:10.1002/chem.200900284

Luengo, C., Brigante, M., Antelo, J., and Avena, M. (2006). Kinetics of phosphate adsorption on goethite: Comparing batch adsorption and ATR-IR measurements. *J. Colloid Interface Sci.* 300, 511–518. doi:10.1016/j.jcis.2006.04.015

Luo, Y., Peng, Y., Li, Y., Li, Y., Feng, C., Li, R., et al. (2024). Phosphorus removal from water using la-based absorbents: Insights into the impacts of crystal structure, surface area, and crystallinity on the removal efficiency and mechanisms. *Sep. Purif. Technol.* 330, 125478. doi:10.1016/j.seppur.2023.125478

Maciá, E. (2005). The role of phosphorus in chemical evolution. *Chem. Soc. Rev.* 34, 691. doi:10.1039/b416855k

Marx, D. and Hutter, J. (2009). *Ab Initio Molecular Dynamics: Basic Theory and Advanced Methods* (Cambridge: Cambridge University Press). doi:10.1017/CBO9780511609633

McLaren, T. I., Smernik, R. J., McLaughlin, M. J., Doolette, A. L., Richardson, A. E., and Frossard, E. (2020). The chemical nature of soil organic phosphorus: A critical review and global compilation of quantitative data. In *Advances in Agronomy* (Elsevier), vol. 160. 51–124. doi:10.1016/bs.agron.2019.10.001

McLaren, T. I., Smernik, R. J., McLaughlin, M. J., McBeath, T. M., Kirby, J. K., Simpson, R. J., et al. (2015). Complex forms of soil organic phosphorus–a major component of soil phosphorus. *Environ. Sci. Technol.* 49, 13238–13245. doi:10.1021/acs.est.5b02948

Menezes-Blackburn, D., Giles, C., Darch, T., George, T. S., Blackwell, M., Stutter, M., et al. (2018). Opportunities for mobilizing recalcitrant phosphorus from agricultural soils: a review. *Plant Soil* 427, 5–16. doi:10.1007/s11104-017-3362-2

Minamisawa, H., Kojima, Y., and Aizawa, M. (2022). Adsorption of inositol phosphate on hydroxyapatite powder with high specific surface area. *Materials* 15, 2176. doi: 10.3390/ma15062176

Missong, A., Bol, R., Willbold, S., Siemens, J., and Klumpp, E. (2016). Phosphorous forms in forest soil colloids as revealed by liquid-state P-NMR. *J. Soil Sci. Plant Nutr.* 179, 159–167

Obersteiner, M., Peñuelas, J., Ciais, P., van der Velde, M., and Janssens, I. A. (2013). The phosphorus trilemma. *Nature Geoscience* 6, 897–898. doi:10.1038/ngeo1990

Ofoegbu, S. U. (2019). Technological challenges of phosphorus removal in high-phosphorus ores: Sustainability implications and possibilities for greener ore processing. *Sustainability* 11, 6787. doi:10.3390/su11236787

Ognalaga, M., Frossard, E., and Thomas, F. (1994). Glucose-1-phosphate and Myo-inositol Hexaphosphate Adsorption Mechanisms on Goethite. *Soil Sci. Soc. Am. J.* 58, 332–337. doi:10.2136/sssaj1994.03615995005800020011x

Okano, K., Uemoto, M., Kagami, J., Miura, K., Aketo, T., Toda, M., et al. (2013). Novel technique for phosphorus recovery from aqueous solutions using amorphous calcium silicate hydrates (a-CSHs). *Water Research* 47, 2251–2259. doi:10.1016/j.watres.2013.01.052

Osman, A. I., Zhang, Y., Lai, Z. Y., Rashwan, A. K., Farghali, M., Ahmed, A. A., et al. (2023). Machine learning and computational chemistry to improve biochar fertilizers: a review. *Environ. Chem. Lett.* 21, 3159–3244. doi:10.1007/s10311-023-01631-0

Parfitt, R. L. and Atkinson, R. J. (1976). Phosphate adsorption on goethite (-FeOOOH). *Nature* 264, 740–742. doi:10.1038/264740a0

Paul, K. W., Kubicki, J. D., and Sparks, D. L. (2007). Sulphate adsorption at the Fe (hydr)oxide–H2O interface: Comparison of cluster and periodic slab DFT predictions. *Eur. J. Soil Sci.* 58, 978–988. doi:10.1111/j.1365-2389.2007.00936.x

Perdew, J. P., Burke, K., and Ernzerhof, M. (1996). Generalized Gradient Approximation Made Simple. *Phys. Rev. Lett.* 77, 3865–3868. doi:10.1103/PhysRevLett.77.3865

Persson, P., Nilsson, N., and Sjöberg, S. (1996). Structure and Bonding of Orthophosphate Ions at the Iron Oxide–Aqueous Interface. *J. Colloid Interface Sci.* 177, 263–275. doi:10.1006/jcis.1996.0030

Powell, K. J., Brown, P. L., Byrne, R. H., Gajda, T., Hefter, G., Sjöberg, S., et al. (2005). Chemical speciation of environmentally significant heavy metals with inorganic ligands. Part 1: The Hg^{2+}– Cl^-, OH^-, CO_3^{2-}, SO_4^{2-}, and PO_4^{3-} aqueous systems (IUPAC Technical Report). *Pure Appl. Chem.* 77, 739–800. doi:10.1351/pac200577040739

Rahnemaie, R., Hiemstra, T., and van Riemsdijk, W. H. (2007). Geometry, Charge Distribution, and Surface Speciation of Phosphate on Goethite. *Langmuir* 23, 3680–3689. doi:10.1021/la062965n

Rakovan, J., Becker, U., and Hochella, M. F. (1999). Aspects of goethite surface microtopography, structure, chemistry, and reactivity. *Am. Mineral.* 84, 884–894. doi:10.2138/am-1999-5-623

Ren, X., Yang, S., Tan, X., Chen, C., Sheng, G., and Wang, X. (2012). Mutual effects of copper and phosphate on their interaction with γ-Al2O3: Combined batch macroscopic experiments with DFT calculations. *J. Hazard. Mater.* 237–238, 199–208

Rietra, R. P. J. J., Hiemstra, T., and van Riemsdijk, W. H. (2001). Interaction between Calcium and Phosphate Adsorption on Goethite. *Environ. Sci. Technol.* 35, 3369–3374. doi:10.1021/es000210b

Rose, J., Flank, A.-M., Masion, A., Bottero, J.-Y., and Elmerich, P. (1997). Nucleation and Growth Mechanisms of Fe Oxyhydroxide in the Presence of PO $_4$ Ions. 2. P K-Edge EXAFS Study. *Langmuir* 13, 1827–1834. doi:10.1021/la961039d

Rose, J., Manceau, A., Bottero, J.-Y., Masion, A., and Garcia, F. (1996). Nucleation and Growth Mechanisms of Fe Oxyhydroxide in the Presence of PO $_4$ Ions. 1. Fe K-Edge EXAFS Study. *Langmuir* 12, 6701–6707. doi:10.1021/la9606299

Ruttenberg, K. and Sulak, D. (2011). Sorption and desorption of dissolved organic phosphorus onto iron (oxyhydr)oxides in seawater. *Geochim. Cosmochim. Acta* 75, 4095–4112. doi:10.1016/j.gca.2010.10.033

Schaumann, G. and Thiele-Bruhn, S. (2011). Molecular modeling of soil organic matter: Squaring the circle? *Geoderma* 166, 1–14. doi:10.1016/j.geoderma.2011.04.024

Schulten, H.-R. and Leinweber, P. (2000). New insights into organic-mineral particles: Composition, properties and models of molecular structure. *Biol Fertil Soils* 30, 399–432. doi:10.1007/s003740050020

Schulten, H. R. and Schnitzer, M. (1993). A state of the art structural concept for humic substances. *Naturwissenschaften* 80, 29–30. doi:10.1007/BF01139754

Schwertmann, U. (1993). Relations between iron oxides, soil color, and soil formation. In *SSSA Special Publications*, eds. J. M. Bigham and E. J. Ciolkosz (Soil Science Society of America). 51–69. doi:10.2136/sssaspecpub31.c4

Senn, H. M. and Thiel, W. (2009). QM/MM Methods for Biomolecular System. *Angew. Chem. Int. Ed. Engl.* 48, 1198

Shaheen, S. M., Wang, J., Baumann, K., Ahmed, A. A., Hsu, L.-C., Liu, Y.-T., et al. (2022). Stepwise redox changes alter the speciation and mobilization of phosphorus in hydromorphic soils. *Chemosphere* 288, 132652. doi:10.1016/j.chemosphere.2021.132652

Sheals, J., Sjoberg, S., and Persson, P. (2002). Adsorption of glyphosate on goethite: Molecular characterization of surface complexes. *Environ. Sci. Technol.* 36, 3090–3095. doi:10.1021/es010295w

Stewart, J. J. P. (2007). Optimization of parameters for semiempirical methods V: Modification of NDDO approximations and application to 70 elements. *J. Mol. Model.* 13, 1173–1213. doi:10.1007/s00894-007-0233-4

Strauss, R., Brummer, G., and Barrow, N. (1997a). Effects of crystallinity of goethite: II. Rates of sorption and desorption of phosphate. *Eur. J. Soil Sci.* 48, 101–114. doi:10.1111/j.1365-2389.1997.tb00189.x

Strauss, R., Brümmer, G., and Barrow, N. (1997b). Effects of crystallinity of goethite: I. Preparation and properties of goethites of differing crystallinity. *Eur. J. Soil Sci.* 48, 87–99. doi:10.1111/j.1365-2389.1997.tb00188.x

Tejedor-Tejedor, M. I. and Anderson, M. A. (1990). The protonation of phosphate on the surface of goethite as studied by CIR-FTIR and electrophoretic mobility. *Langmuir* 6, 602–611. doi:10.1021/la00093a015

Tsao, T. M., Chen, Y. M., and Wang, M. K. (2011). Origin, separation and identification of environmental nanoparticles: A review. *J. Environ. Monit.* 13, 1156. doi:10.1039/c1em10013k

Turner, B. L., Mahieu, N., and Condron, L. M. (2003). Quantification of myo-inositol hexakisphosphate in alkaline soil extracts by solution ^{31}p nmr spectroscopy and spectral deconvolution. *Soil Science* 168, 469–478. doi:10.1097/01.ss.0000080332.10341.ed

Urrutia, O., Guardado, I., Erro, J., Mandado, M., and García-Mina, J. M. (2013). Theoretical chemical characterization of phosphate-metal-humic complexes and relationships with their effects on both phosphorus soil fixation and phosphorus availability for plants. *J. Sci. Food Agric.* 93, 293–303

Van Emmerik, T. J., Sandström, D. E., Antzutkin, O. N., Angove, M. J., and Johnson, B. B. (2007). 31p solid-state nuclear magnetic resonance study of the sorption of phosphate onto gibbsite and kaolinite. *Langmuir* 23, 3205–3213. doi:10.1021/la062765b

VandeVondele, J. and Hutter, J. (2007). Gaussian basis sets for accurate calculations on molecular systems in gas and condensed phases. *J. Chem. Phys.* 127, 114105. doi:10.1063/1.2770708

VandeVondele, J., Krack, M., Mohamed, F., Parrinello, M., Chassaing, T., and Hutter, J. (2005). Quickstep: Fast and accurate density functional calculations using a mixed Gaussian and plane waves approach. *Comput. Phys. Commun.* 167, 103–128. doi:10.1016/j.cpc.2004.12.014

Vanommeslaeghe, K., Hatcher, E., Acharya, C., Kundu, S., Zhong, S., Shim, J., et al. (2009). CHARMM general force field: A force field for drug-like molecules compatible with the CHARMM all-atom additive biological force fields. *J. Comput. Chem.* , NA–NAdoi:10.1002/jcc.21367

Vepraskas, M. J., Richardson, J. L., Tandarich, J. P., and Teets, S. J. (1999). Dynamics of hydric soil formation across the edge of a created deep marsh. *Wetlands* 19, 78–89. doi:10.1007/BF03161736

Villalobos, M., Cheney, M. A., and Alcaraz-Cienfuegos, J. (2009). Goethite surface reactivity: II. A microscopic site-density model that describes its surface area-normalized variability. *J. Colloid Interface Sci.* 336, 412–422. doi:10.1016/j.jcis.2009.04.052

Wang, H., Zhu, J., Fu, Q., Hong, C., Hu, H., and Violante, A. (2016). Phosphate adsorption on uncoated and humic acid-coated iron oxides. *J Soils Sediments* 16, 1911–1920. doi:10.1007/s11368-016-1383-8

Wang, H., Zhu, J., Fu, Q., and Hu, H. (2015a). Adsorption of phosphate on pure and humic acid-coated ferrihydrite. *J Soils Sediments* 15, 1500–1509. doi:10.1007/s11368-015-1095-5

Wang, H., Zhu, J., Fu, Q.-L., Xiong, J.-W., Hong, C., Hu, H.-Q., et al. (2015b). Adsorption of phosphate onto ferrihydrite and ferrihydrite-humic acid complexes. *Pedosphere* 25, 405–414. doi:10.1016/S1002-0160(15)30008-4

Weng, Y., Vekeman, J., Zhang, H., Chou, L., Elskens, M., and Tielens, F. (2020). Unravelling phosphate adsorption on hydrous ferric oxide surfaces at the molecular level. *Chemosphere* 261, 127776. doi:10.1016/j.chemosphere.2020.127776

Xiu, F., Zhou, L., Xia, S., and Yu, L. (2016). Adsorption mechanism of water molecule on goethite (010) surface. *J. Ocean Univ. China* 15, 1021–1026. doi:10.1007/s11802-016-3171-x

Xu, C.-y., Li, J.-y., Xu, R.-k., and Hong, Z.-n. (2017). Sorption of organic phosphates and its effects on aggregation of hematite nanoparticles in monovalent and bivalent solutions. *Environmental Science and Pollution Research* 24, 7197–7207. doi:10.1007/s11356-017-8382-1

Yan, J., Jiang, T., Yao, Y., Lu, S., Wang, Q., and Wei, S. (2016). Preliminary investigation of phosphorus adsorption onto two types of iron oxide-organic matter complexes. *Journal of Environmental Sciences* 42, 152–162. doi:10.1016/j.jes.2015.08.008

Yan, Y. P., Liu, F., Li, W., Liu, F., Feng, X. H., and Sparks, D. L. (2014). Sorption and desorption characteristics of organic phosphates of different structures on aluminium (oxyhydr)oxides: Sorption-desorption of organic P on Al oxyhydroxides. *Eur. J. Soil Sci.* 65, 308–317. doi:10.1111/ejss.12119

Zhong, B., Stanforth, R., Wu, S., and Chen, J. P. (2007). Proton interaction in phosphate adsorption onto goethite. *Journal of Colloid and Interface Science* 308, 40–48. doi:10.1016/j.jcis.2006.12.055

Zimmer, D., Kahle, P., and Baum, C. (2016). Loss of soil phosphorus by tile drains during storm events. *Agricultural Water Management* 167, 21–28. doi:10.1016/j.agwat.2015.12.017

Zimmer, D., Panten, K., Frank, M., Springer, A., and Leinweber, P. (2019). Sulfur-enriched bone char as alternative p fertilizer: Spectroscopic, wet chemical, and yield response evaluation 9, 21. doi:10.3390/agriculture9010021

Appendices

List of Publications

This thesis is based on the following publications, which are included in these appendices.

1. Ashour A. Ahmed, S. Gypser, P. Leinweber, D. Freese, and O. Kühn. Infrared spectroscopic characterization of phosphate binding at the goethite–water interface. Phys. Chem. Chem. Phys. **2019**, 21, 4421-4434.

2. Ashour A. Ahmed, S. Gypser, D. Freese, P. Leinweber, and O. Kühn. Molecular level picture of the interplay between pH and phosphate binding at the goethite–water interface. Phys. Chem. Chem. Phys. **2020**, 22, 26509-26524.

3. S. M. Shaheen, J. Wang, K. Baumann, Ashour A. Ahmed, L.-C. Hsu, Y.-T. Liu, S.-L. Wang, O. Kühn, P. Leinweber, J. Rinklebe. Stepwise redox changes alter the speciation and mobilization of phosphorus in hydromorphic soils. Chemosphere **2022**, 288, 132652.

4. P. B. Ganta, O. Kühn, Ashour A. Ahmed. QM/MM simulations of organic phosphorus adsorption at the diaspore-water interface. Phys. Chem. Chem. Phys. **2019**, 21, 24316-24325.

5. P. B. Ganta, O. Kühn, Ashour A. Ahmed. QM/MM molecular dynamics investigation of the binding of organic phosphates to the 100 diaspore surface. Front. For. Glob. Change **2020**, 3, 71.

6. P. B. Ganta, O. Kühn, Ashour A. Ahmed. Ab Initio Molecular Dynamics Simulations of the Interaction between Organic Phosphates and Goethite. Molecules **2021**, 26(1), 160.

7. P. B. Ganta, M. Morshedizad, O. Kühn, P. Leinweber, Ashour A. Ahmed. The Binding of Phosphorus Species at Goethite: A Joint Experimental and Theoretical Study. Minerals **2021**, 21, 323.

8. Ashour A. Ahmed, M. Morshedizad, O. Kühn, P. Leinweber. Deciphering competitive interactions: Phosphate and organic matter binding on goethite through experimental and theoretical insights. Sci. Total Environ. **2024**, 940, 173510.

9. Y. Luo, Y. Peng, Y. Li, Y. Li, C. Feng, R. Li, B. Gao, R. Xiao, X. Zhang, G. Qu, M. Li, Ashour A. Ahmed, S. G. Al-Solaimani, P. S. Hooda, J. Rinklebe, Z. Zhang, S. S. Lee, S. M. Shaheen. Phosphorus removal from water using La-based absorbents: Insights into the impacts of crystal structure, surface area, and crystallinity on the removal efficiency and mechanisms. Sep. Purif. Technol. **2023**, 330, 125478.

10. Ashour A. Ahmed, P. Leinweber, O. Kühn. Advances in understanding the phosphate binding to soil constituents: A Computational chemistry perspective. Sci. Total Environ. **2023**, 887, 163692.

11. Osman, Y. Zhang, Z. Y. Lai, A. K. Rashwan, M. Farghali, Ashour A. Ahmed, Y. Liu, B. Fang, Z. Chen, A. Al-Fatesh, D. W. Rooney, C. L. Yiin, P.-S. Yap. Machine learning and computational chemistry to improve biochar fertilizers: a review. Environ. Chem. Lett. **2023**, 21, 3159–3244.

12. P. Gros, Ashour A. Ahmed, O. Kühn, P. Leinweber. Glyphosate binding in soil as revealed by sorption experiments and quantum-chemical modeling. Sci. Total Environ. **2017**, 586, 527–535.

13. Ashour A. Ahmed, P. Gros, O. Kühn, P. Leinweber. Molecular level investigation of the role of peptide interactions in the glyphosate analytics. Chemosphere **2018**, 196, 129–134.

14. P. Gros, Ashour A. Ahmed, O. Kühn, P. Leinweber. Influence of metal ions on glyphosate detection by FMOC-Cl. Environ. Monit. Assess. **2019**, 191, 244.

15. Ashour A. Ahmed, P. Leinweber, O. Kühn. Unravelling the nature of glyphosate binding to goethite surfaces by ab initio molecular dynamics simulations. Phys. Chem. Chem. Phys. **2018**, 20, 1531–1539.

Notice: All publications included in the appendices are reproduced with permission from the respective publishers: Royal Society of Chemistry, Elsevier, Springer Nature, Frontiers, and MDPI.

Contributions

My contributions to the publications, listed in the same order as above, are detailed below. I am credited with:

1-2. Conceptualization, conducting the modeling work, analysis and interpretation of both experimental and modeling work, methodology development, visualization, writing the original manuscript, and reviewing and editing the manuscript.

3. Performing the quantum chemical calculations, analyzing the modeling results, writing the modeling part, and reviewing, editing, and proofreading.

4-7. Conceptualization, methodology development, funding acquisition, contribution to writing the original manuscript, supervising the PhD student, discussing and interpreting the results, and reviewing and editing the manuscript.

8. Conceptualization, conducting the modeling work, all experimental and modeling analysis and interpretation, methodology development, visualizing and interpreting the results, writing the original manuscript, and reviewing and editing the manuscript.

9. Scientific concepts, discussing and interpreting the results, and writing, reviewing, and editing the manuscript.

10. Conceptualization, formal analysis, methodology, visualization, original draft writing, writing, reviewing, and editing the manuscript.

11. Writing the modeling part of this review article.

12 and 14. Conceptualization, conducting modeling work, analysis and interpretation, methodology development, visualization, writing the original manuscript with P. Gros, and reviewing and editing the manuscript.

13. Conceptualization, conducting modeling work, analysis and interpretation, methodology development, visualization, writing the original manuscript, and reviewing and editing the manuscript.

15. Conceptualization, conducting the work, all analysis and interpretation, methodology development, visualization, writing the original manuscript, and reviewing and editing the manuscript.

Publication 1

Ashour A. Ahmed, S. Gypser, P. Leinweber, D. Freese, and O. Kühn. Infrared spectroscopic characterization of phosphate binding at the goethite–water interface. Phys. Chem. Chem. Phys. **2019**, 21, 4421-4434.

Contribution: Ashour A. Ahmed is credited with conceptualization, conducting the modeling work, modeling analysis and interpretation of both experimental and modeling work, methodology development, visualization, and writing the original manuscript. Ashour A. Ahmed and co-authors are responsible for reviewing, and editing the manuscript.

URL: https://doi.org/10.1039/c8cp07168c

QR:

Ashour Ahmed IR

Reproduced with the permission of the Royal Society of Chemistry (RSC)

PCCP

PAPER

Check for updates

Cite this: *Phys. Chem. Chem. Phys.*, 2019, **21**, 4421

Infrared spectroscopic characterization of phosphate binding at the goethite–water interface†

Ashour A. Ahmed,[ab] Stella Gypser,[c] Peter Leinweber,[d] Dirk Freese[c] and Oliver Kühn[ab]

Received 20th November 2018,
Accepted 22nd January 2019

DOI: 10.1039/c8cp07168c

rsc.li/pccp

The interaction between phosphates and soil mineral surfaces, such as Fe- and Al-(oxyhydr)oxides, plays a crucial role in the immobilization of P and thus its availability for plants. The reactions of phosphates with Fe-hydroxides and especially goethite have been studied extensively. But a molecular-level picture of the phosphate binding mechanisms at the goethite–water interface is still lacking. Therefore, in the current contribution we have explored the molecular binding mechanisms for the adsorbed phosphate at the goethite–water interface by performing sorption kinetics experiments for orthophosphate and characterizing the adsorbed species by FT-IR spectroscopy. In parallel, periodic DFT calculations have been performed to explore the interaction mechanisms and to assign the IR spectra for monodentate (**M**) and bidentate (**B**) orthophosphate complexes at two different goethite surface planes (010 and 100) in the presence of water. In general, our interaction energy results give evidence that the mono-protonated **B** phosphate complex is favored to be formed at the goethite–water interface, although the **M** motif could exist as a minor fraction. Moreover, it was found that water plays an important role in controlling the phosphate adsorption process at the goethite surfaces. The interfacial water molecules form H-bonds (HBs) with the phosphate as well as with the goethite surface atoms. Furthermore, some water molecules form covalent bonds with goethite's Fe atoms while others dissociate at the surface to protons and hydroxyl groups. The present theoretical assignment of IR spectra introduces a benchmark for characterizing experimental IR data for the adsorbed KH_2PO_4 species at the goethite–water interface. In particular, the IR spectra of the mono-protonated (2O + 1Fe) **B** complex at the 010 goethite surface plane and the **M** complex at the 100 goethite surface plane were found to be consistent with the experimental data. In order to explore the role of different abundances of surface planes and binding motifs, IR spectra obtained from weighted averages have been analyzed. The results confirmed the conclusions drawn from interaction energy calculations.

1. Introduction

Phosphorus (P) plays an important role in the environmental nutrient cycle. P is central to all forms of life and its efficient use in fertilizers is one of the conditions for providing food for a rapidly increasing human population. Facing the projected peak P scenario,[1] substantial research activities have been triggered to improve our knowledge towards a more efficient and sustainable use of P resources.[2,3] One major factor playing a role in the P immobilization and, thus, efficiency is the interaction between phosphates and soil solid-phase components. In general, phosphates bind strongly to soil mineral surfaces and here especially to Fe- and Al-(oxyhydr)oxides.[4] The reactions of phosphates with Fe-hydroxides have been studied thoroughly.[5–10] Major findings concerned the adsorption rate and kinetics of phosphate binding to soil Fe-particles, revealing a biphasic behavior with a fast initial adsorption step followed by a slower reaction phase.[10–13] During the transition from fast to slow adsorption phases, the formation of initial mononuclear complexes and the conversion to binuclear complexes and the competition with anions on the surface or precipitation events

[a] University of Rostock, Institute of Physics, Albert-Einstein-Str. 23-24, D-18059 Rostock, Germany. E-mail: ashour.ahmed@uni-rostock.de
[b] University of Rostock, Department of Life, Light, and Matter (LLM), Albert-Einstein-Str. 25, D-18059 Rostock, Germany
[c] Brandenburg University of Technology Cottbus-Senftenberg, Chair of Soil Protection and Recultivation, Konrad-Wachsmann-Allee 6, 03046 Cottbus, Germany
[d] University of Rostock, Chair of Soil Science, Justus-von-Liebig-Weg 6, D-18059 Rostock, Germany

† Electronic supplementary information (ESI) available. See DOI: 10.1039/c8cp07168c

were discussed to take place.[14] Furthermore, in early adsorption experiments with synthetic Fe- and Al-hydroxides the formation of stable inner-sphere surface complexes on metal ions and ligand exchange have been detected.[15,16]

Particularly, the mineral goethite received much attention and, thus, goethite surface properties are well characterized. This is primarily due to the fact that goethite is the most common ferric iron, Fe(III), oxyhydroxide in soils and its reactivity couples to a wide range of environmental processes. Therefore, it is a frequently used mineral for experimental and theoretical investigations of phosphate-surface reactions.[11,17–20]

Fourier-transform infrared (FT-IR) spectroscopic measurements were widely used to investigate the spectral features of dissolved phosphate species and those adsorbed on Fe-oxide surfaces. Characteristic mid-infrared bands from symmetric and antisymmetric P–O(H) vibrations can be detected even at low phosphate concentrations and depend on the symmetry of the ion.[6,19,21,22] Therefore, the coordination geometry concluded from the IR spectrum is a helpful tool to identify the phosphate binding mechanisms to the mineral surfaces. However, Villalobos *et al.*[23] and Kubicki *et al.*[17] pointed out that FT-IR spectroscopy of phosphate adsorption on goethite has general limitations in predicting the bonding of surface complexes. This is due to the presence of different crystal faces for powdered goethite samples as well as several binding motifs for the complexes between phosphate and each goethite crystal face. This might lead to broad FT-IR bands and different assignments of surface complexes. As a result, different opinions exist regarding the assignment of the binding motifs (monodentate and/or bidentate) of phosphate to the goethite surface. Tejedor-Tejedor and Anderson[22] and also Luengo *et al.*[11] described bidentate P complexes as the predominant binding motifs at the goethite surface with varying protonation states. Persson *et al.*[19] and Loring *et al.*[24] interpreted their IR results by formation of a monodentate binding motif for phosphate at goethite. In view of this debate, combining molecular simulations and experimental work provides the only means for clarifying the above contradicting explanations to achieve a better understanding for the phosphate–goethite complexation process and the existing binding motifs.

The sorption/desorption processes of phosphate to/from soil minerals can be understood and the role of the sorptive surfaces elucidated by calculation of binding energies and other physical parameters.[25] In a number of papers, Kubicki and co-workers have addressed the binding of phosphates to mineral surfaces. The pH dependence of phosphate binding to goethite (α-FeOOH, modeled as a small cluster of two edge-sharing iron octahedra including a few explicit water molecules) has been described using density functional theory (DFT).[25] Based on calculated IR spectra and reaction energies,[6] it was concluded that the dominant form at low pH is a bi-protonated bidentate form, whereas at neutral pH a mono-protonated monodentate species is dominant. This tendency was confirmed in a study by Kubicki *et al.*[26] where emphasis has been placed on the correlation with IR and EXAFS data. Moreover, DFT simulations with periodic boundary conditions (PBC) have been applied to study the phosphate adsorption on a variety of goethite surface planes. Here, IR spectra were obtained for cluster models extracted from the PBC simulation box.[17]

Despite these studies, a systematic molecular-level picture of phosphate binding mechanisms at the goethite–water interface is still lacking. In particular, there are neither experimental nor systematic theoretical studies focusing on the overall phosphate–goethite–water interactions and the individual (phosphate–goethite, phosphate–water, and goethite–water) interactions for different goethite surface planes at a molecular scale. Therefore, our main target in the current contribution is to explore the molecular binding mechanisms for the adsorption of phosphate at the goethite surface in the presence of water. This will be achieved by carrying out sorption kinetics experiments for orthophosphate at the goethite surface followed by characterization of the adsorbed species by FT-IR spectroscopy. Moreover, PBC-DFT calculations will be performed using the mixed Gaussian and plane wave approach. Specifically, the interaction mechanisms for orthophosphate with two different goethite surface planes in the presence of water will be explored. Contributions of individual phosphate–goethite, phosphate–water, and goethite–water interactions will be addressed. Furthermore, the competition between phosphate, water, and the hydroxyl (OH^-) group for adsorption sites will be investigated. Finally, IR vibrational frequencies will be calculated for different phosphate–goethite complexes and the corresponding spectra will be assigned.

2. Methods

2.1. Experiment

2.1.1. Materials. The synthetic and commercially available adsorbent used in this study was goethite (99%, Alfa Aesar, Massachusetts, USA). The crystallinity and composition of the synthetic goethite were confirmed by X-ray diffraction analysis (Fig. S1 in the ESI†) using an Empyrean powder diffractometer (PANalytical, Almelo, Netherlands) with Cu Kα radiation (λ = 0.15418 nm). Diffraction data were recorded from 4.6° to 84.9° 2θ with a step-size of 0.0131 and a step time of 58.4 s. Determination of the *d*-values of the diffraction pattern and verification of the calculated orthorhombic lattice parameter (a = 4.61 Å, b = 9.96 Å, and c = 3.02 Å) were performed by using an open access version of XPowder.[27] A specific surface area of 17.2 $m^2\ g^{-1}$ was determined with an Autosorb-1 (Quantachrome, Odelzhausen, Germany) using a five-point Brunauer–Emmett–Teller (BET)-measurement and nitrogen as an adsorptive medium. KH_2PO_4 and $CaCl_2$ (VWR Chemicals, Darmstadt, Germany) were of analytical grade.

2.1.2. Adsorption kinetics. Phosphate adsorption kinetics experiments have been conducted at pH 6.3 with 4 replicates and blank value (without goethite sample) by using batch experiments with a solid–solution ratio of 1 : 20. Here, 1.5 g of goethite and 30 ml of a KH_2PO_4–$CaCl_2$ solution were used. The $CaCl_2$ electrolyte solution has been selected as an adsorption solution in this study to represent the main constituent of the

 This journal is © the Owner Societies 2019

real soil solution. We have applied a pH of 6.3 in this experiment to mimic the agronomic soils that mostly have a pH range of 5.0–6.8. In addition, phosphate minerals are soluble at pH 6.3 and thus these conditions will prevent phosphate precipitation during the adsorption experiment.[28] The solid–solution ratio of 1 : 20 has been chosen based on several adsorption tests with different solid–solution ratios. The practical reasons for this selection are mainly related to having sufficient material for FT-IR measurements and the available volume of centrifuge tubes. For adsorption, an initial phosphate concentration of 150 μmol l^{-1} was chosen to achieve a low and incomplete loading of the goethite surface according to adsorption capacities mentioned in previous studies.[11,12,20,29,30] The adsorption reaction mixture was horizontally shaken at 150 revolutions per min (rpm). Through this reaction kinetics, the phosphate concentrations in the solution have been determined at different reaction times (2, 6, 24, 48, 168, 336, 672, 1344, and 2688 h). Specifically, the adsorption mixtures have been centrifuged at the mentioned times for 15 min at 2000 rpm and a clear supernatant was filtrated by using P-poor Whatman 512 1/1 filters to separate it from the goethite solid matter. The equilibrium phosphate concentration was measured by the method of Murphy and Riley.[31] Here, the amount of phosphate lost from solution was assumed to be completely adsorbed by the mineral phase.

2.1.3. Fourier transform infrared (FT-IR) spectroscopy. For FT-IR spectroscopic measurements, phosphate–goethite-suspensions at 2688 h reaction time have been centrifuged and the obtained solid samples were taken for the analysis. This longer reaction time was selected to ensure that we describe the phosphate–goethite complexation reaction at the equilibrium. In particular, the mid- and long-term fixation/availability of P in agricultural soils is of importance. These samples were dried for 24 h at 40 °C and stored in a desiccator and analyzed without further treatment prior to IR spectroscopic measurements. IR spectroscopic analyses were carried out by measurement of the absorbance in the FT-IR Drift mode (Tensor 27 HTS-XT, Bruker, Massachusetts, USA) with 40 scans per sample, a wavenumber range from 400 to 4000 cm^{-1}, and a resolution of 1.9 cm^{-1}. For evaluation, all spectra together were truncated in the range of 800 to 1300 cm^{-1}, normalized with respect to the highest absorbance and the goethite spectrum was subtracted from the absorption spectra by using the software Essential FTIR® (Operant LLC, Virginia, USA).

2.2. Theory

2.2.1. Molecular modeling. We have considered two different goethite surface planes (010 and 100 according to the *Pnma* space group). This choice was motivated by the stability of the 010 surface[32,33] and the abundance of the 100 surface plane.[34–38] The selected surface planes exhibit two kinds of Fe atoms with two different coordination numbers. For the bare 010 and 100 goethite surface planes, each surface Fe atom is coordinated by four and five O atoms, respectively. Therefore, this will give us the opportunity to explore different binding motifs between phosphate and goethite. These two surfaces

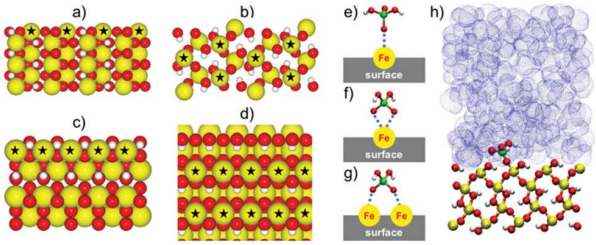


Fig. 1 Side and top views of the 010 goethite surface planes (a) and (b) as well as for the 100 goethite surface planes (c) and (d) according to the *Pnma* space group, schematic view of the possible binding motifs (**M@010** and **M@100** (e), (2O + 1Fe) **B@010** (f), (2O + 2Fe) **B@100** (g)), and phosphate–goethite(100)–water model (h). White, red, green, and yellow colors correspond to H, O, P, and Fe atoms, respectively. Atoms labeled by a star refer to the surface Fe atoms. Water molecules in (h) are represented by blue spheres for better visualization.

have been modelled by periodic slabs, constructed by repetition of the goethite unit cell[39] in the relevant directions (see Fig. 1a–d). The goethite orthorhombic unit cell used in the current contribution consists of four FeOOH formula units (16 atoms) with lattice constants a = 9.9560 Å, b = 3.0215 Å, and c = 4.6080 Å. These lattice constants are almost the same as the values determined experimentally (see Fig. S1 in the ESI†). To simulate these surfaces, a layer of about 20 Å vacuum was added between the periodic slabs perpendicular to the surface plane. In the vacuum region, phosphate was added at the top of each surface plane in two different starting configurations to construct monodentate (**M**) and bidentate (**B**) binding motifs (see Fig. 1e–g). This has been done by constructing either one covalent bond (**M** motif) or two covalent bonds (**B** motif) between the phosphate O atoms and the goethite Fe atoms. The shortest distances between the adjacent Fe atoms are around 4.6 Å for the 010 goethite surface plane and 3.0 Å for the 100 surface plane. Therefore, the formation of the **B** binding motif between phosphate and the surface will mainly take place between two phosphate O atoms and one surface Fe atom (2O + 1Fe) for the 010 surface plane (**B@010**) and two phosphate O atoms and two surface Fe atoms (2O + 2Fe) for the 100 surface plane (**B@100**).[40] To mimic the soil solution and its impact on the phosphate–goethite interaction, water molecules at a density of about 1 g cm^{-3} have been introduced into the vacuum region between the slabs to construct the final simulation box (for example, see Fig. 1h, which contains α-FeOOH (256 atoms) + 1 phosphate molecule + 150 water molecules = 714 atoms). Note that in contrast to previous work,[17] the present simulation box is considerably larger, thus giving results less influenced by finite size effects. The solvation procedure involved filling the vacuum region of the box with water molecules by using the solvation tool provided by the Packmol software.[41] To model the relevant pH solution of the present sorption experiment, the phosphate molecule has been introduced onto the surface in the form of the KH_2PO_4 species. Therefore, we have 4 phosphate–goethite–water model systems, *i.e.* **M@010**, (2O + 1Fe) **B@010**, **M@100**, and (2O + 2Fe) **B@100**.

The interaction of individual molecules (phosphate, water, and the OH^- group) with the goethite surface in vacuum has

been simulated as well. Here, three models have been built for each goethite surface plane (010 and 100). The first model involved complexation of a single KH_2PO_4 molecule with the goethite surface. The second model considers complexation of a single H_2O molecule with the goethite surface. The third model involved complexation of a single OH^- group in the presence of K^+ as a counter ion with the goethite surface. All these complexes have been constructed in vacuum without adding solvent water molecules to the simulation box. In each case, the single fragment (KH_2PO_4, H_2O, or OH^-) was complexed to the goethite surface in the form of a **M** binding motif. The aim of introducing these models is to investigate (1) the role of the aqueous solution in the phosphate–goethite binding process, (2) the competition among phosphate, water, and the OH^- group regarding their interaction with the goethite surface, and (3) the pH effect on the phosphate–goethite binding process.

2.2.2. Computational details. For all the phosphate–goethite models in water as well as in vacuum, DFT-based geometry optimization has been carried out using the quickstep code[42] implemented in the CP2K simulation package.[43] Here, the hybrid Gaussian and plane-wave (GPW) method[44] has been applied for calculating the DFT electronic ground state structure. The Perdew–Burke–Ernzerhof (PBE) functional[45] has been used together with the Goedecker–Teter–Hutter (GTH) pseudopotentials.[46] The electronic density cutoff for atomic core electrons was chosen as 500 Ry. The double-ζ valence polarized (DZVP) basis set optimized for the GTH pseudopotentials has been used.[47] The empirical D3 dispersion correction by Grimme was employed.[48] PBC have been applied in all three spatial directions. The total electronic energy was converged with a convergence threshold for the self-consistent field energy of 10^{-8} Hartree.

To characterize the complexation reaction, phosphate + goethite surface $\rightarrow$ phosphate–goethite-complex, the interaction energy (E_{int}) between the phosphate species and the goethite surface plane for all optimized complexes was calculated as follows (for more details see the ESI†):

$$E_{int} = E_{phosphate\text{–}goethite\text{-}complex} - (E_{phosphate} + E_{goethite\ surface}) \quad (1)$$

where $E_{phosphate\text{–}goethite\text{-}complex}$, $E_{phosphate}$, and $E_{goethite\ surface}$ are the total electronic energies of the geometry optimized phosphate–goethite-complex, phosphate, and goethite surface, respectively. For all interaction energies, the effect of the basis set superposition error (BSSE) has been corrected using the counterpoise scheme.[49]

At the same level of theory IR vibrational frequencies and IR intensities have been calculated for the optimized phosphate–goethite complexes **M@010**, **B@010**, **M@100**, and **B@100**. The vibrational frequencies have been scaled by a factor of 0.986.[50] IR spectra presented below have been obtained by including a phenomenological Gaussian broadening of width 30 cm^{-1}. The calculated spectra for the different phosphate–goethite complexes were normalized individually to unity. It is important to mention that these calculated spectra correspond to the overall spectra of the adsorbed phosphate at the goethite surfaces. This means that every spectrum includes molecular vibrations of the phosphate–goethite complex and the goethite surface itself. In order to quantify the contribution of the phosphates, normal mode displacements have been analyzed to generate spectra due to modes that are dominated by phosphate vibrations (*i.e.* phosphate-related spectra).

3. Results and discussion

3.1. Adsorption kinetics and FT-IR spectroscopy

After 2 h adsorption time, the whole amount of phosphate in the solution was essentially completely adsorbed onto the goethite surface yielding a phosphate surface coverage of 0.18 μmol m^{-2}. Assuming a regular distribution of the adsorbed phosphate at the goethite surface, this reported surface coverage indicates that the average separation distance between the neighboring phosphate molecules is about 3–5 nm. In general, there is no observation of a difference in the phosphate uptake for different reaction times. This is due to the low initial phosphate concentration in solution, competition of hydroxyl and phosphate ions for adsorption sites and the negatively charged oxide surface.[8,51,52]

Regarding FT-IR spectroscopy, comparison of the positions of P–O bands and the assignment of the adsorbed complex and its molecular symmetry are difficult due to the shift of the peak position based on reaction conditions, sample treatment, adsorbed phosphate content, pH, and/or moisture.[6,19,22,53–55] Due to that, the number and not the exact position of vibrations were recommended as characteristics by Arai and Sparks.[6] Previous studies advised an analysis of metal–phosphate complexes in the spectral region from 940 to 1200 cm^{-1} due to the expected position of the two α-FeOOH absorption bands at 828 and 927 cm^{-1} in the goethite spectrum.[22,24] However, the present analysis will focus on a wider spectroscopic range (800–1300 cm^{-1}) for a better correlation with theory below.

The overall FT-IR spectrum that contains the molecular vibrations of the goethite surface and phosphate–goethite complex is presented in Fig. 2a. This spectrum exhibited mainly three peaks at 827, 927, and 1132 cm^{-1} and one shoulder at 1050 cm^{-1} (see Table 1). If only the number of bands were included as described by Arai and Sparks,[6] a C_{3v} symmetry point group can be assumed for the phosphate–goethite complex based on the three main bands. Referring to the dissolved phosphate species[6] and reference phosphate complexes[56] included in Table 1 that have C_{3v} symmetry point groups, the observed vibrations in the present study could be assigned to be due to a monodentate complex. However, if the vibrational frequency at the shoulder is counted, a C_{2v} symmetry point group must be considered for the phosphate–goethite complex. In this case, the bidentate phosphate–goethite complex could be assigned for the present experiment. This is mainly based on the assignment of the dissolved phosphate species[6] and reference phosphate complexes[56] that have C_{2v} symmetry point groups (see Table 1). One should note that in another approach

 This journal is © the Owner Societies 2019

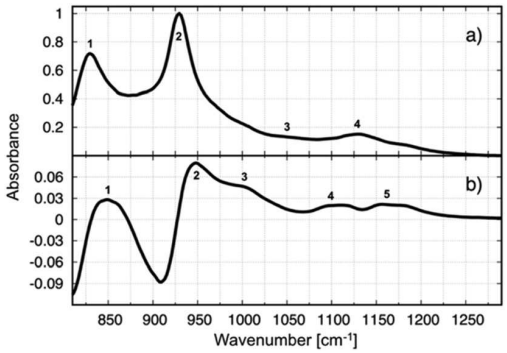


Fig. 2 Normalized overall experimental FT-IR spectrum of adsorbed phosphate on the goethite surface at pH 6.3 after an adsorption time of 2688 h (a) and the phosphate-related spectrum (b) that was obtained by subtraction of the spectrum of pure goethite from the overall spectrum. Notice that the phosphate-related spectrum exhibits negative and positive features in the range below 900 cm^{-1}. Moreover, shifts in the peak position can be observed when comparing both spectra.

focusing on the position of P–O bands, Tejedor-Tejedor and Anderson[22] assigned a non-protonated monodentate complex ($FePO_4$) at 1001 and 1025 cm^{-1}, a non-protonated bidentate complex (Fe_2PO_4) at 1044 and 1096 cm^{-1}, and a mono-protonated bidentate complex (Fe_2HPO_4) at 982, 1006 and 1123 cm^{-1} (see Table 1). According to this assignment, the present peak at 1132 cm^{-1} would be due to a mono-protonated bidentate phosphate–goethite complex (Fe_2HPO_4). In addition, the shoulder at 1050 cm^{-1} could refer to the presence of a small proportion of non-protonated bidentate complex (Fe_2PO_4) and/or mono-protonated monodentate complex ($FeHPO_4$). Moreover, the two pronounced peaks at 827 and 927 cm^{-1} could be due to molecular vibrations related to the goethite surface and not to the phosphate–goethite complex as described before in the literature.[22,24]

More information about the possible binding motifs for the phosphate–goethite complex is provided by the interpretation of the difference IR spectrum relevant to the phosphate–goethite complex only (see Fig. 2b). In the following, we will refer to this spectrum as the phosphate-related spectrum. It is obtained by subtraction of the pure goethite spectrum from the overall spectrum. The phosphate-related spectrum exhibits four main spectral bands around 850, 948, 1110, and 1165 cm^{-1} and one shoulder around 1000 cm^{-1} (see Table 1). The first two intense peaks around 850 and 948 cm^{-1} in this spectrum are similar to the observed ones for the overall spectrum (at 827 and 927 cm^{-1}) but with a band position shift of about 25 cm^{-1}.

Table 1 Experimental IR frequencies of dissolved phosphate species, reference phosphate complexes, adsorbed phosphate on goethite and present calculated vibrational frequencies (features of the IR spectra and other relevant vibrational frequencies) for the adsorbed KH_2PO_4 on goethite for the optimized complexes of **M@010**, **B@010**, **M@100**, and **B@100**. $FePO_4$: non-protonated monodentate, $FeHPO_4$: mono-protonated monodentate, Fe_2PO_4: non-protonated bidentate, and Fe_2HPO_4: mono-protonated bidentate

Study	Species and description		Wavenumber [cm^{-1}]						
Dissolved phosphate species									
Ref. 6	PO_4^{3-} (T_d)				1006				
	HPO_4^{2-} (C_{3v})		850	989			1077		
	$H_2PO_4^-$ (C_{2v})		870	940			1074		1160
	H_3PO_4 (C_{3v})		888		1006				1179
Reference phosphate complexes									
Ref. 56	$Co(NH_3)_5PO_4$ (C_{3v} & monodentate)			934	980	1030			
	$(CH_3O)PO_3^{2-}$ (C_{3v} & monodentate)		755		975			1095	
	$Co(NH_2CH_2CH_2NH_2)PO_4$ (C_{2v} & bidentate)			900	915		1050	1085	
	$(CH_3O)_2PO_2^-$ (C_{2v} & bidentate)		815				1050	1110	1220
Phosphate–goethite complexes									
Ref. 22	150 μmol l^{-1} P, pH 5				1006		1043	1098	1123
	150 μmol l^{-1} P, pH 6				1000	1023	1044	1099	1127
	$FePO_4$				1001	1025			
	Fe_2PO_4 and/or $FeHPO_4$						1044	1096	
	Fe_2HPO_4			982	1006				1123
Ref. 53	pH 5			940	1010		1042		1120
	pH 6			940	1004		1050	1110	
	pH 7			945			1050	1094	
Present experiment	Overall spectrum		827	927			1050		1132
	Phosphate-related spectrum		850	948	1000		1110		1165
					(990–1010)		(1095–1120)		(1156 & 1175)
Present theory	**M@010**	Features	800	890	965	1035	1110		1200
		Other relevant frequencies		819	943	993	1049		
	B@010	Features	850		970		1122		1223
		Other relevant frequencies		830	923	954	992 & 1007	1035 & 1069	1107
	M@100	Features	814	930			1050		1171
		Other relevant frequencies		838	853	945	957	999	
	B@100	Features	830	890	950		1048		1137
		Other relevant frequencies		826	829	862	930	974	

The presence of these two peaks in both spectra as well as the negative regions reveals that the phosphate–goethite complex could contribute to the observed spectral peaks in the overall spectrum. At the same time, there could be a strong coupling between goethite and phosphate motions. The observation of phosphate-related features in the range of 825–950 cm^{-1} is in good agreement with the reported spectral bands for Co–phosphate[56] and phosphate–goethite[53] complexes (see Table 1).

In the following the analysis will focus on the three bands around 948, 1110, and 1165 cm^{-1} and the shoulder around 1000 cm^{-1}, which are clearly related to the phosphate–goethite complex. A closer look at the phosphate-related spectrum shows the following: the observed band at 948 cm^{-1} is a narrow intense peak while the other bands are broad and less intense. The shoulder around 1000 cm^{-1} is distributed in the range of 990–1010 cm^{-1}. The band around 1110 cm^{-1} is mainly distributed in the range of 1095–1120 cm^{-1} while the band around 1165 cm^{-1} corresponds to a bimodal peak with maxima located around 1156 and 1175 cm^{-1}.

According to the assignment by Arai and Sparks,[6] a C_{2v} symmetry would involve four bands due to a bidentate motif, whereas a C_{3v} symmetry would lead to three bands only, which could results from a monodentate motif. Thus, in the present case this doesn't provide a clear-cut assignment.

Compared with the results of Tejedor-Tejedor and Anderson,[22] the present peaks around 948 and 1165 cm^{-1} could not be clearly assigned. On the other hand, the observed vibrations in the present study around 1000 cm^{-1} (range: 990–1010 cm^{-1}) could be assigned to a mono-protonated bidentate complex (Fe_2HPO_4) and/or a non-protonated monodentate complex ($FePO_4$). Vibrations around 1110 cm^{-1} (range: 1095–1120 cm^{-1}) could be assigned to a non-protonated bidentate complex ($FePO_4$) and/or a mono-protonated bidentate complex (Fe_2HPO_4). Thus, considering the assignment of Tejedor-Tejedor and Anderson,[22] the present IR spectrum indicates the presence of a mixture of monodentate and bidentate complexes with a majority of the mono-protonated bidentate complex.

In contrast, Krumina *et al.*[53] assigned the vibrational peaks at 940–945, 1004–1012, 1042–1050, 1085–1094, and 1110–1128 cm^{-1} (see Table 1) at different pH values as a series of monodentate phosphate surface complexes in different protonation states. According to this assignment, the present vibrational bands might indicate a mono-protonated monodentate complex ($FeHPO_4$).

This discussion clearly shows the yet unsolved general problem of assignment of phosphate–goethite binding motifs to IR features. This is to some extent due to variations in experimental conditions, but also due to the fact that observed IR spectra will always reflect binding at different surface planes of the mineral particles at the same time. Therefore, in the following we will first discuss our simulation results for well-defined systems, which could serve as a reference for assignment. Subsequently, it will be shown how mixing of spectra due to different motifs can improve the agreement with experiments.

3.2. Structure and energetics of phosphate at the goethite–water interface

Goethite bulk Fe atoms are saturated with octahedral coordination by O^{2-} and OH^- in a $FeO_3(OH)_3$ structure while the Fe atoms of the neutral bare goethite surfaces are unsaturated and surface plane dependent. Hence, the goethite surface plane plays an important role in controlling the mechanisms and strength of the reaction of phosphate with the goethite surface. To unravel this role, we will discuss our results with respect to the interaction of phosphate with the 010 and 100 goethite surface planes. Both surfaces may exhibit similar **M** binding motifs, but different **B** binding motifs with phosphates.

3.2.1. Phosphate binding at the 010 goethite surface plane.

For the most abundant phosphate species in the present experimental study (KH_2PO_4), stable **M** (see Fig. 3a) and 2O + 1Fe **B** (Fig. 3b) complexes are formed between phosphate and the goethite surface. The length of the Fe–O covalent bond for the **M** complex (1.94 Å) is shorter than for the **B** complex (1.98 & 2.03 Å, see Table 2). These two complexes have a high interaction energy between phosphate and goethite (see Table 2) with the **B** complex being more stable than the **M** complex.

Regarding the phosphate–water interaction, one proton (H^+) transfers from phosphate to water for both **M** and **B** complexes. This transferred proton stays in contact with its original phosphate donating O atom *via* formation of a H-bond (HB). In contrast, the second proton in the $H_2PO_4^-$ species remained bonded to its phosphate O atom. In addition, other HBs between water H atoms and phosphate O atoms can be observed.

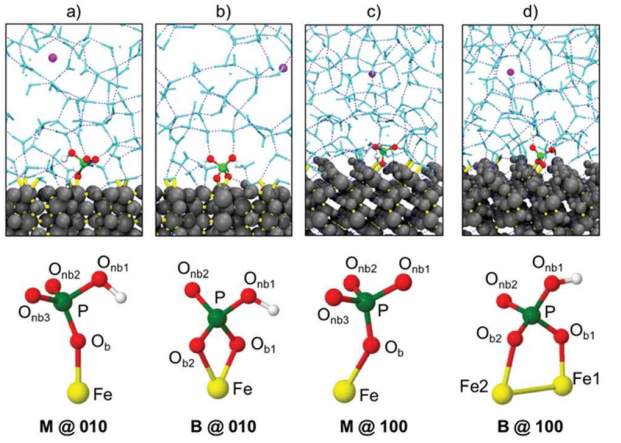


Fig. 3 Upper panel: Geometry optimized structures of the phosphate–goethite–water complexes for the **M@010** motif (a), the (2O + 1Fe) **B@010** (b) motif, **M@100** motif (c), and (2O + 2Fe) **B@100** motif (d). Goethite and water atoms are colored in gray and cyan, respectively. For phosphate, atoms are colored in green (P), red (O), white (H), and purple (K). Intramolecular and intermolecular covalent bonds with goethite atoms are colored in yellow and HBs are colored in blue. Lower panel: Relevant fragments of the optimized binding motifs shown in the upper panel. Here Fe atoms are colored in yellow. O_b and O_{nb} refer to the bonded and non-bonded phosphate O atoms to the goethite surface Fe atoms. Comparing these equilibrium structures with the starting configurations in Fig. 1, one can observe proton transfer processes from phosphate to water and to the surface.

This journal is © the Owner Societies 2019

Table 2 Interaction energies between phosphate (KH_2PO_4) and goethite as well as selected distances for the optimized complexes of **M@010**, **B@010**, **M@100**, and **B@100**. Moreover, these results indicate that water as an aqueous solution competes with the goethite surface regarding their binding to phosphate yielding less binding in the presence of water (−59 kcal mol^{-1}, for **M@010**) than in the vacuum case (−83 kcal mol^{-1}, for **M@010**)

Surface plane	Binding motif	E_{int} [kcal mol^{-1}]	Distance [Å]		
			$Fe_{goethite}$–O_P	Fe–P	P–O_P
010	**M**	−59	1.94	3.41	1.53, 1.54, 1.54, 1.66
	B (2O + 1Fe)	−101	1.98 & 2.03	2.58	1.53, 1.56, 1.58, 1.62
100	**M**	−74	2.12	3.48	1.55, 1.56, 1.58, 1.58
	B (2O + 2Fe)	−102	1.95 & 2.16	3.15 & 3.26	1.51, 1.57, 1.59, 1.61

Regarding the water–goethite interaction, the surrounding water molecules approach the goethite surface and form covalent bonds with goethite. Mainly this takes place between water O atoms (O_{H_2O}) and most of the Fe active sites at the 010 goethite surface plane. The Fe–O_{H_2O} covalent bond lengths are in the range of 1.87–2.06 Å. Furthermore, some of these water molecules dissociate at the goethite surface to protons (H^+) and hydroxyl groups (OH^-). Regardless of these covalent bonds formed at the surface, water through its H atoms forms HBs with the goethite surface O atoms.

For reference, let us discuss the interaction of the individual molecular systems (phosphate, water, and the OH^- group) with the goethite surface in vacuum. The calculated interaction energies for the goethite complexes with H_2O, KH_2PO_4, and KOH are −30, −83, and −162 kcal mol^{-1}, respectively. This indicates that the strength of the adsorption process at the goethite surface increases in the order H_2O < phosphate < KOH. This means that phosphate can replace the adsorbed H_2O molecules at the goethite surface. Moreover, at high pH and predominance of the OH^- groups in the equilibrium solution, OH^- can replace the adsorbed phosphate at the goethite surface resulting in a strong drop in the phosphate adsorption. These findings agree with experimental results, such as those of Liu *et al.*[57] and Antelo *et al.*,[58] that reported a decrease of the phosphate adsorption upon increasing the soil solution pH. Moreover, these results indicate that water as an aqueous solution competes with the goethite surface regarding their binding to phosphate resulting in less binding in the presence of water (−59 kcal mol^{-1}) than in the vacuum case (−83 kcal mol^{-1}). This points to the vital role of water and the necessity of including water in molecular simulations as an aqueous solution for the phosphate–goethite binding process.

3.2.2. Phosphate binding at the 100 goethite surface plane. At the 100 goethite surface plane (Fig. 3c and d), the **B** complex is more stable than the **M** complex for the $H_2PO_4^-$ species (see Table 2). Consequently, this indicates that the **B** complex has a higher tendency to be formed. Furthermore, the **M@100** complex is more stable than the corresponding **M@010** one. In contrast, the **B** complexes have almost the same stability at the 100 and 010 goethite surface planes.

For both complexes at the 100 goethite surface, the interfacial water molecules interact with the goethite surface *via* the formation of covalent bonds between the water O_{H_2O} atoms and goethite Fe atoms. Moreover, HBs are formed between the water H_{H_2O} and the goethite O atoms. In addition, dissociation of some water molecules is observed at the surface to protons and hydroxyl groups. The thus produced ions form covalent bonds with the goethite surface. Moreover, for both **M** and **B** complexes, one proton transfers from phosphate to water (see Fig. 3c, d and especially the lower panel). For the **M@100** complex, the second proton transfers to the surface. For both motifs at the 100 surface plane, the transferred protons stay in contact with the original phosphate donating O atoms *via* the formation of HBs.

Similar to the 010 goethite surface case, the competition among phosphate, water, and the OH^- group regarding their interaction with the 100 goethite surface plane has been studied in vacuum. The interaction energies for the goethite complexes with H_2O, KH_2PO_4, and KOH are −22, −81, and −199 kcal mol^{-1}, respectively. This means that the adsorption strength at the 100 goethite surface plane increases in the order H_2O < phosphate < KOH. This order is exactly the same as obtained in the case of the 010 goethite surface plane. It confirms again that phosphate has the ability to replace the adsorbed water molecules at the goethite surface but the OH^- groups can replace both phosphate and water at the surface.

3.2.3. Theory–experiment correlation. The applied pH in the present experimental study suggests the predominance of the $H_2PO_4^-$ species. The calculated strength of the binding motifs of the $H_2PO_4^-$ species at both goethite surface planes increases in the order **M@010** (−59 kcal mol^{-1}) < **M@100** (−74 kcal mol^{-1}) < 2O + 1Fe **B@010** (−101 kcal mol^{-1}) ≈ 2O + 2Fe **B@100** (−102 kcal mol^{-1}), see Table 2. This reveals that both **B** motifs (2O + 1Fe **B** and 2O + 2Fe **B**) are the most abundant binding motifs at the studied surface planes for the used pH (*i.e.* in the presence of $H_2PO_4^-$ species). It is important to mention here that all these binding motifs observed in this case are mono-protonated motifs and also hydrogen-bonded to their original hydroxyl H atom. Thus, one can conclude that the mono-protonated **B** motif is the predominant binding motif at low phosphate loading and the experimentally studied pH. Moreover, the mono-protonated **M** binding motif might exist but in a minor fraction. In principle, this is in agreement with an assignment of the present experimental IR spectrum according to Tejedor-Tejedor and Anderson,[22] *i.e.* to a mixture of minority monodentate and majority bidentate complexes. This assignment will be discussed in more detail in the following section.

3.3. Analysis of IR spectra

All calculated IR spectra of the adsorbed phosphate species at the goethite surface for the different phosphate–goethite complexes are presented in Fig. 4. Here, the overall IR spectra due to molecular vibrations of the goethite surface and phosphate–goethite

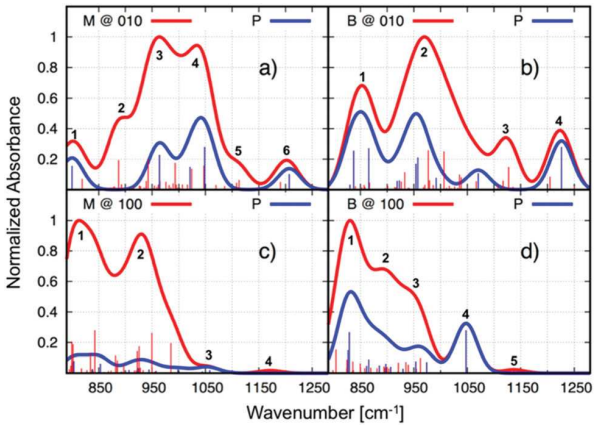


Fig. 4 Calculated IR spectra (sticks and phenomenologically broadened with a half-width of 30 cm^{-1}) of the adsorbed phosphate species (KH_2PO_4) at the goethite surface for the optimized complexes of **M@010** (a), **B@010** (b), **M@100** (c), and **B@100** (d). Red color refers to the overall spectrum due to the goethite surface and the phosphate–goethite complexes while blue color refers to contributions of the phosphate–goethite complexes only (phosphate-related spectrum).

complexes as well as the phosphate-related IR spectra have been introduced.

For the **M@010** binding motif, the overall IR spectrum in the range of 800–1300 cm^{-1} exhibits six features (four peaks and two shoulders) around 800, 890, 965, 1035, 1110, and 1200 cm^{-1} (see Fig. 4a). Comparing the overall spectrum to the corresponding phosphate-related spectrum, one observes that not all features in this range originate from phosphate molecular vibrations. Fig. 4a shows that features 2 and 5 are due to goethite surface vibrations only. All other features in the **M@010** spectrum contain contributions from the phosphate–goethite complex and the goethite surface, although features 1 and 6 are dominated by phosphate vibrations. For the **B@010** complex, Fig. 4b shows that the overall IR spectrum exhibits four features around 850, 970, 1122, and 1223 cm^{-1}. Here, phosphate vibrations are dominant for features 1 and 4. Notice that shifts in the peak position can be observed when comparing both spectra.

At the 100 goethite surface plane, the overall spectrum for the **M** complex exhibits four features around 814, 930, 1050, and 1171 cm^{-1} (see Fig. 4c). Comparing the overall and the phosphate-related spectra, one notices that in this case the goethite vibrations give the dominant contribution to the spectrum in the whole range. For the **B@100** complex, Fig. 4d shows that the overall spectrum exhibits five features around 830, 890, 950, 1048, and 1137 cm^{-1}. Phosphate vibrations contribute strongly to all features except feature 5. Feature 4 is solely due to phosphate modes. Feature 2 in the overall spectrum is reduced to a shoulder in the phosphate spectrum. The opposite holds true for feature 3.

Finally, we comment on the relative intensities of the different panels in Fig. 4. Specifically, the intensities of the highest peaks for the different complexes have the order **M@100** > **B@100** > **M@010** > **B@010** with scaling factors of 1×(**M@100**) = 7.4 × (**B@100**) = 9.2 × (**M@010**) = 9.9 × (**B@010**). In the case of the phosphate-related spectra, the intensities of the highest peaks have the order **M@100** > **B@100** > **M@010** > **B@010** with scaling factors of 1×(**M@100**) = 1.7×(**B@100**) = 2.3×(**M@010**) = 2.4×(**B@010**). Thus, under the assumptions of equal contributions to a measured spectrum, the **M@100** complex would be clearly dominant, in terms of both the overall and the phosphate-related IR spectra.

The assigment of the IR spectra for the different binding motifs is provided in Tables 3 and 4, see also the definition of atom labels in Fig. 3. Overall, the calculated IR spectra and their assignment are strongly dependent on the binding motif type of the phosphate–goethite complex as well as the goethite crystal surface plane. It is important to emphasize that the experimental IR spectrum is due to a combination of all different binding motifs at the different surface planes (not only 010 and 100) present in the real sample. Furthermore, the experimental IR measurements have been conducted for dried samples. Thus, a one-to-one comparison is rather difficult if not impossible. Therefore, below we will present a systematic study of the effect of varying composition on the IR spectral features. First, however, the assignment of the spectra for the different motifs will be discussed.

Let us first compare the calculated phosphate-related IR spectra with the corresponding experimental IR spectrum (Fig. 2); for the assignment see Tables 3 and 4. The difference spectrum shows negative and positive features in the range below 900 cm^{-1}, which could involve band shifts as discussed before. This hinders straightforward comparison, but one can state that all cases except **M@010** predict a strong phosphate-related band around 850 cm^{-1} (for more details, see the ESI†). The situation is more favourable if the focus is set on the spectral range of 925–1280 cm^{-1} (see Fig. 5). The overall behavior and in particular the dominant peak at 950 cm^{-1} is best reproduced by the **B@010** and the **M@100** complexes. The shoulder in the experimental spectrum at about 1000 cm^{-1} is seen in the case of the **M@100** complex. In addition, a qualitative agreement between the experimental spectrum and that for the **B@010** complex can be found in the range of 1050–1200 cm^{-1}, *i.e.* in both cases one observes two bands. Up to this point, one could conclude an abundance of the **B@010** and the **M@100** complexes under the present experimental conditions.

In order to use the information contained in the full spectral range and to also account for possible interaction-induced peak shifts, we will focus on the comparison of the overall experimental and theoretical spectra in the following. At first glance, the results in Fig. 6 indicate a reasonable agreement in particular for the **M@100** and **B@010** complexes. Here, the **M@100** complex shows a better agreement with the experiment as far as the first two peaks are concerned. However, a reasonable agreement with the last experimental peak can be observed only if the **B@010** complex is considered. More specifically the experimental peak observed at 827 cm^{-1} could be due to molecular vibrations related to the **B@010**, **M@100**, and/or

 This journal is © the Owner Societies 2019

Table 3 Assignment of the IR spectra calculated for the adsorbed $H_2PO_4^-$ on goethite for the optimized complexes of **M@010** and **B@010** binding motifs. Underlined frequencies refer to those vibrations having high phosphate contributions. O_b and O_{nb} refer to the bonded and non-bonded phosphate O atoms at the goethite surface. sym., asym., and str. are abbreviations for symmetric, antisymmetric, and stretching, respectively

Binding motif	Frequencies in cm^{-1} and their description
M@010	Feature 1 (peak around 800 cm^{-1})
	801: P–3O_{nb} complex vibration + P–O–H bending vibration 819: Fe–O–H surface bending vibrations
	Feature 2 (shoulder around 890 cm^{-1})
	887 & 893: Fe–O–H surface bending vibrations
	Feature 3 (peak around 965 cm^{-1})
	943: Fe–O–H surface bending vibrations 964: O_b–P–2$O_{nb1,3}$ sym. str. + P–O–H bending vibration + Fe–O–H surface bending vibrations 976, 982, 989 & 993: Fe–O–H surface bending vibrations
	Feature 4 (peak around 1035 cm^{-1})
	1021: mainly O_b–P–O_{nb3} asym. str. + O_{nb1}–P–O_{nb2} sym. str. + P–O–H wagging vibration 1024 & 1047: Fe–O–H surface bending vibrations 1049: P–O_{nb3} str. vibration + O_b–P–2$O_{nb2,3}$ asym str. + P–O–H wagging vibration + Fe–O–H surface bending vibrations
	Feature 5 (shoulder around 1110 cm^{-1})
	1070 & 1077: Fe–O–H surface bending vibrations 1108 & 1113: sym scissoring of four Fe–O–H groups
	Feature 6 (peak around 1200 cm^{-1})
	1190: Fe–O–H surface bending vibrations 1207: P–O–H bending vibration
B@010	Feature 1 (peak around 850 cm^{-1})
	830 & 838: P–O–H bending vibration + Fe–O–H surface bending vibrations 866: 2O_b–P–2O_{nb} sym. str. + P–O–H bending vibration
	Feature 2 (peak around 970 cm^{-1})
	919, 923 & 954: O_{b2}–P–O_{nb1} asym. str. + Fe–O–H surface bending vibrations 957: 2O_b–P–O_{nb2} sym. str. + Fe–O–H surface bending vibrations 992: O_{b1}–P str. vibration + O_{b1}–P–2O_{nb} asym. str. 1007: Fe–O–H scissoring vibrations + small contribution of O_{b1}–P–O_{nb2} sym. str. vibration 1035 & 1039: small contribution of 2O_b–P–O_{nb} asym. str. + Fe–O–H scissoring 1067: small contribution of 2O_b–P–O_{nb2} asym. str. + Fe–O–H & P–O_{nb}–H_P scissoring vibration 1071: P–O_{b2} str. vibration + 2O_b–P–O_{nb2} asym. str. + P–O_{nb}–H_P rocking vibration + Fe–O–H scissoring vibration
	Feature 3 (peak around 1122 cm^{-1})
	1107: sym. scissoring for two Fe–O–H groups 1117 & 1127: low contribution of (P–2O_b asym. str. and P–O–H scissoring vibration) + Fe–O–H surface bending vibrations
	Feature 4 (peak around 1223 cm^{-1})
	1205: Fe_2–O–H surface bending vibrations 1227: P–O–H bending vibration

B@100 complex(es), while the peak observed at 927 cm^{-1} could correspond to the **M@010**, **B@010**, and/or **M@100** complex(es). Furthermore, the observed peak at 1132 cm^{-1} could be assigned as being due to the **B@010** complex, whereas the shoulder at 1050 cm^{-1} could be assigned to the **M@100** complex. Given the fact that experimental spectra will be affected by the presence of different crystal planes and therefore binding motifs, one might ask whether a weighted average of the present theoretical results would lead to an improved agreement with experiment. Of course, this neglects the possible presence of other crystal planes as well as effects due to, *e.g.*, surface coverage and drying conditions.

Calculated spectra obtained by weighted averaging are shown in Fig. 7 and compared with the overall experimental IR spectrum of the adsorbed phosphate at the goethite surface. For better comparison with Fig. 6 we have combined the

Table 4 Assignment of the IR spectra calculated for the adsorbed $H_2PO_4^-$ on goethite for the optimized complexes of **M@100** and **B@100** binding motifs. Underlined frequencies refer to those vibrations having high phosphate contributions. O_b and O_{nb} refer to the bonded and non-bonded phosphate O atoms at the goethite surface. sym., asym., and str. are abbreviations for symmetric, antisymmetric, and stretching, respectively

Binding motif	Frequencies in cm^{-1} and their description
M@100	Feature 1 (peak around 814 cm^{-1})
	800 & 802: Fe–O–H surface bending vibrations
	804: P–3O_{nb} sym. str. + Fe–O–H surface bending vibrations
	834 & 843: Fe–O–H surface bending vibrations
	838: P–3O_{nb} sym. str. + Fe–O–H surface bending vibrations
	853: P–2O_{nb} (str. + bending) vibration + Fe–O–H surface bending vibrations
	Feature 2 (peak around 930 cm^{-1})
	881, 884, 885 & 897: Fe–O–H surface bending vibrations
	907: O_b–P–2O_{nb} sym. str. + Fe–O–H surface bending vibrations
	923: Fe–O–H surface bending vibrations
	924: O_b–P–2$O_{nb2,3}$ asym. str. + Fe–O–H surface bending vibrations
	926 & 928: small contribution of P–2O_{nb} asym. str. + Fe–O–H surface bending vibrations
	945: mainly P–O_b str. vibration (characteristic for **M** motif) + O_b–P–2$O_{nb1,2}$ sym. str. and asym. with O_{nb3} + Fe–O–H surface bending vibrations
	950: Fe–O–H surface bending vibrations
	957: mainly P–O_{nb1} str. vibration + P–3O_{nb} asym. str.
	985: Fe–O–H surface bending vibrations
	999: (O_b–P–2$O_{nb2,3}$ sym. str.) and asym. with O_{nb1} + Fe–O–H surface bending vibrations
	Feature 3 (peak around 1050 cm^{-1})
	1044: O_b–P–O_{nb2} asym. str. + Fe–O–H surface bending vibrations
	1058: O_b–P–O_{nb3} asym. str. + Fe–O–H surface bending vibrations
	Feature 4 (peak around 1171 cm^{-1})
	1171: Fe–O–H surface bending vibrations
B@100	Feature 1 (peak around 830 cm^{-1})
	805: Fe–O–H surface bending vibrations
	825 & 836: Fe–O–H twisting vibration
	826 & 829: O_{b2}–P–2O_{nb} sym. str. + Fe–O–H surface bending vibrations
	859: small contribution of 2O_b–P–2O_{nb} sym. str. + Fe–O–H surface bending vibrations
	862: O_{b1}–P–O_{nb1} sym. str. + Fe–O–H surface bending vibrations
	866: O_{b1}–P–2O_{nb} sym. str. + Fe–O–H surface bending vibrations
	Feature 2 (shoulder around 890 cm^{-1})
	885: 2O_b–P asym. str. + surface Fe–O sym. str.
	897: O_{b1}–P–O_{nb1} asym. str. + Fe–O–H surface bending vibrations
	907: O_{b1}–P–O_{nb1} asym. str. + Fe–O–H surface bending vibrations
	Feature 3 (shoulder around 950 cm^{-1})
	930: P–O_{nb1} str. vibration + P–O–H bending vibration + Fe–O–H surface bending vibrations
	953: O_{b2}–P–O_{nb1} asym. str. vibration + P–O–H bending vibration + Fe–O–H surface bending vibrations
	974: mainly P–O–H bending vibration + Fe–O–H surface bending vibrations
	Feature 4 (peak around 1048 cm^{-1})
	1048: mainly P–O_{nb2} str. vibration + low contribution of O_{b1}–P–1O_{nb1} sym. str. and asym with O_{nb2}
	Feature 5 (peak around 1137 cm^{-1})
	1137: Fe–O–H surface bending vibrations

normalized spectra. The respective mixing ratios taking into account the individual intensities will be given as well.

Fig. 7a shows weighted average spectra that have proportions of **M@010 : B@010** varying from 1 : 9 to 9 : 1. (Taking into account the peak intensity ratio 1×(**M@010**) = 1.076(**B@010**) this corresponds to ratios from 1 : 9.7 to 1 : 0.12.) The comparison with experiment clearly improves by decreasing the **M@010 : B@010** proportion from 9 : 1 to 1 : 9. The results for the respective **M@100** and **B@100** complexes are presented in Fig. 7b. Taking into account the peak intensity ratio

 This journal is © the Owner Societies 2019

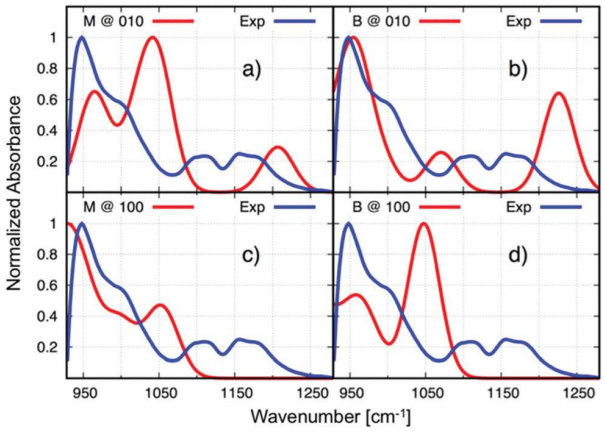


Fig. 5 Experimental IR difference spectrum relevant to the phosphate–goethite complex (in blue) *versus* the phosphate-related spectra calculated for the optimized complexes of **M@010** (a), **B@010** (b), **M@100** (c), and **B@100** (d) in the range of 925–1300 cm^{-1}. Note that the spectra are individually normalized such that the maximum equals unity.

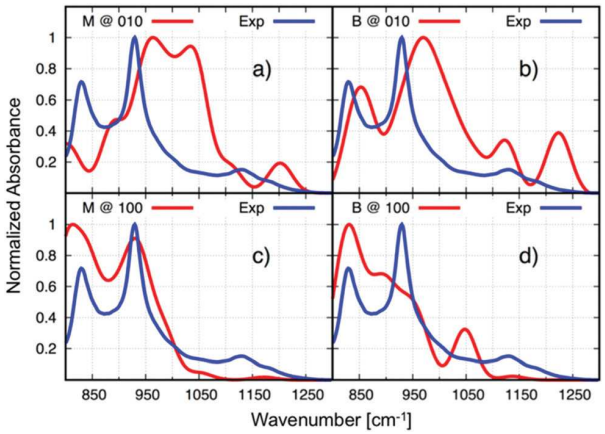


Fig. 6 Overall experimental IR spectrum (in blue) *versus* the calculated overall spectra (red) of the adsorbed phosphate species ($H_2PO_4^-$) at the goethite surface for the optimized complexes of **M@010** (a), **B@010** (b), **M@100** (c), and **B@100** (d). Note that the spectra are individually normalized such that the maximum equals unity.

$1\times$(**M@100**) = $7.4\times$(**B@100**) this corresponds to ratios from 1 : 66.6 to 1 : 0.8. Here, the consistency with the experimental IR spectrum is enhanced upon increasing the **M@100** fraction. However, even the 9 : 1 fraction implies that upon accounting for the IR intensities, there is a high **B@100** fraction (1 : 0.8) needed for good agreement with the experimental spectrum. Comparing panels a and b, one notices that having high proportions of the **M@100** complex is more consistent with the experimental data than having high proportions of the **B@010** complex. An exception is the feature at 1132 cm^{-1} which appears only in the spectra of the **B@010** complex. This suggests mixing spectra of the **B@010** and the **M@100** complexes with different proportions. In this case, the spectra are weighted with proportions of **M@100 : B@010** changing again from 1 : 9 to 9 : 1 (given the intensity ratio $1\times$(**M@100**) = $9.9\times$(**B@010**) this

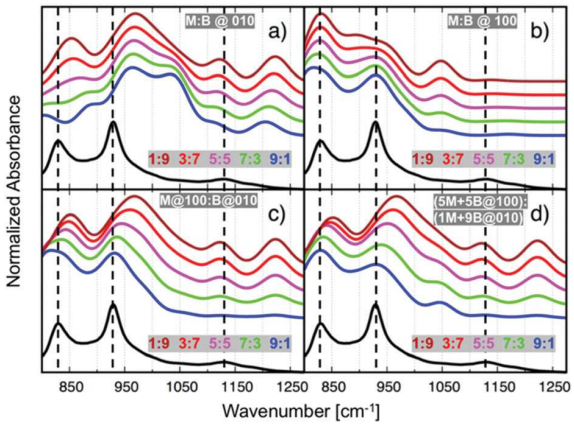


Fig. 7 Overall experimental IR spectrum (in black) *versus* weighted average spectra that are obtained *via* different combinations of the calculated overall spectra with different proportions of **M@010** and **B@010** binding motifs (a), **M@100** and **B@100** binding motifs (b), **M@100** and **B@010** binding motifs (c), and 5**M@100** + 5**B@100** binding motifs and 1**M@010** + 9**B@010** binding motifs (d).

corresponds to 1 : 89 to 1 : 1.1). The results in Fig. 7c show that having a sizeable **M@100** fraction will improve the agreement with respect to the positions of the first two features. On the other hand, the contribution of the **B@010** complex is required to obtain the feature observed around 1132 cm^{-1}. Close inspection reveals that a ratio of **M@100 : B@010** = 7 : 3 (or after taking into account IR intensities 1 : 4.2) is most consistent with experiment. Eventually, we have also made an attempt to include all different binding motifs at both surface planes into the weighted averaging. Reasonable results have been obtained by selecting the combination of 5**M@100** + 5**B@100** with 1**M@010** + 9**B@010**. Then we have mixed these two combinations with different proportions giving the results shown in Fig. 7d. Here, a good agreement is obtained for a ratio of 7 : 3, corresponding to roughly 1**M@100** + 1**B@100** + 0.1**M@010** + 0.8**B@010**, or when peak intensities are taken into account 1**M@100** + 7**B@100** + 1**M@010** + 9**B@010**. In any case, the outlined procedure quantitatively demonstrates the sensitivity of the IR spectrum with respect to the fine details of the composition of the sample.

4. Summary and conclusions

The present study introduced a combination of kinetics of phosphate adsorption on goethite, FT-IR, and periodic DFT calculations in order to draw a molecular-level picture of the phosphate binding mechanisms at the goethite–water interface. For the phosphate adsorption experiment, an initial phosphate concentration of 150 μmol l^{-1} was chosen to achieve a low and incomplete loading of the goethite surface according to adsorption capacities mentioned in previous studies. These results of phosphate adsorption on goethite at a pH range from 4 to 6 varied from 1.4 up to 2.6 μmol m^{-2} depending on background solution or phosphate concentration.[11,12,20,29,30] As goethite is the predominant pedogenic oxide in soils from

temperate regions and the initial phosphate concentrations chosen for the adsorption experiments are only four to tenfold larger than optimal P concentrations for plant nutrition and mean annual concentrations in lysimeter leachates,[59] the results are highly relevant for agriculture and the environment. Here, the individual intermolecular interactions (*i.e.* between each two subsystems including phosphate and goethite, phosphate and water, and goethite and water) for the adsorbed phosphate at the goethite–water interface have been investigated and quantified for the first time. Based on the structures of different binding motifs, a detailed analysis of their IR spectra has been presented and compared to experimental data. Furthermore, it has been shown how the composition of the sample could influence the measured IR spectra. Although this rather pointed to the known difficulty of using IR spectroscopy as a marker for identification of binding motifs, the way of analysis could prove helpful for future investigations. The specific results are summarized in the following.

Phosphate (KH_2PO_4 species) interacts with both goethite surface planes (010 and 100) forming two different complexes (**M** and **B**) at each surface plane. For each phosphate–goethite complex, one proton was found to be transferred from phosphate to water. In all cases, the interfacial water molecules formed HBs with phosphate as well as with the goethite surface. These water molecules approached the surface forming covalent bonds, through water O atoms, with goethite Fe atoms. Moreover, some water molecules were dissociated at the surface to protons and hydroxyl groups that transferred to the surface forming covalent bonds with the goethite surface. All these observations indicate very strong interactions not only between phosphate and the goethite surface but also between water and goethite and between phosphate and water. This demonstrates the crucial role of water in controlling the phosphate adsorption process at the goethite surfaces.

Phosphate and water compete with each other at the goethite surface since both of them could be chemically adsorbed through the formation of covalent bonds. At both goethite surface planes, the competition among phosphate, water, and the OH^- group has been explored to find an increasing importance of the adsorption process in the order $H_2O <$ phosphate $< OH^-$. Based on this observation, one can conclude that phosphate can replace the adsorbed water molecules at the goethite surface but the OH^- groups can replace both phosphate and water. This can explain, at a molecular-level, why the phosphate adsorption decreases upon increasing the pH as observed experimentally.

At low phosphate loading and predominance of the $H_2PO_4^-$ species, the calculated interaction energies indicate a predominance of the mono-protonated bidentate binding motif for phosphates at the goethite–water interface with the possibility of a minor fraction of monodentate species.

Correlating this result with features in the IR spectrum is not straightforward. If an attempt is made to assign the current and previously reported experimental IR spectra in terms of individual binding motifs, the following can be concluded: (i) peaks around 1032 and 1050 cm^{-1} are related to **B@010** and **M@100** motifs, respectively, (ii) the peak around 927 cm^{-1} could come from the motifs **M@010**, **B@010**, and **M@100**, (iii) the peak around 827 cm^{-1} could stem from all considered motifs, and (iv) the interaction with goethite is most dominant in the range below 1000 cm^{-1}. Taking the overall experimental spectrum as a reference, we found that the spectra of the **B@010** and **M@100** complexes are in reasonable agreement with the experimental data. Still, an improvement could be achieved by taking weighted averages of spectra due to different motifs. Here, it was concluded that **M** and **B** motifs of 1 : 8 ratio perform best, regardless of the surface plane. In this respect, it is important to emphasize that the rather different IR intensities of the different motifs cannot be ignored in the analysis. The conclusion drawn from the IR spectrum confirms the interaction energy calculations according to which the mono-protonated **B** motifs are the dominant species and **M** exists as a minor fraction only.

Conflicts of interest

There are no conflicts to declare.

Acknowledgements

This work belongs to the InnoSoilPhos-project, funded by the German Federal Ministry of Education and Research (BMBF) in the frame of the BonaRes-program (No. 031A558). This research was performed within the scope of the Leibniz ScienceCampus "Phosphorus Research" Rostock. Furthermore, we thank Dr A. Schleicher (Helmholtz Center Potsdam, German Research Centre for Geosciences GFZ, Telegrafenberg, 14473 Potsdam, Germany) for supporting XRD-measurements and analysis. The authors thank the North German Supercomputing Alliance for providing HPC resources (project mvp00016).

References

1 D. Cordell, J.-O. Drangert and S. White, The story of phosphorus: Global food security and food for thought, *Glob. Environ. Change*, 2009, **19**, 292–305.

2 J. D. Edixhoven, J. Gupta and H. H. G. Savenije, Recent revisions of phosphate rock reserves and resources: reassuring or misleading? An in-depth literature review of global estimates of phosphate rock reserves and resources, *Earth Syst. Dyn. Discuss.*, 2013, **4**, 1005–1034.

3 M. Obersteiner, J. Peñuelas, P. Ciais, M. van der Velde and I. A. Janssens, The phosphorus trilemma, *Nat. Geosci.*, 2013, **6**, 897–898.

4 J. Kruse, M. Abraham, W. Amelung, C. Baum, R. Bol, O. Kühn, H. Lewandowski, J. Niederberger, Y. Oelmann, C. Rüger, J. Santner, M. Siebers, N. Siebers, M. Spohn, J. Vestergren, A. Vogts and P. Leinweber, Innovative methods in soil phosphorus research: A review, *J. Plant Nutr. Soil Sci.*, 2015, **178**, 43–88.

 This journal is © the Owner Societies 2019

5 Y. Arai and D. L. Sparks, Phosphate Reaction Dynamics in Soils and Soil Components: A Multiscale Approach, *Advances in Agronomy*, Elsevier, 2007, pp. 135–179.

6 Y. Arai and D. L. Sparks, ATR-FTIR Spectroscopic Investigation on Phosphate Adsorption Mechanisms at the Ferrihydrite–Water Interface, *J. Colloid Interface Sci.*, 2001, **241**, 317–326.

7 N. J. Barrow, A mechanistic model for describing the sorption and desorption of phosphate by soil, *J. Soil Sci.*, 1983, **34**, 733–750.

8 R. Chitrakar, S. Tezuka, A. Sonoda, K. Sakane, K. Ooi and T. Hirotsu, Phosphate adsorption on synthetic goethite and akaganeite, *J. Colloid Interface Sci.*, 2006, **298**, 602–608.

9 P. Hinsinger, Bioavailability of soil inorganic P in the rhizosphere as affected by root-induced chemical changes: a review, *Plant Soil*, 2001, **237**, 173–195.

10 J. Torrent, U. Schwertmann and V. Barron, Fast and slow phosphate sorption by goethite-rich natural materials, *Clays Clay Miner.*, 1992, **40**, 14–21.

11 C. Luengo, M. Brigante, J. Antelo and M. Avena, Kinetics of phosphate adsorption on goethite: comparing batch adsorption and ATR-IR measurements, *J. Colloid Interface Sci.*, 2006, **300**, 511–518.

12 J. McLaughlin, J. Ryden and J. Syers, Development and evaluation of a kinetic model to describe phosphate sorption by hydrous ferric oxide gel, *Geoderma*, 1977, **18**, 295–307.

13 I. R. Willett, C. J. Chartres and T. T. Nguyen, Migration of phosphate into aggregated particles of ferrihydrite, *J. Soil Sci.*, 1988, **39**, 275–282.

14 J. Torrent, Interactions between phosphate and iron oxide, *Soils Environ.*, Catena Verlag, Reiskirchen, Germany, 1997, pp. 321–344.

15 S. Goldberg and G. Sposito, On the mechanism of specific phosphate adsorption by hydroxylated mineral surfaces: A review, *Commun. Soil Sci. Plant Anal.*, 1985, **16**, 801–821.

16 R. L. Parfitt, Anion Adsorption by Soils and Soil Materials, *Advances in Agronomy*, Elsevier, 1979, pp. 1–50.

17 J. D. Kubicki, K. W. Paul, L. Kabalan, Q. Zhu, M. K. Mrozik, M. Aryanpour, A.-M. Pierre-Louis and D. R. Strongin, ATR-FTIR and Density Functional Theory Study of the Structures, Energetics, and Vibrational Spectra of Phosphate Adsorbed onto Goethite, *Langmuir*, 2012, **28**, 14573–14587.

18 R. L. Parfitt, Phosphate reactions with natural allophane, ferrihydrite and goethite, *J. Soil Sci.*, 1989, **40**, 359–369.

19 P. Persson, N. Nilsson and S. Sjöberg, Structure and Bonding of Orthophosphate Ions at the Iron Oxide–Aqueous Interface, *J. Colloid Interface Sci.*, 1996, **177**, 263–275.

20 R. Strauss, G. W. Brummer and N. J. Barrow, Effects of crystallinity of goethite: II. Rates of sorption and desorption of phosphate, *Eur. J. Soil Sci.*, 1997, **48**, 101–114.

21 A. C. Chapman and L. E. Thirlwell, Spectra of phosphorus compounds—I the infra-red spectra of orthophosphates, *Spectrochim. Acta*, 1964, **20**, 937–947.

22 M. I. Tejedor-Tejedor and M. A. Anderson, The protonation of phosphate on the surface of goethite as studied by CIR-FTIR and electrophoretic mobility, *Langmuir*, 1990, **6**, 602–611.

23 M. Villalobos, M. A. Cheney and J. Alcaraz-Cienfuegos, Goethite surface reactivity: II. A microscopic site-density model that describes its surface area-normalized variability, *J. Colloid Interface Sci.*, 2009, **336**, 412–422.

24 J. S. Loring, M. H. Sandström, K. Norén and P. Persson, Rethinking Arsenate Coordination at the Surface of Goethite, *Chem. – Eur. J.*, 2009, **15**, 5063–5072.

25 K. D. Kwon and J. D. Kubicki, Molecular Orbital Theory Study on Surface Complex Structures of Phosphates to Iron Hydroxides: Calculation of Vibrational Frequencies and Adsorption Energies, *Langmuir*, 2004, **20**, 9249–9254.

26 J. D. Kubicki, K. D. Kwon, K. W. Paul and D. L. Sparks, Surface complex structures modelled with quantum chemical calculations: carbonate, phosphate, sulphate, arsenate and arsenite, *Eur. J. Soil Sci.*, 2007, **58**, 932–944.

27 J. D. Martin, XPowder: A software package for qualitative and quantitative powder X-ray diffraction analysis, 2016, http://www.xpowder.com/.

28 S. E. Johnson and R. H. Loeppert, Role of Organic Acids in Phosphate Mobilization from Iron Oxide, *Soil Sci. Soc. Am. J.*, 2006, **70**, 222–234.

29 O. K. Borggaard, Effect of Surface Area and Mineralogy of Iron Oxides on Their Surface Charge and Anion-Adsorption Properties, *Clays Clay Miner.*, 1983, **31**, 230–232.

30 D. Freese, P. G. Weidler, D. Grolimund, H. Sticher and A. Flow-Through, Reactor with an Infinite Sink for Monitoring Desorption Processes, *J. Environ. Qual.*, 1999, **28**, 537–543.

31 J. Murphy and J. P. Riley, A modified single solution method for the determination of phosphate in natural waters, *Anal. Chim. Acta*, 1962, **27**, 31–36.

32 F. Xiu, L. Zhou, S. Xia and L. Yu, Adsorption mechanism of water molecule on goethite (010) surface, *J. Ocean Univ. China*, 2016, **15**, 1021–1026.

33 H. Guo and A. S. Barnard, Thermodynamic modelling of nanomorphologies of hematite and goethite, *J. Mater. Chem.*, 2011, **21**, 11566–11577.

34 J. Rakovan, U. Becker and M. F. Hochella, Aspects of goethite surface microtopography, structure, chemistry, and reactivity, *Am. Mineral.*, 1999, **84**, 884–894.

35 R. M. Cornell and U. Schwertmann, *The iron oxides: structure, properties, reactions, occurrences, and uses*, Wiley-VCH, Weinheim, 2nd completely rev. and extended edn, 2003.

36 K. W. Paul, J. D. Kubicki and D. L. Sparks, Sulphate adsorption at the Fe (hydr)oxide–H_2O interface: comparison of cluster and periodic slab DFT predictions, *Eur. J. Soil Sci.*, 2007, **58**, 978–988.

37 J. D. Kubicki, K. W. Paul and D. L. Sparks, Periodic density functional theory calculations of bulk and the (010) surface of goethite, *Geochem. Trans.*, 2008, **9**, 4.

38 J. D. Kubicki, D. Tunega and S. Kraemer, A density functional theory investigation of oxalate and Fe(II) adsorption onto the (010) goethite surface with implications for ligand- and reduction-promoted dissolution, *Chem. Geol.*, 2017, **464**, 14–22.

39 A. Szytuła, A. Burewicz, Ž. Dimitrijević, S. Kraśnicki, H. Rżany, J. Todorović, A. Wanic and W. Wolski, Neutron

Diffraction Studies of α-FeOOH, *Phys. Status Solidi B*, 1968, **26**, 429–434.
40 A. A. Ahmed, P. Leinweber and O. Kühn, Unravelling the nature of glyphosate binding to goethite surfaces by ab initio molecular dynamics simulations, *Phys. Chem. Chem. Phys.*, 2018, **20**, 1531–1539.
41 L. Martínez, R. Andrade, E. G. Birgin and J. M. Martínez, PACKMOL: A package for building initial configurations for molecular dynamics simulations, *J. Comput. Chem.*, 2009, **30**, 2157–2164.
42 J. VandeVondele, M. Krack, F. Mohamed, M. Parrinello, T. Chassaing and J. Hutter, Quickstep: Fast and accurate density functional calculations using a mixed Gaussian and plane waves approach, *Comput. Phys. Commun.*, 2005, **167**, 103–128.
43 J. Hutter, M. Iannuzzi, F. Schiffmann and J. VandeVondele, CP2K: Atomistic Simulations of Condensed Matter Systems, *Wiley Interdiscip. Rev.: Comput. Mol. Sci.*, 2014, **4**, 15–25.
44 B. G. Lippert, J. Hutter and M. Parrinello, A hybrid Gaussian and plane wave density functional scheme, *Mol. Phys.*, 1997, **92**, 477–488.
45 J. P. Perdew, K. Burke and M. Ernzerhof, Generalized Gradient Approximation Made Simple, *Phys. Rev. Lett.*, 1996, **77**, 3865–3868.
46 M. Krack, Pseudopotentials for H to Kr optimized for gradient-corrected exchange–correlation functionals, *Theor. Chem. Acc.*, 2005, **114**, 145–152.
47 J. VandeVondele and J. Hutter, Gaussian basis sets for accurate calculations on molecular systems in gas and condensed phases, *J. Chem. Phys.*, 2007, **127**, 114105.
48 S. Grimme, S. Ehrlich and L. Goerigk, Effect of the damping function in dispersion corrected density functional theory, *J. Comput. Chem.*, 2011, **32**, 1456–1465.
49 H. B. Jansen and P. Ros, Non-empirical molecular orbital calculations on the protonation of carbon monoxide, *Chem. Phys. Lett.*, 1969, **3**, 140–143.
50 I. M. Alecu, J. Zheng, Y. Zhao and D. G. Truhlar, Computational Thermochemistry: Scale Factor Databases and Scale Factors for Vibrational Frequencies Obtained from Electronic Model Chemistries, *J. Chem. Theory Comput.*, 2010, **6**, 2872–2887.
51 C. Shang, J. W. B. Stewart and P. M. Huang, pH effect on kinetics of adsorption of organic and inorganic phosphates by short-range ordered aluminum and iron precipitates, *Geoderma*, 1992, **53**, 1–14.
52 M. Talebi Atouei, R. Rahnemaie, E. Goli Kalanpa and M. H. Davoodi, Competitive adsorption of magnesium and calcium with phosphate at the goethite water interface: Kinetics, equilibrium and CD-MUSIC modeling, *Chem. Geol.*, 2016, **437**, 19–29.
53 L. Krumina, J. P. L. Kenney, J. S. Loring and P. Persson, Desorption mechanisms of phosphate from ferrihydrite and goethite surfaces, *Chem. Geol.*, 2016, **427**, 54–64.
54 M. Nanzyo, Infrared Spectra of Phosphate Sorbed on Iron Hydroxide Gel and the Sorption Products, *Soil Sci. Plant Nutr.*, 1986, **32**, 51–58.
55 T.-T. Zheng, Z.-X. Sun, X.-F. Yang and A. Holmgren, Sorption of phosphate onto mesoporous γ-alumina studied with in-situ ATR-FTIR spectroscopy, *Chem. Cent. J.*, 2012, **6**, 26.
56 R. J. Atkinson, R. L. Parfitt and R. S. C. Smart, Infra-red study of phosphate adsorption on goethite, *J. Chem. Soc., Faraday Trans. 1*, 1974, **70**, 1472.
57 F. Liu, A. De Cristofaro and A. Violante, Effect of pH, phosphate and oxalate on the adsorption/desorption of arsenate on/from goethite, *Soil Sci.*, 2001, **166**, 197–208.
58 J. Antelo, M. Avena, S. Fiol, R. López and F. Arce, Effects of pH and ionic strength on the adsorption of phosphate and arsenate at the goethite–water interface, *J. Colloid Interface Sci.*, 2005, **285**, 476–486.
59 H. Rupp, R. Meissner and P. Leinweber, Plant available phosphorus in soil as predictor for the leaching potential: Insights from long-term lysimeter studies, *Ambio*, 2018, **47**, 103–113.

 This journal is © the Owner Societies 2019

Supplementary Information (SI)

Infrared Spectroscopic Characterization of Phosphate Binding at the Goethite-Water Interface

Ashour A. Ahmed[1,2,*], Stella Gypser[3], Peter Leinweber[2,4], Dirk Freese[3], Oliver Kühn[1,2]

[1] University of Rostock, Institute of Physics, Albert-Einstein-Str. 23-24, D-18059 Rostock, Germany.

[2] University of Rostock, Department of Life, Light, and Matter (LLM), Albert-Einstein-Str. 25, D-18059 Rostock, Germany

[3] Brandenburg University of Technology Cottbus-Senftenberg, Chair of Soil Protection and Recultivation, Konrad-Wachsmann-Allee 6, 03046 Cottbus, Germany

[4] University of Rostock, Chair of Soil Science, Justus-von-Liebig-Weg 6, D-18059 Rostock, Germany

S1. Details about the interaction energy calculations

In general, the effect of water on the phosphate-goethite interaction has been considered during the geometry optimization due to the water-phosphate-goethite interactions based on the electronic and Van der Waals interactions. However, this effect has not been considered explicitly for computing the interaction energy in Eq. 1. In practice, each phosphate-goethite-water model could be considered as three sub-systems (fragments). These fragments are phosphate (fragment1), goethite (fragment2), and water (fragment3). Within CP2K it is possible to calculate the pair interaction energy between two fragments. According to Eq. 1 ($E_{int} = E_{\text{phosphate-goethite-complex}} - (E_{\text{phosphate}} + E_{\text{goethite surface}})$), we have defined phosphate as the first fragment and goethite as the second fragment. Water enters only insofar as it determines the actual geometry of the interacting fragments. The interaction energy is calculated within the BSSE counterpoise correction philosophy, i.e. by performing five energy calculations as follows: total electronic energy of phosphate including only the phosphate basis functions ($E^{\text{phosphate}}_{\text{phosphate}}$), goethite including only the goethite basis functions

($E_{goethite}^{goethite}$), phosphate including the basis functions of phosphate and goethite ($E_{\text{phosphate}}^{\text{phosphate}+goethite}$), goethite including the basis functions of phosphate and goethite ($E_{goethite}^{\text{phosphate}+goethite}$), and finally phosphate-goethite complex including the basis functions of phosphate and goethite ($E_{\text{phosphate}-goethite-complex}^{\text{phosphate}+goethite}$). From these numbers one gets the interaction energy between phosphate and goethite as $E_{int} = E_{\text{phosphate}-goethite-complex}^{\text{phosphate}+goethite} - (E_{\text{phosphate}}^{\text{phosphate}+goethite} + E_{goethite}^{\text{phosphate}+goethite})$. Similarly, the interaction energies between phosphate and water ($E_{int} = E_{\text{phosphate}-water-complex}^{\text{phosphate}+water} - (E_{\text{phosphate}}^{\text{phosphate}+water} + E_{water}^{\text{phosphate}+water})$) and between goethite and water ($E_{int} = E_{goethite-water-complex}^{goethite+water} - (E_{goethite}^{goethite+water} + E_{water}^{goethite+water})$) could be calculated.

S2. X-ray diffraction data

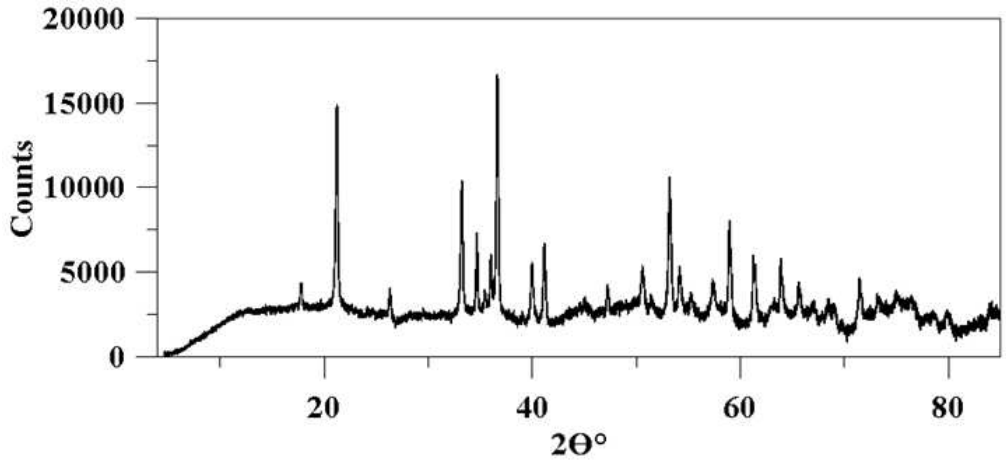


Fig. S1. X-ray diffraction pattern of the synthetic goethite sample used in this study (lattice parameters: a = 4.61 Å, b = 9.96 Å, and c = 3.02 Å).

S3. Comparison between calculated and experimental difference spectra over the full range

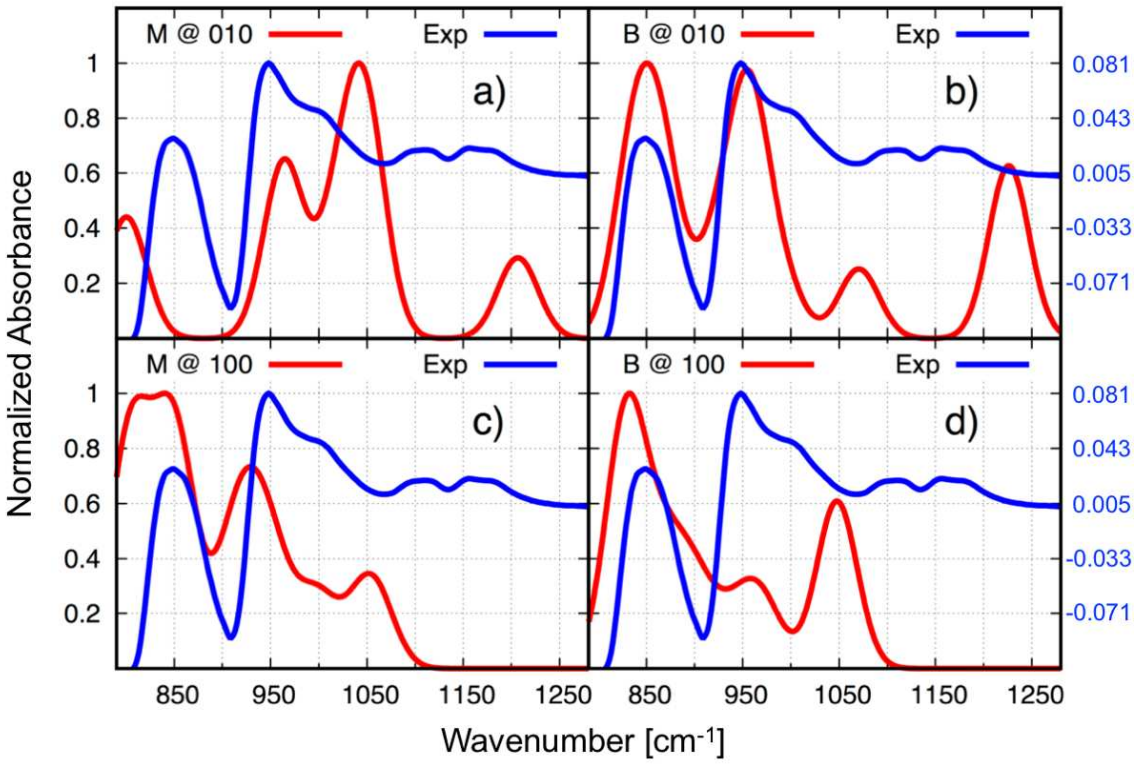


*Fig. S2. Experimental difference IR spectrum relevant to the P-goethite complex (in blue, compare Fig. 2) versus the phosphate-related spectra calculated for **M@010** a), **B@010** b), **M@100** c), and **B@100** d) in the range of 800-1300 cm^{-1}. The original scale for the experimental spectrum was added to the right axis in blue.*

Figure S2 shows that the IR spectrum for the **B@010** complex (Fig. S2b) is closest to the experimental IR spectrum compared to the other calculated spectra. This holds specifically for the first two IR spectral features, i.e. in the spectral range of 80031000 cm^{-1}. Here, it is important to mention that the first feature observed around 850 cm^{-1} for the **B@010** complex involves $2O_b3P32O_{nb}$ symmetric stretching and P3O3H bending vibrations. The second observed feature around 945 cm^{-1} for the same complex corresponds mainly to $2O_b3P3O_{nb2}$ symmetric stretching and $O_{b2}3P3O_{nb1}$ asymmetric stretching vibrations. Moreover, the IR spectrum for the **M@100** complex is also close to the experimental IR spectrum (see Fig. S2c). Here, the first feature seems as a bimodal peak with a local maximum, around 840 cm^{-1}, closer to the experimental feature that corresponds to $P32O_{nb}$ stretching and bending vibrations. Furthermore, the second feature observed around 930 cm^{-1} is due to $P3O_b$ stretching, $P3O_{nb1}$ stretching, $O_b3P32O_{nb1,2}$ symmetric stretching, $P33O_{nb}$ asymmetric stretching, and $O_b3P32O_{nb2,3}$ asymmetric stretching vibrations. For the **M@010** complex (see Fig. S2b), and the **B@100** complex, (see Fig. S2d), one observes a larger deviation in the position for the first two features compared to the experimental ones especially for the first

feature. The first two features in the spectrum of the **M@010** complex are at 800 and 965 cm^{-1} and are due to $P33O_{nb}$ complex vibration and $O_b3P32O_{nb1,3}$ symmetric stretching vibration, respectively, in addition to P3O3H bending vibration. For the **B@100** complex, the first two features existed around 830 and 960 cm^{-1}. The first feature involved an $O_{b2}3P32O_{nb}$ symmetric stretching vibration while the second one involved $P3O_{nb1}$ stretching, $O_{b2}3P3O_{nb1}$ antisymmetric stretching, and P3O3H bending vibrations. For the latter two complexes, the shape of the calculated spectra in the range of 80031000 cm^{-1} is somehow different than the experimental one. This also confirms that spectra of both **B@010** and **M@100** complexes are closer to the experimental spectrum than the other two complexes.

Publication 2

Ashour A. Ahmed, S. Gypser, D. Freese, P. Leinweber, and O. Kühn. Molecular level picture of the interplay between pH and phosphate binding at the goethite–water interface. Phys. Chem. Chem. Phys. **2020**, 22, 26509-26524.

Contribution: Ashour A. Ahmed is credited with conceptualization, conducting the modeling work, modeling analysis and interpretation of both experimental and modeling work, methodology development, visualization, and writing the original manuscript. Ashour A. Ahmed and co-authors are responsible for reviewing, and editing the manuscript.

URL: https://doi.org/10.1039/D0CP04698A

QR:

Ashour Ahmed pH

Reproduced with the permission of the Royal Society of Chemistry (RSC)

PCCP

ROYAL SOCIETY OF CHEMISTRY

PAPER

Check for updates

Cite this: *Phys. Chem. Chem. Phys.*, 2020, **22**, 26509

Molecular level picture of the interplay between pH and phosphate binding at the goethite–water interface†

Ashour A. Ahmed, *[ab] Stella Gypser,[c] Dirk Freese,[c] Peter Leinweber[bd] and Oliver Kühn [ab]

Received 6th September 2020,
Accepted 28th October 2020

DOI: 10.1039/d0cp04698a

rsc.li/pccp

The soil pH plays a substantial role in controlling phosphorus (P) adsorption and mobilization. These processes are strongly affected by the phosphate interaction strength with P-fixing soil minerals such as goethite. The target of the current contribution is to draw a molecular level picture of the interplay between pH and phosphate binding at the goethite–water interface *via* a joint experimental–theoretical approach. Periodic density functional theory (DFT) calculations were carried out to provide a molecular level understanding of the pH dependence of P adsorption. To validate the modeling approach, adsorption experiments of phosphate at goethite were performed in the pH range of 4–12. There was agreement between experiments and simulations in the description of the adsorption behavior by two pH-dependent successive stages. The adsorption increases along the pH change from 4 to 8. A further increase of pH leads to a decrease of adsorption. By comparing with literature data it is concluded that the first stage will be observed only if there is no significant change of the surface charge at low pH. Moreover, the molecular modeling results point to the abundance of the monodentate (**M**) binding motif at both extremely low and high pH ranges. Otherwise, the bidentate (**B**) one is predominant along the intermediate pH range. These observations could resolve the existing debate about the assignment of phosphate–goethite binding motifs. Furthermore, the results point to a decrease of pH upon phosphate sorption due to an induced acidification of soil solution. The present joint experimental–theoretical approach provides a better understanding and description of the existing phosphate sorption experiments and highlights new findings at the atomistic/molecular scale.

Introduction

Phosphorus (P) immobilization and thus its efficiency as fertilizer for plant nutrition is mainly affected by its interaction with soil components such as soil organic matter,[1,2] free metal ions,[3,4] and soil minerals.[5–8] A key point here is the strong interaction between phosphates and soil mineral surfaces and especially with Fe- and Al-(oxyhydr)oxides.[5] Phosphate reactions with Fe-(oxy)hydroxides and particularly with the Fe-mineral goethite have been studied extensively.[9–13] This is due to the fact that goethite is the most common reactive ferric iron Fe(III) oxyhydroxide and also is one of the most common P-fixing minerals found in soils.[6,7,14] Consequently, goethite has been used frequently in many experimental and theoretical studies to investigate the nature of phosphate–surface reactions.[12,15–23] Phosphate adsorption was described previously as a biphasic process with a fast-initial adsorption step and a following slower reaction phase.[15,24–26] During the transition from fast to slow adsorption phases, the formation of initial monodentate (**M**) complexes and the conversion to bidentate (**B**) complexes, the competition with anions on the surface or precipitation events were assumed.[27] Alternatively, the observed temporal effects of the phosphate reaction with the surface could be described by a solid-state diffusion process.[11,19]

The strength of the phosphate–goethite interaction is very sensitive to pH as it determines the surface charge of the goethite surface as well as the protonation state of the phosphate species.[22,28] There are a huge number of studies exploring the effect of pH on phosphate adsorption on goethite.[11,12,19,22,29–38]

[a] *University of Rostock, Institute of Physics, Albert-Einstein-Str. 23-24, D-18059 Rostock, Germany. E-mail: ashour.ahmed@uni-rostock.de*
[b] *University of Rostock, Department of Life, Light, and Matter (LLM), Albert-Einstein-Str. 25, D-18059 Rostock, Germany*
[c] *Brandenburg University of Technology Cottbus-Senftenberg, Chair of Soil Protection and Recultivation, Konrad-Wachsmann-Allee 6, 03046 Cottbus, Germany*
[d] *University of Rostock, Chair of Soil Science, Justus-von-Liebig-Weg 6, D-18059 Rostock, Germany*

† Electronic supplementary information (ESI) available. See DOI: 10.1039/d0cp04698a

Almost all of these studies reported a common significant effect of the solution pH on the adsorption reaction strength that decreased with increasing solution pH. This common behavior of a decrease of phosphate adsorption at higher pH was attributed to the repulsion between phosphate anions and the increasingly negatively charged surface sites, and the competition between phosphate anions and OH^- groups. Furthermore, Hingston *et al.*[29] found that a specific adsorption (*i.e.* direct contact with the surface *via* short-range interactions) at the surface occurs only in the regions having a positive charge. Therefore, goethite exhibits a high affinity to adsorb phosphate anions at pH below the point of zero charge (PZC) since the surface will have a positive net charge and thus a positive electric potential. By increasing the solution pH, the potential becomes less positive and then negative at pH > PZC which makes further specific adsorption more difficult.[30] Moreover, Hiemstra and Van Riemsdijk[32] showed that the phosphate adsorption process will be accompanied by adsorption of protons (H^+) at the goethite surface. This was confirmed by Strauss *et al.*[19] since they suggested that high surface charge was produced by diffusion of protons (H^+) from and to the surface along with the phosphate adsorption process. In addition, they assumed that phosphate ions are not only adsorbed to external surface sites but also penetrated into meso- and micro-pores between the domains of the goethite crystals and were then adsorbed on internal surface sites. Their results also showed that the rate of this adsorption reaction is pH dependent with a slower initial reaction at high pH which is mainly affected by the surface charge. Further, it was found that both singly and triply coordinated OH groups at the goethite surface contribute to the charging behavior of the surface but only the singly coordinated OH groups are responsible for the phosphate binding process.[32]

Background electrolyte solutions play an important role as well in the phosphate adsorption process by controlling the surface electric potential.[15,36,39] Specifically, Barrow *et al.*[39] showed a decrease in phosphate adsorption on increasing the NaCl electrolyte concentration at relatively low pH (pH < 4). Here, increasing the electrolyte concentration led to a decrease in the electric potential (*i.e.* less positive) of the positively charged surface and thus led to a weaker adsorption. In contrast, increasing the NaCl concentration at pH > 4 led to a less negative electric potential and thus a stronger phosphate adsorption. This effect became more pronounced with increasing phosphate concentration as well.[33] This observation was confirmed by Rietra *et al.*[36] and Antelo *et al.*[22] Furthermore, Chitrakar *et al.*[12] showed a different adsorption behavior for phosphate enriched seawater at the goethite surface in which the phosphate adsorption increased with increasing solution pH up to around 7 and then decreased strongly with a further increase of pH. This was attributed to the competition of major and minor seawater constituents for surface sites compared to the single electrolyte case. Similar behavior was observed by Boukemara *et al.*[37] since their phosphate adsorption increased followed by a decrease stage. Moreover, they observed a pH increase along the acidic pH range and a pH decrease at pH > 7. This was explained by a ligand exchange reaction that would release OH^- groups at lower pH and consume more OH^- groups at higher pH.

At a molecular scale, great efforts were made to investigate the binding motifs of the adsorbed phosphate species at Fe-oxide surfaces by using Fourier-Transform Infrared (FT-IR) spectroscopy.[7,10,18,31,40] However, due to the presence of different surface planes for goethite and several binding motifs for the phosphate–goethite complex, FT-IR could not provide an unequivocal assignment of the formed binding motifs.[16,41] As a result, different opinions have been put forward with respect to the phosphate–goethite binding motifs. Tejedor-Tejedor and Anderson[31] assigned the complexes according to the positions of P–O vibrational bands. Arai and Sparks[10] characterized the formed complexes according to the number of P–O bands and not the exact position. Persson *et al.*[18] and Loring *et al.*[42] interpreted their results by the formation of only **M** binding motifs with different protonation states depending on pH. In view of the existing debate about assignment of the P–goethite complexes and several factors affecting the P adsorption process, microscopic models could be used to provide a better description and understanding of the existing phosphate sorption experiments in the literature under different experimental conditions. Atomistic/molecular modeling and computational chemistry applied to simplified model systems could be considered as a first step towards such a microscopic understanding.

Using computational chemistry methods and especially density functional theory (DFT), Kubicki and coworkers have simulated the phosphate binding process and its pH dependence for a small goethite cluster model with a few explicit water molecules.[43] This study suggested the formation of a diprotonated **B** complex at pH 4–6, either a deprotonated **B** or a monoprotonated **M** complex at pH 7.5–7.9, and a deprotonated **M** complex at pH 12.8. Further, Kubicki *et al.*[16] have performed periodic DFT based molecular dynamics simulations for different goethite surface planes to investigate the binding behavior of the HPO_4^{2-} species. The results predicted the formation of **M** complexes at the 001, 210, 101, and 100 surface planes and **B** complexes at the 010, 101, and 100 surface planes. Recently, we have carried out periodic DFT calculations to explore the binding mechanism of phosphate at two different goethite surface planes (010 and 100) in the presence of water with a density of 1 g cm^{-3}.[7] This study simulated the binding of KH_2PO_4 species (*i.e.* around pH 6) with two binding motifs (*i.e.* **M** and **B**) at each surface plane. The results indicated the abundance of the monoprotonated **B** motif at the goethite–water interface. Moreover, the best agreement between the theoretical and experimental IR spectra was obtained assuming the presence of **B** and **M** motifs at a ratio of 8 : 1. Further, the role of water in controlling the phosphate–goethite binding process *via* promoting specific binding motifs, formation of H-bonds (HBs), adsorption and dissociation at the surface, as well as proton transfer processes has been demonstrated. Such a detailed atomistic investigation of the pH dependent phosphate binding mechanisms at the goethite–water interface is still lacking. In addition, most of the pH dependent phosphate adsorption experiments did not account for the effect on the pH change produced due to the phosphate sorption

 This journal is © the Owner Societies 2020

process itself.[22,32–36,38] Therefore, our objective in the present study is to draw a molecular level picture of the effect of pH on phosphate binding at the goethite–water interface *via* a joint experimental–theoretical approach.

The main approach in the present study is to apply atomistic/molecular modeling and simulation to explore the pH dependence of the phosphate adsorption process at the goethite surface. Here, periodic boundary condition (PBC)–DFT calculations were performed to investigate the interaction mechanism for *ortho*phosphate with two different goethite surface planes in the presence of water. Moreover, the individual contributions of phosphate–goethite, phosphate–water, and goethite–water interactions were explored. Further, the competition between phosphate, water, and the hydroxyl (OH^-) group for adsorption sites was investigated. The structure and energetics of phosphate at the goethite–water interface were explored, at both 010- and 100-goethite surface planes and at different pH-values including all possible phosphate species. To validate the present modeling approach, adsorption experiments of phosphate at goethite were carried out at different pH values. Moreover, the pH change associated with the progressing adsorption reaction was investigated. The present systematic study allows discussion of the possible induced pH change upon phosphate sorption *versus* the externally controlled pH change.

Methods

Molecular modeling

The general schematic representation of our molecular modeling approach for the phosphate binding at the goethite–water interface is given in Fig. 1. Here, each phosphate–goethite–water model (see Fig. 1a) consists of (1) – a goethite surface plane, (2) – a phosphate species with a specific binding motif to the surface, and (3) – water molecules that surround both phosphate and goethite. In order to explore the effect of surface composition and morphology on phosphate binding, two different goethite surface planes (010 and 100 according to the centrosymmetric *Pnma* space group) have been considered. These two goethite surface planes are stable and abundant and exhibit two kinds of surface saturation due to different coordination numbers of Fe atoms.[44–48] For the bare 010- and 100-goethite surface planes, each surface Fe atom is coordinated by four and five O atoms, respectively. Therefore, this will give us the opportunity to explore different binding motifs between phosphate and goethite. These two surfaces have been modeled by periodic slabs, constructed by repetition of the goethite unit cell[49] in the relevant directions (see Fig. 1b and c). To simulate these surfaces, a layer of about 20 Å vacuum was added between the periodic slabs perpendicular to the surface plane (see Fig. 1a). In the vacuum region, phosphate was added at the top of each surface plane in two different starting spatial configurations to construct monodentate (**M**) and bidentate (**B**) binding motifs (see Fig. 1d–f). This has been done by constructing one covalent bond (for **M** motif) and two covalent bonds (for **B** motif) between the phosphate O atoms and the goethite Fe atoms. The formation of the **B** binding motif mainly takes place between two phosphate O atoms and one surface Fe atom (2O + 1Fe) for the 010-surface plane and two phosphate O atoms and two surface Fe atoms (2O + 2Fe) for the 100-surface plane.[6] Water molecules at a density of about 1 g cm^{-3} have been introduced into the vacuum region between the slabs to construct the final simulation box (see Fig. 1a).

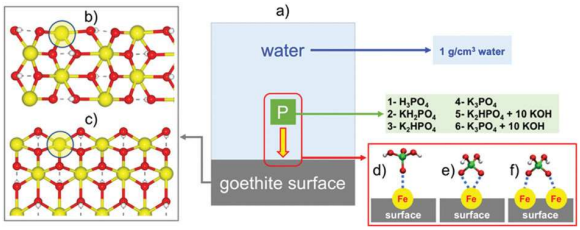


Fig. 1 Molecular modeling approach for phosphate binding at the goethite–water interface involving schematic representation of the phosphate–goethite–water model (a), side view of the modeled 010- (b) as well as the 100-goethite surface planes (c) according to the Pnma space group (dashed lines refer to hydrogen bonds and circles around the surface Fe atoms refer to two different coordination numbers of surface Fe atoms (4 for 010- and 5 for 100-goethite surface planes)), and schematic view of the possible binding motifs between phosphate and goethite (**M** motif at both 010- and 100-surfaces (d), (2O + 1Fe) **B** motif at the 010-surface (e), (2O + 2Fe) **B** motif at the 100-surface (f)). H, O, P, and Fe atoms are colored white, red, green, and yellow, respectively.

To simulate the present sorption experiment and to investigate the effect of pH on phosphate binding, 6 different models have been constructed for each binding motif. In these models, the phosphate molecule has been introduced to the surface with different species involving "KH_2PO_4", "K_2HPO_4", and "K_3PO_4". This will provide us with information about the effect of the deprotonation process on phosphate binding. In addition, the "H_3PO_4" species has been included as well to simulate extremely high acidic conditions (very low pH, *i.e.* around pH 2). Moreover, two other cases representing high pH conditions have been introduced as well to understand the effect of the presence of hydroxyl (OH^-) groups on this binding process. These two models involved addition of 10 KOH molecules to each simulation box containing K_2HPO_4 and K_3PO_4. These models are denoted as "K_2HPO_4(II)" and "K_3PO_4(II)" which correspond to (1 K_2HPO_4 + 10 KOH) and (1 K_3PO_4 + 10 KOH), respectively. Therefore, in total we have 24 phosphate–goethite–water model systems, *i.e.* 6 **M** and 6 **B** binding motifs at each surface plane. It should be noted that these models will cover the most important issues affecting the pH dependence of the phosphate adsorption process. Specifically, these involve the phosphate deprotonation process (which is linked to the pK_a effect), changing the surface charge by KOH groups (which could be connected to the PZC and electric potential effect), and the surface morphology *via* modeling of two surface planes (this is linked to the surface area, PZC, and electric potential effects). Regarding the system size, each model system consists of about 700 atoms. For example, the K_2HPO_4–goethite–water model consists of 256 atoms in the goethite (FeOOH) surface model + 1 phosphate molecule (8 atoms) + 150 water molecules (450 atoms) = 714 atoms in total. For more details about the molecular modeling approach, see ref. 7.

Computational details

All the initial geometries of the phosphate–goethite models involving the surrounding water molecules have been optimized using the Broyden–Fletcher–Goldfarb–Shanno (BFGS) algorithm in the quickstep code[50] implemented in the CP2K simulation package.[51] Here, the hybrid Gaussian and plane-wave (GPW) method[52] has been applied for calculating the DFT electronic ground state structure. The Perdew–Burke–Ernzerhof functional (PBE)[53] has been used together with the Goedecker–Teter–Hutter (GTH) pseudopotentials.[54] The electronic density cutoff for atomic core electrons was chosen as 500 Ry. The double-ζ valence polarized (DZVP) basis set optimized for the GTH pseudopotentials[55] has been used. The empirical dispersion correction D3 by Grimme was employed.[56] PBCs have been applied in all the three spatial directions. Moreover, the total energy value was tuned to be accurate up to 10^{-12} hartree with a convergence threshold for the self-consistent-field (SCF) energy of 10^{-8} hartree.

The complexation reaction, phosphate + goethite surface → phosphate–goethite complex, has been characterized by calculating the interaction energy (E_{int}) between the phosphate species and the goethite surface plane for each phosphate–goethite model in the presence of the surrounding water molecules as follows:

$$E_{int} = E_{\text{P–goethite complex}} - (E_P + E_{goethite}) \quad (1)$$

where $E_{\text{P–goethite complex}}$, E_P, and $E_{goethite}$ are the total electronic energies of the geometry optimized phosphate–goethite complex, phosphate species, and goethite surface, respectively. For all the calculated interaction energies, the effect of the basis set superposition error (BSSE) has been corrected using the counterpoise scheme.[57] It should be noted that these interaction energy values might be not exactly the same as the experimentally measured adsorption energies. Nevertheless, these values are representative of the strength of the phosphate adsorption process in specific environments which is directly proportional to the PO–Fe bond energy formation. Furthermore, the effect of the surrounding water molecules on the phosphate–goethite complexation reaction has been considered during the geometry optimization process due to the electronic and van der Waals interactions within the water–phosphate–goethite complexes. Water molecules participate only insofar as they determine the actual geometry of the interacting fragments. More details are given in the ESI.†

Goethite characterization

Phosphate adsorption experiments have been carried out in a batch setup on synthetic and commercially available goethite (99%, Alfa Aesar, Massachusetts, USA). The crystallinity and composition of goethite were confirmed by X-ray diffraction analysis using an Empyrean powder diffractometer (PANalytical, Almelo, Netherlands) with Cu Kα radiation (λ = 0.15418 nm). The determination of the *d*-values of the diffraction pattern and verification of the calculated lattice parameter were performed by using an open access version of XPowder (J. Daniel Martin). The specific surface area (SAA) of 17.2 $m^2\ g^{-1}$ was determined using an Autosorb-1 (Quantachrome, Odelzhausen, Germany) with a five-point BET-measurement and nitrogen gas as an adsorptive medium. For the detailed characterization results, see Ahmed *et al.* (2019).[7]

The point of zero charge (PZC) was determined using potentiometric titration. Specifically, 0.5 g of goethite was weighed into 50 ml PE-tubes and 10 ml KCl solution of different concentrations (0.02 M, 0.2 M, and 2.0 M) was added separately. These solutions were diluted with ultrapure water to a total volume of 20 ml, leading to final KCl concentrations of 0.01 M, 0.1 M, and 1.0 M, respectively. The goethite/KCl mixtures were equilibrated for 4 days at 25 °C and shaken for 1 h d^{-1} to reach an equilibration pH value prior to the titration procedure. The number of the adsorbed protons (H^+) on the goethite surface at each pH was determined by subtracting the titration curve of the blank solution from the titration curve of the suspension. The PZC derived from the titration curves is 8.8 (see Fig. S4 in the ESI†).

Adsorption experiments

Adsorption was studied at different pH values of 4, 6, 8, 10, and 12. Prior to each sorption experiment, both goethite (5 g) and phosphate (1 l of 0.15 mmol l^{-1} KH_2PO_4 solution) were adjusted to the desired pH in ultrapure water. For pH 4, 0.1 M HCl was used, while for the pH values from 6 to 12, KOH solutions in the concentration range from 0.1 to 5 M were used. The pH adjustment was made using a Potentiometric Compact Titrator G20S and a combined DGi115-SC pH electrode (Mettler-Toledo, Ohio, USA) under continuous stirring. After this adjustment, the goethite samples were dried at 40 °C. For each adsorption experiment, 40 ml of phosphate solution was mixed with 0.5 g of goethite to achieve a solid–solution ratio of 1 : 80. The goethite–solution mixture was shaken horizontally at 150 motions min^{-1} for 24 h, and the phosphorus concentration in the solution was determined after an equilibration time of 168 h. Specifically, the samples were centrifuged for 15 min at 3500 rpm, and the clear supernatant was filtrated by using P-poor Whatmann 512 $\frac{1}{2}$ folded filters. The concentrations of P and Fe were determined using inductively coupled plasma atomic emission spectroscopy (ICP-AES). The amount of phosphorus lost from the KH_2PO_4 solution was assumed to be completely adsorbed by the goethite surface. The adsorption experiments were done in duplicate.

In general, the pH effect is commonly addressed experimentally using a buffer solution which provides a fixed pH value.[7,22,58] This doesn't account for the influence on pH of the phosphate sorption itself. Because such an effect is expected for real soil conditions, we have followed here the pH change along the adsorption process. The pH change during the reaction time of the phosphate adsorption process was measured in a reference experiment that was treated exactly under the same conditions as for the actual phosphate adsorption experiment. Based on the measured pH change, the amount of adsorbed phosphate on goethite was referred to both initial and final pH. In addition, CO_2 might influence the adsorption behavior at

 This journal is © the Owner Societies 2020

higher pH and was therefore not excluded explicitly to simulate more natural conditions. Thus, the total carbon content (C_{Total}) present in the solid goethite samples was measured using a CNS elemental analyzer (Vario EL III, Elementar) prior to adsorption and after a reaction time of 168 h.

Adsorption isotherms with different background electrolytes were studied at pH 6. Here, 0.5 g of goethite and 50 ml of reaction solution were used to achieve a solid–solution ratio of 1 : 100. The reaction solutions consisted of 0.01 M $CaCl_2$ or 0.01 M KCl, with initial P concentrations of 0.5, 1, 1.5, 2, 2.5, 3, 3.5, 4, 4.5, and 5 mmol KH_2PO_4 l^{-1}. To keep the pH value constant, a phosphate buffer solution made up of KH_2PO_4 and $Na_2HPO_4 \times H_2O$ was used. The goethite-solution mixture was shaken horizontally at 150 motions min^{-1}, and the phosphate concentration in the solution was determined after a reaction time of 24 h.

Results

P-Binding at the 010-goethite surface plane

At very low pH and specifically in the presence of *ortho*-phosphoric acid (H_3PO_4), stable **M** (see Fig. 2a and Fig. S2a in the ESI†) and 2O + 1Fe **B** (Fig. 2b and Fig. S2b in the ESI†) complexes are formed between phosphate and the goethite surface. The length of the Fe–O covalent bond for the **M** complex (1.94 Å) is shorter than that of the **B** complex (2.01 and 2.08 Å, see Table 1). These two complexes have high interaction energies between phosphate and goethite, *i.e.* −139 kcal mol^{-1} for **M** and −75 kcal mol^{-1} for **B** (see Fig. 3 and Table 1). This indicates higher stability of the **M** complex compared to the **B** complex at low pH. Moreover, proton (H^+) transfer processes from phosphate to water as well as to the goethite surface have been observed for both **M** and **B** binding motifs at the goethite–water interface (see Fig. 2a, b and Fig. S2a, b in the ESI†). For the **M** complex, one proton is transferred to water and a second one to the goethite surface. Two protons are transferred from phosphate to water in the case of the **B** complex. For both complexes, the transferred protons stay in contact with their original phosphate donating O atoms *via* formation of hydrogen bonds (HBs). In addition, for both **M** and **B** complexes the third proton in the H_3PO_4 species stays covalently bonded to its phosphate O atom without transfer. This means that these observed P-complexes are mono-protonated **M** and **B** complexes and act as donors for two HBs. It is important to mention that for the **B** complex case this proton is bound to one phosphate O atom, that is, it is participating in the bidentate binding motif at the goethite surface. This could be the reason for the higher stability for formation of the **M** complex between phosphate and the goethite surface with respect to the **B** complex at very low pH (*i.e.* in the presence of H_3PO_4 species).

Regarding the water–goethite interaction, the surrounding water molecules approached the goethite surface and formed covalent bonds with goethite. Mainly this takes place between water O atoms (O_{H_2O}) and most of the Fe active sites at the 010-goethite surface plane. The Fe–O_{H_2O} covalent bond lengths are in the range of 1.87–2.06 Å. Further, some of these water molecules dissociated at the goethite surface into protons (H^+) and hydroxyl groups (OH^-). Consequently, these produced ions (H^+ and OH^-) transferred to the surface forming covalent bonds with the conjugated charged surface atoms (O and Fe, respectively). Regardless of these covalent bonds formed at the surface, water through its H atoms forms HBs with goethite surface O atoms. All these observations point to the influential effect of water in controlling the phosphate–goethite complexation reaction and its strong interaction with phosphate as well as with the goethite surface. The interaction energies per single water molecule between phosphate and water, and between goethite and water are −1.5 to −2.3 and −7.7 to −16.7 kcal mol^{-1}, respectively (see Table 1). These values are calculated by assuming equal contributions for the water molecules regarding their interaction with phosphate and goethite. All the reported energies for phosphate–goethite, phosphate–water, and goethite–water interactions indicate a very strong interaction between these three subsystems and show that the goethite–water interaction is stronger than the phosphate–water interaction.

Upon increasing the pH, *i.e.* using KH_2PO_4 instead of H_3PO_4, mainly three key points have been observed. First, the

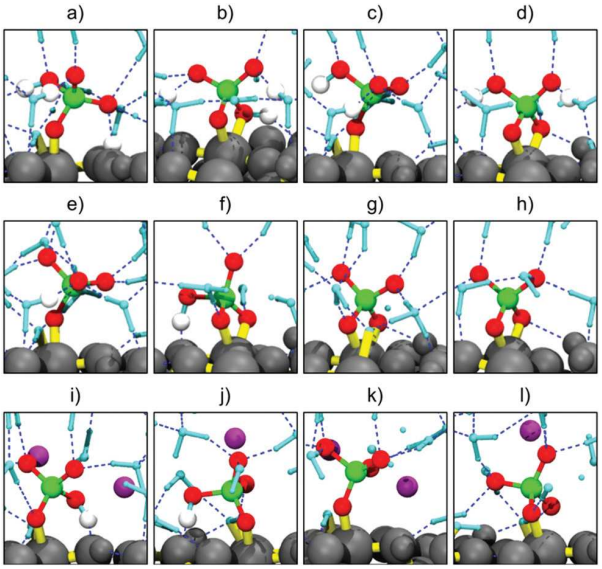


Fig. 2 Relevant fragments of the binding motifs for the geometry optimized structures of the phosphate–goethite–water complexes for the H_3PO_4 species at the 010-goethite surface plane (**M** motif (a), **B** (2O + 1Fe) motif (b)), KH_2PO_4 species with **M** motif (c) and **B** (2O + 1Fe) motif (d), K_2HPO_4 species with **M** motif (e) and **B** (2O + 1Fe) motif (f), K_3PO_4 species with two **B** (2O + 1Fe) motifs (g and h), K_2HPO_4 species in the presence of 10 KOH molecules with two **M** motifs (i and j), and K_3PO_4 species in the presence of 10 KOH molecules with two **M** motifs (k and l). Goethite and water atoms are colored gray and cyan, respectively. For phosphate, atoms are colored green (P), red (O), white (H), and purple (K). Intramolecular and intermolecular covalent bonds including goethite atoms are colored yellow and HBs are colored blue. An extended version of the geometry optimized structures of these phosphate–goethite–water models is given in Fig. S2 in ESI.†

Table 1 Interaction energies between phosphate and goethite, phosphate and water, and goethite and water as well as selected distances for the optimized complexes of different modeled binding motifs (**M** and (2O + 1Fe) **B**) at the 010-goethite surface planes. The reported values for the interaction energies between phosphate and water, and between goethite and water are given per single water molecule

		E_{int} [kcal mol^{-1}]			Distance [Å]		
Species	Binding motif	P-Goethite	P-H_2O/H_2O	Goethite–H_2O/H_2O	$Fe_{goethite}$–O_P	Fe–P	P–O_P
H_3PO_4	**M**	−139	−1.5	−7.7	1.94	3.25	1.53, 1.54, 1.57, 1.63
	B	−75	−2.3	−16.7	2.01 and 2.08	2.71	1.52, 1.52, 1.55, 1.71
KH_2PO_4	**M**	−59	−3.0	−7.1	1.94	3.41	1.53, 1.54, 1.54, 1.66
	B	−101	−2.4	−18.5	1.98 and 2.03	2.58	1.53, 1.56, 1.58, 1.62
K_2HPO_4	**M**	−62	−4.8	−8.5	1.94	3.37	1.53, 1.57, 1.57, 1.60
	B	−117	−3.5	−18.6	2.07 and 2.08	2.60	1.52, 1.57, 1.57, 1.62
K_3PO_4	**M** → **B**	−117	−5.0	−10.0	2.01 and 2.05	2.65	1.56, 1.56, 1.57, 1.58
	B	−150	−4.5	−17.6	1.93 and 1.97	2.54	1.55, 1.57, 1.57, 1.58
K_3PO_4 + 10 KOH	**M**	−68	−5.1	−9.9	1.93	3.19	1.55, 1.56, 1.56, 1.61
	B ≈ **M**	−97	−5.0	−11.2	2.06 and 2.27	2.71	1.56, 1.56, 1.56, 1.57
K_2HPO_4 + 10 KOH	**M**	−62	−3.5	−9.9	2.04	3.04	1.54, 1.54, 1.55, 1.65
	B → **M**	−73	−3.3	−10.1	1.97 and 3.62	3.02	1.53, 1.54, 1.57, 1.62

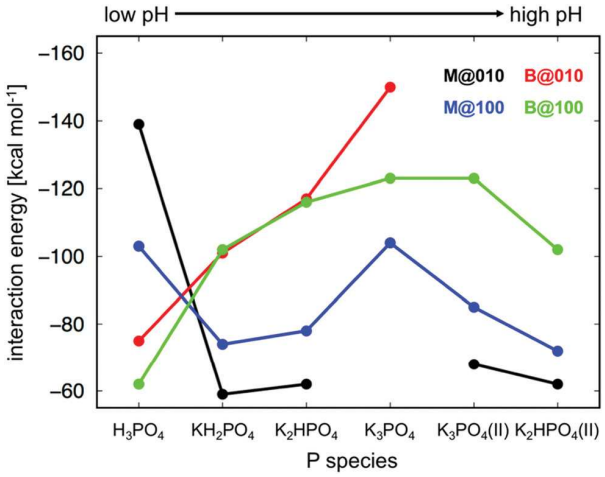


Fig. 3 Interaction energies between phosphate and goethite of stable **M** and **B** modeled binding motifs at the 010- and 100-goethite surface planes for different phosphate species (H_3PO_4, KH_2PO_4, K_2HPO_4, K_3PO_4, K_2HPO_4 + 10 KOH ($K_3PO_{4(II)}$), K_3PO_4 + 10 KOH ($K_2HPO_{4(II)}$)). The numerical values are given in Tables 1 and 2. Note that missing points indicate that the binding motif for the respective species is not stable.

interaction energy between phosphate and goethite for the **M** complex in the presence of KH_2PO_4 (Fig. 2c and Fig. S2c in the ESI†) decreased (−59 kcal mol^{-1}, see Fig. 3 and Table 1), leading to lower stability for the **M** complex at the goethite–water interface compared to the H_3PO_4 case (−139 kcal mol^{-1}). Second, the corresponding interaction energy for the **B** complex (Fig. 2d and Fig. S2d in ESI†) increased, leading to higher stability for the **B** complex (−101 kcal mol^{-1}). Third, the **B** complex has a higher interaction energy than the **M** complex in the presence of KH_2PO_4, indicating its higher stability. Furthermore, both complexes showed one proton transfer process from phosphate to water and formation of a HB with its original phosphate donating O atom. Similar to the H_3PO_4 case, the second proton in the KH_2PO_4 species remained bonded to its phosphate O atom. Again, this refers to formation of mono-protonated complexes for the KH_2PO_4 species. Focusing on the geometry-optimized structure of the **B** complex, one can notice that the remaining proton is not bound to the phosphate O atoms participating in the bidentate binding motif at the goethite–water interface (see Fig. 2d and Fig. S2d in ESI†). In addition to formation of two Fe–O covalent bonds (1.98 and 2.03 Å) for the **B** complex and one Fe–O covalent bond (1.94 Å) for the **M** complex, this explains the higher stability for formation of the **B** complex compared to the **M** complex in the presence of KH_2PO_4 species. Finally, covalent bonds between water and goethite, water dissociation at the goethite surface, HBs between water and goethite, and HBs between water and phosphate can be observed.

At higher pH, *i.e.* going from KH_2PO_4 to K_2HPO_4, two main observations can be made. First, the stability of both **M** and **B** complexes (see Fig. 2e, f and Fig. S2e, f in ESI†) is enhanced. Second, the **B** complex shows higher stability than the **M** complex (−62 kcal mol^{-1} for **M** and −117 kcal mol^{-1} for **B**, see Fig. 2 and Table 1). In addition, one proton is transferred from phosphate to water only in the case of the **M** complex. This indicates the formation of a mono-protonated **B** complex and a non-protonated **M** complex, but with a HB to the original proton of the K_2HPO_4 species. Moreover, like the previous cases, strong interactions are observed between water and goethite *via* formation of covalent bonds and HBs. Further, water dissociation at the goethite surface and HBs between water and phosphate are found as well in this case.

For the non-protonated phosphate species (K_3PO_4), the interaction energy and thus the probability of formation of the **B** complex has its largest value. Note that in this case upon geometry optimization two **B** complexes are found, according to the two different starting **M** and **B** configurations. Both have higher stability (−117 and −150 kcal mol^{-1}, see Fig. 2g, h, Fig. S2g, h in ESI† and Fig. 3, Table 1) than the corresponding complexes formed in the case of K_2HPO_4. This is an indication of increased stability of **B** complexes upon increasing the soil solution pH. All other interactions among phosphate, goethite, and water are similar to the previous cases.

Next, we investigate even higher pH values and especially consider the presence of excess hydroxyl (OH^-) groups (see Fig. 2i–l and Fig. S2i–l in ESI†). The results show the formation

 This journal is © the Owner Societies 2020

of two complexes in the case of K_3PO_4(II), one of them being a pure **M** complex with an Fe–O covalent bond having a length of 1.93 Å. The second complex has a character between **M** and **B** binding motifs with Fe–O bond lengths of 2.06 and 2.27 Å. For the K_2HPO_4(II) case, mainly two **M** complexes result from the two different starting configurations (**M** and **B**). Overall, these results point to the instability of **B** complexes at very high pH (*i.e.* in the presence of excess OH^-- groups). Moreover, these two **M** complexes have a lower stability/interaction energy than that observed at lower pH (see Fig. 3 and Table 1). This suggests a lower probability of formation of both **M** and **B** complexes at high pH due to the competition between phosphate and OH^- towards their interactions with the goethite surface. This is revealed by the formation of more covalent bonds between the hydroxyl (OH^-) groups and the goethite surface in this case compared to all the previous cases. To confirm the observed instability of the formed binding motifs at high pH, relatively short molecular dynamics (MD) simulations (about 13 ps at a temperature of about 300 K) have been performed for two **B** complexes, *i.e.* for the K_2HPO_4 and K_2HPO_4(II) cases. The results confirm the formation of a stable **B** phosphate–goethite complex during the whole MD trajectory for the K_2HPO_4 case (see the Fe–O distances contributed to the B motif in Fig. 4). In contrast, for the K_2HPO_4(II) case the **B** motif was not stable and has been transformed into an **M** motif after about only 2 ps due to dissociation of one Fe–O bond (see Fig. 4 and 5).

P-Binding at the 100-goethite surface plane

In the following, the results of phosphate binding at the 100-goethite surface plane in the presence of water will be briefly introduced. At low pH and especially in the presence of H_3PO_4 (see Fig. 6a, b and Fig. S3a, b in ESI†), the observed **M** complex has a higher interaction energy than the **B** complex and thus a higher tendency of formation (−103 kcal mol^{-1} for **M** and −62 kcal mol^{-1} for **B**, see Fig. 3 and Table 2). The length of the Fe–O covalent bond for the **M** complex (2.02 Å) is intermediate between those for the **B** complex (1.95 and 2.38 Å, see Table 2).

Switching from H_3PO_4 to KH_2PO_4 (Fig. 6c, d and Fig. S3c, d in ESI†), the stability of the **M** complex decreased while the stability of the **B** complex increased, leading to higher stability of the **B** complex (−102 kcal mol^{-1}, see Fig. 3 and Table 2) compared to the **M** complex (−74 kcal mol^{-1}) in the presence of

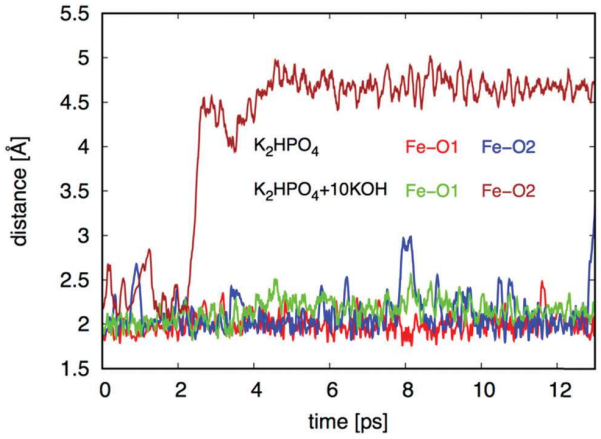


Fig. 4 Intermolecular distances between the phosphate O atoms (O1 and O2) and the surface Fe atom that are contributing to the 2O + 1Fe **B** motifs formed at the 010-goethite surface plane along the MD trajectory for the K_2HPO_4 (in red and blue) and "K_2HPO_4 + 10 KOH = K_2HPO_4(II)" (in green and brown) model cases. For the latter case, **B** → **M** transformation is observed after about 2 ps by dissociation of the second bond (Fe–O2, in brown).

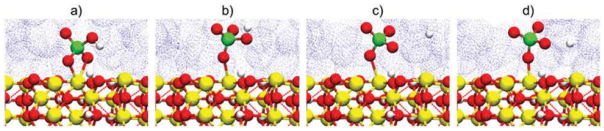


Fig. 5 Selected snapshots (a–d) along the MD trajectory of the "K_2HPO_4 + 10 KOH" model showing the **B** → **M** binding motif's transformation at high pH. Atoms are colored yellow (Fe), green (P), red (O), white (H), and purple (K). For better visualisation, the water molecules in the simulation box are represented by blue points. Moving from (a) to (b) the **B** → **M** transformation process is shown. Moving from (b) to (c) proton transfer from phosphate to water is shown. Moving from (c) to (d) structure reorganization of phosphate and approaching of its original proton take place.

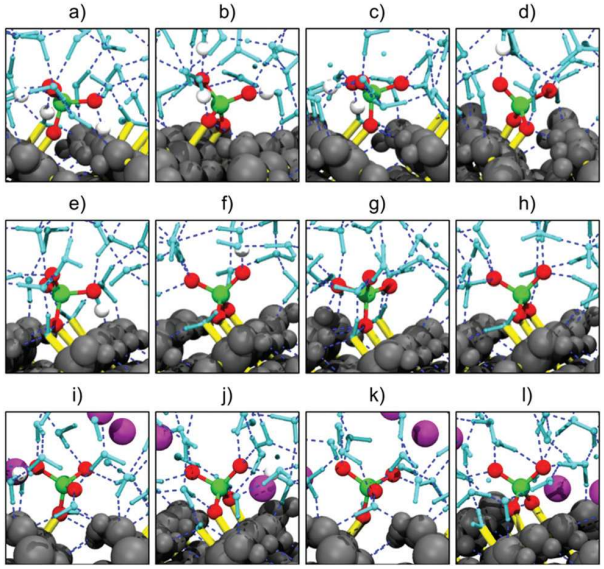


Fig. 6 Relevant fragments of the binding motifs for the geometry optimized structures of the phosphate–goethite–water complexes for the H_3PO_4 species at the 100-goethite surface plane (**M** motif (a), **B** (2O + 2Fe) motif (b)), KH_2PO_4 species with **M** motif (c) and **B** (2O + 2Fe) motif (d), K_2HPO_4 species with **M** motif (e) and **B** (2O + 2Fe) motif (f), K_3PO_4 species with **M** motif (g) and **B** (2O + 2Fe) motif (h), K_2HPO_4 species in the presence of 10 KOH molecules with **M** motif (i) and **B** (2O + 2Fe) motif (j), and K_3PO_4 species in the presence of 10 KOH molecules with **M** motif (k) and **B** (2O + 2Fe) motif (l). Goethite and water atoms are colored gray and cyan, respectively. For phosphate, atoms are colored green (P), red (O), white (H), and purple (K). Intramolecular and intermolecular covalent bonds including goethite atoms are colored yellow and HBs are colored blue. An extended version of the geometry optimized structures of these phosphate–goethite–water models is given in Fig. S3 in ESI.†

Table 2 Interaction energies between phosphate and goethite, phosphate and water, and goethite and water as well as selected distances for the optimized complexes of different modeled binding motifs (**M** and (2O + 2Fe) **B**) at the 100-goethite surface planes. The reported values for the interaction energies between phosphate and water, and between goethite and water are given per single water molecule

		E_{int} [kcal mol^{-1}]			Distance [Å]		
Species	Binding motif	P-Goethite	P-H_2O/H_2O	Goethite–H_2O/H_2O	$Fe_{goethite}$–O_P	Fe–P	P–O_P
H_3PO_4	**M**	−103	−1.9	−6.0	2.02	3.50	1.53, 1.56, 1.57, 1.58
	B	−62	−2.2	−9.0	1.95 and 2.38	3.19 and 3.54	1.55, 1.57, 1.58, 1.58
KH_2PO_4	**M**	−74	−2.5	−6.0	2.12	3.48	1.55, 1.56, 1.58, 1.58
	B	−102	−2.0	−9.1	1.95 and 2.16	3.15 and 3.26	1.51, 1.57, 1.59, 1.61
K_2HPO_4	**M**	−78	−2.2	−5.9	2.21	3.39	1.54, 1.55, 1.57, 1.61
	B	−116	−2.7	−5.9	1.99 and 2.05	3.15 and 3.25	1.52, 1.57, 1.58, 1.61
K_3PO_4	**M**	−104	−3.1	−5.5	2.11	3.46	1.55, 1.56, 1.57, 1.58
	B	−123	−3.5	−7.8	2.08 and 2.09	3.24 and 3.28	1.55, 1.56, 1.58, 1.59
K_3PO_4 + 10 KOH	**M**	−85	−3.4	−6.4	2.06	3.41	1.55, 1.55, 1.57, 1.58
	B	−123	−3.3	−7.3	2.04 and 2.16	3.16 and 3.38	1.55, 1.55, 1.57, 1.59
K_2HPO_4 + 10 KOH	**M**	−72	−3.2	−7.6	2.07	3.42	1.55, 1.56, 1.58, 1.58
	B	−102	−2.9	−6.6	2.09 and 2.17	3.30 and 3.34	1.55, 1.56, 1.57, 1.59

KH_2PO_4 species. Consequently, this indicates that the **B** complex has a higher tendency to be formed in this case. This observation is not only valid for the KH_2PO_4 case but also for the K_2HPO_4 and K_3PO_4 species as well. Moreover, with increasing pH from KH_2PO_4 to K_3PO_4 (Fig. 6c–h and Fig. S3c–h in ESI†), the stability of formation of both **M** and **B** complexes increases as well.

In the presence of the K_3PO_4 species with excess hydroxyl (OH^-) groups, K_3PO_4 + 10 KOH molecules (see Fig. 6k, l and Fig. S3k, l in ESI†), the stability of formation of the **B** complex doesn't change compared to the K_3PO_4 case. However, the interaction energy for the **M** complex is decreased under these conditions with respect to the K_3PO_4 case. For the K_2HPO_4 + 10 KOH case (Fig. 6i, j and Fig. S3i, j in ESI†), both **M** and **B** complexes formed are less stable than those for the K_2HPO_4 case in the absence of OH^- groups. Summing up, the stability of **M** and **B** complexes for the "K_2HPO_4 + 10 KOH" and "K_3PO_4 + 10 KOH" cases shows a decrease at high pH due to the presence of the competing OH^- groups.

For all cases at the 100-goethite surface, the interfacial water molecules interact with the goethite surface *via* formation of covalent bonds between the O_{H2O} and goethite Fe atoms as well as formation of HBs between the water H_{H2O} and goethite O atoms. In addition, dissociation of some water molecules was observed at the surface to protons and hydroxyl groups. These produced ions transferred to the surface and formed covalent bonds. Moreover, for all complexes, involving the H_3PO_4, KH_2PO_4, and K_2HPO_4 species, protons have been transferred from phosphate to water as well as to the surface (see Fig. 6a–f and Fig. S3a–f in ESI†).

Experimental P adsorption

Fig. 7 collects experimental data (present results and literature values) for phosphate adsorption depending on the solution pH. Overall the figure shows that phosphate adsorption is significantly affected by the reaction solution pH. For the present data (see Fig. 7 and Fig. S5 in ESI†), the amount of adsorbed phosphate was represented with respect to both the initial solution pH (start of the adsorption experiment, *i.e.* at time = 0 h) and the final solution pH (at 168 h equilibration time).

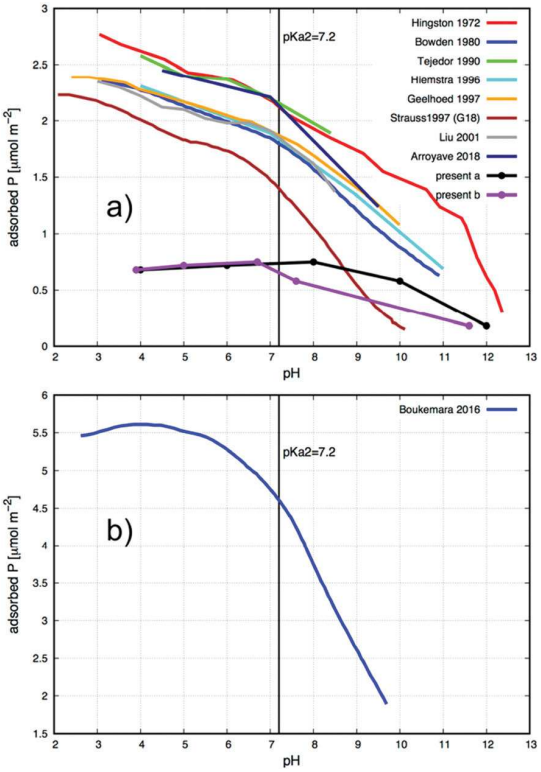


Fig. 7 Panel a: Effect of pH on phosphate (P) adsorption for the present study (considering the initial pH in black "present a" and the final pH in magenta "present b", measured points connected by lines for clarity) and from the literature (digitized and interpolated). The latter includes data by Hingston *et al.*,[29] Bowden *et al.*,[30] Tejedor-Tejedor and Anderson,[31] Hiemstra and Van Riemsdijk,[32] Geelhoed *et al.*,[33] Liu *et al.*,[35] and Arroyave.[38] For more details see also Table 3. The same data are given in µmol g^{-1} in Fig. S7 in ESI.† Panel b: The P adsorption behavior by Boukemara *et al.*[37] that exhibits a higher adsorption capacity compared to all data shown in panel a. The pK_{a2} value for P dissociation is given by a vertical line.

The decrease of the solution pH was slightly lower at low pH, *i.e.* for the initial pH 4.0 the final pH was 3.9 and for the initial

 This journal is © the Owner Societies 2020

pH 6.0 the final pH was 5.0, whereas for initial pH values 8.0 and 10.0, the corresponding final pH values were 6.7 and 7.6, respectively. At initial pH 12.0, the decrease of the solution pH weakened with a final pH of 11.6 (for more details, see Table S3 in ESI†). Considering the initial pH, phosphate adsorption was highest for pH 8 with an adsorption capacity of 0.75 μmol m^{-2} (12.93 μmol g^{-1}) after an equilibration time of 168 h, followed by pH 6 (0.72 μmol m^{-2} = 12.38 μmol g^{-1}) and pH 4 (0.68 μmol m^{-2} = 11.68 μmol g^{-1}). The extent of adsorption decreased at pH 10 (adsorption capacity = 0.58 μmol m^{-2} = 10.04 μmol g^{-1}) and was lowest for pH 12 (0.18 μmol m^{-2} = 3.08 μmol g^{-1}, see Fig. S5 in ESI†). According to the current results, the phosphate adsorption could be described by two pH-dependent successive stages (see Fig. S5 in ESI).† The first stage involves enhancement of phosphate adsorption upon increasing the solution pH specifically in the range of 4–8. Following this stage, a strong drop in phosphate adsorption is observed based on a further increase in solution pH (see adsorption at pH 10 and pH 12 in Fig. S5 in ESI†). It is important to mention that no changes in concentration were detected for dissolved Fe in the equilibrium solution during phosphate adsorption. The measured C_{Total} for the goethite samples without adsorbed phosphate was in the range of 2.88–3.72 μmol m^{-2} for the pH values in the range of 4–10. At pH 12, a relatively high amount of C_{Total} (7.73 μmol m^{-2}) was adsorbed on the goethite surface. Upon phosphate adsorption, the amount of C_{Total} adsorbed on goethite decreased to the range of 2.57–3.98 μmol m^{-2} for the pH range 4–12 (see Table S4 in ESI†).

The adsorption isotherms at pH 6 based on the initial phosphate concentration are shown in Fig. S6 in ESI.† Phosphate adsorption in a 0.01 M $CaCl_2$ electrolyte solution shows a linear increase from 0.55 mmol m^{-2} for an initial phosphate concentration of 0.5 mmol l^{-1}, up to 3.74 mmol m^{-2} for an initial phosphate concentration of 5 mmol l^{-1}. In contrast, phosphate adsorption was quite constant in the range from 0.57 to 0.62 mmol m^{-2} in the case of using 0.01 M KCl as a background electrolyte solution. Only a very weak increase in adsorption with increasing phosphate concentration was detected (Fig. S6, ESI†). This gives an indication for the influential role of the background electrolyte in the phosphate adsorption process at mineral surfaces. It should be noted that there were no changes detected for dissolved Fe, Ca, and K metal ions during the phosphate adsorption process.

Many studies have been conducted to investigate the influence of pH on phosphate adsorption on goethite (see Table 3).[11,12,19,22,29–38] To introduce and compare with some pH-dependent phosphate adsorption data, the free software "GetData Graph Digitizer" was used to digitize the plots of relevant literature data. Most of the reported adsorption capacities of phosphate on goethite in the literature vary from 0.07 to 5.62 μmol m^{-2} (3.1–2570.0 μmol g^{-1}). In almost all of these studies the phosphate adsorption on goethite is significantly affected by the reaction solution pH and it decreased with increasing pH (see Fig. 7). The study of Li and Stanforth[34] showed a significantly higher adsorption capacity of P on the goethite surface (5.58–46.11 μmol m^{-2} = 310.9–2568.1 μmol g^{-1}) due to higher initial P concentration and also high P precipitate content at the surface (see Table 3 and Fig. S8 in ESI†). By distinguishing between the adsorption and surface precipitation processes at the goethite surface, the real P adsorption capacity was in the range of 1.8–4.1 μmol m^{-2} (100–230 μmol g^{-1}). In addition, the studies by Boukemara *et al.*[37] and Chitrakar *et al.*[12] showed relatively high adsorption capacities of phosphate on goethite as well (see Fig. 7b, Table 3, and Fig. S9 in ESI†). In the present study, the adsorption capacity values of phosphate are lower in comparison to previous studies. This is due to starting the sorption experiment with a low initial phosphate concentration (0.15 mmol l^{-1}) to achieve a low and incomplete phosphate loading at the goethite surface.[7] Moreover, the use of background electrolyte solutions during phosphate adsorption additionally affects the amount of adsorbed P on the goethite surface (see Table 3 and Fig. S10, S11 in ESI†). Nevertheless, the curves show a similar trend of decreasing phosphate adsorption with increasing pH.

Discussion

Let us start with the discussion of the present experimental results in light of previous related studies. The present study shows that the phosphate adsorption slightly increases upon increasing the pH from 4 to 8 reaching its maximum point at pH 8 (see Fig. 7 and Fig. S5 in ESI†). Further increasing the solution pH (from 8 to 12) led to a strong and rapid decrease in phosphate adsorption (see Fig. S5 in ESI†). The details depend on whether initial or final pH values are used. If the final pH is considered, a strong decrease in phosphate adsorption already takes place at a pH above 6.7 (see the adsorption decrease at pH 7.6, Fig. S5 in ESI†). Since there is no explicit attempt made to exclude CO_2 during stirring of the goethite samples and phosphate solutions for pH adjustment, the amount of adsorbed CO_3^{2-} increased at pH 12 (see Table S4 in ESI†). This could result as well in a more negative surface charge, decreasing the amount of phosphate adsorption. Therefore, the slope of phosphate adsorption can be steeper in the alkaline pH range than observed in experiments without CO_2 influence. Nevertheless, the observed progressive decrease in phosphate adsorption is consistent with the results reported for similar phosphate adsorption experiments on goethite (see Fig. 7 and Fig. S7–S13 in ESI†).[11,12,19,22,29–38]

It should be clear that in addition to the pK_a effect of the conjugated acids of phosphate anions on the phosphate adsorption process, the goethite's PZC value is a key factor controlling this process. The reported goethite PZC values for the present study and other literature data collected in Table 3 vary from 6.4 to 9.7.[11,12,19,22,29–38] For pH > PZC, the goethite surface has a net negative charge. Under these conditions, goethite exhibits a high affinity to attract cations such as protons (H^+) and free metal ions (M^{n+}) and repel anions such as phosphate species ($H_2PO_4^-$ to PO_4^{3-}). Therefore, the observed strong decrease in the phosphate adsorption process

Table 3 Collected data from the literature for the pH dependence of the phosphate (P) adsorption process on goethite under different experimental setups, involving pH, specific surface area (SSA), initial P concentration, electrolyte solution, reaction time, and point of zero charge (PZC). For graphical representation of selected data, see Fig. 7

Study ref.	pH	SSA, $m^2\ g^{-1}$	Adsorbed P μmol g^{-1}	Adsorbed, P μmol m^{-2}	Initial P, mmol l^{-1}	Electrolyte	Equilibration time, h	PZC
29	3–12	32	9.7–88.6	0.3–2.8	1.00	0.1 M NaCl	24	7.8
39	3–10	49	23.0–101.4	0.5–2.1	0.34	0.01 M NaCl	24	>8
			35.3–99.0	0.7–2.0	0.34	0.1 M NaCl		
			41.2–94.1	0.8–1.9	0.34	1.0 M NaCl		
30	3–11	80	5.6–188.8	0.07–2.4	0.2	0.01 M KCl	24 h	8.4
31	4–8.4	81	152.9–208.7	1.9–2.6	100	0.01 M NaCl	20	9.7
32	4–11	105	72.2–242.1	0.7–2.3	0.2	0.01 M $NaNO_3$	20	9.5
33	2.5/3–8.5/10	96.4	104.5–230.4	1.1–2.4	1.00	0.01 M KNO_3	20	9.2
			86.1–158.0	0.9–1.6	0.08	0.01 M KNO_3		
			74.6–113.0	0.8–1.2	0.02	0.01 M KNO_3		
			136.6–225.9	1.4–2.3	1.00	0.5 M KNO_3		
			123.5–157.3	1.3–1.6	0.08	0.5 M KNO_3		
			76.3–112.9	0.8–1.2	0.02	0.5 M KNO_3		
19	2–10/11	18	2.7–40.7	0.2–2.2	0.81	0.01 M $NaNO_3$	1	6.4
		23	4.4–63.2	0.2–2.8				6.8
		46	5.1–127.4	0.1–2.7				6.9
		60	14.4–169.5	0.2–2.8				6.9
		132	26.7–354.7	0.2–2.7				7.0
34	2.5–8.8	55.7	310.9–2568.1 (adsorption and precipitation)	5.6–46.1	<500	0.001 M NaCl	24	7.4
			100–230 (adsorption only)	1.8–4.1				
35	3–8.5	82	112.0–193.0	1.4–2.4	20	0.1 M KCl	24	7.8
36	4–10	96.4	99.0–196.6	1.0–2.0	0.50	0.01 M $NaNO_3$	24	9.25
			134.0–196.5	1.4–2.0	0.50	0.1 M $NaNO_3$		
22	4.5–10	70.8	75.7–178.5	1.1–2.5	—	0.01 M KNO_3	15–18	9.3
			97.179.4	1.4–2.5		0.1 M KNO_3		
12	2–11	—	190.2–794.1	—	1.61	H_2O	24	—
	2–8		53.4–338.0			Seawater		
37	2.5–9.5	29.6	55.8–166.0	1.9–5.6	—	H_2O	—	8.2
38	4.5–9.5	89.7	111.5–220.0	1.2–2.5	0.005–0.13	0.1 M NaCl	6	8.6
Present	4–12	17.2	3.1–12.9	0.2–0.8	0.15	H_2O	168	8.8

for the present experiment at pH > 8 (see the adsorption decrease at pH = 10 > PZC = 8.8, Fig. 7 and Fig. S5 in ESI†) could be explained by the lower affinity for PO_4^{3-} adsorption. This low affinity is mainly produced by the increase in the surface negative charge due to the adsorbed phosphate at the surface and also by the competition between PO_4^{3-} and OH^- groups at the surface. It should be noted that Fig. 7 and Fig. S7–S13 in ESI† show that phosphate adsorption on goethite in most of the previous studies decreases with increasing solution pH even at low pH. Nevertheless, the rate of the decrease in most studies is increasing at higher pH values. This becomes more prominent when the pH exceeds the PZC (6.4–9.7) value for the corresponding experiment. This confirms the observed stronger decrease in P adsorption at higher pH and the role of PZC in controlling such behavior. Moreover, it was observed that phosphate adsorption increases at higher pH with increasing concentration of the background electrolyte solution (see Fig. S10 and S11 in ESI†).[15,33,36,39] This is in accordance with the present study showing an increase of phosphate adsorption at pH 6 with an increase in the ionic strength of the $CaCl_2$ electrolyte solution (see Fig. S6 in ESI†). On the other hand, increasing the ionic strength of the KCl electrolyte solution does not affect phosphate adsorption. This indicates that pH, the kind of background electrolyte, the electrolyte ionic strength, and the initial phosphate application have a significant influence on the phosphate adsorption process and thus the amount and kind of formed surface complexes.

Focusing on Fig. 7 one notices an unusual slight increase in phosphate adsorption upon increasing the reaction pH from 4 to 8. This observation is in accordance with the behavior of phosphate adsorption at goethite observed by Chitrakar *et al.*[12] in the presence of seawater. They found that the adsorption increases with increasing solution pH up to 7 (see Fig. S9 in ESI†). The results are confirmed as well by a similar behavior observed by Boukemara *et al.*[37] in which the adsorption increased with increasing solution pH up to 4 (see Fig. 7b). However, in general such behavior is not a common observation in the literature for adsorption of phosphates on pure goethite surfaces and in the presence of pure water or background electrolyte solution.[11,12,19,22,29–38] To some extent, this could be due to the variations in the experimental setup and conditions, concentration of phosphate species, pH buffer used, purity, crystallinity, and SSA of goethite, and also existing ions and thus their ionic strength in the reaction solution. Chitrakar *et al.*[12] suggested that the different behavior observed for phosphate adsorption in seawater might be due to the competition of seawater constituents, mainly between phosphate and carbonate. Therefore, the C_{Total} (CO_2 and/or carbonate groups (CO_3^{2-})) in the goethite samples might affect the present phosphate adsorption.

 This journal is © the Owner Societies 2020

Next, let us compare our present modeling results with those obtained in previous simulation as well as experimental studies. Regarding the structures of the phosphate–goethite complexes, the present optimized geometries in water have Fe–P distances in the range of 2.54–3.54 Å (see Tables 1 and 2). This covers the range of the distances predicted by Kwon and Kubicki[43] (3.21–3.37 Å) and Kubicki *et al.*[16] (3.25–3.55 Å) as well as the distances inferred from X-ray absorption spectroscopy of colloidal phosphate iron complexes (3.05–3.39 Å)[59] and phosphate minerals such as vivianite (3.19–3.43 Å).[60] Specifically, the calculated Fe–P distances for the binding motifs **M**@010 (3.02–3.41), **M**@100 (3.39–3.50), and **B**@100 (3.15–3.54) are closer to the measured ones by X-ray absorption (3.05–3.43 Å) than those for the **B**@010 (2.54–2.71) complexes. Further, the calculated bond lengths in the present study between the chemisorbed water and goethite ($Fe–O_{H_2O}$) are 1.87–2.06 and 2.01–2.09 Å for the 010- and 100-goethite surface planes. This is in accordance with those for the solvated goethite surface that are measured by the crystal truncation rod technique (2.15 Å)[61] and calculated by DFT (2.04 Å).[62] With respect to the energetics of phosphate–goethite complexes, Kwon and Kubicki[43] suggested formation of a diprotonated **B** complex at pH 4–6 ($H_2PO_4^-$), either a deprotonated **B** or a monoprotonated **M** complex at pH 7.5–7.9 (HPO_4^{2-}), and a deprotonated **M** complex at pH 12.8 (PO_4^{3-}). This could be considered as an agreement with our findings. However, they predicted that both monoprotonated **M** and non-protonated **B** complexes are not stable for the $H_2PO_4^-$ species. A reason for this discrepancy could be the use of a small cluster model in ref. 43 containing only two octahedral iron atoms connected to each other in an edge-sharing fashion with a few explicit water molecules. On the other hand, Kubicki *et al.*[16] have performed DFT-based molecular dynamics simulations for larger periodic goethite models. Their calculated average binding energies of phosphate at goethite indicated that formation of **M**@100 and **B**@100 complexes is favored for the HPO_4^{2-} species. This outcome is in accordance with the present findings. For the **M**@010 and **B**@010 complexes, positive adsorption energies have been reported, which disagrees with the present results. The reason for this discrepancy is not obvious, because different computational setups have been used in terms of system size and methods. While in ref. 16 thermal fluctuations have been included (although it should be noted that for the rather short trajectories used, standard deviations take large values), the present study focused on geometry-optimized structures only. Further, Belelli *et al.*[63] have simulated the phosphate adsorption at goethite by introducing periodic slab models and performing DFT calculations. They predicted the abundance of the protonated **B** complex at pH 3.1 and pH 12.8 and the non-protonated **B** complex along the pH range of 4.2–7.9. Their observations at pH 3.1 and pH = 4.2–7.9 are consistent with our findings related to the abundance of the **B** complex at both goethite surfaces for the modeled $H_2PO_4^-$, HPO_4^{2-}, and PO_4^{3-} species. Regarding the water–goethite interaction by using DFT calculations, Long *et al.*[64] predicted chemisorption and dissociation of water at the 010-goethite surface. This comes in good agreement with our observation that water molecules proceed towards the goethite surface and form covalent bonds and some of them dissociate at the surface into protons and hydroxyl groups.

With respect to the adsorption and energetics of phosphate and other oxyanions on iron and aluminum oxides, calorimetric measurements reported that the molar heats of sulfate and phosphate sorption on amorphous aluminum hydroxide are +0.7 and −1.6 kcal mol^{-1}, respectively.[65] This indicates that phosphate adsorption on aluminum hydroxide is more favored compared to sulphate adsorption. Moreover, both reported values are smaller than our calculated interaction energies of the phosphate–goethite complexes. In principle, this points to stronger adsorption for phosphate at goethite compared to aluminum hydroxide. Furthermore, the measured molar heat of adsorption values of chromate on hematite and ferrihydrite are −1.5 and −1.8 kcal mol^{-1}, respectively.[66] However, the DFT results of the same study predicted the **M** complex to be the most favored complex at hematite with an adsorption energy of −33.2 kcal mol^{-1} with minority of the **B** complex with −10.3 kcal mol^{-1}. At ferrihydrite, the DFT results predicted unfavorable binding for chromate with positive adsorption energy values (+9.6 kcal mol^{-1} for the **M** complex and from +1.2 to +6.5 kcal mol^{-1} for the **B** complex). Regardless of the discrepancy between the experimental and theoretical results, all the reported values are smaller compared to the calculated interaction energies in the present study. In this context, one should mention the discrepancy present for the reported heats of oxyanion sorption on oxides due to the use of different experimental approaches. This is even more relevant when there is a comparison between direct calorimetric measurements and thermodynamic data derived from the temperature dependence of isotherms;[66] for more details see ref. 67–69.

In the following, we will discuss our molecular modeling results based on the pH dependence by introducing three pH ranges. These ranges are low pH (only H_3PO_4 species), intermediate pH ($H_2PO_4^-$, HPO_4^{2-}, and PO_4^{3-} assuming the absence of hydroxyl (OH^-) groups), and high pH (HPO_4^{2-} and PO_4^{3-} species + hydroxyl (OH^-) groups). It is important to mention that the present sorption experiment assumes abundance of two phosphate species involving $H_2PO_4^-$ (pH: 2.1–7.2) and HPO_4^{2-} (pH: 7.2–12.4). This is mainly based on the reported values for the phosphate dissociation and recombination equilibrium constants.[70] However, our present modeling approach involved all possible cases to have a global understanding of the pH dependence of the P binding at the goethite–water interface. Based on the introduced three pH ranges, formation of the **M** complex between phosphate and both goethite surface planes is more favored than the **B** complex at low pH (*i.e.* H_3PO_4, extremely high acidic conditions). Here, both **M** and **B** complexes at the 100-surface plane are less stable than the corresponding ones at the 010-surface plane. This indicates that the most stable **M** complex at low pH occurs at the 010-goethite surface plane.

For both surfaces and moving from low to intermediate pH ranges, the observed behavior in the presence of H_3PO_4 is reversed, leading to a decrease of the stability of **M** complexes and an increase of the stability of **B** complexes. Over the

intermediate pH range, formation of the **B** complex is more favored than the **M** complex. With increasing pH from $H_2PO_4^-$ to PO_4^{3-} the stability of formation of both **M** and **B** complexes increases. This means that within this range the P binding increases with the increasing pH level (see Fig. 3). This is in good agreement with the observed increase in phosphate adsorption upon increasing the pH for the present study from pH 4 to pH 8 (see Fig. 7 and Fig. S5 in ESI†) as well for other studies by Chitrakar *et al.*[12] and Boukemara *et al.*[37] In addition to the formed covalent bonds and HBs within the phosphate–goethite–water systems that will be discussed later, the electrostatic interaction is a key point influencing this observation. As it was introduced before and also according to our modeling setup, the goethite surface exhibits a positive net charge at pH < PZC. In addition, there is no significant change in the goethite surface charge in the intermediate pH range. Therefore, the main change upon increasing the reaction pH will be the phosphate deprotonation process from $H_2PO_4^-$ to PO_4^{3-}. Taking these facts into account, one can easily understand now that the electrostatic interaction for the phosphate–goethite complexes increases in the order of $H_2PO_4^-$ < HPO_4^{2-} < PO_4^{3-}. This provides an explanation for the experimental observation regarding this issue (the present study and studies by Chitrakar *et al.*[12] and Boukemara *et al.*[37]). It should be highlighted that such behavior will be observed only under certain conditions in which the goethite surface is positively charged with no substantial change with increasing pH below its PZC. This assumption matches the measured surface charge density in the present study (see Fig. S4 in ESI†). A first look at Fig. S4 (ESI†) indicates a large linear change in the charge density with 1 C m^{-2} for 1 pH unit or in total 7 C m^{-2} change along the whole acidic range. However, when we translate this change to one goethite unit cell (with an area of about 46 $Å^2$ = 46 × 10^{-20} m^2) which is sufficient enough to bind one phosphate anion or even more, this would produce about 322 × 10^{-20} C for 7 pH units. This is a negligible change in the surface charge compared to the change produced from the phosphate deprotonation process. Further, it should be noted that the present study and those by Chitrakar *et al.*[12] and Boukemara *et al.*[37] were very unique in carrying out the experiments without using either buffer or background electrolyte. On the other hand, if the surface charge changes considerably, the adsorption will decrease upon increasing the pH due to enhanced repulsion between the increasingly negatively charged phosphate and goethite surface. In this case, the common behavior observed for most previous studies[11,12,19,22,29–38] will predominate (Fig. 7 and Fig. S7–S13 in ESI†). Furthermore, all the **M** complexes in this intermediate pH range at the 100-goethite surface plane are more stable than the corresponding **M** complexes at the 010-goethite surface (see Fig. 3 and Tables 1, 2). This could be explained based on the fact that each surface Fe atom for the modeled 010- and 100-goethite surface planes is coordinated by four and five O atoms, respectively. Consequently, one may attribute this observation to the saturation of the Fe atom participating in the **M** motif with six coordination bonds with O atoms for the 100-goethite surface plane, compared with the same **M** binding motifs at the 010-surface (here the Fe atom is coordinated by five O atoms). Therefore, one can conclude that mostly the **M** binding motif stability increases with increasing coordination of its contributing Fe atom. In contrast, the **B** complexes in the presence of $H_2PO_4^-$ and HPO_4^{2-} have mostly the same stability at both 100- and 010-goethite surface planes. Moreover, both starting configurations with **M** and **B** complexes at the 010-goethite surface and in the presence of PO_4^{3-} yield only **B** complexes indicating the formation of only this complex under these conditions. The observed PO_4^{3-} **B** complex is more stable at the 010-goethite surface plane than at the 100-goethite surface plane.

At high pH, the stability of formation of both **M** and **B** complexes at both 010- and 100-goethite surface planes decreases compared to the relevant species in the intermediate pH range. This means that increasing the pH level into the proposed high pH range will decrease the P binding. This is in accordance with the experimental observation of a strong drop in phosphate adsorption at high pH and especially at pH > PZC (see Fig. 7). This is valid for the present experiment as well as for most of the previous experiments in the literature related to phosphate adsorption at goethite surfaces (see Fig. 7 and Fig. S7–S13 in ESI†).[11,12,19,22,29–38,71] As discussed above, this strong decrease is mainly due to the presence of OH^- groups at the goethite surface and thus their competition reaction with phosphates. This is obvious from the comparison of the binding strengths (see Tables 1 and 2) of phosphate at both goethite surfaces for the HPO_4^{2-} and PO_4^{3-} species in the intermediate pH range and the corresponding species (HPO_4^{2-} + 10 KOH and PO_4^{3-} + 10 KOH) in the high pH range. The binding energy values indicate the vital role of the competitive OH^- groups in decreasing the P binding. This is also confirmed by the MD simulation results that highlight the weakness of the **B** complex and its transformation into the **M** complex due to the presence of 10 KOH molecules (see Fig. 4 and 5). This agrees well with the outcome of our recent study[7] in which we found that the binding strength at both 010- and 100-goethite surface planes has the order H_2O < phosphate < KOH. This means that phosphate could replace the adsorbed water molecules at the goethite surface, but the OH^- groups can replace both phosphate and water at the surface. This is also revealed in the current study by the observation of more adsorbed OH^- groups on both modeled goethite surface planes at high pH. As a consequence of the OH^- adsorption at the goethite surface, the surface becomes negatively charged which takes place at pH > PZC. Hence, the electrostatic interaction will play a role in repelling the negatively charged phosphate species (mainly HPO_4^{2-} and/or PO_4^{3-}) from approaching the negatively charged goethite surface. This molecular level observation agrees with and confirms the suggestion by Boukemara *et al.*[37] in which the competition effect of OH^- could be the reason for decreasing phosphate adsorption at higher pH. Eventually this provides a detailed explanation for the experimentally observed progressive decrease in phosphate adsorption at goethite surfaces at high pH.

Formation of the **M** complex in the modeled high pH range at the 010-goethite surface plane will be more favored than the **B** complex at low pH. However, still the **B** complex is more

 This journal is © the Owner Societies 2020

favored than the **M** complex at the 100-goethite surface plane under the same conditions. It should be noted that both **M** and **B** complexes at the 100-goethite surface plane and in the presence of the competing OH^- groups are more favored than the corresponding ones at the 010-surface plane. Translating such information to Geochemistry, it points to the critical role of the goethite composition (such as purity, crystallinity, existing crystal planes, and SSA of goethite) and experimental setup (such as phosphate source, initial concentration of phosphate species, pH, pH buffer, existing ions, electrolyte, and electrolyte ionic strength) in controlling phosphate adsorption at the goethite surface.

At both goethite surfaces, proton (H^+) transfer from phosphate to water as well as to goethite has been observed over all the pH ranges containing H_3PO_4, $H_2PO_4^-$, and HPO_4^{2-} species. This observation confirms the prediction by Hiemstra and Van Riemsdijk[32] that protons (H^+) will be adsorbed at the goethite surface during the phosphate adsorption process. Moreover, our observation is in accordance as well with the suggestion by Strauss *et al.*[19] that diffusion of protons (H^+) from and to the surface will take place along with the phosphate adsorption process. From this observation it could be concluded that the proton transfer process will lead to a decrease of the solution pH value. This molecular level understanding for this observation could be supported and confirmed by the observed decrease in solution pH during the present adsorption experiment at all pH values (see Table S3 in ESI†). This agrees as well with the observed pH decrease at pH $>$ 7 by Boukemara *et al.*[37] This explains and is in accordance with the observation of the possible induced soil acidification process due to phosphate sorption.[72–74] In other words, in cases where there is no buffer solution used during the addition of phosphates to soils, the soil may become more acidic with time due to the sorption process. It should be emphasized that such a conclusion couldn't be drawn from most adsorption experiments. This is due to the fact that most of these experiments have been performed under specific pH value(s), *i.e.* controlled by using acid/base buffers.

Summary and conclusions

In summary, we have introduced a molecular level picture of the pH dependence of the phosphate binding mechanism at the goethite–water interface through a joint experimental–theoretical approach. We have employed different molecular models for the phosphate–goethite–water molecular systems to cover qualitatively a large number of the existing phosphate sorption experiments. Each model involved binding of only one phosphate species of 6 studied cases (H_3PO_4, KH_2PO_4, K_2HPO_4, K_3PO_4, K_2HPO_4 + 10 KOH, and K_3PO_4 + 10 KOH) at one goethite surface plane of two studied cases (010 and 100) in the presence of water molecules to simulate the sorption solution medium. For each phosphate species, two separate models have been constructed involving monodentate (**M**) and bidentate (**B**) binding motifs between phosphate and the goethite surface. For each model periodic DFT calculations have been performed for better understanding the detailed interactions at the goethite–water interface. To validate and confirm our molecular modeling approach, adsorption experiments of phosphate at goethite have been carried out at different pH levels in the pH range of 4–12. Here, we have used low initial phosphate concentration (0.15 mmol l^{-1}) to achieve a low and incomplete phosphate loading at the goethite surface. Such conditions are more compatible with the molecular modeling in the present study in which only one adsorbed phosphate molecule at the goethite surface has been simulated.

The molecular modeling results point to the stability and thus abundance of the **M** binding motif under extremely acidic conditions (*i.e.* in the presence of H_3PO_4 species). By increasing the pH into an intermediate range (*i.e.* in the absence of OH^- groups), the **B** binding motif becomes predominant. At extremely high pH (*i.e.* in the presence of OH^- groups), the **M** binding motif becomes abundant again, *i.e.* similar to the very low pH case. These observations should be useful to resolve the existing debate about the assignment of the phosphate–goethite binding motifs. Moreover, the importance of water in controlling such binding reactions, and the competition between phosphate, water, and the hydroxyl groups at goethite have been explored.

The present experiment demonstrated two successive adsorption stages based on the pH; the first stage was described by a slight increase of phosphate adsorption upon increasing the pH from 4 to 8, while the second one exhibited a strong decrease in phosphate adsorption upon a further increase in pH from 8 to 12. This is in good agreement with the present theoretical results and thus gives support for the provided molecular level picture. However, it should be noted that the unusual first stage will be observed only if the goethite surface exhibits a positive net charge and there is no significant change with increasing pH below PZC. If the surface charge changes considerably, the common behavior of an adsorption decrease will be observed, as manifested by most previous experiments. This could be explained as well using the present simulations and in particular by considering the most relevant species for common sorption experiments. Specifically, considering the "H_3PO_4" (pH: around 2), "KH_2PO_4" (pH: 2.1–7.2), and "K_2HPO_4 + 10 KOH" (pH: 7.2–12.4) models at the 010-goethite surface yields a decrease in phosphate adsorption upon pH increase. Another point needs to be stressed if a comparison with experiment is being made. Experimental adsorption results are affected by the presence of different crystal planes and thus binding motifs. Hence, fitting the present theoretical results to a particular experiment could be done by assuming a weighted average of the result obtained for different surface planes and binding motifs. Of course, to make really quantitative predictions one should include more surface planes as well as effects due to, *e.g.*, surface coverage, purity, crystallinity, and SSA of the goethite surface.

The present experimental–theoretical results indicate that phosphate sorption may induce soil acidification although the impact of this effect depends on the overall chemical conditions of soil. For soil chemistry applications this means that P-fertilization

may support soil acidification not only by the acidity from common P-fertilizers but also by induced acidity from the adsorption of surplus phosphate that was not taken up by crops but bound to pedogenic oxides. Finally, the agreement with the present and other experimental and theoretical studies in addition to introducing fundamental explanations to the observed sorption behaviors come together to validate our molecular modeling approach. However, further modification of the present modeling approach could explain the effects of background electrolytes and their ionic strength on the pH dependent P binding at the goethite surfaces. In addition, this model could be used to describe the binding mechanisms of other anions on goethite.

Funding

This work belongs to the InnoSoilPhos-project, funded by the German Federal Ministry of Education and Research (BMBF) in the frame of the BonaRes-program (No. 031A558).

Conflicts of interest

There are no conflicts to declare.

Acknowledgements

This research was performed within the scope of the Leibniz ScienceCampus ''Phosphorus Research'' Rostock. The authors thank the North German Supercomputing Alliance for providing HPC resources (project mvp00016).

References

1 P. Gros, A. Ahmed, O. Kühn and P. Leinweber, Glyphosate binding in soil as revealed by sorption experiments and quantum-chemical modeling, *Sci. Total Environ.*, 2017, **586**, 527–535, DOI: 10.1016/j.scitotenv.2017.02.007.

2 A. A. Ahmed, P. Gros, O. Kühn and P. Leinweber, Molecular level investigation of the role of peptide interactions in the glyphosate analytics, *Chemosphere*, 2018, **196**, 129–134, DOI: 10.1016/j.chemosphere.2017.12.162.

3 O. Urrutia, I. Guardado, J. Erro, M. Mandado and J. M. García-Mina, Theoretical chemical characterization of phosphate-metal-humic complexes and relationships with their effects on both phosphorus soil fixation and phosphorus availability for plants, *J. Sci. Food Agric.*, 2013, **93**, 293–303.

4 P. Gros, A. A. Ahmed, O. Kühn and P. Leinweber, Influence of metal ions on glyphosate detection by FMOC-Cl, *Environ. Monit. Assess.*, 2019, **191**, 244, DOI: 10.1007/s10661-019-7387-2.

5 J. Kruse, M. Abraham, W. Amelung, C. Baum, R. Bol, O. Kühn, H. Lewandowski, J. Niederberger, Y. Oelmann, C. Rüger, J. Santner, M. Siebers, N. Siebers, M. Spohn, J. Vestergren, A. Vogts and P. Leinweber, Innovative methods in soil phosphorus research: a review, *J. Plant Nutr. Soil Sci.*, 2015, **178**, 43–88, DOI: 10.1002/jpln.201400327.

6 A. A. Ahmed, P. Leinweber and O. Kühn, Unravelling the nature of glyphosate binding to goethite surfaces by *ab initio* molecular dynamics simulations, *Phys. Chem. Chem. Phys.*, 2018, **20**, 1531–1539, DOI: 10.1039/C7CP06245A.

7 A. A. Ahmed, S. Gypser, P. Leinweber, D. Freese and O. Kühn, Infrared spectroscopic characterization of phosphate binding at the goethite–water interface, *Phys. Chem. Chem. Phys.*, 2019, **21**, 4421–4434, DOI: 10.1039/C8CP07168C.

8 P. B. Ganta, O. Kühn and A. A. Ahmed, QM/MM simulations of organic phosphorus adsorption at the diaspore–water interface, *Phys. Chem. Chem. Phys.*, 2019, **21**, 24316–24325, DOI: 10.1039/C9CP04032C.

9 Y. Arai and D. L. Sparks, Phosphate Reaction Dynamics in Soils and Soil Components: A Multiscale Approach, in *Adv. Agron.*, Elsevier, 2007, pp. 135–179, , DOI: 10.1016/S0065-2113(06)94003-6.

10 Y. Arai and D. L. Sparks, ATR-FTIR Spectroscopic Investigation on Phosphate Adsorption Mechanisms at the Ferrihydrite–Water Interface, *J. Colloid Interface Sci.*, 2001, **241**, 317–326, DOI: 10.1006/jcis.2001.7773.

11 N. J. Barrow, A mechanistic model for describing the sorption and desorption of phosphate by soil, *J. Soil Sci.*, 1983, **34**, 733–750, DOI: 10.1111/j.1365-2389.1983.tb01068.x.

12 R. Chitrakar, S. Tezuka, A. Sonoda, K. Sakane, K. Ooi and T. Hirotsu, Phosphate adsorption on synthetic goethite and akaganeite, *J. Colloid Interface Sci.*, 2006, **298**, 602–608, DOI: 10.1016/j.jcis.2005.12.054.

13 P. Hinsinger, Bioavailability of soil inorganic P in the rhizosphere as affected by root-induced chemical changes: a review, *Plant Soil*, 2001, **237**, 173–195, DOI: 10.1023/A:1013351617532.

14 T. M. Tsao, Y. M. Chen and M. K. Wang, Origin, separation and identification of environmental nanoparticles: a review, *J. Environ. Monit.*, 2011, **13**, 1156, DOI: 10.1039/c1em10013k.

15 C. Luengo, M. Brigante, J. Antelo and M. Avena, Kinetics of phosphate adsorption on goethite: comparing batch adsorption and ATR-IR measurements, *J. Colloid Interface Sci.*, 2006, **300**, 511–518, DOI: 10.1016/j.jcis.2006.04.015.

16 J. D. Kubicki, K. W. Paul, L. Kabalan, Q. Zhu, M. K. Mrozik, M. Aryanpour, A.-M. Pierre-Louis and D. R. Strongin, ATR-FTIR and Density Functional Theory Study of the Structures, Energetics, and Vibrational Spectra of Phosphate Adsorbed onto Goethite, *Langmuir*, 2012, **28**, 14573–14587, DOI: 10.1021/la303111a.

17 R. L. Parfitt, Phosphate reactions with natural allophane, ferrihydrite and goethite, *J. Soil Sci.*, 1989, **40**, 359–369, DOI: 10.1111/j.1365-2389.1989.tb01280.x.

18 P. Persson, N. Nilsson and S. Sjöberg, Structure and Bonding of *Ortho*phosphate Ions at the Iron Oxide–Aqueous Interface, *J. Colloid Interface Sci.*, 1996, **177**, 263–275, DOI: 10.1006/jcis.1996.0030.

19 R. Strauss, G. W. Brummer and N. J. Barrow, Effects of crystallinity of goethite: II. Rates of sorption and desorption of phosphate, *Eur. J. Soil Sci.*, 1997, **48**, 101–114, DOI: 10.1111/j.1365-2389.1997.tb00189.x.

 This journal is © the Owner Societies 2020

20 M. Talebi Atouei, R. Rahnemaie, E. Goli Kalanpa and M. H. Davoodi, Competitive adsorption of magnesium and calcium with phosphate at the goethite water interface: Kinetics, equilibrium and CD-MUSIC modeling, *Chem. Geol.*, 2016, **437**, 19–29, DOI: 10.1016/j.chemgeo.2016.05.004.

21 L. Krumina, J. P. L. Kenney, J. S. Loring and P. Persson, Desorption mechanisms of phosphate from ferrihydrite and goethite surfaces, *Chem. Geol.*, 2016, **427**, 54–64, DOI: 10.1016/j.chemgeo.2016.02.016.

22 J. Antelo, M. Avena, S. Fiol, R. López and F. Arce, Effects of pH and ionic strength on the adsorption of phosphate and arsenate at the goethite–water interface, *J. Colloid Interface Sci.*, 2005, **285**, 476–486, DOI: 10.1016/j.jcis.2004.12.032.

23 R. J. Atkinson, R. L. Parfitt and R. S. C. Smart, Infra-red study of phosphate adsorption on goethite, *J. Chem. Soc., Faraday Trans. 1*, 1974, **70**, 1472, DOI: 10.1039/f19747001472.

24 J. Torrent, U. Schwertmann and V. Barron, Fast and slow phosphate sorption by goethite-rich natural materials, *Clays Clay Miner.*, 1992, **40**, 14–21.

25 J. R. McLaughlin, J. C. Ryden and J. K. Syers, Development and evaluation of a kinetic model to describe phosphate sorption by hydrous ferric oxide gel, *Geoderma*, 1977, **18**, 295–307, DOI: 10.1016/0016-7061(77)90038-6.

26 I. R. Willett, C. J. Chartres and T. T. Nguyen, Migration of phosphate into aggregated particles of ferrihydrite, *J. Soil Sci.*, 1988, **39**, 275–282, DOI: 10.1111/j.1365-2389.1988.tb01214.x.

27 J. Torrent, Interactions between phosphate and iron oxide, in *Soils Environ.*, Catena Verlag, Reiskirchen, Germany, 1997, pp. 321–344.

28 Y. Gao and A. Mucci, Acid base reactions, phosphate and arsenate complexation, and their competitive adsorption at the surface of goethite in 0.7 M NaCl solution, *Geochim. Cosmochim. Acta*, 2001, **65**, 2361–2378, DOI: 10.1016/S0016-7037(01)00589-0.

29 F. J. Hingston, A. M. Posner and J. P. Quirk, Anion adsorption by goethite and gibbsite: I. The role of the proton in determining adsorption envelopes, *J. Soil Sci.*, 1972, **23**, 177–192, DOI: 10.1111/j.1365-2389.1972.tb01652.x.

30 J. Bowden, S. Nagarajah, N. Barrow, A. Posner and J. Quirk, Describing the adsorption of phosphate, citrate and selenite on a variable-charge mineral surface, *Soil Res.*, 1980, **18**, 49, DOI: 10.1071/SR9800049.

31 M. I. Tejedor-Tejedor and M. A. Anderson, The protonation of phosphate on the surface of goethite as studied by CIR-FTIR and electrophoretic mobility, *Langmuir*, 1990, **6**, 602–611, DOI: 10.1021/la00093a015.

32 T. Hiemstra and W. H. Van Riemsdijk, A Surface Structural Approach to Ion Adsorption: The Charge Distribution (CD) Model, *J. Colloid Interface Sci.*, 1996, **179**, 488–508, DOI: 10.1006/jcis.1996.0242.

33 J. S. Geelhoed, T. Hiemstra and W. H. Van Riemsdijk, Phosphate and sulfate adsorption on goethite: single anion and competitive adsorption, *Geochim. Cosmochim. Acta*, 1997, **61**, 2389–2396, DOI: 10.1016/S0016-7037(97)00096-3.

34 L. Li and R. Stanforth, Distinguishing Adsorption and Surface Precipitation of Phosphate on Goethite (α-FeOOH), *J. Colloid Interface Sci.*, 2000, **230**, 12–21, DOI: 10.1006/jcis.2000.7072.

35 F. Liu, A. De Cristofaro and A. Violante, Effect of pH, phosphate and oxalate on the adsorption/desorption of arsenate on/from goethite, *Soil Sci.*, 2001, **166**, 197–208.

36 R. P. J. J. Rietra, T. Hiemstra and W. H. van Riemsdijk, Interaction between Calcium and Phosphate Adsorption on Goethite, *Environ. Sci. Technol.*, 2001, **35**, 3369–3374, DOI: 10.1021/es000210b.

37 L. Boukemara, C. Boukhalfa, L. Reinert and L. Duclaux, Characterization of Phosphate Adsorption on Goethite Macroscopic and Spectroscopic Analyses, *J. Mater. Environ. Sci.*, 2016, **7**, 2541–2550.

38 J. M. Arroyave, V. Puccia, G. P. Zanini and M. J. Avena, Surface speciation of phosphate on goethite as seen by InfraRed Surface Titrations (IRST), *Spectrochim. Acta, Part A*, 2018, **199**, 57–64, DOI: 10.1016/j.saa.2018.03.043.

39 N. Barrow, J. Bowden, A. Posner and J. Quirk, Describing the effects of electrolyte on adsorption of phosphate by a variable charge surface, *Soil Res.*, 1980, **18**, 395, DOI: 10.1071/SR9800395.

40 A. C. Chapman and L. E. Thirlwell, Spectra of phosphorus compounds—I the infra-red spectra of *ortho*phosphates, *Spectrochim. Acta*, 1964, **20**, 937–947, DOI: 10.1016/0371-1951(64)80094-1.

41 M. Villalobos, M. A. Cheney and J. Alcaraz-Cienfuegos, Goethite surface reactivity: II. A microscopic site-density model that describes its surface area-normalized variability, *J. Colloid Interface Sci.*, 2009, **336**, 412–422, DOI: 10.1016/j.jcis.2009.04.052.

42 J. S. Loring, M. H. Sandström, K. Norén and P. Persson, Rethinking Arsenate Coordination at the Surface of Goethite, *Chem. – Eur. J.*, 2009, **15**, 5063–5072, DOI: 10.1002/chem.200900284.

43 K. D. Kwon and J. D. Kubicki, Molecular Orbital Theory Study on Surface Complex Structures of Phosphates to Iron Hydroxides: Calculation of Vibrational Frequencies and Adsorption Energies, *Langmuir*, 2004, **20**, 9249–9254, DOI: 10.1021/la0487444.

44 F. Xiu, L. Zhou, S. Xia and L. Yu, Adsorption mechanism of water molecule on goethite (010) surface, *J. Ocean Univ. China*, 2016, **15**, 1021–1026, DOI: 10.1007/s11802-016-3171-x.

45 H. Guo and A. S. Barnard, Thermodynamic modelling of nanomorphologies of hematite and goethite, *J. Mater. Chem.*, 2011, **21**, 11566, DOI: 10.1039/c1jm10381d.

46 J. Rakovan, U. Becker and M. F. Hochella, Aspects of goethite surface microtopography, structure, chemistry, and reactivity, *Am. Mineral.*, 1999, **84**, 884–894, DOI: 10.2138/am-1999-5-623.

47 R. M. Cornell and U. Schwertmann, *The iron oxides: structure, properties, reactions, occurrences, and uses, 2nd, completely rev. and extended ed*, Wiley-VCH, Weinheim, 2003.

48 J. D. Kubicki, D. Tunega and S. Kraemer, A density functional theory investigation of oxalate and Fe(II) adsorption onto the (010) goethite surface with implications for ligand- and reduction-promoted dissolution, *Chem. Geol.*, 2017, **464**, 14–22, DOI: 10.1016/j.chemgeo.2016.08.010.

49 A. Szytuła, A. Burewicz, ž. Dimitrijević, S. Kraśnicki, H. Rżany, J. Todorović, A. Wanic and W. Wolski, Neutron Diffraction Studies of α-FeOOH, *Phys. Status Solidi B*, 1968, **26**, 429–434, DOI: 10.1002/pssb.19680260205.

50 J. VandeVondele, M. Krack, F. Mohamed, M. Parrinello, T. Chassaing and J. Hutter, Quickstep: fast and accurate density functional calculations using a mixed Gaussian and plane waves approach, *Comput. Phys. Commun.*, 2005, **167**, 103–128, DOI: 10.1016/j.cpc.2004.12.014.

51 J. Hutter, M. Iannuzzi, F. Schiffmann and J. VandeVondele, CP2K: Atomistic Simulations of Condensed Matter Systems, *Wiley Interdiscip. Rev.: Comput. Mol. Sci.*, 2014, **4**, 15–25, DOI: 10.1002/wcms.1159.

52 B. G. Lippert, J. Hutter and M. Parrinello, A hybrid Gaussian and plane wave density functional scheme, *Mol. Phys.*, 1997, **92**, 477–488, DOI: 10.1080/002689797170220.

53 J. P. Perdew, K. Burke and M. Ernzerhof, Generalized Gradient Approximation Made Simple, *Phys. Rev. Lett.*, 1996, **77**, 3865–3868, DOI: 10.1103/PhysRevLett.77.3865.

54 M. Krack, Pseudopotentials for H to Kr optimized for gradient-corrected exchange-correlation functionals, *Theor. Chem. Acc.*, 2005, **114**, 145–152, DOI: 10.1007/s00214-005-0655-y.

55 J. VandeVondele and J. Hutter, Gaussian basis sets for accurate calculations on molecular systems in gas and condensed phases, *J. Chem. Phys.*, 2007, **127**, 114105, DOI: 10.1063/1.2770708.

56 S. Grimme, S. Ehrlich and L. Goerigk, Effect of the damping function in dispersion corrected density functional theory, *J. Comput. Chem.*, 2011, **32**, 1456–1465, DOI: 10.1002/jcc.21759.

57 H. B. Jansen and P. Ros, Non-empirical molecular orbital calculations on the protonation of carbon monoxide, *Chem. Phys. Lett.*, 1969, **3**, 140–143, DOI: 10.1016/0009-2614(69)80118-1.

58 N. Y. Acelas, S. M. Mejia, F. Mondragón and E. Flórez, Density functional theory characterization of phosphate and sulfate adsorption on Fe-(hydr)oxide: Reactivity, pH effect, estimation of Gibbs free energies, and topological analysis of hydrogen bonds, *Comput. Theor. Chem.*, 2013, **1005**, 16–24.

59 T. J. Daou, S. Begin-Colin, J. M. Grenèche, F. Thomas, A. Derory, P. Bernhardt, P. Legaré and G. Pourroy, Phosphate Adsorption Properties of Magnetite-Based Nanoparticles, *Chem. Mater.*, 2007, **19**, 4494–4505, DOI: 10.1021/cm071046v.

60 R. A. Fry, K. D. Kwon, S. Komarneni, J. D. Kubicki and K. T. Mueller, Solid-State NMR and Computational Chemistry Study of Mononucleotides Adsorbed to Alumina, *Langmuir*, 2006, **22**, 9281–9286, DOI: 10.1021/la061561s.

61 S. K. Ghose, G. A. Waychunas, T. P. Trainor and P. J. Eng, Hydrated goethite (α-FeOOH) (100) interface structure: Ordered water and surface functional groups, *Geochim. Cosmochim. Acta*, 2010, **74**, 1943–1953, DOI: 10.1016/j.gca.2009.12.015.

62 J. D. Kubicki, K. W. Paul and D. L. Sparks, Periodic density functional theory calculations of bulk and the (010) surface of goethite, *Geochem. Trans.*, 2008, **9**, 4, DOI: 10.1186/1467-4866-9-4.

63 P. G. Belelli, S. A. Fuente and N. J. Castellani, Phosphate adsorption on goethite and Al-rich goethite, *Comput. Mater. Sci.*, 2014, **85**, 59–66, DOI: 10.1016/j.commatsci.2013.12.030.

64 L. Zhou, F. Xiu, M. Qiu, S. Xia and L. Yu, The adsorption and dissociation of water molecule on goethite (010) surface: A DFT approach, *Appl. Surf. Sci.*, 2017, **392**, 760–767, DOI: 10.1016/j.apsusc.2016.09.038.

65 C. Appel, D. Rhue, N. Kabengi and W. Harris, Calorimetric Investigation of the Nature of Sulfate and Phosphate Sorption on Amorphous Aluminum Hydroxide, *Soil Sci.*, 2013, **178**, 180–188, DOI: 10.1097/SS.0b013e3182979e93.

66 N. J. Kabengi, M. Chrysochoou, N. Bompoti and J. D. Kubicki, An integrated flow microcalorimetry, infrared spectroscopy and density functional theory approach to the study of chromate complexation on hematite and ferrihdyrite, *Chem. Geol.*, 2017, **464**, 23–33, DOI: 10.1016/j.chemgeo.2017.01.017.

67 N. J. Kabengi, S. H. Daroub and R. D. Rhue, Energetics of arsenate sorption on amorphous aluminum hydroxides studied using flow adsorption calorimetry, *J. Colloid Interface Sci.*, 2006, **297**, 86–94, DOI: 10.1016/j.jcis.2005.10.050.

68 O. R. Harvey and R. D. Rhue, Kinetics and energetics of phosphate sorption in a multi-component Al(III)–Fe(III) hydr(oxide) sorbent system, *J. Colloid Interface Sci.*, 2008, **322**, 384–393, DOI: 10.1016/j.jcis.2008.03.019.

69 S. Luther, N. Brogfeld, J. Kim and J. G. Parsons, Study of the thermodynamics of chromium(III) and chromium(VI) binding to iron(II/III)oxide or magnetite or ferrite and magnanese(II) iron(III) oxide or jacobsite or manganese ferrite nanoparticles, *J. Colloid Interface Sci.*, 2013, **400**, 97–103, DOI: 10.1016/j.jcis.2013.02.036.

70 K. J. Powell, P. L. Brown, R. H. Byrne, T. Gajda, G. Hefter, S. Sjöberg and H. Wanner, Chemical speciation of environmentally significant heavy metals with inorganic ligands. Part 1: The Hg^{2+}–Cl^-, OH^-, CO_3^{2-}, SO_4^{2-}, and PO_4^{3-} aqueous systems (IUPAC Technical Report), *Pure Appl. Chem.*, 2005, **77**, 739–800, DOI: 10.1351/pac200577040739.

71 J. Kim, W. Li, B. L. Philips and C. P. Grey, Phosphate adsorption on the iron oxyhydroxides goethite (α-FeOOH), akaganeite (β-FeOOH), and lepidocrocite (γ-FeOOH): a 31P NMR Study, *Energy Environ. Sci.*, 2011, **4**, 4298, DOI: 10.1039/c1ee02093e.

72 S. R. Baker, S. A. Watmough and M. C. Eimers, Phosphorus forms and response to changes in pH in acid-sensitive soils on the Precambrian Shield, *Can. J. Soil Sci.*, 2015, **95**, 95–108, DOI: 10.4141/cjss-2014-035.

73 N. J. Barrow, Modelling the effects of pH on phosphate sorption by soils, *J. Soil Sci.*, 1984, **35**, 283–297, DOI: 10.1111/j.1365-2389.1984.tb00283.x.

74 W. M. H. Saunders, The effect of different phosphate fertilisers on soil pH and the consequent effect on phosphate retention, *N. Z. J. Agric. Res.*, 1958, **1**, 675–682, DOI: 10.1080/00288233.1958.10431576.

 This journal is © the Owner Societies 2020

Supporting Information (SI)

Molecular level picture of the interplay between pH and phosphate binding at the goethite–water interface

Ashour A. Ahmed[1,2*], Stella Gypser[3], Dirk Freese[3], Peter Leinweber[2,4], Oliver Kühn[1,2]

[1] University of Rostock, Institute of Physics, D-18059 Rostock, Albert-Einstein-Str. 23-24, Germany

[2] University of Rostock, Department of Life, Light, and Matter (LLM), Albert-Einstein-Str. 25, D-18059 Rostock, Germany

[3] Brandenburg University of Technology Cottbus-Senftenberg, Chair of Soil Protection and Recultivation, Konrad-Wachsmann-Allee 6, 03046 Cottbus, Germany

[4] University of Rostock, Chair of Soil Science, Justus-von-Liebig-Weg 6, D-18059 Rostock, Germany

Emails:

Dr. Ashour A. Ahmed: ashour.ahmed@uni-rostock.de

Dr. Stella Gypser: stella.gypser@b-tu.de

Prof. Dirk Freese: dirk.freese@b-tu.de

Prof. Peter Leinweber: peter.leinweber@uni-rostock.de

Prof. Oliver Kühn: oliver.kuehn@uni-rostock.de

Contents

- Modeling goethite with unsaturated active sites
- Interaction Energy Calculations
- Adsorption Energy Calculations
- Tables
- Figures

Modeling goethite with unsaturated active sites

In the following we introduce the idea behind our modeling approach and why we modeled the goethite with unsaturated active sites (bare surfaces):

1. In general, the main objective in the present study is to unravel the interplay between pH and phosphate binding at the goethite3water interface and how this is affected by the surface morphology and degree of saturation. So, it would be better to involve here bare surfaces with different surface saturation centers (Fe surface atoms were surrounded by 4 and 5 O^{23}/OH^{3} groups) and different morphologies.

2. The reported goethite PZC values in literature data vary from 6.4 to 9.7 but mostly they are around pH 9 (see Table 3 in the main manuscript). This means that below pH 9 (or for some cases below pH 6.4) the surrounding water molecules will dissociate and donate more protons than hydroxyl groups to the goethite surface leading to a positively charged surface. This explains that the goethite surface at pH below pH 9 (or for some case pH 6.4) will be partially unsaturated and have the ability to attract/adsorb anions such as phosphate and/or hydroxyl groups at its surface. Considering the fact that most soils are acidic,[1,2] gives the motivation to model the goethite surface as a partially unsaturated one.

3. It is well-known from sorption experiments that the phosphate adsorption decreases with increasing the soil solution pH.[335] This means that in the presence of OH^{3} at high pH, OH^{3} groups can replace the adsorbed phosphate indicating a stronger adsorption for OH^{3} than for phosphate at mineral surfaces. This behavior has been observed and explained in more details at a molecular level by our group[6,7] and in the current contribution as well. The results indicated that phosphate can replace water molecules from the goethite surface, but phosphate could be replaced by OH^{3} groups. This shows that the reverse reaction, i.e. replacement of OH^{3} groups by phosphate, is mainly a non-spontaneous reaction and unlikely to take place. This indicates that formation of inner-sphere complexes of phosphate with goethite surfaces could happen mainly due to direct reaction of phosphate with the surface unsaturated centers and not with a ligand-exchange mechanism. Consequently, this points to the necessity of the presence of some unsaturated centers at the mineral surface to form inner-sphere complexes with phosphates. So, this means that one should model goethite surfaces with some unsaturation centers.

All these points motivated us to model the goethite surfaces with unsaturated centers (at different degree of saturations). This holds true unless one is studying a high pH

range which, for this reason, we studied high pH by adding KOH molecules to simulate the existing hydroxyl groups at high pH.

Interaction Energy Calculations

In the following we comment on the calculation of interaction energies according to Eq. 1 of the main text. At the optimized geometry the total system can be decomposed into three sub-systems (fragments), i.e. phosphate (fragment1), goethite (fragment2), and water (fragment3). For each pair of fragments the interaction energy has been calculated within the BSSE counterpoise correction philosophy. That is, the interaction energy is calculated by performing five energy calculations using the same simulation box dimensions as follows: 1- total electronic energy of phosphate including only the phosphate basis functions ($E^{\text{phosphate}}_{\text{phosphate}}$), 2- goethite including only the goethite basis functions ($E^{goethite}_{goethite}$), 3- phosphate including the basis functions of phosphate and goethite ($E^{\text{phosphate}+goethite}_{\text{phosphate}}$), 4- goethite including the basis functions of phosphate and goethite ($E^{\text{phosphate}+goethite}_{goethite}$), and 5- phosphate3goethite complex including the basis functions of phosphate and goethite ($E^{\text{phosphate}+goethite}_{\text{phosphate}-goethite\ complex}$). Eventually, the interaction energy between phosphate and goethite was calculated as $E_{int} = E^{\text{phosphate}+goethite}_{\text{phosphate}-goethite\ complex} - (E^{\text{phosphate}+goethite}_{\text{phosphate}} + E^{\text{phosphate}+goethite}_{goethite})$, which corresponds to Eq. 1 in the main text where a simplified notation has been used. Similarly, the interaction energies between phosphate and water as well as between goethite and water have been calculated for each water3phosphate3goethite complex.

Adsorption Energy Calculations

In an alternative approach for calculating the adsorption energy (E_{ads}) of phosphate at the goethite surface, an explicit consideration for the surrounding water molecules has been introduced. For each phosphate3goethite model, a corresponding model involving phosphate as dissolved aqueous species (not bound to the goethite surface) has been created. Each model system has been optimized at the same level as for the inner-sphere phosphate3goethite complexes as described in the main text (see section 2.2). The adsorption energy (E_{ads}) has been calculated here as follows:

$$E_{ads} = E_{\text{inner-sphere complex}} - E_{\text{aqueous}} \quad \text{(S1)}$$

where, $E_{\text{inner-sphere complex}}$ and E_{aqueous} are the total electronic energies of the inner-sphere phosphate3goethite complexes and the corresponding cases in which

phosphate is dissolved aqueous species involving surrounding water molecules. During the geometry optimization process, some structural changes for the water molecules are taking place which are not directly related to the phosphate adsorption process at the goethite surface. To avoid spurious effects due to such changes, the energy of the water molecules is omitted from the total energy, thus giving the corrected adsorption energy (E^c_{ads}) as follows:

$$E^c_{ads} = (E_{\text{inner-sphere complex}} - E_{\text{water/inner}}) - (E_{\text{aqueous}} - E_{\text{water/aqueous}}) \quad \text{(S2)}$$

where, $E_{water/inner}$ and $E_{water/aqueous}$ are the total electronic energies of the surrounding water molecules to the inner-sphere phosphate3goethite complexes and the corresponding cases in which phosphate is dissolved in water. It should be noted that the calculated adsorption energy values in Eqs. S13S2 do not refer only to the phosphate adsorption energy on goethite, but they involve all other reactions/changes between structures of the inner-sphere complexes and the corresponding cases in which phosphate is dissolved in water. These values correspond to different processes such as water adsorption, water dissociation in solution and at the surface, proton transfer from and to phosphate, water, and goethite, formation of hydrogen bonds (HBs), and formation of water clusters such as dimers, trimers, and so on. Therefore, these calculated values are rather large and they depend on number of water molecules involved in the system. To eliminate this arbitrariness, the adsorption energies are given in Tables S132 per one water molecule i.e. they are calculated according to the above equations and then divided by number of water molecules involved for each phosphate3goethite complex.

It should be noted that there is no significant change between the calculated adsorption energies in Eqs. S13S2 (see Tables S13S2) for the different phosphate3goethite binding motifs. So, one couldn't draw a conclusion on the phosphate3goethite binding mechanism and thus its pH-dependence using these values. This is because these values are related to all the reactions/changes taking place upon the structural change between the whole inner-sphere phosphate3goethite optimized geometry and the corresponding dissolved phosphate one. Therefore, the calculated interaction energies in Eq. 1 in the main manuscript are more specific and better to interpret the phosphate3goethite binding and the pH-dependence as well.

Tables

Table S1. Relative energies between dissolved phosphate species in water at the goethite surface and inner-sphere phosphate–goethite complexes at both 010- and 100-goethite surface planes.

species	Relative energies per H_2O molecule [kcal mol^{-1}]			
	0103surface plane		1003surface plane	
	M	**B**	**M**	**B**
H_3PO_4	-30.6	-28.8	-30.6	-30.2
KH_2PO_4	-30.7	-28.8	-31.0	-30.5
K_2HPO_4	-30.3	-27.5	-31.5	-30.0
K_3PO_4	-31.3	-28.9	-32.7	-31.0
K_3PO_4 + 10 KOH	-30.3	-27.5	-31.5	-30.0
K_2HPO_4 + 10 KOH	-31.3	-28.9	-32.7	-31.0

Table S2. Corrected relative energies between dissolved phosphate species in water at the goethite surface and inner-sphere phosphate–goethite complexes at both 010- and 100-goethite surface planes.

species	Relative energies per H_2O molecule [kcal mol^{-1}]			
	0103surface plane		1003surface plane	
	M	**B**	**M**	**B**
H_3PO_4	-29.0	-36.7	-29.8	-31.6
KH_2PO_4	-29.8	-38.9	-30.7	-32.2
K_2HPO_4	-30.4	-38.1	-30.7	-30.8
K_3PO_4	-32.0	-38.2	-31.5	-33.4
K_3PO_4 + 10 KOH	-30.3	-27.5	-31.5	-30.0
K_2HPO_4 + 10 KOH	-31.3	-28.9	-32.7	-31.0

Table S3. Change of pH during the P adsorption.

Time [h]	pH 4	pH 6	pH 8	pH 10	pH 12
0	4.028	5.988	8.026	10.031	11.953
2	4.026	5.144	7.333	8.180	11.736
24	3.904	4.810	6.307	7.170	11.619
168	3.926	4.982	6.683	7.553	11.561

Table S4. Total carbon content (C_{Total}) in the solid goethite samples prior to the P adsorption process and after an adsorption reaction time of 168 h.

prior to adsorption		after 168 h reaction time	
pH	C_{Total} [µmol m^{-2}]	pH	C_{Total} [µmol m^{-2}]
4	3.30	4	2.75
6	3.72	6	2.57
8	2.88	8	2.72
10	3.46	10	3.32
12	7.73	12	3.98

Figures

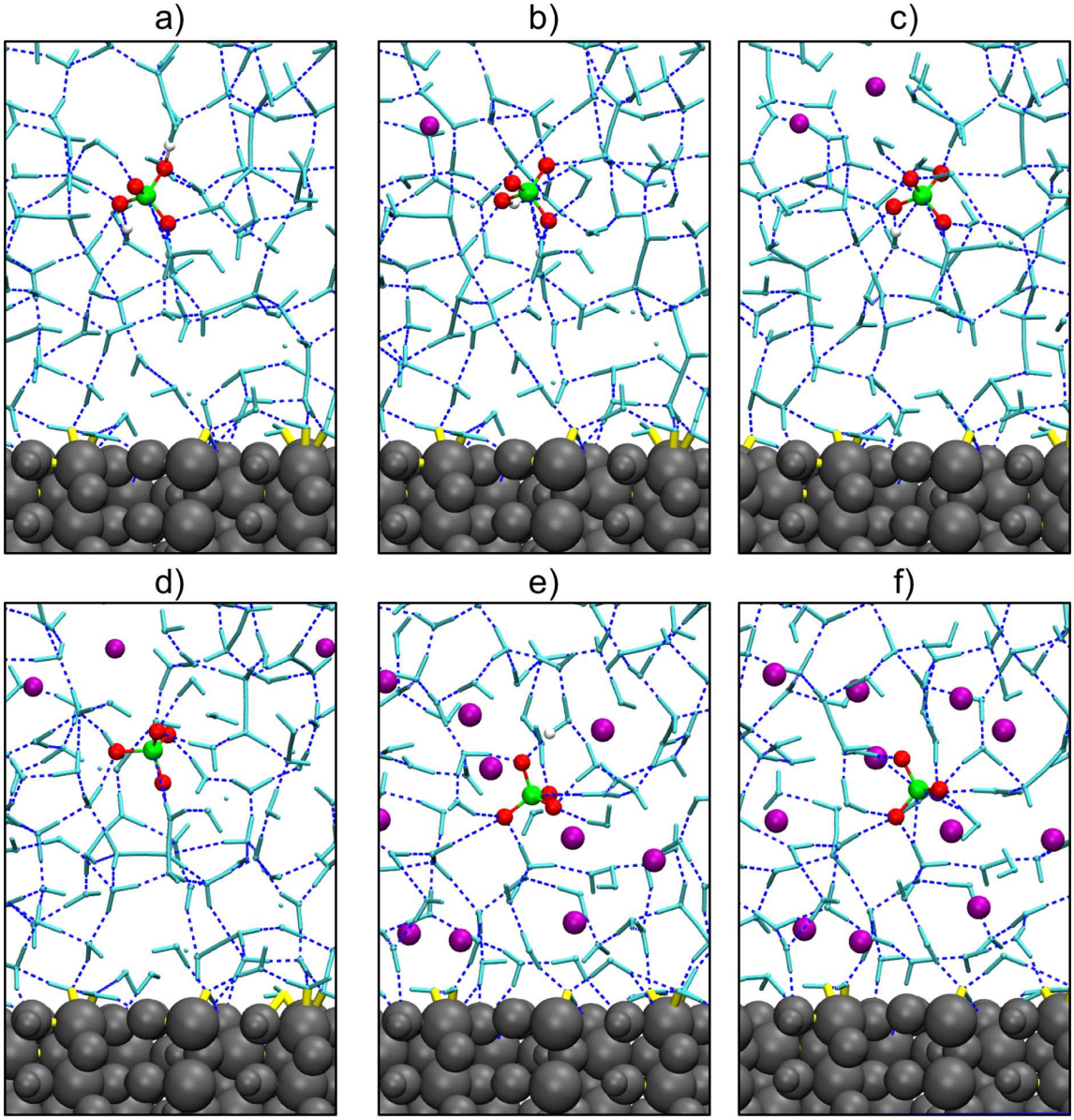


*Fig. S1. Geometry optimized structures of the dissolved phosphate species in water at the goethite surface for the H_3PO_4 species at the 010-goethite surface plane (a), KH_2PO_4 species (b), K_2HPO_4 species (c), K_3PO_4 species (d), K_2HPO_4 species in the presence of 10 KOH molecules (e), and K_3PO_4 species in the presence of 10 KOH molecules with two **M** motifs (f). Goethite, and water atoms are colored in gray and cyan, respectively. For phosphate, atoms are colored in green (P), red (O), white (H), and purple (K). Intramolecular and intermolecular covalent bonds including goethite atoms are colored in yellow and HBs are colored in blue.*

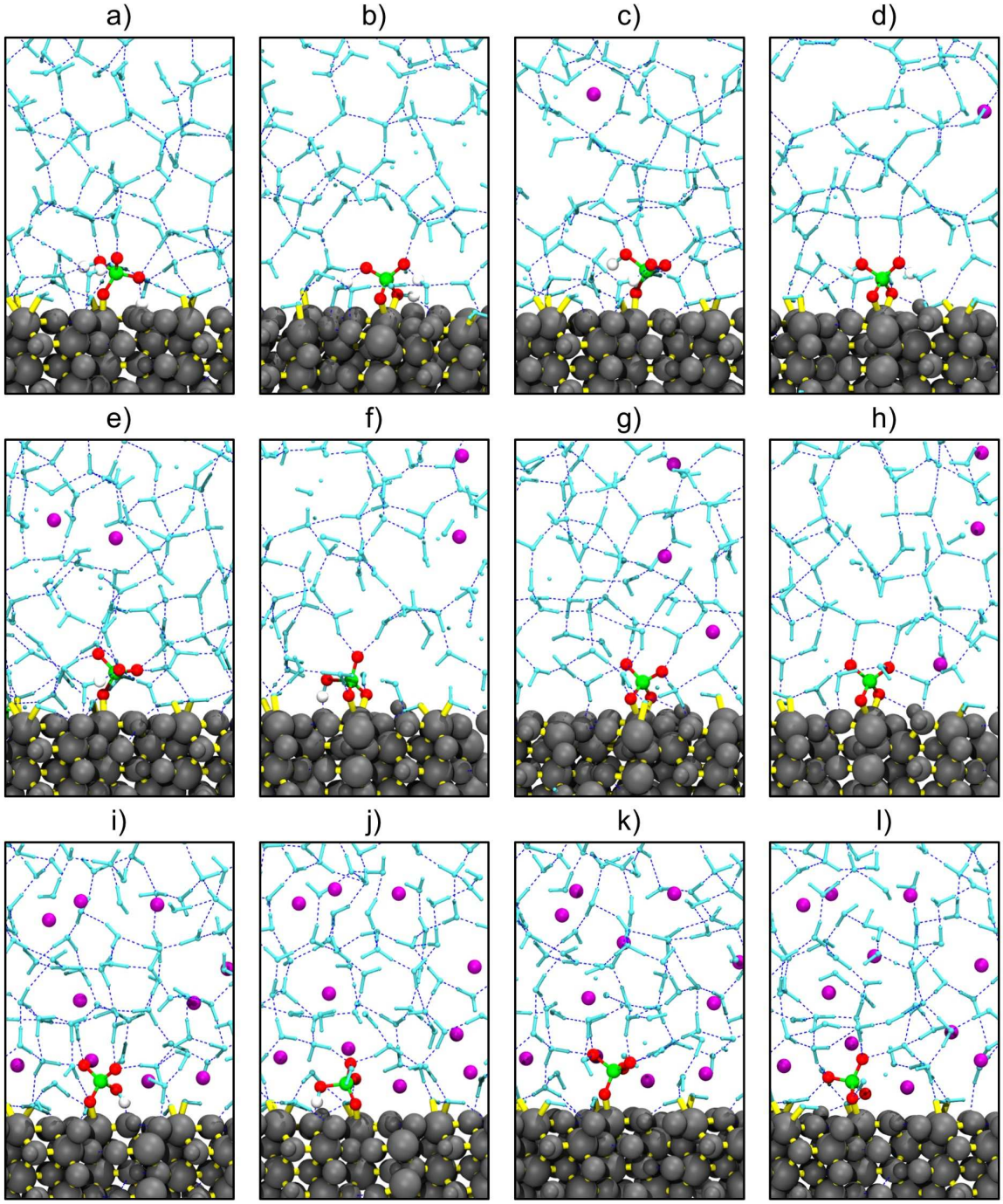


*Fig. S2. Geometry optimized structures of the inner-sphere phosphate–goethite–water complexes for the H_3PO_4 species at the 010-goethite surface plane (**M** motif (a), **B** (2O+1Fe) motif (b)), KH_2PO_4 species with **M** motif (c) and **B** (2O+1Fe) motif (d), K_2HPO_4 species with **M** motif (e) and **B** (2O+1Fe) motif (f), K_3PO_4 species with two **B** (2O+1Fe) motifs (g and h), K_2HPO_4 species in the presence of 10 KOH molecules with two **M** motifs (i and j), and K_3PO_4 species in the presence of 10 KOH molecules with two **M** motifs (k and l). Goethite, and water atoms are colored in gray and cyan, respectively. For phosphate, atoms are colored in green (P), red (O), white (H), and purple (K). Intramolecular and intermolecular covalent bonds including goethite atoms are colored in yellow and HBs are colored in blue.*

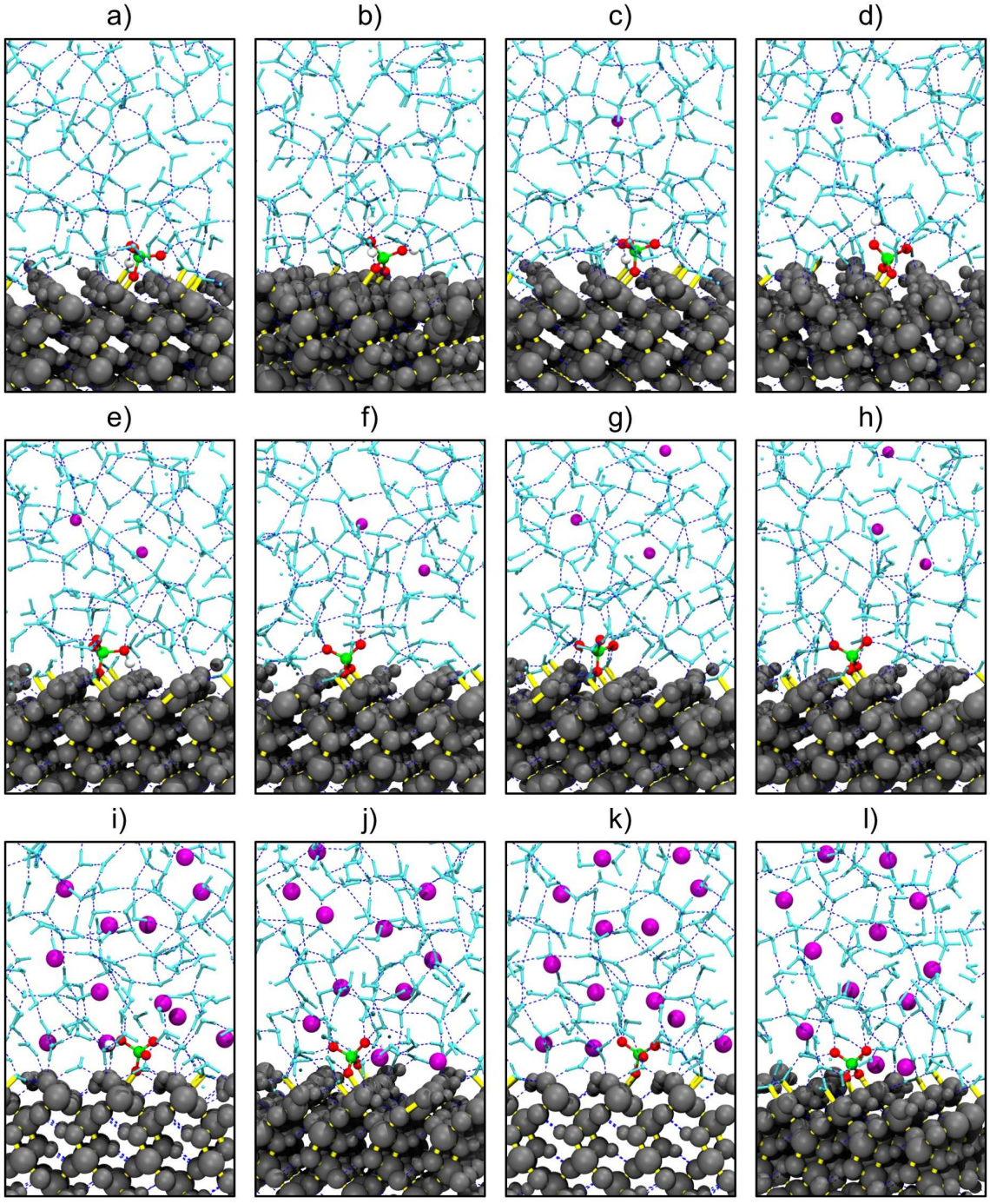


*Fig. S3. Geometry optimized structures of the inner-sphere phosphate–goethite–water complexes for the H_3PO_4 species at the 100-goethite surface plane (**M** motif (a), **B** (2O+2Fe) motif (b)), KH_2PO_4 species with **M** motif (c) and **B** (2O+2Fe) motif (d), K_2HPO_4 species with **M** motif (e) and **B** (2O+2Fe) motif (f), K_3PO_4 species with **M** motif (g) and **B** (2O+2Fe) motif (h), K_2HPO_4 species in the presence of 10 KOH molecules with **M** motif (i) and **B** (2O+2Fe) motif (j), and K_3PO_4 species in the presence of 10 KOH molecules with **M** motif (k) and **B** (2O+2Fe) motif (l). Goethite, and water atoms are colored in gray and cyan, respectively. For phosphate, atoms are colored in green (P), red (O), white (H), and purple (K). Intramolecular and intermolecular covalent bonds including goethite atoms are colored in yellow and HBs are colored in blue.*

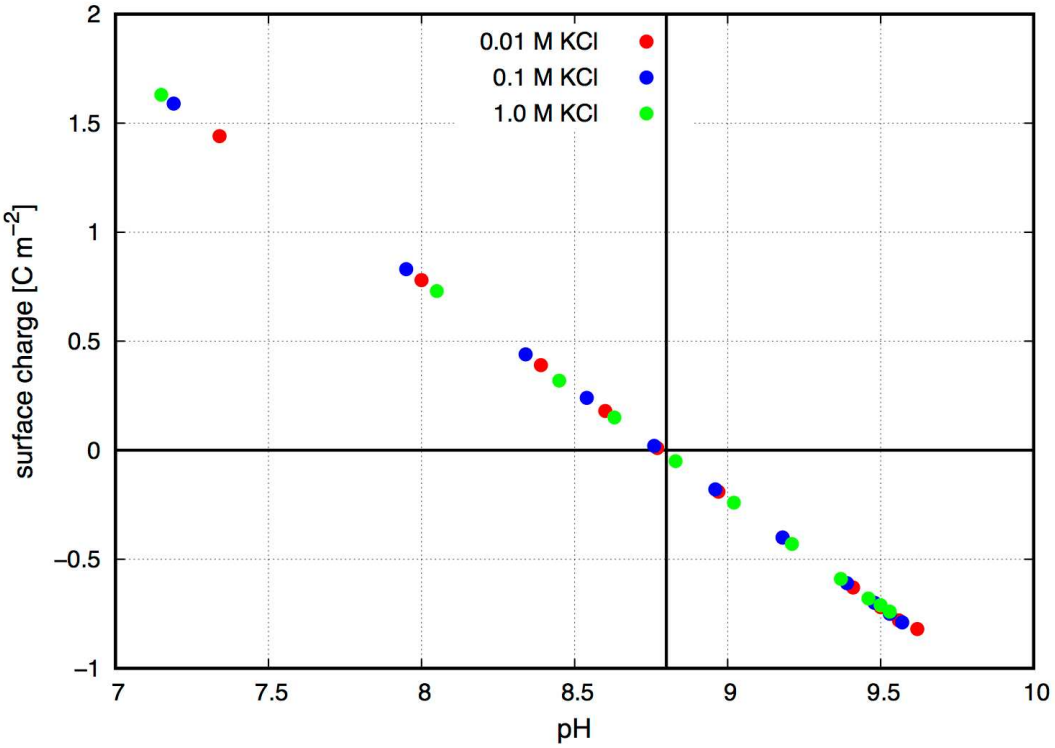


Fig. S4. Goethite surface charge in C m^{-2} versus the solution pH at different ionic strengths of the KCl background electrolyte. Here the data refer to a point of zero charge (PZC) for goethite at 8.8.

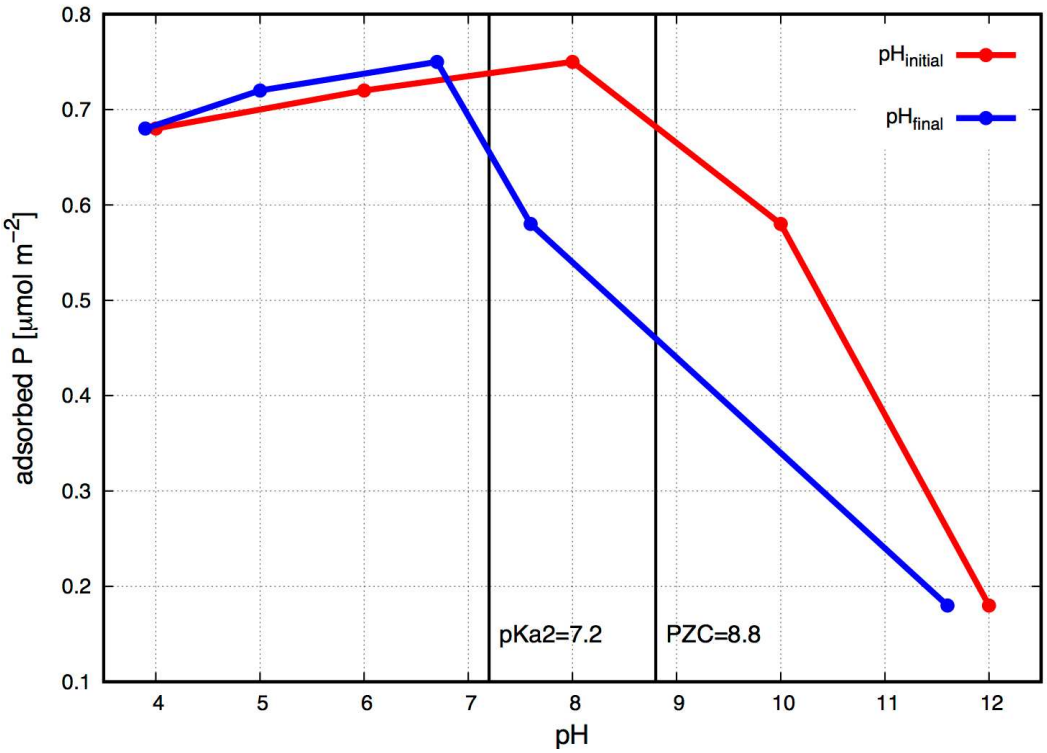


Fig. S5. Effect of pH on the phosphate (P) adsorption for the present study (considering the initial pH in red and the final pH in blue.

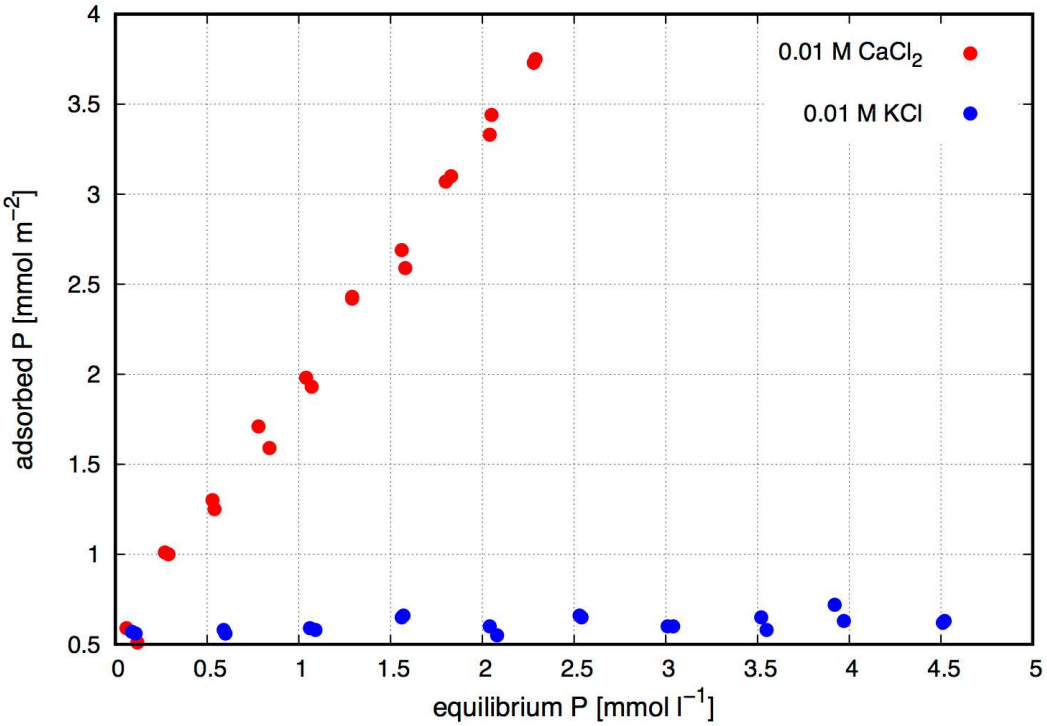


Fig. 6. Effect of background electrolyte solution on the P adsorption at goethite surfaces. Here, two background electrolyte solutions (0.01 M $CaCl_2$ and 0.01 M KCl) were used at pH 6.

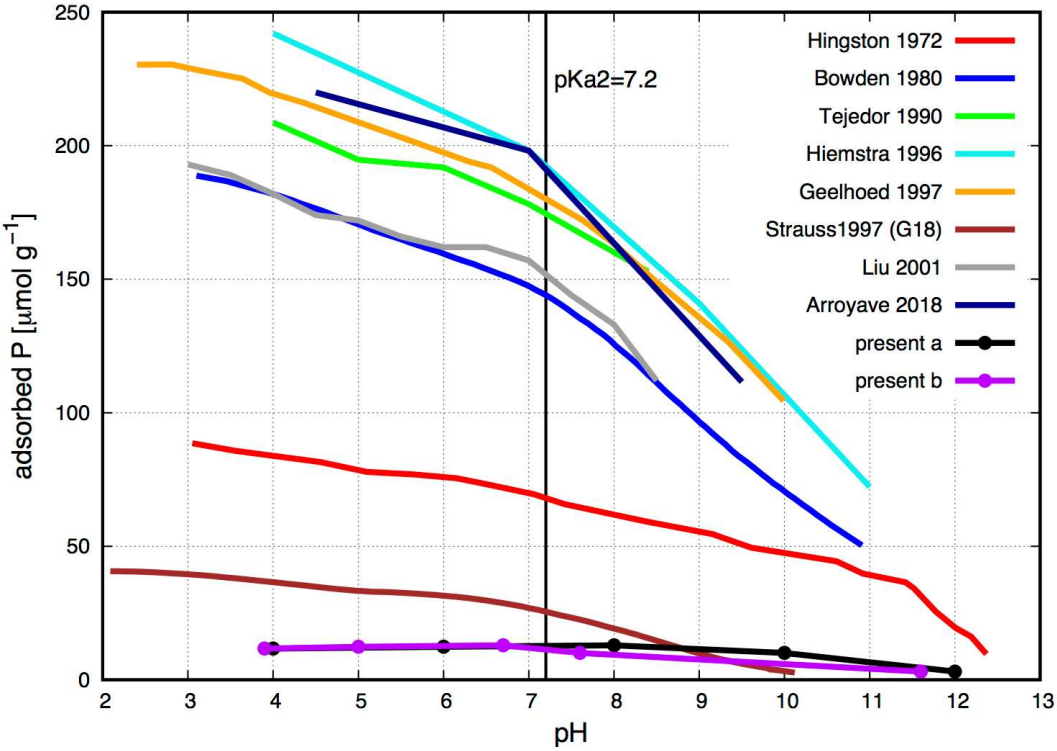


Fig. S7. Effect of pH on the phosphate (P) adsorption for the present study (considering the initial pH in black "present a" and the final pH in magenta "present b") and from literature. The latter includes data by Hingston et al.,[1] Bowden et al.,[2] Tejedor-Tejedor and Anderson,[3] Hiemstra and Van Riemsdijk,[4] Geelhoed et al.,[5] Liu et al.,[6] and Arroyave[7]. This figure is exactly the same as Fig. 7 in the main text but here the amount of adsorbed P is calculated with respect to the mass of goethite sample i.e. in µmol g^{-1}.

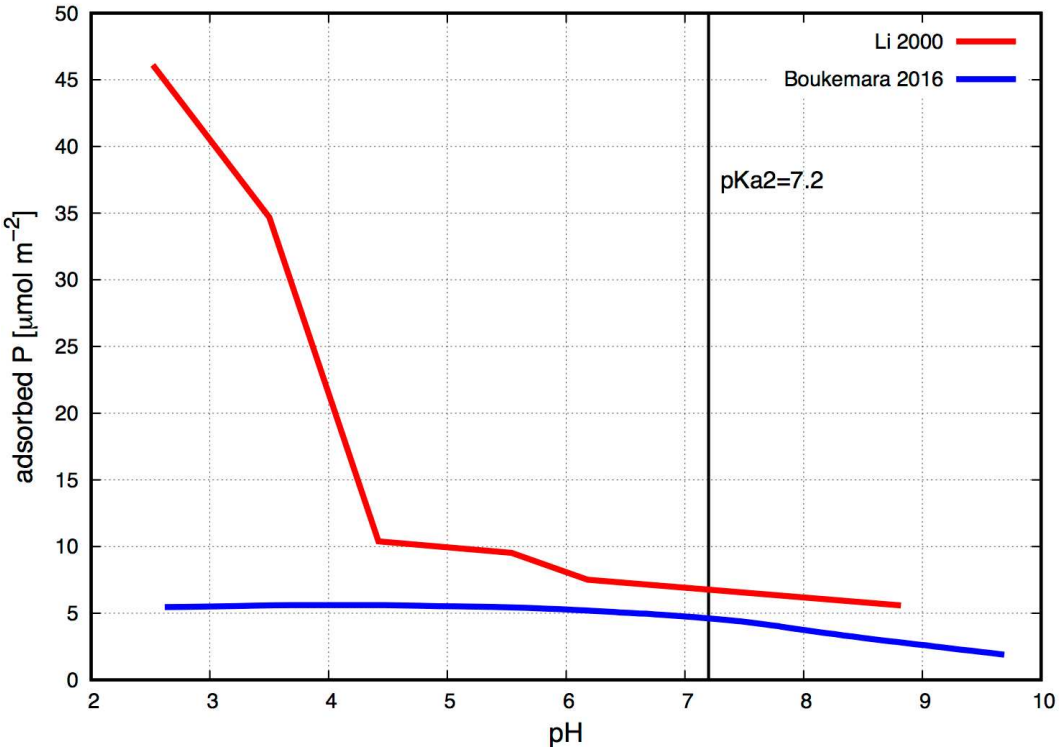


Fig. S8. Effect of pH on the P adsorption at high P surface coverage. The plotted data are collected from previous studies by Li and Stanforth[8] and Boukemara et al.[9]

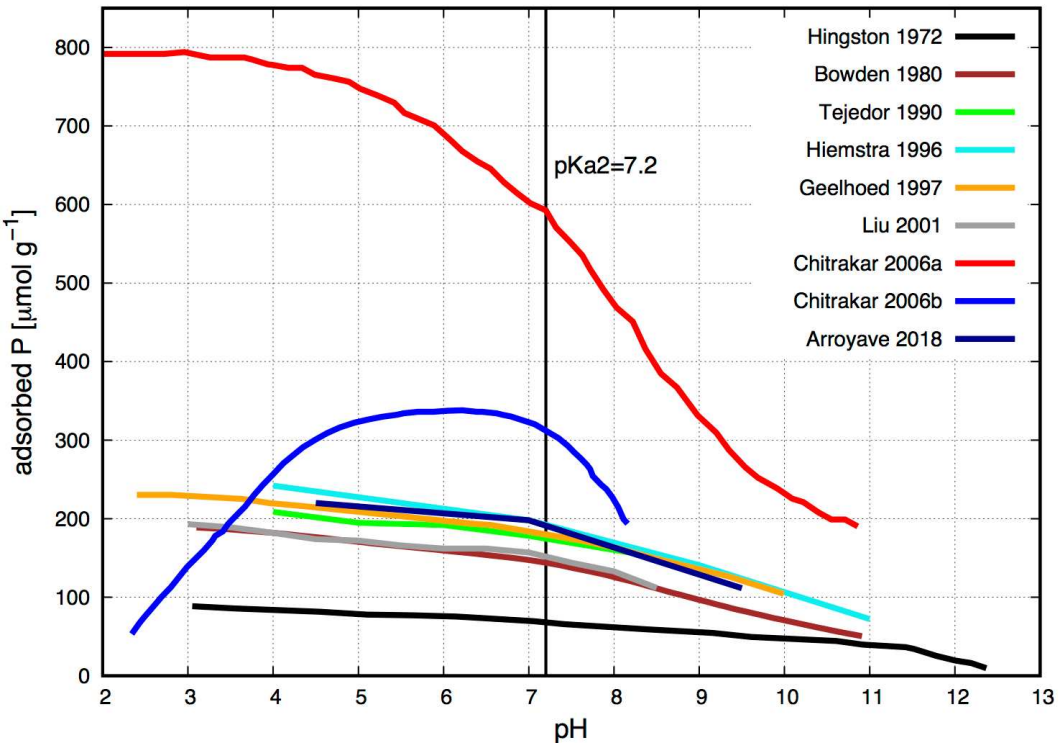


Fig. S9. Effect of pH on the P adsorption at goethite surfaces for a previous study by Chitrakar et al.[10] (adsorption in pure water is represented in red "Chitrakar 2006a" and in sea water in blue "Chitrakar 2006a"). To show how different this study than other literature studies, the studies by Hingston et al.,[1] Bowden et al.,[2] Tejedor-Tejedor and Anderson,[3] Hiemstra and Van Riemsdijk,[4] Geelhoed et al.,[5] Liu et al., [6], and Arroyave[7] are represented as well. Here the amount of adsorbed P is expressed in µmol.g^{-1}.

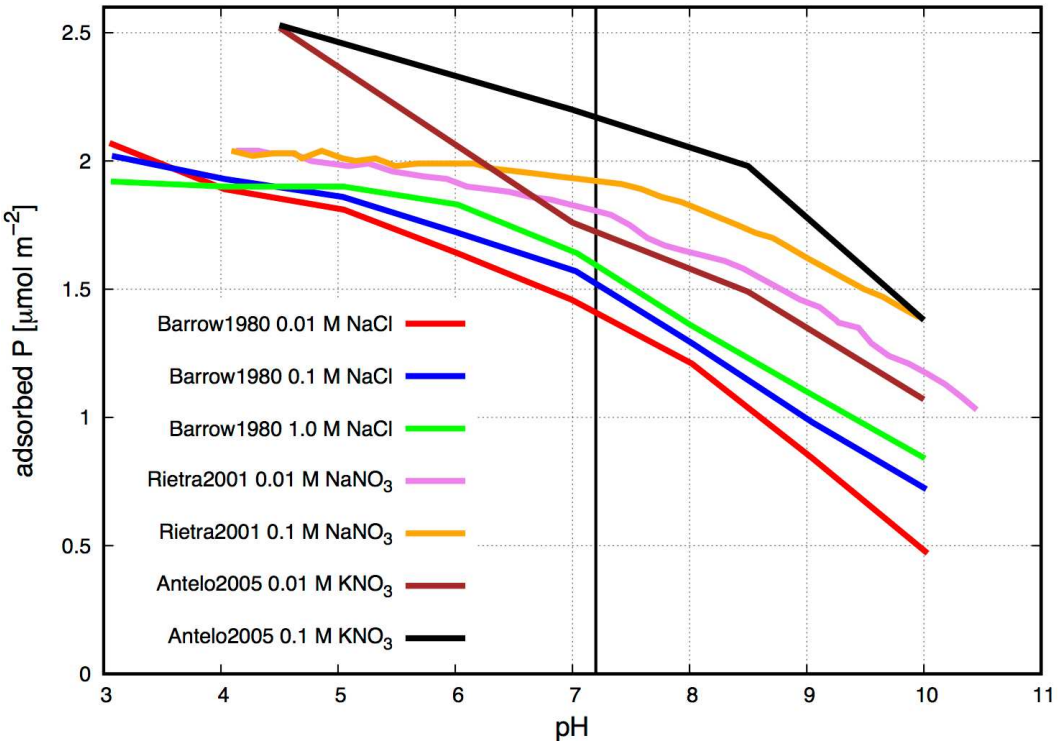


Fig. S10. Effect of pH on the P adsorption at goethite surfaces at different background electrolyte solutions and with different electrolyte concentrations. The plotted data are collected from previous studies by Barrow et al.,[11] Rietra et al.,[12] and Antelo et al.[13]

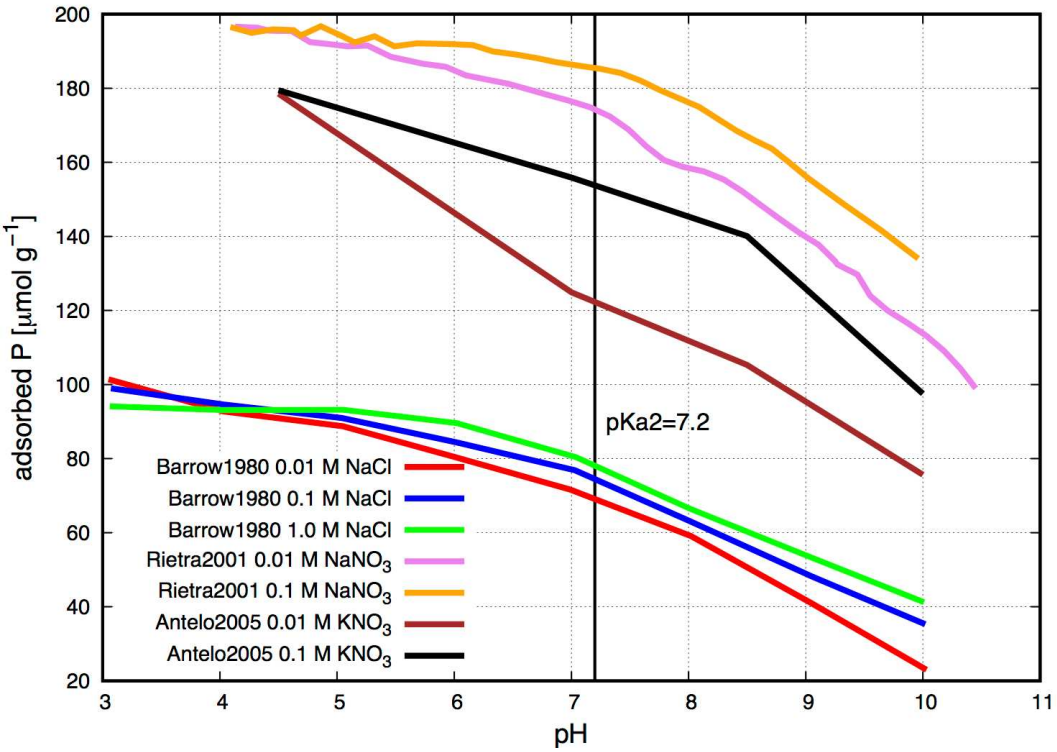


Fig. S11. Effect of pH on the P adsorption at goethite surfaces at different background electrolyte solutions and with different electrolyte concentrations. This Figure corresponds exactly to Fig. S9 but here the amount of adsorbed P is calculated with respect to the mass of goethite sample i.e. in µmol g^{-1}.

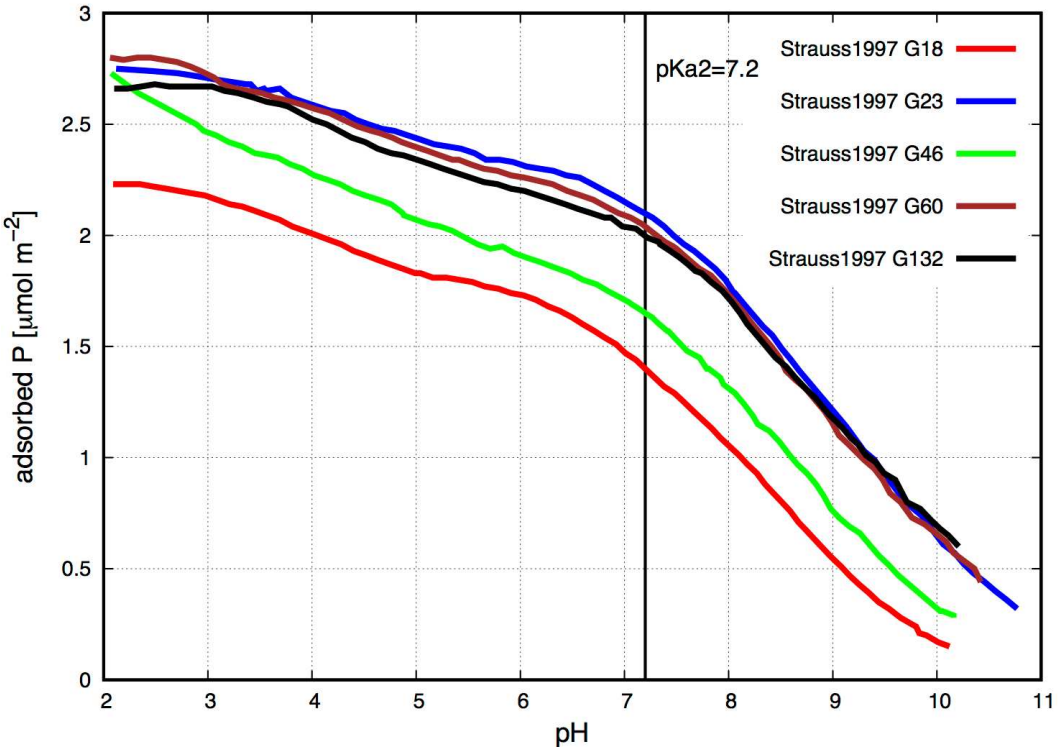


Fig. S12. Effect of pH on the P adsorption at goethite surfaces with different specific surface area (SSA) in the range from 18 to 132 m² g^{-1}. G18 to G132 refer to goethite samples with SSA values of 18 to 132 m² g^{-1}, respectively. Here the amount of adsorbed P is calculated with respect to the surface area i.e. in µmol m^{-2}. The plotted data are collected from a previous study by Strauss et al.[14]

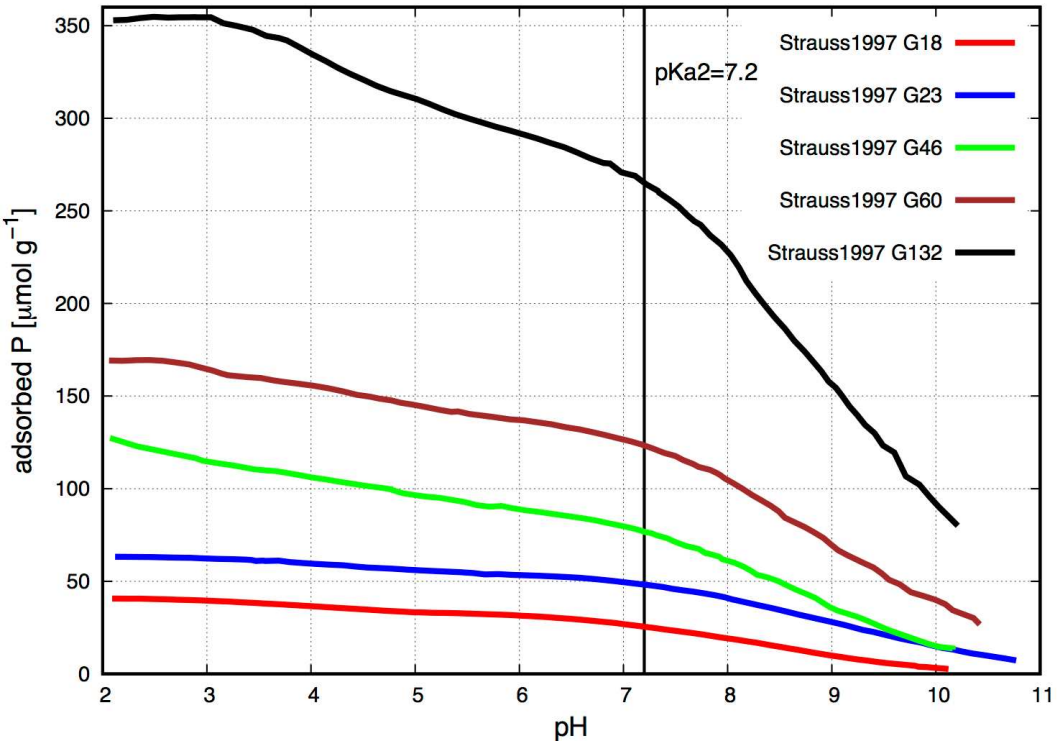


Fig. S13. Effect of pH on the P adsorption at goethite surfaces with different specific surface area which corresponds exactly to Fig. S10. Here the amount of adsorbed P is calculated with respect to the mass of goethite sample i.e. in µmol g^{-1}.

Note: The Figures S73S13 are plotted based on data collected from pervious literature of phosphate sorption experiments.

References

[1] F.J. Hingston, A.M. Posner, J.P. Quirk, Anion adsorption by goethite and gibbsite: i. The role of the proton in determining adsorption envelopes, J. Soil Sci. 23 (1972) 1773192.

[2] J. Bowden, S. Nagarajah, N. Barrow, A. Posner, J. Quirk, Describing the adsorption of phosphate, citrate and selenite on a variable-charge mineral surface, Soil Res. 18 (1980) 49.

[3] M.I. Tejedor-Tejedor, M.A. Anderson, The protonation of phosphate on the surface of goethite as studied by CIR-FTIR and electrophoretic mobility, Langmuir. 6 (1990) 6023611.

[4] T. Hiemstra, W.H. Van Riemsdijk, A surface structural approach to ion adsorption: The charge distribution (CD) model, J. Colloid Interface Sci. 179 (1996) 4883508.

[5] J.S. Geelhoed, T. Hiemstra, W.H. Van Riemsdijk, Phosphate and sulfate adsorption on goethite: Single anion and competitive adsorption, Geochim. Cosmochim. Acta. 61 (1997) 238932396. https://doi.org/10.1016/S0016-7037(97)00096-3.

[6] F. Liu, A. De Cristofaro, A. Violante, Effect of pH, phosphate and oxalate on the adsorption/desorption of arsenate on/from goethite, Soil Sci. 166 (2001).

[7] J.M. Arroyave, V. Puccia, G.P. Zanini, M.J. Avena, Surface speciation of phosphate on goethite as seen by InfraRed Surface Titrations (IRST), Spectrochim. Acta. A. Mol. Biomol. Spectrosc. 199 (2018) 57364.

[8] L. Li, R. Stanforth, Distinguishing Adsorption and Surface Precipitation of Phosphate on Goethite (³ -FeOOH), J. Colloid Interface Sci. 230 (2000) 12321.

[9] L. Boukemara, C. Boukhalfa, L. Reinert, L. Duclaux, Characterization of Phosphate Adsorption on Goethite Macroscopic and Spectroscopic Analyses, J. Mater. Environ. Sci. 7 (2016) 25413 2550.

[10] R. Chitrakar, S. Tezuka, A. Sonoda, K. Sakane, K. Ooi, T. Hirotsu, Phosphate adsorption on synthetic goethite and akaganeite, J. Colloid Interface Sci. 298 (2006) 6023608.

[11] N. Barrow, J. Bowden, A. Posner, J. Quirk, Describing the effects of electrolyte on adsorption of phosphate by a variable charge surface, Soil Res. 18 (1980) 395.

[12] R.P.J.J. Rietra, T. Hiemstra, W.H. van Riemsdijk, Interaction between Calcium and Phosphate Adsorption on Goethite, Environ. Sci. Technol. 35 (2001) 336933374.

[13] J. Antelo, M. Avena, S. Fiol, R. López, F. Arce, Effects of pH and ionic strength on the adsorption of phosphate and arsenate at the goethite3water interface, J. Colloid Interface Sci. 285 (2005) 4763486.

[14] R. Strauss, G.W. Brummer, N.J. Barrow, Effects of crystallinity of goethite: II. Rates of sorption and desorption of phosphate, Eur. J. Soil Sci. 48 (1997) 1013114.

Publication 3

S. M. Shaheen, J. Wang, K. Baumann, Ashour A. Ahmed, L.-C. Hsu, Y.-T. Liu, S.-L. Wang, O. Kühn, P. Leinweber, J. Rinklebe. Stepwise redox changes alter the speciation and mobilization of phosphorus in hydromorphic soils. Chemosphere **2022**, 288, 132652.

Contribution: Ashour A. Ahmed is credited with performing the quantum chemical calculations, analyzing the modeling results, writing the modeling part, reviewing, editing, and proofreading.

URL: https://doi.org/10.1016/j.chemosphere.2021.132652

QR:



Reproduced with the permission of Elsevier

Chemosphere 288 (2022) 132652

Contents lists available at ScienceDirect

Chemosphere

journal homepage: www.elsevier.com/locate/chemosphere

Stepwise redox changes alter the speciation and mobilization of phosphorus in hydromorphic soils

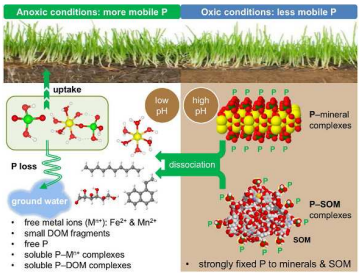
Sabry M. Shaheen [a,b,c], Jianxu Wang [d,a], Karen Baumann [e], Ashour A. Ahmed [f,g], Liang-Ching Hsu [h], Yu-Ting Liu [i], Shan-Li Wang [j], Oliver Kühn [f,g], Peter Leinweber [e,g], Jörg Rinklebe [a,k,*]

[a] University of Wuppertal, School of Architecture and Civil Engineering, Institute of Foundation Engineering, Water- and Waste-Management, Laboratory of Soil- and Groundwater-Management, Pauluskirchstraße 7, 42285, Wuppertal, Germany
[b] King Abdulaziz University, Faculty of Meteorology, Environment, and Arid Land Agriculture, Department of Arid Land Agriculture, Jeddah, 21589, Saudi Arabia
[c] University of Kafrelsheikh, Faculty of Agriculture, Department of Soil and Water Sciences, 33 516, Kafr El-Sheikh, Egypt
[d] State Key Laboratory of Environmental Geochemistry, Institute of Geochemistry, Chinese Academy of Sciences, 550082, Guiyang, PR China
[e] University of Rostock, Faculty of Agricultural and Environmental Science, Soil Sciences, Justus-von-Liebig-Weg 6, 18051, Rostock, Germany
[f] University of Rostock, Institute of Physics, D-18059, Rostock, Albert-Einstein-Str. 23-24, Germany
[g] University of Rostock, Department of Life, Light, and Matter (LLM), Albert-Einstein-Str. 25, D-18059, Rostock, Germany
[h] Department of Soil and Environmental Sciences, National Chung-Hsing University, 145 Xingda Rd., Taichung, 402, Taiwan
[i] Department of Soil and Environmental Sciences & Innovation and Development Center of Sustainable Agriculture, National Chung-Hsing University, 145 Xingda Rd., Taichung, 402, Taiwan
[j] Department of Agricultural Chemistry, National Taiwan University, 1 Sect. 4, Roosevelt Rd., Taipei, 10617, Taiwan
[k] University of Sejong, Department of Environment, Energy and Geoinformatics, Guangjin-Gu, Seoul, 05006, Republic of Korea

HIGHLIGHTS

- Stepwise and repeated redox cycles alter P speciation and affect its mobilization.
- P, Fe^{2+} and DOC mobilized under low E_H in toe-, mid-, and upper-slope arable soil.
- Acidic/reductive dissolution of Fe-oxide/carbonate governed P release under low E_H.
- Aromatic carbon compounds governed P release under high E_H in upper slope soil.
- Fe–P and Ca–P decreased under low E_H and organic-P and Ca–P increased under high E_H.

GRAPHICAL ABSTRACT



ARTICLE INFO

Handling Editor: X. Cao

Keywords:
Hydromorphic arable soils
Phosphorus loss
Sustainable management

ABSTRACT

Sustainable engineering and management of hydromorphic arable soils need deep knowledge about the redox-mediated interactions between nutrients and soil colloids. Consequently, we examined the redox-mediated interactions of P with metal oxides and organic carbon (OC) in toe-, mid-, and upper-slope arable soils under dynamic redox changes using geochemical (biogeochemical microcosm), spectroscopic (XANES), and molecular (quantum chemical calculations (QCC)) approaches. We controlled the redox potential (E_H) in two directions i.e.,

* Corresponding author. University of Wuppertal, School of Architecture and Civil Engineering, Institute of Foundation Engineering, Water- and Waste-Management, Laboratory of Soil- and Groundwater-Management, Pauluskirchstraße 7, 42285, Wuppertal, Germany.
E-mail addresses: shaheen@uni-wuppertal.de (S.M. Shaheen), rinklebe@uni-wuppertal.de (J. Rinklebe).

https://doi.org/10.1016/j.chemosphere.2021.132652
Received 29 June 2021; Received in revised form 15 October 2021; Accepted 22 October 2021
Available online 22 October 2021
0045-6535/© 2021 Elsevier Ltd. All rights reserved.

XANES
Quantum chemical calculations

1) slowly oxidizing direction (SOD; E_H increased from −286 to +564 mV); and 2) slowly reducing direction (SRD; E_H decreased from +564 to −148 mV). In the SOD of all soils, P, Fe^{2+} and OC mobilized at $E_H \leq 200$ mV, due to the pH decrease from 7.2 to 4.1 and dissolution of Fe-oxyhydroxides/carbonates, as indicated by the decrease of Fe–P and Ca–P determined by P–*K*-edge-XANES. At $E_H > 200$ mV, P immobilized due to the strong P binding with Fe^{3+} as suggested by QCC. In the SRD of mid-slope-soil, P immobilized with decreasing E_H, due to pH increase and P retention by aromatic carbon and/or precipitation by carbonates, as supported by increase of organic-P and Ca–P. These findings help for management of P in arable soils.

1. Introduction

Arable soils are distributed worldwide and highly affected by acidity and intermittent water logging (Hens and Quynh, 2016). In various arable soils (e.g., in Northern Germany), high precipitation plus restricted drainage may cause an increase in the groundwater table (Zimmer et al., 2016), which can lead to a low soil redox potential (E_H) and vice versa. This reversible process may affect the water regime, and thus affect the mobilization of nutrients and pollutants due to redox changes (from low E_H (high water table) to high E_H (low water table and vice versa) (Shaheen et al., 2014a; Baumann et al., 2021a). Consequently, mobilization of nutrients in arable soils with redoximorphic characters is of increasing interest from agro-environmental point of view. Phosphorus (P) is a macronutrient element for plants (Bünemann, 2011); however, high P mobilization and its potential loss from soils to water can enhance eutrophication and thus cause environmental problems (Barcellos et al., 2019). Therefore, understanding the release of P is required to assess its bioavailability and potential loss in soils and/or stream bank sediments (Siddique et al., 2000; Felicien et al., 2016; Rahutomo et al., 2018; Bernardo et al., 2018).

Phosphorus in soils can occur as different species including organic-, Fe-, Mn-, Al-, Mg- and Ca–P complexes (Baumann et al., 2021b; Zhang et al., 2021). Therefore, the content and forms of soil organic matter (SOM), sesquioxides, and/or Ca compounds may affect P mobilization in soils, particularly under wet-dry-cycles as affected by the associated changes of E_H (Baumann et al., 2021a) Redox changes can lead to associated changes in pH, as a result of proton consumption and/or decomposition of SOM and production of organic acids (Reddy and DeLaune, 2013; Khan et al., 2019; Baumann et al., 2021a). The E_H/pH changes may affect the compounds of dissolved organic carbon (DOC) in soil (Stumm and Morgan, 1996; Shaheen et al., 2014b; Afsar et al., 2020). Those changes can also affect the P binding to metal ions of lower and higher oxidation state and/or their oxides. Moreover, the redox changes may cause dissolution (under reducing/acidic) or precipitation (under oxidizing/alkaline conditions) of Fe-oxides, and thus mobilize or immobilize P in soil. For instance, if a soil becomes anoxic, Fe(III) will be reduced to Fe(II) and in turn the Fe-oxides will be dissolved so that the bound P will be released and vice versa (Søndergaard, 2009; Reddy and DeLaune, 2013). Accordingly, several authors found an increase of dissolved concentrations of P and Fe in wetland soils under reducing conditions (Shenker et al., 2005; Prem et al., 2015; Gu et al., 2019; Zhang et al., 2021). However, the relations between P mobilization in one side and the composition of DOC and chemistry of Fe on the other side are not clear under slow stepwise redox changes in ground water affected arable soils. Moreover, P species in the sediment phase of soils under particular and different redox conditions have not been studied. Hence, there is a knowledge gap about 1) the impact of slowly controlled redox changes (from the initial case (high E_H) to low E_H; then, from low E_H to high E_H (slowly oxidation direction; SOD); thereafter, from high E_H to low E_H again (slowly reducing direction; SRD)) and the relevant effects of pH, sesquioxides, and DOC on the mobilization and speciation of P in soils, 2) the effects of stepwise adjusted redox-states on the P binding to metal ions of lower and higher oxidation state and/or their oxides and SOM, 3) how redox-induced alterations affect aliphatic and aromatic carbon and subsequently the mobilization and species of P in soils, and 4) the impact of slope position (e.g., toe, mid, and upper) on the redox-induced changes of soil properties and the associated changes of P mobilization.

We hypothesized that stepwise changes of E_H will lead to changes in 1) pH, 2) the binding process between P with metal ions and their oxides and SOM, 3) the proportion of aliphatic and aromatic carbon compounds of DOC, 4) the dissolution or precipitation of carbonates, 5) the distribution of P species in the soil which affect P release into soil solution.

Specifically, we aimed to elucidate and quantify for the first time, systematically the impacts of stepwise changes of E_H from SOD to SRD and the E_H-dependent changes of pH, Fe, Mn, Al, DOC, and DIC on the dissolved concentrations of P and P-species in the solid phase of groundwater affected arable soils. Further, we investigated P binding reactions with metal ions of different oxidation states and SOM at a molecular level by quantum chemical calculations (QCC).

2. Materials and methods

2.1. Soil sampling and characterization

Three arable soil samples were collected from the top horizon (7–14 cm) of three profiles in a field, near Rostock, Northern Germany (Baumann et al., 2021b). The 7–14 cm depth was selected to avoid surface effects including compacted subsurface horizons during soil core sampling, to sample the central part of the ploughed horizon (0–25 cm) and to be able to align soil information with results of parallel experiments. The profiles were excavated by drilling at the bottom of a slight slope (toe-slope arable soil (TS); Eutric Stagnosol (Colluvic)), at the middle slope position (mid-slope arable soil (MS); Eutric Stagnosol), and at the upper slope (upper-slope arable soil (US); Stagnic Eutric Cambisol) (Table S1). More details are included in the supporting information (SI) and reported in Baumann et al. (2021a,b).

2.2. Automated biogeochemical microcosm experiment

To simulate fluctuating groundwater levels and the associated changes of E_H, we incubated the soils in biogeochemical microcosms (MCs) (Figure S1). This equipment enables the simulation of various anoxic/oxic directions that may occur in the soils when the groundwater level changes. This happens by adjusting the E_H automatically using addition of nitrogen gas to lower E_H or synthetic air/oxygen to increase E_H (Yu and Rinklebe, 2011; Frohne et al., 2011; Rinklebe et al., 2016, 2020; Shaheen et al., 2014b, 2021). Briefly, glass vessels were used in triplicate for the TS and MS and in duplicate for the US. Each vessel was filled with 210 g of the soil sample and 1680 mL of tap water to create soil slurry. Fifteen gram of wheat straw and 10 g of glucose were mixed with the soil samples in each MC as a source of carbon for microorganisms. The system is equipped with a stirrer, platinum (Pt) electrode, a pH electrode, and a temperature electrode to measure E_H, pH, and temperature in a high temporal resolution (10 min). The measured E_H values were calculated and standardized relative to the standard hydrogen electrode according to the procedure of Wolkersdorfer (2008).

The soil samples were incubated and the redox conditions were controlled stepwise at two directions (i.e., SOD and ROD) after the initial case as follow: initial case (1 h after incubation; E_H = +374, +360, +471 mV in the TS, MS, and US, respectively); SOD (from reducing

conditions (E_H = −262, −286, −127 mV) to oxidizing conditions (E_H = +447, +440, +564 mV, in the TS, MS, and US, respectively); then ROD (from oxidizing conditions (E_H = +447, +440, +564 mV) to reducing conditions (E_H = +191, −148, +407 mV), in the TS, MS, and US, respectively). The total incubation period was 600 h (about 400 h for the SOD and 200 h for the ROD). The slurry was centrifuged at 4000 rpm for 15 min and filtered using 0.45-μm Whatman filter paper to get the well-established "dissolved fraction" as defined by others (Guo et al., 2007; El-Naggar et al., 2018, 2021). Therefore, here we used the <0.45 μm filtrate as dissolved fraction.

The dissolved form of P, Fe, Mn, and Al was analyzed in triplicates using ICP-AES (Ultima 2, Horiba Jobin Yvon, Germany). The Fe^{2+} was extracted and determined according to the method of Harvey et al. (1955). The DOC and DIC concentrations were measured using a C/N-analyzer (multi N/C 2100 S, Analytik Jena). The specific UV absorbance (SUVA) was measured and used to calculate aromaticity by the formula: aromaticity = 6.52 * SUVA + 3.63 (Weishaar et al., 2003). The entire procedure was carried out under exclusion of oxygen in a glove box (Whitley A35, Shipley, UK).

After sampling and centrifugating the slurry, selected samples of the remained soil-sediments were sampled and dried using freeze dryer (Alpha 1–2/LD Plus freeze dryer; Martin Christ, Osterode Germany), and crushed and mixed under exclusion of oxygen in the glove box (Whitley A35 Anaerobic Work Station, Don Whitley Scientific, Shipley, UK). More details are included in the SI.

2.3. Phosphorus speciation in sediments

Phosphorus species in the freeze dried solid-phase sediments collected from the three soils under different conditions, were measured using P *K*-edge XANES at the BL16A beamline of NSRRC in Taiwan. The P *K*-edge XANES spectra data processing and LCF were performed with the Athena software (Ravel and Newville, 2005; Beauchemin et al., 2003; Hurtarte et al., 2019; Gustafsson et al., 2020). The distributions of P species were determined using LCF across the region from 10 eV below to 30 eV above the P absorption edge. The reference materials used in the LCF included: (1) labile P (KH_2PO_4); (2) Al–P (P adsorbed to boehmite); (3) Fe–P (P co-precipitated with iron oxyhydroxides); (4) Ca–P (apatite); (5) organic P (lecithin). More details are included in the SI. The details of the principal components analysis results are provided in Table S5, S6, and S7.

2.4. Molecular modeling approach

To explore the impact of stepwise changes of E_H from SOD to SRD on the P mobility at a molecular level, we simulated the binding process of ortho-phosphate (inorganic phosphate, P_i) with the relevant metal ions as well as with DOC present in soil solutions. Specifically, this was done by modeling the complexation reaction of P_i individually with each relevant metal ion M^{n+} (Ca^{2+}, Al^{3+}, Fe^{2+}, Fe^{3+}, Mn^{2+}, Mn^{3+}, and Mn^{4+}). To simulate the pH effect on this binding process, P_i was modeled with two phosphate species involving $H_2PO_4^{1-}$ (pH: 2.1–7.2) and HPO_4^{2-} (pH: 7.2–12.4) species (Powell et al., 2005). Similarly, the binding process of P_i with relevant DOC molecules at different oxidizing/-reducing conditions was simulated. All calculations were performed at the B3LYP-D3/6–311++G(d,p)/CPCM level of theory (Hehre et al., 1972; Lee et al., 1988; Cossi et al., 2003; Grimme et al., 2011) using the Gaussian 16 program package (Frisch et al., 2016). More details about the molecular modeling approach are given in the SI.

3. Results and discussion

3.1. Redox directions and induced changes of pH

The average E_H values (mV) of all soils varied from −262 to +447 in the TS, −286 mV to +440 in the MS soil, and from −137 to +564 in the US (Fig. 1). The E_H decreased from +374, +360, and +471 mV in the initial sampling to −262, −286, and −137 mV in the TS, MS, and US, respectively. In the SOD, the E_H was forced from reducing conditions (−262, −286, and −137) to oxidizing conditions (+447, +440, and +564 mV) in the TS, MS, and US, respectively. In the SRD, the E_H was forced from oxidizing conditions (+447, +440, and +564 mV) to reducing conditions (+191, −148, +407 mV) in the TS, MS, and US, respectively. Only the MS reached a lower E_H value than the TS and US (Fig. 1). The variations of E_H and pH are given in the SI (Figures S2-S4; Table S2).

The TS and MS showed a wider range of E_H than the US. This might be because of the higher carbon content in the TS and MS (1.5–1.6%) than in the US (1.1%) (Table S1). This original soil carbon content plus the added carbon in the form of straw and glucose may favor the microbially mediated reduction, and thus lead to a lower E_H in the TS and MS (−286 mV) than in the US (−137 mV). Soil organic matter (as a source of electrons) and high microbial activities are crucial factors that control reduction in soils (Megonigal et al., 2004; Husson, 2013; Gross et al., 2018; Baumann et al., 2021b).

The weaker response in E_H decrease in the SRD of the US than the MS may indicate its higher redox buffer capacity. This response could be explained by the relatively high content of clay, total Fe and Al, and poorly crystalline Fe oxides in the US as compared with the TS and MS (Table S1). In addition, the abundance of organic matter and the activity of microbial communities may restrict the OM decomposition (Fierer and Schimel, 2002; Baumann et al., 2009, 2021b; Moche et al., 2015), and thus may have led to a smaller drop in E_H in the SRD of the US compared with the TS and MS. The phospholipid fatty acids data (Fig S5) suggested that the US contained a lower total microbial biomass than the TS and MS. This could also be an explanation for a smaller E_H drop in the SRD compared with the SOD. Several types of microorganisms were present in our soils (Fig S5), which indicate that they affect various biogeochemical processes including the oxidation-reduction process (Reddy and DeLaune, 2013). The three soils contain PLFA biomarker for gram-positive bacteria (GPB), actinomycetes, gram-negative bacteria (GNB), fungi and further general PLFA which are summarized as residual soil microbial biomass (Fig. S5). Bacterial biomass (GPB + GNB) is higher than fungal biomass in the three soils. Flooding is unfavorable for fungi and actinomycetes that might go into stationary phase or suffer under osmotic stress. Labile organic matter such as glucose and necromass can be taken up and transformed preferentially by GNBs which can affect redox conditions. Under flooded conditions these bacterial groups might be able to take over important biogeochemical transformation processes leading to changes in redox conditions.

The average initial pH value of the three soils was 6.8, 7.2, and 6.6, and decreased under low E_H to 4.3, 4.9, and 4.1 in the TS, MS, and US, respectively (Fig. 1). Then, the pH was around the values of 4.5 during the SOD in the TS and US. However, in the MS, pH increased to 8.0 with increasing E_H and increased even more to 8.3 in the SRD despite a decrease of E_H down to −148 mV in the end of the SRD (Fig. 1).

In the SOD of all soils, the decrease in pH under low E_H conditions might be due to the dissolution of microbial CO_2 in solution and the organic acids production by the microbial decomposition of SOM (Yu et al., 2007; Reddy and DeLaune, 2013; Shaheen et al., 2014b). The carbon amendment (straw and glucose) can also contribute to the decrease of pH under reducing conditions due to the formation of organic acids during carbon transformation (Glinski et al., 1992; Shaheen et al., 2021). In the SRD of the MS, an increase in pH during decreasing E_H may be due to the protons consumption for the reduction of NO_3^-, Mn^{4+} and/or Fe^{3+}(Reddy and DeLaune, 2013). The dissolution of $Fe(OH)_3$ to form Fe^{2+} that releases OH^- can be also a reason for an increasing pH during reducing conditions in this soil.

3.2. Mobilization of P and E_H/pH dynamics

The replicates average concentration (mg L^{-1}) of dissolved P (<0.45

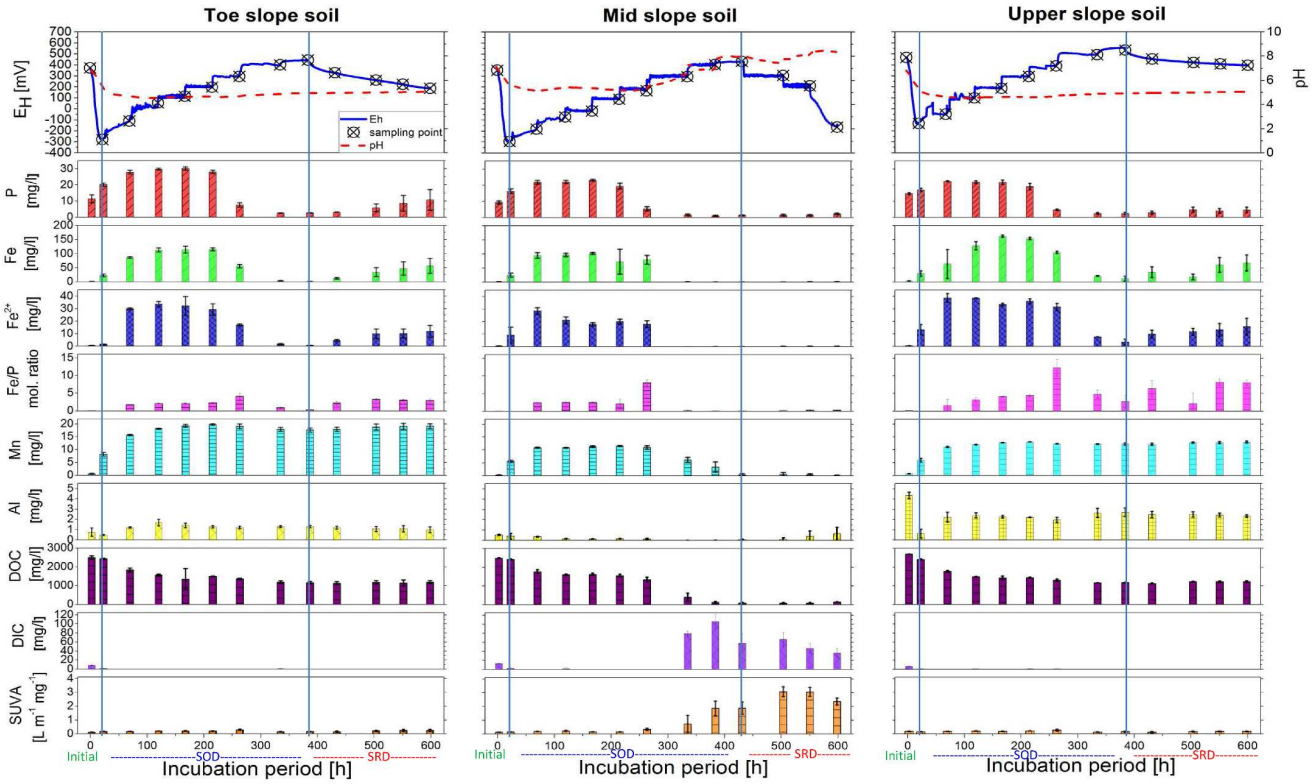


Fig. 1. Temporal course of mean EH and pH and the concentrations of dissolved P, iron, manganese, aluminum, dissolved organic and inorganic carbon and SUVA in the soil suspension of the toe, mid-, and upper-slope soil. Note: the abscissa scale and the symbol and unit of the studied parameters are placed in the left panel and they applicable for the three panels to avoid overcrowding in the figure. SOD: slowly oxidizing direction; SRD: slowly reducing direction.

μm filtrate-P) strongly increased up to 31.2 with decreasing E_H and decreased down to 0.71 with increasing E_H in the SOD of all soils. Then, with decreasing E_H in the SRD, it was increased again to 10.8 in the TS, 2.3 in the MS, and to 4.6 in the US (Fig. 1). The minimum, maximum, mean, and median values are presented in Table S2. The concentrations of dissolved P were negatively correlated with E_H in all soils (R = −0.66 (TS), −0.83 (MS), −0.85 (US); $P < 0.01$; Table S3). The low P concentrations under low E_H in the SRD compared with the SOD might be caused by the release of potentially labile P in the SOD. In the SOD, increasing the mobilization of P under low E_H and vice versa could be explained by the associated reductive dissolution of P-binding Fe(III) minerals, which was supported by the higher concentrations of dissolved Fe and Fe^{2+} (Fig. 1) (see Section 3.3).

The highest P concentrations (mg L^{-1}) were recorded in the TS (2.4–31.2), followed by the US (1.9–23.1); then, the MS (0.7–23.8) (Fig. 1). The higher P mobilization in the TS might be due by the higher concentrations of labile P in the TS than the MS and US (Table S1). The high P mobilization in the top arable soils may increase P loss under low E_H, which might be reached due to precipitation and/or restricted drainage if ground water level rises.

The E_H-dependent changes in pH were stronger in the MS than the TS and US (Fig. 1). The P release increased in the MS at low E_H and decreased at high E_H and pH in the SOD; however, in the SRD, P was immobilized under alkaline pH, although the E_H was low (−148 mV; Fig. 1). Therefore, the concentrations of dissolved P were negatively correlated with pH only in this soil (Table S3). The higher P mobilization at low pH might be due to the release of P associated to carbonates and oxides. The lower P mobilization at high pH in the MS could be likely due to its precipitation with carbonates, which is supported by the higher content of total Ca (7.6 gkg^{-1}) in the MS than the TS and US (1.9–2.7 gkg^{-1}; Table S1) (see Section 3.4).

3.3. Impact of Fe–Mn–Al oxides on P mobilization under redox changes

Concentrations of total dissolved Fe (Fe) and ferrous ions (Fe^{2+}) in the <0.45 μm filtrate showed a pattern similar to P in the SOD and SRD in all soils, while the total dissolved Mn showed a similar trend to P in the MS (Fig. 1). Therefore, concentrations of dissolved P were significantly positively correlated with Fe and Fe^{2+} in the three soils (R = 0.60–0.91; $P < 0.01$; Table S3), and with Mn in the MS (R = 0.78; $P < 0.01$; Table S3). Total dissolved Al did not show a clear response to the E_H changes; therefore, the relation between P and Al was non-significant (Table S3). This may mean that the impact of Fe oxides on P mobilization in the soils is higher than Mn–Al oxides, which is in agreement with the higher Fe oxides content than Mn and Al oxides in the soils (Table S1). Also, a significant portion of P in these soils was distributed in the oxide fraction as reported by Baumann et al. (2021b). This demonstrates that the associated P with Al–Fe–Mn-oxides could be released if these oxides were microbially dissolved under reducing/acidic conditions and Fe^{3+} reduced to Fe^{2+} (Weber et al., 2006; Unger et al., 2009). Therefore, the average concentrations of Fe^{2+} increased under low E_H up to 42.2 mg L^{-1} and decreased under oxic conditions down to 0.08 mg L^{-1} in the three soils (Fig. 1). We assume that the reductive dissolution of Fe oxides may did not only lead to the release of Fe^{2+} but also to the release of their associated P to soil solution. Therefore, the increase of P mobilization under reducing acidic conditions could likely be due to the reductive/acidic dissolution of Fe–Mn oxides by anaerobic bacteria (Fig. S5), resulting in the release of associated P, and vice versa (Afsar et al., 2020; Zhang et al., 2021). In this respect, Søndergaard (2009) reported that at an E_H above ~200 mV, Fe^{3+} has a high P sorption capacity, whereas at lower E_H, Fe^{3+} is reduced and P is released.

The LCF of P *K*-edge XANES sample spectra and the proportions of P

species (% of total P) in the sediments of the TS, MS, and US are presented in Fig. 2. The proportions of P species with r-factor (0.001–0.007) are presented in Table S4. Data of Fig. 2 and Table S4 suggested that Al–P was the dominant species (32–52%), followed by Fe–P (14–47%), Ca–P (7–31%), and then organic-P (0–13%). We assumed that the higher portion of Al–P than the other P species in our soils indicated that the Al–P was more stable than Fe–P because Al-oxides are less redox-sensitive than Fe-oxides (Takeno, 2005). In addition, the higher portion of Al–P might be attributed to P re-adsorbed onto Al hydroxides or other phases with a similar bonding configuration. The dominance of Al–P in the bulk soils of similar soils was reported by Baumann et al. (2021b). Except for the initial sampling point (1 h after flooding), the portion of Fe–P (as % total P) increased under oxic conditions (≥+200 mV), and varied from 27 to 47%, 17–28%, and 38–44% in the TS, MS, and US, respectively. On the other side, the portion of Fe–P (as % total P) decreased under reducing conditions (≤+100 mV), and varied from 24 to 37, 15 to 23, and 30–34% in the TS, MS, and US, respectively (Table S4). We did not interpret the initial sampling because the geochemical equilibrium was not reached 1 h after flooding.

As suggested by the *K*-edge XANES results, the lower portion of Fe–P under reducing conditions in comparison to oxic conditions may support our interpretation in the way that Fe-oxides were dissolved under low E_H and the associated P was mobilized. The increase of Fe–P portion under high E_H might mean that oxides were formed under oxic conditions and P was bound and thus the dissolved P concentrations decreased.

In the SRD of the MS, the impact of pH on the oxide precipitation (particularly Mn) and thus on P release was stronger than the impact of E_H because the pH increased to values higher than 8.0 despite the E_H decreased to −148 mV (Fig. 1). Under these alkaline conditions, the concentrations of dissolved P, Fe, Fe^{2+} and Mn were lower in the MS than the TS and US, which suggests that these metal ions might have been precipitated in the oxides form and the dissolved P might have been retained/bounded to these oxides.

The *K*-edge XANES data (Fig. 2) of the MS supported this interpretation and showed that the portion of Fe–P was higher (17.2–23.5%; Table S4) under alkaline (pH = 8.3) conditions than weakly acidic (pH = 6.8) conditions (16.9–20.4%; Table S4) in this soil, which validated our previous interpretation. The QCC data (Section 3.5) also supported this explanation by pointing to a stronger P binding in soils with metal ions of higher oxidation state (such as Fe^{3+}) and/or with their metal-oxides than metal ions of lower oxidation state (such Fe^{2+}). Moreover, in the SRD of the MS, P immobilized with decreasing E_H, due to pH increase and P precipitation by carbonates, as supported by increase of Ca–P (Fig. 2).

The Fe:P molar ratios of soil solutions differed widely among the soils and also under the different redox conditions (Fig. 1). The average Fe:P molar ratio in the US was higher (4.85) than the TS (2.07) and MS (1.55). In the TS, the Fe:P molar ratio was higher (1.7–4.1) under E_H≤+300 mV; then, it decreased to 0.33 at E_H above +300 mV in the SOD; thereafter, increased again (3.2) with decreasing E_H in the SRD (Fig. 1). In the US, the Fe:P molar ratio was low (1.6) under strongly reducing conditions (E_H ≤ −100 mV), then increased (up to 12.3) with increasing E_H to +401 mV, but decreased again to 2.7 with increasing E_H to +564 mV in the SOD; thereafter, increased again to 8.2 with decreasing E_H (to +419 mV) in the SRD (Fig. 1). However, in the MS, the Fe:P molar ratio was high (up to 8.1) under reducing conditions (E_H≤+200 mV), then decreased to 0.01 with increasing E_H (to +447 mV) in the SOD; thereafter, remained low (0.29) in the SRD, despite the decrease in E_H to −148 mV, which might be due to the associated increase of pH, along with the decrease of E_H in the SRD (Fig. 1).

The Fe:P molar ratio of soil solution under reducing-oxidizing conditions can be used to assess the ability of Fe oxides to immobilize P under oxic conditions, and can also be used to assess the potential risk of P loss from soil to water (Zak et al., 2004; Shenker et al., 2005; Baken et al., 2015; Van der Grift et al., 2016; Gu et al., 2019). The higher Fe:P molar ratios found in the US than the TS and MS could be related to its higher oxalate-Fe content (Table S1). The sharp increase of Fe:P molar ratio at +300, +181, and +401 mV in the TS, MS, and US, respectively, could be likely explained by the associated decrease of dissolved P under these E_H values (4-fold lower than its concentration at the previous E_H value (+205, +101, and +304 mV, respectively; Fig. 1)).

In their study, Zak et al. (2004), proposed that an Fe:P molar ratio of 3.0 could be used as a threshold value to assess the potential loss of P from peat soils to surface water. Also, Baken et al. (2015) and Gu et al. (2019) used the ratio to assess the potential loss of P from agricultural and wetlands to surface water. These results showed that if the Fe:P

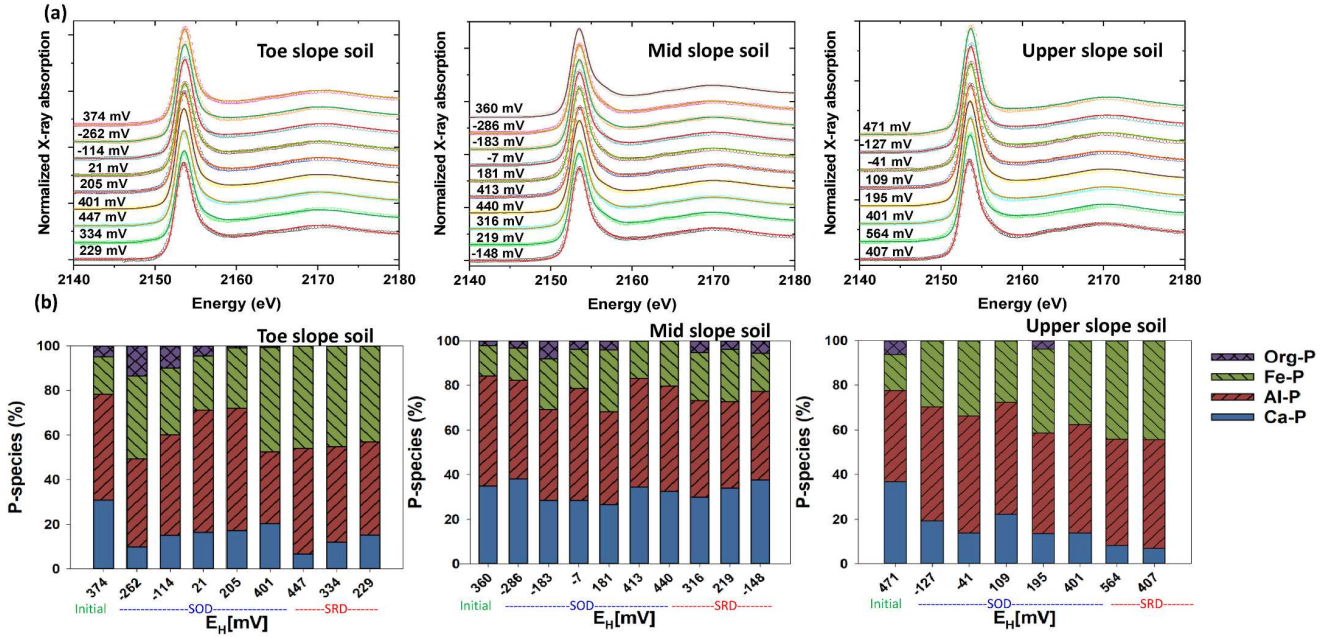


Fig. 2. a) P K-edge XANES spectra data (open circles) with LCF fits (solid lines) and b) proportions of P (% of total P) for the sediments collected under reducing and oxidizing conditions in the two redox cycles of the toe-, mid-, and upper slope soils.

molar ratio was >3.0, high concentrations of dissolved P under reducing conditions will be decreased to concentrations below 0.031 mg L^{-1} under oxic conditions. Conversely, a Fe:P molar ratio <3.0 in the anaerobic soil solution would enhance the loss of dissolved P to water because the precipitated Fe-oxides are not enough to immobilize the released P under reducing conditions. Therefore, the average Fe:P molar ratios recorded under anaerobic conditions (E_H < +100 mV) in the present study (1.7–2.0 in the TS; 2.1–2.4 in the MS; and 1.6–4.4 in the US) suggested that the TS and MS pose a greater threat of leaching P from the soil to waters when the spoil is being reduced than the US. Also, the TS and MS have a lower position in the landscape than the US and they were therefore more subjected to higher groundwater levels over a longer time. As a result, anaerobic condition might have occurred longer than in US, which might have increased the mobilization and potential loss of P in the TS and MS.

3.4. Impact of organic carbon compounds on P mobilization under redox changes

The data of Fig. 1 demonstrated that the dynamics of E_H and pH affected DOC, DIC, and SUVA and thus affected the composition of DOC in the studied soils, particularly in the MS. Weishaar et al. (2003) used SUVA values to estimate the proportion of the aliphatic and aromatic compounds of DOC in soil solution. Accordingly, the higher SUVA at high E_H and pH in the SOD of the MS indicated a more pronounced aromaticity of DOC under these conditions, while the lower SUVA under anoxic/acidic conditions indicated a predominance of aliphaticity of DOC under these conditions.

In the SOD of all soils, particularly the MS, the release of P and DOC increased at low E_H and decreased at high E_H (Fig. 1). In the SRD, the concentrations of P and DOC decreased, while the SUVA increased with decreasing E_H (Fig. 1). The P correlated positively with DOC in all soils and the relation was stronger in the MS ($R = 0.77$; $P \leq 0.01$) than in the TS ($R = 0.31$; $P \leq 0.05$) and US ($R = 0.51$ $P \leq 0.05$) (Table S3). The relationships between dissolved P and SUVA ($R = -0.71$; $P \leq 0.01$) and DIC ($R = -0.0.79$; $P \leq 0.01$) were significantly negative only in the MS ($R = -0.71$ for SUVA; $P \leq 0.01$ and $R = -0.0.79$; $P \leq 0.01$ for DIC). These results suggested that the redox-induced changes of DOC, DIC, and SUVA affected the mobilization of P in the soils, particularly in the MS.

The association between P and DOC in the three soils might be explained by the microbial decomposition of SOM under low E_H, and release of both P and DOC from the decomposed SOM. The DOC release can occur due to the production of soluble organic metabolites by the soil microbial biomass under reductive conditions prior to fermentation (Kalbitz et al., 2000; Shaheen et al., 2014b); then, the associated P can also be released. The release of DOC from SOM decomposition occurred in parallel to the release of dissolved P when the soil is reduced, which may mean that P released together with the low molecular and labile organic matter under low E_H. Also we assume that the release of P and DOC can be due to the reduction induced dissolution of Fe- and Mn oxyhydroxides at the low E_H. The solubilized DOC might be derived from OM originally bound onto Fe- and Mn oxyhydroxides. Indeed, Fe- and Mn oxyhydroxides strongly adsorb OM (Chorover and Amistadi, 2001; Shaheen et al., 2014b). However, when soils become water saturated, microorganisms that normally use oxygen as the terminal electron acceptor for OM oxidation will change to other electron acceptors such as Fe and Mn. This shift results in the reductive dissolution of Fe- and Mn oxyhydroxides, followed by a release of associated substances including DOC and P (Grybos et al., 2009; Zhang et al., 2012; Shaheen et al., 2014b).

However, under high E_H (and high pH in the MS), dissolved P might have been sorbed/retained again to organic carbon, as supported by the XANES data (Fig. 2) which showed that a significant portion of organic-P was detected under high pH in the SRD of the MS.

The immobilization of P under alkaline conditions in the SRD of the MS could also be explained by the precipitation of phosphates forming insoluble calcium phosphate, particularly under the presence of higher content of total calcium (Ca) in this soil (7.6 g kg^{-1}) than the TS (2.7 g kg^{-1}) and US (1.9 g kg^{-1}) (Table S1). The P *K*-edge XANES analysis supported this assumption and revealed that the portion of Ca–P was clearly higher under alkaline than under acidic conditions in this soil (Fig. 2), which demonstrated that a significant part of P might have been precipitated with Ca compounds under high pH in this soil.

In the MS, the significantly higher values of SUVA (high portion of aromatic carbon compounds) and DIC under alkaline conditions in the SRD compared with those under acidic conditions in the SOD (Fig. 1) may also have contributed to the decrease of P mobilization in this soil.

Analyses of the organic matter compounds in the studied bulk soils (Fig S6A) using Py-FIMS showed that the studied soils were rich in aromatic compounds (e.g., alkyl aromatics, phenols/lignin monomers, lignin dimers, and heterocyclic nitrogen and nitriles), and the proportion (% of total ion intensity) of these aromatic compounds exceeded that of the aliphatic compounds. Also, the Py-FIMS analyses of the organic matter compounds in the sediment phase of the MS (Figure S6B) showed that the proportion (% of total ion intensity) of the aromatic compounds was higher under oxic/alkaline than under reducing/acidic conditions. These results supported the SUVA data and indicated that in the MS, P might be immobilized under oxic/alkaline conditions, due to the retention of P by aromatics.

The QCC data (Section 3.5; Fig S11) also supported this explanation and suggested that aromatic compounds could bind P stronger than aliphatic carbon compounds. The P *K*-edge XANES data also supported this assumption by showing an increase in the portion of organically bound-P under high pH (Fig. 2).

3.5. Molecular level picture for the P mobilization process

Considering the most abundant P_i species ($H_2PO_4^{1-}$) for most soils, the calculated reaction free energies (ΔG) for the M^{n+}–P_i complexation reactions pointed to spontaneous chemical reactions of phosphate with each free metal ion (Fig. 3 and Table S5). For all metal ions, ΔG values showed that the monodentate (**M**) M^{n+}–P_i complexes are more favored

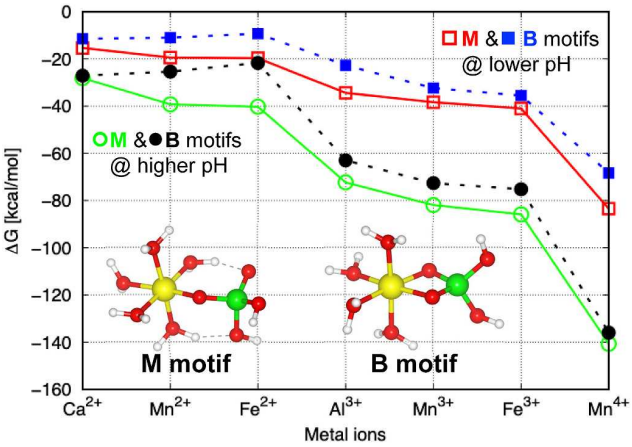


Fig. 3. Calculated reaction free energies (ΔG) for the complexation reaction between phosphate and the relevant free metal ions. Red and blue colors correspond to **M** and **B** binding motifs, respectively, for the M^{n+}–P_i complexes at lower pH (i.e., considering the $H_2PO_4^{1-}$ species). Similarly, green and black colors correspond to **M** and **B** M^{n+}–P_i complexes at higher pH (i.e., considering the HPO_4^{2-} species). ΔG data points are connected with lines for better visualization. As an example, optimized geometries for the **M** and **B** Fe^{3+}–P_i complexes are shown. H, O, P, and Fe atoms are visualized in white, red, green, and yellow colors, respectively. Dashed lines refer to H-bonds (HBs). (For interpretation of the references to color in this figure legend, the reader is referred to the Web version of this article.)

than the bidentate (**B**) ones. The reasons behind this observation were discussed in the SI (Table S5; Figures S6-S8). For both **M** and **B** complexes, the calculated ΔG values indicated that stability of the M^{n+}–P_i complexes increases with respect to the metal ion valency in the order divalent < trivalent < tetravalent metal ion (Fig. 3, Table S5, and Fig. S8). According to the ΔG values, the stability and thus binding strength (in kcal/mol) of these **M** P_i–M^{n+} complexes increase in the order Ca^{2+} (~−15) < Mn^{2+} (~−19) ≈ Fe^{2+} (~−20) < Al^{3+} (~−34) < Mn^{3+} (~−38) < Fe^{3+} (~−41) < Mn^{4+} (~−84). Here, one could observe that tetravalent ion (Mn^{4+}) and trivalent ions (Mn^{3+} and Fe^{3+}) bind phosphate four and two times stronger, respectively, compared to the corresponding divalent ones (Mn^{2+} and Fe^{2+}). This suggests that phosphates could bind strongly and thus immobilize in soil through their complexation reaction with the free metal ions of higher oxidation state (such as Al^{3+}, Mn^{3+}, Fe^{3+}, and Mn^{4+}) and/or their oxides. In the same context, own recent modeling results showed strong complexation reactions (adsorption) for the P-containing compounds with Al^{3+}/Fe^{3+}–oxide surfaces (Ahmed et al., 2018, 2019, 2020; Ganta et al., 2019, 2020, 2021a, b). Specifically, the interaction energies of the adsorbed P_i at goethite varied from −59 to −150 kcal/mol based on several factors involving surface morphology, surface saturation, crystal plane, water, and pH. In contrast, phosphates will bind weaker and thus will be more available if the interaction takes place with free metal ions of lower oxidation state (such as Ca^{2+}, Mn^{2+}, and Fe^{2+}). This means that binding of phosphates in soils (and especially binding to metal ions and metal-oxides) will be overall weaker under reducing conditions. Hence more P will be available in solution by applying reducing conditions to soil samples, which yield more Fe^{2+} and Mn^{2+} with respect to the existing Fe^{3+}, $Mn^{3+}$and Mn^{4+} metal ions.

With respect to the P binding to SOM, Figure S10 showed that this P binding is very small (ΔG_B changes from +6.4 to −6.6) compared to the binding to free metal ions and metal-oxide surfaces (Ahmed et al., 2018, 2019, 2020; Ganta et al., 2019, 2020, 2021a, b). This means that one could expect more available P from those bound to DOC/SOM compared to the P forms that are bound to metal ions and their oxide surfaces. Regarding OM, phosphate binds to the oxidized OM forms stronger than the corresponding reduced ones. In addition, aromatic DOC can bind P stronger than the aliphatic DOC. More details about the molecular binding behavior of phosphate to OM are given in the SI (pages 14–15). Combining the binding behavior and strength of P to metal ions, metal oxides, and organic matter, one could suggest the higher release of P under reducing conditions (lower E_H values) as well as the lower P release under oxidizing conditions. This is similar to the same experimental observations in Section 3.2. Moreover, our results refer as well to the importance of redox chemistry of Fe oxides together with Mn oxides in controlling the redox-induced mobilization of P in soils. In addition, based on the binding strength introduced above, the modeling results come in accord with the experimental results that Al–P could be the dominant species followed by Fe–P, Ca–P, and then organic-P.

At higher pH (i.e. considering the HPO_4^{2-} species), possible precipitation of metal ions by existing hydroxyl (OH^-) groups in soil solution could happen as well but still the M^{n+}–P_i complexation reaction is more favored (Fig. S9). Further, the **M** M^{n+}–P_i complexes were found to be more stable than the **B** ones similar to the lower pH case (Fig. 3). In addition, it was found here as well that the M^{n+}–P_i binding strength decreased under reducing conditions. Furthermore, the results showed that the M^{n+}–P_i complexes are more favored and thus more strongly bound at higher pH than at lower pH. Therefore, these results confirm the higher release of P under reducing and acidic (lower pH values) conditions as well as the lower P release under oxidizing and alkaline conditions (Fig. S11). However, it should be noted that the pH effect on the P mobilization is not uniform and similar for all soil components. For example, our modeling results showed that P binds stronger to organic compound at lower pH than at higher pH (see ΔG_B for carboxylic and carboxylate groups in Fig. S10). The same observation was obtained for metal oxide surfaces. This might refer to the higher release of P under alkaline (higher pH values) conditions considering metal oxides and organic matter. This shows the complex behavior of pH on the P binding and thus the P mobility but could explain and support also the experimental observations of P mobilization under alkaline conditions as shown in the mid-slope soil.

4. Conclusions and environmental implications

Phosphorus can cause environmental problems when undesired mobilization from soil to water occurs. Raising groundwater table from coincidence of heavy rainfall with restricted drainage system probably results in low redox potentials in soils which may promote the reductive dissolution of iron oxides and release of bound P-compounds towards waterways, causing eutrophication. Consequently, controlling the loss of P at the field scale is essential to reduce the associated eutrophication risk. Effective management of P loss in groundwater-affected arable soils needs more insights into the processes/factors and potential mechanisms which may govern the redox-induced mobilization of P. We examined the redox-induced mobilization and speciation of P under different redox directions in hydromorphic arable soils to understand these processes, and develop mitigation strategies. Our study demonstrated that the higher solubility of P at low E_H and Ph may enhance its bioavailability, but also may increase its leaching and potential loss. The release of P was higher in the TS and MS than in the US and thus the TS and MS demonstrate a greater threat than the US of leaching P to adjacent waters when the soil is reduced. The results might be an aid for a sustainable management of P in hydromorphic arable soils and further wetland soils. The results may also be an aid for the decision makers in the studied area to develop some practices, such as controlled drainage or reactive ditches for trapping mobilized P and to mitigate P losses.

However, these results need to be verified at meso- (e.g., lysimeter) and macro-(field) scale. Also, more studies are needed to examine and investigate the impact of redox-induced changes of soil organic matter fractions and dissolved organic carbon compounds on the release kinetics and speciation of organic and inorganic P in different soils.

Credit author statement

Sabry M. Shaheen: Investigation, conducting the experiment, data processing, and writing the original draft. Jianxu Wang: conducting the experiment, XANES analyses, Software and visualization, and editing. Karen Baumann: Editing and proof reading. Ashour A. Ahmed: Performing the quantum chemical calculations, Analyzing the modeling results, Writing the modeling part, editing and proof reading. Liang-Ching Hsu: XANES analyses, treading the XANES data, LCF, creating figures, and editing. Yu-Ting Liu: XANES analyses, editing and proof reading. Shan-Li Wang: XANES analyses, editing and proof reading. Oliver Kühn: Contributing to quantum chemical calculations, analyzing the modeling results and writing the modeling part, editing and proof reading. Peter Leinweber: Review, editing and proof reading. Jörg Rinklebe: Scientific concept, research idea, Supervision, coordination, experimental guiding, technical facilities, foundation, editing and proof reading, and corresponding author.

Declaration of competing interest

The authors declare that they have no known competing financial interests or personal relationships that could have appeared to influence the work reported in this paper.

Acknowledgements

We thank the German Federal Ministry of Education and Research (BMBF) who funded the InnoSoilPhos-project (http://www.innosoilphos.de/default.aspx), in the frame of the BonaRes-program (No. 521 031B0509A). Also, we thank the team of Laboratory of Soil- and

Groundwater-Management at Wuppertal University for the technical support.

Appendix A. Supplementary data

Supplementary data to this article can be found online at https://doi.org/10.1016/j.chemosphere.2021.132652.

References

Afsar, M.Z., Goodwin, C., Beebe Jr., T.P., Jaisi, D.P., Jin, Y., 2020. Quantification and molecular characterization of organo-mineral associations as influenced by redox oscillations. Sci. Total Environ. 704, 135454.

Ahmed, A.A., Gypser, S., Leinweber, P., Freese, D., Kühn, O., 2019. Infrared spectroscopic characterization of phosphate binding at the goethite–water interface. Phys. Chem. Chem. Phys. 21, 4421–4434.

Ahmed, A.A., Leinweber, P., Kühn, O., 2018. Unravelling the nature of glyphosate binding to goethite surfaces by ab initio molecular dynamics simulations. Phys. Chem. Chem. Phys. 20, 1531–1539.

Ahmed, A.A., Gypser, S., Freese, D., Leinweber, P., Kühn, O., 2020. Molecular level picture of the interplay between pH and phosphate binding at the goethite–water interface. Phys. Chem. Chem. Phys. 22, 26509–26524.

Baken, S., Verbeeck, M., Verheyen, D., Diels, J., Smolders, E., 2015. Phosphorus losses from agricultural land to natural waters are reduced by immobilization in iron-rich sediments of drainage ditches. Water Res. 71, 160–170.

Barcellos, D., Melo, H., Gabriel, N.N., Romildo Lopesde Oliveira Filho, R.L.O., 2019. Xosé LuisOtero, X. L.; Ferreira, T.O. Phosphorus enriched effluents increase eutrophication risks for mangrove systems in northeastern Brazil. Mar. Pollut. Bull. 142, 58–63.

Baumann, K., Marschner, P., Smernik, R.J., Baldock, J.A., 2009. Residue chemistry and microbial community structure during decomposition of eucalypt, wheat and vetch residues. Soil Biol. Biochem. 41, 1966–1975.

Baumann, K., Nastah, S., Shaheen, S.M., Rinklebe, J., Leinweber, P., 2020a. Phosphorus cycling and spring barley crop response to varying redox potential. Vadose Zone J. 19, e20088.

Baumann, K., Shaheen, S.M., Hu, Y., Gros, P., Heilmann, E., Morshedizad, M., Wang, J., Wang, S.L., Rinklebe, J., Leinweber, P., 2020b. Speciation and sorption of phosphorus in agricultural soil profiles of redoximorphic character. Environ. Geochem. Health 42, 3231–3246.

Beauchemin, S., Hesterberg, D., Chou, J., Beauchemin, M., Simard, R.R., Sayers, D.E., 2003. Speciation of phosphorus in phosphorus-enriched agricultural soils using X-ray absorption near-edge structure spectroscopy and chemical fractionation. J. Environ. Qual. 32, 1809–1819.

Bernardo, M.P., Guimaraes, G.G.F., Majaron, V.F., Ribeiro, C., 2018. Controlled release of phosphate from layered double hydroxide structures: dynamics in soil and application as smart fertilizer. ACS Sustain. Chem. Eng. 6, 5152–5161.

Bünemann, E.K., Oberson, A., Frossard, E. (Eds.), 2011. Phosphorus in Action; Biological Processes in Soil Phosphorus Cycling. Springer, Heidelberg, Germany.

Cossi, M., Rega, N., Scalmani, G., Barone, V., 2003. Energies, structures, and electronic properties of molecules in solution with the C-PCM solvation model. J. Comput. Chem. 24, 669–681.

El-Naggar, A., Shaheen, S.M., Chang, S., Hou, D., Ok, Y.S., Rinklebe, J., 2021. Biochar surface functionality plays a vital role in (im)mobilization and phytoavailability of soil vanadium. ACS Sustain. Chem. Eng. 9, 6864–6874.

El-Naggar, A., Shaheen, S.M., Ok, Y.S., Rinklebe, J., 2018. Biochar affects the dissolved and colloidal concentrations of Cd, Cu, Ni, and Zn and their phytoavailability and potential mobility in a mining soil under dynamic redox-conditions. Sci. Total Environ. 624, 1059–1071.

Felicien, W.L., Wight, J.P., Gaston, L.A., Blazier, M.A., Kovar, J.L., 2016. Phosphorus runoff from Coastal Plain forest soil in Louisiana. Commun. Soil Sci. Plant Anal. 47 (10), 1283–1295.

Fierer, N., Schimel, J.P., 2002. Effects of drying-rewetting frequency on soil carbon and nitrogen transformations. Soil Biol. Biochem. 34, 777–787.

Frisch, M.J., Trucks, G.W., Schlegel, H.B., Scuseria, G.E., Robb, M.A., 2016. Gaussian 16. Gaussian, Inc., Wallingford CT.

Frohne, T., Rinklebe, J., Diaz-Bone, R.A., Du Laing, G., 2011. Controlled variation of redox conditions in a floodplain soil: impact on metal mobilization and biomethylation of arsenic and antimony. Geoderma 160, 414–424.

Ganta, P.B., Kühn, O., Ahmed, A.A., 2020. QM/MM molecular dynamics investigation of the binding of organic phosphates to the 100 diaspore surface. Front. For. Glob. Change. 3, 7.

Ganta, P.B., Kühn, O., Ahmed, A.A., 2019. QM/MM simulations of organic phosphorus adsorption at the diaspore–water interface. Phys. Chem. Chem. Phys. 21, 24316–24325.

Ganta, P.B., Morshedizad, M., Kühn, O., Leinweber, P., Ahmed, A.A., 2021a. The binding of phosphorus species at goethite: a joint experimental and theoretical study. Minerals 11, 323.

Ganta, P.B., Kühn, O., Ahmed, A.A., 2021b. Ab initio molecular dynamics simulations of the interaction between organic phosphates and goethite. Molecules 26, 160.

Glinski, J., Stahr, K., Stepniewska, Z., Brzezinska, M., 1992. Changes of redox and pH conditions in a flooded soil amended with glucose and nitrate under laboratory conditions. J. Plant Nutr. Soil Sci. 155, 13–17.

Grimme, S., Ehrlich, S., Goerigk, L., 2011. Effect of the damping function in dispersion corrected density functional theory. J. Comput. Chem. 32, 1456–1465.

Gross, A., Pett-Ridge, J., Silver, W., 2018. Soil oxygen limits microbial phosphorus utilization in humid tropical forest soils. Soil Syst 2, 65. https://doi.org/10.3390/soilsystems2040065.

Grybos, M., Davranche, M., Gruau, G., Petitjean, P., Pedrot, M., 2009. Increasing pH drives organic matter solubilization from wetland soils under reducing conditions. Geoderma 154, 13–19.

Gu, S., Gruau, G., Dupas, R., Petitjean, P., Li, Q., Pinay, G., 2019. Respective roles of Fe-oxyhydroxide dissolution, pH changes and sediment inputs in dissolved phosphorus release from wetland soils under anoxic conditions. Geoderma 338, 365–374.

Guo, L., Warnken, K.W., Santschi, P.H., 2007. Retention behavior of dissolved uranium during ultrafiltration: implications for colloidal U in surface waters. Mar. Chem. 107, 156–166.

Gustafsson, J.P., Braun, S., Tuyishime, J.R.M., Adediran, G.A., Warrinnier, R., Hesterberg, D., 2020. A probabilistic approach to phosphorus speciation of soils using P K-edge XANES spectroscopy with linear combination fitting. Soil Syst. 4, 26. https://doi.org/10.3390/soilsystems4020026.

Harvey Jr., A.E., Smart, J.A., Aims, E.S., 1955. Simultaneous spectrophotometric determination of iron (II) and total iron with 1, 10-phenanthroline. Anal. Chem. 27 (1), 26–29.

Hehre, W.J., Ditchfield, R., Pople, J.A., 1972. Self—consistent molecular orbital methods. XII. Further extensions of Gaussian—type basis sets for use in molecular orbital studies of organic molecules. J. Chem. Phys. 56, 2257–2261.

Hens, L., Quynh, L.X., 2016. Environmental space. In: Hens, L., Quynh, L.X. (Eds.), Reference Module in Earth Systems and Environmental Sciences. Elsevier Ltd, Oxford. U.K. https://doi.org/10.1016/B978-0-12-409548-9.09739-6.

Hurtarte, L.C.C., Souza-Filho, L.F.S., Oliveira Santos, W., Vergütz, L., Prietzel, J., Hesterberg, D., 2019. Optimization of data processing minimizes impact of self-absorption on phosphorus speciation results by P K-edge XANES. Soil Syst 3, 61.

Husson, O., 2013. Redox potential and pH as drivers of soil/plant/microorganism systems: a transdisciplinary overview pointing to integrative opportunities for agronomy. Plant Soil 362, 389–417.

Kalbitz, K., Solinger, S., Park, J.-H., Michalzik, B., Matzner, E., 2000. Controls on the dynamics of dissolved organic matter in soil: a review. Soil Sci. 165, 277–304.

Khan, S.U., Hooda, P.S., Blackwell, M.S.A., Busquets, R., 2019. Microbial biomass responses to soil drying-rewetting and phosphorus leaching. Front. Environ. Sci. 7, 133 https://doi.org/10.3389/fenvs.2019.00133.

Lee, C., Yang, W., Parr, R.G., 1988. Development of the Colle-Salvetti correlation-energy formula into a functional of the electron density. Phys. Rev. B37, 785–789.

Megonigal, J.P., Hines, M.E., Visscher, P.T., 2004. Anaerobic metabolism: linkages to trace gases and aerobic processes. In: Schlesinger, W.H. (Ed.), Biogeochemistry. Elsevier-Pergamon, Oxford, pp. 317–424.

Moche, M., Gutknecht, J., Schulz, E., Langer, U., Rinklebe, J., 2015. Monthly dynamics of microbial community structure and their controlling factors in three floodplain soils. Soil Biol. Biochem. 90, 169–178.

Powell, K.J., Brown, P.L., Byrne, R.H., Gajda, T., Hefter, G., Sjöberg, S., Wanner, H., 2005. Chemical speciation of environmentally significant heavy metals with inorganic ligands. Part 1: the Hg2+– Cl–, OH–, CO32–, SO42–, and PO43– aqueous systems (IUPAC Technical Report). Pure Appl. Chem. 77, 739–800.

Prem, M., Hansen, H.C.B., Wenzel, W., Heiberg, L., Sørensen, H., Borggaard, O.K., 2015. High spatial and fast changes of iron redox state and phosphorus solubility in a seasonally flooded temperate wetland soil. Wetlands 35, 237–246.

Rahutomo, S., Kovar, J.L., Thompson, M.L., 2018. Varying redox potential affects P release from stream bank sediments. PLoS One 13 (12). https://doi.org/10.1371/journal.pone.0209208.

Ravel, B., Newville, M., 2005. ATHENA, ARTEMIS, HEPHAESTUS: data analysis for X-ray absorption spectroscopy using IFEFFIT. J. Synchrotron Radiat. 12, 537–541.

Reddy, K.R., DeLaune, R.D., 2008. Biogeochemistry of Wetlands: Science and Applications. Taylor & Francis Group, LLC, Boca Raton, London, New York.

Rinklebe, J., Shaheen, S.M., El-Naggar, A., Wang, H., Du Laing, G., Alessi, D.S., Ok, Y.S., 2020. Redox-induced mobilization of Ag, Sb, Sn, and Tl in the dissolved, colloidal and solid phase of a biochar-treated and un-treated mining soil. Environ. Int. 140, 105754.

Rinklebe, J., Shaheen, S.M., Yu, K., 2016. Release of As, Ba, Cd, Cu, Pb, and Sr under pre-definite redox conditions in different rice paddy soils originating from the U.S.A. and Asia. Geoderma 270, 21–32.

Shaheen, S.M., Rinklebe, J., Frohne, T., White, J.R., DeLaune, R.D., 2014b. Biogeochemical factors governing cobalt, nickel, selenium, and vanadium dynamics in periodically flooded Egyptian North Nile Delta rice soils. Soil Sci. Soc. Am. J. 78, 1065.

Shaheen, S.M., Wang, J., Baumann, K., Wang, S.-L., Leinweber, P., Rinklebe, J., 2021. Redox-induced mobilization of phosphorus in groundwater affected arable soil profiles. Chemosphere 275, 129928.

Shaheen, S.M., Rinklebe, J., Rupp, H., Meissner, R., 2014a. Lysimeter trials to assess the impact of different flood-dry-cycles on the dynamics of pore water concentrations of As, Cr, Mo and V in a contaminated floodplain soil. Geoderma 228–229, 5–13.

Shenker, M., Seitelbach, S., Brand, S., Haim, A., Litaor, I., 2005. Redox reactions and phosphorus release in re-flooded soils of an altered wetland. Eur. J. Soil Sci. 56, 515–525.

Siddique, M.T., Robinson, J.S., Alloway, B.J., 2000. Phosphorus reactions and leaching potential in soils amended with sewage sludge. J. Environ. Qual. 29, 1931–1938.

Søndergaard, M., 2009. Redox Potential. In: Encyclopedia of Inland Waters. https://doi.org/10.1016/B978-012370626-3.00115-0.

Stumm, W., Morgan, J.J., 1996. Aquatic Chemistry: Chemical Equilibria and Rates in Natural Waters. Wiely, New Yrk.

Takeno, N., 2005. Atlas of Eh-pH diagrams. Geological survey of Japan open file report 419, 102.
Unger, I.M., Kennedy, A.C., Muzika, R.M., 2009. Flooding effects on soil microbial communities. Appl. Soil Ecol. 42, 1–8.
Van der Grift, B., Behrends, T., Osté, L.A., Schot, P.P., Wassen, M.J., 2016. Griffioen, J. Fe hydroxyphosphate precipitation and Fe(II) oxidation kinetics upon aeration of Fe (II) and phosphate-containing synthetic and natural solutions. Geochem. Cosmochim. Acta 186, 71–90.
Weber, K., Achenbach, L., Coates, J., 2006. Microorganisms pumping iron: anaerobic microbial iron oxidation and reduction. Nat. Rev. Microbiol. 4, 752–764.
Weishaar, J.L., Aiken, G.R., Bergamaschi, B.A., Fram, M.S., Fujii, R., Mopper, K., 2003. Evaluation of specific ultraviolet absorbance as an indicator of the chemical composition and reactivity of dissolved organic carbon. Environ. Sci. Technol. 37, 4702–4708.
Wolkersdorfe, C., 2008. Water Management at Abandoned Flooded Underground Mines: Fundamentals, Tracer Tests, Modelling, Water Treatment (Mining and the Environment). Springer, ISBN 978-3-540-77331-3, 465. https://www.wolkersdorfer.info/en/redoxprobes.html.
Yu, K., Böhme, F., Rinklebe, J., Neue, H.U., DeLaune, R.D., 2007. Major biogeochemical processes in soils - A microcosm incubation from reducing to oxidizing conditions. Soil Sci. Soc. Am. J. 71, 1406–1417.
Yu, K., Rinklebe, J., 2011. Advancement in soil microcosm apparatus for biogeochemical research. Ecol. Eng. 37, 2071–2075.
Zak, D., Gelbrecht, J., Steinberg, C.E.W., 2004. Phosphorus retention at the redox interface of peatlands adjacent to surface waters in northeast Germany. Biogeochemistry 70, 359–370.
Zhang, S., Yang, X., Hsu, L.-C., Liu, Y.-T., 2021. Soil acidification enhances the mobilization of phosphorus under anoxic conditions in an agricultural soil: investigating the potential for loss of phosphorus to water and the associated environmental risk. Sci. Total Environ. 793, 148531.
Zhang, W., White, J.R., DeLaune, R.D., 2012. Diverted Mississippi River Sediment as a Potential Phosphorus Source to Louisiana Water Quality. J. Freshw. Ecol. 47, 575–586.
Zimmer, D., Kahle, P., Baum, C., 2016. Loss of soil phosphorus by tile drains during storm events. Agric. Water Manag. 167, 21–28.

Supplementary Materials

Stepwise redox changes alter the speciation and mobilization of phosphorus in hydromorphic soils

Sabry M. Shaheen[1,2,3], Jianxu Wang[4,1], Karen Baumann[5], Ashour A. Ahmed[6,7], Liang-Ching Hsu[8], Yu-Ting Liu[9], Shan-Li Wang[10], Oliver Kühn[6,7], Peter Leinweber[5,7], Jörg Rinklebe[1,11*]

[1]University of Wuppertal, School of Architecture and Civil Engineering, Institute of Foundation Engineering, Water- and Waste-Management, Laboratory of Soil- and Groundwater-Management, Pauluskirchstraße 7, 42285 Wuppertal, Germany; E-mail: shaheen@uni-wuppertal.de (Shaheen); rinklebe@uni-wuppertal.de (Rinklebe); ORCiD: 0000-0002-5618-8175 (Shaheen); 0000-0001-7404-1639 (Rinklebe)
[2]King Abdulaziz University, Faculty of Meteorology, Environment, and Arid Land Agriculture, Department of Arid Land Agriculture, Jeddah 21589, Saudi Arabia
[3]University of Kafrelsheikh, Faculty of Agriculture, Department of Soil and Water Sciences, 33 516 Kafr El-Sheikh, Egypt
[4]State Key Laboratory of Environmental Geochemistry, Institute of Geochemistry, Chinese Academy of Sciences, 550082 Guiyang, P.R. China
[5]University of Rostock, Faculty of Agricultural and Environmental Science, Soil Science, Justus-von-Liebig-Weg 6, 18051 Rostock, Germany
[6]University of Rostock, Institute of Physics, D-18059 Rostock, Albert-Einstein-Str. 23-24, Germany
[7]University of Rostock, Department of Life, Light, and Matter (LLM), Albert-Einstein-Str. 25, D-18059 Rostock, Germany
[8]Department of Soil and Environmental Sciences, National Chung-Hsing University, 145 Xingda Rd., Taichung 402, Taiwan
[9]Department of Soil and Environmental Sciences & Innovation and Development Center of Sustainable Agriculture, National Chung-Hsing University, 145 Xingda Rd., Taichung 402, Taiwan,
[10]Department of Agricultural Chemistry, National Taiwan University, 1 Sect. 4, Roosevelt Rd., Taipei 10617, Taiwan
[11]University of Sejong, Department of Environment, Energy and Geoinformatics, Guangjin-Gu, Seoul 05006, Republic of Korea

* Corresponding Author: rinklebe@uni-wuppertal.de

reference materials were selected on the basis of a high similarity of their spectra with the spectra of major components of soil samples as identified by principal components analysis (PCA). We used the function of fit all combinations to fit each sample, and then the best combination was chosen based on the R-factor values and visual check of fitting spectra. The details of the principal components analysis PCA results are shown in the appendix (Table S5, S6, and S7).

Molecular modeling approach

One major factor controlling the Phosphorus (P) mobilization process and thus availability to plants is the P interaction with soil components such as free metal ions, (Urrutia et al. 2013), (Gros, 2019), soil minerals, (Kruse, 2015), (Ganta, 2019) and soil organic matter (SOM) (Gros, 2017), (Ahmed, 2018) . A key point is the strong interaction between phosphates and soil mineral surfaces especially Fe- and Al-(oxyhydr)oxides (Kruse, 2015). Extensive experimental and theoretical efforts at a molecular scale have been introduced to investigate the binding strength and mechanism of the phosphate reactions with these mineral surfaces (Ahmed, 2018; Ganta, 2019; Arai, 2007; Arroyave, 2018). The applied molecular modeling approaches have provided a deeper description and atomistic understanding of the phosphate adsorption experiments at metal-oxyhydroxide surfaces at different experimental conditions. Such a detailed atomistic investigation for the phosphate binding nature with free metal ions and soil organic matter (SOM) is still lacking. Therefore, our main objectives in this section are 1- to simulate the phosphate binding process with the relevant metal ions as well as with some organic matter (OM) present in soil solutions and 2- how the redox conditions and soil pH control this binding process.

Our objectives were addressed by modeling the complexation reaction of ortho-phosphate (inorganic phosphate, P_i) with the following dominant metal ions in soils: Ca^{2+}, Al^{3+}, Fe^{2+}, Fe^{3+}, Mn^{2+}, Mn^{3+}, and Mn^{4+}. To provide a realistic approach, P_i and the free metal ions (M^{n+}) were modeled according to their abundant chemical species in the soil solution at the relevant pH values. Each M^{n+} was modelled as an octahedral metal aqua complex. In addition, the most abundant P_i species ($H_2PO_4^{13}$) was taken into account, see Fig. S7. Using these reactants, simulations of 1:1 complex formation between each M^{n+} and the P_i species were performed. For each $M^{n+}3P_i$ complex, two possible binding motifs (mono-dentate and bi-dentate) have been modeled, see Fig. S7. A mono-dentate (**M**) binding motif was constructed by the formation of only one coordination bond from one P_i O atom to the free metal ion M^{n+}. A bi-dentate (**B**) motif involved the formation of two coordination bonds from two P_i O atoms to M^{n+}. For each $M^{n+}3P_i$ complex, the free metal ion was saturated with water molecules up to the octahedral coordination state (i.e.

each metal ion is surrounded in total by 6 coordination bonds). The stability of the formed $M^{n+}3P_i$ complexes and their P binding strengths were characterized by considering the following chemical substitution/exchange reactions and calculating the relevant reaction-free energies (&G).

For **M** binding motifs:

$$1\ [M(H_2O)_6]^{n+} + 1\ H_2PO_4^{13\ 3} \rightarrow 1\ [(H_2O)_5M(H_2PO_4)]^{n31} + 1\ H_2O \qquad \text{(Eq. 1)}$$

For **B** binding motifs:

$$1\ [M(H_2O)_6]^{n+} + 1\ H_2PO_4^{13\ 3} \rightarrow 1\ [(H_2O)_4M(H_2PO_4)]^{n31} + 2\ H_2O \qquad \text{(Eq. 2)}$$

For example, &G for the substitution reaction in Eq. 1 is calculated as follows:

$$\&G = G([(H_2O)_5M3(H_2PO_4)]^{n31} + G(H_2O)\ 3\ G([M(H_2O)_6]^{n+})\ 3\ G(H_2PO_4^{13}) \qquad \text{(Eq. 3)}$$

where, $G([(H_2O)_4M3GLP]^{n-1})$, $G(H_2O)$, $G([M(H_2O)_6]^{n+})$, and $G(H_2PO_4^{13})$ are the free energies of the $M^{n+}3P_i$ complexes, H_2O, metal aqua-complexes, and $H_2PO_4^{13}$, respectively.

To study the pH effect on the P binding process, similar $M^{n+}3P_i$ complexation reactions to Eqs. 1-2 were simulated but here P_i is modeled with the HPO_4^{23} species instead of the $H_2PO_4^{13}$ one. The HPO_4^{23} species represents a higher pH (pH: 7.2312.4) than the $H_2PO_4^{13}$ species (pH: 2.137.2) (Powell, et al 2005). Similar to Eqs. 1-2, the $M^{n+}3P_i$ complexation reactions at higher pH were simulated by considering the following chemical reactions:

For **M** binding motifs, $1\ [M(H_2O)_6]^{n+} + 1\ HPO_4^{23\ 3} \rightarrow 1\ [(H_2O)_5M(HPO_4)]^{n32} + 1\ H_2O$ (Eq. 4)

For **B** binding motifs, $1\ [M(H_2O)_6]^{n+} + 1\ HPO_4^{23\ 3} \rightarrow 1\ [(H_2O)_4M(HPO_4)]^{n32} + 2\ H_2O$ (Eq. 5)

The corresponding reaction free energies (&G) for the $M^{n+}3P_i$ complexation reaction in Eqs. 4-5 were calculated in the same way as in Eq. 3. Furthermore, the binding process between free metal ions and hydroxyl (OH^3) groups at higher pH (which is the first step to the precipitation process of metal ions) has been modeled. This was considered due to the presence of OH^3 groups at higher pH which may lead to precipitation of the existing free metal ions in soil solution. The $M^{n+}3OH$ complexation reaction was simulated by considering of the following exchange reaction of one water (H_2O) molecule by one OH group for the octahedral metal aqua-complexes ($[M(H_2O)_6]^{n+}$):

$$1\ [M(H_2O)_6]^{n+} + 1\ OH^3 \rightarrow 1\ [(H_2O)_5M(OH)]^{n31} + 1\ H_2O \qquad \text{(Eq. 6)}$$

The reaction-free energies (&G) for the $M^{n+}3OH$ exchange reactions were calculated similarly to Eq. 3.

To understand the $M^{n+}3P_i$ complexation reactions and determine &G for all related chemical reactions, full geometry optimization was performed for the initial geometries of the octahedral metal aqua-complexes ($[M(H_2O)_6]^{n+}$), both phosphate species ($H_2PO_4^{13}$ and HPO_4^{23}), water (H_2O), a hydroxyl group (OH^3), $M^{n+}3OH$ complexes ($[(H_2O)_5M(OH)]^{n31}$), and $M^{n+}3P_i$ complexes ($[(H_2O)_5M(H_2PO_4)]^{n-1}$, $[(H_2O)_4M(H_2PO_4)]^{n-1}$, $[(H_2O)_5M(HPO_4)]^{n-2}$, and $[(H_2O)_4M(HPO_4)]^{n-2}$) using

density functional theory (DFT). Specifically, the B3LYP hybrid functional (Ganta, et al 2019), (Gros, et al 2017) combined with the 6-311++G(d,p) basis set (Ahmed, et al 2018) have been applied. Moreover, the Grimme D3 dispersion correction (Arai and Sparks 2007) has been involved to improve the spatial configurations for the optimized geometries of the $M^{n+}3P_i$ complexes and to yield more accurate reaction-free energy values. To mimic the environmental aqueous solution in soil samples around the $M^{n+}3P_i$ complexes and their separate fragments, water solvent has been introduced for all studied geometries by implicit treatment. This was modeled by the conductor-like polarizable continuum model (CPCM) (Arai and Sparks 2001; Barrow, 1983). Moreover, harmonic vibrational frequencies were calculated for all optimized geometries. All these geometries are characterized to be true minima by having zero gradient norms and positive harmonic vibrational frequencies. All the present calculations have been performed by using the Gaussian16 program package (Chitrakar, et al, 2006).

To explore how strong the interaction between P and OM is and how this is affected by the redox conditions, the binding process between phosphate and selected OM fragments was studied. Here, the main focus on selecting the OM fragments was based on the hierarchy of reducing conditions for a specific OM fragment from its oxidized form to the corresponding reduced form. To the best of our knowledge, organic carboxylic acids9class is one of the most oxidized OM forms which would be reduced first to the corresponding aldehyde form and further reduction would lead to the alcohol form and eventually reaching to hydrocarbon. The second factor in the OM selection was based on the OM abundance in soils to introduce here a reliable model. So maleic acid was selected here as a representative case for studying the $OM3P_i$ interactions. Then its aldehyde, alcohol, and hydrocarbon forms were considered as well. In addition, n-butanoic acid (simple aliphatic carboxylic acid with the same C-chain length as for maleic acid) and also its aldehyde, alcohol, and hydrocarbon forms were modeled to check the hydrophilicity effect on the $OM3P_i$ interactions. To check the aromaticity effect on the P binding to organic matter, benzoic acid as aromatic carboxylic acid and its reduced forms were considered. In addition to the alcohol form (benzyl alcohol), phenol was modeled as well to check how the difference in their chemical structures affects the P binding process. For each carboxylic acid compound, two models were introduced representing the neutral form (i.e. carboxylic acid form) and the deprotonated one (carboxylate form). Therefore, in total, we introduce here 16 representative OM molecular systems to model the $OM3P_i$ interactions. For each OM molecular system, an initial geometry for the $OM3P_i$ complex was constructed by selecting the expected preferential binding situations between P_i and the OM molecule. Full geometry optimization was performed for the initial geometries of all $OM3P_i$ complexes and all modeled OM molecules at the same level of theory

used for the $M^{n+}3P_i$ complexes. For the complexation reaction, 1 OM fragment + 1 P_i ($H_2PO_4^{13}$) → $OM3P_i$ complex, the reaction energy or specifically binding energy (E_B) between phosphate and the OM fragment is calculated as follows:

$$E_B = E(OM3P_i)\ 3\ (E(OM) + E(H_2PO_4^{13})) \qquad \text{(Eq. 7)}$$

where, $E(OM3P_i)$, E(OM), and $E(H_2PO_4^{13})$ are the electronic energies of the $OM3P_i$ complex, OM fragment, and $H_2PO_4^{13}$, respectively. Similarly, the corresponding binding free energies ($\&G_B$) of the $OM3P_i$ complexes were calculated by including the zero-point energy and thermal correction to the Gibbs free energy.

In the following, important notes related to the present molecular modeling approach and its outcome will be introduced:

- It should be noted that the $M^{n+}3P_i$ complex reactions (see Eqs. 134) are not formation reactions, but they are substitution/exchange reactions. The formation of one/two coordination bond(s) between the free metal ions and phosphate was considered next to the dissociation of one/two coordination bond(s) between the free metal ions and one/two water molecule(s). This means that the dissociation of one/two water molecule(s) from modeled metal aqua-complexes ($[M(H_2O)_6]^{n+}$) should take place first and this process is always accompanied by energy gain (i.e. &E is positive). Following this process, the formation of one/two new coordination bond(s) between P_i and metal ions will take place giving rise to the octahedral $M^{n+}3P_i$ complex ($(H_2O)_5M3P_i$ for **M** binding motif and $(H_2O)_4M3P_i$ for **B** one). The latter process is mainly accompanied by energy release (&E is negative). Energies (&E and &G) of the overall substitution/exchange reaction are mainly affected by both individual reactions in which the overall energy is the sum of the individual components of energy.
- For each metal ion, &G values for the overall substitution/exchange reaction in Eq.1 and Eq.2 are negative (see Fig. 3 in the main manuscript). This means that these reactions are spontaneous and all formed monodentate (**M**) and bidentate (**B**) binding motifs for the $M^{n+}3P_i$ complexes are expected to be strongly bound and thermally stable. Moreover, the results showed that the exchange reaction in Eq.1 is more spontaneous (&G values are more negative) than that in Eq.2. This indicates that the **M** $M^{n+}3P_i$ complexes are more favored than the **B** ones for the present models. This also means that the second formed coordination bond for the **B** $M^{n+}3P_i$ complexes is less stable and less favored compared to the first coordination bond. This can be rationalized by having a closer look at the optimized geometries for the **M** and **B** $M^{n+}3P_i$ complexes (see Fig. S8). One substantial factor for the instability of the **B** complexes versus the **M** complexes is the angle/ring stain in the **B** complexes (see Fig. S8). All the **B** complexes exhibit four-membered rings with stained and abnormal bond angles

compared to the corresponding angles for the **M** complexes. The calculated P3O3M^{n+} angles for the **B** complexes (89.0395.4 °) are significantly smaller than those for the **M** complexes (122.53135.3 °, see Table S4). Further, the other contributed bond angles to the formed four-membered rings, O3M^{n+}3O (60.0377.0 °) and O3P3O (92.63111.6 °), for the **B** complexes are relatively small compared to the **M** complexes case. Moreover, the formation of H-bonds (HBs) is another key factor controlling the stability of these $M^{n+}3P_i$ complexes. All the **M** $M^{n+}3P_i$ complexes exhibit 2 intramolecular HBs of moderate strength (Hinsinger, 2001) which stabilize the **M** complexes as compared to the **B** complexes (see Fig. S8 and Table S6). These intramolecular HBs are observed between two phosphate O atoms and H atoms of two water molecules coordinated to the metal ions in the $M^{n+}3P_i$ complexes. For the **M** complex of the Mn^{4+} metal ion, which is the most stable complex, a proton transfer (PT) process is observed. Here, a proton (H^+) was transferred from a coordinated water molecule to the deprotonated phosphate O atom for one HB (see the $Mn^{4+}3P_i$ complex in Fig. S8). Lengths of the observed HBs for the **M** complexes vary from 2.61 to 2.85 Å (see Table S4). As a consequence of these factors, the observed $M^{n+}3O_P$ bond length for each **M** $M^{n+}3P_i$ complex (1.8232.30 Å) is always shorter and thus stronger than the observed ones for the corresponding **B** complex (1.843 2.55 Å).

- It should be noted that the Coulomb interaction gives the main contribution to the calculated &G values. In contrast, the contribution of the dispersion (van der Waals) interaction to the &G values is relatively small (see Fig. S9).
- It should be noted that both trivalent ions (Mn^{3+} and Fe^{3+}) bind phosphate two times stronger compared to the corresponding divalent ones (Mn^{2+} and Fe^{2+}). Moreover, the tetravalent Mn^{4+} ion binds phosphate four times stronger compared to the Mn^{2+} ion.
- At higher pH (i.e. considering the HPO_4^{23} species instead of the $H_2PO_4^{13}$ species), similar results for the $M^{n+}3P_i$ complexation reactions were observed as for the lower pH case. Briefly, both **M** ($[(H_2O)_5M3HPO_4]^{n32}$) and **B** ($[(H_2O)_4M3HPO_4]^{n32}$) $M^{n+}3P_i$ complexes are thermally stable and strongly bound (see Fig. 3 in the main manuscript). In addition, Fig. 3 in the main text shows that the **M** $M^{n+}3P_i$ complexes are more stable compared to the **B** ones at higher pH as well. This is due to the same reasons discussed above for the lower pH case. Mainly, the binding/stability order of the $M^{n+}3P_i$ complexes formed at higher pH followed a similar trend compared to the lower pH case. Furthermore, the results showed that the **c**alculated reaction-free energies (&G) for the $M^{n+}3P_i$ complexation reactions are more negative at higher pH than at lower pH. This refers to more favored $M^{n+}3P_i$ complexes and thus more strongly bound at higher pH than the lower pH case. Higher &G values and thus stability for the $M^{n+}3P_i$

complexes at higher pH could be explained by the higher Coulomb interaction between M^{n+} and Pi for the higher pH case. This is mainly due to increasing the negative charge on the phosphate anion from lower pH ($H_2PO_4^{13}$) to higher pH (HPO_4^{23}). Due to the higher P binding at higher pH, one could expect more available P at lower pH.

- It should be noted that possible precipitation of metal ions by hydroxyl (OH^3) groups at higher pH could happen in parallel to the $M^{n+}3P_i$ complexation reaction. In brief, the results in Fig. S10 referred to a high possibility for these metal ions to react with OH groups but the reaction between phosphate and metal ions is still more favored which confirms that the binding of phosphate increases at higher pH.
- For the binding process between the $H_2PO_4^{13}$ phosphate species and the modeled OM fragments/compounds, the results involving the optimized geometries for the $OM3P_i$ complexes and their binding energies and free energies ($\&E_B$ and $\&G_B$) are represented in Fig. S11. The results showed that the P binding to organic matter ($\&E_B$ changes from -1.9 to -18.6 and $\&G_B$ changes from +6.4 to -6.6) is very small compared to the binding to free metal ions or to metal-oxide surfaces. This means that one could expect more available P from those bound to DOM/SOM compared to the P forms that are bound to metal ions and their oxide surfaces. Regarding OM, phosphate binds to the oxidized OM forms stronger than to the corresponding reduced ones. This could be observed by increasing the P binding strength to OM from hydrocarbons to carboxylic acids (this is valid for all three general models (benzoic, maleic, and butanoic acids) introduced in Fig. S11). This would lead to the conclusion that more P would be available under reducing conditions. Furthermore, the same binding strength of P to OM from hydrocarbons to carboxylic acids indicates that phosphate binds to the hydrophilic OM stronger than to the hydrophobic ones. This could be confirmed as well by comparing the P binding to maleic acid (more hydrophilic OM) and butanoic acid (less hydrophilic OM compared to maleic acid) and their alcohol, aldehyde, and hydrocarbon forms. Here, one observes that all maleic acid forms bind P stronger than the corresponding forms of butanoic acid.
- Here, the reason for stronger P binding in the case of hydrophilic OM is due to their ability to form HBs which would increase the stability of these $OM3P_i$ complexes. In contrast, the main contribution to the hydrophobic $OM3P_i$ complexes is coming from the dispersion interaction. Moreover, for a specific functional group (i.e. focusing on one group such as the carboxylic group, aldehyde, alcohol, or hydrocarbon), aromatic OM can bind P stronger than the aliphatic OM. This could be observed by increasing the P binding strength ($\&E_B$ and $\&G_B$) from butanoic acid (aliphatic OM) to benzoic acid (aromatic OM) and all corresponding reduced forms. For

aromatic OM, phenol was added to the models to check the difference in the P binding strength between alcohols (OH is not attached directly to aromatic rings) and phenols (OH is attached directly to aromatic rings). The calculated binding free energies ($\&G_B$) for the $OM3P_i$ complexes referred to a slightly stronger binding to P in the case of phenol compared to benzyl alcohol.

- In summary, based on all the detailed information about the nature of binding between P and free metal ions and their oxide surfaces, it would be clear from a chemical point of view that P mobilization could be enhanced under reducing conditions. This is valid whether P is bound to OM, free metal ions, or metal-oxide surfaces but the free metal ions and their oxides could be the most important factor condoling the mobilization process. Moreover, enhancement of this P mobilization process under reducing conditions could be improved at lower pH.

Eventually, it is important to introduce some general points regarding the validity of the present molecular modeling approach to help in understanding P mobility under reducing conditions. We are completely aware of the considerable complexity of the soil system, being a highly heterogeneous and interactive molecular system containing inorganic minerals (e.g., clays and metal-oxide surfaces), SOM (the most complex existing biomaterial), most metal ions (in free and/or complexed states), soil solution (with many electrolyte and different pH values) and gases, with the details differing from site to site. Considering all this complexity, molecular modeling of the entire soil system is rather very difficult if not impossible. Therefore, we are not introducing the present molecular modeling data as a complete picture and/or final solution for the P mobilization issue in soil. However, we introduce here an attempt or one step forward toward understanding the P mobilization process at a molecular level. In general, the P mobilization is strongly correlated to how strong the P binding to soil components (e.g., minerals, SOM, metal ions). Regarding minerals, we have extensively investigated in several papers the binding mechanism and binding motifs formed for the adsorbed P at Fe- and Al- oxide surfaces with different surface planes (Ahmed, et al, 2018, 2020; Ganta, et al, 2019, 2020, 2021a,b). In this previous modeling work, we have referred to the effect of surface morphology, surface saturation, crystal plane, water, P species, and pH on the P adsorption process and the formed P complexes and thus the P mobilization process. Therefore, we are focusing here mainly on the P binding to metal ions and organic matter. However, it should be mentioned that the present modeling approach (i.e., including metal ions and organic matter) fits well with the present topic (i.e., the effect of redox potential). This is because most of the selected metal ions and all organic matter exhibit oxidized and reduced species. So, investigating the P binding strength to those selected species would provide a direct relation to the P binding and thus P mobilization under different

reducing conditions. In this context, it is important to emphasize that our modeling approach is aiming to present a qualitative behavior rather than a direct quantitative comparison between the calculated P binding strengths and the P mobilization process under experimental conditions. Moreover, it is important to mention that the outcome of this modeling approach led to a better understanding of the main geochemical processes in pure systems and thus the P mobilization process under different redox potential conditions.

Table S8. Reaction free energies (&G) for the complexation reaction between phosphate and the relevant free metal ions as well as selected distances and angles for the **M** and **B** $M^{n+}3P_i$ optimized complexes. $M^{n+}3O_P$ and $M^{n+}3P$ refer to the distance between M^{n+} and O, and P atoms of phosphate, respectively. O3P3O, $O3M^{n+}3O$, and $P3O3M^{n+}$ refer to the most contributed angles to the **M** and **B** $M^{n+}3P_i$ complexes.

metal ion	**M** binding motif					**B** binding motif					
	&G [kcal mol^{-1}]	distance [Å]			Angle [deg.]	&G [kcal mol^{-1}]	distance [Å]		Angle [deg.]		
		$M^{n+}3O_P$	$M^{n+}3P$	HB (O3O)	$P3O3M^{n+}$		$M^{n+}3O_P$	$M^{n+}3P$	O3P3O	$O3M^{n+}3O$	$P3O3M^{n+}$
Ca^{2+}	-15.4	2.35	3.53	2.72 & 2.84	130.5	-11.4	2.48 & 2.55	3.03	111.6	60.0	93.0 & 95.4
Mn^{2+}	-19.4	2.03	3.15	2.70 & 2.81	123.7	-11.0	2.09 & 2.12	2.59	107.3	71.7	89.0 & 90.1
Fe^{2+}	-19.7	2.00	3.10	2.71 & 2.81	122.5	-9.2	2.05 & 2.06	2.56	106.5	73.4	89.9
Al^{3+}	-34.4	1.82	3.05	2.63 & 2.81	129.5	-22.7	1.90 & 1.91	2.50	99.2	76.8	91.9 & 92.0
Mn^{3+}	-38.4	1.87	3.10	2.65 & 2.81	128.0	-32.3	1.94	2.55	99.0	75.2	92.9
Fe^{3+}	-41.0	1.85	3.04	2.61 & 2.77	125.6	-35.5	1.91 & 1.92	2.52	98.4	76.0	92.2 & 92.9
Mn^{4+}	-83.5	1.83	3.13	2.81 & PT	135.3	-68.3	1.84 & 1.86	2.55	92.6	77.0	95.1 & 95.2

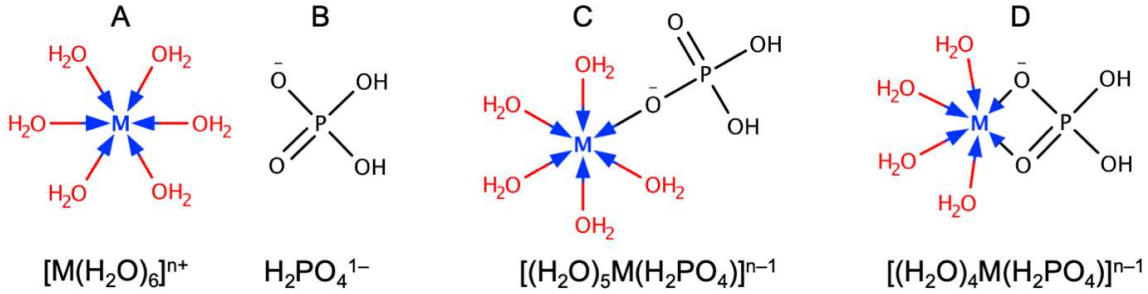


Figure S7 Chemical structures for the modeled free metal ions A), phosphate B), and mono(**M**)-dentate C) and bi(**B**)-dentate D) binding motifs of the $M^{n+}3P_i$ complexes.

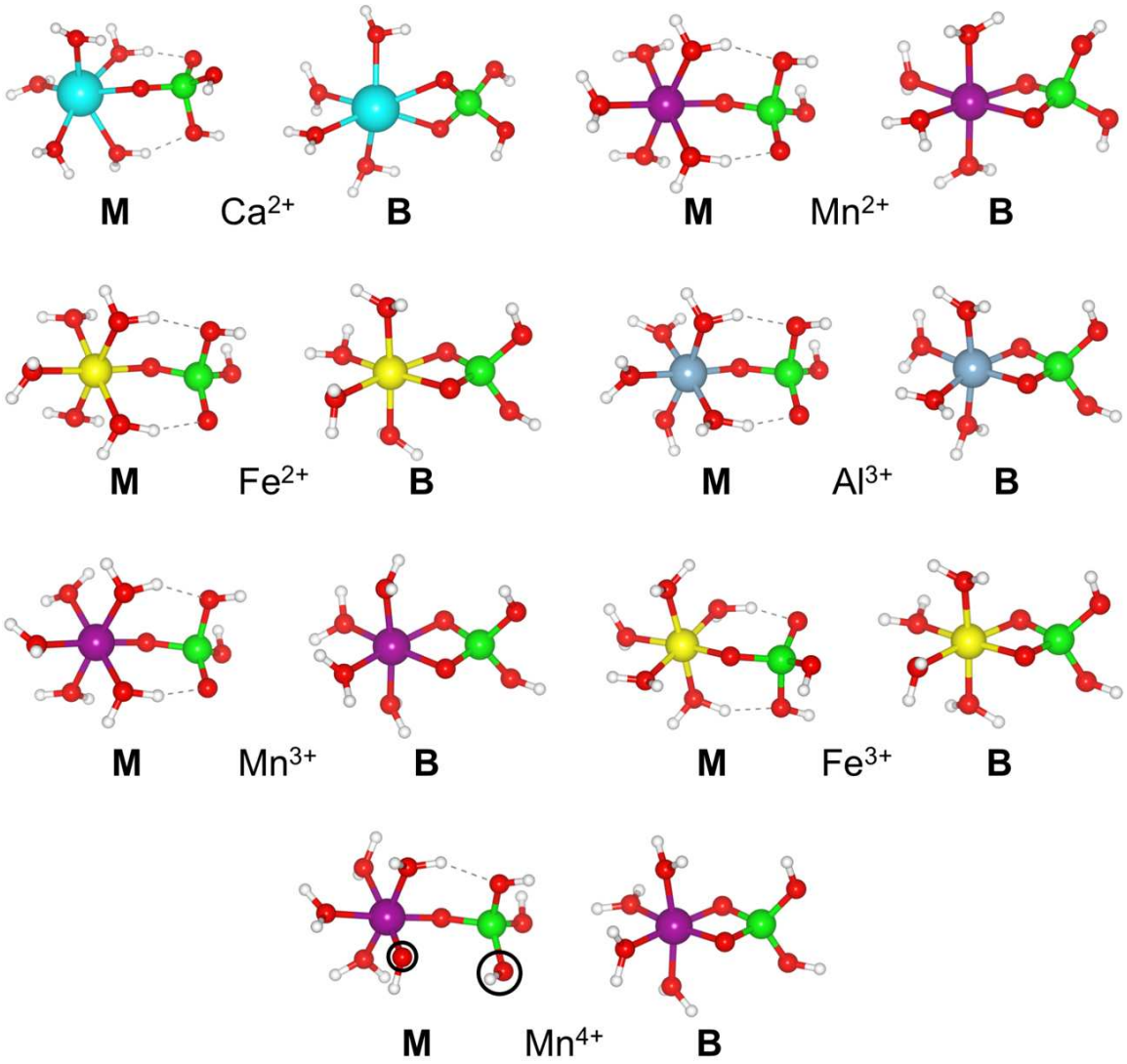


Figure S8 Optimized geometries for the **M** and **B** binding motifs of the $M^{n+}3P_i$ complexes. H, O, P, Ca, Mn, Fe, and Al atoms are visualized in white, red, green, cyan, purple, yellow, and light blue colors, respectively. Dashed lines refer to H-bonds (HBs). Circles are made around O and H atoms for the Mn^{4+} case to show the proton transfer (PT) process from water to phosphate.

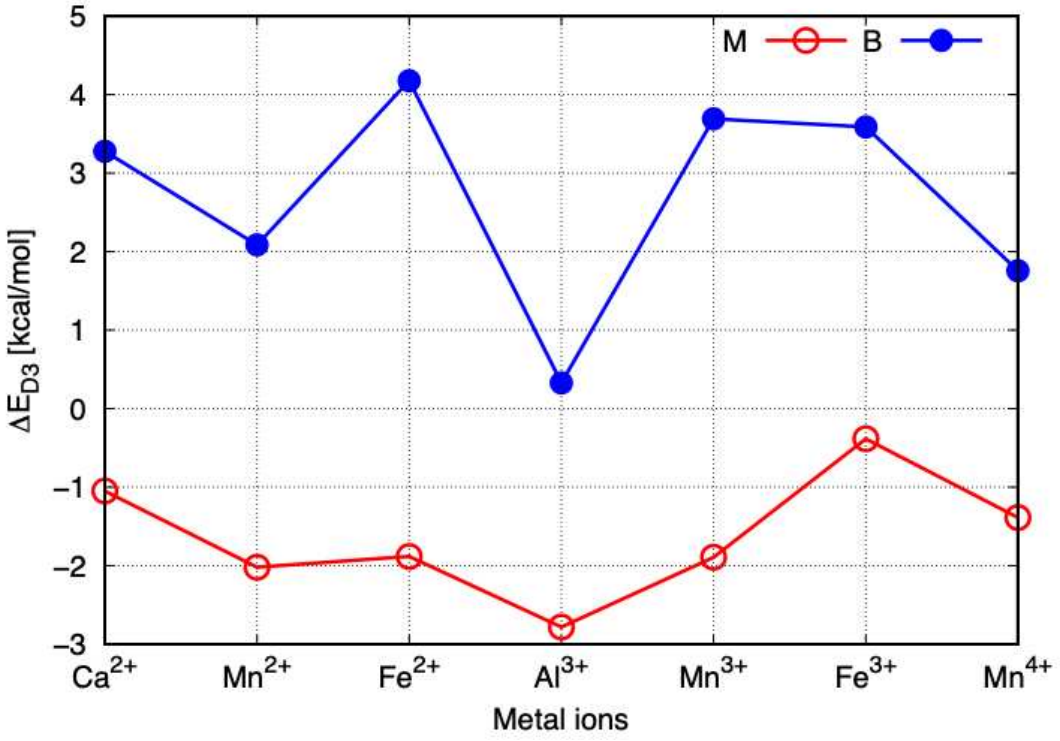


Figure S9 Calculated reaction energies due to the dispersion interactions (&E_{D3}) for the $M^{n+}3P_i$ complexation reaction in both **M** and **B** binding motifs. Red and blue colors correspond to **M** and **B** binding motifs for the $M^{n+}3P_i$ complexes, respectively. Data points are connected with lines for better visualization.

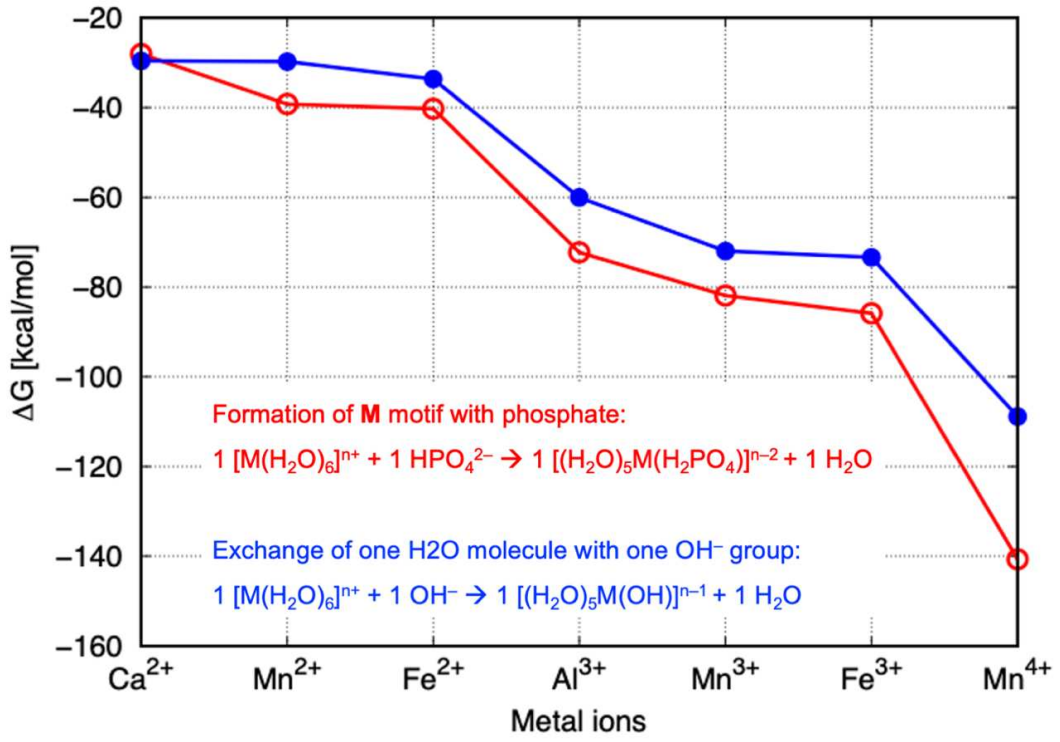


Figure S10 Calculated reaction free energies (&G) of the exchange reactions for relevant metal aqua-complexes by replacement of one water molecule either by one $H_2PO_4^{23}$ species to form $M^{n+}3P_i$ complex

with **M** binding motif (represented in red) or one OH^3 group (in blue). Data points are connected with lines for better visualization.

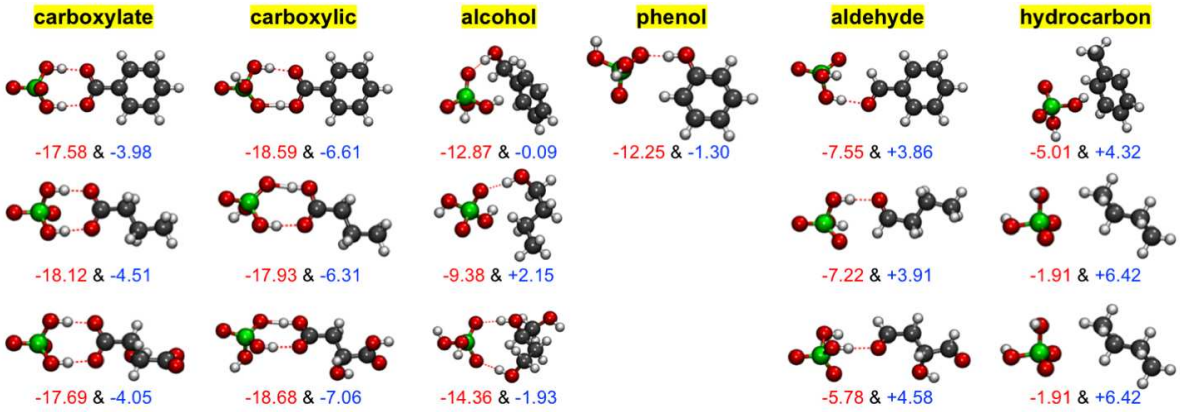


Figure S11 Optimized geometries for the $OM3P_i$ complexes formed between the $H_2PO_4^{13}$ species and each modeled organic matter (OM) functional group. The reaction/binding energy ($\&E_B$) and corresponding reaction/binding free energy ($\&G_B$) are given for each $OM3P_i$ complex in red and blue, respectively. H, O, P, and C atoms are visualized in white, red, green, and gray colors, respectively. Dashed red lines refer to H-bonds (HBs).

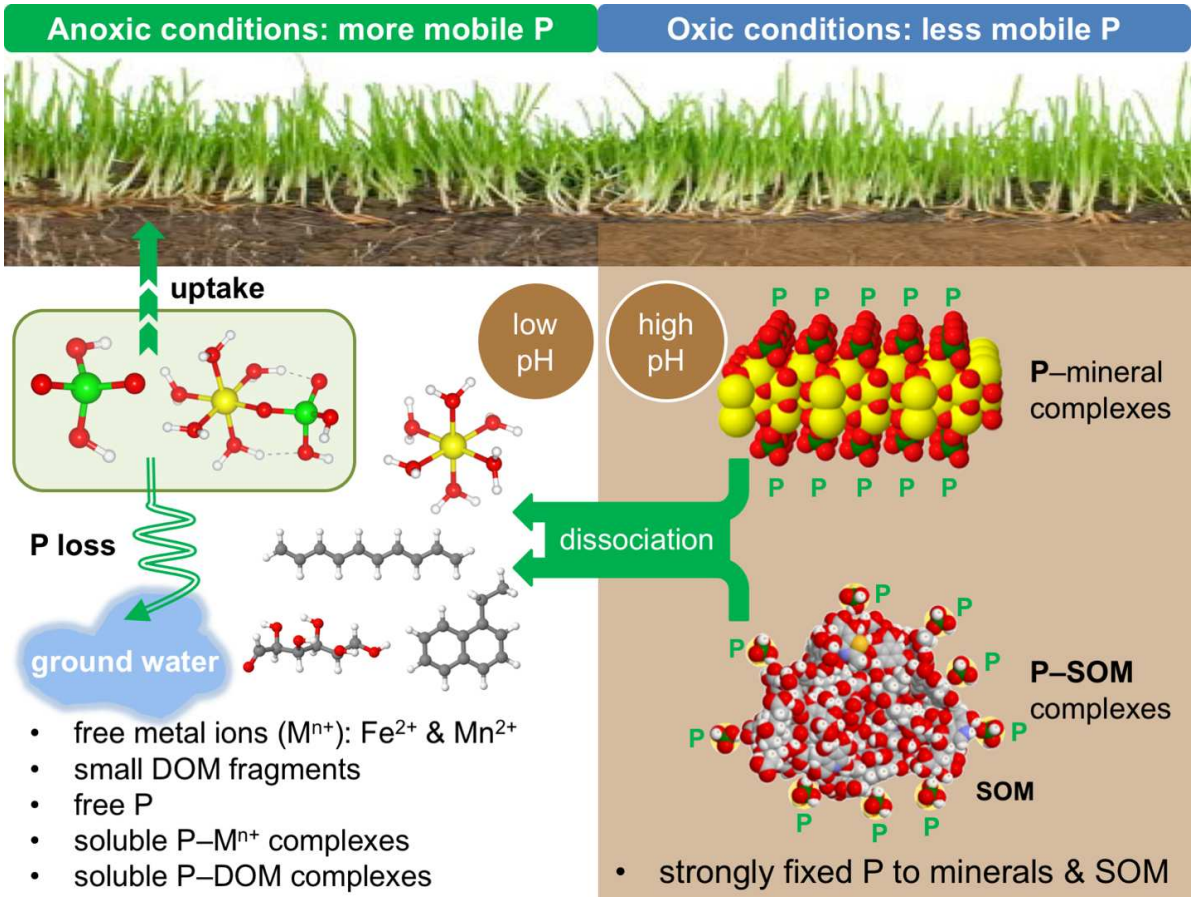


Figure S12 Conceptual model shows the different redox conditions and their effect on P mobility and P losses. H, C, N, O, P, and Fe atoms are visualized as spheres with white, gray, blue, red, green, and yellow colors, respectively; SOM: soil organic matter, DOM: dissolved organic matter.

References

Ahmed, A.A.; P. Gros, O. Kühn, P. Leinweber, Molecular level investigation of the role of peptide interactions in the glyphosate analytics, Chemosphere 196 (2018) 1293134.

Ahmed, A.A.; P. Leinweber, O. Kühn, Unravelling the nature of glyphosate binding to goethite surfaces by ab initio molecular dynamics simulations, Phys. Chem. Chem. Phys. 20 (2018) 153131539.

Ahmed, A.A.; S. Gypser, D. Freese, P. Leinweber, O. Kühn, Molecular level picture of the interplay between pH and phosphate binding at the goethite3water interface, Phys. Chem. Chem. Phys. 22 (2020) 26509326524.

Ahmed, A.A.; S. Gypser, P. Leinweber, D. Freese, O. Kühn, Infrared spectroscopic characterization of phosphate binding at the goethite3water interface, Phys. Chem. Chem. Phys. 21 (2019) 442134434.

Antelo, J.; M. Avena, S. Fiol, R. López, F. Arce, Effects of pH and ionic strength on the adsorption of phosphate and arsenate at the goethite3water interface, J. Colloid Interface Sci. 285 (2005) 4763486.

Arai, Y.; D.L. Sparks, ATR3FTIR Spectroscopic Investigation on Phosphate Adsorption Mechanisms at the Ferrihydrite3Water Interface, J. Colloid Interface Sci. 241 (2001) 3173326.

Arai, Y.; D.L. Sparks, Phosphate Reaction Dynamics in Soils and Soil Components: A Multiscale Approach, in: Adv. Agron., Elsevier, 2007: pp. 1353179.

Arroyave, J.M.; V. Puccia, G.P. Zanini, M.J. Avena, Surface speciation of phosphate on goethite as seen by InfraRed Surface Titrations (IRST), Spectrochim. Acta. A. Mol. Biomol. Spectrosc. 199 (2018) 573 64.

Barrow, N.J.; A mechanistic model for describing the sorption and desorption of phosphate by soil, J. Soil Sci. 34 (1983) 7333750.

Baumann, K.; Shaheen, S. M.; Hu, Y.; Gros, P.; Heilmann, E.; Morshedizad, M.; Wang, J.; Wang, S. L.; Rinklebe, J.; Leinweber, P. Speciation and sorption of phosphorus in agricultural soil profiles of redoximorphic character. Environ. Geochem. Health. 2020, 42, 323133246

Blume, H.-P., Stahr, K., Leinweber, P., 2011. Bodenkundliches Praktikum. 3. Auflage, Spektrum Akademischer Verlag, Heidelberg, p. 255.

Chapman, A.C., L.E. Thirlwell, Spectra of phosphorus compounds4 I the infra-red spectra of orthophosphates, Spectrochim. Acta. 20 (1964) 9373947.

Chitrakar, R. .; S. Tezuka, A. Sonoda, K. Sakane, K. Ooi, T. Hirotsu, Phosphate adsorption on synthetic goethite and akaganeite, J. Colloid Interface Sci. 298 (2006) 6023608.

Frostegård, Å., Tunlid, A., Bååth, E. Microbial biomass measured as total lipid phosphate in soils of different organic content. Journal of Microbiological Methods 1991, 14, 151-163.

Ganta, P.B.; M. Morshedizad, O. Kühn, P. Leinweber, A.A. Ahmed, The Binding of Phosphorus Species at Goethite: A Joint Experimental and Theoretical Study. Minerals. 11 (2021b) 323.

Ganta, P.B.; O. Kühn, A.A. Ahmed, Ab Initio Molecular Dynamics Simulations of the Interaction between Organic Phosphates and Goethite. Molecules. 26 (2021a) 160.

Ganta, P.B.; O. Kühn, A.A. Ahmed, QM/MM Molecular Dynamics Investigation of the Binding of Organic Phosphates to the 100 Diaspore Surface, Front. For. Glob. Change. 3 (2020).

Ganta, P.B.; O. Kühn, A.A. Ahmed, QM/MM simulations of organic phosphorus adsorption at the diaspore3 water interface, Phys. Chem. Chem. Phys. 21 (2019) 24316324325.

Geelhoed, J.S.; T. Hiemstra, W.H. Van Riemsdijk, Phosphate and sulfate adsorption on goethite: Single anion and competitive adsorption, Geochim. Cosmochim. Acta. 61 (1997) 238932396.

Gros, P.; A. Ahmed, O. Kühn, P. Leinweber, Glyphosate binding in soil as revealed by sorption experiments and quantum-chemical modeling, Sci. Total Environ. 586 (2017) 5273535.

Gros, P.; A.A. Ahmed, O. Kühn, P. Leinweber, Influence of metal ions on glyphosate detection by FMOC-Cl, Environ. Monit. Assess. 191 (2019).

Hiemstra, T.; W.H. Van Riemsdijk, A Surface Structural Approach to Ion Adsorption: The Charge Distribution (CD) Model, J. Colloid Interface Sci. 179 (1996) 4883508.

Hinsinger, P.; Bioavailability of soil inorganic P in the rhizosphere as affected by root-induced chemical changes: a review, Plant Soil. 237 (2001) 1733195.

Kruse, J.; M. Abraham, W. Amelung, C. Baum, R. Bol, O. Kühn, H. Lewandowski, J. Niederberger, Y. Oelmann, C. Rüger, J. Santner, M. Siebers, N. Siebers, M. Spohn, J. Vestergren, A. Vogts, P. Leinweber, Innovative methods in soil phosphorus research: A review, J. Plant Nutr. Soil Sci. 178 (2015) 43388.

Langer, U., Rinklebe, J. Priming effect after glucose amendment in two different soils evaluated by SIR- and PLFA-technique Ecological Engineering 2011, 37, 465-473

Li, L.; R. Stanforth, Distinguishing Adsorption and Surface Precipitation of Phosphate on Goethite (³ -FeOOH), J. Colloid Interface Sci. 230 (2000) 12321.

Liu, F.; A. De Cristofaro, A. Violante, Effect of pH, phosphate and oxalate on the adsorption/desorption of arsenate on/from goethite, Soil Sci. 166 (2001).

Persson, P.; N. Nilsson, S. Sjöberg, Structure and Bonding of Orthophosphate Ions at the Iron Oxide3 Aqueous Interface, J. Colloid Interface Sci. 177 (1996) 2633275.

Powell, K.J.; P.L. Brown, R.H. Byrne, T. Gajda, G. Hefter, S. Sjöberg, H. Wanner, Chemical speciation of environmentally significant heavy metals with inorganic ligands. Part 1: The $Hg^{2+}3$ Cl^{3}, OH^{3}, CO_3^{23}, SO_4^{23}, and PO_4^{33} aqueous systems (IUPAC Technical Report), Pure Appl. Chem. 77 (2005) 7393800.

Rietra, R.P.J.J.; T. Hiemstra, W.H. van Riemsdijk, Interaction between Calcium and Phosphate Adsorption on Goethite, Environ. Sci. Technol. 35 (2001) 336933374.

Rinklebe, J., Langer, U. Microbial diversity in three floodplain soils at the Elbe River (Germany). Soil Biology & Biochemistry 2006, 38, 2144-2151.

Rinklebe, J., Langer, U. Relationship between soil microbial biomass determined by SIR and PLFA analysis in floodplain soils. Journal of Soils and Sediments 2010, 10, 4-8.

Schnitzer, M.; Schulten, H.-R. The analysis of soil organic matter by pyrolysis field ionization mass spectrometry, Soil Sci. Soc. Am. J., 1992, 56, 181131817.

Schulten, H.-R. Pyrolysis and soft ionization mass spectrometry of aquatic/terrestrial humic substances and soils. J. Appl. Anal. Pyrolysis 1987, 12, 1493186.

Tejedor-Tejedor, M.I.; Anderson, M.A. The protonation of phosphate on the surface of goethite as studied by CIR-FTIR and electrophoretic mobility, Langmuir. 6 (1990) 6023611.

Urrutia, O.; I. Guardado, J. Erro, M. Mandado, J.M. García-Mina, Theoretical chemical characterization of phosphate-metal-humic complexes and relationships with their effects on both phosphorus soil fixation and phosphorus availability for plants, J Sci Food Agric. 93 (2013) 2933303.

Weishaar, J. L.; Aiken, G. R.; Bergamaschi, B. A.; Fram, M. S.; Fujii, R.; Mopper, K. Evaluation of specific ultraviolet absorbance as an indicator of the chemical composition and reactivity of dissolved organic carbon. Environ. Sci. Technol. 2003, 37, 470234708.

White, D.C., Davis, W.M., Nickels, J.S., King, J.D., Bobbie, R.J., 1979. Determination of the sedimentary microbial biomass by extractable lipid phosphate. Oecologia 40, 51-62.

Wolersdorfer, C., 2008 . Water Management at Abandoned Flooded Underground Mines: Fundamentals, Tracer Tests, Modelling, Water Treatment (Mining and the Environment)., 465 pp. Springer, ISBN 978-3-540-77331-3; https://www.wolkersdorfer.info/en/redoxprobes.html

Yu, K.; Rinklebe J. Advancement in soil microcosm apparatus for biogeochemical research. Ecol. Eng. 2011, 37, 207132075.

Publication 4

P. B. Ganta, O. Kühn, Ashour A. Ahmed. QM/MM simulations of organic phosphorus adsorption at the diaspore-water interface. Phys. Chem. Chem. Phys. **2019**, 21, 24316-24325.

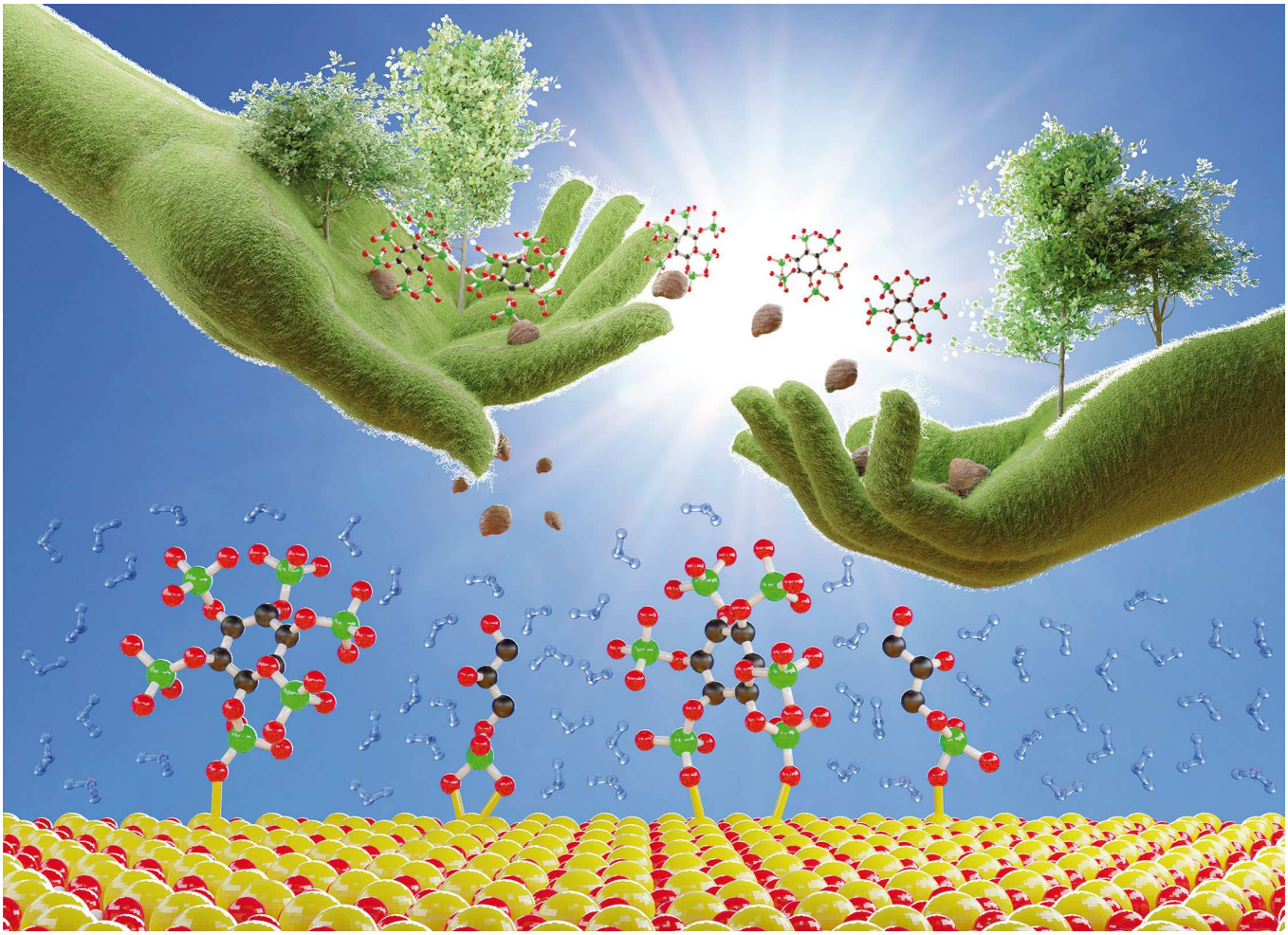
Contribution: Ashour A. Ahmed is credited with the conceptualization of the scientific approach for this study, development of the methodology, acquisition of funding, contribution to writing the original manuscript, and supervising the PhD student (Mr. P.B. Ganta). Ashour A. Ahmed, along with the co-authors, has discussed and interpreted the results and contributed to writing, reviewing, and editing the manuscript.

URL: https://doi.org/10.1039/C9CP04032C

QR:

Ashour Ahmed QM/MM1

Reproduced with the permission of the Royal Society of Chemistry (RSC)

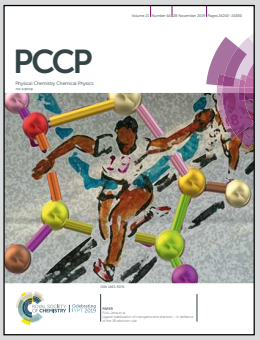


Showcasing research from the Group of Prof. Oliver Kühn at the University of Rostock, Germany

QM/MM simulations of organic phosphorus adsorption at the diaspore–water interface

The focus of the junior group led by Dr Ashour Ahmed is on the establishment of atomistic simulation techniques into the field of environmental chemistry and physics. A major target is phosphorous, its transport and immobilization in the soil. The present work highlights the nature and strength of the binding of the most abundant organic phosphates in forest eco-systems to the diaspore surface. For the diaspore–water interface, different binding motifs are explored. Further, the role of water in controlling binding strengths *via* formation of H-bonds and proton transfers, adsorption and dissociation at the surface is demonstrated.

As featured in:



See Ashour A. Ahmed *et al.*, *Phys. Chem. Chem. Phys.*, 2019, **21**, 24316.

ROYAL SOCIETY OF CHEMISTRY | Celebrating IYPT 2019

rsc.li/pccp

Registered charity number: 207890

PCCP

PAPER

Check for updates

Cite this: *Phys. Chem. Chem. Phys.*, 2019, **21**, 24316

QM/MM simulations of organic phosphorus adsorption at the diaspore–water interface†

Prasanth B. Ganta, [a] Oliver Kühn [ab] and Ashour A. Ahmed *[ab]

Received 18th July 2019,
Accepted 27th August 2019

DOI: 10.1039/c9cp04032c

rsc.li/pccp

Phosphorus (P) immobilization and thus its availability for plants are mainly affected by the strong interaction of phosphates with soil components especially soil mineral surfaces. The related reactions have been studied extensively *via* sorption experiments especially by carrying out adsorption of *ortho*-phosphates onto Fe-oxide surfaces. But a molecular-level understanding of the P-binding mechanisms at the mineral–water interface is still lacking, especially for forest eco-systems. Therefore, the current contribution provides an investigation of the molecular binding mechanisms for two abundant phosphates in forest soils, inositol hexaphosphate (IHP) and glycerolphosphate (GP), at the diaspore mineral surface. Here a hybrid electrostatic embedding quantum mechanics/molecular mechanics (QM/MM) based molecular dynamics simulation has been applied to explore the diaspore–IHP/GP–water interactions. The results provide evidence for the formation of different P-diaspore binding motifs involving monodentate (**M**) and bidentate (**B**) for GP and two (**2M**) as well as three (**3M**) monodentates for IHP. The interaction energy results indicated the abundance of the GP **B** motif compared to the **M** one. The IHP **3M** motif has a higher total interaction energy compared to its **2M** motif, but exhibits a lower interaction energy per bond. Compared to GP, IHP exhibited stronger interaction with the surface as well as with water. Water was found to play an important role in controlling these diaspore–IHP/GP–water interactions. The interfacial water molecules form moderately strong H-bonds (HBs) with GP and IHP as well as with the diaspore surface. For all the diaspore–IHP/GP–water complexes, the interaction of water with the diaspore exceeds that with the studied phosphates. Furthermore, some water molecules form covalent bonds with diaspore Al atoms while others dissociate at the surface to protons and hydroxyl groups leading to proton transfer processes. Finally, the current results confirm the previous experimental conclusions indicating the importance of the number of phosphate groups, HBs, and proton transfers in controlling the P-binding at soil mineral surfaces.

1 Introduction

Phosphorus (P) is a vital element supporting global food systems by enhancing soil fertility, plant growth and consequently the nutritional security of the world population. A P peak scenario has been predicted to arise this century[1] and thus P scarcity could become one of the most important global food security challenges. Knowledge about substantial P leaching as well as about a more efficient and sustainable use of P resources is still limited and needs to be enhanced.[2–4] For instance, P leaching accompanies heavy rains through the dispersion of rain water with soluble and adsorbed P.[5] In rain water, minerals retain about 50% of the existing P in the soil solution.[4,6] A major factor in the context of P efficiency is the interaction between P-containing compounds and soil components.[7] Specifically, phosphates bind strongly to soil mineral surfaces and especially to Fe- and Al-(oxyhydr)oxides.[8–10] This strong binding will reduce the availability of P to the plants and consequently reduce the P efficiency. Molecular level insight into this interaction could trigger a deeper understanding of the fate of P in the environment and eventually lead to smarter fertilisers with increased P efficiency.[4,8,11]

Organic and inorganic P (P_o and P_i) containing compounds play a substantial role in controlling the P environmental cycle. The most abundant P compounds in soils and especially forest ecosystems are orthophosphates,[12] inositolhexaphosphates (IHPs)[13–15] and glycerolphosphates (GPs).[16–18] In addition, Fe- and Al-(oxyhydr)oxides are among the most common P-fixing minerals found in forest soils.[19] The colloids of these minerals can adsorb P at their surfaces forming colloidal P complexes. Goethite (α-FeOOH) is one of the most abundant reactive soil minerals having a ferric ion (Fe^{3+}) in an iron oxyhydroxide chemical formula within the orthorhombic crystal system. In general, phosphates and especially orthophosphates show strong interactions with goethite and thus, these interactions are thoroughly studied.[20–23] Here, it was found that the

[a] *Institute of Physics, University of Rostock, Albert-Einstein-Str. 23-24, D-18059 Rostock, Germany. E-mail: ashour.ahmed@uni-rostock.de*
[b] *Department of Life, Light, and Matter (LLM), University of Rostock, Albert-Einstein-Str. 25, D-18059 Rostock, Germany*

† Electronic supplementary information (ESI) available. See DOI: 10.1039/c9cp04032c

This journal is © the Owner Societies 2019

number of phosphate groups in a certain P_o compound determines the stability of its complex with the mineral surface.[24] For instance, IHP with its six phosphate groups generally exhibits a strong binding and high stability compared with other P_o compounds with a smaller number of phosphate groups. Ognalaga *et al.*[25] showed that IHP interacts with goethite *via* the formation of inner-sphere complexes between the IHP phosphate groups and the goethite surface Fe atoms. It was suggested that IHP binds to the goethite surface by up to four phosphate groups. The remaining non-interacting phosphate groups induce a modification of the electro-chemical properties, for instance, IHP adsorption causes particle dispersion and a net increase of the negative charge of the surface. The IHP organic moiety affects only the conformational flexibility of the binding motif. In addition, very little dissolution of the goethite surface has been observed during the adsorption process. Adsorption experiments and FTIR results by Celi *et al.*[26] confirmed the above conclusions by Ognalaga *et al.*[25] In contrast, FTIR and adsorption experiments by Guan *et al.*[27] showed that only three phosphate groups in IHP were bound to the amorphous aluminium hydroxide while others remained free.

The binding capabilities of IHP can be compared with those of GP which has a single phosphate group only. Li *et al.*[28] suggested that GP adsorbs onto the goethite surface by forming inner-sphere complexes through the phosphate group. Moriguchi *et al.*[29] showed that GP adsorbs onto hydrated iron (Fe^{3+}) oxide precipitates. In addition, GP exhibits strong interaction with boehmite, α-Al_2O_3 and $Al(OH)_3$,[30] and also with ferric oxide.[31]

Despite the presence of quite a few studies reporting on the binding of IHP and GP to the goethite surface, almost nothing is known about the interaction of these P_o compounds with the diaspore surface. Diaspore (α-AlOOH) is isomorphous with goethite having an Al^{3+} oxidation state instead of Fe^{3+}. Compared with goethite it exhibits a higher surface energy.[32] In soil minerals amorphous Fe/Al hydroxide mixtures are present, thus having a more detailed knowledge about the P interaction with diaspore will provide a better understanding of the P interaction with these soil mineral components.

Accompanying experimental studies, molecular level simulations are emerging as an important tool in soil sciences.[33] For instance, Kubicki *et al.*[34,35] analysed different phosphate–goethite complexes in terms of their fingerprints in infrared vibrational spectra. Recently, Ahmed *et al.*[23] performed *ab initio* simulations of infrared spectra and the associated binding motifs for the phosphate at the goethite–water interface. A comparison with experiments emphasised the importance of combining the results from different binding motifs and surface planes in order to account for the heterogeneous nature of the samples. A similar statistical approach has been proven useful also for the description of the interactions of pollutants with soil organic matter.[36,37] Taking into account solvating water molecules in the simulations is essential for a realistic description of the P–mineral surface interaction, which has also been concluded from a study of glyphosate at the goethite–water interface.[38]

A similar molecular level analysis of the IHP and GP interaction with the diaspore surface is missing so far, which provides motivation for the present study. The main objective of this work is to characterise the adsorption of IHP and GP at the diaspore–water interface on the basis of periodic boundary quantum mechanics/molecular mechanics (QM/MM)[39] molecular dynamics simulations. To this end, a systematic analysis of the binding motifs, proton transfers, intramolecular and intermolecular hydrogen bonds (HB), interaction energies and the competition between water and IHP/GP adsorption onto the diaspore surface will be presented.

2 Computational details

2.1 Model systems

The interaction of IHP and GP with diaspore will be investigated by considering the 010 diaspore surface plane (according to the *Pnma* space group) which corresponds to the 001 diaspore surface plane within the *Pbnm* space group. The orthorhombic diaspore unit cell has 16 atoms, *i.e.*, four AlO(OH) formula units with lattice constants a = 4.4007, b = 9.4253, and c = 2.8452 Å (according to the *Pbnm* space group), see Fig. 1a. The surface plane slab was generated by repetition of the diaspore unit cell as $5a \times 2b \times 4c$, Fig. 1b and c. This slab model consists of 640 atoms (160 Al, 160 H, and 320 O atoms). Each top surface Al atom of the slab is coordinated by four O atoms, see Fig. 1c. This means that in the present contribution the diaspore has been simulated as an unsaturated surface. The main reason for that is the diaspore has point of zero charge (PZC) around 6.[40] Consequently, at pH below 6, the diaspore surface will be partially unsaturated and exhibit a positive charge. Thus it has the ability to attract/adsorb anions such as phosphates and/or hydroxyl groups. More details about modeling of the diaspore surface is given in the ESI.† It is important to mention that here we are simulating common and normal acidic soil conditions, *i.e.* in the pH range of 3–6.

The initial binding motifs are modelled to have phosphate group(s) of GP and IHP interacting with the Al atoms of the diaspore surface. GP has one phosphate group, see Fig. 2a, and IHP has six phosphate groups, see Fig. 2b. To differentiate between phosphate groups in the IHP, each phosphorus is color-coded and denoted as Px, where x = 1, 2..., 6 and the corresponding oxygens are denoted as Ox1 (non-protonated oxygen), Ox2 and Ox3 (OH functional group oxygens), and Ox4 (oxygen bonded with carbon) with the same color as the

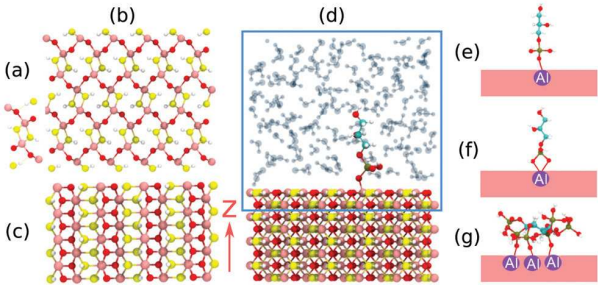


Fig. 1 Diaspore unit cell (a), top view (b) and side view of the modelled diaspore surface (c), the diaspore–GP–water complex (d), the **M** motif (e), the **B** motif (f), and the **3M** motif (g). Pink, red, yellow, white and lime colors correspond to Al, bridging oxygen, hydroxyl oxygen, hydrogen and phosphorus respectively.

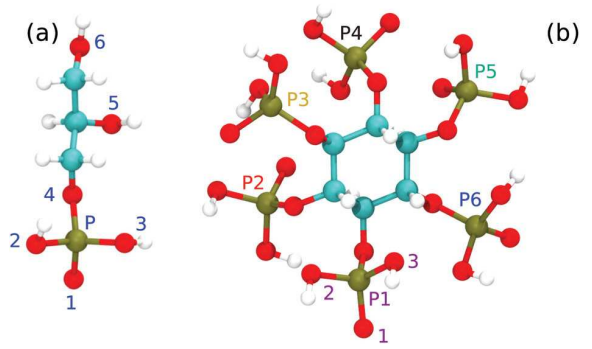


Fig. 2 Molecular structure of glycerolphosphate ($C_3H_9O_6P$, GP) (a) and inositol hexaphosphate ($C_6H_{18}O_{24}P_6$, IHP) (b). In general all the phosphate groups are equivalent. The oxygen and phosphorus atoms are labelled to ease the discussion of diaspore–IHP/GP–water interactions.

corresponding phosphate, see Fig. 2b. More details about modelling of IHP and GP are given in the ESI.†

A vacuum layer of about 18 Å was added between the periodic slabs perpendicular (along the z axis) to the studied surface plane. Then, GP was added into the vacuum region with its long axis perpendicular to the surface and solvated, see Fig. 1d. Here, the GP's phosphate group was aligned to bind to the surface Al atoms *via* two different binding motifs. These motifs involved the formation of diaspore–GP complexes with monodentate (**M**, 1 covalent bond between 1 phosphate O atom and 1 surface Al atom), see Fig. 1e and bidentate (**B**, 2 covalent bonds between 2 phosphate O atoms and 1 surface Al atom), see Fig. 1f bonds. The same binding motifs have been considered for the diaspore–IHP complex. In addition, another binding motif (**3M**, 3 phosphate O atoms with 3 Al atoms) Fig. 1g was modelled for the IHP interaction with the diaspore surface. The choice of the latter motif is mainly based on the experimental studies in ref. 25 and 27 which concluded a higher number of IHP–surface bonds. It is important to mention that having different starting configurations for each binding motif could give more insight into understanding the diaspore–IHP/GP interactions. However, this was not possible within a reasonable time due to the size of the modeled systems and the used computationally expensive QM/MM level of theory. To simulate the soil solution and its vital role in controlling the interaction of the P containing compounds with the mineral surfaces,[38] the modelled diaspore–IHP/GP complexes are solvated with water at a density of about 1 g cm^{-3} using the solvate plugin provided by the VMD package,[41] see Fig. 1d. For each model, the slab bottom layer atoms were kept fixed to approximate the properties of the underlying extended diaspore bulk and to diminish artefacts due to the interaction with water of the next box image. Except for these fixed atoms, all other MM atoms including the MM water molecules are left fully flexible during the MD simulations.

2.2 QM/MM setup

The accuracy provided by the *ab initio* methods comes at high computational costs which restricts the applicability to systems with a few hundred atoms at best. The modelled diaspore–IHP/GP–water complexes include about 1200 atoms and therefore cannot reasonably be treated by pure *ab initio* methods. Reducing the system size, however, always bears the danger of artefacts due to the finite simulation box in combination with periodic boundary conditions. Setting the focus on the adsorption of the P-compounds, *i.e.* a process which is local at the mineral–water surface, a full *ab initio* treatment is not necessary and a hybrid QM/MM approach is the method of choice.[39] In the present case, the QM (reactive) part is chosen to include the top two layers of the diaspore surface (160 atoms), IHP (54 atoms)/GP (19 atoms), and solvating water within a layer of ≈10 Å perpendicular to the surface (≈114 atoms). The size of the QM box is $5a \times 2b \times 22$ Å *i.e.* 22.0035 × 18.8506 × 22 Å, where a and b are the diaspore lattice constants. The remaining part of the system is treated at the MM level. Thereby electrostatic embedding is used, including the polarization of the QM atoms by the MM atoms. The QM/MM implementation is performed employing the CP2K[42] package, where QM is treated by the quickstep code[43] and MM by the FIST package.[44] For the QM method, density functional theory (DFT) was adopted with the hybrid Gaussian and plane wave (GPW) dual basis method, wherein the atom centered Gaussian basis describes the wave function and the auxiliary plane waves describe the electron density. The core electrons are replaced by Goedecker–Teter–Hutter (GTH) pseudopotentials[45] and the Perdew–Burke–Ernzerhof (PBE)[46] version of generalized gradient approximation (GGA) was used as an exchange–correlation functional. To account for the van der Waals forces, the D3 empirical dispersion correction[47] was adopted. The electronic density cut-off of the auxiliary plane wave basis is set to 500 Ry. The double-ζ valence polarized (DZVP-MOLOPT-SR-GTH), MOLOPT[48] basis sets that reduce the computational cost for condensed phase systems and minimize the basis set superposition error (BSSE) are used except for water atoms. The single-ζ valence basis set was selected for the water atoms to further reduce the computational costs. An SCF energy convergence study was performed for various configurations and a convergence threshold of 10^{-5} was chosen. In the MM part, water is modeled using a SPC[49] based water model and the surface is modelled with CLAYFF force fields,[50] see Tables S1 and S2 in the ESI.† These force fields are suitable to simulate mineral surfaces and their corresponding water interfaces. CHARMM force fields for IHP and GP are obtained *via* the SwissParm force field generation tool,[51] see Table S3 and Fig. S1 in the ESI.† The QM/MM driver in CP2K is the Gaussian expansion of the electrostatic potential method (GEEP),[52] wherein the MM atom charges are described using Gaussians to prevent electron spill out and to accelerate QM/MM electrostatic calculations. More details about the current implementation of the QM/MM approach are given in the ESI.† The parameters used in the current QM/MM approach are validated by comparing pair correlation functions and P–O–Al bond formations observed in pure QM and QM/MM trajectories as shown in Fig. S2 and S3 in the ESI.† Periodic boundary conditions (PBC) are applied in all the three spatial directions to the whole molecular system involving the diaspore surface, phosphate species (IHP/GP), and all water molecules. A total of 25 ps *NVT*-MD simulations are performed with a time step of 0.5 fs. To maintain the average

 This journal is © the Owner Societies 2019

temperature of the system around 300 K, the canonical sampling through velocity rescaling thermostat (CSVR)[53] approach is used with 100 fs time constant. The first 10 ps are considered as equilibration (see Fig. S4 in the ESI†) of the system and the production trajectory (remaining 15 ps) was used for analysis of the diaspore–IHP/GP–water interactions.

To characterize the complexation reaction between the modeled phosphate species (IHP/GP) and the diaspore surface, the interaction energy (E_{int}) between each phosphate species and the diaspore surface is calculated at every 100 fs along the production trajectory. For example, for the complexation reaction diaspore + GP → diaspore–GP–complex, E_{int} between GP and the diaspore surface is calculated as follows:

$$E_{int} = E_{diaspore-GP-complex} - (E_{diaspore} + E_{GP}) \quad (1)$$

where, $E_{diaspore-GP-complex}$, E_{GP}, and $E_{diaspore}$ are the total electronic energies of the diaspore–GP–complex, GP, and the diaspore surface, respectively. Here, the BSSE is corrected using the counterpoise scheme.[54] Similarly, the interaction energies between IHP and diaspore, water and diaspore, GP and water, and IHP and water are calculated. For each model, the interaction energy between each of the two subsystems is calculated for 150 snapshots along the production trajectory and the time-averaged value is presented here. For more details regarding the calculation of interaction energies, see the ESI.† Energies related to the interaction with water will also be given as per the water molecule, *i.e.* by dividing the total energy by the total number of water molecules in the box.

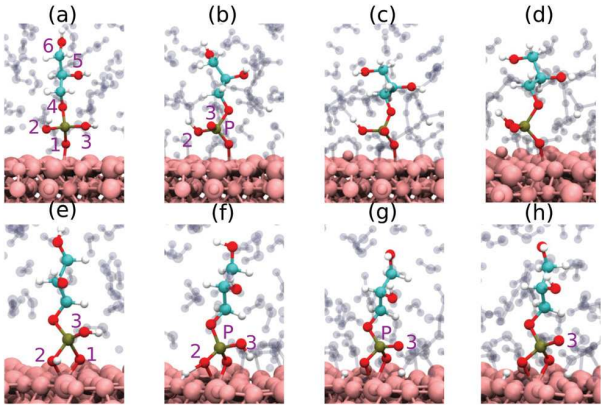


Fig. 3 Snapshots along the trajectories of diaspore–GP–water models. Initial **M** (O + Al) motif (a), proton transfer from O3 to water (b), at 20 ps (c), a stable **M** motif at 25 ps (d), the initial **B** (2O + Al) motif (e), proton transfer from O2 to diaspore (f), proton transfer from O3 to diaspore (g), a stable **B** motif at 25 ps (h).

3 Results and discussion

3.1 Diaspore–GP–water interactions

3.1.1 GP M motif. In this model, initially the long side of GP was placed perpendicular to the diaspore surface in forming an **M** binding motif between the GP's non-protonated oxygen atom (O1) and the central surface Al atom, see Fig. 3a. The MD simulation results show that a stable monodentate complex is formed between GP and the diaspore with an Al–O1 average bond length of 1.90 Å. P–Ox and Al–Ox interatomic distances are given in the ESI† (Fig. S5b and S6a). Two proton transfer events are observed from O3 and O5 of GP to water, see Fig. 3c and d. It is to be noted that the proton transfer events are not entirely a consequence of diaspore–GP binding, but they are also observed in the simulations carried out in the bulk, see Fig. S7 and S8 (ESI†). The average geometry of the PO_4 moiety is rather close to that of a free tetrahedral PO_4^{3-} with a RMSD of 0.06 Å (see Table 1 and Fig. S5a, b and S6a in the ESI†).

On average 7 HBs are observed between GP and water in the production trajectory. In the following, HB strengths are analysed using their geometrical correlations expressed in terms of the coordinates q_1 and q_2,[55–57] where $q_1 = \frac{1}{2}(r_1 - r_2)$ Å and $q_2 = (r_1 + r_2)$ Å. Here r_1 and r_2 denote the distance between donor oxygen and hydrogen (O_D–H) and the distance between hydrogen and acceptor oxygen (H···O_A), respectively, see Fig. 4. Thus, for a linear HB q_1 and q_2 denote the deviation of the hydrogen from the center of the HB and the total HB length, respectively. In addition $q_1 < 0$ indicates that the hydrogen stays with the donor oxygen, whereas $q_1 > 0$ denotes a proton transfer to the acceptor. A HB will be called strong if r_2 is about 1.2–1.5 Å and thus q_2 is about 2.2–2.5 Å. In addition $r_1 \approx r_2$ *i.e.* q_1 is close to zero. Similarly, moderate and weak HBs

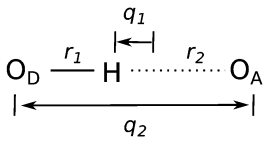


Fig. 4 Definition of HB coordinates q_1 and q_2.[56]

Table 1 Time-averaged interaction energies (E_{int} according to eqn (1) divided by the number of bonds in the motif) of diaspore–IHP/GP, selected bond lengths and distances as well as the RMSD of the average phosphate geometry from that of the isolated PO_4^{3-} one (*cf.* Fig. S5 and S6 in the ESI). Here, 'motif' denotes the final motif adopted in the production trajectory, Al and O_p denote covalent bonded Al and IHP/GP O atoms. The P denotes the phosphorus atom of the phosphate group bonded to Al and **2M(1)** and **2M(2)** denote the two different **2M** motifs of IHP

P_o	Motif	E_{int}/bond (kcal mol^{-1})	Al–OP (Å)	Al–P (Å)	RMSD(PO_4^{3-}) (Å)
GP	**M**	−63	1.90	3.3	0.06
	B	−148	2.03 & 2.05	2.65	0.10
IHP	**2M(1)**	−170	1.84 & 1.87	3.15 & 3.25	0.06 & 0.10
	2M(2)	−115	1.91 & 2.07	2.92 & 3.19	0.10 & 0.19
	3M	−145	1.90 & 1.88 & 1.86	3.25 & 3.17 & 3.18	0.07 & 0.08 & 0.10

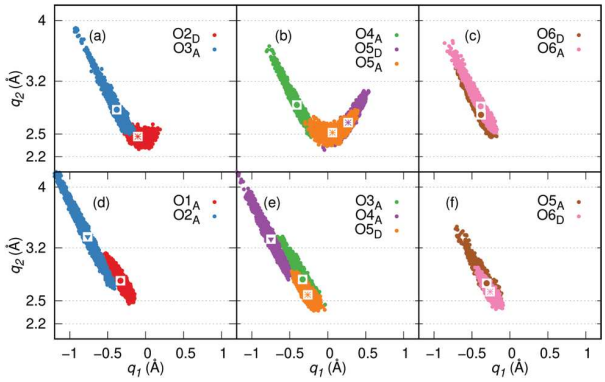


Fig. 5 HB correlation q_2 *vs.* q_1 of the GP **M** motif (a–c) and the GP **B** motif (d–f), respectively, along the production trajectory. The points in white square boxes denote the average values of q_1 and q_2. Here, the symbols *, ● and ▼ denote strong to moderately strong HB, moderately strong HB and moderately strong to weak HB respectively.

have r_2 distances in the range of 1.5–2.2 (q_2 from 2.5–3.2 Å and $r_1 < r_2$) and 2.2–3.2 Å (q_2 from 3.2–4 Å and $r_1 \ll r_2$), respectively.[58]

The trajectory data will be analysed by taking snapshot geometries for all the observed HBs. In addition the averaged q_2 and q_1 lengths will be given. The results for the GP **M** motif are shown in Fig. 5. Panel (a) considers the O2 atom which forms a moderate to strong HB and O3 being involved in a weak to moderately strong HB. According to Fig. 5b O4 forms a weak to moderately strong HB, whereas from O5 a proton is transferred to a water oxygen ($r_2 < r_1$). The transferred proton forms a moderate to strong HB with the donating O5. In addition, O5 is an acceptor for a HB with a water H atom. From Fig. 5c we notice that O6 acts as both, donor and acceptor for moderately strong HBs. From the overall analysis of HB strengths, 3 (O2, $O5_D$, and $O5_A$) strong to moderately strong HBs and 4 (O3, O4, $O6_D$, and $O6_A$) moderately strong HBs are observed. In this study H-bond analysis is performed only for the QM part of the system because we are mainly interested in the interface region. This region is our reactive system which includes all reactions concerning and affecting the surface binding/adsorption process.

Regarding the diaspore–water interaction, an average of 19 water molecules (out of 20 possible) formed **M** binding motifs (Al–O_{H_2O}) with the diaspore surface. The oxygen atoms of water, O_{H_2O} are bound to the surface Al atoms of the diaspore with average bond lengths in the range of 1.8 to 2.0 Å. Around five protons transferred to the diaspore surface after dissociation of a few water molecules near the surface. In addition to the proton transfers and covalent bonds, moderate to strong HBs are also observed between water and diaspore, see Fig. S9a and b in the ESI.†

The analysis of the time averaged interaction energies of the production trajectory provides a quantitative measure for the significance of the bonds and proton transfers discussed above. The average interaction energy between diaspore and GP is around −63 kcal mol^{-1}, see Table 1. The average interaction energy values per water molecule with diaspore and GP are −9.8 and −2.2 kcal mol^{-1} respectively. This indicates that water has a stronger interaction with diaspore than with GP due to several **M** motifs (1Al–1O_{H_2O}), proton transfers and HBs formed between water and the diaspore surface. This appears to be a general observation valid for all the studied diaspore–IHP/GP–water models (see below).

3.1.2 GP B motif. The starting configuration the phosphate group is placed in a **B** (2O + 1Al) motif with a surface Al atom and the long side of GP perpendicular to the diaspore surface, see Fig. 3e. A stable **B** motif complex is observed throughout the trajectory, see Fig. S10 in the ESI.† The average covalent bond length of Al–O1 and Al–O2 is 2.03 and 2.05 Å, respectively. Note that these bond lengths are larger than those of the **M** motif, see Table 1. The distance between the P atom and the bonded Al atom has an average value of around 2.65 Å, which is shorter than the one observed in the **M** motif, see Table 1. Hence, establishing a cyclic closed-membered ring structure at the Al site in the **B** motif requires the O1–P–O2 angle to widen, while P moves closer to the surface. As a consequence the average geometry of the PO_4 moiety has a RMSD value of 0.10 Å with respect to the free tetrahedral PO_4^{3-} (see Table 1 and Fig. S5c and S6b in the ESI†).

The proton bonded to oxygen O2 is transferred to the surface in the first 5 ps of the trajectory, see Fig. 3f and thus both oxygens bonded to the Al atom are non-protonated in the production trajectory. This could be the reason for similar covalent bond lengths for the Al–O1 and Al–O2 bonds. The P–O*x* and Al–O*x* interatomic distances are given in the ESI† (Fig. S5c and S6b). Observe that O3 is closer to Al compared to the **M** motif, see Fig. S6a and b in the ESI.† In contrast to the **M** motif, two protons are transferred from O2 and O3 to the surface, see Fig. 3h. Moderately strong HBs are formed between oxygens O1, O2 and protons transferred to the surface, see Fig. S5c in the ESI.†

Similar to the **M** motif, GP forms an average of 7 HBs with water. Geometrical correlations and HB strengths can be taken from Fig. 5. Observe that 2 (O5 and O6) strong to moderately strong HBs, 3 (O1, O3, and O5) moderately strong HBs and 2 (O2 and O4) moderately strong to weak HBs are formed, see Fig. 5d–f. Altogether, GP often forms moderately strong HBs with water see Fig. S11a and b in the ESI.† The interaction of water with the diaspore surface in the **B** motif is similar to the interaction of water with the diaspore in the **M** motif.

The average interaction energy between GP and diaspore for the **B** motif is −295 kcal mol^{-1}, *i.e.* −148 kcal mol^{-1} per bond, see Table 1. This interaction energy is more than twice of the interaction energy calculated per bond in the **M** motif case. The increased interaction energy is due to the two proton transfer processes from GP to the diaspore surface. Therefore, the formation of the **B** motif is more favourable compared to the formation of the **M** motif. The average interaction energy per water molecule with GP is −0.78 kcal mol^{-1}. A weaker GP–water interaction energy is observed compared to the **M** motif case since in the latter two proton transfers to the water solvation shell are found.

3.2 Diaspore–IHP–water interactions

3.2.1 IHP 2M motifs. Here, two different initial configurations of the diaspore–IHP–water model have been modelled and both

 This journal is © the Owner Societies 2019

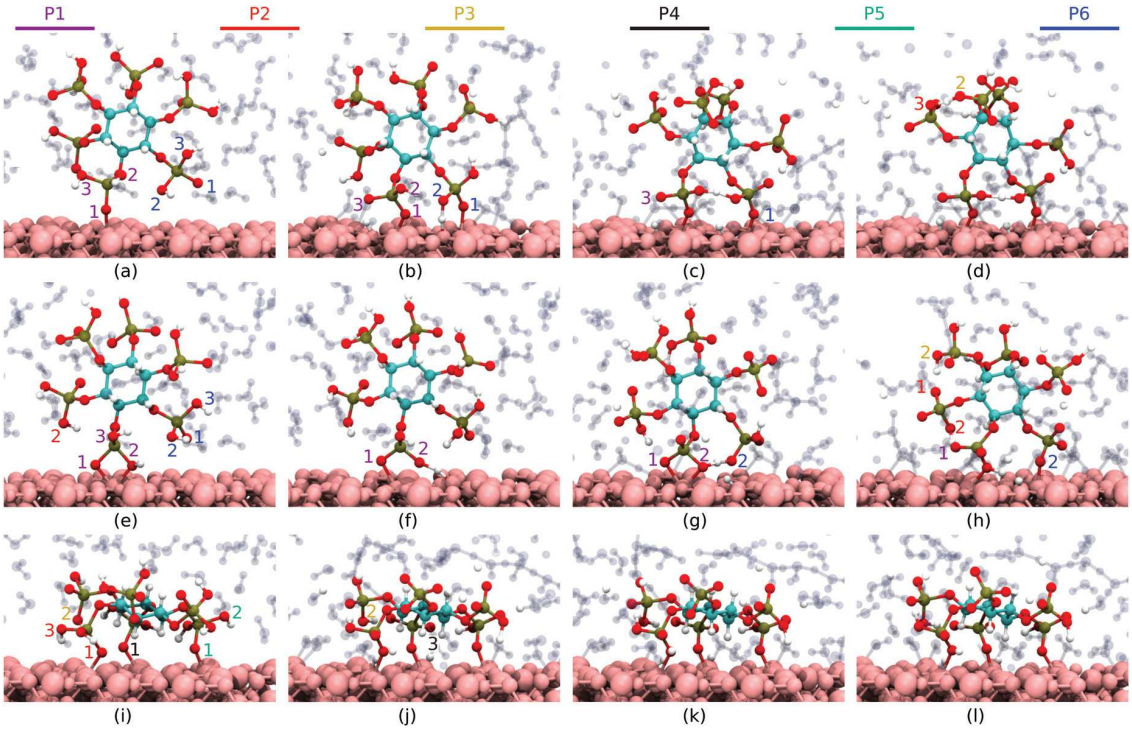


Fig. 6 Snapshots along the trajectories of diaspore–IHP–water models. Here, the phosphate groups are color-coded and the oxygen label color denotes the phosphate group it belongs to. Initial **M** (O + Al) motif (a), proton transfer from O13 and O62 to the surface and formation of the Al2–O61 covalent bond (b), proton sharing between P1 and P6 phosphate groups (c), a stable **2M** motif (d), the initial **B** (2O + Al) motif (e), proton transfer from O12 to the surface (f), proton sharing and HB between P1 and P6 phosphate groups (g), HB between P1 and P2 phosphate groups and a broken Al2–O62 covalent bond (h), the initial **3M** motif (i), proton transfer from O43 to the surface and protonation of O32 (j), and a stable **3M** motif (k) and (l).

cases finally transformed to **2M** motifs (2 covalent bonds between 2 phosphate's 2 O atoms and 2 surface Al atoms). In the first case, **2M(1)**, a non-protonated IHP phosphate oxygen atom (O11) is aligned to form a **M** motif with a surface Al atom (Al1) and the remaining part of IHP is aligned perpendicular to the diaspore surface, see Fig. 6a. The MD results show that within 2 ps, O61 forms a covalent bond with another surface Al atom (Al2), adjacent to Al1. A stable **2M** binding motif is observed between IHP and diaspore with Al1–O11 and Al2–O61 average covalent bond lengths of 1.84 and 1.87 Å, see Fig. S12b in the ESI† and Fig. 6d, respectively. Further, the average geometries of the PO_4 moieties deviate from that of a free tetrahedral PO_4^{3-} with RMSD values of 0.06 and 0.10 Å (see Table 1 and Fig. S5d and S6c in the ESI†).

The series of events which unfolds to form the stable **2M(1)** motif starting from Fig. 6a is as follows: from O13 a proton is transferred to the surface, followed by HB formation between the transferred proton and the donating oxygen O13. After a few fs a HB to the surface from O62 oxygen of the P6 phosphate group is formed, see Fig. 6b. After the formation of this HB, the P6 phosphate group is now close to the surface and the non-protonated oxygen atom (O61) of the P6 phosphate makes a covalent bond with Al2. The formation of HBs between IHP's phosphate group and the surface supported the formation of the Al2–O61 covalent bond. For P–O1*x*, P–O6*x*, Al1–O1*x* and Al2–O6*x* interatomic distances, where x = 1, 2, 3, and 4, see Fig. S5d and S6c in the ESI.† Notice that the bond lengths, P–O–Al angle and distances observed between Al1 and the P1 phosphate group are shorter than those between Al2 and the P6 phosphate group, *i.e.* the two binding sites are not equivalent. The distance between Al1 and all P atoms along the course of the trajectory is shown in Fig. S12a in the ESI.†

A total of two proton transfer processes is observed from IHP to the surface, one proton transfers from O13 and it forms a moderately strong HB with the donating oxygen atom O13. Another proton transfers from O62 to form a moderately strong to weak HB with O62, see Fig. 7a ($r_2 < r_1$). In addition to the intermolecular HBs, strong to moderately strong intramolecular

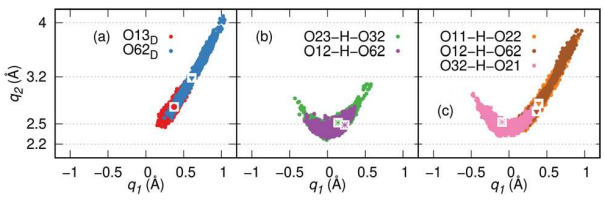


Fig. 7 HB correlation q_2 *vs.* q_1 of O13, O62 and protons transferred to the surface in IHP **2M(1)** motif (a), intramolecular HBs in IHP observed in the IHP **2M(1)** motif (b) and the IHP **2M(2)** motif (c). The points in white square boxes denote the average value of q_1 and q_2 along the course of the corresponding production trajectory. Here, the symbols *, ● and ▼ denote strong to moderately strong HB, moderately strong HB and moderately strong to weak HB respectively.

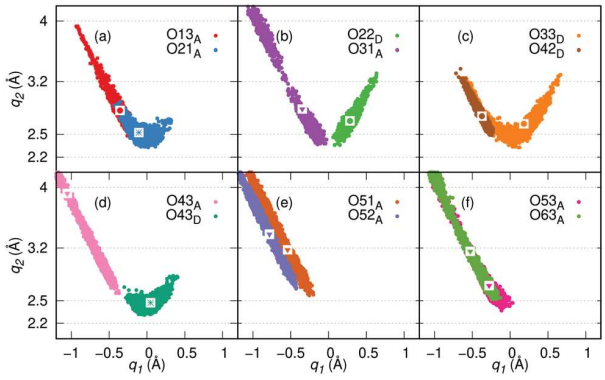


Fig. 8 HB correlation q_2 *vs.* q_1 of IHP and water in the IHP **2M(1)** motif (a–f). The points in white square boxes denote the average value of q_1 and q_2 along the course of the corresponding production trajectory. Here, the symbols *, ● and ▼ denote strong to moderately strong HB, moderately strong HB and moderately strong to weak HB, respectively.

HBs are observed in IHP, namely O12–H–O62 and O23–H–O32 (see Fig. 7b). Regarding the IHP interaction with water, a total of 5 proton transfers are observed from IHP to water with an average of 19 HBs between IHP and water. Upon analyzing HB strengths between IHP and water using the q_2 *vs.* q_1 correlation, 2 (O21 and O43) strong to moderately strong HBs, 4 (O13, O22, O33, and O42) moderately strong HBs and 6 (O31, $O43_A$, O51, O52, O53, and O63) moderately strong to weak HBs are formed, see Fig. 8. Note that in Fig. 8b O22 exhibits a proton transfer ($r_2 < r_1$). In addition, it is also observed that the water molecules tend to move closer to the diaspore surface during the course of the simulation, see Fig. S12c and d in the ESI.†

The time-averaged interaction energy between IHP and the diaspore surface is −340 kcal mol^{-1}, *i.e.* −170 kcal mol^{-1} per bond, see Table 1. The interaction energy of IHP with diaspore is higher than that of the GP **B** motif. The average interaction energy per water molecule with IHP is −6.9 kcal mol^{-1}. Observe that the interaction of water with IHP is stronger than that with GP.

Given the size and flexibility of IHP a number of different configurations can be expected for a given motif. Exemplarily, we discuss a second **2M** motif, in the following called **2M(2)**. It has been obtained starting with a **B** motif, where the phosphate group is placed such that the surface Al atom forms a **B** motif with O11 and O12 oxygens and the remaining part is aligned perpendicular to the diaspore surface, see Fig. 6e. The stable **2M(2)** motif which is obtained is shown in panel (h). The P6 phosphate group forms an additional covalent bond with another surface Al atom (Al2), which is adjacent to the P1 phosphate group bonded surface Al atom (Al1). The average covalent bond length of Al1–O12 and Al2–O62 is 1.91 and 2.07 Å, respectively. Further, the average geometries of the PO_4 moieties deviate from that of a free tetrahedral PO_4^{3-} with RMSD values of 0.10 and 0.19 Å (see Table 1 and Fig. S5e and S6d in the ESI†).

One proton transfer occurs from IHP to diaspore which forms a HB with the bonded oxygens O12 and O62. The series of events that led to the formation of **2M(2)** is as follows: a proton is transferred from O12 to the diaspore surface followed by intramolecular HB formation between O12 and O62 (O12–H–O62), see Fig. 6f. The HB pulls O62 close to the surface, see Fig. 6g and supports the formation of the Al2–O62 covalent bond. After a few ps, the covalent bond between the non-protonated oxygen O11 and Al1 (see Fig. S13 in the ESI†) is distorted by a moderately strong to weak intramolecular HB formed between O11 and O22 (O11–H–O22). In addition two moderately strong to weak intramolecular HBs (O11–H–O22 and O12–H–O62) are present (see Fig. 6h and 7c).

In addition to the O11–H–O22 intramolecular HB, another reason for dissociation of the Al1–O11 covalent bond in the initial **B** motif could be that IHP has a strong interaction with water. The phosphate groups of IHP often form moderately strong HBs with the surrounding water molecules. A total of three proton transfers and 17 HBs are observed between IHP and water molecules. These interactions lead to a considerable fluctuation of IHP with respect to the diaspore surface, causing dissociation of the covalent bond in the **B** motif.

The average interaction energy between IHP and the diaspore surface is −230 kcal mol^{-1} *i.e.* −115 kcal mol^{-1} per bond, see Table 1. The average interaction energy per water molecule with IHP is −6 kcal mol^{-1}. The interaction energy per bond is smaller than that for **2M(1)**, implying that eventually **2M(2)** could transform into **2M(1)** on a longer time scale. Observe that the P1–O12 average bond length (1.64 Å) is larger than the average bond length observed between phosphorus and the corresponding Al-bonded oxygen in the IHP **2M(1)** motif, see Fig. S5d and e in the ESI.† Also, the P1–O12–Al1 angle is smaller than the angle observed between P, corresponding Al-bonded oxygen and Al in the IHP **2M(1)** motif, see Fig. S5d and e in the ESI.†

There are several reasons for the higher stability of **2M(1)** as compared to **2M(2)**. Most importantly there is a difference in the deprotonation state, *i.e.* in the case of **2M(1)** a total of seven proton transfers are observed, whereas only four are found for **2M(2)**. In addition, the intramolecular HB O12–H–O62, which is close to the binding sites, could have a stabilizing function. It is much stronger for **2M(1)** as compared to **2M(2)**.

Analyzing the binding mechanisms in the IHP **2M** motif cases, one can conclude that intermolecular HBs, proton transfer processes and intramolecular HBs play a prominent role in deciding the stability of the IHP binding motifs with the diaspore surface.

3.2.2 IHP 3M motif. Initially, IHP has been aligned parallel to the surface with non-protonated oxygens of three phosphate groups forming the **3M** motif with the surface, see Fig. 6i. A stable **3M** motif is observed along the whole trajectory. The average Al1–O21, Al2–O41 and Al3–O51 covalent bond length is 1.90, 1.88 and 1.86 Å, respectively (P2–O2*x*, P4–O4*x*, P5–O5*x*, Al1–O2*x*, Al2–O4*x* and Al3–O5*x* interatomic distances, where *x* = 1, 2, 3, and 4 are given in Fig. S5e and S6f in the ESI†). Further, the average geometries of the PO_4 moieties deviate from that of a free tetrahedral PO_4^{3-} with RMSD values of 0.07, 0.08, and 0.10 Å (see Table 1 and Fig. S5e and S6f in the ESI†). Two protons transferred from O32 and O43 to the diaspore surface. The proton transferred from O43 was kept within a HB close to O43.

This journal is © the Owner Societies 2019

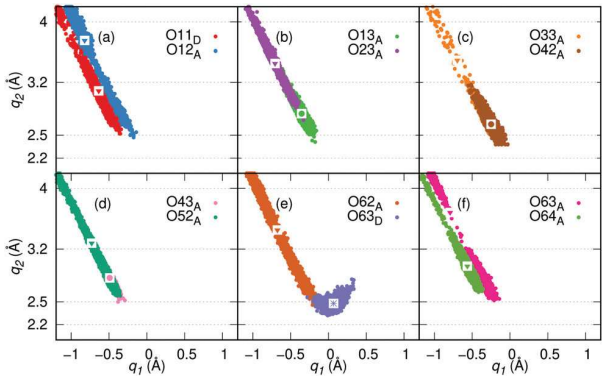


Fig. 9 HB correlation q_2 *vs.* q_1 of IHP and water in the IHP **3M** motif (a–f). The points in white square boxes denote the average value of q_1 and q_2 along the course of the corresponding production trajectory. Here, the symbols *, ● and ▼ denote strong to moderately strong HB, moderately strong HB and moderately strong to weak HB respectively.

A total of 4 proton transfers are observed from IHP to water with an average of 17 HBs between them. Upon analyzing a few HBs, in Fig. 9, 8 (O11, O12, O23, O33, O52, O62, O63, and O64) moderately strong to weak HBs, 3 (O13, O42, and O43) moderately strong HBs, and 1 (O63) strong to moderately strong HB are observed over the course of the trajectory. Thus, similar to the **2M** motifs, IHP and water form predominantly moderately strong HBs (*cf.* Fig. S11c and d in the ESI†).

The interaction energy between IHP and diaspore is -436 kcal mol^{-1}, *i.e.* -145 kcal mol^{-1} per bond, see Table 1. Thus the additional bond in the **3M** motif does not yield an increase in the stability per bond compared to the stable **2M** motif. This may be caused by steric and strain effects due to the fact that the positions of the phosphate groups in IHP do not fit the positions of the possible Al binding sites at the surface. The average interaction energy per water molecule with IHP is -6.8 kcal mol^{-1}, similar to the interaction energies observed in the **2M** motif cases.

4 Summary and conclusions

The interaction between the reactive hydroxide surface of the mineral diaspore with organic phosphates has been investigated for the exemplary cases of IHP and GP. To this end, periodic boundary QM/MM simulations of GP and IHP at the diaspore–water interface have been performed. The analysis of the individual interactions, *i.e.* diaspore–IHP/GP, IHP/GP–water, and diaspore–water, provided information about the factors that control the binding mechanisms and the stability of different motifs. Besides the actual covalent P–O–Al bonds, HBs and proton transfers were found to be vital for understanding the relative stability of the binding motifs. In fact the proper description of the various deprotonation steps has been one of the main motivations for using the computationally expensive QM/MM approach.

Upon analyzing the diaspore–GP–water complexes, the interaction energy per bond of the **B** motif is found to exceed the one of the **M** motif by a factor of 2.4. The higher interaction energy of the **B** motif is to some extent due to the larger number of deprotonation steps, *i.e.* two more protons transfer from GP to the surface in the case of **B**.

Regarding the diaspore–IHP–water complexes, the IHP **3M** motif is found to have a higher interaction energy compared to the most stable **2M(1)** motif, but exhibits a 1.2 times weaker interaction energy per bond. A possible reason could be the mismatch between the positions of the phosphate groups in IHP and the surface Al sites, which introduces some strain into the **3M** motif. This mismatch makes the formation of a fourth P–O–Al bond rather unlikely. We have also shown that the **B** motif is not stable and if chosen initially it transforms into a **2M** motif.

The HBs between GP/IHP and water as well as diaspore have been characterized using correlations between their geometries along the trajectory. Most of the HBs can be classified as being of moderate strength. In the case of GP, compared to **B** the **M** motif exhibits a stronger interaction with water and has two more proton transfers to the water. For IHP the interaction with the solvating water is of similar strength for **2M** and **3M**. In all cases the interaction of water with diaspore exceeds that with phosphate.

GP and IHP are abundant species in forest soils. Based on the present investigation of their interaction with the diaspore–water interface it becomes clear that once the two species compete for the same active sites of the respective mineral particle, binding of IHP will dominate. Although the interaction energy per bond of the GP **B** and the IHP **3M** motifs is similar, IHP's larger number of phosphate groups allows for more covalent bonds to the surface and more HBs to the solvating water. Note that this should hold true under low concentration conditions, *i.e.* not regarding surface coverage effects.

Correlating the current analysis with experiments, our simulations confirm the general observation that the number of phosphate groups is the most important parameter controlling the P-binding strength.[31] As far as the suggestion by Ognalaga *et al.*,[25] that IHP binds to the goethite surface by up to four phosphate groups, is concerned, our findings provide evidence that the **4M** motif is not stable at the studied diaspore surface that is structurally isomorphous to goethite. Further, our results are in accordance with the observation that stable binding motifs include only IHP/GP's phosphate groups and do not affect the organic moiety, *i.e.* no dissociation of C–H, C–O, and C–O–P bonds occurs.[26,28] In addition, our simulations confirm the general notion regarding the importance of HBs and proton transfers in deciding on the stable binding motif.[59]

Conflicts of interest

There are no conflicts to declare.

Acknowledgements

We gratefully acknowledge the financial support from the German Research Foundation (DFG) as a part of the SPP 1685

Priority program ''Ecosystem Nutrition: Forest strategies for limited phosphorus resources'' (PBG, OK, AA) and the InnoSoilPhos-project (AA), funded by the German Federal Ministry of Education and Research (BMBF) in the frame of the BonaRes-program (No. 031A558). This research was performed within the scope of the Leibniz Science Campus ''Phosphorus Research Rostock''. The authors thank the North German Super computing Alliance for providing HPC resources (project mvp00016). The authors would like to thank Prof. Peter Leinweber (Chair of Soil Science, Rostock University) for helpful discussions.

References

1 D. Cordell and T.-S. Neset, *Global Environ. Change*, 2014, **24**, 108–122.
2 R. Bol, G. Gruau, P.-E. Mellander, R. Dupas, M. Bechmann, E. Skarbøvik, M. Bieroza, F. Djodjic, M. Glendell, P. Jordan, B. Van der Grift, M. Rode, E. Smolders, M. Verbeeck, S. Gu, E. Klumpp, I. Pohle, M. Fresne and C. Gascuel-Odoux, *Front. Mater. Sci.*, 2018, **5**, 276:1–276:16.
3 A. Missong, S. Holzmann, R. Bol, V. Nischwitz, H. Puhlmann, K. v. Wilpert, J. Siemens and E. Klumpp, *Sci. Total Environ*, 2018, **634**, 305–315.
4 R. Bol, D. Julich, D. Brödlin, J. Siemens, K. Kaiser, M. A. Dippold, S. Spielvogel, T. Zilla, D. Mewes, F. von Blanckenburg, H. Puhlmann, S. Holzmann, M. Weiler, W. Amelung, F. Lang, Y. Kuzyakov, K.-H. Feger, N. Gottselig, E. Klumpp, A. Missong, C. Winkelmann, D. Uhlig, J. Sohrt, K. von Wilpert, B. Wu and F. Hagedorn, *J. Soil Sci. Plant Nutr.*, 2016, **179**, 425–438.
5 J. Boy, C. Valarezo and W. Wilcke, *Eur. J. Soil Sci.*, 2008, **59**, 1209–1227.
6 S. Holzmann, A. Missong, H. Puhlmann, J. Siemens, R. Bol, E. Klumpp and K. v. Wilpert, *J. Soil Sci. Plant Nutr.*, 2015, **179**, 443–453.
7 P. Gros, A. Ahmed, O. Kühn and P. Leinweber, *Sci. Total Environ*, 2017, **586**, 527–535.
8 J. Kruse, M. Abraham, W. Amelung, C. Baum, R. Bol, O. Kühn, H. Lewandowski, J. Niederberger, Y. Oelmann, C. Rüger, J. Santner, M. Siebers, N. Siebers, M. Spohn, J. Vestergren, A. Vogts and P. Leinweber, *J. Soil Sci. Plant Nutr.*, 2015, **178**, 43–88.
9 M. Hens and R. Merckx, *Environ. Sci. Technol.*, 2001, **35**, 493–500.
10 X. Jiang, R. Bol, V. Nischwitz, N. Siebers, S. Willbold, H. Vereecken, W. Amelung and E. Klumpp, *J. Environ. Qual.*, 2015, **44**, 1772–1781.
11 J. Peñuelas, J. Sardans, A. Rivas-ubach and I. A. Janssens, *Global Change Biol.*, 2011, **18**, 3–6.
12 R. H. Newman and K. R. Tate, *Commun. Soil Sci. Plant Anal.*, 1980, **11**, 835–842.
13 B. L. Turner, M. J. Papházy, P. M. Haygarth and I. D. Mckelvie, *Philos. Trans. R. Soc., B*, 2002, **357**, 449–469.
14 J. Gerke, *Plants*, 2015, **4**, 253–266.
15 A. Doolette, R. Smernik and W. Dougherty, *Soil Sci. Soc. Am. J.*, 2009, **73**, 919–927.
16 A. Missong, R. Bol, S. Willbold, J. Siemens and E. Klumpp, *J. Soil Sci. Plant Nutr.*, 2016, **179**, 159–167.
17 A. G. Vincent, J. Vestergren, G. Gröbner, P. Persson, J. Schleucher and R. Giesler, *Plant Soil*, 2013, **367**, 149–162.
18 H. K. Pant, P. R. Warman and J. Nowak, *Commun. Soil Sci. Plant Anal.*, 1999, **30**, 757–772.
19 T. M. Tsao, Y. M. Chen and M. K. Wang, *J. Environ. Monit.*, 2011, **13**, 1156–1163.
20 R. Chitrakar, S. Tezuka, A. Sonoda, K. Sakane, K. Ooi and T. Hirotsu, *J. Colloid Interface Sci.*, 2006, **298**, 602–608.
21 J. Torrent, U. Schwertmann and V. Barron, *Clays Clay Miner.*, 1992, **40**, 14–21.
22 R. L. Parfitt and R. J. Atkinson, *Nature*, 1976, **264**, 740–742.
23 A. A. Ahmed, S. Gypser, P. Leinweber, D. Freese and O. Kühn, *Phys. Chem. Chem. Phys.*, 2019, **21**, 4421–4434.
24 G. Anderson and E. Z. Arlidge, *J. Soil Sci.*, 1962, **13**, 216–224.
25 M. Ognalaga, E. Frossard and F. Thomas, *Soil Sci. Soc. Am. J.*, 1994, 332–337.
26 L. Celi, S. Lamacchia, F. A. Marsan and E. Barberis, *Soil Sci.*, 1999, **164**, 574–585.
27 X.-H. Guan, C. Shang, J. Zhu and G.-H. Chen, *J. Colloid Interface Sci.*, 2006, **293**, 296–302.
28 H. Li, B. Wan, Y. Yan, Y. Zhang, W. Cheng and X. Feng, *J. Soil Sci. Plant Nutr.*, 2017, **181**, 557–565.
29 T. Hori, M. Moriguchi, M. Sasaki, S. Kitagawa and M. Munakata, *Anal. Chim. Acta*, 1985, **173**, 299–303.
30 Y. P. Yan, F. Liu, W. Li, F. Liu, X. H. Feng and D. L. Sparks, *Eur. J. Soil Sci.*, 2014, **65**, 308–317.
31 G. Anderson and E. Z. Arlidge, *Eur. J. Soil Sci.*, 1962, **13**, 216–224.
32 H. Guo and A. S. Barnard, *J. Mater. Chem.*, 2011, **21**, 11566–11577.
33 *Molecular Modeling of Geochemical Reactions*, ed. J. D. Kubicki, Wiley and Sons, Chichester, 2016.
34 J. D. Kubicki and H. D. Watts, *Minerals*, 2019, **9**, 141.
35 J. D. Kubicki, K. W. Paul, L. Kabalan, Q. Zhu, M. K. Mrozik, M. Aryanpour, A.-M. Pierre-Louis and D. R. Strongin, *Langmuir*, 2012, **28**, 14573–14587.
36 A. A. Ahmed, O. Kühn, S. G. Aziz, R. H. Hilal and P. Leinweber, *Sci. Total Environ*, 2014, **476–477C**, 98–106.
37 A. A. Ahmed, P. Leinweber and O. Kühn, *J. Theor. Comput. Chem.*, 2014, **13**, 1450009.
38 A. A. Ahmed, P. Leinweber and O. Kühn, *Phys. Chem. Chem. Phys.*, 2018, **20**, 1531–1539.
39 H. M. Senn and W. Thiel, *Angew. Chem., Int. Ed.*, 2009, **48**, 1198–1229.
40 M. Kosmulski, *J. Colloid Interface Sci.*, 2009, **337**, 439–448.
41 W. Humphrey, A. Dalke and K. Schulten, *J. Mol. Graphics*, 1996, **14**, 33–38.
42 CP2K, Open source molecular dynamics code., www.cp2k.org.
43 J. VandeVondele, M. Krack, F. Mohamed, M. Parrinello, T. Chassaing and J. Hutter, *Comput. Phys. Commun.*, 2005, **167**, 103–128.
44 C. Mundy, S. Balasubramanian, K. Bagchi, J. Hutter, A. S. I. Kuo, T. Laino and J. VandeVondele, Frontiers in Simulation Technology (FIST).

 This journal is © the Owner Societies 2019

45 M. Krack, *Theor. Chem. Acc.*, 2005, **114**, 145–152.
46 J. P. Perdew, K. Burke and M. Ernzerhof, *Phys. Rev. Lett.*, 1996, **77**, 3865–3868.
47 S. Grimme, J. Antony, S. Ehrlich and H. Krieg, *J. Phys. Chem.*, 2010, **132**, 154104.
48 J. VandeVondele and J. Hutter, *J. Chem. Phys.*, 2007, **127**, 114105.
49 H. J. C. Berendsen, J. R. Grigera and T. P. Straatsma, *J. Phys. Chem.*, 1987, **91**, 6269–6271.
50 R. T. Cygan, J. J. Liang and A. G. Kalinichev, *J. Phys. Chem. B*, 2004, **108**, 1255–1266.
51 V. Zoete, M. A. Cuendet, A. Grosdidier and O. Michielin, *J. Comput. Chem.*, 2011, **32**, 2359–2368.
52 T. Laino, F. Mohamed, A. Laio and M. Parrinello, *J. Chem. Theory Comput.*, 2006, **2**, 1370–1378.
53 G. Bussi, D. Donadio and M. Parrinello, *J. Chem. Phys.*, 2007, **126**, 014101.
54 S. Boys and F. Bernardi, *Mol. Phys.*, 1970, **19**, 553–566.
55 T. Strassner, *Angew. Chem.*, 2006, **45**, 6420–6421.
56 H.-H. Limbach, P. M. Tolstoy, N. Pérez-Hernández, J. Guo, I. G. Shenderovich and G. S. Denisov, *Isr. J. Chem.*, 2009, **49**, 199–216.
57 T. Zentel and O. Kühn, *Theor. Chem. Acc.*, 2017, **136**, 87.
58 M. J. Minch, *J. Chem. Educ.*, 1999, **76**, 759.
59 B. B. Johnson, E. Quill and M. J. Angove, *J. Colloid Interface Sci.*, 2012, **367**, 436–442.

This journal is © the Owner Societies 2019

Supplementary Information:

QM/MM simulations of organic phosphorus adsorption at the diaspore-water interface

Prasanth B. Ganta,[a] Oliver Kühn,[a,b] and Ashour A. Ahmed,[a,b‡]

[a]University of Rostock, Institute of Physics, Albert-Einstein-Str. 23-24, D-18059 Rostock, Germany

[b]University of Rostock, Department of Life, Light, and Matter (LLM), Albert-Einstein-Str. 25, D-18059 Rostock, Germany

prasanth.ganta@uni-rostock.de

oliver.kuehn@uni-rostock.de

ashour.ahmed@uni-rostock.de

CONTENTS

1. Force fields used in the current simulations
2. Description and validation of the present QM/MM approach
3. Modeling of diaspore surface with unsaturated active sites
4. Model conditions (soil pH and pKa for phosphates)
5. Proton transfer in the bulk and at the interface
6. Description of the interaction energy calculations

1. Force fields used in the current simulations

The MM level interaction between the diaspore (α-AlOOH) surface and water is defined based on the CLAYFF force fields [S1]. It is to be noted that the CLAYFF force fields are compatible with SPC water model. The total energy of the MM system using CLAYFF is given by:

$$\mathrm{E_{sys}} = \mathrm{E_{bond}} + \mathrm{E_{angle}} + \mathrm{E_{vdW}} + \mathrm{E_{coulomb}}$$

where, $\mathrm{E_{bond}}$ and $\mathrm{E_{angle}}$ are energies due to bond stretching and angle bending. $\mathrm{E_{vdW}}$ and $\mathrm{E_{coulomb}}$ denote energies due to van der Waals (vdW) and electrostatic interactions. The total energy is sum of bonded interactions (bond/angle) and nonbonded interactions (vdW and electrostatic). The bond stretching energy is defined as:

$$\mathrm{E_{bond}} = \mathrm{k_b}(\mathrm{r_{ij}} - \mathrm{r_0})^2$$

where, $\mathrm{k_b}$ denotes force constant, $\mathrm{r_{ij}}$ denotes distance between $\mathrm{i,j}$ atoms, and $\mathrm{r_0}$ denotes equilibrium bond length. Similarly the energy of the angle bend is given by:

$$\mathrm{E_{angle}} = \mathrm{k_\theta}(\theta_{\mathrm{ijk}} - \theta_0)^2$$

where, $\mathrm{k_\theta}$ denotes a force constant, θ_{ijk} is bond angle between i, j and k atoms and θ_0 is equilibrium bond angle.

Table S1: Bond and angle parameters for diaspore and water

bond stretch				
species i	species j		$\mathrm{k_b}$ (kcal/mol Å^2)	$\mathrm{r_0}$(Å)
water hydrogen	water oxygen		554.1349	1.0
hydroxyl hydrogen	hydroxyl oxygen		554.1349	1.0
angle bend				
species i	species j	species k	$\mathrm{k_\theta}$ (kcal/mol rad^2)	θ_0 (deg)
water hydrogen	water oxygen	water hydrogen	45.7696	109.47
aluminium	hydroxyl oxygen	hydroxyl hydrogen	30.0	109.47

The short range vdW interaction energy is represented as:

$$\mathrm{E_{vdW}} = \sum_{\mathrm{vdW}}^{\mathrm{i<j}} \mathrm{D_{o,ij}} \left[\left(\frac{\mathrm{R_{o,ij}}}{\mathrm{r_{ij}}} \right)^{12} - 2 \left(\frac{\mathrm{R_{o,ij}}}{\mathrm{r_{ij}}} \right)^{6} \right]$$

where, $\mathrm{D_{o,ij}}$ and $\mathrm{R_{o,ij}}$ are empirical parameters. For unlike atoms, the parameters can be calculated using:

$$\mathrm{R_{o,ij}} = \frac{1}{2}(\mathrm{R_{o,i}} + \mathrm{R_{o,j}})$$

$$\mathrm{D_{o,ij}} = \sqrt{\mathrm{D_{o,i}} \mathrm{D_{o,j}}}$$

The long range coulomb interaction energy is given by:

$$\mathrm{E_{coulomb}} = \sum_{\mathrm{coulomb}}^{\mathrm{i<j}} e^2 \frac{\mathrm{q_i q_j}}{4\pi\epsilon_0 \mathrm{r_{ij}}}$$

Table S2: Nonbonded parameters for diaspore and water

species	charge (e)	D_0(kcal mol^{-1})	R_0(Å)
water hydrogen	0.41		
water oxygen	-0.82	0.1554	3.5532
bridging oxygen	-1.05	0.1554	3.5532
aluminium	1.575	1.3298e-6	4.7943
hydroxyl hydrogen	0.425		
hydroxyl oxygen	-0.95	0.1554	3.5532

where, q_i, q_j denote partial charges, e denotes electron charge and ϵ_0 is the dielectric permittivity of vacuum.

The MM level interaction between IHP/GP and water is defined with the CHARMM force field parameters obtained from SwissParm, a force field generation tool [S2]. Here also, the water is defined based on the SPC water model.

Table S3: Nonbonded parameters for IHP, GP

species	charge (e)	D_0(kcal mol^{-1})	R_0(Å)
CR	0.2800	0.0550	3.8754
O2CM	-0.7000	0.1200	3.0290
ORC2P	-0.5512	0.1520	3.1537
ORPOH	-0.7712	0.1520	3.1537
ORCOH	-0.6800	0.1520	3.1537
PO4	1.5136	0.5850	3.8308
HCMM	0.0000	0.0220	2.3519
HOCO	0.5000	0.0460	0.4000
HORCOH	0.4000	0.0460	0.4000

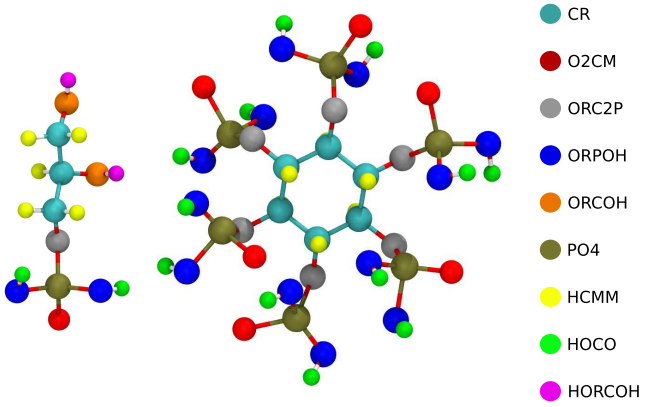


Figure S1: IHP and GP color-coded to denote atoms listed in Table S3.

2. Description and validation of the present QM/MM approach

For the current applied electrostatic embedding QMMM approach, the MM parameters are used for calculating

- interaction between the MM subsystems
- coupling interaction between the QM and MM subsystems

The whole MM subsystem consists of two subsystems, 1- bottom six layers of diaspore surface (480 atoms) and 2- about 175 water molecules in the simulation box. Here, the CLAYFF parameters for the diaspore surface and the SPC model parameters for water molecules (which are completely compatible with the CLAYFF parameters) are sufficient to simulate the diaspore-water interactions.

Regarding QM and MM coupling the following approach is implemented:

- QM(water+diaspore+IHP/GP) interaction with MM(diaspore): Here, $\text{water}_{\text{QM}} - \text{diaspore}_{\text{MM}}$ and $\text{diaspore}_{\text{QM}} - \text{diaspore}_{\text{MM}}$ interactions are defined with respect to two compatible force fields CLAYFF and SPC based water model. Regarding $\text{IHP/GP}_{\text{QM}} - \text{diaspore}_{\text{MM}}$ interactions, the long range interactions are ignored, since the corresponding parameters are not available.
- QM(water+diaspore+IHP/GP) interaction with MM(water): Here, MM water is defined based on SPC water model which is compatible with both CLAYFF (diaspore) and CHARMM (IHP/GP) force fields.

To validate our approach, pure QM(DFT) NVT-MD simulation using IHP **2M(1)** model is performed for 5 ps. The trajectory analysis showed similar pair correlation functions between the corresponding QM and QMMM trajectories, please refer Fig. S2. In addition, the trajectories obtained using pure QM and QMMM have similar Al-O-P bond formations, please ref Fig. S3.

3. Modeling of diaspore surface with unsaturated active sites

- Diaspore has a point of zero charge (PZC) around 6 [S3, S4]. This means that below pH 6 the surrounding water molecules will dissociate and donate more protons than hydroxyl groups to the diaspore surface leading to a positively charged surface. This explains that the diaspore surface at pH below 6 will be partially unsaturated and has the ability to attract/adsorb anions such as phosphate and/or hydroxyl groups at its surface. Hence, this adsorption process (or binding reaction) could happen mainly by direct reaction to the unsaturated surface centers (active sites) without need for a ligand-exchange mechanism. Conversely, above pH 6 the surface will be negatively charged and more saturated by hydroxyl groups from water. Here the surface saturation will increase upon increasing the solution pH and the surface will have the ability to attract cations and repel anions. Under these conditions, the chemisorption process of anions at surfaces (i.e. inner-sphere complexes) should take place via a ligand-exchange mechanism. Considering the fact that most soils and especially forest soils are acidic [S5, S6], gives the motivation to model the diaspore surface as a partially unsaturated one.
- In addition to the poor knowledge of the molecular reaction mechanisms of the phosphate binding at the diaspore surface, diaspore has been modeled in the current contribution for two main reasons. The first one is that diaspore

is isomorphous with goethite (α-FeOOH) which is most abundant and common mineral containing iron atom in the form of ferric (Fe^{+3}). Hence, by investigating the adsorption process at both diaspore and goethite surfaces with same degree of unsaturation the effect of central metal ion (Fe/Al) on adsorption process could be understood in more detail. The second reason is arising from the fact that Fe/Al hydroxide mixtures are highly abundant in soils thus affecting P fixation and release. It is to be noted that goethite has PZC around 9 [S3]. Therefore, goethite surface will be unsaturated below pH 9 and thus can adsorb phosphate and form inner-sphere complexes via a direct interaction mechanism and not a ligand-exchange one. Keeping in mind the PZC of diaspore and goethite one may expect the amorphous Fe/Al hydroxide mixtures should have PZC values in the range of pH 6-9. So according to reported PZC values, which are in that range, a more realistic model for both diaspore and goethite should be partially unsaturated and not saturated completely. This holds true unless one is studying a high pH range which, however, is not in the focus of the present investigation.

- It is well-known from sorption experiments that the phosphate adsorption decreases with increasing the soil solution pH [S7, S8]. This means that in the presence of OH^- at high pH, OH^- groups can replace the adsorbed phosphate indicating a stronger adsorption for OH^- than for phosphate at mineral surfaces. This behaviour has been observed and explained in more details at a molecular level by our group [S9, S10]. The modelling results indicated that phosphate can replace the competing water molecules at the goethite surface, but phosphate could be replaced by OH^- groups. This shows that the reverse reaction, i.e. replacement of OH^- groups by phosphate, is mainly a non-spontaneous reaction and unlikely to take place. This indicates that formation of inner-sphere complexes of phosphate with goethite/diaspore surfaces could happen mainly due to direct reaction of phosphate with the surface unsaturated centers and not with a ligand-exchange mechanism. Consequently, this points to the necessity of the presence of some unsaturated centers at the mineral surface to form inner-sphere complexes with phosphates.

4. Model conditions (soil pH and pKa for phosphates)

As mentioned in the previous section and according to the diaspore‘s PZC value, we are simulating common and normal acidic soil conditions, i.e. at pH in the range of 3-6. Consequently, the diaspore surface was modeled with active unsaturated centers. According to the best of our knowledge, there are some differences and conflicts between the available pKa values for IHP and GP. For example, the estimated pKa values by the “ChemAxon” software are 0.14 for IHP and 1.5 for GP. Experimentally, it was mentioned that IHP is a relatively reactive phosphate compound having 12 dissociable protons with pKa values in the range of about 1.5 to 10 [S11]. In view of these conflicts, we have started our simulation with the neutral forms for both IHP and GP. However, we have observed deprotonation of the phosphates (IHP and GP) in the first few pico-seconds (ps) of the simulation trajectories (see Figs. S7 and S8), according to the acidic character of these phosphates which is thus properly taking into account by our modelling approach.

5. Proton transfer in the bulk and at the interface

The proton transfer events have been triggered by the surface. But in general, these processes could take place either in the presence or absence of the surface (i.e. for simulations carried out in the bulk). To investigate such goal practically,

two additional MD simulations have been performed with the same applied approach. One simulation was carried out with GP in the presence of the diaspore surface with a separation distance of about 5 Å between them. The second simulation involved GP in a pure water without diaspore. Both simulations showed proton transfer processes during the simulation trajectory (see Figs. S7 and S8).

6. Description of the interaction energy calculations

In general, the effect of water on the calculated diaspore-phosphate interaction has been considered during the MD trajectory due to the diaspore-phosphate-water interactions based on the electronic and Van der Waals interactions. Here phosphate refers to GP and IHP. However, this effect has not been considered explicitly for computing the interaction energy in Eq. 1. In practice, each diaspore-phosphate-water model could be considered as three sub-systems (fragments). These fragments are diaspore (fragment1), IHP/GP (fragment2) and water (fragment3). Within CP2K it is possible to calculate the pair interaction energy between two fragments. According to Eq. 1 of the main paper

$$\mathrm{E_{int}} = \mathrm{E_{diaspore-phosphate-complex}} - (\mathrm{E_{diaspore}} + \mathrm{E_{phosphate}}),$$

we have defined diaspore as the first fragment and phosphate as the second fragment. Water enters only insofar as it determines the actual geometry of the interacting fragments. The interaction energy is calculated within the BSSE counterpoise correction philosophy, i.e. by performing five energy calculations as follows: diaspore including only the diaspore basis functions ($\mathrm{E^{diaspore}_{diaspore}}$), total electronic energy of phosphate including only the phosphate basis functions ($\mathrm{E^{phosphate}_{phosphate}}$), diaspore including the basis functions of phosphate and diaspore ($\mathrm{E^{diaspore+phosphate}_{diaspore}}$), phosphate including the basis functions of phosphate and diaspore ($\mathrm{E^{diaspore+phosphate}_{phosphate}}$) and finally diaspore-phosphate complex including the basis functions of diaspore and phosphate ($\mathrm{E^{diaspore+phosphate}_{diaspore-phosphate-complex}}$). From these numbers one gets the interaction energy between diaspore and phosphate as $\mathrm{E_{int}} = \mathrm{E^{diaspore+phosphate}_{diaspore-phosphate-complex}} - (\mathrm{E^{diaspore+phosphate}_{diaspore}} + \mathrm{E^{diaspore+phosphate}_{phosphate}})$. Similarly, the interaction energies between phosphate and water ($\mathrm{E_{int}} = \mathrm{E^{phosphate+water}_{phosphate-water-complex}} - (\mathrm{E^{phosphate+water}_{phosphate}} + \mathrm{E^{phosphate+water}_{water}})$) and between diaspore and water ($\mathrm{E_{int}} = \mathrm{E^{diaspore+water}_{diaspore-water-complex}} - (\mathrm{E^{diaspore+water}_{diaspore}} + \mathrm{E^{diaspore+water}_{water}})$) could be calculated.

References

[S1] R. T. Cygan, J. J. Liang, A. G. Kalinichev, Molecular models of hydroxide, oxyhydroxide, and clay phases and the development of a general force field, J. Phys. Chem. B 108 (2004) 1255–1266.

[S2] V. Zoete, M. A. Cuendet, A. Grosdidier, O. Michielin, Swissparam: A fast force field generation tool for small organic molecules, J. Comput. Chem. 32 (2011) 2359–2368.

[S3] M. Kosmulski, pH-dependent surface charging and points of zero charge. IV. Update and new approach, J. Colloid Interface Sci. 337 (2009) 439 – 448.

[S4] C.-b. Huang, L. Zhang, Y.-h. Wang, Y. Lan, Separation of aluminosilicates and diaspore from diasporic-bauxite by selective flocculation, J. Cent. South Univ. Technol. 15 (2008) 520–525.

[S5] E. Slessarev, Y. Lin, N. Bingham, J. E Johnson, Y. Dai, J. Schimel, O. Chadwick, Water balance creates a threshold in soil pH at the global scale, Nature 540 (2016) 567–569.

[S6] Breemen, C. Driscoll, J. Mulder, Acidic deposition and internal proton in acidification of soils and waters, Nature 307 (1984) 599-604 307 (1984) 599–604.

[S7] B. Barja, M. Dos Santos AFONSO, Aminomethylphosphonic acid and glyphosate adsorption onto goethite: A comparative study, Environ. Sci. Technol. 39 (2005) 585–92.

[S8] J. Sheals, S. Sjoberg, P. Persson, Adsorption of glyphosate on goethite: Molecular characterization of surface complexes, Environ. Sci. Technol. 36 (2002) 3090–3095.

[S9] A. A. Ahmed, P. Leinweber, O. Kühn, Unravelling the nature of glyphosate binding to goethite surfaces by ab initio molecular dynamics simulations, Phys. Chem. Chem. Phys. 20 (2018) 1531–1539.

[S10] A. A. Ahmed, S. Gypser, P. Leinweber, D. Freese, O. Kühn, Infrared spectroscopic characterization of phosphate binding at the goethite-water interface, Phys. Chem. Chem. Phys. 21 (2019) 4421–4434.

[S11] A. J. Costello, T. Glonek, T. C. Myers, 31P Nuclear magnetic resonance pH titrations of myo-inositol hexaphosphatex, Carbohydr. Res. 46 (1976) 159 – 171.

FIGURES

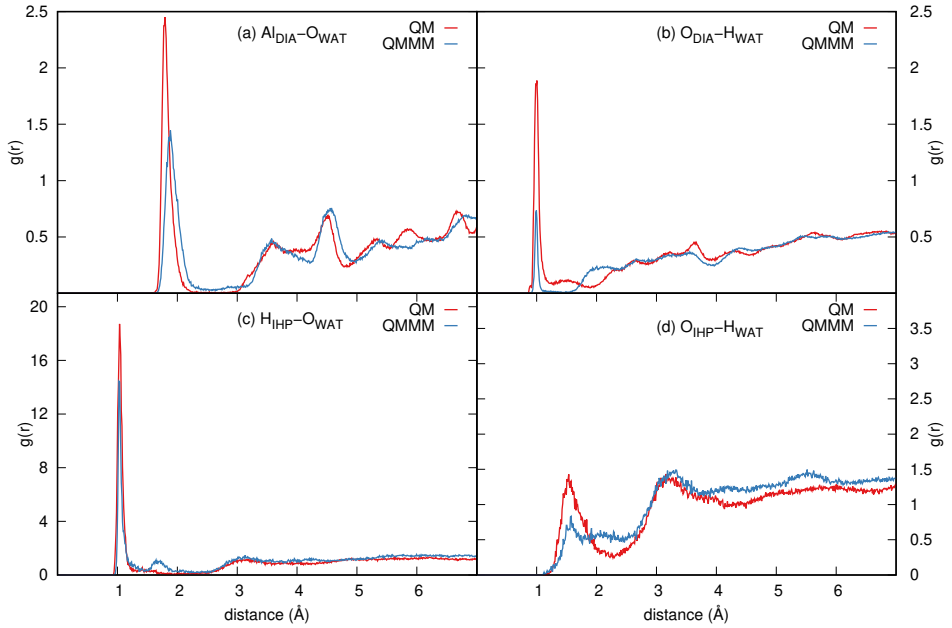


Figure S2: Comparison of pair correlation functions calculated using QM and QMMM methods. Al of diaspore and oxygens of water (a), oxygens of diaspore and hydrogens of water (b), hydrogens of IHP and oxygens of water (c), oxygens of IHP and hydrogens of water (d). The red and black lines denote correlation function obtained using QM method and QMMM method respectively.

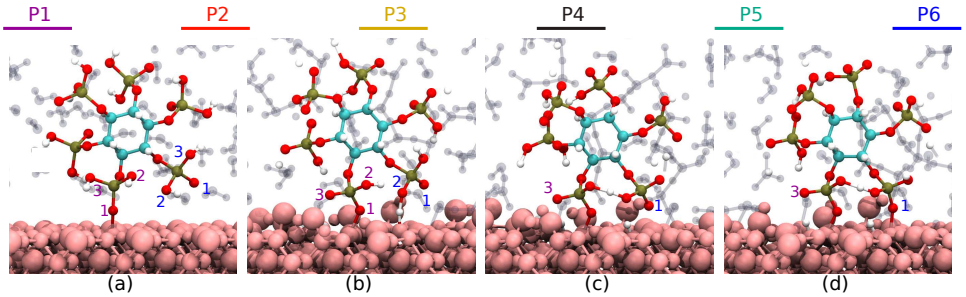


Figure S3: Snapshots along the trajectory of IHP **2M(1)** model simulated using QM (DFT) only. Initial M(O + Al) motif (a), proton transfer from O13 and O62 to surface (b), proton sharing between P1 and P6 phosphate groups (c), and formation of Al2-O61 covalent bond (d). Similar events are observed in IHP **2M(1)** model trajectory simulated using QM/MM.

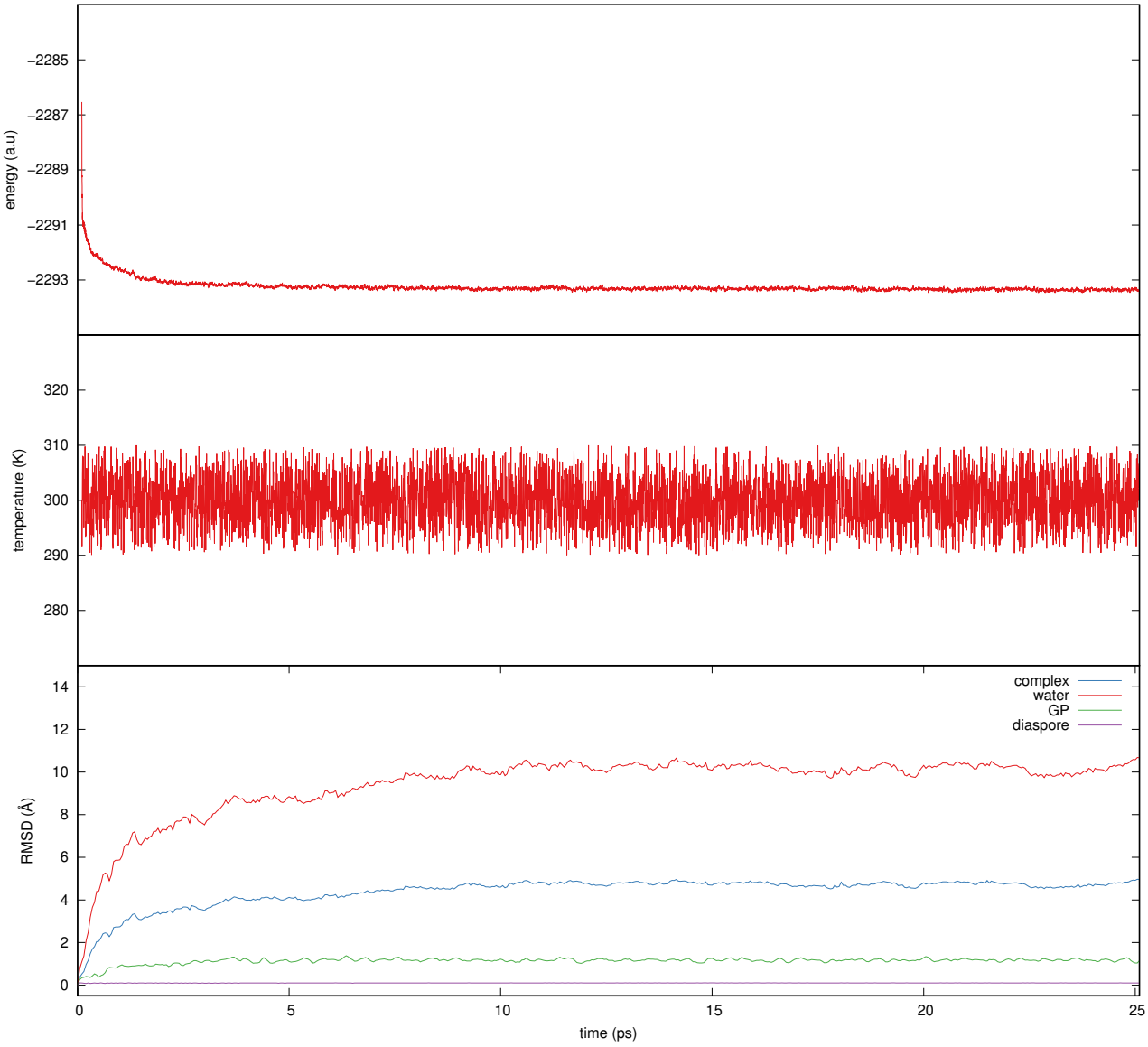


Figure S4: GP **M** motif potential energy (top), temperature (middle), root mean square deviation (RMSD, bottom) along MD trajectory. This figure suggests that the GP **M** motif diaspore-GP-water complex is equilibrated within the first 10 ps of the whole trajectory.

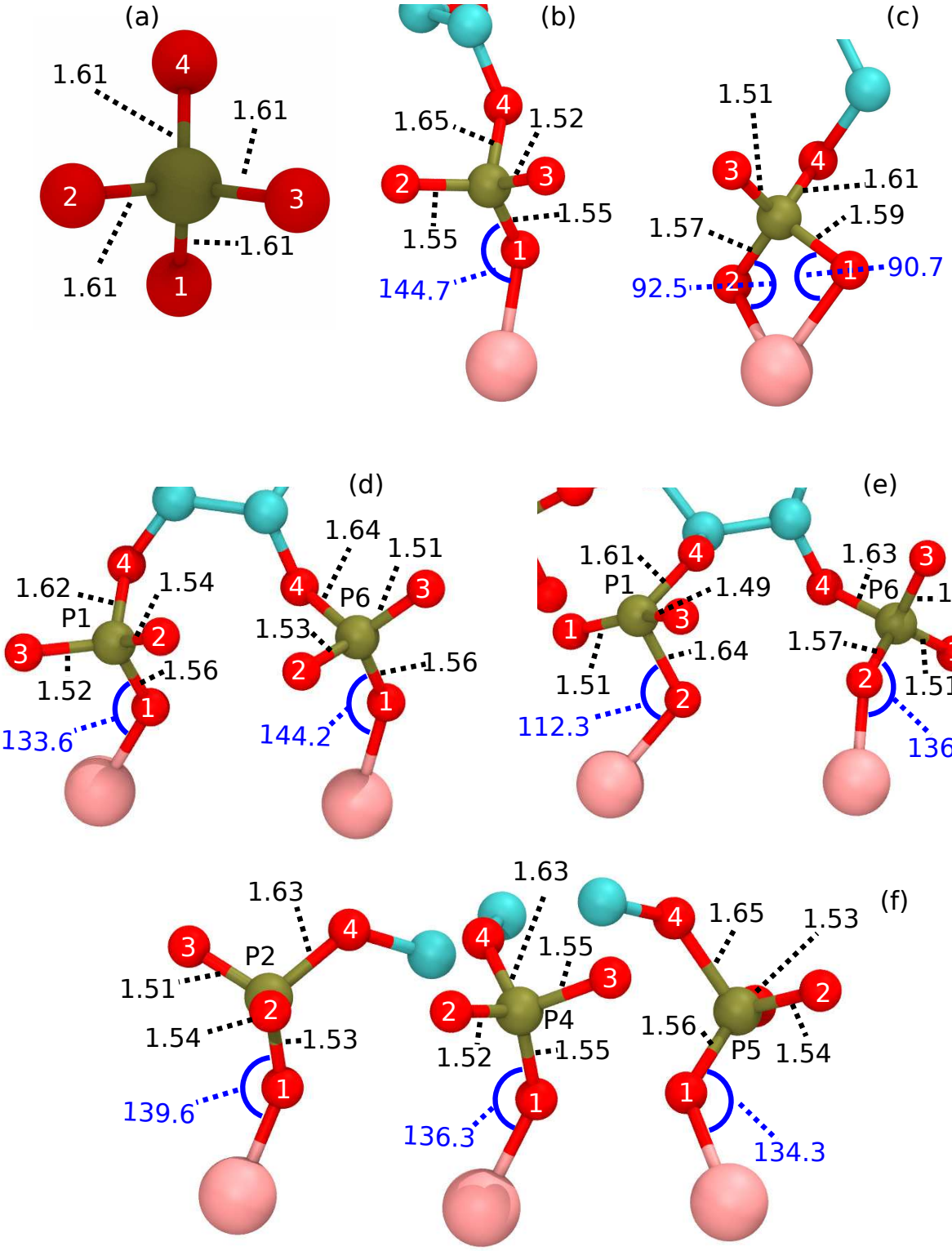


Figure S5: Interatomic distances between phosphorus and corresponding oxygens of orthophosphate (a), GP **M** motif (b), GP **B** motif (c), IHP **2M(1)** motif (d), IHP **2M(2)** motif (e), IHP **3M** motif (f). Note that P-O-Al angle is also provided for relevant cases, where O and Al are covalently bonded. Only Al bonded phosphate groups and Al are shown in all motifs for better visualisation.

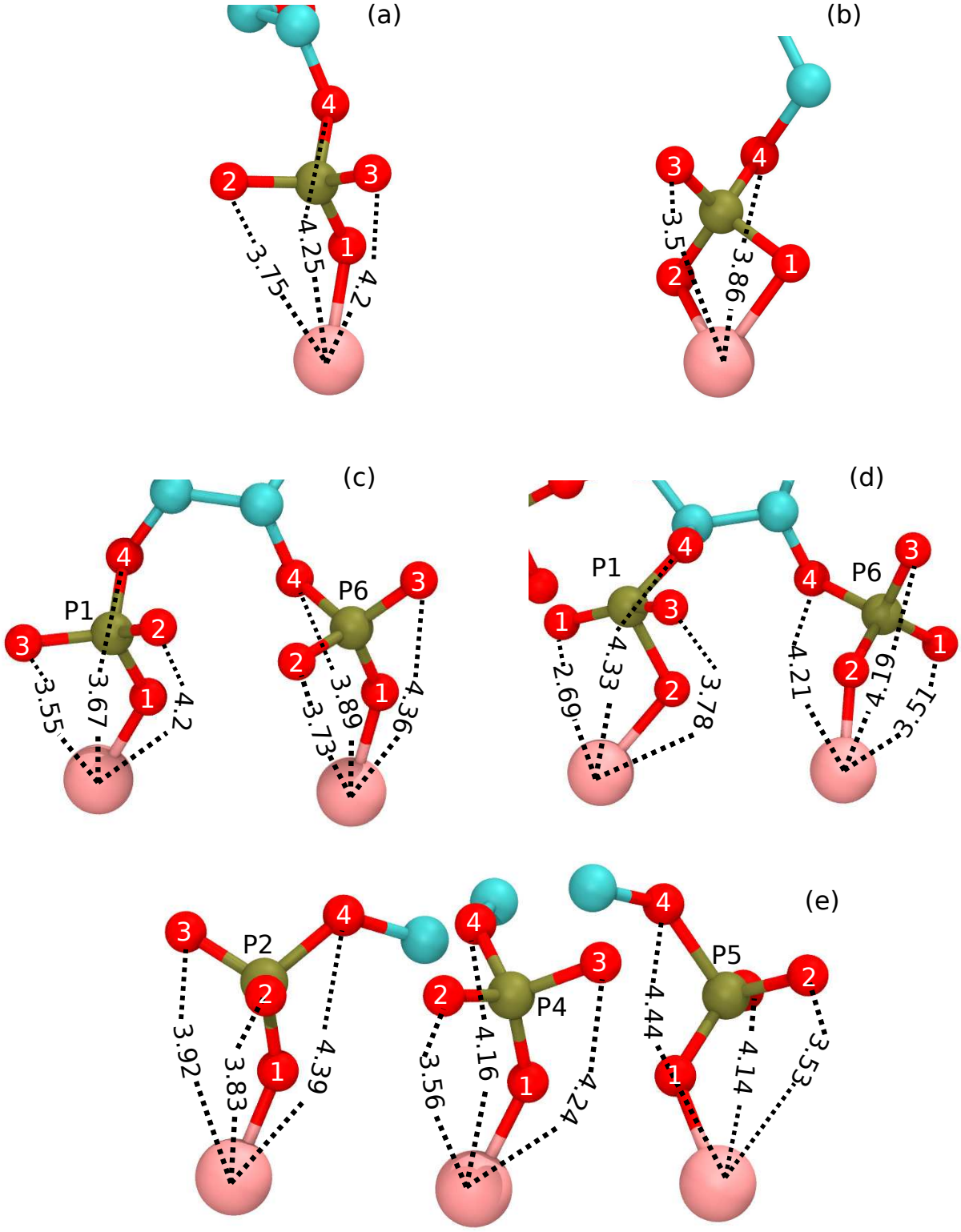


Figure S6: Interatomic distances between Al-nonbonded oxygens in phosphate group and Al. GP **M** motif (a), GP **B** motif (b), IHP **2M(1)** motif (c), IHP **2M(2)** motif (d), IHP **3M** motif (e).

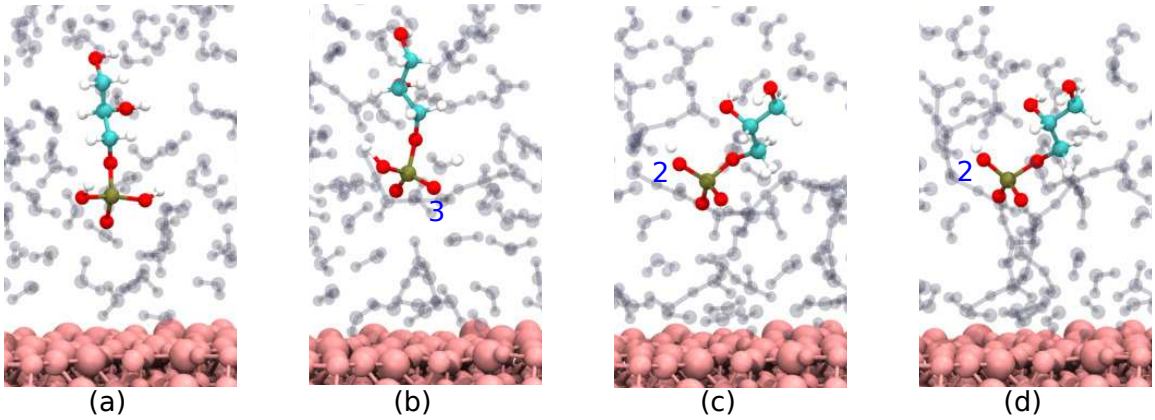


Figure S7: Snapshots along 10 ps trajectory of diaspore-GP-water model with GP above 5 Å from diaspore surface. Initial configuration (a), proton transfer from O3 to water (b), proton transfer from O2 to water (c) and (d).

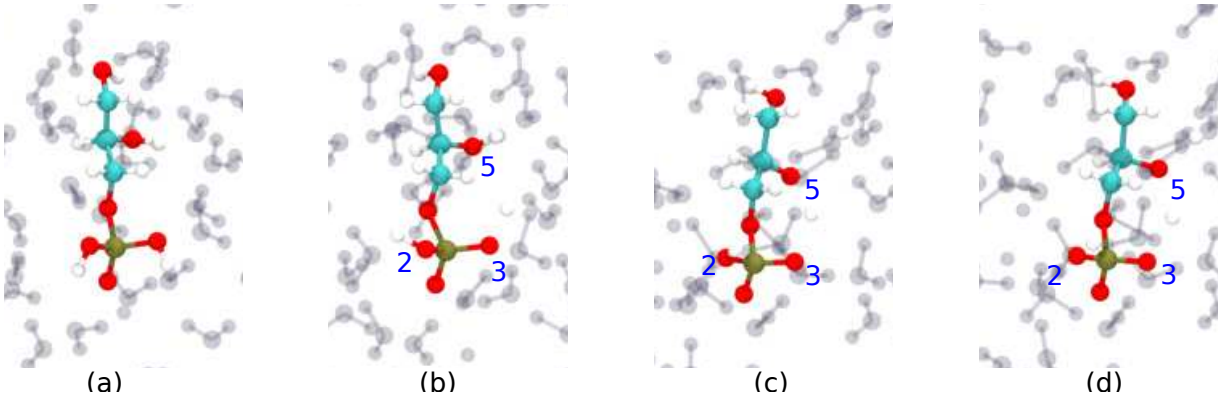


Figure S8: Snapshots along 10 ps trajectory of GP-water model. Initial configuration (a), proton transfer from O3 to water (b), proton transfer from O5 to water (c) and proton transfer from O2 to water (d).

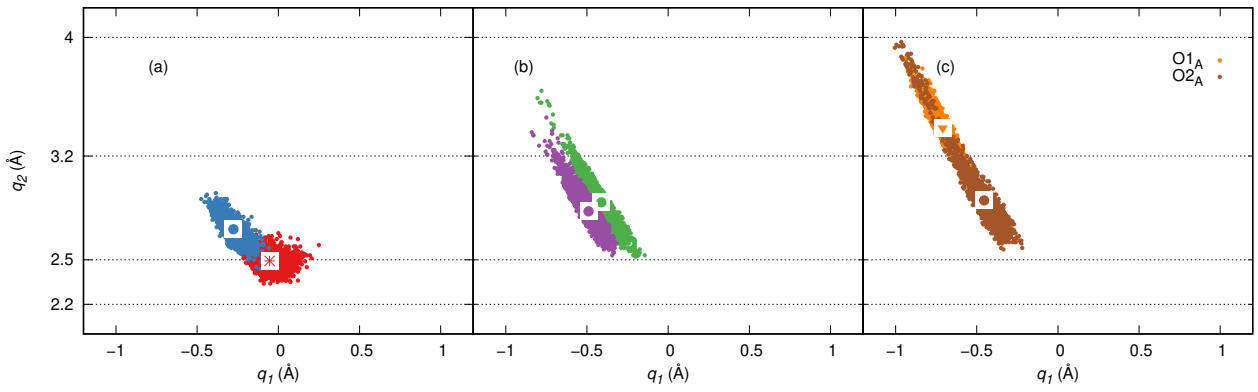


Figure S9: HB correlation q_2 vs. q_1 of a few diaspore oxygens and water molecules in GP **M** motif (a), (b) and HBs strength between O1, O2 and protons transferred to diaspore in GP **B** motif (c). Here, the symbols $*$, $\bullet$ and $\blacktriangledown$ denote strong to moderately strong HB, moderately strong HB and moderately strong to weak HB respectively.

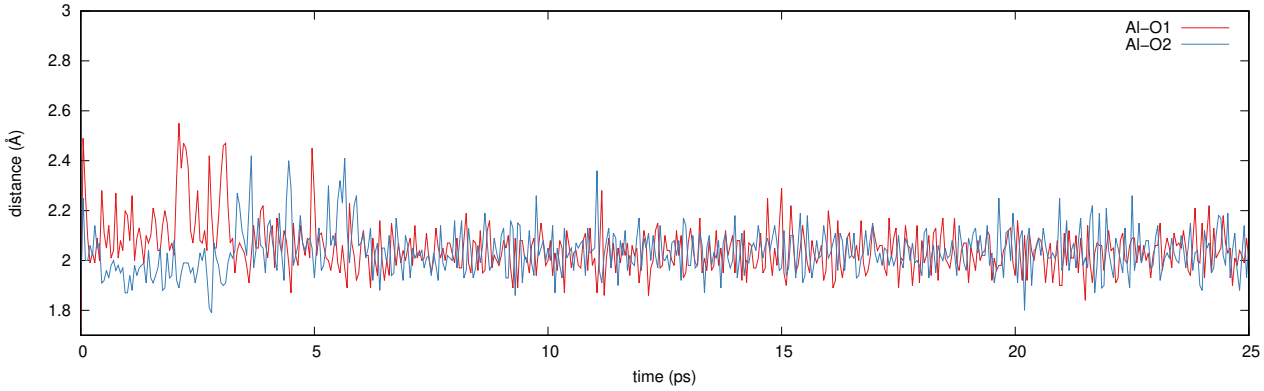


Figure S10: Al-O bond lengths in GP **B** motif with **B** motif along MD trajectory. Observe that a stable **B** motif is maintained until the end of the trajectory.

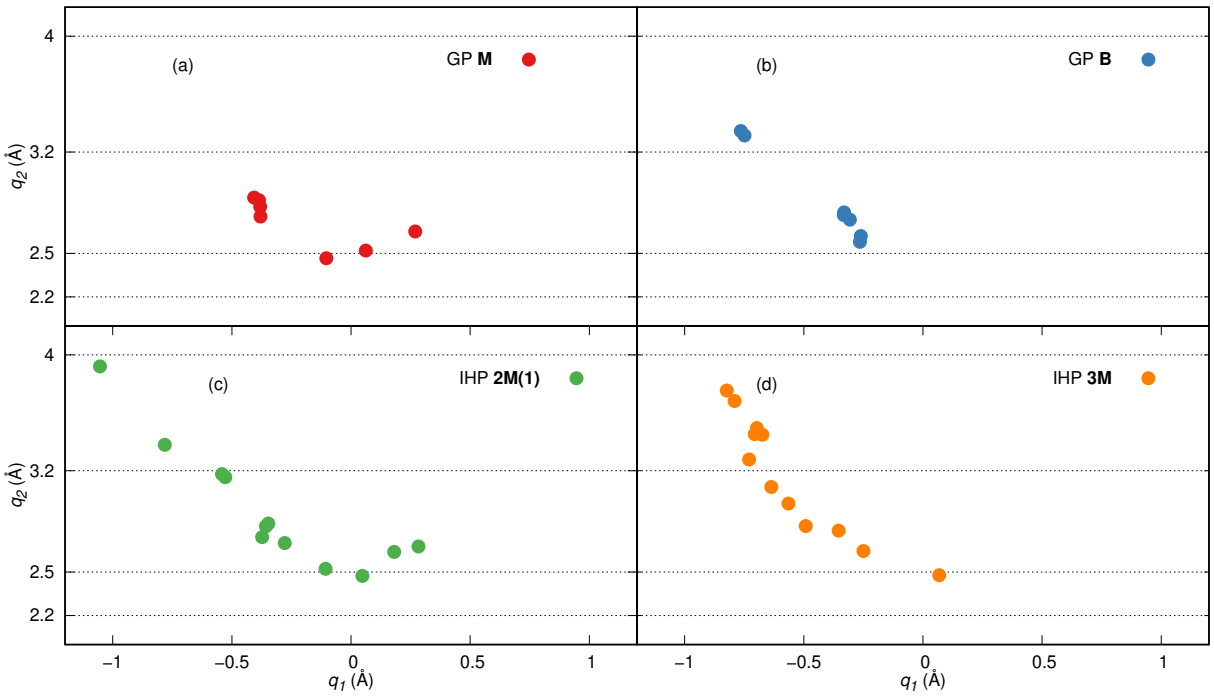


Figure S11: HB correlation q_2 vs. q_1 of selected HBs observed in IHP/GP with water. Observe that IHP and GP often formed moderately strong HBs with water.

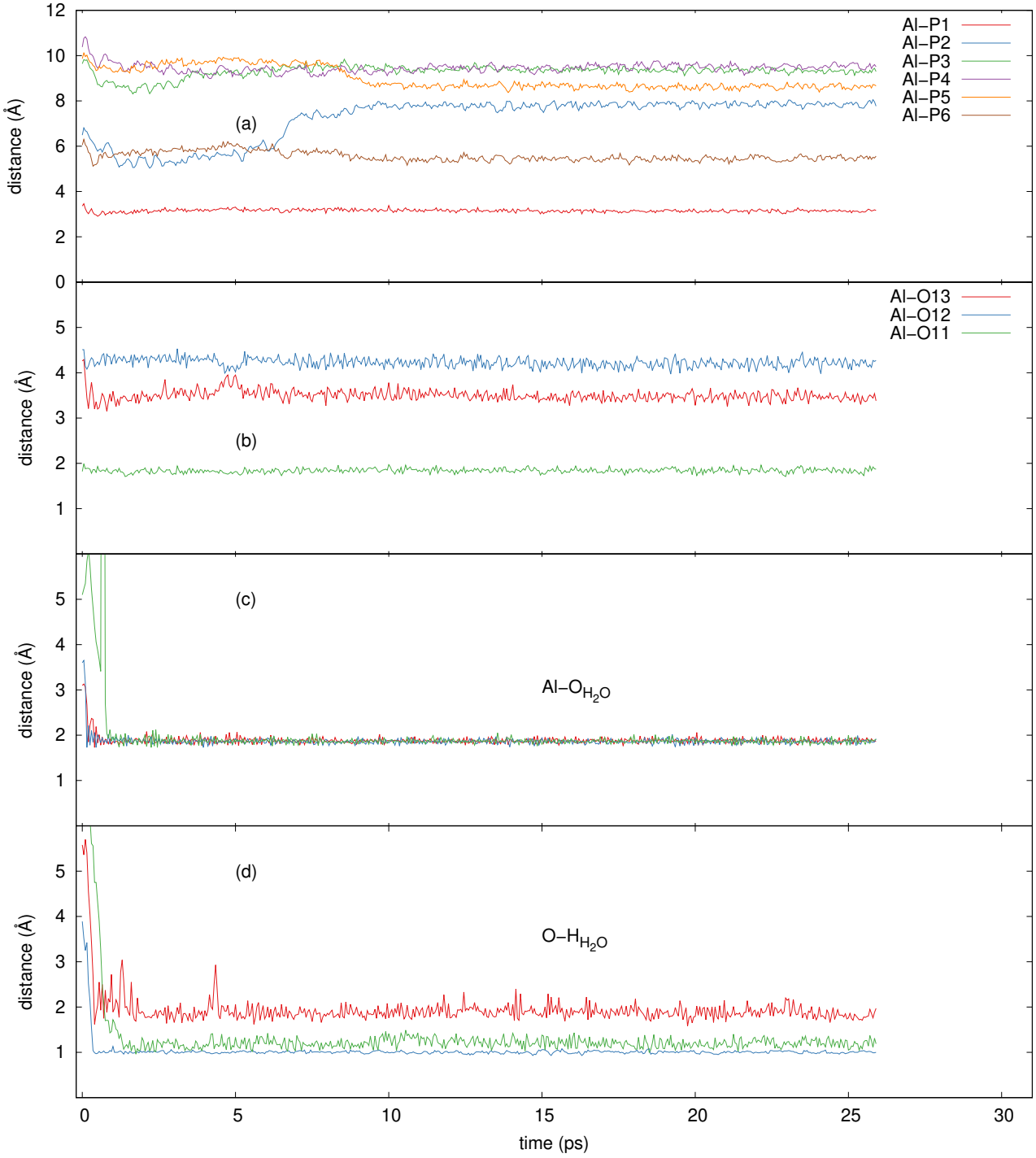


Figure S12: In IHP **2M(1)** motif, distance between surface Al1 contributed to **M** motif and all phosphorus atoms in IHP (a), distance between surface Al1 contributed to **M** motif and bonded phosphate oxygens (b), distance between a few different surface Al and water oxygens (c), distance between a few different diaspore oxygens and water hydrogens (d).

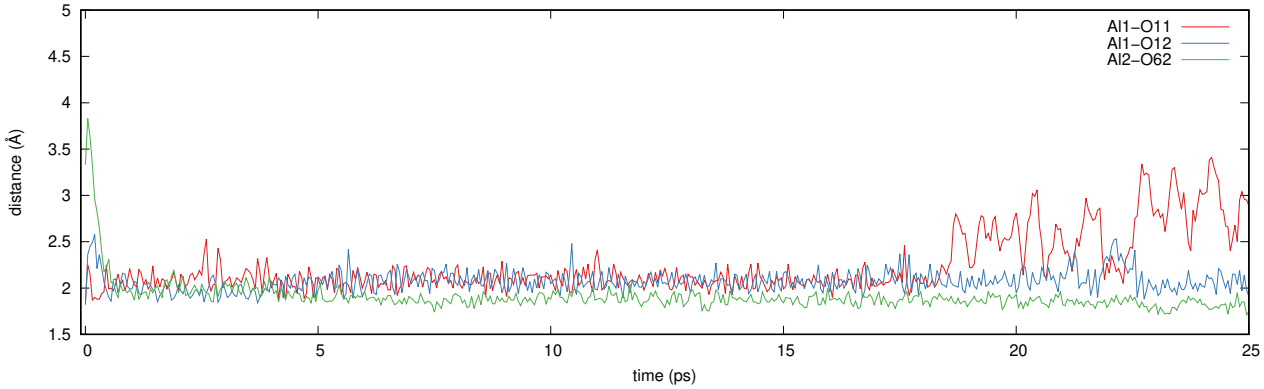


Figure S13: Al-O bond lengths in IHP **2M(2)** motif along MD trajectory. Observe disassociation of Al1-O11 and formation of Al2-O62 resulting in **2M** motif until the end of the trajectory.

Publication 5

P. B. Ganta, O. Kühn, Ashour A. Ahmed. QM/MM molecular dynamics investigation of the binding of organic phosphates to the 100 diaspore surface. Front. For. Glob. Change **2020**, 3, 71.

Contribution: Ashour A. Ahmed is credited with the conceptualization of the scientific approach for this study, development of the methodology, acquisition of funding, contribution to writing the original manuscript, and supervising the PhD student (Mr. P.B. Ganta). Ashour A. Ahmed, along with the co-authors, has discussed and interpreted the results and contributed to writing, reviewing, and editing the manuscript.

URL: https://doi.org/10.3389/ffgc.2020.00071

QR:



This is an open-access article distributed under the terms of the Creative Commons Attribution License (CC BY). The use, distribution or reproduction in other forums is permitted, provided the original author(s) and the copyright owner(s) are credited and that the original publication in this journal is cited, under accepted academic practice.

frontiers in Forests and Global Change

ORIGINAL RESEARCH
published: 17 June 2020
doi: 10.3389/ffgc.2020.00071

QM/MM Molecular Dynamics Investigation of the Binding of Organic Phosphates to the 100 Diaspore Surface

Prasanth B. Ganta[1], *Oliver Kühn*[1,2] *and Ashour A. Ahmed*[1,2]*

[1] *Institute of Physics, University of Rostock, Rostock, Germany,* [2] *Department of Life, Light, and Matter (LLM), University of Rostock, Rostock, Germany*

The fate of phosphorus (P) in the eco-system is strongly affected by the interaction of phosphates with soil components and especially reactive soil mineral surfaces. As a consequence, P immobilization occurs which eventually leads to P inefficiency and thus unavailability to plants with strong implications on the global food system. A molecular level understanding of the mechanisms of the P binding to soil mineral surfaces could be a key for the development of novel strategies for more efficient P application. Much experimental work has been done to understand P binding to several reactive and abundant minerals especially goethite (α-FeOOH). Complementary, atomistic modeling of the P-mineral molecular systems using molecular dynamics (MD) simulations is emerging as a new tool in environmental science, which provides more detailed information regarding the mechanisms, nature, and strength of these binding processes. The present study characterizes the binding of the most abundant organic phosphates in forest soils, inositol hexaphosphate (IHP), and glycerolphosphate (GP), to the 100 diaspore (α-AlOOH) surface plane. Here, different molecular models have been introduced to simulate typical situations for the P-binding at the diaspore/water interface. For all models, quantum mechanics/molecular mechanics (QM/MM) based MD simulations have been performed to explore the diaspore–IHP/GP–water interactions. The results provide evidence for the formation of monodentate (**M**) and bidentate (**B**) motifs for GP and **M** and as well as two monodentate (**2M**) motifs for IHP with the surface. The calculated interaction energies suggest that GP and IHP prefer to form the **B** and **2M** motif, respectively. Moreover, IHP exhibited stronger binding than GP with diaspore and water. Further, the role of water in controlling binding strengths via promoting of specific binding motifs, formation of H-bonds, adsorption and dissociation at the surface, as well as proton transfer processes is demonstrated. Finally, the P-binding at the 100 diaspore surface plane is weaker than that at the 010 plane, studied previously (Ganta et al., 2019), highlighting the influential role of the coordination number of Al atoms at the top surface of diaspore.

Keywords: P-efficiency, P-adsorption, inositolhexaphosphate (IHP), glycerolphosphate (GP), diaspore (AlOOH), QM/MM simulations

OPEN ACCESS

Edited by:
Friederike Lang,
University of Freiburg, Germany

Reviewed by:
Zachary E. Kayler,
University of Idaho, United States
Daniel Tunega,
University of Natural Resources and Life Sciences Vienna, Austria

***Correspondence:**
Ashour A. Ahmed
ashour.ahmed@uni-rostock.de

Specialty section:
This article was submitted to Forest Soils, a section of the journal Frontiers in Forests and Global Change

Received: *12 December 2019*
Accepted: *20 May 2020*
Published: *17 June 2020*

Citation:
Ganta PB, Kühn O and Ahmed AA (2020) QM/MM Molecular Dynamics Investigation of the Binding of Organic Phosphates to the 100 Diaspore Surface. Front. For. Glob. Change 3:71. doi: 10.3389/ffgc.2020.00071

1. INTRODUCTION

Phosphorus (P) is essential for plant growth and plays an important role in photosynthesis, energy storage, cell growth, and many other plant processes. It has been pointed out that P scarcity could arise in near future (Cordell and Neset, 2014) and to cope with this situation there is a need to understand the P cycle in forest and agro-ecosystems (Bol et al., 2016, 2018; Missong et al., 2018). In general, phosphates bind to soil components like soil organic matter (Gros et al., 2017, 2019; Ahmed et al., 2018a) and to soil minerals like Fe/Al(oxyhydr)oxides (Hens and Merckx, 2001; Jiang et al., 2015; Kruse et al., 2015; Ahmed et al., 2019) and amorphous Fe/Al hydroxide mixtures (Gypser et al., 2018). The P bound to soil minerals forms colloidal P complexes and consequently becomes unavailable to plants causing P ineÿ ciency (Holzmann et al., 2015; Bol et al., 2016). These colloidal P complexes disperse during heavy rains and accumulate in specific regions resulting in P leaching which further reduces P availability to plants (Boy et al., 2008). Molecular level understanding of P adsorption onto these soil minerals could support e" orts to improve P availability to plants (Bol et al., 2016).

Goethite (α-FeOOH) is one of the most common and abundant soil minerals that interacts strongly with phosphates (Parfitt and Atkinson, 1976; Torrent et al., 1992; Chitrakar et al., 2006; Kubicki et al., 2012; Ahmed et al., 2019). It is a highly reactive soil mineral containing ferric ions (Fe^{+3}) with common surface planes as 010, 100, 110, 021 (according to *Pnma* space group) (Cornell and Schwertmann, 2003). The surface iron atoms are coordinated by 3, 4, 5, or more atoms depending on the surface plane as well as the pH of the environment. Consequently, goethite exhibits di" erent levels of saturation according to the interaction with its environment. The same holds true for most minerals, i.e., minerals exhibit a net positive or negative surface charge based on surface (un)saturation and pH (Cornell and Schwertmann, 2003). Hence, the type of surface plane, its termination and saturation are important factors that influence the adsorption of phosphates onto soil minerals. For instance, Ahmed et al. (2018b) studied glyphosate adsorption at goethite surface with three di" erent degrees of (un)saturation (Fe surface atoms coordinated by 3, 4, and 5 O^{-2}/OH^{-} groups) and showed the e" ect of the surface's (un)saturation on phosphate binding stability.

In addition to surface saturation and pH, the Fe and Al ratio in amorphous Fe/Al hydroxides is also vital for understanding the phosphates' interaction with soil minerals. Gypser et al. (2018) showed the influence of the Fe:Al ratio in amorphous Fe/Al hydroxide mixtures on phosphate adsorption/desorption rates. The omnipresent Al in weathering environment results in most of Fe oxides in soils being substituted by Al and goethite is no exception (Cornell and Schwertmann, 2003). Diaspore (α-AlOOH) is isomorphous with goethite with Al^{+3} oxidation state exhibiting a higher surface energy compared to goethite (Guo and Barnard, 2011). Since amorphous Fe/Al hydroxide mixtures exist in soils, analyzing phosphate binding to diaspore provides additional insight into the P interaction with these amorphous mixtures.

Orthophosphates (Newman and Tate, 1980), inositolhexaphosphate (IHP) (Turner et al., 2002; Doolette et al., 2009; Gerke, 2015), and glycerolphosphate (GP) (Pant et al., 1999; Vincent et al., 2013; Missong et al., 2016) are the most abundant phosphates in soils. Orthophosphate interaction with goethite has been studied extensively (Parfitt and Atkinson, 1976; Torrent et al., 1992; Chitrakar et al., 2006; Ahmed et al., 2019). Yan et al. (2014) studied sorption of di" erent phosphates involving GP and IHP on aluminum (oxyhydr)oxides. They found that the maximum adsorbed phosphate normalized to the mass of adsorbent increases with decreasing crystallinity of the minerals: α–Al_2O_3 < boehmite < amorphous $Al(OH)_3$. Moreover, they concluded that the phosphate adsorption, interfacial reactions, and phosphate fate in the environment are strongly a" ected by molecular structure and size of phosphates, and degree of crystallinity and crystal structure of mineral surfaces. Li et al. (2017) suggested that GP adsorbs onto the goethite surface through its phosphate group forming inner-sphere complexes. IHP has six phosphate groups, and in general it exhibits strong binding with P-fixing minerals compared to other phosphates with fewer phosphate groups. Anderson and Arlidge (1962) suggested that the total number of phosphate groups in a compound determines the stability of its interaction with minerals. Ognalaga et al. (1994) showed that IHP forms inner-sphere complexes with goethite through its phosphate groups and suggested that up to four phosphate groups could be involved in binding with the mineral surface; the remaining non-interacting phosphate groups could alter the electrochemical properties of the surroundings. However, Guan et al. (2006) revealed that only three phosphate groups were bound to aluminum hydroxide while the other three groups remained free. This was based on adsorption experiments of IHP on amorphous aluminum hydroxide, FTIR characterization, and quantum chemical calculations.

Quantum chemical calculations become increasingly important when it comes to develop a mechanistic understanding of chemical processes in general. Although not yet widely used, computational chemistry approaches to environmentally relevant questions are recognized as tools to complement experimental investigations. Interestingly, as early as 1973 Tossell et al. (1973) studied electronic structure and bonding in iron oxide minerals with molecular simulations and validated this approach with experimental studies. Kwon and Kubicki (2004) used molecular simulations to resolve controversies in experimental studies related to phosphate surface complexes on iron hydroxides. In another study, Kubicki et al. (2012) demonstrated that phosphate interaction with goethite involves a variety of surface complexes in multiple configurations, which explained the diÿ culties one faces when interpreting, e.g., IR spectra. Moreover, Ahmed et al. (2018b) explored the possible binding mechanisms for glyphosate (GLP) with three goethite surface planes (010, 001, and 100) in the presence of water via ab initio molecular dynamics simulations. The results showed the prominence of water in controlling the GLP–goethite–water interactions. Further (Ahmed et al., 2019) investigated the molecular level mechanism of phosphate binding at the goethite–water interface referring to the possible phosphate

binding motifs formed at the modeled goethite surface planes. Moreover, the theoretical assignment of IR spectra in the latter study introduced a benchmark for characterizing experimental IR data for a distribution of adsorbed phosphate species. This incomplete list already indicates the huge potential of computational chemistry as an emerging powerful tool for detailed investigations of complex geochemical reactions and especially reaction mechanisms of P-species in soil (for a more complete overview, see also Kubicki, 2016).

Which computational methods are available today? Thinking of it in terms of a hierarchy (Kubicki, 2016; Ozboyaci et al., 2016), quantum mechanics (QM) methods are at the top because they provide, at least in principle, an unbiased ab initio description in terms of the molecular Schrödinger equation. In practice, such a treatment is not feasible except for the simplest cases. Density Functional Theory (DFT) has emerged as a low-cost alternative, which despite of the involved approximations often provides reliable results even for systems with hundreds of atoms (Kubicki, 2016). At the bottom of the hierarchy there are molecular mechanics (MM) methods, which are based on parameterized empirical functions (force fields) describing bonded and non-bonded interactions. This allows to treat millions of atoms, but unless special purpose force fields are used chemical reactions, i.e., bond making and breaking, cannot be simulated (González, M.A., 2011). Here, the hybrid QM/MM approach comes into play, combining the accuracy of QM methods with the eÿ ciency of MM methods. In this approach, the reactive region of the molecular system is treated at the QM level while the remaining part of the system enters at the MM level (Senn and Thiel, 2009). By this, the bond changes, proton transfer events and hydrogen bonds (HBs), e.g., at water-mineral interfaces can be properly described. Besides providing energies in dependence on nuclear positions, forces on the nuclei can be calculated as well. This is prerequisite for molecular dynamics simulations which gives statistical information including thermally accessible configurations (Marx and Hutter, 2009).

In an earlier hybrid QM/MM study of IHP and GP binding to the 010 diaspore surface plane we have demonstrated a strong interaction of IHP/GP with the diaspore surface (Ganta et al., 2019). Here, IHP forms multiple intramolecular HBs with three of its phosphate groups bound to the surface, while GP is bound through its single phosphate group only. Overall, it has been found that proton transfers from phosphate to water or surface have a stabilizing e" ect, most likely due to the interaction of the HBs dipole with surface charges. Moreover, in case of IHP intramolecular HBs can be formed, which lead to a steric constraint that could weaken the binding to the surface. Since the interaction of IHP and GP with diaspore is not yet fully explored, in the present work we extend our previous study in two directions, i.e., we consider a chemically di" erent surface plane and incorporate the e" ect of saturation of the diaspore surface on phosphates adsorption. In our previous work (Ganta et al., 2019), IHP/GP and water showed strong and spontaneous interactions with an unsaturated diaspore surface (010 in *pnma*) where the surface Al atoms are coordinated by four oxygens (O^{-2}/OH^{-} groups). Here, a more saturated diaspore surface (100 in *pnma*) is selected where the surface Al atoms are coordinated by five oxygens i.e., O^{-2}/OH^{-} groups. The main objective of current work is to characterize the binding mechanism of IHP and GP at this diaspore–water interface and also to understand the e" ect of (un)saturation of the diaspore surface on this binding mechanism.

2. MOLECULAR MODELING APPROACH

In general, the surface charge of a certain mineral can be determined as a function of pH via its point of zero charge (PZC) (Tan, 2011). For pH > PZC, the mineral surface is saturated with negative surface charges which attract cations. In contrast, for pH < PZC, the mineral surface is unsaturated with positive surface charges which attract anions. The phosphates in general exhibit overall negative charge and hence can be adsorbed at the partially unsaturated 100 diaspore surface (according to the *Pnma* space group) (Tan, 2011). The diaspore unit cell has four AlO(OH) units i.e., total of 16 atoms with lattice constants $a = 9.4253$, $b = 2.8452$, $c = 4.4007$ Å (see **Figure 1C**). The 100 surface plane model is generated by repetition of the diaspore unit cell as $1a \times 8b \times 5c$ along x, y, z axes, respectively (see **Figure 1D**). In total, the used diaspore slab consists of 640 atoms (160 Al, 160 H, and 320 O atoms). Observe that the surface Al atoms are coordinated by five oxygen atoms (see **Figure S3B**). The phosphates IHP and GP (see **Figures 1A,B**) are modeled to have their phosphate group(s) interacting via inner-sphere complexes with surface Al atoms of diaspore (see **Figures 1F–H**, **Figures S2A–C**). The diaspore-IHP/GP complexes are then solvated using the *solvate* plugin from the VMD package (Humphrey et al., 1996) with a water layer of about 18 Å perpendicular to the surface along the x axis and with a density of $\approx 1\,\mathrm{g\,cm^{-3}}$ (see **Figure 1E**). Since we are interested in IHP/GP interaction at diaspore–water interface, the QM part of the system (see dashed box in **Figure 1E**) includes the top layer of diaspore (160 atoms), IHP (54 atoms)/GP (19 atoms), and a few water molecules ($\approx$ 53 molecules depending on the setup) surrounding IHP/GP within layer of $\approx$ 10 Å perpendicular to the diaspore surface. The enclosing QM box has a size of $22 \times 8b \times 5c$ Å i.e., $22 \times 22.7616 \times 22.0035$ Å, where b, c are diaspore lattice constants (see **Figure 1E**). The remaining part of the system is treated at the MM level.

The initial motifs of diaspore–GP complexes include the monodentate motif **M** (1Al + 1O) (see **Figure 1F**) and bidentate motif **B** (2Al + 2O, here both oxygens are from same phosphate group) (see **Figure 1G**). Note that in contrast to this setup, in the 010 case the two oxygens bind to the same Al atom. In addition to these two, the diaspore–IHP complexes include the four monodentate motif **4M** (4Al + 4O) as experimental studies suggest that IHP forms multiple bonds with the goethite surface (Ognalaga et al., 1994; Guan et al., 2006) (see **Figure 1H**, **Figure S2C**). Note that in principle even more initial conditions/motifs could be sampled. But considering the size of the modeled systems here and the used computationally expensive QM/MM level of theory the initial configurations for the MD simulations are limited to the most common and experimentally observed binding motifs. More technical details

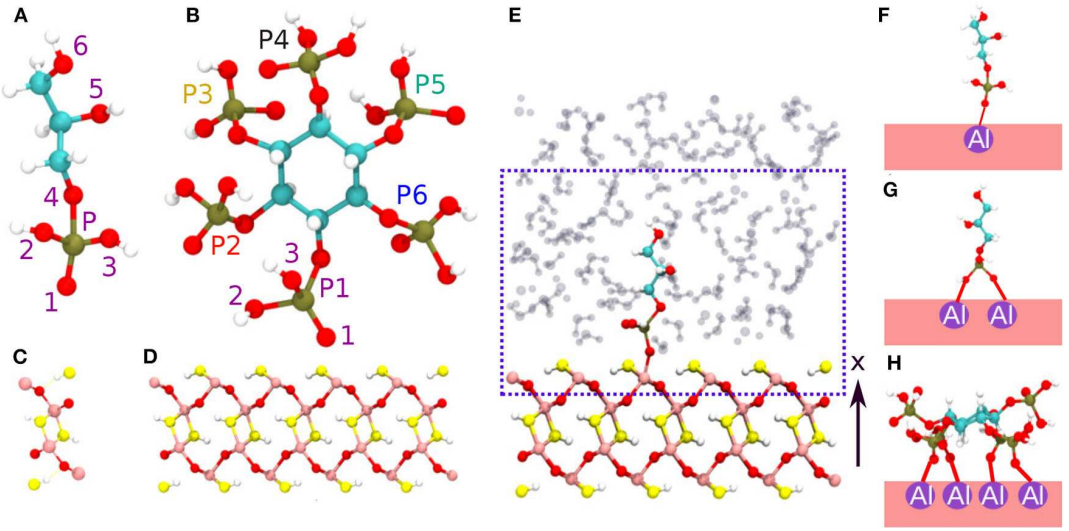


FIGURE 1 | Phosphates GP **(A)** and IHP **(B)**. The oxygen and phosphorus atoms are labeled here to ease the discussion of diaspore–IHP/GP–water interactions. Diaspore unit cell **(C)**, side view of the modeled diaspore surface **(D)**, diaspore–GP–water complex and the blue box including atoms described at quantum mechanical level of theory (QM part) and remaining atoms at molecular mechanics level (MM part) **(E)**, **M** motif **(F)**, **B** motif **(G)**, **4M** motif **(H)**. Pink, red, yellow, white, lime, and cyan colors correspond to Al, bridging oxygen, hydroxyl oxygen, hydrogen, phosphorus, and carbon, respectively.

about QM and MM methods and their mutual interaction adopted here is given in **Supplementary Material**. The QM/MM based MD simulations are performed for 25 ps with 0.5 fs time step and with an average temperature of 300 K maintained using canonical sampling through the velocity rescaling thermostat (CSVR) (Bussi et al., 2007). Here, for each molecular model the first 10 ps of the MD trajectory is assigned for equilibration. The last 15 ps of the trajectory is considered as the production trajectory which is used for analysis of interactions at diaspore–water interface with IHP/GP.

To analyze the interaction energies of the complexes, snapshots are taken at every 100 fs of the production trajectory and interaction energies between diaspore and IHP/GP ($E_{diaspore-IHP/GP}$), IHP/GP and water ($E_{IHP/GP-water}$), and diaspore and water ($E_{diaspore-water}$) are calculated. For example, the interaction energy E_{int} between diaspore and GP for a certain diaspore–GP–water snapshot is calculated as follows:

$$E_{int} = E_{diaspore-GP} - (E_{diaspore} + E_{GP}) \quad (1)$$

where $E_{diaspore-GP}$, E_{GP}, and $E_{diaspore}$ denote electronic energies of the diaspore–GP complex, GP and diaspore surface, respectively. Likewise, the interaction energies for each pair of diaspore, IHP/GP and water are calculated at every 100 fs during the corresponding production trajectory. The interaction energies with water are divided by the total number of water molecules involved in the simulation box for better comparison. More details regarding the calculation of interaction energies are given in Ganta et al. (2019).

The HBs strength between IHP/GP and water as well as for the intramolecular HBs of one IHP motif are analyzed using geometrical correlations of distances between atoms in HB as

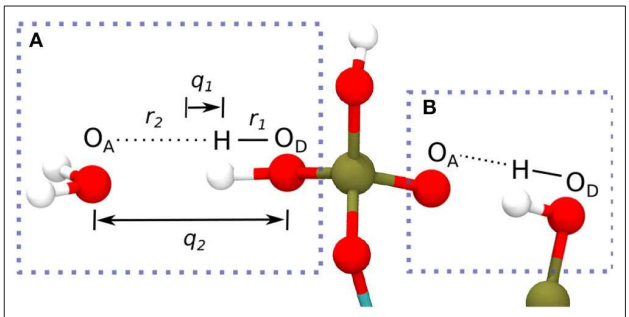


FIGURE 2 | Definition of coordinates q_1 and q_2 in a HB between water's oxygen (O_A) and IHP's oxygen (O_D) from a phosphate group **(A)** (Limbach et al., 2009), intramolecular HB in IHP **(B)**.

discussed in Strassner (2006), Limbach et al. (2009), Yan and Kühn (2010), and Zentel and Kühn (2017). The quantities q_1 and q_2 in **Figures 4**, **6** below are defined as the deviation of the hydrogen from HB center assuming a linear HB (q_1) and the total HB length (q_2) (see **Figure 2A**). Geometrically q_1 and q_2 are defined as $q_1 = \frac{1}{2}(r_1 - r_2)$ Å and $q_2 = (r_1 + r_2)$ Å where r_1, r_2 denote the distance between donor oxygen and hydrogen (O_D—H) and distance between hydrogen and acceptor oxygen ($H\cdots O_A$), respectively (see **Figure 2A**). The same holds true for intramolecular HBs between phosphate groups for the IHP case (see **Figure 2B**).

A HB will be called strong if $q_1 \approx 0$ and q_2 is in the range 2.2-2.5 Å. Similarly, moderate and weak HBs have q_2 distances ranging from 2.5 to 3.2 and 3.2 to 4 Å, respectively. Also if $q_1 < 0$ the hydrogen atom stays with the donor oxygen and if $q_1 > 0$

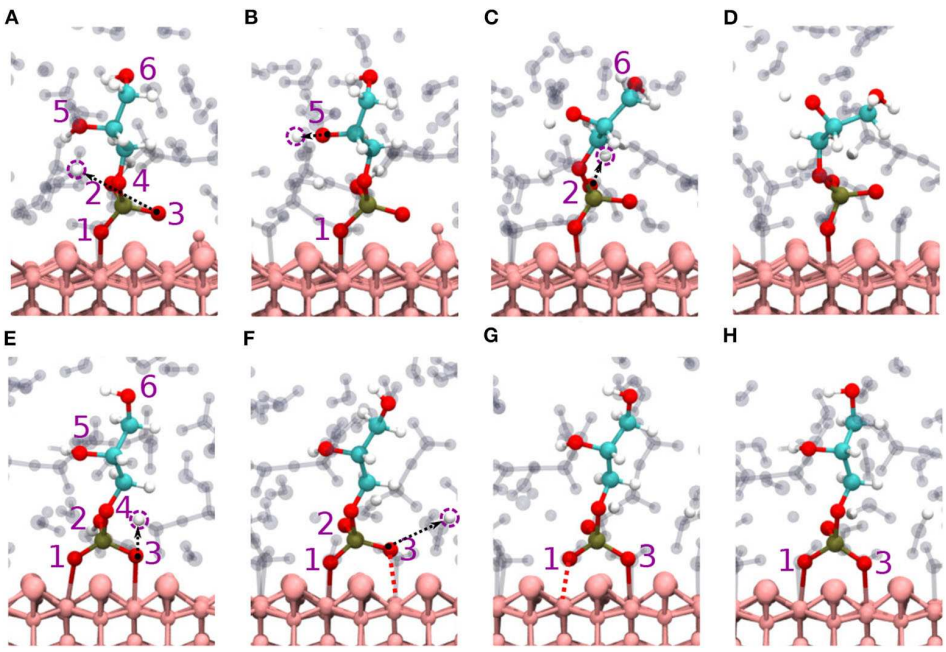


FIGURE 3 | Diaspore–GP–water snapshots displaying proton transfer events and GP dynamics along trajectories. Proton transfers observed during production trajectory of **M** motif from O3 to water **(A)** from O5 to water **(B)**, and from O2 to water **(C)**, GP **M** motif at 25 ps **(D)**. Proton transfer events in **B** (2Al+2O) motif from O3 to water **(E)**, from O2 to water and momentary dissociation of Al1-O1 bond **(F)**, momentary dissociation of Al2-O3 bond **(G)**, GP **B** motif at 25 ps **(H)**.

the hydrogen atom (proton) transferred to the acceptor oxygen. In the following a HB analysis is performed for the QM part of the system only as the emphasis of this study is on the interface region where the binding/adsorption process takes place.

3. RESULTS AND DISCUSSION

3.1. Diaspore–GP–Water Interactions

3.1.1. GP M Motif

For the GP-**M** initial condition a stable monodentate (1Al+1O) motif is observed between GP and the diaspore surface over the course of the production trajectory with the Al-O1 average bond length of 2.3 Å (see **Figures 3A–D**). The average geometry of the PO_4 moiety here has root mean square deviation (RMSD) value of 0.17 Å with respect to free tetrahedral PO_4^{3-} (see **Figure S2D**).

Proton transfer events from GP to the diaspore surface are not observed, instead three proton transfer events are found from O3, O5, and O2 oxygens of GP to water (see **Figures 3A–C**), respectively. On average, eight HBs are observed between GP and water in the production trajectory. Here, the GPs oxygen atoms act as HB donors (Ox_D) as well as acceptors (Ox_A). Exemplary analysis of six of the above eight HBs shows that four ($O2_A$, $O3_A$, $O5_A$, $O5_D$) are strong to moderately strong HBs and two ($O1_A$, $O6_A$) moderately strong to weak HBs (see **Figures 4A–C**).

Regarding the diaspore–water interaction, an average of 17 water molecules (out of 40 surface Al atoms) formed **M** binding motifs (Al-O_{H_2O}) with the diaspore surface and have average bond length of 1.9-2.3 Å. Also moderately strong HBs are observed between water and diaspore (see **Figure S1A**). This scheme of diaspore–water interactions is also observed for the other diaspore–IHP/GP–water models studied below. For the average diaspore–water interaction energy per water molecule one obtains about −3 kcal/mol for all considered models.

The time averaged interaction energy per surface bond between diaspore and GP is around −23 kcal/mol (see **Table 1**). The average GP–water interaction energy per water molecule is −2.6 k cal/mol.

3.1.2. GP B Motif

The **B** motif (2Al+2O i.e., Al1-O1 and Al2-O3) is observed over the course of the production trajectory with Al1-O1 and Al2-O3 covalent bond length ranging from 2-2.7 and 1.9-2.7 Å with an average value of 2.4 and 2.3 Å, respectively (see **Figures 3E–H**). Most notably the Al2-O3 and Al1-O1 bonds are elongated and compressed in an alternating see-saw fashion as seen in **Figures 3F,G**. The **B** motif's average geometry of the PO_4 moiety has a RMSD value of 0.17 Å with respect to the free tetrahedral PO_4^{3-}.

Proton transfer events are observed from O3 and O2 oxygens to water (see **Figures 3E,F**), respectively. The **B** motif features on average a total of seven HBs between GP and water. According to **Figures 4D–F**, four ($O1_A$, $O2_A$, $O2_D$, $O5_D$) strong to moderately strong HBs and two ($O1_A$, $O6_D$) moderately strong to weak HBs are formed between GP and water.

The average interaction energy per surface bond between diaspore and GP for the **B** motif is around −15 kcal/mol. The

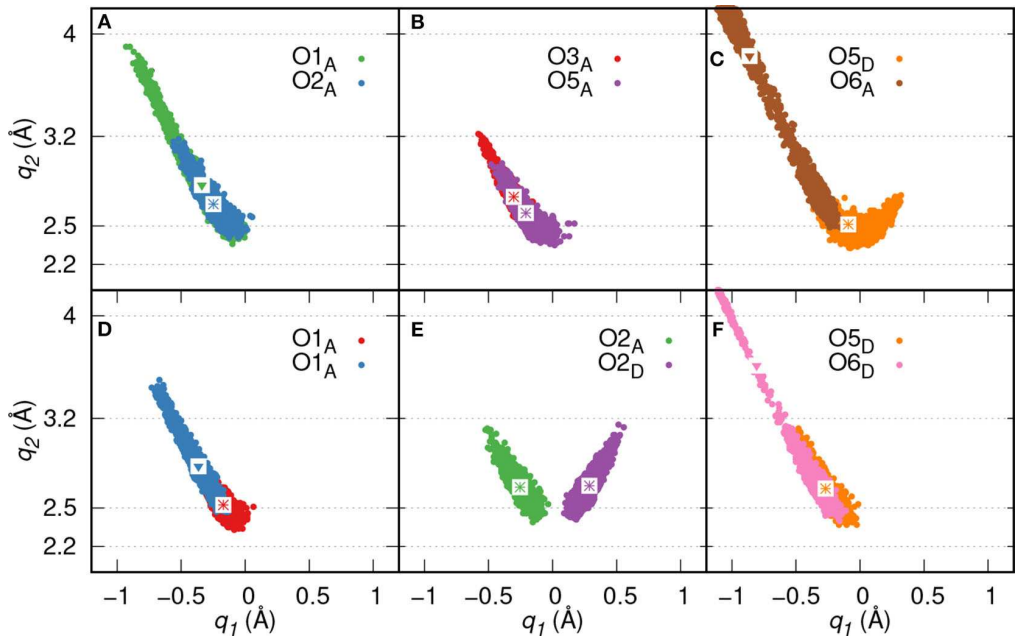


FIGURE 4 | HB correlation q_2 *vs.* q_1 of HBs formed between GP and water in GP's **M** motif **(A–C)** and **B** motif **(D–F)**, respectively. The average q_1 and q_2 coordinate pairs are shown as points in white square boxes. A strong to moderately strong HB is denoted as * while a moderately strong HB and a moderately strong to weak HB are denoted as • and ▼, respectively.

TABLE 1 | The per bond time averaged interaction energies (calculated with Equation 1) of diaspore–IHP/GP complexes and some selected bond lengths and distances.

			100 diaspore surface		
***P*o**	**Motif**	**E_{int}/bond (kcal/mol)**	**Al-O_P (Å)**	**Al-P (Å)**	**RMSD(PO_4^{3-}) (Å)**
GP	**M**	−23	2.3	3.4	0.17
	B	−15	2.3 and 2.4	3.3	0.17
IHP	**M(1)**	−33	2.4	3.5	0.16
	M(2)	−18	2.7	3.6	0.19
	2M	−109	2.1 and 2.2	3.3 and 3.4	0.18 and 0.17
			010 diaspore surface (Ganta et al., 2019)		
GP	**B**	−148	2.03 and 2.05	2.65	0.1
IHP	**3M**	−145	1.90 and 1.88 and 1.86	3.25 and 3.17 and 3.18	0.07 and 0.08 and 0.1

*The RMSD difference between average phosphate geometry and isolated tetrahedral PO_4^{3-} (see **Figure S2D**) is also provided. Here, P_o denotes phosphate and motif denotes average motif observed during production trajectory. Further, Al-O_P denotes bond distance between covalent bonded Al and O_P oxygen of IHP/GP.*

per surface bond interaction energy here is smaller than for the **M** motif due to GP's see-saw type of motion over the surface. Nevertheless, the total interaction energy observed here is larger than for the **M** motif and hence the **B** motif is more likely to form.

Note that due to the formation of a strong to moderately strong HB with water, the O3 oxygen in **M** cannot easily transform into the **B** motif, i.e., the barrier is too high to be sampled in the present trajectory (see **Figure 4B**). The average GP–water interaction energy per water molecule is around −2.3 kcal/mol. The smaller value as compared with **M** could be due to the additional proton transfer event observed in that case.

3.2. Diaspore–IHP–Water Interactions

3.2.1. IHP M Motifs

Here, two initial configurations (**M**, **B** motifs) of the diaspore–IHP–water model resulted in two di! erent **M** final motifs. In the first case, **M(1)**, the initial configuration was an **M** motif, wherein O11 oxygen is aligned to form a **M** motif with a surface Al atom (see **Figure S2A**). A stable **M** motif is observed throughout the production trajectory with average Al-O11 bond length of 2.4 Å (see **Figures 5A–D**). The series of events that are observed during the formation of the **M(1)** motif are: a proton transfer from O12 to water (see **Figure 5A**), followed by intramolecular proton transfer from O62 to O12 and formation of O13-H-O61 intramolecular HB (see **Figure 5B**). After a few femtoseconds, the O12-H-O62 HB is formed and a proton transfer is observed from O32 to water (see **Figure 5C**) to reach the final **M** motif in **Figure 5D**. The events in **Figures 5A–C** occurred within 2 ps of the simulation trajectory. Overall, a total of three protons transfer events are observed from IHP to water from O12, O53, and O32 (see **Figures 5A–C**), respectively. On average IHP has formed 19 HBs with water over the course of the production trajectory. Analyzing for illustration 12 out of these 19 HBs, IHP has formed nine ($O12_A$, $O21_A$, $O22_A$, $O23_A$, $O31_A$, $O43_A$, $O51_A$, $O53_A$,

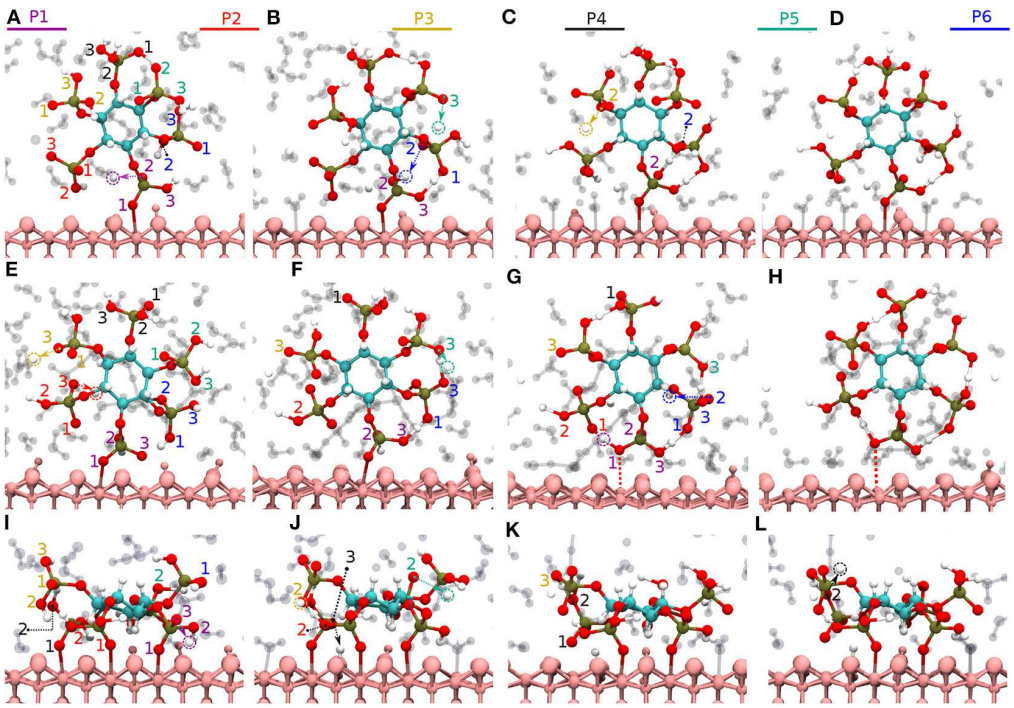


FIGURE 5 | Diaspore–IHP–water snapshots displaying proton transfer events and IHP dynamics along trajectories. The phosphate groups are color-coded and the oxygen atom label color denotes to the phosphate group it belongs. In **M(1)** motif, proton transfer from O12 to water **(A)**, proton transfer from O53 to water and intramolecular proton transfer from O62 to O12 **(B)**, moderately strong O12-H-O62 HB and proton sharing between O12 to O62 oxygens and proton transfer from O32 to water **(C)**, **M(1)** motif at 25 ps **(D)**. In **M(2)** motif, dissociation of Al2-O13 covalent bond due to O13-H-O61 HB and proton transfers from O23 and O33 to water **(E)**, proton transfer from O53 to water and formation of O53-H-O63 HB **(F)**, dissociation of Al1-O11 bond due to formation of O11-H-O21 HB **(G)**, **M(2)** motif at 25ps **(H)**. In **2M** motif, dissociation of Al4-O51 bond and proton transfer from O13 to water **(I)**, proton transfer from O43 to diaspore and from O32 to water, also proton sharing and HB between O22 and O32 **(J)**, and between O33 and O42 followed by dissociation of Al3-O41 bond **(K)**, proton transfer from O42 to water and **2M** motif at 25 ps **(L)**.

$O63_D$) strong to moderately strong HBs, two ($O33_D$, $O41_A$) moderately strong HBs and one ($O31_A$) moderately strong to weak HB with water (see **Figures 6A–E**). Interestingly, IHP also forms multiple intramolecular HBs, for instance, O13-H-O61, O41-H-O52, and O12-H-O62 (see **Figures 5A–C**). Analyzing the strength of the intramolecular HBs between P1 and P6 phosphate groups, one finds two (O13-H-O61, O12-H-O62) moderately strong HBs (see **Figure 6F**). The average geometry of PO_4 moiety has a RMSD value of 0.16 Å with respect to the free tetrahedral PO_4^{3-}.

The time averaged interaction energy per surface bond between diaspore and IHP is around −33 kcal/mol (see **Table 1**) and between IHP and water is around −5.5 kcal/mol per water molecule. Notice that IHP exhibits a larger interaction energy with water as well with the diaspore surface compared to GP.

For the **M(2)** motif, the initial configuration had the O11 and O13 oxygens aligned such as to form a **B** motif with adjacent surface Al atoms (see **Figure S2B**). The Al2-O13 covalent bond is dissociated during the trajectory and the **B** motif is transformed into the **M(2)** motif (see **Figures 5E,F**). Over the course of the production trajectory the Al1-O11 bond length ranges from 2.4 to 3.2 Å with an average of 2.7 Å. In more detail, the series of events that unfold in this case are as follows: From the O23 and O33 oxygens, two protons are transferred to water and the Al2-O13 covalent bond is dissociated (see **Figure 5E**). After a few femtoseconds, a proton transfer is observed from O53 to water followed by formation of an intramolecular HB between O53 and O63 oxygens (see **Figure 5F**). Also formation of the intramolecular O13-H-O61 HB is observed. With progressing simulation time an intramolecular proton transfer event is observed from O12 to O21, followed by formation of O11-H-O21 HB. Afterwards, the Al1-O11 covalent bond weakens at around 6 ps and its bond length ranges from 2.4 to 3.2 Å further on (see **Figure 5G**, **Figure S1B**). In addition, a proton transfer is observed from O62 to water (see **Figure 5G**). The snapshot at 25 ps shows that multiple inter- and intramolecular HBs are observed for IHP (see **Figure 5H**). Their characterization in terms of HB geometries leads to a similar distribution of HB strengths as for **M(1)**. Overall the average geometry of PO_4 moiety has RMSD value of 0.19 Å with respect to the free tetrahedral PO_4^{3-}.

The average interaction energy per surface bond between the diaspore surface and IHP in this case is around −18 kcal/mol. The interaction energy observed here is smaller than for the **M(1)**

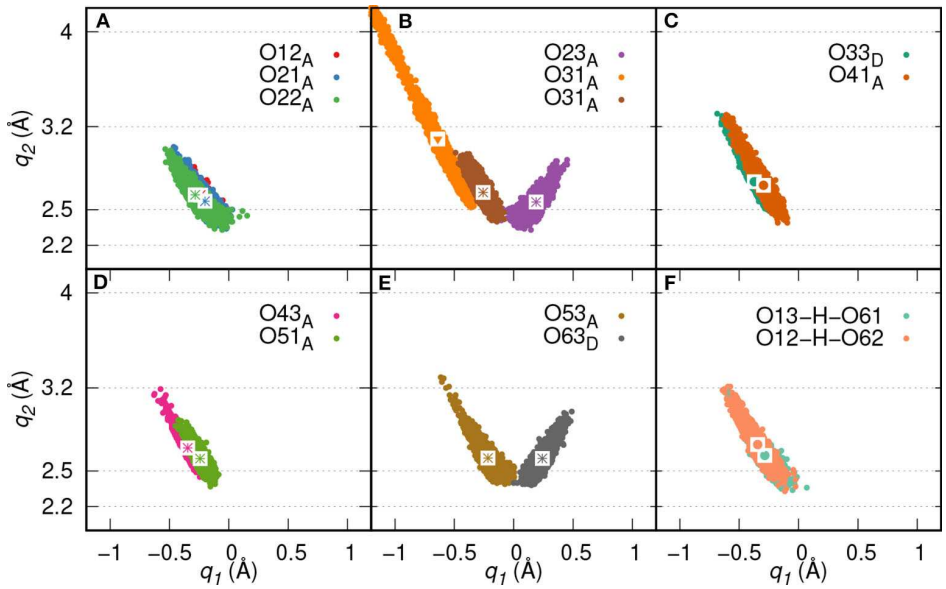


FIGURE 6 | HB correlation q_2 vs. q_1 of HBs formed between IHP and water **(A–E)** and between P1 and P6 phosphate groups **(F)** along trajectory of IHP's **M(1)** motif. The average q_1 and q_2 coordinate pairs are shown as points in white square boxes. A strong to moderately strong HB is denoted as * while a moderately strong HB and a moderately strong to weak HB are denoted as • and ▼, respectively.

case as the Al1-O11 bond length is longer due to formation of O13-H-O61 and O12-H-O21 intramolecular HBs. The observed interaction energy between IHP and water here is −5.7 kcal/mol per water molecule which is slightly higher than for the **M(1)** case, probably due to additional proton transfer from IHP to water.

3.2.2. IHP 2M Motif

Here, IHP is initially aligned parallel to surface with the non-protonated oxygens of the four phosphate groups forming a **4M** motif, i.e., Al1-O11, Al2-O21, Al3-O41, Al4-O51 covalent bonds with the surface (see **Figure S2C**). However, only a stable **2M** motif is observed along the production trajectory with average bond lengths of Al1-O11, Al2-O21 as 2.13 and 2.22 Å, respectively. The events observed during simulation that led to the formation of **2M** motif are as follows: within a few picoseconds, the Al-O51 bond is dissociated transforming **4M** into a **3M** motif. A proton transfer is observed from O13 oxygen to water and from O43 oxygen to diaspore (see **Figures 5I,J**). Further, an intramolecular HB is observed between O22 and O32 oxygens and two proton transfer events from O32 and O52 to water (see **Figure 5J**). The Al3-O41 covalent bond is disassociated due to intramolecular HB formed between O33 and O42 oxygens (see **Figure 5K**), followed by a proton transfer event from O42 to water (see **Figure 5L**). Totally four proton transfer events are observed from IHP to water and an average of 19 HBs are formed between IHP and water. The inter- and intra-molecular HBs have a similar distribution of strengths as for **M(1)** and **M(2)**. The average geometry of the PO_4 moieties deviate from that of free tetrahedral PO_4^{3-} with RMSD values of 0.18 and 0.17 Å.

The interaction energy between IHP and diaspore in the **2M** motif is −109 kcal/mol per bond (see **Table 1**). The interaction energy is larger here compared to **M(1)** and **M(2)** motifs due to the additional covalent bond and a proton transfer from IHP to the diaspore surface. Hence, the **2M** motif is more likely to form compared to both the **M(1)** and **M(2)** motifs. The average interaction energy per water molecule with IHP is −5.9 kcal/mol which is slightly larger than the IHP–water interaction energy observed in **M(1)** motif case due to additional proton transfer from IHP to water here.

3.3. Effect of Surface Saturation

In the following we will compare the present results with those of our previous work for the 010 surface plane (Ganta et al., 2019). The 010 diaspore surface plane is relatively unsaturated, i.e. the surface Al atoms are coordinated by only four oxygen atoms (see **Figure S3A**). In contrast, for the present more saturated 100 plane, surface Al atoms are coordinated by five oxygens (see **Figure S3B**). Also the 010 diaspore surface plane exhibits higher electrostatic potential compared to the 100 surface plane as shown in **Figure S6**.

For the 010 plane the largest total interaction energy was observed for the **B** and **3M** motif in case of GP and IHP, respectively (see **Table 1**). In case of 100 plane, the **B** and **2M** motifs dominate the total interaction energies. Comparing the two **B** motifs for GP one finds that the binding to 010 being 10 times stronger than to 100 surface plane. The reason for the weaker interaction energy in case of 100 is due to see-saw type

of motion of GP yielding a weakening/strengthening of Al1-O1 and Al2-O3 bonds which is not observed for the 010 plane. This can be attributed to the fact that in case of 010 plane the two oxygens are coordinated to the same Al, whereas for 100 plane the coordination is with two neighboring Al atoms, whose distances is such as to require unfavorably large O_P-P-O_P angles for strong binding. Further stabilization of the GPs **B** motif in the 010 plane case comes from two additional proton transfers observed from GP to the diaspore surface.

Regarding the total interaction energies, the dominant binding motifs for the diaspore–IHP complexes are also di! erent for 010 (**3M**) and 100 (**2M**). In case of 100 the total interaction energy is about two times smaller than for 010. Comparing the two motifs we note in particular that the interaction with the two surfaces is di! erent. This is nicely illustrated by the fact that no stable **4M** motif could be observed for the 100 case. One reason for the transformation of the **4M** motif to **2M** motif is that the Al-O_P bonds (regions R1 and R2, see **Figures S5A–C**) at the 100 diaspore surface are inclined due to O_P and surface hydroxyl oxygen repulsion. Hence the movement of oxygens in the Al-O_P bonds (regions R1 and R2) is restricted to the space between consecutive surface hydroxyl oxygens or to move away from surface (see **Figures S5A–C**). Consequently, upon equilibration the oxygens in the Al-O_P bonds could dissociate from diaspore as they are confined between consecutive surface hydroxyl oxygens (see **Figures S5A–C**). In contrast for the 010 diaspore–IHP case, the oxygens in the Al-O_P bonds (regions R3 and R4, **Figures S5E–G**) are not restricted and they are free to move. Hence a stable **3M** motif is observed over the course of production trajectory (see **Figures S5E–G**). Looking at it from a geometric point of view, Al-Al distances on the 010 surface are about 4.4–5.4 Å which is much larger than the 2.4 Å for the 100 surface where the **2M** motif forms (see **Figures S5D,H**). Given the typical distances between the phosphate groups in IHP, bonding to the 100 surface plane yields a higher strain and thus it becomes weaker as compared with the 010 surface plane.

In case of the 100 surface the diaspore–water interaction energy is 3.4 times smaller compared to the 010 case. In fact less than half of surface Al atoms formed **M** motifs with water compared to the 010 diaspore surface. Also the radial distribution function of diaspore surface oxygens with water hydrogens in **Figure S4** shows higher water accumulation near the 010 diaspore surface compared to the 100 diaspore surface which suggests stronger interaction for the 010 diaspore surface with water.

4. SUMMARY AND CONCLUSIONS

In our previous study (Ganta et al., 2019), a strong and spontaneous binding of IHP and GP with the 010 diaspore surface has been described, which provided the motivation for studying the e! ect of surface saturation on these interactions. Therefore, the more saturated 100 diaspore surface has been investigated here using periodic boundary QM/MM based MD simulations. The analysis of the MD trajectories showed the importance of inter- and intramolecular HBs in the formation of final motifs and also shed light on e! ects that lead to disassociation and association of P-O-Al bonds in the diaspore–IHP/GP–water complexes.

In case of the diaspore–GP–water complexes, the **B** motif's interaction energy per bond is 1.5 times smaller than the **M** motif. But considering the total average interaction energy, GP is more likely to form a **B** motif with the 100 diaspore surface.

Regarding the diaspore–IHP–water complexes, the interaction energy per bond follows the order **2M** > **M(1)** > **M(2)**. Here, the **M(2)** motif's interaction energy is 1.8 times smaller than the **M(1)** motif due to longer Al-O_p bond length, i.e., due to movement of IHP away from the diaspore surface. Thus the **2M** motif will be also dominating considering the total interaction energy. This is due to the additional covalent bond and a proton transfer to the diaspore surface. Hence IHP is likely to form a **2M** motif with the 100 diaspore surface.

Regarding the water interaction with 100 diaspore and IHP/GP, it can be concluded that the average IHP-water interaction energy is about 2.3 times larger than the GP-water one due to IHP's higher water accessible surface area. Both IHP and GP show proton transfer events to water and formation of strong to moderately strong HBs with water. The diaspore–water interaction energy is only 1.1 times that of the GP-water case, but 2.8 times smaller than IHP-water one. Thus, water has a stronger interaction with IHP than with the 100 diaspore surface.

Of course, studying a particular perfect surface plane can at best give qualitative trends if compared to real surfaces of mineral particles in soil. Studying two abundant surface planes, however, it is possible to pinpoint important factors which influence the behavior of P-compounds at the mineral/water interface. The present investigation focused on the e! ects of surface saturation and thus electrostatic potential on IHP/GP adsorption. The soil minerals exhibit a positive charge with an unsaturated surface and active sites for pH < PZC. For a pH far below PZC a higher positive charge, i.e, more unsaturated surface is observed (Cornell and Schwertmann, 2003; Tan, 2011). The IHP and GP adsorption onto goethite (with PZC around 9–10) is decreased with increasing pH and reached near zero values for pH around 10 (Celi et al., 1999; Li et al., 2017). This shows that the mineral surface saturation varies with pH and thus the ability of a mineral to adsorb phosphates. Higher surface saturation leads to more negative charges on the 100 surface as compared to the 010 case. Phosphates in water are partially deprotonated and thus have an e! ective negative charge. Thus the phosphate groups will be attracted stronger to the 010 diaspore surface plane. The denser distribution of water around the 010 surface compared to the 100 surface and transformation of IHP's **M** and **B** motifs to **2M** motif highlight the stronger electrostatic potential of 010 surface than 100.

Comparing our previous study (Ganta et al., 2019) with the present one, it can be concluded that the diaspore surfaces with di! erent degrees of saturation exhibit di! erent interaction energies with phosphates. Moreover, both surface planes form multiple bonds with IHP while the **B** binding motif dominates for GP. The overall interaction energies show that IHP is bound to diaspore stronger than GP and this confirms the prevailing view that the number of phosphate groups is a decisive parameter

determining the adsorption strength (Anderson and Arlidge, 1962). This could also explain why higher percentages of IHP is found in the forest soil colloid samples than GP as revealed by liquid-state NMR measurements (Missong et al., 2016). However, not all available phosphate groups will contribute to the binding, with details depending on the surface saturation. The present study also stresses the importance of inter- and intra-molecular HBs and the observation that IHP is less protonated than solution counterparts when pH < PZC as shown by Johnson et al. (2012). For both modeled diaspore surfaces, there is no observed dissociation for the bonds involved in C-O, C-H, and C-O-P as suggested by Celi et al. (1999) and Li et al. (2017). In the present case of IHP we cannot confirm the suggestion of a **4M** motif made by Ognalaga et al. (1994).

DATA AVAILABILITY STATEMENT

All datasets generated for this study are included in the article/**Supplementary Material**.

AUTHOR CONTRIBUTIONS

PG has performed the present work and analyzed the results. AA and OK have suggested, designed, and supervised the scientific approach for the present study. All authors have discussed and interpreted the present results and contributed to writing the submitted manuscript.

ACKNOWLEDGMENTS

All authors gratefully acknowledge the financial support by the German Research Foundation (DFG) as a part of the SPP 1685 Priority program Ecosystem Nutrition: Forest strategies for limited phosphorus resources. AA would like to thank the financial support by the InnoSoilPhos-project, funded by the German Federal Ministry of Education and Research (BMBF) in the frame of the BonaRes-program (No. 031A558). This research was performed within the scope of the Leibniz Science Campus Phosphorus Research Rostock. The authors thank the North German Supercomputing Alliance for providing HPC resources (project mvp00016).

SUPPLEMENTARY MATERIAL

The Supplementary Material for this article can be found online at: https://www.frontiersin.org/articles/10.3389/! gc.2020.00071/full#supplementary-material

REFERENCES

Ahmed, A. A., Gros, P., Kühn, O., and Leinweber, P. (2018a). Molecular level investigation of the role of peptide interactions in the glyphosate analytics. *Chemosphere* 196, 129–134. doi: 10.1016/j.chemosphere.2017.12.162

Ahmed, A. A., Gypser, S., Leinweber, P., Freese, D., and Kühn, O. (2019). Infrared spectroscopic characterization of phosphate binding at the goethite-water interface. *Phys. Chem. Chem. Phys.* 21, 4421–4434. doi: 10.1039/C8CP07168C

Ahmed, A. A., Leinweber, P., and Kühn, O. (2018b). Unravelling the nature of glyphosate binding to goethite surfaces by ab initio molecular dynamics simulations. *Phys. Chem. Chem. Phys.* 20, 1531–1539. doi: 10.1039/C7CP06245A

Anderson, G., and Arlidge, E. Z. (1962). The adsorption of inositol phosphates and glycerophosphate by soil clays, clay minerals, and hydrated sesquioxides in acid media. *J. Soil Sci.* 13, 216–224. doi: 10.1111/j.1365-2389.1962.tb00699.x

Bol, R., Gruau, G., Mellander, P.-E., Dupas, R., Bechmann, M., Skarbøvik, E., et al. (2018). Challenges of reducing phosphorus based water eutrophication in the agricultural landscapes of Northwest Europe. *Front. Mar. Sci.* 5:276. doi: 10.3389/fmars.2018.00276

Bol, R., Julich, D., Brödlin, D., Siemens, J., Kaiser, K., Dippold, M. A., et al. (2016). Dissolved and colloidal phosphorus fluxes in forest ecosystems–an almost blind spot in ecosystem research. *J. Soil Sci. Plant Nutr.* 179, 425–438. doi: 10.1002/jpln.201600079

Boy, J., Valarezo, C., and Wilcke, W. (2008). Water flow paths in soil control element exports in an andean tropical montane forest. *Eur. J. Soil Sci.* 59, 1209–1227. doi: 10.1111/j.1365-2389.2008.01063.x

Bussi, G., Donadio, D., and Parrinello, M. (2007). Canonical sampling through velocity rescaling. *J. Chem. Phys.* 126, 014101:1–014101:6. doi: 10.1063/1.2408420

Celi, L., Lamacchia, S., Marsan, F. A., and Barberis, E. (1999). Interaction of inositol hexaphosphate on clays: adsorption and charging phenomena. *Soil Sci.* 164, 574–585. doi: 10.1097/00010694-199908000-00005

Chitrakar, R., Tezuka, S., Sonoda, A., Sakane, K., Ooi, K., and Hirotsu, T. (2006). Phosphate adsorption on synthetic goethite and akaganeite. *J. Colloid Interface Sci.* 298, 602–608. doi: 10.1016/j.jcis.2005.12.054

Cordell, D., and Neset, T.-S. (2014). Phosphorus vulnerability: a qualitative framework for assessing the vulnerability of national and regional food systems to the multi-dimensional stressors of phosphorus scarcity. *Glob. Environ. Chang.* 24, 108–122. doi: 10.1016/j.gloenvcha.2013.11.005

Cornell, R. M., and Schwertmann, U. (2003). *The Iron Oxides: Structure, Properties Reactions Occurrence and Uses*. Weinheim: Wiley-VCH Verlag GmbH and Co. KGaA.

Doolette, A., Smernik, R., and Dougherty, W. (2009). Spiking improved solution phosphorus31 nuclear magnetic resonance identification of soil phosphorus compounds. *Soil Sci. Soc. Am. J.* 73, 919–927. doi: 10.2136/sssaj2008.0192

Ganta, P. B., Kühn, O., and Ahmed, A. A. (2019). QM/MM simulations of organic phosphorus adsorption at the diaspore–water interface. *Phys. Chem. Chem. Phys.* 21, 24316–24325. doi: 10.1039/C9CP04032C

Gerke, J. (2015). Phytate (inositol hexakisphosphate) in soil and phosphate acquisition from inositol phosphates by higher plants: a review. *Plants* 4, 253–266. doi: 10.3390/plants4020253

González, M.A. (2011). Force fields and molecular dynamics simulations. *Collect. SFN 2011* 12, 169–200. doi: 10.1051/sfn/201112009

Gros, P., Ahmed, A., Kühn, O., and Leinweber, P. (2017). Glyphosate binding in soil as revealed by sorption experiments and quantum-chemical modeling. *Sci. Tot. Environ.* 586, 527–535. doi: 10.1016/j.scitotenv.2017.02.007

Gros, P., Ahmed, A. A., Kühn, O., and Leinweber, P. (2019). Influence of metal ions on glyphosate detection by FMOC-Cl. *Environ. Model. Assess.* 191:244. doi: 10.1007/s10661-019-7387-2

Guan, X.-H., Shang, C., Zhu, J., and Chen, G.-H. (2006). ATR-FTIR investigation on the complexation of myo-inositol hexaphosphate with aluminum hydroxide. *J. Colloid Interface Sci.* 293, 296–302. doi: 10.1016/j.jcis.2005.06.070

Guo, H., and Barnard, A. S. (2011). Thermodynamic modelling of nanomorphologies of hematite and goethite. *J. Mater. Chem.* 21, 11566–11577. doi: 10.1039/c1jm10381d

Gypser, S., Hirsch, F., Schleicher, A. M., and Freese, D. (2018). Impact of crystalline and amorphous iron- and aluminum hydroxides on mechanisms of phosphate adsorption and desorption. *J. Environ. Sci.* 70, 175–189. doi: 10.1016/j.jes.2017.12.001

Hens, M., and Merckx, R. (2001). Functional characterization of colloidal phosphorus species in the soil solution of sandy soils. *Environ. Sci. Technol.* 35, 493–500. doi: 10.1021/es0013576

Holzmann, S., Missong, A., Puhlmann, H., Siemens, J., Bol, R., Klumpp, E., et al. (2015). Impact of anthropogenic induced nitrogen input and liming on phosphorus leaching in forest soils. *J. Soil Sci. Plant Nutr.* 179, 443–453. doi: 10.1002/jpln.201500552

Humphrey, W., Dalke, A., and Schulten, K. (1996). VMD – visual molecular dynamics. *J. Mol. Graph.* 14, 33–38. doi: 10.1016/0263-7855(96)00018-5

Jiang, X., Bol, R., Nischwitz, V., Siebers, N., Willbold, S., Vereecken, H., et al. (2015). Phosphorus containing water dispersible nanoparticles in arable soil. *J. Environ. Qual.* 44, 1772–1781. doi: 10.2134/jeq2015.02.0085

Johnson, B. B., Quill, E., and Angove, M. J. (2012). An investigation of the mode of sorption of inositol hexaphosphate to goethite. *J. Colloid Interface Sci.* 367, 436–442. doi: 10.1016/j.jcis.2011.09.066

Kruse, J., Abraham, M., Amelung, W., Baum, C., Bol, R., Kühn, O., et al. (2015). Innovative methods in soil phosphorus research: a review. *J. Soil Sci. Plant Nutr.* 178, 43–88. doi: 10.1002/jpln.201400327

Kubicki, J. D. (ed.). (2016). *Molecular Modeling of Geochemical Reactions*. Chichester: Wiley and Sons.

Kubicki, J. D., Paul, K. W., Kabalan, L., Zhu, Q., Mrozik, M. K., Aryanpour, M., et al. (2012). ATR–FTIR and Density Functional Theory study of the structures, energetics, and vibrational spectra of phosphate adsorbed onto goethite. *Langmuir* 28, 14573–14587. doi: 10.1021/la303111a

Kwon, K. D., and Kubicki, J. D. (2004). Molecular orbital theory study on surface complex structures of phosphates to iron hydroxides-calculation of vibrational frequencies and adsorption energies. *Langmuir* 20, 9249–9254. doi: 10.1021/la0487444

Li, H., Wan, B., Yan, Y., Zhang, Y., Cheng, W., and Feng, X. (2017). Adsorption of glycerophosphate on goethite: a macroscopic and infrared spectroscopic study. *J. Soil Sci. Plant Nutr.* 181, 557–565. doi: 10.1002/jpln.201700517

Limbach, H.-H., Tolstoy, P. M., Pérez-Hernández, N., Guo, J., Shenderovich, I. G., and Denisov, G. S. (2009). Oho hydrogen bond geometries and NMR chemical shifts: from equilibrium structures to geometric H/D isotope e! ects, with applications for water, protonated water, and compressed ice. *Isr. J. Chem.* 49, 199–216. doi: 10.1560/IJC.49.2.199

Marx, D., and Hutter, J. (2009). *Ab Initio Molecular Dynamics: Basic Theory and Advanced Methods*. Cambridge, UK: Cambridge University Press.

Missong, A., Bol, R., Willbold, S., Siemens, J., and Klumpp, E. (2016). Phosphorous forms in forest soil colloids as revealed by liquid-state P-NMR. *J. Soil Sci. Plant Nutr.* 179, 159–167. doi: 10.1002/jpln.201500119

Missong, A., Holzmann, S., Bol, R., Nischwitz, V., Puhlmann, H., Wilpert, K., et al. (2018). Leaching of natural colloids from forest topsoils and their relevance for phosphorus mobility. *Sci. Tot. Environ.* 634, 305–315. doi: 10.1016/j.scitotenv.2018.03.265

Newman, R. H., and Tate, K. R. (1980). Soil phosphorus characterisation by 31 P Nuclear Magnetic Resonance. *Commun. Soil Sci. Plant Anal.* 11, 835–842. doi: 10.1080/00103628009367083

Ognalaga, M., Frossard, E., and Thomas, F. (1994). Glucose-1-phosphate and myo-inositol hexaphosphate adsorption mechanisms on goethite. *Soil Sci. Soc. Am. J.* 332–337. doi: 10.2136/sssaj1994.03615995005800020011x

Ozboyaci, M., Kokh, D. B., Corni, S., and Wade, R. C. (2016). Modeling and simulation of protein-surface interactions: achievements and challenges. *Q. Rev. Biophys.* 49:e4. doi: 10.1017/S0033583515000256

Pant, H. K., Warman, P. R., and Nowak, J. (1999). Identification of soil organic phosphorus by 31 P Nuclear Magnetic Resonance spectroscopy. *Commun. Soil. Sci. Plant Anal.* 30, 757–772. doi: 10.1080/00103629909370244

Parfitt, R. L., and Atkinson, R. J. (1976). Phosphate adsorption on goethite (α-FeOOOH). *Nature* 264, 740–742. doi: 10.1038/264740a0

Senn, H. M., and Thiel, W. (2009). QM/MM methods for biomolecular systems. *Angew. Chem.* 48, 1198–1229. doi: 10.1002/anie.200802019

Strassner, T. (2006). Isotope e! ects in chemistry and biology. Edited by amnon kohen and hans-heinrich limbach. *Angew. Chem.* 45, 6420–6421. doi: 10.1002/anie.200585384

Tan, K. (2011). *Principles of Soil Chemistry, Fourth Edition*. Books in Soils, Plants, and the Environment. New York, NY: Taylor & Francis.

Torrent, J., Schwertmann, U., and Barron, V. (1992). Fast and slow phosphate sorption by goethite-rich natural materials. *Clays Clay Miner.* 40, 14–21. doi: 10.1346/CCMN.1992.0400103

Tossell, J. A., Vaughan, D. J., and Johnson, K. H. (1973). Electronic structure of ferric iron octahedrally coordinated to oxygen. *Nat. Phys. Sci.* 244, 42–45. doi: 10.1038/physci244042a0

Turner, B. L., Papházy, M. J., Haygarth, P. M., and Mckelvie, I. D. (2002). Inositol phosphates in the environment. *Philos. Trans. R. Soc. B* 357, 449–469. doi: 10.1098/rstb.2001.0837

Vincent, A. G., Vestergren, J., Gröbner, G., Persson, P., Schleucher, J., and Giesler, R. (2013). Soil organic phosphorus transformations in a boreal forest chronosequence. *Plant Soil* 367, 149–162. doi: 10.1007/s11104-013-1731-z

Yan, Y., and Kühn, O. (2010). Geometric correlations and infrared spectrum of adenine-uracil hydrogen bonds in $CDCl_3$ solution. *Phys. Chem. Chem. Phys.* 12, 15695–15703. doi: 10.1039/c0cp00009d

Yan, Y. P., Liu, F., Li, W., Liu, F., Feng, X. H., and Sparks, D. L. (2014). Sorption and desorption characteristics of organic phosphates of di! erent structures on aluminium (oxyhydr)oxides. *Eur. J. Soil Sci.* 65, 308–317. doi: 10.1111/ejss.12119

Zentel, T., and Kühn, O. (2017). Properties of hydrogen bonds in the protic ionic liquid ethylammonium nitrate. *Theor Chem Acc.* 136:87. doi: 10.1007/s00214-017-2119-6

Conflict of Interest: The authors declare that the research was conducted in the absence of any commercial or financial relationships that could be construed as a potential conflict of interest.

Copyright © 2020 Ganta, Kühn and Ahmed. This is an open-access article distributed under the terms of the Creative Commons Attribution License (CC BY). The use, distribution or reproduction in other forums is permitted, provided the original author(s) and the copyright owner(s) are credited and that the original publication in this journal is cited, in accordance with accepted academic practice. No use, distribution or reproduction is permitted which does not comply with these terms.

frontiers

Supplementary Material

1 ADDITIONAL QM/MM TECHNICAL DETAILS

The electrostatic embedding QM/MM method is implemented here using the CP2K package (CP2K, 5.1, 2017) where QM is simulated by the quickstep method (VandeVondele et al., 2005) and MM by FIST (Mundy et al., 2017). For the QM part, density functional theory (DFT) is adopted in which Goedecker-Teter-Hutter (GTH) pseudopotentials (Krack, 2005) and the Perdew-Burke-Ernzerhof (PBE) (Perdew et al., 1996) exchange correlation functional are used together with the D3 empirical dispersion correction (Grimme et al., 2010). The double-ζ valence polarised (DZVP-MOLOPT-SR-GTH), MOLOPT (VandeVondele and Hutter, 2007) basis set has been selected for all QM atoms except water for which single-ζ valance basis was selected to reduce computational costs.The HBs between diaspore-water and between water molecules could be well defined using these basis sets (Kubicki, 2016). The SCF convergence threshold of 10^{-5} hartree was chosen. The counterpoise scheme (Boys and Bernardi, 1970) is used to correct the basis set superposition error (BSSE) for interaction energies.

For the MM part of the modeled system, the bottom three layers of diaspore surface (480 atoms) has been modeled with CLAYFF force fields (Cygan et al., 2004), water with SPC based water model (Berendsen et al., 1987) and IHP/GP using the CHARMM force fields obtained via SwissParam force field generation tool (Zoete et al., 2011). The SPC based water model is compatible with both CLAYFF and CHARMM force fields. More details about force fields used here are given in (Ganta et al., 2019). The QM/MM coupling driver is part of the CP2K package, namely we used the gaussian expansion of the electrostatic potential method (GEEP) (Laino et al., 2006). The QM/MM simulations here are performed within a canonical (NVT) ensemble that means simulation of molecular systems at constant number of atoms (N), volume (V), and temperature (T).

REFERENCES

Berendsen, H. J. C., Grigera, J. R., and Straatsma, T. P. (1987). The missing term in effective pair potentials. *J. Phys. Chem.* 91, 6269–6271. doi:10.1021/j100308a038

Boys, S. and Bernardi, F. (1970). The calculation of small molecular interactions by the differences of separate total energies: Some procedures with reduced errors. *Mol. Phys.* 19, 553–566. doi:10.1080/00268977000101561

Cimas, Á., Tielens, F., Sulpizi, M., Gaigeot, M.-P., and Costa, D. (2014). The amorphous silica–liquid water interface studied byab initiomolecular dynamics (AIMD): local organization in global disorder. *Journal of Physics: Condensed Matter* 26, 244106. doi:10.1088/0953-8984/26/24/244106

CP2K (5.1, 2017). *Open source molecular dynamics code* (www.cp2k.org)

Cygan, R. T., Liang, J. J., and Kalinichev, A. G. (2004). Molecular models of hydroxide, oxyhydroxide, and clay phases and the development of a general force field. *J. Phys. Chem. B* 108, 1255–1266. doi:10.1021/jp0363287

Gaigeot, M.-P. (2010). Theoretical spectroscopy of floppy peptides at room temperature. a dftmd perspective: gas and aqueous phase. *Phys. Chem. Chem. Phys.* 12, 3336–3359. doi:10.1039/B924048A

Ganta, P. B., Kühn, O., and Ahmed, A. A. (2019). QM/MM simulations of organic phosphorus adsorption at the diaspore–water interface. *Phys. Chem. Chem. Phys.* 21, 24316–24325. doi:10.1039/C9CP04032C

González, M.A. (2011). Force fields and molecular dynamics simulations. *Collect. SFN 2011* 12, 169–200. doi:10.1051/sfn/201112009

Grimme, S., Antony, J., Ehrlich, S., and Krieg, H. (2010). A consistent and accurate ab initio parametrization of density functional dispersion correction (DFT-D) for the 94 elements H-Pu. *J. Phys. Chem.* 132, 154104:1–154104:15

Groenhof, G. (2013). *Introduction to QM/MM Simulations* (Totowa, NJ: Humana Press). 43–66. doi:10.1007/978-1-62703-017-5_3

Huang, P., Pham, T. A., Galli, G., and Schwegler, E. (2014). Alumina(0001)/water interface: Structural properties and infrared spectra from first-principles molecular dynamics simulations. *The Journal of Physical Chemistry C* 118, 8944–8951. doi:10.1021/jp4123002

Ingólfsson, H. I., Lopez, C. A., Uusitalo, J. J., de Jong, D. H., Gopal, S. M., Periole, X., et al. (2014). The power of coarse graining in biomolecular simulations. *WIREs Computational Molecular Science* 4, 225–248. doi:10.1002/wcms.1169

Krack, M. (2005). Pseudopotentials for H to Kr optimized for gradient-corrected exchange-correlation functionals. *Theor. Chem. Acc.* 114, 145–152. doi:10.1007/s00214-005-0655-y

Kubicki, J. D. (ed.) (2016). *Molecular Modeling of Geochemical Reactions* (Chichester: Wiley and Sons)

Kubicki, J. D. and Watts, H. D. (2019). Quantum mechanical modeling of the vibrational spectra of minerals with a focus on clays. *Minerals* 9, 141. doi:10.3390/min9030141

Laino, T., Mohamed, F., Laio, A., and Parrinello, M. (2006). An efficient linear-scaling electrostatic coupling for treating periodic boundary conditions in qm/mm simulations. *J. Chem. Theory Comput.* 2, 1370–1378. doi:10.1021/ct6001169. PMID: 26626844

Marx, D. and Hutter, J. (2009). *Ab Initio Molecular Dynamics: Basic Theory and Advanced Methods* (Cambridge University Press). doi:10.1017/CBO9780511609633

Mundy, C., Balasubramanian, S., Bagchi, K., Hutter, J., Kuo, A. S. I., Laino, T., et al. (2017). *Frontiers in Simulation Technology (FIST)* (www.cp2k.org)

Ozboyaci, M., Kokh, D. B., Corni, S., and Wade, R. C. (2016). Modeling and simulation of protein–surface interactions: achievements and challenges. *Q. Rev. Biophys.* 49, e4. doi:10.1017/S0033583515000256

Perdew, J. P., Burke, K., and Ernzerhof, M. (1996). Generalized gradient approximation made simple. *Phys. Rev. Lett.* 77, 3865–3868. doi:10.1103/PhysRevLett.77.3865

Senn, H. M. and Thiel, W. (2009). QM/MM methods for biomolecular systems. *Angew. Chem.* 48, 1198–1229

VandeVondele, J. and Hutter, J. (2007). Gaussian basis sets for accurate calculations on molecular systems in gas and condensed phases. *J. Chem. Phys.* 127, 114105:1–114105:8. doi:10.1063/1.2770708

VandeVondele, J., Krack, M., Mohamed, F., Parrinello, M., Chassaing, T., and Hutter, J. (2005). Quickstep: Fast and accurate density functional calculations using a mixed gaussian and plane waves approach. *Comput. Phys. Commun.* 167, 103–128. doi:https://doi.org/10.1016/j.cpc.2004.12.014

Zoete, V., Cuendet, M. A., Grosdidier, A., and Michielin, O. (2011). Swissparam: A fast force field generation tool for small organic molecules. *J. Comput. Chem.* 32, 2359–2368. doi:10.1002/jcc.21816

2 FIGURES

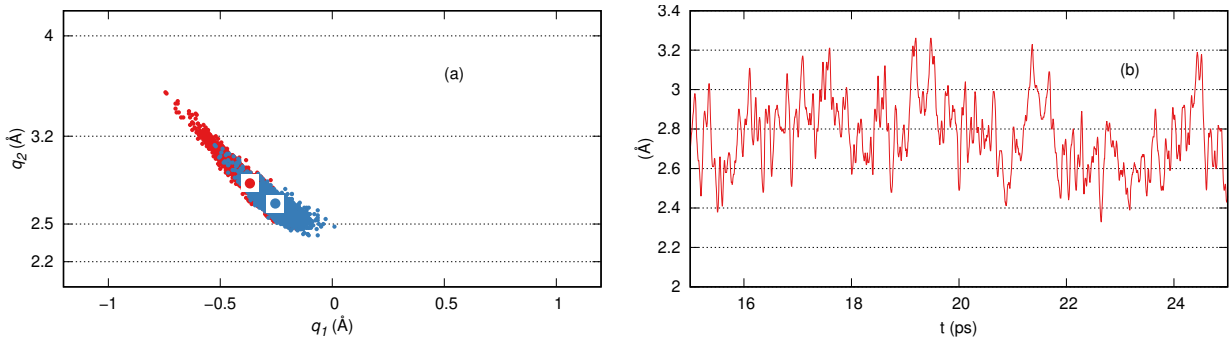


Figure S1: Correlation plot of hydrogen bond (HB) length (q_2) and deviation of the H atom from the HB center (q_1) of two HBs formed between the diaspore surface and water for the diaspore–GP–water **M** motif (a) Al1-O11 bond length for the diaspore–IHP–water **M(2)** motif (b).

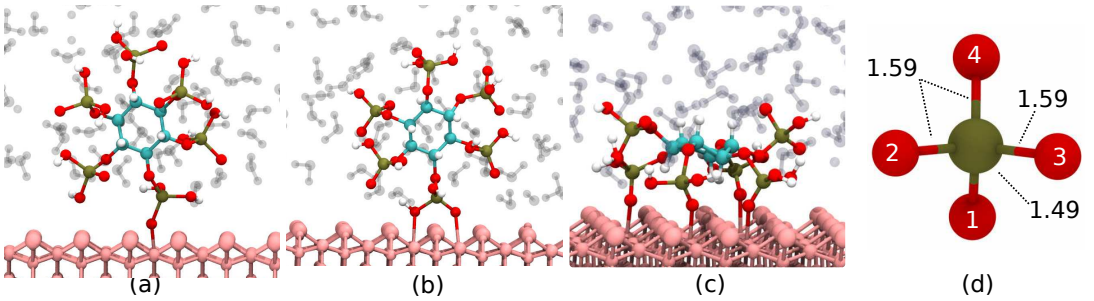


Figure S2: Diaspore–IHP–water initial binding motifs, **M(1)** case intial motif: **M** (a), **M(2)** case intial motif: **B** (b), **2M** case intial motif: **4M** (c), free tetrahedral PO_4^{3-} (d).

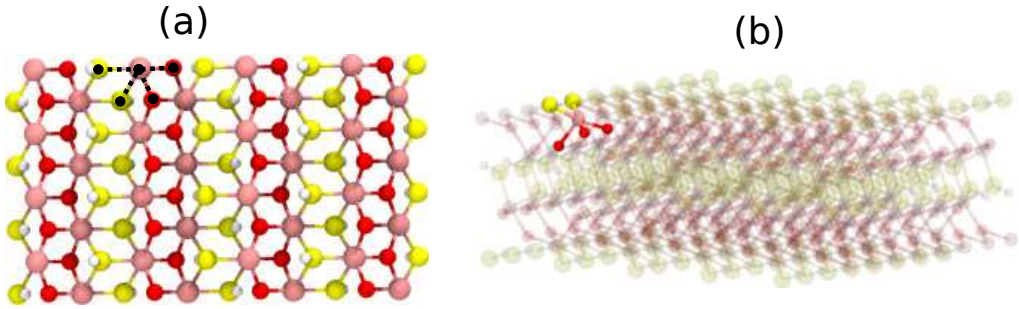


Figure S3: Side view of the neutral and pure 010 and 100 diaspore surface planes. Surface Al atoms of the diaspore 010 surface plane are coordinated by four oxygen atoms (a) and 100 diaspore surface plane are coordinated by five oxygen atoms (b). Pink, red, yellow and white colors correspond to Al, bridging oxygen, hydroxyl oxygen and hydrogen respectively.

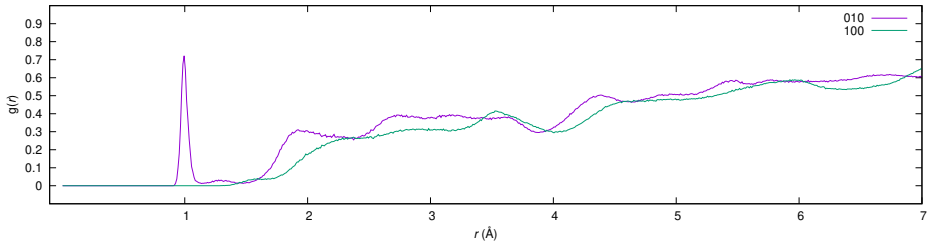


Figure S4: Comparison of radial distribution functions calculated for the 010 and 100 diaspore surface oxygen atoms and water hydrogen atoms.

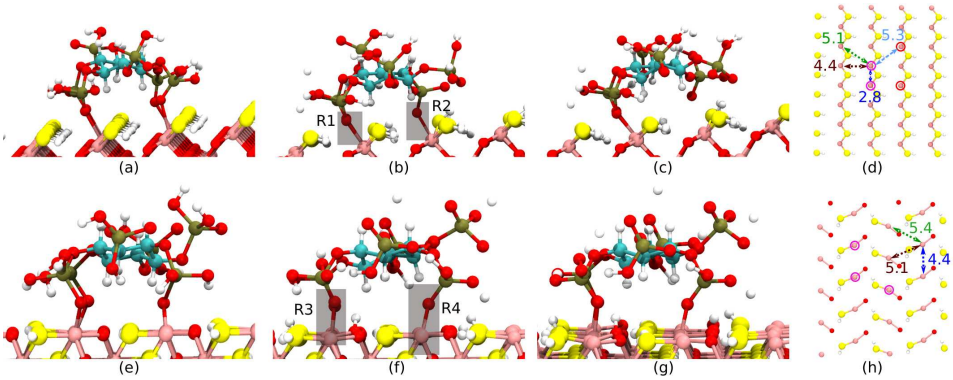


Figure S5: Snapshots along the MD trajectory for the 100 diaspore–IHP–water **2M** motif (a-c) and the top view of surface atoms showing interatomic Al-Al distances (d). Similarly, the snapshots of **3M** motif (e-g) and top view of surface atoms showing interactomic Al-Al distances (h). The circle around Al atom denote the site of Al-O_P bonds in **2M** and **3M** motif, respectively wherein the red circle denotes the site where Al-O_P bond dissociated. Note that water is ignored in this image for better view.

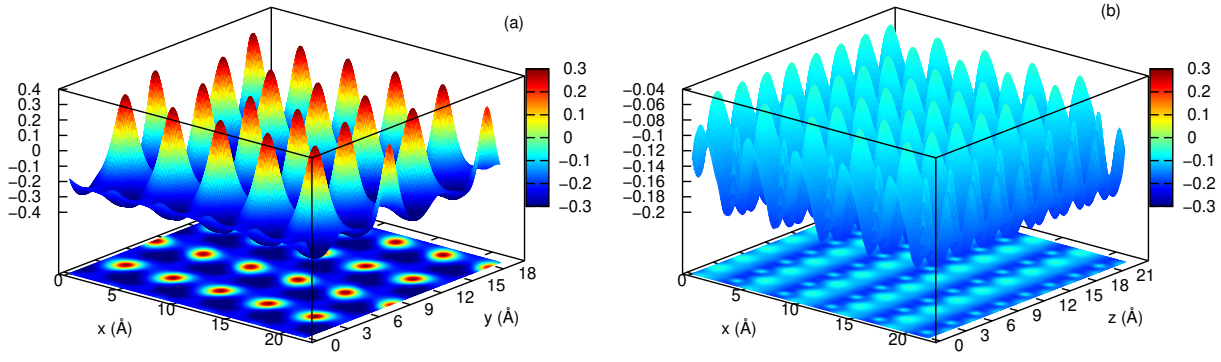


Figure S6: Electrostatic potential (a.u.) at 1 Å (perpendicular to surface) for the bare 010 diaspore surface plane (a) as well as for the bare 100 diaspore surface plane (b). These have been calculated for bare surfaces without involving phosphates and water.

Publication 6

P. B. Ganta, O. Kühn, Ashour A. Ahmed. Ab Initio Molecular Dynamics Simulations of the Interaction between Organic Phosphates and Goethite. Molecules **2021**, 26(1), 160.

Contribution: Ashour A. Ahmed is credited with the conceptualization of the scientific approach for this study, development of the methodology, acquisition of funding, contribution to writing the original manuscript, and supervising the PhD student (Mr. P.B. Ganta). Ashour A. Ahmed, along with the co-authors, has discussed and interpreted the results and contributed to writing, reviewing, and editing the manuscript.

URL: https://doi.org/10.3390/molecules26010160

QR:



Licensee MDPI, Basel, Switzerland. This open-access article is distributed under the terms and conditions of the Creative Commons Attribution (CC BY) license (http://creativecommons.org/licenses/by/4.0/).

molecules

MDPI

Article

Ab Initio Molecular Dynamics Simulations of the Interaction between Organic Phosphates and Goethite

Prasanth B. Ganta [1], Oliver Kühn [1,2] and Ashour A. Ahmed [1,2,*]

[1] Institute of Physics, University of Rostock, Albert-Einstein-Str. 23-24, D-18059 Rostock, Germany; prasanth.ganta@uni-rostock.de (P.B.G.); oliver.kuehn@uni-rostock.de (O.K.)
[2] Department of Life, Light, and Matter (LLM), University of Rostock, Albert-Einstein-Str. 25, D-18059 Rostock, Germany
* Correspondence: ashour.ahmed@uni-rostock.de; Tel.: +49-381-498-6943

Abstract: Today's fertilizers rely heavily on mining phosphorus (P) rocks. These rocks are known to become exhausted in near future, and therefore effective P use is crucial to avoid food shortage. A substantial amount of P from fertilizers gets adsorbed onto soil minerals to become unavailable to plants. Understanding P interaction with these minerals would help efforts that improve P efficiency. To this end, we performed a molecular level analysis of the interaction of common organic P compounds (glycerolphosphate (GP) and inositol hexaphosphate (IHP)) with the abundant soil mineral (goethite) in presence of water. Molecular dynamics simulations are performed for goethite–IHP/GP–water complexes using the multiscale quantum mechanics/molecular mechanics method. Results show that GP forms monodentate (**M**) and bidentate mononuclear (**B**) motifs with **B** being more stable than **M**. IHP interacts through multiple phosphate groups with the **3M** motif being most stable. The order of goethite–IHP/GP interaction energies is GP **M** < GP **B** < IHP **M** < IHP **3M**. Water is important in these interactions as multiple proton transfers occur and hydrogen bonds are formed between goethite–IHP/GP complexes and water. We also present theoretically calculated infrared spectra which match reasonably well with frequencies reported in literature.

Keywords: P–inefficiency; goethite; glycerolphosphate; inositol hexaphosphate; MD simulations; QMMM; binding energies; infrared spectra

check for updates

Citation: Ganta, P.B.; Kühn, O.; Ahmed, A.A. Ab Initio Molecular Dynamics Simulations of the Interaction between Organic Phosphates and Goethite. *Molecules* **2021**, *26*, 160. https://doi.org/10.3390/molecules26010160

Received: 12 November 2020
Accepted: 23 December 2020
Published: 31 December 2020

Publisher's Note: MDPI stays neutral with regard to jurisdictional claims in published maps and institutional affiliations.

Copyright: © 2020 by the authors. Licensee MDPI, Basel, Switzerland. This article is an open access article distributed under the terms and conditions of the Creative Commons Attribution (CC BY) license (https://creativecommons.org/licenses/by/4.0/).

1. Introduction

Phosphorus (P) scarcity is becoming one of the major global environmental challenges, which needs attention on par with climate change because of the foreseen P peak scenario [1–3]. The P in today's fertilizer is mostly from mined P rocks, and given the current mining rate they are predicted to be exhausted within next 50–100 years [4,5]. Complicating the situation further, the P rock reserves are available only in few countries and a P peak scenario could affect regions like UK, Western Europe, and India who obtain these resources mainly through imports [2,6,7]. As P rock reserves dwindle with time, the food security of P-importing countries is in question, which, in the long-term, might flip oil based economies to P based economies. The oil crisis in the 1970s emphasized the need for renewable energy sources, but unfortunately for the peak P crisis there is no alternative but to develop ways to increase, reuse, and secure the domestic P production [1,6–8].

The P input to soil (P fertilizers or from nature) is not fully available to plants as most of it is bound to soil organic matter [9–11] or soil minerals [12–16]. To overcome this, fertilizers are often applied in the agriculture industry to maintain and boost the agricultural production. As a side effect, P bound to minerals runs off along water paths during heavy rains and in the long-term causes eutrophication of waterways [17]. Recent studies show that the soil minerals in rain water retain about 50% of P in the soil solution [18,19]. In addition, heavy rains further decrease P efficiency as P-bound soil minerals, i.e., P colloid complexes, disperse with rain water and accumulate in specific regions unavailable

to plants [20]. Methods that support effective extraction of P from these colloids would increase domestic P sources which in turn would improve the food security of global population.

Orthophosphate (OP) is one of the most abundant inorganic phosphate, which exists mainly in the form of phosphate ions ($H_2PO_4^{1-}$, HPO_4^{2-}, PO_4^{3-}) [21,22]. Regarding organic phosphates, inositol hexaphosphate (IHP) [23–25] and glycerolphosphate (GP) [26–28] are some of the abundant and most common organic phosphates in soil. Often they are present in soil as oxyanions with deprotonated phosphate groups [29–31]. Therefore, the negatively charged phosphates bind to positively charged soil mineral surfaces to form P colloids. The most common P-fixing minerals are Fe and Al(oxyhydr)oxides [32–34] and Ca–oxides [33]. Goethite (α-FeOOH) is one of the most reactive and abundant mineral that interacts with phosphates [35]. Strong interactions have been reported for OP [15,36–39] as well as for IHP [30,31,40,41] and GP [29], especially at low to medium pH. The interaction of phosphates with goethite or most minerals is through bonded and non-bonded interactions, for instance, covalent bonds, hydrogen bonds (HBs), van der Waals (vdW) interactions, and electrostatic attraction to form surface complexes [33,42,43]. Numerous studies show that P compounds with a single phosphate group form one to two covalent bonds between the phosphate group's oxygens and surface iron atoms [15,36,44] within inner-sphere complexes. IHP may bind through one to four of its six phosphate groups [31,40,41,45] to form covalent bonds with surface iron atoms. In contrast, Johnson et al. [30] suggested that IHP forms outer-sphere complexes. In addition to the covalent bonds and electrostatic interaction between phosphates and goethite, water also plays an important role for the stability of these complexes. In fact, the P colloids often exist in a solvated state in both arable and forest soils. The study by Ahmed et al. [46] showed the importance of water in surface complexation reactions and highlighted how water maneuvers the phosphate interaction with mineral by forming strong to moderately strong HBs with phosphates [47,48].

A molecular level study of solvated P colloids could provide additional insight into these interactions and improve our understanding of P availability to plants [13]. Molecular simulations are efficient tools to achieve this with proven track record [42,49]. For instance, Kwon and Kubicki [50] resolved controversies in experimental studies related to phosphate surface complexes on iron hydroxides. They correlated different types of phosphate binding motifs with goethite to pH and suggested that binding motifs change with pH. Aquino et al. [51] estimated goethite's point of zero charge (PZC) to 9.1 which fits well with experimental values of 6.4–9.7 [22,52,53]. Kubicki et al. [44] explored phosphate and goethite binding motifs and their corresponding stability at different surface planes to find dominant motifs that contribute significantly to infrared (IR) spectra. Ahmed et al. [15] showed that an analysis of theoretical spectra for different motifs could provide an estimate of their ratio of abundance at the goethite surface.

The main objective of the current study is to unravel the interactions of IHP/GP at the 010 goethite–water interface. This is achieved by analyzing binding motifs, interaction energies, and IR spectra obtained using periodic boundary quantum mechanics/molecular mechanics (QM/MM) [54] molecular dynamics simulations.

2. Modeling and Computations

2.1. Goethite Surface

Goethite is an orthorhombic crystal containing ferric (Fe^{3+}) iron which is coordinated by six oxygen atoms [35]. The bulk oxygens are triply coordinated and they are of two distinct types: (1) bridging oxygen coordinated by three iron atoms plus a HB and (2) hydroxyl oxygens coordinated by three iron atoms and one proton, see Figure 1c. Its unit cell contains 16 atoms, i.e., four FeO(OH) units with lattice constants $a = 9.95$, $b = 3.01$, $c = 4.62$ Å. Some common goethite surface planes are 010, 100, 021, and 110 (as per Pnma space group). The IHP and GP interactions with goethite are studied here by considering the 010 goethite surface which is known for its high stability [55,56], see

Figure 1c. The unsaturated and undercoordinated iron and oxygen atoms at the goethite surface generate an overall positive surface charge that attracts IHP/GP and also water to the surface. Compared to bulk, the surface iron atoms are coordinated by only four oxygens while the bridging and hydroxyl oxygens are coordinated by only two irons instead of three. Modeling an undercoordinated surface supports experimental studies that phosphate (IHP [31] and GP [29]) adsorption occurs mostly at pH lower than the goethite PZC, where its surface is unsaturated and has positive surface charge [29,31].

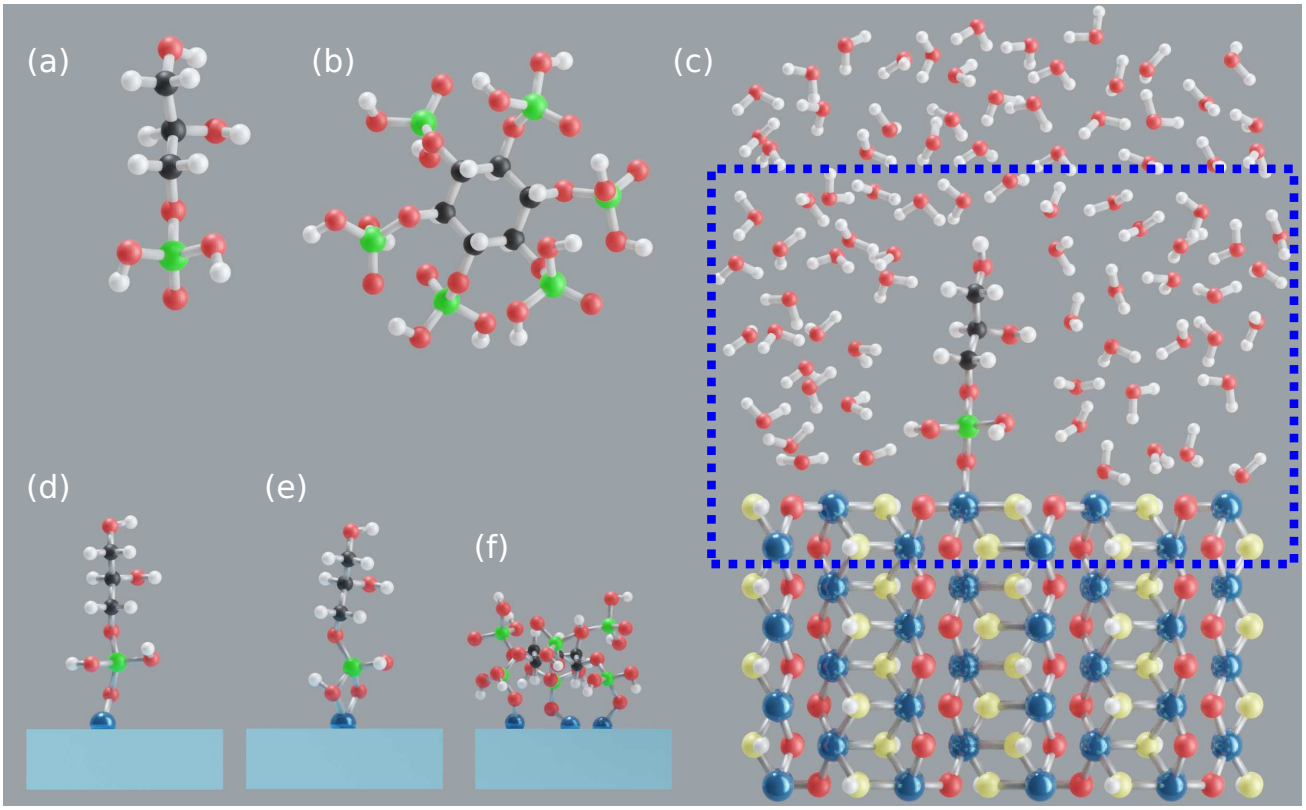


Figure 1. GP [$C_3H_9O_6P$] (**a**), IHP [$C_6H_{18}O_{24}P_6$] (**b**), goethite-GP-water complex (**c**), **M** motif (**d**), **B** motif (**e**), and **3M** motif (**f**). Blue, red, yellow, white, black, and green colors correspond to iron, bridging oxygen, hydroxyl oxygen, hydrogen, carbon, and phosphorus atoms, respectively. The dotted line denotes the QM box.

2.2. Model Systems

First, a surface slab is modeled by repetition of the goethite unit cell as $2a \times 4b \times 5c$. Then, GP (see Figure 1a) is added onto the goethite slab to form covalent bond(s) with a surface iron atom, see Figure 1c. The binding motifs considered for goethite–GP complex are based on experimental studies related to OP [22,57] and organic compounds with monophosphate groups [29,43] interacting with goethite. The study by Li et al. [29] of GP adsorption on goethite suggests that GP predominantly forms monodentate mononuclear motifs (**M**, 1Fe+1O a covalent bond between Fe atom and phosphate free oxygen, see Figure 1d). However, considering OP's [58] interaction with goethite, an additional motif called bidentate mononuclear motif (**B**, 1Fe + 2O two covalent bonds between Fe atom and unprotonated and protonated phosphate O atoms, see Figure 1e) is modeled. The bidentate binuclear motif (**BB**, 2Fe+2O, two covalent bonds between two surface Fe atoms and two oxygens from phosphate, see Figure S4a) which is commonly discussed for OP interaction with goethite [22,36,50] is not considered here as the distance between consecutive Fe atoms does not match the range of distances between oxygen atoms in the phosphate group.

Similarly, IHP (see Figure 1b) is added onto the goethite surface to form goethite–IHP complexes. The IHP interaction with goethite is different compared to GP because of the additional phosphate groups. Guan et al. [45] studied IHP adsorption onto aluminum hydroxide and showed that IHP binds to the surface through two phosphate groups. Moreover, Celi et al. [31] and Ognalaga et al. [40] suggested that IHP interacts with goethite through multiple phosphate groups. Unlike for OP and GP, there is no suggestion for a clear dominant motif for IHP interaction with goethite. Therefore, in addition to the **M** and **B** motifs, a tridentate motif **3M** (**3M**, 3Fe + 3O three covalent bonds between three surface Fe atoms and one protonated, two unprotonated phosphate O atoms, see Figure 1f) is considered. The **3M** motif is considered here based on the goethite surface Fe atom's and IHP O atom's structural flexibility to form bonds.

The complexes discussed so far are solvated to include the effects of water on their interactions. The goethite–IHP/GP complexes are solvated perpendicular to the studied surface plane up to $\approx$ 18 Å using VMD [59] at a density of $\approx$ 1 g cm^{-3}, see Figure 1c. To ease the discussion about the interactions, the Fe/Al-bonded oxygens are denoted as O_p. Note that even though the initial motifs considered here may not include all possible surface configurations they should allow us to draw conclusions from common motifs.

2.3. Computational Details

The atoms in the modeled complexes are separated into two regions as required by the QM/MM method [54,60]. The atoms of the reactive region (QM) of goethite–IHP/GP–water complexes include the top goethite layer, phosphate, and water within $\approx$ 10 Å from goethite surface. The average number of QM atoms in each model is around 350–400 depending on the complex; the total average number of atoms per each model is around 1200–1250. The atoms excluded from the QM region are described at the MM level with classical force fields (FF). Note that simulating the above complexes with 1200+ atoms using pure QM methods is a computational roadblock [42,61], and to overcome this the QM/MM approach is adopted here.

The potential and forces of the QM subsystems are calculated using density functional theory (DFT) as implemented in the Quickstep code [62]. Here, the nucleus and highly localized core electrons of atoms are replaced by Goedecker–Teter–Hutter (GTH) pseudopotentials [63], while the valance electrons are described with the double-ζ valance-polarized MOLOPT (DZVP–MOLOPT–SR–GTH) basis set [64]. For water atoms, the valance electrons are defined with the simpler single-ζ valance (SZV–MOLOPT–SR–GTH) basis set to further reduce computational cost. The exchange correlation interactions and vdW interactions are included with Perdew–Burke–Ernzerhof (PBE) [65] exchange correlation functional and D3 empirical dispersion correction [66], respectively. The MM part is simulated with the FIST module [67], which is an integral part of CP2K [68,69]. The goethite surface is modeled with the CLAYFF FF [70] and the water with the single point charge (SPC) water model [71]. For phosphates IHP and GP, CHARMM FF are obtained from SwissParm, a FF generation tool [72]. Both CLAYFF and CHARMM FFs are compatible with the SPC water model.

The interaction between QM and MM subsections is simulated by Gaussian expansion of the electrostatic potential method (GEEP) [73] which is part of CP2K. This method defines MM charges as smeared out Gaussians and adopts efficient screening techniques to reduce the computational cost in calculating mutual interaction energies between QM and MM subsystems. There is a variety of QM/MM methods available that differ based on the level of theory used to define QM and MM mutual interactions. Here, the electrostatic embedding type of QM/MM method is employed which allows MM atoms to polarize QM atoms and thus to include the effect of surrounding atoms onto the reactive region [60]. For all complexes, the QM box size is $2a \times 22 \times 5c$, i.e., 19.9 × 22 × 23.1 Å, see Figure 1c, and the remaining region is MM.

Molecular Dynamics (MD) simulations are employed to sample the equilibrium dynamics including reactive events. As the phosphate interaction at goethite–water interface

involve proton transfer events and covalent bond changes [46–48], using the QM/MM MD technique is mandatory. Specifically, the electron density cut-off for the auxiliary plane wave basis set is chosen to be 500 Ry with SCF convergence threshold of 10^{-4} Hartree. The MD simulations are performed for 25 ps with a 0.5 fs time step and the temperature is maintained at 300K with canonical sampling through the velocity rescaling thermostat (CSVR) [74].

Each model has been equilibrated for about 10 ps. Interaction energies and information about geometries have been obtained from a subsequent 15 ps production trajectory. Specifically, the interaction energy between the goethite surface and IHP is calculated for every 100 fs (i.e., 150 snapshots) along the production trajectory by using

$$E_{int} = E_{goe-IHP-complex} - (E_{goe} + E_{IHP}). \quad (1)$$

The terms $E_{goe-IHP-complex}$, E_{IHP}, and E_{goe} denote total electronic energy of the goethite–IHP–complex, IHP, and goethite surface, respectively. The basis set superposition error (BSSE) in interaction energies is corrected using the counterpoise scheme [75]. The interaction energies that involve water are divided by the total number of water molecules in the simulation box to obtain per water molecule interaction energies for better comparison.

Infrared (IR) spectra for IHP and GP adsorbed onto goethite are calculated using the TRAVIS [76] software. In TRAVIS the IR spectra are obtained by Voronoi tessellation of the electron density yielding molecular dipole moments from bulk phase MD simulations [77,78]. This was done along a 30 ps equilibrium trajectory. The electron density is calculated for each 4 fs, i.e, every 8th snapshot of production trajectory and the massive ($\approx$ 2 TB) electron density files are compressed using the bqb compression tool [79] compatible with TRAVIS. The compressed bqb files are then provided to TRAVIS software to calculate IR spectra. Here, the IR spectra are calculated for the frequency range of 950 to 1250 cm^{-1}, where the characteristic peaks related to phosphate stretching modes are observed.

3. Results and Discussion

3.1. Goethite–GP–Water Interactions

3.1.1. GP **M** Motif

A stable **M** motif is observed throughout the production trajectory with an average Fe–O_p bond length of 2.0 Å and average Fe–P distance of 3.2 Å, see Figure 2b. During early stages of equilibration, GP has formed an average of seven HBs with water, of which one is strong enough for a proton transfer to happen from GP to water, see Figure 3a. By the end of the equilibration, GP is twice deprotonated with one proton transfer to water and another to surface, see Figure 3a–b. A proton transfer is observed from GP to water (see Figure 3c) in the production trajectory; therefore, GP is three times deprotonated and its phosphate group completely deprotonated. In Figure 3b, a proton transfer event is observed from goethite surface oxygen to water. On average 8 HBs are observed between GP and water over the course of the production trajectory, see Figure S4b. The HBs are calculated using the VMD [59] plugin with HB donor–acceptor distance selected as 3 Å. Figure 3d shows a stable GP **M** motif at 25 ps.

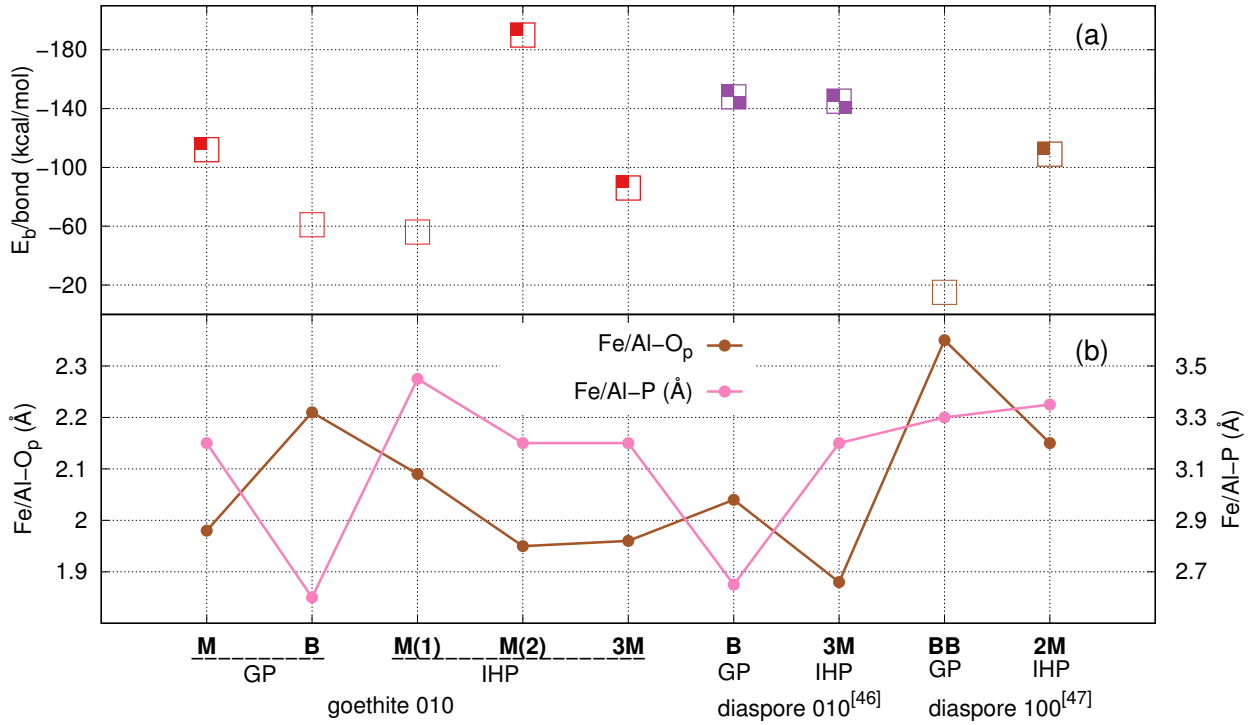


Figure 2. Comparison plot of interaction energies per bond E_b (**a**) and Fe–O_p, Fe–P distances (**b**). Panels (**a**,**b**) also contain data for diaspore–IHP/GP–water complexes [47,48]. In the top figure, the number of filled subsquares denote the total number of proton transfers from IHP/GP to surface and center of box denotes the binding energy. The square with zero filled subsquares denotes zero proton transfers from phosphate to the surface.

The average interaction energy between goethite and GP calculated using Equation (1) is −112 kcal/mol, see Figure 2a. The average GP–water interaction energy per water molecule is −2.3 kcal/mol. The accumulation of water around the goethite surface suggests that water experiences a strong electrostatic pull from goethite surface, see Figure S5. The average goethite–water interaction energy is −6.8 kcal/mol, which is larger than the GP–water interaction energy. The stronger goethite–water interaction is due to multiple Fe–O_{H_2O} covalent bonds (see Figure S4c), proton transfers, and HBs between goethite active sites and water.

3.1.2. GP **B** Motif

The initial **B** motif was found stable during the production trajectory with a mean average Fe–O_p bond length of 2.21 Å and Fe–P distance of 2.6 Å. The mean average Fe–O_p bond length observed here is longer than in the **M** motif case, probably due to the repulsion between the bonded oxygens, see Figure 2b. In contrast to the **M** motif, proton transfer events are not observed from GP to the goethite surface. GP formed an average of eight HBs with water during equilibration stage and of these two yielded proton transfers from GP to water, see Figure 3e–f. Therefore, GP is deprotonated twice at the end of equilibration and during the production trajectory it formed an average of eight HBs with water. The snapshots in Figure 3g and h show the GP **B** motif at 20 and 25 ps, respectively.

The goethite–GP per bond interaction energy here is −61 kcal/mol per bond which is less than for the GP **M** motif because of the additional proton transfer observed in the latter case. However, the total interaction energy (−122 kcal/mol) here is higher than for the GP **M** motif, see Figure 2a. The GP–water interaction energy is −1.9 kcal/mol, which is smaller than for **M** motif case, probably due to the additional proton transfer from GP to water in the **M** motif.

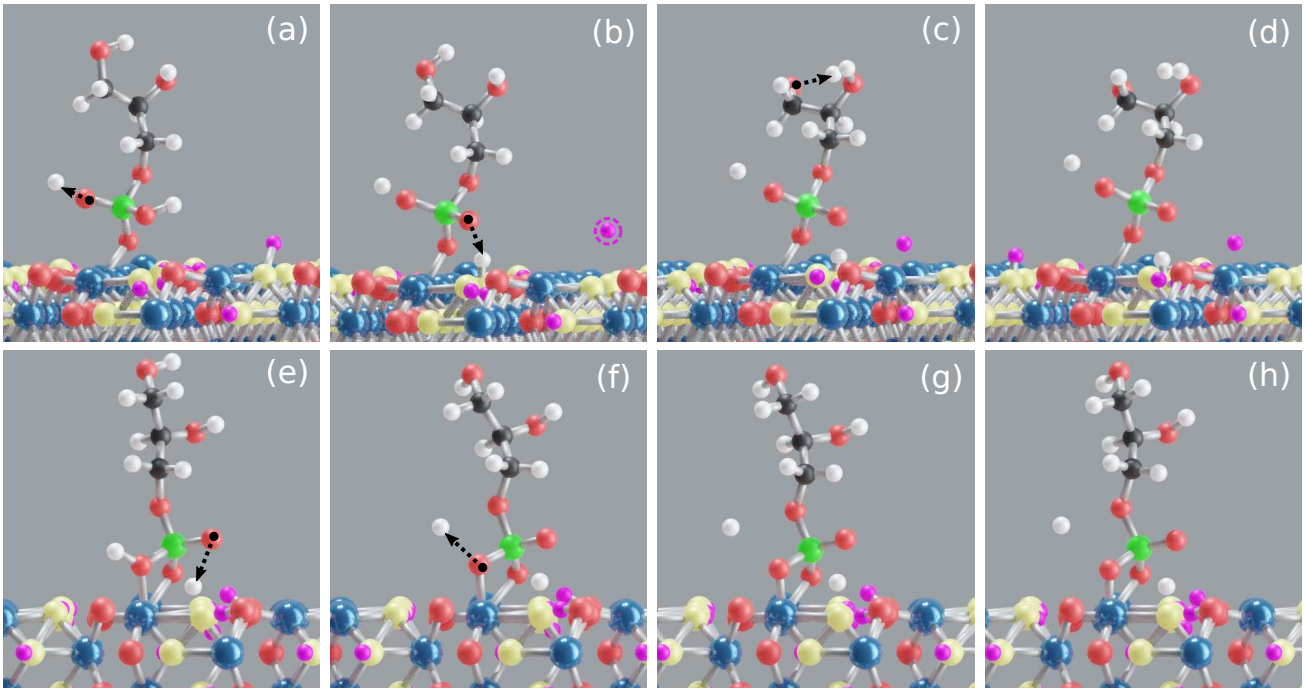


Figure 3. Snapshots of goethite–GP–water models along the simulation trajectory. Proton transfer from GP to water (**a**), a proton transfer from GP to surface and from surface to water (**b**), a proton transfer from GP to water (**c**), a stable **M** motif at 25 ps (**d**), proton transfers from GP to water (**e**,**f**), and **B** motif at 20 ps (**g**) and 25 ps (**h**). As proton transfer events are common in these interactions, the goethite surface hydrogen atoms and GP's hydrogen atoms are shown in violet and white colors to avoid confusion. Moreover, the surrounding water is ignored here for better visualization. Snapshots (**a**,**b**,**e**,**f**) are from equilibration phase.

3.1.3. Discussion of Goethite–GP–Water Interactions

The study by Li et al. [29] of GP on goethite suggested the formation of only the **M** motif and considered that the **B** motif could not be formed due to steric hindrance of the organic moiety in the GP molecule. In addition, Persson et al. [43] suggested a dominant **M** motif for monomethyl phosphate (MMP; CH_3–H_2PO_4) adsorption onto goethite. However, similar to our previous studies [47,48], we find that GP forms stable and strong **B** or **BB** motifs, see Figure 2a. In addition, Lü et al. [80] suggested that molecules with similar binding mechanism like GP such as glucose 6-phosphate and adenosine mono/triphosphates form nonprotonated bidentate complexes within first ten minutes after mixing. Furthermore, OP is known to form **M**, **B**, and **BB** motifs when interacting with goethite [33,44,50,58]. This raises the question of why the **M** motif could be the dominant species for GP on goethite, despite the fact that the binding energy for the **B** motif is stronger, see Figure 2a. Note that the interaction energies presented in Figure 2a are per bond. For IHP, we found a transformation of **B** motif to **M** motif on diaspore surface [47,48] because of intermolecular HBs in IHP and its strong interaction with water. Based on this, and on the study by Li et al. [29], one might assume that GP's HBs with water or its steric hinderance might hinder the **B** motif. Nevertheless, Abdala et al. [58] showed that at low (1.25 $\mu molm^{-2}$), medium (2.5 $\mu molm^{-2}$), and high (10 $\mu molm^{-2}$) surface loading of OP onto goethite, the observed motifs are at low **B** (48%), **BB** (47%), and **M** ($\approx$0); at medium **B** (77%), **BB** (25%), and **M** ($\approx$0); and at high **B** ($\approx$0), **BB** (18%), and **M** (77%). This clearly shows that for low surface loading the **B** and **BB** motifs are dominant motifs whereas for high surface loading the **B** motif is not formed in the first place. In addition to surface loading, the surface type is also vital in deciding the dominant motifs of phosphates on surface [15,44]. For the 010 goethite surface, the theoretical study of single phosphate molecule interaction at goethite–water interface by Ahmed et al. [15,46] showed that the

B motif has a stronger binding than **M**. Further, the protonation state of GP's phosphate group here could be understood from the study of Sheals et al. [81] of glyphosate (GLP, H_2PO_3–CH_2–NH_2–CH_2–COO) on goethite; the twice deprotonated phosphate species dominate at the low surface adsorption densities and the monoprotonated phosphate species dominate at high surface adsorption densities. Correlating the current study with the above literature, the GP binds through a **B** motif with a twice deprotonated phosphate group dominantly at low surface adsorption density. At high surface adsorption density, GP binds preferentially through a **M** motif with a monoprotonated phosphate group.

The Fe–P distance observed here for the GP **M** motif is within the range of Fe–P distances observed in literature for goethite–phosphate complexes: 3.13–3.37 [82], 3.17–3.32 [83], 3.38 [44], 3.20 [46], and 3.41 [15], see Figure 2b. For the **B** motif, even though the calculated phosphate bond in this motif exhibits a strong interaction energy [46–48], it is not often discussed in experimental studies [22,44]. X-ray absorption studies of Abdala et al. [58] showed that the Fe–P distance observed for **B** motif case is around 2.85 Å, which is close to the value observed here, see Figure 2b. Furthermore, similar Fe–P values are observed for **B** motif in theoretical studies, i.e., 2.64 [46] and 2.58 Å [15]. Comparing the present interaction energies with other systems we notice the following. The present **B** motif exhibits stronger binding energy than the **M** motif, similar to the OP [46] and GLP [15] interaction with 010 goethite surface. Moreover, OP and GLP bind more strongly with goethite than with water, as observed for GP and water here. This suggests that phosphates often have the ability to replace water from goethite surface.

3.2. Goethite–IHP–Water Interaction

3.2.1. IHP **M** Motifs

Here, the initial **M** (Fe–O_p) and **B** (O_p–Fe–O_p) motifs (see Figure S3a,b) resulted in two different **M** motifs. **M(1)** corresponds to the initial **M** configuration, with an average Fe–O_p bond length and Fe–P distance of 2.09 and 3.45 Å, respectively, see Figure 2b. Two proton transfer events are observed from IHP to water in the equilibration stage, see Figure 4a,b. Moreover, a proton transfer is observed from goethite to water, see Figure 4a. During the production trajectory, IHP is twice deprotonated and the protonation state of IHP has not altered. It has formed an average of 22 HBs with water. In addition, intramolecular HBs are observed between adjacent phosphate groups along the whole MD trajectory, see Figure 4b–d. Similar to our previous studies [47,48], the HBs formed between IHP and water and the intramolecular HBs in IHP are mostly strong to moderately strong HBs. Figure 4d shows the **M(1)** motif at 25 ps. The average goethite–IHP and IHP–water interaction energies observed here are −56 and −5.5 kcal/mol, respectively. The goethite-water interaction energy here is −5.7 kcal/mol which is less than in the GP's **M** motif.

In **M(2)** motif case, the initial configuration was the **B** motif (see Figure S3b), which transformed to form **M(2)**. Here, one of the Fe–O_p bonds is dissociated, and for the other bond the average Fe–O_p bond length and Fe–P distance is found to be 1.95 and 3.2 Å, respectively, see Figure 2b. In the equilibration phase, a proton transfer event is observed from IHP's oxygen to the surface (see Figure 4a), followed by formation of an intramolecular HB between the same oxygen and an adjacent phosphate group, see Figure 4b. IHP has formed around 20 HBs with water and two of them are apparently strong enough such that proton transfer events are observed from IHP to water. In addition, IHP has formed multiple intramolecular HBs between phosphate groups, see Figure 4f–h. During the production trajectory, IHP is three times deprotonated with one proton transfer to surface and two to water. One of the protons transferred from IHP to water formed an HB with the goethite surface, see Figure 4g–h. The time averaged goethite–IHP interaction energy observed here is −190 kcal/mol which is higher than the **M(1)** motif case due to additional proton transfers from IHP to goethite surface observed here, see Figure 2e–h.

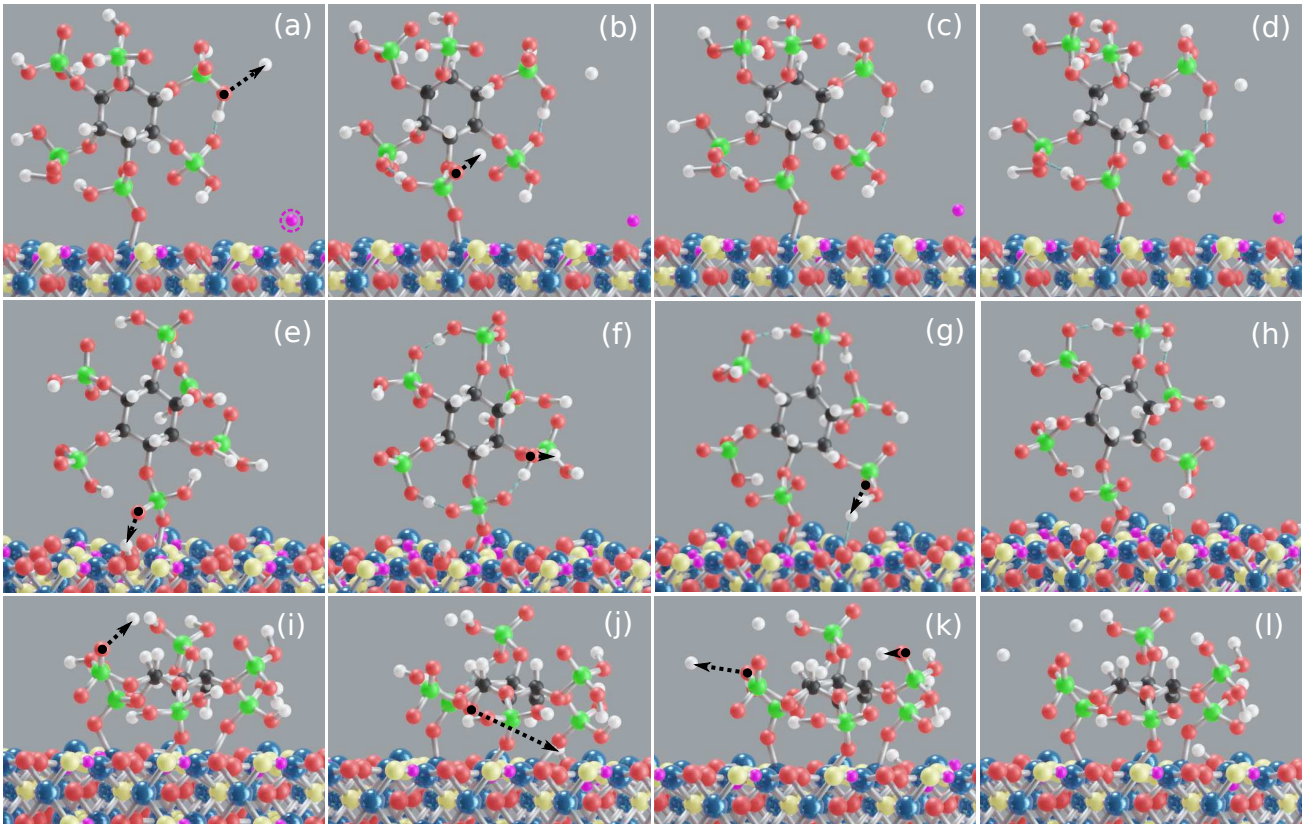


Figure 4. Snapshots of goethite–IHP–water models along the simulation trajectory. In **M(1)** motif, proton transfer from IHP to water and from goethite surface oxygen to water (**a**), intramolecular HB and a proton transfer from IHP to water (**b**), and **M(1)** motif at 17 and 25 ps (**c**,**d**). In **M(2)** motif, proton transfer from IHP to surface (**e**), protons transfer from IHP to water (**f**,**g**), and **M(2)** motif at 25 ps (**h**). In **3M** motif, three proton transfers from IHP to water (**i**,**k**) and a proton transfer from IHP to surface (**j**), **3M** motif at 25 ps (**l**). As proton transfer events are common in these interactions, the goethite surface hydrogen atoms and IHP's hydrogen atoms are shown in violet and white colors to avoid confusion. Moreover, the surrounding water is ignored here for better visualization. Snapshots that show proton transfers are from the equilibration phase.

3.2.2. IHP **3M** Motif

Here, IHP is aligned parallel to the surface to form three Fe–O_p covalent bonds as shown in Figure 1c. A stable **3M** motif is observed during the production trajectory with mean average Fe–O_p bond length of 1.96 Å and the corresponding mean average Fe–P distance of 3.2 Å, see Figure 2b, respectively. During equilibration, IHP has formed an average of 22 HBs with water of which three transformed to proton transfers from IHP to water, see Figure 4i,k. Furthermore, one proton transfer is observed from IHP to the surface, see Figure 4j. The equilibrated IHP is four times deprotonated with three proton transfers to water and one to the surface. The average number of HBs formed between IHP and water in production trajectory is around 23. The Figure 4l shows the IHP **3M** motif at 25 ps.

The time averaged goethite–IHP interaction energy per bond observed here is −86 kcal/mol. The goethite–IHP per bond interaction energy here is small compared to the **M(2)** motif case, but the overall interaction energy is higher than for both **M** motif cases, see Figure 2a. The IHP–water interaction energy is −7.8 kcal/mol which is higher than for the IHP **M** motif cases because of an additional proton transfer from IHP to water.

3.2.3. Discussion of Goethite–IHP–Water Interactions

Evaluating the interaction of the IHP phosphate groups with goethite, the **B** motif is found to be unstable here, similar to our previous studies [47,48] for IHP interaction with diaspore. To our knowledge, studies in literature have not mentioned the existence of **B** or **BB** motifs for IHP interacting with minerals. However, the **M** motif is often observed in theoretical studies [45,47,48] for IHP. Interestingly, for the number of phosphate groups which will bind to the surface different suggestions exist, ranging from four [40], three [45,47], two [47,48], one [47,48], and 0 [30]. The present **M** and **3M** stable motifs add to the list. The goethite–water interaction energy observed here is less than in the GP case. The weaker interaction of water in the latter case is in line with the study by Celi et al. [31] who showed that IHP adsorption on goethite makes the surface more negative than in case of OP.

Numerous studies show that IHP has the ability to compete with OP for the same binding sites and it could release and replace OP on goethite [23]. Comparing IHP and GP interaction energies, IHP exhibits stronger adsorption onto goethite than GP (see Figure 2a) which is in line with experiment [84] and our previous studies [47,48] for diaspore. Therefore, IHP has the ability to replace GP and the order of adsorption energies is IHP > GP > water. The Fe–P distances observed here are in close match to the values observed in experimental [58,82] and theoretical studies [15,44,46,83] of OP adsorption onto goethite. This is in line with Celi et al. [85] suggestion that IHP phosphate groups react with goethite in the same way as OP. Compared to GP, one could also infer that the changes in the phosphate group's geometry observed upon binding to goethite is similar for IHP and GP.

3.3. Theoretical IR Spectra of GP and IHP Adsorbed onto Goethite

The IR spectra of IHP/GP adsorbed onto goethite are calculated only for the stable motifs observed above, i.e, **M** and **B** of GP and **M** and **3M** of IHP. These motifs remained stable also during the extended trajectory used to calculate spectra, see Figures S6 and S7. The theoretical spectra calculated for these motifs are normalized and illustrated in Figure 5. The spectral analysis here is confined to 950–1250 cm^{-1} mainly to focus on the [P–O] stretching modes which are dominant in this range [22,86,87]. Therefore, the discussion below is mainly focused on phosphate ion bondings observed in the production trajectory and the corresponding IR spectra from literature. However, the peak positions of the IR spectra are known to shift differently with environmental factors such as water content and pH [50]. Especially nonprotonated oxygens of phosphate group are more sensitive to water hydrogens and hydroxyl groups and form HBs which might influence the spectra [50,88,89]. Both IHP and GP form strong to moderately strong HBs with surrounding water [47,48] and also contain nonprotonated oxygens, see Figures 3 and 4. Therefore, the calculated spectra here should reflect these interactions. The charge superscript is ignored when representing the phosphate ion bondings, e.g., FeH_2PO_4 or $FeHPO_4$, as these complexes are part of GP or IHP but not a molecule on their own.

Arai and Sparks [90] predicted the type of aqueous phosphate species based on the number of bands in IR spectra and the corresponding symmetry. According to their study, the aqueous phosphate species and their corresponding symmetry with number of bands (in parentheses) are PO_4–$T_d(1)$, HPO_4–$C_{3v}(3)$, H_2PO_4–$C_{2v}(4)$, and H_3PO_4–$C_{3v}(3)$. The study also showed that after OP binds to goethite the symmetry is reduced and the aqueous phosphate IR bands further split to form additional bands. Here, the symmetry of the phosphate group/s of IHP and GP is further reduced compared to OP bonded to goethite because of the P–O–C connection. Therefore, in the current study the spectrum assignment is performed based on the phosphate group moiety and its binding motif with goethite rather than symmetry.

Before we start the analysis some limitations about this approach should be mentioned. In an experimental set-up the IR spectra are obtained for an ensemble of molecules interacting with different goethite surface types. In contrast, here the analysis is performed for a single IHP/GP molecule interacting with only one goethite surface type. Furthermore,

the IR bands and their corresponding assignments may vary based on pH, experimental conditions, and surface crystallinity [44]. Ahmed et al. [15] provided a novel approach to this problem by calculating weighted averages of theoretical IR spectra involving simultaneously the most common and abundant motifs and surface planes. This study also emphasized the idea that an abundant motif's characteristics dominate the overall spectra which is in line with experimental studies [22,57].

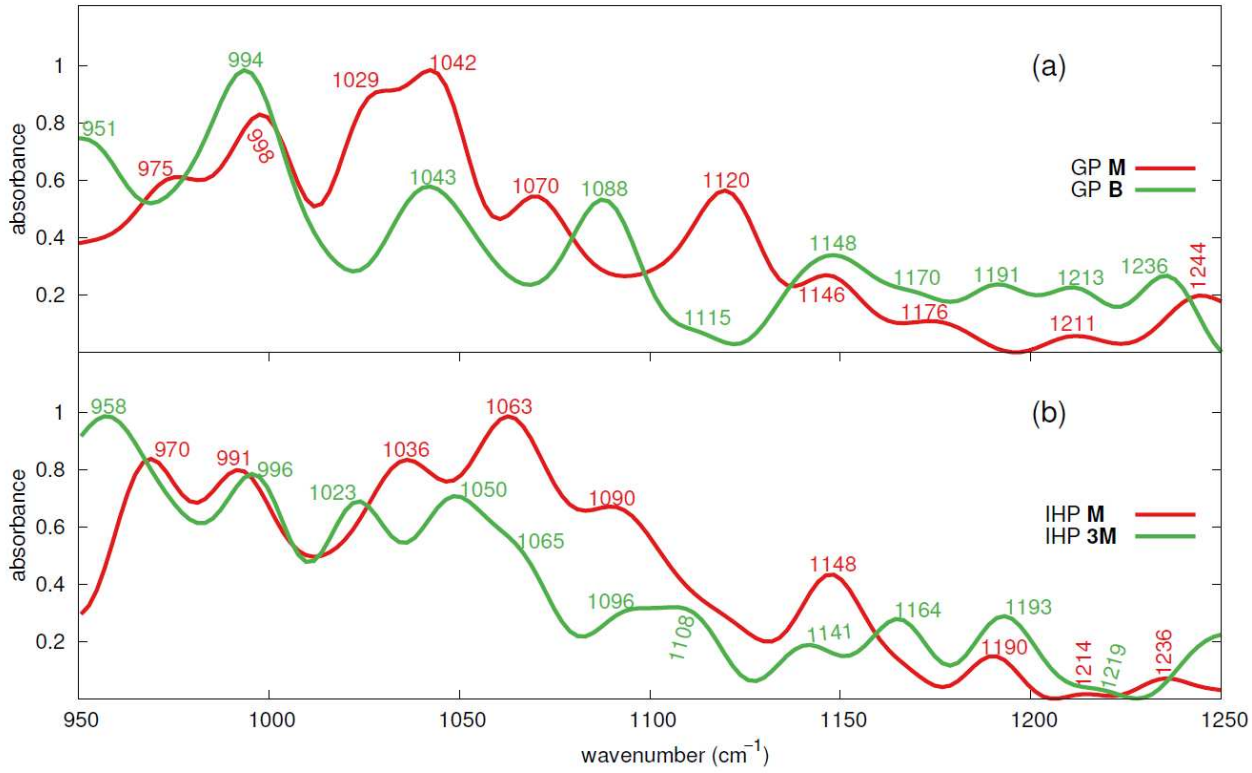


Figure 5. Calculated IR spectra of GP **M** and **B** motifs (**a**) and IHP **M** and **3M** motifs (**b**).

3.3.1. GP IR Spectra

In the GP **M** motif case, a deprotonated phosphate species is observed throughout the production trajectory. Therefore, the phosphate species observed here is $FePO_4$. The IR spectrum for GP exhibits ten bands at 975, 998, 1029, 1042, 1070, 1120, 1146, 1176, 1211, and 1244 cm^{-1} in the frequency range 950–1250 cm^{-1}, see Figure 5a. The first six peaks are of high to moderately high intense, whereas the remaining ones are less intense. The peaks at 1176 and 1211 cm^{-1} are less intense and wide ranged peaks distributed in frequency range of 1165 to 1187 cm^{-1} and 1200 to 1224cm^{-1}. In the GP **B** motif case also a deprotonated phosphate species is also observed throughout the simulation trajectory. Here, the GP exhibits ten bands at 951, 994, 1043, 1088, 1115, 1148, 1170, 1191, 1213, and 1236 cm^{-1}. Here, only the first four bands are of high to moderately high intense and the remaining ones are less intense, see Figure 5a. The bands at 1115 cm^{-1} and 1170 cm^{-1} are shoulder bands distributed in the range of 1109 to 1119 cm^{-1} and 1164 to 1175 cm^{-1}, respectively. The GP **M** and **B** motif cases have matching bands within ± 6 cm^{-1} of frequencies at 996, 1041, 1117, 1147, 1173, 1212, and 1240 cm^{-1}. In the following we compare these findings with previous studies.

GP **M** motif case: Lincoln and Stranks [91] studied phosphate binding to Co in the $Co(NH_3)_5PO_4$ complex and assigned bands at 980 and 1030 cm^{-1} to [P–OCo] and [P–O] modes of monodentate deprotonated phosphate group ($CoPO_4$), respectively. Tribe et al. [83] assigned bands at 979 and 1032 cm^{-1} to [P–O] modes of $FePO_4$ phosphate

species for glyphosate adsorption onto goethite. Therefore, the bands at 975 and 1029 cm^{-1} here are assigned to [P–OFe] and [P–O] modes. Compared to the study by Li et al. [29] of GP adsorption onto goethite, the bands at 998, 1042, 1120, and 1146 cm^{-1} could be assigned to [P–O] stretching mode, see Table 1 and Figure 5. The band at 998 cm^{-1} could also be assigned to [P–OFe] stretching mode as multiple studies [15,22,57,83] assigned bands around this frequency to the same stretching mode. Tribe et al. [83] assigned a band at 1063 cm^{-1} to [P–O] stretching mode for the $FeHPO_4$ complex, and therefore the band at 1070 cm^{-1} here could be assigned to a [P–O] stretching mode. The less intense band at 1176 cm^{-1} might correspond to [P–O] asymmetric stretching mode as Li et al. [29] assigned a band at 1180 cm^{-1} to [P–O] or [P–OH] for HPO_4 phosphate species of aqueous GP. Moreover, Persson et al. [57] assigned a band at 1178 cm^{-1} to [P–O] stretching mode for FeH_2PO_4 and Kubicki et al. [44] listed a band at 1176 cm^{-1} for the $FeHPO_4$ phosphate species. The band at 1211 cm^{-1} could be assigned to stretching modes of [C–C–C] and [C–O–C] of glycerol group based on the assignment by Nakagawa and Oyama [92] of 1210 cm^{-1} frequency observed in glycerol–water interactions [93]. Regarding the next band at 1244 cm^{-1}, Kubicki et al. [44] assigned the band at 1250 cm^{-1} to [P–O–H] bending vibrations and in addition, Ahmed et al. [15] assigned the band at 1227 cm^{-1} to [P–O–H] bending vibrations for OP on 010 goethite surface. Therefore, the band at 1244 cm^{-1} here could be assigned to GP's unprotonated phosphate oxygens interaction with water hydrogens.

GP **B** motif case: Ahmed et al. [15] study of OP on 010 goethite surface assigned bands at 957 and 964 cm^{-1} to [O–P–2OFe] and [2O–P–OFe] symmetric stretching modes and Persson et al. [57] assigned the band at 966 cm^{-1} to [P–O] stretching mode. Therefore, the band at 951 cm^{-1} could be assigned to [P–O] or [P–OFe] stretching modes. The band at 994 cm^{-1} frequency is close to 998 cm^{-1} frequency found in GP **M** motif case, and therefore it is assigned the same modes, [P–O] or [P–OFe] stretching modes, as the latter frequency. The bands at 1043, 1115, and 1148 cm^{-1} could be assigned to [P–O] stretching mode as per Li et al. [29] study while the band at 1088 cm^{-1} could be assigned to [P=O] [29] or [P–O] [83] stretching modes, see Table 1. The band at 1170 cm^{-1} is assigned [P–O] mode which is the same mode assigned for the band at 1176 cm^{-1} in GP **M** motif case. The band at 1191 and 1213 cm^{-1} could be assigned to [C–C–C] and [C–O–C] stretching modes of glycerol group as assigned for 1211 cm^{-1} frequency observed in GP **M** motif case. The band at 1236 cm^{-1} is assigned the same mode as 1244 cm^{-1} in GP **M** motif case.

Comparing IR spectra of GP **M** and **B** motifs, we conclude that several common band assignments are observed between both cases. The bands between 951 and 998 cm^{-1} are assigned to [P–O] or [P–OFe] stretching modes, and the ones between 1029 and 1176 cm^{-1} are assigned to [P–O] stretching mode except for 1088 cm^{-1} frequency which could be assigned to [P=O] stretching mode as well. The bands between 1191 and 1213 cm^{-1} are assigned to [C–C–C] and [C–O–C] stretching modes of glycerol group, respectively, while the bands between 1236 and 1244 cm^{-1} are assigned to unprotonated phosphate oxygens interaction with water hydrogens. The comparison of spectra calculated here with spectra from the experimental study by Li et al. [29] is shown in Figure S2a. Moreover, spectral peaks characteristic to water are analyzed in light of peaks from literature, see Figure S8.

Table 1. Experimental and theoretical IR frequencies from selected studies related to phosphates OP, GP, IHP, and others on goethite are listed below. The IR frequencies calculated here for GP and IHP on goethite are also presented here. The symbols †, ‡, •, ○, ▲, · · · , and ⋆ denote [P–O], [P=O], [P–OFe], [P–OH], [P–O–C], [P–O· · · H], and [C–C–C] plus [C–O–C] modes, respectively. The symbols are assigned to frequencies only when specifically mentioned in reference experimental study. The frequency assigned to multiple modes is denoted as •/○ represent [P–OFe] or [P–OH] modes while •&/○ represent [P–OFe] and/or [P–OH] mode.

Study and Description	Wavenumber [cm^{-1}]										
goethite–OP											
Ref.Tejedor and Anderson [22]											
pH 6.0, 190 µmol P/g of Gt		1004	1030	1045		1099		1128			
Fe_2HPO_4	982 •/○	1006 •						1123 ‡			
Fe_2PO_4				1044 †		1096 †					
$FePO_4$		1001 •&/†	1025 †								
Ref. Persson et al. [57]											
pH 4.2−5.7 [FeH_2PO_4]		1001 •/○		1049 ○				1122 †	1178 †		
pH 7.9 [$FeHPO_4$]		1001 •/○		1049 ○				1122 †			
pH 13 [$FePO_4$]	966 †			1057 †							
Ref. Kubicki et al. [44]											
pH 4.22 [FeH_2PO_4]	982	1009		1044		1091	1122	1157		1195	
pH 7.51 [$FeHPO_4$]			1022	1043	1084		1124		1177		
Ref. Ahmed et al. [15]											
pH 6.3		1000					1110		1165		
M@010 [$FeHPO_4$]	964		1021	1049							1207
B@010 [$FeHPO_4$]	957	992	1007	1035	1071						1227
M@100 [$FePO_4$]	957	999		1044	1058						
B@100 [Fe_2HPO_4]	953	974		1048							
goethite–[organic P-compounds]											
Ref. Persson et al. [43] (MMP)											
pH 2.6 $FeHPO_4$		1003 †		1051 †				1140 †		1185	
pH 9.9 $FePO_4$		990 †		1051 †				1120 †		1185	
Ref. Tribe et al. [83] (GLP)											
$FeHPO_3$		1001 •	1020 •	1030 †	1063 ○		1118 †				
$FePO_3$	973 †	979 †		1032 †	1068 †	1084 †	1095 †	1102 †			
Ref. Li et al. [29] (GP)											
pH 3		1008 †		1052 †		1098 ‡		1139 †			
pH 9		998 †		1044 †		1092 ‡		1126 †			
current work											
M [$FePO_4$]	975 †/•	998 †/•	1029 †	1042 †	1070 †		1120 †	1146 †	1176 †		1211 ⋆	1244 ○
B [$FePO_4$]	951 †/•	994 †/•		1043 †		1088 †/‡	1115 †	1148 †	1170 †	1191 ⋆	1213 ⋆	1236 ○
goethite–IHP											
Ref. Yan et al. [41]											
pH 5		998 †			1075 †			1135 †	1166 •		
Ref. Yan et al. [94]											
pH 5		1010			1071			1134	1164		
pH 6		998			1068			1131			
Ref. Johnson et al. [30]											
fitted band centers	974 †	991 ▲	1011 ▲	1043 ···	1074 †	1099 †		1128	1160 †	1187 †	1220 ‡	
current work											
M	970 †/▲	991 †/▲		1036 ···	1063 †	1090 †			1148 †/•	1190 †	1214 ‡	1236 ○
3M	958 †/▲	996 †/▲	1023 ▲	1050 ···	1065 †	1096 †	1108 †	1141 †/•	1164 †/•	1193 †	1219 ‡	

3.3.2. IHP IR Spectra

IHP has six phosphate groups and hence the theoretical spectra calculated here would include the characteristics of different types of phosphate species originating from the six phosphate groups. In addition, intermolecular HBs are also common between adjacent phosphate groups which shift or alter intensity of the IR spectra [88,89]. In the IHP **M** case, the six phosphate groups transformed to two types of phosphate species, HPO_4 (2) and H_2PO_4 (4), in the production trajectory. The IR spectra for IHP **M** case exhibited bands at 970, 991, 1036, 1063, 1090, 1148, 1190, 1214, and 1236 cm^{-1}, see Figure 5b. The first five bands are high intense bands while the latter ones are moderately intense to often less

intense. The band at 1090 cm^{-1} is a shoulder band distributed in the frequency range of 1084 to 1099 cm^{-1} while the band at 1214 is a least intense flat band distributed in the frequency range of 1205 to 1222 cm^{-1}. In IHP **3M** motif case all possible phosphate species, PO_4 (1), HPO_4 (2), H_2PO_4 (3), are observed in the production trajectory. The IR spectra have bands at 958, 996, 1023, 1050, 1065, 1096, 1108, 1141, 1164, 1193, and 1219 cm^{-1}. The bands at 1065 and 1219 cm^{-1} are shoulder bands distributed in the frequency range of 1059 to 1071 cm^{-1} and 1212–1225 cm^{-1}, respectively. The bands at 1096 and 1108 cm^{-1} are maxima of a bimodal peak which is distributed in the frequency range of 1084 to 1116 cm^{-1}. The IHP **M** and IHP **3M** motif cases have matching bands within ± 6 cm^{-1} of frequencies at 964, 993, 1064, 1093, 1144, 1191, and 1217 cm^{-1}. The IHP spectra obtained here are deconvoluted into Gaussian functions using the PeakFit v4 software [95] to compare current results with Johnson et al. [30] study. PeakFit v4 is the same software used by Johnson et al. [30] for deconvolution of IHP spectra. The deconvoluted spectra and the corresponding fitted band centers are presented in Figure S1.

IHP **M** case: Guan et al. [45] assigned bands between 970–985 cm^{-1} and 970 cm^{-1} frequency to [P–O–C] stretching mode for IHP adsorbed onto aluminum hydroxide and for IHP in water, respectively. In contrast, Johnson et al. [30] assigned a fitted band center at 974 cm^{-1} to [P–O] mode but he assigned fitted band center at 991 and 1011 cm^{-1} to [P–O–C] stretching mode. Therefore, the peaks at 970 and 991 cm^{-1} (fitted band centers at 967 and 992 cm^{-1}, respectively, see Figure S1a) could be assigned to [P–O] or [P–O–C] stretching modes. The band at 1036 cm^{-1} (fitted band center 1036 cm^{-1}) might correspond to the intermolecular HBs between adjacent phosphate groups or between a phosphate group and water adsorbed to goethite surface. This assignment is based on the study of Johnson et al. [30], where the fitted band center at 1043 cm^{-1} is assigned to P–O···H (H from the phosphate group or water adsorbed to goethite surface). The high intense peak at 1063 cm^{-1} with fitted band center at peak center could be assigned to [P–O] stretching mode of HPO_4 as per Johnson et al. [30] and Yan et al. [41] studies, see Table 1. The next peak is at 1090 cm^{-1} (fitted band center at 1091 cm^{-1}) and it could be assigned to [P–O] mode as Johnson et al. [30] assigned a fitted band at 1099 to such a mode. The fitted band center at 1120 cm^{-1} which does not have a specific assigned peak (see Figure S1a) might correspond to [P–O] stretching mode as Johnson et al. [30] assigned fitted band center at 1128 cm^{-1} to [P–O] stretching mode. The peak at 1148 cm^{-1} (fitted band centers at 1147 and 1165 cm^{-1}) might correspond to [P–OFe] stretching mode as Guan et al. [45] and Yan et al. [41] assigned bands 1148 cm^{-1}, 1157 cm^{-1}, and 1166 cm^{-1} to [P-OAl] and [P-OFe] stretching modes, respectively. It could also be assigned to [P–O] mode as Johnson et al. [30] assigned 1160 cm^{-1} band center to such a mode. The peak at 1190 cm^{-1} the fitted band center is at peak center and it is assigned to [P–O] mode as per Johnson et al. [30]. The band at 1214 cm^{-1} (fitted band center at 1213 cm^{-1}) could be assigned to [P=O] stretching mode. This is because, Celi et al. [31] suggested that after IHP adsorption onto goethite the [P=O] stretching band observed for aqueous IHP at 1223 cm^{-1} frequency might shift to lower frequencies. In addition, Johnson et al. [30] assigned the fitted band center at 1220 cm^{-1} to [P=O] stretching mode. Bands within 1230 and 1250 cm^{-1} are not common in goethite–IHP-related studies, see Table 1, and therefore the band at 1239 cm^{-1} is assigned to [P–O–H] bending vibrations based on Ahmed et al. [15]'s study.

IHP **3M** motif case: The first band at 958 cm^{-1} could be assigned to [P–O] or [P–O–C] stretching modes based on reasons for assignment of 970 cm^{-1} band in IHP **M** motif case. The next band at 996 cm^{-1} is assigned to [P–O] or [P–O–C] stretching modes for the same reasons as given for the assignment of the 977 cm^{-1} band in IHP **M** motif case. The band at 1023 cm^{-1} (fitted band center at 1022 cm^{-1}) could be assigned to [P–O–C] stretching mode, as Johnson et al. [30] assigned the fitted band center at 1011 cm^{-1} to such a mode. Similar to the band at 1036 cm^{-1} for IHP **M** motif case, the band at 1050 cm^{-1} (fitted band center at 1048 cm^{-1}) here could be assigned to inter- and intramolecular HBs among adjacent phosphate groups and a phosphate group with water bound to goethite, respectively. The next bands at 1065 and 1096 cm^{-1} (corresponding fitted band centers at

1068 and 1092 cm^{-1}) are assigned to [P–O] stretching modes similar to peaks at 1063 and 1090 cm^{-1} of IHP **M** motif case, see Table 1. The peak at 1108 cm^{-1} with fitted band center at 1113 cm^{-1} could be assigned to [P–O] stretching mode based on Johnson et al. [30] assignment of fitted band center at 1127 cm^{-1} to [P–O] stretching mode. The band at 1141 cm^{-1} (fitted band center at 1140 cm^{-1}) is assigned to [P–OFe] stretching mode as Guan et al. [45] assigned the band at 1048 cm^{-1} to [P–OAl] stretching mode. It could also be assigned to [P–O] mode since Yan et al. [41] assigned the band at 1135cm^{-1} to [P–O] mode. The band 1164 cm^{-1} (fitted band center at 1165cm^{-1}) is assigned to [P–OFe] or [P–O] mode, as Yan et al. [41] assigned the band at 1166 cm^{-1} to [P–OFe] stretching mode and Johnson et al. [30] assigned fixed band center at 1162 to [P–O] mode. The peaks at 1193 and 1219 cm^{-1} are assigned to [P–O] and [P=O] modes for the same reasons given the assignment of peaks at 1190 and 1214 cm^{-1} in IHP **M** motif case.

Summarizing the IHP **M** and **3M** motifs' IR spectra, and their assignments based on literature (see Table 1), we conclude the following. The bands in the frequency range of 958 to 996 cm^{-1} could be mainly assigned to [P–O] or [P–O–C] stretching modes. The bands around 1043 cm^{-1} are assigned to intermolecular HBs between IHPs phosphate groups and intramolecular HBs between IHP phosphate groups and water adsorbed to goethite. The bands observed in the range of 1063 to 1108 cm^{-1} are assigned to [P–O] stretching modes and the ones in 1141–1164 cm^{-1} frequency range are assigned to [P–OFe] or [P–O] modes. The peaks around 1191 cm^{-1} are assigned to [P–O] modes and the ones around 1217 cm^{-1} are assigned to [P=O] modes. The comparison of IHP spectra with spectra from the experimental study of Yan et al. [41] is shown in Figure S2b. A few selected frequency ranges where the IR spectra of water could be characterized are analyzed, see Figure S8.

4. Summary and Conclusions

The world population is expected to increase 34% by 2050 and will reach 9.1 billion [96], challenging the agricultural industry to meet the nutritional needs. Unfortunately, agricultural production is heavily dependent on the soon to be exhausted P rocks. Therefore, there is a need to find ways to recycle and secure P resources to support the raising global population. The current study focused on P interaction with soil minerals, a significant factor that causes P inefficiency and P loss in soil. The present results are expected to provide additional insight into organic P interaction at goethite–water interface.

Analysis of binding energies (see Figure 2) show that the GP **B** motif exhibits stronger overall binding energy than the **M** motif. This is in contrast to the suggestion by Li et al. [29] that GP might not form **B** motif due to steric hinderance of organic moiety. However, based on interaction energies calculated here and the study by Abdala et al. [58], we conclude that GP forms a **B** motif at low goethite surface loading, while at high loading the **M** motif dominates.

Regarding IHP, it is found to interact with goethite through multiple phosphate groups and its **3M** motif has a higher interaction energy than the **M** motif. Furthermore, its **B** motif is unstable which transformed to the **M** motif. The transformation of the **B** to the **M** motif has occurred in our previous studies [47,48] as well, confirming that IHP phosphate groups are more likely to form **M** motifs with goethite. The IHP interaction energy with goethite is stronger than for GP which suggests that it could replace GP to bind with goethite. This is in line with the results of De Groot and Golterman [97] which showed that IHP can replace OP and inhibit it from further adsorption.

The energy required for phosphate to replace a OH^- from the surface could not be estimated from that study. However, Ahmed et al. [15] showed that OH^- has a higher interaction energy than OP and water and thus could replace both. However, in contrast, Li et al. [29] showed that GP replaces OH^- at the goethite surface at a high rate. Therefore, understanding the priority of adsorption is important as a non-replaceable hydroxyl group at the surface could restrict the IHP interaction with goethite and also reduce the range of binding motifs. The current study proposes a competitive adsorption study for multiple

instances of IHP/GP in presence of water and OH^- at the goethite surface to understand effect of high surface loading and influence of OH^- on binding motifs.

Finally, we have investigated the IR signatures of the different binding motifs. The IR spectra calculated for GP **M** and **B** motifs match reasonably with phosphates related IR spectra from literature. This suggests that both motifs might exist simultaneously on the goethite surface. However, given the similarity of spectra, the proportion of these motifs could not be estimated as done by Ahmed et al. [15]. The calculated IR spectra for IHP also matches well with the IR spectra from literature. This validates the current modeling approach for simulating the interactions of IHP and GP at goethite–water interface.

Supplementary Materials: The following are available online, Figure S1: Fitted IR spectra of IHP, Figure S2: Comparison of GP and IHP spectra with experimental spectra, Figure S3: Initial motifs of IHP and GP, Figure S4: GP **BB** motif, HBs between GP and surrounding water and water bonded to surface Fe atoms, Figure S5: Pair correlation function for surface Fe atoms and water oxygens, Figure S6: Fe-O_p covalent bond lengths along simulation trajectories between 25 and 55 ps, Figure S7: Binding energy of IHP **M(1)** motif along simulation trajectory between 25 and 55 ps, Figure S8: IR spectra of GP M and B motif cases and IHP M and 3M motif cases.

Author Contributions: P.B.G. is responsible for formal analysis, investigation, methodology, visualization and writing—original draft. A.A.A. and O.K. are responsible for conceptualization, funding acquisition, methodology, supervision, writing—review and editing. All authors have read and agreed to the published version of the manuscript.

Funding: We gratefully acknowledge the financial support by the German Research Foundation (DFG) as a part of the SPP 1685 Priority program "Ecosystem Nutrition: Forest strategies for limited phosphorus resources" (P.B.G., O.K., A.A.A.) and the InnoSoilPhos-project (A.A.A.), funded by the German Federal Ministry of Education and Research (BMBF) in the frame of the BonaRes-program (No. 031A558). This research was performed within the scope of the Leibniz Science Campus "Phosphorus Research Rostock". The authors thank the North German Super computing Alliance for providing HPC resources (project mvp00016).

Data Availability Statement: Not applicable.

Conflicts of Interest: The authors declare no conflict of interest. The funders had no role in the design of the study; in the collection, analyses, or interpretation of data; in the writing of the manuscript; or in the decision to publish the results.

References

1. Cordell, D.; Drangert, J.O.; White, S. The Story of Phosphorus: Global Food Security and Food for Thought. *Glob. Environ. Chang.* **2009**, *19*, 292–305. [CrossRef]
2. Cordell, D.; Neset, T.S.S. Phosphorus Vulnerability: A Qualitative Framework for Assessing the Vulnerability of National and Regional Food Systems to the Multi-Dimensional Stressors of Phosphorus Scarcity. *Glob. Environ. Chang.* **2014**, *24*, 108–122. [CrossRef]
3. Reitzel, K.; Bennett, W.W.; Berger, N.; Brownlie, W.J.; Bruun, S.; Christensen, M.L.; Cordell, D.; van Dijk, K.; Egemose, S.; Eigner, H.; et al. New Training to Meet the Global Phosphorus Challenge. *Environ. Sci. Technol.* **2019**, *53*, 8479–8481. [CrossRef]
4. Steen, I. Phosphorus Availability in the 21st Century : Management of a Non-Renewable Resource. *Phosphorus Potassium* **1998**, *217*, 25–31.
5. Smil, V. Phosphorus in the Environment: Natural Flows and Human Interferences. *Annu. Rev. Environ. Resour.* **2000**, *25*, 53–88. [CrossRef]
6. Rosmarin, A. The Precarious Geopolitics of Phosphorous. *Down Earth Sci. Environ. Fortn.* **2004**, *30*, 27–31.
7. Withers, P. Closing the Phosphorus Cycle. *Nat. Sustain.* **2019**, 1001–1002. [CrossRef]
8. Withers, P.; Forber, K.; Lyon, C.; Rothwell, S.; Doody, D.; Jarvie, H.; Martin-Ortega, J.; Jacobs, B.; Cordell, D.; Patton, M.; et al. Towards Resolving the Phosphorus Chaos Created by Food Systems. *Ambio A J. Hum. Environ.* **2019**. [CrossRef]
9. Ahmed, A.A.; Gros, P.; Kühn, O.; Leinweber, P. Molecular Level Investigation of the Role of Peptide Interactions in the Glyphosate Analytics. *Chemosphere* **2018**, *196*, 129–134. [CrossRef]
10. Gros, P.; Ahmed, A.; Kühn, O.; Leinweber, P. Glyphosate Binding in Soil as Revealed by Sorption Experiments and Quantum-Chemical Modeling. *Sci. Total Environ.* **2017**, *586*, 527–535. [CrossRef]
11. Gros, P.; Ahmed, A.A.; Kühn, O.; Leinweber, P. Influence of Metal Ions on Glyphosate Detection by FMOC-Cl. *Environ. Model. Assess.* **2019**, *191*, 244. [CrossRef] [PubMed]

12. Hens, M.; Merckx, R. Functional Characterization of Colloidal Phosphorus Species in the Soil Solution of Sandy Soils. *Environ. Sci. Technol.* **2001**, *35*, 493–500. [CrossRef] [PubMed]
13. Kruse, J.; Abraham, M.; Amelung, W.; Baum, C.; Bol, R.; Kühn, O.; Lewandowski, H.; Niederberger, J.; Oelmann, Y.; Rüger, C.; et al. Innovative Methods in Soil Phosphorus Research: A Review. *J. Soil Sci. Plant Nutr.* **2015**, *178*, 43–88. [CrossRef] [PubMed]
14. Jiang, X.; Bol, R.; Nischwitz, V.; Siebers, N.; Willbold, S.; Vereecken, H.; Amelung, W.; Klumpp, E. Phosphorus Containing Water Dispersible Nanoparticles in Arable Soil. *J. Environ. Qual.* **2015**, *44*, 1772–1781. [CrossRef] [PubMed]
15. Ahmed, A.A.; Gypser, S.; Leinweber, P.; Freese, D.; Kühn, O. Infrared Spectroscopic Characterization of Phosphate Binding at the Goethite-Water Interface. *Phys. Chem. Chem. Phys.* **2019**, *21*, 4421–4434. [CrossRef] [PubMed]
16. Gypser, S.; Hirsch, F.; Schleicher, A.M.; Freese, D. Impact of Crystalline and Amorphous Iron- and Aluminum Hydroxides on Mechanisms of Phosphate Adsorption and Desorption. *J. Environ. Sci.* **2018**, *70*, 175–189. [CrossRef]
17. Sharpley, A.N.; Chapra, S.C.; Wedepohl, R.; Sims, J.T.; Daniel, T.C.; Reddy, K.R. Managing Agricultural Phosphorus for Protection of Surface Waters: Issues and Options. *J. Environ. Qual.* **1994**, *23*, 437–451. [CrossRef]
18. Holzmann, S.; Missong, A.; Puhlmann, H.; Siemens, J.; Bol, R.; Klumpp, E.; von Wilpert, K. Impact of Anthropogenic Induced Nitrogen Input and Liming on Phosphorus Leaching in Forest Soils. *J. Soil Sci. Plant Nutr.* **2015**, *179*, 443–453. [CrossRef]
19. Bol, R.; Julich, D.; Brödlin, D.; Siemens, J.; Kaiser, K.; Dippold, M.A.; Spielvogel, S.; Zilla, T.; Mewes, D.; von Blanckenburg, F.; et al. Dissolved and Colloidal Phosphorus Fluxes in Forest Ecosystems—An Almost Blind Spot in Ecosystem Research. *J. Soil Sci. Plant Nutr.* **2016**, *179*, 425–438. [CrossRef]
20. Boy, J.; Valarezo, C.; Wilcke, W. Water Flow Paths in Soil Control Element Exports in an Andean Tropical Montane Forest. *Eur. J. Soil Sci.* **2008**, *59*, 1209–1227. [CrossRef]
21. Newman, R.H.; Tate, K.R. Soil Phosphorus Characterisation by 31 P Nuclear Magnetic Resonance. *Commun. Soil Sci. Plant Anal.* **1980**, *11*, 835–842. [CrossRef]
22. Tejedor-Tejedor, M.I.; Anderson, M.A. The Protonation of Phosphate on the Surface of Goethite as Studied by CIR-FTIR and Electrophoretic Mobility. *Langmuir* **1990**, *6*, 602–611. [CrossRef]
23. Turner, B.L.; Papházy, M.J.; Haygarth, P.M.; Mckelvie, I.D. Inositol Phosphates in the Environment. *Philos. Trans. R. Soc. B* **2002**, *357*, 449–469. [CrossRef] [PubMed]
24. Doolette, A.; Smernik, R.; Dougherty, W. Spiking Improved Solution Phosphorus31 Nuclear Magnetic Resonance Identification of Soil Phosphorus Compounds. *Soil Sci. Soc. Am. J.* **2009**, *73*. [CrossRef]
25. Gerke, J. Phytate (Inositol Hexakisphosphate) in Soil and Phosphate Acquisition from Inositol Phosphates by Higher Plants: A Review. *Plants* **2015**, *4*, 253–266. [CrossRef]
26. Pant, H.K.; Warman, P.R.; Nowak, J. Identification of Soil Organic Phosphorus by 31 P Nuclear Magnetic Resonance Spectroscopy. *Commun. Soil. Sci. Plant Anal.* **1999**, *30*, 757–772. [CrossRef]
27. Vincent, A.G.; Vestergren, J.; Gröbner, G.; Persson, P.; Schleucher, J.; Giesler, R. Soil Organic Phosphorus Transformations in a Boreal Forest Chronosequence. *Plant Soil* **2013**, *367*, 149–162. [CrossRef]
28. Missong, A.; Bol, R.; Willbold, S.; Siemens, J.; Klumpp, E. Phosphorous Forms in Forest Soil Colloids as Revealed by Liquid-State P-NMR. *J. Soil Sci. Plant Nutr.* **2016**, *179*, 159–167. [CrossRef]
29. Li, H.; Wan, B.; Yan, Y.; Zhang, Y.; Cheng, W.; Feng, X. Adsorption of Glycerophosphate on Goethite: A Macroscopic and Infrared Spectroscopic Study. *J. Soil Sci. Plant Nutr.* **2017**, *181*, 557–565. [CrossRef]
30. Johnson, B.B.; Quill, E.; Angove, M.J. An Investigation of the Mode of Sorption of Inositol Hexaphosphate to Goethite. *J. Colloid Interface Sci.* **2012**, *367*, 436–442. [CrossRef]
31. Celi, L.; M, P.; Marsan, F.A.; Barberis, E. Effects of pH and Electrolytes on Inositol Hexaphosphate Interaction with Goethite. *Soil Sci. Soc. Am. J.* **2001**, *65*, 753–760. [CrossRef]
32. Tsao, T.M.; Chen, Y.M.; Wang, M.K. Origin, Separation and Identification of Environmental Nanoparticles: A Review. *J. Environ. Monit.* **2011**, *13*, 1156–1163. [CrossRef]
33. Tan, K. *Principles of Soil Chemistry*, 4th ed.; Books in Soils, Plants, and the Environment; Taylor & Francis: Abingdon, UK, 2011.
34. Brady, N. *The Nature and Properties of Soils*, 15th ed.; Pearson Education Ltd.: Pearson, Harlow, UK, 2017.
35. Cornell, R.M.; Schwertmann, U. *The Iron Oxides: Structure, Properties Reactions Occurrence and Uses*; Wiley-VCH Verlag GmbH and Co. KGaA: Weinheim, Germany, 2003. [CrossRef]
36. Parfitt, R.L.; Atkinson, R.J. Phosphate Adsorption on Goethite (α-FeOOOH). *Nature* **1976**, *264*, 740–742. [CrossRef]
37. Torrent, J.; Schwertmann, U.; Barron, V. Fast and Slow Phosphate Sorption by Goethite-Rich Natural Materials. *Clays Clay Miner.* **1992**, *40*, 14–21. [CrossRef]
38. Chitrakar, R.; Tezuka, S.; Sonoda, A.; Sakane, K.; Ooi, K.; Hirotsu, T. Phosphate Adsorption on Synthetic Goethite and Akaganeite. *J. Colloid Interface Sci.* **2006**, *298*, 602–608. [CrossRef]
39. Ahmed, A.A.; Gypser, S.; Freese, D.; Leinweber, P.; Kuehn, O. Molecular Level Picture of the Interplay between pH and Phosphate Binding at the Goethite–Water Interface. *Phys. Chem. Chem. Phys.* **2020**. [CrossRef] [PubMed]
40. Ognalaga, M.; Frossard, E.; Thomas, F. Glucose-1-Phosphate and Myo-Inositol Hexaphosphate Adsorption Mechanisms on Goethite. *Soil Sci. Soc. Am. J.* **1994**, 332–337. [CrossRef]
41. Yan, Y.; Koopal, L.K.; Liu, F.; Huang, Q.; Feng, X. Desorption of Myo-Inositol Hexakisphosphate and Phosphate from Goethite by Different Reagents. *J. Plant. Nutr. Soil Sci.* **2015**, *178*, 878–887. [CrossRef]
42. Kubicki, J.D. (Ed.) *Molecular Modeling of Geochemical Reactions*; Wiley and Sons: Chichester, UK, 2016.

43. Persson, P.; Andersson, T.; Nelson, H.; Sjöberg, S.; Giesler, R.; Lövgren, L. Surface Complexes of Monomethyl Phosphate Stabilized by Hydrogen Bonding on Goethite (Alpha-FeOOH) Nanoparticles. *J. Colloid Interface Sci.* **2012**, *386*, 350–358. [CrossRef]
44. Kubicki, J.D.; Paul, K.W.; Kabalan, L.; Zhu, Q.; Mrozik, M.K.; Aryanpour, M.; Pierre-Louis, A.M.; Strongin, D.R. ATR–FTIR and Density Functional Theory Study of the Structures, Energetics, and Vibrational Spectra of Phosphate Adsorbed onto Goethite. *Langmuir* **2012**, *28*, 14573–14587. [CrossRef]
45. Guan, X.H.; Shang, C.; Zhu, J.; Chen, G.H. ATR-FTIR Investigation on the Complexation of Myo-Inositol Hexaphosphate with Aluminum Hydroxide. *J. Colloid Interface Sci.* **2006**, *293*, 296–302. [CrossRef] [PubMed]
46. Ahmed, A.A.; Leinweber, P.; Kühn, O. Unravelling the Nature of Glyphosate Binding to Goethite Surfaces by Ab Initio Molecular Dynamics Simulations. *Phys. Chem. Chem. Phys.* **2018**, *20*, 1531–1539. [CrossRef] [PubMed]
47. Ganta, P.B.; Kühn, O.; Ahmed, A.A. QM/MM Simulations of Organic Phosphorus Adsorption at the Diaspore–Water Interface. *Phys. Chem. Chem. Phys.* **2019**, *21*, 24316–24325. [CrossRef] [PubMed]
48. Ganta, P.B.; Kühn, O.; Ahmed, A.A. QM/MM Molecular Dynamics Investigation of the Binding of Organic Phosphates to the 100 Diaspore Surface. *Front. For. Glob. Chang.* **2020**, *3*, 71. [CrossRef]
49. Gerzabek, M.; Aquino, A.; Haberhauer, G.; Tunega, D.; Lischka, H. Molecular Modelling—Opportunities for Soil Research. *Bodenkultur* **2001**, *52*, 133–146.
50. Kwon, K.D.; Kubicki, J.D. Molecular Orbital Theory Study on Surface Complex Structures of Phosphates to Iron Hydroxides: Calculation of Vibrational Frequencies and Adsorption Energies. *Langmuir* **2004**, *20*, 9249–9254. [CrossRef]
51. Aquino, A.J.; Tunega, D.; Haberhauer, G.; Gerzabek, M.H.; Lischka, H. Acid–Base Properties of a Goethite Surface Model: A Theoretical View. *Geochim. Cosmochim. Acta* **2008**, *72*, 3587–3602. [CrossRef]
52. Strauss, R.; BrÜmmer, G.; BARROW, N. Effects of Crystallinity of Goethite: II. Rates of Sorption and Desorption of Phosphate. *Eur. J. Soil Sci.* **1997**, *48*, 101–114. [CrossRef]
53. Kosmulski, M. pH-Dependent Surface Charging and Points of Zero Charge. IV. Update and New Approach. *J. Colloid Interface Sci.* **2009**, *337*, 439–448. [CrossRef]
54. Senn, H.M.; Thiel, W. QM/MM Methods for Biomolecular Systems. *Angew. Chem.* **2009**, *48*, 1198–1229. [CrossRef]
55. Xiu, F.; Zhou, L.; Xia, S.; Yu, L. Adsorption Mechanism of Water Molecule on Goethite (010) Surface. *J. Ocean Univ. China* **2016**, *15*, 1021–1026. [CrossRef]
56. Guo, H.; Barnard, A.S. Thermodynamic Modelling of Nanomorphologies of Hematite and Goethite. *J. Mater. Chem.* **2011**, *21*, 11566–11577. [CrossRef]
57. Persson, P.; Nilsson, N.; Sjöberg, S. Structure and Bonding of Orthophosphate Ions at the Iron Oxide–Aqueous Interface. *J. Colloid Interface Sci.* **1996**, *177*, 263–275. [CrossRef]
58. Abdala, D.B.; Northrup, P.A.; Arai, Y.; Sparks, D.L. Surface Loading Effects on Orthophosphate Surface Complexation at the Goethite/Water Interface as Examined by Extended X-Ray Absorption Fine Structure (EXAFS) Spectroscopy. *J. Colloid Interface Sci.* **2015**, *437*, 297–303. [CrossRef]
59. Humphrey, W.; Dalke, A.; Schulten, K. VMD—Visual Molecular Dynamics. *J. Mol. Graph.* **1996**, *14*, 33–38. [CrossRef]
60. Groenhof, G. Introduction to QM/MM Simulations. In *Biomolecular Simulations: Methods and Protocols*; Monticelli, L., Salonen, E., Eds.; Humana Press: Totowa, NJ, USA, 2013; pp. 43–66. [CrossRef]
61. Ozboyaci, M.; Kokh, D.B.; Corni, S.; Wade, R.C. Modeling and Simulation of Protein–Surface Interactions: Achievements and Challenges. *Q. Rev. Biophys.* **2016**, *49*, e4. [CrossRef]
62. VandeVondele, J.; Krack, M.; Mohamed, F.; Parrinello, M.; Chassaing, T.; Hutter, J. Quickstep: Fast and Accurate Density Functional Calculations Using a Mixed Gaussian and Plane Waves Approach. *Comput. Phys. Commun.* **2005**, *167*, 103–128. [CrossRef]
63. Krack, M. Pseudopotentials for H to Kr Optimized for Gradient-Corrected Exchange-Correlation Functionals. *Theor. Chem. Acc.* **2005**, *114*, 145–152. [CrossRef]
64. VandeVondele, J.; Hutter, J. Gaussian Basis Sets for Accurate Calculations on Molecular Systems in Gas and Condensed Phases. *J. Chem. Phys.* **2007**, *127*. [CrossRef]
65. Perdew, J.P.; Burke, K.; Ernzerhof, M. Generalized Gradient Approximation Made Simple. *Phys. Rev. Lett.* **1996**, *77*, 3865–3868. [CrossRef]
66. Grimme, S.; Antony, J.; Ehrlich, S.; Krieg, H. A Consistent and Accurate Ab Initio Parametrization of Density Functional Dispersion Correction (DFT-D) for the 94 Elements H-Pu. *J. Phys. Chem.* **2010**, *132*. [CrossRef] [PubMed]
67. Mundy, C.J.; Balasubramanian, S.; Bagchi, K.; Hutter, J.; Kuo, A.S.I.; Laino, T.; VandeVondele, J. Frontiers in Simulation Technology (FIST). (accessed by CP2K, version 5.1). 2017. Available online: www.cp2k.org (accessed on 12 November 2020).
68. CP2K. Open Source Molecular Dynamics Code. version 5.1, Released October 24, 2017 (r18096). Available online: https://www.cp2k.org/ (accessed on 12 November 2020).
69. Kühne, T.D.; Iannuzzi, M.; Del Ben, M.; Rybkin, V.V.; Seewald, P.; Stein, F.; Laino, T.; Khaliullin, R.Z.; Schütt, O.; Schiffmann, F.; et al. CP2K: An electronic structure and molecular dynamics software package—Quickstep: Efficient and accurate electronic structure calculations. *J. Chem. Phys.* **2020**, *152*, 194103. [CrossRef]
70. Cygan, R.T.; Liang, J.J.; Kalinichev, A.G. Molecular Models of Hydroxide, Oxyhydroxide, and Clay Phases and the Development of a General Force Field. *J. Phys. Chem. B* **2004**, *108*, 1255–1266. [CrossRef]

71. Berendsen, H.J.C.; Grigera, J.R.; Straatsma, T.P. The Missing Term in Effective Pair Potentials. *J. Phys. Chem.* **1987**, *91*, 6269–6271. [CrossRef]
72. Zoete, V.; Cuendet, M.A.; Grosdidier, A.; Michielin, O. SwissParam: A Fast Force Field Generation Tool for Small Organic Molecules. *J. Comput. Chem.* **2011**, *32*, 2359–2368. [CrossRef] [PubMed]
73. Laino, T.; Mohamed, F.; Laio, A.; Parrinello, M. An Efficient Linear-Scaling Electrostatic Coupling for Treating Periodic Boundary Conditions in QM/MM Simulations. *J. Chem. Theory Comput.* **2006**, *2*, 1370–1378. [CrossRef] [PubMed]
74. Bussi, G.; Donadio, D.; Parrinello, M. Canonical Sampling through Velocity Rescaling. *J. Chem. Phys.* **2007**. [CrossRef]
75. Boys, S.F.; Bernardi, F. The Calculation of Small Molecular Interactions by the Differences of Separate Total Energies: Some Procedures with Reduced Errors. *Mol. Phys.* **1970**, *19*, 553–566. [CrossRef]
76. Brehm, M.; Kirchner, B. TRAVIS—A Free Analyzer and Visualizer for Monte Carlo and Molecular Dynamics Trajectories. *J. Chem. Inf. Model.* **2011**, *51*, 2007–2023. [CrossRef]
77. Thomas, M.; Brehm, M.; Fligg, R.; Vöhringer, P.; Kirchner, B. Computing Vibrational Spectra from Ab Initio Molecular Dynamics. *Phys. Chem. Chem. Phys.* **2013**, *15*, 6608–6622. [CrossRef]
78. Thomas, M.; Brehm, M.; Kirchner, B. Voronoi Dipole Moments for the Simulation of Bulk Phase Vibrational Spectra. *Phys. Chem. Chem. Phys.* **2015**, *17*, 3207–3213. [CrossRef] [PubMed]
79. Brehm, M.; Thomas, M. An Efficient Lossless Compression Algorithm for Trajectories of Atom Positions and Volumetric Data. *J. Chem. Inf. Model.* **2018**, *58*, 2092–2107. [CrossRef] [PubMed]
80. Lü, C.; Yan, D.; He, J.; Zhou, B.; Li, L.; Zheng, Q. Environmental Geochemistry Significance of Organic Phosphorus: An Insight from Its Adsorption on Iron Oxides. *J. Appl. Geochem.* **2017**, *84*, 52–60. [CrossRef]
81. Sheals, J.; Sjoberg, S.; Persson, P. Adsorption of Glyphosate on Goethite: Molecular Characterization of Surface Complexes. *Environ. Sci. Technol.* **2002**, *36*, 3090–3095. [CrossRef]
82. Rose, J.; Flank, A.M.; Masion, A.; Bottero, J.Y.; Elmerich, P. Nucleation and Growth Mechanisms of Fe Oxyhydroxide in the Presence of PO4 Ions. 2. P K-Edge EXAFS Study. *Langmuir* **1997**, *13*, 1827–1834. [CrossRef]
83. Tribe, L.; Kwon, K.D.; Trout, C.C.; Kubicki, J.D. Molecular Orbital Theory Study on Surface Complex Structures of Glyphosate on Goethite: Calculation of Vibrational Frequencies. *Environ. Sci. Technol.* **2006**, *40*, 3836–3841. [CrossRef]
84. Anderson, G.; Arlidge, E.Z. The Adsorption of Inositol Phosphates and Glycerophosphate by Soil Clays, Clay Minerals, and Hydrated Sesquioxides in Acid Media. *J. Soil Sci.* **1962**, *13*, 216–224. [CrossRef]
85. Celi, L.; Lamacchia, S.; Marsan, F.A.; Barberis, E. Interaction of Inositol Hexaphosphate on Clays: Adsorption and Charging Phenomena. *Soil Sci.* **1999**, *164*, 574–585. [CrossRef]
86. Colthup, N.B.; Daly, L.H.; Wiberley, S.E. Compounds Containing Boron, Silicon, Phosphorus, Sulfur, or Halogen. In *Introduction to Infrared and Raman Spectroscopy*, 3rd ed.; Colthup, N.B., Daly, L.H., Wiberley, S.E., Eds.; Academic Press: San Diego, CA, USA, 1990; Chapter 12, pp. 355–385. [CrossRef]
87. Olsson, R.; Giesler, R.; Loring, J.S.; Persson, P. Adsorption, Desorption, and Surface-Promoted Hydrolysis of Glucose-1-Phosphate in Aqueous Goethite (Alpha-Feooh) Suspensions. *Langmuir* **2010**, *26*, 18760–18770. [CrossRef]
88. Del Bene, J.E.; Jordan, M.J.T. Vibrational Spectroscopy of the Hydrogen Bond: An Ab Initio Quantum-Chemical Perspective. *Null* **1999**, *18*, 119–162. [CrossRef]
89. Fornaro, T.; Burini, D.; Biczysko, M.; Barone, V. Hydrogen-Bonding Effects on Infrared Spectra from Anharmonic Computations: Uracil–Water Complexes and Uracil Dimers. *J. Phys. Chem. A* **2015**, *119*, 4224–4236. [CrossRef]
90. Arai, Y.; Sparks, D. ATR–FTIR Spectroscopic Investigation on Phosphate Adsorption Mechanisms at the Ferrihydrite–Water Interface. *J. Colloid Interface Sci.* **2001**, *241*, 317–326. [CrossRef]
91. Lincoln, S.; Stranks, D. Phosphato Complexes of Cobalt(III). I. General Structural and Hydrolytic Properties. *Aust. J. Chem.* **1968**, *21*, 37–56. [CrossRef]
92. Nakagawa, H.; Oyama, T. Molecular Basis of Water Activity in Glycerol–Water Mixtures. *Front. Chem.* **2019**, *7*, 731. [CrossRef]
93. Kataoka, Y.; Kitadai, N.; Hisatomi, O.; Nakashima, S. Nature of Hydrogen Bonding of Water Molecules in Aqueous Solutions of Glycerol by Attenuated Total Reflection (ATR) Infrared Spectroscopy. *Appl. Spectrosc.* **2011**, *65*, 436–441. [CrossRef] [PubMed]
94. Yan, Y.; Wan, B.; Zhang, Y.; Zhang, L.; Liu, F.; Feng, X. In Situ ATR-FTIR Spectroscopic Study of the Co-Adsorption of Myo-Inositol Hexakisphosphate and Zn(II) on Goethite. *Soil Res.* **2018**, *56*, 526–534. [CrossRef]
95. Peak Fit v4. *Peak Separation and Analysis Software*; SPSS Science, Inc.: Chicago, IL, USA, 2003.
96. FAO. FAO's Director-General on How to Feed the World in 2050. *Popul. Dev. Rev.* **2009**, *35*, 837–839. [CrossRef]
97. De Groot, C.J.; Golterman, H.L. On the Presence of Organic Phosphate in Some Camargue Sediments: Evidence for the Importance of Phytate. *Hydrobiologia* **1993**, *252*, 117–126. [CrossRef]

Supplementary Information:

Ab Initio Molecular Dynamics Simulations of the Interaction between Organic Phosphates and Goethite

Prasanth B. Ganta,[a] Oliver Kühn,[a,b] and Ashour A. Ahmed,[a,b*]

[a]University of Rostock, Institute of Physics, Albert-Einstein-Str. 23-24, D-18059 Rostock, Germany

[b]University of Rostock, Department of Life, Light, and Matter (LLM), Albert-Einstein-Str. 25, D-18059 Rostock, Germany

* corresponding author

prasanth.ganta@uni-rostock.de

oliver.kuehn@uni-rostock.de

ashour.ahmed@uni-rostock.de

FIGURES

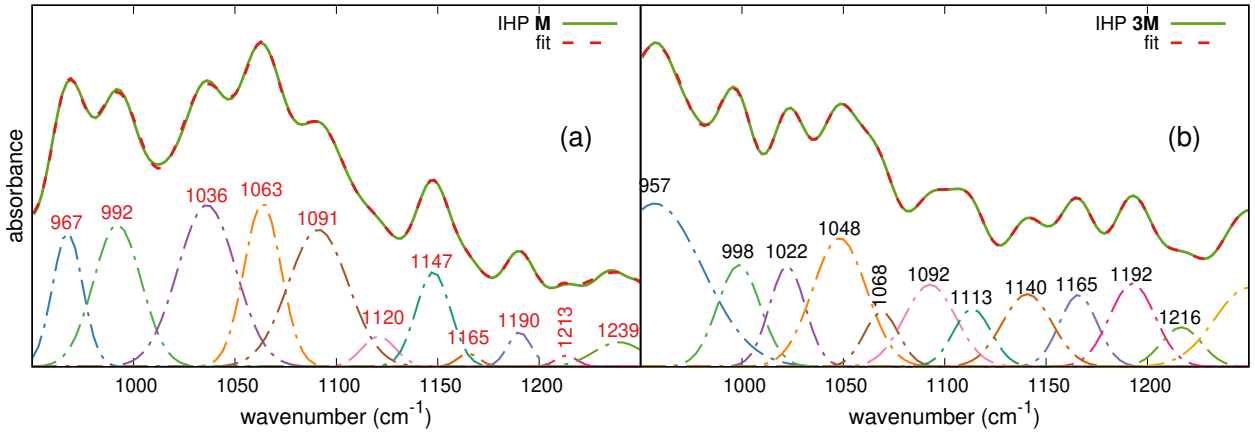


Figure S1: Fitted IR spectra of IHP bonded through **M** (a) and **3M** motifs (b).

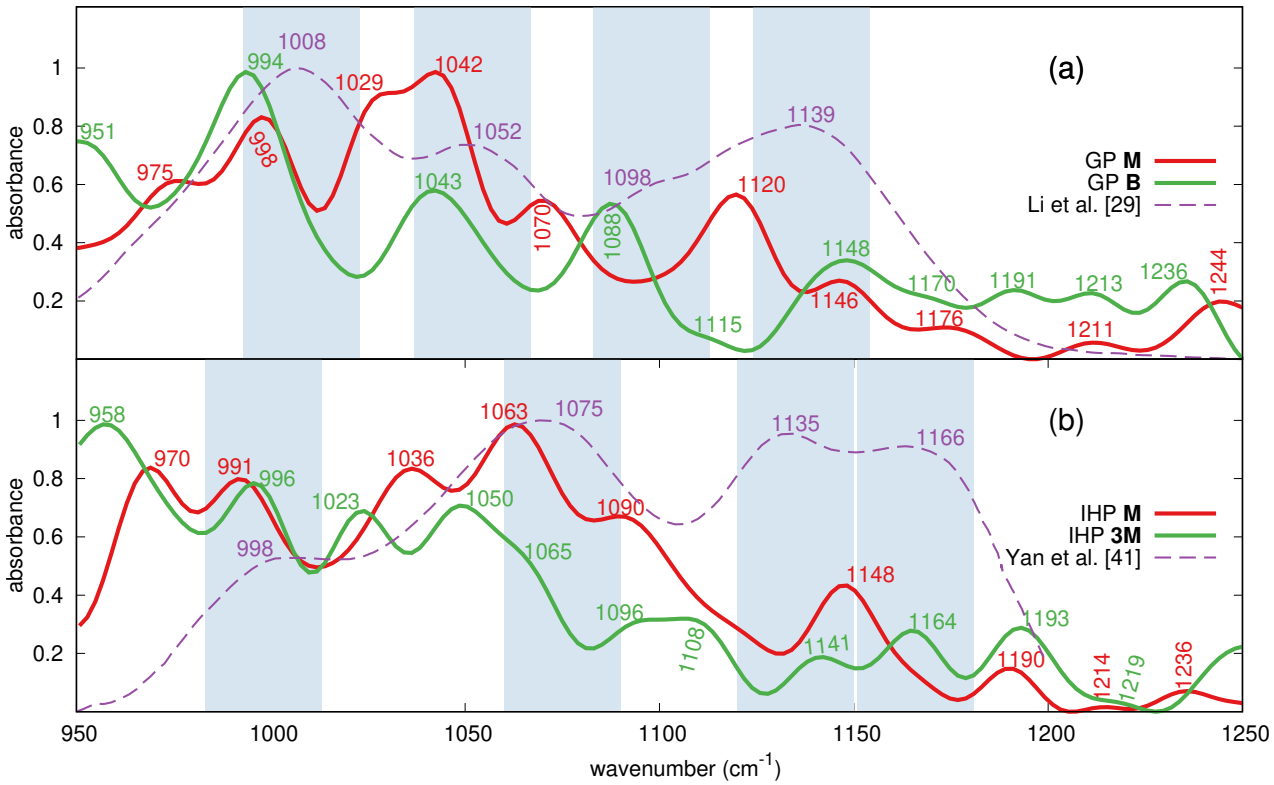


Figure S2: Comparision of GP and IHP spectra with experimental spectra from Li *et al.* [29] and Yan *et al.* [41] studies, respectively. The blue rectangle denotes region within ± 15 cm^{-1} around frequencies observed in experimental studies.

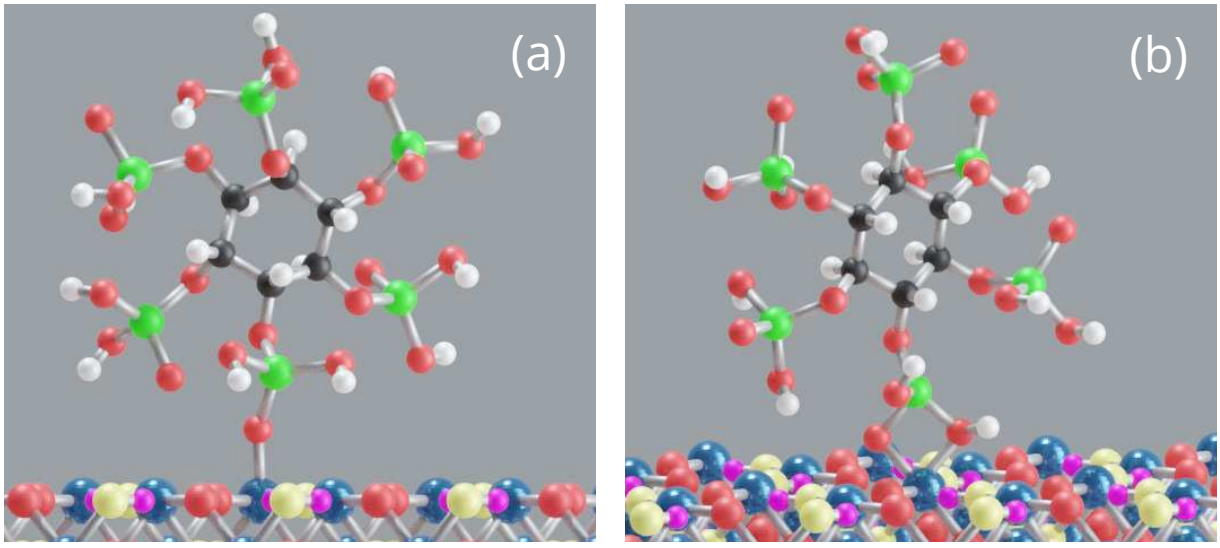


Figure S3: Initial motifs of IHP: **M** motif (a), **B** motif (b).

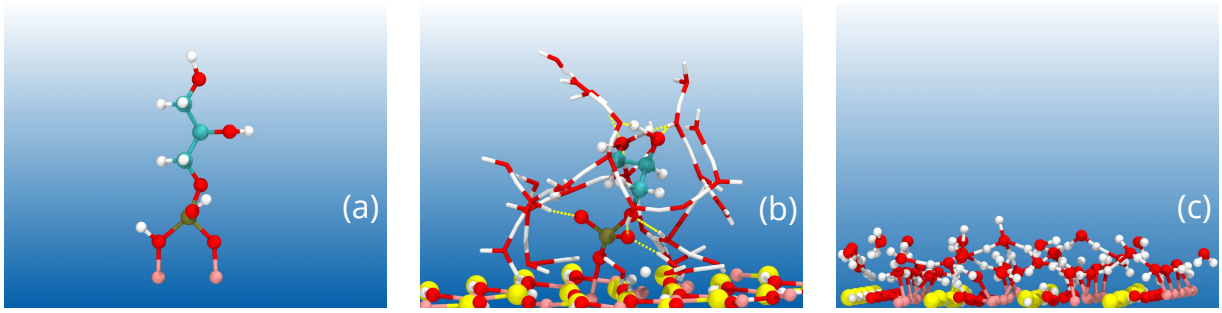


Figure S4: GP **BB** motif (a), HBs (yellow dotted lines) between GP and surrounding water (b), water bonded to surface Fe atoms (c). Pink, red, yellow, white and lime colors correspond to iron, oxygen, hydroxyl oxygen, hydrogen and phosphorus, respectively.

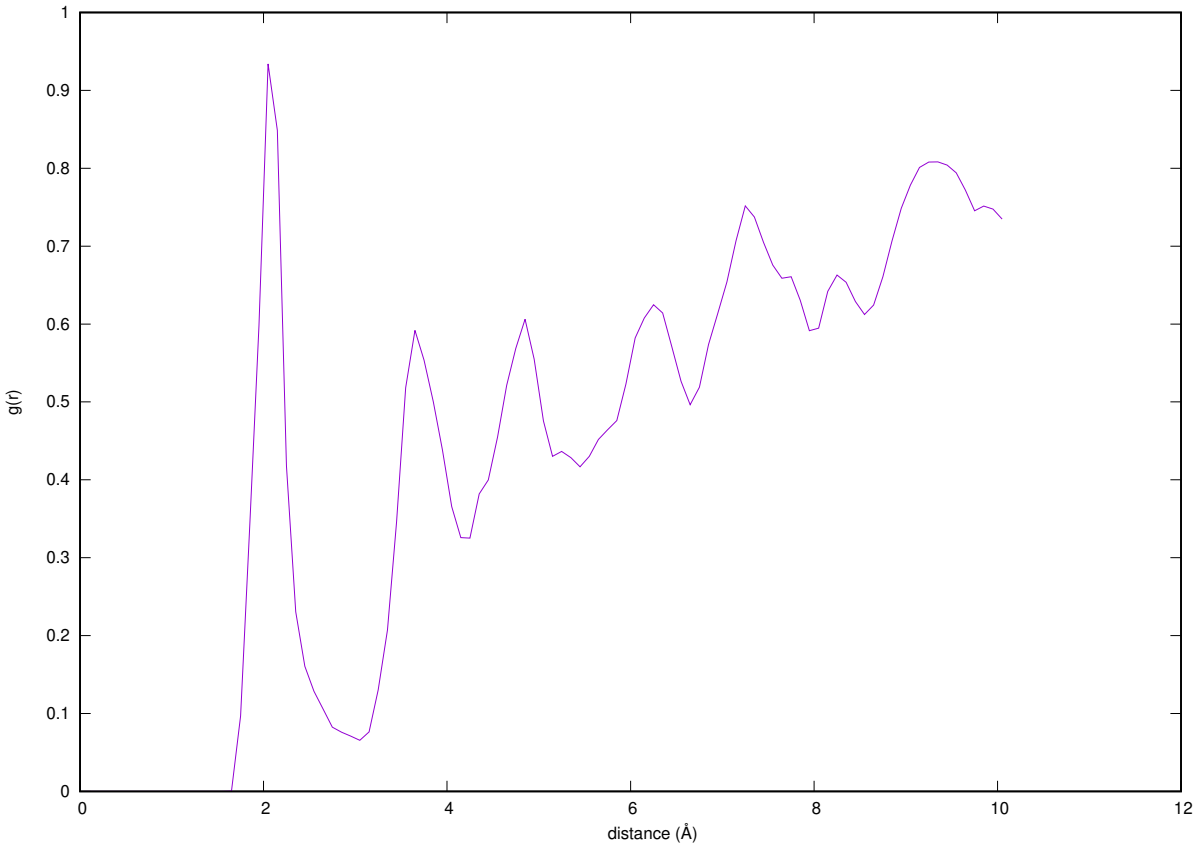


Figure S5: Pair correlation function calculated for surface Fe atoms of goethite and oxygens of water observed for GP **M** motif case.

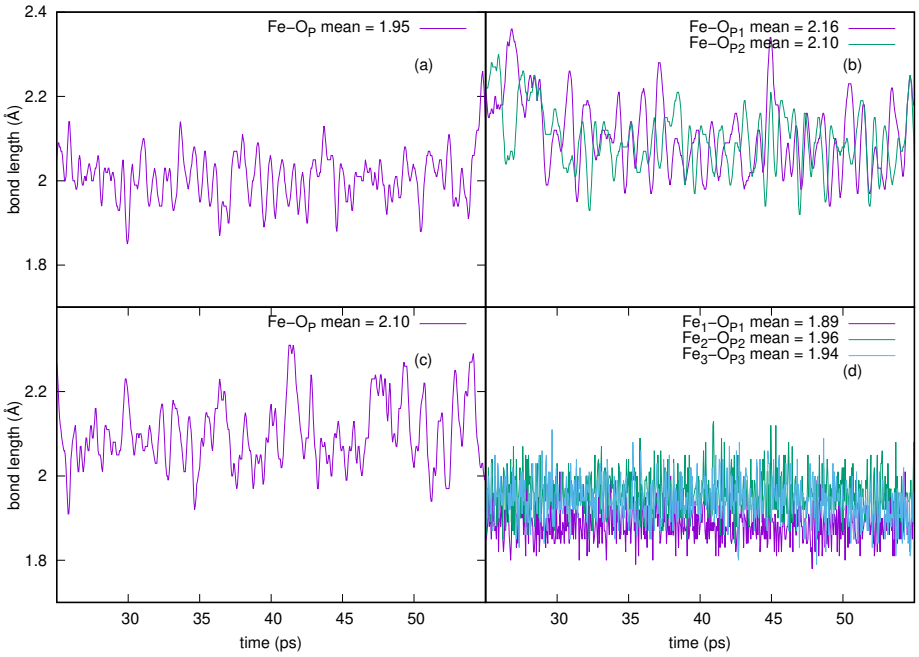


Figure S6: Covalent bond lengths of Fe-O$_P$ bonds for GP **M**(Fe–O$_P$) and **B**(Fe–O$_{P1}$, Fe–O$_{P2}$) motifs (a,b) and IHP **M**(Fe–O$_P$) and **3M**(Fe–O$_{P1}$, Fe–O$_{P2}$, Fe–O$_{P3}$) motifs (c,d) between 25–55 ps.

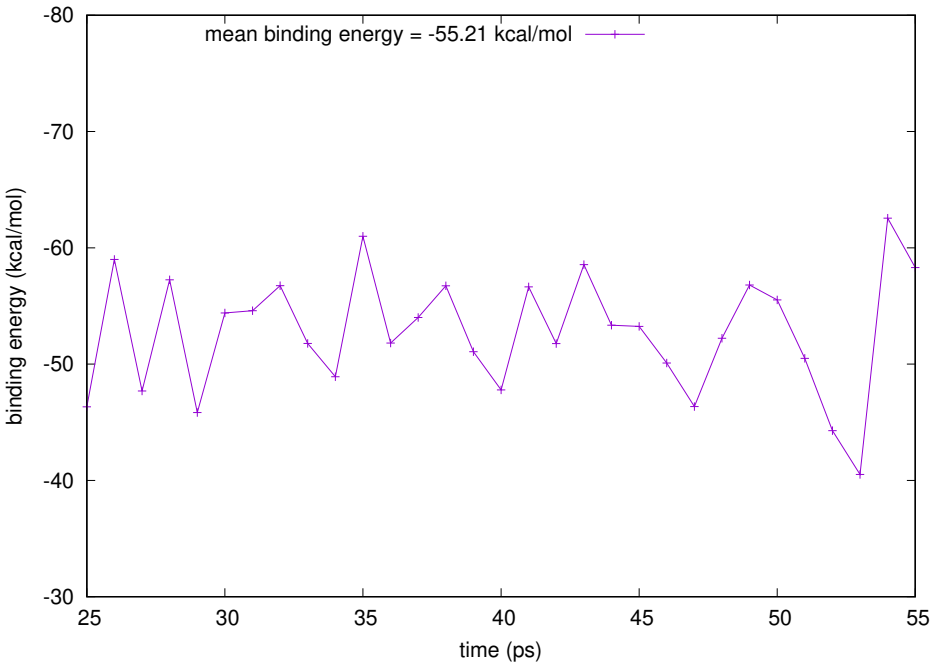


Figure S7: Binding energies along the simulation trajectory of IHP **M** motif in the time range of 25–50 ps.

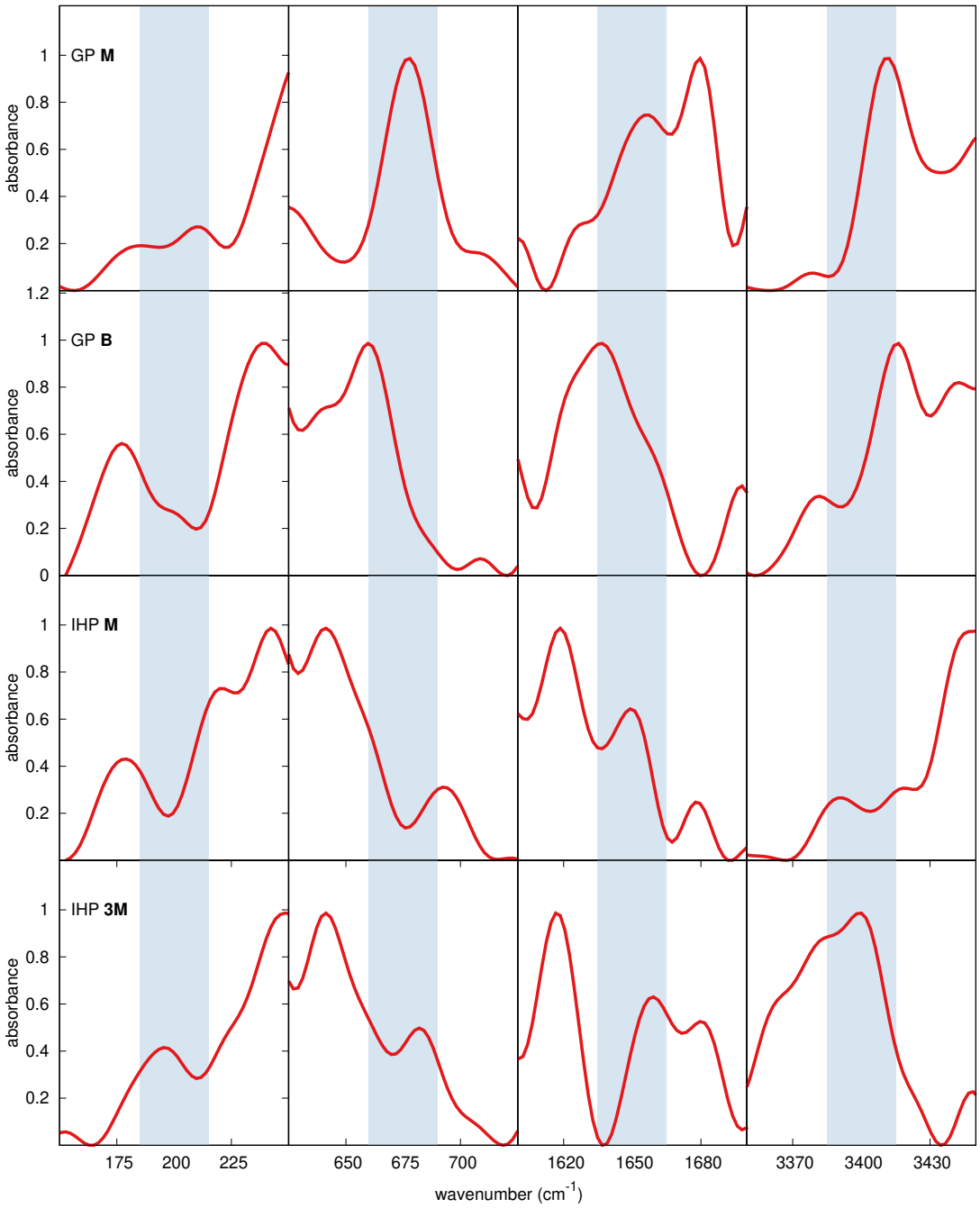


Figure S8: IR spectra of GP **M** and **B** motif cases (first and second rows) and IHP **M** and **3M** motif cases (third and fourth rows) for a selected freqency ranges. Brubach et al. [S1] showed that bands at 200, 675, 1650 and 3400 cm^{-1} are characteristic to water IR spectra and assigned the first two bands to hydrogen movement in intermolecular HBs and the last two to intramolecular [H–O–H] bending and [O–H] stretching modes. A similar assignment for [H–O–H] bending and [O–H] stretching modes is also observed in studies by Libnau et al. [S2] and Maréchal [S3]. The blue rectangle denotes a region within ± 15 cm^{-1} around frequencies 200, 675, 1650 and 3400 cm^{-1}. The overall picture shows that peaks in selected freqency ranges of the calculated IR spectra match mostly with the peaks from the literature [S3, S2, S1].

References

[S1] J.-B. Brubach, A. Mermet, A. Filabozzi, A. Gerschel, P. Roy, Signatures of the hydrogen bonding in the infrared bands of water, J. Chem. Phys. 122 (2005) 184509.

[S2] F. O. Libnau, O. M. Kvalheim, A. A. Christy, J. Toft, Spectra of water in the near- and mid-infrared region, Vibrational Spectroscopy 7 (1994) 243–254.

[S3] Y. Maréchal, Infrared spectra of water. I. Effect of temperature and of H/D isotopic dilution, J. Chem. Phys. 95 (1991) 5565–5573.

Publication 7

P. B. Ganta, M. Morshedizad, O. Kühn, P. Leinweber, Ashour A. Ahmed. The Binding of Phosphorus Species at Goethite: A Joint Experimental and Theoretical Study. Minerals **2021**, 21, 323.

Contribution: Ashour A. Ahmed is credited with the conceptualization of the scientific approach for this study, development of the methodology, acquisition of funding, contribution to writing the original manuscript, and supervising the PhD student (Mr. P.B. Ganta). Ashour A. Ahmed, along with the co-authors, has discussed and interpreted the results and contributed to writing, reviewing, and editing the manuscript.

URL: https://doi.org/10.3390/min11030323

QR:



Licensee MDPI, Basel, Switzerland. This article is an open-access article distributed under the terms and conditions of the Creative Commons Attribution (CC BY) license (http://creativecommons.org/licenses/by/4.0/).

minerals

MDPI

Article

The Binding of Phosphorus Species at Goethite: A Joint Experimental and Theoretical Study

Prasanth B. Ganta [1], Mohsen Morshedizad [2], Oliver Kühn [1,3], Peter Leinweber [2,3] and Ashour A. Ahmed [1,3,*]

[1] Institute of Physics, University of Rostock, Albert-Einstein-Str. 23–24, D-18059 Rostock, Germany; prasanth.ganta@uni-rostock.de (P.B.G.); oliver.kuehn@uni-rostock.de (O.K.)
[2] Chair of Soil Science, University of Rostock, Justus-von-Liebig-Weg 6, D-18059 Rostock, Germany; mohsen.morshedizad3@uni-rostock.de (M.M.); peter.leinweber@uni-rostock.de (P.L.)
[3] Department of Life, Light, and Matter (LLM), University of Rostock, Albert-Einstein-Str. 25, D-18059 Rostock, Germany
* Correspondence: ashour.ahmed@uni-rostock.de; Tel.: +49-381-498-6943

Abstract: Knowledge of the interaction between inorganic and organic phosphates with soil minerals is vital for improving soil P-fertility. To achieve an in-depth understanding, we combined adsorption experiments and hybrid ab initio molecular dynamics simulations to analyze the adsorption of common phosphates, i.e., orthophosphate (OP), glycerolphosphate (GP) and inositolhexaphosphate (IHP), onto the 100 surface plane of goethite. Experimental adsorption data per mol P-molecule basis fitted to the Freundlich model show the adsorption strength increases in the order GP < OP < IHP, and IHP adsorption being saturated faster followed by GP and OP. Modeling results show that OP and GP form stable monodentate (**M**) and binuclear bidentate (**B**) motifs, with **B** being more stable than **M**, whereas IHP forms stable **M** and **3M** motifs. Interfacial water plays an important role through hydrogen bonds and proton transfers with OP/GP/IHP and goethite. It also controls the binding motifs of phosphates with goethite. Combining both experimental and modeling results, we propose that the **B** motif dominates for OP, whereas GP forms **M** and IHP forms a combination of **M** and **3M** motifs. The joint approach plausibly explains why IHP is the predominant organically bound P form in soil. This study could be considered as a preliminary step for further studies for understanding the mechanisms of how microbes and plants overcome strong IHP–mineral binding to implement the phosphate groups into their metabolism.

Keywords: P-fertility; orthophosphate; glycerolphosphate; inositolhexaphosphate; goethite; adsorption; surface complexation; MD simulations; QMMM

check for updates

Citation: Ganta, P.B.; Morshedizad, M.; Kühn, O.; Leinweber, P.; Ahmed, A.A. The Binding of Phosphorus Species at Goethite: A Joint Experimental and Theoretical Study. *Minerals* **2021**, *11*, 323. https://doi.org/10.3390/min11030323

Academic Editor: Daniel Tunega

Received: 4 February 2021
Accepted: 16 March 2021
Published: 20 March 2021

Publisher's Note: MDPI stays neutral with regard to jurisdictional claims in published maps and institutional affiliations.

Copyright: © 2021 by the authors. Licensee MDPI, Basel, Switzerland. This article is an open access article distributed under the terms and conditions of the Creative Commons Attribution (CC BY) license (https://creativecommons.org/licenses/by/4.0/).

1. Introduction

The phosphorus (P) adsorption capacity of soil is a crucial factor affecting the P-immobilization process and thus soil fertility, and fate of P in natural environments [1–4]. This adsorption capacity, defined as the amount of adsorbed substance (adsorbate), reached in a saturated solution for a specific adsorbent [5], is fundamentally influenced by the diverse interactions of P with soil constituents, involving free metal ions [6,7], soil minerals [8–11], and soil organic matter [12,13]. In particular, the strong interaction between phosphates and soil mineral surfaces, and especially Fe- and Al-(oxyhydr)oxides, plays a very important role in controlling this process [8,14–18]. The Fe-oxides are widespread in surface environments and constitute a major component of highly weathered soils and sediments. They have attracted considerable attention due to their high P-adsorption capacity [19–21]. Phosphate adsorption on iron oxide surfaces shows a biphasic behavior consisting of a rapid and strong ligand exchange step followed by a slower step [22–25]. The latter phase was described previously by the formation of monodentate (**M**) complexes and conversion into bidentate (**B**) complexes, the competition with other anions, and/or

precipitation events [26]. Alternatively, the slower phase has been assigned to a diffusion process of phosphate ions from an outer-sphere complex to the surface [16,23,27,28].

The extent of P-uptake during these processes depends on reactive surface groups and the degree of crystallinity or porosity of iron oxides [27,29]. In soils, sediments and natural environments, goethite is the most frequent and widespread form of iron oxyhydroxides [30]. It has high crystallinity with a specific surface area varying from 18 to 132 $m^2 g^{-1}$ [27,31] depending on synthesis conditions which may thus influence the P-adsorption capacity of minerals [32]. Goethite has been studied extensively since it is considered as one of the most reactive surfaces for P compounds in the environment [33]. However, conflicting discussions are still present about the nature of binding motifs of the adsorbed phosphate species and the relative abundance of **M** complexes [34,35] versus **B** ones [36,37]. This could be due to the presence of different surface planes for goethite and several binding motifs for the goethite–phosphate complexes in addition to the different setups and conditions of adsorption experiments reported in literature. Consequently, different opinions have been put forward to assign the goethite–phosphate binding motifs based on infrared (IR) spectroscopy. This involves assignment either by the positions of P–O vibrational bands [36], the number of P–O bands and not their exact position [15], or formation of only an **M** motif with different protonation states depending on pH [38]. Molecular modeling is considered as a powerful tool to resolve such conflicting discussions by providing a molecular level description for the nature of the formed goethite–phosphate complexes.

By using molecular modeling, Kwon and Kubicki [39] studied the binding process of phosphate at goethite and suggested the abundance of the diprotonated **B** complex at pH 4–6 and the deprotonated **B** or monoprotonated **M** complex at pH 7.5–7.9. In a further study [40], they predicted the formation of **M** complexes at the 001, 210, 101, and 100 surface planes and **B** complexes at the 010, 101, and 100 surface planes. Recently, we have simulated the binding mechanism of phosphate at the goethite water interface at about pH 6, considering two different goethite surface planes [10]. The outcome of this study pointed to the abundance of the monoprotonated **B** motif at the goethite–water interface and the importance of water in controlling this binding process via promoting of specific binding motifs, formation of H-bonds (HBs), adsorption and dissociation at the surface, and proton transfer processes. Furthermore, the assignment of calculated IR spectra in this study introduced a new approach for characterizing experimental IR data of adsorbed phosphate species. Investigations at a molecular level for the binding of other P-compounds to soil reactive surfaces have also been reported. For example, the mechanism, nature, strength, and different possible binding motifs of interaction of glyphosate, the most used herbicide, with goethite, as well as with representative models for soil organic matter, have been explored [9]. Moreover, we studied the interaction of organic phosphate such as glycerolphosphate (GP) and inositolphosphate (IHP) at the diaspore(α-AlOOH)–water interface by focusing on two diaspore surface planes [11,41]. The results revealed stronger interactions for both GP and IHP at the 010 diaspore surface plane compared to the 100 surface plane. Further, IHP binds stronger to both surfaces via three phosphate groups compared to GP.

Such a detailed atomistic investigation for the binding mechanisms of both inorganic and organic phosphates at the goethite–water interface is still lacking. Therefore, our objective in the present study is to introduce a molecular level understanding for the binding mechanism of phosphate at the goethite–water interface via a joint experimental/theoretical approach. Specifically, adsorption experiments have been performed for orthophosphate (OP), GP, and IHP on the pure synthetic goethite surface at constant pH and ionic strength. Further, the simulation of these adsorption experiments have been carried out by molecular modeling for the binding processes of OP/GP/IHP at the goethite–water interface, applying hybrid quantum mechanics/molecular mechanics (QM/MM)-based molecular dynamics (MD) simulations.

2. Materials and Methods

2.1. Goethite Preparation and Adsorption Experiments

Goethite was prepared as described by Dultz et al. [42], i.e., a 10 M NaOH solution was added to a 0.5 M $FeCl_3$ solution ($FeCl_3 \cdot 6H_2O$, Merck AG) with stirring continuously to bring the pH to 12. The resulting ferrihydrite was aged for 120 h at 55 °C to be converted to goethite. Then, the suspension was subjected to pH adjustment to pH 6 by adding 0.1 M HCl and followed by centrifugation-washing cycles with distilled water until the electrical conductivity was lower than 10 $\mu S\,cm^{-1}$. The so-prepared goethite was freeze-dried and stored as powder for further analysis and experiments.

The results of X-ray diffraction (XRD) analysis confirmed the well-crystallinity of goethite samples; see Figure S1. The measured specific surface area (SAA) of goethite by Brunauer-Emmett-Teller (BET, N_2 adsorption; Nova 4000e, Quantachrome, Boynton Beach, FL, USA) method is 64.5 $m^2\,g^{-1}$. This value lies in the reported common range values of SSA of goethite in the literature [27,33,43]. It should be noted that different SSA values of goethite were reported in the literature. This could be due to the sensitivity of the BET method to the type of adsorbent, lack of an appropriate linearity criterion (a linear region within the standard pressure range assuming that monolayer adsorption will occur in this pressure range), and presence of micro pores [44]. The mean hydrodynamic diameter of goethite particles is 1.6 ± 0.2 µm as determined by a particle sizer (Zetapals, Brookhaven, Holtsville, NY, USA) on a 100 mgL^{-1} suspension treated with a dispersant agent (0.01 mM $Na_4P_2O_7$, pH 8) and sonicated for 30 s (Labsonic M, Sartorius Stedim, Göttingen, Germany). The measured point of zero charge (PZC) of goethite particles is 6.3; see Figure S2.

In the present study, the adsorption of three different phosphate compounds involving inorganic orthophosphate (OP, potassium dihydrogen phosphate, CAS number: 7778-77-0) and organic phosphates (α-glycerol phosphate (GP, CAS number: 17603-42-8) and myo-inositol hexakisphosphate (IHP, CAS number: 83-86-3)) on goethite was performed. Here, a stock solution of 10 mM P of each P compound was prepared in 0.01 M $CaCl_2$ solution. For each experiment, 200 mg sample of goethite was weighed into a 50 mL centrifuge tube and equilibrated with 40 mL of each initial P concentration. Here, twelve different initial P concentrations (0, 0.05, 0.1, 0.15, 0.2, 0.3, 0.5, 1, 2, 3, 5, and 10 mM P) were considered. Each initial concentration was prepared by the dilution of the P stock in 0.01 M $CaCl_2$ background electrolyte solution, adjusted at pH 5. After an equilibrium period of 24 h at 25 °C under end-over-end shaking at 20 rpm, samples were centrifuged at 4500 g for 15 min. The P content in the filtered supernatant was quantified by inductively coupled plasma-optical emission spectroscopy (ICP-OES) method.

It is noteworthy that all adsorption experiments were performed in triplicate and data were presented as the means of three repeats. Moreover, all used P compounds (myo-inositol hexakisphosphate: $C_6H_{18}O_{24}P_6$; α-glycerol phosphate: $C_3H_9O_6P$; potassium dihydrogen phosphate: KH_2PO_4) in the present experiments were of analytical grade chemicals and purchased from Carl Roth GmbH and Sigma-Aldrich. Working solutions were prepared fresh daily by adding accurate quantities of the prepared P stocks into 0.01 M $CaCl_2$ solution.

To describe the adsorption behaviors of P compounds on goethite, the adsorption data were fitted to the Freundlich [45], Langmuir [46], and Temkin [47] models. The Freundlich model provides a two-parameter equation that describes the relationship between the equilibrium concentration and the adsorbed one onto heterogeneous surfaces through the following equation:

$$Q_{ads} = K_f C_e^{n_f} \quad (1)$$

that is rewritten in a linear form as follows:

$$\ln Q_{ads} = \ln K_f + n_f \ln C_e \quad (2)$$

where Q_{ads} is the amount of adsorbate adsorbed per unit mass (or surface area) of adsorbent, C_e is the adsorbate equilibrium concentration in solution, K_f is Freundlich adsorption

constant (sometimes it is defined as Freundlich unit adsorption capacity), and n_f is the non-linearity exponent (Freundlich exponent) [45]. In the present study, Q_{ads}, C_e, and K_f are expressed in μmol m^{-2}, μmol L^{-1} and μmol$^{1-n_f}$ L^{n_f} m^{-2}, respectively. Notice that the Freundlich model assumes that the adsorption enthalpy depends on the amount of adsorbate. In the limit of small Q_{ads} where the adsorption enthalpy should not depend on Q_{ads} one could describe the isotherm by a Langmuir model as well. The Langmuir adsorption theory assumes that the adsorbate forms a monolayer on a homogeneous adsorbent surface. The following equation expresses the Langmuir isotherm:

$$Q_{ads} = Q_{max} \frac{K_l C_e}{1 + K_l C_e} \tag{3}$$

that is rewritten in a linear form as follows:

$$\frac{C_e}{Q_{ads}} = \frac{C_e}{Q_{max}} + \frac{1}{K_l Q_{max}} \tag{4}$$

where Q_{max} is the maximum amount of the adsorbate which is required to form a monolayer by complete saturation of all binding sites (it is defined also as the maximum monolayer coverage capacity or simply as monolayer capacity [5], μmol m^{-2}), K_l is the Langmuir adsorption constant (L μmol^{-1}), which is mainly related to the adsorption energy [46]. The Temkin model exhibits a factor considering the adsorbent–adsorbate interaction with a uniform distribution of binding energies. The model is expressed by the following equation:

$$Q_{ads} = \frac{RT}{b_T} \ln A_T + \frac{RT}{b_T} \ln C_e = B_T \ln A_T + B_T \ln C_e \tag{5}$$

where R is the universal gas constant (8.314 J K mol^{-1}), T is the absolute temperature (K), b_T is Temkin isotherm constant (J mol^{-1}), A_T is Temkin isotherm equilibrium binding constant (L μmol^{-1}), and B_T is constant related to the heat of adsorption. It is important to mention that our adsorption isotherm data were fitted by two ways. The first way is based on the normal linearization technique while the second way is based on non-linear equations solver function that was described by Bolster and Hornberger [48]. Fitted parameters obtained by both ways were compared to each other and the best fit parameters were selected based on error measures. Non-linear equations solver was found to be more appropriate compared to the linearization technique, and thus the corresponding parameters were selected and presented in the present contribution. For better understanding for the P adsorption behavior, the calculated adsorption coefficients are interpreted on three different bases (per mol P (i.e., per mole of P element), per mol molecule (i.e., per mole of P--containing molecule (OP, GP, and IHP)), and per mass (i.e., per mass (mg) of P--containing molecule)).

2.2. Molecular Modeling and Computational Details

The current molecular modeling approach for the binding process of phosphates at the goethite–water interface is illustrated in Figure 1. Here, three different abundant phosphates are considered, i.e., OP (H_3PO_4), GP ($C_3H_9O_6P$), and IHP ($C_6H_{18}O_{24}P_6$), to study the complexation reaction of each phosphate with the goethite surface in the presence of water (see Figure 1a–c). Each constructed goethite–phosphate–water complex model (for example, see Figure 1d), consists of 1– the goethite surface, 2– a phosphate compound with a specific binding motif to the surface, and 3– water molecules surrounding the goethite–phosphate complex. Here, the 100 goethite surface is considered, which is one of the most abundant goethite surface planes in soil systems [33,49]. This goethite surface plane is modeled by the repetition of the goethite unit cell (lattice constants : $a = 9.95, b = 3.01, c = 4.62$ Å) as $1a \times 8b \times 5c$ which consists of 640 atoms (160 Fe, 160 H, and 320 O atoms). The binding motifs formed between these phosphates and the goethite surface are modeled based on previous literature studies [9–11,41,50–52]. The initial motifs

of OP and GP with the goethite surface include monodentate (**M**, 1Fe+1O one covalent bond between phosphate non-protonated O atom and a surface Fe atom) and bidentate (**B**, 2Fe+2O i.e., two covalent bonds between two phosphate O atoms, one protonated and other non-protonated and two surface Fe atoms); see Figure 1e–f. For IHP, an additional, **4M** (4Fe+4O i.e., four covalent bonds between four separate phosphates non-protonated oxygens and four surface Fe atoms) are considered since IHP is known to interact with goethite through multiple phosphate groups, see Figure 1g. To simulate the effect of water on the goethite–OP/GP/IHP complexes, each modeled binding motif is solvated with water molecules at a density of $\approx 1\ g\,cm^{-3}$ perpendicular to the studied surface plane with height of ≈18 Å by using the visual molecular dynamics (VMD) package (see Figure 1d) [53]. To ease the discussion about the interactions, oxygen atoms bonded to surface Fe atoms are denoted as O_p.

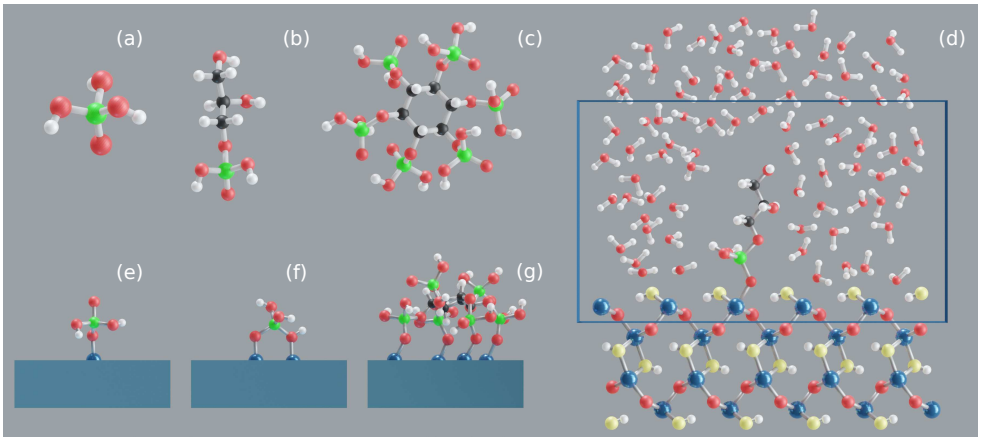


Figure 1. OP (**a**), GP (**b**), IHP (**c**), solvated goethite–GP complex highlighting QM box (**d**), goethite–OP **M** motif (**e**) and **B** motif (**f**), goethite–IHP **4M** motif (**g**). Blue, red, yellow, white, black and green colors correspond to iron, oxygen, hydroxyl oxygen, hydrogen, carbon and phosphorus atoms, respectively.

Due to the large size for the modeled goethite–OP/GP/IHP–water complexes (each model consists of more than 1200 atoms), the simulation of these systems with pure ab initio methods is computationally expensive and thus not feasible [54,55]. Therefore, the present models will be studied by molecular dynamics (MD) simulations based on the electrostatic embedding QM/MM hybrid approach. It should be noted that the present QM/MM approach has been validated for studying the P binding process at mineral/water interfaces. Specifically, this was achieved in two recent studies by comparing outcome of the QM/MM approach with corresponding results from pure DFT calculations [11] as well as experimental IR spectra [52]. Here, the reactive part (system of interest) is described at a QM level of theory, while the remaining part is described using MM. The QM part includes 1– OP/GP/IHP, 2– the goethite top surface layer (160 atoms), and 3– water molecules within a layer of about 10 perpendicular to the surface (≈55 molecules). The total QM box size is $22 \times 8b \times 5c$, i.e., $22 \times 24.08 \times 23.1$ Å. The QM part is simulated with density functional theory (DFT) as implemented in the quickstep code in CP2K [56]. A hybrid Gaussian and plane wave (GPW) dual basis method is used with ionic cores described by Goedecker-Teter-Hutter (GTH) pseudopotentials [57] in combination with the Perdew-Burke-Ernzerhof (PBE) [58] exchange correlation functional and the Grimme D3 empirical dispersion correction [59]. The valence electrons of all atoms are defined with the double-ζ valence polarized MOLOPT (DZVP-MOLOPT-SR-GTH) basis set except water for which the single-ζ valence (SZV-MOLOPT-SR-GTH) basis set is used to reduce computational cost [60]. The SCF convergence threshold was chosen to be 10^{-4} hartree. The MM part is described by classical force fields (FF) with FIST module in CP2K [61]. The goethite surface is modeled with the CLAYFF FF [62] while water is modeled with the single point

charge (SPC) water model [63] and OP/GP/IHP with CHARMM FF using the SwissParm tool [64]. Both CLAYFF and CHARMM FFs are compatible with the SPC water model. The interaction between the QM and MM parts in CP2K is implemented using the Gaussian expansion of the electrostatic potential method (GEEP) [65], wherein the MM charge is distributed by defining it using Gaussians instead of point charges to avoid electron spilling. QM/MM-based canonical (NVT, i.e., constant number of atoms N, volume V and temperature T) MD simulations are performed for 25 ps with a 0.5 fs time step while the temperature was maintained at 300 K using velocity rescaling thermostat (CSVR) [66]. The first 10 ps of each trajectory are assigned for the equilibration, and the remaining 15 ps (production trajectory) are used for analysis. The interaction energy between each phosphate and the goethite surface is calculated for every 100 fs (i.e., 150 snapshots) along the production trajectory by using:

$$E_{int} = E_{G-P\,complex} - (E_G + E_P) \quad (6)$$

where, $E_{G-P\,complex}$, E_P, and E_G denote the total electronic energies of the goethite–phosphate complex, the phosphate (OP/GP/IHP), and the goethite surface, respectively. The interaction energies involving water are divided by the number of water molecules in the simulation box for better comparison. The basis set superposition error (BSSE) in interaction energies is corrected using counterpoise scheme [67].

3. Results and Discussion

3.1. Adsorption Isotherms

Despite some data scatter in OP adsorption, Figure 2 shows that almost the maximum adsorption capacities are reached for goethite and the selected range of P concentrations is sufficient to achieve the equilibrium. Here, the sequence of adsorbed P (Q_{ads}) values per mol P is IHP > OP > GP (see Figure 2). For most cases, the coefficients of determination (R^2) values indicated that the Freundlich equation fitted the adsorption data better than the Langmuir and Temkin models; see Table 1. This comes in accord with the study by Tellinghuisen and Bolster [68] that discussed the statistical reasons leading to better fitting for the Freundlich equation case compared to Langmuir and Temkin models for the P adsorption on soils. The Freundlich adsorption constant (capacity) K_f ranged from 0.22 to 4.79 μmol$^{1-n_f}$ L^{n_f} m^{-2}. The order of K_f values suggests that IHP exhibits the strongest adsorption and the highest capacity at the goethite surface, followed by OP and GP (GP < OP < IHP). The magnitude of the Freundlich exponent n_f, that ranged from 0.07 to 0.29 (see Table 1), gives an indication that the sorption mechanism is dominated by adsorption and not absorption [69,70]. Furthermore, the exponent points to the diversity of the energies associated with adsorption of P compounds on the goethite surface. Moreover, n < 1 for all cases indicates that upon increasing the P concentration/loading the binding energy between the surfaces and P compounds is reduced. The order of the n_f values (IHP < GP < OP) suggests that the binding energy decreases with increasing the P loading in the order OP < GP < IHP. This means that affinity of the goethite surface to adsorb/bind a P molecule, with increasing the P concentration, increases in the order IHP < GP < OP. According to the Langmuir model, the maximum monolayer adsorption capacities (Q_{max}) are 1.2, 7.64 and 8.35 μmol m^{-2}, respectively, for GP, OP and IHP (see Table 1). This shows that the order of saturation of the goethite surface with P per mol P is GP < OP < IHP. This trend fits well with that one observed based on the Freundlich K_f values. The Langmuir parameter K_l increased in the order 0.001 (OP) < 0.003 (GP) < 0.06 (IHP) L μmol^{-1}. This constant is mainly related to the adsorption energy and could give information on how strong (i.e., strength) the goethite–P interaction/binding process is. Therefore, based on Langmuir model, one expects that the goethite–P interaction increases in the order OP < GP < IHP. The same order but with different values was obtained from Temkin binding constant A_T which is also related to the binding strength, see Table 1. The Temkin B_T values for OP (0.75), GP (0.13) and IHP (0.52) suggest that the heat of adsorption increases in the

order GP < IHP < OP. Regardless the Temkin constant B_T, all other parameters from the represented isotherm models in the present contribution refer to stronger adsorption and higher capacity for the IHP case compared to OP and GP cases by considering the number of P moles.

Considering the size and chemical structure of IHP (six phosphate groups), GP and OP (only one phosphate group), the adsorption data were presented as well in terms of whole P molecular system. Specifically, both Q_{ads} and C_e concentrations and all related fitted adsorption isotherm parameters are represented per mole and per mass of the whole P--containing molecule (OP, GP, and IHP), see Table 1. It should be noted that n_f and R^2 values for all P compounds do not change upon changing the interpretation/representation of P concentration (Q_{ads} and C_e). In addition, the order of all adsorption parameters (k_f, n_f, k_l, Q_{max}, B_T, A_T) does not change for OP and GP by different interpretations for the P concentration (i.e., per mol P versus per mol molecule and per mass bases). Here, the only change was observed for the IHP case. By considering the number of moles of the P adsorbed molecules (i.e., per mol molecule), the K_f, Q_{max} and B_T values for IHP decreased by a factor of six, while the corresponding K_l and A_T values increased by a factor of six (see Table 1). In principle, this means that the goethite adsorption capacity will decrease to one sixth by considering the whole IHP molecule compared to considering six P moles of each IHP mole. Consequently, the binding/adsorption strength between the goethite surface and each IHP mole will increase by a factor of six compared to the case of considering only one mole of P. In addition, the orders of K_f (GP < OP < IHP), K_l (OP < GP < IHP) and A_T (OP < GP < IHP) do not change compared to the mol P basis. In contrast, the orders of Q_{max} (GP < IHP < OP) and B_T (IHP < GP < OP) changed comparing with considering the mol P cases. Same orders were obtained by considering the P concentration as mass of the adsorbed P molecule. With respect to the K_l order, one can suggest that GP has stronger interaction than OP with the goethite surface. In contrast, the B_T order suggests that OP has stronger interaction than IHP.

In a study evaluating the adsorption properties of goethite, Celi et al. [71] reported the adsorption ratio of 3:2 between IHP and OP at pH 4.5. Later, Martin et al. [72] confirmed the greater affinity of IHP than of OP for goethite, indicating that the maximum amount of adsorbed P were 3.6 and 2.4 $\mu mol\,P\,m^{-2}$ for IHP and OP, respectively. Likewise, Celi and Barberis [73] found that goethite shows a higher affinity for IHP (deduced from Langmuir K_l values) than for other organic and inorganic phosphates. Li et al. [74] reported a maximum GP adsorption of 1.95 $\mu mol\,P\,m^{-2}$ at pH 5 which is close to the value of 1.20 $\mu mol\,P\,m^{-2}$ observed here. However, the lower adsorption of GP as compared to that reported by Li et al. [74] may be due to the differences in experimental conditions. Specifically, Li et al. [74] conducted their adsorption experiment by β--glycerophosphate at a goethite sample with SAA of 46.4 $m^2\,g^{-1}$ and PZC of 9.2 in 0.1 M KCl as a background electrolyte. Overall, both organic and inorganic phosphates exhibited affinity for goethite. Parfitt [29], compared the adsorption of OP on goethite in $CaCl_2$ solution, and reported that larger amounts of specifically adsorbed P reflect more reactive and available adsorption sites on the goethite. This was explained by thermal gravimetric analyses that indicated that goethite contains 24% structural OH [74]. Similarly, Guzman et al. [75] showed the affinity for phosphate (exponent coefficient of Freundlich equation) for goethite on a surface area basis. Details of IHP adsorption on goethite have been extensively studied [71,72,76,77]. Ognalaga et al. [50] investigated the adsorption of IHP on synthetic goethite and attributed it solely to the inner-sphere complexation of phosphate groups with reactive OH groups. Celi et al. [71] and Ognalaga et al. [50] suggested that four of the six phosphate groups of each IHP molecule were involved in bonding to goethite while the other two remained free.

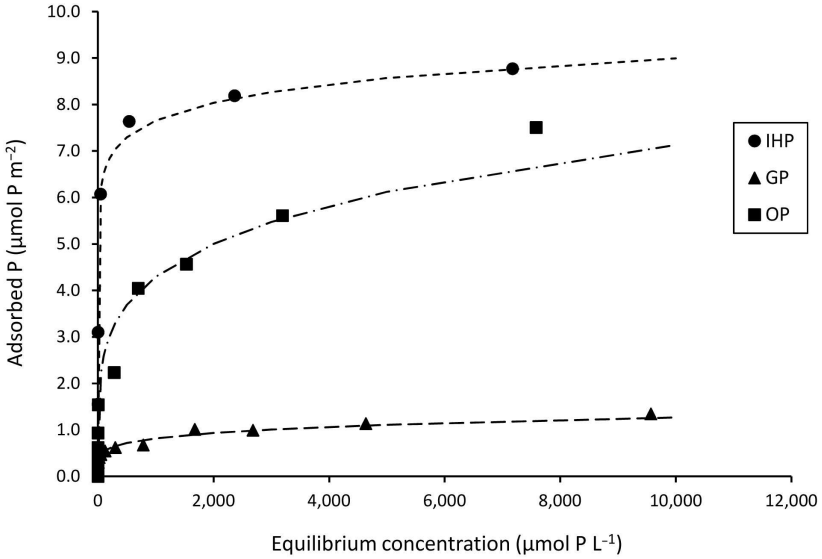


Figure 2. Adsorption isotherms of OP, GP, and IHP on goethite at 0.01 M $CaCl_2$ electrolyte solution (pH 5). Points represent the original data and dashed lines represent the fitted isotherms according to Freundlich model.

Table 1. Freundlich, Langmuir and Temkin isotherm coefficients (K_f, n_f, K_l, $A_T$and B_T) of OP, GP and IHP adsorption on goethite at pH 5 in 0.01 M $CaCl_2$.

Sorbate	Freundlich			Langmuir			Temkin		
	n_f	K_f	R^2	Q_{max}	K_l	R^2	B	A_T	R^2
OP (µmol P)	0.29 ± 0.08	0.57 ± 0.23	0.97	7.64 ± 2.36	0.001 ± 0.001	0.88	0.75 ± 0.16	0.49 ± 0.23	0.83
GP (µmol P)	0.19 ± 0.01	0.22 ± 0.02	0.98	1.20 ± 0.06	0.003 ± 0.001	0.81	0.13 ± 0.03	0.89 ± 0.30	0.92
IHP (µmol P)	0.07 ± 0.001	4.79 ± 0.02	0.98	8.35 ± 0.04	0.06 ± 0.002	0.92	0.52 ± 0.01	3104.43 ± 467.8	0.99
OP (µmol)	0.29 ± 0.08	0.57 ± 0.23	0.97	7.64 ± 2.36	0.001 ± 0.001	0.88	0.75 ± 0.16	0.49 ± 0.23	0.83
GP (µmol)	0.19 ± 0.01	0.22 ± 0.02	0.98	1.20 ± 0.06	0.003 ± 0.001	0.81	0.13 ± 0.03	0.89 ± 0.30	0.92
IHP (µmol)	0.07 ± 0.001	0.90 ± 0.002	0.98	1.39 ± 0.006	0.36 ± 0.0009	0.92	0.09 ± 0.0004	18,444.8 ± 148.6	0.99
OP (mg)	0.29 ± 0.07	0.14 ± 0.06	0.97	1.04 ± 0.4	0.01 ± 0.01	0.88	0.10 ± 0.02	3.6 ± 1.1	0.83
GP (mg)	0.20 ± 0.01	0.05 ± 0.003	0.98	0.21 ± 0.01	0.02 ± 0.004	0.81	0.02 ± 0.001	5.19 ± 1.53	0.92
IHP (mg)	0.07 ± 0.001	0.61 ± 0.001	0.98	0.92 ± 0.004	0.55 ± 0.01	0.92	0.06 ± 0.0002	7427.1 ± 112.6	0.99

3.2. Molecular Modeling of P Interactions at the Goethite--Water Interface

3.2.1. Orthophosphate

The MD simulations showed that OP maintained the initial motifs (see Figure 1e–f) and formed stable **M** and **B** motifs throughout the simulation trajectory, see Figure 3a–h, respectively. The time averaged Fe–O_p bond length and Fe–P distance observed for the **B** motif are shorter than those for the **M** motif which is probably due to higher stability in the former case, see Table 2. Here, the total interaction energy between OP and the goethite surface of the goethite–OP complex for the **B** and **M** motifs are –82 and –35 kcal mol^{-1}, respectively. The interaction energy per bond of goethite–OP in the **B** motif being higher than in the **M** motif suggests that the alignment of OP with the goethite surface favors the formation of an additional Fe–O_p covalent bond in the **B** motif.

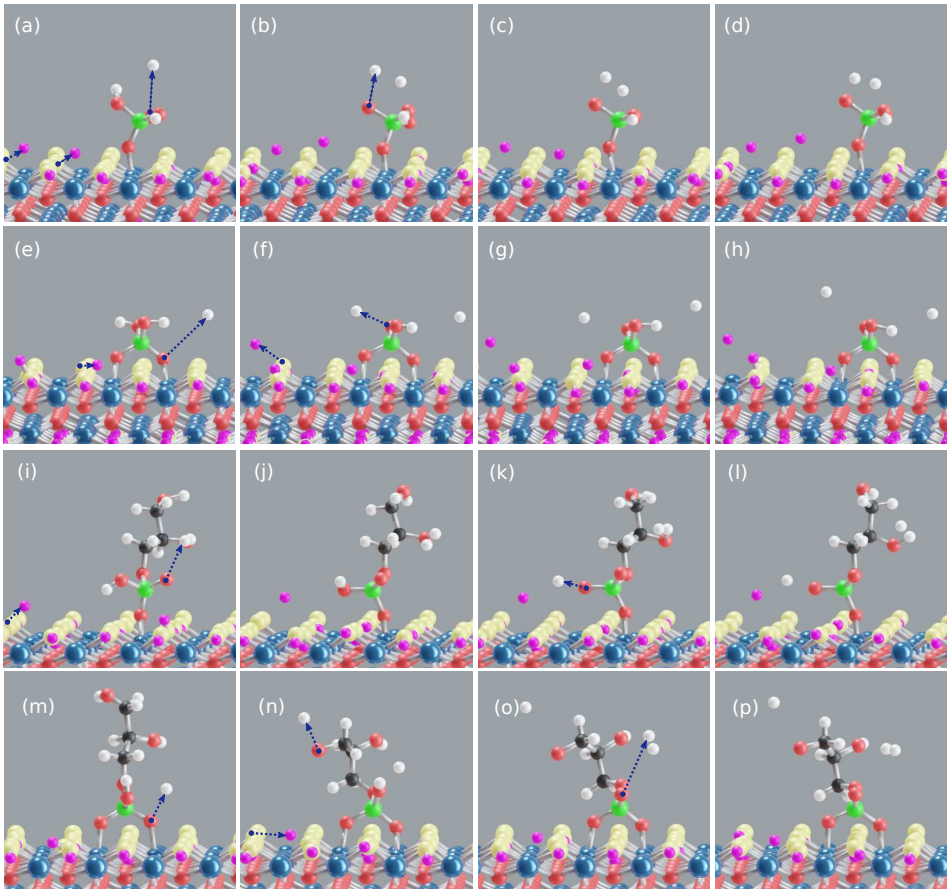


Figure 3. Snapshots along the simulation trajectories of the goethite--OP/GP/IHP--water complexes. OP **M** motif (**a**–**d**), OP **B** motif (**e**–**h**), GP **M** motif (**i**–**l**), GP **B** motif (**m**–**p**). Arrows denote proton transfers from phosphates to water and from goethite to water. For all cases, the first two snapshots are from equilibration phase while the last two are from production, except for OP **M** motif case where only (**a**) is from equilibration phase. The last snapshot for each case is taken at 25 ps. The goethite's hydrogen atoms and OP/GP/IHP's hydrogen atoms are shown in violet and white colors, respectively, for clear visualization of proton transfer events. Blue, red, yellow, black and green colors correspond to iron, bridging oxygen, hydroxyl oxygen, carbon and phosphorus atoms, respectively. The surrounding water is ignored here for better visualization.

Table 2. The interaction energies per number of bonds (E_{int}/bond) and selected interatomic distances Fe–O_p and Fe–P observed along the trajectories of goethite–OP/GP/IHP–water complexes.

P	Motif	E_{int}/bond (kcal mol^{-1})	Fe–O_p (Å)	Fe–P (Å)
OP	**M**	–35	2.1	3.5
	B	–41	2.01 & 1.97	3.19 & 3.2
GP	**M**	–48	1.99	3.19
	B	–38	2.01 & 2.03	3.19 & 3.1
IHP	**M(1)**	–85	2.0	3.1
	M(2)	–69	2.03	3.2
	3M	–72	2.01 & 1.98 & 1.94	3.1 & 3.2 & 3.4

For both **M** and **B** motifs, two protons are transferred from OP to water (see Figure 3a,b,e,f), forming an average of five HBs each. Consequently, the calculated OP–water interaction energy per water molecule for **M** (-1.7 kcal mol^{-1}) and **B** (-1.6 kcal mol^{-1}) motifs is essentially the same. In addition, proton transfers are observed from goethite to water, see Figure 3a,e,f. The proton transfers observed here occurred only during the

equilibration phase of the complexes and OP remained twice deprotonated in the production trajectory for both cases. The goethite–water interaction energy per single water molecule (−4.8 kcal mol^{-1}) is lower than the goethite–OP interaction energy for both **M** and **B** motifs. The goethite–water interaction energy is higher than OP–water interaction energies in both motif cases because of goethite's larger solvent accessible surface area (SASA), proton transfer events from goethite to water (see Figure 3), formation of multiple Fe–O_{H_2O} **M** motifs (on average 15 of 40 surface Fe atoms, see Figure S6) and HBs between goethite and water.

3.2.2. Glycerolphosphate

GP is aligned perpendicular to the goethite surface to form initial **M** and **B** motifs, as shown in Figures 1d and S3c–d. The MD simulations show that these initial motifs are stable during the whole trajectory (see Figure 3i–p, respectively). The time averaged Fe–O_p bond length and Fe–P distance observed for the **M** motif are close to the corresponding values for the **B** motif case; see Table 2. GP forms an average of six and eight HBs with water in the **M** and **B** motifs, respectively. It also exhibits multiple proton transfers to water, two in the **M** motif case and three in the **B** motif. The proton transfer events observed for both cases occurred during the equilibration phase. The total interaction energy between GP and goethite for the **B** motif (−76 kcal mol^{-1}) is higher than for the **M** motif (−48 kcal mol^{-1}) due to additional covalent bond in former motif. The higher overall goethite–GP interaction energy of the **B** motif indicates that it is a more favorable motif than the **M** one. However, the goethite–GP interaction energy per bond for the **B** motif is lower than for the **M** motif, suggesting comparatively unfavorable conditions for Fe–O_p bonds in former motif. This is in contrast to the case of OP. The difference comes from the glycerol group in GP. Both OP and GP interact through the phosphate, but through the glycerol group, GP has a higher SASA and exhibits stronger interaction with water than OP (OP/GP–water interaction energies will be discussed below). In the GP **B** motif case, two oxygens of GP's phosphate group are bound to two individual Fe atoms and when the glycerol group interacts with flexible water atoms, GP fluctuates with water while the surface Fe atoms competitively pull O_p oxygens towards the surface as a counteraction. This may induce strain in the Fe–O_p bonds for the **B** motif and, therefore, the goethite–GP interaction energy per bond for the **B** motif is less compared to the **M** motif. The stretch in the Fe–O_p bonds found in the GP **B** motif is larger than in the OP **B** motif, see Figure S4, which signifies a strain in the Fe–O_p bonds in the former case. In addition, GP is found to oscillate occasionally in a seesaw type of motion over the surface which randomly stretches one of the Fe–O_p bonds to its extreme (maximum Fe–O_p bond length found ≈2.4 Å), see Figure S5. A similar observation was made for GP on 100 diaspore surface [41] which is isomorphous with goethite [33]. The study by Xu et al. [78] showed that GP induces more negative charges onto hematite mineral surface than OP, which might also influence the strength of the Fe–O_p covalent bonds.

Regarding GP–water interaction energies, GP exhibited a slightly stronger interaction with water for the **B** motif (−2.8 kcal mol^{-1}) case than for the **M** motif one (−2.5 kcal mol^{-1}). This is due to additional proton transfer observed from GP to water for the **B** motif case (see Figure 3m–o). The GP–water interaction energy here is higher than that of OP–water due to additional glycerol group in GP which contains two polar OH groups that interact strongly with water. Similar to goethite–OP–water complexes, proton transfer is observed from goethite to water in both motifs here; see Figure 3i,n.

3.2.3. Inositolhexaphosphate

IHP was initially aligned perpendicular to the goethite surface to form **M** and **B** motifs (see Figure S3a–b), and parallel to the goethite surface to form the proposed **4M** motif (see Figure 1g). In contrast to goethite–OP–water and goethite–GP–water cases, transformation of initial binding motifs between IHP and the goethite surface with time is observed. The simulation results show that the initial **M** and **B** motifs resulted in two similar conform-

ers of **M** motif type; namely, **M(1)** and **M(2)**. On the other hand, the starting **4M** binding motif transformed along the MD trajectory into a **3M** motif. The transformations observed here happened within the equilibration phase of each complex. The corresponding Fe–O_p bond lengths and Fe–P distances of the relatively long-lived binding motifs [**M(1)**, **M(2)**, **3M**] are in close range and lie within half angstrom difference (see Table 2). The **M(1)** motif's goethite–IHP interaction energy is higher than that for the **M(2)** one (see Table 2). This is probably because of the strain in the Fe–O_p bond in the **M(2)** motif due to intramolecular HBs between the phosphate group bound to Fe and its adjacent phosphate groups (see Figure 4h). The **3M** motif has a higher total interaction energy than both **M** motifs due to additional covalent bonds and proton transfer from IHP to the goethite surface. However, the interaction energy per bond between IHP and goethite for the **3M** binding motif is less than for the **M(1)** motif. Thus, in spite of the **3M** motif being the more favorable motif compared to the **M** motifs, the alignment of IHP with goethite as in the **3M** motif weakens the overall strength of the individual Fe–O_p bonds.

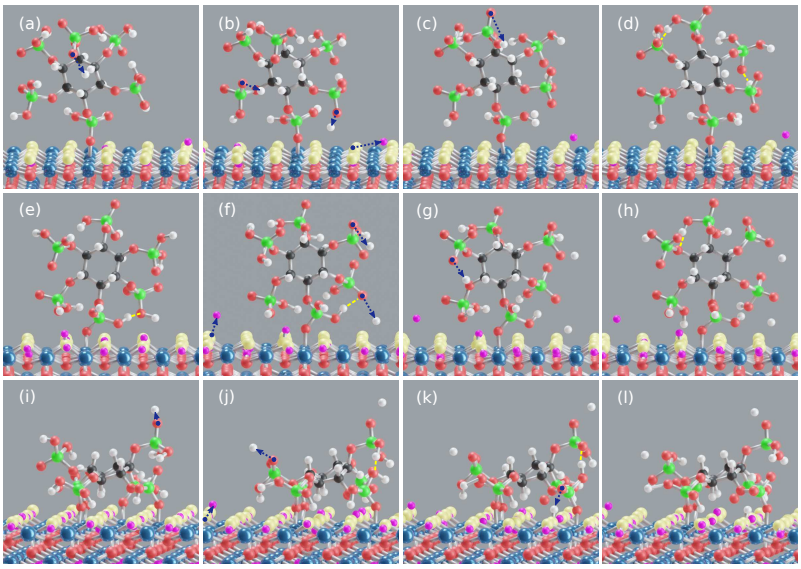


Figure 4. Snapshots along the simulation trajectories of the goethite–IHP–water complexes. IHP **M** motif (**a**–**d**), IHP **B** motif (**e**–**h**), IHP **3M** motif (**i**–**l**). Arrows denote proton transfers from phosphates to water and from goethite to water. The yellow dotted lines denote intramolecular HBs between IHP's phosphate groups. For all cases, the first two snapshots are from equilibration phase while the last two are from production, except for the IHP **3M** motif case where only (**i**) is from the equilibration phase. The last snapshot for each case is taken at 25 ps. The goethite's hydrogen atoms and IHP's hydrogen atoms are shown in violet and white colors, respectively, for clear visualization of proton transfer events. Blue, red, yellow, black and green colors correspond to iron, oxygen, hydroxyl oxygen, carbon and phosphorus atoms, respectively. The surrounding water is ignored here for better visualization.

Even though an additional proton transfer is observed from IHP to water for the **M(1)** motif, the IHP–water interaction energy (-7.3 kcal mol^{-1}) is very close to that for the **M(2)** motif case (-7.2 kcal mol^{-1}). This could be probably due to higher number of time averaged HBs observed for the **M(2)** motif case (25) compared to the **M(1)** case (23). The IHP–water interaction energy observed for the **3M** motif case (-3.1 kcal mol^{-1}) is lower than those for both **M** cases due to fewer proton transfer processes (2) and HBs (15) observed in the **3M** motif case.

The stronger interaction of IHP with water is vital for understanding the reason for transformation of initial **B** and **4M** motifs to **M(2)** and **3M** final motifs, respectively. For initial **B** motif case, when IHP interacts with flexible water molecules it fluctuates with respect to goethite surface which might induce strain in one of the Fe–O_p covalent bonds

leading to its dissociation. In addition, an intramolecular HB is observed between the Fe bonded phosphate group and its adjacent phosphate group, see Figure 4l. In our previous work on IHP interaction at the diaspore(100)–water interface (diaspore isostructural with goethite), [41] the initial **4M** motif was transformed into a **2M** motif. The reason is that the Al–O_p covalent bonds are inclined and restricted between diaspore's surface hydroxyl groups. Moreover, when IHP interacts with water and fluctuates during the equilibration phase, the restricted Al–O_p covalent bonds under unfavorable conditions do not have an alternative but to dissociate and move towards water. The same reason holds true here for the transformation process of the initial **4M** motif to a stable **3M** binding motif.

3.3. Discussion of Experimental and Modeling Results

In what follows, we will correlate the present modeling results and the adsorption isotherms as per mole of P--compound. It is important to emphasize that the experimental adsorption results are due to a combination of all different binding motifs at the existing different surface planes (not only the 100 goethite surface plane) in the real goethite sample. Therefore, a direct quantitative comparison is rather difficult and thus we are aiming here to present a qualitative behavior. First, let us recollect that K_f, K_l and B_T relate to the phosphate's binding energy and that n_f relates to the binding energy of the next incoming P molecule to surface (i.e., binding affinity). Since the Freundlich isotherm provided the best fit to the experimental data for all cases (see Table 1), we will discuss the theoretical results in Table 2 in the context of K_f and n_f. Analyzing the strength of phosphate interaction shows that the K_f values are in line with the order of overall binding energies observed here, i.e., GP **B** < OP **B** < IHP **3M**. The K_f value for OP adsorption is more than twice that of the GP adsorption, suggesting a significant difference between OP and GP interaction with goethite. In light of these results, combined with the theoretical binding energy values (see Table 2), one could suggest that OP might predominantly form **B** motif and GP might form **M** motif as the predominant binding motif. Therefore, the binding strength order could be updated as GP **M** < OP **B** < IHP **3M**. Comparing K_f values for IHP and OP, the K_f for IHP adsorption is about 1.58 times that for OP adsorption, which is very close to the reported adsorption ratio by Celi et al. [71] and Martin et al. [72]. Correlating this ratio to the present calculated binding energies would suggest that one should rather use the average of all three bonding motifs, i.e., both **M** and **3M** binding motifs for the adsorbed IHP molecule are present at the goethite surface. Therefore, based on both experimental and theoretical binding strength values, one could suggest that the overall binding strength increases in the order GP (**M**) < OP (**B**) < IHP (**M + 3M**).

The order of n_f values (IHP < GP < OP, see Table 1) suggests that IHP adsorption leads to a faster saturation of the goethite surface than GP and OP. Even though IHP binds to goethite through a few phosphate groups, the remaining phosphate groups (often deprotonated) would induce more negative charges to the surface compared to OP and GP cases [71,78]. Moreover, it was found that GP leads to a more negatively charged surface than OP [78]. This explains the reason why the n_f value for GP is lower than for OP.

Let us compare the present modeling results with previous experimental and theoretical studies. In the case of OP, experimental [36,79,80] and theoretical [10,40] results pointed to a formation of both, i.e., **M** and **B**, motif,s with goethite. Specifically, for the 100 goethite surface studied here, Kubicki et al. [40] and Ahmed et al. [10] demonstrated that OP often exists in a doubly deprotonated state forming both **M** and **B** binding motifs but with the predominance of the **B** one. This is confirmed by the present MD results, i.e., OP has formed stable **M** and **B** motifs and remained twice as

deprotonated in the production trajectory with the **B** motif exhibiting higher interaction energy with the goethite surface compared to the **M** motif. Even though the **B** motif is the more stable motif under the present conditions, it is not always the dominant one, a topic which has been highly debated in the literature [39,40,79,80]. For instance, Persson et al. [80] interpreted their FTIR spectra of the OP adsorption at goethite and hematite by the formation of only **M** binding motifs with different protonation states. This analysis

was done as a function of total phosphate concentration, pH, and time. In contrast, Tejedor-Tejedor and Anderson [36] proposed that the **B** motif is the dominant motif, for low surface coverage of OP on goethite over the pH range of 3.6–8.0. Further, they proposed that the **M** motif exists at low surface coverage but as a non-dominant motif. By using DFT calculations, Kwon and Kubicki [39] concluded that the **B** motif is dominant between pH 4–6. Recently, a joint approach by Ahmed et al. [51] involving adsorption experiments and DFT simulations showed that the **M** motif is dominant at both extremely low and high pH values, while the **B** motif is dominant in the intermediate pH range.

Keeping in mind that the present simulations correspond to a low surface coverage scenario and acidic pH, one can conclude that the stable **M** and **B** motifs with abundance of the **B** one here are in line with the studies of Tejedor-Tejedor and Anderson [36], Ahmed et al. [51], and Abdala et al. [79]. Moreover, the time averaged Fe–P distance observed in both motifs (3.5 Å for the **M** motif and 3.19–3.2 Å for the **B** motif) are within the range of values reported in literature, thus giving further support for the present model. For instance, an extended X-ray absorption fine structure study of adsorbed OP on goethite [79] showed that the distances between the surface Fe atoms and the adsorbed phosphate P atoms (i.e., Fe–P distances) for **M** and **B** binding motifs are 3.6 and 3.28 Å, respectively. The Fe–P distances from other studies are in the range of 3.48–3.55 Å for the **M** motif and 3.13–3.37 Å for the **B** motif [10,40,81,82].

Compared to OP, GP adsorption on goethite has not been extensively studied and hence, the information about its binding motifs with goethite is limited. Li et al. [74] showed that GP forms inner-sphere complexes with goethite by replacing water and hydroxyl groups from surface active sites. The study also proposes that GP forms only **M** motifs at the goethite surface based on FTIR spectra analysis. The **B** motif is sterically hindered by the organic moiety. Additionally, Hartree-Fock simulations and FTIR spectra studies by Persson et al. [83] of monomethyl phosphate (CH_3–H_2PO_4), an organic P with a single phosphate group like GP, showed that it forms mostly **M** motifs with goethite. Adsorption isotherms and FTIR spectra by Sheals et al. [34] proposed that glyphosate binds predominantly through an **M** motif but **B** motifs might be formed at low P concentration and neutral pH. By using periodic DFT based MD simulations, Ahmed et al. [9] studied the glyphosate binding process at the goethite–water interface by considering three goethite surface planes. The results indicated that the **M** binding motif is the most dominant one at the 100 goethite surface plane, although both **M** and **B** motifs exist at the 100, 010 and 001 surface planes. Summing up these literature data, the **M** motif is the dominant motif for GP like molecules at the 100 goethite surface. This could be supported by our recent study [52] about the P binding at the 010 goethite surface plane. We found that the calculated total interaction energy for the GP **B** motif (-122 kcal mol^{-1}) is higher than for the **M** motif (-112 kcal mol^{-1}). However, the goethite–GP interaction energy per bond for the **B** motif is lower than for the **M** motif. This suggests unfavorable conditions for Fe–O_p bonds for the **B** case. This is in accord with outcome of the present contribution. In addition, the calculated interaction energy indicated that the 010 goethite surface plane binds GP stronger than the corresponding 100 surface plane. Regarding the Fe–P distances observed for both GP motifs at both 010 and 100 goethite surface planes, the distances are within the range of Fe–P distances observed for OP on goethite in the literature [10,40,79,81,82]. This suggests that the GP's phosphate group interacts with goethite surface in a similar way to the OP case.

There is no consensus in the literature about the number of IHP's phosphate groups that bind to goethite surface or about dominant binding motifs. The binding motifs observed for goethite–IHP complexes in the current study (**M** and **3M**) have been found in literature before [11,41]. Similarly, we have observed the same binding motifs (i.e., **M** and **3M**) for IHP at the 010 goethite surface plane [52]. Similar to the GP case, the calculated interaction energy referred to stronger interaction for IHP at the 010 goethite surface plane compared to the 100 surface plane. It is important to mention that it is not clear yet in literature which binding motif is the dominant one. For instance, **3M** [11,84], **2M** [11,41]

and **1M** [11] are different binding motifs observed for IHP on minerals. In contrast, Johnson et al. [77] proposed that IHP interacts with goethite by forming outer-sphere complexes. Interestingly, none of the above mentioned studies for IHP suggest that it forms a bidentate binuclear (**B**) motif. Similar to our previous studies [11,41], we found that the initial **B** motif of IHP was not stable due to the strong interaction of IHP with water and intramolecular HBs. Therefore, we propose that IHP phosphate groups form **M** motif with goethite surface.

De Groot and Golterman [85] showed that IHP adsorption onto goethite had an inhibitory effect on OP adsorption and it can release adsorbed OP from the goethite surface. The same could be inferred from binding energies here, where the goethite–IHP binding energies are larger than for goethite–OP complexes. The goethite–GP binding energies are also less than goethite–IHP and one might suggest that IHP might replace GP as well from goethite surface. The same could be inferred from the adsorption strengths order calculated from experiments here. The Fe–P distances observed here show that they are close to the Fe–P distances for OP on goethite [10,40,79,81,82] which suggests that IHP's organic moiety might not influence the individual phosphate groups interaction with goethite but only the conformational flexibility of the overall binding motif [11,41]. This comes in accord with the observation by Celi et al. [71] that phosphate groups of IHP react with a goethite surface similar to OP.

4. Summarizing Discussion

The current study contributes to the efforts in understanding the interaction of phosphates with soil minerals. Here, both experimental and theoretical approaches are adopted to characterize inorganic (OP) and organic (GP, IHP) phosphates interaction with abundant and reactive goethite mineral. The goethite–OP/GP/IHP–water complexes are simulated with the multiscale QM/MM method which provides molecular level insights into adsorption experiments performed for OP/GP/IHP on goethite. The binding energies and interaction mechanisms of phosphates adsorption on goethite from the modeling study are correlated to adsorption data fitted to the Freundlich isotherm, which provided a uniformly better fit than the Langmuir and Temkin models. The model coefficients provided an overview of the pattern of phosphate interactions with goethite and the QM/MM simulations demonstrate, at the molecular level, the attributes that build these pattern.

The modeling results show that OP forms stable **M** and **B** motifs and OP **B** motif has higher interaction energy per bond than OP **M** motif. This suggests that goethite–OP interaction favors the additional covalent bond, which makes the OP **B** motif more stable. For goethite–GP complexes, the order of interaction energies is same as OP case, except that GP **B** motif interaction energy per bond is lower than GP **M** motif. Compared to OP, the GP **B** motif is weaker than OP **B** motif due to a strain in Fe–O_p bonds in former case. The strain is due to GP interaction with water molecules. In addition, Xu et al. [78] study shows that adsorption of GP induces more negative charges on the hematite surface than OP which might strain the Fe–O_p bonds further. Therefore, the literature [34,74] and the calculated binding energies in the present contribution show that GP's dominant motif might be the **M** or **B** motif depending on the GP interaction with environmental molecules. IHP forms **M** and **3M** motifs with multiple intramolecular HBs between adjacent phosphate groups [77]. IHP's **3M** motif exhibits the strongest binding energy with the goethite surface among all goethite–OP/GP complexes here. This comes in accord with our recent study [52] for the binding of GP and IHP at the 010 goethite surface plane. In that study, the **3M** binding motif of IHP showed the strongest interaction with goethite compared to all other existing binding motifs for GP and IHP. Therefore, we propose that the **3M** motif might be the most dominant motif at low surface loading.

The adsorption data from experiment fitted to Freundlich model show that the order of adsorption strength (K_f) is GP < OP < IHP whereas the order of incoming P binding strength with surface (n_f) is IHP < GP < OP. Based on the magnitude and order of experimental K_f values combined with theoretical binding strength values, one could suggest that the overall binding strength increases in the order GP (**M**) < OP (**B**) < IHP (**M**

+ 3M). This shows that GP might often form **M** motif, whereas OP might form **B**, and IHP might form both **M** and **3M** motifs. The n_f order suggests that IHP adsorption on goethite saturates its surface faster than for the GP and OP cases. The fact that GP adsorption induces more negative charges on goethite than OP supports our suggestions that GP would often form **M** and not **B** motifs and eventually its interaction energy would be less than OP.

Eventually, the present experimental and theoretical results, in agreement with the pertinent literature, plausibly explain why IHP is the predominant organically bound P form in soil. A challenge for further studies and application is to understand and explore the mechanisms by which microbes and plants can overcome the strong IHP--mineral binding and incorporate the phosphate groups into their metabolism.

Supplementary Materials: The following are available online at www.mdpi.com/xxx/s1, Figure S1: XRD pattern for pure goethite sample, Figure S2: Effect of pH on goethite zeta potential, Figure S3: Initial motifs of IHP GP, Figure S4: Sum of covalent bond lengths in OP and GP **B** motifs, Figure S5: Seesaw movement of GP's phosphate group, Figure S6: Multiple covalent bonds between surface irons atoms and water molecules.

Author Contributions: P.B.G. and M.M. performed the modeling and experimental work, respectively, and wrote the manuscript draft. A.A.A., P.L. and O.K. are responsible for conceptualization, funding acquisition, methodology, supervision, writing–review and editing of the present contribution. All authors have read and agreed to the published version of the manuscript.

Funding: We are grateful to S. Dultz, Soil Science, University of Hannover, for preparing and characterizing the goethite. We gratefully acknowledge the financial support by the German Research Foundation (DFG) as a part of the SPP 1685 Priority program "Ecosystem Nutrition: Forest strategies for limited phosphorus resources" (P.B.G., O.K., A.A.A.) and the InnoSoilPhos-project (A.A.A.), funded by the German Federal Ministry of Education and Research (BMBF) in the frame of the BonaRes-program (No. 031A558). This research was performed within the scope of the Leibniz Science Campus "Phosphorus Research Rostock". The authors thank the North German Super computing Alliance for providing HPC resources (project mvp00016).

Institutional Review Board Statement: Not applicable.

Informed Consent Statement: Not applicable.

Data Availability Statement: Not applicable.

Conflicts of Interest: The authors declare no conflict of interest. The funders had no role in the design of the study; in the collection, analyses, or interpretation of data; in the writing of the manuscript, or in the decision to publish the results.

References

1. Tisdale, S.L. (Ed.) *Soil Fertility and Fertilizers*, 5th ed.; Prentice Hall: Upper Saddle River, NJ, USA, 1993.
2. Andersen, D.S.; Helmers, M.J.; Burns, R.T. Phosphorus Sorption Capacity of Six Iowa Soils before and after Five Years of Use as Vegetative Treatment Areas. *Appl. Eng. Agric.* **2015**, 611–620, doi:10.13031/aea.31.11128.
3. Wang, Y.; Zhang, T.; O'Halloran, I.; Tan, C.; Hu, Q. A Phosphorus Sorption Index and Its Use to Estimate Leaching of Dissolved Phosphorus from Agricultural Soils in Ontario. *Geoderma* **2016**, *274*, 79–87, doi:10.1016/j.geoderma.2016.04.002.
4. Roy, E.D.; Willig, E.; Richards, P.D.; Martinelli, L.A.; Vazquez, F.F.; Pegorini, L.; Spera, S.A.; Porder, S. Soil Phosphorus Sorption Capacity after Three Decades of Intensive Fertilization in Mato Grosso, Brazil. *Agric. Ecosyst. Environ.* **2017**, *249*, 206–214, doi:10.1016/j.agee.2017.08.004.
5. Everett, D.H. Manual of Symbols and Terminology for Physicochemical Quantities and Units, Appendix II: Definitions, Terminology and Symbols in Colloid and Surface Chemistry. *Pure Appl. Chem.* **1972**, *31*, 577–638, doi:10.1351/pac197231040577.
6. Urrutia, O.; Guardado, I.; Erro, J.; Mandado, M.; García-Mina, J.M. Theoretical Chemical Characterization of Phosphate-Metal–Humic Complexes and Relationships with Their Effects on Both Phosphorus Soil Fixation and Phosphorus Availability for Plants. *J. Sci. Food Agric.* **2013**, *93*, 293–303, doi:10.1002/jsfa.5756.
7. Gros, P.; Ahmed, A.A.; Kühn, O.; Leinweber, P. Influence of Metal Ions on Glyphosate Detection by FMOC-Cl. *Environ. Model. Assess.* **2019**, *191*, 244, doi:10.1007/s10661-019-7387-2.
8. Kruse, J.; Abraham, M.; Amelung, W.; Baum, C.; Bol, R.; Kühn, O.; Lewandowski, H.; Niederberger, J.; Oelmann, Y.; Rüger, C.; et al. Innovative Methods in Soil Phosphorus Research: A Review. *J. Soil Sci. Plant Nutr.* **2015**, *178*, 43–88, doi:10.1002/jpln.201400327.

9. Ahmed, A.A.; Leinweber, P.; Kühn, O. Unravelling the Nature of Glyphosate Binding to Goethite Surfaces by Ab Initio Molecular Dynamics Simulations. *Phys. Chem. Chem. Phys.* **2018**, *20*, 1531–1539, doi:10.1039/C7CP06245A.
10. Ahmed, A.A.; Gypser, S.; Leinweber, P.; Freese, D.; Kühn, O. Infrared Spectroscopic Characterization of Phosphate Binding at the Goethite-Water Interface. *Phys. Chem. Chem. Phys.* **2019**, *21*, 4421–4434, doi:10.1039/C8CP07168C.
11. Ganta, P.B.; Kühn, O.; Ahmed, A.A. QM/MM Simulations of Organic Phosphorus Adsorption at the Diaspore–Water Interface. *Phys. Chem. Chem. Phys.* **2019**, *21*, 24316–24325, doi:10.1039/C9CP04032C.
12. Gros, P.; Ahmed, A.; Kühn, O.; Leinweber, P. Glyphosate Binding in Soil as Revealed by Sorption Experiments and Quantum-Chemical Modeling. *Sci. Total Environ.* **2017**, *586*, 527–535, doi:10.1016/j.scitotenv.2017.02.007.
13. Ahmed, A.A.; Gros, P.; Kühn, O.; Leinweber, P. Molecular Level Investigation of the Role of Peptide Interactions in the Glyphosate Analytics. *Chemosphere* **2018**, *196*, 129–134, doi:10.1016/j.chemosphere.2017.12.162.
14. Arai, Y.; Sparks, D. Phosphate Reaction Dynamics in Soils and Soil Components: A Multiscale Approach. In *Advances in Agronomy*; Elsevier: Amsterdam, The Netherlands, 2007; Volume 94, pp. 135–179, doi:10.1016/S0065-2113(06)94003-6.
15. Arai, Y.; Sparks, D. ATR–FTIR Spectroscopic Investigation on Phosphate Adsorption Mechanisms at the Ferrihydrite–Water Interface. *J. Colloid Interface Sci.* **2001**, *241*, 317–326, doi:10.1006/jcis.2001.7773.
16. Barrow, N.J. A Mechanistic Model for Describing the Sorption and Desorption of Phosphate by Soil. *J. Soil Sci.* **1983**, *34*, 733–750, doi:10.1111/j.1365-2389.1983.tb01068.x.
17. Chitrakar, R.; Tezuka, S.; Sonoda, A.; Sakane, K.; Ooi, K.; Hirotsu, T. Phosphate Adsorption on Synthetic Goethite and Akaganeite. *J. Colloid Interface Sci.* **2006**, *298*, 602–608, doi:10.1016/j.jcis.2005.12.054.
18. Hinsinger, P. Bioavailability of Soil Inorganic P in the Rhizosphere as Affected by Root-Induced Chemical Changes: A Review. *Plant Soil* **2001**, *237*, 173–195, doi:10.1023/A:1013351617532.
19. Ryan, J.; Curtin, D.; Cheema, M. Significance of Iron Oxides and Calcium Carbonate Particle Size in Phosphate Sorption by Calcareous Soils. *Soil Sci. Soc. Am. J.* **1985**, *49*, 74–76, doi:10.2136/sssaj1985.03615995004900010014x.
20. Baken, S.; Verbeeck, M.; Verheyen, D.; Diels, J.; Smolders, E. Phosphorus Losses from Agricultural Land to Natural Waters Are Reduced by Immobilization in Iron-Rich Sediments of Drainage Ditches. *Water Res.* **2015**, *71*, 160–170, doi:10.1016/j.watres.2015.01.008.
21. Bortoluzzi, E.C.; Pérez, C.A.; Ardisson, J.D.; Tiecher, T.; Caner, L. Occurrence of Iron and Aluminum Sesquioxides and Their Implications for the P Sorption in Subtropical Soils. *Appl. Clay Sci.* **2015**, *104*, 196–204, doi:10.1016/j.clay.2014.11.032.
22. Torrent, J.; Schwertmann, U.; Barron, V. Fast and Slow Phosphate Sorption by Goethite-Rich Natural Materials. *Clays Clay Miner.* **1992**, *40*, 14–21, doi:10.1346/CCMN.1992.0400103.
23. Luengo, C.; Brigante, M.; Antelo, J.; Avena, M. Kinetics of Phosphate Adsorption on Goethite: Comparing Batch Adsorption and ATR-IR Measurements. *J. Colloid Interface Sci.* **2006**, *300*, 511–518, doi:10.1016/j.jcis.2006.04.015.
24. McLaughlin, J.; Ryden, J.; Syers, J. Development and Evaluation of a Kinetic Model to Describe Phosphate Sorption by Hydrous Ferric Oxide Gel. *Geoderma* **1977**, *18*, 295–307, doi:10.1016/0016-7061(77)90038-6.
25. Willett, I.R.; Chartres, C.J.; Nguyen, T.T. Migration of Phosphate into Aggregated Particles of Ferrihydrite. *J. Soil Sci.* **1988**, *39*, 275–282, doi:10.1111/j.1365-2389.1988.tb01214.x.
26. Torrent, J. Interactions between Phosphate and Iron Oxide. In *Soils and Environment*; Catena Verlag: Reiskirchen, Germany, 1997; Volume 30, pp. 321–344.
27. Strauss, R.; Brummer, G.; Barrow, N. Effects of Crystallinity of Goethite: II. Rates of Sorption and Desorption of Phosphate. *Eur. J. Soil Sci.* **1997**, *48*, 101–114, doi:10.1111/j.1365-2389.1997.tb00189.x.
28. Neupane, G.; Donahoe, R.J.; Arai, Y. Kinetics of Competitive Adsorption/Desorption of Arsenate and Phosphate at the Ferrihydrite– Water Interface. *Chem. Geol.* **2014**, *368*, 31–38, doi:10.1016/j.chemgeo.2013.12.020.
29. Parfitt, R.L. Phosphate Reactions with Natural Allophane, Ferrihydrite and Goethite. *J. Soil Sci.* **1989**, *40*, 359–369, doi:10.1111/j.1365-2389.1989.tb01280.x.
30. Langmuir, D. *Aqueous Environmental Geochemistry*; Prentice Hall: Upper Saddle River, NJ, USA, 1997.
31. Villalobos, M.; Trotz, M.A.; Leckie, J.O. Variability in Goethite Surface Site Density: Evidence from Proton and Carbonate Sorption. *J. Colloid Interface Sci.* **2003**, *268*, 273–287, doi:10.1016/j.jcis.2003.07.044.
32. Houben, G.; Kaufhold, S. Multi-Method Characterization of the Ferrihydrite to Goethite Transformation. *Clay Miner.* **2011**, *46*, 387–395, doi:10.1180/claymin.2011.046.3.387.
33. Cornell, R.M.; Schwertmann, U. *The Iron Oxides: Structure, Properties Reactions Occurrence and Uses*; Wiley-VCH Verlag GmbH and Co. KGaA: Weinheim, Germany, 2003; doi:10.1002/3527602097.
34. Sheals, J.; Sjoberg, S.; Persson, P. Adsorption of Glyphosate on Goethite: Molecular Characterization of Surface Complexes. *Environ. Sci. Technol.* **2002**, *36*, 3090–3095, doi:10.1021/es010295w.
35. Olsson, R.; Giesler, R.; Loring, J.S.; Persson, P. Adsorption, Desorption, and Surface-Promoted Hydrolysis of Glucose-1-Phosphate in Aqueous Goethite (Alpha-Feooh) Suspensions. *Langmuir* **2010**, *26*, 18760–18770, doi:10.1021/la1026152.
36. Tejedor-Tejedor, M.I.; Anderson, M.A. The Protonation of Phosphate on the Surface of Goethite as Studied by CIR-FTIR and Electrophoretic Mobility. *Langmuir* **1990**, *6*, 602–611, doi:10.1021/la00093a015.
37. Kim, J.; Li, W.; Philips, B.L.; Grey, C.P. Phosphate Adsorption on the Iron Oxyhydroxides Goethite (Alpha-FeOOH), Akaganeite (Beta-FeOOH), and Lepidocrocite (Gamma-FeOOH): A 31P NMR Study. *Energy Environ. Sci.* **2011**, *4*, 4298, doi:10.1039/c1ee02093e.

38. Loring, J.S.; Sandström, M.H.; Norén, K.; Persson, P. Rethinking Arsenate Coordination at the Surface of Goethite. *Chem. Eur. J.* **2009**, *15*, 5063–5072, doi:10.1002/chem.200900284.
39. Kwon, K.D.; Kubicki, J.D. Molecular Orbital Theory Study on Surface Complex Structures of Phosphates to Iron Hydroxides: Calculation of Vibrational Frequencies and Adsorption Energies. *Langmuir* **2004**, *20*, 9249–9254, doi:10.1021/la0487444.
40. Kubicki, J.D.; Paul, K.W.; Kabalan, L.; Zhu, Q.; Mrozik, M.K.; Aryanpour, M.; Pierre-Louis, A.M.; Strongin, D.R. ATR–FTIR and Density Functional Theory Study of the Structures, Energetics, and Vibrational Spectra of Phosphate Adsorbed onto Goethite. *Langmuir* **2012**, *28*, 14573–14587, doi:10.1021/la303111a.
41. Ganta, P.B.; Kühn, O.; Ahmed, A.A. QM/MM Molecular Dynamics Investigation of the Binding of Organic Phosphates to the 100 Diaspore Surface. *Front. For. Glob. Chang.* **2020**, *3*, 71, doi:10.3389/ffgc.2020.00071.
42. Dultz, S.; Steinke, H.; Mikutta, R.; Woche, S.K.; Guggenberger, G. Impact of Organic Matter Types on Surface Charge and Aggregation of Goethite. *Colloid Surf. A* **2018**, *554*, 156–168, doi:10.1016/j.colsurfa.2018.06.040.
43. Antelo, J.; Avena, M.; Fiol, S.; López, R.; Arce, F. Effects of pH and Ionic Strength on the Adsorption of Phosphate and Arsenate at the Goethite– Water Interface. *J. Colloid Interface Sci.* **2005**, *285*, 476–486, doi:10.1016/j.jcis.2004.12.032.
44. Rouquerol, J.; Llewellyn, P.; Rouquerol, F. Is the Bet Equation Applicable to Microporous Adsorbents? In *Studies in Surface Science and Catalysis*; Elsevier: Amsterdam, The Netherlands, 2007; Volume 160, pp. 49–56, doi:10.1016/S0167-2991(07)80008-5.
45. Freundlich, H. Über Die Adsorption in Lösungen. *Z. Phys. Chem.* **1907**, *57U*, doi:10.1515/zpch-1907-5723.
46. Langmuir, I. The Adsorption of Gases on Plane Surfaces of Glass, Mica and Platinum. *J. Am. Chem. Soc.* **1918**, *40*, 1361–1403, doi:10.1021/ja02242a004.
47. Tempkin, M.I.; Pyzhev, V. Kinetics of Ammonia Synthesis on Promoted Iron Catalyst. *Acta Phys. Chim. USSR* **1940**, *12*, 327–356.
48. Bolster, C.H.; Hornberger, G.M. On the Use of Linearized Langmuir Equations. *Soil Sci. Soc. Am. J.* **2007**, *71*, 1796–1806, doi:10.2136/sssaj2006.0304.
49. Rakovan, J.; Becker, U.; Hochella, M.F. Aspects of Goethite Surface Microtopography, Structure, Chemistry, and Reactivity. *Am. Mineral.* **1999**, *84*, 884–894, doi:10.2138/am-1999-5-623.
50. Ognalaga, M.; Frossard, E.; Thomas, F. Glucose-1-Phosphate and Myo-Inositol Hexaphosphate Adsorption Mechanisms on Goethite. *Soil Sci. Soc. Am. J.* **1994**, 332–337, doi:doi:10.2136/sssaj1994.03615995005800020011x.
51. Ahmed, A.A.; Gypser, S.; Freese, D.; Leinweber, P.; Kuehn, O. Molecular Level Picture of the Interplay between pH and Phosphate Binding at the Goethite–Water Interface. *Phys. Chem. Chem. Phys.* **2020**, doi:10.1039/D0CP04698A.
52. Ganta, P.B.; Kühn, O.; Ahmed, A.A. Ab Initio Molecular Dynamics Simulations of the Interaction between Organic Phosphates and Goethite. *Molecules* **2021**, *26*, 160, doi:10.3390/molecules26010160.
53. Humphrey, W.; Dalke, A.; Schulten, K. VMD – Visual Molecular Dynamics. *J. Mol. Graph.* **1996**, *14*, 33–38.
54. Ozboyaci, M.; Kokh, D.B.; Corni, S.; Wade, R.C. Modeling and Simulation of Protein–Surface Interactions: Achievements and Challenges. *Q. Rev. Biophys.* **2016**, *49*, e4, doi:10.1017/S0033583515000256.
55. Kubicki, J.D. (Ed.) *Molecular Modeling of Geochemical Reactions*; Wiley and Sons: Hoboken, NJ, USA, 2016.
56. VandeVondele, J.; Krack, M.; Mohamed, F.; Parrinello, M.; Chassaing, T.; Hutter, J. Quickstep: Fast and Accurate Density Functional Calculations Using a Mixed Gaussian and Plane Waves Approach. *Comput. Phys. Commun.* **2005**, *167*, 103–128, doi:10.1016/j.cpc.2004.12.014.
57. Krack, M. Pseudopotentials for H to Kr Optimized for Gradient-Corrected Exchange-Correlation Functionals. *Theor. Chem. Acc.* **2005**, *114*, 145–152, doi:10.1007/s00214-005-0655-y.
58. Perdew, J.P.; Burke, K.; Ernzerhof, M. Generalized Gradient Approximation Made Simple. *Phys. Rev. Lett.* **1996**, *77*, 3865–3868, doi:10.1103/PhysRevLett.77.3865.
59. Grimme, S.; Antony, J.; Ehrlich, S.; Krieg, H. A Consistent and Accurate Ab Initio Parametrization of Density Functional Dispersion Correction (DFT-D) for the 94 Elements H-Pu. *J. Phys. Chem.* **2010**, *132*, 154104:1–154104:15, doi:10.1063/1.3382344.
60. VandeVondele, J.; Hutter, J. Gaussian Basis Sets for Accurate Calculations on Molecular Systems in Gas and Condensed Phases. *J. Chem. Phys.* **2007**, *127*, 114105:1–114105:8, doi:10.1063/1.2770708.
61. Mundy, C.J.; Balasubramanian, S.; Bagchi, K.; Hutter, J.; Kuo, A.S.I.; Laino, T.; VandeVondele, J. Frontiers in Simulation Technology (FIST), 2017. Available online: www.cp2k.org (accessed on 4 February 2021).
62. Cygan, R.T.; Liang, J.J.; Kalinichev, A.G. Molecular Models of Hydroxide, Oxyhydroxide, and Clay Phases and the Development of a General Force Field. *J. Phys. Chem. B* **2004**, *108*, 1255–1266, doi:10.1021/jp0363287.
63. Berendsen, H.J.C.; Grigera, J.R.; Straatsma, T.P. The Missing Term in Effective Pair Potentials. *J. Phys. Chem.* **1987**, *91*, 6269–6271, doi:10.1021/j100308a038.
64. Zoete, V.; Cuendet, M.A.; Grosdidier, A.; Michielin, O. SwissParam: A Fast Force Field Generation Tool for Small Organic Molecules. *J. Comput. Chem.* **2011**, *32*, 2359–2368, doi:10.1002/jcc.21816.
65. Laino, T.; Mohamed, F.; Laio, A.; Parrinello, M. An Efficient Linear-Scaling Electrostatic Coupling for Treating Periodic Boundary Conditions in QM/MM Simulations. *J. Chem. Theory Comput.* **2006**, *2*, 1370–1378, doi:10.1021/ct6001169.
66. Bussi, G.; Donadio, D.; Parrinello, M. Canonical Sampling through Velocity Rescaling. *J. Chem. Phys.* **2007**, *126*, 014101:1–014101:6, doi:10.1063/1.2408420.
67. Boys, S.F.; Bernardi, F. The Calculation of Small Molecular Interactions by the Differences of Separate Total Energies: Some Procedures with Reduced Errors. *Mol. Phys.* **1970**, *19*, 553–566, doi:10.1080/00268977000101561.

68. Tellinghuisen, J.; Bolster, C.H. Least-Squares Analysis of Phosphorus Soil Sorption Data with Weighting from Variance Function Estimation: A Statistical Case for the Freundlich Isotherm. *Environ. Sci. Technol.* **2010**, *44*, 5029–5034, doi:10.1021/es100535b.
69. Ahmed, A.A.; Kühn, O.; Aziz, S.G.; Hilal, R.H.; Leinweber, P. How Soil Organic Matter Composition Controls Hexachlorobenzene-Soil-Interactions: Adsorption Isotherms and Quantum Chemical Modeling. *Sci. Total Environ.* **2014**, *476*, 98–106.
70. Ahmed, A.A.; Thiele-Bruhn, S.; Aziz, S.G.; Hilal, R.H.; Elroby, S.A.; Al-Youbi, A.O.; Leinweber, P.; Kühn, O. Interaction of Polar and Nonpolar Organic Pollutants with Soil Organic Matter: Sorption Experiments and Molecular Dynamics Simulation. *Sci. Total Environ.* **2015**, *508*, 276–287, doi:10.1016/j.scitotenv.2014.11.087.
71. Celi, L.; Lamacchia, S.; Marsan, F.A.; Barberis, E. Interaction of Inositol Hexaphosphate on Clays: Adsorption and Charging Phenomena. *Soil Sci.* **1999**, *164*, 574–585, doi:10.1097/00010694-199908000-00005.
72. Martin, M.; Celi, L.; Barberis, E. Desorption and Plant Availability of Myo-Inositol Hexaphosphate Adsorbed on Goethite. *Soil Sci.* **2004**, *169*, 115–124, doi:10.1097/01.ss.0000117787.98510.9d.
73. Celi, L.; Barberis, E. Abiotic Reactions of Inositol Phosphates in Soil. In *Inositol Phosphates: Linking Agriculture and the Environment*; Turner, B.L., Richardson, A., Mullaney, E.J., Eds.; CABI Publishing: Wallingford, UK, 2007.
74. Li, H.; Wan, B.; Yan, Y.; Zhang, Y.; Cheng, W.; Feng, X. Adsorption of Glycerophosphate on Goethite: A Macroscopic and Infrared Spectroscopic Study. *J. Soil Sci. Plant Nutr.* **2017**, *181*, 557–565, doi:10.1002/jpln.201700517.
75. Guzman, G.; Alcantara, E.; Barron, V.; Torrent, J. Phytoavailability of Phosphate Adsorbed on Ferrihydrite, Hematite, and Goethite. *Plant Soil* **1994**, *159*, 219–225, doi:10.1007/BF00009284.
76. Celi, L.; M, P.; Marsan, F.A.; Barberis, E. Effects of pH and Electrolytes on Inositol Hexaphosphate Interaction with Goethite. *Soil Sci. Soc. Am. J.* **2001**, *65*, 753–760, doi:10.2136/sssaj2001.653753x.
77. Johnson, B.B.; Quill, E.; Angove, M.J. An Investigation of the Mode of Sorption of Inositol Hexaphosphate to Goethite. *J. Colloid Interface Sci.* **2012**, *367*, 436–442, doi:10.1016/j.jcis.2011.09.066.
78. Xu, C.Y.; Li, J.Y.; Xu, R.K.; Hong, Z.N. Sorption of Organic Phosphates and Its Effects on Aggregation of Hematite Nanoparticles in Monovalent and Bivalent Solutions. *Environ. Sci. Pollut. Res.* **2017**, *24*, 7197–7207, doi:10.1007/s11356-017-8382-1.
79. Abdala, D.B.; Northrup, P.A.; Arai, Y.; Sparks, D.L. Surface Loading Effects on Orthophosphate Surface Complexation at the Goethite/Water Interface as Examined by Extended X-Ray Absorption Fine Structure (EXAFS) Spectroscopy. *J. Colloid Interface Sci.* **2015**, *437*, 297–303, doi:10.1016/j.jcis.2014.09.057.
80. Persson, P.; Nilsson, N.; Sjöberg, S. Structure and Bonding of Orthophosphate Ions at the Iron Oxide–Aqueous Interface. *J. Colloid Interface Sci.* **1996**, *177*, 263–275, doi:10.1006/jcis.1996.0030.
81. Rose, J.; Flank, A.M.; Masion, A.; Bottero, J.Y.; Elmerich, P. Nucleation and Growth Mechanisms of Fe Oxyhydroxide in the Presence of PO4 Ions. 2. P K-Edge EXAFS Study. *Langmuir* **1997**, *13*, 1827–1834, doi:10.1021/la961039d.
82. Tribe, L.; Kwon, K.D.; Trout, C.C.; Kubicki, J.D. Molecular Orbital Theory Study on Surface Complex Structures of Glyphosate on Goethite: Calculation of Vibrational Frequencies. *Environ. Sci. Technol.* **2006**, *40*, 3836–3841, doi:10.1021/es052363a.
83. Persson, P.; Andersson, T.; Nelson, H.; Sjöberg, S.; Giesler, R.; Lövgren, L. Surface Complexes of Monomethyl Phosphate Stabilized by Hydrogen Bonding on Goethite (Alpha-FeOOH) Nanoparticles. *J. Colloid Interface Sci.* **2012**, *386*, 350–358, doi:10.1016/j.jcis.2012.07.042.
84. Guan, X.H.; Shang, C.; Zhu, J.; Chen, G.H. ATR-FTIR Investigation on the Complexation of Myo-Inositol Hexaphosphate with Aluminum Hydroxide. *J. Colloid Interface Sci.* **2006**, *293*, 296–302, doi:10.1016/j.jcis.2005.06.070.
85. De Groot, C.J.; Golterman, H.L. On the Presence of Organic Phosphate in Some Camargue Sediments: Evidence for the Importance of Phytate. *Hydrobiologia* **1993**, *252*, 117–126, doi:10.1007/BF00000133.

Supplementary Information

The Binding of Phosphorus Species at Goethite: A Joint Experimental and Theoretical Study

Prasanth B. Ganta,[1] Mohsen Morshedizad,[2] Oliver Küuhn,[1,3] Peter Leinweber,[2,3] and Ashour A. Ahmed,[1;3*]

[1] Institute of Physics, University of Rostock, Albert-Einstein-Str. 23-24, D-18059 Rostock, Germany
[2] Chair of Soil Science, University of Rostock, Justus-von-Liebig-Weg 6, D-18059 Rostock, Germany
[3] Department of Life, Light, and Matter (LLM), University of Rostock, Albert-Einstein-Str. 25, D-18059 Rostock, Germany

Correspondence: ashour.ahmed@uni-rostock.de; Tel.: +49381-498-6943

FIGURES

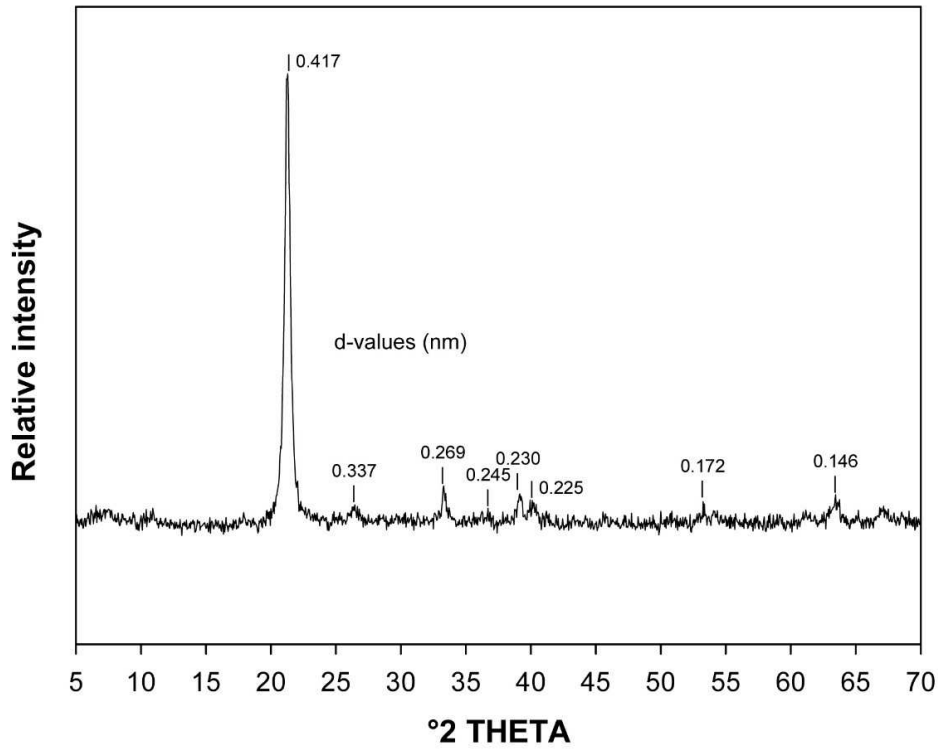


Figure S1: XRD pattern for pure goethite sample.

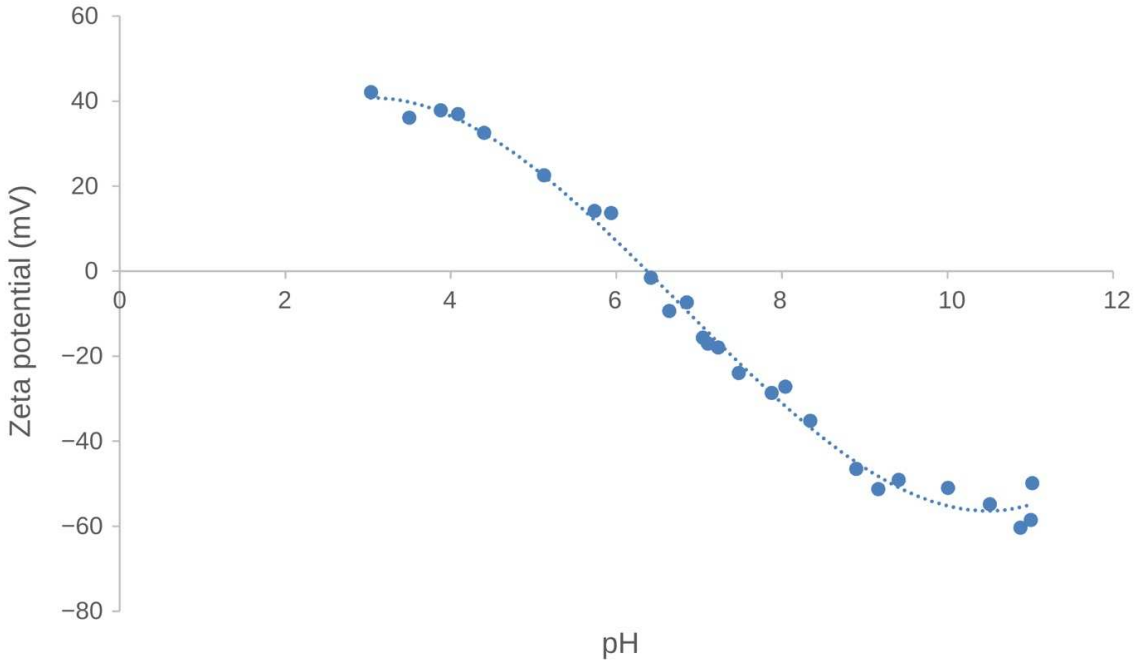


Figure S2: Effect of pH on electrophoretic zeta potential of goethite particles. Dashed line shows polynomial fitting to all data points representing the PZC of 6.3 (R^2 = 0.99).

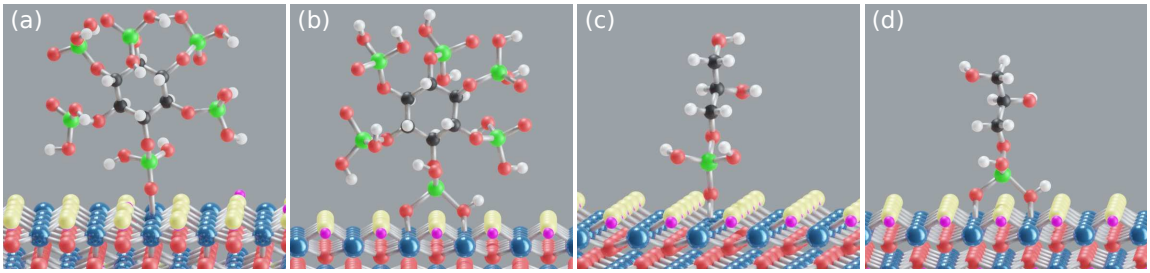


Figure S3: Initial motifs of IHP: **M**, **B** motifs (a,b) and GP **M**, **B** motifs (c,d).

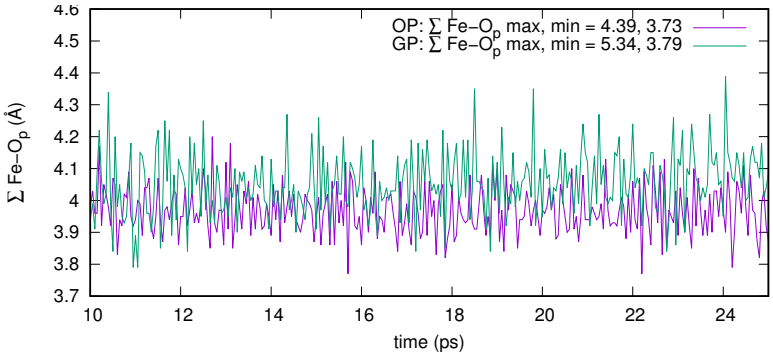


Figure S4: Sum of $Fe3O_P$ bond lengths observed in goethite3OP and goethite3GP **B** motifs.

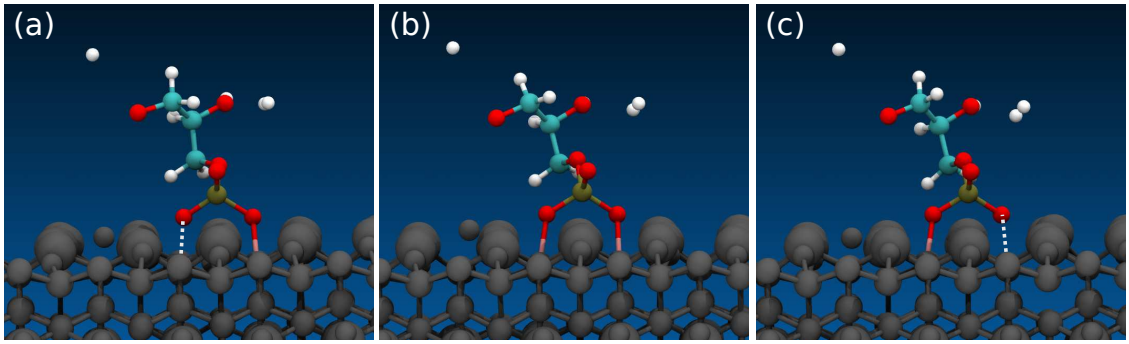


Figure S5: Seesaw movement of the bound GP's phosphate group to the goethite surface for the **B** motif case. (a) and (c) show momentarily elongated Fe3O bonds (left and right bonds, respectively) passing through a more stable **B** motif as shown in (b).

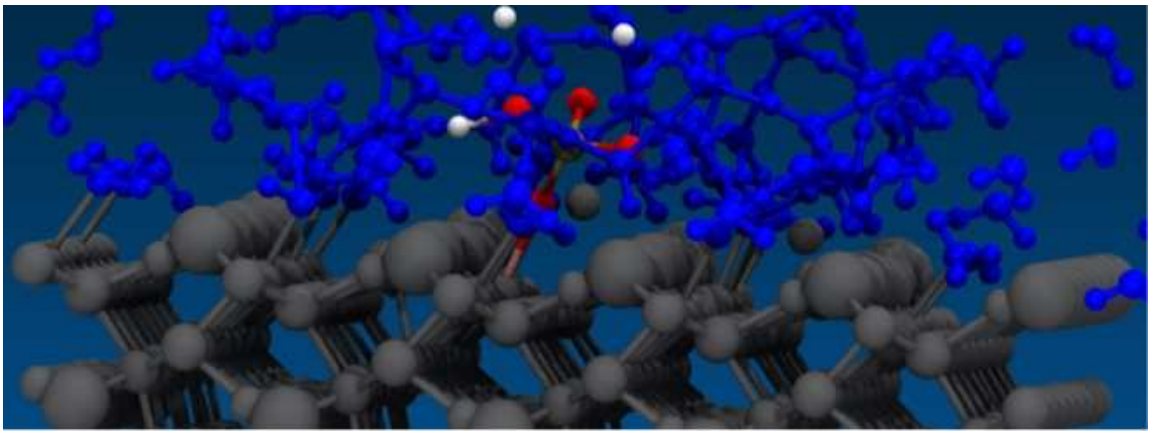


Figure S6: Multiple $Fe3O_{water}$ **M** motifs formed between water oxygen atoms and goethite surface Fe atoms.

Publication 8

Ashour A. Ahmed, M. Morshedizad, O. Kühn, P. Leinweber. Deciphering competitive interactions: Phosphate and organic matter binding on goethite through experimental and theoretical insights. Sci. Total Environ. **2024**, 940, 173510.

Contribution: Ashour A. Ahmed is credited with conceptualization, conducting the modeling work, all experimental and modeling analysis and interpretation, methodology development, visualization, and writing the original manuscript. Ashour A. Ahmed, Oliver Kühn, and Peter Leinweber are responsible for funding acquisition, reviewing, and editing the manuscript. Ashour A. Ahmed, along with the co-authors, has discussed and interpreted the results and contributed to writing, reviewing, and editing the manuscript.

URL: https://doi.org/10.1016/j.scitotenv.2024.173510

QR:



Reproduced with the permission of Elsevier

Science of the Total Environment 940 (2024) 173510

Contents lists available at ScienceDirect

Science of the Total Environment

journal homepage: www.elsevier.com/locate/scitotenv

Deciphering competitive interactions: Phosphate and organic matter binding on goethite through experimental and theoretical insights

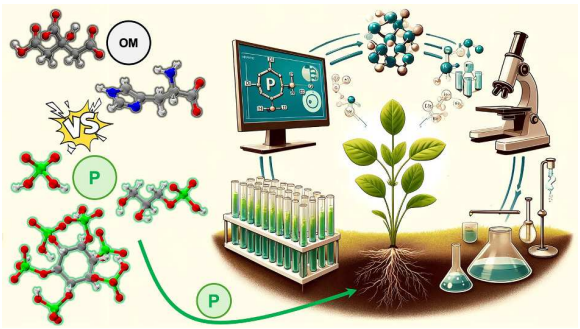
Ashour A. Ahmed [a,*], Mohsen Morshedizad [b], Oliver Kühn [a], Peter Leinweber [b]

[a] Institute of Physics, University of Rostock, Albert-Einstein-Str. 23-24, D-18059 Rostock, Germany
[b] Chair of Soil Science, University of Rostock, Justus-von-Liebig-Weg 6, D-18059 Rostock, Germany

HIGHLIGHTS

- OM affects P adsorption at the goethite-water interface, influenced by multiple factors.
- OP adsorption is highly inhibited by OM, especially with citrate covering the surface.
- OM's impact on GP adsorption varies with GP concentration levels.
- Electrostatic interactions regulate P-OM competition at the goethite surface.
- Computational chemistry is crucial for understanding P binding and mobility.

GRAPHICAL ABSTRACT



ARTICLE INFO

Editor: Daniel Alessi

Keywords:
Phosphates
P adsorption
Organic matter coadsorption
Mineral surfaces
Molecular modeling
MD simulations

ABSTRACT

The adsorption of phosphorus (P) onto active soil surfaces plays a pivotal role in immobilizing P, thereby influencing soil fertility and the filter function of soil to protect freshwater systems from eutrophication. Competitive anions, such as organic matter (OM), significantly affect the strength of this P-binding, eventually controlling P mobility and release, but surprisingly, these processes are insufficiently understood at the molecular level. In this study, we provide a molecular-level perspective on the influence of OM on P binding at the goethite-water interface using a combined experimental-theoretical approach. By examining the impact of citric acid (CIT) and histidine (HIS) on the adsorption of orthophosphate (OP), glycerol phosphate (GP), and inositol hexaphosphate (IHP) through adsorption experiments and molecular dynamics simulations, we address fundamental questions regarding P binding trends, OM interaction with the goethite surface, and the effect of OM on P adsorption. Our findings reveal the complex nature of P adsorption on goethite surfaces, where the specific OM, treatment conditions (covering the surface with OM or simultaneous co-adsorption), and initial concentrations collectively shape these interactions. P adsorption on goethite exhibits a binding strength increasing in the order of GP < OP < IHP. Crucially, this trend remains consistent across all adsorption experiments, regardless of the presence or absence of OM, CIT, or HIS, and irrespective of the specific treatment method. Notably, OP is particularly susceptible to inhibition by OM, while adsorption of GP depends on specific OM treatments. Despite being less sensitive to OM, IHP shows reduced adsorption, especially at higher initial P concentrations. Of significance is the strong inhibitory effect of CIT, particularly evident when the surface is pre-covered, resulting in a

* Corresponding author.
E-mail address: ashour.ahmed@uni-rostock.de (A.A. Ahmed).

https://doi.org/10.1016/j.scitotenv.2024.173510
Received 21 March 2024; Received in revised form 21 May 2024; Accepted 23 May 2024
Available online 26 May 2024
0048-9697/© 2024 The Authors. Published by Elsevier B.V. This is an open access article under the CC BY-NC-ND license (http://creativecommons.org/licenses/by-nc-nd/4.0/).

substantial 70 % reduction in OP adsorption compared to bare goethite. The sequence of goethite binding affinity to P and OM underscores a higher affinity of CIT and HIS compared to OP and GP, suggesting that OM can effectively compete with both OP and GP and replace them at the surface. In contrast, the impact of OM on IHP adsorption appears insignificant, as IHP exhibits a higher affinity than both CIT and HIS towards the goethite surface. The coverage of goethite surfaces with OM results in the blocking of active sites and the generation of an unfavorable electric potential and field, inhibiting anion adsorption and consequently reducing P binding. It is noteworthy that electrostatic interactions predominantly contribute more to the binding of P and OM to the surface compared to dispersion interactions.

1. Introduction

Phosphorus (P) is indispensable for all life forms, and its efficient utilization in fertilizers is essential for sustaining a rapidly growing human population (Maciá, 2005). The affinity of soil for P adsorption, alongside the capacity and strength of this process, significantly influences P immobilization. This significantly affects soil fertility and the fate of P in natural environments such as transfer from soil to freshwater systems, where P accelerates eutrophication (Ahmed et al., 2023; Andersen et al., 2015; Roy et al., 2017; Tisdale and Tisdale, 1993; Y. T. Wang et al., 2016). These aspects are significantly influenced by the diverse interactions of P with soil constituents involving free metal ions (Gros et al., 2019; Urrutia et al., 2013), soil minerals (Ahmed et al., 2019; Ganta et al., 2021; Kruse et al., 2015; Kubicki et al., 2012; Liu et al., 2022), and soil organic matter (Ahmed et al., 2018a; Debicka et al., 2023; Gros et al., 2017). Among these constituents, mineral surfaces such as Fe- and Al-(oxyhydr)oxides, calcium phosphates, silicates, and carbonates exhibit a strong affinity for binding phosphates (Bellier et al., 2006; Liu et al., 2012; Minamisawa et al., 2022; Okano et al., 2013; Tunesi et al., 1999). Notably, Fe- and Al-(oxyhydr)oxides play a pivotal role as the principal adsorbents of phosphates in soils (Borggaard, 2001; Borggaard et al., 2004; Elzinga and Sparks, 2007; Zhong et al., 2007). The high affinity of phosphates for these oxides stems from their ability to form stable covalent bonds with the surfaces of these oxides, termed inner-sphere surface complexes (Ahmed et al., 2019; Dimirkou et al., 2002; Kruse et al., 2015; Y. T. Wang et al., 2016). Among these oxyhydroxides, goethite (α-FeOOH) stands out as the most prevalent pedogenic reactive ferric iron Fe(III) mineral and plays a critical role in P fixation in soils (Arai and Sparks, 2007; Chitrakar et al., 2006; Cornell and Schwertmann, 2003; Tsao et al., 2011).

Considerable experimental and theoretical research endeavors have been directed towards exploring the mechanisms involved in the adsorption and binding of phosphates to oxyhydroxides and particularly the goethite surface. Examples of such studies include those by Ahmed et al. (2023), Amadou et al. (2022), Antelo et al. (2005), Arroyave et al. (2018), Boukemara et al. (2016), Luengo et al. (2006), and Y. T. Wang et al. (2016). These studies, along with others, aimed to clarify the impact of key factors such as the type, nature, and molecular configuration of both the phosphate and the adsorbent (Ognalaga et al., 1994; Ruttenberg and Sulak, 2011; Yan et al., 2014), P concentration (Arroyave et al., 2018; Luengo et al., 2006), characteristics of mineral surfaces including their planes (Ahmed et al., 2019), surface crystallinity and morphology (Gypser et al., 2018), specific surface area, point of zero charge of the adsorbent surface (Strauss et al., 1997a, 1997b), binding motifs (Ahmed et al., 2019; Arai and Sparks, 2001; Kubicki et al., 2012; Tejedor-Tejedor and Anderson, 1990), water and solution pH (Ahmed et al., 2020; Arroyave et al., 2018; Gao and Mucci, 2001; Geelhoed et al., 1998, 1997; Strauss et al., 1997a), presence of background electrolytes with their respective ionic strengths (Barrow et al., 1980; Geelhoed et al., 1998, 1997), redox potential (Shaheen et al., 2022), and the presence of other competitive inorganic (Gao and Mucci, 2001; Geelhoed et al., 1997; Hongshao and Stanforth, 2001) and/or organic (Geelhoed et al., 1998; Guppy et al., 2005; Kubicki and Ohno, 2020) anions on the process and strength of P binding.

Regarding the role of OM in P adsorption, organic acids demonstrate a strong affinity to adsorb onto Al- and Fe-hydroxide surfaces, influencing various physicochemical properties of reactive surfaces. These properties include specific surface area, reactive OH groups, surface charge, and electrostatic properties, consequently altering the interactions between phosphates and the adsorption sites (Gu et al., 1994; Kaiser and Guggenberger, 2003; Yan et al., 2016). Moreover, sorption experiments, along with infrared (IR) and X-ray spectroscopy as well as Density Functional Theory (DFT) analyses, indicated that organic acids tend to form inner-sphere complexes under acidic conditions and outer-sphere complexes under basic conditions, highlighting the significant role of the hydrogen bonding interactions (Duckworth and Martin, 2001; Han et al., 2020). As a result, organic acids compete effectively with phosphates for adsorption onto the surface, leading to enhanced phosphate mobility and surface dissolution (Furrer and Stumm, 1986; Guppy et al., 2005; Han et al., 2020). Notably, Geelhoed et al. (1998) found that citrate adsorption decreased phosphate adsorption at the goethite surface at low pH. Moreover, Johnson and Loeppert (2006) found that organic acids effectively release adsorbed P from ferrihydrite, with the efficiency increasing in the order oxalate ~ malonate ~ succinate < tartrate < malate < citrate. Additionally, Antelo et al. (2007) and Fu et al. (2013) observed a significant decrease in P adsorption upon covering the goethite surface with humic acid (HA). Moreover, H. Wang et al. (2016) and Wang et al. (2015a, 2015b) reported that humic acids reduce the specific surface area and isoelectric point of iron oxides (goethite, hematite, and ferrihydrite), thereby significantly decreasing P adsorption. In contrast, Borggaard et al. (2005) reported a limited effect on P adsorption at aluminum oxide, ferrihydrite, and goethite upon covering the surfaces with soil-derived OM. In a recent long-term desorption study by Gypser et al. (2019), utilizing competitive inorganic and organic anions to release adsorbed P from Fe- and Al-hydroxides, it was found that P desorption increased in the order $CaCl_2$ < $CaSO_4$ < humic acid < citric acid. A further desorption study by Gypser et al. (2021) showed that goethite exhibited the highest desorption, followed by gibbsite and then ferrihydrite upon applying both organic and inorganic competitors. Furthermore, a joint experimental-theoretical approach by Kubicki and Ohno (2020) demonstrated that salicylate can replace adsorbed phosphate on the goethite surface.

Despite considerable efforts in the literature, the mechanism underlying the competition between phosphates and organic acids at reactive surfaces, particularly in soil environments, has not been fully understood, especially at the molecular level. This challenge is attributed to the limitations of current analytical techniques, coupled with the complex and heterogeneous nature of soil constituents (Dakora and Phillips, 2002; Han et al., 2020). Even for a specific mineral surface, variations in surface planes, crystallinity, morphology, saturation, and binding motifs further complicate the analysis (Ahmed et al., 2023). To address this gap and tackle this complexity, a joint approach involving sorption experiments and molecular dynamics (MD) simulations (Ahmed et al., 2023; Kubicki, 2016; Osman et al., 2023) is proposed offering a promising avenue for gaining deeper insights into the nature of the interaction between each P and OM species with the adsorbent surface. Therefore, the primary objective of the present study is to investigate the impact of OM on P adsorption and the competitive interactions between OM and P through a combined experimental-

theoretical approach. This contribution delves into the adsorption behavior of three distinct phosphate molecules involving orthophosphate (OP), glycerol phosphate (GP), and inositol hexaphosphate (IHP) on the goethite surface under controlled conditions, including constant pH and ionic strength. These phosphates are selected for their prevalence in both natural and agricultural soil environments and for their distinct chemical structures and properties, including inorganic versus organic phosphates, monophosphate versus multi-phosphate, and various functional groups associated with organic phosphates. This selection facilitates the investigation of a broad spectrum of P compounds, encompassing different levels of complexity and significance in soil and environmental chemistry. For each phosphate molecule, three different adsorption scenarios are considered involving the adsorption onto bare goethite, adsorption onto goethite covered with OM, and simultaneous co-adsorption of P and OM onto bare goethite. This investigation utilizes two common soil OM compounds, citric acid (CIT), and histidine (HIS) (Negassa et al., 2008; Werdin-Pfisterer et al., 2012; Westergaard Strobel et al., 1999), to elucidate the underlying mechanisms.

It should be highlighted that the unique aspect of this study lies in its combination of experimental and theoretical approaches, providing molecular-level insights into how OM influences P adsorption on goethite surfaces. By examining the complex interactions between different types of OM and P, the findings will elucidate how OM variants, treatment conditions, and initial P concentrations impact P mobility and soil fertility. Furthermore, this research will uncover the significant role of electrostatic environments and P-OM complexes in either enhancing or inhibiting P adsorption, offering new perspectives for sustainable soil fertility management.

2. Materials and methods

2.1. Goethite preparation

Goethite was prepared according to (Dultz et al., 2018), where a 10 M NaOH solution was added to a 0.5 M $FeCl_3$ solution ($FeCl_3.6H_2O$, Merck AG) with stirring continuously to bring the pH to 12. The resulting material was aged for 120 h at 55 °C to be converted to goethite. Then the suspension was subjected to pH adjustment to 6 by adding 0.1 M HCl and followed by centrifugation-washing cycles with distilled water until the electrical conductivity was lower than 10 μS cm^{-1}. The prepared goethite was freeze-dried and stored as a powder for further analysis and experiments. For details about the purity, crystallinity, particle size, and specific surface area of goethite, refer to our earlier investigation by Ganta et al. (2021).

2.2. Reagents

All studied OM (citric acid (CIT): $C_6H_8O_7$; L-histidine (HIS): $C_6H_9N_3O_2$) and P compounds (potassium dihydrogen phosphate (orthophosphate (OP)): KH_2PO_4, α-glycerol phosphate (GP): $C_3H_9O_6P$, and myo-inositol hexaphosphate (IHP): $C_6H_{18}O_{24}P_6$) used in the experiments were of analytical grade chemicals and purchased from Carl Roth GmbH and Sigma-Aldrich, respectively. Working solutions were prepared fresh daily by adding accurate quantities of reagents to the water solution of 0.01 M $CaCl_2$ as a background electrolyte.

2.3. Adsorption experiments

The adsorption experiments were conducted using three distinct approaches: 1. Single-component adsorption: In this approach, we employed pure goethite as an adsorbent for OP, GP, and IHP (see Ganta et al. (2021)), 2. Organic matter-exposed goethite adsorption: Here, we examined the adsorption of various P compounds (OP, GP, and IHP) on goethite surfaces that had been previously exposed to (covered with) organic matter (OM) substances; and 3. Co-adsorption of P and OM: In this approach, we investigated the simultaneous adsorption of both P and OM at the bare surfaces of goethite. Two abundant OM substances present in the soil, each characterized by carboxylic groups that compete for binding with phosphates on the goethite surface, were utilized: citric acid (CIT) and L-histidine (HIS). CIT, a common low-molecular-weight organic ligand primarily derived from plant root exudations or organic matter decomposition (Kpomblekou-A and Tabatabai, 2003), leverages its hydroxyl and carboxyl active groups to influence phosphorus availability through processes such as ligand exchange, chelation, and complexation reactions (Drouillon and Merckx, 2003). HIS, another OM substance, incorporates carboxylic and amino groups, offering the potential to competitively bind with phosphates on the goethite surface.

In the first set of adsorption experiments, we prepared a 250 mM P L^{-1} stock solution for each P reagent (OP, GP, and IHP) in a 0.01 M $CaCl_2$ solution. A 20 mg sample of goethite was placed in a 50 mL centrifuge tube and equilibrated with 40 mL of each of ten different initial P concentrations (ranging from 0 to 5 mM P L^{-1}, in particular, 0, 0.05, 0.1, 0.15, 0.2, 0.3, 0.5, 1, 2, 3, and 5 mM P L^{-1}), achieved by dilution of the P stock in a 0.01 M $CaCl_2$ solution with a pH value of 5. After a 24-h equilibrium period at 25 °C under end-over-end shaking at 20 rpm, samples were centrifuged at 4500 *g* for 15 min. The P content in the filtered supernatant was quantified using inductively coupled plasma-optical emission spectroscopy (ICP-OES) at a wavelength of 214.914 nm.

In the second series of experiments, P adsorption isotherms were determined after the equilibrium adsorption of OM compounds to goethite. To ensure a similar magnitude of OM coverage for the goethite surface, it was necessary to acquire the sorption coefficients of CIT and HIS. Like the P adsorption procedure, the same was repeated for CIT and HIS compounds as adsorbents. The only difference was that the addition of background electrolytes to OM suspensions was excluded. The C content in the supernatant was determined by a TOC analyzer (Dimatec Analysentechnik GmbH, 45,141 Essen, Germany). Based on the OM adsorption data, the equivalent C concentrations of CIT and HIS were extrapolated to achieve the same coverage of 500 μmol C g^{-1} goethite. Subsequently, a two-stage adsorption process was conducted with (1) equilibrating 20 mg of goethite with 40 mL of CIT/HIS solution for 24 h, centrifugation, and decanting the supernatant and (2) following the same P adsorption procedure using OP, GP, and IHP solutions as described above.

In the last series, a competition experiment was carried out with the addition of CIT and HIS reagents (similar concentrations related to the adsorption rate of 500 μmol C g^{-1}) to the background electrolyte (0.01 M $CaCl_2$ solution) and adjusting the pH value to 5. The P adsorption procedure was then repeated as described previously. It is noteworthy that all series of adsorption experiments were performed in triplicate and data were presented as the means of three repeats.

The sorption data were fitted to the Freundlich (Freundlich, 1907) and Langmuir (Langmuir, 1918) models. The equations representing the Freundlich (1) and Langmuir (2) isotherms are as follows:

$$Q_{ads} = K_f \, C_{eq}{}^{nf} \tag{1}$$

where Q_{ads} is the amount of adsorbate adsorbed per unit mass (or surface area) of adsorbent, C_{eq} is the adsorbate equilibrium concentration in solution, and K_f and n_f are the Freundlich unit capacity factor (sorption capacity) and non-linearity Freundlich exponent, respectively. Here, Q_{ads}, C_{eq}, and K_f are expressed in μmol m^{-2}, μmol L^{-1}, and mol^{1-nf} L^{nf} m^{-2}, respectively.

$$Q_{ads} = \left(Q_{max} \, K_l \, C_{eq}\right) / \left(1 + K_l \, C_{eq}\right) \tag{2}$$

where Q_{max} is the maximum amount of the adsorbate required to form a monolayer by having a complete saturation of all binding sites (μmol m^{-2}), K_l is the Langmuir adsorption constant (L μmol^{-1}) that is related to the sorption energy.

Non-linear regression was carried out for both adsorption isotherm equations. Moreover, the standard error of the regression (SER) for all data sets was calculated. More details about Freundlich and Langmuir

isotherms and the data fitting are provided in the Supporting information.

2.4. Molecular modeling and computational details

To model the binding/adsorption of phosphate at the goethite surface and investigate the influence of OM on this binding process at a molecular level, several molecular models were constructed. The overall molecular modeling approach employed in this study is illustrated in Fig. 1. Three different phosphates, namely OP (H_2PO_4), GP ($C_3H_8O_6P$), and IHP ($C_6H_{12}O_{24}P_6$), were considered to analyze the complexation reactions between each phosphate and the goethite surface in the presence of water (refer to Fig. 1). Each constructed phosphate-goethite-water complex model, exemplified in Fig. 1, comprises the following components: 1) the goethite surface, 2) a single adsorbed phosphate molecule on the surface, and 3) water molecules surrounding the phosphate-goethite complex. Moreover, two additional molecular models were designed to investigate the binding behavior and strength of OM with the goethite surface. Here, each model featured a single OM molecule, either CIT or HIS, instead of the phosphate molecule in the case of P-goethite-water models.

Furthermore, models were developed that incorporated a one-to-one ratio of P to OM at the goethite surface to investigate the competition between P and OM towards their interaction with the goethite surface. Specifically, for CIT, molecular models were created, including 1OP-1CIT-goethite, 1GP-1CIT-goethite, and 1IHP-1CIT-goethite. Similarly, analogous molecular models were established for HIS. For each 1P:1OM pair, two molecular models were considered. One model placed the 1P-1OM complex directly on the goethite surface, while the other positioned the 1P-1OM complex in the bulk solution, away from the goethite surface.

For each complex involving P-goethite, OM-goethite, and 1P:1OM-goethite, the chosen goethite surface is the 100 surface (according to the Pnma space group), recognized as one of the most prevalent surface planes in soil systems (Cornell and Schwertmann, 2003; Rakovan et al., 1999). This goethite surface plane is modeled by replicating the goethite unit cell (lattice constants a = 9.95, b = 3.01, and c = 4.62 Å) twice in the x-direction, twelve times in the y-direction, and eight times in the z-direction. This results in a supercell of dimensions x = 19.9, y = 36.12, and z = 36.96 Å, composed of 3072 atoms (768 Fe, 768 O, and 1536H atoms). The initial configurations of the P-goethite, OM-goethite, and 1P:1OM-goethite complexes are designed so that the phosphates (OP/GP/IHP) and OM (CIT and HIS) molecules, as well as 1P-1OM complexes, are nearby and bound to the goethite surface except for the cases of 1P-1OM complexes in the bulk solution. This design is based on insights from previous simulation studies (Ahmed et al., 2020, 2019, 2018b; Ganta et al., 2021, 2020a). To account for the influence of water on the P-goethite, OM-goethite, and 1P:1OM-goethite complexes, each modeled complex is solvated by water with a density of ≈ 1 g cm^{-3}. The water molecules were added perpendicular to the studied surface plane, extending to a height of ≈ 130 Å in the x direction. This results in a final supercell with dimensions x = 150, y = 36.12, and z = 36.96 Å.

Due to the substantial size of the P-goethite, OM-goethite, and 1P:1OM-goethite complexes being modeled (each comprising approximately 20 thousand atoms, including water), employing ab initio methods for simulation is computationally impractical (Kubicki, 2016; Ozboyaci et al., 2016). Consequently, the investigation of these models was conducted through molecular dynamics (MD) simulations utilizing an atomistic representation via force-field molecular mechanics. It is important to highlight that the present force-field-based simulations of the P binding process at goethite-water interfaces have been validated against corresponding QM/MM simulations that were previously

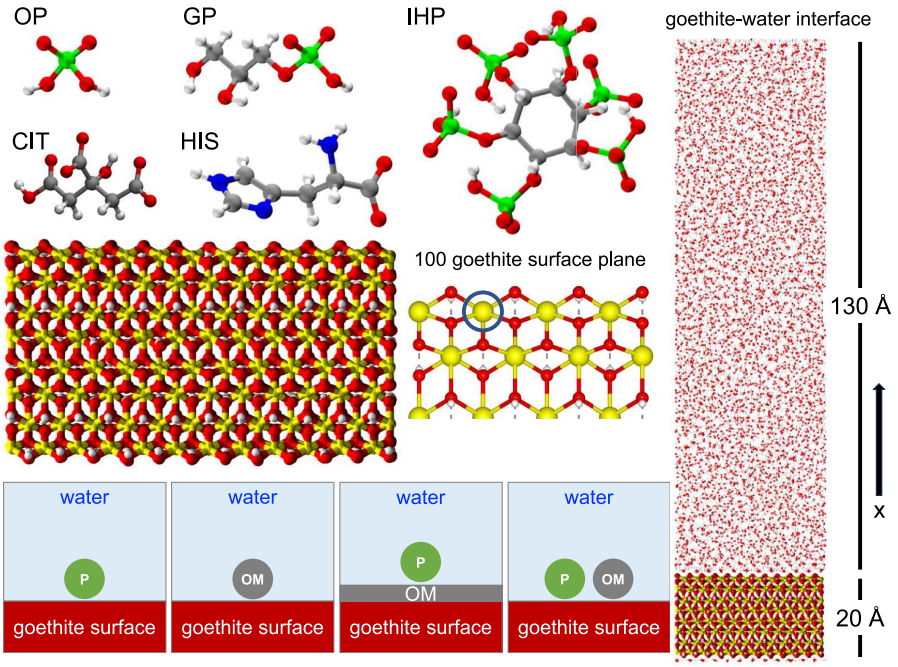


Fig. 1. Illustration of the molecular modeling approach examining the impact of organic matter (OM) on the binding of phosphorus (P) at the interface between goethite and water. It includes representations of the chemical and three-dimensional structures of modeled P compounds (OP, GP, and IHP) and OM compounds (CIT and HIS). The figure also presents two side views of the modeled 100-goethite surface plane (according to the Pnma space group), with one providing a comprehensive view and the other zooming in on the coordination number of surface Fe atoms, highlighted within a circle (dashed lines denote hydrogen bonds). Additionally, schematic representations of four adsorption scenarios are provided: P adsorption at the goethite surface, OM adsorption at the goethite surface, P adsorption at the goethite surface previously covered with OM, and simultaneous co-adsorption of P and OM at the goethite surface. Furthermore, the figure displays a representative example depicting the goethite-water interface. Different atoms are depicted in varying colors: H, C, N, O, P, and Fe atoms are visualized in white, red, gray, blue, green, and yellow, respectively.

validated against pure DFT calculations and experimental IR spectra (Ganta et al., 2020a, 2019). Here, the goethite surface is represented using the CLAYFF force field (Cygan et al., 2004), while water is modeled using the single point charge (SPC) water model (Berendsen et al., 1987), and P (OP/GP/IHP) and OM (CIT and HIST) are represented with the CHARMM force field (Jo et al., 2008). Both the CLAYFF and CHARMM force fields are compatible with the SPC water model. The simulations are conducted under periodic boundary conditions in all three dimensions.

For each molecular model, an energy minimization was carried out, followed by a two-step canonical (NVT, i.e., constant number of atoms N, volume V, and temperature T) MD simulation, consisting of approximately 5 ns for equilibration and 20 ns for the production trajectory that were utilized for MD analysis. The time step was set to 2 fs, and a straight cutoff of 12 Å was employed in conjunction with the Verlet neighbor list scheme. Temperature control was achieved using the velocity-rescaling thermostat with a coupling constant of 0.1 ps, maintaining the temperature at 300 K (Bussi et al., 2007). The interaction energy between every two subsystems of the P-goethite, OM-goethite, and 1P:1OM-goethite complexes in the presence of water was calculated along the production trajectory based on electrostatic Coulomb and van der Waals interactions. All calculations and corresponding analyses were conducted using the GROMACS program package, version 2019.4 (Abraham et al., 2015; Van Der Spoel et al., 2005).

To mimic the experimental pH condition (pH 5), the molecular models of P and OM were configured based on the most prevalent species for each molecular structure. Specifically, OP was represented as H_2PO4^-, GP as GP^-, IHP as IHP^{6-}, CIT as CIT^{2-}, and HIS as HIS^-. Additionally, all simulation boxes were neutralized with sodium ions (Na^+).

3. Results and discussion

3.1. Experimental results

3.1.1. General overview

The results of the adsorption experiments provide valuable insights into the interactions between phosphates and the goethite surface. Specifically, the P adsorption (per mol P) exhibits a consistent order of GP < OP < IHP across all experimental conditions, indicating a systematic variation in adsorption capacity (see Fig. 2 and Fig. S1 in the Supporting information). This pattern highlights IHP consistently having the highest adsorption capacity, while GP consistently shows the lowest values. Importantly, this trend consistently holds across all treatments employed in the present adsorption experiments, whether involving organic matter (OM), acetic acid (CIT), or histidine (HIS), or not, and irrespective of the specific treatment approach, including covering the surface with OM and simultaneous co-adsorption. This order remains stable despite variations in individual adsorption capacities, indicating a robust trend beyond the specific experimental conditions employed in this study.

The adsorption data presented here were subjected to fitting with various adsorption isotherm models. Among these models, Langmuir and Freundlich exhibited superior fitting performance, as evidenced by SER values. Notably, the Freundlich model consistently outperformed the Langmuir model in all adsorption experiments, demonstrating lower SER values, except for the GP adsorption on the goethite surface covered with CIT, as indicated in Table 1. A comprehensive discussion follows, incorporating precise numerical comparisons, focusing on the relevant Freundlich and Langmuir fitted parameters in the context of OP, GP, and IHP adsorption under various treatments. This discussion will be organized as follows: initially examining the impact of each goethite

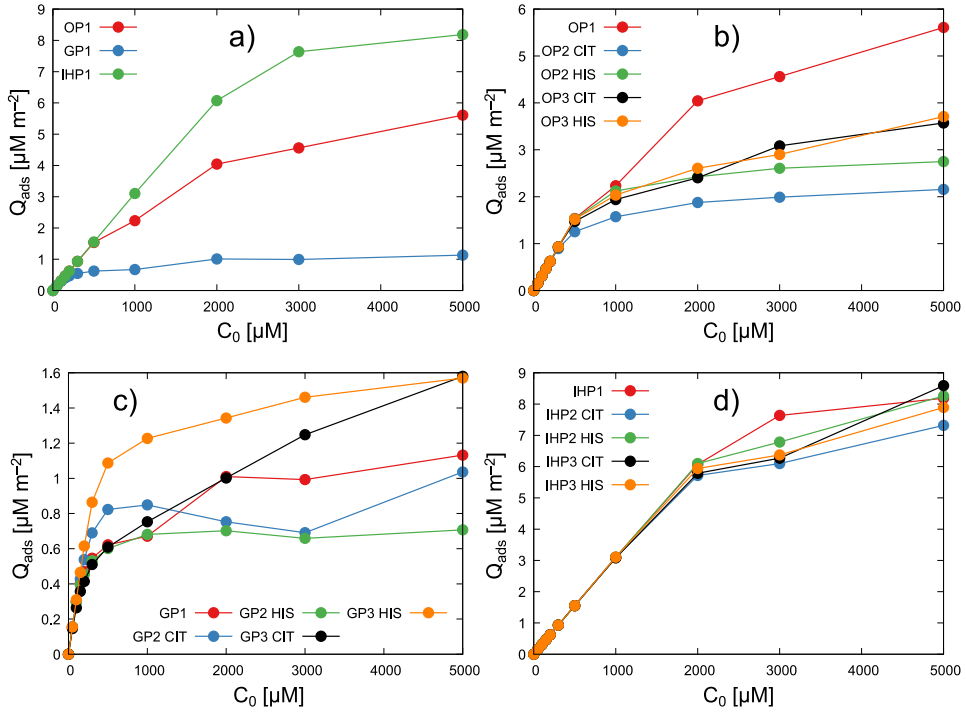


Fig. 2. The relationship between P adsorption per unit surface area (Q_{ads}, µmol m^{-2}) and the corresponding initial P concentration (C_0, µmol L^{-1}) for orthophosphate (OP), glycerol phosphate (GP), and inositol hexaphosphate (IHP) under various experimental conditions. Panel (a) illustrates OP, GP, and IHP adsorption on the bare goethite surface, while panels (b), (c), and (d) showcase P adsorption at the goethite surface with different experimental conditions for OP, GP, and IHP, respectively. The numerical symbols 1, 2, and 3 represent P adsorption on bare goethite, goethite covered with organic matter (OM), and P plus OM co-adsorption, respectively. This notation applies to OP, GP, and IHP. CIT and HIS denote adsorption in the presence of citric acid or histidine, respectively, whether through covering the surface coverage with OM or co-adsorption. Lines connect data points for clarity.

Table 1
Freundlich and Langmuir isotherms coefficients of adsorption of phosphates (OP, GP, and IHP) at goethite at different experimental conditions: adsorption of phosphates at pure goethite (P@G), adsorption of phosphates at covered goethite with organic matter (OM, P@CIT-G, and P@HIS-G), and simultaneous co-adsorption of phosphates and organic matter at goethite (P + CIT@G and P + HIS@G). OM here are citric acid (CIT) and L-histidine (HIS). K_f, K_l, and Q_{max} are expressed in $mol^{1-nf} L^{nf} m^{-2}$, L μmol^{-1}, and $\mu mol\ m^{-2}$, respectively.

Treatments	OP						GP						IHP					
	Freundlich			Langmuir			Freundlich			Langmuir			Freundlich			Langmuir		
	K_f	n_f	*SER*	Q_{max}	K_l	*SER*	K_f	n_f	*SER*	Q_{max}	K_l	*SER*	K_f	n_f	*SER*	Q_{max}	K_l	*SER*
P@G	0.685	0.259	0.521	6.252	0.002	0.660	0.208	0.199	0.074	0.949	0.018	0.164	4.660	0.074	1.233	8.049	0.070	1.234
P@CIT-G	0.624	0.150	0.194	1.851	0.076	0.310	0.365	0.112	0.123	0.831	0.093	0.108	2.822	0.120	0.708	6.471	0.209	0.758
P@HIS-G	1.202	0.100	0.284	2.487	0.202	0.434	0.295	0.110	0.067	0.658	0.078	0.079	4.654	0.068	1.252	7.593	0.113	1.275
P + CIT@G	0.751	0.181	0.335	2.861	0.035	0.551	0.096	0.327	0.055	1.399	0.003	0.185	2.376	0.160	0.770	7.162	0.088	0.915
P + HIS@G	0.829	0.171	0.455	2.863	0.093	0.571	0.599	0.113	0.194	1.308	0.324	0.253	4.020	0.080	1.254	7.270	0.049	1.276

treatment on the variations in adsorption among OP, GP, and IHP, and subsequently, analyzing how the different treatments influence the adsorption of each P molecular system (OP, GP, and IHP).

In the context of the Langmuir isotherm, the parameter Q_{max}, representing the maximum adsorption capacity, plays a pivotal role in assessing the adsorption strength and the surface's affinity. It signifies the quantity of adsorbate required to occupy all active binding sites and establish a complete monolayer saturation. The Q_{max} values exhibit an ascending order of GP < OP < IHP across all experimental conditions. In the absence of OM, IHP consistently exhibits markedly higher adsorption capacity than both OP and GP, see Table 1, Fig. 2, and Figs. S1–S2 in the Supporting information. Specifically, IHP's adsorption capacity is approximately 1.3 times that of OP and nearly 8.5 times that of GP. The sequence of adsorption (GP < OP < IHP) is consistent with the observations made by Amadou et al. (2022) for the adsorption of the same phosphates on the goethite surface. Similarly, Yan et al. (2014) noted a similar trend, with GP exhibiting the least affinity and IHP demonstrating the highest affinity when adsorbed on amorphous $Al(OH)_3$ surfaces. However, this trend was reversed when the same phosphates were adsorbed onto the gibbsite (Amadou et al., 2022) and the boehmite (Yan et al., 2014). Further, Yan et al. (2014) found that on α-Al_2O_3 surfaces, IHP had the least affinity, OP had the highest, and GP fell in between. These findings highlight the influence of both phosphate molecular structure and mineral surface type and crystallinity on the adsorption process. In this context, Yan et al. (2014) indicated that the mass-based phosphorus adsorption capacities increase with decreasing mineral crystallinity, following the sequence of α-Al_2O_3 < boehmite < amorphous $Al(OH)_3$.

3.1.2. Impact of OM treatments on P adsorption behavior

When covering the goethite surface with CIT, IHP's adsorption capacity is roughly 3.5 times that of OP and approximately 7.8 times that of GP. In the case of HIS, IHP's adsorption capacity is approximately 3.1 times that of OP and nearly 11.5 times that of GP. These findings emphasize a more pronounced influence of organic coatings on diminishing P adsorption capacities, particularly for GP in the presence of HIS and for OP in the presence of CIT. In simultaneous co-adsorption scenarios with CIT, IHP's maximum adsorption capacity is approximately 2.5 times that of OP and around 5.1 times that of GP. Similarly, with HIS, IHP's maximum adsorption capacity is approximately 2.5 times also that of OP and nearly 5.5 times that of GP. In conclusion, these comparisons relevant to the maximum adsorption capacity reveal no significant difference between CIT and HIS in simultaneous co-adsorption scenarios. However, a noteworthy reduction is observed in the case of OM coatings compared to the simultaneous co-adsorption of phosphates and OM.

Regarding the Freundlich isotherm, the combination of both the Freundlich unit capacity (K_f) and exponent (n_f) is crucial in assessing adsorption strength. Higher values for both K_f and the exponent n_f are indicative of more robust adsorption and elevated capacities. This holds for the exponent n_f, especially in scenarios where the equilibrium concentration (C_{eq}) is higher than 1. It should be noted that a minor alteration in the exponent tends to have a more pronounced impact on adsorption strength than changes in K_f alone. Thus, caution is advised when interpreting the fitted Freundlich isotherm parameters, emphasizing the need to consider both K_f and, particularly, n_f, especially when n_f varies significantly for data from different adsorption experiments. In the present study, K_f values exhibit an ascending order of GP < OP < IHP across all experimental conditions. This sequence implies that in the context of goethite surface adsorption, IHP demonstrates the most robust adsorption and possesses the highest capacity, followed by OP and GP. This comes in accord with the conclusion obtained by the Langmuir Q_{max} values. As for the Freundlich exponent (n_f), it is crucial to underscore that this exponent can offer insights not only into the adsorption strength but also into the adsorption mechanism. Specifically, n_f values below 1, observed in all present adsorption experiments, indicate that the sorption mechanism is primarily dominated by

adsorption rather than absorption (Ahmed et al., 2015, 2014). Moreover, n_f values below 1 imply that as the P concentration/loading increases, the binding energy between P compounds and the surfaces diminishes. In other words, for lower n_f values, the affinity of the goethite surface to adsorb/bind a P molecule decreases as the P concentration/loading rises. The validation and clarification of understanding and interpretation of both K_f and n_f in this manner are demonstrated in Fig. S3 in the Supporting information. A detailed interpretation of the various treatments is provided in the subsequent discussion.

In the absence of OM, the sequence of n_f values for the adsorbed phosphates on goethite (IHP (0.074) < GP (0.199) < OP (0.259), see Table 1) suggests a reduction in binding energy with increasing P loading, following the order OP < GP < IHP. This implies that the bare goethite surface exhibits an increasing affinity to adsorb P in the order IHP < GP < OP as the P concentration increases. Despite IHP demonstrating the most robust initial adsorption, the untreated goethite surface shows the highest affinity for OP at elevated P concentrations. This phenomenon can be attributed to the larger molecular size of IHP, which occupies and blocks more active adsorption sites on the goethite surface and experiences significant self-repulsion among IHP molecules, compared to the smaller OP molecules. Therefore, while IHP initially binds strongly, its large size and resultant steric effects reduce the overall number of available adsorption sites, making OP more favorable at higher concentrations.

For goethite covered with CIT, the n_f values sequence (GP (0.112) < IHP (0.120) < OP (0.150)) suggests that the affinity of the CIT-covered surface to adsorb/bind a P molecule increases with P concentration in the order GP < IHP < OP. Similar to the case of bare goethite, the CIT-covered surface exhibits the highest binding affinity for OP, but the lowest for GP at high P concentrations. This is indicative not only of the surface interaction but also of relatively stronger interactions between CIT and OP compared to GP. In the scenario of goethite covered with HIS, the n_f values sequence (IHP (0.068) < OP (0.100) < GP (0.110)) suggests that the affinity of the HIS-covered surface to adsorb/bind a P molecule increases with P concentration, following the order IHP < OP < GP. This implies that, at higher P concentrations, the HIS-covered surface exhibits a preference for GP binding, highlighting relatively stronger interactions between HIS and GP. This could substantiate the conclusion on the enhanced adsorption of GP on goethite in the case of co-adsorption with organic matter, specifically HIS.

In the context of co-adsorption of P with CIT on the goethite surface, the sequence of n_f values (IHP (0.160) < OP (0.181) < GP (0.327)) implies that the surface's affinity to adsorb/bind a P molecule rises with increasing P concentration, following the order IHP < OP < GP. This suggests that, at higher P concentrations, the surface demonstrates a preference for GP binding, emphasizing favorable interactions and complexation between CIT and GP at high GP concentrations. Similarly,

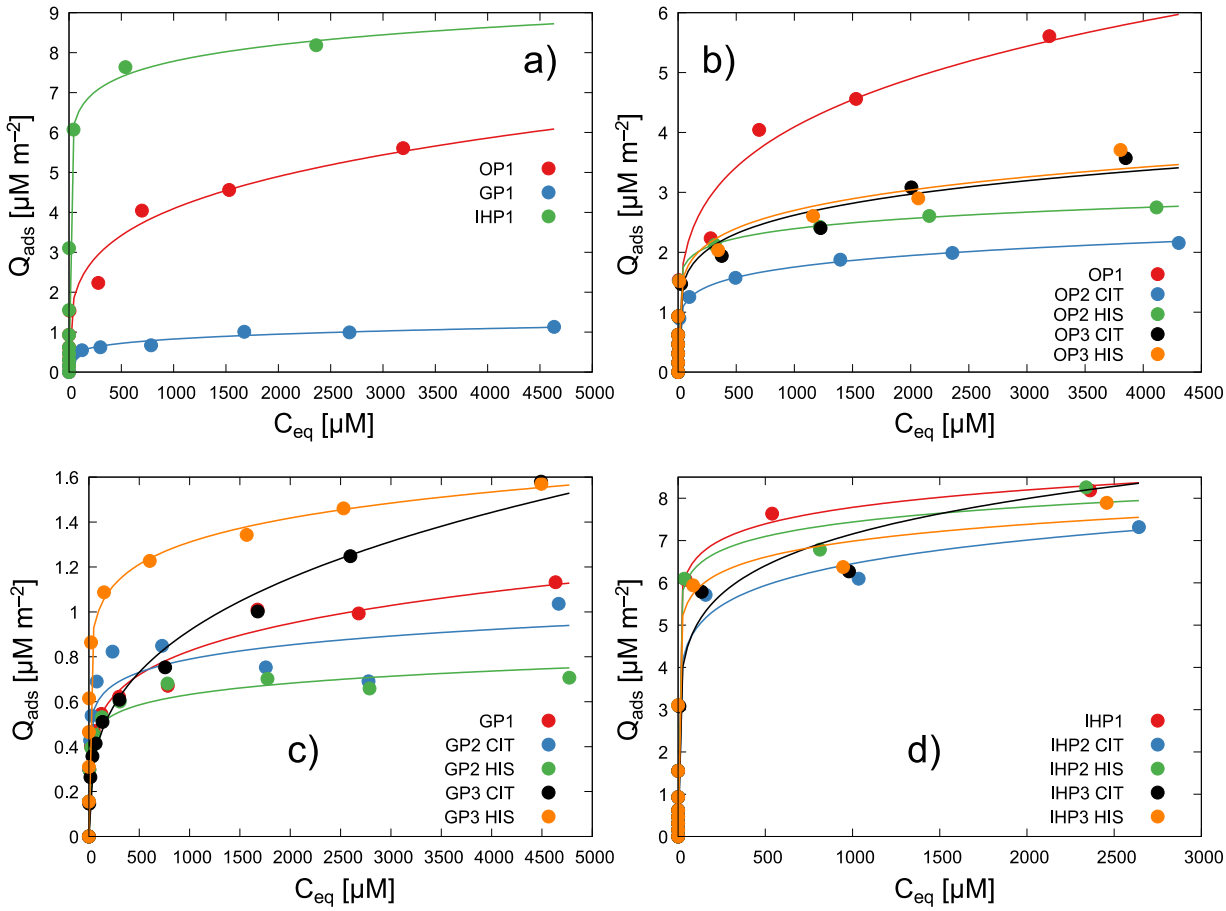


Fig. 3. The relationship between P adsorption per unit surface area (Q_{ads}, μmol m^{-2}) and the corresponding equilibrium P concentration (C_{eq}, μmol L^{-1}) in solution for OP, GP, and IHP under various experimental conditions fitted according to Freundlich isotherm. Panel (a) shows OP, GP, and IHP adsorption on the bare goethite surface, while panels (b), (c), and (d) showcase P adsorption at the goethite surface with different experimental conditions for OP, GP, and IHP, respectively. The numerical symbols 1, 2, and 3 represent P adsorption on bare goethite, goethite covered with organic matter (OM), and P plus OM co-adsorption, respectively. These annotations apply to OP, GP, and IHP. CIT and HIS denote adsorption in the presence of citric acid or histidine, respectively, whether through covering the surface coverage with OM or co-adsorption.

in the context of co-adsorption, but with HIS instead of CIT, the sequence of n_f values (IHP (0.080) < GP (0.113) < OP (0.171)) indicates that the surface's affinity to adsorb/bind a P molecule increases with P concentration in the order IHP < GP < OP. This implies that, at higher P concentrations, the surface exhibits a preference for binding OP followed by GP, highlighting favorable interactions and complexation of HIS with OP and GP at high P concentrations.

3.1.3. Impact of OM on OP adsorption

Let us discuss the adsorption patterns of OP on the goethite surface under two distinct scenarios: firstly, examining the impact of OM on OP adsorption when goethite is covered/coated with OM, and secondly, considering the simultaneous co-adsorption of OP and OM on goethite. Notably, when the goethite surface was covered with CIT, a pronounced decrease in OP adsorption was evident compared to the OP adsorption at bare goethite (see Fig. 3b). The maximum adsorption capacity decreased from 6.25 to 1.85 μmol m^{-2} (see Table 1), representing a reduction by factor 3.4. This translates to a 70 % decrease in the maximum adsorption capacity of OP to goethite when the surface is covered with CIT. This underscores the inhibitory impact of CIT on OP adsorption, likely attributed to CIT molecules occupying binding sites on the goethite surface, consequently restricting the availability of sites for OP adsorption. Likewise, the application of HIS to the goethite surface led also to a notable decrease in OP adsorption. In this instance, the maximum adsorption capacity decreased from 6.25 to 2.49 μmol m^{-2}, representing a reduction by factor 2.5 (~ 60 % decrease). Analogous to CIT, this decrease can be attributed to the strong adsorption affinity of HIS for the goethite surface, effectively competing with OP for the available binding sites and consequently diminishing OP adsorption.

The highlighted stronger inhibitory influence of CIT on OP adsorption is attributed to its higher affinity for surface sites. This is linked to the presence of more reactive functional groups in CIT compared to HIS. CIT possesses three carboxylate functional groups and one hydroxyl group, all of which are active and capable of binding to the goethite surface through ligand exchange and/or complexation reactions. In contrast, HIS contains one carboxylate and one amino group, providing it with the potential to bind to the goethite surface. Furthermore, under the current experimental conditions (pH 5), the increased negative charge of CIT (−2 for citrate) compared to HIS (−1) is notable for its involvement in binding to the positively charged active sites on the goethite surface through electrostatic interactions. This indicates that the nature of OM plays a crucial role in determining the degree of inhibition in P adsorption, with the presence of reactive and charged functional groups being a key determining factor.

The present results and their interpretation are consistent with those of Antelo et al. (2007), who noted a significant decrease in P adsorption when the goethite surface was coated with soil-derived humic acid (HA). Moreover, studies conducted by Dultz et al. (2018) and Kaiser and Guggenberger (2003) demonstrated that OM rich in acidic functional groups promotes aggregation with goethite, influencing specific surface area and micropore clogging. H. Wang et al. (2016) and Wang et al. (2015a) confirmed that the addition of humic acid reduces the specific surface area and isoelectric point of iron oxides, thereby affecting P adsorption. Furthermore, Fu et al. (2013) used Fourier transform infrared spectrometry (FTIR) to reveal fewer hydroxyl groups on goethite after soil-derived HA adsorption, resulting in inhibited adsorption and weaker P affinity. Their investigation illustrated that coating the goethite surface with HA can significantly reduce OP adsorption by as much as 27.8 %. Several other studies, including those of H. Wang et al. (2016), Wang et al. (2015a), and Weng et al. (2008) highlighted that adsorbed HA on iron oxides leads to a reduction in P adsorption. In contrast, Borggaard et al. (2005) reported a limited effect on P adsorption at aluminum oxide, ferrihydrite, and goethite upon covering the surfaces with soil-derived OM.

The simultaneous co-adsorption of OM and OP on the goethite surface led to a decrease in OP adsorption compared to the adsorption on bare goethite. This reduction was nearly identical for both CIT and HIS, with the maximum adsorption capacity decreasing by factor 2.2 (~ 54 % decrease) compared to the bare goethite case. This suggests similar competitive effects of both CIT and HIS when present simultaneously in the solution with OP. This may also imply comparable complexation reactions in the solution between CIT and OP, as well as HIS and OP. Furthermore, under both CIT and HIS treatments, OP exhibited a more significant reduction in adsorption when the goethite surface was covered with OM compared to the scenario where OP was co-adsorbed simultaneously with OM. This reduction can be attributed to the fact that in the covering scenario, OM (CIT and HIS) already bound to the goethite surface block most of the active binding sites, impeding OP adsorption to a greater extent compared to the competition between OM and OP in the co-adsorption scenario. Notably, this behavior is more pronounced in the case of CIT than HIS, indicating the greater affinity of CIT to undergo stronger adsorption at the goethite surface and block more active sites than the HIS case. Eventually, this emphasizes the substantial influence of surface modification, wherein the presence of OM, whether as a coating on the goethite surface or co-adsorbed with OP, plays a pivotal role in reducing OP adsorption. This highlights the significance of taking surface modifications into account when studying the behavior of P compounds in environmental systems.

The observed decrease in P adsorption, particularly concerning the co-adsorption of OM and OP, aligns with the findings of previous studies conducted by Sibanda and Young (1986), Antelo et al. (2007), and Fu et al. (2013). These studies suggested that OM derived from soil exhibited a competitive interaction with phosphate, leading to the inhibition of OP adsorption by goethite. For example, Sibanda and Young (1986) investigated the competitive effect of humic acid (HA) and fulvic acid (FA) on P adsorption on goethite, gibbsite, and two tropical soils at pH values of 4 and 7. They observed reductions in P adsorption when applying HA and FA across all cases, with this effect being more pronounced for P adsorption on goethite and gibbsite in the presence of HA at a lower pH (pH 4). Further, Antelo et al. (2007) studied the competitive impact of HA on phosphate adsorption onto goethite across varying pH and ionic strength conditions. Their findings revealed a significant influence of HA presence on P adsorption, with a more pronounced effect observed at lower pH levels compared to higher pH levels. This was attributed to the greater adsorption capacity of HA at the goethite surface under acidic conditions. At pH 4.5, HA could reduce P adsorption by as much as 45 %, while at pH 7.0, the reduction was up to 25 %. They also observed a relatively higher reduction in P adsorption when the goethite surface had previously adsorbed HA, in contrast to the simultaneous adsorption of P and HA. This aligns with our current observation regarding the stronger impact of covering the surface with OM on P (particularly OP) adsorption compared to the concurrent co-adsorption of P and OM. Moreover, Fu et al. (2013) explored a notable decrease in P adsorption when co-adsorbed with soil-derived HA. Similar to our findings, Antelo et al. (2007) also noted a larger reduction in P adsorption when the surface was pre-covered with HA compared to the simultaneous co-adsorption scenario. In contrast, Borggaard et al. (2005) observed only limited reductions in P adsorption on goethite, ranging from 4 % to 11.5 %, in the presence of HA during co-adsorption scenarios. These minor effects can be attributed to the low concentrations of HA used, which are comparable to naturally occurring dissolved organic carbon concentrations in mineral soils. Additionally, the nature and composition of the organic matter within the employed HA likely contribute to these limited effects. Furthermore, Borggaard et al. (2005) reported that the sequence of HA and phosphate addition whether they were added simultaneously, or HA was added before phosphate did not influence the amount of phosphate adsorbed by goethite.

3.1.4. Impact of OM on GP adsorption

For GP, the adsorption behavior at the goethite surface is complex and influenced by several factors, including initial P concentrations,

adsorption conditions or treatment type (coverage versus co-adsorption), and the type of OM (CIT versus HIS). Key observations reveal essential insights into this complexity. Generally, co-adsorption with OM (CIT or HIS) on the goethite surface enhanced GP adsorption compared to the bare goethite surface. The maximum adsorption capacity increased from 0.95 μmol m^{-2} for bare goethite to 1.40 and 1.31 μmol m^{-2} for co-adsorption with CIT and HIS, respectively, representing increases of 1.5 and 1.4 times for CIT and HIS cases. This corresponds to enhancements of 47 % and 38 % in the maximum adsorption of GP when co-adsorbed with CIT and HIS, respectively. This enhancement may be attributed to the potential formation of stable complexes between GP and OM (CIT and HIS), wherein these complexes exhibit a higher tendency to bind and adsorb onto the goethite surface compared to the individual GP scenario. A possible mechanism for this adsorption could be via OM (CIT and HIS) serving as bridges between the goethite surface and GP, thereby facilitating GP binding and the subsequent adsorption process. A comparison between CIT and HIS in the co-adsorption process with GP indicates higher and more favorable adsorption for GP in the presence of HIS at an initial GP concentration of up to 3 mM, suggesting a more favorable interaction/complexation for GP with HIS than with CIT. This is supported by the higher Freundlich unit capacity K_f in the HIS case (0.599) in comparison to the CIT scenario (0.096), see Table 1. However, a further increase in the initial concentration reverses this observation, enhancing GP adsorption in the presence of CIT compared to HIS and leading to a higher maximum adsorption capacity for CIT (1.40 μmol m^{-2}) compared to HIS (1.31 μmol m^{-2}) at high GP concentrations. This could be explained by the higher affinity of CIT for the goethite surface compared to HIS as observed for the OP case, thus stabilizing more GP molecules in the presence of CIT, especially at high GP concentrations. This is bolstered by the higher Freundlich exponent n_f in the CIT case (0.327) compared to the HIS scenario (0.113), as shown in Table 1. This points to a higher affinity of the surface to adsorb more GP molecules in the CIT case than in the HIS case, with an increase in P concentration.

Covering the goethite surface with OM (CIT or HIS) resulted in an overall decrease in GP adsorption compared to that on the bare goethite surface. This reduction can be attributed to the occupation of binding sites on the goethite surface by OM, limiting the availability of sites for GP adsorption. In general, the maximum adsorption capacity decreased from 0.95 μmol m^{-2} for bare goethite to 0.83 and 0.66 μmol m^{-2} for CIT and HIS-covered surfaces, respectively. This corresponds to a reduction by factors 1.15 and 1.44 for the CIT and HIS cases, representing reductions of approximately 13 % and 31 %, respectively. This highlights the inhibitory effect of OM, particularly HIS when the surface is pre-covered with OM before GP adsorption. A detailed examination of GP adsorption on the goethite surface covered with OM reveals a two-step adsorption process based on the initial concentration. At initial GP concentrations up to 1 mM, GP exhibits higher and more favorable adsorption in the presence of OM compared to GP adsorption on bare goethite. This suggests a favorable complexation for GP with OM, particularly CIT, enhancing GP adsorption. This is supported by an increase in the Freundlich unit capacity (K_f) for GP adsorption in the order of bare goethite (0.208) < goethite covered with HIS (0.295) < goethite covered with CIT (0.365), as indicated in Table 1. However, at initial concentrations exceeding 1 mM, this trend reverses, resulting in reduced GP adsorption in the presence of CIT and HIS, leading to lower maximum adsorption capacities at higher GP concentrations compared to the bare goethite case. This is supported by the lower Freundlich exponent (n_f) in the presence of CIT (0.112) and HIS (0.110) compared to the bare goethite scenario (0.199), as shown in Table 1. This reduction can be attributed to the increased blocking of active binding sites at the goethite surface at higher GP concentrations.

3.1.5. Impact of OM on IHP adsorption

In the case of IHP adsorption onto goethite surfaces, the impact of OM is notably less substantial compared to OP and GP. At low initial P concentrations, up to 2 mM, Fig. 2d depicts an insignificant alteration in IHP adsorption when covering the goethite surface with OM and simultaneous co-adsorption, either with CIT or HIS. Despite the observed reduction in IHP adsorption, especially at higher initial IHP concentrations (see Fig. 2d), this decrease is relatively small for both scenarios. For the goethite surface covered with CIT and HIS, it becomes evident that IHP exhibits lower adsorption when goethite is coated with CIT, particularly at elevated initial P concentrations (see Fig. 2d). This highlights the inhibitory effect of OM, particularly CIT when the surface is pre-covered with OM before IHP adsorption. This is evident in the maximum IHP adsorption capacity, which decreased from 8.05 μmol m^{-2} in the case of bare goethite to 6.47 and 7.59 μmol m^{-2} for CIT and HIS cases, respectively. This represents a reduction of 1.24 and 1.06 times for the CIT and HIS cases, corresponding to reductions of approximately 20 % and 6 %, respectively. For the IHP co-adsorption with individual CIT and HIS on the goethite surface, there is negligible difference between both cases. They resulted in maximum adsorption capacities of 7.16 and 7.27 μmol m^{-2} for co-adsorption with CIT and HIS, respectively. This corresponds to reductions of 11 % and 10 % in the maximum adsorption capacity for the CIT and HIS cases, respectively. Comparing the co-adsorption and covering the surface scenarios for HIS, a slighter reduction in the IHP maximum adsorption capacity (4 %) is observed in the case of co-adsorption. In contrast, a slightly lower reduction in the IHP maximum adsorption capacity (9 %) is observed in the case of goethite covered with CIT rather than undergoing simultaneous co-adsorption. Eventually, these findings highlight the limited impact of OM on altering the adsorption of IHP on goethite surfaces, especially at lower P concentrations. Nevertheless, at higher P concentrations, there are subtle variations in adsorption behavior depending on the type and application scenarios of OM, although these variations are relatively minor.

3.2. Simulation results

To validate our interpretations of the present experimental outcomes, MD simulations were conducted to address key questions: Does the order of P binding/adsorption at the goethite surface follow as GP < OP < IHP? Does organic matter (OM) exhibit significant binding to the goethite surface, leading to competition with P and consequent reduction in P binding? Does CIT bind more strongly to the goethite surface than HIS? What about the binding nature particularly for OM (electrostatic versus van der Waals interactions)? Does OM produce an unfavorable electrostatic field around the adsorbed OM molecule/molecules preventing/limiting the P adsorption? If OM competes with P and diminishes binding, how does OM (CIT and HIS) enhance GP adsorption in the co-adsorption scenario? Which exerts a stronger binding effect, IHP or OM? If IHP exhibits stronger binding, how does OM reduce IHP binding?

The present molecular modeling approach is focused on characterizing the relatively large model size of the P/OM-goethite-water complexes through MD simulations employing force-field-based molecular mechanics. Consequently, the current study will revolve around discussing the processes of P binding and the impact of OM, without delving into the intricacies of bond formation and dissociation. These aspects, extensively discussed in our previous studies, entailed a comprehensive understanding of the P-binding mechanism to soil constituents at the quantum mechanics level (Ahmed et al., 2023, 2020, 2019, 2018b; Ganta et al., 2021, 2020a, 2020b, 2019; Shaheen et al., 2022). Those studies aimed to elucidate the effects of various key factors on the P-binding process and its strength. These factors include the type and nature of P-containing compounds, the molecular configuration of both the phosphate and the adsorbent, characteristics of mineral surfaces including their planes and morphology, binding motifs, water and solution pH, and redox potential. For example, phosphates like OP and GP with single phosphate groups form stable monodentate (**M**) and bidentate (**B**) binding motifs. On the other hand, phosphates containing

multiple phosphate groups like IHP can bind to mineral surfaces through more than one phosphate group, forming various stable motifs like **M**, 2 **M**, and 3 **M**. The interaction energies of phosphates and water with goethite and diaspore surfaces increase in the order water < GP < OP < IHP (Ganta et al., 2021, 2020a), indicating that phosphates could displace water molecules at these surfaces, with IHP potentially replacing OP and GP. Additionally, water plays a critical role in controlling phosphate binding through hydrogen bond formation, dissociation at the surface, proton transfer processes, and covalent/coordination bond formation with the surface. Intramolecular hydrogen bonds between adjacent phosphate groups in IHP can induce strain into IHP-mineral complexes, affecting motif stability and leading to the dissociation of certain covalent bonds and instability of specific motifs.

3.2.1. *Characterization of the goethite-water interface*

To comprehend the binding mechanism of P and OM at the goethite

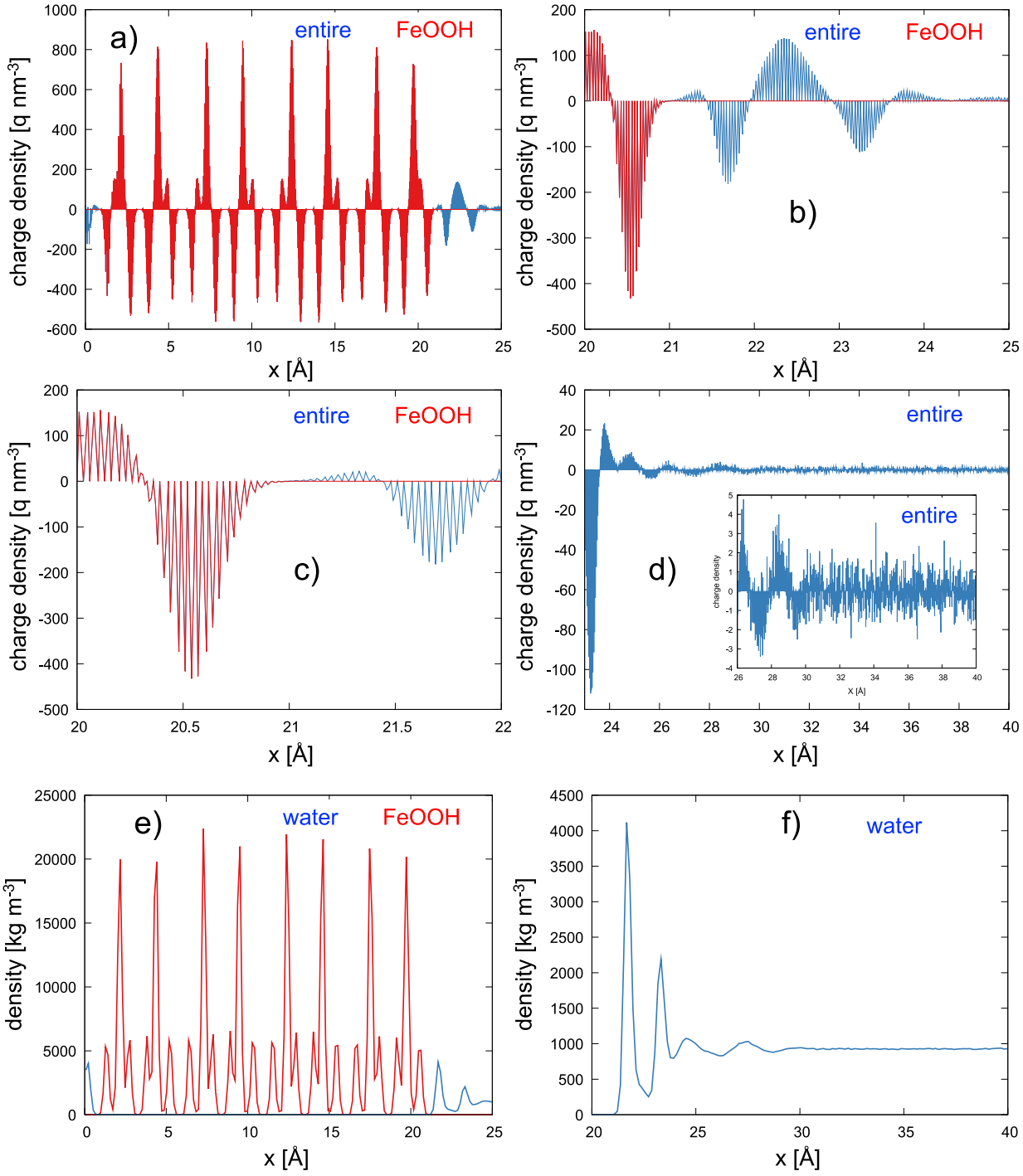


Fig. 4. Visualization of the distribution of charge density (a–d) along the axis perpendicular (x) to the interface for both the goethite surface (red) and the entire system (blue) at various distances within the simulation box. The simulation box spans from x = 0 to x = 150 Å, with goethite primarily positioned around x = 0–20 Å during the MD simulation. In addition, the mass density (e–f) along various distances in the simulation box is presented.

surface, as well as their competitive interactions, our initial focus will be on characterizing the goethite-water interface. Fig. 4 illustrates the distribution of charge density of a goethite-water molecular model along the x-axis of the simulation box, perpendicular to the goethite-water interface. It is important to note that the charge distribution is integrated over the other axes (y and z). In this representation, intense peaks with positive charges depicted in red correspond to Fe atoms of the goethite, while smaller peaks are attributed to H atoms of the goethite surface. Conversely, intense negative peaks depicted in red correspond to O atoms of the goethite surface. Among these peaks, the relatively smaller ones proximate to the H-peaks represent hydroxide ions (OH^-) of the goethite, whereas the relatively larger ones, farther from the H-peaks, correspond to non-protonated oxygen atoms of the goethite, i.e., O^{2-}. Observing the surface reveals termination with negatively charged OH^- (peak around 20.5 Å for O atoms), followed in the direction of the goethite bulk by two subsequent positively charged peaks around 20.1 Å (for H atoms) and 19.7 Å (for Fe atoms). This suggests the presence of a positively active site at the goethite surface capable of binding and adsorbing anions such as phosphates and carboxylates, despite the negatively charged O atoms at the surface top. Due to the surface termination with a negative charge, certain water molecules engage with the surface by aligning themselves with H atoms (positively charged) facing the surface within the Helmholtz layer, which generates the initial small positively charged peak around 21.3 Å, illustrated in blue in Fig. 4. Subsequently, the majority of water molecules near the surface reorient so that O atoms face the surface while H atoms face towards the bulk of the water. This leads to the emergence of the primary and largest negatively charged peak of water (O atoms) at the interface around 21.7 Å, succeeded by the largest positively charged peak of water (H atoms) around 22.4 Å. For further elaboration and clarification, this distribution of charge density along the goethite-water interface including the Helmholtz layer and the interpretation of peaks corresponding to Fe^{3+}, O^{2-}, and OH^- of goethite, and $O^{\delta-}$ and $H^{\delta+}$ of water are illustrated in Fig. S4 in the Supporting information. The strong electrostatic interaction between water and the surface at the interface, coupled with the presence of active sites at the surface, leads to a high density of water at the surface, decreasing in the direction of the water bulk, thus conforming to the normal distribution and density of liquid water (refer to Fig. 4b, d–f). For example, in Fig. 4e–f, water exhibits significantly high mass density near the surface, with the first layer reaching approximately four times the normal density of liquid water (about 4000 kg m^{-3}). The density decreases to around twice the normal density (2000 kg m^{-3}) in the second layer. Moving away from the surface, water density gradually decreases, reaching normal liquid density at approximately 10 Å from the surface.

The electric potential of the goethite-water system described above exhibits positive values along the x-axis, with peaks representing maximum positive charge densities observed at the positions of Fe atoms, as shown in Fig. 5a. This generally suggests the propensity of these Fe atoms to attract anions. Specifically focusing on the goethite surface without considering interfacial water (illustrated in red Fig. 5a), traversing away around the positions of Fe atoms results in a decrease in the electric potential and vice versa. However, for the entire system, i.e., in the goethite-water system, the electric potential progressively increases as moving from the bulk goethite towards the surface, with the highest potentials observed at the interface between the surface and water. Consequently, anions in the bulk water/solution are more likely to be strongly attracted to the surface due to the increasing positive potential. When moving from the goethite surface towards the bulk water and increasing the distance, the electric potential exhibits a linear increase, as depicted in Fig. 5a–b. This trend reflects the influence of the positively charged surface on the surrounding water molecules and the gradual accumulation of positive charge density towards the bulk water. The corresponding electric field which is the negative gradient of the electric potential along the x-axis of the simulation box is presented in Fig. 5c–d. It is important to note that the electric field points away from positively charged objects and towards negatively charged objects, with its magnitude directly proportional to the rate of change of the electric potential. In this regard, interpreting these findings in terms of chemistry suggests that at the goethite-water interface or in its vicinity, an attractive electric potential (electric field) is generated, facilitating the adsorption of anions like phosphates and carboxylates onto the surface.

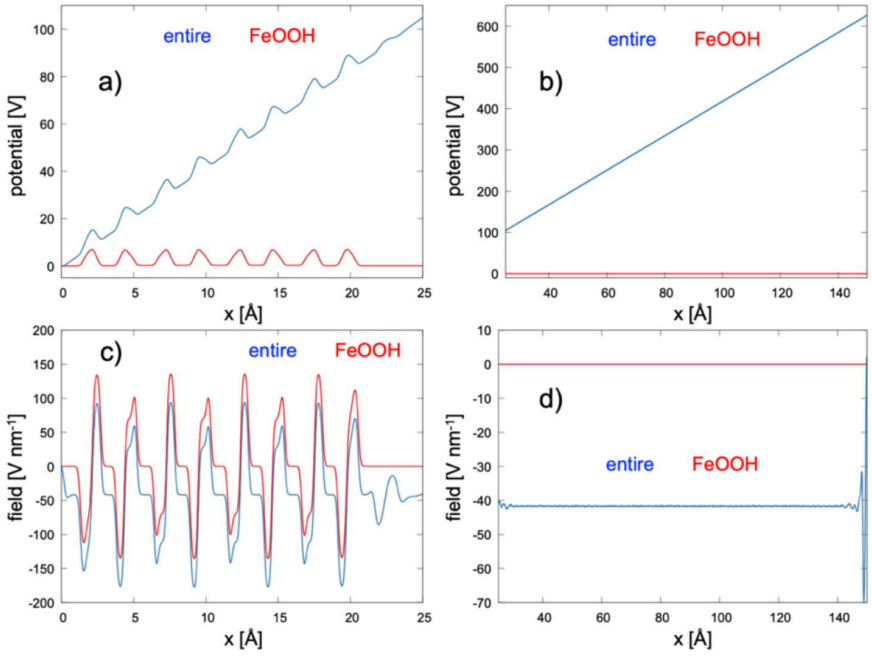


Fig. 5. The electric potential and corresponding electric field along the axis perpendicular (x) to the interface for both the goethite surface (depicted in red) and the entire system (depicted in blue) at different distances within the simulation box.

3.2.2. Single-molecule adsorption at the goethite-water interface

Moving to scenarios involving the adsorption of single P (OP, GP, or IHP) or OM (CIT or HIS) at the goethite-water interface, no significant differences are observed in the characteristics of the goethite-water interface across these various situations when compared to the case of the bare goethite-water interface. This is evident from various calculated properties observed at both the interface and within the bulk water. For instance, one can examine the electric potential, electric field, and density profiles along the simulation box, as depicted in Fig. 6, along with the radial distribution function of water shown in Fig. 10. This indicates a negligible impact on the goethite-water interface in the presence of individual P or OM entities at the surface, irrespective of their size, charge, or any other physical or chemical attribute. As a result, the goethite surface within these interfaces particularly in the region of the Helmholtz layer would similarly promote the favorable adsorption of additional anions from the bulk water, akin to the behavior observed at the bare goethite-water interface.

Regarding the binding of individual P and OM at the goethite-water interface, the dynamic configurations during the MD simulations, the center of mass motion and partial density along the simulation box perpendicular to the interface, minimum distance from the surface, and interaction energy and its contributing components, as well as hydrogen bonding with the surface and water, will be presented and discussed in the following sections.

The dynamic behavior of OP, GP, IHP, CIT, and HIS binding at the goethite-water interface was investigated using MD simulations over a 20 ns period for each case. Fig. 7 presents overlays of 100 snapshots taken at equidistant time intervals during the simulations, providing insights into the binding dynamics of these molecules. In addition, individual snapshots along the MD simulations showing the dynamic behavior of P and OM are provided in the Supporting information, see Figs. S5–S9. Fig. 7a–d depicts the binding behavior of OP and GP, showing that they initially bind to the goethite surface at the start of the simulations before diffusing towards the water bulk, suggesting a weak binding affinity to the surface. In contrast, both IHP and CIT (Fig. 7e–h and m–p) exhibit close contact with the surface and movement at the surface along its plane throughout the simulation duration, without diffusing into the bulk water. This suggests a strong binding affinity of IHP and CIT to the goethite surface. Additionally, HIS displays an intermediate behavior, remaining in close contact with the surface for more than half of the simulation time before exhibiting diffusion back and forth between the surface and the water bulk, see Fig. 7i–l. This suggests an intermediate binding affinity of HIS to the goethite surface, falling between the weakly bound cases of OP and GP and the strongly bound cases of IHP and CIT.

The observed binding tendencies of P and OM to the goethite surface, as discussed earlier, are corroborated by analyzing the calculated center of mass (COM) motion of OP, GP, IHP, CIT, and HIS along the x-axis of the simulation box throughout the MD simulation. The COM motion

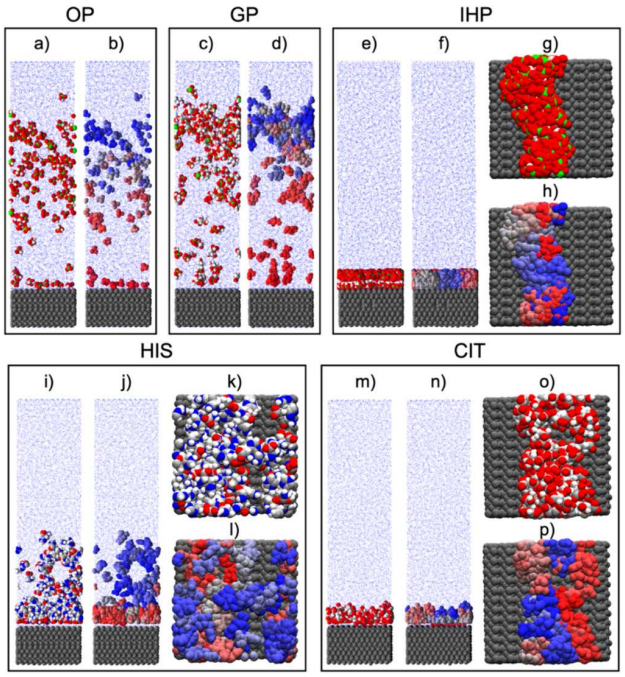


Fig. 7. Overlays of 100 snapshots captured at equidistant time intervals during MD simulations depicting the adsorption of each OP, GP, IHP, CIT, and HIS at the goethite surface. Side view overlays are provided for OP ((a) and (b)) and GP ((c) and (d)), while both side and top views are presented for the strongly bound IHP (side: (e) and (f), and top: (g) and (h)), HIS (side: (i) and (j), and top: (k) and (l)), and CIT (side: (m) and (n), and top: (o) and (p)). Each P and OM is represented in two styles. First ((a), (c), (e), (g), (i), (k), (m), and (o)), atoms are color-coded: H, C, N, O, and P atoms are portrayed in white, red, gray, blue, and green, respectively. Second ((b), (d), (f), (g), (i), (l), (n), and (p)), P and OM molecules transition from red (start of the simulation: 0 ns) to blue (end of the simulation: 20 ns), illustrating the dynamic behavior of P and OM at the goethite surface throughout the MD simulation.

reveals an intermediate level of movement for HIS along the x-axis compared to a higher degree of motion for OP and GP, and a lower degree for IHP and CIT, as depicted in Fig. S10a–b in the Supporting information. The trend in COM motion follows the sequence: IHP < CIT < HIS < OP < GP. This hierarchy suggests a binding affinity of the goethite surface to P and OM that increases in the order of GP < OP < HIS < CIT < IHP.

Furthermore, a similar trend was observed for the calculated minimum distances between each P or OM molecule and the goethite surface. In essence, these minimum distances provide insights into the proximity and interactions among different components of the molecular system

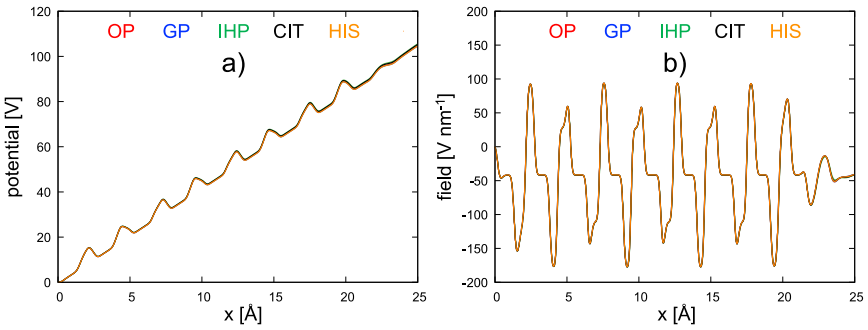


Fig. 6. The electric potential (a) and electric field (b) along the axis perpendicular (x) to the interface for the entire system within the simulation box. These MD simulations involve the individual adsorption of every single P (OP, GP, or IHP) or OM (CIT or HIS) molecule at the goethite surface.

throughout the simulation. Specifically, the minimum distance increased along the MD simulation in the sequence: IHP < CIT < HIS < OP < GP, as illustrated in Fig. S10c–d in the Supporting information. In the same context, distributions of each P and OM, along with accompanying Na^+ ions, along the x-axis of the simulation box are illustrated in Fig. 8 through their partial densities. Fig. 8a reveals that during the MD simulation trajectory, IHP, CIT, and HIS are predominantly located near the goethite surface, indicating their high affinity to bind to the surface. While both OP and GP exhibit peaks in proximity to the surface, their presence extends into the bulk water, suggesting a lower affinity to bind to the surface, particularly for GP. The partial densities of Na^+ ions accompanying P and OM confirm this observed behavior, see Fig. 8b. In conclusion, all these observations align consistently, indicating a rise in the binding affinity of the goethite surface to P and OM in the sequence: GP < OP < HIS < CIT < IHP, as evidenced by Figs. 7–8 and Fig. S10 in the Supporting information.

In terms of the interactions within each P/OM-goethite-water molecular model involving all components, our simulations indicate nearly identical water-water interactions with no significant variations observed among the molecular models containing P (OP, GP, and IHP) and OM (CIT and HIS) at the goethite-water interface, as depicted in the radial distribution function and the distribution of hydrogen bonds (HBs) in Fig. 9a–b. Here, water-water HBs are characterized as moderately strong, predominantly electrostatic, with donor-acceptor (D-A) distances ranging from 2.4 to 3.6 Å, centered around a maximum of 2.8 Å. Similarly, almost identical HBs with consistent strength and distribution are observed between the goethite surface and interfacial water molecules, see Fig. 9d. Nevertheless, contrary to the HBs observed between water molecules (water-water) and those formed between goethite and water (goethite-water), all P and OM species investigated in this study exhibit stronger HBs with water molecules, as depicted in Fig. 9c. Notably, among these species, IHP displays the most robust HBs, followed by CIT and OP, while GP and HIS demonstrate relatively weaker interactions. Specifically, the distributions of HBs observed for P and OM with water reveal peaks of D-A distances, with maxima at 2.62 Å for IHP, 2.68 Å for both OP and CIT, with CIT having higher intensity, and 2.73 Å for both GP and HIS, with GP displaying relatively higher intensity. Furthermore, the total number of HBs observed during the MD simulation for P and OM with water is tallied at each time step, as depicted in Fig. S8 in the Supporting information. On average, the number of these HBs fluctuates around 8.9 for OP, 11.0 for GP, 11.1 for HIS, 14.7 for CIT, and 29.4 for IHP. Analyzing the combination of the number of HBs with their strength reveals the highest affinity of IHP in its interaction with water, an intermediate affinity for CIT, and the lowest affinity for GP, HIS, and OP, particularly for the OP case. This finding aligns with the calculated interaction energy of each P or OM with the surrounding water molecules within a range of 11 Å, as depicted in Fig. 10. Eventually, all the observed HBs at the goethite-water interface in the presence of P and OM come in accord with the FTIR observations by Norén and Persson (2007) that highlighted the significant role of the HBs in the binding process at the goethite-water interface.

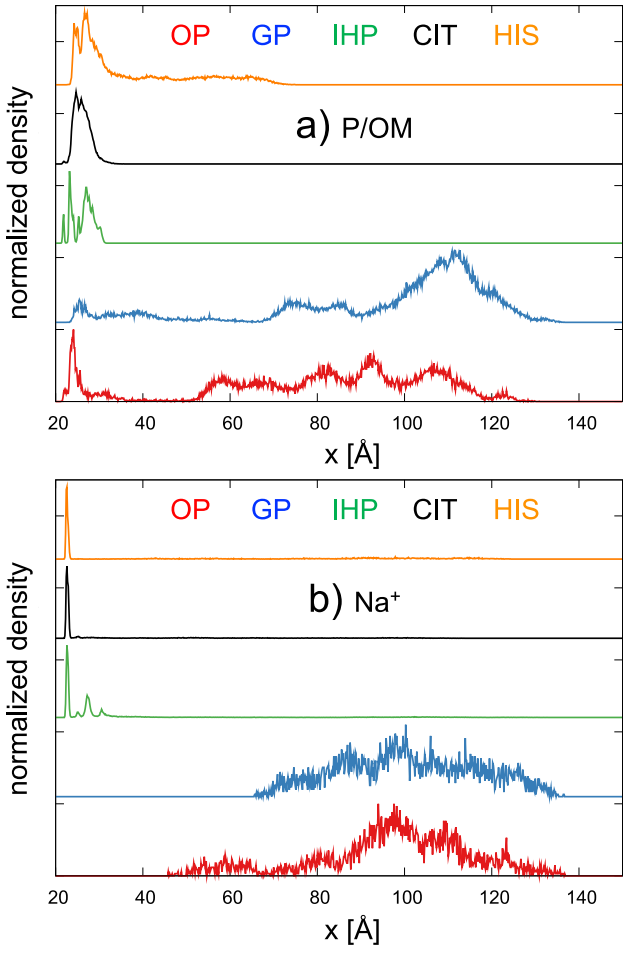


Fig. 8. The partial density of each OP, GP, IHP, CIT, and HIS (a), along with their corresponding accompanying Na^+ ions (b), along the axis perpendicular (x) to the interface throughout the entire simulation box. These MD simulations correspond to the individual adsorption of each OP, GP, IHP, CIT, and HIS at the goethite surface. Note: partial density indicates the probability of finding a particular particle in space.

The interaction energies provide crucial insights into the competitive binding behaviors of different P and OM compounds with goethite, offering valuable information for understanding P dynamics in the soil environment and thus managing soil fertility and. Based on the calculated interaction energies, the binding strength of P compounds (OP, GP, and IHP) and OM (CIT and HIS) with the goethite surface follows the order: GP (−0.5 kcal mol^{-1}) < OP (−4.8) < HIS (−21.9) < CIT (−31.4) < IHP (−93.5) (refer to Fig. 10a–b and Table S1 in the Supporting information). This hierarchy indicates that among the P compounds, IHP exhibits the strongest binding to the goethite surface, followed by OP, which binds more strongly than GP. The significant interaction energy of IHP (−93.5 kcal mol^{-1}) suggests a strong affinity for the goethite surface, likely due to its multi-phosphate structure, which provides multiple binding sites. OP, with an interaction energy of −4.8 kcal mol^{-1}, binds more strongly than GP, which has the weakest interaction energy of −0.5 kcal mol^{-1}. This observation is consistent with our previous quantum mechanics/molecular mechanics (QM/MM) results (Ganta et al., 2021), which also indicate a similar order of P binding affinity towards goethite. Furthermore, these findings are consistent with the results of current adsorption experiments involving OP, GP, and IHP at the goethite surface under diverse experimental conditions, which suggest a binding/adsorption hierarchy of GP < OP < IHP, as illustrated in Figs. 2a, 3a, and Figs. S1–S2 in the Supporting information. Moreover, CIT with an interaction energy of −31.4 kcal mol^{-1}, exhibits a stronger binding compared to HIS, which has an interaction energy of −21.86 kcal mol^{-1}. The strong interaction of CIT can be attributed to its multiple carboxyl groups, which can form multiple bonds with the surface.

It is worth highlighting that electrostatic Coulomb interactions predominantly contribute to the total interaction energies reported in Fig. 10, in contrast to the dispersion (in this case, Lennard Jones, LJ) interaction energy, see Figs. S12-S13 in the Supporting information. This predominance primarily stems from the repulsive component outweighing the attractive part of the LJ potential in the interaction between each P or OM and the goethite surface. This occurrence arises from the proximity of both P and OM compounds to the goethite surface, resulting in positive dispersion interaction energy. GP exhibits

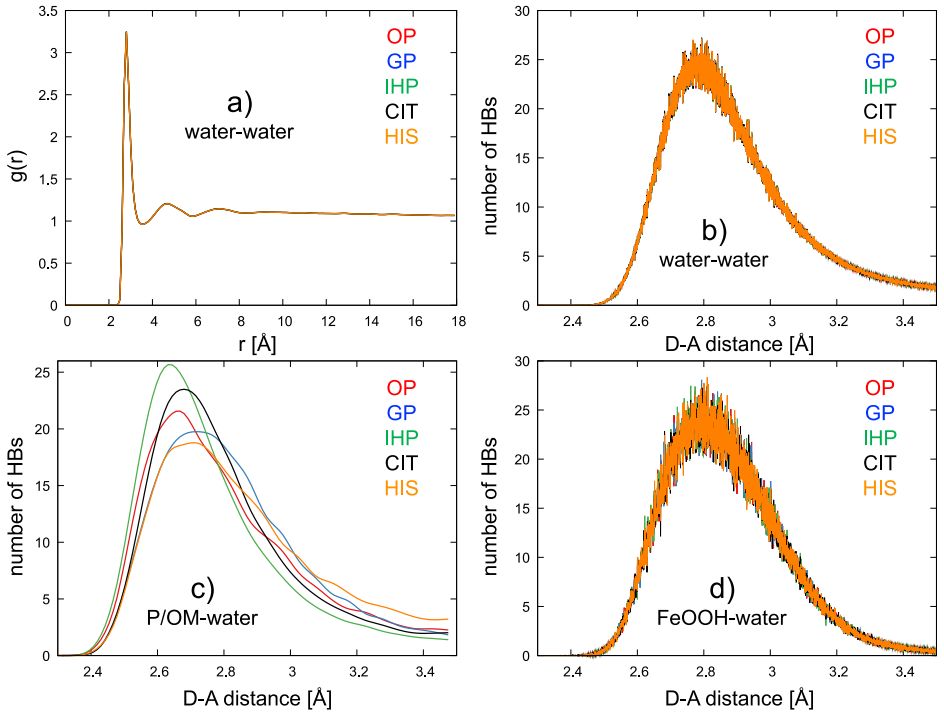


Fig. 9. The radial distribution function of water (a) and the number of hydrogen bonds (HBs) within water (b), between water and each of P and OM (c), and between the goethite surface and water (d) for the adsorption of each OP, GP, IHP, CIT, and HIS at the goethite surface.

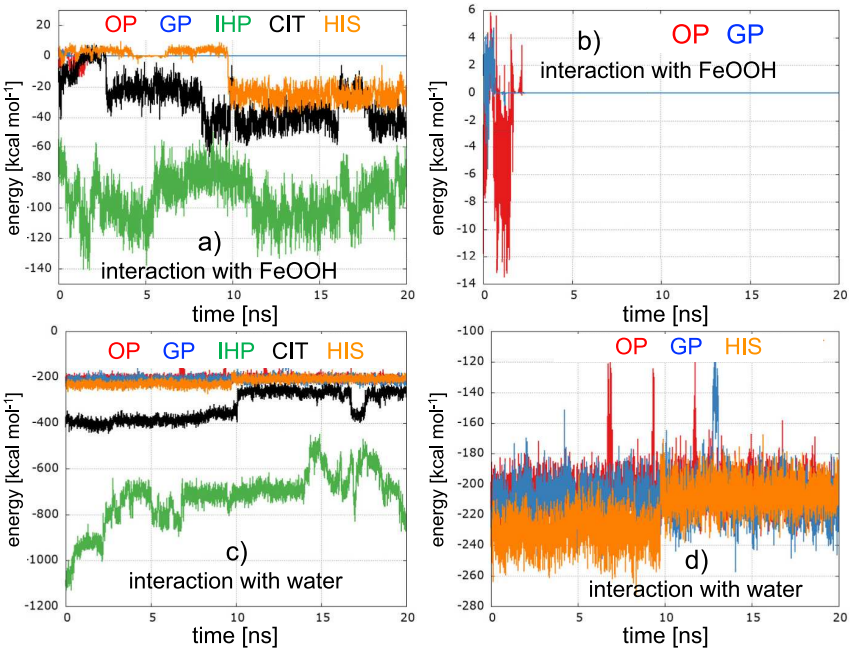


Fig. 10. The total interaction energy (combining electrostatic and dispersion contributions) of each P (OP, GP, and IHP) and OM (CIT and HIS) with both the goethite surface (a–b) and water (c–d) throughout the MD simulation. Additionally, Fig. S14 in the Supporting information shows the interaction energy of both OP and GP with the surface within the first 2.5 ns of the MD simulation.

exceptional behavior, as depicted in Fig. S13 in the Supporting information, owing to its relatively distant positioning from the surface, as illustrated in Figs. 7–8. This results in the prevalence of dispersion interactions over electrostatic interactions, thereby contributing to the relative stability of GP at the surface.

The prevalence of electrostatic Coulomb interactions was also observed in the interaction energy between each P or OM and water. The total interaction energy of P compounds (OP, GP, and IHP) and OM (CIT and HIS) with water exhibited a similar order to that observed with the goethite surface, with the order being: OP (-204 kcal mol^{-1}) $\leq$ GP

(−209) < HIS (−219) < CIT (−330) < IHP (−724) (refer to Fig. 10c–d and Table S1 in the Supporting information). These electrostatic interactions are corroborated by the number of HBs observed for P and OM with water, following the order: OP < GP < HIS < CIT < IHP (see Fig. S11 in the Supporting information), along with the strength of the HBs shown in Fig. 9c, as discussed earlier.

Regarding the effect of OM on the P binding at the goethite surface, the interaction energy showed that both CIT and HIS display stronger binding to goethite compared to OP and GP, see Fig. 10a. This implies that CIT and HIS possess the capability to displace OP and GP from the goethite surface competitively. Consequently, coating the surface with CIT or HIS could impede the adsorption of OP and GP by blocking the active sites at the goethite surface, thereby promoting their desorption and mobilization processes. This elucidates why CIT and HIS can impede the P adsorption, particularly for GP and OP, as observed in the present experiments, see Figs. 2b–c and 3b–c. This inhibitory effect is more pronounced in the case of CIT due to its superior adsorption (and interaction energy with the goethite surface) thus blocking more active sites at the goethite surface compared to HIS. This finding concurs with the present experimental results and clarifies why CIT exerts a potent inhibitory effect on P binding to the goethite surface.

In the case of IHP, its adsorption on the goethite surface covered with OM (CIT or HIS) remains largely unaffected due to its stronger binding affinity to the goethite surface compared to both CIT and HIS, see Fig. 10a. This strong affinity allows IHP not only to be influenced by OM but also positions it as a strong competitor, potentially reducing the binding affinity of CIT and HIS and replacing them at the surface. This explains the experimental observation of minimal changes in the impact of OM on IHP adsorption, see Figs. 2d and 3d. Despite being relatively minor in affecting IHP adsorption, the more noticeable decrease in IHP adsorption observed when the surface is covered with CIT compared to HIS can be attributed to the more pronounced inhibitory effect of CIT compared to HIS. This can be traced back to the stronger binding and higher affinity of CIT to the surface compared to HIS, as discussed earlier in the context of the OP and GP cases.

3.2.3. *Covering the goethite surface with OM*

To delve deeper into the impact of OM on the P binding process at the goethite surface, we constructed two models featuring goethite surfaces covered with a monolayer of either CIT or HIS. Each model included 38 individual molecules (anions) of CIT or HIS to form the monolayer. To counterbalance the negative charge from the HIS (−38) and CIT (−78) molecules, an equivalent number of sodium ions (Na^+) was introduced into each simulation box, which spanned 150 Å perpendicular to the goethite-water interface. The overlay of snapshots captured during MD simulations of the goethite surface covered with HIS and CIT individually is depicted in Fig. 11. These simulations reveal that the majority of HIS and CIT molecules tend to adhere to the surface, forming monolayers that cover and block all active sites at the surface. Consequently, this diminishes the likelihood of anions such as phosphates being adsorbed at the surface in the presence of the formed OM monolayer. According to these MD simulations, approximately 34–35 CIT molecules remain adsorbed at the surface, with about 3–4 molecules diffusing into the bulk water during the simulation. Conversely, in the case of HIS, around 28 molecules remain adsorbed at the surface, while approximately 10 molecules diffuse into the bulk water throughout the simulation. Once again, this underscores the strong affinity of CIT to bind to the goethite surface compared to HIS, with electrostatic interactions playing a significant role. Moreover, upon the formation of monolayers of OM (CIT and HIS) on the goethite surface, dissolution of the goethite surface was observed along the MD simulation, especially for the CIT case, see the dissolved gray goethite atoms in Fig. 11. In addition to enhancing the phosphate mobility, this surface dissolution process comes in accord with the surface dissolution observed in the literature, e.g., see (Duckworth and Martin, 2001; Guppy et al., 2005; Han et al., 2020).

In terms of the electrostatic effect, the electric potential along the x-axis exhibits negative values, primarily attributed to the accumulation of negatively charged OM molecules forming the monolayer at the surface, alongside the diffusion of some molecules into the bulk water, as discussed previously. Fig. 12 illustrates peaks indicating maximum positive charge densities observed at the positions of Fe atoms. This electric potential gradually decreases to more negative values when moving from the bulk goethite towards the surface, with the lowest potentials observed at the interface between the surface and water. Consequently, anions present in the bulk water or solution are unlikely to bind to the

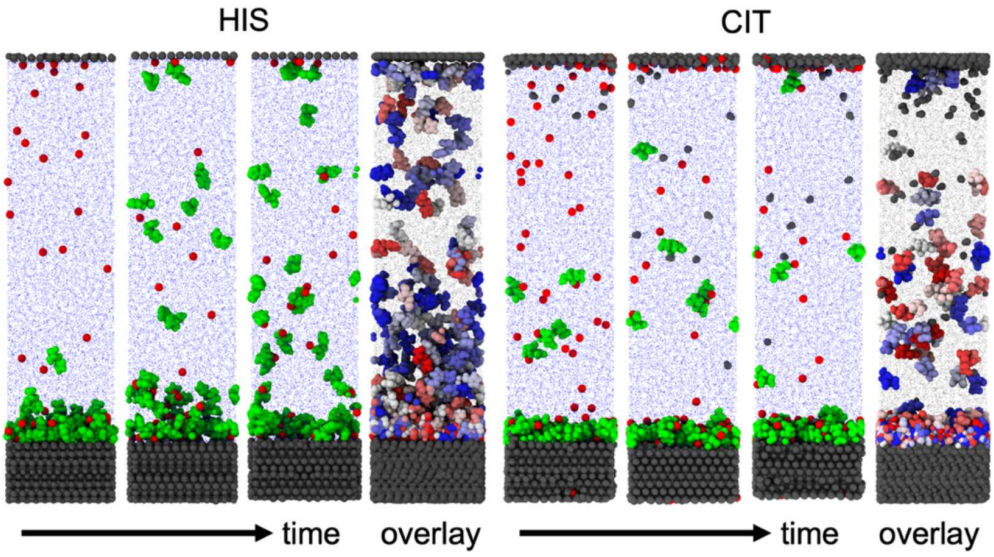


Fig. 11. Snapshots taken during MD simulations showing the dynamic behavior of the goethite surface covered with a monolayer of 38 HIS molecules (left 4 panels) and 38 CIT molecules (right 4 panels). The first three left configurations/panels of each case, namely HIS and CIT, depict the specific arrangement, with HIS and CIT molecules colored in green, goethite in gray, Na^+ ions in red, and water in blue points. Additionally, overlays of snapshots captured during MD simulations illustrate the evolving behavior of these two cases. In the overlays, CIT and HIS molecules transition from red (start of the simulation: 0 ns) to blue (end of the simulation: 20 ns), while goethite remains in gray.

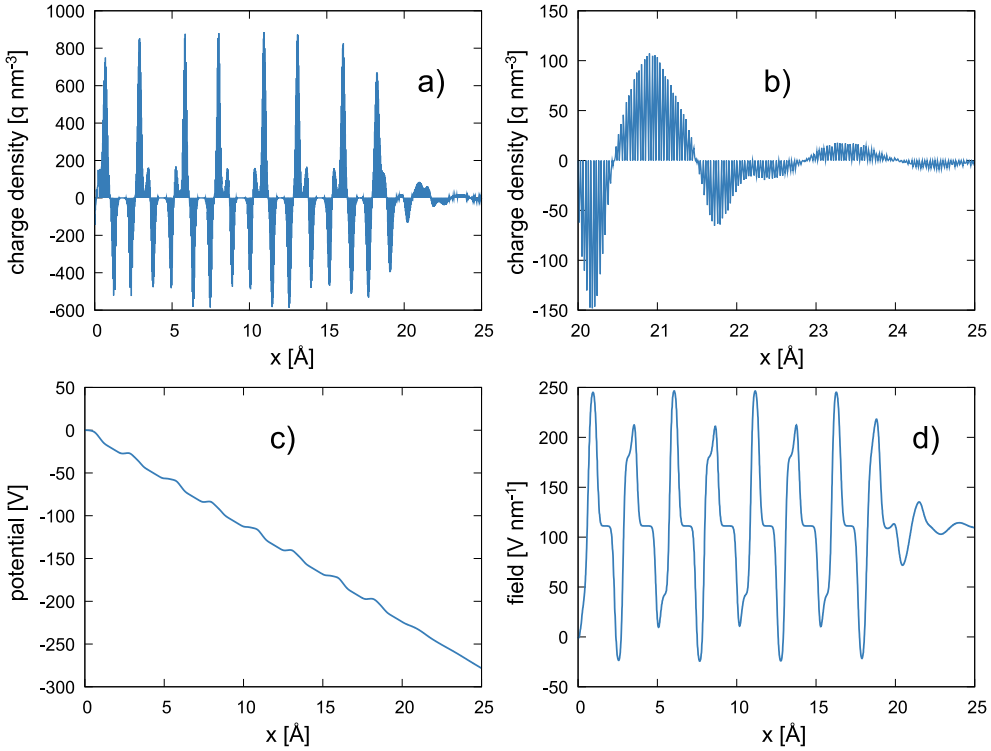


Fig. 12. The distribution of charge density (a–b), electric potential (c), and electric field (d) along the axis perpendicular (x) to the interface of the entire system for the goethite surface covered with a monolayer of 38 HIS molecules. For comparison with the interface between the bare goethite surface and water, see Fig. S15 in the Supporting information.

surface due to the increasing negative potential. This highlights the pivotal role played by both CIT and HIS as inhibitors in the P-binding process. It elucidates the experimental finding regarding the substantial influence of OM on P adsorption, particularly when the goethite surface is pre-covered with OM before the adsorption process, notably in cases involving OP and GP, as depicted in Figs. 2b–c and 3b–c.

Furthermore, the observed negative potential for goethite covered with OM aligns with the expectations proposed by (Sibanda and Young, 1986) and (Fu et al., 2013). They suggested that an unfavorable electrostatic potential or field could be generated around the adsorbed humic acid molecules, potentially hindering P adsorption. While comparing the outcomes of the present study with those of others who have applied humic substances (HSs), such as (Sibanda and Young, 1986) and (Fu et al., 2013), it is important to highlight that the HSs are not as pure as the OM applied in the present study. Typically, all HSs contain some minerals, such as metal ions/clusters/colloids, which are likely predominantly composed of Al and Fe. However, the key distinction lies in the composition of OM utilized in our study, particularly at high surface coverage, compared to the HSs (HA and FA) which have a higher concentration of carboxylate and hydroxyl groups. These groups enhance the negative charge on the goethite surface, initiating discussions on the unfavorable electric potential and field at the surface.

3.2.4. *Co-adsorption at the goethite-water interface*

To examine how OM affects the GP binding process at the goethite surface in the co-adsorption scenario, we developed two models incorporating CIT or HIS separately on goethite surfaces alongside GP, i.e., GP-CIT and GP-HIS. Two initial configurations were established for each model. In one configuration, the combination of GP with each OM (CIT or HIS) was positioned on the surface, while in the second configuration, the combination was situated in the bulk water, far from the surface. For both configurations (whether on the surface or in the bulk water), the formation of stable complexes between GP and both HIS and CIT individually was observed during the MD simulation. For instance, Fig. 13a–b illustrates the interaction between GP and each of CIT and HIS at some periods along the MD simulation trajectory.

Furthermore, it was noted that GP exhibited stronger binding and interaction energy with the goethite surface in the presence of CIT and HIS compared to when GP was alone, see Fig. 13a–d. These observations align with experimental findings indicating that the surface prefers binding GP in the presence of HIS and CIT in the co-adsorption scenario compared to when GP is alone, see Figs. 2c, 3c, and 13a–d. Despite CIT binding relatively more strongly to the surface than HIS, GP demonstrates stronger binding in the presence of HIS compared to the CIT case due to the formation of a more stable complex between GP and HIS, see Fig. 13a–c. As a result, the more stable GP-HIS complex exhibits stronger binding to the goethite surface compared to the GP-CIT complex, ultimately leading to enhanced GP adsorption in the presence of HIS. This finding confirms our interpretation of the present experiments of the formation of GP-OM complexes, which result in higher adsorption compared to the scenario where GP is alone.

Although the co-adsorption of GP in the presence of HIS enhanced GP adsorption, intriguingly, IHP demonstrated lower binding to the surface in the presence of HIS compared to bare IHP adsorption, as depicted in Fig. 13e–f. This is evidenced by the lower interaction energy between IHP and the surface observed in Fig. 13e, compared to that for bare IHP adsorption, i.e., adsorption of IHP in the absence of OM. These findings are consistent with present experimental observations regarding the effect of OM on IHP adsorption in the co-adsorption scenario. This reduced interaction is attributed to the weakened interaction between IHP and the surface, as well as the distance between IHP and the surface observed at certain intervals during the MD simulation. This can be understood by observing a second peak of the partial density for IHP in the presence of HIS at around 30 Å, far from the goethite surface, as shown in Fig. 13f. This aspect is also evident from Fig. 14, which illustrates the dynamic behavior of the co-adsorption of IHP with HIS at the

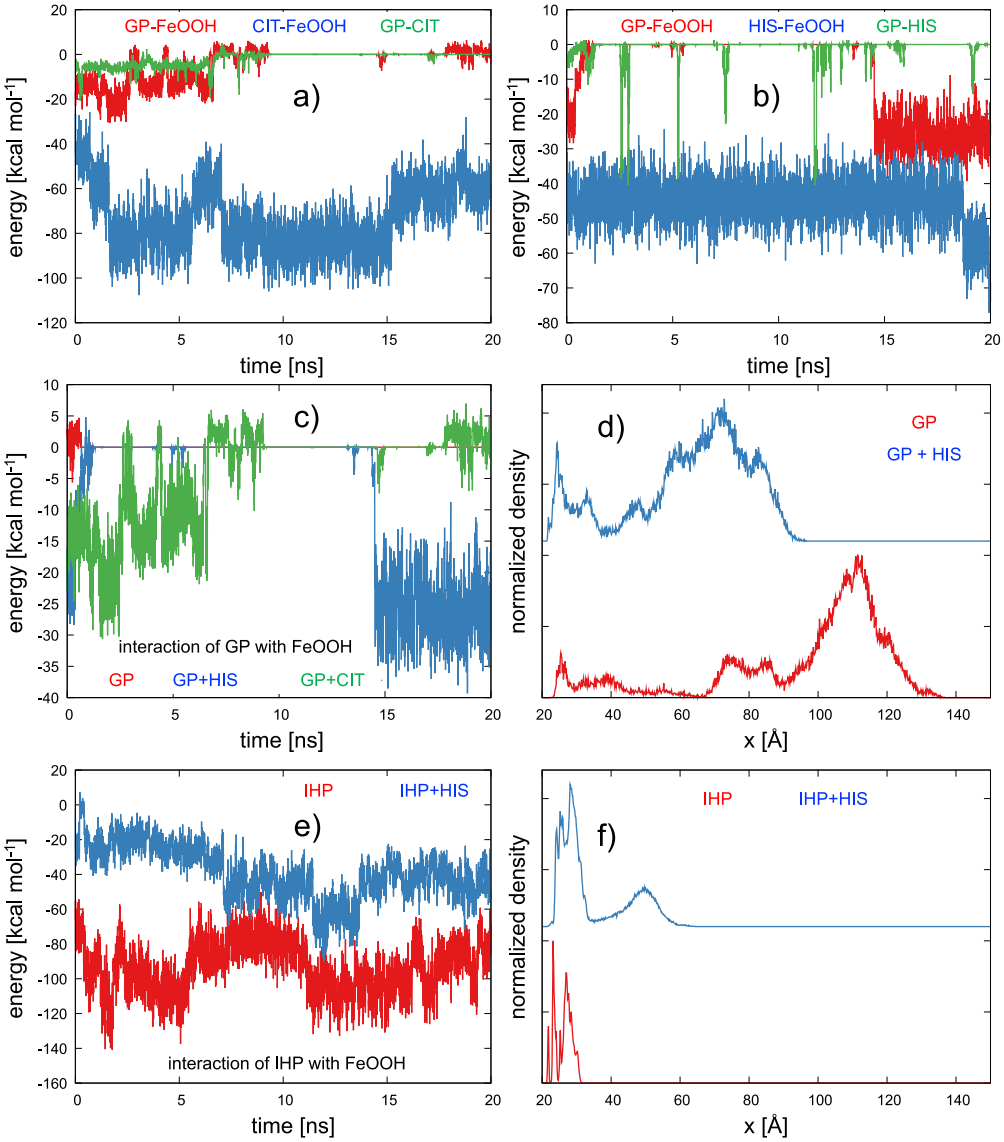


Fig. 13. The total interaction energy (comprising both electrostatic and dispersion components) during the MD simulation of GP co-adsorption with CIT (a) and HIS (b). In these panels, GP-FeOOH, CIT-FeOOH, GP-CIT, HIS-FeOOH, and GP-HIS denote the interaction energy between each pair of components, where, for instance, GP-FeOOH represents the interaction between GP and the goethite surface. Additionally, panels (c) and (d) illustrate the influence of OM on GP in the co-adsorption scenario through the interaction energy (c) and partial density along the axis perpendicular (x) to the interface throughout the entire simulation box (d). Similarly, panels (e) and (f) demonstrate the impact of HIS on IHP in the co-adsorption scenario via the interaction energy (e) and partial density (f). Here, GP + HIS and GP + CIT signify GP in the presence of HIS and CIT, respectively, with the same notation applying to IHP.

goethite surface, showing instances where IHP moves away from and returns to the surface.

4. Summary

The present contribution provides a molecular-level perspective on how organic matter (OM) influences phosphorus (P) adsorption at the goethite-water interface, using a combined experimental-theoretical approach. We examined the impact of citric acid (CIT) and histidine (HIS) on the adsorption of orthophosphate (OP), glycerol phosphate (GP), and inositol hexaphosphate (IHP).

Our findings highlight the complexity of P adsorption on goethite, which is influenced by the chemical structure of both P and OM, treatment conditions, and initial P concentrations. Notably, IHP shows the highest affinity for goethite, while GP shows the lowest. OP is highly sensitive to OM inhibition, with CIT causing a 70 % reduction in adsorption capacity, whereas IHP is less affected, with only a 20 % reduction. GP experiences a 31 % reduction with HIS coverage. These reductions occur when the goethite surface is pre-covered by OM. The order of OM addition (simultaneous or pre-covered) significantly affects P adsorption inhibition. Simultaneous co-adsorption with OM leads to inhibition of P adsorption by 54 % for OP and 10 % for IHP with no significant difference between CIT and HIS. Surprisingly, co-adsorption of OM with GP increases adsorption capacity by 47 % for CIT and 38 % for HIS.

Molecular modeling results reveal the behavior of the Helmholtz layer at the goethite-water interface. At low surface loading, either with P or OM, the interface exhibits a favorable electric potential, promoting the adsorption of anions. This electrostatic environment explains all experimental observations concerning the intrinsic affinity of bare

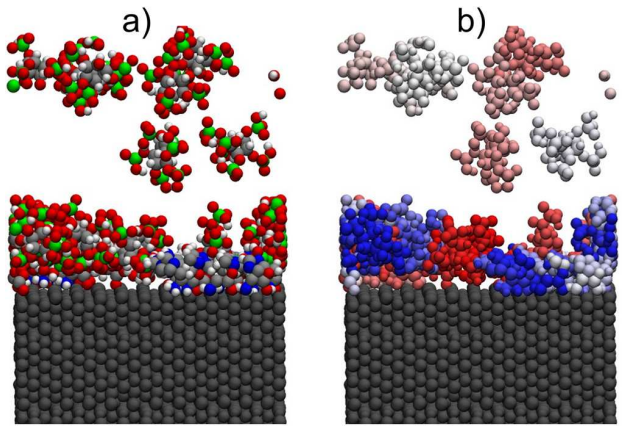


Fig. 14. Overlays of snapshots captured during MD simulations depict the evolving behavior of IHP adsorption in the presence of HIS in the co-adsorption scenario. In panel (e), atoms are color-coded as follows: white (H), red (O), blue (N), silver (C), green (P), and gray (representing the entire goethite). In panel (f), IHP and HIS molecules transition from red (start of the simulation: 0 ns) to blue (end of the simulation: 20 ns), while the goethite remains depicted in gray. Water molecules are excluded from visualization for clarity.

goethite for anions and supports further adsorption at low P and OM concentrations. Moreover, HIS shows intermediate binding affinity, falling between OP and GP (weak) and IHP and CIT (strong), with a goethite binding affinity in the order GP < OP < HIS < CIT < IHP. This order aligns with experimental findings, showing the increasing P adsorption trend: GP < OP < IHP. Both CIT and HIS bind more strongly to goethite than OP and GP, leading to competition and inhibition of OP and GP adsorption. Pre-covered surfaces with OM present an unfavorable negative electric potential, hindering P adsorption, with CIT showing a more pronounced inhibitory effect. This supports our experimental results, explaining the inhibitory effect of OM, particularly CIT, on P adsorption. Furthermore, this elucidates all experimental observations concerning the inhibitory effect on the adsorption of anions at a surface already pre-covered with adsorbed anions. Despite the general inhibitory effect of OM, its presence in solution enhances GP binding due to the formation of GP-OM complexes with a higher affinity for goethite surfaces.

Our results are consistent with prior research on similar and different minerals, as well as whole soil samples. The inclusion of mechanistic insights through MD simulations enhances the reliability of our conclusions. Although our study focused on two organic molecular systems (HIS and CIT), the consistent behavior across various conditions suggests broader applicability.

In conclusion, our study provides crucial insights into the molecular-level influence of OM on P binding at surfaces, affecting P mobility and soil fertility, which is essential for sustaining a growing human population. Several challenges remain in understanding the dynamics of P adsorption and release. Future research should explore OM variants with more carboxylate groups, aromatic OM with carboxylate groups, and naturally occurring humic substances. Additionally, examining the effects of electrolytes and ionic strength, understanding the role of inorganic anions, characterizing P and OM binding at the goethite-water interface, and assessing sequential adsorption by P and OM are necessary. Addressing these issues will enhance our understanding of P, OM, and mineral interactions, providing valuable insights into P fate and transport in natural settings. By integrating experimental and theoretical approaches, we can advance our knowledge and contribute to sustainable soil fertility management and environmental conservation practices.

Funding

This research belongs mainly to the InnoSoilPhos project, funded by the German Federal Ministry of Education and Research (BMBF) in the frame of the BonaRes program (No. 031A558).

CRediT authorship contribution statement

Ashour A. Ahmed: Conceptualization, Data curation, Formal analysis, Funding acquisition, Investigation, Methodology, Validation, Visualization, Writing – original draft, Writing – review & editing. **Mohsen Morshedizad:** Investigation, Methodology. **Oliver Kühn:** Conceptualization, Funding acquisition, Writing – review & editing. **Peter Leinweber:** Conceptualization, Funding acquisition, Writing – review & editing.

Declaration of competing interest

The authors declare no conflict of interest. The funders had no role in the design of the study; in the collection, analyses, or interpretation of data; in the writing of the manuscript, or in the decision to publish the results.

Data availability

No data was used for the research described in the article.

Appendix A. Supplementary data

Supplementary data to this article can be found online at https://doi.org/10.1016/j.scitotenv.2024.173510.

References

Abraham, M.J., Murtola, T., Schulz, R., Páll, S., Smith, J.C., Hess, B., Lindahl, E., 2015. GROMACS: high performance molecular simulations through multi-level parallelism from laptops to supercomputers. SoftwareX 1–2, 19–25. https://doi.org/10.1016/j.softx.2015.06.001.

Ahmed, A.A., Kühn, O., Aziz, S.G., Hilal, R.H., Leinweber, P., 2014. How soil organic matter composition controls hexachlorobenzene–soil-interactions: adsorption isotherms and quantum chemical modeling. Sci. Total Environ. 476–477, 98–106. https://doi.org/10.1016/j.scitotenv.2013.12.096.

Ahmed, A.A., Thiele-Bruhn, S., Aziz, S.G., Hilal, R.H., Elroby, S.A., Al-Youbi, A.O., Leinweber, P., Kühn, O., 2015. Interaction of polar and nonpolar organic pollutants with soil organic matter: sorption experiments and molecular dynamics simulation. Sci. Total Environ. 508, 276–287. https://doi.org/10.1016/j.scitotenv.2014.11.087.

Ahmed, A.A., Gros, P., Kühn, O., Leinweber, P., 2018a. Molecular level investigation of the role of peptide interactions in the glyphosate analytics. Chemosphere 196, 129–134. https://doi.org/10.1016/j.chemosphere.2017.12.162.

Ahmed, A.A., Leinweber, P., Kühn, O., 2018b. Unravelling the nature of glyphosate binding to goethite surfaces by ab initio molecular dynamics simulations. Phys. Chem. Chem. Phys. 20, 1531–1539. https://doi.org/10.1039/C7CP06245A.

Ahmed, A.A., Gypser, S., Leinweber, P., Freese, D., Kühn, O., 2019. Infrared spectroscopic characterization of phosphate binding at the goethite–water interface. Phys. Chem. Chem. Phys. 21, 4421–4434. https://doi.org/10.1039/C8CP07168C.

Ahmed, A.A., Gypser, S., Freese, D., Leinweber, P., Kühn, O., 2020. Molecular level picture of the interplay between pH and phosphate binding at the goethite–water interface. Phys. Chem. Chem. Phys. 22, 26509–26524. https://doi.org/10.1039/D0CP04698A.

Ahmed, A.A., Leinweber, P., Kühn, O., 2023. Advances in understanding the phosphate binding to soil constituents: a computational chemistry perspective. Sci. Total Environ. 887, 163692 https://doi.org/10.1016/j.scitotenv.2023.163692.

Amadou, I., Faucon, M.-P., Houben, D., 2022. Role of soil minerals on organic phosphorus availability and phosphorus uptake by plants. Geoderma 428, 116125. https://doi.org/10.1016/j.geoderma.2022.116125.

Andersen, D.S., Helmers, M.J., Burns, R.T., 2015. Phosphorus sorption capacity of six Iowa soils before and after five years of use as vegetative treatment areas. Appl. Eng. Agric. 611–620. https://doi.org/10.13031/aea.31.11128.

Antelo, J., Avena, M., Fiol, S., López, R., Arce, F., 2005. Effects of pH and ionic strength on the adsorption of phosphate and arsenate at the goethite–water interface. J. Colloid Interface Sci. 285, 476–486. https://doi.org/10.1016/j.jcis.2004.12.032.

Antelo, J., Arce, F., Avena, M., Fiol, S., López, R., Macías, F., 2007. Adsorption of a soil humic acid at the surface of goethite and its competitive interaction with phosphate. Geoderma 138, 12–19.

Arai, Y., Sparks, D.L., 2001. ATR–FTIR spectroscopic investigation on phosphate adsorption mechanisms at the ferrihydrite–water interface. J. Colloid Interface Sci. 241, 317–326. https://doi.org/10.1006/jcis.2001.7773.
Arai, Y., Sparks, D.L., 2007. Interactions between phosphate and iron oxide. In: Advances in Agronomy. Elsevier, pp. 135–179. https://doi.org/10.1016/S0065-2113(06)94003-6.
Arroyave, J.M., Puccia, V., Zanini, G.P., Avena, M.J., 2018. Surface speciation of phosphate on goethite as seen by InfraRed Surface Titrations (IRST). Spectrochim. Acta A Mol. Biomol. Spectrosc. 199, 57–64. https://doi.org/10.1016/j.saa.2018.03.043.
Barrow, N., Bowden, J., Posner, A., Quirk, J., 1980. Describing the effects of electrolyte on adsorption of phosphate by a variable charge surface. Soil Res. 18, 395. https://doi.org/10.1071/SR9800395.
Bellier, N., Chazarenc, F., Comeau, Y., 2006. Phosphorus removal from wastewater by mineral apatite. Water Res. 40, 2965–2971. https://doi.org/10.1016/j.watres.2006.05.016.
Berendsen, H.J.C., Grigera, J.R., Straatsma, T.P., 1987. The missing term in effective pair potentials. J. Phys. Chem. 91, 6269–6271. https://doi.org/10.1021/j100308a038.
Borggaard, O.K., 2001. Soil Chemistry in a Pedological Context, 5. rev. ed. Royal Veterinary and Agricultural University, København.
Borggaard, O.K., Szilas, C., Gimsing, A.L., Rasmussen, L.H., 2004. Estimation of soil phosphate adsorption capacity by means of a pedotransfer function. Geoderma 118, 55–61. https://doi.org/10.1016/S0016-7061(03)00183-6.
Borggaard, O.K., Raben-Lange, B., Gimsing, A.L., Strobel, B.W., 2005. Influence of humic substances on phosphate adsorption by aluminium and iron oxides. Geoderma 127, 270–279. https://doi.org/10.1016/j.geoderma.2004.12.011.
Boukemara, L., Boukhalfa, C., Reinert, L., Duclaux, L., 2016. Characterization of phosphate adsorption on goethite macroscopic and spectroscopic analyses. J. Mater. Environ. Sci. 7, 2541–2550.
Bussi, G., Donadio, D., Parrinello, M., 2007. Canonical sampling through velocity rescaling. J. Chem. Phys. 126, 014101 https://doi.org/10.1063/1.2408420.
Chitrakar, R., Tezuka, S., Sonoda, A., Sakane, K., Ooi, K., Hirotsu, T., 2006. Phosphate adsorption on synthetic goethite and akaganeite. J. Colloid Interface Sci. 298, 602–608. https://doi.org/10.1016/j.jcis.2005.12.054.
Cornell, R.M., Schwertmann, U., 2003. The iron Oxides: Structure, Properties, Reactions, Occurrences, and Uses, 2nd, completely rev. and extended ed ed. Wiley-VCH, Weinheim.
Cygan, R.T., Liang, J.-J., Kalinichev, A.G., 2004. Molecular models of hydroxide, oxyhydroxide, and clay phases and the development of a general force field. J. Phys. Chem. B 108, 1255–1266. https://doi.org/10.1021/jp0363287.
Dakora, F.D., Phillips, D.A., 2002. Root exudates as mediators of mineral acquisition in low-nutrient environments. Plant Soil 245, 35–47. https://doi.org/10.1023/A:1020809400075.
Debicka, M., Morshedizad, M., Leinweber, P., 2023. The effects of dissolved organic matter derived from agricultural waste materials on phosphorus sorption in sandy soils. Agriculture 13, 2164. https://doi.org/10.3390/agriculture13112164.
Dimirkou, A., Ioannou, A., Doula, M., 2002. Preparation, characterization and sorption properties for phosphates of hematite, bentonite and bentonite–hematite systems. Adv. Colloid Interf. Sci. 97, 37–61. https://doi.org/10.1016/S0001-8686(01)00046-X.
Drouillon, M., Merckx, R., 2003. The role of citric acid as a phosphorus mobilization mechanism in highly P-fixing soils. Gayana Botánica 60. https://doi.org/10.4067/S0717-66432003000100009.
Duckworth, O.W., Martin, S.T., 2001. Surface complexation and dissolution of hematite by C 1 -C 6 dicarboxylic acids at pH = 5.0. Geochim. Cosmochim. Acta 65, 4289–4301. https://doi.org/10.1016/S0016-7037(01)00696-2.
Dultz, S., Steinke, H., Mikutta, R., Woche, S.K., Guggenberger, G., 2018. Impact of organic matter types on surface charge and aggregation of goethite. Colloids Surf. A Physicochem. Eng. Asp. 554, 156–168. https://doi.org/10.1016/j.colsurfa.2018.06.040.
Elzinga, E.J., Sparks, D.L., 2007. Phosphate adsorption onto hematite: an in situ ATR-FTIR investigation of the effects of pH and loading level on the mode of phosphate surface complexation. J. Colloid Interface Sci. 308, 53–70. https://doi.org/10.1016/j.jcis.2006.12.061.
Freundlich, H., 1907. Über die Adsorption in Lösungen. Z. Für Phys. Chem. 57U https://doi.org/10.1515/zpch-1907-5723.
Fu, Z., Wu, F., Song, K., Lin, Y., Bai, Y., Zhu, Y., Giesy, J.P., 2013. Competitive interaction between soil-derived humic acid and phosphate on goethite. Appl. Geochem. 36, 125–131. https://doi.org/10.1016/j.apgeochem.2013.05.015.
Furrer, G., Stumm, W., 1986. The coordination chemistry of weathering: I. Dissolution kinetics of δ-Al2O3 and BeO. Geochim. Cosmochim. Acta 50, 1847–1860. https://doi.org/10.1016/0016-7037(86)90243-7.
Ganta, P.B., Kühn, O., Ahmed, A.A., 2019. QM/MM simulations of organic phosphorus adsorption at the diaspore–water interface. Phys. Chem. Chem. Phys. 21, 24316–24325. https://doi.org/10.1039/C9CP04032C.
Ganta, P.B., Kühn, O., Ahmed, A.A., 2020a. Ab initio molecular dynamics simulations of the interaction between organic phosphates and goethite. Molecules 26, 160. https://doi.org/10.3390/molecules26010160.
Ganta, P.B., Kühn, O., Ahmed, A.A., 2020b. QM/MM molecular dynamics investigation of the binding of organic phosphates to the 100 diaspore surface. Front. For. Glob. Change 3. https://doi.org/10.3389/ffgc.2020.00071.
Ganta, P.B., Morshedizad, M., Kühn, O., Leinweber, P., Ahmed, A.A., 2021. The binding of phosphorus species at goethite: a joint experimental and theoretical study. Minerals 11, 323. https://doi.org/10.3390/min11030323.
Gao, Y., Mucci, A., 2001. Acid base reactions, phosphate and arsenate complexation, and their competitive adsorption at the surface of goethite in 0.7 M NaCl solution. Geochim. Cosmochim. Acta 65, 2361–2378. https://doi.org/10.1016/S0016-7037(01)00589-0.
Geelhoed, J.S., Hiemstra, T., Van Riemsdijk, W.H., 1997. Phosphate and sulfate adsorption on goethite: single anion and competitive adsorption. Geochim. Cosmochim. Acta 61, 2389–2396. https://doi.org/10.1016/S0016-7037(97)00096-3.
Geelhoed, J.S., Hiemstra, T., Van Riemsdijk, W.H., 1998. Competitive interaction between phosphate and citrate on goethite. Environ. Sci. Technol. 32, 2119–2123. https://doi.org/10.1021/es970908y.
Gros, P., Ahmed, A., Kühn, O., Leinweber, P., 2017. Glyphosate binding in soil as revealed by sorption experiments and quantum-chemical modeling. Sci. Total Environ. 586, 527–535. https://doi.org/10.1016/j.scitotenv.2017.02.007.
Gros, P., Ahmed, A.A., Kühn, O., Leinweber, P., 2019. Influence of metal ions on glyphosate detection by FMOC-Cl. Environ. Monit. Assess. 191 https://doi.org/10.1007/s10661-019-7387-2.
Gu, Baohua, Schmitt, Juergen, Chen, Zhihong, Liang, Liyuan, McCarthy, J.F., 1994. Adsorption and desorption of natural organic matter on iron oxide: mechanisms and models. Environ. Sci. Technol. 28, 38–46. https://doi.org/10.1021/es00050a007.
Guppy, C.N., Menzies, N.W., Moody, P.W., Blamey, F.P.C., 2005. Competitive sorption reactions between phosphorus and organic matter in soil: a review. Soil Res. 43, 189. https://doi.org/10.1071/SR04049.
Gypser, S., Hirsch, F., Schleicher, A.M., Freese, D., 2018. Impact of crystalline and amorphous iron- and aluminum hydroxides on mechanisms of phosphate adsorption and desorption. J. Environ. Sci. 70, 175–189. https://doi.org/10.1016/j.jes.2017.12.001.
Gypser, S., Schütze, E., Freese, D., 2019. Crystallization of single and binary iron- and aluminum hydroxides affect phosphorus desorption. J. Plant Nutr. Soil Sci. 182, 741–750. https://doi.org/10.1002/jpln.201700543.
Gypser, S., Schütze, E., Freese, D., 2021. Single and binary Fe- and Al-hydroxides affect potential phosphorus mobilization and transfer from pools of different availability. Soil Syst. 5, 33. https://doi.org/10.3390/soilsystems5020033.
Han, J., Kim, M., Ro, H.-M., 2020. Factors modifying the structural configuration of oxyanions and organic acids adsorbed on iron (hydr)oxides in soils. A review. Environ. Chem. Lett. 18, 631–662. https://doi.org/10.1007/s10311-020-00964-4.
Hongshao, Z., Stanforth, R., 2001. Competitive adsorption of phosphate and arsenate on goethite. Environ. Sci. Technol. 35, 4753–4757. https://doi.org/10.1021/es010890y.
Jo, S., Kim, T., Iyer, V.G., Im, W., 2008. CHARMM-GUI: a web-based graphical user interface for CHARMM. J. Comput. Chem. 29, 1859–1865. https://doi.org/10.1002/jcc.20945.
Johnson, S.E., Loeppert, R.H., 2006. Role of organic acids in phosphate mobilization from Iron oxide. Soil Sci. Soc. Am. J. 70, 222. https://doi.org/10.2136/sssaj2005.0012.
Kaiser, K., Guggenberger, G., 2003. Mineral surfaces and soil organic matter. Eur. J. Soil Sci. 54, 219–236. https://doi.org/10.1046/j.1365-2389.2003.00544.x.
Kpomblekou-A, K., Tabatabai, M.A., 2003. Effect of low-molecular weight organic acids on phosphorus release and phytoavailabilty of phosphorus in phosphate rocks added to soils. Agric. Ecosyst. Environ. 100, 275–284. https://doi.org/10.1016/S0167-8809(03)00185-3.
Kruse, J., Abraham, M., Amelung, W., Baum, C., Bol, R., Kühn, O., Lewandowski, H., Niederberger, J., Oelmann, Y., Rüger, C., Santner, J., Siebers, M., Siebers, N., Spohn, M., Vestergren, J., Vogts, A., Leinweber, P., 2015. Innovative methods in soil phosphorus research: a review. J. Plant Nutr. Soil Sci. 178, 43–88. https://doi.org/10.1002/jpln.201400327.
Kubicki, J.D. (Ed.), 2016. Molecular Modeling of Geochemical Reactions: An Introduction. Wiley, Chichester, West Sussex, United Kingdom.
Kubicki, J.D., Ohno, T., 2020. Integrating density functional theory modeling with experimental data to understand and predict sorption reactions: exchange of salicylate for phosphate on goethite. Soil Syst. 4, 27. https://doi.org/10.3390/soilsystems4020027.
Kubicki, J.D., Paul, K.W., Kabalan, L., Zhu, Q., Mrozik, M.K., Aryanpour, M., Pierre-Louis, A.-M., Strongin, D.R., 2012. ATR-FTIR and density functional theory study of the structures, energetics, and vibrational spectra of phosphate adsorbed onto goethite. Langmuir ACS J. Surf. Colloids 28, 14573–14587. https://doi.org/10.1021/la303111a.
Langmuir, I., 1918. The adsorption of gases on plane surfaces of glass, mica and platinum. J. Am. Chem. Soc. 40, 1361–1403. https://doi.org/10.1021/ja02242a004.
Liu, Q., Guo, L., Zhou, Y., Dai, Y., Feng, L., Zhou, J., Zhao, J., Liu, J., Qian, G., 2012. Phosphate adsorption on biogenetic calcium carbonate minerals: effect of a crystalline phase. Desalination Water Treat. 47, 78–85. https://doi.org/10.1080/19443994.2012.696798.
Liu, X., Tournassat, C., Grangeon, S., Kalinichev, A.G., Takahashi, Y., Marques Fernandes, M., 2022. Molecular-level understanding of metal ion retention in clay-rich materials. Nat. Rev. Earth Environ. 3, 461–476. https://doi.org/10.1038/s43017-022-00301-z.
Luengo, C., Brigante, M., Antelo, J., Avena, M., 2006. Kinetics of phosphate adsorption on goethite: comparing batch adsorption and ATR-IR measurements. J. Colloid Interface Sci. 300, 511–518. https://doi.org/10.1016/j.jcis.2006.04.015.
Maciá, E., 2005. The role of phosphorus in chemical evolution. Chem. Soc. Rev. 34, 691. https://doi.org/10.1039/b416855k.
Minamisawa, H., Kojima, Y., Aizawa, M., 2022. Adsorption of inositol phosphate on hydroxyapatite powder with high specific surface area. Materials 15, 2176. https://doi.org/10.3390/ma15062176.
Negassa, W., Dultz, S., Schlichting, A., Leinweber, P., 2008. Influence of specific organic compounds on phosphorus sorption and distribution in a tropical soil. Soil Sci. 173, 587–601. https://doi.org/10.1097/SS.0b013e3181847eef.

Norén, K., Persson, P., 2007. Adsorption of monocarboxylates at the water/goethite interface: the importance of hydrogen bonding. Geochim. Cosmochim. Acta 71, 5717–5730. https://doi.org/10.1016/j.gca.2007.04.037.
Ognalaga, M., Frossard, E., Thomas, F., 1994. Glucose-1-phosphate and myo-inositol hexaphosphate adsorption mechanisms on goethite. Soil Sci. Soc. Am. J. 58, 332–337. https://doi.org/10.2136/sssaj1994.03615995005800020011x.
Okano, K., Uemoto, M., Kagami, J., Miura, K., Aketo, T., Toda, M., Honda, K., Ohtake, H., 2013. Novel technique for phosphorus recovery from aqueous solutions using amorphous calcium silicate hydrates (A-CSHs). Water Res. 47, 2251–2259. https://doi.org/10.1016/j.watres.2013.01.052.
Osman, A.I., Zhang, Y., Lai, Z.Y., Rashwan, A.K., Farghali, M., Ahmed, A.A., Liu, Y., Fang, B., Chen, Z., Al-Fatesh, A., Rooney, D.W., Yiin, C.L., Yap, P.-S., 2023. Machine learning and computational chemistry to improve biochar fertilizers: a review. Environ. Chem. Lett. 21, 3159–3244. https://doi.org/10.1007/s10311-023-01631-0.
Ozboyaci, M., Kokh, D.B., Corni, S., Wade, R.C., 2016. Modeling and simulation of protein–surface interactions: achievements and challenges. Q. Rev. Biophys. 49 https://doi.org/10.1017/S0033583515000256.
Rakovan, J., Becker, U., Hochella, M.F., 1999. Aspects of goethite surface microtopography, structure, chemistry, and reactivity. Am. Mineral. 84, 884–894. https://doi.org/10.2138/am-1999-5-623.
Roy, E.D., Willig, E., Richards, P.D., Martinelli, L.A., Vazquez, F.F., Pegorini, L., Spera, S. A., Porder, S., 2017. Soil phosphorus sorption capacity after three decades of intensive fertilization in Mato Grosso. Brazil. Agric. Ecosyst. Environ. 249, 206–214. https://doi.org/10.1016/j.agee.2017.08.004.
Ruttenberg, K.C., Sulak, D.J., 2011. Sorption and desorption of dissolved organic phosphorus onto iron (oxyhydr)oxides in seawater. Geochim. Cosmochim. Acta 75, 4095–4112. https://doi.org/10.1016/j.gca.2010.10.033.
Shaheen, S.M., Wang, J., Baumann, K., Ahmed, A.A., Hsu, L.-C., Liu, Y.-T., Wang, S.-L., Kühn, O., Leinweber, P., Rinklebe, J., 2022. Stepwise redox changes alter the speciation and mobilization of phosphorus in hydromorphic soils. Chemosphere 288, 132652. https://doi.org/10.1016/j.chemosphere.2021.132652.
Sibanda, H.M., Young, S.D., 1986. Competitive adsorption of humus acids and phosphate on goethite, gibbsite and two tropical soils. J. Soil Sci. 37, 197–204. https://doi.org/10.1111/j.1365-2389.1986.tb00020.x.
Strauss, R., Brümmer, G.W., Barrow, N.J., 1997a. Effects of crystallinity of goethite: I. Preparation and properties of goethites of differing crystallinity. Eur. J. Soil Sci. 48, 87–99. https://doi.org/10.1111/j.1365-2389.1997.tb00188.x.
Strauss, R., Brummer, G.W., Barrow, N.J., 1997b. Effects of crystallinity of goethite: II. Rates of sorption and desorption of phosphate. Eur. J. Soil Sci. 48, 101–114. https://doi.org/10.1111/j.1365-2389.1997.tb00189.x.
Tejedor-Tejedor, M.I., Anderson, M.A., 1990. The protonation of phosphate on the surface of goethite as studied by CIR-FTIR and electrophoretic mobility. Langmuir 6, 602–611. https://doi.org/10.1021/la00093a015.
Tisdale, S.L., Tisdale, S.L. (Eds.), 1993. Soil Fertility and Fertilizers, 5th ed. Prentice Hall, Upper Saddle River, N.J.
Tsao, T.M., Chen, Y.M., Wang, M.K., 2011. Origin, separation and identification of environmental nanoparticles: a review. J. Environ. Monit. 13, 1156. https://doi.org/10.1039/c1em10013k.
Tunesi, S., Poggi, V., Gessa, C., 1999. Phosphate adsorption and precipitation in calcareous soils: the role of calcium ions in solution and carbonate minerals. Nutr. Cycl. Agroecosyst. 53, 219–227. https://doi.org/10.1023/A:1009709005147.
Urrutia, O., Guardado, I., Erro, J., Mandado, M., García-Mina, J.M., 2013. Theoretical chemical characterization of phosphate-metal-humic complexes and relationships with their effects on both phosphorus soil fixation and phosphorus availability for plants: theoretical chemical characterization of phosphate-metal-humic complexes. J. Sci. Food Agric. 93, 293–303. https://doi.org/10.1002/jsfa.5756.
Van Der Spoel, D., Lindahl, E., Hess, B., Groenhof, G., Mark, A.E., Berendsen, H.J.C., 2005. GROMACS: fast, flexible, and free. J. Comput. Chem. 26, 1701–1718. https://doi.org/10.1002/jcc.20291.
Wang, H., Zhu, J., Fu, Q., Hu, H., 2015a. Adsorption of phosphate on pure and humic acid-coated ferrihydrite. J. Soils Sediments 15, 1500–1509. https://doi.org/10.1007/s11368-015-1095-5.
Wang, H., Zhu, J., Fu, Q.-L., Xiong, J.-W., Hong, C., Hu, H.-Q., Violante, A., 2015b. Adsorption of phosphate onto ferrihydrite and ferrihydrite-humic acid complexes. Pedosphere 25, 405–414. https://doi.org/10.1016/S1002-0160(15)30008-4.
Wang, Y.T., Zhang, T.Q., O'Halloran, I.P., Tan, C.S., Hu, Q.C., 2016. A phosphorus sorption index and its use to estimate leaching of dissolved phosphorus from agricultural soils in Ontario. Geoderma 274, 79–87. https://doi.org/10.1016/j.geoderma.2016.04.002.
Wang, H., Zhu, J., Fu, Q., Hong, C., Hu, H., Violante, A., 2016. Phosphate adsorption on uncoated and humic acid-coated iron oxides. J. Soils Sediments 16, 1911–1920. https://doi.org/10.1007/s11368-016-1383-8.
Weng, L., Van Riemsdijk, W.H., Hiemstra, T., 2008. Humic nanoparticles at the oxide−water Interface: interactions with phosphate ion adsorption. Environ. Sci. Technol. 42, 8747–8752. https://doi.org/10.1021/es801631d.
Werdin-Pfisterer, N.R., Kielland, K., Boone, R.D., 2012. Buried organic horizons represent amino acid reservoirs in boreal forest soils. Soil Biol. Biochem. 55, 122–131. https://doi.org/10.1016/j.soilbio.2012.06.012.
Westergaard Strobel, B., Bernhoft, I., Borggaard, O.K., 1999. Low-molecular-weight aliphatic carboxylic acids in soil solutions under different vegetations determined by capillary zone electrophoresis. Plant Soil 212, 115–121. https://doi.org/10.1023/A:1004637126429.
Yan, Y.P., Liu, F., Li, W., Liu, F., Feng, X.H., Sparks, D.L., 2014. Sorption and desorption characteristics of organic phosphates of different structures on aluminium (oxyhydr) oxides: sorption-desorption of organic P on Al oxyhydroxides. Eur. J. Soil Sci. 65, 308–317. https://doi.org/10.1111/ejss.12119.
Yan, J., Jiang, T., Yao, Y., Lu, S., Wang, Q., Wei, S., 2016. Preliminary investigation of phosphorus adsorption onto two types of iron oxide-organic matter complexes. J. Environ. Sci. 42, 152–162. https://doi.org/10.1016/j.jes.2015.08.008.
Zhong, B., Stanforth, R., Wu, S., Chen, J.P., 2007. Proton interaction in phosphate adsorption onto goethite. J. Colloid Interface Sci. 308, 40–48. https://doi.org/10.1016/j.jcis.2006.12.055.

Supporting information (SI)

Deciphering competitive interactions: Phosphate and organic matter binding on goethite through experimental and theoretical insights

Ashour A. Ahmed[a,*], Mohsen Morshedizad[b], Oliver Kühn[a], Peter Leinweber[b]

[a] Institute of Physics, University of Rostock, Albert-Einstein-Str. 23-24, D-18059 Rostock, Germany

[b] Chair of Soil Science, University of Rostock, Justus-von-Liebig-Weg 6, D-18059 Rostock, Germany

Corresponding Author: Ashour A. Ahmed (ashour.ahmed@uni-rostock.de)

Sorption isotherms

To investigate and describe the adsorption behaviors of P compounds on goethite in the absence or presence of OM substances, the sorption data were fitted to the Freundlich and Langmuir models as the most widely used analytical isotherms. The Freundlich model is a two-parameter equation that describes the relationship between the equilibrium concentration of adsorbed and free adsorbates onto heterogeneous surfaces based on an assumed uniform adsorption energy distribution. The model considers that sorption energy decreases exponentially with increasing saturation in the surface and can be expressed as:

$$Q_{ads} = K_f C_{eq}^{nf} \quad (1)$$

where Q_{ads} is the amount of adsorbate adsorbed per unit mass (or surface area) of adsorbent, C_{eq} is the adsorbate equilibrium concentration in solution, and K_f and n_f are the Freundlich unit capacity factor (sorption capacity) and non-linearity Freundlich exponent, respectively (Freundlich, 1907). In the present study, Q_{ads}, C_{eq}, and K_f are expressed in µmol m^{-2}, µmol L^{-1}, and mol^{1-nf} L^{nf} m^{-2}, respectively. Notice that the Freundlich model assumes that the adsorption enthalpy depends on the amount of adsorbate. In the limit of small Q_{ads} where the adsorption enthalpy should not depend on Q_{ads}, one could describe the isotherm by a Langmuir model as well. The Langmuir adsorption theory assumes that the adsorbate forms a monolayer on a homogenous adsorbent surface. The following equation expresses the Langmuir isotherm:

$$Q_{ads} = (Q_{max} K_l C_{eq} / (1 + K_l C_{eq}) \quad (2)$$

where Q_{max} is the maximum amount of the adsorbate required to form a monolayer by having a complete saturation of all binding sites (µmol m^{-2}), K_l is the Langmuir adsorption constant (L μmol^{-1}) that is related to the sorption energy (Langmuir, 1918). To determine the Freundlich and Langmuir constants, non-linear regression was carried out for both adsorption isotherm equations (1) and (2). Moreover, the standard error of the regression (SER) for all data sets was calculated. SER provides an absolute measure of the typical distance that data points deviate from the regression line. Therefore, SER offers a more reliable indication of the goodness-of-fit than R^2, especially when dealing with non-linear regression.

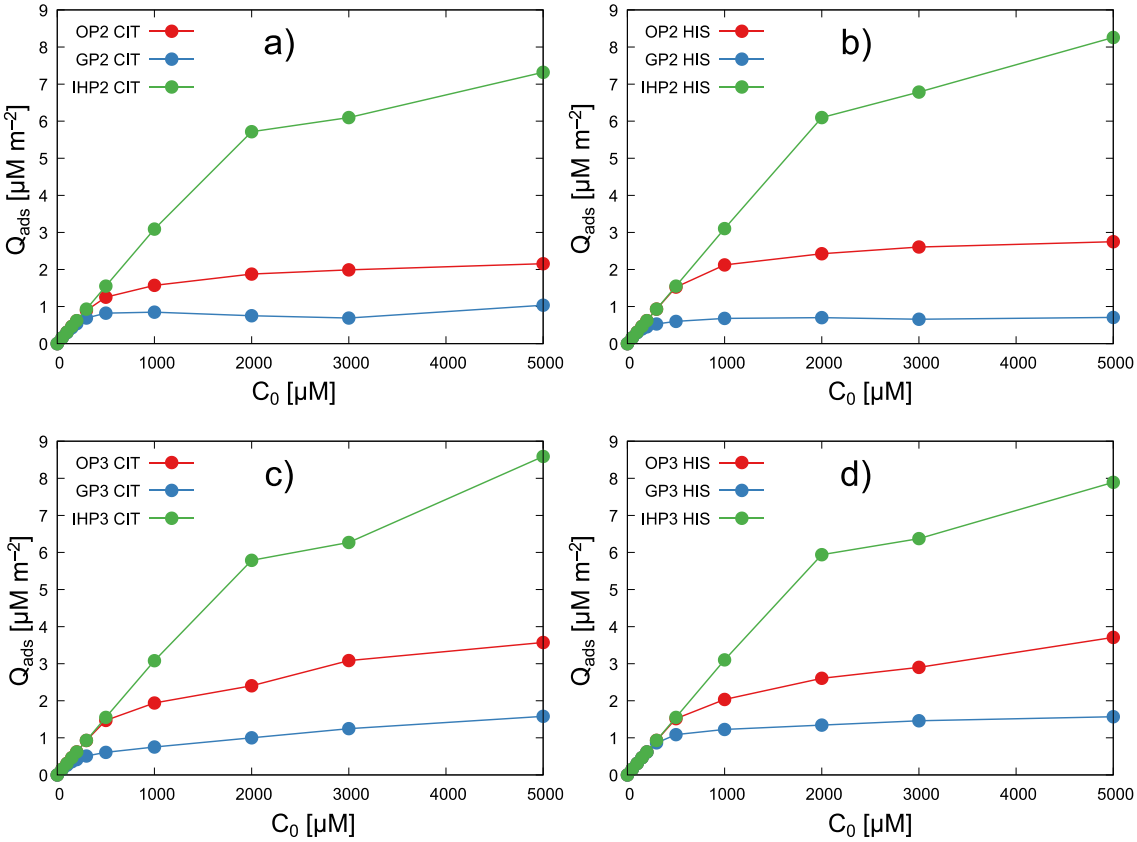


Figure S1. The relationship between P adsorption per unit surface area (Q_{ads}, µmol m^{-2}) and the corresponding initial P concentration (Q_e, µmol L^{-1}) for orthophosphate (OP), glycerolphosphate (GP), and inositolhexaphosphate (IHP) under various experimental conditions. Panel (a) illustrates P adsorption on the goethite surface covered with citric acid (CIT), panel (b) illustrates P adsorption on the goethite surface covered with histidine (HIS), panel (c) showcases co-adsorption of P and CIT on the goethite surface, and panel (d) showcases co-adsorption of P and HIS on the goethite surface. The numerical symbols 2 and 3 represent P adsorption on goethite covered with organic matter (OM), and P plus OM co-adsorption, respectively. Lines connect data points for clarity.

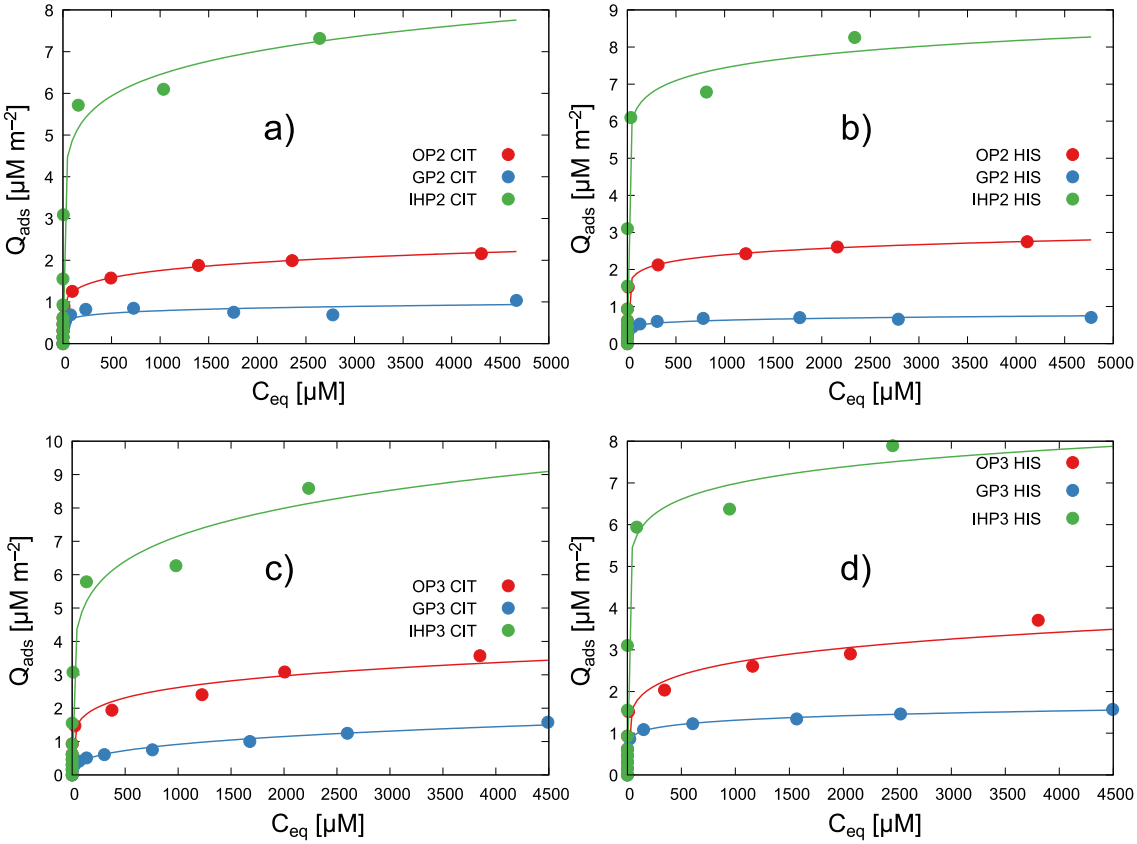


Figure S2. The relationship between P adsorption per unit surface area (Q_{ads}, µmol m^{-2}) and the corresponding equilibrium P concentration (Q_e, µmol L^{-1}) in solution for orthophosphate (OP), glycerolphosphate (GP), and inositolhexaphosphate (IHP) under various experimental conditions fitted according to Freundlich isotherm. Panel (a) illustrates P adsorption on the goethite surface covered with citric acid (CIT), panel (b) illustrates P adsorption on the goethite surface covered with histidine (HIS), panel (c) showcases co-adsorption of P and CIT on the goethite surface, and panel (d) showcases co-adsorption of P and HIS on the goethite surface. The numerical symbols 2 and 3 represent P adsorption on goethite covered with organic matter (OM), and P plus OM co-adsorption, respectively.

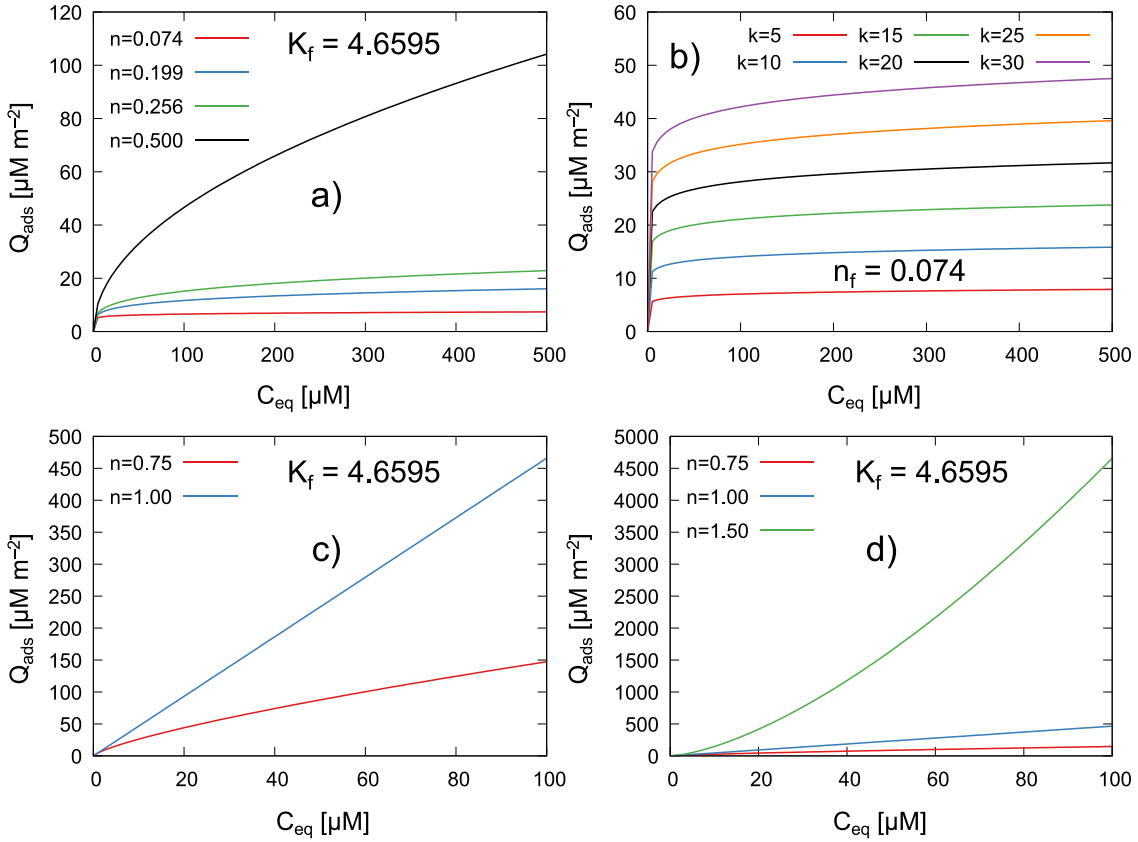


Figure S3. Demonstrations illustrating the relationship between the adsorbed adsorbate and the Freundlich parameters K_f and n_f are depicted. All panels indicate that higher values of K_f and n_f signify stronger adsorption and increased capacities. Panels a), c), and d) demonstrate that minor changes in the exponent n_f result in a more pronounced impact on adsorption strength (greater enhancement) compared to alterations in K_f value as in panel b). For $n_f < 1$, the affinity for binding more adsorbate at the surface decreases with increasing concentration. Conversely, for $n_f > 1$, the affinity for binding more adsorbate at the surface increases with increasing concentration, as seen in panel d). When $n_f = 1$, the affinity for binding more sorbate remains constant with increasing concentration, as shown in panel c). This latter case indicates absorption rather than adsorption.

Molecular Modeling

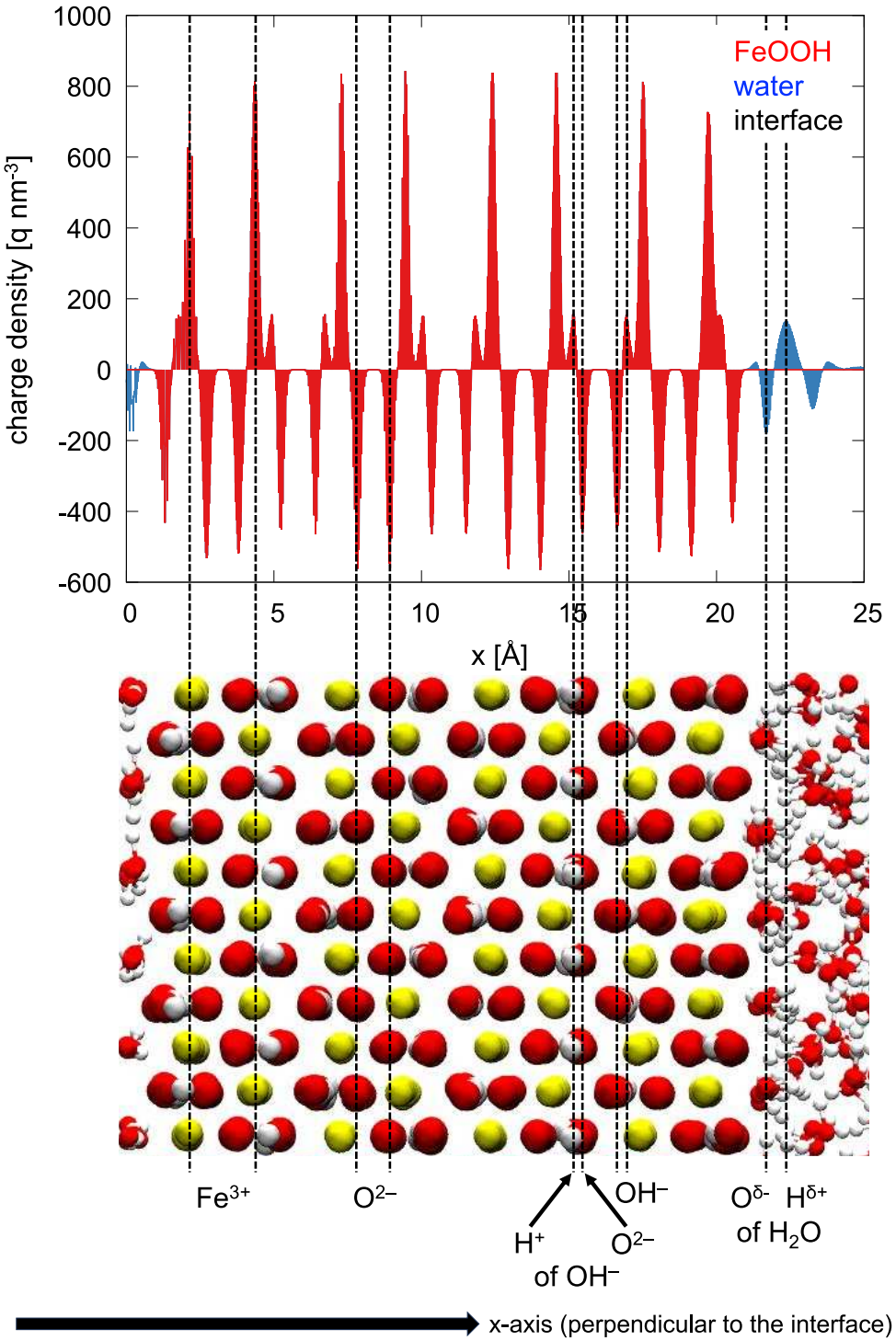


Figure S4. Visualization illustrating the distribution of charge density along the perpendicular axis (x) to the interface for the goethite (red)-water (blue) system, with the interpretation of peaks corresponding to Fe^{3+}, O^{2-}, and OH^{-} of goethite, and $O^{\cdot\,-}$ and $H^{\cdot\,+}$ of water. The simulation box extends from x = 0 to x = 150 Å, with goethite predominantly located around x = 0-20 Å.

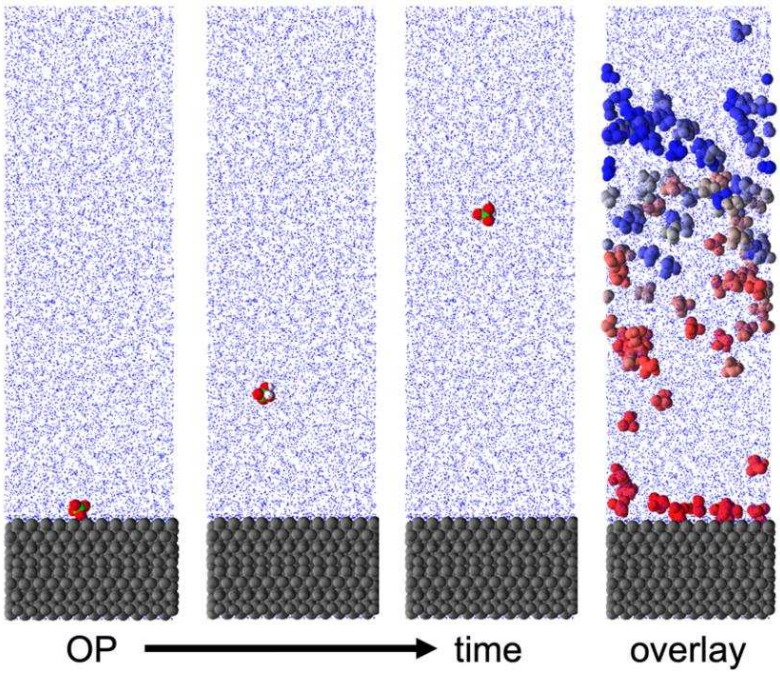


Figure S5. Snapshots taken during MD simulations showing the dynamic behavior of the OP binding at the goethite surface (left 3 panels) and overlay (right panel) of snapshots during the MD simulation. For all configurations, goethite is represented in gray while water is in blue points. For snapshots, H, O, and P atoms are visualized in white, red, and green, respectively. For the overlay, OP molecules transition from red (start of the simulation: 0 ns) to blue (end of the simulation: 20 ns).

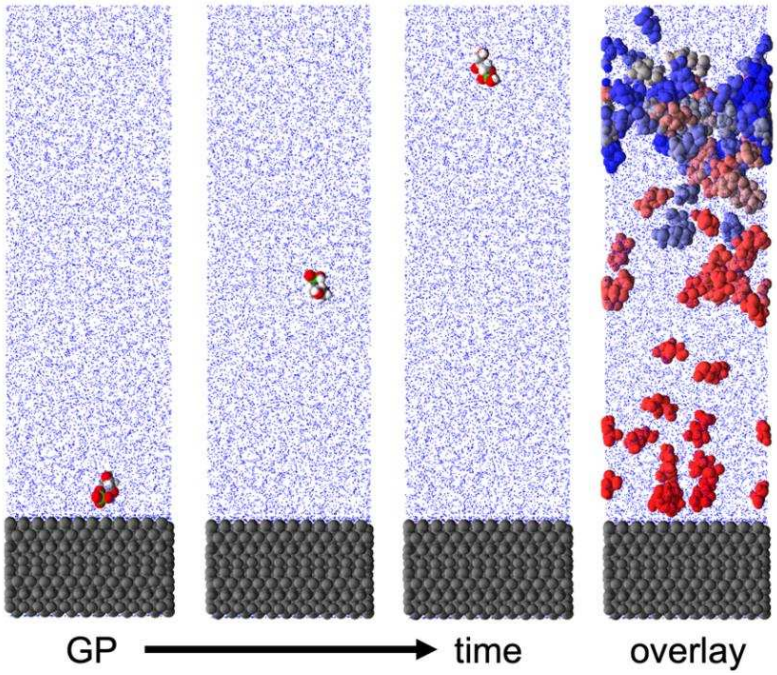


Figure S6. Snapshots taken during MD simulations showing the dynamic behavior of the GP binding at the goethite surface (left 3 panels) and overlay (right panel) of snapshots during the MD simulation. For all configurations, goethite is represented in gray while water is in blue points. For snapshots, H, C, O, and P atoms are visualized in white, gray, red, and green, respectively. For the overlay, GP molecules transition from red (start of the simulation: 0 ns) to blue (end of the simulation: 20 ns).

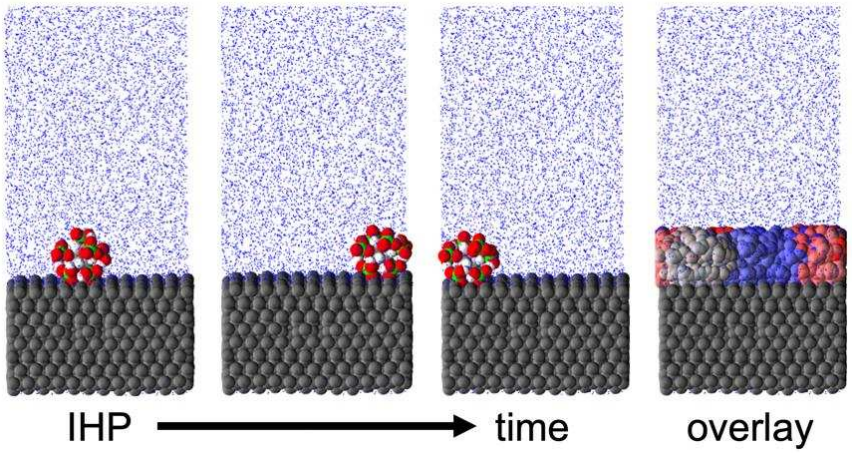


Figure S7. Snapshots taken during MD simulations showing the dynamic behavior of the IHP binding at the goethite surface (left 3 panels) and overlay (right panel) of snapshots during the MD simulation. For all configurations, goethite is represented in gray while water is in blue points. For snapshots, H, C, O, and P atoms are visualized in white, gray, red, and green, respectively. For the overlay, IHP molecules transition from red (start of the simulation: 0 ns) to blue (end of the simulation: 20 ns).

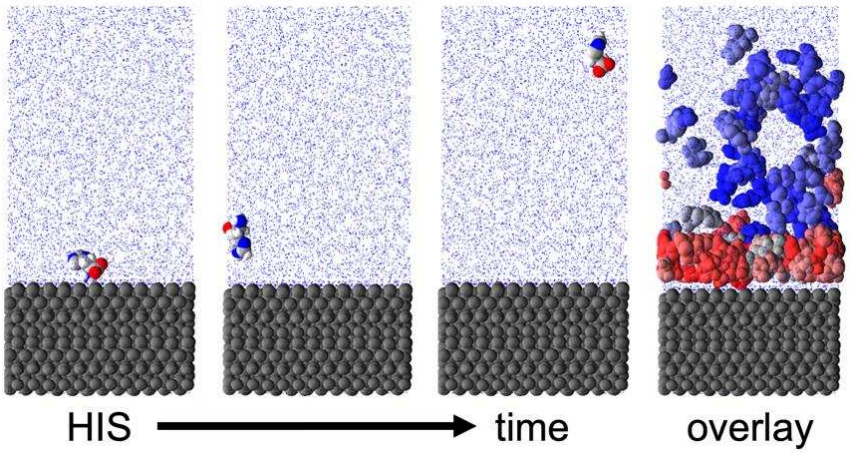


Figure S8. Snapshots taken during MD simulations showing the dynamic behavior of the HIS binding at the goethite surface (left 3 panels) and overlay (right panel) of snapshots during the MD simulation. For all configurations, goethite is represented in gray while water is in blue points. For snapshots, H, C, N, and O atoms are visualized in white, gray, blue, and red, respectively. For the overlay, HIS molecules transition from red (start of the simulation: 0 ns) to blue (end of the simulation: 20 ns).

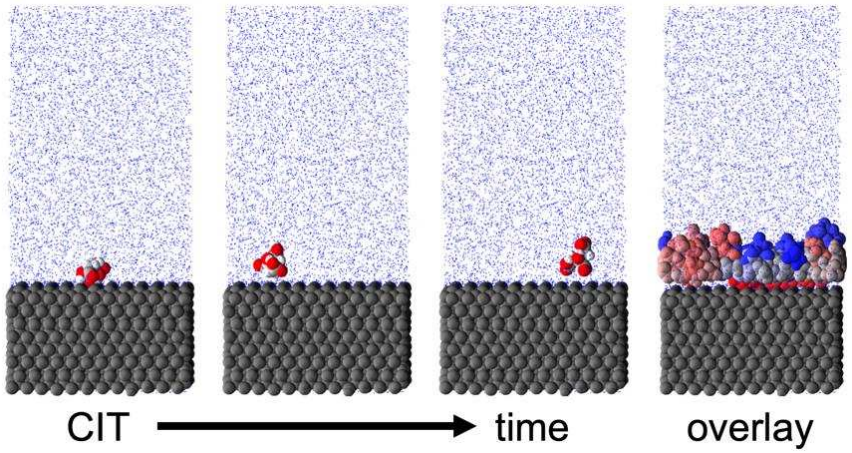


Figure S9. Snapshots taken during MD simulations showing the dynamic behavior of the CIT binding at the goethite surface (left 3 panels) and overlay (right panel) of snapshots during the MD simulation. For all configurations, goethite is represented in gray while water is in blue points. For snapshots, H, C, and O atoms are visualized in white, gray, and red, respectively. For the overlay, CIT molecules transition from red (start of the simulation: 0 ns) to blue (end of the simulation: 20 ns).

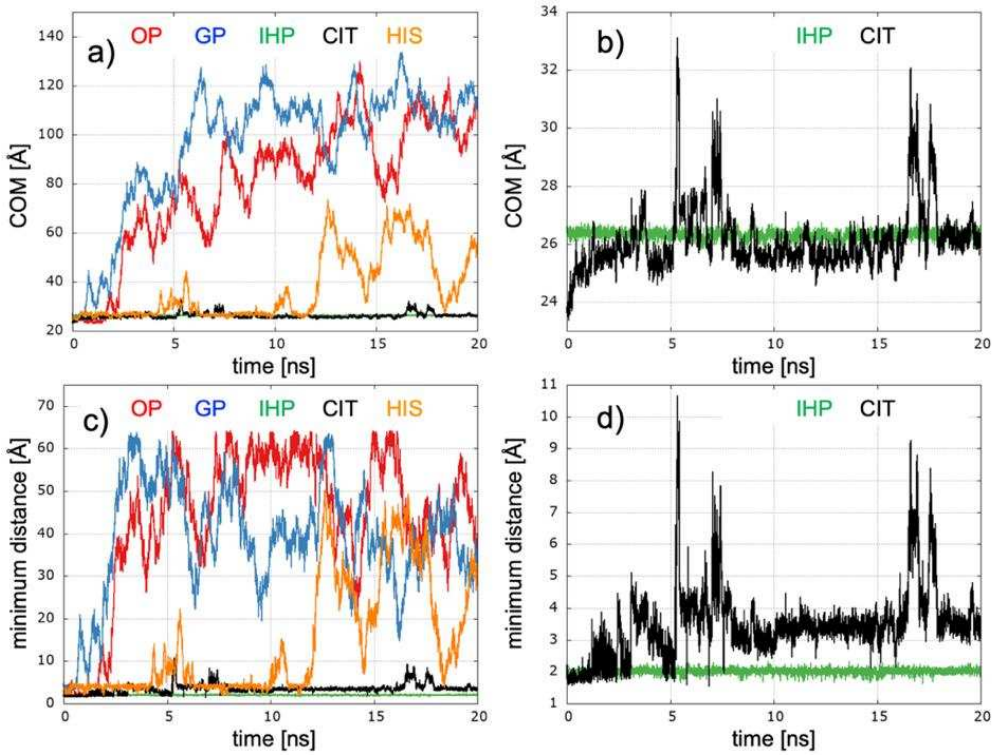


Figure S10. The center of mass motion of each OP, GP, IHP, CIT, and HIS at the goethite surface during the MD simulations (a-b) and the minimum distance between each P or OM and the goethite surface (c-d).

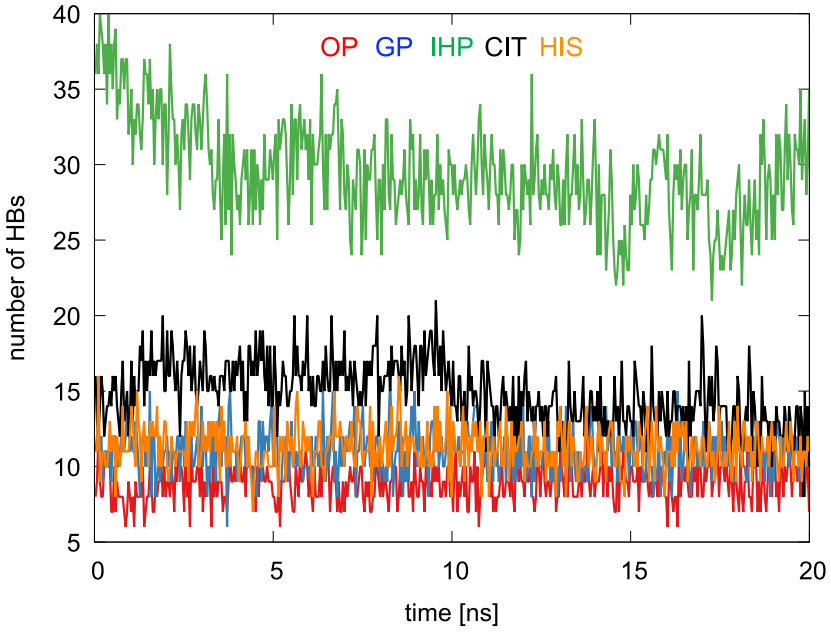


Figure S11. The number of hydrogen bonds (HBs) formed by each P (OP, GP, and IHP) and OM (CIT and HIS) with water molecules throughout the MD simulations.

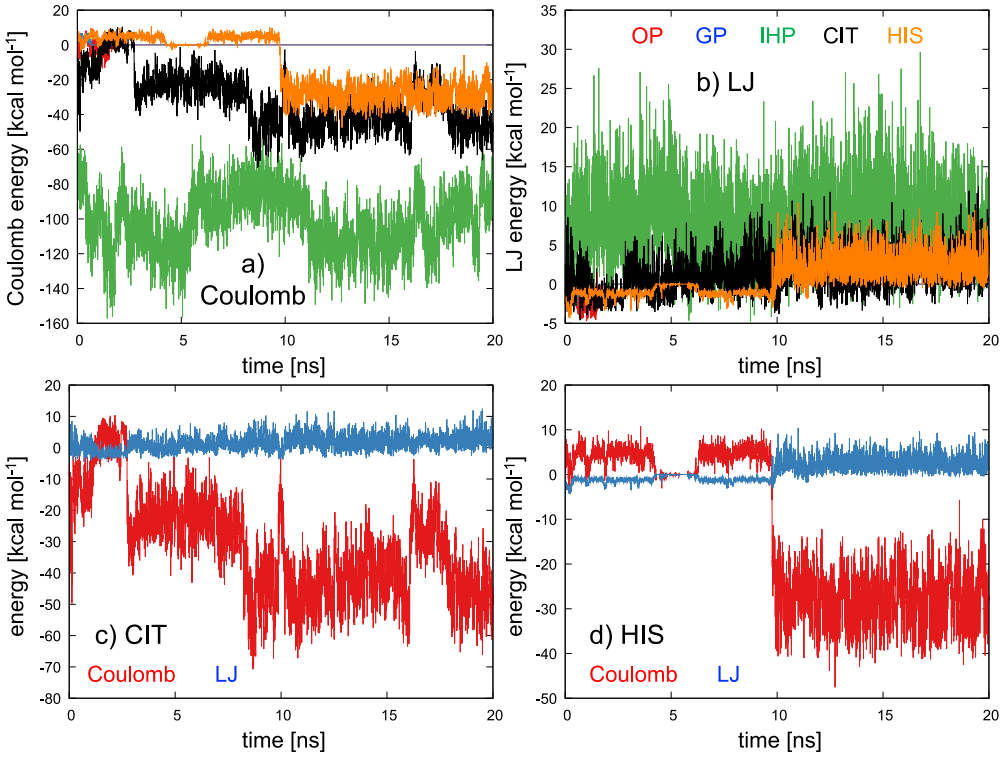


Figure S12. The Coulomb electrostatic (a) and Lennard-Jones (LJ) dispersion (b) interaction energies of each P (OP, GP, and IHP) and OM (CIT and HIS) with the goethite surface throughout the MD simulation. Additionally, both the Coulomb electrostatic and Lennard-Jones (LJ) dispersion interaction energies of CIT (c) and HIS (d) with the goethite surface.

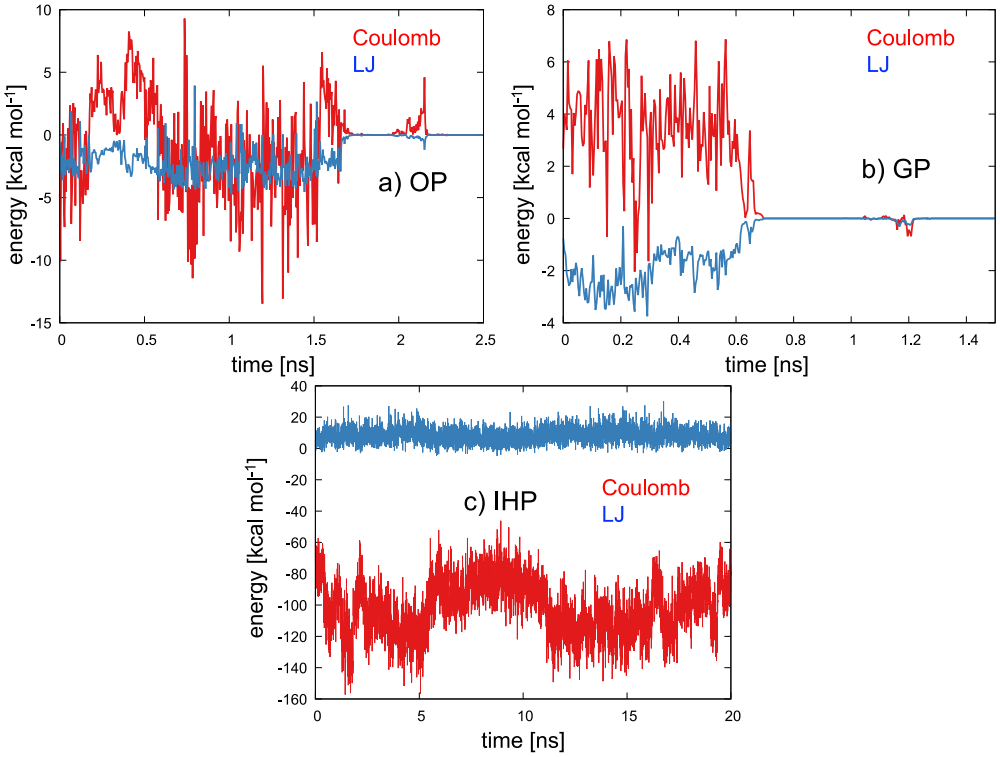


Figure S13. The Coulomb electrostatic and Lennard-Jones (LJ) dispersion interaction energies of OP (a), GP (b), and IHP (d) with the goethite surface.

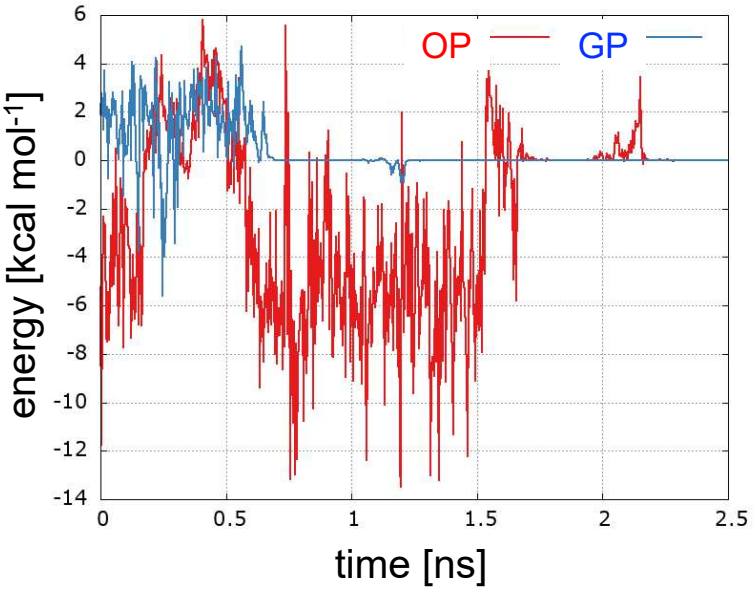


Figure S14. The total interaction energy (combining electrostatic and dispersion contributions) of each OP and GP with both the goethite surface throughout the first 2.5 ns of the MD simulation.

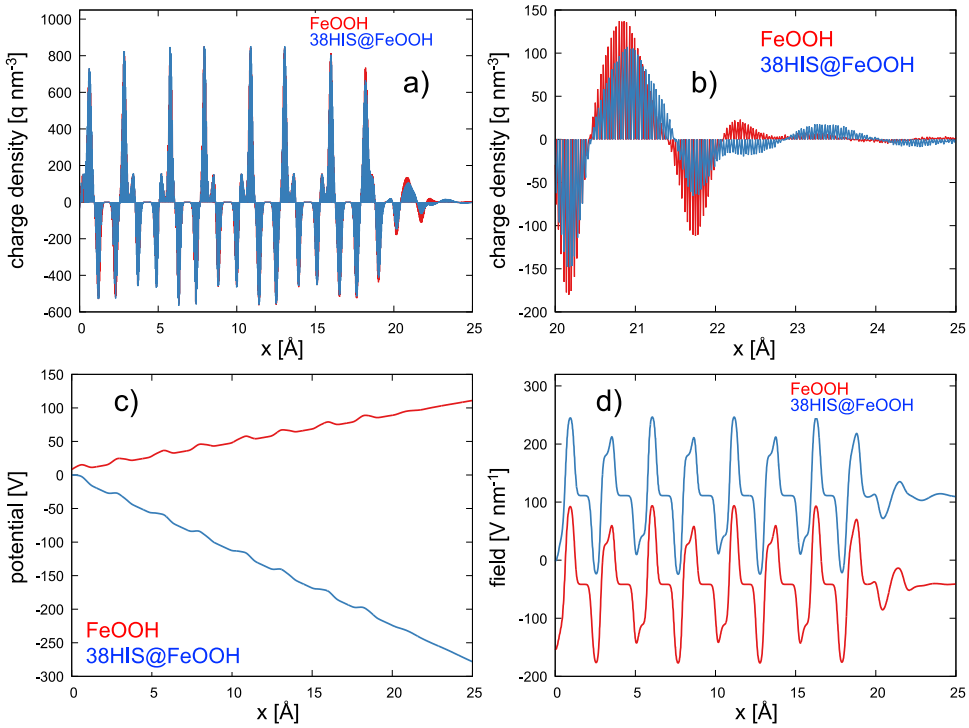


Figure S15. The distribution of charge density (a-b), electric potential (c), and electric field (d) along the axis perpendicular (x) to the interface of the entire system for two scenarios: the interface between the bare goethite surface and water (in red) and the case of the goethite surface covered with a monolayer of 38 HIS molecules (in blue).

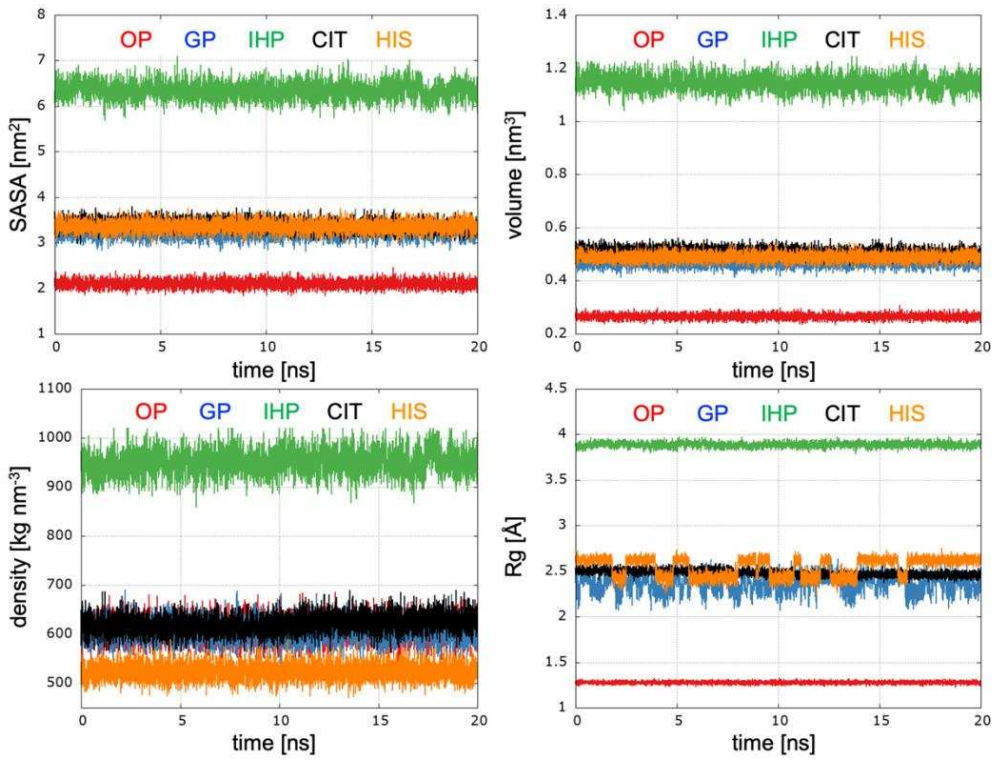


Figure S16. The surface accessible surface area (SASA, a), volume (b), mass density (c), and radius of gyration (R_g, d) of each OP, GP, IHP, CIT, and HIS during the MD simulations.

Table S1. The averaged total interaction energy in kcal mol^{-1} (combining electrostatic (Coulomb) and dispersion (LJ) contributions) between each pair of individual components (P and goethite, P and water, goethite and water) in the P-goethite-water system. The same applies to OM instead of P.

P/OM	total interaction energy [kcal mol^{-1}]		
	P/OM-goethite	P/OM-water	Goethite-water
GP	0.05 (-0.46)	-209	-2958
OP	-0.26 (-4.75)	-204	-2958
IHP	-93.49	-724	-2882
HIS	-11.75 (-21.86)	-219	-2949
CIT	-29.86 (-31.37)	-330	-2936

Note: The interaction energy values presented in the table are averaged over the entire equilibrium MD simulation runs. For all P and OM complexes with goethite (except the IHP-goethite complex), dissociation of the complex occurs during certain periods. To account for this and accurately calculate the interaction energy only during the periods when the complex is intact, the interaction energies (shown in blue in parentheses) are averaged only for the moments of non-zero interaction energies over the equilibrium MD simulation runs.

Publication 9

Y. Luo, Y. Peng, Y. Li, Y. Li, C. Feng, R. Li, B. Gao, R. Xiao, X. Zhang, G. Qu, M. Li, Ashour A. Ahmed, S. G. Al-Solaimani, P. S. Hooda, J. Rinklebe, Z. Zhang, S. S. Lee, S. M. Shaheen. Phosphorus removal from water using La-based absorbents: Insights into the impacts of crystal structure, surface area, and crystallinity on the removal efficiency and mechanisms. Sep. Purif. Technol. **2023**, 330, 125478.

Contribution: Ashour A. Ahmed is credited with scientific concepts. Ashour A. Ahmed, along with the co-authors, has discussed and interpreted the results and contributed to writing, reviewing, and editing the manuscript.

URL: https://doi.org/10.1016/j.seppur.2023.125478

QR:



Reproduced with the permission of Elsevier

Separation and Purification Technology 330 (2024) 125478



Contents lists available at ScienceDirect

Separation and Purification Technology

journal homepage: www.elsevier.com/locate/seppur



Phosphorus removal from water using La-based absorbents: Insights into the impacts of crystal structure, surface area, and crystallinity on the removal efficiency and mechanisms

Yuan Luo [a,b], Yaru Peng [a,b], Yimeng Li [a,b], Yage Li [a], Chuchu Feng [a,b], Ronghua Li [a,b,*], Bin Gao [c], Ran Xiao [d], Xiu Zhang [e], Guangzhou Qu [a,b], Manlin Li [f], Ashour A. Ahmed [g], Samir G. Al-Solaimani [h], Peter S. Hooda [i], Jörg Rinklebe [j], Zengqiang Zhang [a,b], Sang Soo Lee [k,*], Sabry M. Shaheen [h,j,l,*]

[a] College of Natural Resources and Environment, Northwest A&F University, Yangling, Shaanxi Province 712100, China
[b] Key Laboratory of Plant Nutrition and the Agri-environment in Northwest China, Ministry of Agriculture and Rural Affairs, Yangling, Shaanxi Province 712100, China
[c] Department of Civil and Environmental Engineering, Rensselaer Polytechnic Institute, Troy, NY 12180, USA
[d] Interdisciplinary Research Center for Agriculture Green Development in Yangtze River Basin, College of Resources and Environment, Southwest University, Chongqing 400715, China
[e] North Minzu University Ningxia Key Laboratory for the Development and Application of Microbial Resources in Extreme Environments, Yinchuan, 750021, China
[f] College of Chemistry & Pharmacy, Northwest A&F University, Yangling, Shaanxi Province 712100, China
[g] University of Rostock, Institute of Physics, Rostock, Albert-Einstein-Str. 23-24, Germany
[h] King Abdulaziz University, Faculty of Meteorology, Environment, and Arid Land Agriculture, 21589 Jeddah, Saudi Arabia
[i] Faculty of Engineering, Computing and the Environment, Kingston University London, Kingston Upon Thames KT1 2EE, London, UK
[j] University of Wuppertal, School of Architecture and Civil Engineering, Institute of Foundation Engineering, Water- and Waste-Management, Laboratory of Soil- and Groundwater-Management, Pauluskirchstraße 7, 42285 Wuppertal, Germany
[k] Department of Environmental and Energy Engineering, Yonsei University, Wonju, 26493, Republic of Korea
[l] University of Kafrelsheikh, Faculty of Agriculture, Department of Soil and Water Sciences, 33516, Kafr El-Sheikh, Egypt

ARTICLE INFO

Handling Editor: Z Bao

Keywords:
Water nutrients
Structured adsorbents
Chemical separation
Lanthanum oxides crystallinity
Purification mechanisms

ABSTRACT

Removal of nutrients and pollutants from water using structured adsorbents is of great interest. Lanthanum (La) oxide/hydroxides and their derivative composites are promising platforms for phosphate (P) removal from wastewater. However, various key factors including crystal structure, specific surface area (S_{BET}) and crystallinity restrict their P removal performance. In this study, LaOCl, a novel adsorbent with tetragonal crystal, and La_2O_3, a traditional adsorbent with hexagonal crystal, were prepared at different calcination temperatures and tested as P adsorbents. Due to different crystal structures, LaOCl and La_2O_3 exhibit significant differences in P adsorption. LaOCl crystal is more stable than La_2O_3 in solution. The main LaOCl crystal phase is not changed after P adsorption, while La_2O_3 transformed into $La(OH)_3$ due to proton capturing form H_2O. The Cl^- on LaOCl can be used as a ligand for P ions exchange. It is different from OH^- exchange which increases the pH sharply. The isoelectric points (IEP) of LaOCl is slightly higher than La_2O_3. All of these factors, caused by the different structures of LaOCl, keep its P adsorption capacity and rate high in acidic conditions. The Langmuir maximum P adsorption capacity of LaOCl is 164.52 mg/g, which is 2.3 times greater than La_2O_3. The LaOCl adsorbent exhibited a faster adsorption rate than La_2O_3. It is able to reduce the $H_2PO_4^-$ concentration from 50 mg/L (pH ~ 5.0) to < 0.002 mgP/L in 180 min, while the residual P concentration is about 11.27 mgP/g by La_2O_3 in the same time. The P adsorption capacity was found positively correlated with crystallinity at pH 3.0 but with S_{BET} only in pH 5.0 ~ 9.0 range for LaOCl. However, S_{BET} and crystallinity are not the main factors influencing the P adsorption capacity of La_2O_3. Following P adsorption, both adsorbents were verified for P desorption. The results showed the amount of P desorbed was small, thus the adsorbents have the ability to lock P in natural water. Overall, this study provides essential perspectives on the effects of crystal structure, surface area, and crystallinity on P adsorption and the scientific basis for developing new and functionalized La-based adsorbents.

* Corresponding authors.
E-mail addresses: rh.lee@nwsuaf.edu.cn (R. Li), cons@yonsei.ac.kr (S. Soo Lee), shaheen@uni-wuppertal.de (S.M. Shaheen).

https://doi.org/10.1016/j.seppur.2023.125478
Received 30 July 2023; Received in revised form 13 October 2023; Accepted 22 October 2023
Available online 25 October 2023
1383-5866/© 2023 Elsevier B.V. All rights reserved.

1. Introduction

Surface water eutrophication has received wide attention for decades because of the excessive surface runoff of phosphorus (P) from agricultural soils into waters, which has posed a severe threat to aquatic ecosystems and also presents a huge challenge for water dephosphorization [1,2]. The biological method usually referred to as the activated sludge treatment, is capable of removing most phosphorus by phosphorus-accumulating bacteria, but for trace level of phosphorus (e.g., below 0.1 mg P/L) in waters/wastewaters, its efficiency is often limited [3,4]. Chemical precipitation is useful for a high level of P reduction but also cannot meet the requirement of environmental limit (<0.02 mg P/L), given the engineering cost and benefit analysis [4]. By contrast, adsorption is thought to be an efficient method due to its advantages of low cost, easy operation, and high efficiency in media with low levels of P [5–7]. Lanthanum (La), an environment-friendly and abundant rare earth element in the crust, has a strong affinity for P ions with a solubility product constant of 3.7×10^{-23} for $LaPO_4$ [8]. In the past decades, La-based adsorbents, including La oxide/hydroxide and their derivative composites, have received extensive attention [9,10]. For example, the highest P adsorption capacity of purchased La_2O_3 is 46.95 mg/g, which is 2.25 times that of Al_2O_3 [11], while the hollow La_2O_3 nanosphere synthesized by the template method is up to 198.68 mg/g due to its high (S_{BET}) [12]. Amorphous $La(OH)_3$ synthesized by co-precipitation method and the high crystallinity $La(OH)_3$ purchased from the market have adsorption capacities of 107.53 mg/g and 55.56 mg/g, respectively [13]. Also, $La(OH)_3$ nanorod (LH-1, LH-2 and LH-3) synthesized by hydrothermal method, the P adsorption capacity of LH-3 can reach up to 170.1 mg/g because of its high S_{BET} and small particle size [14]. In addition, the combination of La (hydr)oxides with other metals and carriers to prepare composite adsorbents was considered an effective strategy to improve P adsorption. The P adsorption capacities of La/Al and La/Fe (hydr)oxide composites are 76.3 mg/g and 123.46 mg/g because metal doping caused changes in the crystal structure and surface morphology [15,16]. $La(OH)_3$ loaded on silica aerogel and porous biomass surface can achieve P adsorption capacities of 153.8 mg/g and 180.5 mg/g due to the synergistical relationship between $La(OH)_3$ and matrix [17,18]. However, the above studies mainly based on La_2O_3 and $La(OH)_3$ as active components, i.e., La_2O_3 and $La(OH)_3$ or as combined with carriers and other metals for P removal. The S_{BET} and crystallinity of such adsorbents have obvious influence on P adsorption. Therefore, using novel La-containing crystal and exploring how crystal structure, surface area and crystallinity affect P removal are very important and necessary at present. These initiatives are likely to lead to development of La-based adsorbents synthesis for superior P removal.

LaOCl is a rare earth oxychloride with a tetragonal structure (space group P4/nmm, No. 129), which structure formed from the $(LaO)_n^{n+}$ and Cl^- layers [19]. Due to its structural feature and chemical stability, it has been widely applied in many fields, such as emission display devices, sensors and catalysis. The introduction of other rare earth cations, including europium (Eu), dysprosium (Dy), terbium (Te), etc., in LaOCl lattice can prepare monochromatic or multi-colour luminescent materials [20–22]. Moreover, coating LaOCl on alumina substrates is an effective way to produce CO_2 sensors with a better response than SnO_2-La_2O_3 and $BaTiO_3$-CuO [23]. And LaOCl is able to promote the oxidation and chlorination of alkanes and separate the photogenerated electrons and holes rapidly when act as a catalyst [24–26]. However, not much attention has been given to LaOCl as an efficient adsorbent to remove P from wastewater. In a recent study, Li et al. unexpectedly found that LaOCl in different crystal Fe/La oxide composites plays an important role in P removal, but the effects of $S_{BET}$and crystallinity on the P adsorption were not investigated, and hence further investigations are needed [27]. Simultaneously, compared with the conventional adsorbent La_2O_3 with hexagonal phase (space group P-3 m1 No.164), the differences in P adsorption performances and underlying mechanisms modulated by crystal structures are still unclear.

In order to clarify these issues, two adsorbents, LaOCl and La_2O_3, were prepared at different temperatures, characterized and employed for P adsorption in solutions. The crystal structure and morphology, surface area, and Zeta potential were characterized. The effects of solution pH, reaction time and P species on P adsorption were tested. The reusability and P removal in natural water were studied, and the P adsorption mechanisms were determined by X-ray diffraction (XRD), Fourier transform infrared (FTIR) spectroscopy and X-ray photoelectron spectroscopy (XPS) characterization.

2. Materials and methods

2.1. Main reagents

$LaCl_3{\cdot}7H_2O$ and $C_6H_8O_7{\cdot}H_2O$ were purchased from Aladdin Biochemical Technology Co., Ltd. $La(NO_3)_3{\cdot}nH_2O$ was purchased from Sinopharm Group Chemical Reagent Co., Ltd. HCl was purchased from Xilong Science Co., Ltd. KH_2PO_4, $K_2HPO_4{\cdot}3H_2O$, $NH_3{\cdot}H_2O$ and NaOH were purchased from Guangdong Guanghua Technology Co., Ltd. All reagents were of analytical purity.

2.2. Preparation of adsorbents

For the LaOCl preparation, 37.1 g $LaCl_3{\cdot}7H_2O$ and 21.0 g $C_6H_8O_7{\cdot}H_2O$ were dissolved in a beaker with 50 mL deionized water and transferred to an oven to dry the liquid and foam. The formed dry gel was ground to fine powder by agate grinding and transferred to a muffle furnace at different temperatures (500, 600, 700, and 800 °C) for 2 h calcination. The corresponding products were named as LC500, LC600, LC700 and LC800, respectively, according to the calcination temperature.

As for the La_2O_3 synthesis, 50 g $La(NO_3)_3{\cdot}nH_2O$ was dissolved in a beaker with 500 mL deionized water. After complete dissolution, $NH_3{\cdot}H_2O$ was added to the $La(NO_3)_3$ solution dropwise until pH stabilized at 11.0. The suspension was aged at room temperature for 12 h. After that, the white precipitate was collected and washed with deionized water 3 times to clear impurities. Then, the solid was ground, transferred to a muffle furnace and calcined at different temperatures (500, 600, 700 and 800 °C) for 2 h. The corresponding products were labeled as LO500, LO600, LO700 and LO800, respectively.

2.3. Characterization of adsorbents

A Bruker D8 Advance X-ray analyzer (GER) measured the XRD pattern of the sample, and the crystal structure was identified by Jade 6.0. The surface morphology was observed by a SU8220 SEM (JPN) and the Brunauer-Emmet-Teller specific surface area (S_{BET}) was measured by a Micromeritics 2420 automatic adsorption apparatus (USA) based on the N_2 adsorption–desorption isotherms at 77 K. The zeta potential was measured by a Malvern Zetasizer (UK, ZEN3600). The surface functional groups were determined by a FTIR spectrometer (USA, Thermo Nicolet Is10) using a KBr slice. Additionally, the electron binding energy was collected by an XPS spectrometer (USA, Thermo Fischer). The results were analyzed by Avantage software and using C − C binding energy 284.8 eV as calibration.

2.4. Adsorption experiment

2.4.1. Effects of solution pH on adsorption capacity

In a typical batch test, 0.02 g LaOCl (or La_2O_3) was added into a series of glass bottles containing 200 mg/L P solutions (pH 3.0, 5.0, 7.0, 9.0, and 11.0). After mixing for 6 h in a shaker (180 r/min, 25 °C), the suspension was separated using a 0.45 μm membrane filter. The pH value of the filtrate was measured by a Mettler-Toledo pH meter, and the residual P concentration (i.e., the equilibrium concentration in solution) was measured by the ammonium molybdate spectrophotometric

method. The relative error was less than 1.9 % for a 2 mg P/L standard sample (GB/T 11893–1989). The amount of P adsorbed (q_e, mg/g) was calculated according to equation (1).

$$q_e = \frac{(ci - ce)V}{m} \quad (1)$$

where c_i is the initial P concentration (mg/L); c_e is the residual P concentration after adsorption (mg/L); V is the solution volume (L); m is the adsorbent mass (g).

2.4.2. Adsorption isotherm experiment

A 1000 mg P/L phosphate stock solution was prepared and subsequently diluted to solutions of different P concentrations (50 mg/L,100 mg/L,150 mg/L, 200 mg/L, 250 mg/L, 300 mg/L, 350 mg/L, 400 mg/L). The pH of these solutions was adjusted to 3.0 using 0.1 mol/L HCl and NaOH. 0.02 g LC800 (or LO800) was added into 20 mL of the above P solutions. After adsorption for 6 h in a shaker (180 r/min, 25 °C), the suspension was separated and the P concentration was measured. The P adsorption capacities were fitted to both Langmuir and Freundlich models. The two relevant equations are as follows:

$$q_e = \frac{q_{max} K_L c_e}{1 + K_L c_e} \quad (2)$$

$$q_e = K_F c_e^{1/n} \quad (3)$$

Where q_e and q_{max} are the equilibrium adsorption capacity and Langmuir maximum adsorption capacity, mg/g, respectively; K_L is the Langmuir constant, L/mg; c_e is the equilibrium concentration in solution, mg/L; K_F is a Freundlich constant, $(mg{\cdot}L^{1/n})/(g{\cdot}mg^{1/n})$; n is a measure of the adsorption intensity or surface heterogeneity. $1/n$ less than 1 means good adsorption performance of adsorbents, while $1/n$ higher than 1 means poor adsorption performance [28].

2.4.3. Adsorption kinetic experiment

To explore the adsorption rate of the adsorbents for different P species and the role of Cl in the adsorption process, P solutions with a concentration of 50 mg/L were prepared directly using KH_2PO_4 and K_2HPO_4. Then, 0.02 g LC800 (or LO800) was mixed with 20 mL of the above P solution in 50 mL glass bottles and transferred to a shaker (180 r/min, 25 °C). During the adsorption process, adsorption solution samples were collected in triplicate at 1, 3, 5, 10, 15, 30, 60, 120, 180 and 360 min. After filtration, the Cl^- concentration was measured by using an ion electrode (BXS-CL, Hangzhou Qiwei Instrument Co., LTD). The P adsorption capacity data were fitted to both pseudo-first-order (PFO) and pseudo-second-order (PSO) models. The corresponding two equations to PFO and PSO are shown as follows.

$$q_t = q_e(1 - e^{-k_1 t}) \quad (4)$$

$$q_t = \frac{q_e^2 k_2 t}{1 + q_e k_2 t} \quad (5)$$

where, q_t is the adsorption capacity (mg/g) at time t, q_e is the adsorption amount (mg/g) at equilibrium, k_1 is the primary rate constant (h^{-1}); k_2 is the secondary rate constant (g/(mg·h)).

2.4.4. Adsorption-desorption and P removal in natural water

Several phosphate desorption reagents including NaOH (1 mol/L), Na_2CO_3 (1 mol/L), NaCl (1 mol/L), and $Na_2C_2O_4$ (0.2 mol/L) solutions were used for P desorption study. In a typical adsorption–desorption experiment, 0.04 g LC800 (or LO800) was added into 40 mL of 200 mg/L P solution in a centrifuge tube. After 6 h of adsorption, the suspension was separated with a centrifuge entirely. Then, the solid was mixed with a desorption reagent for 6 h. During the desorption process, the P concentration in the liquid phase was determined.

To conduct a real water purification test, approximately 2 L water sample was collected from a landscape lake in Northwest A&F University, and it was then filtered through a 0.45 μm membrane to remove suspended particles. Next, the adsorbents were added to the water sample at different concentrations (ranging from 0.2 to 1.0 g/L) in centrifugal tubes, and the mixtures were transferred to a shaker (180 r/min, 25 °C) and agitated for 6 h to allow for adsorption to occur. After adsorption, the soluble P (SP) was measured after persulfate digestion, while the soluble reactive P (SRP) was measured without persulfate digestion [29].

3. Results and discussion

3.1. Material characterization

LC500 presented a porous structure with a large amount of separated spherical pores existing in its matrix. The aperture distribution of these pores ranged from 50 to 300 nm, with the strut thicknesses in the range of 10 ~ 100 nm (Fig. 1a, b). Upon increasing the temperature to 600 °C, the pore became irregular and narrow in LC600 (Fig. 1e, f). The results indicated that the calcination temperature at 500 ~ 600 °C retained the native pore structure generation during the foaming of the gel precursor. Upon further increasing the temperature to 700 °C, the surface pore structure vanished, and numerous regular and thick nanosheet crystals appeared on LC700. The nanosheet thicknesses ranged from 20 to 80 nm (Fig. 1i, j). The surface morphology of LC800 was similar to that of LC700, but the nanosheet thickness slightly increased (Fig. 1m, n). By contrast, the LO500 and LO600 were in phases of loose and irregular sheet-like crystals (Fig. 1c, d, g, h). Upon increasing the calcination temperature, the size of the nanosheets grew, and the shape became noticeably regular. For example, the grain of LO800 showed a hexagonal surface morphology, and the thickness of individual nanosheets ranged from 20 to 70 nm (Fig. 1o, p).

As shown in Fig. 2(a), the diffraction peaks centered at 2-theta of 12.8°, 25.2°, 25.9°, 30.7°, 33.9°, 40.5°, 43.8°, 50.7°, 51.3°, 56.6°, 58.1°, and 63.9° matched with the crystal planes of (001), (101), (002) (110), (102), (112), (200), (113), (211), (212), (104), and (220) in the tetragonal phase of LaOCl (JCPDS code No. 34——1494), and there were no secondary phases or impurity peaks. For La_2O_3, the diffraction peaks located at 2-theta of 26.1°, 29.2°, 29.9°, 39.5°, 46.0°, 52.2°, 55.4°, and 62.2° corresponded to the (100), (002), (011), (012), (110), (103), (103) (112), and (202) crystal planes (JCPDS code No. 73——2141) in hexagonal phase (Fig. 2b). The above results confirmed the production of pure LaOCl and La_2O_3 materials. Meanwhile, all diffraction peaks of LaOCl and La_2O_3 became narrower, stronger, and sharper with increasing the temperature from 500 to 800 °C, which indicated that the increase in calcination temperature enhanced the crystallinity [30,31]. The intensity ratio of the main peaks for LC500, LC600, LC700, and LC800 was 0.26, 0.41, 0.62, and 1.0, respectively. Similarly, for LO500, LO600, LO700, and LO800, the intensity ratio of the major peaks was 0.14, 0.30, 0.61, and 1.0, respectively. The S_{BET} and Zeta potential results are shown in Fig. 2(c, d) and Table 1. It was observed that the S_{BET} of La_2O_3 was noticeably higher than that of LaOCl. With the increase of calcination temperature, the S_{BET} of LaOCl increased from 13.8 m^2/g (500 °C) to 14.5 m^2/g (600 °C) and then decreased to 8.6 m^2/g (800 °C), while the S_{BET} of La_2O_3 decreased from 26.8 m^2/g (500 °C) to 9.2 m^2/g (800 °C). The results indicated that increasing the calcination temperature would lead to a decrease in the surface area, which is evident from the surface morphology of the adsorbent depicted in Fig. 1a-p. The decrease in surface area can be attributed to sintering and particle agglomeration, which cause the collapse of the pore structure, as well as volatilization of components and the formation of larger crystals at higher temperatures. Furthermore, the measurement of Zeta potential revealed that LaOCl has a higher IEP than La_2O_3, which can be mainly attributed to differences in their crystal structures (as depicted in Fig. 2d).

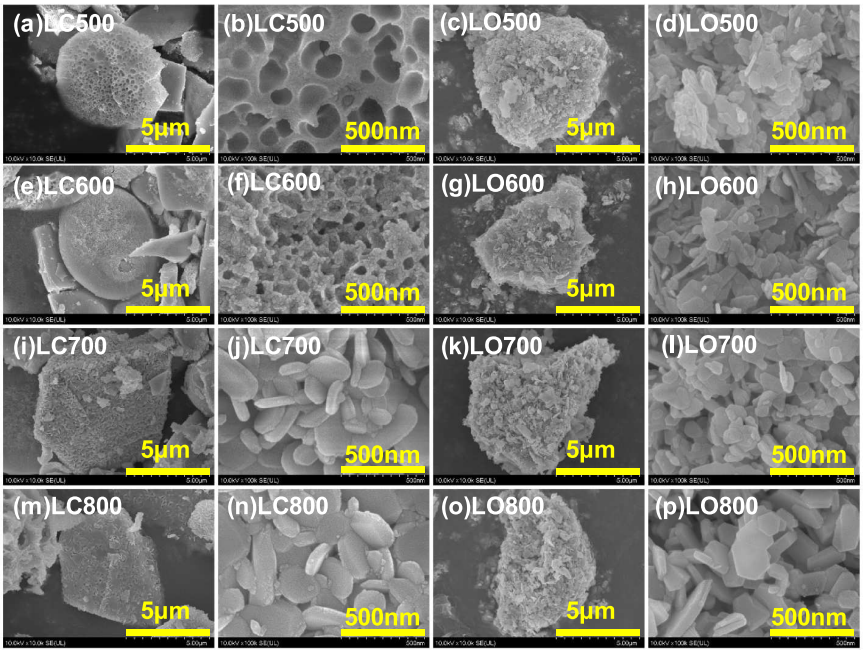


Fig. 1. SEM images of (a, b) LC500, (c, d) LO500, (e, f) LC600, (g, h) LO600, (i, j) LC700, (k, l) LO700, (m, n) LC800, and (o, p) LO800.

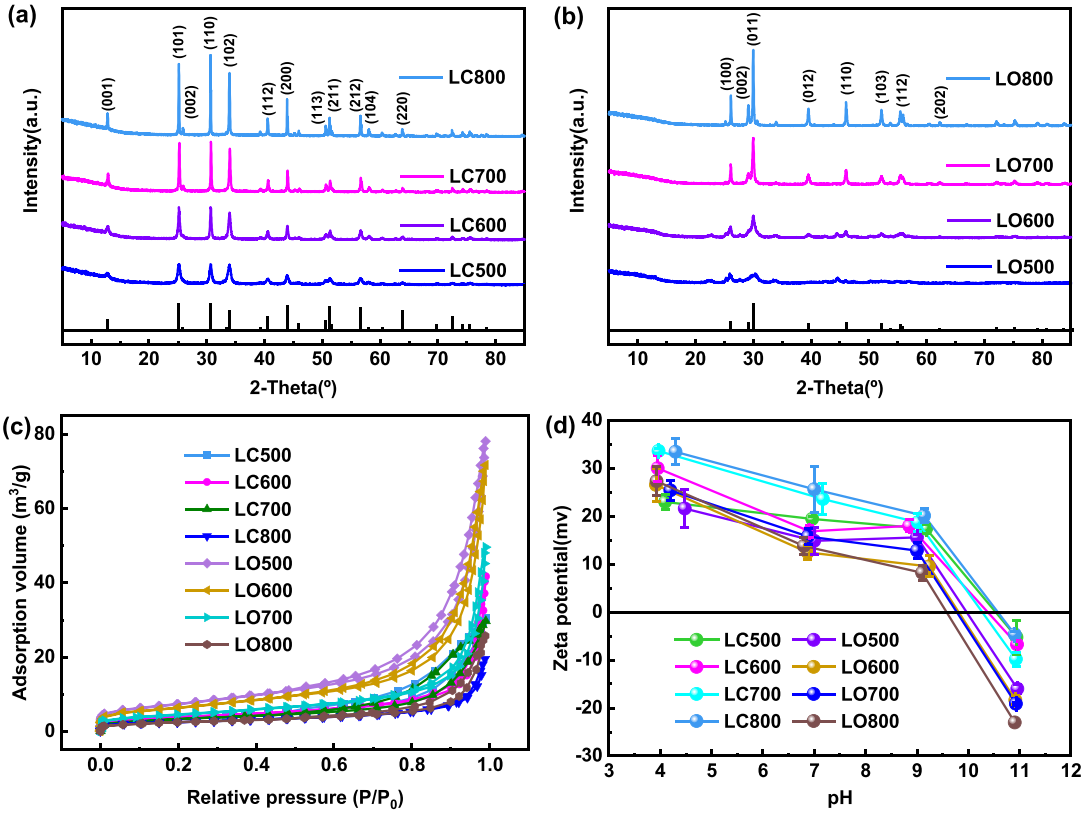


Fig. 2. XRD patterns of (a) LaOCl and (b) La_2O_3 samples; (c) N_2 adsorption–desorption isotherms; (d) Zeta potential in different pH.

Table 1
S_{BET} and IEP results of LaOCl and La_2O_3.

Adsorbents	LC500	LC600	LC700	LC800	LO500	LO600	LO700	LO800
S_{BET} (m^2/g)	13.8	14.5	12.2	8.6	26.8	23.1	16.2	9.2
IEP	10.53	10.37	10.26	10.58	9.96	9.81	9.77	9.57

3.2. Adsorption of P under different pH conditions

As shown in Fig. 3(a) and (b), all adsorbents showed a decrease in the P adsorption capacity upon increasing the solution pH. The trends of P adsorption with pH change are similar to previous La-based adsorbents to P adsorption, such as La_2O_3, $La(OH)_3$ and $La(OH)_3/Fe_3O_4$ composites [11,13,32]. An important reason is that the affinity of La(III) to $H_2PO_4^-$ is higher than HPO_4^{2-} [33,34]. The most abundant P species in the pH range of 3.0 to 6.0 is $H_2PO_4^-$, while HPO_4^{2-} in the range of 8.2 to 11.0 (Fig. 3d). For the P adsorption at the initial pH range of 3.0–5.0, the pH changed to 3.0–5.5 after P adsorption by LaOCl. In contrast, La_2O_3 caused a significant increase in pH to 6.2 ~ 7.3, which markedly decreased the $H_2PO_4^-$ ratio in solutions (as shown in Fig. 3c). Simultaneously, the increase in pH caused a transformation of adsorption sites from highly reactive, positively charged adsorption sites ($La-OH_2^+$) to low reactive, neutral or negative sites ($La-OH$ or $La-O^-$), which is

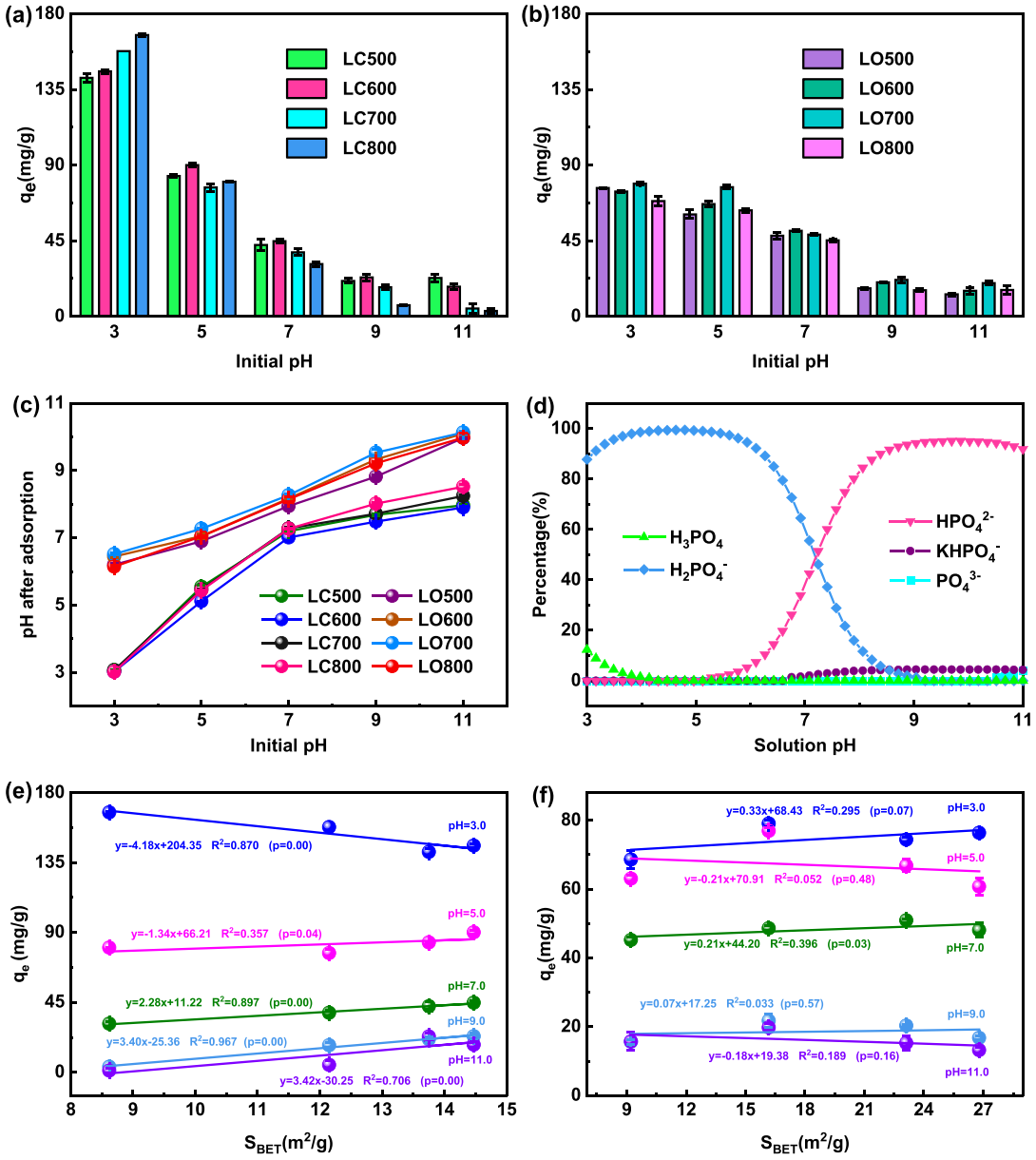


Fig. 3. P adsorption capacities of (a) LaOCl and (b) L_2O_3 in the different initial pH; (c) the solution pH of after P adsorption; (d) the P species in different solution pH when the P concentration is 200 mg/L; linear regression analysis of the relationship between S_{BET} and P adsorption capacity for (e) LaOCl and (f) L_2O_3 in different pHs.

related to IEP values [11]. The IEP were greater than 10.26 for LaOCl and greater than 9.57 for La_2O_3 (Table 1).

In addition, the maximum P adsorption capacity is different at different pH points of LaOCl and La_2O_3. This can be attributed to differences in crystallinity and S_{BET}. The crystal face exposition is correlated with the crystallinity, which is an important factor for adsorption free energy [35]. Simultaneously, the number of active adsorption sites is related to S_{BET}. The difference in the maximum P adsorption of LaOCl or La_2O_3 in different pH conditions is the integrated impacts of the two factors. As shown in Fig. 3(a), the P adsorption capacity increased with the crystallinity at pH 3.0 for LaOCl, which may be related to the selective binding of specific crystal face of LaOCl to the $H_2PO_4^-$. However, the result was not found under other pH conditions. And for La_2O_3, no clear link between crystallinity and P adsorption capacity was found. The correlation between S_{BET} and P adsorption capacity was further analyzed at different pH points. For LaOCl, the P adsorption capacity was found significantly related to the S_{BET} of adsorbent at pH 3.0–11.0 ($p < 0.05$) with a positive correlation between S_{BET} and adsorption capacity at pH > 3 and a negative correlation at pH 3.0 (Fig. 3e). However, for La_2O_3, the positive correlation between S_{BET} and adsorption capacity was only found at pH 7.0, with the correlation coefficient of $R^2 = 0.396$ (Fig. 3f). According to above analysis, the P adsorption capacity was mainly affected by crystallinity at pH 3.0 but by S_{BET} in pH 5.0 ~ 9.0 range for LaOCl, and S_{BET} and crystallinity are not the main factors influencing the P adsorption capacity for La_2O_3.

3.3. Adsorption isotherms and kinetics

In order to exclude the influence of morphology or surface area and reveal the performance and mechanism of LaOCl and La_2O_3 adsorbing P ions, LC800 and LO800 with high crystallinity and minor surface area differences were used to carry out the subsequent experiments. As shown in Fig. 4(a), the P adsorption capacity increased and then reached to a stable state for both adsorbents. According to the result of data fitting, the Langmuir and Freundlich models could fit the P adsorption capacity well ($R^2 > 0.97$) (Table 2), which proved that P adsorption on both adsorbents involved physical and chemical interaction. The Langmuir maximum adsorption capacity of LC800 is 164.52 mg/g, which is about 2.3 times that of La_2O_3. And the 1/n value fitted with Freundlich model of LC800 is 0.0218 and for LO800 is 0.0862, which proved that both adsorbents are good materials for P adsorption, and LC800 is better than LO800 [28]. In order to further compare the P adsorption capacity, some typical La-based adsorbents are summarized in Table S1. It can be seen that the LaOCl has noticeable advantage compared with most other La-based adsorbents for P adsorption, such as the P adsorption capacity of LaOCl is 3.5 times that of commercial La_2O_3, 3.0 times that of commercial $La(OH)_3$, 2.2 times that of $La/Al(OH)_3$ composite, and 16.1 times that of phoslock, etc. (Table S1).

The P adsorption capacity as a function of time is shown in Fig. 4(b). The saturated P adsorption capacity of LC800 with the $H_2PO_4^-$ species was significantly higher than that of LO800, as it was explained above i.e., the lower P adsorption capacities for La_2O_3 in comparison to LaOCl in the pH range of 3.0–5.0. In contrast, the P adsorption capacity of LC800 with the HPO_4^{2-} species was lower than that of LO800. The main reason playing a role here is the solution pH. With the same P level (50 mg/L), the initial pH of K_2HPO_4 solution was about 8.4. Another important finding is that the $H_2PO_4^-$ solution as high as 50 mg P/L was quickly reduced to an ultra-low level (approximately 0.002 mg P/L) (which is far below the P concentration (0.02 mg/L) that triggers eutrophication) by LC800, but the residual P concentration was about 11.27 mg P/g by LO800 after 3 h of adsorption. Such fast adsorption rate and superior adsorption capacity are attributed to the high IEP and surface ligand of

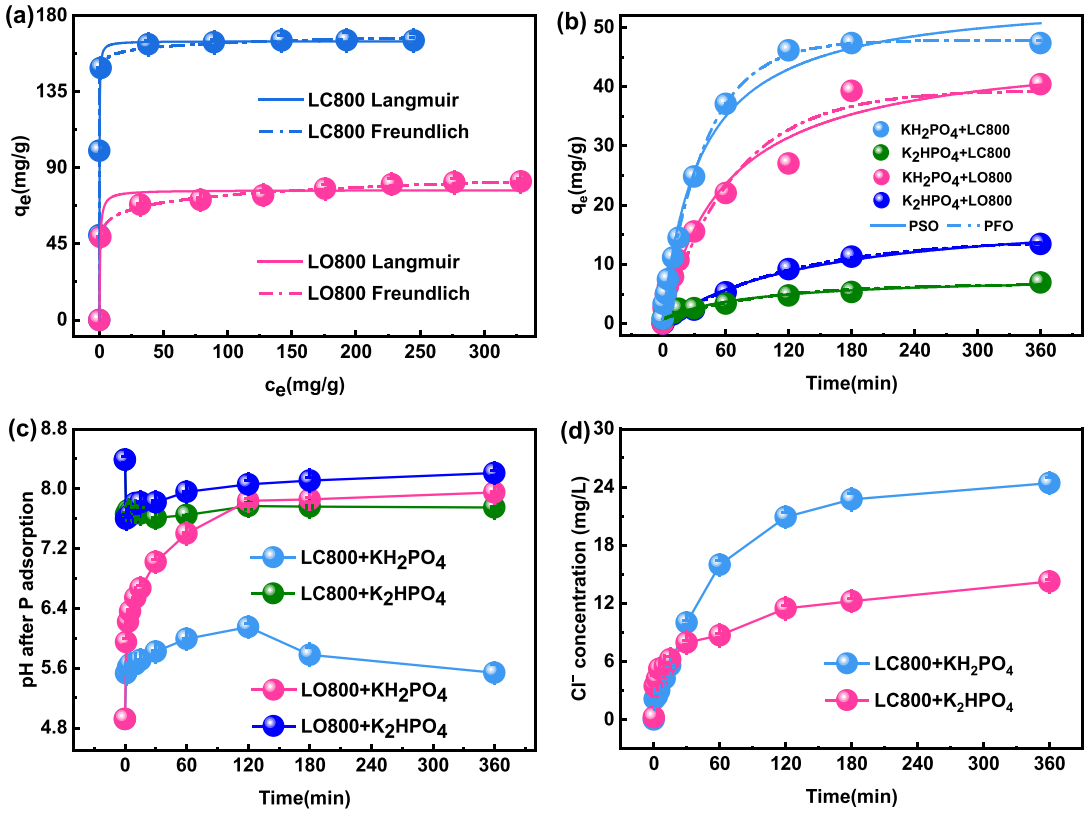


Fig. 4. (a) The isotherm curves of P adsorption by LC800 and LO800; (b) The kinetic curves of P adsorption by LC800 and LO800; (c) the changes of solution pH and (d) the Cl^- concentration during the P adsorption process.

Table 2
The fitting parameters of P adsorption isotherms by LC800 and LO800.

Adsorbent	Langmuir			Freundlich		
	q_{max} (mg·g^{-1})	K_L (L·mg^{-1})	R^2	$1/n$	K_F [(mg·g^{-1})·(L·mg^{-1})$^{1/n}$]	R^2
LC800	164.52	9.20	0.997	0.0218	148.88	0.988
LO800	71.26	2.40	0.975	0.0862	49.44	0.996

LaOCl. The adsorption process of LC800 and LO800 to $H_2PO_4^-$ ion can be observed more visually by the colour development reaction in Fig. S1 and S2. The kinetic model fitting results revealed that there are only small differences in R^2 between PFO and PSO fitting data for both adsorbents (Table 3). However, the k_1 and k_2 values of LC800 were higher than those of LO800 for $H_2PO_4^-$ or HPO_4^{2-} adsorption, which testified that the adsorption rate of LC800 to both ions is faster than LO800. In the meanwhile, the k_2 of LC800 for P adsorption is between $4.64 \times 10^{-4} \sim 1.42 \times 10^{-3}$ g/(mg·min), which is higher than hollow La_2O_3 ($k_2 = 6.3 \times 10^{-5}$) [12], but is almost in the same order of magnitude with $La(OH)_3$ prepared by a hydrothermal method ($5.8 \sim 8.2 \times 10^{-4}$) [14]. In addition, the pH value and the Cl^- content during the adsorption process are shown in Fig. 4(c) and (d). For the adsorption of $H_2PO_4^-$, the pH after adsorption to the two adsorbents increased dramatically, and the La_2O_3 experiment group showed much higher growth than LaOCl. This is an important reason that the P adsorption capacity of LC800 is higher than LO800 at the pH 5.0. For the adsorption of HPO_4^{2-}, the pH decreased firstly in both experiment groups, and then in the LO800 group it increased slightly, but the solution pH of LO800 group was only slightly higher than that of LC800. Therefore, LC800 has no obvious advantage compared with LO800. According to Fig. 4(d), it can be seen that Cl^- concentration in KH_2PO_4 solution is much higher than that in K_2HPO_4 solution, which demonstrates that the replacement of Cl^- by P ions is noticeably affected by the solution pH.

3.4. Adsorbent regeneration and evaluation of real water application

The amount of desorbed P was relatively small for both P-loaded LC800 and LO800 (Fig. 5a). Using 1 mol/L NaOH as a desorption reagent, approximately 7.7 % and 23.0 % of P desorbed from P-loaded LC800 and P-loaded LO800, respectively. Similarly, when employing 1 mol/L Na_2CO_3 solution for P desorption, about 2.4 % and 8.9 % of P was released from P-loaded LC800 and P-loaded LO800, respectively. Furthermore, no P was desorbed from the P-loaded LaOCl and La_2O_3 in NaCl and $Na_2C_2O_4$ solutions. The results are similar to previous studies by Wu et al. [36]. They also found that the P loaded on La oxide/hydroxides can be desorbed effectively only when some specific conditions are met, such as high NaOH concentration (12.5 mol/L), liquid/solid ratio (6 mL/g) and temperature (140 °C) or strong acid solution (0.5 mol/L HCl) [11,13]. Although effective P desorption methods have been proposed, these conditions possibly make application uneconomical in practice.

Based on the strong affinity of La for P, LaOCl and La_2O_3 application in natural waters to make P inactive lastingly is an excellent measure to control eutrophication. Therefore, LC800 and LO800 were further tested for phosphorous removal from lake water with SP concentration 0.095 ± 0.011 mg P/L, SRP concentration 0.042 ± 0.004 mg P/L, and pH 7.91 ± 0.07. The results are presented in Fig. 5b. Both adsorbents can further remove phosphorus in natural water to further lower concentrations. With the controlled adsorbent dosage, the SP and SRP can reach below 0.02 mg/L, but LC800 has an advantage when the dosage of adsorbents increases continually. To sum up, these results indicated the feasibility of LaOCl and La_2O_3 for P removal in real contaminated waterbodies.

3.5. Mechanisms of P adsorption by LaOCl and La_2O_3

As shown in Fig. 6 (a), the most vigorous diffraction peak was weakened obviously (intensities ratio of the diffraction peak after P adsorption (I_e) to the diffraction peak without P adsorption (I_i), $I_e/I_i = 0.44$) after the adsorption of KH_2PO_4 by LC800 (LC800 − H2P). And several new and faint diffraction peaks appeared at 2-theta of 19.9°, 28.9°and 31.2° in LC800 − H2P, which were contributed to the crystal planes of (1 0 1), (2 0 0) and (1 0 2) in $LaPO_4{\cdot}0.5H_2O$ (JCPDS code No. 46—1439). The main reason is that LC800 adsorbed numerous $H_2PO_4^-$ and HPO_4^{2-} on its surface, and then a small amount of LaPO4··0.5H_2O crystal formed as the evolution of the La − P complex [37,38]. After P adsorption from K_2HPO_4 solution by LC800 (LC800 − HP), except for the weakness of the peak intensity ($I_e/I_i = 0.79$), the peak position of LC800 − HP did not change compared to the LC800 case. On the other hand, after P adsorption from KH_2PO_4 and K_2HPO_4 solutions by LO800 (LO800 − H2P and LO800 − HP), the diffraction peaks of La_2O_3 were transformed into peaks of $La(OH)_3$ completely (Fig. 6b). The result demonstrated that the LaOCl crystal structure is more stable than La_2O_3 in solutions, and this is why the pH rose sharply after P adsorption by La_2O_3.

The FTIR spectra of LC800 and LO800 before and after the P adsorption were also investigated (Fig. 6c-f), and the functional group information was analyzed as reported in Table 4. As a result of the adsorption of the KH_2PO_4 species, the P − O stretching vibrational peaks (1056 and 1012 cm^{-1}) and P − O bending vibrational peaks (616 and 539 cm^{-1}) appeared clearly in LC800 − H2P sample. On the other hands, the La − O (528 cm^{-1}) and La − OH (3565 cm^{-1}) stretching vibrational peaks disappeared entirely (Fig. 6c, e), which suggested that La − O and La − OH were the active sites of LC800 adsorbing $H_2PO_4^-$. A possible adsorption mechanism is that the La − O group protonated in solutions firstly, converting into La − OH. Subsequently, the − OH originating from La − O protonation and the pristine adsorbent surface are replaced by P ions. Upon adsorption of the K_2HPO_4 spices by LC800, the La − OH (3565 cm^{-1}) stretching vibrational peak was unchanged, the La − O (528 cm^{-1}) peak broadened and moved to lower frequency, and a sharp stretching vibrational peak of P − O appeared only at the 1056 cm^{-1} band (Fig. 6c, e). Consequently, the inner-sphere complexation between HPO_4^{2-} and La(III) sites possibly happened [34,39]. For the P adsorption by LO800, LO800 − H2P sample appeared with clear and intense P − O stretching and bending vibrational peaks (1056, 1012, 616, and 539 cm^{-1}), proving that P was adsorbed successfully.

Table 3
The fitting parameters of P adsorption kinetics by LC800 and LO800.

Adsorbent	P solutions	PFO			PSO		
		k_1 (min^{-1})	Q_e (mg/g)	R^2	k_2 (g/mg min^{-1})	Q_e (mg/g)	R^2
LC800	KH_2PO_4	2.46×10^{-2}	50.56	0.998	4.64×10^{-4}	59.08	0.988
	K_2HPO_4	1.03×10^{-2}	6.37	0.956	1.42×10^{-3}	7.79	0.968
LO800	KH_2PO_4	1.48×10^{-2}	39.46	0.954	3.57×10^{-4}	47.03	0.969
	K_2HPO_4	8.34×10^{-3}	14.25	0.989	3.69×10^{-4}	19.18	0.986

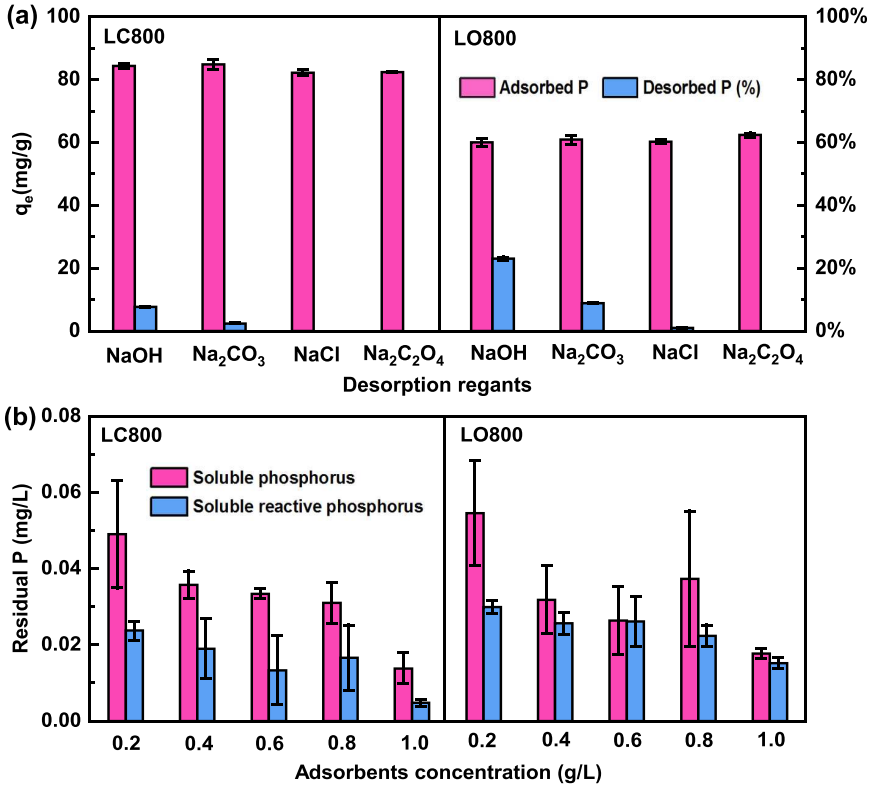


Fig. 5. Desorption P from P-loaded (a) LC800 and (b) LO800 in different solutions; (c) LC800 and LO800 for P removal in real contaminated water.

Meanwhile, the intensity of La − OH stretching and deformation vibrational peaks (3609 and 648 cm^{-1}) increased noticeably. The phenomenon made it challenging to distinguish the function of − OH during the P adsorption process. However, in accordance with the La − OH peak upon adsorption of the K_2HPO_4 spices by LO800, it can be found that the peak intensities (3609 and 648 cm^{-1}) of LO800 − H2P were dramatically weaker than LO800 − HP. Therefore, this suggests that the − OH group acts as a ligand being exchanged during the adsorption of $H_2PO_4^-$ ion by LO800. Moreover, both LC800 − H2P and LO800 − H2P showed obvious and sharp P − O bending vibrational peaks (616 and 539 cm^{-1}), while the two characteristic peaks in LC800 − HP and LO800 − HP were very weak or non-existent, which demonstrated a clear variation in the adsorbents' affinity towards $H_2PO_4^-$ and HPO_4^{2-} ions [33,34].

For further confirmation of the P adsorption mechanism, LC800, LC800-HP, LC800H2P, LO800, LO800-HP and LO800H2P were analyzed using XPS. As shown in Fig. 7(a), upon adsorption of the $H_2PO_4^-$ and HPO_4^{2-} ions, the binding energy of La $3d_{5/2}$ peak shifted from 834.4 eV to 834.5 eV and 835.9 eV for LC800, and 833.5 eV to 835.0 eV and 835.4 eV for LO800. The electron arrangement of La is [Xe] $6s^25d^1$, and the valence of La^{3+} in the oxidation state is difficult to be changed [44]. Therefore, the main reason for this phenomenon is the interaction of La with P ions, which weakened the shielding effect of the outer electrons on the inner electrons, thus shifting the binding energy to higher levels. Moreover, the energy gap (△E) between the La $3d_{5/2}$ main peaks and La $3d_{5/2}$ satellite peaks of LC800 and LO800 was ~ 4.3 eV, and the values were about ~ 4.2 eV and ~ 3.4 eV for LC800 − HP and LC800 − H2P, and ~ 3.7 eV and ~ 3.5 eV for LO800 − HP and LO800 − H2P respectively. It is reported that the △E for pure La_2O_3 and $La(OH)_3$ is about 4.5 and 3.8 eV, respectively, and 3.1–3.6 eV for pure $LaPO_4$ [45,46]. It can be seen that the La − O only has a small change after LC800 adsorbing HPO_4^{2-} ions, but the La − O translated into La − PO_4 after LC800 adsorbing $H_2PO_4^-$ obviously. The results are consistent with XRD and FTIR analysis discussed above. For LO800, the La − O changed into La − OH or La − PO_4 completely, and there is a transformation of La − OH to La − PO_4 because of the △E of LO800 − H2P (~3.5 eV) being lower than $La(OH)_3$ (~3.8 eV). Moreover, the P 2p peaks are centered at 133.6 eV for LC800 − H2P and LC800 − HP, and at 133.5 eV for LO800 − HP and LO800H2P. According to the area of P 2p peak, it can be speculated that this is because of the P content on the materials (i.e. LC800 − H2P > LO800 − H2P > LO800 − HP > LC800 − HP) (Fig. 7c). The O 1 s peak of LC800 was composed of lattice oxygen (M − O, 529.1 eV) and hydroxyl oxygen (M − OH, 531.5 eV), but the binding energy lowered to about 0.3 eV in LO800 [6]. After the P adsorption, the M − O peaks in LC800 and LO800 decreased or disappeared, while the M − OH/P − O peaks enhanced (Fig. 7d, e). The results indicate that P was adsorbed successfully or surface protonation occurred on the adsorbents [47–49]. Additionally, the Cl $2p_{1/2}$ and Cl $2p_{3/2}$ peaks were located at 200.5 eV and 198.9 eV for each, and the peak at 195.6 eV is La $4p_{3/2}$ [50,51]. After P adsorption by LC800, the Cl 2p peak position did not change in LC800 − HP and LC800 − H2P samples, but the intensity and area decreased dramatically, especially for LC800 − H2P sample, which proved that P ions may replace Cl atom during adsorption process (Fig. 7f). At the meanwhile, the La $4p_{3/2}$ peak moved from 195.6 eV to 195.8 and 196.9 eV respectively after P adsorption. This result is consistent with the conclusion of the La 3d peak. As indicated above, the possible P adsorption reactions are shown in (1) to (10) (1 ~ 5 for LaOCl and 6 ~ 10 for La_2O_3), and the corresponding adsorption schematic is depicted in Fig. 8. The adsorbents adding to the P solutions first adsorb water, experiencing a protonation process. Electrostatic attraction occurs when the solution pH is below the adsorbent IEP. The surface − OH and Cl^- on LaOCl can be replaced by P ions at low solution pH, then the exchanges being severely hindered, and the surface complexation was the main adsorption mechanism with increasing the solution pH gradually. However, unlike LaOCl, the La_2O_3 adsorbed a large amount of water once added to solutions, producing numerous − OH on its surface and inner crystal. Then P ions

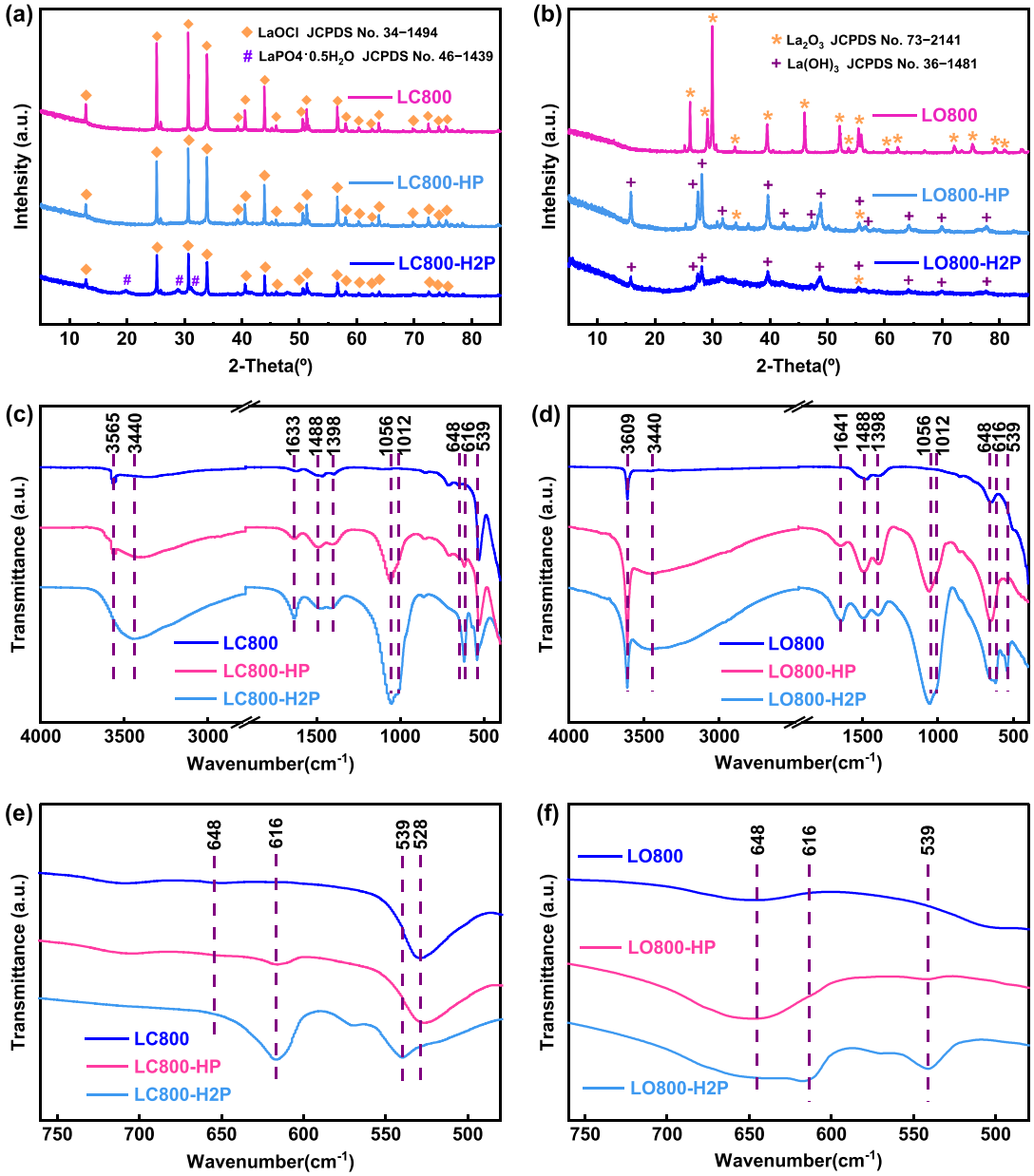


Fig. 6. (a) XRD patterns of LC800 and (b) LO800 after P adsorption; (c) The FTIR spectra of LC800 and (d) LO800 before and after P adsorption; (e)and (f) are the corresponding partial enlargements.

Table 4
FTIR spectra peaks of different functional groups.

Wavenumber	Bond origin	Reference
528 cm^{-1}	La − O stretching vibration from LaOCl	[40]
539 cm^{-1} and 616 cm^{-1}	P − O bending vibration	[6,8,16]
648 cm^{-1}	La − OH deformation vibration from La_2O_3 or $La(OH)_3$	[41,42]
1012 cm^{-1} and 1056 cm^{-1}	P − O stretching vibration	[6,11,41]
~1398 cm^{-1} and ~ 1488 cm^{-1}	CO_3^{2-} stretching vibration	[42,43]
1633 cm^{-1} ~ 1641 cm^{-1}	−OH bending vibration of H_2O	[8,16,43]
3440 cm^{-1}	−OH stretching vibration of H_2O	[8,42,43]
3565 cm^{-1} and 3609 cm^{-1}	La − OH stretching vibration from LaOCl and $La(OH)_3$ for each	[41,42]

were adsorbed by ligand exchange and surface complexation depending on the solution pH conditions.

$$Cl - La - O + H_2O \rightarrow Cl - La - OH^+ + OH^- \quad (1)$$

$$Cl - La - OH^+ + H_2O \rightarrow Cl - La - OH_2^+ + OH^- \quad (2)$$

$$Cl - La - OH_2^+ + H_2PO_4^-/HPO_4^{2-} \rightarrow Cl - La - OH_2 - H_2PO_4/HPO_4 \quad (3)$$

$$Cl - La - OH_2^+ + H_2PO_4^-/HPO_4^{2-} \rightarrow La - H_2PO_4/HPO_4 + Cl^-/OH^- \quad (4)$$

$$Cl - La - O + HPO_4^{2-} \rightarrow ClOLa - O - HPO_3 \quad (5)$$

$$La - O + H_2O \rightarrow La - OH^+ + OH^- \quad (6)$$

$$La - OH + H_2O \rightarrow La - OH_2^+ + OH^- \quad (7)$$

$$La - OH_2^+ + H_2PO_4^-/HPO_4^{2-} \rightarrow La - OH_2 - H_2PO_4/HPO_4 \quad (8)$$

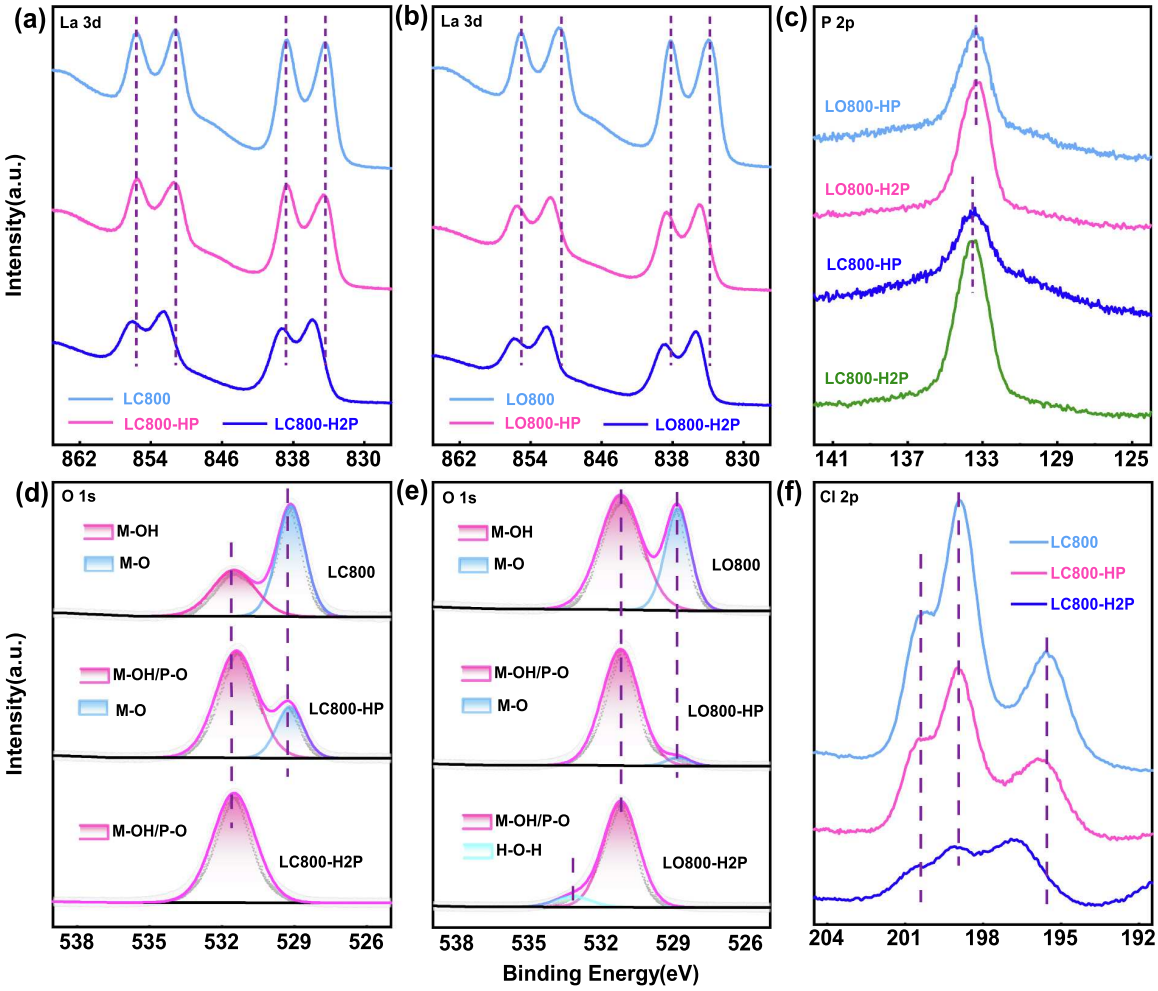


Fig. 7. (a) La3d high-resolution spectra of LC800, LC800HP and LC − 800H2P, (b) La3d high-resolution spectra of LO800, LO800 − HP and LO − 800H2P, (c) high-resolution spectra of P 2p, (d) O1s split peak fits of LC800, LC800HP and LC − 800H2P, (e) O1s split peak fits of LO800, LO800 − HP and LO − 800H2P, (f) Cl 2p and La 4p3/2 high-resolution spectra of LC800, LC800 − HP and LC − 800H2P.

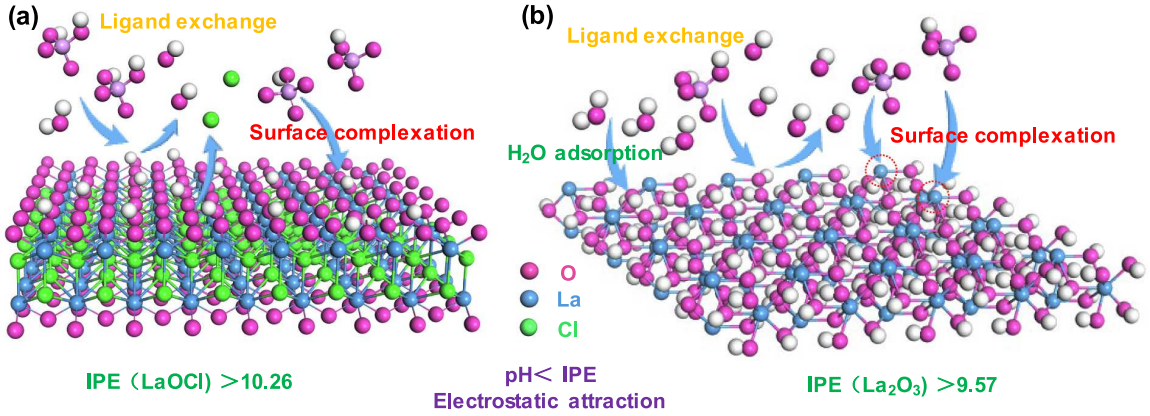


Fig. 8. Possible adsorption mechanism of P on LaOCl and La_2O_3.

$$La - OH + H_2PO_4^-/HPO_4^{2-} \rightarrow La - H_2PO_4/HPO_4 + OH^- \quad (9)$$

$$La - O + HPO_4^{2-} \rightarrow O - La - O - HPO_3 \quad (10)$$

4. Conclusions

In this study, tetragonal LaOCl and hexagonal La_2O_3 were successfully prepared by different preparation methods and calcination temperatures. The comparison of their P adsorption performances studied here for was the first time. The crystal structure has an obvious impact on their P adsorption performances. The stability in water, the special exchange of ligand Cl^-, and the high IEP enhance the P adsorption capacity of LaOCl. The maximum P adsorption capacity of LaOCl is 2.3 times greater than that of La_2O_3 in pH 3.0. The P adsorption rate of LaOCl is also higher than that of La_2O_3. In addition, the influence of surface area and crystallinity on P adsorption capacity differed with the solution pH changing. The two adsorbents were difficult to desorb P after adsorption, but both were able to reduce P in natural water to trace levels. So, the application of both adsorbents in natural water to lock P or using their P-loaded materials to further resolve other environmental issues, such as passivation for heavy metals and reduction for greenhouse gases should be considered in future research directions. As a whole, this study provides some new perspectives for P removal from waters rich in P and wastewater, which is important for creating novel La-based adsorbents in the future.

CRediT authorship contribution statement

Yuan Luo: Performing the experiments, investigation, analysis, data collection, methodology, and writing the draft manuscript. **Yaru Peng:** Investigation, analysis, data collection and validation, and helping in writing the original draft of manuscript. **Yimeng Li:** Investigation, analysis, data collection and validation, and helping in writing the original draft of manuscript. **Yage Li:** Investigation, analysis, data collection and validation, and helping in writing the original draft of manuscript. **Chuchu Feng:** Investigation, analysis, data collection and validation, and helping in writing the original draft of manuscript. **Ronghua Li:** Supervision, foundation, conceptualization, research idea, experimental guiding, technical facilities, review, editing. **Bin Gao:** Revising, editing, and proof reading for the entire manuscript. **Ran Xiao:** Data analysis and validation, visualization, creating figures, writing and editing. **Xiu Zhang:** Data analysis and validation, visualization, creating figures, writing and editing. **Guangzhou Qu:** Data analysis and validation, visualization, creating figures, writing and editing. **Manlin Li:** Data analysis and validation, visualization, creating figures, writing and editing. **Ashour A. Ahmed:** Revising, editing, and proof reading for the entire manuscript. **Samir G. Al-Solaimani:** Revising, editing, and proof reading for the entire manuscript. **Peter S. Hooda:** Revising, editing, and proof reading for the entire manuscript. **Jörg Rinklebe:** Revising, editing, and proof reading for the entire manuscript. **Zengqiang Zhang:** Revising, editing, proof reading for the entire manuscript. **Sang Soo Lee:** Revising, editing, proof reading for the entire manuscript. **Sabry M. Shaheen:** Scientific concept, coordination, writing, editing, proof reading for the entire manuscript.

Declaration of Competing Interest

The authors declare that they have no known competing financial interests or personal relationships that could have appeared to influence the work reported in this paper.

Data availability

The data that has been used is confidential.

Acknowledgments

The National Natural Science Foundation of China (32172679) and the Open Research Fund of Key Laboratory of Biogas Institute of Ministry of Agriculture and Rural Affairs, China (2020–005) financially supported this work. The authors Sabry Shaheen and Samir Al-Solaimani are also thankful to the Deanship of Scientific Research at King Abdulaziz University for the financial support of their research project (Project ID: IFPRC-127-155-2020). We also thank Ran Zhao, Hong Zhang, Yingcui Yu, and Yajie Zuo (College of Natural Resources and Environment, Northwest A&F University), for their help in sample characterization.

Appendix A. Supplementary data

Supplementary data to this article can be found online at https://doi.org/10.1016/j.seppur.2023.125478.

References

[1] E. Ortiz-Reyes, R. Anex, A life cycle impact assessment method for freshwater eutrophication due to the transport of phosphorus from agricultural production, J. Clean. Prod. 177 (2018) 474–482.
[2] B. Ringeval, L. Augusto, H. Monod, D. van Apeldoorn, L. Bouwman, X. Yang, D. L. Achat, L.P. Chini, K. Van Oost, B. Guenet, R. Wang, B. Decharme, T. Nesme, S. Pellerin, Phosphorus in agricultural soils: drivers of its distribution at the global scale, Glob. Chang. Biol. 23 (2017) 3418–3432.
[3] R. Liu, L. Chi, X. Wang, Y. Sui, Y. Wang, H. Arandiyan, Review of metal (hydr)oxide and other adsorptive materials for phosphate removal from water, J. Environ. Chem. Eng. 6 (2018) 5269–5286.
[4] B. Wu, J. Wan, Y. Zhang, B. Pan, I.M.C. Lo, Selective phosphate removal from water and wastewater using sorption: process fundamentals and removal mechanisms, Environ. Sci. Tech. 54 (2020) 50–66.
[5] R. Li, J. Wang, Z. Zhang, M. Awasthi, D. Du, P. Dang, Q. Huang, Y. Zhang, L. Wang, Recovery of phosphate and dissolved organic matter from aqueous solution using a novel CaO-MgO hybrid carbon composite and its feasibility in phosphorus recycling, Sci. Total Environ. 642 (2018) 526–536.
[6] H. Fu, Y. Yang, R. Zhu, J. Liu, M. Usman, Q. Chen, H. He, Superior adsorption of phosphate by ferrihydrite-coated and lanthanum-decorated magnetite, J. Colloid Interface Sci. 530 (2018) 704–713.
[7] Y. Yang, K. Yuen Koh, R. Li, H. Zhang, Y. Yan, J.P. Chen, An innovative lanthanum carbonate grafted microfibrous composite for phosphate adsorption in wastewater, J. Hazard. Mater. 392 (2020), 121952.
[8] W. Shi, Y. Fu, W. Jiang, Y. Ye, J. Kang, D. Liu, Y. Ren, D. Li, C. Luo, Z. Xu, Enhanced phosphate removal by zeolite loaded with Mg–Al–La ternary (hydr)oxides from aqueous solutions: Performance and mechanism, Chem. Eng. J. 357 (2019) 33–44.
[9] Y. Zhi, C. Zhang, R. Hjorth, A. Baun, O.W. Duckworth, D.F. Call, D.R.U. Knappe, J. L. Jones, K. Grieger, Emerging lanthanum (III)-containing materials for phosphate removal from water: A review towards future developments, Environ. Int. 145 (2020), 106115.
[10] Q. He, H. Zhao, Z. Teng, Y. Wang, M. Li, M.R. Hoffmann, Phosphate removal and recovery by lanthanum-based adsorbents: A review for current advances, Chemosphere 303 (2022), 134987.
[11] J. Xie, Y. Lin, C. Li, D. Wu, H. Kong, Removal and recovery of phosphate from water by activated aluminum oxide and lanthanum oxide, Powder Technol. 269 (2015) 351–357.
[12] Y. Chang, Z. Wei, X. Chang, G. Ma, L. Meng, T. Liu, L. Yang, Y. Guo, X. Ma, Hollow hierarchically porous La_2O_3 with controllable multishells: A high-performance adsorbent for phosphate removal, Chem. Eng. J. 421 (2021), 127816.
[13] J. Xie, Z. Wang, S. Lu, D. Wu, Z. Zhang, H. Kong, Removal and recovery of phosphate from water by lanthanum hydroxide materials, Chem. Eng. J. 254 (2014) 163–170.
[14] L. Fang, B. Wu, J.K.M. Chan, I.M.C. Lo, Lanthanum oxide nanorods for enhanced phosphate removal from sewage: A response surface methodology study, Chemosphere 192 (2018) 209–216.
[15] R. Xu, M. Zhang, R.J.G. Mortimer, G. Pan, Enhanced phosphorus locking by novel Lanthanum/Aluminum–Hydroxide composite: Implications for eutrophication control, Environ. Sci. Tech. 51 (2017) 3418–3425.
[16] J. Yu, C. Xiang, G. Zhang, H. Wang, Q. Ji, J. Qu, Activation of lattice oxygen in LaFe (Oxy)hydroxides for efficient phosphorus removal, Environ. Sci. Tech. 53 (2019) 9073–9080.
[17] B. Zhang, L. Xu, Z. Zhao, S. Peng, C. Yu, X. Zhang, Y. Zong, D. Wu, Enhanced phosphate removal by nano-lanthanum hydroxide embedded silica aerogel composites: Superior performance and insights into specific adsorption mechanism, Sep. Purif. Technol. 285 (2022), 120365.
[18] Z. Zhao, Z. Li, L. Wu, Y. Song, M. Roger Razanajatovo, Q. Sun, T. Jiao, Q. Peng, Q. Zhang, Rational design of the nanocomposite by in-situ sub-10 nm La(OH)3 formation for selective phosphorus removal in waters, Sep. Purif. Technol. 312 (2023), 123306.

[19] G. Waetzig, G. Horrocks, R. Davidson, J.W. Jude, G.V. Villalpando, L. Zuin, S. Banerjee, In a different light: deciphering optical and X-ray sensitization mechanisms in an expanded Palette of LaOCl phosphors, J. Phys. Chem. C 122 (2018) 16412–16423.
[20] G. Li, Z. Hou, C. Peng, W. Wang, Z. Cheng, C. Li, H. Lian, J. Lin, Electrospinning derived one-dimensional LaOCl: Ln3+ (Ln = Eu/Sm, Tb, Tm) nanofibers, nanotubes and microbelts with multicolor-tunable emission properties, Adv. Funct. Mater. 20 (2010) 3446–3456.
[21] Y. Lan, C. Chen, J. Li, X. Xia, X. Mao, H. Zhou, Formation and growth of LaOCl:Eu3+ crystal in KCl-LiCl molten flux and its luminescent properties, Ceram. Int. 47 (2021) 4793–4802.
[22] G. Waetzig, G. Horrocks, J. Jude, G. Villalpando, L. Zuin, S. Banerjee, Ligand-mediated control of dopant oxidation state and X-ray excited optical luminescence in Eu-doped LaOCl, Inorg. Chem. 57 (2018) 5842–5849.
[23] A. Marsal, G. Dezanneau, A. Cornet, J.R. Morante, A new CO_2 gas sensing material, Sens. Actuators B 95 (2003) 266–270.
[24] H. Borges, A. Giroir-Fendler, C. Mirodatos, P. Chanaud, A. Julbe, Catalytic membrane reactor for oxidative coupling of methane. Part II—Catalytic properties of LaOCl membranes, Catal. Today 25 (1995) 377–383.
[25] S. Podkolzin, E. Stangland, M. Jones, E. Peringer, J. Lercher, Methyl chloride production from methane over lanthanum-based catalysts, J. Am. Chem. Soc. 129 (2007) 2569–2576.
[26] Y. Lin, W. Su, X. Wang, X. Fu, X. Wang, LaOCl-coupled polymeric carbon nitride for overall water splitting through a one-photon excitation pathway, Angew. Chem. Int. Ed. 59 (2020) 20919–20923.
[27] M. Li, Y. Luo, D. Zhao, S. Qiu, L. Zhang, K. Zhang, C. Song, F. Wang, Different La/Fe oxide composites for efficient phosphate removal from wastewater: Properties and mechanisms, J. Environ. Chem. Eng. 10 (2022), 107329.
[28] F. Chen, H. Li, X. Jia, Z. Wang, X. Liang, Y. Qin, W. Chen, T. Ao, Characteristic and model of phosphate adsorption by activated carbon electrodes in capacitive deionization, Sep. Purif. Technol. 236 (2020), 116285.
[29] B. Li, M. Brett, The influence of dissolved phosphorus molecular form on recalcitrance and bioavailability, Environ. Pollut. 182 (2013) 37–44.
[30] E. Goharshadi, T. Mahvelati, M. Yazdanbakhsh, Influence of preparation methods of microwave, sol–gel, and hydrothermal on structural and optical properties of lanthania nanoparticles, J. Iran. Chem. Soc. 13 (2016) 65–72.
[31] M. Bellardita, A. Paola, B. Megna, L. Palmisano, Absolute crystallinity and photocatalytic activity of brookite TiO_2 samples, Appl Catal B 201 (2017) 150–158.
[32] B. Wu, L. Fang, J. Fortner, X. Guan, I. Lo, Highly efficient and selective phosphate removal from wastewater by magnetically recoverable $La(OH)_3/Fe_3O_4$ nanocomposites, Water Res. 126 (2017) 179–188.
[33] J. Zhang, Z. Shen, W. Shan, Z. Mei, W. Wang, Adsorption behavior of phosphate on lanthanum(III)-coordinated diamino-functionalized 3D hybrid mesoporous silicates material, J. Hazard. Mater. 186 (2011) 76–83.
[34] L. Zhang, L. Wan, N. Chang, J. Liu, C. Duan, Q. Zhou, X. Li, X. Wang, Removal of phosphate from water by activated carbon fiber loaded with lanthanum oxide, J. Hazard. Mater. 190 (2011) 848–855.
[35] H. Luo, Y. Wan, Y. Cai, Z. Dang, H. Yin, Enhanced phosphate adsorption by Mg-stirred leaf biochar in a complex water matrix via active MgO facet exposure, ACS ES&T Engineering 2 (2022) 2254–2265.
[36] L. Lai, Q. Xie, L. Chi, W. Gu, D. Wu, Adsorption of phosphate from water by easily separable Fe_3O_4@SiO_2 core/shell magnetic nanoparticles functionalized with hydrous lanthanum oxide, J. Colloid Interface Sci. 465 (2016) 76–82.
[37] Z. Zhong, X. Lu, R. Yan, S. Lin, X. Wu, M. Huang, Z. Liu, F. Zhang, B. Zhang, H. Zhu, X. Guo, Phosphate sequestration by magnetic La-impregnated bentonite granules: A combined experimental and DFT study, Sci. Total Environ. 738 (2020), 139636.
[38] Y. Zhang, M. Wang, X. Gao, J. Qian, B. Pan, Structural evolution of lanthanum hydroxides during long-term phosphate mitigation: Effect of nanoconfinement, Environ. Sci. Tech. 55 (2021) 665–676.
[39] Y. Wu, X. Li, Q. Yang, D. Wang, Q. Xu, F. Yao, F. Chen, Z. Tao, X. Huang, Hydrated lanthanum oxide-modified diatomite as highly efficient adsorbent for low-concentration phosphate removal from secondary effluents, J. Environ. Manage. 231 (2019) 370–379.
[40] X. Zhu, L. Hope-Weeks, D. Ramirez, R. Baghi, V. Charles, Y. He, Controllable decomposition of lanthanum oxychloride through different annealing conditions, J. Alloy. Compd. 800 (2019) 29–34.
[41] Y. Luo, K. Xie, Y. Feng, Q. He, K. Zhang, S. Shen, F. Wang, Synthesis of a La(OH)3 nanorod/walnut shell biochar composite for reclaiming phosphate from aqueous solutions, Colloids Surf A Physicochem Eng Asp 610 (2021), 125736.
[42] T. Levan, M. Che, J. Tatibouet, M. Kermarec, Infrared study of the formation and stability of $La_2O_2CO_3$ during the oxidative coupling of methane on La_2O_3, J. Catal. 142 (1993) 18–26.
[43] Y. Zhang, B. Kong, Z. Shen, J. Qian, B. Pan, Phosphorus binding by lanthanum modified pyroaurite-like clay: Performance and mechanisms, ACS ES&T Engineering 1 (2021) 1565–1575.
[44] P. D'Haese, G. Douglas, A. Verhulst, E. Neven, G. Behets, B. Vervaet, K. Finsterle, M. Lürling, B. Spears, Human health risk associated with the management of phosphorus in freshwaters using lanthanum and aluminium, Chemosphere 220 (2019) 286–299.
[45] Y. Pang, X. Zhou, E. Vovk, C. Guan, S. Li, A. van Bavel, Y. Yang, Understanding lanthanum oxide surface structure by DFT simulation of oxygen 1s calibrated binding energy in XPS after in situ treatment, Appl. Surf. Sci. 548 (2021), 149214.
[46] S. Jørgensen, J. Horst, O. Dyrlie, Y. Larring, H. Ræder, T. Norby, XPS surface analyses of $LaPO_4$ ceramics prepared by precipitation with or without excess of PO_4^{3-}, Surf. Interface Anal. 34 (2002) 306–310.
[47] M. Mallet, K. Barthélémy, C. Ruby, A. Renard, S. Naille, Investigation of phosphate adsorption onto ferrihydrite by X-ray Photoelectron Spectroscopy, J. Colloid Interface Sci. 407 (2013) 95–101.
[48] L. Fang, R. Liu, J. Li, C. Xu, L. Huang, D. Wang, Magnetite/Lanthanum hydroxide for phosphate sequestration and recovery from lake and the attenuation effects of sediment particles, Water Res. 130 (2018) 243–254.
[49] B. Liu, Z. Liu, H. Wu, S. Pan, Y. Sun, Y. Xu, Insight into simultaneous selective removal of nitrogen and phosphorus species by lanthanum-modified porous polymer: Performance, mechanism and application, Chem. Eng. J. 415 (2021), 129026.
[50] Q. Shao, C. Yan, M. Gao, W. Du, J. Chen, Y. Yang, J. Gan, Z. Wu, W. Sun, Y. Jiang, Y. Liu, M. Gao, H. Pan, New Insights into the effects of Zr substitution and carbon additive on $Li_{3-x}Er_{1-x}Zr_xCl_6$ Halide Solid Electrolytes, ACS Appl. Mater. Interfaces 14 (2022) 8095–8105.
[51] K. Kim, D. Kim, T. Kim, B. Kim, D. Ko, J. Lee, Y. Han, J.C. Jung, H. Na, Synthesis of mesoporous lanthanum hydroxide with enhanced adsorption performance for phosphate removal, RSC Adv. 9 (2019) 15257–15264.

Publication 10

review article

Ashour A. Ahmed, P. Leinweber, O. Kühn. Advances in understanding the phosphate binding to soil constituents: A Computational Chemistry perspective. Sci. Total Environ. **2023**, 887, 163692.

Contribution: Ashour A. Ahmed is responsible for conceptualization, formal analysis, methodology, visualization, and original draft writing. Ashour A. Ahmed and co-authors are responsible for funding acquisition, writing3review, and editing of the present contribution.

URL: https://doi.org/10.1016/j.scitotenv.2023.163692

QR:



Reproduced with the permission of Elsevier

Science of the Total Environment 887 (2023) 163692

Contents lists available at ScienceDirect

Science of the Total Environment

journal homepage: www.elsevier.com/locate/scitotenv

Review

Advances in understanding the phosphate binding to soil constituents: A Computational Chemistry perspective

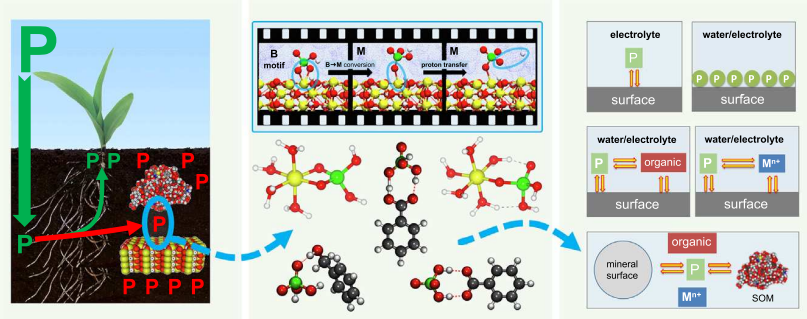
Ashour A. Ahmed [a,b,*], Peter Leinweber [b,c], Oliver Kühn [a,b]

[a] Institute of Physics, University of Rostock, Albert-Einstein-Str. 23-24, D-18059 Rostock, Germany
[b] Department of Life, Light, and Matter (LLM), University of Rostock, Albert-Einstein-Str. 25, D-18059 Rostock, Germany
[c] Chair of Soil Science, University of Rostock, Justus-von-Liebig-Weg 6, D-18059 Rostock, Germany

HIGHLIGHTS

- Phosphorus (P) is an indispensable element to all forms of life.
- P efficiency, recovery, and cycle are affected by the P binding to soil constituents.
- The P binding depends on but not limited to surfaces, water, pH, and redox potential.
- Computational Chemistry is a promising tool in the P research.
- Challenges and further modifications for better understanding are highlighted.

GRAPHICAL ABSTRACT



ARTICLE INFO

Editor: Daniel Alessi

Keywords:
Phosphates
P binding
Mineral surfaces
Molecular modeling
MD simulations

ABSTRACT

Phosphorus (P) is an indispensable element to all forms of life and its efficient use in fertilizers is one of the conditions for food security. The efficiency of P fertilizers is affected by P mobilization and P fixation, both depending on the P binding strength to soil constituents. This review provides an overview of the P binding to soil constituents, especially to P-fixing mineral surfaces and its investigation using state-of-the-art Computational Chemistry (**CC**). A particular focus will be on goethite (α-FeOOH), which is highly significant in the context of P fixation in soils, given its prevalence, high susceptibility to P, and wide distribution across both oxic and anoxic environments. First, a brief overview will be given on experimental efforts related to the P adsorption at mineral surfaces and the factors affecting this process. Here, we will discuss the process of P adsorption, with a focus on important factors that influence this process, such as pH, surface crystallinity and morphology, competing anions, and electrolyte solutions. We will also explore the various techniques used to study this process and investigate the resulting binding motifs. Next, a brief introduction into common **CC** methods, techniques, and applications is presented, highlighting the advantages and limitations of each approach. Then, a comprehensive discussion of a wide range of the most relevant computational studies related to the phosphate binding issue will be provided. This will be followed by the main part of this review which is focusing on a possible strategy to cope with the soil heterogeneity by breaking down the complexity of P behavior in soil into well-defined models that can be discussed in terms of particular key factors. Hence, different molecular model systems and molecular simulations are introduced to reveal the P binding to soil organic matter (SOM), metal ions, and mineral surfaces. Simulation results provided an in-depth understanding of the P binding problem and explained at a molecular level the effects of surface plane, binding motif, kind and valency of metal ions, SOM composition, water, pH, and redox potential on the P binding in soil. On this basis, an overall molecular picture of P binding in soil can be then obtained by combining results for the different models. Eventually, challenges and further modifications of the existing molecular modeling approaches are discussed, such as steps necessary to bridge the molecular with the mesoscale.

* Corresponding author at: Institute of Physics, University of Rostock, Albert-Einstein-Str. 23-24, D-18059 Rostock, Germany.
E-mail address: ashour.ahmed@uni-rostock.de (A.A. Ahmed).

http://dx.doi.org/10.1016/j.scitotenv.2023.163692
Received 7 November 2022; Received in revised form 31 March 2023; Accepted 19 April 2023
Available online 06 May 2023
0048-9697/© 2023 Elsevier B.V. All rights reserved.

Contents

1. Introduction . . . 2
2. Experimental efforts. . . . 3
3. Computational Chemistry . . . 8
4. Computational efforts . . . 10
   4.1. General overview . . . 10
   4.2. Towards squaring the circle . . . 11
      4.2.1. The pH effect on the P binding . . . 14
      4.2.2. IR spectra of phosphate-goethite complexes . . . 15
      4.2.3. Organic phosphates . . . 17
      4.2.4. Effect of surface central metal ion . . . 18
      4.2.5. Redox potential . . . 19
5. Summary and conclusions . . . 21

Abbreviations . . . 23
CRediT authorship contribution statement . . . 23
Funding . . . 23
Data availability . . . 23
Declaration of competing interest . . . 23
Acknowledgments . . . 23
References . . . 23

1. Introduction

Soil is an important source for life on earth providing us with fiber, food, and fuel. It acts as a water filter and growing medium, provides habitat for billions of organisms, and supplies most of the antibiotics. From a Chemistry point of view, soil is a very heterogeneous complex natural system containing various metal ions (in free and/or complexed states), reactive inorganic minerals (e.g., clays and metal-oxides), soil organic matter (SOM, the most complex biomaterial), soil solution (with many electrolytes and different pH values) and gases (Schulten and Schnitzer, 1993; Schulten and Leinweber, 2000; Leinweber et al., 1999; Schaumann and Thiele-Bruhn, 2011; Di Iorio et al., 2022). Soil composition is greatly differing in space, i.e., from site to site, and time. The soil composition and quantity of its constituents are key factors in controlling many critical environmental issues involving for example the phosphorus (P) availability and thus soil fertility (Lehmann et al., 2020). P is central to all forms of life and its efficient use in fertilizers is one of the conditions for providing food for a rapidly increasing human population (Maciá, 2005). Phosphate rock is the main source for the P fertilizers. A P peak scenario has been projected for this century and thus P scarcity could become one of the most important global food security challenges (Cordell et al., 2009; Jupp et al., 2021).

Facing the projected peak P scenario, substantial research activities involving novel P research platforms have been established to improve our knowledge towards a more efficient and sustainable use of P resources and P recovery and recycling (Jupp et al., 2021; Cordell and White, 2011; Kruse et al., 2015; Withers et al., 2015; McLaren et al., 2020; Alam et al., 2021; van der Bom et al., 2022; Keyikoglu et al., 2022). The main objective is to understand the processes controlling P acquisition by arable crops, P cycling, and P inputs into waterways. Sorption/desorption and kinetics experiments and characterization tools such as cutting-edge spectroscopic, microscopic, and molecular techniques are applied to achieve this goal. For instance, a comprehensive meta-analysis of soil ^{31}P-NMR data, based on 258 soil samples from 41 publications, revealed that inorganic P (orthophosphate) constitutes the majority of total P stocks in soil, accounting for $57 \pm 7\%$ (Menezes-Blackburn et al., 2018); monoester and diester P (i.e., organic P) represented approximately $33 \pm 2\%$ and $4 \pm 0\%$, respectively. The efficiency of P immobilization is largely controlled by its interaction with various soil constituents, including SOM (Gros et al., 2017; Ahmed et al., 2018a; Liu et al., 2022), free metal ions (Gros et al., 2019; Urrutia et al., 2013), and soil minerals (Kruse et al., 2015; Liu et al., 2022; Ahmed et al., 2018b; Ahmed et al., 2019; Ganta et al., 2019). Among these soil constituents, soil mineral surfaces such as Fe- and Al-(oxyhydr)oxides, calcium phosphates, silicates, and carbonates exhibit a strong affinity to bind phosphates (Tunesi et al., 1999; Liu et al., 2012; Bellier et al., 2006; Okano et al., 2013; Minamisawa et al., 2022). In particular, Fe- and Al-(oxyhydr)oxides act as the main phosphate adsorbents in soils (Borggaard, 2001; Borggaard et al., 2004; Elzinga and Sparks, 2007; Zhong et al., 2007). The strong binding of phosphates to Fe- and Al-(oxyhydr)oxides is attributed to the formation of stable inner-sphere surface complexes (i.e., formation of covalent bond(s) between phosphates and oxide surfaces) (Kruse et al., 2015; Parfitt, 1979; Goldberg and Sposito, 1985; Dimirkou et al., 2002; Luengo et al., 2006; Wang et al., 2016). Among these oxyhydroxides, goethite (α-FeOOH) is known to be the most prevalent reactive ferric iron Fe(III) form and is of utmost importance to the P fixation issue in soils (Ahmed et al., 2019; Barrow, 1983; Arai and Sparks, 2001; Cornell and Schwertmann, 2003; Chitrakar et al., 2006; Arai and Sparks, 2007; Tsao et al., 2011; Ahmed et al., 2020; Ganta et al., 2020a; Ganta et al., 2021). It exhibits the largest susceptibility to phosphorus compared to other iron minerals (Ofoegbu, 2019). This is driven by the remarkable thermodynamic stability of goethite and its widespread occurrence in soils in both oxic and anoxic environments (Cornell and Schwertmann, 2003; Schwertmann, 1993; Schwertmann, 1958; Torrent et al., 1992). Consequently, considerable research effort has been directed towards unravelling the mechanisms underlying the adsorption and binding of phosphates to the goethite surface (Luengo et al., 2006; Wang et al., 2016; Chitrakar et al., 2006; Ahmed et al., 2020; Ganta et al., 2021; Hingston et al., 1972; Barrow et al., 1980; Bowden et al., 1980; Tejedor-Tejedor and Anderson, 1990; Hiemstra and Van Riemsdijk, 1996; Geelhoed et al., 1997; Strauss et al., 1997a; Li and Stanforth, 2000; Liu et al., 2001; Rietra et al., 2001; Antelo et al., 2005; Boukemara et al., 2016; Arroyave et al., 2018; Amadou et al., 2022).

The objective of the present review is to provide a concise overview of the phosphate-soil binding problem and the state-of-the-art of molecular modeling and its application to that problem. This review will focus on recent advancements in our understanding of how phosphate binds to the most relevant soil constituents for the issue of P-fixation, i.e. the Fe- and Al-oxyhydroxide mineral surfaces. The discussion will mainly center around goethite that has high thermodynamic stability, and its isomorphous Al-oxyhydroxide mineral surface, diaspore. We will explore the latest findings from atomistic simulations, cutting-edge spectroscopic, microscopic, and molecular techniques, which have all played a significant role in improving our knowledge of P immobilization and cycling in soil systems. Moreover, it will be shown that molecular simulations can provide a complementary description and in-depth understanding of experimental findings. After a general overview on related experimental studies in Section 2, a brief introduction into methods of Computational Chemistry

will be given in Section 3. Then, different model systems and molecular simulations revealing the phosphate binding to soil constituents and especially mineral surfaces at molecular level will be discussed in Section 4.2 after a general overview on the relevant computational efforts in literature in Section 4.1. Finally, a summary and conclusions will be presented in Section 5.

2. Experimental efforts

Adsorption experiments and isotherms (e.g., Freundlich (1907), Langmuir (1918), Tempkin and Pyzhev (1940), and BET (Brunauer et al., 1938) models) are of utmost importance to characterize the phosphate binding behavior and the binding strength between phosphates and reactive surfaces. There is a growing interest in investigating the competition between phosphate and other adsorbates (such as organic molecules) towards their adsorption to Fe- and Al-mineral surfaces as well as to soil samples (Borggaard et al., 2005; Borggaard and Gimsing, 2008; Negassa et al., 2008a; Waiman et al., 2013). However, the main focus has been on adsorption of a single phosphate (i.e., one phosphate molecular system) at a particular and well-defined mineral surface (Ahmed et al., 2019; Ganta et al., 2021; Shang et al., 1996; Wang et al., 2013; Ahmed et al., 2012). From a kinetic perspective, phosphate adsorption is often described as a biphasic process with a fast initial adsorption step followed by a slower reaction phase (Luengo et al., 2006; Torrent et al., 1992; McLaughlin et al., 1977; Willett et al., 1988). It was suggested that formation of initial monodentate (**M**, i.e., formation of one covalent bond) and conversion to bidentate (**B**, i.e., formation of two covalent bonds) complexes, competition reactions with anions on the surface, and/or precipitation could take place in the transition period between the fast and slow phases (Torrent, 1997). Alternatively, the observed temporal effects of the phosphate reaction with the surface could be due to diffusion processes (Barrow, 1983; Strauss et al., 1997a).

The adsorption of phosphate on Fe- and Al-(oxyhydr)oxide surfaces is a multifaceted process that is affected by a range of factors, including the pH of the solution, the molecular structure of both the phosphate and the adsorbent, the P concentration, the crystallinity and morphology of the surface, the specific surface area (SSA), the point of zero charge (PZC) of the adsorbent surface, the presence of other competing inorganic and/or organic anions, as well as background electrolytes and their ionic strengths (Geelhoed et al., 1997; Strauss et al., 1997a, 1997b; Geelhoed et al., 1998; Gao and Mucci, 2001; Hongshao and Stanforth, 2001; Guppy et al., 2005; Yan et al., 2014; Ognalaga et al., 1994; Ruttenberg and Sulak, 2011; Gypser et al., 2018). To provide comprehensive insights into the impact of these factors, an extensive range of literature data concerning adsorption capacities has been collected and compiled in Tables 1 and 2. Table 1 provides an overview of the adsorption of orthophosphate on the goethite surface under different experimental conditions (initial P concentration, electrolyte solution, pH, adsorption time) and surface properties (SSA and PZC). Furthermore, some of these data are graphically represented in Fig. 1 to illustrate the adsorption pH dependence and its interdependence with other critical factors, such as SSA, electrolyte solution, and ionic strength. This figure emphasizes the significance of these variables and their impact on the adsorption process, thereby underlining the importance of considering them when designing effective adsorption systems.

Table 1
Compiled data from relevant literature to the adsorption of orthophosphate at goethite under different experimental conditions, involving the initial P concentration, specific surface area (SSA) of goethite and its point of zero charge (PZC), solution pH, electrolyte solution and its ionic strength, and adsorption time. For the data by Li and Stanforth (2000), * denotes both adsorption and precipitation together, while ** denotes adsorption only.

Study ref.	Adsorbed P		Initial P	SSA	PZC	pH	Electrolyte	Time
	μmol P g^{-1}	μmol P m^{-2}	mM	m^2g^{-1}				h
Hingston et al. (1972)	9.7–88.6	0.3–2.8	1.00	32	7.8	3–12	0.1 M NaCl	24
Barrow et al. (1980)	23.0–101.4	0.5–2.1	0.34	49	>8	3–10	0.01 M NaCl	24
	35.3–99.0	0.7–2.0					0.1 M NaCl	
	41.2–94.1	0.8–1.9					1.0 M NaCl	
Bowden et al. (1980)	5.6–188.8	0.07–2.4	0.2	80	8.4	3–11	0.01 M KCl	24
Tejedor-Tejedor and Anderson (1990)	50.0–208.7	0.6–2.6	≈ 1–6	81	9.7	3.5–8.5	0.01 M NaCl	20
Hiemstra and Van Riemsdijk (1996)	72.2–242.1	0.7–2.3	0.2	105	9.5	4–11	0.01 M $NaNO_3$	20
Geelhoed et al. (1997)	104.5–230.4	1.1–2.4	1.00	96.4	9.2	2.5–8.5	0.01 M KNO_3	20
	86.1–158.0	0.9–1.6	0.08				0.01 M KNO_3	
	74.6–113.0	0.8–1.2	0.02				0.01 M KNO_3	
	136.6–225.9	1.4–2.3	1.00				0.5 M KNO_3	
	123.5–157.3	1.3–1.6	0.08				0.5 M KNO_3	
	76.3–112.9	0.8–1.2	0.02				0.5 M KNO_3	
Strauss et al. (1997a)	2.7–40.7	0.2–2.2	0.016–1.613	18	6.4	2–11	0.01 M $NaNO_3$	1
	4.4–63.2	0.2–2.8		23	6.8			
	5.1–127.4	0.1–2.7		46	6.9			
	14.4–169.5	0.2–2.8		60	6.9			
	26.7–354.7	0.2–2.7		132	7.0			
Li and Stanforth (2000)	310.9–2568.1*	5.6–46.1	–	55.7	7.4	2.5–8.8	0.001 M NaCl	24
	100–230**	1.8–4.1						
Liu et al. (2001)	112.0–193.0	1.4–2.4	20	82	7.8	3–8.5	0.1 M KCl	24
Rietra et al. (2001)	99.0–196.6	1.0–2.0	0.50	96.4	9.25	4–10	0.01 M $NaNO_3$	24
	134.0–196.5	1.4–2.0	0.50				0.1 M $NaNO_3$	
Antelo et al. (2005)	75.7–178.5	1.1–2.5	–	70.8	9.3	4.5–10	0.01 M KNO_3	15–18
	97.179.4	1.4–2.5	–				0.1 M KNO_3	
Chitrakar et al., (2006)	190.2–794.1	–	1.61	–	–	2–11	H_2O	24
	53.4–338.0					2–8	Seawater	
Luengo et al. (2006)		0.4–1.7	0.007–0.055	57		4.5–10.5	0.1 M KNO_3	0–6
Wang et al. (2016)	160.2	1.65	0.4	97.2	8.08	4.5	1.0 mM $NaNO_3$	24
	131.6	1.35	0.4	97.2	8.08	6.5	1.0 mM $NaNO_3$	24
	79.02	0.81	0.4	97.2	8.08	8.5	1.0 mM $NaNO_3$	24
Boukemara et al. (2016)	55.8–166.0	1.9–5.6	–	29.6	8.2	2.5–9.5	H_2O	–
Arroyave et al. (2018)	111.5–220.0	1.2–2.5	0.005–0.13	89.7	8.6	4.5–9.5	0.1 M NaCl	6
Ahmed et al. (2020)	3.1–12.9	0.2–0.8	0.15	17.2	8.8	4–12	H_2O	168
Ganta et al. (2021)	492.78	7.64	0.05–10.0	64.5	6.3	5	0.01 M $CaCl_2$	24
Amadou et al. (2022)	90.65	–	32.26	–	–	5.5	0.1 M KCl	24
Overall range	2.7–2568.1	0.1–46.1	0.005–500	17.2–132	6.3–9.7	2–12	0.00–1.0	0–168

Table 2
Compiled data from relevant literature to the adsorption of inorganic and organic phosphates (involving orthophosphate (OP), glycerolphosphate (GP), and inositolphosphate (IHP)) on soils and mineral surfaces under different experimental conditions, involving the initial P concentration, specific surface area (SSA) of the mineral surface and its point of zero charge (PZC), solution pH, electrolyte solution and its ionic strength, and adsorption time.

Study ref.	Adsorbent	P	Adsorbed P		Initial P	SSA	PZC	pH	Electrolyte	Time
			μmol P g^{-1}	μmol P m^{-2}	mM	$m^2 g^{-1}$				h
Barrow (1972)	Soil	OP	200–800	–	0.0065	–	–	4.2	0.0–20 mM $CaCl_2$	24
			100–200	–		–	–	6.2		
Yan et al. (2014)	Amorphous $Al(OH)_3$	OP	698.17	9.56	–	73.0	9.3	5	0.1 M KCl	–
		GP	279.78	3.83						
		IHP	1168.99	16.01						
	Boehmite	OP	170.75	1.49	–	114.6	9.2			
		GP	197.0	1.72						
		IHP	83.77	0.73						
	α-Al_2O_3	OP	26.40	2.83	–	9.3	8.9			
		GP	23.76	2.55						
		IHP	10.53	1.13						
Wang et al. (2015a)	Ferrihydrite	OP	723.8	1.97	0–1	368.2	6.88	4.5	1.0 mM $NaNO_3$	24
			548.3	1.49				6.5		
			380.6	1.03				8.5		
	Hematite	OP	71.73	2.42	0.4	60.8	8.15	4.5		
			60.35	2.03				6.5		
			30.81	1.04				8.5		
Gypser et al. (2018)	Gibbsite	OP	2.99–16.36	3.44–18.81	0.15–2.0	0.87	–	6	0.01 M $CaCl_2$	2688
	Ferrihydrite		201.44–921.59	0.80–3.66	1.0–5.0	251.8	–			
Ganta et al. (2021)	Goethite	OP	492.78	7.64	0.05–10.0	64.5	6.3	5	0.01 M $CaCl_2$	24
		GP	77.40	1.20						
		IHP	538.58	8.35						
Amadou et al. (2022)	Goethite	OP	90.65	–	32.26	–	–	5.5	0.1 M KCl	24
		GP	45.10							
		IHP	120.71							
	Gibbsite	OP	675.77	–	32.26	–	–	5.5		
		GP	1828.97							
		IHP	201.2							
Overall range			10.53–1828.97	0.73–18.81	0.0–32.26			4.2–8.5	0.0–100 mM	24–2688

Meanwhile, Table 2 represents data related to the adsorption of both inorganic and organic phosphates on various Fe- and Al-(oxyhydr)oxide and soil samples. Table 1 and Fig. 1a depict that the reported adsorption capacities of phosphate in various experimental setups ranged between 0.07 and 2.8 μmol P m^{-2} in most of the studies reviewed. Notably, Li and Stanforth (Li and Stanforth, 2000) reported the highest adsorption capacities (5.6–46.1 μmol P m^{-2}) due to a high initial phosphate concentration and high phosphate precipitate content on the surface, see Fig. 1b, as evidenced by their distinction between adsorption and precipitation using zeta potential measurements with increasing surface coverage. Excluding the phosphate precipitates, the adsorption capacity would drop to 1.81–4.1 μmol P m^{-2}. Additionally, Chitrakar et al. (Chitrakar et al., 2006) (794.1 μmol P g^{-1}), Boukemara et al. (Boukemara et al., 2016) (5.6 μmol P m^{-2}), and Ganta et al. (Ganta et al., 2021) (7.64μmol P m^{-2}) observed relatively high adsorption capacities of phosphate on goethite, see Fig. 1b-c. The significant impact of the initial P concentration on the adsorption process is evident from almost all collected results in Tables 1-2. For example, Geelhoed et al. (1997) demonstrated that varying initial P concentrations lead to different degrees of enhancement in the adsorption process, as indicated in Table 1. These findings emphasize the critical role of experimental conditions and surface properties in regulating phosphate adsorption. This is obvious from the broad range of experimental conditions and surface properties employed in Table 1, including various initial P concentrations (0.005–500 mM), SSA (17.2–132 $m^2 g^{-1}$), PZC (6.3–9.7), background electrolytes with varying ionic strengths (0.00–1.0 M), and adsorption time (0–168 h).

The studies conducted by Yan et al. (2014), Ganta et al. (2021), and Amadou et al. (2022) investigated the adsorption behavior of inorganic and organic phosphates, namely orthophosphate (OP), glycerolphosphate (GP), and inositolhexaphosphate (IHP), on well-defined mineral surfaces, including goethite, gibbsite, boehmite, α-Al_2O_3, and amorphous $Al(OH)_3$. The results indicated that the order of adsorption affinity for the phosphates varied depending on the mineral surface. Specifically, GP had the lowest affinity, while IHP had the highest affinity on both goethite and amorphous $Al(OH)_3$ surfaces, and the order was reversed for both gibbsite and boehmite. For the α-Al_2O_3 surfaces, IHP had the lowest affinity, while OP had the highest affinity, and GP had intermediate affinity. These findings confirm the impact of both the molecular structure of the phosphates and the type and crystallinity of the mineral surface on controlling the adsorption process. According to Yan et al. (2014), the mass-based P adsorption capacities (in μmol P g^{-1}, see Table 2) were observed to increase with decreasing crystallinity of the minerals, in the order of α-Al_2O_3 < boehmite < amorphous $Al(OH)_3$, as reported in this context. The relevance of the molecular structure and crystallinity of the mineral surface on P adsorption is also evident from the data in Table 2 of studies by Wang et al. (2015a) and Gypser et al. (2018). In the same context, the data provided in Table 1 and Fig. 1d-e by Strauss et al. (1997a) highlight the significant impact of the crystallinity and specific surface area (SSA) on the P adsorption process.

In terms of competing anions, it is well-established that arsenate and phosphate exhibit strong competition for adsorption at the surfaces of Al- and Fe-hydroxides (Antelo et al., 2005; Gao and Mucci, 2001; Hongshao and Stanforth, 2001; Han et al., 2020; Li et al., 2021). Typically, this competition ultimately results in arsenate being the dominant competitor over phosphate, indicating that arsenate has a higher affinity for adsorption at these surfaces. This affinity can be influenced by both the properties of the surface and the experimental conditions. For example, (Antelo et al., 2005) found that changes in pH and ionic strength have a greater impact on phosphate adsorption at goethite compared to arsenate adsorption. Specifically, their results showed that phosphate adsorption was higher in acidic media across most ionic strengths, but lower in basic media and at low ionic strengths. In contrast, carbonate, nitrate, and sulfate are generally considered weak competitors for adsorption at similar concentrations (Geelhoed et al., 1997; Han et al., 2020; Appel et al., 2013). However, under certain conditions, carbonate and silicate can be effective adsorbent precursors through cation precipitation (Han et al., 2020). On the other hand, organic acids compete with phosphate and other oxyanions for sorption sites and dissolve Al- and Fe-hydroxide surfaces. Sorption experiments,

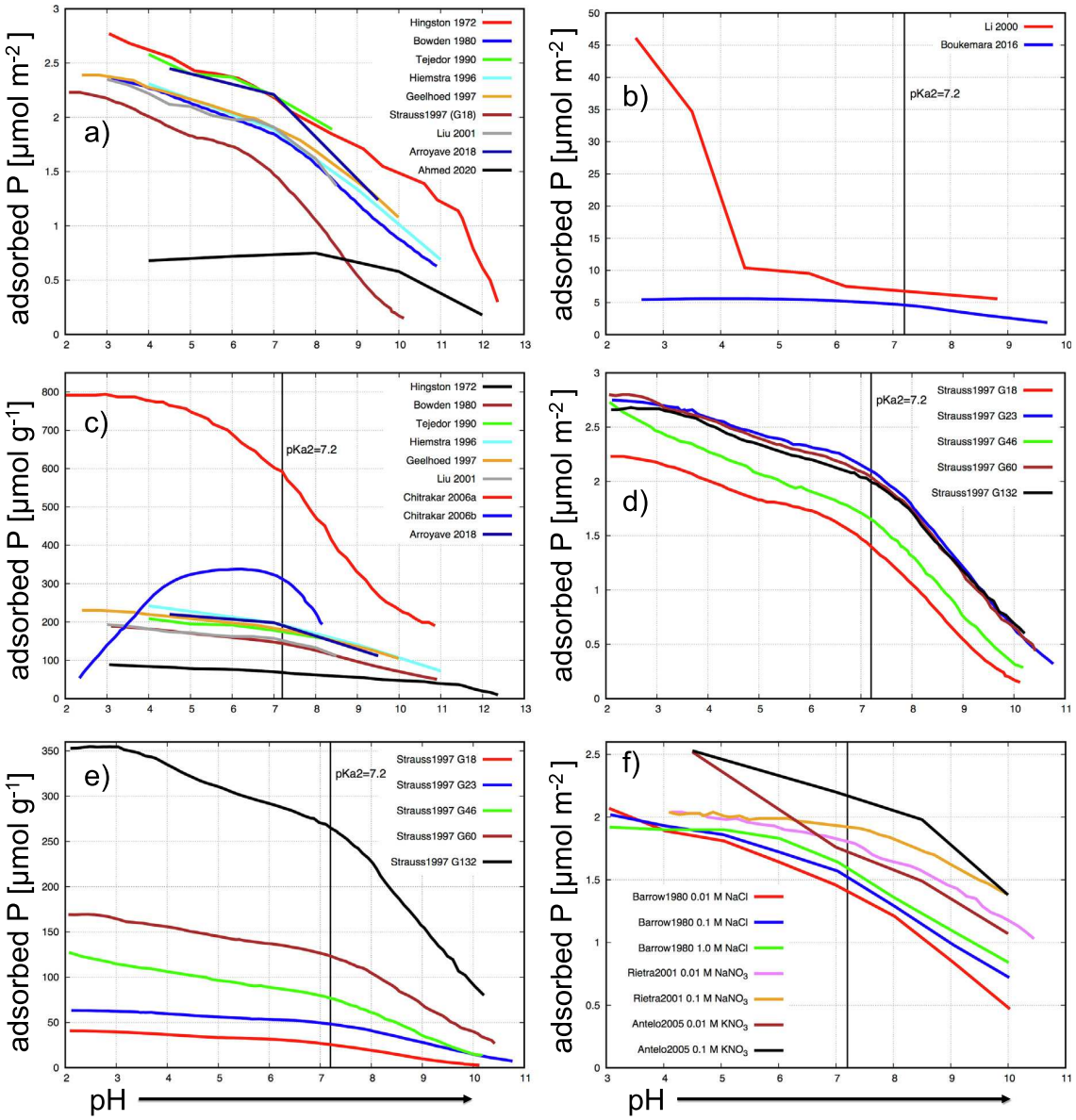


Fig. 1. Effect of the solution pH a)-f), specific surface area (SSA, d)-e)), and background electrolyte and ionic strength f) on the adsorption of inorganic phosphate (orthophosphate) at the goethite surface. The presented data are collected (digitized and interpolated) from literature studies by Hingston et al. (1972), Bowden et al. (1980), Barrow et al. (1980), Tejedor-Tejedor and Anderson (1990), Hiemstra and Van Riemsdijk (1996), Geelhoed et al. (1997), Strauss et al. (1997a), Li and Stanforth (2000), Liu et al. (2001), Rietra et al. (2001), Antelo et al. (2005), Chitrakar et al. (2006), Boukemara et al. (2016), Arroyave et al. (2018), and Ahmed et al. (2020). It should be highlighted that the adsorbed concentrations in μmol m^{-2} here for P (as an element) and phosphate (as an anion) are exactly the same. The same holds true for the adsorbed concentrations in μmol g^{-1}. For Strauss et al. (1997a) plotted data d)-e), G18 to G132 labels refer to goethite samples with SSA values of 18 to 132 m^2 g^{-1}, respectively.

as well as IR, X-ray, and DFT analyses, have indicated that organic acids tend to form inner-sphere complexes under acidic conditions, whereas outer-sphere complexes are formed under basic conditions (Han et al., 2020). For instance, Persson and Axe (2005) observed that oxalate and malonate form a **B** complex at goethite at low pH. The finding in case of oxalate was confirmed later by Kubicki et al. (Kubicki et al., 2017a) using DFT calculations. In addition, Norén and Persson (2007) showed that acetate, benzoate and cyclohexanecarboxylate form hydrated and non-hydrated outer-sphere complexes when adsorbed at the goethite surface. Duckworth and Martin (2001) concluded that oxalate, malonate and glutarate form **B** complex at the hematite surface, whereas succinate and adipate formed an **M** complex. They also observed that oxalate, glutarate, malonate and adipate increase the dissolution of the hematite surface. Hug and Bahnemann (2006) investigated the formation of a **B** complex of oxalate at lepidocrocite, which was later confirmed by Borowski et al. (2018), along with the formation of an **M** complex. These investigations demonstrate that organic acids have a strong affinity for adsorption onto Fe-hydroxide surfaces, allowing them to compete with phosphates and increase their mobility at the surface. Johnson and Loeppert (2006) found that organic acids effectively release adsorbed P from ferrihydrite, with efficiency increasing in the order oxalate = malonate = succinate < tartrate < malate < citrate. Geelhoed et al. (1998) found that phosphate decreased citrate adsorption at the goethite surface over a wide pH range, while citrate adsorption decreased phosphate adsorption only at low pH. Wang

et al. (2016, 2015a, 2015b) reported that humic acids significantly decrease P adsorption at goethite, hematite, and ferrihydrite. In a recent long-term desorption study, Gypser et al. (2019) used inorganic and organic competitive sorptives to release adsorbed P from Fe- and Al-hydroxides, finding that P desorption increased in the order $CaCl_2$ < $CaSO_4$ < humic acid < citric acid. In a further desorption study, Gypser et al. (2021) showed that goethite exhibited the highest desorption, followed by gibbsite and then ferrihydrite, when using organic and inorganic competitors. Kubicki and Ohno (2020) used a joint experimental-theoretical approach to show that salicylate can replace adsorbed phosphate on the goethite surface. In a P adsorption experiment in a real soil sample, Negassa et al. (2008b) found that the order of P release in the soil solution was glucose < tryptophan < lipid < albumin < lignin < mixture < histidine, which changed upon treating the soil sample with H_2O_2. Despite significant efforts in the literature, the specific mechanism for the competition reaction has not been fully verified.

For the solution pH, a significant role in controlling the phosphate adsorption at goethite was found in a number of studies (Barrow, 1983; Arai and Sparks, 2001; Chitrakar et al., 2006; Ahmed et al., 2020; Hingston et al., 1972; Bowden et al., 1980; Tejedor-Tejedor and Anderson, 1990; Hiemstra and Van Riemsdijk, 1996; Geelhoed et al., 1997; Strauss et al., 1997a; Li and Stanforth, 2000; Liu et al., 2001; Rietra et al., 2001; Antelo et al., 2005; Boukemara et al., 2016; Arroyave et al., 2018). This is due to the fact that pH not only determines the surface charge and the degree of saturation of pedogenic oxides as being the most phosphate-affine soil minerals, but also the protonation state of the phosphate species (Antelo et al., 2005; Gao and Mucci, 2001). Almost all of these studies reported a significant effect of the solution pH on the adsorption capacity that decreased with increasing the solution pH, see Fig. 1. This common behavior at higher pH is plausibly explained by the repulsion between phosphate anions and the increasingly negatively charged surface sites, and the competition between phosphate anions and hydroxyl (OH^-) groups. Therefore, goethite exhibits a high affinity to adsorb phosphate anions at pH below the PZC since the surface will have a positive net charge and thus positive electric potential. By increasing the solution pH, the potential becomes less positive and then negative at pH > PZC, which hinders further adsorption (Bowden et al., 1980). Moreover, Hiemstra and Van Riemsdijk (1996) and Strauss et al. (1997a) showed that the phosphate adsorption process will be accompanied by adsorption of protons (H^+) at the goethite surface.

A different adsorption behavior at the goethite surface was observed by Chitrakar et al. (2006) for phosphate enriched seawater containing major anions such as Cl^- and SO_4^{2-} and minor anions such as NO_3^- and CO_3^{2-}. Here, low phosphate adsorption was observed at pH about 2 and increased with increasing the solution pH up to around 7 and then decreased strongly by further pH increase. The observed low adsorption in the first phase was attributed to the competition of both major and minor anions present in seawater with the mono-valent phosphate species ($H_2PO_4^-$) towards their adsorption at the reactive goethite surface sites. The adsorption drop at pH > 7 was assigned to the repulsion of both HPO_4^{2-} and PO_4^{3-} species with the negatively charged surface sites as wells as their competition with OH^- groups. A previous study conducted by Gao and Mucci (2001) also observed a similar trend in phosphate adsorption at the goethite surface in the presence of competing arsenate ions. Specifically, they found that the adsorption of phosphate increased as the solution pH increased, reaching a maximum at around pH 6 before decreasing again. Similar behavior was observed as well by Boukemara et al. (2016) since their phosphate adsorption increased slightly with increasing the solution pH up to 4 and then followed by a significant decrease stage. Moreover, Ahmed et al. (2020) observed two pH-dependent successive stages for the phosphate adsorption at the goethite surface in pure water. In the first stage, the phosphate adsorption increased upon increasing the solution pH specifically in the range of 4–8. Following to this stage, a strong drop in the phosphate adsorption was observed based on a further increase in the solution pH. The latter two observed successive stages will be explained at a molecular level in Section 4.2.1. This brief discussion of P adsorption should also serve for illustration of one of the challenges in soil research, that is, experiments are often conducted for rather different types of samples and under different conditions. Any simulation at the molecular level that aims to connect to these macroscopic observations has to cope with this situation as will be discussed in this review.

The impact of the nature of the background electrolyte and ionic strength on phosphate adsorption can be inferred from a review of the literature data, including studies conducted by Barrow et al. (1980), Rietra et al. (2001), Antelo et al. (2005), and Ahmed et al. (2020), see Table 1 and Fig. 1f. For instance, Barrow et al. (1980) showed a decrease in the phosphate adsorption by increasing the NaCl background electrolyte concentration at pH < 4. Here, increasing the electrolyte concentration led to a decrease in the electric potential (i.e. less positive) of the positively charged surface and thus led to a weaker adsorption. In contrast, increasing the NaCl concentration at pH > 4 led to a less negative electric potential and thus a stronger phosphate adsorption. This effect is more pronounced with increasing the phosphate concentration as well (Geelhoed et al., 1997). This observation was confirmed by Rietra et al. (2001) and Antelo et al. (2005). Recently, Ahmed et al. (2020) provided evidence for the influential role of the background electrolyte in the phosphate adsorption at mineral surfaces by using 0.01 M $CaCl_2$ and 0.01 M KCl electrolyte solutions at pH 6. Almost constant adsorption was observed for the KCl solution, while a significant increase in the phosphate adsorption was observed for the $CaCl_2$ solution. The behavior of the KCl solution is almost similar to what observed by Arai and Sparks (2001) for the NaCl solution. Specifically, it was observed that increasing the ionic strength of NaCl led to a slight increase in P adsorption at pH values above 7.5, whereas no significant changes were observed in the pH range of 4–7.5. For the $CaCl_2$ solution, the behavior comes in accord with a previous study by Barrow (Barrow, 1972), where they investigated the impact of Ca^{+2} ion concentration on the adsorption of phosphate on two soil samples of high sorption capacity and different pH values (4.2 and 6.2), see Table 2. The results showed that the presence of Ca^{+2} ions led to an increase in phosphate adsorption due to the electric potential developed at the soil surface. This electric potential is influenced by electrolyte concentration, which affects the charge distribution and adsorption activity. As noted by Barrow and Shaw (1979), changes in activity coefficient and concentration both contribute to the complexity of the adsorption process. Eventually, these findings suggest that the concentration of electrolytes, such as Ca^{+2} ions, can significantly impact phosphate adsorption by altering the charge distribution and adsorption activity.

Fourier-transform infrared (FTIR) spectroscopy has been used widely to investigate the binding motifs of the adsorbed phosphate species at Fe-oxide surfaces (Ahmed et al., 2019; Arai and Sparks, 2001; Tejedor-Tejedor and Anderson, 1990; Chapman and Thirlwell, 1964; Persson et al., 1996; Lefèvre, 2004). Characteristic mid-infrared bands from symmetric and anti-symmetric P–O(H) vibrations can be detected based on the symmetry of the phosphate ion even at low phosphate concentrations (Arai and Sparks, 2001; Tejedor-Tejedor and Anderson, 1990; Chapman and Thirlwell, 1964; Persson et al., 1996). Therefore, the coordination geometry concluded from the IR spectrum could provide hints to the phosphate binding motifs and thus the relevant binding mechanisms at the mineral surfaces. Although much about the phosphate binding process by soil mineral surfaces could be learned from IR spectra, the question remains whether it is able to provide a conclusive assignment about the binding motifs. Considerable difficulties such as the presence of different surface planes for goethite (and other mineral surfaces) and several binding motifs for the phosphate–goethite (phosphate–mineral) complexes in addition to the different setups and conditions of adsorption experiments might inhibit a clear FTIR assignment (Villalobos et al., 2009; Kubicki et al., 2012). As a result, various points of view have been propounded to analyze the IR spectra and assign the corresponding phosphate–goethite binding motifs. For example, in an approach by Tejedor-Tejedor and Anderson (1990), the P binding motifs (complexes) were assigned according to position of the P—O vibrational bands. Alternatively, Arai and Sparks (2001) characterized the P complexes according to the number of P—O bands rather than the exact position. In a third approach, the dominant P complexes of adsorption experiments were assigned as only monodentate binding motifs

with different protonation states (mono-, bi-, and non-protonated) depending on pH (for example, see (Persson et al., 1996; Loring et al., 2009; Krumina et al., 2016)). Recently, Arroyave et al. (2018) employed a novel spectroscopic technique, infrared surface titration (IRST), to systematically explore the surface speciation of phosphate at goethite under different experimental conditions, including solution pH and surface loading. In addition, other advanced spectroscopic techniques such as P *K*-edge X-ray absorption near-edge structure (XANES) spectroscopy, extended X-ray absorption fine structure (EXAFS) spectroscopy, and liquid ^{31}P nuclear magnetic resonance (NMR) spectroscopy have been extensively used to investigate the speciation of inorganic (X-ray) and organic (NMR) P species adsorbed at mineral surfaces and in soil (McLaren et al., 2020; Turner et al., 2003; Dougherty et al., 2005; McLaren et al., 2015; Kruse and Leinweber, 2008; Andersson et al., 2016). ^{31}P NMR spectroscopy has the ability to differentiate between surface adsorbed phosphate in inner-sphere complexes, phosphate in surface Al-phosphate precipitates, and precipitated phosphate from residual solution (Johnson et al., 2002; Kim and Kirkpatrick, 2004; Van Emmerik et al., 2007; Li et al., 2013a). XANES and EXAFS techniques are powerful tools for distinguishing between P adsorption and surface precipitation, and for analyzing the bonding configurations of binding motifs at mineral/water interfaces. They provide both direct and indirect observations of these processes, making them essential for understanding the mechanisms involved (Hesterberg et al., 1999; Khare et al., 2005, 2007; Abdala et al., 2015). However, it is important to note that EXAFS is limited in its ability to detect changes in the protonation environment of surface complexes. All these cutting-edge spectroscopic techniques have led to significant contributions in identifying binding motifs of adsorbed phosphate species on Fe- and Al-(oxyhydr)oxide surfaces, as evidenced by a comprehensive overview presented in Table 3 (Ahmed et al., 2019; Elzinga and Sparks, 2007; Zhong et al., 2007; Luengo et al., 2006; Arai and Sparks, 2001; Tejedor-Tejedor and Anderson, 1990; Arroyave et al., 2018; Gypser et al., 2018; Persson et al., 1996; Kubicki et al., 2012; Krumina et al., 2016; Kim and Kirkpatrick, 2004; Li et al., 2013a; Khare et al., 2007; Abdala et al., 2015; Parfitt and Atkinson, 1976; Sigg and Stumm, 1981; Nanzyo, 1986; Nilsson et al., 1992; Rahnemaie et al., 2007; Li et al., 2010; Kim et al., 2011; Zheng et al., 2012; Li et al., 2013b). However, given the complexity of this field, further research is necessary to deepen our understanding of the topic and to unveil additional insights.

To sum up this brief and selective overview it should be stated that the considerable experimental efforts not always lead to an unequivocal picture of the phosphate adsorption process. Given the multitude of influencing factors it is not surprising that, for instance, the actual assignment of the phosphate–goethite complexes is still a matter of debate. Here Computational Chemistry can help by providing a complementary description and in-depth understanding of the experimental findings. Specifically, it will be shown in this review how Computational Chemistry can deliver a systematic investigation of possible molecular mechanisms and binding motifs for the phosphate binding process with soil mineral surfaces and other reactive soil constituents at different experimental conditions.

Table 3
Compiled data from relevant literature to the identified binding motifs of adsorbed orthophosphate on Al- and Fe-mineral surfaces using various techniques. **M**, **M**H, and **M**H_2 denote non-protonated, mono-protonated, and bi-protonated monodentate binding motifs, respectively. Same notions hold true for the bidentate binuclear (**B**) and bidentate mononuclear (**BM**) binding motifs.

Study ref.	Binding motifs	Adsorbent	Technique	pH
Parfitt and Atkinson (1976)	**B**	Goethite	IR	3.6–9.7
Sigg and Stumm (1981)	**B**, **B**H, **M**, **M**H, **M**H_2	Goethite	Acid-base titration	3–10
Nanzyo (1986)	**B** (pH > 11)	Fe-oxide gel	IR	2.3–12.3
Tejedor-Tejedor and Anderson (1990)	**B**, **B**H (low P loading) **M**H (high P loading)	Goethite	CIR-FTIR	3.5–8.5
Nilsson et al. (1992)	**M**, **M**H, **M**H_2	Goethite	Potentiometry	3–9
Persson et al. (1996)	**M**, **M**H, **M**H_2	Goethite	FTIR	3.1–12.8
Arai and Sparks (2001)	**B** (pH ≥ 7.5) Not applicable (pH < 7.5)	Ferrihydrite	ATR-FTIR	4.0–9.0
Kim and Kirkpatrick (2004)	**M**, **M**H	Boehmite, γ-Al_2O_3	NMR	3–5
Kwon and Kubicki (2004)	**B**H_2 (pH 4–6) **B** or **M**H (pH 7.5–7.9) **M** (pH 12.8)	Goethite	DFT	
Luengo et al. (2006)	**B**, **B**H	Goethite	ATR-IR	4.5–9.0
Rahnemaie et al. (2007)	**B** (low P loading) **M**H (low pH and high P loading)	Goethite	CD, DFT	4–12
Elzinga and Sparks (2007)	**BM**H, **M**H (3.5–7.9) **M** (pH 8.5–9.0)	Hematite	ATR-FTIR	3.5–8.9
Khare et al. (2007)	B	Ferrihydrite	XANES	6
Zhong et al. (2007)	**B**H, **M**H_2 (pH 3.5) **B**H, **M**H, **M**H_2 (pH > 3.5)	Goethite	Potentiometry	3.5–8.0
Li et al. (2010)	**B**H, **B**	Boehmite	NMR	3–11
Kim et al. (2011)	B **M** (high pH)	Goethite, akaganeite, lepidocrocite	NMR	3–11
Zheng et al. (2012)	**M**H_2 (pH 4.1) **B** (pH 9.0)	γ-Al_2O_3	ATR-FTIR	4.1 and 9.0
Kubicki et al. (2012)	**M**, **B**	Goethite	ATR-FTIR, DFT	4.2–8.0
Li et al. (2013a)	**B**, **B**H	Corundum (α-Al_2O_3)	NMR, ATR-FTIR, DFT	3–11
Li et al. (2013b)	**B**, minor **M**	Boehmite, corundum, gibbsite	NMR	4–10
Abdala et al. (2015)	**B**, **BM**, **M**	Goethite	EXAFS	4.5
Krumina et al. (2016)	**M**, **M**H, **M**H_2	goethite, ferrihydrite	IR, potentiometry	3–12
Arroyave et al. (2018)	**M**H (low P loading and all pH) **M**H_2 (high P loading and pH < 5.5) **M**H (high P loading and pH > 5.5)	Goethite	CD, IRST	4.5–9.5
Gypser et al. (2018)	**M**H or **B** **M**H, **B**H **B**H or **B** **M**H_2	Ferrihydrite Gibbsite Fe-hydroxides Al-hydroxide	FTIR	6
Ahmed et al. (2019)	major **BM**H, **M**H (010-surface plane) major **M**, **B**H (100-surface plane)	Goethite	FTIR, DFT	6.3

3. Computational Chemistry

Computational Chemistry (**CC**) is based on the fundamental laws of Physics and provides access to molecular geometries, thermodynamics, spectroscopic data, chemical reaction kinetics, and dynamics of molecular systems. It can simulate pure phases (gas, liquid, and solid), solutions, and interfaces. Therefore, **CC** is considered as an indispensable tool in Chemistry and related cross-disciplinary areas like Biochemistry, Chemical Physics, and Material Science. Despite the growing relevance and wide applicability of **CC**, Environmental Chemistry and especially biogeochemical processes occurring in soil have not received much attention so far. This is due to the considerable complexity of the problem with soil being an extremely heterogeneous multi-component natural material and habitat. Therefore, developing relevant molecular models and introducing molecular simulation techniques into this field requires a multi-disciplinary effort (Ahmed et al., 2012, 2014, 2015; Dettmann et al., 2021). As a reward, **CC** could be developed as a promising tool for understanding P-related processes in soil at a molecular level. It has already been appreciated that sorption/desorption of phosphates to/from soil constituents such as mineral surfaces can be simulated by **CC** methods (Kwon and Kubicki, 2004). Moreover, effects of the soil surface composition and its spatial configuration, soil solution, ionic strength, and solution pH were explored (Kubicki, 2016). Further, relevant spectroscopic data (IR, UV, NMR, XPS, and XANES) for the characterization of the phosphate binding can be calculated and interpreted using an arsenal of versatile computational tools (Cramer, 2004; Jensen, 2017).

CC involves different levels of theory with different accuracy and computational efficiency (Kubicki, 2016; Cramer, 2004; Jensen, 2017; Koch and Holthausen, 2008; Kmiecik et al., 2016; Senn and Thiel, 2009; Stewart, 2007; Elstner et al., 1998). On the simplest level, molecular mechanics (MM) describes the energy of molecular systems by empirical potentials for bonded and non-bonded particles. Here, three main resolution levels representing the MM particles are involved namely all-atom, united-atom, and coarse-grained representations. For all-atom representation, each atom is described as a particle (point charge) with an implicit treatment for electrons. For the united-atom representation, a group of atoms (e.g., CH_3 group) is defined as one single particle sometimes called pseudo-atom. In the coarse-grained representation, a group of atoms, functional groups, or even molecules are defined as a new particle usually called bead. For all these representation levels, bonded interactions involve all individual interactions between particles forming bonds, angles, proper and improper dihedral angles. Non-bonded interactions are described mainly by electrostatic and van der Waals potentials for the non-bonded particles. A complete set of empirical potentials and relevant parameters describing the potential energy of a molecular system is called a force field. MM methods can simulate millions of atoms at moderate computational cost, but usually cannot describe bond formation and dissociation. As an alternative approach, quantum mechanics (QM) describes the chemical bonds via explicit treatment of nuclei and electrons by solving the Schrödinger equation. In principle, QM can be classified into three main categories involving ab initio, density functional theory (DFT), and semi-empirical (SE) methods (Cramer, 2004). Ab initio methods are computationally expensive and not applicable for P-related problems beyond simple model systems. SE methods use various approximations and empirical parameters and, therefore, are less computationally expensive compared to ab initio methods and thus applicable to P-related problems with model size of a few hundred atoms. DFT is the most prominent method because it provides a compromise between efficiency and accuracy. DFT is based on the electron density which is calculated in terms of the so-called Kohn-Sham molecular orbitals. In practice, the quality of the DFT results depends on the so-called exchange-correlation functional. Many DFT functionals exist, some developed for special purposes and others for the general use. The Becke, three-parameter, Lee–Yang–Parr (B3LYP) (Lee et al., 1988) and Perdew-Burke-Ernzerhof (PBE) (Perdew et al., 1996) functionals are the most common ones used for simulating phosphate related processes. Moreover, the quality of the simulation results is affected by the chosen basis set used to represent the electronic wave function. In general, two kinds of basis sets involving Gaussian atom-centered and periodic plane-wave basis functions are used to describe molecules and extended systems (e.g., surfaces and crystals), respectively. To speed up the calculations, often the core orbitals are described by an effective core potential (ECP) or so-called pseudo-potentials and only the valence orbitals are described explicitly by a basis sets (e.g., Goedecker–Teter–Hutter (GTH) pseudo-potentials have been used in Sections 4.2.1–4.2.4). Each class of basis sets (i.e., Gaussian and plane-wave) has advantages and limitations. An efficient Gaussian and plane-waves (GPW) method has been developed acquiring benefits and advantages of both worlds (Lippert et al., 1997; VandeVondele et al., 2005; Kühne et al., 2020). Long-range van der Waals dispersion interactions are not described by standard functionals. An efficient way to account for dispersion is the inclusion of empirical corrections such as GD3 (Grimme et al., 2011). Notwithstanding the success of these developments in DFT, practical calculations become unfeasible for larger systems containing more than a few hundred atoms. Therefore, QM (DFT) for the reactive part of a system is usually combined with MM for, e.g., the solvent into the hybrid QM/MM method. In general, QM/MM schemes differ in the way QM and MM calculations are linked (e.g. electrostatic embedding used in the applications below), an overview can be found in Ref. Senn and Thiel (2009).

Regardless the **CC** level of theory, different techniques can be applied to obtain a stable geometry (i.e., the nuclear coordinates) or the so-called optimized structure being an energetic minimum of the system on the potential energy surface. Most algorithms give access only to local optimization in which the optimization converges to the closest local minimum on the potential energy surface for nuclear motion. Such a minimum on the potential surface can be characterized by the matrix of second derivatives with respect to the coordinates (Hessian). In particular so-called normal mode coordinates can be introduced that can be used to obtain IR vibrational spectra.

Statistical properties taking into account the random motion of the nuclei due to finite temperature can be obtained using molecular dynamics (MD), for an overview on related techniques see Ref. Marx and Hutter (2009). Solving Newton's equations, a trajectory is generated, which samples the thermal ensemble at a given temperature. The trajectory data can be used to obtain, e.g., average geometries. This way the whole system is treated explicitly on equal footing. A simplification arises in so-called implicit models. In this case, the solvent molecules are described as a classical dielectric medium that is polarized by the electron density in the reactive quantum region and acting back on it. Polarizable continuum model (PCM), conductor-like polarizable continuum model (CPCM), and **co**nductor-like **s**creening **mo**del (COSMO), universal **s**olvation **m**odel based on the full solute electron **d**ensity (SMD) are among the most popular implicit solvation models (Klamt and Schüürmann, 1993; Barone and Cossi, 1998; Cossi et al., 2003; Tomasi et al., 2005; Klamt, 2005; Marenich et al., 2009). Another important aspect is how to mimic the in principle macroscopic systems like surfaces. This could be approximated either in terms of a finite cluster or by using a periodic treatment. To model surface related processes (either for crystalline or amorphous materials), using periodic boundary condition (PBC) is the standard approach. Here, a well-defined unit cell is repeated in two dimensions to construct the surface of interest. To study interfacial processes, slab models are used which involve an (artificial) periodicity with respect to the direction perpendicular to the surface.

We have summarized the advantages and limitations of various levels of theory and techniques, along with other relevant aspects discussed in this review, in Tables 4 and 5. This serves to showcase the power of Computational Chemistry. In particular, Table 4 provides an overview about the advantages and limitations of various computational chemistry methods, including ab-initio (AI), density functional theory (DFT), and semi-empirical (SE) methods for quantum mechanics (QM); all-atom (AA), united-atom (UA), and coarse-grained (CG) representations for molecular mechanics (MM); and the hybrid QM/MM approach. Table 5 compares and contrasts the benefits and drawbacks of different approaches, such as stationary calculations versus molecular dynamics simulations, cluster

Table 4
Advantages and limitations of the different Computational Chemistry methods reviewed in this review article, involving QM (ab-intio (AI), DFT, and semi-empirical (SE) methods), MM (all-atom (AA), united-atom (UA), and coarse-grained (CG) representations,), and the hybrid QM/MM methods.

Level	Sub-level	Advantages	Limitations
QM	Ab-initio	Independent of any experimental data. Provides the highest level of accuracy among all the reviewed methods. Simulates chemical reactions, transition states, and excited states.	Computationally expensive. Limited to small systems (tens of atoms). MD simulations hardly feasible.
	DFT	Provides a good balance between accuracy and computational cost. Versatile tool for molecules, materials science, and solid-state physics. Simulates chemical reactions, transition states, and excited states. Predicts electronic and thermodynamic properties of materials and molecules.	Use empirical parameters that limit its accuracy. Results are dependent on the choice of functional. Dispersion interactions between atoms or molecules has to be corrected for. Limited in both time and length scales of MD simulations.
	SE	Less computationally expensive than AI and DFT, making it more efficient. Feasible for medium-sized systems (hundreds to thousands of atoms). It can access longer time scales (MD simulations) compared to AI and DFT. Simulates chemical reactions, transition states, and excited states.	Use extensive empirical parameters. Needs ab initio calculations or experiments for parameterization. Parameters may not be transferable to other molecular systems. Less accurate than ab initio and DFT.
MM	All-atom	Computationally cheaper and faster than all QM methods. Describes large molecular systems (thousands to millions of atoms). Often accurate in reproducing experimental observables. Useful for limited computer resources.	Based solely on empirical parameters. Requires QM calculations or experiments for parameterization. Generally less accurate than all QM methods. Cannot simulate chemical reactions and electronic properties.
	United-atom	Computationally cheaper and faster compared to all-atom representations. It has almost the same accuracy as AA representation. Describes systems of the same or larger sizes than for all-atom representations.	Shares the same limitations as all-atom force field methods. Not suitable for studying systems with high degrees of flexibility or capturing subtle structural details.
	CG	Reduces complexity of molecular systems. Lowest computational cost compared to all other reviewed methods. Suitable for large molecular systems (millions of atoms). Enables access to longer time and length scales in simulations. Describes slow processes like adsorption/desorption, diffusion, Protein folding, and self-assembly.	Requires all-atom calculations and/or experiments for parameterization. Parameters may not be transferable to other molecular systems. Less accurate than all other reviewed methods. Loss of atomistic details may limit the ability to study the detailed structure of molecular systems.
QM/MM		Computationally more efficient than pure QM simulations. Versatile and applicable to various complex molecular systems. Provides accurate reaction modeling with environmental effects. Provides valuable insights into the nature of chemical reactions, as well as the properties of transition and excited states	Requires specialized software, and good expertise. Affected by the quality of FF parameters and the QM method. Interpretation can be challenging due to the complexity of calculations and analysis.

Table 5
Advantages and limitations of the some important techniques and aspects in Computational Chemistry.

	Advantages	Limitations
	Stationary versus dynamic calculations	
Stationary	Computationally efficient and quick assessment of electronic structure. Useful for calculating properties like energies, orbitals, and frequencies. Provide insights into reactivity and reaction mechanisms	Limited in accounting for temperature, pressure, and dynamics. Do not provide information on time-dependent behavior. Do not account for effects of fluctuations and thermal motions.
Dynamics	Account for time-dependent behavior, interactions, and fluctuations. Examine effects of temperature, pressure, and environment. Provide insights into reactions and complex systems	Computationally demanding and require significant resources. Accuracy is dependent on the chosen MM and/or QM method(s).
	Cluster (non-periodic) versus periodic calculations	
Cluster	Study molecules and systems without periodicity. Explore a wide range of properties (structure, reactivity, spectroscopic). Study reactions and processes at interfaces (adsorption, catalysis).	Less efficient for large systems. Do not capture all electronic and structural effects of periodicity. Accuracy can be affected by choice of basis set and method.
Periodic	Model bulk materials and periodic systems. Study periodicity properties e.g., band structures and phonon spectra. Study systems with defects and their effect on properties.	Computationally demanding. Periodicity can limit accuracy, especially for surfaces and interfaces. Supercell size and shape can affect accuracy.
	Vacuum calculations versus (implicit and explicit) solvation methods	
Vacuum	Less computationally demanding than solvated calculations. Useful for gas-phase reactions and intrinsic properties of molecules. Used as a benchmark for comparing with different theoretical methods.	Ignore solvent influence, which is critical in many processes. Overestimate barriers, energies, and bond lengths. Less accurate results.
Implicit	Less computationally demanding than explicit solvation methods. Provide good compromise between accuracy and cost. Useful for large systems and long timescales. Suitable for studying reaction thermodynamics and kinetics.	Relies on empirical parameters. Not transferable and may need recalibration. May not fully capture solvation effects. Accuracy is dependent on the chosen solvent model.
Explicit	More accurate representation of solvation effects. Provides insight into reaction mechanisms and dynamics. Applicable for a wide range of solvents.	Computationally demanding for large systems or long timescales. Accuracy is dependent on the quality of force field. Analysis could be challenging for huge systems.
	Gaussian, plane-wave, and hybrid Gaussian/plane-wave (GPW) basis sets	
Gaussian	Widely used and well-established. Efficient and accurate for various molecular systems. Versatile and easily tailored to different levels of theory.	Not suitable for periodic systems. Large basis sets are computationally expansive. Accuracy is significantly affected by the chosen basis set.
Plane-wave	Well-suited for periodic systems and periodic boundary conditions. Applicable to wide range of materials. Ideal for high-performance computing and parallel processing.	Computationally demanding for large systems. Pseudopotentials may introduce inaccuracies in some calculations. Accuracy can be affected by choice of pseudopotential and energy cutoff.
GPW	Accurately describes electronic structure of various systems. Computationally efficient for periodic systems. Easily adaptable to different system sizes and shapes.	Requires specialized software and expertise. Accuracy depends on parameter choices. Computationally demanding for large or complex systems.

calculations versus periodic calculations, vacuum calculations versus solvation methods, and hybrid Gaussian/plane-wave basis sets versus both individual Gaussian and plane-wave basis sets.

4. Computational efforts

4.1. General overview

Concerning P-related processes, the main focus of this review is on the phosphate-surface binding mechanisms and in particular the possible binding motifs. In general, a binding motif refers to a binding situation between two or more molecular systems (or fragments in the same molecular system) to form a complex in a specific manner and sometimes with a specific sequence. Each binding motif has its own energy and thus a specific stability. The characterization of the phosphate binding motifs provides direct information on stability of a specific phosphate-surface complex and thus helps in understanding and controlling the P mobilization process. A brief overview about application of **CC** methods to phosphate related processes is given in the following. Thereby, the focus will be on phosphate binding motifs and the development of new fertilizers.

CC has been applied in the field of P research to provide a comprehensive understanding of the phosphate binding to soil constituents and especially mineral surfaces. For instance, Kubicki and co-workers have addressed the phosphate binding using DFT calculations in a number of papers. In an early investigation, they have studied the phosphate binding to goethite and its pH dependence by applying an embedded-molecular-cluster approach (Kwon and Kubicki, 2004; Kubicki et al., 2007). Here, goethite was modeled as a small cluster of two edge-sharing iron octahedra (each iron ion was saturated with water molecules and OH^- groups) with only a few explicit water molecules to mimic the surrounding solvent molecules. By comparing the experimental IR vibrational frequencies with the calculated ones, it was suggested that a diprotonated bidentate (**B**) complex forms at pH 4–6, a deprotonated **B** or a monoprotonated monodentate (**M**) complex at pH 7.5–7.9, and a deprotonated **M** complex at pH 12.8. Moreover, the reaction energies of the modeled adsorption process (phosphate species + goethite model → phosphate-goethite complex) have been calculated for all the modeled complexes. These calculated reaction energies pointed to the overall abundance of the monoprotonated **M** complex among all other phosphate-goethite complexes along the whole modeled pH range. Next to the monoprotonated **M** complex, the diprotonated **B** complex is favored at low pH (i.e., pH 4–6). Moreover, the effects of surface charge distributions, phosphate speciation, competitive water, pH, and hydrogen bonds on the phosphate binding to the same small cluster have been investigated (Rahnemaie et al., 2007; Acelas et al., 2013). According to Rahnemaie et al. (2007), a deprotonated **B** complex is more favorable at low P loading, while a monoprotonated **M** complex is more favorable at low pH and high P loading. In contrast, Acelas et al. (2013) found a mixture of diprotonated **B** and **M** complexes, with the **B** complex being more abundant in the pH range of 4.2–5.7, and a mixture of monoprotonated **B** and monoprotonated **M** complexes at pH 7.9. Similar studies have investigated the binding of phosphate to a cluster model of boehmite (γ-AlOOH) (Li et al., 2010), correndum (α-Al_2O_3) (Li et al., 2013a), γ-Al_2O_3 (Ren et al., 2012), aqueous uranium complexes (Kubicki et al., 2009), and ferrihydrite (Khare et al., 2007). For example, Li et al. (2010) observed a mixture of

deprotonated and monoprotonated **B** complexes, with the deprotonated form being more abundant. Similarly, Li et al. (2013a) found a mixture of deprotonated and monoprotonated **B** complexes at pH 5, while at pH 9, the deprotonated **B** complex was the dominant species. The aforementioned observations were made using cluster calculations, which may not be the most accurate approach for describing extended or periodic systems.

Kubicki et al. (2012) have extended their investigations of phosphate-surface binding motifs by performing periodic DFT calculations. Thereby, they have taken into account different goethite surface planes and carried out stationary calculations and MD simulations for the HPO_4^{2-} species. Moreover, IR vibrational frequencies have been calculated for extracted molecular clusters and used to assign the phosphate binding motifs. The results predicted the formation of **M** complexes at the 001, 210, 101, and 100 surface planes and **B** complexes at the 010, 101, and 100 surface planes. Similarly, Belelli et al. (2014) utilized periodic DFT calculations to investigate the behavior of phosphate complexes on pure and Al-rich goethite surfaces. Their analysis included several phosphate complexes that had not been previously explored in theoretical studies. In particular, they examined bidentate binuclear (**B**), bidentate mononuclear (**BM**), monodentate mononuclear (**B**), and monodentate binuclear (**MB**) complexes, with their respective monoprotonated and nonprotonated species, on the 110 planes of both pure and Al-rich goethite surfaces. Their findings indicated that all of the examined complexes could potentially form on both pure and Al-rich goethite surfaces. Nevertheless, the analysis of the calculated and experimental vibrational frequencies suggested a prevalence of protonated **BM** complexes at pH 3.1, **B** complexes within the pH range of 4.2–7.9, and protonated **B** complexes at pH 12.8. In addition, Weng et al. (2020) performed short molecular dynamics (MD) simulations (3 ps) using periodic DFT calculations to study the behavior of three distinct phosphate complexes, namely **M**, **B** (chemisorption), and outer-sphere (physisorption) configurations, on the 100 goethite surface plane. The authors found that the chemisorption configuration of **M** was more abundant than the physisorbed configuration, accounting for 83 % and 17 % of the total adsorbed species on the surface, respectively, based on weighing the binding energy according to the Maxwell-Boltzmann distribution. Furthermore, they reported an extraordinarily high binding/adsorption energy of −2.13 eV for the physisorbed configuration. Moreover, Ahmed et al. in a number of contributions have investigated the binding of inorganic and organic P compounds to soil constituents such as mineral surfaces, free metal ions, and SOM (Gros et al., 2017; Ahmed et al., 2018a; Gros et al., 2019; Ahmed et al., 2018b, 2019; Ganta et al., 2019; Ahmed et al., 2020; Ganta et al., 2021, 2020b; Shaheen et al., 2022). These contributions have addressed the P binding mechanisms taking into account the effects of surface morphology, surface saturation, surface central metal ion exchange, metal ions and their valency, SOM composition, water, pH, and redox potential on the P binding. The results of these investigations will be summarized in Section 4.2.

CC methods were also used to aid the development of new P-fertilizers. In particular, García-Mina and coworkers have focused on new efficient P-fertilizers in a joint experimental-theoretical effort (Baigorri et al., 2013, 2019; Urrutia et al., 2014). These new fertilizers comprise soluble phosphate-metal-humic complexes that are more sustainable and provide a bio-available P source. These complexes have been proposed to occur naturally in soil by Gerke et al. (1995) and characterized later by Guardado et al. (2007) and Urrutia et al. (2013). The structure of these fertilizers have been characterized experimentally by fluorescence, FTIR, ^{31}P NMR, and 2D ^{1}H-^{31}P WISE NMR spectroscopy (Baigorri et al., 2013, 2019; Urrutia et al., 2014; Guardado et al., 2008). Erro et al. (2012) showed that the complexes prevent P soil fixation and enhance root-phosphorus uptake. Moreover, phosphate-metal-humic complexes (metal = Al^{3+} and Zn^{2+}, humic acid = salicylate) have been modeled using a semi-empirical method (Guardado et al., 2008). The molecular modeling results showed that the stability of the phosphate-metal-humic complexes is inversely proportional to stability of the corresponding metal-humic complexes. This came in accord with the joint experimental characterization by FTIR and fluorescence spectroscopy that pointed to a relationship between the P fixation and the stabilization of the metal-carboxylate bond. Moreover, this might explain why a relatively small amount of humic-complexed metal is involved in phosphate fixation. In another study, similar complexes have been modeled for Fe^{3+}, Al^{3+}, and Ca^{2+} at the B3LYP/PCM level of theory (Urrutia et al., 2013). The calculated reaction/relative Gibbs free energies showed that the stability of formation of complexes between phosphate and metal-humic complexes has the order $Fe^{3+} \geq Al^{3+} > Ca^{2+}$. These results were qualitatively consistent with the experimental results by Guardado et al. (2007) and specifically with the apparent stability constants calculated by the Scatchard (1949) method. Moreover, the modeling results were in accord with the observed significant decrease in the phosphate adsorption in the presence of phosphate-metal-humic complexes for the joint adsorption experiments on soil samples in the presence of pure phosphate, phosphate + humic acid, and phosphate-metal-humic complexes (Urrutia et al., 2013). The order of the P adsorption decrease was $Fe^{3+} > Al^{3+} > Ca^{2+}$ indicating to the P protection by inhibiting the binding of the stable phosphate-metal-humic complexes with the P binding sites in soils. This means that more phosphate will be available for plants when considering metal-humic complexes and especially for the Fe^{3+} case. In conclusion together with experimental results, **CC** investigations provided evidence for the importance of the phosphate-metal-humic complexes as potential candidates for novel phosphate-based fertilizers and especially for crops cultivated in soils with high P fixation ability.

The above overview discussing the computational efforts performed to gain a better understanding of the binding of phosphate to Fe- and Al-surfaces, is presented in Table 6. This table compiles data from relevant literature studies that have investigated the binding motifs of adsorbed phosphates on Al- and Fe-mineral surfaces using different levels of theory and molecular simulation techniques (Ahmed et al., 2019; Ganta et al., 2019; Ahmed et al., 2020; Ganta et al., 2020a, 2021; Kubicki et al., 2012; Li et al., 2013a; Rahnemaie et al., 2007; Li et al., 2010; Kwon and Kubicki, 2004; Kubicki et al., 2007; Acelas et al., 2013; Belelli et al., 2014; Weng et al., 2020; Ganta et al., 2020b; Shaheen et al., 2022; Frisch et al., 2004). The table provides information on the various binding motifs of adsorbed phosphates at Fe- and Al-mineral surfaces, along with the molecular modeling and computational approaches used. By comparing the methods employed in each literature study reviewed in Table 6 with those presented in Tables 4 and 5, it is possible to judge on the potential accuracy of each approach. In this context, it is important to emphasize that the contributions made by Ahmed et al. (Ahmed et al., 2019; Ganta et al., 2019; Ahmed et al., 2020; Ganta et al., 2020a; Ganta et al., 2021; Ganta et al., 2020b) stand out in terms of the level of **CC** among the reviewed literature in this table. These studies employed periodic calculations with considerably larger simulation boxes, which incorporated bigger phosphate-mineral-water molecular models with explicit solvation using a water density of 1 g.cm^{-3}. Moreover, these simulations utilized molecular dynamics based on either DFT or QM(DFT)/MM in combination with the hybrid Gaussian and plane-wave basis sets, and took into account the long-range dispersion correction.

4.2. Towards squaring the circle

The fate of P in soil is determined by multiscale biogeochemical processes bridging molecular to macroscopic length and time scales. In addition, soil is a very complex and heterogeneous medium and P-binding is affected by many factors, see Sections 1–3. At this time, broader-scope **CC** investigations at the molecular level are only emerging and the link to the mesoscale and beyond is yet to be established. However, simplified atomistic and molecular modeling approaches and **CC** methods applied in P research are a first step towards understanding the fate of P in the environment at microscopic and macroscopic scales. In particular, molecular simulations based on atomistic models give access to fundamental understanding of the related chemical reactions, binding mechanisms, and relevant binding motifs that could not be obtained otherwise. But, already the molecular modeling of phosphate binding in soil faces the challenge of soil heterogeneity. As a remedy, it has been shown to be advantageous to break down the problem into well-defined soil constituents (e.g., SOM, metal ions, or mineral surfaces) and to address a particular key factor

Table 6
Compiled data from relevant literature to the identified binding motifs of adsorbed phosphates (orthophosphate (OP), glycerolphosphate (GP), and inositolhexaphosphate (IHP)) on Al- and Fe-mineral surfaces using different levels of theory and molecular simulation techniques. Different modeled and abundant binding motifs of adsorbed phosphate at Fe- and Al-mineral surfaces are given. Brief details about the molecular modeling and computational approaches are given as well. d = 1 denotes explicit solvation with water density of 1 g.cm^{-3}, else the number written refers to the number of water molecules. For a row with more than one binding motifs, ∗ denotes a major binding motif. Parentheses followed the binding motifs, refer to formation or abundance of this/these motif(s) at under the conditions stated in the parentheses. 001, 100, 010, 101, and 210 refer to the different goethite surface planes. GO, MD, and vib. freq., and vac denote geometry optimization, molecular dynamics simulation, vibrations frequencies calculations, and vacuum, respectively.

Study Ref.	P	Surface	Periodic/	Water	Binding motifs		Level of	Technique	Vibr.	Code
			Cluster		Modeled	Abundant	Theory		Freq.	
Kwon and Kubicki (2004)	OP	Goethite	Cluster	A few	6 motifs	**B**H_2 (pH 4-6) **B** or **M**H (pH 7.5–7.9) **M** (pH 12)	B3LYP	GO	Yes	G03 (Frisch et al., 2004)
Kubicki et al. (2007)	OP	Goethite	Cluster	A few	6 motifs	**M**H∗, **B**	B3LYP	GO	Yes	G03
Rahnemaie et al. (2007)	OP	Goethite	Cluster	A few	4 motifs	**B** (low P loading) **M**H (low pH, high P loading)	BP86	GO	Yes	Spartan 04 (2003)
Li et al. (2010)	OP	Boehmite	Cluster	4–8	3 motifs	**B**∗, **B**H	B3LYP	GO	Yes	G03
Kubicki et al. (2012)	OP	Goethite	Periodic 100, 010, 001, and 210 planes (vac 10 Å)	31	10 motifs	**M**H (001, 210, 101, 100) **B**H (010, 101, 100)	PBE + U, B3LYP	MD (3 ps), GO	Yes	VASP (Kresse and Furthmüller, 1996), G03
Li et al. (2013a)	OP	Corundum	Cluster	8–18	4 motifs	**B**, **B**H (pH 5) **B** (pH 9)	B3LYP	GO	Yes	G03
Acelas et al. (2013)	OP	Fe-hydroxide	Cluster	A few	9 motifs	**B**H_2^+, **M**H_2 (pH 4.2-5.7) **B**H, **M**H (7.9)	B3LYP	GO	Yes	G09 (Frisch et al., 2013)
Belelli et al. (2014)	OP	Goethite	Periodic 110 planes (vac 14 Å)	A few	8 motifs	**BM**H (pH 3.1) **B** (pH 4.2-7.9) **B**H (pH 12.8)	PBE+U	GO	Yes	VASP
Ahmed et al. (2019)	OP	Goethite	Periodic 010 and 100 planes (vac 20 Å)	d = 1	4 motifs	**BM**H (010) **M** (100) **M**:**B** = 1:8 (IR)	PBE-D3	GO	Yes	CP2K (Kühne et al., 2020; Hutter et al., 2014)
Ahmed et al. (2020)	OP	Goethite	Periodic 010 and 100 (vac 20 Å)	d = 1	24 motifs	**M** (low pH) **B** (intermediate pH) **M** (high pH)	PBE-D3	GO, MD	Yes	CP2K
Weng et al. (2020)	OP	Goethite	Periodic 100 planes (vac 15 Å)	12–32	2 motifs	**M**	optPBE-vdW	MD (3 ps)	Yes	VASP
Ganta et al. (2019, 2020b)	GP IHP	Diaspore	Periodic 010 and 100 planes (vac 18 Å)	d = 1	4 motifs 8 motifs	B∗, **M** 3**M**∗, 2**M** (010) 2**M**∗,**M** (100)	QM/MM	MD (25 ps)	No	CP2K
Ganta et al. (2020a, 2021)	GP IHP	Goethite	Periodic 010 and 100 planes (vac 18 Å)	d = 1	4 motifs 8 motifs	B∗, **M** 3**M**∗, **M**	QM/MM	MD (25 ps)	No	CP2K
Shaheen et al. (2022)	OP	Metal ions	Cluster	A few	4 motifs	**M**H	B3LYP-D3	GO	Yes	G16 [184]

(e.g., surface Chemistry, morphology, and saturation, kind and valency of metal ions, SOM composition, water, pH, and redox potential). An overall molecular picture for the P binding in soil could then be obtained by combining information from all these approaches. Vital for the success of this bottom-up modeling is the validation with respect to experiments and in particular targeted experiments on controlled samples. For example, a SOM model set consisting of >30 representative molecular systems covering most abundant SOM functional groups has been developed and tested against experimental data on well-controlled SOM modifications of soil samples characterized by high resolution mass spectrometry and X-ray absorption near-edge spectroscopy (XANES) (Gros et al., 2017; Ahmed et al., 2012, 2014, 2015). In the P-context, the binding with SOM, free metal ions, and mineral surfaces with different surface planes and different central metal ions have been modeled at different pH conditions and validated against experiments in Refs. Ahmed et al., (2018b), Ahmed et al. (2019), Ganta et al. (2019), Ahmed et al. (2020), Ganta et al. (2021, 2020b), Shaheen et al. (2022).

In general, the binding strength between the phosphate species and the soil component model can be characterized by calculating the interaction energy (E_{int}) for the complexation reaction, phosphate (A) + soil component model (B) → A-B complex using the following expression:

$$E_{int} = E_{A-B\,complex} - (E_A + E_B). \quad (1)$$

Here, $E_{A-B\,complex}$, E_A, and E_B are the total electronic energies of the phosphate-(soil component model) complex, phosphate species, and the soil component model, respectively. In the reporting calculation results, the basis set superposition error (BSSE), which would predict a too strong stabilization of the complex A-B as compared with the fragments A and B, is corrected using the counterpoise scheme (Boys and Bernardi, 1970). It should emphasized that there is no additional geometry relaxation taken into account for the individual fragments (A and B) and their energies are calculated based on their geometries in the A-B complex. Moreover, it should be highlighted that the calculated interaction energies are representative for the strength of the phosphate binding process in a specific environment and are directly proportional to the PO–Fe bond energy formation. However, their values might deviate from the experimentally measured adsorption energies, which correspond to binding free energies. Including change in the free energy, combining enthalpy and entropy, gives direct access to how spontaneous a certain chemical reaction will occur (see Section 4.2.5). Although free energy calculations are feasible for small molecular systems, in particular when using the harmonic approximation for nuclear motion, they become very time-consuming for large systems (as the introduced molecular models in Sections 4.2.1–4.2.4) (Pohorille and Chipot, 2007; Goette and Grubmüller, 2009).

In the following, an illustrative overview about different molecular modeling approaches related to the phosphate binding to soil constituents will be provided. Effects of key factors such as solution pH, crystal surface planes (surface morphology and surface saturation), binding motifs, and the influence of water on the phosphate binding process at two goethite surface planes will be presented in Section 4.2.1. Simulations of IR spectra as a tool to assign the phosphate-goethite binding motifs will be discussed in Section 4.2.2. Later, effects of organic phosphates and surface central ion replacement on the phosphate binding process will be highlighted in Sections 4.2.3 and 4.2.4. Finally, the results on the effect of the redox potential combined with the pH effect involving the binding process of phosphate with metal ions and SOM will be presented in Section 4.2.5.

Technically, periodic boundary calculations were performed to simulate the binding process of phosphates at mineral surfaces in the presence of explicit water in Sections 4.2.1–4.2.4. Specifically, in Sections 4.2.1 and 4.2.2, DFT calculations were performed for different phosphate-goethite-water models at the GPW/PBE/GTH/GD3 level of theory using the CP2K simulation package (Perdew et al., 1996; Lippert et al., 1997; VandeVondele et al., 2005; Kühne et al., 2020; Grimme et al., 2011; Hutter et al., 2014; Krack, 2005; VandeVondele and Hutter, 2007). The focus in Sections 4.2.1 and 4.2.2 is on inorganic phosphate (orthophosphate), while the main focus in Sections 4.2.3 and 4.2.4 is on relatively large organic phosphates. Consequently, Sections 4.2.3 and 4.2.4 involve larger phosphate-goethite/diaspore-water models (each molecular model contains >1200 atoms) compared to the introduced models in Section 4.2.1. Hence, hybrid electrostatic embedding QM/MM based MD simulations were applied (Laino et al., 2006). The QM region was described at the same level of theory as in Sections 4.2.1 and 4.2.2. The MM region was simulated using both compatible CLAYFF and CHARMM force fields (Cygan et al., 2004; Vanommeslaeghe et al., 2009). For each model, 25 ps MD simulations (NVT ensemble) were performed and the last 15 ps were assigned as production trajectories and used for analysis. Eventually, in Section 4.2.5, cluster calculations with implicit solvent treatment were performed to investigate the binding mechanisms of phosphates to metal ions and organic matter. Specifically, the calculations were carried out at the B3LYP/GD3/CPCM level of theory using the Gaussian simulation package (Lee et al., 1988; Grimme et al., 2011; Cossi et al., 2003; Frisch et al., 2016; Hehre et al., 1972). For more details about the molecular modeling approaches discussed in Section 4.2 and the relevant computational setup, see (Ahmed et al., 2019; Ganta et al., 2019; Ahmed et al., 2020; Ganta et al., 2020a; Ganta et al., 2021; Ganta et al., 2020b; Shaheen et al., 2022).

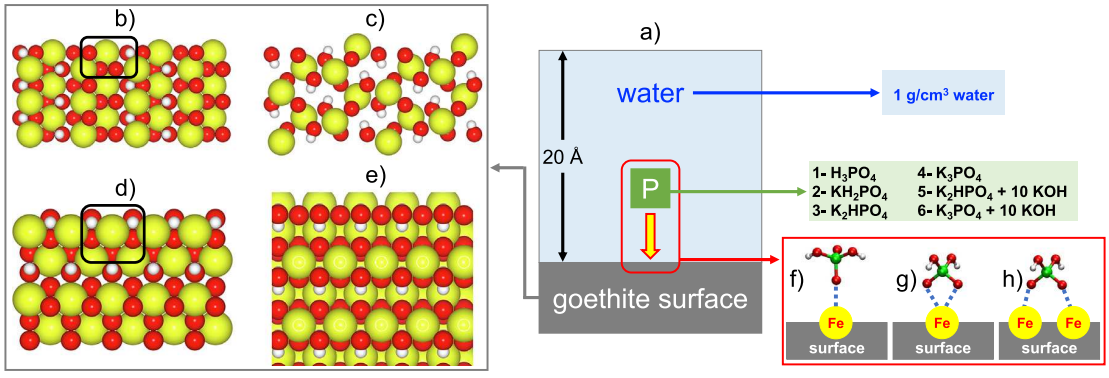


Fig. 2. Molecular modeling approach for the phosphate binding at the goethite-water interface including schematic representation of the phosphate-goethite-water model a), side and top views of the modeled 010- b) and c) as well as the 100-goethite surface planes d) and f), respectively, according to the Pnma space group (rectangles around the surface Fe atoms refer to two different coordination numbers of surface Fe atoms (4 for 010- and 5 for 100-goethite surface planes)), and schematic view of the possible binding motifs between phosphate and goethite (**M** motif at both 010- and 100-surfaces (f), (2O + 1Fe) **B** motif at the 010-surface (g), (2O + 2Fe) **B** motif at the 100-surface (h)). H, O, P, and Fe atoms are colored white, red, green, and yellow, respectively. Different phosphate species are considered in the simulations involving H_3PO_4, KH_2PO_4, K_2HPO_4, K_3PO_4, K_2HPO_4 + 10 KOH molecules, and K_3PO_4 + 10 KOH molecules. Note that the binding motifs have been constructed either by one covalent bond (**M** motif) or by two covalent bonds (**B** motif) between the phosphate O atoms and the goethite Fe atoms.

4.2.1. The pH effect on the P binding

In order to explore the effects of solution pH, crystal surface planes (i.e., surface morphology and surface saturation), binding motifs, and water on the phosphate adsorption at mineral surfaces, a molecular modeling focusing on phosphate binding at the goethite-water interface has been introduced (Ahmed et al., 2020). In accord with experimental studies, different molecular models for the phosphate-goethite-water molecular systems have been employed. Each model involved binding of a single phosphate species of 6 studied cases (H_3PO_4, KH_2PO_4, K_2HPO_4, K_3PO_4, K_2HPO_4 + 10 KOH, and K_3PO_4 + 10 KOH) at one goethite surface plane being either of 010 or 100 type. Further, water has been included with a density of 1 $g.cm^{-3}$ to mimic the adsorption solution medium, see Fig. 2. The focus on these two surface planes was motivated by the stability of the 010-surface (Xiu et al., 2016; Guo and Barnard, 2011) and the abundance of the 100-surface plane (Cornell and Schwertmann, 2003; Rakovan et al., 1999; Paul et al., 2007; Kubicki et al., 2008; Kubicki et al., 2017b). Moreover, these two surfaces provide the opportunity to explore different binding motifs between phosphate and goethite since they exhibit two kinds of surface Fe atoms with different coordination numbers, see Fig. 2b and d. For each phosphate species, two different models have been constructed involving **M** and **B** binding motifs between phosphate and the goethite surface, see Fig. 2f-h. In total, 24 phosphate-goethite-water molecular models have been introduced involving 6 **M** and 6 **B** motifs at each surface plane. For each model, the overall interactions (phosphate-goethite-water) and the individual interactions (phosphate-goethite, phosphate-water, and goethite-water) have been explored. The interaction energy (E_{int}) between the phosphate species and the goethite surface for the complexation reaction, phosphate + goethite surface → phosphate-goethite complex, was calculated according to Eq. (1).

For the 010-goethite surface plane, the simulation results point to the stability and thus abundance of the **M** binding motif at extremely acidic and alkaline conditions (i.e., in the presence of the H_3PO_4 species and excess OH^- groups, respectively), see Fig. 3. In the intermediate pH range (i.e., in the absence of OH^- groups), the **B** binding motif becomes predominant. Moreover, with increasing the pH from $H_2PO_4^-$ to PO_4^{3-} in this range, the stability of formation of phosphate complexes for both **M** and **B** binding motifs increases as well. Comparing the energy values for the modeled HPO_4^{2-} and PO_4^{3-} cases with and without OH^- groups, a clear drop in the stability of the binding motifs becomes obvious at the 010-goethite surface in the presence of the competing OH^- groups. A similar trend has been observed as well at the 100-goethite surface plane confirming the experimentally found strong drop in phosphate adsorption at the goethite surface at high pH. This observed experimental behavior could be explained as well by the simulations results that indicate that the binding at goethite increases in the order water < phosphate < OH^-. Based on this molecular level picture, one can conclude that phosphate can replace the adsorbed water molecules at the goethite surface but the OH^- groups can replace both adsorbed phosphate and water molecules leading to the strong adsorption drop at high pH.

Although there are similarities in the binding at the 010- and 100-goethite surface planes, there are considerable differences due to different surface morphology and saturation. For example, the geometrical difference of the **B** binding motif can be considered as a significant distinction between both surfaces which comes back to the surface morphology. The shortest distances between the adjacent surface Fe atoms are around 4.6 Å for the 010- and 3.0 Å for the 100-goethite surface plane. Therefore, the 010-goethite surface plane favors to form the (2O + 1Fe) **B** motif (i.e., it takes place between two phosphate O atoms and one surface Fe atom, see Fig. 2g), while the 100-surface favors to form the (2O + 2Fe) **B**@100 (i.e., it takes place between two phosphate O atoms and two surface Fe atoms, see Fig. 2h). Moreover, all **M** complexes over the whole pH range except for the H_3PO_4 case are more stable at the 100-goethite surface plane compared to the corresponding **M** complexes at the 010-goethite surface. This could be plausibly explained based on the extent of the surface saturation. Here, each surface Fe atom for the modeled 010- and 100-goethite surface planes is coordinated by four and five O atoms, respectively. Consequently, formation of the **M** binding motif would lead to surface Fe atoms coordinated with six (for the 100-goethite surface) and five (for the

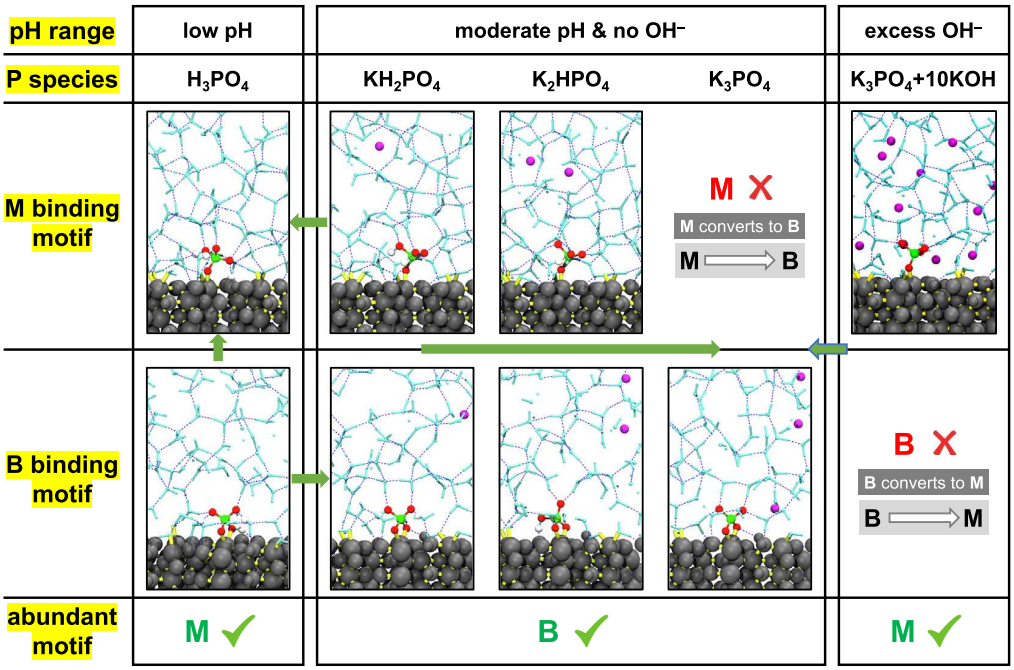


Fig. 3. Geometry-optimized structures of the phosphate-goethite-water complexes for the H_3PO_4, KH_2PO_4, K_2HPO_4, K_3PO_4, and K_3PO_4 + 10 KOH molecules at the 010 goethite surface plane. For each species, two binding motifs are represented including **M** and **B** (2O + 1Fe). Goethite and water atoms are colored in gray and cyan, respectively. For phosphate, atoms are colored in green (P), red (O), white (H), and purple (K). Intramolecular and intermolecular covalent bonds included goethite atoms are colored in yellow and HBs are colored in blue. Arrows indicate to the direction of increasing the interaction energy between the phosphate species and the goethite surface (i.e., direction of increasing the stability).

010-goethite surface) coordination bonds. Therefore, one can conclude that mostly the **M** binding motif is more stable at the 100-goethite surface plane compared to the 010-surface plane due to the complete saturation (i.e., six coordination bonds) for the former case. Moreover, the **B** complexes in the presence of the competing OH^- groups are only stable and abundant at the 100-goethite surface plane. In contrast, both **M** and **B** complexes at extremely low pH are more stable at the 010-goethite surface plane than the corresponding ones at the 100-goethite surface plane with predominance of the **M** complex at both goethite surface planes. Furthermore, the **B** complex for the PO_4^{3-} case is more stable at the 010-goethite surface plane than at the 100-goethite surface plane. Eventually, all these information demonstrate the importance of the kind of surface plane (saturation and morphology), the binding motif (either **M** or **B**), and pH in controlling the P binding. Thus, these pieces of information could serve as a reference to predict the phosphate binding motifs at goethite surfaces under specific pH conditions. Additionally, they could aid in identifying the prevalent crystallographic planes of goethite surfaces if the binding motifs are determined experimentally.

At both goethite surface planes, water shows a great potential in controlling the phosphate adsorption process, and the competition with phosphate and the hydroxyl (OH^-) groups at the goethite surface. Specifically, the interfacial water molecules interact with the goethite surface via formation of covalent bonds between water O atoms (O_{H_2O}) and goethite Fe atoms as well as formation of H-bonds (HBs) between water H atoms (H_{H_2O}) and goethite O atoms. In addition, dissociation of some water molecules is observed at the surface to protons (H^+) and hydroxyl (OH^-) groups. Consequently, these produced ions (H^+ and OH^-) will form covalent bonds with the conjugated charged surface atoms. This comes in accord with the experimental observations by Hiemstra and Van Riemsdijk (Hiemstra and Van Riemsdijk, 1996) and Strauss et al. (Strauss et al., 1997a) in which they found adsorption of protons (H^+) at the goethite surface during phosphate adsorption. Moreover, protons have been transferred from phosphate to water as well as to the surface. This in turn leads to a more acidic solution. Therefore, the P-fertilization process might induce soil acidity as a consequence of the phosphate adsorption at the mineral surfaces and proton transfer process.

The simulation results have been validated against pH dependent phosphate adsorption experiments (Ahmed et al., 2020). The experiments showed two successive adsorption stages based on the pH (see Fig. 1), the first stage was described by a slight increase of the phosphate adsorption upon increasing the pH from 4 to 8, while the second one exhibited a strong adsorption decrease upon a further pH increase from 8 to 12. It is worth noting that similar observations have been reported in previous studies on phosphate adsorption, as those conducted by Gao and Mucci (2001), Chitrakar et al. (2006), and Boukemara et al. (2016), which were previously discussed in Section 2. All these come in a good agreement with the provided molecular level picture. However, it should be noted that the uncommon first stage will be observed for adsorption of phosphate in the absence of competing ions only if the goethite surface exhibits a positive net charge and there is no significant change with increasing the pH below PZC. If the surface charge changes considerably, the common behavior of an adsorption decrease will be observed, as manifested by most previous experiments. This could be explained in the light of the simulation results by considering the most relevant phosphate species for common sorption experiments. Specifically, considering the H_3PO_4 (pH: around 2), $H_2PO_4^-$ (pH: 2.1–7.2), and HPO_4^{2-} + 10 KOH (pH: 7.2–12.4) models at the 010-goethite surface, yields a decrease in the phosphate adsorption upon the pH increase. Here, it should be critically stressed that adsorption experiments are affected by many factors involving e.g., the specific surface area (SSA), surface coverage, purity, and crystallinity of the goethite surface as well as the presence of different crystal planes and thus binding motifs. Interestingly, the joint experimental-theoretical results indicate that the phosphate sorption decreases the solution pH. This behavior will be observed only if there is no buffer solution used in the adsorption experiment and it becomes more significant at higher pH conditions. This means that P-fertilization may support soil acidification not only by the acidity from common P-fertilizers but also by induced acidity from the adsorbed phosphate by pedogenic oxides.

Regarding the energetics of phosphate-goethite complexes, Kwon and Kubicki (2004) suggested formation of a diprotonated **B** complex at pH 4–6 ($H_2PO_4^-$), either a deprotonated **B** or a monoprotonated **M** complex at pH 7.5–7.9 (HPO_4^{2-}), and a deprotonated **M** complex at pH 12.8 (PO_4^{3-}). This comes in accord with the outcome of the presented molecular modeling approach in this section by Ahmed et al. (2020) see Fig. 3. In contrast, Kwon and Kubicki (2004) predicted that both monoprotonated **M** and non-protonated **B** complexes are not stable for the $H_2PO_4^-$ species. This discrepancy might be due to modeling the goethite surface in that study (Kwon and Kubicki, 2004) by a small cluster of only two edge-sharing iron octahedra with only a few explicit water molecules. On the other hand, Kubicki et al. (2012) have performed periodic DFT-MD simulations for larger goethite models and the results evidenced the stability of both **M**@100 and **B**@100 complexes for the HPO_4^{2-} species in agreement with the findings by Ahmed et al. (2020). Further, Kubicki et al. (2012) reported positive adsorption energies for the **M**@010 and **B**@010 complexes which contradicts the negative adsorption energies reported by Ahmed et al. (2020). The reason might come back to different computational setups in terms of molecular models and their system size, levels of theory, and computational techniques. Further, Belelli et al. (2014) predicted using periodic DFT calculations the abundance of the protonated **B** complex at pH 3.1 and pH 12.8 and non-protonated **B** complex along the pH range of 4.2–7.9. Their observations at pH 3.1 and the pH range of 4.2–7.9 are consistent with the findings by Ahmed et al. (2020) related to the abundance of the **B** complex at both goethite surfaces for the modeled $H_2PO_4^-$, HPO_4^{2-}, and PO_4^{3-} species. Moreover, both Belelli et al. (2014) and Ahmed et al. (2020) reported consistent findings of the abundance of the **B** motif at the 100-goethite surface plane at high pH, specifically at pH 12.8. For the goethite-water interaction, DFT calculations by Zhou et al. (2017) predicted chemisorption and dissociation of water at the 010-goethite surface. This is consistent with the results reported by Ahmed et al. (2020), which showed that water molecules can form covalent bonds with the surface and some of them dissociate at the surface to protons (H^+) and hydroxyl (OH^-) groups, see Fig. 3.

The outcome of the molecular modeling approach by Ahmed et al. (2020) has been validated as well by comparing bond distances with other calculations and experimental extended X-ray absorption fine structure (EXAFS). For the optimized geometries of phosphate-goethite complexes in the presence of water, Fe—P distances fall within the range of 2.54–3.54 Å (Ahmed et al., 2020). This covers the range of the distances predicted by Kwon and Kubicki (2004) (3.21–3.37 Å) and Kubicki et al. (2012) (3.25–3.55 Å) as well as the distances obtained by EXAFS for colloidal phosphate-Fe complexes (3.05–3.39 Å) (Rose et al., 1997) and phosphate minerals such as vivianite (3.19–3.43 Å) (Rose et al., 1996). Moreover, the calculated Fe—P distances for the **M** binding motif at the 010-surface (3.02–3.41 Å), **M** motif at the 100-surface (3.39–3.50 Å), and **B** motif at the 100-surface (3.15–3.54 Å) are closer to the measured ones by X-ray (3.05–3.43 Å) than those for the **B** motif at the 010-surface (2.54–2.71 Å). Further, the calculated bond lengths of the adsorbed water molecules and goethite (Fe-O_{H_2O}) for the 010- (1.87–2.06 Å) and 100- (2.01–2.09 Å) goethite surface planes come in a good agreement with those measured by crystal truncation rod (2.15 Å) (Ghose et al., 2010) and calculated by DFT (2.04 Å) (Kubicki et al., 2008) for the solvated goethite surface.

4.2.2. IR spectra of phosphate-goethite complexes

IR spectroscopy provides a sensitive probe of the type of chromophore and its chemical environment. As mentioned in Section 2, there are different strategies for the assignment of IR spectral features to binding motifs of phosphates at the mineral surface, which potentially could lead to controversial conclusions. In order to address this question with **CC** methods, one has to take into account that models usually describe perfect surfaces for the chosen particular plane, whereas mineral particles in soil will have various crystal planes hosting imperfections (Cornell and Schwertmann,

2003; Guo and Barnard, 2011; Rakovan et al., 1999; Catalano, 2011). To cope with this situation, it was suggested to combine **CC** simulation results from different surface planes and different binding motifs into an effective model (Ahmed et al., 2019). Specifically, IR spectra have been calculated for the phosphate-goethite complexes at both 010- and 100-goethite surface planes. The focus was on the most abundant phosphate species for common soils (i.e., $H_2PO_4^-$). IR vibrational frequencies and corresponding IR intensities have been calculated for the optimized **M** and **B** phosphate-goethite complexes at both goethite surface planes (i.e, **M**@010, **B**@010, **M**@100, and **B**@100). For each binding motif, the overall IR spectrum of the adsorbed phosphate has been generated by considering all molecular vibrations related to the phosphate-goethite complex and to the goethite surface itself. In order to quantify the contribution of the phosphates, vibrational motions have been analyzed to generate spectra due to modes that are dominated by phosphate vibrations (i.e., phosphate-related spectra). In parallel, phosphate adsorption kinetics experiments at pH 6.3 have been carried out and the adsorbed phosphate has been characterized by FTIR spectroscopy.

The calculated spectra for the adsorbed phosphate of both **M** and **B** binding motifs at both 010- and 100-goethite surface planes versus the corresponding experimental FTIR spectrum are presented in Fig. 4. The experimental spectrum exhibits three main peaks (at 827, 927, and 1132 cm^{-1}) and one shoulder (at 1050 cm^{-1}). According to the approach related to the number of bands (Arai and Sparks, 2001), the experimental spectrum could be assigned to an **M** complex by tacking only the three main bands. By considering the shoulder in addition to the main bands, the **B** complex could be assigned for the same spectrum. According to the approach by Tejedor-Tejedor and Anderson (Tejedor-Tejedor and Anderson, 1990), the peak at 1132 cm^{-1} could be assigned to a monoprotonated **B** motif, the shoulder at 1050 cm^{-1} could be assigned to a small proportion of nonprotonated **B** and/or monoprotonated **M**, and the pronounced peaks at 827 and 927 cm^{-1} could be assigned to the goethite surface only and not to the phosphate-goethite complex (Tejedor-Tejedor and Anderson, 1990; Loring et al., 2009). A closer analysis of the reported IR data by Ahmed et al. (2019), with particular focus on phosphate-related spectra, suggests the following interpretation. Fig. 4 shows a good agreement between the theoretical and experimental IR spectra, especially for the **B**@010 (Fig. 4b) and **M**@100 (Fig. 4c) complexes. This might hint to the abundance of the 010-goethite surface plane in the goethite sample for the experiments that reported the predominance of the **B** motif. In contrast, the 100-plane could be the dominating plane for those experiments reported **M** as the most abundant motif. Therefore, possible explanation for the contradiction between experiments could be understood in the light of these simulation results. Moreover, by considering the first two experimental peaks, the **M**@100 complex shows a better agreement with the experiment, see Fig. 4c. However, a reasonable agreement with the last peak can be observed only if the **B**@010 complex is considered, see Fig. 4b. An attempt to assign both Ahmed et al. (2019) and previously reported experimental IR spectra in terms of individual binding motifs has led to the following conclusions: (1) experimental peaks around 1132 and 1050 cm^{-1} could be due to **B**@010 and **M**@100 motifs, respectively, (2) the peak around 927 cm^{-1} could be due to the **M**@010, **B**@010, and **M**@100 binding motifs, (3) the peak around 827 cm^{-1} could originate from all considered motifs, and (4) the interaction with goethite is most dominant in the range below 1000 cm^{-1}.

Considering the overall experimental spectrum as a reference, reasonable agreement was mainly achieved for the phosphate-goethite spectra of **B**@010 (Fig. 4b) and **M**@100 (Fig. 4c). This indicates the abundance of the **M** complex at the 100-surface plane combined with the **B** complex at the 010-surface plane. But also the **M** complex at the 010-surface plane (Fig. 4a) and the **B** complex at the 100-surface plane (Fig. 4d) could be present. This would explain the agreement of some pronounced peaks for the latter complexes with the corresponding experimental ones (see the labeled peaks with transparent blue rectangles). This suggests the conclusion that the overall spectrum should involve contributions (theoretical spectra) of all different complexes based on the proportion of the existing complexes at specific surface plane as well as proportion of the existing surface planes. For this purpose, overall spectra with different proportions and combinations of the relevant complexes and surface planes have been calculated (i.e., by taking weighted averages of spectra of different motifs). The outcome of this approach is shown in Fig. 5.

Comparing the weighted average spectra with the experiment, one finds an improvement of agreement by increasing the **B**:**M** proportion from 1:9 to 9:1 for the 010-goethite surface plane, (see Fig. 5a). In contrast, the theoretical spectra for the 100-surface plane are improved by decreasing the **B**:**M**

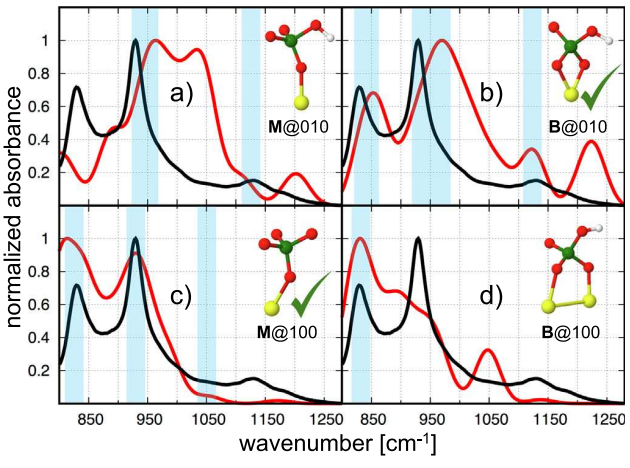


Fig. 4. Overall experimental IR spectrum (in black) versus the calculated overall spectra (in red) of the adsorbed phosphate species ($H_2PO_4^-$) at the goethite surface for **M** binding motif at the 010 surface plane a), **B** binding motif at the 010 surface plane b), **M** binding motif at the 100 surface plane c), and **B** binding motif at the 100 surface plane d). For each binding motif, a small Fe-phosphate cluster is extracted and shown here for better visualization. Atoms are colored in yellow (Fe), green (P), red (O), and white (H). Transparent blue rectangles are added to show the agreement between the calculated and experimental spectra. "Right symbols" refer to the best agreement.

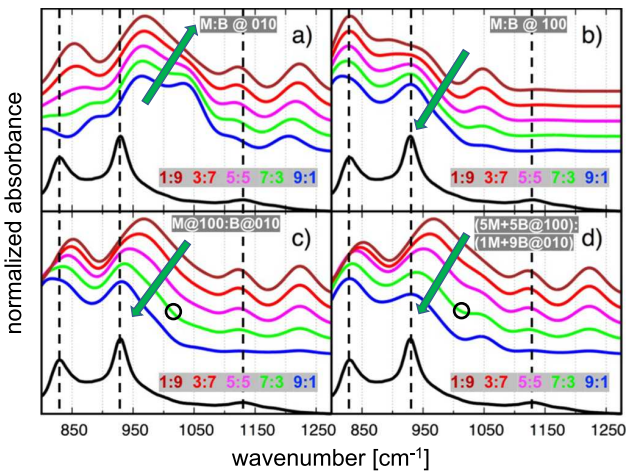


Fig. 5. Overall experimental IR spectrum (in black) versus weighted average spectra that are obtained via different combinations of the calculated overall spectra with different proportions of **M**@010 and **B**@010 binding motifs (a), **M**@100 and **B**@100 binding motifs (b), **M**@100 and **B**@010 binding motifs (c), and 5 **M**@100 + 5**B**@100 binding motifs and 1 **M**@010 + 9**B**@010 binding motifs (d). Arrows are added to indicate to the direction of increasing the agreement level between the calculated and experimental spectra. Black circles refer to the best agreement.

proportion, see Fig. 5b. This points to the abundance and necessity of considering both **B**@010 and **M**@100 binding motifs. Comparing Fig. 5a and b, one observes that having high proportions of the **M**@100 complex is more consistent with the experimental data than having high proportions of the **B**@010 complex. Mixing of both **B**@010 and **M**@100 complexes (Fig. 5c) shows that including the **M**@100 fraction will improve the agreement with respect to the positions of the first two features. Nevertheless, the contribution of the **B**@010 complex is absolutely necessary to obtain the feature around 1132 cm^{-1}. An attempt involving all different binding motifs at both surface planes has been considered as well. Here, the best agreement between the theoretical and experimental IR spectra (Fig. 5d) indicated that the **B** motif is the most abundant binding motif at low phosphate loading and predominance of the $H_2PO_4^-$ species with **B**:**M** ratio of 8:1 regardless of the surface plane. The conclusion drawn from the IR spectrum confirms the interaction energy calculations according to which the monoprotonated **B** motifs are the dominant species and **M** motifs exist as a minor fraction only. Eventually, this theoretical assignment of IR spectra introduced a benchmark for characterizing experimental IR data for the adsorbed phosphates species at the goethite-water interface.

4.2.3. Organic phosphates

In-depth molecular level understanding of the phosphate binding mechanisms at mineral-water interfaces and especially for organically bound phosphates is lacking and substantial efforts should put forward to achieve this goal. As a starting point, the molecular binding mechanisms for two abundant organic phosphates (inositol hexaphosphate (IHP) and glycerolphosphate (GP)) at the goethite surface have been investigated at a molecular level. Specifically, two goethite surface planes (010 and 100) with different binding motifs of each phosphate-goethite model have been considered. The phosphate binding mechanisms have been explored by analyzing the phosphate-goethite-water geometries and the relevant interactions along the production trajectory of the QM/MM based MD simulations. In order to highlight the difference between adsorption of organic and inorganic phosphates, the adsorption of orthophosphate (OP) at the 100-goethite surface plane has been simulated as well with the same **CC** method and setup.

For the 100-goethite surface plane, MD simulations showed that OP and GP form stable **M** and **B** binding motifs, see Fig. 6. In general, the total interaction energy values showed that the **B** binding motif is more stable than the **M** one for both OP and GP. OP exhibits stronger binding to the goethite surface than GP for the **B** binding motif while it is the other way round for the **M** motif. This highlights the importance of the binding motif type as a key factor in controlling the phosphate-mineral binding process. Considering the interaction energy per bond, OP has a higher interaction energy for the **B** motif than the **M** motif. This suggests that OP favors to form an additional covalent bond with goethite and thus makes the **B** motif more favorable. This comes in accord with the outcome of the QM calculations involving interaction energies (Section 4.2.1) and the corresponding IR spectra (Section 4.2.2) that suggested the abundance of the **B** motif for OP at both 010- and 100-goethite surface planes. In contrast, the interaction energy per bond for the **B** motif of GP is lower than that for the **M** motif. This comes back to the strain in the formed covalent bonds between GP and goethite (Fe–O_P bonds) due to the interaction of the GP polar organic moiety with water molecules. For the same reason, the **B** motif for GP is less stable than that for OP. In the same context, Xu et al. (2017) showed that the GP adsorption induces more negative charge on hematite surface compared to the OP case which might strain the Fe–O_P bonds. Moreover, Li et al. (2017) suggested that GP might not form a **B** binding motif due to steric hinderance of the organic moiety. Combining the calculated interaction energies with previous experimental studies would suggest the dependence of the dominant GP binding motif (**M** or **B**) on the environmental condition and how GP is interacting with the surrounding environment

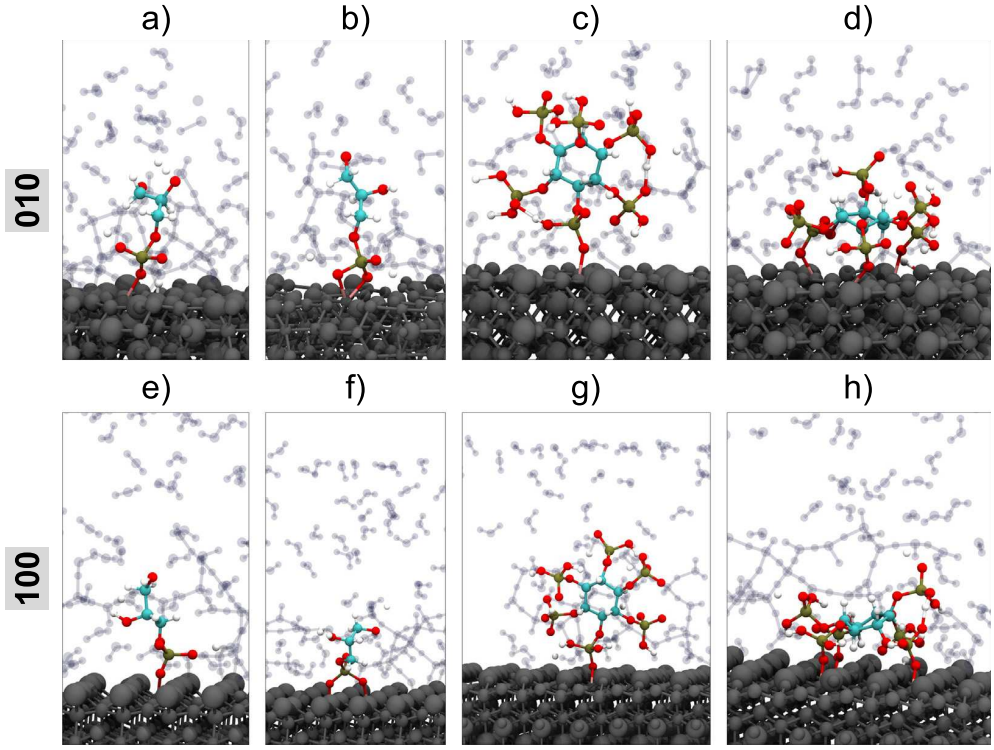


Fig. 6. Snapshots of the equilibrated adsorbed GP and IHP molecules at the goethite surface planes in the presence of water. **M** GP motif at the 010 goethite surface plane a), **B** (2O + 1Fe) GP motif at the 010 surface plane b), **M** IHP motif at the 010 surface plane c), 3 **M** IHP motif at the 010 surface plane d), **M** GP motif at the 100 surface plane e), **B** (2O + 2Fe) GP motif at the 100 surface plane f), **M** IHP motif at the 100 surface plane g), and 3 **M** IHP motif at the 100 surface plane h). H, O, P, and C atoms are visualized in white, red, lime, and cyan colors, respectively. For good visualization, all the goethite surface atoms are represented by gray color and water molecules are kept transparent.

(Li et al., 2017; Sheals et al., 2002). GP might form a **B** motif at low phosphate loading and **M** motif at high loading.

For IHP at the 100-goethite surface, the MD simulations showed that IHP forms stable **M** and 3 **M** binding motifs with multiple intramolecular HBs between adjacent phosphate groups, see Fig. 6. The interaction energy per bond for the 3 **M** motif is relatively lower than for the corresponding **M** motif due to the steric hinderance of the large organic moiety of IHP. However, the total interaction energy of the 3 **M** binding motif exceeds significantly that of the corresponding **M** motif. Thus, this shows that the 3 **M** motif is more stable than the **M** one. Moreover, the overall phosphate binding strength at the 100-goethite surface increases in the order OP **M** < GP **M** < GP **B** < OP **B** < IHP **M** < IHP 3 **M**. This shows that IHP binds to goethite stronger than both OP and GP regardless the binding motif type. In addition, this suggests that IHP could replace the adsorbed OP and GP at the goethite surface that comes in accord with the results by De Groot and Golterman (1993) that showed that IHP can replace OP and inhibit further OP adsorption. Moreover, this indicates that the number of phosphate groups is a key factor in controlling the adsorption strength (Anderson and Arlidge, 1962). This could explain the higher abundance of IHP compared to GP in forest soil colloid samples as revealed by liquid-state NMR measurements (Missong et al., 2016). However, it is important to emphasize that not all phosphate groups would contribute to the inner-sphere complexes with mineral surfaces. For instance, according to the simulation results IHP does not form a 4 **M** binding motif. Further, the binding strength order indicates that the IHP 3 **M** binding motif exhibits the highest interaction energy with the goethite surface among all phosphate-goethite complexes. Therefore, the 3 **M** motif could be proposed as the most dominant binding motif at low surface loading.

For the 010-goethite surface plane, GP and IHP exhibit phosphate-goethite binding motifs and phosphate-goethite-water interactions similar to the 100-goethite case. GP forms stable **M** and **B** binding motifs and IHP forms stable **M** and **3 M** motifs, see Fig. 6. Moreover, the binding strength order for GP and IHP (GP **M** < GP **B** < IHP **M** < IHP 3 **M**) is the same as for the 100-goethite surface. Comparing both 010- and 100-goethite surface planes underlines the influential role of the surface morphology and degree of the surface saturation in controlling the phosphate binding at mineral surfaces. In general, the less saturated 010-goethite surface plane binds both GP and IHP stronger than the more saturated 100-surface plane regardless of the binding motif type.

Joint adsorption experiments fitted to the Freundlich model showed that the adsorption strength (K_f) increases in the order GP < OP < IHP (Ganta et al., 2021). This comes in accord with experimental studies performed by Yan et al. (2014) and Amadou et al. (2022) investigating the affinity for OP, GP, and IHP to adsorb varied depending on the mineral surface. Their results indicated that GP had the lowest affinity, while IHP had the highest affinity on both goethite and amorphous $Al(OH)_3$ surfaces. These findings confirm the role of the molecular structure of phosphates in controlling the adsorption process, see the relevant data in Table 2. While the binding strength of the incoming phosphate molecule at the covered surface with the existing phosphate molecules (n_f) for the joint adsorption experiments (Ganta et al., 2021) increases in the order IHP < GP < OP. Based on the magnitude and order of both experimental and theoretical binding strength values, it can be suggested that the overall binding strength increases in the order GP (**M**) < OP (**B**) < IHP (**M** + 3 **M**). According to this order, GP might predominantly form an **M** motif whereas OP might form **B** and IHP might tend to form both **M** and 3 **M** motifs. The fact that GP adsorption induces more negative charge on goethite compared to OP, supports the suggestions that GP would tend to form **M** and not **B** motifs and eventually its interaction energy would be less than OP. The n_f order suggests that IHP adsorption at goethite saturates its surface faster than that for the GP and OP cases. This finding potentially explains why IHP is the most common form of phosphate found in soil. Furthermore, this highlights the significance of utilizing experimental and theoretical methods to enhance our comprehension at a molecular level of such phenomena.

For both goethite surfaces, the MD simulations showed that interfacial water molecules play an important role in controlling interactions and the binding mechanisms and thus binding motifs between these phosphates (OP, GP, and IHP) and goethite. Some of the interfacial water molecules form covalent bonds with goethite Fe atoms, while others dissociate at the surface to protons (H^+) and hydroxyl (OH^-) groups leading to proton transfer processes. Furthermore, water form HBs with OP, GP, and IHP as well as with the goethite surface. These HBs can be characterized using correlations between their geometries along the trajectory, see Fig. 7. This characterization type provides a quantification of the strength of a particular type of HB (weak, moderate, and strong) and the relevant proton transfer process (Guo et al., 2012; Ahmed et al., 2013). Most of the analyzed HBs for the phosphate-mineral-water systems are classified as being of moderate strength. For all models, the interaction of water with the goethite surface exceeds that of the studied phosphates.

4.2.4. Effect of surface central metal ion

Besides the most abundant Fe(III)-oxides like goethite or hematite, AlOOH-type reactive minerals like diaspore or boehmite are important soil constituents. To investigate the effect of the central metal ion of mineral surfaces on the phosphate binding process, the reactive mineral surface diaspore (α-AlOOH) can be considered. It is isomorphous with goethite having an Al^{3+} oxidation state instead of Fe^{3+}. In the following, results are shown for the binding of both GP and IHP at both 010- and 100-diaspore surface planes in the presence of water using the same setup, conditions, and techniques as for the geothite surface in Section 4.2.3.

For the 010-diaspore surface plane, the simulations showed formation of different stable phosphate-diaspore binding motifs involving **M** and **B** for GP as well as 2 **M** and 3 **M** for IHP, see Fig. 8. For GP, the interaction energy results indicated that the **B** motif is more stable than the **M** one. Here, the interaction energy per bond for the **B** motif is 2.4 times of that for the **M** motif. This higher interaction energy could be due to stability of the second bond formed between GP and the surface in addition to transfer of two more protons from GP to the surface in the case of **B**. For IHP, the 3 **M** motif has a higher total interaction energy compared to its 2 **M** motif but exhibits a lower interaction energy per bond. This means that the third bond in the 3 **M** binding motif might be less favorable than the first two bonds. A possible reason could be the mismatch between the positions of the phosphate groups in IHP and the surface Al sites, which introduces some strain into the 3 **M** motif. This mismatch makes the formation of a fourth phosphate-Al bond rather unlikely. For the same reason, the **B** motif, as a starting configuration, is not stable for IHP and transforms spontaneously along the MD simulation into a 2 **M** motif. IHP exhibited stronger interaction with the surface as well as with water compared to GP. Although the interaction energies per bond of the GP **B** and the IHP 3 **M** motifs are

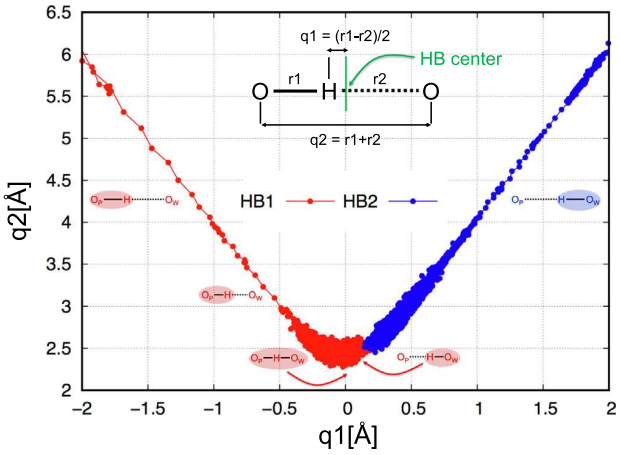


Fig. 7. Representative examples of observed HBs (HB1 and HB2) for the phosphates binding process to mineral surfaces in the presence of water. Here, q1 is the deviation of the H atom from the center of the HB (i.e., it refers to proton transfer) and q2 is the O—O HB length that indicates the HB strength.

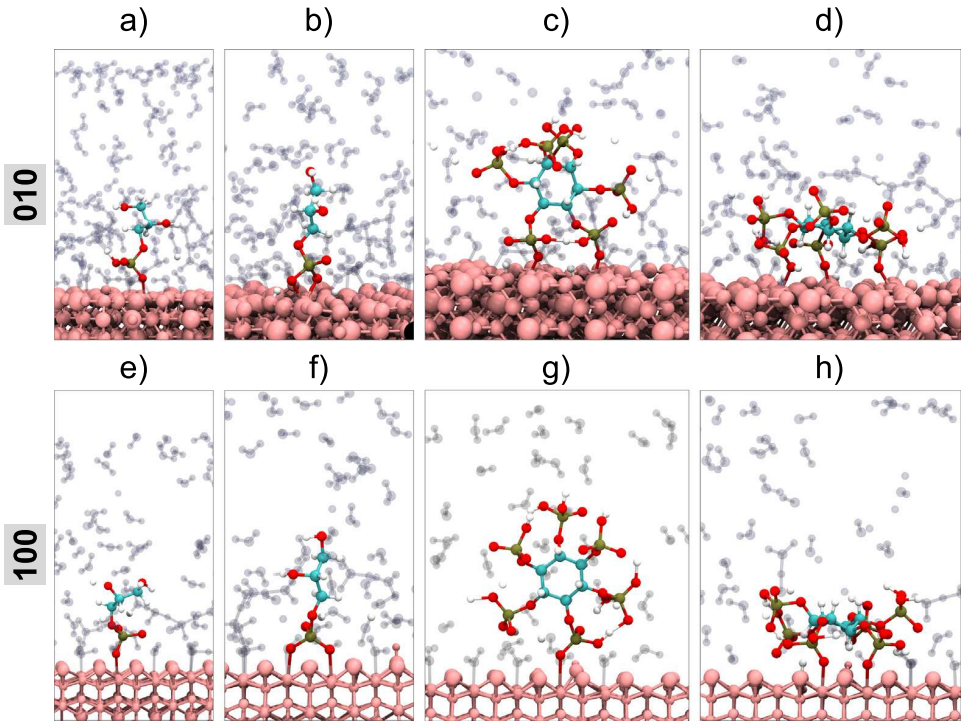


Fig. 8. Snapshots of the equilibrated adsorbed GP and IHP molecules at the diaspore surface planes in the presence of water. **M** GP motif at the 010 diaspore surface plane a), B (2O + 1Fe) GP motif at the 010 surface plane b), 2 **M** IHP motif at the 010 surface plane c), 3 **M** IHP motif at the 010 surface plane d), **M** GP motif at the 100 surface plane e), B GP motif (2O + 2Fe) at the 100 surface plane f), **M** IHP motif at the 100 surface plane g), and 2 **M** IHP motif at the 100 surface plane h). H, O, P, and C atoms are visualized in white, red, lime, and cyan colors, respectively. For good visualization, all the diaspore surface atoms are represented by pink color and water molecules are kept transparent.

similar, IHP via more phosphate groups compared to GP can form more covalent bonds with the surface and more HBs with the surrounding water molecules. Like the phosphate binding at goethite (Sections 4.2.1, 4.2.2, and 4.2.3), water plays a vital role in controlling the stability of these binding motifs and the overall diaspore-GP/IHP-water interactions via HBs and proton transfers. For GP, the **M** motif exhibits a stronger interaction with water and has two more proton transfers to water compared to the **B** motif. For IHP, the interaction with the solvating water molecules is of similar strength for 2 **M** and 3 **M** binding motifs. For all phosphate-diaspore-water models, the interaction of water with the diaspore surface exceeds that with phosphates (GP and IHP).

For the more saturated diaspore surface plane (100), two stable binding motifs (**M** and **B**) for GP and two stable binding motifs (**M** and 2 **M**) for IHP have been observed along the MD simulations. Here, GP and IHP favor **B** and 2 **M** motifs, respectively. Concerning the water interaction, the average interaction energy of water with IHP is higher than that with GP due to the higher water accessible surface area of IHP. IHP and GP showed proton transfer processes to water and formation of intermediate and strong HBs with water.

Comparing both 010- and 100-diaspore surfaces indicates that the less saturated surface plane (010) binds GP and IHP stronger than the more saturated one (100) for all binding motifs. This comes in accord with the same conclusion for the goethite surface, see Section 4.2.3. One key factor here is that higher surface saturation would lead in general to more negative charges and lower electrostatic potential at the 100-surface plane compared to the 010-surface. Therefore, phosphates (that are partially deprotonated and thus have effective negative charges) and water will be strongly bound/adsorbed to the 010- surface plane compared to the 100-surface. This comes along with a higher density distribution of water around the 010-surface compared to the 100-surface, see Ganta et al. (2020b). In addition, the surface morphology plays a key role, i.e. different dominant binding motifs have been observed based on the surface plane. The distribution of the surface central metal ions (i.e., Al^{3+} or Fe^{3+} in case of goethite) and their positions for both surface planes gives GP and IHP the opportunity to form more stable multiple covalent bonds with the 010-diaspore surface plane compared to the 100-surface. For IHP, the 010-diaspore surface plane dominates the 3 **M** motif while the 100-surface plane dominates the 2 **M** motif. In contrast, the **B** binding motif for GP is dominant at both surface planes with significantly higher abundance at the 010-diapsore surface plane. Moreover, both diaspore surface planes like goethite bind IHP stronger than GP indicating to the higher abundance of IHP in soils (Anderson and Arlidge, 1962; Missong et al., 2016).

Comparing the phosphate binding at both mineral surfaces (goethite and diaspore) leads to the following conclusions. Overall, goethite binds phosphates stronger than diaspore for most of the binding motifs. For all **M** motifs, phosphates bind to goethite stronger than diaspore. For the GP **B** binding motifs, goethite binds GP stronger than diaspore for the 100-surface plane and the other way round for the 010-surface plane. For the IHP 3 **M** binding motifs, diaspore binds IHP stronger than goethite for both surface planes. This discovery highlights the crucial role of the molecular structure of both the phosphate and the adsorbent surface, as supported by numerous experimental studies, such as those conducted by Yan et al. (2014), Ganta et al. (2021), Amadou et al. (2022), Wang et al. (2015a) and Gypser et al. (2018), as shown in Table 2.

4.2.5. Redox potential

In soil samples, the redox potential (E_h), that measures the tendency of a certain species or even a complex system to gain or lose electrons, might change. This change could be temporary (i.e., for minutes, hours, or days) and/or spatially (i.e., in micro sites, soil horizons and pedogenic soil patterns in landscapes, soil types, or landscapes) (Vepraskas et al., 1999; Gao et al., 2002; Fiedler et al., 2007). In general, the change of E_h is affected by several factors involving precipitation, infiltration, water filled pore space and groundwater level, microbial activity, and quality and quantity of available organic matter (Fiedler et al., 2007; Zimmer et al., 2016). For example, E_h might drop when soil moisture is replacing the O_2 containing

gas phase from the pore space, e.g., by infiltration of precipitation or by increasing groundwater levels. As these changes essentially go along with the soil water regime, the P binding in soil and its potential mobilization will be affected (Baumann et al., 2020a). Consequently, effects of redox changes on the fate of major plant nutrients and soil pollutants have received much attention in recent years (Frohne et al., 2011; El-Naggar et al., 2018; Baumann et al., 2020b). Nevertheless, a molecular level picture for the redox potential effect on the P binding is still lacking and some efforts should be introduced in this direction for better understanding. In an attempt to investigate the impact of redox potential on the phosphate binding at a molecular level, the binding process of orthophosphate with the relevant metal ions as well as with dissolved organic matter present in soil solutions has been simulated (Shaheen et al., 2022). Specifically, this was done by modeling the complexation reaction between phosphate and each of the series of metal ions M^{n+} (Ca^{2+}, Al^{3+}, Fe^{2+}, Fe^{3+}, Mn^{2+}, Mn^{3+}, and Mn^{4+}). Each M^{n+} ion was modeled as an octahedral metal aqua-complex, see Fig. 9. Two possible binding motifs (**M** and **B**) have been considered. **M** and **B** binding motifs were constructed by formation of one and two coordination bond(s) from phosphate O atom(s) to the free metal ion M^{n+}, respectively (see Fig. 9). For each M^{n+}-P complex, the free metal ion was saturated with water molecules up to the octahedral coordination state. Stability of the M^{n+}-P complexes and their P binding strengths were characterized by calculating the relevant reaction energies and free energies (ΔE and ΔG) according to reaction equation given in Fig. 9. To simulate the pH effect on this binding process, phosphate was modeled with two species involving $H_2PO_4^-$ (pH: 2.1–7.2) and HPO_4^{2-} (pH: 7.2–12.4) (Powell et al., 2005). Similarly, the binding of P to relevant organic matter molecules at different oxidizing/reducing conditions was simulated and corresponding reaction energies and free energies were calculated as in Eq. (1).

For the M^{n+}-$H_2PO_4^-$ complexation reactions, the calculated reaction free energies ΔG predict spontaneous chemical reactions between phosphate and each free metal ion, see Fig. 9. For all metal ions, the **M** M^{n+}-P complexes are more favored than the **B** ones. For both **M** and **B** complexes, the stability of the M^{n+}-P complexes increases with respect to the metal ion valency in the order divalent < trivalent < tetravalent metal ion. It was observed that the tetravalent ion (Mn^{4+}) and trivalent ions (Mn^{3+} and Fe^{3+}) bind phosphate four and two times stronger, respectively, than the corresponding divalent ones (Mn^{2+} and Fe^{2+}), see Fig. 9. This suggests that phosphates could bind strongly and thus immobilize in soil through their complexation reaction with free metal ions of higher oxidation state (such as Al^{3+}, Fe^{3+}, Mn^{3+}, and Mn^{4+}) and/or their oxides. Here, it is worth noting that in general, phosphates tend to bind more strongly to mineral surfaces than free metal ions in the soil solution. This is due to the fact that mineral surfaces can provide a range of binding sites for phosphates, including cation exchange sites, surface hydroxyl groups, and specific adsorption sites. These binding sites can interact with phosphates through a variety of chemical and physical mechanisms, leading to the formation of stable surface complexes that are difficult to desorb. On the other hand, free metal ions in the soil solution may be subject to competition from other dissolved species and may be more easily mobilized or removed from the system. To provide an example, the binding energies calculated for the complexation of M^{n+} with $H_2PO_4^-$ were found to be −20 and −41 kcal/mol for Fe^{2+} and Fe^{3+}, respectively. However, when examining the interaction energies between the adsorbed $H_2PO_4^-$ species and goethite, a wide range of values were observed, varying from −59 to −102 kcal/mol depending on factors such as surface morphology, surface saturation, crystal plane, presence of water, and pH. This means that binding of phosphates in soils (and especially binding to metal ions and metal-oxides) will be overall weaker under reducing conditions.This is because all different reductive dissolution mechanisms (e.g., proton-promoted dissolution, ligand-promoted dissolution, microbial reduction, electrochemical reduction, and photochemical reduction) that can occur for Fe(III) mineral surfaces such as goethite can ultimately lead to the release of free metal ions into solution, typically Fe(II) or Fe(III) that can then be reduced to Fe(II) in solution (Han et al., 2020). The specific mechanism and extent of dissolution will depend on a range of factors, including the nature of the reducing agent or conditions, the surface chemistry of the mineral, and the presence of other dissolved species that may affect the reaction kinetics or pathways. Regardless of the specific mechanism, the end result is typically the release of metal ions into solution. Hence more available P in solution could be expected by applying reducing conditions to soil samples, which yield more Fe^{2+} and Mn^{2+} with respect to the existing Fe^{3+}, Mn^{3+}, and Mn^{4+} metal ions.

Regarding organic matter (OM), the calculated binding energies and free energies are very small compared to those for free metal ions and metal-oxide surfaces, see Fig. 10 (Ahmed et al., 2019; Ganta et al., 2019; Ahmed et al., 2020; Ganta et al., 2020a, 2021, 2020b; Shaheen et al., 2022). Therefore, one could expect more available P from those bound to dissolved organic carbon (DOC)/SOM than the P bound to metal ions and their oxide surfaces. Within OM, aromatic DOC can bind P stronger than the aliphatic DOC. Furthermore, it was found that phosphate binds to the

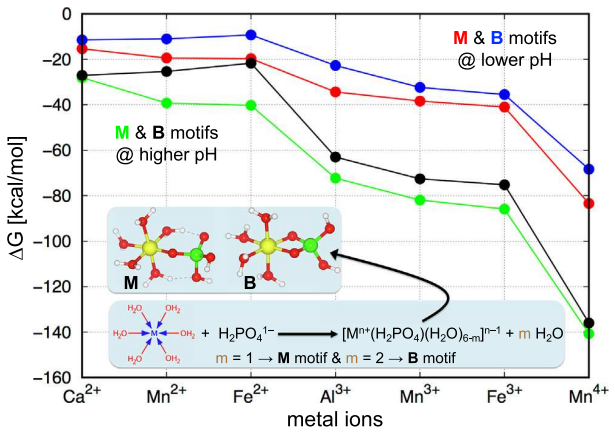


Fig. 9. Calculated reaction free energies (ΔG) for the complexation reaction between phosphate and the relevant free metal ions. Red and blue colors correspond to **M** and **B** binding motifs for the M^{n+}-P complexes, respectively. As an example, optimized geometries for the **M** and **B** Fe^{3+}-P complexes are shown. H, O, P, and Fe atoms are visualized in white, red, green, and yellow colors, respectively. Dashed lines refer to H-bonds (HBs).

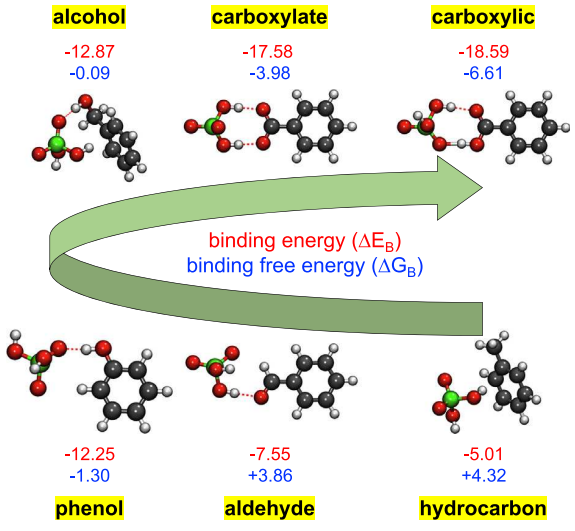


Fig. 10. Optimized geometries for selected OM–P complexes formed between the $H_2PO_4^-$ species and modeled organic matter (OM) functional groups. The reaction/binding energy (ΔE_B) and corresponding reaction/binding free energy (ΔG_B) are given for each OM–P complex in red and blue, respectively. H, O, P, and C atoms are visualized in white, red, green, and gray colors, respectively. Dashed red lines refer to H-bonds (HBs).

oxidized OM forms stronger than the corresponding reduced ones. This would highlight a general message and suggest the higher release of P under reducing conditions (lower E_h values) as well as the lower P release under oxidizing conditions. This is valid for organic matter, metal ions, and metal oxides. This in turn highlights the importance of redox chemistry of Fe oxides together with Mn oxides in controlling the redox-induced mobilization of P in soils. Furthermore, the modeling results come in accord with joint experimental results that Al—P could be the dominant species followed by Fe—P, Ca—P, and then organic-P (Shaheen et al., 2022). This outcome is mainly based on two key factors involving the binding strength discussed above and proportions of soil constituents and especially the existing free metal ions in soil solution (and in particular Fe^{3+} and Al^{3+}).

By considering the HPO_4^{2-} species (i.e., at higher pH), possible precipitation of metal ions by OH^- groups in soil solution could take place, however, the M^{n+}-P complexation reaction would be more favored. Similar to the lower pH case, the **M** M^{n+}-P complexes are more favored than the **B** ones and the M^{n+}-P binding strength decreases under reducing conditions as well, see Fig. 9. Furthermore, the M^{n+}-P complexes are more favored and thus more strongly bound at higher pH than at lower pH. This confirms the higher release of P under reducing and acidic (lower pH) conditions and the lower P release under oxidizing and alkaline conditions observed in a microcosm experiment with controlled redox oscillations (Shaheen et al., 2022). However, it must be stressed here that the pH effect on the P mobilization is not uniform and similar for all soil constituents. For example, the outcome of the molecular modeling approach indicated that P binds stronger to organic compounds at lower pH than at higher pH (see ΔG_B for carboxylic and carboxylate groups in Fig. 10). The same observation was made for metal oxide surfaces. In accord with experiment, this points to a higher release of P under alkaline (higher pH values) conditions considering metal oxides and organic matter. It shows the complex influence of pH on the P binding and thus the P mobility.

5. Summary and conclusions

Complementary to the huge body of experimental studies, molecular modeling approaches are capable of providing an in-depth molecular level understanding of the P binding in soil. In this review, this has been demonstrated by focusing on effects of some key factors controlling the P binding process and its strength (e.g., kind of the P-containing compound and its species, the quality and quantity of soil constituents, mineral surfaces and surface planes, binding motifs, water, solution pH, and redox potential). In general, we can conclude that in soil phosphate binds to metal ions and mineral surfaces stronger than to organic matter. For the binding to organic matter, the dispersion interaction and HBs are the main contributors. In contrast, phosphate binds to metal ions and mineral surfaces through inner-sphere complexes (i.e., by formation of covalent/coordination bonds) in addition to the important role of both HBs and the dispersion interaction. Accordingly, more available and mobile P could be expected from the P species bound to SOM compared to those bound to metal ions and mineral surfaces. In the same context, one can conclude that phosphate can bind stronger to soils that are rich in pedogenic oxides and vice versa. Moreover, phosphate binds weaker to soil constituents and especially to metal ions and metal-oxides under reducing conditions (low E_h) compared to oxidizing conditions. Therefore, more available P is expected upon reducing conditions in soil, e.g. by flooding. Specific aspects of P binding are summarized in what follows.

For mineral surfaces, their nature and surface planes are key factors that control the P binding process. For most binding motifs, goethite (α-FeOOH) binds phosphates stronger than diaspore (α-AlOOH). For the examples discussed here, this holds for all **M** motifs. There are some differences though that reflect the specific surface and adsorbate properties. The surface morphology (via different positions of surface metal ions) influences the binding process and controls the binding motifs and their strength. Favorable surface metal positions with respect to the phosphate oxygen atoms support and enhance formation of inner-sphere complexes. Otherwise, a strain of possible covalent bonds in the phosphate-mineral complexes exists leading sometimes to dissociation. As an example, orthophosphate (OP) favors to form the (2O + 1Fe) **B** binding motif at 010-goethite surface plane and the (2O + 2Fe) **B** motif at the 100-surface plane. The phosphate adsorption is affected as well by the kind and number of phosphate groups of the interacting phosphate species with mineral surfaces. Phosphates with a single phosphate group such as OP and GP can form stable **M** and **B** motifs. Nevertheless, the dominant motif could change depending on the surface loading, nature of mineral surface, surface plane, pH, … etc. In general, the surface saturation plays a vital role in the phosphate adsorption process where the general trend is that a more saturated surface will interact weaker with phosphates and vice versa. Further, the polar organic moiety of GP interacts with the surrounding water molecules that might hinder the interaction between phosphate and the mineral surface leading to a significant effect on stability of the binding motif. Phosphates containing multiple phosphate groups such as IHP could bind to mineral surfaces through more than one phosphate group forming various stable binding motifs, e.g., **M**, 2 **M**, and 3 **M** motifs; the latter two motifs are the dominant binding motifs for IHP. IHP binds to mineral surface stronger than monophosphates (OP and GP) with the order GP < OP < IHP. Further, the induced negative charge by phosphates at both surfaces increases in the order OP < GP < IHP. This could plausibly explain why the binding strength of a new incoming phosphate molecule at a particular surface covered with phosphate molecules is increasing in the order IHP < GP < OP.

Water plays an important role in controlling the phosphate binding process at mineral surfaces via formation of H-bonds (HBs) with phosphates and surfaces, dissociation at the surface producing H^+ and OH^- ions, proton transfer process to and from phosphates and surfaces, and formation of covalent/coordination bonds with the surface. Proton transfer processes from phosphates to water could lead to more acidic solution, which points to a possible induced soil acidity upon P-fertilization. The intermolecular HBs between phosphates (especially GP and IHP) and water molecules induced strain into the phosphate-mineral complexes leading to instability of particular binding motifs. This instability effect is directly related to the water accessible surface area of the phosphate species. Interestingly, IHP exhibits intramolecular HBs between the adjacent phosphate groups that could induce a strain into the IHP-mineral complexes leading to dissociation of some covalent bonds and thus instability of some binding motifs such as **B** and 4 **M**. The interaction energies of phosphates and water with the goethite and diaspore surfaces increases in the order water < GP < OP < IHP. This means that phosphates (OP, GP, and IHP) could replace water at the diaspore and goethite surfaces and IHP could replace OP and GP. This plausibly explains why IHP is the most abundant organically bound phosphate in soil.

The molecular modeling and simulation results by Ahmed et al. highlight the complex influence of the pH effect and its substantial role in controlling the P binding and thus P mobilization in soil. The pH effect is not uniform for all soil constituents. For example, the P binding to free metal ions increases upon increasing the solution pH. However, a different general trend was observed for organic matter and mineral surfaces in which the P binding decreases by increasing the solution pH. Another behavior has been observed for the P binding at mineral surfaces. Here, a slight increase in the phosphate adsorption upon increasing the pH is followed by a significant drop upon further pH increase and especially at pH > PZC. The first stage (i.e., the P adsorption increase) will be observed only if there is no significant change of the surface charge at pH < PZC. These observations suggest a higher release of P under alkaline conditions (i.e., higher pH) considering organic matter and metal oxides. On the other hand, P bound to free metal ions might be released easier at lower pH than at higher pH. This leads to the conclusion that binding of P to a specific soil is significantly influenced by the quality and quantity of soil constituents and the solution pH. In addition to the binding strength at mineral surfaces, the pH showed a significant effect in controlling the binding motifs. At both extremely low and high pH conditions, **M** was found to be the predominant motif for OP at both 010- and 100-goethite surface planes. In contrast, the **B** motif is predominant along the intermediate pH range,

i.e., in the absence of excess of OH^- groups. This was confirmed by calculated IR spectra whose interpretation points to the abundance of the **B** motif with **B**:**M** ratio of 8:1. In general, calculated IR spectra showed a significant dependence on the kind of surface planes and binding motif. This suggests that a comparison between theory and experiment cannot be made based on a single motif only. Specifically, for the phosphate-goethite case the best agreement with the experimental spectra was obtained including the **B**@010 and **M**@100 binding motifs with high proportions of the **B**@010 complex. This procedure could resolve the existing debate about the assignment of phosphate–goethite binding motifs. Therefore, this type of analysis can be recommended for characterizing experimental IR spectra for similar cases.

Further modifications and challenges of the existing molecular modeling approaches should be considered to address open critical questions in the field of P research at a molecular level. For example, but not limited, some key open questions are suggested as follows:

- How to setup molecular modeling approaches that are capable to differentiate between surface complexation and precipitation of phosphates at mineral surfaces (see Fig. 11a)?
- How to explain effects of background electrolytes and their ionic strength on the P binding process (see Fig. 11b)?
- How to describe the binding mechanisms at different P loading/concentrations (see Fig. 11c) and how the incoming P interacts with a mineral surface covered by existing phosphates?
- How to explore effects of free metal ions and organic matter in the solution on the P binding and how they compete with phosphates towards their interactions with reactive surfaces (see Fig. 11d-f)?
- How to rigorously and systemically model and simulate the impact of surface imperfections on the P binding process?
- How to explore the mechanisms by which microbes and plants can overcome the strong P-mineral binding and incorporate the phosphate groups into their metabolism?
- How to describe binding mechanisms of other anions and adsorbates at soil reactive surfaces?
- How to calculate and interpret IR spectra for different phosphates absorbed at soil constituents involving mineral surfaces as a function of pH?
- How to explore the temperature dependence of the P-binding process?
- How to simulate the P-adsorption isotherms and study the adsorption kinetics?
- How to explore more complex systems containing various reactive soil constituents?
- How to design new smart P fertilizers based on different bio-available materials such as phosphate-metal-humic complexes and bare and modified bone char (BC)?

Finally, a comment on the general conditions at which **CC** can possibly make a contribution to soil science. **CC** is well established and there exists an arsenal of methods from highly accurate to approximate, suitable for small to large systems, respectively. The actual challenge is provided by the complexity of soil as a heterogeneous medium comprising a mixture of organic and inorganic components of a wide range of sizes. Molecular models must account for this situation and they can do so only by focusing on a range of possible setups designed by chemical intuition. Of course, given the nature of soil this will never capture the full complexity in a statistical sense. Molecular models must be validated against experiment. There is a huge body of experimental literature, e.g. on sorption under specific conditions and for specific soils. The heterogeneity of soil, however, makes a one-to-one comparison with simulation results a difficult task. Therefore, validation should preferentially be done against targeted experiments under well-defined controllable conditions. Subsequently, the mechanistic insight could be transferred to other experiments if applicable. Within this frame, **CC** can already contribute to the understanding of processes in soil and their dependence on chemical conditions. To connect to mesoscale diffusion processes, coarse-grained models will be needed. Computational tools are already available and suitable models need to be developed based on the lessons learned from atomistic and molecular level simulations.

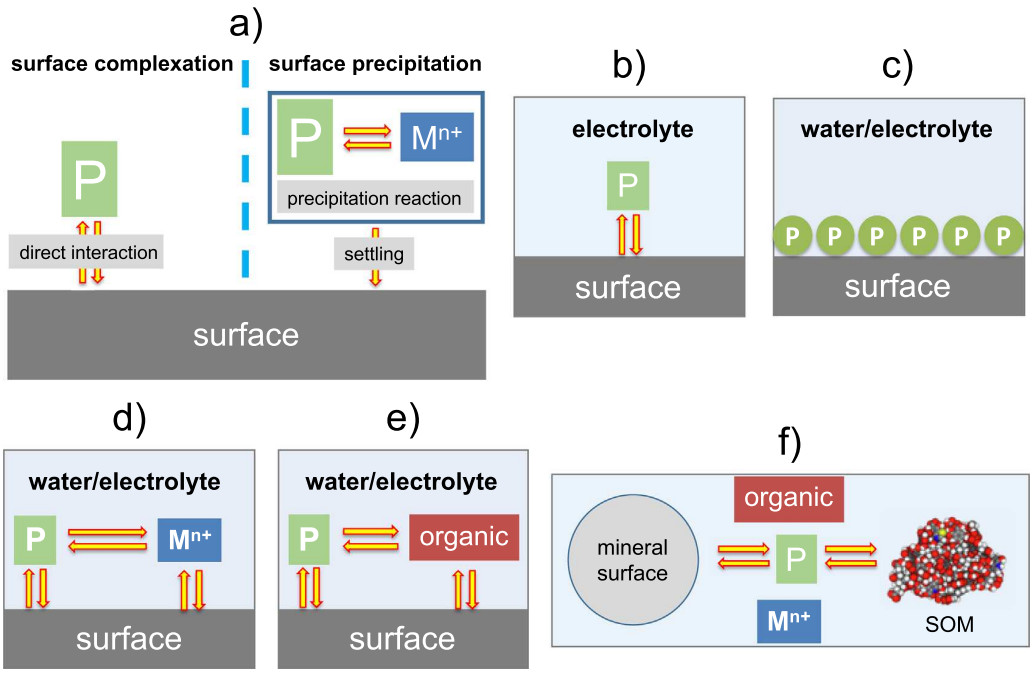


Fig. 11. Schematic representations for some critical scientific points related to the "P in soil" topic. For example, how to differentiate between surface complexation and precipitation of phosphates at mineral surfaces a), effect of electrolyte solutions and their ionic strengths on the phosphate binding process b), effect of the phosphate loading (concentration) on the phosphate binding process c), effect of the existing free metal ions in solution on the phosphate binding process d), effect of the organic matter on the phosphate binding process e),and overall effect of different factors on the phosphate binding process f).

Abbreviations

CC	Computational Chemistry
MD	molecular dynamics
PBC	periodic boundary condition
NVT	constant particle number, temperature, and volume
MM	molecular mechanics
QM	quantum mechanics
DFT	density functional theory
GPW	the hybrid Gaussian and plane-wave approach
PBE	the Perdew–Burke–Ernzerhof DFT functional
B3LYP	the Becke, three-parameter, Lee–Yang–Parr DFT functional
ECP	effective core potential
GTH	Goedecker–Teter–Hutter pseudopotentials
BSSE	basis set superposition error
GD3	the empirical dispersion correction D3 by Grimme
SE	semi-empirical methods
PCM	polarizable continuum model
CPCM	conductor-like polarizable continuum model
COSMO	**co**nductor-like **s**creening **mo**del
SMD	universal **s**olvation **m**odel based on the full solute electron **d**ensity
FTIR	Fourier-transform infrared
IRST	infrared surface titration
ATR	attenuated total reflectance
CIR	cylindrical internal reflection
CD	charge distribution model
UV	ultraviolet
NMR	nuclear magnetic resonance
XPS	X-ray photo-electron spectroscopy
XANES	X-ray absorption near-edge spectroscopy
EXAFS	extended X-ray absorption fine structure
OP	orthophosphate
GP	glycerolphosphate
IHP	inositolhexaphosphate
M^n+	metal ion
OM	organic matter
SOM	soil organic matter
DOM	dissolved organic matter
DOC	dissolved organic carbon
M	monodentate (i.e., formation of one covalent/coordination bond)
B	bidentate (i.e., formation of two covalent/coordination bonds)
HBs	hydrogen bonds
PZC	point of zero charge
SSA	specific surface area
BC	bone char

CRediT authorship contribution statement

A.A. Ahmed is responsible for conceptualization, formal analysis, methodology, visualization, and writing-original draft. All authors are responsible for funding acquisition, writing–review and editing of the present contribution. All authors have read and agreed to the submitted version of this review.

Funding

The research by Ahmed et al. involved in this review belongs mainly to the InnoSoilPhos project, funded by the German Federal Ministry of Education and Research (BMBF) in the frame of the BonaRes program (No. 031A558) as well as to the German Research Foundation (DFG) as a part of the SPP 1685 Priority program “Ecosystem Nutrition: Forest strategies for limited phosphorus resources”.

Data availability

No data was used for the research described in the article.

Declaration of competing interest

The authors declare no conflict of interest. The funders had no role in the design of the study; in the collection, analyses, or interpretation of data; in the writing of the manuscript, or in the decision to publish the results.

Acknowledgments

The research by Ahmed et al. involved in this review was performed within the scope of the Leibniz Science Campus “Phosphorus Research Rostock”. The authors are grateful to Mr. P. B. Ganta who was working under supervision of A.A. Ahmed and O. Kühn within the frame of the SPP 1685 priority program. The authors thank the North German Supercomputing Alliance for providing HPC resources (project mvp00016).

References

Abdala, D.B., Northrup, P.A., Arai, Y., Sparks, D.L., 2015. Surface loading effects on orthophosphate surface complexation at the Goethite/Water Interface as examined by extended X-ray absorption fine structure (EXAFS) spectroscopy. J. Colloid Interface Sci. 437, 297–303. https://doi.org/10.1016/j.jcis.2014.09.057.

Acelas, N.Y., Mejia, S.M., Mondragón, F., Flórez, E., 2013. Density functional theory characterization of phosphate and sulfate adsorption on fe-(Hydr)Oxide: reactivity, pH effect, estimation of gibbs free energies, and topological analysis of hydrogen bonds. Comput. Theor. Chem. 1005, 16–24. https://doi.org/10.1016/j.comptc.2012.11.002.

Ahmed, A.A., Kühn, O., Leinweber, P., 2012. Controlled experimental soil organic matter modification for study of organic pollutant interactions in soil. Sci. Total Environ. 441, 151–158. https://doi.org/10.1016/j.scitotenv.2012.09.042.

Ahmed, A.A., Kühn, O., Hilal, R.H., Shibl, M.F., 2013. Structure and cooperativity of the hydrogen bonds in sodium dihydrogen triacetate. Int. J. Quantum Chem. 113, 1394–1400. https://doi.org/10.1002/qua.24328.

Ahmed, A.A., Kühn, O., Aziz, S.G., Hilal, R.H., Leinweber, P., 2014. How soil organic matter composition controls hexachlorobenzene-soil-interactions: adsorption isotherms and quantum chemical modeling. Sci. Total Environ. 476–477C, 98–106. https://doi.org/10.1016/j.scitotenv.2013.12.096.

Ahmed, A.A., Thiele-Bruhn, S., Aziz, S.G., Hilal, R.H., Elroby, S.A., Al-Youbi, A.O., Leinweber, P., Kühn, O., 2015. Interaction of polar and nonpolar organic pollutants with soil organic matter: sorption experiments and molecular dynamics simulation. Sci. Total Environ. 508C, 276–287. https://doi.org/10.1016/j.scitotenv.2014.11.087.

Ahmed, A.A., Gros, P., Kühn, O., Leinweber, P., 2018. Molecular level investigation of the role of peptide interactions in the glyphosate analytics. Chemosphere 196, 129–134. https://doi.org/10.1016/j.chemosphere.2017.12.162.

Ahmed, A.A., Leinweber, P., Kühn, O., 2018. Unravelling the nature of glyphosate binding to goethite surfaces by ab initio molecular dynamics simulations. Phys. Chem. Chem. Phys. 20, 1531–1539. https://doi.org/10.1039/C7CP06245A.

Ahmed, A.A., Gypser, S., Leinweber, P., Freese, D., Kühn, O., 2019. Infrared spectroscopic characterization of phosphate binding at the goethite-water Interface. Phys. Chem. Chem. Phys. 21, 4421–4434. https://doi.org/10.1039/C8CP07168C.

Ahmed, A.A., Gypser, S., Freese, D., Leinweber, P., Kühn, O., 2020. Molecular level picture of the interplay between pH and phosphate binding at the goethite-water Interface. Phys. Chem. Chem. Phys. 22, 26509–26524. https://doi.org/10.1039/D0CP04698A.

Alam, M.M., Srinivasan, V., Mueller, A.V., Gu, A.Z., 2021. Status and advances in Technologies for Phosphorus Species Detection and Characterization in natural environment- a comprehensive review. Talanta 233, 122458. https://doi.org/10.1016/j.talanta.2021.122458.

Amadou, I., Faucon, M.P., Houben, D., 2022. Role of soil minerals on organic phosphorus availability and phosphorus uptake by plants. Geoderma 428, 116125. https://doi.org/10.1016/j.geoderma.2022.116125.

Anderson, G., Arlidge, E.Z., 1962. The adsorption of inositol phosphates and glycerophosphate by soil clays, clay minerals, and hydrated sesquioxides in acid media. J. Soil Sci. 13, 216–224. https://doi.org/10.1111/j.1365-2389.1962.tb00699.x.

Andersson, K.O., Tighe, M.K., Guppy, C.N., Milham, P.J., McLaren, T.I., Schefe, C.R., Lombi, E., 2016. XANES demonstrates the release of calcium phosphates from alkaline vertisols to moderately acidified solution. Environ. Sci. Technol. 50, 4229–4237. https://doi.org/10.1021/acs.est.5b04814.

Antelo, J., Avena, M., Fiol, S., López, R., Arce, F., 2005. Effects of pH and ionic strength on the adsorption of phosphate and arsenate at the goethite-water interface. J. Colloid Interface Sci. 285, 476–486. https://doi.org/10.1016/j.jcis.2004.12.032.

Appel, C., Rhue, D., Kabengi, N., Harris, W., 2013. Calorimetric investigation of the nature of sulfate and phosphate sorption on amorphous aluminum hydroxide. Soil Sci. 178, 180–188. https://doi.org/10.1097/SS.0b013e3182979e93.

Arai, Y., Sparks, D., 2001. ATR–FTIR spectroscopic investigation on phosphate adsorption mechanisms at the ferrihydrite-water interface. J. Colloid Interface Sci. 241, 317–326. https://doi.org/10.1006/jcis.2001.7773.

Arai, Y., Sparks, D., 2007. Phosphate reaction dynamics in soils and soil components: a multiscale approach. Advances in Agronomy. 94. Elsevier, pp. 135–179. https://doi.org/10.1016/S0065-2113(06)94003-6.

Arroyave, J.M., Puccia, V., Zanini, G.P., Avena, M.J., 2018. Surface speciation of phosphate on goethite as seen by InfraRed surface titrations (IRST). Spectrochim. Acta A Mol. Biomol. Spectrosc. 199, 57–64. https://doi.org/10.1016/j.saa.2018.03.043.

Baigorri, R., Urrutia, O., Erro, J., Mandado, M., Pérez-Juste, I., Garcia-Mina, J.M., 2013. Structural characterization of anion-calcium-humate complexes in phosphate-based fertilizers. ChemSusChem 6, 1245–1251. https://doi.org/10.1002/cssc.201300024.

Baigorri, R., Erro, J., Urrutia, Ó., Martinez, J.M., Mandado, M., Martín-Pastor, M., García-Mina, J.M., 2019. Both chemical and crystalline phase configuration influence the molecular features of humic acids in humic–calcium–phosphates fertilizers. RSC Adv. 9, 25790–25796. https://doi.org/10.1039/C9RA04383G.

Barone, V., Cossi, M., 1998. Quantum calculation of molecular energies and energy gradients in solution by a conductor solvent model. J. Phys. Chem. A 102, 1995–2001. https://doi.org/10.1021/jp9716997.

Barrow, N.J., 1972. Influence of solution concentration of calcium on the adsorption of phosphate, sulfate, and molybdate by soils. Soil Sci. 113.

Barrow, N.J., 1983. A mechanistic model for describing the sorption and desorption of phosphate by soil. J. Soil Sci. 34, 733–750. https://doi.org/10.1111/j.1365-2389.1983.tb01068.x.

Barrow, N., Bowden, J., Posner, A., Quirk, J., 1980. Describing the effects of electrolyte on adsorption of phosphate by a variable charge surface. Soil Res. 18, 395. https://doi.org/10.1071/SR9800395.

Barrow, N.J., Shaw, T.C., 1979. Effects of ionic strength and nature of the cation on desorption of phosphate from soil. J. Soil Sci. 30, 53–65. https://doi.org/10.1111/j.1365-2389.1979.tb00964.x.

Baumann, K., Nastah, S., Shaheen, S.M., Rinklebe, J., Leinweber, P., 2020. Phosphorus cycling and spring barley crop response to varying redox potential. Vadose Zone J., 19 https://doi.org/10.1002/vzj2.20088.

Baumann, K., Shaheen, S.M., Hu, Y., Gros, P., Heilmann, E., Morshedizad, M., Wang, J., Wang, S.L., Rinklebe, J., Leinweber, P., 2020. Speciation and sorption of phosphorus in agricultural soil profiles of redoximorphic character. Environ. Geochem. Health 42, 3231–3246. https://doi.org/10.1007/s10653-020-00561-y.

Belelli, P.G., Fuente, S.A., Castellani, N.J., 2014. Phosphate adsorption on goethite and Al-rich goethite. Comput. Mater. Sci. 85, 59–66. https://doi.org/10.1016/j.commatsci.2013.12.030.

Bellier, N., Chazarenc, F., Comeau, Y., 2006. Phosphorus removal from wastewater by mineral apatite. Water Res. 40, 2965–2971. https://doi.org/10.1016/j.watres.2006.05.016.

van der Bom, F.J.T., Kopittke, P.M., Raymond, N.S., Sekine, R., Lombi, E., Mueller, C.W., Doolette, C.L., 2022. Methods for assessing laterally-resolved distribution, speciation and bioavailability of phosphorus in soils. Rev. Environ. Sci. Biotechnol. 21, 53–74. https://doi.org/10.1007/s11157-021-09602-z.

Borggaard, O.K., 2001. Soil chemistry in a pedological context. 5. rev. ed ed.;. Royal Veterinary and Agricultural University OCLC: 476766674.

Borggaard, O.K., Gimsing, A.L., 2008. Fate of glyphosate in soil and the possibility of leaching to ground and surface waters: a review. Pest Manag. Sci. 64, 441–456. https://doi.org/10.1002/ps.1512.

Borggaard, O., Szilas, C., Gimsing, A., Rasmussen, L., 2004. Estimation of soil phosphate adsorption capacity by means of a pedotransfer function. Geoderma 118, 55–61. https://doi.org/10.1016/S0016-7061(03)00183-6.

Borggaard, O., Raben-Lange, B., Gimsing, A., Strobel, B., 2005. Influence of humic substances on phosphate adsorption by aluminium and iron oxides. Geoderma 127, 270–279. https://doi.org/10.1016/j.geoderma.2004.12.011.

Borowski, S.C., Biswakarma, J., Kang, K., Schenkeveld, W.D., Hering, J.G., Kubicki, J.D., Kraemer, S.M., Hug, S.J., 2018. Structure and reactivity of oxalate surface complexes on lepidocrocite derived from infrared spectroscopy, DFT-calculations, adsorption, dissolution and photochemical experiments. Geochim. Cosmochim. Acta 226, 244–262. https://doi.org/10.1016/j.gca.2018.01.024.

Boukemara, L., Boukhalfa, C., Reinert, L., Duclaux, L., 2016. Characterization of phosphate adsorption on goethite macroscopic and spectroscopic analyses. J. Mater. Environ. Sci. 7, 2541–2550.

Bowden, J., Nagarajah, S., Barrow, N., Posner, A., Quirk, J., 1980. Describing the adsorption of phosphate, citrate and selenite on a variable-charge mineral surface. Soil Res. 18, 49. https://doi.org/10.1071/SR9800049.

Boys, S., Bernardi, F., 1970. The calculation of small molecular interactions by the differences of separate total energies. Some procedures with reduced errors. Mol. Phys. 19, 553–566. https://doi.org/10.1080/00268977000101561.

Brunauer, S., Emmett, P.H., Teller, E., 1938. Adsorption of gases in multimolecular layers. J. Am. Chem. Soc. 60, 309–319. https://doi.org/10.1021/ja01269a023.

Catalano, J.G., 2011. Weak interfacial water ordering on isostructural hematite and corundum (001) surfaces. Geochim. Cosmochim. Acta 75, 2062–2071. https://doi.org/10.1016/j.gca.2011.01.025.

Chapman, A., Thirlwell, L., 1964. Spectra of phosphorus compounds—I the infra-red spectra of orthophosphates. Spectrochim. Acta 20, 937–947. https://doi.org/10.1016/0371-1951(64)80094-1.

Chitrakar, R., Tezuka, S., Sonoda, A., Sakane, K., Ooi, K., Hirotsu, T., 2006. Phosphate adsorption on synthetic goethite and akaganeite. J. Colloid Interface Sci. 298, 602–608. https://doi.org/10.1016/j.jcis.2005.12.054.

Cordell, D., White, S., 2011. Peak phosphorus: clarifying the key issues of a vigorous debate about long-term phosphorus security. Sustainability 3, 2027–2049. https://doi.org/10.3390/su3102027.

Cordell, D., Drangert, J.O., White, S., 2009. The story of phosphorus: global food security and food for thought. Glob. Environ. Change 19, 292–305. https://doi.org/10.1016/j.gloenvcha.2008.10.009.

Cornell, R.M., Schwertmann, U., 2003. The Iron Oxides: Structure, Properties, Reactions, Occurrences, and Uses. 2nd, completely rev. and extended ed. Wiley-VCH, Weinheim.

Cossi, M., Rega, N., Scalmani, G., Barone, V., 2003. Energies, structures, and electronic properties of molecules in solution with the C-PCM solvation model. J. Comput. Chem. 24, 669–681. https://doi.org/10.1002/jcc.10189.

Cramer, C.J., 2004. Essentials of Computational Chemistry: Theories and Models. 2nd ed. Wiley, Chichester, West Sussex, England; Hoboken, NJ.

Cygan, R.T., Liang, J.J., Kalinichev, A.G., 2004. Molecular models of hydroxide, oxyhydroxide, and clay phases and the development of a general force field. J. Phys. Chem. B 108, 1255–1266. https://doi.org/10.1021/jp0363287.

De Groot, C.J., Golterman, H.L., 1993. On the presence of organic phosphate in some camargue sediments: evidence for the importance of phytate. Hydrobiologia 252, 117–126. https://doi.org/10.1007/BF00000133.

Dettmann, L.F., Kühn, O., Ahmed, A.A., 2021. Coarse-grained molecular dynamics simulations of nanoplastics interacting with a hydrophobic environment in aqueous solution. RSC Adv. 11, 27734–27744. https://doi.org/10.1039/D1RA04439G.

Di Iorio, E., Circelli, L., Angelico, R., Torrent, J., Tan, W., Colombo, C., 2022. Environmental implications of interaction between humic substances and iron oxide nanoparticles: a review. Chemosphere 303, 135172. https://doi.org/10.1016/j.chemosphere.2022.135172.

Dimirkou, A., Ioannou, A., Doula, M., 2002. Preparation, characterization and sorption properties for phosphates of hematite, bentonite and bentonite-hematite systems. Adv. Colloid Interface Sci. 97, 37–61. https://doi.org/10.1016/S0001-8686(01)00046-X.

Dougherty, W.J., Smernik, R.J., Chittleborough, D.J., 2005. Application of spin counting to the solid-state 31 P NMR analysis of pasture soils with varying phosphorus content. Soil Sci. Soc. Am. J. 69, 2058–2070. https://doi.org/10.2136/sssaj2005.0017.

Duckworth, O.W., Martin, S.T., 2001. Surface complexation and dissolution of hematite by C 1 -C 6 dicarboxylic acids at pH = 5.0. Geochim. Cosmochim. Acta 65, 4289–4301. https://doi.org/10.1016/S0016-7037(01)00696-2.

El-Naggar, A., Shaheen, S.M., Ok, Y.S., Rinklebe, J., 2018. Biochar affects the dissolved and colloidal concentrations of cd, cu, ni, and zn and their phytoavailability and potential mobility in a mining soil under dynamic redox-conditions. Sci. Total Environ. 624, 1059–1071. https://doi.org/10.1016/j.scitotenv.2017.12.190.

Elstner, M., Porezag, D., Jungnickel, G., Elsner, J., Haugk, M., Frauenheim, T., Suhai, S., Seifert, G., 1998. Self-consistent-charge density-functional tight-binding method for simulations of complex materials properties. Phys. Rev. B 58, 7260–7268. https://doi.org/10.1103/PhysRevB.58.7260.

Elzinga, E.J., Sparks, D.L., 2007. Phosphate adsorption onto hematite: an in situ ATR-FTIR investigation of the effects of pH and loading level on the mode of phosphate surface complexation. J. Colloid Interface Sci. 308, 53–70. https://doi.org/10.1016/j.jcis.2006.12.061.

Erro, J., Urrutia, O., Baigorri, R., Aparicio-Tejo, P., Irigoyen, I., Storino, F., Mandado, M., Yvin, J.C., Garcia-Mina, J.M., 2012. Organic complexed superphosphates (CSP): physicochemical characterization and agronomical properties. J. Agric. Food Chem. 60, 2008–2017. https://doi.org/10.1021/jf204821j.

Fiedler, S., Vepraskas, M.J., Richardson, J., 2007. Soil redox potential: importance, field measurements, and observations. Advances in Agronomy. 94. Elsevier, pp. 1–54. https://doi.org/10.1016/S0065-2113(06)94001-2.

Freundlich, H., 1907. Über die adsorption in Lösungen. Z. Phys. Chem., 57U https://doi.org/10.1515/zpch-1907-5723.

Frisch, M., Trucks, G., Schlegel, H.E.A., Scuseria, G., Robb, M., Cheeseman, J., Montgomery Jr., J., Vreven Jr., T., Kudin Jr., K., Burant Jr., J., 2004. Gaussian 03, revision C. 02.

Frisch, M.J., Trucks, G.W., Schlegel, H.B., Scuseria, G.E., Robb, M.A., Cheeseman, J.R., Scalmani, G., Barone, V., Mennucci, B., Petersson, G.A., Nakatsuji, H., Caricato, M., Li, X., Hratchian, H.P., Izmaylov, A.F., Bloino, J., Zheng, G., Sonnenberg, J.L., Hada, M., Ehara, M., Toyota, K., Fukuda, R., Hasegawa, J., Ishida, M., Nakajima, T., Honda, Y., Kitao, O., Nakai, H., Vreven, T., Montgomery, J.A., Peralta, J.E., Ogliaro, F., Bearpark, M., Heyd, J.J., Brothers, E., Kudin, K.N., Staroverov, V.N., Kobayashi, R., Normand, J., Raghavachari, K., Rendell, A., Burant, J.C., Iyengar, S.S., Tomasi, J., Cossi, M., Rega, N., Millam, J.M., Klene, M., Knox, J.E., Cross, J.B., Bakken, V., Adamo, C., Jaramillo, J., Gomperts, R., Stratmann, R.E., Yazyev, O., Austin, A.J., Cammi, R., Pomelli, C., Ochterski, J.W., Martin, R.L., Morokuma, K., Zakrzewski, V.G., Voth, G.A., Salvador, P., Dannenberg, J.J., Dapprich, S., Daniels, A.D., Foresman, J.B., Ortiz, J.V., Cioslowski, J., Farkas, Fox, D.J., 2013. Gaussian 09.

Frisch, M.J., Trucks, G.W., Schlegel, H.B., Scuseria, G.E., Robb, M.A., Cheeseman, J.R., Scalmani, G., Barone, V., Mennucci, B., Petersson, G.A., Nakatsuji, H., Caricato, M., Li, X., Hratchian, H.P., Izmaylov, A.F., Bloino, J., Zheng, G., Sonnenberg, J.L., Hada, M., Ehara, M., Toyota, K., Fukuda, R., Hasegawa, J., Ishida, M., Nakajima, T., Honda, Y., Kitao, O., Nakai, H., Vreven, T., Montgomery, J.A., Peralta, J.E., Ogliaro, F., Bearpark, M., Heyd, J.J., Brothers, E., Kudin, K.N., Staroverov, V.N., Kobayashi, R., Normand, J., Raghavachari, K., Rendell, A., Burant, J.C., Iyengar, S.S., Tomasi, J., Cossi, M., Rega, N., Millam, J.M., Klene, M., Knox, J.E., Cross, J.B., Bakken, V., Adamo, C., Jaramillo, J., Gomperts, R., Stratmann, R.E., Yazyev, O., Austin, A.J., Cammi, R., Pomelli, C., Ochterski, J.W., Martin, R.L., Morokuma, K., Zakrzewski, V.G., Voth, G.A., Salvador, P., Dannenberg, J.J., Dapprich, S., Daniels, A.D., Foresman, J.B., Ortiz, J.V., Cioslowski, J., Fox, D.J., Farkas, 2016. Gaussian 16. 2016. R.C. Gaussian Inc., Wallingford CT.

Frohne, T., Rinklebe, J., Diaz-Bone, R.A., Du Laing, G., 2011. Controlled variation of redox conditions in a floodplain soil: impact on metal mobilization and biomethylation of arsenic and antimony. Geoderma 160, 414–424. https://doi.org/10.1016/j.geoderma.2010.10.012.

Ganta, P.B., Kühn, O., Ahmed, A.A., 2019. QM/MM simulations of organic phosphorus adsorption at the diaspore-water Interface. Phys. Chem. Chem. Phys. 21, 24316–24325. https://doi.org/10.1039/C9CP04032C.

Ganta, P.B., Kühn, O., Ahmed, A.A., 2020. Ab initio molecular dynamics simulations of the interaction between organic phosphates and goethite. Molecules 26, 160. https://doi.org/10.3390/molecules26010160.

Ganta, P.B., Kühn, O., Ahmed, A.A., 2020. QM/MM molecular dynamics investigation of the binding of organic phosphates to the 100 diaspore surface. Front. For. Glob. Change 3, 71. https://doi.org/10.3389/ffgc.2020.00071.
Ganta, P.B., Morshedizad, M., Kühn, O., Leinweber, P., Ahmed, A.A., 2021. The binding of phosphorus species at goethite: a joint experimental and theoretical study. Minerals 11, 323. https://doi.org/10.3390/min11030323.
Gao, Y., Mucci, A., 2001. Acid Base reactions, phosphate and arsenate complexation, and their competitive adsorption at the surface of goethite in 0.7 M NaCl solution. Geochim. Cosmochim. Acta 65, 2361–2378. https://doi.org/10.1016/S0016-7037(01)00589-0.
Gao, S., Tanji, K.K., Scardaci, S.C., Chow, A.T., 2002. Comparison of redox indicators in a Paddy soil during Rice-growing season. Soil Sci. Soc. Am. J. 66, 805–817. https://doi.org/10.2136/sssaj2002.8050.
Geelhoed, J.S., Hiemstra, T., Van Riemsdijk, W.H., 1997. Phosphate and sulfate adsorption on goethite: single anion and competitive adsorption. Geochim. Cosmochim. Acta 61, 2389–2396. https://doi.org/10.1016/S0016-7037(97)00096-3.
Geelhoed, J.S., Hiemstra, T., Van Riemsdijk, W.H., 1998. Competitive interaction between phosphate and citrate on goethite. Environ. Sci. Technol. 32, 2119–2123. https://doi.org/10.1021/es970908y.
Gerke, J., Meyer, U., Römer, W., 1995. Phosphate, Fe and Mn uptake of N2 fixing red clover and ryegrass from an Oxisol as affected by P and model humic substances application. 1. Plant parameters and soil solution composition. Z. Für Pflanzenernähr. Bodenkd. 158, 261–268. https://doi.org/10.1002/jpln.19951580309.
Ghose, S.K., Waychunas, G.A., Trainor, T.P., Eng, P.J., 2010. Hydrated goethite (α-FeOOH) (100) Interface structure: ordered water and surface functional groups. Geochim. Cosmochim. Acta 74, 1943–1953. https://doi.org/10.1016/j.gca.2009.12.015.
Goette, M., Grubmüller, H., 2009. Accuracy and convergence of free energy differences calculated from nonequilibrium switching processes. J. Comput. Chem. 30, 447–456. https://doi.org/10.1002/jcc.21073.
Goldberg, S., Sposito, G., 1985. On the mechanism of specific phosphate adsorption by hydroxylated mineral surfaces: a review. Commun. Soil Sci. Plant Anal. 16, 801–821. https://doi.org/10.1080/00103628509367646.
Grimme, S., Ehrlich, S., Goerigk, L., 2011. Effect of the damping function in dispersion corrected density functional theory. J. Comput. Chem. 32, 1456–1465. https://doi.org/10.1002/jcc.21759.
Gros, P., Ahmed, A., Kühn, O., Leinweber, P., 2017. Glyphosate binding in soil as revealed by sorption experiments and quantum-chemical modeling. Sci. Total Environ. 586, 527–535. https://doi.org/10.1016/j.scitotenv.2017.02.007.
Gros, P., Ahmed, A.A., Kühn, O., Leinweber, P., 2019. Influence of metal ions on glyphosate detection by FMOC-Cl. Environ. Monit. Assess. 191, 244. https://doi.org/10.1007/s10661-019-7387-2.
Guardado, I., Urrutia, O., García-Mina, J.M., 2007. Size distribution, complexing capacity, and stability of phosphate-metal-humic complexes. J. Agric. Food Chem. 55, 408–413. https://doi.org/10.1021/jf062894y.
Guardado, I., Urrutia, O., Garcia-Mina, J.M., 2008. Some structural and electronic features of the interaction of phosphate with metal-humic complexes. J. Agric. Food Chem. 56, 1035–1042. https://doi.org/10.1021/jf072641k.
Guo, H., Barnard, A.S., 2011. Thermodynamic modelling of nanomorphologies of hematite and goethite. J. Mater. Chem. 21, 11566. https://doi.org/10.1039/c1jm10381d.
Guo, J., Tolstoy, P.M., Koeppe, B., Golubev, N.S., Denisov, G.S., Smirnov, S.N., Limbach, H.H., 2012. Hydrogen bond geometries and proton tautomerism of homoconjugated anions of carboxylic acids studied via H/D isotope effects on 13 C NMR chemical shifts. J. Phys. Chem. A 116, 11180–11188. https://doi.org/10.1021/jp304943h.
Guppy, C.N., Menzies, N.W., Moody, P.W., Blamey, F.P.C., 2005. Competitive sorption reactions between phosphorus and organic matter in soil: a review. Soil Res. 43, 189. https://doi.org/10.1071/SR04049.
Gypser, S., Hirsch, F., Schleicher, A.M., Freese, D., 2018. Impact of crystalline and amorphous iron- and aluminum hydroxides on mechanisms of phosphate adsorption and desorption. J. Environ. Sci. 70, 175–189. https://doi.org/10.1016/j.jes.2017.12.001.
Gypser, S., Schütze, E., Freese, D., 2019. Crystallization of single and binary iron- and aluminum hydroxides affect phosphorus desorption. J. Plant Nutr. Soil Sci. 182, 741–750. https://doi.org/10.1002/jpln.201700543.
Gypser, S., Schütze, E., Freese, D., 2021. Single and binary Fe- and Al-hydroxides affect potential phosphorus mobilization and transfer from pools of different availability. Soil Syst. 5, 33. https://doi.org/10.3390/soilsystems5020033.
Han, J., Kim, M., Ro, H.M., 2020. Factors modifying the structural configuration of oxyanions and organic acids adsorbed on iron (hydr)oxides in soils. A review. Environ Chem Lett 18, 631–662. https://doi.org/10.1007/s10311-020-00964-4.
Hehre, W.J., Ditchfield, R., Pople, J.A., 1972. Self—consistent molecular orbital methods. XII. Further extensions of Gaussian—type basis sets for use in molecular orbital studies of organic molecules. J. Chem. Phys. 56, 2257–2261. https://doi.org/10.1063/1.1677527.
Hesterberg, D., Zhou, W., Hutchison, K.J., Beauchemin, S., Sayers, D.E., 1999. XAFS study of adsorbed and mineral forms of phosphate. J Synchrotron Rad 6, 636–638. https://doi.org/10.1107/S0909049599000370.
Hiemstra, T., Van Riemsdijk, W., 1996. A surface structural approach to ion adsorption: the charge distribution (CD) model. J. Colloid Interface Sci. 179, 488–508. https://doi.org/10.1006/jcis.1996.0242.
Hingston, F.J., Posner, A.M., Quirk, J.P., 1972. Anion adsorption by goethite and gibbsite: I. The role of the proton in determining adsorption envelopes. J. Soil Sci. 23, 177–192. https://doi.org/10.1111/j.1365-2389.1972.tb01652.x.
Hongshao, Z., Stanforth, R., 2001. Competitive adsorption of phosphate and arsenate on goethite. Environ. Sci. Technol. 35, 4753–4757. https://doi.org/10.1021/es010890y.
Hug, S.J., Bahnemann, D., 2006. Infrared spectra of oxalate, malonate and succinate adsorbed on the aqueous surface of rutile, anatase and lepidocrocite measured with in situ ATR-FTIR. J. Electron Spectrosc. Relat. Phenom. 150, 208–219. https://doi.org/10.1016/j.elspec.2005.05.006.
Hutter, J., Iannuzzi, M., Schiffmann, F., VandeVondele, J., 2014. CP2K: atomistic simulations of condensed matter systems. Wiley Interdiscip. Rev. Comput. Mol. Sci. 4, 15–25. https://doi.org/10.1002/wcms.1159.
Jensen, F., 2017. Introduction to computational chemistry. third edition. John Wiley & Sons.
Johnson, S.E., Loeppert, R.H., 2006. Role of organic acids in phosphate mobilization from iron oxide. Soil Sci. Soc. Am. J. 70, 222. https://doi.org/10.2136/sssaj2005.0012.
Johnson, B.B., Ivanov, A.V., Antzutkin, O.N., Forsling, W., 2002. 31 P nuclear magnetic resonance study of the adsorption of phosphate and phenyl phosphates on -Al 2 O 3. Langmuir 18, 1104–1111. https://doi.org/10.1021/la001537t.
Jupp, A.R., Beijer, S., Narain, G.C., Schipper, W., Slootweg, J.C., 2021. Phosphorus recovery and recycling – closing the loop. Chem. Soc. Rev. 50, 87–101. https://doi.org/10.1039/D0CS01150A.
Keyikoglu, R., Khataee, A., Yoon, Y., 2022. Layered double hydroxides for removing and recovering phosphate: recent advances and future directions. Adv. Colloid Interf. Sci. 300, 102598. https://doi.org/10.1016/j.cis.2021.102598.
Khare, N., Hesterberg, D., Martin, J.D., 2005. XANES investigation of phosphate sorption in single and binary systems of iron and aluminum oxide minerals. Environ. Sci. Technol. 39, 2152–2160. https://doi.org/10.1021/es049237b.
Khare, N., Martin, J.D., Hesterberg, D., 2007. Phosphate bonding configuration on ferrihydrite based on molecular orbital calculations and XANES fingerprinting. Geochim. Cosmochim. Acta 71, 4405–4415. https://doi.org/10.1016/j.gca.2007.07.008.
Kim, Y., Kirkpatrick, R.J., 2004. An investigation of phosphate adsorbed on aluminium oxyhydroxide and oxide phases by nuclear magnetic resonance: phosphate adsorbed on aluminium phases. Eur. J. Soil Sci. 55, 243–251. https://doi.org/10.1046/j.1365-2389.2004.00595.x.
Kim, J., Li, W., Philips, B.L., Grey, C.P., 2011. Phosphate adsorption on the iron oxyhydroxides goethite (α-FeOOH), akaganeite (β-FeOOH), and lepidocrocite (γ-FeOOH): a 31P NMR study. Energy Environ. Sci. 4, 4298. https://doi.org/10.1039/c1ee02093e.
Klamt, A., 2005. COSMO-RS: From Quantum Chemistry to Fluid Phase Thermodynamics and Drug Design. 1st ed. Elsevier.
Klamt, A., Schüürmann, G., 1993. COSMO: a new approach to dielectric screening in solvents with explicit expressions for the screening energy and its gradient. J. Chem. Soc. Perkin Trans. 2, 799–805. https://doi.org/10.1039/P29930000799.
Kmiecik, S., Gront, D., Kolinski, M., Wieteska, L., Dawid, A.E., Kolinski, A., 2016. Coarse-grained protein models and their applications. Chem. Rev. 116, 7898–7936. https://doi.org/10.1021/acs.chemrev.6b00163.
Koch, W., Holthausen, M.C., 2008. A chemist's guide to density functional theory. 2nd ed., 5. reprint ed. Wiley-VCH, Weinheim.
Krack, M., 2005. Pseudopotentials for H to kr optimized for gradient-corrected exchange-correlation functionals. Theor. Chem. Accounts 114, 145–152. https://doi.org/10.1007/s00214-005-0655-y.
Kresse, G., Furthmüller, J., 1996. Efficient iterative schemes for ab initio total-energy calculations using a plane-wave basis set. Phys. Rev. B 54, 11169–11186. https://doi.org/10.1103/PhysRevB.54.11169.
Krumina, L., Kenney, J.P., Loring, J.S., Persson, P., 2016. Desorption mechanisms of phosphate from ferrihydrite and goethite surfaces. Chem. Geol. 427, 54–64. https://doi.org/10.1016/j.chemgeo.2016.02.016.
Kruse, J., Leinweber, P., 2008. Phosphorus in sequentially extracted fen peat soils: a K-edge X-ray absorption near-edge structure (XANES) spectroscopy study. Z. Pflanzenernähr. Bodenk. 171, 613–620. https://doi.org/10.1002/jpln.200700237.
Kruse, J., Abraham, M., Amelung, W., Baum, C., Bol, R., Kühn, O., Lewandowski, H., Niederberger, J., Oelmann, Y., Rüger, C., Santner, J., Siebers, M., Siebers, N., Spohn, M., Vestergren, J., Vogts, A., Leinweber, P., 2015. Innovative methods in soil phosphorus research: a review. J. Plant Nutr. Soil Sci. 178, 43–88. https://doi.org/10.1002/jpln.201400327.
Kubicki, J.D., 2016. Molecular modeling of geochemical reactions: An introduction. Chichester, West Sussex, United Kingdom, Wiley.
Kubicki, J.D., Ohno, T., 2020. Integrating density functional theory modeling with experimental data to understand and predict sorption reactions: exchange of salicylate for phosphate on goethite. Soil Syst. 4, 27. https://doi.org/10.3390/soilsystems4020027.
Kubicki, J.D., Kwon, K.D., Paul, K.W., Sparks, D.L., 2007. Surface complex structures modelled with quantum chemical calculations: carbonate, phosphate, sulphate, arsenate and arsenite. Eur. J. Soil Sci. 58, 932–944. https://doi.org/10.1111/j.1365-2389.2007.00931.x.
Kubicki, J.D., Paul, K.W., Sparks, D.L., 2008. Periodic density functional theory calculations of bulk and the (010) surface of goethite. Geochem. Trans. 9, 4. https://doi.org/10.1186/1467-4866-9-4.
Kubicki, J.D., Halada, G.P., Jha, P., Phillips, B.L., 2009. Quantum mechanical calculation of aqueuous uranium complexes: carbonate, phosphate, organic and biomolecular species. Chem. Cent. J. 3, 10. https://doi.org/10.1186/1752-153X-3-10.
Kubicki, J.D., Paul, K.W., Kabalan, L., Zhu, Q., Mrozik, M.K., Aryanpour, M., Pierre-Louis, A.M., Strongin, D.R., 2012. ATR–FTIR and density functional theory study of the structures, energetics, and vibrational spectra of phosphate adsorbed onto goethite. Langmuir 28, 14573–14587. https://doi.org/10.1021/la303111a.
Kubicki, J.D., Tunega, D., Kraemer, S., 2017. A density functional theory investigation of oxalate and Fe(II) adsorption onto the (010) goethite surface with implications for ligand- and reduction-promoted dissolution. Chem. Geol. 464, 14–22. https://doi.org/10.1016/j.chemgeo.2016.08.010.
Kubicki, J.D., Tunega, D., Kraemer, S., 2017. A density functional theory investigation of oxalate and Fe(II) adsorption onto the (010) goethite surface with implications for ligand- and reduction-promoted dissolution. Chem. Geol. 464, 14–22. https://doi.org/10.1016/j.chemgeo.2016.08.010.
Kühne, T.D., Iannuzzi, M., Del Ben, M., Rybkin, V.V., Seewald, P., Stein, F., Laino, T., Khaliullin, R.Z., Schütt, O., Schiffmann, F., Golze, D., Wilhelm, J., Chulkov, S., Bani-Hashemian, M.H., Weber, V., Borštnik, U., Taillefumier, M., Jakobovits, A.S., Lazzaro,

A., Pabst, H., Müller, T., Schade, R., Guidon, M., Andermatt, S., Holmberg, N., Schenter, G.K., Hehn, A., Bussy, A., Belleflamme, F., Tabacchi, G., Glöß, A., Lass, M., Bethune, I., Mundy, C.J., Plessl, C., Watkins, M., VandeVondele, J., Krack, M., Hutter, J., 2020. CP2K: an electronic structure and molecular dynamics software package - quickstep: efficient and accurate electronic structure calculations. J. Chem. Phys. 152, 194103. https://doi.org/10.1063/5.0007045.

Kwon, K.D., Kubicki, J.D., 2004. Molecular orbital theory study on surface complex structures of phosphates to iron hydroxides: calculation of vibrational frequencies and adsorption energies. Langmuir 20, 9249–9254. https://doi.org/10.1021/la0487444.

Laino, T., Mohamed, F., Laio, A., Parrinello, M., 2006. An efficient linear-scaling electrostatic coupling for treating periodic boundary conditions in QM/MM simulations. J. Chem. Theory Comput. 2, 1370–1378. https://doi.org/10.1021/ct6001169.

Langmuir, I., 1918. The adsorption of gases on plane surfaces of glass, mica and platinum. J. Am. Chem. Soc. 40, 1361–1403. https://doi.org/10.1021/ja02242a004.

Lee, C., Yang, W., Parr, R.G., 1988. Development of the colle-salvetti correlation-energy formula into a functional of the electron density. Phys. Rev. B 37, 785–789. https://doi.org/10.1103/PhysRevB.37.785.

Lefèvre, G., 2004. In situ fourier-transform infrared spectroscopy studies of inorganic ions adsorption on metal oxides and hydroxides. Adv. Colloid Interface Sci. 107, 109–123. https://doi.org/10.1016/j.cis.2003.11.002.

Lehmann, J., Bossio, D.A., Kögel-Knabner, I., Rillig, M.C., 2020. The concept and future prospects of soil health. Nat. Rev. Earth Environ. 1, 544–553. https://doi.org/10.1038/s43017-020-0080-8.

Leinweber, P., Schulten, H.R., Jancke, H., 1999. New evidence for the molecular composition of soil organic matter in vertisols. Soil Sci. 164, 857–870.

Li, L., Stanforth, R., 2000. Distinguishing adsorption and surface precipitation of phosphate on goethite (α-FeOOH). J. Colloid Interface Sci. 230, 12–21. https://doi.org/10.1006/jcis.2000.7072.

Li, W., Feng, J., Kwon, K.D., Kubicki, J.D., Phillips, B.L., 2010. Surface speciation of phosphate on boehmite (γ-AlOOH) determined from NMR spectroscopy. Langmuir 26, 4753–4761. https://doi.org/10.1021/la903484m.

Li, W., Pierre-Louis, A.M., Kwon, K.D., Kubicki, J.D., Strongin, D.R., Phillips, B.L., 2013. Molecular level investigations of phosphate sorption on corundum (α-Al_2O_3) by 31P solid state NMR, ATR-FTIR and quantum chemical calculation. Geochim. Cosmochim. Acta 107, 252–266. https://doi.org/10.1016/j.gca.2013.01.007.

Li, W., Feng, X., Yan, Y., Sparks, D.L., Phillips, B.L., 2013. Solid-state NMR spectroscopic study of phosphate sorption mechanisms on aluminum (Hydr)oxides. Environ. Sci. Technol., 130725144353009 https://doi.org/10.1021/es400874s.

Li, H., Wan, B., Yan, Y., Zhang, Y., Cheng, W., Feng, X., 2017. Adsorption of glycerophosphate on goethite: a macroscopic and infrared spectroscopic study. J. Soil Sci. Plant Nutr. 181, 557–565. https://doi.org/10.1002/jpln.201700517.

Li, X., Yan, L., Zhong, W., Kersten, M., Jing, C., 2021. Competitive arsenate and phosphate adsorption on α-FeOOH, LaOOH, and nano-TiO_2: two-dimensional correlation spectroscopy study. J. Hazard. Mater. 414, 125512. https://doi.org/10.1016/j.jhazmat.2021.125512.

Lippert, G., Hutter, J., Parrinello, M., 1997. A hybrid Gaussian and plane wave density functional scheme. Mol. Phys. 92, 477–488. https://doi.org/10.1080/002689797170220.

Liu, F., De Cristofaro, A., Violante, A., 2001. Effect of pH, phosphate and oxalate on the adsorption/desorption of arsenate on/from goethite. Soil Sci. 166.

Liu, Q., Guo, L., Zhou, Y., Dai, Y., Feng, L., Zhou, J., Zhao, J., Liu, J., Qian, G., 2012. Phosphate adsorption on biogenetic calcium carbonate minerals: effect of a crystalline phase. Desalin. Water Treat. 47, 78–85. https://doi.org/10.1080/19443994.2012.696798.

Liu, X., Tournassat, C., Grangeon, S., Kalinichev, A.G., Takahashi, Y., Marques Fernandes, M., 2022. Molecular-level understanding of metal ion retention in clay-rich materials. Nat. Rev. Earth Environ. 3, 461–476. https://doi.org/10.1038/s43017-022-00301-z.

Loring, J.S., Sandström, M.H., Norén, K., Persson, P., 2009. Rethinking arsenate coordination at the surface of goethite. Chem. Eur. J. 15, 5063–5072. https://doi.org/10.1002/chem.200900284.

Luengo, C., Brigante, M., Antelo, J., Avena, M., 2006. Kinetics of phosphate adsorption on goethite: comparing batch adsorption and ATR-IR measurements. J. Colloid Interface Sci. 300, 511–518. https://doi.org/10.1016/j.jcis.2006.04.015.

Maciá, E., 2005. The role of phosphorus in chemical evolution. Chem. Soc. Rev. 34, 691. https://doi.org/10.1039/b416855k.

Marenich, A.V., Cramer, C.J., Truhlarn, D.G., 2009. Universal solvation model based on solute electron density and on a continuum model of the solvent defined by the bulk dielectric constant and atomic surface tensions. J. Phys. Chem. B 113, 6378–6396. https://doi.org/10.1021/jp810292n.

Marx, D., Hutter, J., 2009. Ab Initio Molecular Dynamics: Basic Theory and Advanced Methods. Cambridge University Press, Cambridge https://doi.org/10.1017/CBO9780511609633.

McLaren, T.I., Smernik, R.J., McLaughlin, M.J., McBeath, T.M., Kirby, J.K., Simpson, R.J., Guppy, C.N., Doolette, A.L., Richardson, A.E., 2015. Complex forms of soil organic Phosphorus–A major component of soil phosphorus. Environ. Sci. Technol. 49, 13238–13245. https://doi.org/10.1021/acs.est.5b02948.

McLaren, T.I., Smernik, R.J., McLaughlin, M.J., Doolette, A.L., Richardson, A.E., Frossard, E., 2020. The chemical nature of soil organic phosphorus: a critical review and global compilation of quantitative data. Advances in Agronomy. 160. Elsevier, pp. 51–124. https://doi.org/10.1016/bs.agron.2019.10.001.

McLaughlin, J., Ryden, J., Syers, J., 1977. Development and evaluation of a kinetic model to describe phosphate sorption by hydrous ferric oxide gel. Geoderma 18, 295–307. https://doi.org/10.1016/0016-7061(77)90038-6.

Menezes-Blackburn, D., Giles, C., Darch, T., George, T.S., Blackwell, M., Stutter, M., Shand, C., Lumsdon, D., Cooper, P., Wendler, R., Brown, L., Almeida, D.S., Wearing, C., Zhang, H., Haygarth, P.M., 2018. Opportunities for mobilizing recalcitrant phosphorus from agricultural soils: a review. Plant Soil 427, 5–16. https://doi.org/10.1007/s11104-017-3362-2.

Minamisawa, H., Kojima, Y., Aizawa, M., 2022. Adsorption of inositol phosphate on hydroxyapatite powder with high specific surface area. Materials 15, 2176. https://doi.org/10.3390/ma15062176.

Missong, A., Bol, R., Willbold, S., Siemens, J., Klumpp, E., 2016. Phosphorous forms in Forest soil colloids as revealed by liquid-state ^{31}P-NMR. J. Soil Sci. Plant Nutr. 179, 159–167. https://doi.org/10.1002/jpln.201500119.

Nanzyo, M., 1986. Infrared spectra of phosphate sorbed on iron hydroxide gel and the sorption products. Soil Sci. Plant Nutr. 32, 51–58. https://doi.org/10.1080/00380768.1986.10557480.

Negassa, W., Dultz, S., Schlichting, A., Leinweber, P., 2008. Influence of specific organic compounds on phosphorus sorption and distribution in a tropical soil. Soil Sci. 173, 587–601. https://doi.org/10.1097/SS.0b013e3181847eef.

Negassa, W., Dultz, S., Schlichting, A., Leinweber, P., 2008. Influence of specific organic compounds on phosphorus sorption and distribution in a tropical soil. Soil Sci. 173, 587–601. https://doi.org/10.1097/SS.0b013e3181847eef.

Nilsson, N., Lövgren, L., Sjöberg, S., 1992. Phosphate complexation at the surface of goethite. Chem. Speciat. Bioavailab. 4, 121–130. https://doi.org/10.1080/09542299.1992.11083190.

Norén, K., Persson, P., 2007. Adsorption of monocarboxylates at the water/goethite interface: the importance of hydrogen bonding. Geochim. Cosmochim. Acta 71, 5717–5730. https://doi.org/10.1016/j.gca.2007.04.037.

Ofoegbu, S.U., 2019. Technological challenges of phosphorus removal in high-phosphorus ores: sustainability implications and possibilities for greener ore processing. Sustainability 11, 6787. https://doi.org/10.3390/su11236787.

Ognalaga, M., Frossard, E., Thomas, F., 1994. Glucose-1-phosphate and myo-inositol hexaphosphate adsorption mechanisms on goethite. Soil Sci. Soc. Am. J. 58, 332–337. https://doi.org/10.2136/sssaj1994.03615995005800020011x.

Okano, K., Uemoto, M., Kagami, J., Miura, K., Aketo, T., Toda, M., Honda, K., Ohtake, H., 2013. Novel technique for phosphorus recovery from aqueous solutions using amorphous calcium silicate hydrates (A-CSHs). Water Res. 47, 2251–2259. https://doi.org/10.1016/j.watres.2013.01.052.

Parfitt, R., 1979. Anion adsorption by soils and soil materials. Advances in Agronomy. 30. Elsevier, pp. 1–50. https://doi.org/10.1016/S0065-2113(08)60702-6.

Parfitt, R.L., Atkinson, R.J., 1976. Phosphate adsorption on goethite (α-FeOOOH). Nature 264, 740–742. https://doi.org/10.1038/264740a0.

Paul, K.W., Kubicki, J.D., Sparks, D.L., 2007. Sulphate adsorption at the Fe (Hydr)Oxide–H_2O Interface: comparison of cluster and periodic slab DFT predictions. Eur. J. Soil Sci. 58, 978–988. https://doi.org/10.1111/j.1365-2389.2007.00936.x.

Perdew, J.P., Burke, K., Ernzerhof, M., 1996. Generalized gradient approximation made simple. Phys. Rev. Lett. 77, 3865–3868. https://doi.org/10.1103/PhysRevLett.77.3865.

Persson, P., Axe, K., 2005. Adsorption of oxalate and malonate at the water-goethite interface: molecular surface speciation from IR spectroscopy. Geochim. Cosmochim. Acta 69, 541–552. https://doi.org/10.1016/j.gca.2004.07.009.

Persson, P., Nilsson, N., Sjöberg, S., 1996. Structure and bonding of orthophosphate ions at the iron oxide-aqueous Interface. J. Colloid Interface Sci. 177, 263–275. https://doi.org/10.1006/jcis.1996.0030.

Pohorille, A., Chipot, C., 2007. Free Energy Calculations: Theory and Applications in Chemistry and Biology; Number 86 in Springer Series in Chemical Physics. Springer.

Powell, K.J., Brown, P.L., Byrne, R.H., Gajda, T., Hefter, G., Sjöberg, S., Wanner, H., 2005. Chemical speciation of environmentally significant heavy metals with inorganic ligands. Part 1: the, and aqueous systems (IUPAC technical Report). Pure Appl. Chem. 77, 739–800. https://doi.org/10.1351/pac200577040739.

Rahnemaie, R., Hiemstra, T., van Riemsdijk, W.H., 2007. Geometry, charge distribution, and surface speciation of phosphate on goethite. Langmuir 23, 3680–3689. https://doi.org/10.1021/la062965n.

Rakovan, J., Becker, U., Hochella, M.F., 1999. Aspects of goethite surface microtopography, structure, chemistry, and reactivity. Am. Mineral. 84, 884–894. https://doi.org/10.2138/am-1999-5-623.

Ren, X., Yang, S., Tan, X., Chen, C., Sheng, G., Wang, X., 2012. Mutual effects of copper and phosphate on their interaction with γ-Al_2O_3: combined batch macroscopic experiments with DFT calculations. J. Hazard. Mater. 237–238, 199–208. https://doi.org/10.1016/j.jhazmat.2012.08.032.

Rietra, R.P.J.J., Hiemstra, T., van Riemsdijk, W.H., 2001. Interaction between calcium and phosphate adsorption on goethite. Environ. Sci. Technol. 35, 3369–3374. https://doi.org/10.1021/es000210b.

Rose, J., Manceau, A., Bottero, J.Y., Masion, A., Garcia, F., 1996. Nucleation and growth mechanisms of Fe oxyhydroxide in the presence of PO_4 ions. 1. Fe K-edge EXAFS Study. Langmuir 12, 6701–6707. https://doi.org/10.1021/la9606299.

Rose, J., Flank, A.M., Masion, A., Bottero, J.Y., Elmerich, P., 1997. Nucleation and growth mechanisms of fe oxyhydroxide in the presence of PO_4 ions. 2. P K-Edge EXAFS Study. Langmuir 13, 1827–1834. https://doi.org/10.1021/la961039d.

Ruttenberg, K., Sulak, D., 2011. Sorption and desorption of dissolved organic phosphorus onto iron (oxyhydr)oxides in seawater. Geochim. Cosmochim. Acta 75, 4095–4112. https://doi.org/10.1016/j.gca.2010.10.033.

Scatchard, G., 1949. The attractions of proteins for small molecules and ions. Ann. N. Y. Acad. Sci. 51, 660–672. https://doi.org/10.1111/j.1749-6632.1949.tb27297.x.

Schaumann, G., Thiele-Bruhn, S., 2011. Molecular modeling of soil organic matter: squaring the circle? Geoderma 166, 1–14. https://doi.org/10.1016/j.geoderma.2011.04.024.

Schulten, H.R., Leinweber, P., 2000. New insights into organic-mineral particles: composition, properties and models of molecular structure. Biol. Fertil. Soils 30, 399–432. https://doi.org/10.1007/s003740050020.

Schulten, H.R., Schnitzer, M., 1993. A state of the art structural concept for humic substances. Naturwissenschaften 80, 29–30. https://doi.org/10.1007/BF01139754.

Schwertmann, U., 1958. The effect of pedogenic environments on iron oxide minerals. In: Stewart, B.A. (Ed.), Advances in Soil Science. Advances in Soil Science1. Springer New York, pp. 171–200. https://doi.org/10.1007/978-1-4612-5046-3_5.
Schwertmann, U., 1993. Relations between iron oxides, soil color, and soil formation. In: Bigham, J.M., Ciolkosz, E.J. (Eds.), SSSA Special Publications. Soil Science Society of America, pp. 51–69 https://doi.org/10.2136/sssaspecpub31.c4.
Senn, H.M., Thiel, W., 2009. QM/MM methods for biomolecular system. Angew. Chem. Int. Ed. Engl. 48, 1198.
Shaheen, S.M., Wang, J., Baumann, K., Ahmed, A.A., Hsu, L.C., Liu, Y.T., Wang, S.L., Kühn, O., Leinweber, P., Rinklebe, J., 2022. Stepwise redox changes alter the speciation and mobilization of phosphorus in hydromorphic soils. Chemosphere 288, 132652. https://doi.org/10.1016/j.chemosphere.2021.132652.
Shang, C., Caldwell, D., Stewart, J., Tiessen, H., Huang, P., 1996. Bioavailability of organic and inorganic phosphates adsorbed on short-range ordered aluminum precipitate. Microb. Ecol., 31 https://doi.org/10.1007/BF00175073.
Sheals, J., Sjoberg, S., Persson, P., 2002. Adsorption of glyphosate on goethite: molecular characterization of surface complexes. Environ. Sci. Technol. 36, 3090–3095. https://doi.org/10.1021/es010295w.
Sigg, L., Stumm, W., 1981. The interaction of anions and weak acids with the hydrous goethite (α-FeOOH) surface. Colloids and Surfaces 2, 101–117. https://doi.org/10.1016/0166-6622(81)80001-7.
Spartan '04 Wavefunction Inc, Irvine, CA.
Stewart, J.J.P., 2007. Optimization of parameters for semiempirical methods V: modification of NDDO approximations and application to 70 elements. J. Mol. Model. 13, 1173–1213. https://doi.org/10.1007/s00894-007-0233-4.
Strauss, R., Brummer, G., Barrow, N., 1997. Effects of crystallinity of goethite: II. Rates of sorption and desorption of phosphate. Eur. J. Soil Sci. 48, 101–114. https://doi.org/10.1111/j.1365-2389.1997.tb00189.x.
Strauss, R., Brümmer, G., Barrow, N., 1997. Effects of crystallinity of goethite: I. Preparation and properties of goethites of differing crystallinity. Eur. J. Soil Sci. 48, 87–99. https://doi.org/10.1111/j.1365-2389.1997.tb00188.x.
Tejedor-Tejedor, M.I., Anderson, M.A., 1990. The protonation of phosphate on the surface of goethite as studied by CIR-FTIR and electrophoretic mobility. Langmuir 6, 602–611. https://doi.org/10.1021/la00093a015.
Tempkin, M.I., Pyzhev, V., 1940. Kinetics of ammonia synthesis on promoted iron catalyst. Acta Phys. Chim. USSR 12, 327–356.
Tomasi, J., Mennucci, B., Cammi, R., 2005. Quantum mechanical continuum solvation models. Chem. Rev. 105, 2999–3094. https://doi.org/10.1021/cr9904009.
Torrent, J., 1997. Interactions between phosphate and iron oxide. Soils and Environment. Vol. Adv. GeoEcol30. Catena Verlag, Reiskirchen, Germany, pp. 321–344.
Torrent, J., Schwertmann, U., Barron, V., 1992. Fast and slow phosphate sorption by goethite-rich natural materials. Clay Clay Miner. 40, 14–21.
Tsao, T.M., Chen, Y.M., Wang, M.K., 2011. Origin, separation and identification of environmental nanoparticles: a review. J. Environ. Monit. 13, 1156. https://doi.org/10.1039/c1em10013k.
Tunesi, S., Poggi, V., Gessa, C., 1999. Phosphate adsorption and precipitation in calcareous soils: the role of calcium ions in solution and carbonate minerals. Nutr. Cycl. Agroecosyst. 53, 219–227. https://doi.org/10.1023/A:1009709005147.
Turner, B.L., Mahieu, N., Condron, L.M., 2003. Quantification of myo-inositol hexakisphosphate in alkaline soil extracts by solution 31 P NMR spectroscopy and spectral deconvolution. Soil Sci. 168, 469–478. https://doi.org/10.1097/01.ss.0000080332.10341.ed.
Urrutia, O., Guardado, I., Erro, J., Mandado, M., García-Mina, J.M., 2013. Theoretical chemical characterization of phosphate-metal-humic complexes and relationships with their effects on both phosphorus soil fixation and phosphorus availability for plants. J. Sci. Food Agric. 93, 293–303.
Urrutia, O., Erro, J., Guardado, I., San Francisco, S., Mandado, M., Baigorri, R., Claude Yvin, J., Ma Garcia-Mina, J., 2014. Physico-chemical characterization of humic-metal-phosphate complexes and their potential application to the manufacture of new types of phosphate-based fertilizers. J. Plant Nutr. Soil Sci. 177, 128–136. https://doi.org/10.1002/jpln.201200651.
Van Emmerik, T.J., Sandström, D.E., Antzutkin, O.N., Angove, M.J., Johnson, B.B., 2007. 31P solid-state nuclear magnetic resonance study of the sorption of phosphate onto gibbsite and kaolinite. Langmuir 23, 3205–3213. https://doi.org/10.1021/la062765b.
VandeVondele, J., Hutter, J., 2007. Gaussian basis sets for accurate calculations on molecular systems in gas and condensed phases. J. Chem. Phys. 127, 114105. https://doi.org/10.1063/1.2770708.
VandeVondele, J., Krack, M., Mohamed, F., Parrinello, M., Chassaing, T., Hutter, J., 2005. Quickstep: fast and accurate density functional calculations using a mixed Gaussian and plane waves approach. Comput. Phys. Commun. 167, 103–128. https://doi.org/10.1016/j.cpc.2004.12.014.
Vanommeslaeghe, K., Hatcher, E., Acharya, C., Kundu, S., Zhong, S., Shim, J., Darian, E., Guvench, O., Lopes, P., Vorobyov, I., Mackerell, A.D., 2009. CHARMM general force field: a force field for drug-like molecules compatible with the CHARMM all-atom additive biological force fields. J. Comput. Chem. https://doi.org/10.1002/jcc.21367 pp. NA–NA.
Vepraskas, M.J., Richardson, J.L., Tandarich, J.P., Teets, S.J., 1999. Dynamics of hydric soil formation across the edge of a created deep marsh. Wetlands 19, 78–89. https://doi.org/10.1007/BF03161736.
Villalobos, M., Cheney, M.A., Alcaraz-Cienfuegos, J., 2009. Goethite surface reactivity: II. A microscopic site-density model that describes its surface area-normalized variability. J. Colloid Interface Sci. 336, 412–422. https://doi.org/10.1016/j.jcis.2009.04.052.
Waiman, C.V., Avena, M.J., Regazzoni, A.E., Zanini, G.P., 2013. A real time in situ ATR-FTIR spectroscopic study of glyphosate desorption from goethite as induced by phosphate adsorption: effect of surface coverage. J. Colloid Interface Sci. 394, 485–489. https://doi.org/10.1016/j.jcis.2012.12.063.
Wang, X., Liu, F., Tan, W., Li, W., Feng, X., Sparks, D.L., 2013. Characteristics of phosphate adsorption-desorption onto ferrihydrite: comparison with well-crystalline Fe (Hydr)Oxides. Soil Sci. 178, 1–11. https://doi.org/10.1097/SS.0b013e31828683f8.
Wang, H., Zhu, J., Fu, Q.L., Xiong, J.W., Hong, C., Hu, H.Q., Violante, A., 2015. Adsorption of phosphate onto ferrihydrite and ferrihydrite-humic acid complexes. Pedosphere 25, 405–414. https://doi.org/10.1016/S1002-0160(15)30008-4.
Wang, H., Zhu, J., Fu, Q., Hu, H., 2015. Adsorption of phosphate on pure and humic acid-coated ferrihydrite. J. Soils Sediments 15, 1500–1509. https://doi.org/10.1007/s11368-015-1095-5.
Wang, H., Zhu, J., Fu, Q., Hong, C., Hu, H., Violante, A., 2016. Phosphate adsorption on uncoated and humic acid-coated iron oxides. J Soils Sediments 16, 1911–1920. https://doi.org/10.1007/s11368-016-1383-8.
Weng, Y., Vekeman, J., Zhang, H., Chou, L., Elskens, M., Tielens, F., 2020. Unravelling phosphate adsorption on hydrous ferric oxide surfaces at the molecular level. Chemosphere 261, 127776. https://doi.org/10.1016/j.chemosphere.2020.127776.
Willett, I.R., Chartres, C.J., Nguyen, T.T., 1988. Migration of phosphate into aggregated particles of ferrihydrite. J. Soil Sci. 39, 275–282. https://doi.org/10.1111/j.1365-2389.1988.tb01214.x.
Withers, P.J.A., Elser, J.J., Hilton, J., Ohtake, H., Schipper, W.J., van Dijk, K.C., 2015. Greening the global phosphorus cycle: how green chemistry can help achieve planetary P sustainability. Green Chem. 17, 2087–2099. https://doi.org/10.1039/C4GC02445A.
Xiu, F., Zhou, L., Xia, S., Yu, L., 2016. Adsorption mechanism of water molecule on goethite (010) surface. J. Ocean Univ. China 15, 1021–1026. https://doi.org/10.1007/s11802-016-3171-x.
Xu, C.Y., Li, J.Y., Xu, R.K., Hong, Z.N., 2017. Sorption of organic phosphates and its effects on aggregation of hematite nanoparticles in monovalent and bivalent solutions. Environmental Science and Pollution Research 24, 7197–7207. https://doi.org/10.1007/sll356-017-8382-l.
Yan, Y.P., Liu, F., Li, W., Liu, F., Feng, X.H., Sparks, D.L., 2014. Sorption and desorption characteristics of organic phosphates of different structures on aluminium (oxyhydr)oxides: sorption-desorption of organic P on Al oxyhydroxides. Eur. J. Soil Sci. 65, 308–317. https://doi.org/10.1111/ejss.12119.
Zheng, T.T., Sun, Z.X., Yang, X.F., Holmgren, A., 2012. Sorption of phosphate onto mesoporous -alumina studied with in-situ ATR-FTIR spectroscopy. Chem. Cent. J., 6 https://doi.org/10.1186/1752-153X-6-26.
Zhong, B., Stanforth, R., Wu, S., Chen, J.P., 2007. Proton interaction in phosphate adsorption onto goethite. J. Colloid Interface Sci. 308, 40–48. https://doi.org/10.1016/j.jcis.2006.12.055.
Zhou, L., Xiu, F., Qiu, M., Xia, S., Yu, L., 2017. The adsorption and dissociation of water molecule on goethite (010) surface: a DFT approach. Appl. Surf. Sci. 392, 760–767. https://doi.org/10.1016/j.apsusc.2016.09.038.
Zimmer, D., Kahle, P., Baum, C., 2016. Loss of soil phosphorus by tile drains during storm events. Agric. Water Manag. 167, 21–28. https://doi.org/10.1016/j.agwat.2015.12.017.

Publication 11

review article

A. I. Osman, Y. Zhang, Z. Y. Lai, A. K. Rashwan, M. Farghali, Ashour A. Ahmed, Y. Liu, B. Fang, Z. Chen, A. Al-Fatesh, D. W. Rooney, C. L. Yiin, P.-S. Yap. Machine learning and computational chemistry to improve biochar fertilizers: a review. Environ. Chem. Lett. **2023**, 21, 3159–3244.

Contribution: Ashour A. Ahmed is responsible for writing the modeling part of the present review.

Due to the large size of this review article, only a preview containing the molecular modelling part is provided. The full PDF version can be accessed via the following link or QR code.

URL: https://doi.org/10.1007/s10311-023-01631-0

QR:

Ashour Ahmed review2

Open Access: This article is licensed under a Creative Commons Attribution 4.0 International License, which permits use, sharing, adaptation, distribution, and reproduction in any medium or format, as long as you give appropriate credit to the original author(s) and the source, provide a link to the Creative Commons license, and indicate if changes were made.

Environmental Chemistry Letters
https://doi.org/10.1007/s10311-023-01631-0

REVIEW ARTICLE

Machine learning and computational chemistry to improve biochar fertilizers: a review

Ahmed I. Osman[1] · Yubing Zhang[2] · Zhi Ying Lai[3] · Ahmed K. Rashwan[4] · Mohamed Farghali[5,6] · Ashour A. Ahmed[7] · Yunfei Liu[2] · Bingbing Fang[2] · Zhonghao Chen[2] · Ahmed Al-Fatesh[8] · David W. Rooney[1] · Chung Loong Yiin[3,9] · Pow-Seng Yap[2]

Received: 21 June 2023 / Accepted: 13 July 2023
© The Author(s) 2023

Abstract
Traditional fertilizers are highly inefficient, with a major loss of nutrients and associated pollution. Alternatively, biochar loaded with phosphorous is a sustainable fertilizer that improves soil structure, stores carbon in soils, and provides plant nutrients in the long run, yet most biochars are not optimal because mechanisms ruling biochar properties are poorly known. This issue can be solved by recent developments in machine learning and computational chemistry. Here we review phosphorus-loaded biochar with emphasis on computational chemistry, machine learning, organic acids, drawbacks of classical fertilizers, biochar production, phosphorus loading, and mechanisms of phosphorous release. Modeling techniques allow for deciphering the influence of individual variables on biochar, employing various supervised learning models tailored to different biochar types. Computational chemistry provides knowledge on factors that control phosphorus binding, e.g., the type of phosphorus compound, soil constituents, mineral surfaces, binding motifs, water, solution pH, and redox potential. Phosphorus release from biochar is controlled by coexisting anions, pH, adsorbent dosage, initial phosphorus concentration, and temperature. Pyrolysis temperatures below 600 °C enhance functional group retention, while temperatures below 450 °C increase plant-available phosphorus. Lower pH values promote phosphorus release, while higher pH values hinder it. Physical modifications, such as increasing surface area and pore volume, can maximize the adsorption capacity of phosphorus-loaded biochar. Furthermore, the type of organic acid affects phosphorus release, with low molecular weight organic acids being advantageous for soil utilization. Lastly, biochar-based fertilizers release nutrients 2–4 times slower than conventional fertilizers.

Keywords Climate change · Machine learning and computational chemistry · Phosphorus-loaded biochar · Phosphorus bioavailability · Organic acids · Biochar-based fertilizer

Introduction

Biochar, a carbon-rich material produced through biomass pyrolysis, has garnered significant interest as a potential agricultural amendment and other environmental applications (Farghali et al. 2023; Osman et al. 2022). Biochar offers promising applications in improving soil quality and nutrient management as a nutrition carrier due to biochar's unique properties, such as high porosity and surface area. Phosphorus, on the other side, is an essential nutrient required for plant growth and various physiological processes; however, phosphorus availability in soil is limited due to phosphorus's high reactivity and tendency to form insoluble compounds. Traditional fertilizer practices have been used to combat phosphorus deficiency but have several environmental consequences, including water pollution and soil degradation. As a result, there is a growing need to develop sustainable solutions that increase phosphorus availability while minimizing environmental impacts. The availability of phosphorus in biochar is critical for improving soil fertility and promoting plant growth. However, the phosphorus content in biochar can be relatively stable and not readily available for plant uptake. To significantly improve the bioavailability of phosphorus-loaded biochar, scientists have undertaken a pioneering approach, synergistically combining cutting-edge technologies like machine learning and computational

Extended author information available on the last page of the article

Published online: 17 August 2023

chemistry with meticulous application and optimization of organic acids (Ahmed et al. 2014; Ahmed et al. 2023; Gros et al. 2017).

Here we review biochar with a focus on production methods, phosphorus loading techniques, and the factors affecting phosphorus release to better understand the underlying mechanisms. The review also highlights the strategies and mechanisms involved in maximizing organic acids for enhancing phosphorus bioavailability from biochar in the context of climate-smart agriculture. Interestingly, machine learning, computational chemistry, and organic acids application and optimization can be applied to optimize phosphorus bioavailability, as shown in Fig. 1. The role of phosphorus in crop growth, the problems with traditional fertilizers, the limitations of phosphorus-loaded biochar, and future research directions are discussed. The review uniquely focuses on utilizing organic acids to enhance phosphorus release from loaded biochar. Additionally, it explores the potential application of computational chemistry and machine learning algorithms in identifying the most effective organic acids for improving phosphorus bioavailability.

The insights derived from this review will contribute to optimizing phosphorus management strategies in agriculture and promoting the sustainable utilization of biochar to enhance phosphorus availability. Through an in-depth evaluation of current knowledge, the review identifies gaps, limitations, and future research directions, thereby supporting the development of sustainable agricultural practices that maximize phosphorus utilization while minimizing environmental impacts.

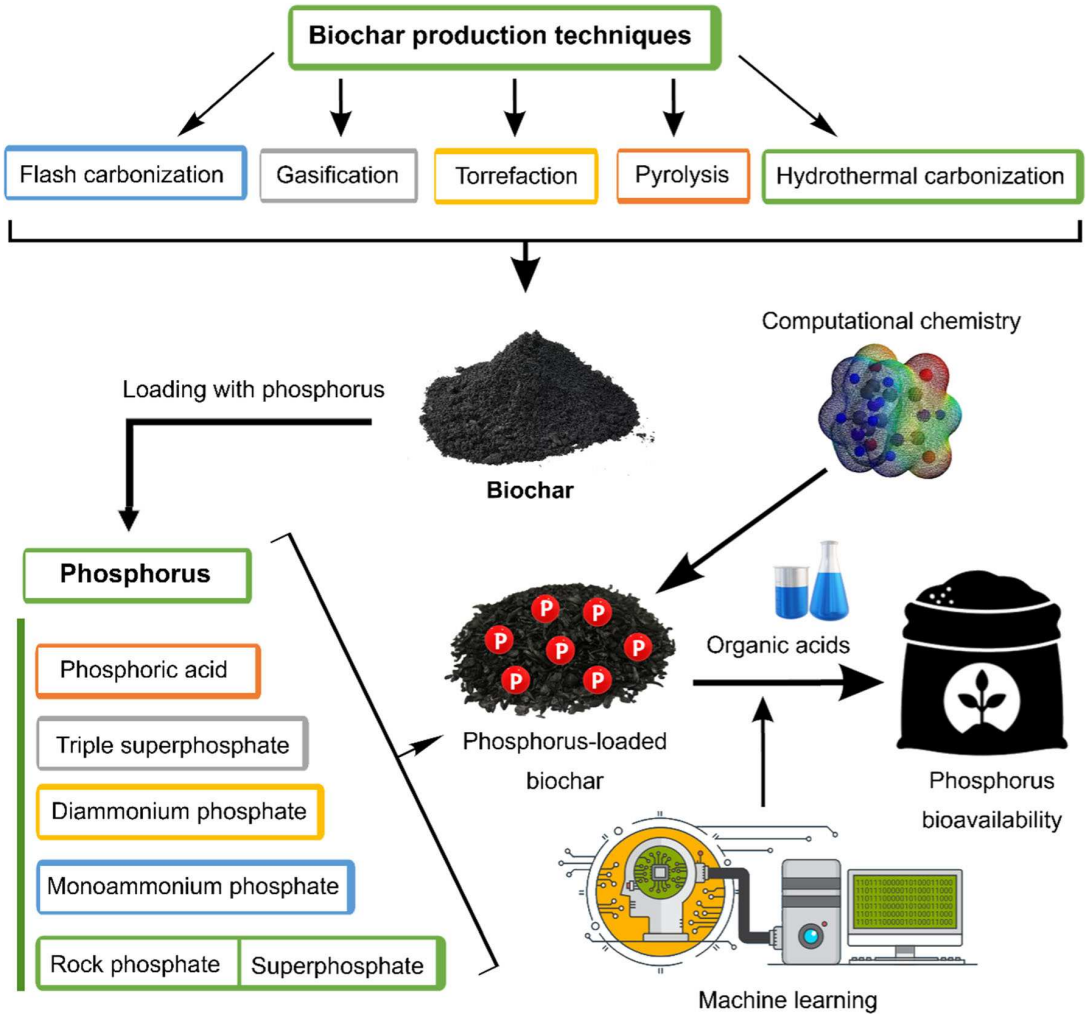


Fig. 1 Biochar-based fertilizer loading with phosphorus and enhancing phosphorus bioavailability using organic acids. This figure illustrates the process of biochar production techniques, loading biochar with phosphorus to make a biochar-based fertilizer, and the subsequent enhancement of phosphorus bioavailability for plants. Various organic acids are employed as effective agents to facilitate phosphorus release. Integrating machine learning and computational chemistry with organic acids application could optimize phosphorus bioavailability

Application of computational chemistry in phosphorus-loaded biochar

Despite extensive experimental efforts, a complete understanding of the underlying mechanisms behind specific chemical reactions or physical processes is not always achieved. The intricate interplay of factors influencing phenomena like phosphorus bioavailability further adds complexity. In this context, computational chemistry is a valuable tool that can complement experimental findings and provide a more profound comprehension of these processes. Additionally, it can offer insights into identifying suitable materials for climate-smart agriculture.

This section will consist of two main subsections. The first subsection will provide a concise introduction to computational chemistry, exploring different levels of theory and highlighting the advantages and limitations associated with each level. Then, we will discuss how computational chemistry enables a systematic investigation of potential molecular mechanisms and binding patterns involved in phosphate binding to reactive soil constituents, even under diverse experimental conditions.

Overview of computational chemistry

Computational chemistry is vital in chemistry and related fields like biochemistry, chemical physics, and material science. Computational chemistry is a discipline that leverages fundamental principles from physics to investigate a wide range of molecular properties and phenomena. Employing advanced computational techniques allows researchers to study molecular structures, thermodynamics, spectroscopic data, reaction rates, and dynamics with high precision and accuracy. It can simulate different phases like gases, liquids, solids, solutions, and interfaces (Ahmed et al. 2023; Cramer 2004; Jensen 2017; Kubicki 2016). Computational chemistry enables the simulation of adsorption/desorption processes, accounting for the impact of surface composition, spatial configuration, solution environment, ionic strength, and solution pH. Furthermore, computational chemistry can calculate and interpret spectroscopic data like infrared, ultraviolet, nuclear magnetic resonance, and X-ray spectroscopy. The accuracy and efficiency of the level of theory significantly impact these calculations and simulations. Despite the growing importance and wide-ranging applications, the use of computational chemistry in environmental chemistry, specifically in studying biogeochemical processes within the soil, has been relatively constrained thus far. This is primarily due to the immense complexity inherent in soil, which is characterized by the heterogeneous nature and multi-component composition, posing unique challenges and requiring interdisciplinary collaborations (Ahmed et al. 2014; Ahmed et al. 2023; Gros et al. 2017; Kubicki 2016; Kwon and Kubicki 2004). However, the integration of molecular simulation techniques and the development of relevant molecular models hold substantial promise. The comprehensive utilization of computational chemistry has great potential in enhancing our molecular-level understanding of phosphorus-related processes, thus improving soil's phosphorus bioavailability.

Computational chemistry encompasses different levels of theory, each offering distinct accuracy and computational efficiency. At the simplest level, molecular mechanics employ empirical potentials to describe the energy of molecular systems, with three primary resolution levels: all-atom, united-atom, and coarse-grained representations (Cramer 2004; Jensen 2017; Kmiecik et al. 2016).

In the all-atom depiction, individual atoms are considered particles, with the treatment of electrons being implicit. On the other hand, the united-atom representation consolidates groups of atoms, such as a CH_2 group, into a single pseudo-atom. Taking a further step, the coarse-grained representation involves grouping atoms, functional groups, or even whole molecules into beads. These various representations encompass both bonded and non-bonded interactions, encompassing potentials for bonds, angles, dihedral angles, electrostatic forces, and van der Waals interactions.

For a more detailed description, quantum mechanics explicitly treats nuclei and electrons, solving the Schrödinger equation. Quantum mechanics can be broadly categorized into three main approaches: ab initio, density functional theory, and semi-empirical methods. Each of these methods provides different levels of accuracy and computational cost in capturing the quantum behavior of molecules (Cramer 2004; Jensen 2017; Kubicki 2016). Ab initio methods are computationally expensive and limited to simple model systems. Semi-empirical methods utilize approximations and empirical parameters, making them computationally more efficient and applicable to larger systems.

Density functional theory, the most prominent method, balances efficiency and accuracy by calculating the electron density using Kohn–Sham molecular orbitals. The choice of the so-called exchange–correlation functional and basis set significantly affects the quality of density functional theory results (Jensen 2017; Lee et al. 1988; Perdew et al. 1996). In practice, computational chemistry employs various basis sets, such as Gaussian atom-centered and periodic plane-wave basis sets, to represent electronic wave functions. Hybrid Gaussian and plane-wave methods have been developed to combine the benefits of both approaches (Kuhne et al. 2020; Lippert et al. 1997). Incorporating long-range van der Waals dispersion interactions often requires the inclusion of empirical dispersion corrections (Chai and Head-Gordon 2008; Grimme et al. 2011).

Moreover, the hybrid QM/MM method combines quantum mechanics (QM) calculations for the reactive part of the system with molecular mechanics (MM) estimates for the rest, such as the solvent (Senn and Thiel 2009). This approach efficiently tackles larger and more complex systems. Various QM/MM schemes, including mechanical and electrostatic embedding, have been developed to link quantum mechanics and molecular mechanics calculations, capturing the interplay between different regions. The hybrid QM/MM method offers advantages such as computational efficiency, versatility, accurate modeling of reactions with environmental effects, and valuable insights into chemical reactions, transition states, and excited states. However, implementing it requires specialized software and expertise, and the results from QM/MM can be influenced by force field parameters and the chosen quantum mechanics method. Additionally, interpreting calculations and analysis can be challenging due to the complexity involved. In this context, in the following, we present a summary of the benefits and limitations of commonly utilized levels of theory, as well as potential levels, for conducting phosphorus research.

Density functional theory (DFT) is widely used in phosphorus research due to DFT's favorable balance between accuracy and computational cost. It offers versatility in studying molecules, materials science, and solid-state physics and enables the simulation of chemical reactions, transition states, and excited states. Moreover, density functional theory can predict materials and molecules' electronic and thermodynamic properties. However, density functional theory has limitations that should be considered. It relies on empirical parameters, which can limit the density functional theory accuracy. The choice of functional theory is crucial and can impact the results. Dispersion interaction corrections are often necessary to account for non-covalent interactions. Moreover, there are limitations in the time and length scales of molecular dynamics simulations within the framework of density functional theory.

Semi-empirical methods provide an alternative to density functional theory and offer certain advantages. They are computationally less expensive compared to ab initio and density functional theory methods, resulting in higher efficiency. These methods are particularly suitable for studying molecular systems containing hundreds to thousands of atoms. They can access longer time scales in molecular dynamics simulations compared to ab initio and density functional theory methods, making them useful for simulating chemical reactions, transition states, and excited states. However, semi-empirical methods have their own limitations. They rely on extensive empirical parameters, which can affect their accuracy. Additionally, parameterization often requires ab initio calculations or experimental data, limiting their transferability to other molecular systems.

When considering molecular mechanics-based methods, the all-atom representation offers several advantages. It is computationally efficient and fast compared to all quantum mechanics methods. It enables the description of large molecular systems containing thousands to millions of atoms and often achieves good accuracy in reproducing experimental observations. This representation is particularly suitable for situations with limited computational resources. However, the all-atom representation relies on empirical parameters, which need to be carefully parameterized through quantum mechanics calculations or experiments. Generally, it has lower accuracy compared to all quantum mechanics methods. Furthermore, the all-atom representation cannot simulate chemical reactions and accurately capture electronic properties.

The coarse-grained representation reduces the complexity of molecular systems by grouping atoms into larger entities, significantly reducing the computational cost. This makes it highly suitable for studying large molecular systems consisting of millions of atoms. The coarse-grained representation also enables access to longer time and length scales in simulations, making it useful for studying slow processes such as adsorption/desorption, diffusion, and self-assembly. However, the coarse-grained representation has limitations. It requires all-atom calculations and/or experiments for parameterization, which can be time-consuming. The potential lack of parameter transferability to other molecular systems is another challenge. Additionally, the coarse-grained representation sacrifices atomistic details, which may limit the ability to study precise molecular structures.

Irrespective of the level of theory in computational chemistry, a wide range of techniques can be employed to achieve stable molecular geometries and optimized structures. Molecular dynamics simulations are utilized to incorporate statistical properties that account for the thermal motion of nuclei at finite temperatures (Marx and Hutter 2009). By solving Newton's equations of motion, molecular dynamics generate trajectories that sample the system's thermal ensemble at a specific temperature, enabling the determination of average geometries and capturing the explicit behavior of the entire system. Implicit solvation models offer a simplification by representing the solvent as a classical dielectric medium that responds to the electron density of the reactive quantum region (Cossi et al. 2003; Klamt and Schuurmann 1993; Marenich et al. 2009). When considering macroscopic systems like surfaces, there are two main approaches: finite cluster models and periodic treatments. Periodic boundary conditions are commonly used for surface-related processes in crystalline or amorphous materials.

In summary, different levels of theory and techniques employed in phosphorus research possess distinct advantages and limitations. The selection of the optimal approach relies on specific research objectives, system size, computational resources, and the desired level of accuracy.

Computational chemistry in phosphorus research

To the best of our knowledge, no molecular modeling study has yet examined the impact of biochar on phosphorus bioavailability. However, computational chemistry has significantly contributed to investigating phosphorus-related processes and enhancing phosphorus bioavailability in soil. It has been employed as a complementary tool to experimental studies, specifically to understand phosphate binding to soil constituents, particularly mineral surfaces. For instance, Kubicki and colleagues made pioneering strides in understanding the phosphate binding process through the use of density functional theory calculations (Kubicki et al. 2009; Kubicki et al. 2007; Kubicki et al. 2012; Kwon and Kubicki 2004). In an early investigation, they utilized an embedded-molecular-cluster approach to study pH-dependent phosphate binding to goethite (α-FeOOH). The goethite surface was represented by a small cluster of two edge-sharing iron octahedra, with a few explicit water molecules simulating the solvent environment. By comparing vibrational frequencies with experimental data, the study proposed the formation of a diprotonated bidentate complex at low pH, a deprotonated bidentate or a monoprotonated monodentate complex at intermediate pH, and a deprotonated monodentate complex at high pH.

Further investigations examined the impact of surface charge distributions, phosphate speciation, competitive water, pH, and hydrogen bonds on phosphate binding to the same small cluster (Acelas et al. 2013; Rahnemaie et al. 2007). Furthermore, the phosphate binding to aqueous uranium complexes as well as various mineral surfaces such as boehmite (γ-AlOOH), corundum (α-Al_2O_3), and ferrihydrite has been explored using similar cluster models (Acelas et al. 2013; Khare et al. 2007; Kubicki et al. 2009; Li et al. 2010; Ren et al. 2012). It should be noted that these observations were obtained through cluster calculations, which may not fully capture the behavior of extended or periodic systems.

Extending the cluster approach applied in previous research on phosphate-surface binding motifs, Kubicki et al. (2012) conducted periodic density functional theory calculations. Their study encompassed goethite surface planes and employed stationary calculations and molecular dynamics simulations to analyze the HPO_4^{2-} species. Additionally, infrared spectroscopy vibrational frequencies were calculated for extracted molecular clusters, aiding in identifying phosphate binding motifs. The findings indicated the formation of monodentate complexes on the 001, 210, 101, and 100 surface planes, while bidentate complexes were observed on the 010, 101, and 100 surface planes. Similarly, Belelli et al. (2014) utilized periodic calculations to investigate the behavior of phosphate complexes on pure and aluminum (Al)-rich goethite surfaces (110 planes), exploring previously unexplored complexes. Their vibrational frequency calculations, compared with experimental data, indicated the prevalence of protonated bidentate mononuclear complexes at pH 3.1, bidentate binuclear complexes within the pH range of 4.2–7.9, and protonated bidentate binuclear complexes at pH 12.8. Furthermore, Weng et al. (2020) performed molecular dynamics simulations using periodic density functional theory calculations to study the phosphate binding on the 100 goethite surface plane. The results demonstrated that the monodentate complex is the most abundant, followed by the physisorbed configuration.

Furthermore, Ahmed et al. (2020) investigated the interaction between inorganic and organic phosphorus compounds and diverse soil components. These components include mineral surfaces, free metal ions, and soil organic matter, as illustrated in Fig. 2 (Ahmed et al. 2019; Ganta et al. 2019, 2020a, b; Ganta et al. 2021; Shaheen et al. 2022). Their calculations involved larger simulation boxes, incorporating phosphate-mineral–water molecular models with explicit solvation at a water density of 1 $g.cm^{-3}$. The simulations employed molecular dynamics with density functional theory or quantum mechanics/molecular mechanics (QM/MM) methods, using hybrid Gaussian and plane-wave basis sets and accounting for long-range dispersion correction. To elucidate the mechanisms underlying phosphorus binding, their investigations considered multiple factors, including surface morphology, saturation, central metal ion exchange, metal ion valency, soil organic matter (SOM) composition, water, pH, and redox potential. The research yielded important insights into phosphate binding in soils, revealing more robust binding to mineral surfaces and metal ions than organic matter (Ahmed et al. 2019; Shaheen et al. 2022).

Phosphate formed inner-sphere complexes through covalent or coordination bonds with mineral surfaces and metal ions while binding to the organic matter involved dispersion interactions and hydrogen bonds. Hydrogen bonds and dispersion interactions also played significant roles in the binding to metal ions and mineral surfaces. Consequently, phosphate species bound to organic matter may contribute to readily available and mobile phosphorus compared to mineral surfaces. Furthermore, soils rich in pedogenic oxides are expected to have stronger phosphate binding, while soils with lower concentrations exhibit weaker binding. Under reducing conditions, phosphate

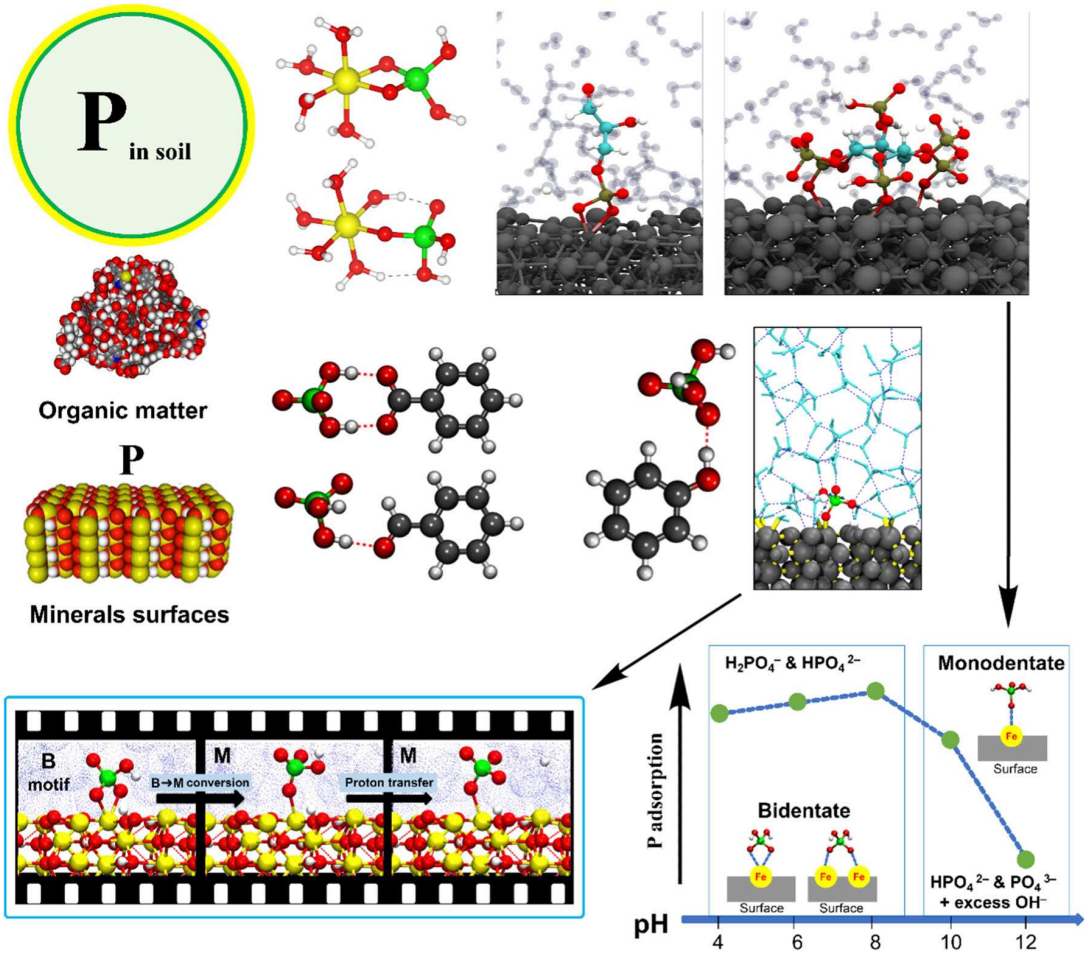


Fig. 2 Interaction between phosphate and various soil constituents. This interaction includes optimized structures of orthophosphate complexes with metal ions (in monodentate and bidentate binding motifs), organic molecules, and the goethite surface in the presence of water. Additionally, the binding of glycerolphosphate and inositolphosphate complexes to the goethite surface in the presence of water is shown. The influence of pH on orthophosphate binding at the goethite surface and the dynamic behavior and conversion of binding arrangements and proton transfer are depicted. In the figure, "M" and "B" represent monodentate and bidentate binding motifs, respectively. Goethite atoms are depicted in gray, while orthophosphate (PO_4^{3-}) atoms are color-coded with green (P, phosphorus), red (O, oxygen), and white (H, hydrogen)

shows weaker binding to soil constituents, especially metal ions and metal oxides, compared to oxidizing conditions. This suggests that reduced soil conditions can increase phosphorus availability. The subsequent paragraphs will delve further into the computational chemistry perspective of the phosphate binding process.

The results obtained from molecular modeling and simulations conducted by Ahmed and colleagues have shed light on the intricate influence of pH on the binding and mobilization of phosphorus in soil. Notably, the pH effect is not uniform across all soil constituents (Ahmed et al. 2020; Shaheen et al. 2022). While phosphate binding to free metal ions increases with higher solution pH, binding to organic matter and mineral surfaces decreases as the pH rises. This implies that the composition of soil constituents and solution pH significantly impact phosphorus binding in a specific soil. Moreover, pH is crucial in determining phosphate binding motifs on mineral surfaces. For instance, monodentate binding motifs dominate at 010 and 100 goethite surface planes under extremely low and high pH conditions, while the bidentate binding motif prevails in the intermediate pH range.

Additionally, mineral surfaces' nature and surface planes notably affect phosphorus binding. For instance, goethite (α-FeOOH) generally exhibits stronger phosphate binding compared to diaspore (α-AlOOH), particularly for specific binding motifs (Ganta et al. 2019; Ganta et al. 2021). All monodentate binding motifs of phosphates (orthophosphate, glycerolphosphate, and inositol-hexaphosphate) show more robust binding to goethite than

diaspore. However, in the case of the 3 monodentate (3M) binding motif of inositol-hexa-phosphate, diaspore demonstrates stronger binding than goethite for both 010 and 100 surface planes (Ganta et al. 2019; Ganta et al. 2021, 2020a; b).

Moreover, both glycerolphosphate and inositol-hexa-phosphate exhibited stronger binding to the less saturated surface plane of diaspore (010) compared to the more saturated plane (100) for all binding motifs (Ganta et al. 2019, 2020b). This can be attributed to the higher surface saturation of the 100-plane, which results in more negative charges and a lower electrostatic potential than the 010-plane. As a result, phosphates, carrying negative charges due to partial deprotonation, are more strongly bound or adsorbed to the 010-plane than the 100-plane. Furthermore, the surface morphology plays a significant role, as different dominant binding motifs are observed depending on the surface plane. For example, orthophosphate exhibits a preference for the bidentate mononuclear (2O + 1Fe) binding motif on the 010-goethite surface plane, whereas it favors the bidentate binuclear (2O + 2Fe) motif on the 100-surface plane (Ahmed et al. 2019).

Moreover, the distribution and positions of surface central metal ions (such as Al^{3+} in diaspore or Fe^{3+} in goethite) on both surface planes enable glycerolphosphate and inositol-hexa-phosphate to form more stable multiple covalent bonds with the 010-diaspore surface plane compared to the 100-plane. Specifically, the 3 monodentate (3M) binding motif prevails for inositol-hexa-phosphate on the 010-diaspore surface plane, while the 2 monodentate (2M) motif dominates on the 100-plane (Ganta et al. 2019, 2020b). Regarding glycerolphosphate, the bidentate binding motif is dominant on both surface planes, with significantly higher occurrence observed on the 010-diaspore surface plane. Furthermore, the stronger binding of inositol-hexa-phosphate compared to glycerolphosphate on both diaspore surface planes, similar to goethite, suggests a higher prevalence of inositol-hexa-phosphate in soils (Missong et al. 2016).

It was also explored that water plays a vital role in regulating the phosphate binding process on mineral surfaces through diverse mechanisms. It forms hydrogen bonds with phosphates and surfaces, leading to dissociation and the generation of H^+ and OH^- ions. Proton transfer processes occur between phosphates, surfaces, and water, influencing the solution's acidity and potentially inducing soil acidity after phosphorus fertilization. The presence of water molecules introduces strain into phosphate-mineral complexes, especially for phosphates like glycerolphosphate and inositol-hexa-phosphate, which engage in intermolecular hydrogen bonds with water. This strain causes instability in specific binding motifs and depends on the water-accessible surface area of the phosphate species. Inositol-hexa-phosphate also exhibits intramolecular hydrogen bonds between adjacent phosphate groups, contributing to strain and the dissociation of covalent bonds in specific motifs. Interaction energies reveal that phosphates show an increasing affinity for goethite and diaspore surfaces compared to water, enabling them to displace water molecules on these surfaces. Ultimately, all these investigations emphasize the critical role played by water as well as the molecular structure of both phosphates and the adsorbent surface, as supported by numerous experimental studies (Amadou et al. 2022; Ganta et al. 2021; Gypser et al. 2018; Wang et al. 2015a; Yan et al. 2014). In addition, these investigations have resolved debates regarding the assignment of phosphate-mineral binding motifs and can be applied to characterize experimental infrared spectra in similar cases. Further discussion of these findings can be found in the review article (Ahmed et al. 2023).

In conclusion, molecular modeling is a potent tool for unraveling the complexities of phosphorus binding and bioavailability in soil, complementing experimental investigations. It provides crucial insights into the impact of various factors on the binding process, including phosphorus compound type, soil constituents, mineral surfaces, binding motifs, water, solution pH, and redox potential. Phosphate predominantly binds to mineral surfaces and free metal ions, exhibiting a stronger affinity than organic matter. The binding mechanisms involve inner-sphere complexes, covalent/coordination bonds, hydrogen bonds, and dispersion interactions. Various factors, including the characteristics of mineral surfaces, positions of surface metals, properties of phosphate groups, interactions with water, and solution pH, influence phosphate binding. The pH effect on binding is intricate and varies among soil constituents. To enhance our understanding of phosphorus bioavailability in soil, future research should address outstanding questions and challenges in molecular modelings, such as optimizing organic acids to improve phosphorus bioavailability from biochar in climate-smart agriculture. This will drive the development of sustainable soil management strategies and efficient phosphorus fertilizers. Integrating computational chemistry methods with experimental data enables a comprehensive comprehension of molecular systems, propelling advancements in chemistry and related fields.

Machine learning for improved phosphorus bioavailability from biochar

Artificial intelligence enables computers to solve complex challenges and perform tasks like humans. Machine learning algorithms convert input data into new solutions

Environ 821:153256. https://doi.org/10.1016/j.scitotenv.2022.153256

Zheng XB et al (2021) Nitric acid-modified hydrochar enhance Cd^{2+} sorption capacity and reduce the Cd^{2+} accumulation in rice. Chemosphere 284:131261. https://doi.org/10.1016/j.chemosphere.2021.131261

Zhou Z, Yao H (2020) Effects of composting different types of organic fertilizer on the microbial community structure and antibiotic resistance genes. Microorganisms 8:268. https://doi.org/10.3390/microorganisms8020268

Zhou J et al (2019a) Random forests and cubist algorithms for predicting shear strengths of rockfill materials. Appl Sci 9:1621. https://doi.org/10.3390/app9081621

Zhou X et al (2019b) Turning pig manure into biochar can effectively mitigate antibiotic resistance genes as organic fertilizer. Sci Total Environ 649:902–908. https://doi.org/10.1016/j.scitotenv.2018.08.368

Zhou XH et al (2023) Treatment of distiller grain with wet-process phosphoric acid leads to biochar for the sustained release of nutrients and adsorption of Cr(VI). J Hazard Mater 441:129949. https://doi.org/10.1016/j.jhazmat.2022.129949

Zhu D et al (2020) Synthesis and characterization of magnesium oxide nanoparticle-containing biochar composites for efficient phosphorus removal from aqueous solution. Chemosphere 247:125847. https://doi.org/10.1016/j.chemosphere.2020.125847

Zhu J et al (2018) Phosphorus activators contribute to legacy phosphorus availability in agricultural soils: a review. Sci Total Environ 612:522–537. https://doi.org/10.1016/j.scitotenv.2017.08.095

Zhu X et al (2019) The application of machine learning methods for prediction of metal sorption onto biochars. J Hazard Mater 378:120727. https://doi.org/10.1016/j.jhazmat.2019.06.004

Zolfi Bavariani M et al (2019) Influence of pyrolysis temperatures on FTIR analysis, nutrient bioavailability, and agricultural use of poultry manure biochars. Commun Soil Sci Plant Anal 50:402–411. https://doi.org/10.1080/00103624.2018.1563101

Zong Y et al (2022) Comparative study on the potential risk of contaminated-rice straw, its derived biochar and phosphorus modified biochar as an amendment and their implication for environment. Environ Pollut 293:118515. https://doi.org/10.1016/j.envpol.2021.118515

Publisher's Note Springer Nature remains neutral with regard to jurisdictional claims in published maps and institutional affiliations.

Authors and Affiliations

Ahmed I. Osman[1] · Yubing Zhang[2] · Zhi Ying Lai[3] · Ahmed K. Rashwan[4] · Mohamed Farghali[5,6] · Ashour A. Ahmed[7] · Yunfei Liu[2] · Bingbing Fang[2] · Zhonghao Chen[2] · Ahmed Al-Fatesh[8] · David W. Rooney[1] · Chung Loong Yiin[3,9] · Pow-Seng Yap[2]

✉ Ahmed I. Osman
aosmanahmed01@qub.ac.uk

✉ Chung Loong Yiin
clyiin@unimas.my

Mohamed Farghali
mohamed.farghali@aun.edu.eg

Ashour A. Ahmed
ashour.ahmed@uni-rostock.de

[1] School of Chemistry and Chemical Engineering, David Keir Building, Queen's University Belfast, Stranmillis Road, Belfast BT9 5AG, Northern Ireland, UK

[2] Department of Civil Engineering, Xi'an Jiaotong-Liverpool University, Suzhou 215123, China

[3] Department of Chemical Engineering and Energy Sustainability, Faculty of Engineering, Universiti Malaysia Sarawak (UNIMAS), 94300 Kota Samarahan, Sarawak, Malaysia

[4] Department of Food and Dairy Sciences, Faculty of Agriculture, South Valley University, Qena 83523, Egypt

[5] Department of Agricultural Engineering and Socio-Economics, Kobe University, Kobe 657-8501, Japan

[6] Department of Animal and Poultry Hygiene and Environmental Sanitation, Faculty of Veterinary Medicine, Assiut University, Assiut 71526, Egypt

[7] Institute of Physics, University of Rostock, Albert-Einstein-Str. 23-24, 18059 Rostock, Germany

[8] Chemical Engineering Department, College of Engineering, King Saud University, PO Box 800, Riyadh 11421, Saudi Arabia

[9] Institute of Sustainable and Renewable Energy (ISuRE), Universiti Malaysia Sarawak (UNIMAS), 94300 Kota Samarahan, Sarawak, Malaysia

Publication 12

P. Gros, Ashour A. Ahmed, O. Kühn, P. Leinweber. Glyphosate binding in soil as revealed by sorption experiments and quantum-chemical modeling. Sci. Total Environ. **2017**, 586, 527–535.

Contribution: Ashour A. Ahmed is credited with conceptualization, conducting the modeling work, modeling analysis and interpretation, methodology development, visualization, and writing the original manuscript with P. Gros. Ashour A. Ahmed and co-authors are responsible for reviewing, and editing the manuscript.

URL: http://dx.doi.org/10.1016/j.scitotenv.2017.02.007

QR:

Ashour Ahmed GLP-SOM

Reproduced with the permission of Elsevier

Science of the Total Environment 586 (2017) 527–535

Contents lists available at ScienceDirect

Science of the Total Environment

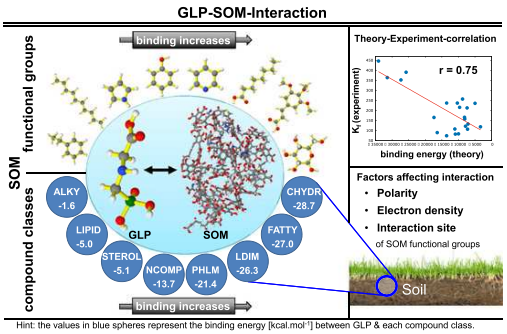
journal homepage: www.elsevier.com/locate/scitotenv

Glyphosate binding in soil as revealed by sorption experiments and quantum-chemical modeling

Peter Gros [a,*], Ashour Ahmed [b,c], Oliver Kühn [b], Peter Leinweber [a]

[a] University of Rostock, Soil Science, Justus-von-Liebig-Weg 6, D-18059 Rostock, Germany
[b] University of Rostock, Institute of Physics, Albert-Einstein-Str. 23-24, D-18051 Rostock, Germany
[c] University of Cairo, Faculty of Science, Department of Chemistry, 12613 Giza, Egypt

GRAPHICAL ABSTRACT



ARTICLE INFO

Article history:
Received 9 December 2016
Received in revised form 1 February 2017
Accepted 1 February 2017
Available online 21 February 2017

Editor: Dr. D. Barcelo

Keywords:
Glyphosate (GLP)
Soil organic matter (SOM)
Sorption isotherms
Molecular modeling
Quantum chemical calculations

ABSTRACT

The herbicide glyphosate (GLP) is supposed to be rapidly degraded or adsorbed strongly by soil solids but findings in soil years after application and concentrations in waters above legal limits question a harmless disappearance. Therefore, we conducted batch sorption experiments with 23 thoroughly characterized arable surface soils, correlated isotherm coefficients with numerous inorganic and organic soil parameters, and investigated GLP-SOM-complexes by quantum-chemical modeling. The Freundlich sorption model yielded the best fits, and coefficients K_f and n_f were correlated positively with the contents of clay/silt. The contents of organic C (C_{org}) and of the mass-spectrometrically determined SOM-compound classes carbohydrates, phenols/lignin monomers, lignin dimers, lipids, alkylaromatics, non-amide N and amides and sterols all were strongly positively correlated with the Freundlich coefficients. Quantum-chemical modeling showed that both GLP phosphonic and carboxylic functional groups interact similarly with the polar SOM functional groups via H-bond formation but the GLP phosphonic moiety is most important in the GLP-SOM-interaction. Moreover, the interaction mechanism between GLP and every modeled SOM-compound class was explored indicating the importance of the polarity, electron density, and site of attack of the SOM fragments in the GLP-SOM-interaction. Partial binding energies were combined to a total binding energy ($E_{B,tot}$) of GLP to the SOM, considering the mass spectrometrically quantified compound classes for each individual soil sample. The resulting strongly positive correlation between the $E_{B,tot}$ and the C_{org} provided compelling new experimental-theoretical evidence for the importance of SOM on the GLP binding and its behavior in the environment. In conclusion, the multitude of binding mechanisms to clay minerals and organic colloids make the occurrence of free GLP rather unlikely but a leaching of GLP complexes via preferential flow path through soil and transfer to waterways rather likely.

© 2017 Elsevier B.V. All rights reserved.

* Corresponding author.
E-mail addresses: peter.gros@uni-rostock.de (P. Gros), ashour.ahmed@uni-rostock.de (A. Ahmed), oliver.kuehn@uni-rostock.de (O. Kühn), peter.leinweber@uni-rostock.de (P. Leinweber).

http://dx.doi.org/10.1016/j.scitotenv.2017.02.007
0048-9697/© 2017 Elsevier B.V. All rights reserved.

1. Introduction

Glyphosate (GLP, N-(phosphonomethyl)-glycine) is the most used non-selective herbicide in the world. For 2017 a total application of 1.35 Mio t is forecasted (Global Analysists Industry Inc., 2011). GLP is highly soluble in water (12 g L^{-1}), has a low partitioning coefficient for the octanol-water system (log $K_{ow} = -3.4$), and is charged according to the soil pH ($pK_{a1} = 0.8$, $pK_{a2} = 2.23$, $pK_{a3} = 5.46$, $pK_{a4} = 10.14$; Tomlin, 1997; Liu et al., 2016). Therefore, early work of Glass (1984) plausibly reported that GLP is strongly bound to mineral surfaces and assumed that it should be nearly immobile in mineral soils. Nevertheless, GLP and its primary metabolite aminomethylphosphonic acid (AMPA) have been detected in ground and surface water (e.g., Coupe et al., 2012; Van Stempvoort et al., 2014) and recently also in the Baltic Sea (Skeff et al., 2015). Since this contradicts the assumed immobility, the influence of soil parameters on GLP sorption mechanisms still is a scientific challenge.

It has been reported that sorption is influenced mainly by (1) soil texture (Sprankle et al., 1975), (2) mineral composition (Dion et al., 2001; Piccolo et al., 1994), and (3) pH (Sidoli et al., 2016; Kumari et al., 2016). For soil organic matter (SOM) negative (e.g. Torstensson, 1985; Gerritse et al., 1996; Ololade et al., 2014; Arroyave et al., 2016) and positive (e.g., Roy et al., 1989; Piccolo et al., 1995; Okada et al., 2016) effects on GLP binding have been reported. Studies on SOM model systems concluded that (1) GLP binds to organic molecules via H-bonds leading to disaggregation of complex structures (Miano et al., 1992), (2) binding is positively influenced by aromatic substances (Albers et al., 2009) and (3) sorption capacity is similar or even higher compared with those of pure soil minerals or bulk soils (Piccolo et al., 1996). Despite these findings from model experiments, the effect of non-extracted, chemically unaltered SOM on GLP sorption in bulk soil samples is still unclear. Furthermore, the molecular structure of SOM also may have an impact on GLP sorption, but this has not yet been studied with bulk soil and SOM.

Pyrolysis field-ionization mass spectrometry (Py-FIMS) is a versatile analytical method for the determination of SOM building blocks (Leinweber et al., 2009), and it has been successfully applied to study the binding of xenobiotics to SOM (e.g. Thiele-Bruhn et al., 2004). Molecular modeling is a flexible tool for the investigation of elementary processes in soils (Ahmed et al., 2016; Schaumann and Thiele-Bruhn, 2011; Sündermann et al., 2015). It complements analytic and kinetic experiments in the development of a molecular level understanding of soil processes such as the interaction of xenobiotics with, for example, SOM or soil minerals. In general, modeling of SOM is not straightforward due to its high variability in chemical composition, spatial architecture, and multi-phase behavior (Senesi et al., 2009). Recently, Ahmed et al. (2014a, 2014b) have developed a new approach for SOM modeling based on SOM characterization by different analytical techniques (Ahmed et al., 2012), which is combined with quantum chemical and molecular dynamics calculations. The model is based on a large test set of separate representative molecules, covering the most relevant functional groups that exist in analytically quantified compound classes (Ahmed et al., 2012). The validity of this model has been demonstrated by comparison with experimental sorption of polar and non-polar xenobiotics on well-characterized soil samples (Ahmed et al., 2016). However, this promising combination of experimental and theoretical approaches has not yet been applied to explore the interaction of GLP with soil components, especially SOM.

The general objective of the present study was to disclose the binding nature between GLP and SOM at a molecular level. Specifically, we want to deduce which soil constituents are involved in GLP binding by correlating their contents with the sorption coefficients from batch experiments. Complementary, we performed quantum chemistry based molecular modeling of GLP-SOM binding by extending the recent SOM model by Ahmed et al. (2016). Linking the molecular modeling with the experimental sorption and correlation results will allows us to develop a molecular level understanding of GLP binding to soil.

2. Materials and methods

2.1. Soils samples and basic soil properties

Soil samples were selected from mineral A-horizons of agricultural sites in Germany and Sweden (Table 1). Agricultural uses involved arable (Ap-horizons, n = 10), grassland (Ah-horizons, n = 6) and short rotation coppice (SRC, Ah-horizons, n = 7). The soils represent most major soil units of agricultural soils in Pleistocene landscapes in Central and Northern Europe. Texture classes ranged from loamy sand to clay, and the pH values from strongly acidic (4.03) to slightly alkaline (7.19). The C_{org} contents range from 2.8 to 31.1 mg kg^{-1} and are typical for agricultural soils with sandy to clayey texture; they represent mineral soils ($C_{org} < 75$ g kg^{-1}). These fields had not been treated with GLP so far.

Air dry samples were sieved <2 mm. Basic properties were analyzed: (1) particle size distribution by combined sieving (sand, 2 to 0.063 mm) and sedimentation (silt, 0.063 to 0.002 mm, and clay, <0.002 mm) analysis according to E DIN ISO 11277:06.1994–06 (Sedimat 4–12, Umwelt-Geräte-Technik GmbH, Müncheberg, Germany), (2) pH in 0.01 M $CaCl_2$ (pH-Meter 540 GLP WTW, Schott, Germany), (3) carbon and nitrogen content via CNS-analysis (VARIO EL analyser, Elementar Analysensysteme GmbH, Hanau, Germany), (4) detailed molecular-chemical composition of SOM.

For most samples (n = 18 archived soil samples) the SOM composition had been analyzed in previous projects by Py-FIMS (Leinweber et al., 1999: sample numbers 18, 19, 20; Jandl et al., 2015: sample numbers 1, 2, 21, 22; Acksel et al., 2016: sample numbers 4, 7, 8, 12, 13; Barth et al., submitted Applied Soil Ecology: sample numbers 3, 5, 6, 11, 16, 17). The methodology of Py-FIMS, also applied to the remaining n = 5 samples (sample numbers 9, 10, 14, 15 and 23) for the present study, has been described in detail by Leinweber et al. (2009). For Py-FIMS analysis about 5 mg of each sample was thermally degraded in the ion source mass spectrometer. The samples were heated under a high vacuum from 110 to 700 °C and 60 magnetic scans were recorded for the mass range of 55 to 500 a.u. Total ion intensity (TII) which is the sum of ion intensities of all recorded marker signals was calculated for each sample. Furthermore, the scans provide information about abundance and chemical structure of the chemical compounds. These chemical compounds are classified into 10 compound classes that are carbohydrates (CHYDR), phenols/lignin monomers (PHLM), lignin dimers (LDIM), lipids, alkenes, fatty acids, and n-alkyl esters (LIPID), alkylaromatics (ALKY), heterocyclic N and nitriles (NCOMP), sterols (STERO), amides (amino acids, peptides, amino sugars)/ (PEPTI), suberin (SUBER) and free fatty acids (*n*-C16 to *n*-C34), (FATTY). The particular ion intensity of each compound class was calculated according to well-established modes of spectra interpretation (Ahmed et al., 2012; Schulten et al., 1999). The contents of these compound classes based on soil weight [mg kg^{-1}] were calculated by multiplying the relative proportions of ion intensity (%TII) of these compound classes with the SOM content ($C_{org} \times 2$, [g kg^{-1}]). This calculation assumed that the total ion intensity is proportional to the SOM content. Detailed descriptions of the Py-FIMS methodology (Schulten, 1999) and statistical evaluations of sample weight and residue, volatilized matter, and total ion intensities were given by Sorge et al. (1993).

2.2. Sorption isotherms

Sorption experiments were carried out according to the method of Waiman et al. (2012) with slight modification. 2 g of soil were added to 10 mL of potassium chloride (KCl, purchased from Carl Roth, p.a.) solution (0.1 M) in 15 mL centrifuge tubes and spiked with GLP (purchased from Dr. Ehrenstorf, 99,0%) at 10 initial concentration levels (0, 10, 15, 20, 25, 30, 50, 75, 100, 150 mg L^{-1}) in five replicates. The concentration level of 0 mg L^{-1} was used for blank subtraction. Sorption was carried out over night for 16 h at room temperature with overhead shaking. Equilibrium soil solution was centrifuged (10 min, 1558 g) and 3 mL of the supernatant were used for determining the GLP

Table 1
Sampling sites and soil properties of tested samples: texture, pH and soil organic carbon content (C_{org}).

Sample						Texture			Texture class	pH	C_{org}
No.	location		use		Horizon	clay (%)	silt (%)	sand (%)	(international, USDA)		g kg^{-1}
1[b]	Ultuna, S	59°47″ N, 17°39″ E	SRC	Cambisol	Ah	58	33	9	clay	6.60	2.8
2[b]	Ultuna, S	59°47″ N, 17°39″ E	SRC	Cambisol	Ah	58	33	9	clay	5.65	4.0
3[d]	Gülzow, D	53°27″ N, 10°29″ E	grassland	Stagnic Luvisol	Ap	5	24	71	sandy loam	6.03	7.1
4[c]	Niendorf, D	53°59″ N, 10°49″ E	grassland	Chernozem	Ap	10	33	57	sandy loam	5.72	7.4
5[d]	Vipperow, D	53°19″ N, 12°41″ E	SRC	Luvisol	Ah	5	22	73	sandy loam	4.03	8.1
6[d]	Cahnsdorf, D	51°51″ N, 13°44″ E	grassland	Luvisol	Ah	2	23	75	loamy sand	6.50	8.3
7[c]	Timmendorf, D	53°59″ N, 10°47″ E	arable	Chernozem	Ap	11	27	61	sandy loam	5.47	8.6
8[c]	Niendorf, D	53°59″ N, 10°49″ E	arable	Chernozem	Ap	10	27	63	sandy loam	5.83	9.2
9	Quersa, D	51°18″ N, 13°38″ E	grassland	Luvisol	Ap	14	24	62	sandy loam	5.57	10.7
10	Quersa, D	51°18″ N, 13°38″ E	grassland	Luvisol	Ap	7	16	77	loamy sand	5.37	12.2
11[d]	Cahnsdorf, D	51°51″ N, 13°44″ E	SRC	Luvisol	Ap	2	23	75	loamy sand	5.36	12.6
12[c]	Großenbrode, D	54°21″ N, 11°05″ E	arable	Chernozem	Ap	17	18	66	sandy loam	6.30	12.8
13[c]	Niendorf, D	53°59″ N, 10°49″ E	arable	Chernozem	Ap	11	27	62	sandy loam	5.90	12.8
14	Quersa, D	51°18″ N, 13°38″ E	arable	Luvisol	Ap	11	28	61	sandy loam	5.34	13.0
15	Quersa, D	51°18″ N, 13°38″ E	arable	Luvisol	Ap	11	30	60	sandy loam	5.48	14.8
16[d]	Vipperow, D	53°19″ N, 12°41″ E	grassland	Luvisol	Ah	5	22	73	sandy loam	4.35	15.1
17[d]	Gülzow, D	53°27″ N, 10°29″ E	SRC	Stagnic Luvisol	Ap	5	24	71	sandy loam	6.60	15.8
18[a]	Bad Lauchstäd, D	51°23″ N, 11°47″ E	arable	Chernozem	Ap	19	75	6	silt loam	6.97	16.3
19[a]	Bad Lauchstäd, D	51°23″ N, 11°47″ E	arable	Chernozem	Ap	21	69	9	silt loam	7.19	19.4
20[a]	Bad Lauchstäd, D	51°23″ N, 11°47″ E	arable	Chernozem	Ap	18	72	10	silt loam	6.39	23.9
21[b]	Enköpping, S	59°33″ N, 17°00″ E	SRC	Cambisol	Ah	39	40	21	clay loam	6.70	27.0
22[b]	Enköpping, S	59°33″ N, 17°00″ E	SRC	Cambisol	Ah	39	40	21	clay loam	5.63	30.0
23	Quersa, D	51°18″ N, 13°38″ E	arable	Luvisol	Ap	16	19	64	sandy loam	5.25	31.1
Min						2.0	16.0	5.8		4.03	2.8
Max						58.0	75.1	76.6		7.19	31.1

S: Sweden, D: Germany; SRC: short rotation coppice.
[a] Leinweber et al. (1999)
[b] Jandl et al. (2015)
[c] Acksel et al. (2016)
[d] Barth et al. (submitted to Applied Soil Ecology).

concentration. For derivatization, 0.5 mL borate buffer solution (pH 9, sodium tetra borate decahydrate purchased from Carl Roth, >99.8%) and 0.5 mL of 9-Fluorenylmethoxycarbonyl chloride (FMOC-Cl, purchased from Sigma Aldrich, >99.9%) in acetonitrile (1 g L^{-1}) were added to the 3 mL supernatant in 15 mL centrifuge tubes. After 2 h reaction with occasionally shaking at room temperature 4 mL of dichlormethane (purchased from Carl Roth, >99.5%) were added and shaken vigorously to remove any byproducts of FMOC-Cl and centrifuged (10 min, 1558 g). Detection of the GLP-FMOC-complex in the aqueous phase was carried out with a Specord 40 UV/Vis-spectrometer (Analytik Jena, Germany) at 265 nm. The limit of detection was 0.233 mg L^{-1} and the limit of quantification 0.260 mg L^{-1}. Blank correction was conducted by measuring the background signal of the method and soil matrix with the zero concentration level (0 mg L^{-1}) for GLP and was further on subtracted from the signals with GLP addition.

Adsorbed amounts of GLP, C_{ads} (mg kg^{-1}), are calculated by subtracting the measured soil equilibrium concentration, C_{eq} (mg L^{-1}), from the initial, C_0, GLP concentration added. The following isotherm model equations (1: Freundlich, 2: Langmuir, 3: Brunauer-Emmet-Teller (BET)) have been applied to our datasets:

$$C_{ads} = K_f C_{eq}^{n_f} \quad (1)$$

where K_f is Freundlich unit capacity (mg^{1-nf} L^{nf} kg^{-1}) and n_f is the Freundlich exponent describing the non-linearity.

$$C_{ads} = q_{L,max} \frac{K_L C_{eq}}{1 + K_L C_{eq}} \quad (2)$$

where K_L (L mg^{-1}) is the unit capacity and $q_{L,max}$ (mg kg^{-1}) is the maximum adsorbed GLP concentration to cover the surface with a monolayer of GLP molecules.

$$C_{ads} = \frac{q_{BET,max} K_{BET} C_{eq}}{(C_{sat} - C_{eq})\left(1 + \frac{(K_{BET}-1) C_{eq}}{C_{sat}}\right)} \quad (3)$$

where K_{BET} (L mg^{-1}) is the BET unit capacity, $q_{BET,max}$ (mg kg^{-1}) is the maximum amount of GLP adsorbed as a monolayer at the soil surface and C_{sat} (g L^{-1}) is the solubility of GLP.

The determination of the isotherm coefficients (1: K_f, n_f; 2: K_L, $q_{L,max}$; 3: K_{BET}, $q_{BET,max}$) was performed in the limit of their linearized forms.

2.3. SOM modeling and quantum chemical calculations

The GLP-SOM-interactions were simulated through 1:1 complex formation between GLP and the relevant SOM fragment, i.e. 1 GLP + 1 SOM-fragment ➔ GLP-SOM-complex. Here, SOM has been modeled by a set of representative SOM fragments covering a broad range of functional groups as well as compound classes of SOM. Based on the Py-FIMS data, the current SOM model was chosen to cover several SOM compound classes involving 1- ALKY (represented by ethylbenzene, and ethylnaphthalene), 2- LIPID (represented by long-chain alkane and conjugated alkene), 3- NCOMP (represented by pyrrole, pyridine, and butanenitrile), 4- phenols (represented by phenol), 5- lignins (represented by phenol and 3,4,5-trimethoxy cinnamic acid), 6- PHLM (was assembled from the modeled phenols and lignins), 7- LDIM (was assembled from the modeled lignins), 8- STEROL (represented by a segment of beta-sitosterol (sterol1) and the whole beta-sitosterol (sterol2)), 9- CHYDR (represented by glucose in the open (glucose1) and cyclic (glucose2) forms), and 10- FATTY (represented by caprylic acid).

The initial geometries for each GLP-SOM-complex were constructed by selecting the expected preferential binding situations between GLP and the SOM fragment. To simulate the aqueous soil solution, which is an important factor controlling the GLP-SOM-interaction, solvation by

water was included via an implicit treatment through the conductor-like polarizable continuum model (CPCM, Cossi et al., 2003). The calculations were performed using density functional theory (DFT). Here, the Becke, three-parameter, Lee-Yang-Parr hybrid functional (B3LYP) (Becke, 1988; Lee et al., 1988) with a 6–311++G(d,p) basis set (Hehre et al., 1972) and Grimme's D3 dispersion correction (Grimme et al., 2011) has been applied. The effect of the basis set superposition error (BSSE) has been corrected using the counterpoise scheme (Jansen and Ros, 1969). Full geometry optimization, using CPCM, was performed for each GLP-SOM-complex as well as for all individual species (GLP and each SOM system) using the gradient minimization technique. Harmonic vibrational frequencies were calculated for all optimized geometries. These geometries are characterized by having zero gradient norms and positive harmonic vibrational frequencies. All calculations have been performed using the Gaussian09 program package (Frisch et al., 2013).

For the complexation reaction, GLP + SOM fragment ➔ GLP-SOM-complex, the binding energy (E_B) between GLP and the SOM fragment is calculated as follows:

$$E_{B_i} = E_{(GLP-i)complex} - (E_{GLP} + E_i) \quad (4)$$

where, E_{B_i} is the binding energy of GLP to the SOM fragment *i*, $E_{(GLP-i)complex}$ is the energy of the complex of GLP with the SOM fragment *i*, E_{GLP} is the energy of GLP, and E_i is the energy of the SOM fragment *i*. Similarly, the corresponding binding free energies (ΔG_{B_i}) of GLP-SOM-complexes were calculated by including the zero point energy and thermal correction to the Gibbs free energy.

The representative SOM fragments collectively form SOM building blocks as determined by Py-FIMS (Ahmed et al., 2012). The average binding energy of GLP to a SOM building block *j*, $\langle E_B \rangle_j$, is given by

$$E_{Bj} = \frac{\sum_i E_{Bi}}{n} \quad (5)$$

where *n* is number of the modeled SOM fragments in the SOM building block *j*. Having a well-characterized soil sample, containing particular proportions of SOM building blocks, one can estimate the dependence of the binding energy of GLP to the whole SOM on the binding energy of GLP to each SOM building block as well as on the proportion of each SOM building block. To this end, one can formulate the binding energy of GLP to whole SOM (E_B^{SOM}, the total binding energy) as follows:

$$E_B^{SOM} = \sum_j E_{Bj} * I_j \quad (6)$$

where I_j is the Py-FIMS ion intensity of particular SOM building blocks *j* (in % SOM). This means that E_B^{SOM} was approximated as sum of the binding energies of GLP to the SOM building blocks weighted by their ion intensities that are determined by Py-FIMS. By replacing E_B with ΔG_B in eqs. 5 and 6, one can introduce the following equations:

$$\Delta G_{Bj} = \frac{\sum_i \Delta G_{Bi}}{n} \quad (7)$$

$$\Delta G_B^{SOM} = \sum_j \Delta G_{Bj} * I_j \quad (8)$$

where $\langle \Delta G_B \rangle_j$ is the binding free energy of GLP to the SOM building block *j*, ΔG_{Bi} is the binding free energy of GLP to the SOM fragment *i*, and ΔG_B^{SOM} is the binding free energy of GLP to the whole SOM.

3. Results and discussion

3.1. Isotherm models and correlation with soil parameters

Three different models (non-linear Freundlich, Langmuir, BET) were tested and, overall, the Freundlich model gave the best fit of the sorption data. The coefficients of the non-linear Freundlich isotherms covered a wide range, i.e. from 74 to 446.5 $mg^{1-nf} L^{nf} kg^{-1}$ (K_f) and 0.40 to 1.21 (n_f) (Table 2). Except for samples 1, 16 and 22 the non-linear Freundlich model described the GLP sorption best. Generally, the coefficients of determination (R^2) were smaller for the Langmuir (mean $R^2 = 0.769$) and the BET models (mean $R^2 = 0.613$), indicating that these models described the GLP sorption worse.

Fig. 1 shows two of the measured isotherms according to Freundlich with highest (sample 22) and lowest (sample 13) sorption behavior. All other 21 sorption isotherms are located between these two shown. Sample 22 is a Cambisol of clay loam texture with high C_{org} content (30.0 g kg^{-1}) whereas sample 13 is a Chernozem of sandy loam texture and morderate C_{org} content (12.8 g kg^{-1}). Both samples have a similar pH ($\Delta pH = 0.27$). These properties, especially coincidence of high clay and C_{org} contents in the Cambisol 22, plausibly explain why it has the highest binding capacity for GLP.

Our comparisons of sorption models agree with earlier works by Hance (1976), Glass (1984) and Piccolo et al. (1994) who also found the non-linear Freundlich model as best fitting sorption data. Therefore, we use only the Freundlich coefficients in further correlations with soil parameters. In summary, the range of K_f and n_f values in Table 2 indicates a weaker GLP sorption in our soils compared to the studies of Wang et al. (2005), almost similar GLP sorption compared to Vereecken (2005), Mamy et al. (2007), Albers et al. (2009), Bergström et al. (2011) and Ghafoor et al. (2013), and a slightly stronger GLP sorption compared to Okada et al. (2016) (See Table 3). Considering the completely different soil mineralogy of the Chinese soils (Wang et al., 2005) the overall good agreement of our sorption coefficients with those from all other studies of soils from temperate regions confirm that the present data set well represents soil and management conditions in Central to Northern Europe.

Sorption of the structurally similar herbicide glufosinate, also a phosphonated derivate of the amino acid glycine, yielded lower K_f values in the range 0.4 to 39.7 in a tropical silty clay and clay (Jariani et al., 2010). For other herbicides also smaller mean K_f values were reported for nonlinear Freundlich isotherm models, e.g., 0.3 for bentazone and 3.3 for isoproturon (Ghafoor et al., 2013), 3.1 for metamitron, 3.8 for phenimediphan, and 4.0 for ethofumasate (Autio et al., 2004). Therefore, these data comparisons indicate a relatively strong GLP sorption, thus supporting the general assumption concerning the fate of this herbicide in soil (Pessagno et al., 2005; Vereecken, 2005).

PEARSON correlation coefficients, r, were determined between the non-linear Freundlich isotherm coefficients (Table 2) and (1) pH and contents of inorganic soil constituents such as mineral size classes integrated in the texture (Table 1), (2) the content of SOM measured as C_{org} (Table 1) and (3) the concentrations of compound classes as derived from Py-FIMS (data in Supplementary Table S1). These data confirm the great diversity of soils under study with respect to SOM contents (2.8 to 31.1 g C_{org} kg^{-1}, Table 1) and composition. The SOM compositions of the investigated Chernozems (n = 8, Table 1), Luvisols (n = 11) and Cambisols (n = 4) well agree with samples from the corresponding soil units worldwide (Leinweber et al., 1999).

Results of correlations are visualized in a two-dimensional diagram that plots the PEARSON correlation coefficients between a soil parameter and K_f on the x-axis versus the correlation between the parameter and n_f on the y-axis. Neither K_f nor n_f shows any correlation with pH (Fig. 1). The K_f values were correlated significantly negatively with sand content and significantly positively with the clay and silt contents. Furthermore, there are close correlations between K_f and the contents of C_{org} as well as the quantity of eight out of the ten compound classes. The

Table 2
Calculated isotherm coefficients of non-linear Freundlich, Langmuir and BET models.

Sample	Freundlich			Langmuir			BET		
	$K_f \pm \sigma[K_f]$	$n_f \pm \sigma[n_f]$	R^2	$K_L \pm \sigma[K_L]$	$q_{L,max} \pm \sigma[q_{L,max}]$	R^2	$K_{BET} \pm \sigma[K_{BET}]$	$C_{BET,max} \pm \sigma[q_{BET,max}]$	R^2
1	118.8 ± 3.3	0.43 ± 0.09	0.352	0.148 ± 0.027	191 ± 66	0.518	875 ± 1170	0.849 ± 1.13	0.013
2	235.9 ± 2.0	1.21 ± 0.07	0.894	0.077 ± 0.007	3259 ± 5504	0.781	17 ± 1055	10,639 ± 677,260	0.000
3	121.6 ± 0.5	0.61 ± 0.01	0.976	1.379 ± 0.120	242 ± 32	0.755	1617 ± 93	0.534 ± 0.03	0.874
4	132.4 ± 0.5	0.69 ± 0.02	0.980	0.328 ± 0.013	592 ± 115	0.939	1674 ± 97	0.583 ± 0.03	0.874
5	213.0 ± 0.6	0.60 ± 0.01	0.984	0.665 ± 0.022	614 ± 74	0.960	3847 ± 129	0.230 ± 0.01	0.959
6	106.8 ± 0.4	0.64 ± 0.01	0.985	0.497 ± 0.022	368 ± 46	0.924	1336 ± 85	0.657 ± 0.04	0.852
7	107.8 ± 1.0	0.73 ± 0.03	0.913	0.778 ± 0.066	278 ± 45	0.764	715 ± 180	2.049 ± 0.52	0.269
8	166.2 ± 0.8	0.68 ± 0.02	0.964	0.910 ± 0.052	375 ± 61	0.882	2070 ± 182	0.503 ± 0.04	0.759
9	237.0 ± 1.6	0.64 ± 0.03	0.927	1.396 ± 0.122	381 ± 88	0.759	3395 ± 267	0.316 ± 0.02	0.790
10	157.5 ± 0.7	0.60 ± 0.02	0.967	2.859 ± 0.278	219 ± 28	0.711	2302 ± 200	0.387 ± 0.03	0.756
11	82.3 ± 0.3	0.75 ± 0.01	0.988	0.260 ± 0.012	437 ± 70	0.921	681 ± 64	1.778 ± 0.17	0.725
12	83.6 ± 0.5	0.73 ± 0.02	0.977	0.249 ± 0.010	459 ± 68	0.935	676 ± 77	1.766 ± 0.20	0.654
13	74.0 ± 0.3	0.82 ± 0.01	0.989	0.112 ± 0.004	759 ± 168	0.958	455 ± 53	3.550 ± 0.41	0.632
14	257.2 ± 1.4	0.51 ± 0.02	0.945	5.794 ± 0.684	257 ± 38	0.642	6322 ± 309	0.129 ± 0.01	0.913
15	215.6 ± 2.5	0.47 ± 0.04	0.785	1.684 ± 0.335	309 ± 91	0.412	3618 ± 399	0.247 ± 0.03	0.662
16	237.2 ± 3.2	0.40 ± 0.04	0.728	2.047 ± 0.191	354 ± 62	0.782	5274 ± 420	0.141 ± 0.01	0.823
17	89.9 ± 0.3	0.73 ± 0.01	0.992	0.327 ± 0.011	409 ± 44	0.957	817 ± 74	1.378 ± 0.12	0.741
18	390.7 ± 3.1	0.58 ± 0.03	0.926	5.059 ± 0.499	321 ± 61	0.715	10,671 ± 782	0.086 ± 0.01	0.812
19	241.3 ± 2.1	0.73 ± 0.04	0.879	4.466 ± 0.644	217 ± 34	0.540	1959 ± 636	0.807 ± 0.26	0.184
20	352.5 ± 3.8	0.72 ± 0.04	0.858	1.423 ± 0.142	524 ± 180	0.722	3149 ± 793	0.516 ± 0.13	0.273
21	364.0 ± 5.6	0.94 ± 0.09	0.732	0.151 ± 0.018	2354 ± 5210	0.632	655 ± 1751	9.004 ± 24.06	0.003
22	446.5 ± 7.4	0.62 ± 0.09	0.678	1.911 ± 0.302	721 ± 118	0.690	10,229 ± 1611	0.096 ± 0.02	0.691
23	425.4 ± 4.2	0.62 ± 0.04	0.894	3.779 ± 0.460	407 ± 109	0.692	40,483 ± 4933	0.016 ± 0.00	0.616
Min	74.0	0.40		0.077	190.9		16.6	0.016	
Max	446.5	1.21		5.794	3259		40,483	10,639	
Mean			0.883			0.765			0.603

strongest correlations were derived for carbohydrates, alkylaromatic compounds, phenols and lignin monomers, N-containing (heterocyclic) compounds, peptides, lignin dimers and lipids. The contents of suberins were weakly correlated with K_f but sterols and fatty acids seemed to have no significant effect on GLP sorption.

The non-correlation between pH and GLP sorption (Fig. 2) disagrees with McConnel et al. (1985), Waiman et al. (2012) and Sidoli et al. (2016) who reported negative correlations between pH and GLP sorption. This discrepancy can be explained by the use of pure minerals at varying pH in the sorption experiments of McConnel et al. (1985) and Waiman et al. (2012). Sidoli et al. (2016) used similar bulk soils but a different methodological approach: a lower range of six initial solute concentrations (0.05 to 5 mg L^{-1}) in triplicates and quantification by the scintillation method. On the other hand, Ghafoor et al. (2013) found no correlation between pH and K_f values although they also used five initial solute concentrations (0.01 to 1.0 mg L^{-1}) in two replicates. Therefore, the pH effect on GLP sorption may have been overestimated on the basis of model studies (McConnel et al., 1985; Waiman et al., 2012), but it is still not completely understood even if publications with similar methodology, samples and concentration ranges are evaluated. For soil texture, the positive effect of clay and silt contents (Fig. 2) confirms all previous reports (e.g., Glass, 1984; Spann and Hargreaves, 1994) and reviews (Vereecken, 2005; Borggaard and Gimsing, 2008).

For the influence of SOM quality two groups of compound classes can be distinguished which favor sorption: (a) substances with phenolic functional groups (alkylaromatics, phenolics/lignin monomers and lignin dimers) and (b) H-bond-providing compounds (N-containing heterocyclic compounds, peptides and carbohydrates). This generalization is in good agreement with findings for model systems, in which H-bonds between GLP and soil humic fractions were detected by IR spectroscopy (Miano et al., 1992; Albers et al., 2009). However, limitations in the sensitivity of previous spectroscopic and spectrometric SOM characterizations prevented a more detailed insight into the influence of SOM moieties on the GLP binding.

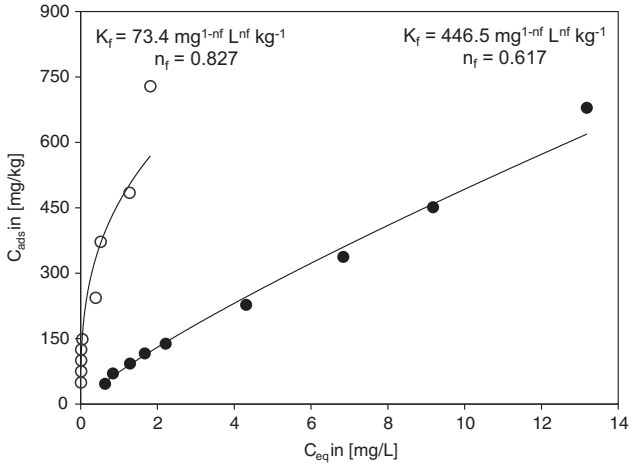


Fig. 1. Isotherm with highest (○, Sample 22) and lowest (•, Sample 13) sorption behavior.

3.2. Quantum chemical modeling

The optimized geometries of the GLP-SOM-complexes compiled in Fig. 3 provide strong evidence for the effect of the high polarity of GLP.

Table 3
Parameters of Freundlich equation (K_f, n_f) reported in various studies.

	K_f [mg^{1-nf} L^{nf} kg^{-1}]	n_f	Number of samples used in publication
Vereecken, (2005), Review	0.6–249	0.26–1.26	30
Wang et al. (2005)	166.2–2751	0.17–0.51	3
Mamy et al. (2016)	17.6–276	0.76–0.88	3
Albers et al. (2009)	21–87	0.69–0.90	6
Bergström et al. (2011)	40–118	0.92–0.95	2
Ghafoor et al. (2013)	24–149	0.92–0.99	16
Okada et al. (2016)	101–457	0.33–0.52	3
Present study	74–446.5	0.40–1.21	23

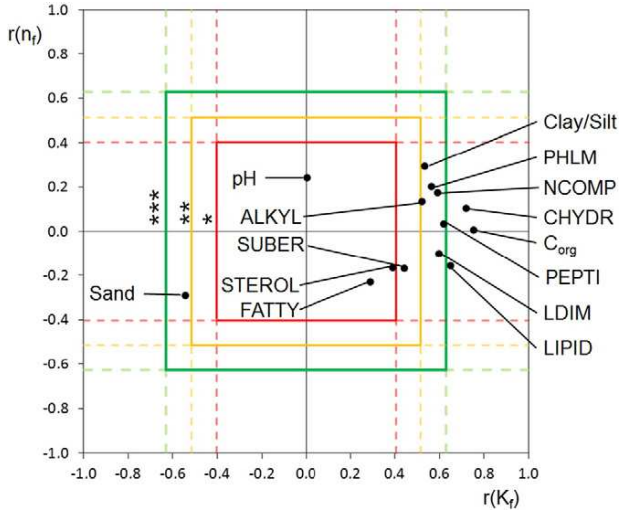


Fig. 2. Plot of Pearson correlation coefficients of soil parameters and SOM compounds versus coefficients of the non-linear Freundlich isotherm model K_f and n_f. Levels of significance are marked as follows: *|P| < 0.5 (red line). **|P| < 0.1 (yellow line). ***|P| < 0.01 (green line).

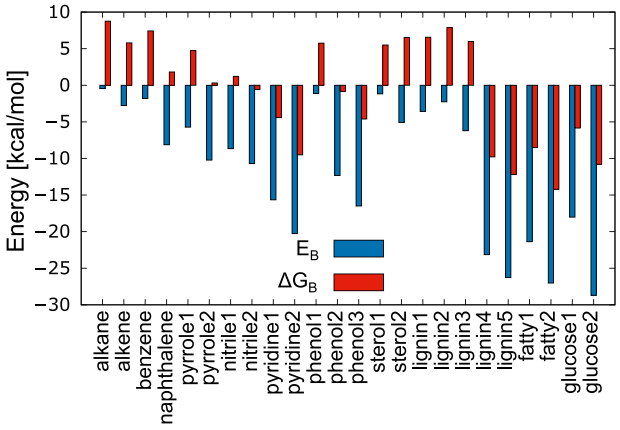


Fig. 4. Binding energies (blue) and binding free energies (red) for GLP with the modeled SOM systems in the GLP-SOM complexes at the B3LYP/D3/6–311++G(d.p) level of theory and using the CPCM model.

It comprises several active polar centers including negative (O atoms of phosphonic and carboxylic groups, and the N atom of the amino group) as well as positive (H atoms of phosphonic, carboxylic, and amino groups) centers of interaction. Accordingly, for GLP one observes several strong interaction motifs, especially with the polar SOM representative fragments that show H-bond formation. A closer look at the optimized geometries of the GLP-SOM-complexes indicates that GLP forms one to four H-bond(s) with the polar SOM fragments. The length of these H-bonds varies from 1.6 to 2.6 Å. Furthermore, similar to our previous work, predominance of the dispersion interaction is observed for the interaction of GLP with those SOM fragments lacking polar functional groups.

With respect to the effect of SOM chemical composition on GLP-SOM-interaction, Fig. 4 and Supplemental Table S2 points to the importance of the SOM polarity. Here, interaction of the hydrophobic SOM systems with GLP yields the lowest binding energies $E_{B,i}$. A close examination reveals that GLP binds to the hydrophobic systems in the order: long-chain conjugated alkene > ethylnaphthalene > long-chain alkane > ethylbenzene. This indicates that an increase of the electron density of the hydrophobic systems will increase the binding energy to GLP. On the other hand, most

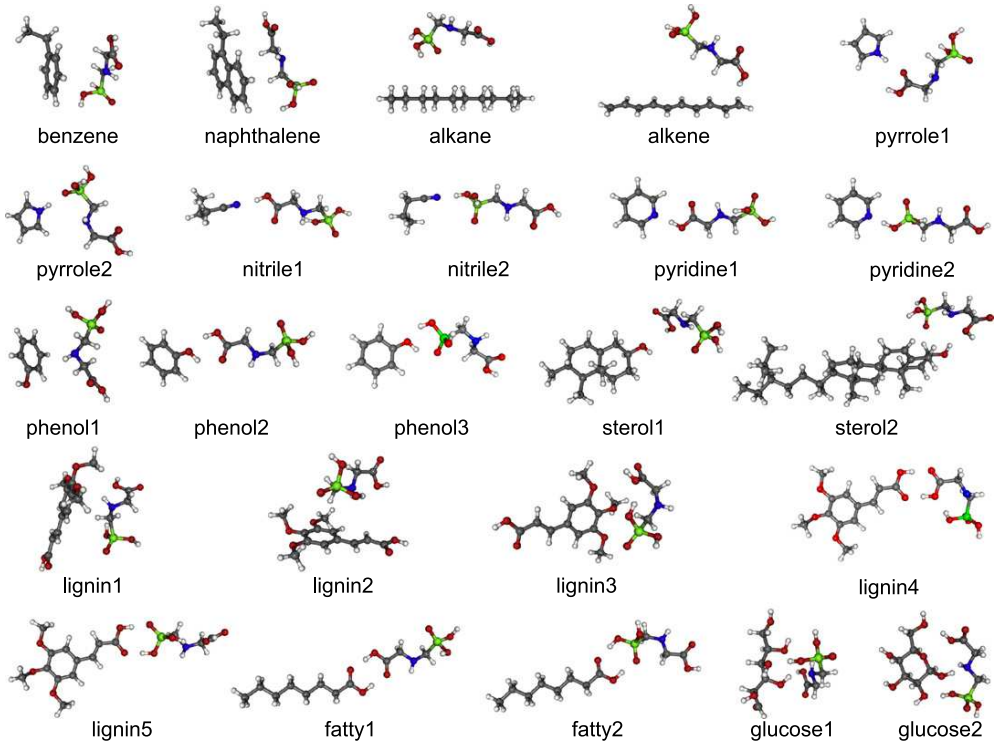


Fig. 3. Optimized geometries of GLP-SOM complexes at the B3LYP/D3/6–311++G(d.p) level of theory and using the CPCM model.

of the polar SOM systems exhibit several binding motifs for interaction with GLP. For N-containing compounds, two stable conformers are obtained for each complex, i.e. between GLP and pyrrole, butanenitrile, and pyridine (see Fig. 3). GLP binds to N-containing compounds in the order: pyridine2 > pyridine1 > nitrile2 > pyrrole2 > nitrile1 > pyrrole1. Thus, binding of GLP to 6-membered N-heterocycles is stronger than to 5-membered N-heterocycles. Clearly, the only difference between pyridine1 and pyridine2, pyrrole1 and pyrrole2, etc. is in the binding motif. The complexes of GLP with pyridine1, pyrrole1, and nitrile1 are due to formation of H-bonds between these SOM systems and the GLP's carboxylic group. In contrast, the second conformer for each complex is the outcome of the interaction of GLP through its phosphonic group. This implies that the GLP phosphonic functional group forms stronger H-bonds with SOM compared to the carboxylic one. This indicates that the GLP phosphonic functional group is more relevant than the carboxylic one for binding to SOM. Furthermore, three stable conformers are observed for the phenol-GLP-complex. The complex with the lowest binding energy (phenol1) is stabilized by the interaction of GLP with the phenol aromatic ring. For the other two complexes (phenol2 and phenol3), two H-bonds are observed for each complex. Here, the H-bonds of the phenolic O—H group of phenol with the GLP phosphonic group (phenol3) are stronger than those with the GLP carboxylic group (phenol2). Therefore, for a SOM fragment comprising polar and non-polar functional groups, the GLP binding strength has a pronounced dependence on the interaction site. Sterols show lower binding energies with GLP compared to phenols. Further, GLP binds to sterol2 stronger than to sterol1. This reflects the increase of binding strength with increasing molecular mass, molecular volume, and/or side chain length. For lignins, five energetically different conformers of the lignin-SOM-complex are found that have distinct binding motifs. The binding of GLP to the lignin monomer increases in the order lignin1 < lignin2 < lignin3 < lignin4 < lignin5. For the first three conformers, GLP interacts through its carboxylic and/or phosphonic functional groups with the lignin methoxy groups giving rise to H-bond(s). Strong double H-bonds between the lignin carboxylic acid and the GLP carboxylic and phosphonic functional groups are observed for the complex conformers lignin4 and lignin5, respectively. Further, GLP shows strong binding with the free fatty acids through interaction of the carboxylic functional group of caprylic acid with the GLP carboxylic (fatty1) and phosphonic (fatty2) functional groups. A strong interaction is observed between GLP and glucose. Finally, GLP shows stronger binding to the cyclic form of glucose (glucose2) than to its open form (glucose1).

If we take into account only the most stable conformer of each GLP-SOM-complex the following picture is obtained. GLP binds to the modeled SOM systems in the order glucose > fatty > lignin > pyridine > phenol > nitrile > pyrrole > alkene > sterol > ethylnaphthalene > alkane > ethylbenzene. This indicates that GLP binds to the hydrophilic SOM systems or hydrophobic ones containing polar functional groups stronger than to the hydrophobic systems lacking any polar functional group. Moreover, as the electron density of the hydrophobic or hydrophilic SOM systems increases, the GLP binding to their sorption sites increases as well. For details, compare the binding of GLP to the following sets of pairs: lignin and phenol, ethylnaphthalene and ethylbenzene, and alkene and alkane. Furthermore, GLP binds to the polycyclic aromatic rings (ethylnaphthalene) stronger than the monocyclic ones (ethylbenzene). Despite the stronger binding of GLP to naphthalenes compared to benzenes, the GLP-benzenes-binding can exceed the GLP-naphthalenes-binding if benzene is substituted by strong electron donating functional groups (such as OH in phenol, OCH_3 in lignin). In addition, GLP binds to N-heterocycles (pyridine and pyrrole) stronger than to alkyl aromatics (ethylnaphthalene and ethylbenzene). The binding energies of GLP to the individual models of SOM fragments have been used to calculate the binding energies of GLP to the corresponding compound classes (see eq. 5 and Supplemental Table S3). This shows that GLP binds to the SOM compound classes in the order: CHYDR (-28.7 kcal mol^{-1}) > FATTY (-27.0 kcal mol^{-1}) > LDIM (-26.3 kcal mol^{-1}) > PHLM (-21.4 kcal mol^{-1}) > NCOMP (-13.7 kcal mol^{-1}) > STEROL (-5.1 kcal mol^{-1}) > LIPID (-5.0 kcal mol^{-1}) > ALKY (-1.6 kcal mol^{-1}). This confirms the conclusion regarding the role of the polarity, electron density, and site of attack of the SOM fragments on the GLP-SOM-interactions.

Since the calculated binding energy for the complexation reaction, GLP + SOM ➔ GLP-SOM-complex, is not a thermodynamic quantity, the corresponding binding free energy (ΔG_B) for this reaction was calculated as well. This binding free energy, that involves the entropy contribution, is more suitable for prediction the complexation reaction or the sorption process. The binding free energies of 13 GLP-SOM-complexes have positive values. This means that these complexes (GLP-benzene, −naphthalene, −alkane, −alkene, −pyrrole1, −pyrrole2, −nitrile1, −phenol1, −sterol1, −sterol2, −lignin1, −lignin2, and −lignin3) are thermodynamically unstable. This indicates weak binding/sorption of GLP to these SOM sorption sites. Nitrile2 and phenol2 show low binding free energies regarding their complexation with GLP. Pyridine1, pyridine2, phenol3, lignin4, lignin5, fatty1, fatty2, glucose1, and glucose2 exhibit very strong interaction with GLP giving rise to relatively high binding free energies. In general, this highlights that the thermal stability for the sorption process depends not only on the sorption site but also on the binding motif. Similar to the calculation of the binding energy of GLP to each compound class, the corresponding binding free energy is calculated (see eq. 7). Accordingly, this shows that the thermal stability of the GLP binding to the SOM compound classes increases in the order: ALKY ($+7.3$ kcal mol^{-1}) < STEROL ($+6.5$ kcal mol^{-1}) < LIPID LIPID ($+4.6$ kcal mol^{-1}) < NCOMP (-3.3 kcal mol^{-1}) < PHLM (-8.4 kcal mol^{-1}) < CHYDR (-10.8 kcal mol^{-1}) < LDIM (-12.2 kcal mol^{-1}) < FATTY (-14.2 kcal mol^{-1}). This indicates unfavorable sorption conditions for GLP to the sorption sites of the ALKY, STEROL, and LIPID compound classes. For the rest of the SOM compound classes, spontaneous sorption process can take place by GLP to their sorption sites having the binding order FATTY > LDIM > CHYDR > PHLM > NCOMP. As a caveat one should keep in mind, that the SOM fragments do not exist as free molecules in soil, i.e. the effect of solvating water or a macromolecular structure might have a potential influence on the present conclusions.

3.3. Theory-experiment-correlation

In the following the results of the binding energy study will be correlated to the experimental data presented in Section 3.1. The binding (free) energy E_B^{SOM} (ΔG_B^{SOM}) gives the theoretical binding strength of GLP to the SOM model. On the experimental side the binding strength is quantified by the Freundlich unit capacity factor K_f. Assuming a linear correlation between K_f and E_B^{SOM} as well as ΔG_B^{SOM} one obtains the following equations:

$$K_f = 71.456 - 0.0095\ E_B^{SOM}$$

$$K_f = 73.918 - 0.0177\ \Delta G_B^{SOM}$$

These fitted equations produced correlation values of $r = 0.75$ and $R^2 = 0.56$ for K_f with E_B^{SOM} (eq. 9) and $r = 0.74$ and $R^2 = 0.55$ for K_f and ΔG_B^{SOM} (eq. 10, for details see Fig. 5). Considering the soil heterogeneity as well as the most significant correlations established in section 3.1 between K_f and the contents of soil organic as well as inorganic matter ($r = 0.42$ to 0.66), the relatively high correlation values ($r = 0.74$ to 0.75) indicate that both equations show a reasonable agreement between the experimental and theoretical data. This agreement supports our theoretical model for studying the GLP-SOM-interactions.

Given the success of our molecular-computational model for describing the GLP-SOM-interactions, it is instructive to compare our current results with that published for binding of hexachlorobenzene

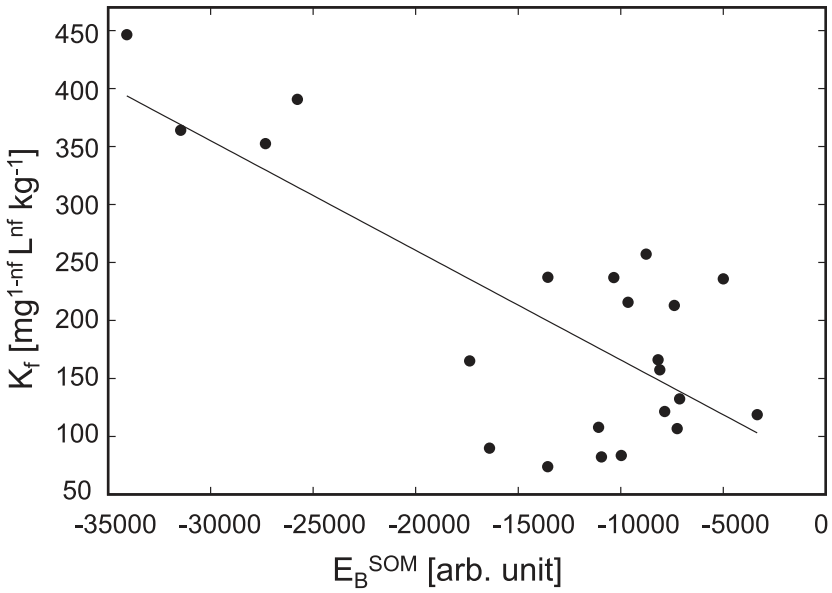


Fig. 5. Correlation of the Freundlich unit capacities (K_f) with the approximated total binding energies in solution (E_B^{SOM}) of GLP for the soil samples.

(HCB) and sulfanilamide (SAA) to similar SOM models (Ahmed et al., 2014a, 2016). In general, GLP binds stronger than HCB and SAA to CHYDR, FATTY, LDIM, PHLM, and NCOMP (for more details see Table S3 in SI). In detail, GLP, HCB, and SAA bind to CHYDR, PHLM, and, NCOMP in the order GLP > SAA > HCB, while they bind to FATTY and LDIM in the order GLP > HCB > SAA. In contrast, STEROL, LIPID, and ALKY bind in the order HCB > SAA > GLP. Using these binding energies for GLP, HCB, and SAA with the different SOM compound classes, the corresponding total binding energies (E_B^{SOM}) for GLP, HCB, and SAA with the whole SOM are calculated (see eq. 6 and Table S3). Finally, these total binding energies indicated a stronger binding for GLP to soil or its surface than for HCB and SAA. This agrees with the experimental findings that sorption of GLP to soil is stronger than sorption of the hydrophobic HCB and hydrophilic SAA (Ghafoor et al., 2013; Ahmed et al., 2015, 2016).

4. Conclusions

(1) The present investigation provides a comprehensive dataset for GLP sorption in untreated soils which obtained from batch sorption experiments with this herbicide. Representativeness of data results from the large number of surface soils that were characterized in depth for relevant physical (texture) and chemical properties such as pH and soil organic matter content and composition.

(2) The complementary chemical-analytical and theoretical modeling approaches provided new evidence for a positive effect of the SOM on GLP sorption, mainly resulting from the interaction of the GLP phosphonic moiety with phenolic and H-bond providing structures within the SOM. Smaller SOM structures with polar character have the potential to form stable complexes with GLP.

(3) These finding have great practical importance: because of the high complexation potential to inorganic components (clay minerals) and organic matter molecules, it appears to be unlikely to find GLP in its free form in soil solution. However, GLP leaching through soil profiles is possible in its complex form with small disaggregated SOM building blocks or even organic-mineral particles of colloidal or clay size. These binding and possible transport mechanisms plausibly explain the detection of GLP in environmental compartments in which it never should end up.

Acknowledgements

Peter Gros acknowledges a PhD-grant from the state of Mecklenburg-Western Pommeria. The modeling part of this work belongs to the InnoSoilPhos-project (http://www.innosoilphos.de/default.aspx), funded by the German Federal Ministry of Education and Research (BMBF) in the frame of the BonaRes-program (No. 031A558). This research was performed within the scope of the Leibniz ScienceCampus Phosphorus Research Rostock.

References

Acksel, A., Amelung, W., Kühn, P., Gehrt, E., Regier, T., Leinweber, P., 2016. Soil organic matter characteristics as indicator of Chernozem genesis in the Baltic Sea region. Geoderma 7, 187–200.

Ahmed, A.A., Kühn, O., Aziz, S.G., Hilal, R.H., Leinweber, P., 2014a. How soil organic matter controls hexachlorobenzene-soil interactions: adsorption isotherms and quantum chemical modelling. Sci. Total Environ. 476-477, 98–106.

Ahmed, A.A., Kühn, O., Leinweber, P., 2012. Controlled experimental soil organic matter modification for study of organic pollutant interactions in soil. Sci. Total Environ. 441, 151–158.

Ahmed, A.A., Leinweber, P., Kühn, O.A., 2014b. Computational study of hexachlorobenzene-soil organic matter interactions. J. Theor. Comput. Chem. 13, 1–16.

Ahmed, A.A., Thiele-Bruhn, S., Aziz, S.G., Hilal, R.H., Elroby, S.A., Al-Youbi, A.O., Leinweber, P., Kühn, O., 2015. Interaction of polar and nonpolar organic pollutants with soil organic matter: sorption experiments and molecular dynamics simulation. Sci. Total Environ. 508, 276–287.

Ahmed, A.A., Thiele-Bruhn, S., Leinweber, P., Kühn, O., 2016. Towards a molecular level understanding of the sulfanilamide-soil organic matter-interaction. Sci. Total Environ. 559, 347–355.

Albers, Chr.N., Banta, G.T., Hansen, P.E., Jacobsen, O.S., 2009. The influence of organic matter on sorption and fate of glyphosate in soil – comparing different soils and humic substances. Environ. Pollut. 157, 2865–2870.

Arroyave, J.M., Waiman, C.C., Zanini, G.P., Avena, M.J., 2016. Effect of humic acid on the adsorption/desorption behavior of glyphosate on goethite. Isotherms and kinetics. Chemosphere 145, 34–41.

Autio, S., Siimes, K., Laitinen, P., Rämö, S., Oinonen, S., Eronen, L., 2004. Adsorption of sugar beet herbicides to Finnish soils. Chemosphere 55, 215–226.

Becke, A.D., 1988. Density-functional exchange-energy approximation with correct asymptotic behavior. Phys. Rev. A 38, 3098–3100.

Bergström, L., Börjesson, E., Stenström, J., 2011. Laboratory and lysimeter studies of glyphosate and aminomethylphosphonic acid in a sand and a clay soil. J. Environ. Qual. 40, 98–108.

Borggaard, O.K., Gimsing, A.L., 2008. Review: fate of glyphosate in soil and the possibility of leaching to ground and surface waters: a review. Pest Manag. Sci. 64, 441–456.

Cossi, M., Rega, N., Scalmani, G., Barone, V., 2003. Energies, structures, and electronic properties of molecules in solution with the C-PCM solvation model. J. Comput. Chem. 24, 669–681.

Coupe, R.H., Kalkhoff, S.J., Capel, P.D., Gregoire, C., 2012. Fate and transport of glyphosate and aminomethylphosphonic acid in surface waters of agricultural basins. Pest Manag. Sci. 68, 16–30.
Dion, H.M., Harsh, J.B., Hill Jr., H.H., 2001. Competitive sorption between glyphosate and inorganic phosphate on clay minerals and low organic matter soils. J. Radioanal. Nucl. Chem. 249, 385–390.
Frisch, M.J., Trucks, G.W., Schlegel, H.B., Scuseria, G.E., Robb, M.A., Cheeseman, J.R., Scalmani, G., Barone, V., Mennucci, B., Petersson, G.A., Nakatsuji, H., Caricato, M., Li, X., Hratchian, H.P., Izmaylov, A.F., Bloino, J., Zheng, G., Sonnenberg, J.L., Hada, M., Ehara, M., Toyota, K., Fukuda, R., Hasegawa, J., Ishida, M., Nakajima, T., Honda, Y., Kitao, O., Nakai, H., Vreven, T., Montgomery Jr., J.A., Peralta, J.E., Ogliaro, F., Bearpark, M., Heyd, J.J., Brothers, E., Kudin, K.N., Staroverov, V.N., Kobayashi, R., Normand, J., Raghavachari, K., Rendell, A., Burant, J.C., Iyengar, S.S., Tomasi, J., Cossi, M., Rega, N., Millam, J.M., Klene, M., Knox, J.E., Cross, J.B., Bakken, V., Adamo, C., Jaramillo, J., Gomperts, R., Stratmann, R.E., Yazyev, O., Austin, A.J., Cammi, R., Pomelli, C., Ochterski, J.W., Martin, R.L., Morokuma, K., Zakrzewski, V.G., Voth, G.A., Salvador, P., Dannenberg, J.J., Dapprich, S., Daniels, A.D., Farkas, Ö., Foresman, J.B., Ortiz, J.V., Cioslowski, J., Fox, D.J., 2013. Gaussian 09, Revision D.01. Gaussian, Inc., Wallingford CT.
Gerritse, R.G., Beltran, J., Hernandez, F., 1996. Adsorption of atrazine, simazine and glyphosate in soils of the Gnangara Mound, Western Australia. Aust. J. Soil Res. 34, 599–607.
Ghafoor, A., Nicholas, J., Jarvisa, N.J., Stenström, J., 2013. Modelling pesticide sorption in the surface and subsurface soils of an agricultural catchment. Pest Manag. Sci. 69, 919–929.
Glass, R.L., 1984. Metal complex formation by glyphosate. J. Agric. Food Chem. 32, 1249–1253.
Global Analysists Industry Inc., 2011.
Grimme, S., Ehrlich, S., Goerigk, L., 2011. Effect of the damping function in dispersion corrected density functional theory. J. Comput. Chem. 32, 1456–1465.
Hance, R.J., 1976. Adsorption of glyphosate by soils. Pestic. Sci. 7, 363–366.
Hehre, W.J., Ditchfield, R., Pople, J.A., 1972. Self-consistent molecular orbital methods. XII. Further extensions of gaussian-type basis sets for use in molecular orbital studies of organic molecules. J. Chem. Phys. 56, 2257–2261.
Horta, M.d.C., Torrent, J., 2007. The Olsen P method as an agronomic and environmental test for predicting phosphate release from acid soils. Nutr. Cycl. Agroecosyst. 77, 283–292.
Jandl, G., Acksel, A., Baum, C., Leinweber, P., 2015. Indicators for soil organic matter quality in no-till soils under perennial crops in Central Sweden. Soil Tillage Res. 148, 74–84.
Jansen, H.B., Ros, P., 1969. Non-empirical molecular orbital calculations on the protonation of carbon monoxide. Chem. Phys. Lett. 3, 140–143.
Jariani, S.M.J., Rosenani, A.B., Samsuri, A.W., Shukor, A.J., Ainie, H.K., 2010. Adsorption and desorption of glufosinate ammonium in soils cultivated with oil palm in Malaysia. Mal. J. Soil Sci. 14, 41–52.
Kumari, K.G.I.D., Moldrup, P., Paradelo, M., Elsgaard, L., de Jonge, L.W., 2016. Soil properties control glyphosate sorption in soils amended with birch wood biochar. Water Air Soil Pollut. 227, 174.
Lee, C., Yang, W., Parr, R.G., 1988. Development of the Colle-Salvetti correlation-energy formula into a functional of the electron density. Phys. Rev. B 37, 785–789.
Leinweber, P., Jandl, G., Eckhardt, K.-U., Schlichting, A., Hofmann, D., Schulten, H.-R., 2009. Analytical pyrolysis and soft-ionization mass spectrometry. In: Senesi, N., Xing, B., Huang, P.M. (Eds.), Biophysico-chemical Processes Involving Natural Nonliving Organic Matter in Environmental Systems. John Wiley & Sons, Inc., New York, pp. 539–588.
Leinweber, P., Schulten, H.-R., Jancke, H., 1999. New evidence for the molecular composition of soil organic matter in Vertisols. Soil Sci. 164, 857–870.
Liu, B., Dong, L., Yu, Q., Li, X., Wu, F., Tan, Z., Luo, S., 2016. Thermodynamic study on the protonation reactions of glyphosate in aqueous solution: potentiometry, calorimetry and NMR spectroscopy. J. Phys. Chem. B 120 (9), 2132–2137.
Mamy, L., Barriuso, E., Gabrielle, B., 2016. Glyphosate fate in soils when arriving in plant residues. Chemosphere 154, 425–433.
Miano, T.M., Piccolo, A., Celano, G., Senesi, N., 1992. Infrared and fluorescence spectroscopy of glyphosate-humic acid complexes. Sci. Total Environ. 123/124, 83–92.
Monsanto Backgrounder, 2005. Glyphosate Half-life in Soil.
Okada, E., Costa, J.L., Bedmar, F., 2016. Adsorption and mobility of glyphosate in different soils under no-till and conventional tillage. Geoderma 263, 78–85.
Ololade, I.A., Oladoja, N.A., Oloye, F.F., Alomaja, F., Akerele, D.D., Iwaye, J., Aikpokpodion, P., 2014. Sorption of glyphosate on soil components: the roles of metal oxides and organic materials. Soil Sediment Contam. Int. J. 23, 571–585.
Pessagno, R.C., Dos Santos Afonso, M., 2005. N-(phosphonomethyl)glycine interactions with soils. J. Argent. Chem. Soc. 93, 97–108.
Piccolo, A., Celano, G., Conte, P., 1996. Adsorption of glyphosate by humic substances. J. Agric. Food Chem. 44, 2442–2446.
Piccolo, A., Gatta, L., Campanella, L., 1995. Interactions of glyphosate herbicide with a humic acid and its iron complex. Ann. Chim. (Rome) 85, 31–40.
Piccolo, A., Gelano, G., Arienzo, M., Mirabella, A., 1994. Adsorption and desorption of glyphosate in some European soils. J. Environ. Sci. Health B29 (6), 1105–1115.
Roy, D.N., Konar, S.K., Banerjee, S., Charles, D.A., Thompson, D.G., Prasad, R., 1989. Persistence, movement and degradation of glyphosate in selected Canadian boreal forest soils. J. Agric. Food Chem. 37, 437–440.
Schaumann, G.E., Thiele-Bruhn, S., 2011. Molecular modeling of soil organic matter: squaring the circle. Geoderma 166, 1–14.
Schulten, H.-R., Leinweber, P., Jancke, H., 1999. New evidence for the molecular composition of soil organic matter in Vertisols. Soil Sci. 164 (11), 857–870.
Senesi, N., Xing, B., Huang, P.M., 2009. Biophysico-chemical Processes Involving Natural Nonliving Organic Matter in Environmental Systems. Wiley & Sons, Hoboken NJ.
Sidoli, P., Baran, N., Angulo-Jaramillo, R., 2016. Glyphosate and AMPA adsorption in soils: laboratory experiments and pedotransfer rules. Environ. Sci. Pollut. Res. 23, 5733–5742.
Skeff, W., Neumann, C., Schulz-Bull, D.E., 2015. Glyphosate and AMPA in the estuaries of the Baltic Sea method optimization and field study. Mar. Pollut. Bull. 100, 577–585.
Spann, K.P., Hargreaves, P.A., 1994. The determination of glyphosate in soils with moderate to high clay content. Pestic. Sci. 40, 41–48.
Sprankle, P., Meggitt, W.F., Penner, D., 1975. Adsorption, mobility, and microbial degradation of glyphosate in the soil. Weed Sci. 23, 229–234.
Sündermann, A., Solc, R., Tunega, D., Haberhauer, G., Gerzabek, M.H., Oostenbrink, C., 2015. Vienna soil-organic-matter modeler–generating condensed-phase models of humic substances. J. Mol. Graph. Model. 62, 253–261.
Thiele-Bruhn, S., Seibicke, T., Schulten, H.-R., Leinweber, P., 2004. Sorption of sulfonamide pharmaceutical antibiotics on whole soils and particle-size fractions: batch experiments and chemical modelling. J. Environ. Qual. 33, 1331–1342.
Tomlin, C.D.S., 1997. The Pesticide Manual: A World Compendium. 11th ed. British Crop Protection Council, Farnham Surrey (UK).
Torstensson, L., 1985. Behaviour of glyphosate in soils and its degradation. In: Grossbard, E., Atkinson, D. (Eds.), The Herbicide Glyphosate. Butterworth, London.
Van Stempvoort, D.R., Roy, J.W., Brown, J., Bickerton, G., 2014. Residues of the herbicide glyphosate in riparian groundwater in urban catchments. Chemosphere 95, 455–463.
Vereecken, H., 2005. Mobility and leaching of glyphosate: a review. Pest Manag. Sci. 61, 1139–1151.
Waiman, C.V., Avena, M.J., Garrido, M., Band, B.F., Zanini, G.P., 2012. A simple and rapid spectrophotometric method to quantify the herbicide glyphosate in aqueous media. Application to adsorption isotherms on soils and goethite. Geoderma 170, 154–158.
Wang, Y.-J., Zhou, D.-M., Sun, R.-J., 2005. Effects of phosphate on the adsorption of glyphosate on three different types of Chinese soils. J. Environ. Sci. 17 (5), 711–715.
Wang, Y.-J., Zhou, D.-M., Sun, R.-J., Cang, L., Hao, X.-Z., 2006. Cosorption of zinc and glyphosate on two soils with different characteristics. J. Hazard. Mater. 137, 76–82.

Supplementary Information

Glyphosate binding in soil as revealed by sorption experiments and quantum-chemical modeling

Peter Gros[1], Ashour Ahmed[2,3], Oliver Kühn[2], Peter Leinweber[1]

[1] University of Rostock, Soil Science, D-18059 Rostock, Germany.

[2] University of Rostock, Institute of Physics, D-18051 Rostock, Germany.

[3] University of Cairo, Faculty of Science, Department of Chemistry, 12613 Giza, Egypt.

peter.gros@uni-rostock.de

ashour.ahmed@uni-rostock.de

oliver.kuehn@uni-rostock.de

peter.leinweber@uni-rostock.de

Table S1: SOM composition determined by pyrolysis field-ionization mass spectrometry (carbohydrates = CHYD, phenols + lignin-monomers = PHLM, lignin-dimers = LDIM, lipids = LIPD, alkyl-aromatics = ALKYL, heterocyclic N-containing compounds = NCOMP, sterols = STEROL, peptides = PEPTI, suberin = SUBER, free fatty acidy = FATTY)

Sample	**TII**	CHYDR		PHLM		LDIM		LIPID		ALKYL		NCOMP		STEROL		PEPTI		SUBER		FATTY	
	10^6 counts mg^{-1}	%TII	mg kg^{-1}	%TII	mg kg^{-1}	%TII	mg kg^{-1}	%TII	mg kg^{-1}	%TII	mg kg^{-1}	%TII	mg kg^{-1}	%TII	mg kg^{-1}	%TII	mg kg^{-1}	%TII	mg kg^{-1}	%TII	mg kg^{-1}
1[b]	20.1	8.7	24.4	15.9	44.5	2.5	7.0	4.7	13.2	13.8	38.6	8.9	24.9	0.2	0.6	3.6	10.1	0.0	0.0	0.1	0.3
2[b]	15.9	9.5	38.0	16.9	67.6	1.8	7.2	4.0	16.0	13.9	55.6	9.3	37.2	0.1	0.4	3.9	15.6	0.0	0.0	0.0	0.0
3[d]	5.0	7.8	55.4	15.2	107.9	3.0	21.3	5.2	36.9	13.2	93.7	8.8	62.5	0.0	0.0	3.0	21.3	0.0	0.0	0.2	1.4
4[c]	88.7	3.8	28.1	9.8	72.5	4.0	29.6	4.5	33.3	11.2	82.9	2.0	14.8	1.2	8.9	4.5	33.3	0.1	0.7	0.2	1.5
5[d]	22.0	5.2	42.1	8.7	70.5	5.2	42.1	9.7	78.6	10.9	88.3	6.8	55.1	2.0	16.2	2.1	17.0	0.1	0.8	2.1	17.0
6[d]	29.7	4.4	36.5	8.8	73.0	4.2	34.9	10.1	83.8	10.6	88.0	6.8	56.4	2.1	17.4	2.0	16.6	0.2	1.7	2.7	22.4
7[c]	42.1	6.9	59.3	10.1	86.9	3.8	32.7	4.2	36.1	10.1	86.9	3.9	33.5	2.0	17.2	6.6	56.8	0.0	0.0	0.0	0.0
8[c]	30.4	3.6	33.1	7.9	72.7	5.0	46.0	4.7	43.2	10.9	100.3	1.9	17.5	1.4	12.9	4.0	36.8	0.1	0.9	0.1	0.9
9	15.1	4.1	43.9	9.9	106.0	2.8	29.5	7.0	74.9	13.1	139.5	2.6	27.4	0.8	8.5	4.5	48.0	0.0	0.5	0.3	2.7
10	51.8	1.6	19.3	4.8	58.6	4.9	60.2	6.1	74.8	9.0	109.8	0.9	11.1	3.1	37.2	2.7	32.8	0.3	4.2	1.4	16.6
11[d]	1.3	7.1	89.5	12.9	162.5	2.3	29.0	3.8	47.9	11.8	148.7	4.7	59.2	0.2	2.5	7.5	94.5	0.0	0.0	0.1	1.3
12[c]	20.8	4.6	58.0	8.8	110.9	5.0	63.0	9.6	121.0	11.2	141.1	6.7	84.4	1.6	20.2	1.9	23.9	0.1	1.3	2.1	26.5
13[c]	44.1	5.0	64.0	9.5	121.6	2.9	37.1	4.7	60.2	11.1	142.1	2.6	33.3	1.0	12.8	5.3	67.8	0.1	1.3	0.5	6.4
14	49.0	1.8	23.7	4.7	60.7	4.9	63.9	6.4	82.6	8.5	110.1	1.1	14.4	3.8	49.7	2.8	36.4	0.3	4.1	1.0	13.0
15	59.6	1.6	22.9	4.6	68.3	4.8	71.4	6.5	96.5	8.9	130.7	0.9	13.6	3.7	54.2	2.6	38.8	0.3	4.8	1.4	20.3
16[d]	17.1	5.7	86.1	8.9	134.4	3.4	51.3	9.3	140.4	10.8	163.1	7.2	108.7	1.6	24.2	2.2	33.2	0.1	1.5	2.2	33.2
17[d]	11.4	6.8	107.4	13.2	208.6	3.9	61.6	7.1	112.2	12.2	192.8	7.9	124.8	1.0	15.8	2.6	41.1	0.0	0.0	0.9	14.2
18[a]	0.5	8.6	140.2	12.9	210.3	1.9	31.0	5.7	92.9	14.9	242.9	7.7	125.5	0.1	1.6	8.3	135.3	0.0	0.0	0.1	1.6
19[a]	1.0	7.0	134.8	10.7	206.6	3.4	65.0	5.5	106.7	13.0	251.2	5.7	110.6	0.7	12.6	7.0	135.8	0.1	1.0	0.1	1.9
20[a]	1.5	5.3	126.7	8.4	200.8	4.8	114.7	5.3	126.7	11.0	262.9	3.7	88.4	1.2	28.7	5.7	136.2	0.1	2.4	0.1	2.4
21[b]	22.0	8.6	232.2	16.3	440.1	2.6	70.2	4.8	129.6	14.4	388.8	8.3	224.1	0.2	5.4	3.3	89.1	0.0	0.0	0.1	2.7
22[b]	32.2	8.2	246.0	14.2	426.0	3.2	96.0	5.9	177.0	12.9	387.0	8.2	246.0	0.6	18.0	3.3	99.0	0.1	3.0	0.4	12.0
23	163.7	1.1	35.1	2.6	81.6	5.2	163.1	6.8	211.9	6.9	213.8	0.7	21.4	6.8	212.3	1.9	59.3	0.6	20.2	2.7	84.4
Min	0.5	1.1	19.3	2.6	44.5	1.8	7.0	3.8	13.2	6.9	38.6	0.7	11.1	0.0	0.0	1.9	10.1	0.0	0.0	0.0	0.0
Max	163.7	9.5	246.0	16.9	440.1	5.2	163.1	10.1	211.9	14.9	388.8	9.3	246.0	6.8	212.3	8.3	136.2	0.6	20.2	2.7	84.4

a) Leinweber et al. (1999); b) Jandl et al. (2015); c) Acksel et al. (2016); d)Bath et al. (submitted Applied Soil Ecology)

Table S2: Calculated binding energies and binding free energies for GLP with the SOM systems in the modeled GLP-SOM-complexes at the B3LYP/D3/6-311++G(d.p) level of theory and using the CPCM model.

modeled SOM systems	E_B [kcal.mol^{-1}]	ΔG_B [kcal.mol^{-1}]
benzene	-0.45	+8.75
naphthalene	-2.77	+5.80
alkane	-1.80	+7.43
alkene	-8.13	+1.82
pyrrole1	-5.72	+4.73
pyrrole2	-10.22	+0.32
nitrile1	-8.67	+1.22
nitrile2	-10.70	-0.58
pyridine1	-15.66	-4.42
pyridine2	-20.25	-9.51
phenol1	-1.11	+5.76
phenol2	-12.34	-0.84
phenol3	-16.50	-4.62
sterol1	-1.17	+5.50
sterol2	-5.09	+6.54
lignin1	-3.57	+6.56
lignin2	-2.26	+7.88
lignin3	-6.21	+5.98
lignin4	-23.15	-9.78
lignin5	-26.25	-12.18
fatty1	-21.38	-8.52
fatty2	-27.02	-14.21
glucose1	-18.02	-5.85
glucose2	-28.70	-10.80

Table S3: Calculated binding energies for GLP, hexachlorobenzene (HCB), and sulfanilamide (SAA) with the modeled SOM compound classes at the B3LYP/D3/6-311++G(d.p) level of theory.

modeled SOM compound classes	ΔG_B [kcal.mol^{-1}]	E_B [kcal.mol^{-1}]		
	GLP	GLP	HCB	SAA
CHYDR	-10.8	-28.7	-6.2	-10.2
PHLM	-8.4	-21.4	-10.8	-11.2
LDIM	-12.2	-26.3	-13.6	-8.7
LIPID	+4.6	-5.0	-8.8	-5.4
ALKY	+7.3	-1.6	-11.0	-6.3
NCOMP	-3.3	-13.7	-5.8	-8.1
STEROL	+6.5	-5.1	-10.5	-8.1
FATTY	-14.2	-27.0	-10.5	-7.5

Publication 13

Ashour A. Ahmed, P. Gros, O. Kühn, P. Leinweber. Molecular level investigation of the role of peptide interactions in the glyphosate analytics. Chemosphere **2018**, 196, 129–134.

Contribution: Ashour A. Ahmed is credited with conceptualization, conducting the modeling work, modeling analysis and interpretation, methodology development, visualization, and writing the original manuscript. Ashour A. Ahmed and co-authors are responsible for reviewing, and editing the manuscript.

URL: https://doi.org/10.1016/j.chemosphere.2017.12.162

QR:

Ashour Ahmed GLP-PEP

Reproduced with the permission of Elsevier

Chemosphere 196 (2018) 129–134

Contents lists available at ScienceDirect

Chemosphere

journal homepage: www.elsevier.com/locate/chemosphere

Short Communication

Molecular level investigation of the role of peptide interactions in the glyphosate analytics

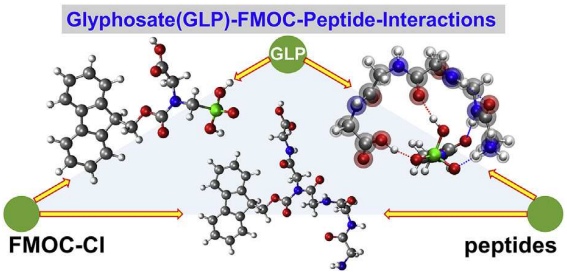
Ashour A. Ahmed [a, b, *], Peter Gros [c], Oliver Kühn [a], Peter Leinweber [c]

[a] University of Rostock, Institute of Physics, D-18059 Rostock, Germany
[b] University of Cairo, Faculty of Science, Department of Chemistry, 12613 Giza, Egypt
[c] University of Rostock, Soil Science, D-18059 Rostock, Germany

HIGHLIGHTS

- This study included calibration experiments and quantum chemical modeling.
- Strong interaction between GLP and peptides in solution has been explored.
- FMOC-Cl showed similar reactions with GLP and peptides.
- Peptides inhibit the GLP derivatization reaction causing the GLP underestimation.
- The presence of peptides may lead to an overestimation of the GLP concentration.

GRAPHICAL ABSTRACT



ARTICLE INFO

Article history:
Received 13 October 2017
Received in revised form
20 December 2017
Accepted 24 December 2017
Available online 27 December 2017

Handling Editor: Klaus Kümmerer

Keywords:
FMOC-Cl
Glyphosate
Peptides
UV spectra
Quantum chemical modeling

ABSTRACT

The detection of the herbicide glyphosate (GLP) in environmental samples is most often conducted after derivatizing the target molecule with the chromophore 9-fluorenylmethyloxycarbonyl chloride (FMOC-Cl). However, this method is sensitive to all primary and secondary amines, which can occur in the sample matrix as well. In order to quantify the interference of primary and secondary amines on GLP detection, we have used well-defined peptides such as pentaglycine (PG) and albumin as well as mixtures of peptides such as peptone. These peptides have been added to the derivatization solution of GLP at different constant concentration levels and UV extinction coefficients have been determined. Data analysis supported by quantum chemical modeling of the GLP–peptide, FMOC–GLP, and FMOC–peptide complexation reactions facilitated the identification of two interfering impacts of peptide on GLP derivatization: (i) increase of the signal due to reaction with FMOC-Cl leading to an overestimation of GLP concentration and (ii) decrease of GLP recovery due to complex formation and therefore inhibition of GLP derivatization, which leads to an underestimation. Specifically, our results indicated that the GLP-peptide- and peptide-FMOC-interactions are mainly affected by type of interfering peptides as well as concentration of each peptide and GLP in the environmental samples.

© 2017 Elsevier Ltd. All rights reserved.

1. Introduction

Glyphosate (GLP) is the most commonly used herbicide worldwide. Although it is assumed that GLP is nearly immobile in soil

* Corresponding author. University of Rostock, Institute of Physics, D-18059 Rostock, Germany.
E-mail addresses: ashour.ahmed@uni-rostock.de (A.A. Ahmed), peter.gros@uni-rostock.de (P. Gros), oliver.kuehn@uni-rostock.de (O. Kühn), peter.leinweber@uni-rostock.de (P. Leinweber).

https://doi.org/10.1016/j.chemosphere.2017.12.162
0045-6535/© 2017 Elsevier Ltd. All rights reserved.

(Borggaard and Gimsing, 2008) it was found in ground and surface waters (Aparicio et al., 2013) and recently in the Baltic Sea (Skeff et al., 2015). This emphasizes the need for reliable analytical methods to support the ongoing discussion of potential risks of unlimited GLP usage. The most frequently employed detection method for GLP is a chromatographic separation of the reversed phase and UV- or fluorescent-spectrometric detection (Stalikas and Konidari, 2001), often combined with mass-spectrometry (Ramirez et al., 2014). Recently, Koskinen et al. (2016) reported that the GLP direct analytical detection methods, i.e. without GLP derivatization, are almost not suitable for the GLP determination in samples of complex and rich matrix constituents such as plant and soil materials. To this end, GLP has to be converted into a non-polar and UV-detectable form *via* a derivatization step such as reaction with 9-fluorenylmethyloxycarbonyl chloride (FMOC-Cl) as described by Hanke et al. (2008).

The composition of environmental samples is generally complex, containing numerous diverse organic and inorganic constituents. These matrix components potentially interact with GLP in solution, e.g., by formation of stable complexes between GLP and multivalent cations (Freuze et al., 2007). Also, polar organic compounds containing phenolic, hydroxylic, carboxylic, and amino functional groups can form stable complexes with GLP *via* H-bond formation with the GLP phosphonic and carboxylic moieties (Gros et al., 2017). Primary and secondary amines such as peptides have the ability to interact with GLP (Castellino et al., 1989) as well as with the derivatization agent FMOC-Cl (Carpino and Han, 1972; Moye and Boning, 1979). This indicates that the GLP detection or quantification may be affected by peptides in the samples. The impact of possibly produced FMOC–peptide complexes can be avoided by chromatographic separation combined with mass-spectrometry (environmental samples with unknown concentration, Vreeken et al., 1998) or blank correction in the data evaluation (samples with known GLP concentrations such as those for sorption isotherms). However, possible interactions between peptides and GLP preventing the derivatization with FMOC-Cl cannot be corrected using the established analytical procedures. This is due to the lack of knowledge about concentration of GLP and peptides, and their interaction strength in environmental samples. Here, we hypothesize that the interaction of peptides with GLP can suppress the GLP reaction with FMOC-Cl, and this inhibiting effect on GLP derivatization may cause underestimations of GLP concentrations. Surprisingly, this possible disturbance of the GLP quantification has not been examined and described in the literature before.

The objective of the present study was to scrutinize possible inhibition effects at a molecular level by investigating the GLP derivatization with FMOC-Cl in the presence of peptides of different compositions. Well-defined peptides such as pentaglycine (PG) and albumin as well as mixtures of peptides such as peptone will be used in the current contribution. Specifically, the interactions between GLP and peptides, FMOC-Cl and GLP, and FMOC-Cl and peptides will be explored experimentally by calibration studies and theoretically by quantum chemical modeling.

2. Materials and methods

2.1. Chemicals and calibration solutions

GLP (CAS: 1071-83-6), FMOC-Cl (CAS: 28920-43-6), dichloromethane (CAS: 75-09-2), sodium tetraborate decahydrate (CAS: 1330-43-4), albumin (pig, CAS: 9048-46-8), and peptone (from casein, CAS: 91079-40-2) were purchased from Sigma Aldrich. PG (CAS: 7093-67-6) was purchased from Fluorochem Ldt. Hydrochloric acid and sodium hydroxide were used for pH adjustment of GLP and PG solutions. All the used chemicals were of analytical grade. Concentration levels of single components for GLP and PG were prepared in the range of 2.96–94.67 $\mu mol\,L^{-1}$ and range of 0.5–32.0 $mg\,L^{-1}$ for albumin and peptone. The GLP calibration solution was also prepared in the presence of three distinct levels of PG, albumin and peptone (0.5, 16.0, and 32.0 $mg\,L^{-1}$). Four replicates per concentration level were prepared.

2.2. Derivatization and UV-detection

The method proposed by Waiman et al. (2012) for complex environmental samples like soil was used for GLP, PG, albumin, and peptone derivatization. Briefly, 0.5 mL borate buffer solution (pH 9) was added to 4 mL of sample solution. Next, an excess concentration of FMOC-Cl (0.5 mL, $c = 1\,g\,L^{-1}$; dissolved in acetonitrile) was added. After vigorously shaking the derivatization solution was allowed to react for 2 h with occasionally shaking. Subsequently, by-products of FMOC-Cl (FMOC-OH) were removed by extracting with 4 mL dichloromethane. The mixture was centrifuged (10 min, 1558xg) to separate the two phases. The supernatant aqueous phases of each derivatization solution were used for UV/Vis spectroscopy at $\lambda = 264$ nm (Specord200, Analytik Jena AG, 07745 Jena, Germany). The averaged signals of the calibration series of the respective analyte were corrected by subtracting the signal intensity of the blank level containing no analyte. In this way effects on signal intensity resulting from matrix constituents were eliminated.

2.3. Quantum chemical modeling

Here, we are mainly focusing on the interaction between GLP and PG that was simulated through 1:1 complex formation between them, i.e. 1GLP + 1PG → GLP–PG complex. Different initial geometries for this complex were constructed by selecting the expected preferential binding situations between GLP and PG. The aqueous solution around the complex was simulated by introducing an implicit treatment through the conductor-like polarizable continuum model (CPCM, Cossi et al., 2003). Full geometry optimization, using CPCM, was performed for the complexes as well as for the individual species (GLP and PG). The calculations have been performed using density functional theory (DFT) implemented in the Gaussian09 program package (Frisch et al., 2013). Specifically, the B3LYP hybrid functional (Becke, 1988; Lee et al., 1988) combined with the 6–311++G (d,p) basis set (Hehre et al., 1972) and Grimme's D3 dispersion correction (Grimme et al., 2011) have been applied. The basis set superposition error (BSSE) has been corrected using the counterpoise scheme (Jansen and Ros, 1969). For more details about the different methods of computational chemistry and their application to soil science, see also Kubicki (2016).

For the complexation reaction, 1GLP + 1PG → GLP–PG complex, the reaction energy (ΔE) is calculated as follows:

$$\Delta E = E_{GLP-PG\ complex} - (E_{GLP} + E_{PG}) \quad (1)$$

where, $E_{GLP-PG\ complex}$, E_{GLP}, and E_{PG}, are the electronic energies of the GLP–PG complex, GLP, and PG, respectively. Similarly, the corresponding reaction free energy (ΔG) is calculated by including the zero-point energy and thermal correction to the Gibbs free energy.

The derivatization reactions of FMOC-Cl with GLP as well as with PG have been simulated at the same level of theory. For PG, we have considered five possibilities for the 1:1 FMOC–PG derivatization reaction according to the five amino groups (for details see Figs. S1 and S2 in the Supplemental Material (SM)). For the derivatization reaction, 1FMOC-Cl + 1GLP(PG) → FMOC–GLP(PG) complex + HCl, the reaction energy (ΔE) is calculated as follows:

$$\Delta E = E_{FMOC-GLP(PG)\ complex} + E_{HCl} - (E_{FMOC-Cl} + E_{GLP(PG)}) \quad (2)$$

where, $E_{FMOC-GLP(PG)\ complex}$, E_{HCl}, $E_{FMOC-Cl}$, and $E_{GLP(PG)}$ are the electronic energies of the FMOC–GLP or FMOC–PG complex, HCl, FMOC-Cl, and GLP or PG, respectively. Moreover, UV spectra for FMOC-Cl as well as for the FMOC–GLP and FMOC–GP complexes have been calculated using linear response time-dependent DFT.

3. Results and discussion

3.1. Quantum chemical modeling

The optimized geometry for the GLP–PG complex in Fig. 1a indicates a strong interaction between GLP and PG. This is due to the high polarity of GLP and PG, which contain several polar functional groups (phosphonic, amino, carboxylic, and amide). The GLP–PG complex formation involves multiple intermolecular interactions. Especially, PG forms a cavity around GLP in addition to formation of intermolecular and intramolecular H-bonds (HBs) and proton transfer. Four intermolecular HBs are observed between PG and the GLP phosphonic and carboxylic functional groups. Here, the GLP phosphonic group is involved in three HBs with O···H bond lengths of 1.53, 1.57, and 1.75 Å. The GLP carboxylic group participated with one weaker HB with O···H bond length of 1.95 Å. This indicates a stronger interaction for the GLP phosphonic group than the corresponding carboxylic one. Moreover, the calculated reaction energy (-38.8 kcal mol^{-1}) and reaction free energy (-17.6 kcal mol^{-1}) indicate that the GLP–PG complex is strongly bound, thermally stable, and can be formed spontaneously. This already hints at the possibility of masking of GLP by peptides in environmental samples.

In order to investigate the competition between PG and FMOC-Cl regarding their interaction with GLP, the FMOC–GLP derivatization reaction has been simulated. The calculated reaction energy and free energy for this reaction are -18.8 and -16.3 kcal mol^{-1}, respectively (for more details, see Fig. 1b and Table S1 in SM). Thus, the reaction is exothermic and can occur spontaneously. Compared to energies of the GLP–PG complex, GLP can interact with peptides *stronger* than with FMOC-Cl.

The interaction of FMOC-Cl with PG has been simulated through a similar derivatization reaction (see Fig. 1c and Fig. S2 in SM). The results indicate complex formation between FMOC-Cl and PG at five interaction sites (five amino groups) with the most stable one at the PG primary amino group. For this complex, the calculated reaction energy and free energy for the FMOC–PG derivatization reaction are -13.9 and -11.8 kcal mol^{-1}, respectively (see Table S1 in SM). Similar to the FMOC–GLP case, these reaction energies also point to a spontaneous complex formation reaction between FMOC-Cl and PG. This indicates that both GLP and PG can form complexes with FMOC-Cl of similar binding strength. Similar reactions with FMOC-Cl can be expected for other peptides such as albumin and peptone.

The calculated UV spectra for FMOC-Cl and its complexes with GLP and PG reveal two peaks at 219 nm and 275 nm (Fig. 2). This agrees well with the experimentally observed UV peaks for FMOC-Cl (Catrinck et al., 2014). For FMOC-Cl, the peak at 275 nm corresponds mainly to π(fluorene ring) $\rightarrow$ π^*(fluorene ring) electronic transitions, while the peak at 219 nm is a result of combination the π(fluorene ring) $\rightarrow$ π^*(fluorene ring) and π(fluorene ring) $\rightarrow$ σ^*(C-Cl) electronic transitions (for more details, see Figs. S3-S5 in SM). For this reason, the peak at 275 nm is not influenced by the binding between GLP and PG or generally between GLP and any peptide, while the one at 219 nm shows a reduced intensity for the complex. Most importantly, however, is the observation that there is essentially no effect of GLP and PG binding on the spectrum. Thus, based on the extinction coefficient one cannot discriminate between the two species, i.e. GLP and peptide in the environmental samples.

3.2. Calibration experiments

The calibration curves of the individual species GLP and PG in

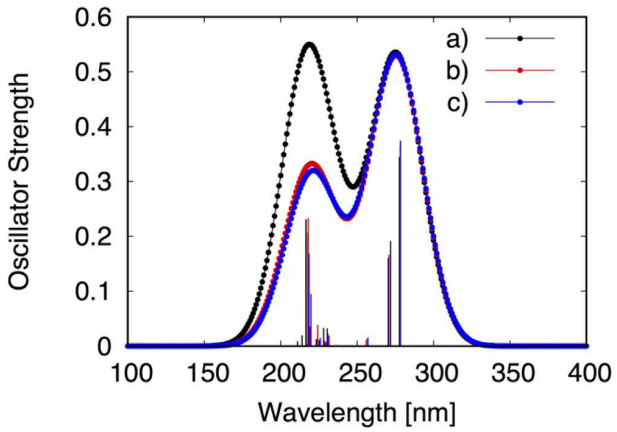


Fig. 2. Calculated UV spectra with their electronic transitions for FMOC-Cl (a) and its complexes with GLP (b) and PG (c) at the TD-DFT/B3LYP/6–311++G (d.p)/CPCM level of theory.

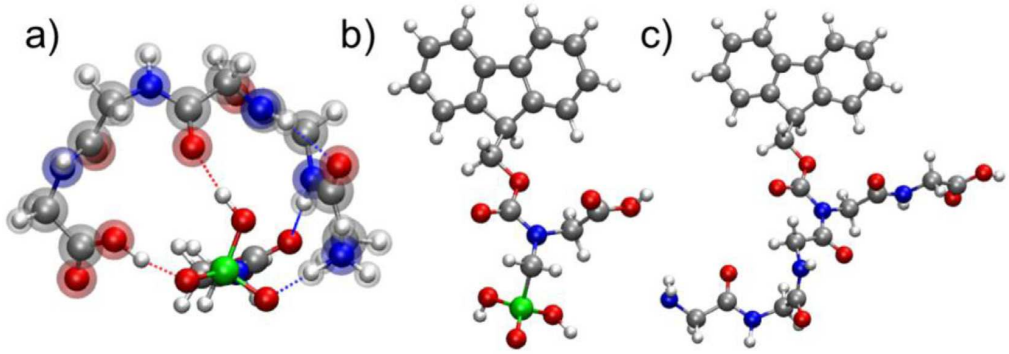


Fig. 1. Optimized geometries of the GLP–PG (a), FMOC–GLP (b), and FMOC–PG complexes (c) at the DFT/B3LYP/D3/6–311++G (d.p) level of theory and using the CPCM model. For the GLP–PG complex, PG atoms are surrounded by transparent spheres for better visualization of the complex formation. Color code: white (H), gray (C), blue (N), red (O), and green (P). (For interpretation of the references to colour in this figure legend, the reader is referred to the Web version of this article.)

aqueous solution show an approximately linear behavior with $R^2 = 0.999$ for GLP and PG within the measured concentration range. The slope of the calibration curve for PG (0.0269 L μmol^{-1}) is almost twice of that for GLP (0.0144 L μmol^{-1}). Since the molar extinction coefficient is the same for both species, this doubled signal intensity (absorbance) of PG in comparison to GLP at equal molar concentrations indicates that the number of FMOC-Cl chromophores per one complexed PG molecule is twice of that per one complexed GLP molecule. Since GLP can react with only one FMOC-Cl molecule, this means that one PG molecule can react with two FMOC-Cl molecules. This is in accord with the quantum chemical results, indicating different sites for FMOC-Cl to PG binding (see also Fig. S2 in SM). Moreover, the calibration curve slope for albumin (1.3134 L μmol^{-1}) indicated that each albumin molecular system has the ability to react with about 90 FMOC-Cl molecules. For peptone, its stoichiometric reaction with FMOC-Cl is not clear because peptone is a mixture of polypeptides and amino acids with not well-defined molar mass. For the same mass/volume concentration (0.5–32.0 mg L^{-1}) of PG, albumin, and peptone, the calibration curve slopes have the order PG (0.0269 L mg^{-1}) > peptone (0.0229 L mg^{-1}) > albumin (0.0199 L mg^{-1}). This means that, for the same mass of these peptides, number of reacted FMOC-Cl molecules with peptides increases in the order albumin < peptone < PG.

For a sample containing GLP and known concentration of peptide (such as PG, albumin, or peptone), a standard blank subtraction for calibration of GLP can correct the increased extinction coming from the FMOC–peptide–complex signal. Of course, this only holds true if these reactions are independent of each other and there is no interference with the remaining matrix. In order to check this, GLP calibration curves have been measured in the presence of constant concentrations of PG as shown in Fig. 3. Here we observe a decreasing in the UV absorbance with increasing the PG concentration, i.e. slope changes like 0.0144 L μmol^{-1} (pure GLP) > 0.0125 L μmol^{-1} (0.5 mg_{PG} L^{-1}) > 0.0056 L μmol^{-1} (16 mg_{PG} L^{-1}) > 0.0023 L μmol^{-1} (32 mg_{PG} L^{-1}). This indicates a decrease in the GLP recovery upon increasing the PG concentration (see Fig. 3 and Table S2 in SM). This observation is readily explained using the quantum chemical results due to the strong binding between GLP and PG. This reduces the availability of GLP for derivatization and thus for reaction with the FMOC-Cl UV sensor. Thus, the 1:1 complex formation reaction between GLP and PG is an example for the matrix interference.

For albumin and peptone, there is no clear trend like what was observed for the PG case. Adding 0.5 mg L^{-1} of albumin or peptone matrix into the GLP solution has no significant effect on the GLP absorbance values and thus the GLP recovery (see Figs. 4 and 5 and Tables S3 and S4 in SM). Almost the observed absorbance values for GLP in the albumin and peptone matrices are in the same range of those observed for pure GLP solution. At 0.37 μmol L^{-1} GLP, low GLP absorbance values are reported in the presence of albumin or peptone compared to the pure GLP. For higher albumin and peptone concentrations (16 and 32 mg L^{-1}), high GLP absorbance values have been observed at low GLP concentrations. This observed GLP overestimation was more significant for the peptide matrices of 16 mg L^{-1} for albumin and 32 mg L^{-1} for peptone. In contrast, low GLP absorbance values have been reported at high concentrations of GLP (94.67 μmol L^{-1}) and peptides (albumin or peptone, 32 mg L^{-1}). This indicates that the GLP analytics may be affected by the molecular composition of the interfering peptides as well as concentrations of these peptides and GLP in the environmental samples.

3.3. Implications for soil samples

Soil samples have unknown concentrations of GLP and peptides (as well as other primary and secondary amines which are present in soil in a range of 9–24 mg g^{-1} of humic substances, Ramunni et al., 1985) which likely interfere with each other. Therefore, a blank cannot be predefined and blank correction is impossible. Since the non-specific nature of FMOC-Cl with respect to GLP and peptides is well-known (Moye and Boning, 1979), calibration experiments with chromatographic separation and mass-spectrometric detection have been performed. For instance, calibration experiments with chromatographic separation yielded recoveries of 70–80% (Roseboom and Berkhoff, 1982) and those with mass-spectrometric detection of FMOC–GLP molecules yielded a recovery of about 67% (Ramirez et al., 2014). Similarly, the use of ^{13}C and ^{15}N isotopic labelled GLP (GLP_{ISO}) standards in combination with chromatographic separation and mass-spectrometric detection led to a recovery of 80% (Grey et al., 2001). In other words, these recoveries indicate that 33%–20% of the existing GLP in the environmental samples are not determined. In view of the present findings (Figs. 3–5), these observations can be explained by formation of stable complexes between GLP and matrix constituents

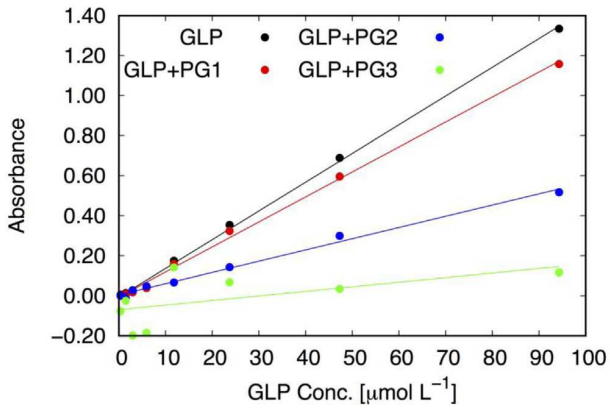


Fig. 3. Calibration curves of GLP in the presence of different concentrations of PG (PG1, PG2, and PG3 correspond to 0.5, 16, and 32 mg L^{-1} of PG). Note that a blank correction for PG has been applied (blank absorbance values are 0.0519, 0.4879, and 0.8882 for PG concentrations of 0.5, 16, and 32 mg L^{-1}, respectively). Black line and points correspond to the pure GLP calibration curve with a blank absorbance value of 0.0293.

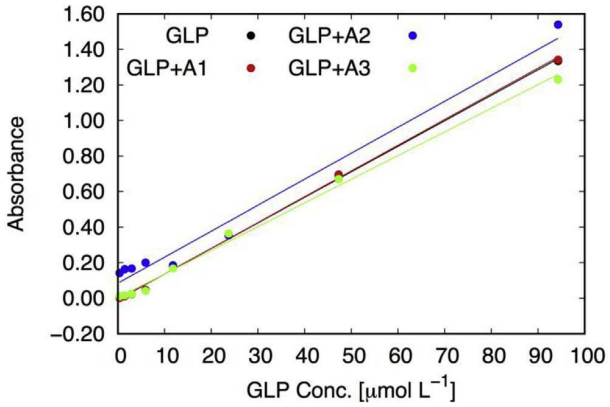


Fig. 4. Calibration curves of GLP in the presence of different concentrations of albumin (A1, A2, and A3 correspond to 0.5, 16, and 32 mg L^{-1} of albumin). Note that a blank correction for albumin has been applied (blank absorbance values are 0.0626, 0.2064, and 0.7090 for albumin concentrations of 0.5, 16, and 32 mg L^{-1}, respectively). Black line and points correspond to the pure GLP calibration curve with a blank absorbance value of 0.0293.

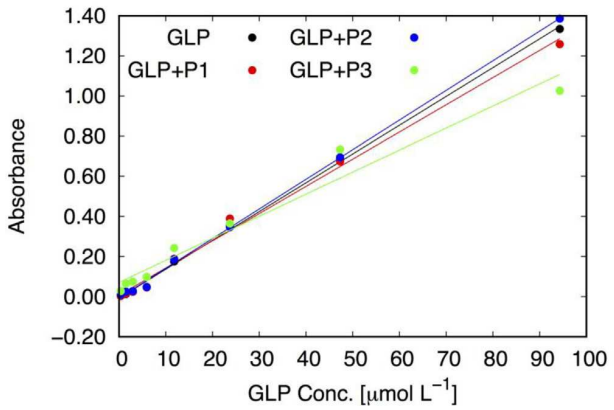


Fig. 5. Calibration curves of GLP in the presence of different concentrations of peptone (P1, P2, and P3 correspond to 0.5, 16, and 32 mg L^{-1} of peptone). Note that a blank correction for peptone has been applied (blank absorbance values are 0.0478, 0.4266, and 0.7589 for peptone concentrations of 0.5, 16, and 32 mg L^{-1}, respectively). Black line and points correspond to the pure GLP calibration curve with a blank absorbance value of 0.0293.

(such as peptides) that inhibit the derivatization of GLP by FMOC-Cl. The use of isotopic labelled standards may not correct these effects since sample GLP, parts of which previously reacted with sample peptides, and added GLP_{ISO} does not exist in the same free form as it is required for a uniform derivatization.

3.4. Implication for samples with high protein content

According to Arkan and Molnár-Perl (2015) who discussed different derivatization techniques for GLP, the most common procedures for serum, urine and blood uses N-(t-butyldimethylsilyl)-N-methyltrifluoroacetamide (MTBSTFA) derivatization and GC detection. Here, the FMOC derivatization approach plays a minor role. Interferences have been observed due to the existing peptides especially in samples with high peptide contents (up to several $mg_{Peptide}$ dL^{-1}) like milk, blood or urine. This may also cause difficulties in quantification of low GLP concentrations if quantification with a derivatization step including FMOC-Cl is chosen.

4. Conclusion

In conclusion, these exemplary experiments and quantum chemical modeling reveal a strong interaction of GLP and peptides (PG, albumin, and peptone) in solution. Both species (GLP and peptides) react similarly with FMOC-Cl and additionally interfere with each other, thus, likely inhibiting the GLP derivatization reaction. As a consequence, two competing effects can occur in soil or similarly complex environmental samples. First, the presence of peptides (or other species binding to FMOC-Cl) may lead to an overestimation of the GLP concentration. Second, the complexation of GLP with peptides (or other species binding to GLP, e.g. metal ions) may cause an underestimation of the GLP concentration. Specifically, our results showed strong interactions between GLP and PG (i.e. underestimation) for all the studied concentration levels of GLP and PG. For albumin and peptone, complex behavior has been explored for their interactions with GLP and FMOC-Cl. At high concentrations of albumin (16 mg L^{-1}) and peptone (32 mg L^{-1}) and low GLP concentrations, high GLP overestimation has been observed. While, GLP underestimation has been reported at the highest concentrations of GLP (94.67 µmol L^{-1}) and peptides (albumin or peptone, 32 mg L^{-1}) used in the current study. This indicates that the GLP-peptide-interaction is mainly affected by type of the existing interfering peptides as well as concentration of each peptide and GLP in the environmental samples. In environmental samples, the magnitudes of these competing effects are not known and even a cancelation of both effects could be possible. This makes an accurate quantitative determination of GLP in such samples using FMOC-Cl complicated. In forthcoming studies these preliminary results will be extended to real soil samples and, thus, the effects of the reactions shown in the present study will be investigated using state-of-the-art GLP detection methods (e.g. LC/MSMS).

Acknowledgements

The modeling part of this work has been performed within the InnoSoilPhos-project (http://www.innosoilphos.de/default.aspx), funded by the German Federal Ministry of Education and Research (BMBF) in the frame of the BonaRes-program (No. 031A558). Peter Gros acknowledges a PhD-grant from the state of Mecklenburg-Western Pommeria. This research was conducted within the scope of the Leibniz ScienceCampus Phosphorus Research Rostock.

Appendix A. Supplementary data

Supplementary data related to this article can be found at https://doi.org/10.1016/j.chemosphere.2017.12.162.

References

Aparicio, V.C., De Gerónimo, E., Marino, D., Primost, J., Carriquiriborde, P., Costa, J.L., 2013. Environmental fate of glyphosate and aminomethylphosphonic acid in surface waters and soil of agricultural basins. Chemosphere 93, 1866–1873. https://doi.org/10.1016/j.chemosphere.2013.06.041.

Arkan, T., Molnár-Perl, I., 2015. The role of derivatization techniques in the analysis of glyphosate and aminomethyl-phosphonic acid by chromatography. Microchem. J. 121, 99–106. https://doi.org/10.1016/j.microc.2015.02.007.

Becke, A.D., 1988. Density-functional exchange-energy approximation with correct asymptotic behavior. Phys. Rev A 38, 3098–3100. https://doi.org/10.1103/PhysRevA.38.3098.

Borggaard, O.K., Gimsing, A.L., 2008. Fate of glyphosate in soil and the possibility of leaching to ground and surface waters: a review. Pest Manag. Sci. 64, 441–456. https://doi.org/10.1002/ps.1512.

Carpino, L.A., Han, G.Y., 1972. 9-Fluorenylmethoxycarbonyl amino-protecting group. J. Org. Chem. 37, 3404–3409. https://doi.org/10.1021/jo00795a005.

Castellino, S., Leo, G.C., Sammons, R.D., Sikorski, J.A., 1989. Phosphorus-31, nitrogen-15, and carbon-13 and NMR of glyphosate: comparison of pH titrations to the herbicidal dead-end complex with 5-enolpyruvoylshikimate-3-phosphate synthase. Biochemistry 28, 3856–3868. https://doi.org/10.1021/bi00435a035.

Catrinck, T.C.P.G., Dias, A., Aguiar, M.C.S., Silvério, F.O., Fidêncio, P.H., Pinho, G.P., 2014. A simple and efficient method for derivatization of glyphosate and AMPA using 9-fluorenylmethyl chloroformate and spectrophotometric analysis. J. Braz. Chem. Soc. https://doi.org/10.5935/0103-5053.20140096.

Cossi, M., Rega, N., Scalmani, G., Barone, V., 2003. Energies, structures, and electronic properties of molecules in solution with the C-PCM solvation model. J. Comput. Chem. 24, 669–681. https://doi.org/10.1002/jcc.10189.

Freuze, I., Jadas-Hecart, A., Royer, A., Communal, P.-Y., 2007. Influence of complexation phenomena with multivalent cations on the analysis of glyphosate and aminomethyl phosphonic acid in water. J. Chromatogr. A 1175, 197–206. https://doi.org/10.1016/j.chroma.2007.10.092.

Frisch, M.J., Trucks, G.W., Schlegel, H.B., Scuseria, G.E., Robb, M.A., Cheeseman, J.R., et al., 2013. Gaussian 09 Revis D01. Gaussian Inc, Wallingford CT.

Grey, L., Nguyen, B., Yang, P., 2001. Liquid chromatography/electrospray ionization/isotopic dilution mass spectrometry analysis of n-(phosphonomethyl) glycine and mass spectrometry analysis of aminomethyl phosphonic acid in environmental water and vegetation matrixes. J. AOAC Int. 84, 1770–1780.

Grimme, S., Ehrlich, S., Goerigk, L., 2011. Effect of the damping function in dispersion corrected density functional theory. J. Comput. Chem. 32, 1456–1465. https://doi.org/10.1002/jcc.21759.

Gros, P., Ahmed, A., Kühn, O., Leinweber, P., 2017. Glyphosate binding in soil as revealed by sorption experiments and quantum-chemical modeling. Sci. Total Environ. 586, 527–535. https://doi.org/10.1016/j.scitotenv.2017.02.007.

Hanke, I., Singer, H., Hollender, J., 2008. Ultratrace-level determination of glyphosate, aminomethylphosphonic acid and glufosinate in natural waters by solid-phase extraction followed by liquid chromatography–tandem mass spectrometry: performance tuning of derivatization, enrichment and detection. Anal. Bioanal. Chem. 391, 2265–2276. https://doi.org/10.1007/s00216-008-2134-5.

Hehre, W.J., Ditchfield, R., Pople, J.A., 1972. Self—consistent molecular orbital

methods. Xii. Further extensions of Gaussian—type basis sets for use in molecular orbital studies of organic molecules. J. Chem. Phys. 56, 2257–2261. https://doi.org/10.1063/1.1677527.

Jansen, H.B., Ros, P., 1969. Non-empirical molecular orbital calculations on the protonation of carbon monoxide. Chem. Phys. Lett. 3, 140–143. https://doi.org/10.1016/0009-2614(69)80118-1.

Koskinen, W.C., Marek, L.J., Hall, K.E., 2016. Analysis of glyphosate and aminomethylphosphonic acid in water, plant materials and soil: analysis of glyphosate and AMPA in water, plant materials and soil. Pest Manag. Sci. 72, 423–432. https://doi.org/10.1002/ps.4172.

Kubicki, J.D. (Ed.), 2016. Molecular Modeling of Geochemical Reactions: an Introduction. Wiley, Chichester, West Sussex, United Kingdom.

Lee, C., Yang, W., Parr, R.G., 1988. Development of the Colle-Salvetti correlation-energy formula into a functional of the electron density. Phys. Rev. B 37, 785–789. https://doi.org/10.1103/PhysRevB.37.785.

Moye, H.A., Boning, A.J., 1979. A versatile fluorogenic labelling reagent for primary and secondary amines: 9-fluorenylmethyl chloroformate. Anal. Lett. 12, 25–35. https://doi.org/10.1080/00032717908082516.

Ramirez, C.E., Bellmund, S., Gardinali, P.R., 2014. A simple method for routine monitoring of glyphosate and its main metabolite in surface waters using lyophilization and LC-FLD+MS/MS. Case study: canals with influence on Biscayne National Park. Sci. Total Environ. 496, 389–401. https://doi.org/10.1016/j.scitotenv.2014.06.118.

Ramunni, A., Scialdone, R., Felleca, D., 1985. Analytical problems in determining peptide nitrogen in the humic fractions of three Italian soils. Org. Geochem. 8, 87–93. https://doi.org/10.1016/0146-6380(85)90056-7.

Roseboom, H., Berkhoff, C.J., 1982. Determination of the herbicide glyphosate and its major metabolite aminomethylphosphonic acid by high-performance liquid chromatography after fluorescence labelling. Anal. Chim. Acta 135, 373–377. https://doi.org/10.1016/S0003-2670(01)93923-6.

Skeff, W., Neumann, C., Schulz-Bull, D.E., 2015. Glyphosate and AMPA in the estuaries of the Baltic Sea method optimization and field study. Mar. Pollut. Bull. 100, 577–585. https://doi.org/10.1016/j.marpolbul.2015.08.015.

Stalikas, C.D., Konidari, C.N., 2001. Analytical methods to determine phosphonic and amino acid group-containing pesticides. J. Chromatogr. A 907, 1–19. https://doi.org/10.1016/S0021-9673(00)01009-8.

Vreeken, R., Speksnijder, P., Bobeldijk-Pastorova, I., Noij, T.H., 1998. Selective analysis of the herbicides glyphosate and aminomethylphosphonic acid in water by on-line solid-phase extraction–high-performance liquid chromatography–electrospray ionization mass spectrometry. J. Chromatogr. A 794, 187–199. https://doi.org/10.1016/S0021-9673(97)01129-1.

Waiman, C.V., Avena, M.J., Garrido, M., Fernández Band, B., Zanini, G.P., 2012. A simple and rapid spectrophotometric method to quantify the herbicide glyphosate in aqueous media. Application to adsorption isotherms on soils and goethite. Geoderma 170, 154–158. https://doi.org/10.1016/j.geoderma.2011.11.027.

Supplementary Material

Molecular level investigation of the role of peptide interactions in the glyphosate analytics

Ashour A. Ahmed[1,2,*], Peter Gros[3], Oliver Kühn[1], Peter Leinweber[3]

[1] University of Rostock, Institute of Physics, D-18059 Rostock, Germany.

[2] University of Cairo, Faculty of Science, Department of Chemistry, 12613 Giza, Egypt.

[3] University of Rostock, Soil Science, D-18059 Rostock, Germany.

ashour.ahmed@uni-rostock.de

peter.gros@uni-rostock.de

oliver.kuehn@uni-rostock.de

peter.leinweber@uni-rostock.de

Figures

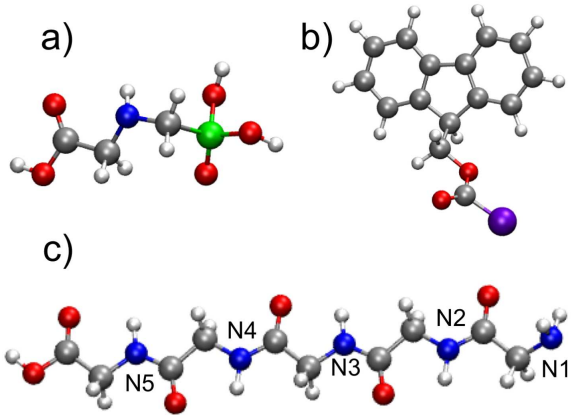


Figure S1. Optimized geometries of GLP (a), FMOC-Cl (b), and PG (c) at the B3LYP/D3/63311++G(d.p) level of theory and using the CPCM model. White, gray, blue, red, green, and violet colors are corresponding to H, C, N, O, P, and Cl atoms, respectively.

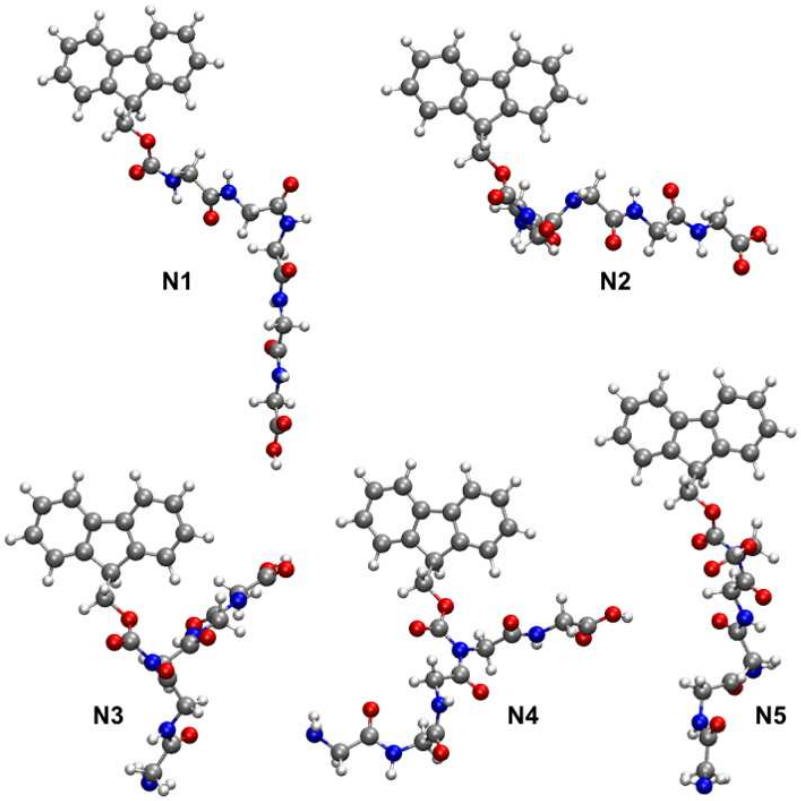


Figure S2. Optimized geometries of the FMOC3PG complexes at the B3LYP/D3/63311++G(d.p) level of theory and using the CPCM model. Here the FMOC-Cl derivatization reactions take place at five different PG amino groups, primary amino group (N1) and four secondary amino groups (N2 to N5 ordered from the PG amino group to the PG carboxylic group). White, gray, blue, red, and green colors are corresponding to H, C, N, O, and P atoms, respectively.

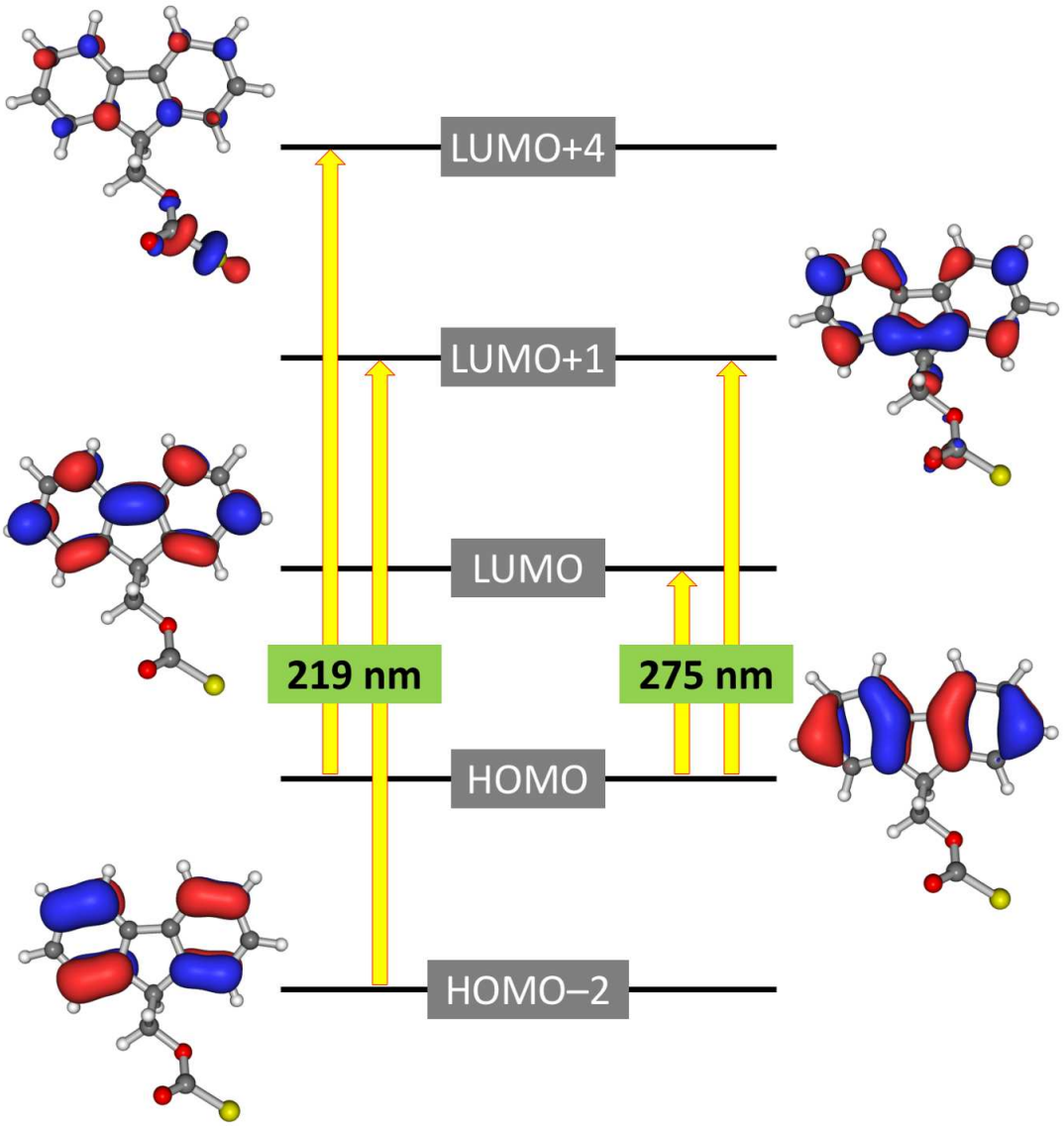


Figure S3. Possible electronic transitions from the highest occupied molecular orbitals (HOMOs) to the lowest unoccupied molecular orbitals (LUMOs) for FMOC-Cl calculated at the TD-DFT/B3LYP/63 311++G(d.p)/ CPCM level of theory.

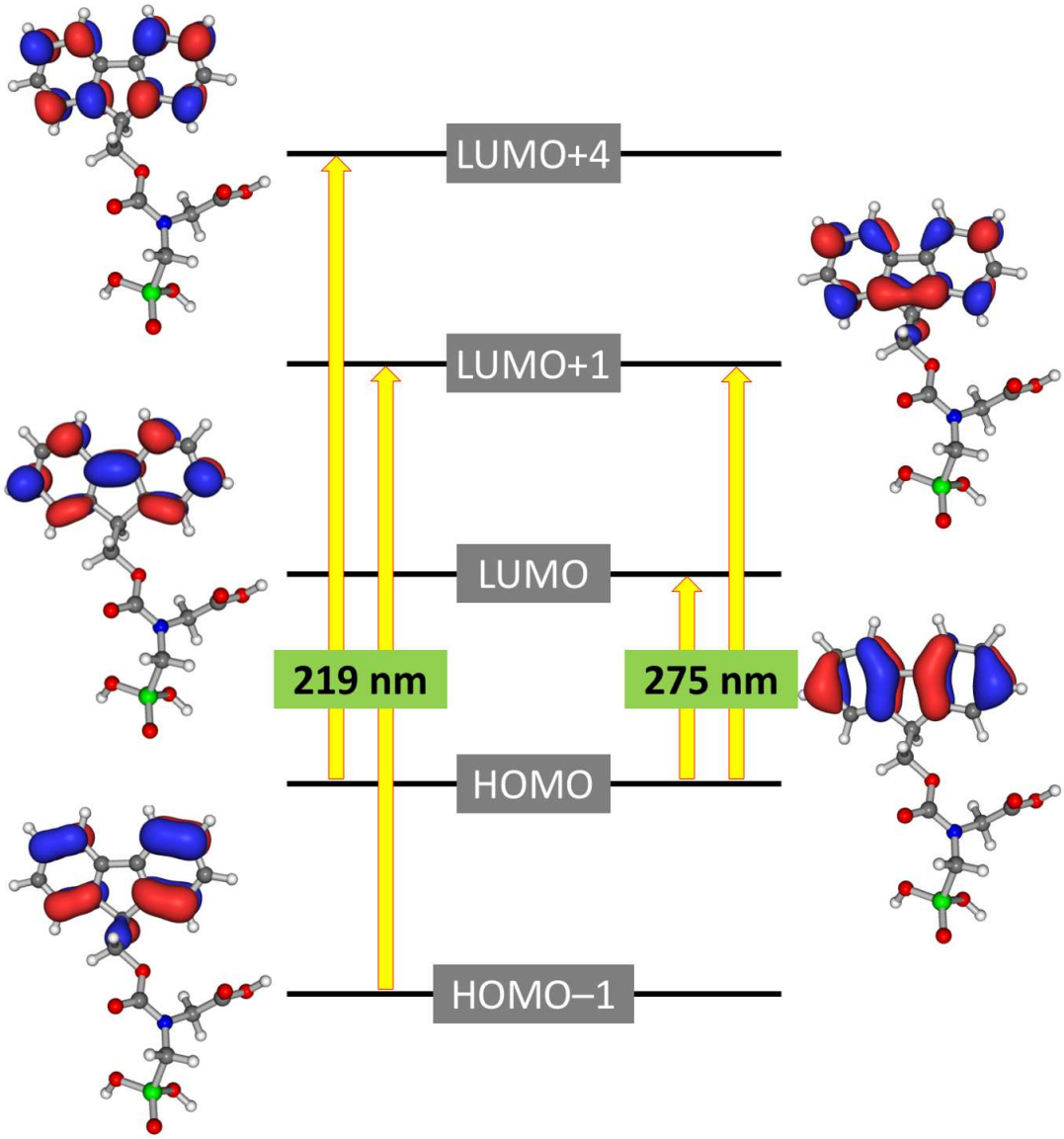


Figure S4. Possible electronic transitions from the highest occupied molecular orbitals (HOMOs) to the lowest unoccupied molecular orbitals (LUMOs) for the FMOC-GLP complex calculated at the TD-DFT/B3LYP/63311++G(d.p)/ CPCM level of theory.

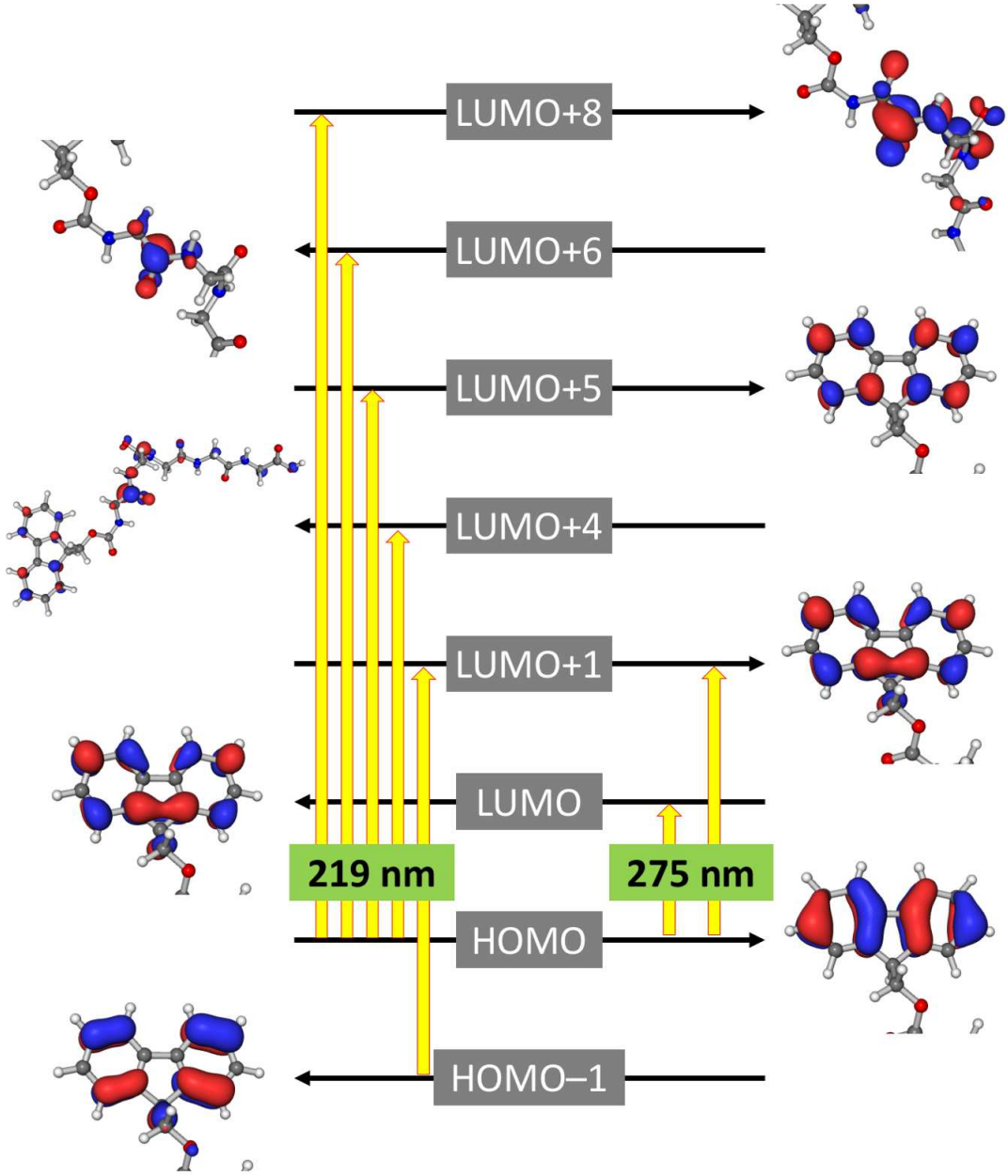


Figure S5. Possible electronic transitions from the highest occupied molecular orbitals (HOMOs) to the lowest unoccupied molecular orbitals (LUMOs) for the FMOC-PG complex calculated at the TD-DFT/B3LYP/63311++G(d.p)/ CPCM level of theory.

Table

Table S1. Calculated reaction energies and free energies at the B3LYP/D3/63311++G(d.p) level of theory and using the CPCM model for the derivatization reactions of FMOC-Cl with GLP and with PG at five different PG amino groups (primary amino group (N1) and four secondary amino groups (N2 to N5 ordered from the PG amino group to the PG carboxylic group)).

	&E (kcal/mol)	&G (kcal/mol)
FMOC-GLP	-18.8	-16.3
FMOC-PG (N1)	-13.9	-11.8
FMOC-PG (N2)	-1.0	3.1
FMOC-PG (N3)	-1.1	1.6
FMOC-PG (N4)	-2.9	0.1
FMOC-PG (N5)	-2.1	1.6

Publication 14

P. Gros, Ashour A. Ahmed, O. Kühn, P. Leinweber. Influence of metal ions on glyphosate detection by FMOC-Cl. Environ. Monit. Assess. **2019**, 191, 244.

Contribution: Ashour A. Ahmed is credited with conceptualization, conducting the modeling work, modeling analysis and interpretation, methodology development, visualization, and writing the original manuscript with P. Gros. Ashour A. Ahmed and co-authors are responsible for reviewing, and editing the manuscript.

URL: https://doi.org/10.1007/s10661-019-7387-2

QR:

Ashour Ahmed FMOC-Cl

Reproduced with the permission of Springer Nature

Environ Monit Assess (2019) 191:244
https://doi.org/10.1007/s10661-019-7387-2

Influence of metal ions on glyphosate detection by FMOC-Cl

Peter Gros · Ashour A. Ahmed · Oliver Kühn · Peter Leinweber

Received: 1 November 2018 / Accepted: 13 March 2019
© Springer Nature Switzerland AG 2019

Abstract Glyphosate (GLP, *N*-(phosphono methyl)glycine) is the most important broadband herbicide in the world, but discussions are controversial regarding its environmental behaviour and distribution. Residue analyses in a variety of environmental samples are commonly conducted by HPLC–MS where GLP needs to be derivatised with 9-fluoromethoxycarnonyl chloride (FMOC-Cl). Since this derivatisation reaction was suspected to be inhibited by metal ions in the sample matrix, the present study provides a comprehensive experimental study of the effect of metal ions (Al^{3+}, Ca^{2+}, Cd^{2+}, Co^{2+}, Cu^{2+}, Fe^{2+}, Fe^{3+}, Mg^{2+}, Mn^{2+}, Zn^{2+}) on derivatisation and GLP recovery. Results show that some metals (Cd^{2+}, Co^{2+}, Cu^{2+}, Mn^{2+} and Zn^{2+}) decreased the GLP recovery down to 19 to 59%. Complementary, quantum chemical modelling of 1:1 GLP–metal complexes as well as their reactivity with respect to FMOC-Cl was performed. Here, a decrease in reactivity of FMOC-Cl towards GLP–metal complexes is observed; i.e. the reaction is non-spontaneous in contrast to the free GLP case. The present results are in accord with previous studies and provide an explanation that full GLP recovery in different matrices was never reached. Remedy strategies to compensate for the inhibition effect are explored such as pH adjustment to acidic or alkaline conditions or addition of ethylenediaminetetraacetic acid (EDTA). In general, our results question the use of internal isotopic labelled standards (ILS) since this presupposes the presence of the analyte and the ILS in the same (free) form.

Keywords Glyphosate (GLP) · FMOC-Cl · Complex formation · Derivatisation · EDTA

Introduction

N-(Phosphonomethyl)glycine (glyphosate, GLP) is a non-selective broadband herbicide developed in 1964 (US Patent 3,160,632 A) and patented for commercial use in 1974 by Monsanto (Franz 1974). In the past decades, glyphosate-based formulations became the most important herbicides with annual use of more than 1 million tonnes worldwide (Global Analysists Industry Inc. 2011). There are concerns about the ecological impact of GLP regarding the distribution in the environment and its effects on organisms. In this respect, it is important to emphasise that the detection of GLP for environmental monitoring and residue analysis in products is challenging due to (i) the molecule's ability to

Electronic supplementary material The online version of this article (https://doi.org/10.1007/s10661-019-7387-2) contains supplementary material, which is available to authorized users.

P. Gros (✉) · P. Leinweber
Soil Science, University of Rostock, Justus-von-Liebig-Weg 6, 18059 Rostock, Germany
e-mail: peter.gros@uni-rostock.de

A. A. Ahmed · O. Kühn
Institute of Physics, University of Rostock, Albert-Einstein-Str. 23-24, 18059 Rostock, Germany

A. A. Ahmed · O. Kühn · P. Leinweber
Department of Life, Light, and Matter (LLM), University of Rostock, Albert-Einstein-Str. 25, 18059 Rostock, Germany

Published online: 26 March 2019

engage in diverse interactions with sample matrix constituents (Arkan and Molnár-Perl 2015) and (ii) the absence of specifics in the molecule's structure (the phosphono, amine and carboxylic moieties are rather abundant in nature) that can be utilised for direct analytical detection (Catrinck et al. 2014).

There is a great variety of interactions of GLP with environmental organic and inorganic substances. For example, the enzyme EPSP synthase binds GLP and is therefore blocked (Hensley et al. 1978) in plant cells and some other microorganisms (Van Bruggen et al. 2018). Recently, interactions of GLP with organic compounds like carbohydrates and peptides in soils have been demonstrated (Gros et al. 2017; Ahmed et al. 2018a) indicating a strong affinity to peptides and carbohydrates due to proton transfer and formation of H–bonds, respectively. Furthermore, the nature of GLP binding to different crystal planes of the mineral goethite has been investigated by ab initio molecular dynamics simulations (Ahmed et al. 2018b). The affinity of GLP to metals in general, resulting in chelating interactions, has been discovered decades ago (Toy et al. 1964). Also, free metal ions like Mn^{2+} form strong and less reactive complexes with GLP so that the interaction of GLP with enzymes is inhibited and therefore, the herbicidal effect is diminished (Bernards et al. 2005).

Complexation of GLP with metals has environmental implications since (i) co-factors like Co^{2+} for enzymatic reactions in cells can be revoked (Ganson and Jensen 1988), (ii) GLP–metal complexes (Fe^{2+}, Fe^{3+}, Al^{3+}, Ca^{2+}, Cd^{2+}, Na^{+} and K^{+}) have diminished toxicity to root growth due to decreased membrane permeability (Hensley et al. 1978; Wang et al. 2004), (iii) sorption of GLP–metal complexes by soil surfaces is different from those of free GLP. For example, GLP complexes with Pb^{2+} are less attracted by soil minerals (Si et al. 2013) and Cu sorption onto montmorillonite is diminished by GLP due to complexation (Undabeytia et al. 1996). As a consequence, the leaching potential and distribution of GLP–metal complexes in the environment is increased.

The characteristics of GLP–metal complexes have been studied intensively over the past years. The coordination of GLP as a ligand in these complexes with different metals as central ions is dependent on the surrounding pH leading to different stability constants (Lundager Madsen et al. 1978, Glass 1984; Subramaniam and Hoggard 1988; Morillo et al. 2002). In the same context, the GLP complexation process with free metal ions has been studied recently by computational chemistry (Caetano et al. 2012). The results indicated that there is no clear trend with respect to binding of divalent and trivalent ions to GLP. Also, the GLP degradation into aminomethylphosphonic acid (AMPA) has been investigated by joint experimental/computational studies (Ascolani Yael et al. 2014; Jaisi et al. 2016). Here, the detection of AMPA after interaction of GLP with metallic ions in aqueous solution was investigated, which revealed the crucial role of metal ions in the GLP degradation process.

Different analytical methods have been used for experimental structural studies. Heineke et al. (1994) and Purgel et al. (2009) proved the participation of all three functional moieties of the GLP molecule in complexes with Al and Co by using nuclear magnetic resonance, infrared and X-ray spectroscopic as well mass spectrometric methods. Daniele et al. (1997) showed by pH-metric measurements that GLP can form complexes with itself. Also, potentiometric studies have been conducted for measuring complex stabilities (Kobylecka et al. 2000) as well as thermal diffractometry and infrared spectroscopy for solubility determination (Ptaszyński and Zwolińska 2001). These methods clearly showed that complexes of GLP with metals are of great variety in structure and, due to their strengths as well as the abundance of metal ions in environmental compartments, GLP is unlikely to exist in its free form.

The GLP quantification is most often conducted by derivatising the molecule with 9-flouromethoxycarbonyl chloride (FMOC-Cl) prior to chromatographic separation from by-products and the following mass spectrometric detection. However, this chemical reaction is affected when GLP is not free in solution, which results in less reactivity (Freuze et al. 2007). For example, compared with pure water samples, recovery was decreased in several groundwater samples tested in an interlaboratory test (Reichert et al. 2006). In particular, the retention time in reversed phase chromatography of derivatised GLP is affected by the presence of metal ions (Skeff et al. 2016). These matrix effects in environmental samples are usually compensated by the use of internal isotopic labelled standards (ILS) in connection with mass spectrometry (Ibanez et al. 2006; Hanke et al. 2008). But, this approach assumes the presence of GLP and its ILS in the same free form. However, because of the likely formation of GLP–metal complexes, these and the added ILS are not equivalent and might undergo different interactions. Therefore, it is necessary to convert GLP into its free form prior to derivatisation as proposed by Ibanez et al. (2006), e.g. by (i) acidification of the sample or (ii) addition of

ethylenediaminetetraacetic acid (EDTA) as a strong complexing agent breaking up the GLP–metal complexes. The acidification of samples to pH about 1 followed by re-alkalisation to pH 9 for optimal derivatisation is a time-consuming step and has the disadvantage that different pH regimes during complex formation affect different GLP–metal species in an unknown way. Since EDTA has higher stability constants with a variety of metal ions compared with those of GLP (Popov et al. 2001; Furia 2006), an exchange of GLP by EDTA as a ligand is likely to convert complexed GLP into its free form and thus diminish interferences during derivatisation. To the best of our knowledge, there is no systematic study testing EDTA as agent for pre-treating water samples with different metal ions as matrix constituents. Most of the reported usages of EDTA during sample preparation employed this reagent after derivatisation to overcome unwanted matrix effects during chromatographic separation (e.g. Hanke et al. 2008; Skeff et al. 2016). The only use of EDTA after a lyophilisation step and prior to derivatisation was described by Ramirez et al. (2014), but without mentioning the necessity of suppressing matrix effects occurring from GLP–metal complexation. Therefore, this study will experimentally test the addition of EDTA as a simple sample treatment step prior to derivatisation of GLP in matrices with different divalent and trivalent metal ions, which are abundant in environmental samples. Specifically, our objective here is to determine the metal influence of GLP recovery by using a simple photometric setup which is suitable to quantify GLP in samples of lower matrix complexity with known concentrations of all constituents and to elucidate their interactions. Furthermore, the influence of different pH regimes during GLP–metal complex formation on GLP recovery as well as possible effects of EDTA during sample preparation will be studied in detail for two metal ions. Here, Cu^{2+} and Fe^{3+} are chosen as representative among the strong complexing divalent and trivalent metal ions with GLP (lg K (Cu^{2+}) = 11.7–16.4, lg K (Fe^{3+}) = 16.1–23.0; Popov et al. 2001). Furthermore, Cu^{2+} and Fe^{3+} are abundant metal ions in environmental samples like soil, plant material and serum as possible interfering matrix constituents. Deeper insight is provided by quantum chemical simulations. This concerns the complexation process between GLP and several metal ions and the derivatisation reaction of FMOC-Cl with free GLP as well as with the metal–GLP complexes and the effect of metal ions on the GLP detection by FMOC-Cl. Independent analysis of the reactions and mechanisms of interaction between GLP and metal ions during derivatisation from an experimental- and a molecular-level quantum-chemical point of view has not been reported so far. Thus, the present study will help to understand the effects of GLP–metal interactions towards a strategy for overcoming these during sample preparation.

Materials and methods

Chemicals

The used chemicals were of p.a. (for analysis) purity grade and were purchased as follows.

Sigma Aldrich: GLP (CAS: 1071-83-6) and FMOC-Cl (CAS: 28920-43-6).
Carl Roth: $AlCl_3 \cdot 6\ H_2O$ (CAS: 7784-13-6), $CaCl_2 \cdot 6\ H_2O$ (CAS: 7774-34-7), $CdCl_2$ (CAS: 10108-64-2), $CoCl_2 \cdot 6\ H_2O$ (CAS: 7791-13-1), $CuCl_2 \cdot 2\ H_2O$ (CAS: 10125-13-0), $ZnCl_2$ (CAS: 7646-85-7), $Na_2EDTA \cdot 2\ H_2O$ (CAS: 6381-92-6), $Na_2B_4O_7 \cdot 10\ H_2O$ (CAS: 1303-96-4) and dichloromethane (CAS: 75-09-2).
Merck: $FeSO_4 \cdot 7\ H_2O$ (CAS: 7782-63-0), $FeCl_3 \cdot 6\ H_2O$ (CAS: 10025-77-1), $MgCl_2 \cdot 6\ H_2O$ (CAS: 7791-18-6) and KOH (CAS: 26288-25-5).
VEB Berlin Chemie: $MnCl_2 \cdot 4\ H_2O$ (CAS: 13446-34-9).
Ultrapure water was received own from laboratory device.

Apparatus

The materials used are UV-VIS spectroscope (Specord 40, Analytik Jena AG, Jena 07745, Germany), pH metre (Mettler Toledo Five Easy Plus with InLab Micro-Pro ISM electrode, 35396 Gießen, Germany), centrifuge (Themo Scientific, Heraeus Multiforce 3SR+, Osterode 37520, Germany).

Experimental design

Study on GLP recovery in the presence of EDTA

For each metal ion, a 50-mL solution of a mixture involving 52.3 μM GLP and 52.3 μM metal ion was

prepared in distilled water under neutral pH conditions. A reference containing only 52.3 μM GLP solution was prepared as blank. Solutions were left to rest for 2 h with occasional shaking. After that, ten aliquots (3 mL) were taken from each solution. Five of these aliquots 0.5 mL of EDTA solution (1.75 mM) and five 0.5 mL of distilled water were added. These treated solutions were shaken again and then left to rest for 30 min. According to the method of Waiman et al. (2012), the samples were derivatised with FMOC-Cl and prepared for photometric measurement at 264 nm. Different derivatisation times (0.5–15 h) for the system (i) GLP, (ii) GLP and Cu^{2+} and (iii) GLP and Fe^{3+} were tested each with and without treatment of EDTA to ensure equilibrium conditions (Fig. S1). Additionally, UV spectra were taken (220–320 nm) from all solution tested for equilibrium conditions to check that no peak shift of the 264-nm GLP–FMOC maximum occurred (Fig. S2).

Study on pH influence

Stock solutions of Fe^{3+}, Cu^{2+} and GLP were prepared and adjusted with hydrochloric acid and potassium hydroxide to pH 4.5, 9 and 12. GLP stock solutions were mixed with the corresponding metal ion solution of similar pH to reach a constant metal ion concentration of 13.3 μM and GLP concentrations of 0, 6.65, 13.3, 26.6, 39.9 and 53.2 μM. The solutions were mixed thoroughly and left to rest for 2 h. After that, the solutions were adjusted to neutral pH with hydrochloric acid and potassium hydroxide to provide same derivatisation preconditions among the samples and for comparability to real environmental samples. From each solution, 6 × 3 mL was taken and filled into 15-mL centrifuge tubes. One half was treated with 0.5 mL EDTA solution (1.75 mM) and the other half with 0.5 mL of distilled water. The solutions were left to rest for 30 min. According to the method of Waiman et al. (2012), the samples were then derivatised with FMOC-Cl and prepared for photometric measurement at 264 nm.

Quantum chemical modelling

The interaction of GLP with several metal ions including Mg^{2+}, Ca^{2+}, Al^{3+}, Cr^{3+}, Mn^{2+}, Fe^{2+}, Fe^{3+}, Co^{2+}, Cu^{2+} and Zn^{2+} was simulated through 1:1 complex formation between GLP and each metal ion. Here, GLP and metal ions were modelled according to their abundant species in solution at the relevant pH. Each metal ion was modelled as octahedral metal aqua complex while GLP was taken as a negatively charged species with total charge − 1 ($[GLP]^{1-}$). The interaction between GLP and the metal ion was modelled by a bidentate binding motif. Here, two covalent bonds were included, i.e. from the GLP's carboxylate and phosphonate groups to the respective metal ion. Thus, the modelled reaction is:

$$1\ [GLP]^{1-} + 1\ \left[M(H_2O)_6\right]^{n+} \rightarrow 1\ \left[(H_2O)_4M\text{–}GLP\right]^{n-1} + 2\ H_2O \quad (1)$$

Full geometry optimisation was performed for the metal complexes ($[M(H_2O)_6]^{n+}$ and $[(H_2O)_4M\text{–}GLP]^{n-1}$), GLP and water. The calculations have been performed using density functional theory (DFT) as implemented in the Gaussian09 program package (Frisch et al. 2013). Specifically, the B3LYP hybrid functional (Becke 1988; Lee et al. 1988) combined with the 6-311++G(d,p) basis set (Hehre et al. 1972) and Grimme's D3 dispersion correction (Grimme et al. 2011) has been applied. Moreover, harmonic vibrational frequencies were calculated for all optimised geometries. These geometries are characterised by having zero gradient norms and positive harmonic vibrational frequencies.

For the metal–GLP complexation reaction in Eq. (1), the reaction energy (ΔE) is calculated as follows:

$$\Delta E = E\left(\left[(H_2O)_4M\text{–}GLP\right]^{n-1}\right) + 2\,E(H_2O) - E\left(\left[M(H_2O)_6\right]^{n+}\right) - E\left([GLP]^{1-}\right) \quad (2)$$

where $E([(H_2O)_4M\text{–}GLP]^{n-1})$, $E(H_2O)$, $E([M(H_2O)_6]^{n+})$ and $E([GLP]^{1-})$ are the electronic energies of the metal–GLP complexes, H_2O, metal aqua complexes and GLP, respectively. Similarly, the corresponding reaction free energy (ΔG) is calculated by including the zero point energy and thermal correction to the Gibbs free energy.

In order to investigate the metal effect on the GLP detection by FMOC-Cl, the derivatisation reactions of FMOC-Cl with free GLP as well as with the metal–GLP complexes ($[(H_2O)_4M\text{–}GLP]^{n-1}$) have been simulated according the following equations.

$$1\ FMOC\text{–}Cl + 1\ [GLP]^{1-} \rightarrow [FMOC\text{–}GLP]^{1-} + HCl \quad (3)$$

$$1\ FMOC\text{–}Cl + 1\ \left[(H_2O)_4M\text{–}GLP\right]^{n-1} \rightarrow \left[(H_2O)_4M\text{–}GLP\text{–}FMOC\right]^{n-1} + HCl \quad (4)$$

At the same level of theory, full geometry optimisation was performed for the initial geometries for FMOC-Cl, HCl, $[FMOC–GLP]^{1-}$ and $[(H_2O)_4M–GLP–FMOC]^{n-1}$ complexes. Also, harmonic vibrational frequencies were calculated for all these optimised geometries. For the derivatisation reactions in Eqs. (3) and (4), the corresponding reaction energies (ΔE) and free energies (ΔG) were calculated in the same way as for Eq. (1).

Results and discussion

Sample pre-treatment with EDTA prior to derivatisation

GLP recovery without EDTA pre-treatment (Tab. 1) was low for Cd^{2+} (19%), Co^{2+} (14%), Cu^{2+} (14%), Mn^{2+} (59%) and Zn^{2+} (20%). The other metal ions lead to GLP recoveries between 94 and 108% when no EDTA was added prior to derivatisation. Recovery of 108% for the GLP–Fe^{3+} complex can be explained by a possible formation of the hydroxo-iron (III) complex which forms precipitates and disturbs spectrophotometric measurements leading to reduced transmission. For Fe^{2+} upon addition of EDTA, this effect seems to be even more pronounced with the recovery reaching 128%. Addition of EDTA (Table 1) strongly increased the GLP recovery for Cd^{2+} (97%), Co^{2+} (93%), Cu^{2+} (105%), Mn^{2+} (95%) and Zn^{2+} (94%). The GLP recoveries in the presence of the other metal ions varied only slightly in comparison with the variant without EDTA pre-treatment.

Table 1 Calculated recoveries in % for GLP in the presence of different metals at pH 7 with and without treatment with EDTA prior to derivatisation

Metal	GLP	GLP + EDTA
Al^{3+}	97 ± 1.2	92 ± 0.2
Ca^{2+}	97 ± 1.1	92 ± 1.1
Cd^{2+}	19 ± 1.9	97 ± 2.0
Co^{2+}	14 ± 2.1	93 ± 2.2
Cu^{2+}	14 ± 0.8	105 ± 2.9
Fe^{2+}	94 ± 1.7	128 ± 0.5
Fe^{3+}	108 ± 1.2	104 ± 1.3
Mg^{2+}	101 ± 1.6	94 ± 2.8
Mn^{2+}	59 ± 3.5	95 ± 2.3
Zn^{2+}	20 ± 1.7	94 ± 0.9

Metals are known to form more or less strong complexes with GLP (Lundager Madsen et al. 1978). According to the low recoveries in Table 1, GLP complexation with Cd^{2+}, Co^{2+}, Cu^{2+}, Mn^{2+} and Zn^{2+} seems to have an inhibiting effect on the derivatisation reaction with FMOC-Cl according to Eq. (4). EDTA is one of the strongest complexing agents (lg K = 8.7–25.7; Furia 2006), and if added, it can compete with GLP as a ligand (lg K = 3.3–23.0; Popov et al. 2001; Freuze et al. 2007) to the metal ion. This will lead to the release of free GLP, which is available for derivatisation afterwards as is apparent from Table 1.

Effect of Cu (II) and Fe (III) ions on the calibration curves for GLP at pH 2 to 12

Results for the pH dependence are shown in Figs. 1 and 2 where measured extinctions are plotted versus added GLP concentrations. Each figure shows the data points of four calibration curves at different pH (2, 4.5, 9, 12) where the Figs. 1b and 2b show the results with EDTA sample pre-treatment. In principle, such calibration curves would be used to connect extinction and concentration of the analyte using Lambert–Beer's law.

For Cu^{2+}, the GLP recovery in Fig. 1 shows that the calibration curves are strongly pH-dependent. With increasing pH prior to derivatisation, the signal intensities increase. Furthermore, sample preparation without using EDTA revealed generally lower signal intensities for the tested pH adjustments compared with those treated with EDTA. Therefore, calculated average GLP recoveries according to the Lambert–Beer's law were lower when no EDTA was added (Fig. 1a; pH 4.5 48%; pH 9 50%; pH 12 69%) and larger when samples have been treated with EDTA (Fig. 1b; pH 4.5 97%; pH 9 100; pH 12 100%).

Extinctions measured for GLP calibration curves under the influence of 13.3 μM Fe^{3+} were not affected at different pH conditions during sample preparation (Fig. 2a; pH 4.5 103%; pH 9 99; pH 12 105%). Data for the treatment with additional EDTA (Fig. 2b; pH 4.5 102%; pH 9 102%; pH 12 104%) were similar, not showing any systematic effect of EDTA.

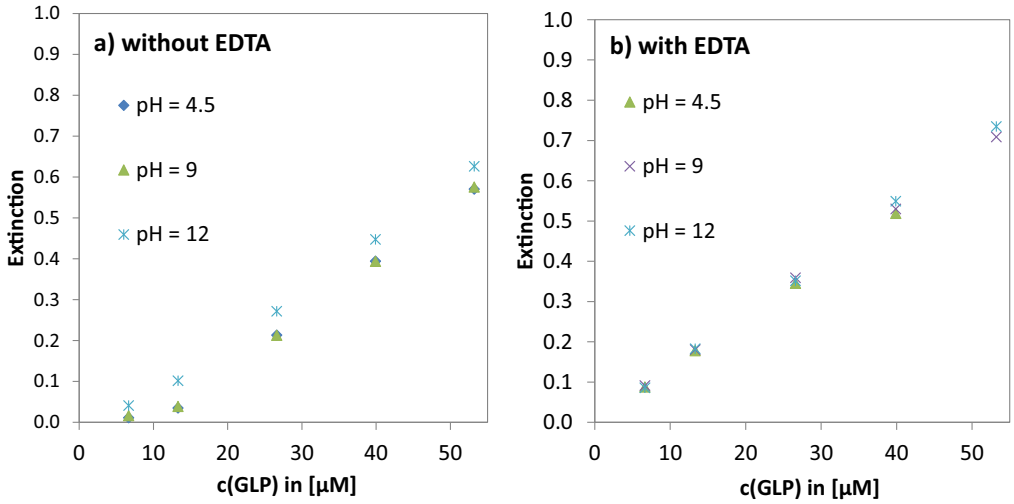


Fig. 1 GLP calibration curves at different pH conditions (2, 4.5, 9 and 12) in the presence of 13.3 µM Cu^{2+} **a** with and **b** without treatment with EDTA prior to derivatisation

The losses in signal intensity (Fig. 1) and, consequently, the lower recovery for GLP under the influence of Cu^{2+} can be plausibly explained by an incomplete reaction between GLP and FMOC-Cl. In contrast, Fe^{3+} had not such an influence (Fig. 2). Although both ions form strong complexes with GLP where complexes of GLP and Fe^{3+} are more stable than those with Cu^{2+} (lg K (Cu^{2+}) = 11.7–16.4, lg K (Fe^{3+}) = 16–23; Popov et al. 2001), the derivatisation with FMOC-Cl obviously was less disturbed by Fe^{3+}.

Therefore, an incomplete derivatisation is not a result of the stability of the metal–GLP complex itself, but probably depends on the protonation state of the GLP amine nitrogen in the metal–GLP complex. This effect could not be overcome by pH adjustment to alkaline conditions after metal–GLP complexation but before derivatisation to achieve free GLP species as recommended by Sancho et al. (1994) or by using borate buffer (pH 9) as proposed by Waiman et al. (2012).

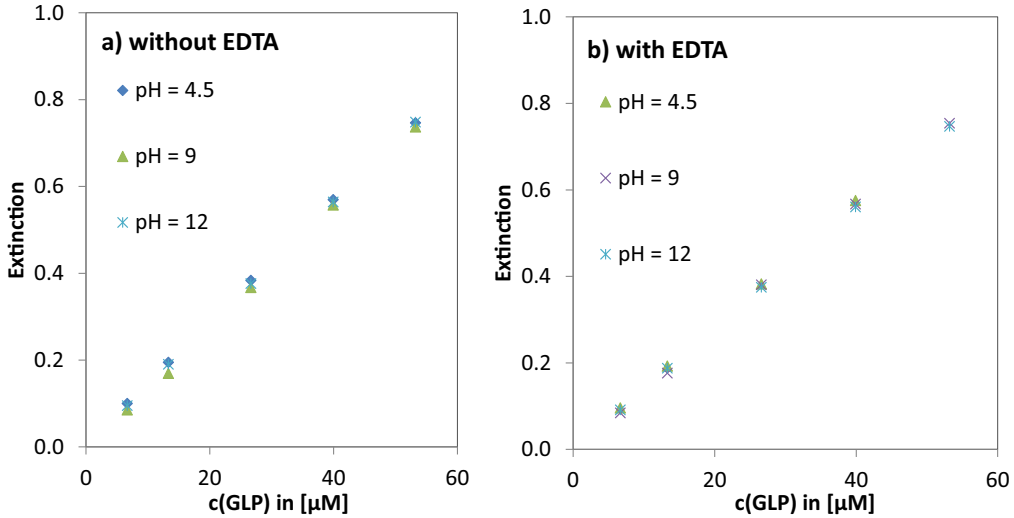


Fig. 2 GLP calibration curves at different pH conditions (2, 4.5, 9 and 12) in the presence of 13.3 µM Fe^{3+} **a** with and **b** without treatment with EDTA prior to derivatisation

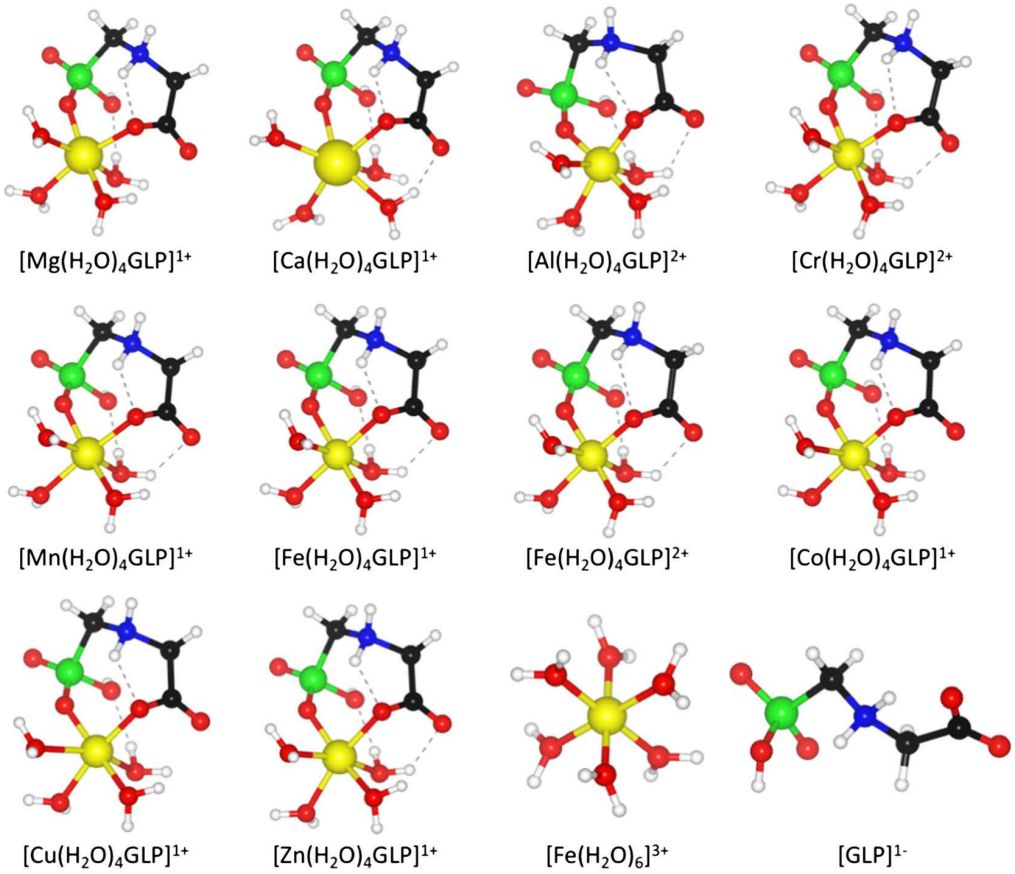


Fig. 3 Optimised geometries of the modelled metal–GLP complexes ($[(H_2O)_4M–GLP]^{n-1}$), Fe^{3+} aqua complex and GLP at the DFT/B3LYP/D3/6–311++G(d,p) level of theory. White, black, blue, red, green and yellow colours correspond to H, C, N, O, P and metal atoms, respectively

Interactions between metals, GLP and FMOC were shown by Skeff et al. (2016) who found that the GLP–metal–FMOC species caused shifts in retention time during separation for HPLC–ESI–MS/MS analysis which was compensated by addition of EDTA after derivatisation. Thus, in view of the results shown in Table 1 as well as in Figs. 1 and 2, one can conclude that the addition of EDTA released free GLP from the metal complexes due to ligand exchange so that improved derivatisation can be achieved. This does not hold true if there is formation of a strong metal–GLP precipitate at low pH.

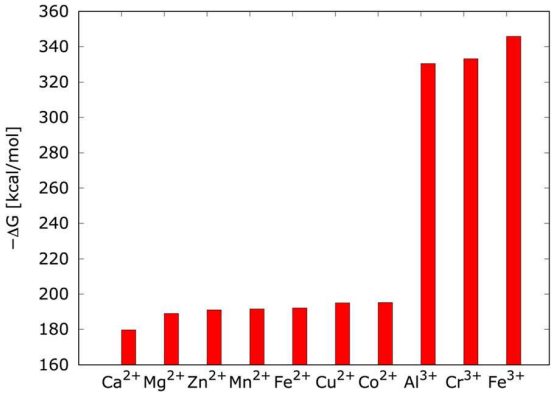


Fig. 4 Calculated free energies (ΔG) in kcal/mol for the metal–GLP reaction for different metal ions at the DFT/B3LYP/D3/6–311++G(d,p) level of theory

Quantum chemical modelling

The optimised gas phase geometries for the metal–GLP complexes having bidentate binding motifs are summarised in Fig. 3. This figure also shows that these metal–GLP complexes involve intramolecular and

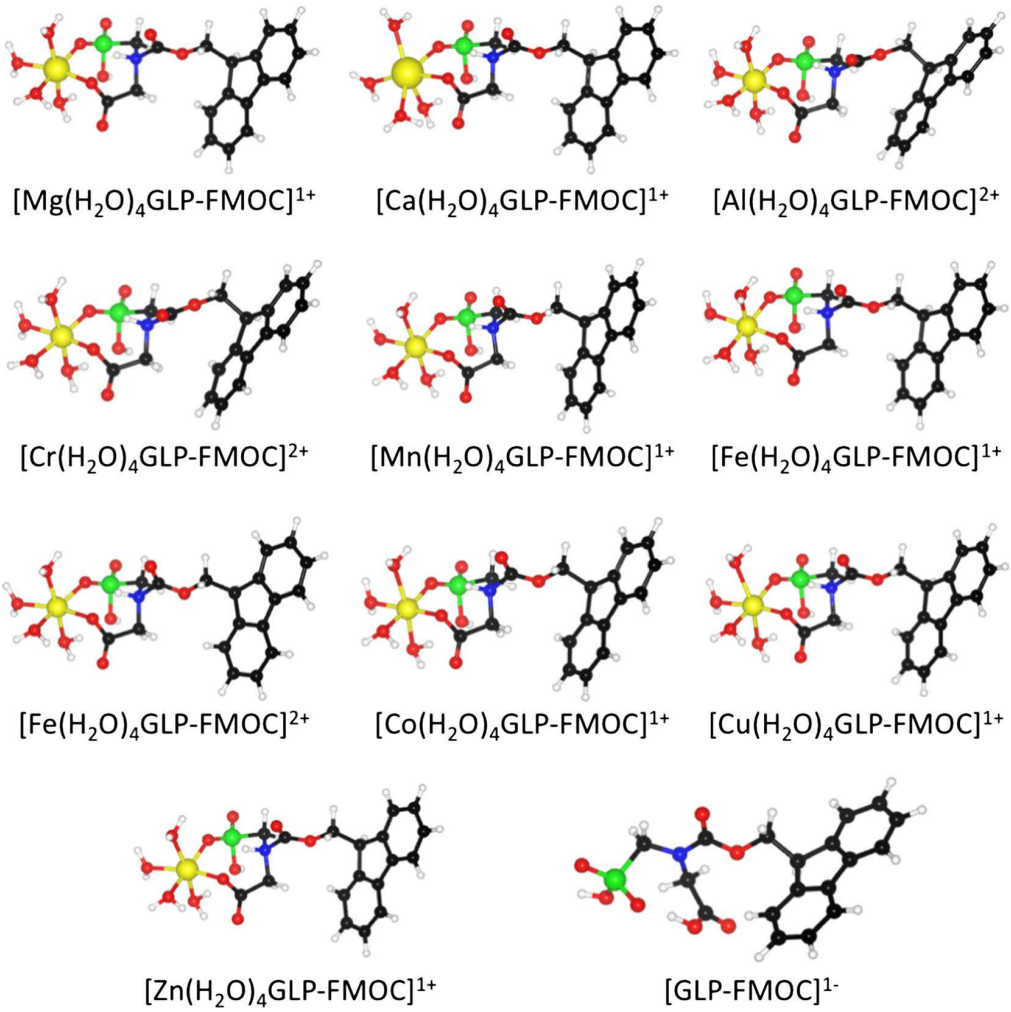


Fig. 5 Optimised geometries of the modelled metal–GLP–FMOC complexes ($[(H_2O)_4M–GLP–FMOC]^{n-1}$) as well as GLP–FMOC complex. White, black, blue, red, green and yellow colours correspond to H, C, N, O, P and metal atoms, respectively

intermolecular H–bonds (HBs). The intramolecular HBs are observed between the GLP amino and carboxylate groups. In addition, the intermolecular HBs are present for the GLP phosphonate and carboxylate groups with the coordinated H_2O molecules. For all metal–GLP complexes, the M^{n+}–O bonds between the metal ion and O atoms of the GLP phosphonate, GLP carboxylate groups and H_2O molecules have bond lengths that decrease in the order H_2O > GLP carboxylate group > GLP phosphonate group. This indicates that interaction of these ligands with the metal ions increases in the order H_2O < GLP carboxylate group < GLP phosphonate group. The shortest M^{n+}–O bond lengths have been observed for the modelled trivalent metal ions that increased in the order $Al^{3+} < Fe^{3+} < Cr^{3+}$. The calculated M^{n+}–O bond lengths involving the GLP phosphonate group, GLP carboxylate group and coordinated H_2O molecules are 1.81, 1.85 and 1.94–1.98 Å for Al^{3+}; 1.85, 1.87 and 1.95–2.01 Å for Fe^{3+}; and 1.89, 1.92 and 2.01–2.08 Å for Cr^{3+}. For the divalent metal ions except for Ca^{2+}, the M^{n+}–O bond lengths involving the GLP phosphonate group, GLP carboxylate group and coordinated H_2O molecules have the ranges 1.94–2.01, 1.95–2.09 and 1.99–2.16 Å, respectively. The longest M^{n+}–O bond lengths have been observed for the Ca^{2+}–GLP complex. In this case, M^{n+}–O bond lengths are

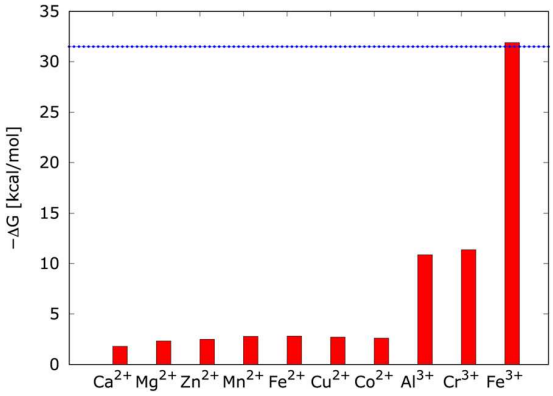


Fig. 6 Calculated reaction free energies (Δ*G*) in kcal/mol for the derivatisation reaction of FMOC-Cl with the metal–GLP complexes for different metal ions at the DFT/B3LYP/D3/6–311++G(d,p) level of theory. Blue line refers to the free energy of the derivatisation reaction of FMOC-Cl with pure GLP

2.30, 2.33 and 2.39–2.43 Å for the GLP phosphonate group, GLP carboxylate group and coordinated H_2O molecules, respectively.

Figure 4 shows that all calculated Δ*G* for the reaction of exchange of two H_2O molecules by one GLP molecule to form the metal–GLP complexes have high negative values. This indicates that this exchange reaction will proceed spontaneously. In addition, every formed metal–GLP complex is expected to be strongly bound and thermally stable. Stability of these metal–GLP complexes for the trivalent metal ions is higher than for the divalent ones. This is in a good agreement with the reported stability constants by Popov et al. (2001) for the metal–GLP complexes formation for divalent and trivalent metal ions (lg $K(M^{2+}) = 3.3–16.4$, lg $K(M^{3+}) = 13.7–23.0$). According to the reaction free energy (Δ*G*) values, the stability of these metal–GLP complexes increases in the order Ca^{2+} (~ − 180 kcal/mol) < Mg^{2+} (~ − 189 kcal/mol) < $Zn^{2+} \approx Mn^{2+} \approx Fe^{2+}$ (~ − 191 kcal/mol) < $Cu^{2+} \approx Co^{2+}$ (~ − 195 kcal/mol) < $Al^{3+} \approx Cr^{3+}$ (~ − 332 kcal/mol) < Fe^{3+} (~ − 346 kcal/mol). It is important to mention that our theoretical Δ*G* values indicate that the GLP complexes with Ca^{2+} and Mg^{2+} have the lowest stability while Cu^{2+} has the highest stability among the divalent metal ions. Thus, the present results show the same trend for the metal–GLP complexes as obtained by Popov et al. (2001) on the basis of experimental data. Moreover, this experimental study showed that Fe^{3+} (lg K $(Fe^{3+}) = 16.1–23.0$) can form a more stable complex with GLP compared with Al^{3+} (lg K $(Al^{3+}) = 13.7–22.1$). This agrees with our theoretical results and thus serves as validation test.

Regarding the derivatisation reaction of FMOC-Cl with the metal–GLP complexes (see Fig. 5), the calculated ΔG for this reaction varies from − 1.8 to − 31.9 kcal/mol (see Fig. 6). This indicates that this derivatisation reaction is a spontaneous reaction, but it is less spontaneous than the metal–GLP complexation reaction. Similarly to the metal–GLP complexation reaction, every formed metal–GLP–FMOC complex is expected to be rather stable. Stability of the metal–GLP–FMOC complexes for the trivalent metal ions is higher than for the divalent ones. According the reaction free energy (Δ*G*) values, the stability of these metal–GLP–FMOC complexes and thus spontaneity of the derivatisation reaction with metal–GLP complexes increase in the order $Ca^{2+} \approx Mg^{2+}$ (~ − 2 kcal/mol) < $Zn^{2+} \approx Mn^{2+} \approx Fe^{2+} \approx Cu^{2+} \approx Co^{2+}$ (~ − 3 kcal/mol) < $Al^{3+} \approx Cr^{3+}$ (~ − 11 kcal/mol) < Fe^{3+} (~ − 32 kcal/mol). In addition, the calculations show that the derivatisation reaction of FMOC-Cl with pure GLP is also a spontaneous reaction (ΔG = − 31.5 kcal/mol). Consequently, one can understand that the derivatisation reaction of FMOC-Cl with pure GLP as well as with GLP complexes with trivalent metal ions, such as Fe^{3+} and Al^{3+}, could proceed easier than with GLP complexes with divalent metal ions. This means that pure GLP and GLP complexes with trivalent metal ions could be detected by FMOC-Cl with higher recoveries compared with GLP complexes with divalent metal ions. This is in overall agreement with experiment, but there are also some exceptions. The latter are seen as high recoveries for Ca^{2+}, Mg^{2+} and Fe^{2+}. Reasons for this discrepancy could be as follows. First, the fact that the reaction free energy has a negative sign does not say anything about the reaction rate. So, this means that some spontaneous reactions especially with low free energy could happen slowly (might be the case for Cd^{2+}, Co^{2+}, Cu^{2+}, Mn^{2+} and Zn^{2+}) and others quickly (e.g. for Ca^{2+}, Mg^{2+} and Fe^{2+}). Second, the metal–GLP complexes might form precipitates and colloids for some metal ions. This process mostly happens at low pH but also can happen at pH below 8. This process will mask GLP and prevent its reaction with FMOC-Cl and consequently will decrease its recovery. Third, although microsolvating water molecules are taken into account, inclusion of the full solvation shell might have an influence on the reaction free energies. Of course, the effect of solvation could be modelled in terms of an implicit solvent model.

However, this neglects entropic effects, which could be important when comparing differently charged species. Finally, it should be emphasised that the recovery in the presence of metal ions is based on extinction changes at a single wavelength of the UV spectrum only. In principle, the UV spectra of the metal–GLP–FMOC complexes could feature more drastic changes, e.g. due to contributions of the metal–ligand chromophore in this spectral range. This could influence the results in a way, such that the assumed relation between extinction and recovery is lost. A possible remedy could be spectral integration along with a detailed theoretical assignment of the UV spectra of the different species.

Conclusions

The present investigation successfully used photometric measurements of GLP recovery and quantum chemical modelling of reaction energies as complementary methods to study the inhibiting effect of metal ions on GLP derivatisation with FMOC-Cl.

GLP recovery was found to depend strongly on the considered metal ion, with particularly low values for Co^{2+}, Cd^{2+}, Cu^{2+}, Mn^{2+} and Zn^{2+}. On the other hand, Al^{3+}, Ca^{2+}, Fe^{3+} and Fe^{2+} showed almost 100% recovery. The behaviour in particular of Fe^{3+} has been rationalised by quantum chemical simulations as being due to the fact that metal–GLP–FMOC complexes are of comparable strength as the GLP–FMOC complex itself. To convert GLP into its free form prior to derivatisation, we followed the strategy by Ibanez et al. 2006 and performed addition of EDTA. Indeed, this yielded generally increased recoveries above 91% in all cases.

Observed low recovery for GLP in the presence of some metal ions could happen due to several interacting factors including (i) slow and therefore incomplete reaction between M–GLP complex and FMOC-Cl, (ii) possibility of precipitate formation of the M–GLP complex and consequently decreased recovery and/or (iii) change in the relevant UV peak position and/or decrease in the peak intensity due to interactions of some metals with the FMOC-Cl chromophore.

The pH of the solution during GLP–metal complex formation has a direct influence on GLP recovery. Comparing Fe^{3+} with Cu^{2+}, it was observed that although Fe^{3+} forms stronger complexes with GLP than Cu^{2+}, the former shows no pH dependence of the recovery, which is in contrast to the latter. We concluded that complex stability is not appropriate to estimate reactivity. Instead, the strength of the metal–GLP–FMOC complex in dependence on pH seems to be key to understanding the limitations of the use of FMOC-Cl.

These findings have considerable practical importance for GLP derivatisation with FMOC-Cl since the use of internal labelled standards presupposes the presence of the same (free) GLP species. However, environmental samples like soil, water or vegetables and fruits containing the minor ($< 1\ mg\ L^{-1}$) or major ($> 1\ mg\ L^{-1}$) elements studied in the present experiments showed inhibiting effects on GLP derivatisation which may sum up and lead to underestimation. Due to the results derived from experiments and theoretical modelling, this may likely account for the effect of general low recoveries of < 50% GLP as observed in a round robin study (Reichert et al. 2006) for groundwater samples. But, according to the present results, full GLP recovery for all tested metal ions was easily achieved by a simple step of EDTA addition prior to derivatisation and is therefore recommended for future use instead of pH adjustments.

Acknowledgements The modelling part of this work has been performed within the InnoSoilPhos-project (http://www.innosoilphos.de/default.aspx), funded by the German Federal Ministry of Education and Research (BMBF) in the frame of the BonaRes-program (No. 031A558). Peter Gros acknowledges a PhDgrant from the state of Mecklenburg-Western Pommerania. This research was conducted within the scope of the Leibniz ScienceCampus Phosphorus Research Rostock.

Compliance with ethical standards

Conflict of interest The authors declare that they have no conflict of interest.

References

Ahmed, A. A., Gros, P., Kühn, O., & Leinweber, P. (2018a). Molecular level investigation of the role of peptide interactions in the glyphosate analytics. *Chemosphere, 196*, 129–134.

Ahmed, A. A., Leinweber, P., & Kühn, O. (2018b). Unravelling the nature of glyphosate binding to goethite surfaces by ab initio molecular dynamics simulations. *Physical Chemistry Chemical Physics, 20*, 1531–1539.

Arkan, T., & Molnár-Perl, I. (2015). The role of derivatization techniques in the analysis of glyphosate and aminomethyl-

phosphonic acid by chromatography. *Microchemical Journal, 121*, 99–106.

Ascolani Yael, J., Fuhr, J. D., Bocan, G. A., Daza Millone, A., Tognalli, N., dos Santos Afonso, M., & Martiarena, M. L. (2014). Abiotic degradation of glyphosate into aminomethylphosphonic acid in the presence of metals. *Journal of Agricultural and Food Chemistry, 62*, 9651–9656.

Becke, A. D. (1988). Density-functional exchange-energy approximation with correct asymptotic behavior. *Physical Review A, 38*, 3098–3100.

Bernards, M. L., Thelen, K. D., Penner, D., Muthukumaran, R. B., & McCracken, J. L. (2005). Glyphosate interaction with manganese in tank mixtures and its effect on glyphosate absorption and translocation. *Weed Science, 53*, 787–794.

Caetano, M. S., Ramalho, T. C., Botrel, D. F., da Cunha, E. F. F., & de Mello, W. C. (2012). Understanding the inactivation process of organophosphorus herbicides: A DFT study of glyphosate metallic complexes with Zn2+, Ca2+, Mg2+, Cu2+, Co3+, Fe3+, Cr3+, and Al3+. *International Journal of Quantum Chemistry, 112*, 2752–2762.

Catrinck, T. C. P. G., Dias, A., Aguiar, M. C. S., Silvério, F. O., Fidêncio, P. H., & Pinho, G. P. (2014). A simple and efficient method for derivatization of glyphosate and AMPA using 9-fluorenylmethyl chloroformate and spectrophotometric analysis. *Journal of the Brazilian Chemical Society, 25*(7), 1194–1199.

Daniele, P. G., De Stefano, C., Prenesti, E., & Sammartano, S. (1997). Copper (II) complexes of *N*-(phosphonomethyl) glycine in aqueous solution: a thermodynamic and spectrophotometric study. *Talanta, 45*, 425–431.

Franz, J. E. (1974). *N-(Phosphonomethyl) glycine phytotoxicant composition. United States Patent No. 3,799,758*. St. Louis: Monsanto Company.

Freuze, I., Jadas-Hecart, A., Royer, A., & Communal, P.-Y. (2007). Influence of complexation phenomena with multivalent cations on the analysis of glyphosate and aminomethyl phosphonic acid in water. *Journal of Chromatography A, 1175*(2), 197–206.

Frisch, M. J., Trucks, G. W., Schlegel, H. B., Scuseria, G. E., Robb, M. A., Cheeseman, J. R., Scalmani, G., Barone, V., Mennucci, B., Petersson, G. A., Nakatsuji, H., Caricato, M., Li, X., Hratchian, H. P., Izmaylov, A. F., Bloino, J., Zheng, G., Sonnenberg, J. L., Hada, M., Ehara, M., Toyota, K., Fukuda, R., Hasegawa, J., Ishida, M., Nakajima, T., Honda, Y., Kitao, O., Nakai, H., Vreven, T., Montgomery, J. A., Peralta, J. E., Ogliaro, F., Bearpark, M., Heyd, J. J., Brothers, E., Kudin, K. N., Staroverov, V. N., Kobayashi, R., Normand, J., Raghavachari, K., Rendell, A., Burant, J. C., Iyengar, S. S., Tomasi, J., Cossi, M., Rega, N., Millam, J. M., Klene, M., Knox, J. E., Cross, J. B., Bakken, V., Adamo, C., Jaramillo, J., Gomperts, R., Stratmann, R. E., Yazyev, O., Austin, A. J., Cammi, R., Pomelli, C., Ochterski, J. W., Martin, R. L., Morokuma, K., Zakrzewski, V. G., Voth, G. A., Salvador, P., Dannenberg, J. J., Dapprich, S., Daniels, A. D., Farkas, Foresman, J. B., Ortiz, J. V., Cioslowski, J., & Fox, D. J. (2013). *Gaussian 09 Revis*. Wallingford: D01 Gaussian Inc..

Furia, T. E. (2006). Stability constants (log K_1) of various metal chelates. In *CRC handbook of food additives*, 2nd edn 1972, from: http://www.coldcure.com/html/stability_constants.html.

Ganson, R. J., & Jensen, R. A. (1988). The essential role of cobalt in the inhibition of the cytosolic isozyme of 3-deoxy-D-arabino-heptulosonate-7-phosphate synthase from *Nicotiana silvestris* by glyphosate. *Archives of Biochemistry and Biophysics, 260*(1), 85–93.

Glass, R. L. (1984). Metal complex formation by glyphosate. *Journal of Agricultural and Food Chemistry, 32*, 1249–1253.

Global Industry Analysts (2011). *Global glyphosate market to reach 1.35 million metric tons by 2017*. According to a new report by Global Industry Analysts, Inc.

Grimme, S., Ehrlich, S., & Goerigk, L. (2011). Effect of the damping function in dispersion corrected density functional theory. *Journal of Computational Chemistry, 32*, 1456–1465.

Gros, P., Ahmed, A. A., Kühn, O., & Leinweber, P. (2017). Glyphosate binding in soil as revealed by sorption experiments and quantum-chemical modelling. *Science of the Total Environment, 586*, 527–535.

Hanke, I., Singer, H., & Hollender, H. (2008). Ultratrace-level determination of glyphosate, aminomethylphosphonic acid and glufosinate in natural waters by solid-phase extraction followed by liquid chromatography–tandem mass spectrometry: performance tuning of derivatization, enrichment and detection. *Analytical and Bioanalytical Chemistry, 391*, 2265–2276.

Hehre, W. J., Ditchfield, R., & Pople, J. A. (1972). Self-consistent molecular orbital methods. XII. Further extensions of Gaussian—type basis sets for use in molecular orbital studies of organic molecules. *The Journal of Chemical Physics, 56*, 2257–2261.

Heineke, D., Franklin, S. F., & Raymond, K. N. (1994). Coordination chemistry of glyphosate: structural and spectroscopic characterization of bis (glyphosate) metal (III) complexes. *Inorganic Chemistry, 33*, 2413–2421.

Hensley, D. L., Beuerman, D. S. N., & Carpenter, P. L. (1978). The inactivation of glyphosate by various soils and metal salts. *Weed Research, 18*, 287–291.

Ibanez, M., Pozo, O. J., Sancho, J. V., Lopez, F. J., & Hernandez, F. (2006). Re-evaluation of glyphosate determination in water by liquid chromatography coupled to electrospray tandem mass spectrometry. *Journal of Chromatography A, 1134*, 51–55.

Jaisi, D. P., Li, H., Wallace, A. F., Paudel, P., Sun, M., Balakrishna, A., & Lerch, R. N. (2016). Mechanisms of bond cleavage during manganese oxide and UV degradation of glyphosate: results from phosphate oxygen isotopes and molecular simulations. *Journal of Agricultural and Food Chemistry, 64*, 8474–8482.

Kobylecka, J., Ptaszynski, B., & Zwolinska, A. (2000). Synthesis and properties of complexes of Lead (II), cadmium (II), and zinc (II) with N-phosphonomethylglycine. *Monatshefte für Chemie, 131*, 1–11.

Lee, C., Yang, W., & Parr, R. G. (1988). Development of the Colle-Salvetti correlation-energy formula into a functional of the electron density. *Physical Review B, 37*, 785–789.

Lundager Madsen, H. E., Christensen, H. H., & Gottlieb-Petersen, C. (1978). Stability constants of copper (II), zinc, manganese (II), calcium and magnesium complexes of N-(phosphonomethyl) glycine (glyphosate). *Acta Chemica Scandinavia, A, 32*, 79–83.

Morillo, E., Undabeytia, T., Maqueda, C., & Ramos, A. (2002). The effect of dissolved glyphosate upon the sorption of copper by three selected soils. *Chemosphere, 47*, 747–752.

Popov, K., Rönkkömäki, H., & Lajunen, L. H. J. (2001). Critical evaluation of stability constants of phosphonic. *Pure and Applied Chemistry, 73*(10), 1641–1677.

Ptaszyński, B., & Zwolińska, A. (2001). Synthesis and properties of solid complexes of lanthanum, cerium, neodymium and erbium with N-phosphonomethylglycine. *Polish Journal of Environmental Studies, 10*(4), 257–262.

Purgel, M., Takács, Z., Jonsson, C. M., Nagy, L., Andersson, I., Bányai, I., Pápai, I., Persson, P., Sjöberg, S., & Tóth, I. (2009). GLP complexation to aluminium (III). An equilibriumand structural study in solution using potentiometry, multinuclear NMR, ATR–FTIR, ESI-MS and DFT calculations. *Journal of Inorganic Biochemistry, 103*, 1426–1438.

Ramirez, C. E., Bellmund, S., & Gardinali, P. R. (2014). A simple method for routine monitoring of glyphosate and its main metabolite in surface waters using lyophilization and LC-FLD + MS/MS. Case study: canals with influence on Biscayne National Park. *Science of the Total Environment, 496*, 389–401.

Reichert, N., Adolph, W., Reding, A.-M., Belvaux, X. (2006). European round robin study for glyphosate residues in surface water and ground water. *SGS Institut Fresenius*.

Sancho, J. V., Lopez, F. J., Hernandeza, F., Hogendoorn, E. A., & van Zoonen, P. (1994). Rapid determination of glufosinate in environmental water samples using 9-fluorenylmethoxycarbonyl precolumn derivatization, large-volume injection and coupled-column liquid chromatography. *Journal of Chromatography A, 678*, 59–67.

Si, Y.-B., Xiang, Y., Tian, C., Si, X.-Y., Zhou, J., & Zhou, D.-M. (2013). Complex interaction and adsorption of glyphosate and Lead in soil. *Soil and Sediment Contamination: An International Journal, 22*(1), 72–84.

Skeff, W., Recknagel, C., & Schulz-Bull, D. E. (2016). The influence of salt matrices on the reversed-phase liquid chromatography behavior and electrospray ionization tandem mass spectrometry detection of glyphosate, glufosinate, aminomethylphosphonic acid and 2-aminoethylphosphonic acid in water. *Journal of Chromatography A, 1475*, 64–73.

Subramaniam, V., & Hoggard, P. E. (1988). Metal complexes of glyphosate. *Journal of Agricultural and Food Chemistry, 36*(6), 1326–1329.

Toy, A. D. F., Forest, P., Uhing, E. H. (1964). Aminomethylenphosphonic acids, salts thereof, and process for their production. *United States Patent office, Patent No. 3, 160,632*.

Undabeytia, T., Cheshire, M. V., & McPhail, D. (1996). Interaction of the herbicide glyphosate with copper in humic complexes. *Chemosphere, 32*(7), 1245–1250.

Van Bruggen, A. H. C., He, M. M., Shin, K., Mai, V., Jeong, K. C., Finckh, M. R., & Morris, J. G., Jr. (2018). Environmental and health effects of the herbicide glyphosate. *Science of the Total Environment, 616–617*, 255–268.

Waiman, C. V., Avena, M. J., Garrido, M., Fernández Band, B., & Zanini, G. P. (2012). A simple and rapid spectrophotometric method to quantify the herbicide glyphosate in aqueous media. Application to adsorption isotherms on soils and goethite. *Geoderma, 170*, 154–158.

Wang, Y., Dongmei, Z., Ruijuan, S., & Huaiman, C. (2004). Toxicity of the interaction of glyphosate and cadmium to wheat. *Frontiers in Ecology and the Environment, 13*(2), 158–160.

Publisher's note Springer Nature remains neutral with regard to jurisdictional claims in published maps and institutional affiliations.

Publication 15

Ashour A. Ahmed, P. Leinweber, O. Kühn. Unravelling the nature of glyphosate binding to goethite surfaces by ab initio molecular dynamics simulations. Phys. Chem. Chem. Phys. **2018**, 20, 1531–1539.

Contribution: Ashour A. Ahmed is credited with conceptualization, conducting the work, all analysis and interpretation, methodology development, visualization, and writing the original manuscript. Ashour A. Ahmed and co-authors are responsible for reviewing, and editing the manuscript.

URL: https://doi.org/10.1039/C7CP06245A

QR:



Reproduced with the permission of the Royal Society of Chemistry (RSC)

PCCP

PAPER

Check for updates

Cite this: *Phys. Chem. Chem. Phys.*, 2018, **20**, 1531

Unravelling the nature of glyphosate binding to goethite surfaces by *ab initio* molecular dynamics simulations†

Ashour A. Ahmed, *[ab] Peter Leinweber[c] and Oliver Kühn[a]

Received 13th September 2017,
Accepted 11th December 2017

DOI: 10.1039/c7cp06245a

rsc.li/pccp

Investigation of the interaction between glyphosate (GLP) and soil minerals is essential for understanding GLP's fate in the environment. Whereas GLP–goethite binding has been discussed extensively, the impact of water as well as of different goethite surface planes has not been studied yet. In this contribution, periodic density functional theory-based molecular dynamics simulations are applied to explore possible binding mechanisms for GLP with three goethite surface planes (010, 001, and 100) in the presence of water. The investigation included several binding motifs of monodentate (**M**) and bidentate (**B**) type. It was found that the binding stability increases in the order **M**@001 < **M**@010 < (2O + 2Fe) **B**@100 < **M**@100 < (1O + 2Fe) **B**@001 < (2O + 1Fe) **B**@010. This behavior has been traced to the presence of intramolecular H-bonds (HBs) in GLP as well as intermolecular HBs between GLP and water, GLP and goethite, and water and goethite. These interactions are accompanied by proton transfer from GLP to water and to goethite, and from water to goethite as well as water dissociation at the goethite surface. Further, it was observed that the OH^- species can replace the adsorbed GLP at the goethite surface, which could explain the well-known drastic drop in GLP adsorption at high pH. The present results highlight the role of water in the GLP–goethite interaction and provide a molecular level perspective on available experimental data.

1. Introduction

There is an ongoing debate about the use of glyphosate (GLP, *N*-(phosphonomethyl)-glycine) in view of its possible carcinogenic effects[1,2] and its occurrence in ground and surface water,[3,4] for instance, in the Baltic Sea.[5] GLP is the most widely used nonselective post-emergent herbicide in the world. It is applied to many food and non-food crops as well as non-crop areas such as roadsides.[6] It has a highly polar character due to its three polar functional groups (amino, carboxylic, and phosphonic groups, see Fig. 1). As a consequence of its chemical properties, GLP is strongly bound to soil constituents, highly soluble in water, and charged according to the soil pH.[7] Due to the chemical similarity between GLP's phosphonate group and inorganic phosphates, they compete with each other for the same sorption sites at soil components.[8,9]

In soil, GLP binds to heavy metals,[6,10] soil organic matter,[11,12] and soil minerals.[13,14] The strong binding to mineral surfaces is commonly taken as an important factor for the deactivation of GLP in soil,[15,16] which leads to a reduction of its mobility and herbicide efficiency.[17,18] Consequently, understanding the nature and extent of the interaction of GLP with soil mineral surfaces is a key point for investigation of the impact and fate of GLP in the environment. Previous experimental studies showed strong adsorption for GLP on soil-abundant mineral surfaces of gibbsite (α-$Al(OH)_3$),[17] bayerite (β-$Al(OH)_3$),[19] manganite (γ-MnOOH),[20] and goethite (α-FeOOH).[21–25]

Particularly, the mineral goethite received much attention over the past few decades because it is the most common ferric

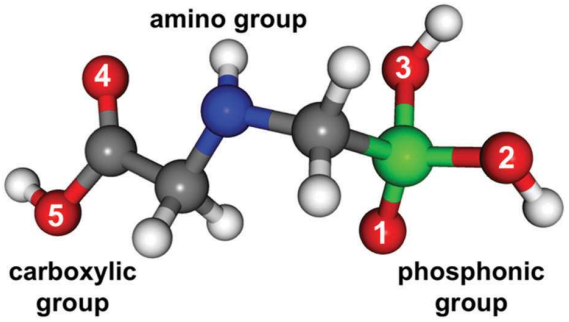


Fig. 1 GLP structure with its three polar (amino, carboxylic, and phosphonic) functional groups. White, gray, blue, red, and green colors are corresponding to H, C, N, O, and P atoms, respectively. Its five oxygen atoms are labelled to aid the discussion of the GLP–goethite-interaction.

[a] *Institute of Physics, University of Rostock, Albert-Einstein-Str. 23-24, D-18059 Rostock, Germany. E-mail: ashour.ahmed@uni-rostock.de*
[b] *Faculty of Science, Department of Chemistry, University of Cairo, 12613 Giza, Egypt*
[c] *University of Rostock, Soil Science, D-18059 Rostock, Germany*

† Electronic supplementary information (ESI) available. See DOI: 10.1039/c7cp06245a

iron Fe(III) oxyhydroxide in soils and its reactivity couples to a wide range of environmental processes. Sheals *et al.*[23] and Barja and Afonso[24] both showed that the GLP adsorption on goethite surface decreases with increasing the soil pH. Sheals *et al.*[23] employed adsorption batch experiments, infrared and photoelectron spectroscopy to find evidence for the formation of intramolecular hydrogen bonds (HBs) between the GLP amino group and both, the carboxylate and the phosphonate groups at low pH. This HB is lost upon deprotonation of the amino group at high pH. In another experimental study, it was observed that the amino and carboxylate functional groups do not contribute to the surface complexation.[24] In contrast, the GLP phosphonate group was found to bind directly to the goethite surface, forming inner-sphere complexes *via* predominantly monodentate (**M**) complexation. This **M** form was supported by a quantum mechanical study using a cluster model.[26] Furthermore, the formation of a minor quantity of bidentate (**B**) complexes is possible at low GLP surface coverage and around neutral pH. Barja and Afonso[24] indicated that GLP adsorbs on goethite surface through the phosphonate group in a **B** form at pH range of 3.5–9.2 and low to moderate surface coverage, and in a **M** form at low pH and high surface coverage. Moreover, they reported that the GLP phosphonate group of the **B** complex is unprotonated, and that of the **M** complex is mostly protonated. Despite these studies, systematic knowledge about the dynamics and mechanism of the GLP–goethite interaction at the molecular level is still lacking. In particular, there are neither experimental nor theoretical studies focusing on the overall GLP–goethite–water interactions and the individual (GLP–goethite, GLP–water, and goethite–water) interactions for different goethite surface planes at a molecular scale.

The main objective of the present contribution is to unravel the nature of binding between GLP and different goethite surface planes at the molecular level by means of periodic density functional theory (DFT) based molecular dynamics (MD) simulations. Specifically, mixed Gaussian and plane wave calculations will be performed for investigation of the interaction of GLP with three different goethite surface planes in the presence of water. Based on previous experimental outcomes,[23,24] only binding of GLP through its phosphonate group with the goethite surfaces will be considered. The individual GLP–goethite, GLP–water, and goethite–water interactions will be addressed. Further, the competition between GLP and water molecules for adsorption sites will be explored. The present exhaustive study of different binding motifs and surface planes using a state-of-the-art computational approach provides a benchmark and starting point for future investigations of interactions of GLP with soil constituents.

2. Molecular modelling and computational details

2.1. Model systems

In order to investigate possible binding motifs between GLP's phosphonate group and goethite, three different goethite surface planes (010, 001, and 100 according to the *Pnma* space group) were considered. These three goethite surface planes have been selected due to the prominent stability of the 010 surface[27,28] and the abundance of the 100 and 001 surfaces.[29–33] Moreover, these three surfaces exhibit three kinds of Fe atoms with three different coordination numbers. In view of the heterogeneity of mineral particles, the present models resemble typical binding situations, but without considering the aspect of imperfections. The three model surfaces were described by periodic slabs, constructed by repetition of the goethite unit cell[34] shown in Fig. 2a in the relevant directions. The goethite orthorhombic unit cell contains four FeOOH formula units (16 atoms, lattice constants are a = 9.9560 Å, b = 3.0215 Å, and c = 4.6080 Å). The 010, 001, and 100 goethite surface planes were generated from $2a \times 2b \times 2c$ (Fig. 2b), $2a \times 4b \times 1c$ (Fig. 2c), and $1a \times 4b \times 3c$ (Fig. 2d) unit cells, respectively. To simulate these surfaces, a layer of about 20 Å vacuum was added between the periodic slabs perpendicular to the surface plane. GLP was added to the vacuum region with its long axis being perpendicular to the surface planes such as to facilitate binding through the phosphonate group. For each surface plane, GLP was situated in two starting spatial configurations to construct **M** and **B** motifs between the phosphonate O atoms and the goethite Fe atoms. Due to the expected importance of solvating water for the GLP–surface interaction, water molecules at a density of about 1 g cm^{-3} were introduced into the vacuum region between the slabs to construct the final simulation box (for example, see Fig. 2e, which contains 128 FeOOH atoms + 1 GLP molecule + 84 water molecules = 398 atoms). The solvation procedure involved filling the box vacuum region with a generic equilibrated 3-point water solvent model (SPC), by using the solvation tool provided by the GROMACS package.[35] Hence, in total there are six GLP–goethite–water models, *i.e.* **M** and **B** at each of the three surface planes. In order to investigate the effect of water we have studied the same GLP–goethite setups, but without water, as well as goethite 010 plus a single water molecule, but without GLP. Further, the effect of pH is estimated using a model containing goethite 010 plus a single OH^- group in vacuum (and K^+ as the counter ion). For each model, the bottom layer atoms of the relevant goethite surface plane were kept fixed to

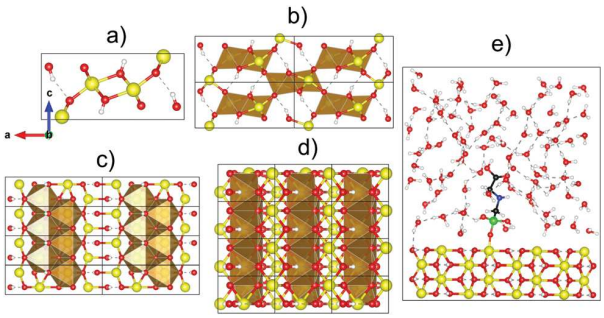


Fig. 2 Goethite unit cell (a), top view for the modelled goethite surface planes 010 (b), 001 (c), and 100 (d) in the *Pnma* space group using a polyhedral representation, and GLP–goethite(010)–water model (e). The polyhedra represent Fe in octahedral coordination. White, black, blue, red, green, and yellow colours are corresponding to H, C, N, O, P, and Fe atoms, respectively.

This journal is © the Owner Societies 2018

approximate the properties of the underlying extended goethite bulk and to decrease the interaction with water of the next box image. All other atoms were left fully flexible.

2.2. Quantum chemical calculations

For the six GLP–goethite–water models, DFT-based Born–Oppenheimer MD simulations have been carried out using the quickstep code[36] implemented in the CP2K simulation package.[37] Here, the hybrid Gaussian and plane-wave (GPW) method[38] was applied for calculating the DFT electronic ground state structure. The Perdew–Burke–Ernzerhof functional (PBE)[39] has been used together with the Goedecker–Teter–Hutter (GTH) pseudopotentials.[40] The electronic density cutoff for atomic core electrons was chosen as 500 Ry. The double-ζ valence polarized (DZVP) basis set optimized for the GTH pseudopotentials[41] has been used for all atomic species included in GLP and the goethite surface model. For O and H atoms of water, the corresponding single-ζ valence (SZV) basis set has been applied to reduce the computational cost. The empirical dispersion correction D3 by Grimme *et al.*[42] was employed. Periodic boundary conditions have been applied in all the three spatial directions as discussed in the previous section. Moreover, the total energy value was tuned to be accurate up to 10^{-10} with a convergence threshold for the SCF energy of 10^{-5}. 25 picoseconds (ps) *NVT*-MD simulations have been performed for each model with a time step of 0.5 femtoseconds (fs) for integrating the equations of motion. The temperature was kept at 300 K through a velocity rescaling thermostat (canonical sampling through velocity rescaling, CSVR) with time constant of 100 fs and temperature tolerance of 10 K. Based on analysis of potential energy, kinetic energy, and temperature, the first 10 ps were assigned for equilibration (for more details see Fig. S1–S3 in the ESI†), the remaining 15 ps (production trajectories) were analysed in terms of dynamics of the individual GLP–goethite-, GLP–water-, and goethite–water-interactions.

To characterize the complexation reaction, GLP + goethite surface → GLP–goethite-complex, snapshots are taken every 50 fs during the production trajectories. For each snapshot, the interaction energy (E_{int}) between GLP and each goethite surface plane for this complexation reaction was calculated as follows (for more detail see ESI†):

$$E_{int} = E_{GLP\text{–}goethite\text{-}complex} - (E_{GLP} + E_{goethite\ surface}) \quad (1)$$

where, $E_{GLP\text{–}goethite\text{-}complex}$, E_{GLP}, and $E_{goethite\ surface}$ are the total electronic energies of the GLP–goethite-complex, GLP, and goethite surface, respectively. Here, the effect of the basis set superposition error (BSSE) has been corrected using the counterpoise scheme.[43]

To investigate the effect of water on the GLP–goethite-interaction, a MD simulation has been performed for one of the GLP–goethite models in vacuum. Here, the same initial configuration for GLP on top of the 010 goethite surface plane in presence of water (Fig. 2e) was selected but without including water. The same box dimensions and all MD parameters have been used exactly as in the water case. Moreover, geometry optimization has been performed for the six GLP–goethite models as well as for the single H_2O and OH^- plus 010 goethite models as introduced above. For the geometry optimization the same level of theory with the same parameters as used in the MD simulations has been employed.

3. Results and discussion

In the goethite bulk, each Fe atom is surrounded by six O atoms (three O^{2-} and three OH^-) to give $FeO_3(OH)_3$ octahedra. For the bare goethite surface, coordination of the surface Fe atoms with the neighbouring O atoms depends on the surface plane. Here, we will discuss three different planes having three different Fe coordination numbers. Specifically, each surface Fe atom is coordinated by three, four, and five O atoms for the 001, 010, and 100 goethite surface planes, respectively (see Fig. 2b–d). For this reason, nature and mechanism of the GLP–goethite interaction as well as water–goethite interaction depend on the goethite surface plane. In the following this dependence will be explored on the basis of MD simulations. Important average bond lengths and interaction energies are summarized in Table 1.

3.1. GLP @ 010 surface plane

Regarding the GLP–goethite-interaction, at the 010 surface plane Fe atoms may exhibit two different binding motifs, *i.e.* **M** and **B**. At the 010 surface plane, the shortest and longest distances between the adjacent Fe atoms are around 4.6 and 5.4 Å, respectively. Therefore, formation of **B** complex between GLP and this surface plane will mainly take place between two GLP phosphonate O atoms and one Fe atom.

3.1.1. Monodentate (M) binding motif. For the **M** motif, GLP was set initially close to a central surface Fe atom through its non-protonated oxygen (O1) of the phosphonate group. In course of the MD equilibration, chemical bond formation occurred between GLP and goethite, water and goethite, and GLP and water.

Regarding the GLP–goethite interaction, a stable **M** complex has been formed between GLP and the goethite surface (see Fig. 3a). Along the production trajectory, the length of the **M** Fe–O1 covalent bond ranges from 1.83 to 2.12 Å with an average of 1.96 Å (see Fig. S4a in ESI†). The distances between the same Fe atom and the other phosphonate O atoms vary in the range

Table 1 Average interaction energies and selected distances obtained from the MD production trajectory for the different modelled binding motifs at the 010, 001, and 100 goethite surface planes. Here, O_{GLP} denotes the GLP O atom(s) bound to $Fe_{goethite}$

Surface plane	Binding motif	E_{int} [kcal mol^{-1}]	Distance [Å]			
			C–N	C–P	$Fe_{goethite}$–O_{GLP}	Fe–P
010	**M**	−110	1.47	1.85	1.96	3.20
	B (2O + 1Fe)	−268	1.48	1.83	2.06 & 2.20	2.64
001	**M**	−68	1.49	1.83	2.02	3.36
	B (1O + 2Fe)	−172	1.46	1.85	1.94 & 1.99	3.02 & 3.35
100	**M**	−154	1.47	1.83	2.04	3.28
	B (2O + 2Fe)	−131	1.47	1.85	2.04 & 2.10	3.10 & 3.21

of 3.32–3.80 Å (O2) and 3.61–4.16 Å (O3) giving rise to averages of 3.56 and 3.93 Å, respectively. The distance between the phosphonate's P atom and the closest Fe atom changes from 3.02 to 3.36 Å with an average of 3.20 Å. Moreover, three proton (H^+) transfer processes have been observed from GLP to the goethite surface as well as to water (see Fig. 3a). Here, one proton is transferred from GLP to the goethite surface forming a strong HB (1.49 Å) with its original donating GLP O2 atom (see Fig. 3a and Fig. S5 in ESI†). This HB enhances formation of the **M** complex between GLP and the goethite surface and retards formation of the corresponding **B** one. For the other two proton transfer processes from GLP to water, both protons show HBs with their original donating GLP O3 and O5 atoms with average H···O distances of 1.86 and 1.89 Å (see Fig. 3a and Fig. S5b, c in ESI†). Moreover, it was observed that the GLP amino group, through its H atom, can form two bifurcated[44] weak intramolecular HBs with two O atoms (one from the phosphonate and one from the carboxylate group with average H···O distances of 2.52 and 2.50 Å, respectively). In general, these observations are in accord with experimental infrared spectra, which indicated that the GLP amino group forms two intramolecular HBs with the GLP phosphonate and carboxylate groups at low pH.[23] This enhances the possibility of formation of the **M** complex compared to the **B** complex.[23]

Regarding the water–goethite interaction, four water molecules approach the goethite surface along the MD simulation and form four **M** binding motifs through their O atoms (O_{H_2O}) with the goethite surface Fe atoms (see Fig. S4b in ESI†). Their average Fe–O_{H_2O} bond lengths are in the range of 1.86–1.99 Å.

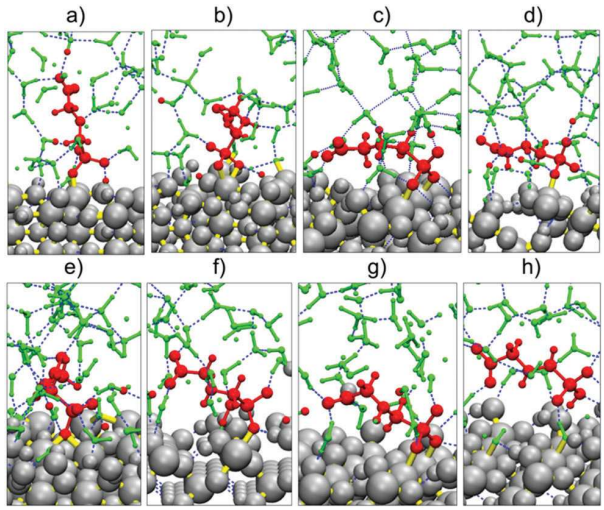


Fig. 3 Snapshot along the equilibrated GLP–goethite–water trajectory for the **M** motif at the 010 goethite surface plane (a), (2O + 1Fe) **B** motif at the 010 surface plane (b), (2O + 2Fe) **B** motif at the 001 surface plane (c), **M** motif at the 001 surface plane (d), (1O + 2Fe) **B** motif at the 001 surface plane (e), **M** motif at the 100 surface plane (f), (2O + 2Fe) **B** motif at the 100 surface plane (g), and outer-sphere complex at the 100 surface plane (h). GLP, goethite, and water atoms are coloured in red, silver, and green, respectively. Intramolecular and intermolecular covalent bonds included goethite atoms are coloured in yellow and HBs are coloured in blue.

Further, two of these four water molecules dissociate at the goethite surface producing two protons (H^+), which transfer to the goethite surface O atoms (O_{FeOOH}) forming covalent bonds. In addition, regardless of the covalent bond formation, water forms five HBs with goethite surface O atoms (see Fig. S4c in ESI†) and four HBs with GLP. These observed HBs between water and the goethite surface have been reported before by Aquino *et al.*[45]

Next, let us draw a quantitative picture of the strength of the GLP–goethite, water–goethite, and GLP–water interactions. Along the production trajectory, the interaction energy between GLP and goethite fluctuates around −110 kcal mol^{-1} (for details, see Fig. S6 in ESI†). The average energies along the trajectory for the interaction of 84 water molecules with GLP and goethite are −389 and −1710 kcal mol^{-1}, respectively. This indicates a very strong interaction between these three subsystems and shows that the water–goethite interaction is stronger than the water–GLP interaction. Recalculating these energies per single water molecule yields interaction energies of −4 and −20 kcal mol^{-1} for the water–GLP and water–goethite interaction, respectively, under the strong assumption of equal contributions for the water molecules regarding their interaction with GLP and goethite.

3.1.2. Bidentate (B) binding motif. In this case GLP was initially placed in a **B** motif between its phosphonate group and the 010 goethite surface. Similar to the **M** motif case, one observes a stable **B** complex formation in water. Here, the **B** complex is formed between two phosphonate O atoms (O1 and O2) and one surface Fe atom (2O + 1Fe) as shown in Fig. 3b. The lengths of these two covalent bonds (Fe–O1 and Fe–O2) forming the **B** motif fluctuate around 2.06 and 2.20 Å. This means that each of these bonds is longer than the **M** Fe–O bond (1.96 Å). The average distance between the third phosphonate O atom and this Fe atom, participating in the **B** motif, (Fe–O3) is 3.56 Å. Here, the GLP phosphonate P atom is closer to the same Fe atom compared to the **M** case, with an average Fe–P distance of 2.64 Å. Furthermore, two protons are transferred from the GLP phosphonate group to the goethite surface O_{FeOOH} atoms (see Fig. 3b). These protons form HBs with their original donating O atoms (O2 and O3) with average H···O bond lengths of 1.79 and 2.48 Å. In addition, a proton transfer occurs from the GLP carboxylate O5 atom to the surrounding water (see Fig. 3b). Compared to the **M** case, the GLP amino group forms weaker intramolecular HBs with the phosphonate group, with an average H···O distance of 2.64 Å. Regarding the water–goethite interaction, **M** complexes between water O_{H_2O} atoms and the surface Fe atoms, water dissociation into H^+ and OH^- at the surface, proton transfer from water to the surface, and HBs between water and the surface are observed along the MD trajectory. Further, HBs between water and GLP are found as well. Finally, the average interaction energy between GLP and goethite for this **B** binding motif is −268 kcal mol^{-1} (see Fig. S6 in ESI†). This value is more than twice the value obtained for the **M** case due to formation of two Fe–O bonds in a cyclic form, the proton transfer from GLP to water and the surface, and saturation of the **B** Fe atom to its octahedral coordination.

 This journal is © the Owner Societies 2018

This indicates to a favoured formation of the **B** motif as compared with the **M** one. Finally, we note that observation of the formation and stability of this (2O + 1Fe) **B** binding motif at the 010 goethite surface is in good agreement with the experimental outcomes suggesting formation of the same binding motif.[23,24]

3.2. GLP @ 001 surface plane

For the 001 goethite surface plane, the shortest distance between any two adjacent surface Fe atoms is around 3.0 Å. Therefore, in principle this plane may exhibit **M** and **B** (2Fe atoms + 2 GLP O atoms) binding motifs for GLP at the surface. In the following, we will discuss the MD simulation results for two different starting configurations.

3.2.1. Monodentate (M) binding motif. For this case, the initial spatial configuration was actually set as a (2O + 2Fe) **B** motif for GLP at the 001 goethite surface plane. During the first three picoseconds of the MD trajectory, a (2O + 2Fe) **B** binding motif (see Fig. 3c) transiently existed, which eventually was disrupted to yield a stable **M** binding motif (see Fig. 3d). More details explaining this **B** → **M** transformation are given in the ESI† (see Fig. S7–S10 in ESI†). For this **M** motif, the average interaction energy between GLP and goethite is −68 kcal mol^{-1} (see Fig. S6 in ESI†). Here, the average distances of the **M** Fe–O and Fe–P bonds are 2.02 and 3.36 Å, respectively. Moreover, the GLP amino group forms two weak intramolecular HBs with the carboxylate and phosphonate groups. In addition, three protons are transferred from GLP to the surrounding water but stayed in contact *via* HBs with the GLP O2 and O5 atoms (see Fig. 3d).

Focusing on the water interaction with goethite and GLP, **M** complexes between water O atoms and the Fe surface atoms, water dissociation at the surface, proton transfer from water to the surface, and intermolecular HBs between water and the surface, and between water and GLP have been found along the MD trajectory.

3.2.2. Bidentate (B) binding motif. Starting with a **M** motif for GLP at the 001 goethite surface plane the configuration turned into a **B** one during the first picoseconds of the MD trajectory. It connects one GLP O atom (O1) in an oxonium fashion with two goethite Fe (Fe1 and Fe2) atoms (1O + 2Fe, see Fig. 3e) that has not been discussed previously. More details about this **M** → **B** transformation are compiled in the ESI† (see Fig. S11–S14 in ESI†). The average interaction energy between GLP and goethite for this (1O + 2Fe) **B** motif is −172 kcal mol^{-1} (see Fig. S6 in ESI†). This indicates that the (1O + 2Fe) **B** binding motif is more stable than the **M** one at the 001 goethite surface plane. The average bond lengths for the two Fe1–O1 and Fe2–O1 bonds are 1.94 and 1.99 Å. The average distances between the GLP P atom and Fe1 and Fe2 atoms involved in the **B** motif are 3.02 and 3.35 Å. Moreover, two protons are transferred from the GLP O3 and O5 atoms to the surrounding water and a third one from the GLP O2 atom to the goethite surface (see Fig. 3e). Two of them form HBs with their original donating GLP O atoms (O2 and O5) with an average H···O bond lengths of 1.65 and 1.74 Å. In addition, the GLP amino group forms an intramolecular HB with the carboxylate one with an average H···O bond length of 2.41 Å.

Compared to the **M** motif at the 001 surface plane, here the same mechanism for the proton transfer processes from GLP to the goethite surface and surrounding water is effective. In addition, similar GLP–goethite–water interactions are found, involving intermolecular GLP–water HBs, goethite–water HBs, goethite(Fe)–(O)water covalent bonds in **M** and 1O + 2Fe **B** forms, water dissociation at the surface, and proton transfer from water to the surface.

3.3. GLP @ 100 surface plane

The distance between the adjacent surface Fe atoms for this surface plane is exactly the same as for the 001 goethite surface plane. Therefore, this plane may exhibit **M** and **B** (2Fe atoms + 2 GLP O atoms) binding motifs for GLP at the surface. For this surface plane, each surface Fe atom is surrounded by 5 O atoms that means that the upper surface layer contains O atoms and not Fe atoms. This already indicates that it could be difficult for GLP to approach the surface Fe atoms through its phosphonate O atoms. For this reason, three cases will be discussed below involving **M**, and **B** and outer-sphere complex formation with the 100 goethite surface plane.

3.3.1. Monodentate (M) binding motif. We have observed a stable **M** motif for GLP at the 100 goethite surface plane along the MD trajectory (see Fig. 3f). Here, the average Fe–O1 bond length is 2.04 Å and the average distances between this Fe atom and the non-bonded phosphonate O atoms (O2 and O3) are 3.54 and 4.52 Å. Further, the average distances of the Fe–P bond is 3.28 Å. Similar to the previous cases, proton transfer processes from the GLP to the surrounding water and goethite surface, formation of intramolecular HBs between GLP amino group and carboxylate group, and formation of goethite–water HBs have been observed. In contrast, the processes involving goethite(Fe)–(O)water covalent bonds, water dissociation at the surface, and proton transfer from water to the surface are not found for this case. Finally, the average interaction energy between GLP and goethite for this **M** motif is −154 kcal mol^{-1} (see Fig. S6 in ESI†).

3.3.2. Bidentate (B) binding motif. Starting with the **B** motif for GLP at the 100 goethite surface plane, we have observed almost the same reactions between the individual subsystems (GLP–goethite, GLP–water, and goethite–water) along the MD trajectory compared to the **M** motif at 100 surface plane. The only difference is that we have in this case a (2O + 2Fe) **B** motif with 2 GLP O atoms + 2 goethite Fe atoms (Fe1 and Fe2 see Fig. 3g). Here, the relevant average distances for the (2O + 2Fe) **B** motif are 2.04 (Fe1–O1), 2.10 (Fe2–O2), 2.57 (O1–O2), 2.95 (Fe1–Fe2), 3.10 (Fe1–P), and 3.21 Å (Fe2–P). The average interaction energy between GLP and the 100 goethite surface plane for this (2O + 2Fe) **B** motif is −131 kcal mol^{-1} (see Fig. S6 in ESI†). This indicates that the **M** binding motif is more favourable than the (2O + 2Fe) **B** one at the 100 goethite surface plane.

3.3.3. Outer-sphere complex formation. The possibility of outer-sphere complex formation between GLP and the 100 goethite surface has been studied by introducing GLP at the surface without direct covalent bond between them. Upon equilibration, two protons have been transferred from GLP to the surrounding water molecules. Furthermore, formation of two **M** covalent

bonds between water and goethite and intermolecular water–goethite HBs have been observed. In fact, there is an indirect interaction between GLP and the goethite surface in which water acts as a bridge (see Fig. 3h). The calculated average interaction energy between GLP and the goethite surface is -43 kcal mol^{-1} (see Fig. S6 in ESI†).

3.4. Effect of water and soil pH

In this section, we will focus on the effect of water as a solvent for the real environmental molecular systems. Here, all the MD simulations have been performed with the previous modeling setup but in vacuum, *i.e.* without water. Four main points will be briefly introduced, including (1) the competition between water and goethite regarding their interaction with GLP, (2) the competition between GLP and water regarding their interaction with the goethite surface, (3) the pH effect, and (4) the stability of the previously discussed binding motifs in the absence of water.

First, we focus on the competition between water and goethite regarding their interaction with GLP. To achieve this goal, exemplary MD simulations have been performed for the same starting configuration as for the **M** complex between GLP and the 010 goethite surface plane (see Fig. 2e) but without including water. As a result, one observes a very strong interaction between GLP and goethite. Snapshots along the MD trajectory are shown in Fig. 4. Here, GLP approaches to the surface with its carboxylate acid group, leading to a situation where GLP interacts through both its carboxylate and phosphonate groups. This gives rise to formation of three HBs (two from the phosphonate and one from the carboxylate group) and one **M** Fe–O bond (see Fig. 4d). Comparing with the situation in the presence of water (see Fig. 3a) we notice that, apparently, water retards the interaction between GLP and the goethite surface and competes with the surface regarding their interactions with GLP. This indicates the possibility of the GLP carboxylate group interaction with the surface in the absence of water. Finally, one can predict that solvation of the carboxylate group is more preferable than formation of a surface bond in the presence of water.

Second, a more detailed view of the competing GLP and water interactions with the goethite surface is obtained by focussing on a single GLP as well as a single water molecule at the bare 010 goethite surface. Geometry optimization has been performed in vacuum for both cases. The obtained optimized geometries are shown in Fig. 5a and b. The calculated interaction energies for GLP and water with goethite are -53 and -31 kcal mol^{-1}, respectively. This indicates that GLP indeed binds stronger than water to goethite and explains why GLP can easily exchange the water molecules at the goethite surface. In passing we note that the difference with respect to the MD results can be explained by the formation of a dissociative **M** binding motif (Fig. 3a) in the MD case. This can increase the interaction energy by two times or more compared to a non-dissociative binding motif (Fig. 5a), in agreement with previous studies.[46]

Third, we discuss the effect of the soil solution pH. To get an estimate of the associated interaction energies, the effect of high pH has been simulated by geometry optimization of a setup where a single OH^- group, in the presence of K^+ as counter ion, forms a **M** binding motif with the 010 goethite surface (Fig. 5c). The resulting interaction energy between the OH^- group and goethite was -80 kcal mol^{-1}, thus indicating a stronger adsorption for OH^- than for GLP at the goethite surface. This means that at high pH, OH^- can replace the adsorbed GLP at the goethite surface yielding a strong drop of the GLP adsorption. This explains at a molecular level the experimental results referring to the GLP adsorption decrease with increasing the soil solution pH.[23,24,47] Of course, the absolute numbers of this comparison in gas phase should be taken with caution and cannot be used for solution phase estimates.

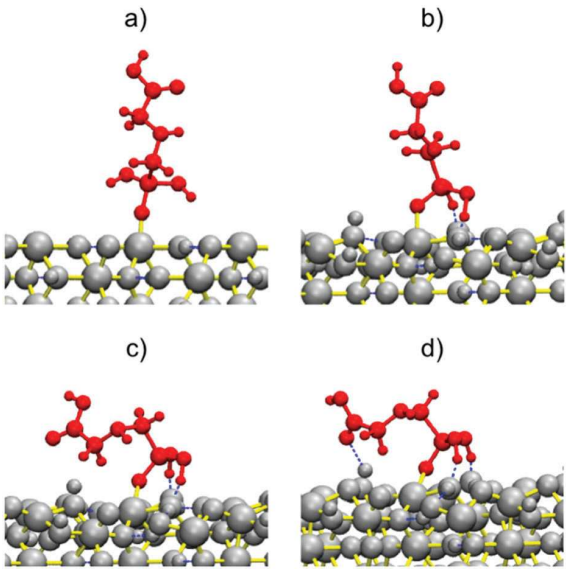


Fig. 4 Four snapshots, from (a–d), characterizing the interaction of GLP with goethite surface in vacuum along the MD trajectory representing the GLP approach to the 010 goethite surface with its carboxylic acid group. The first given snapshot (a) corresponds to the initial configuration of the GLP **M** binding motif at the 010 goethite surface.

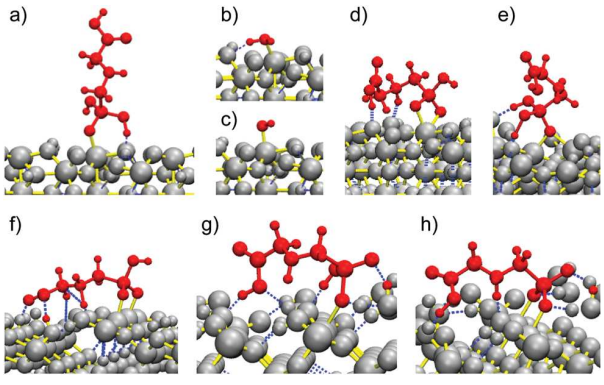


Fig. 5 Vacuum geometry optimized structures for the GLP **M** motif (a), H_2O (b), OH^- (c), and GLP (2O + 1Fe) **B** motif (d) at the 010 goethite surface plane; GLP (1O + 2Fe) **B** motif (e) and GLP (2O + 2Fe) **B** motif (f) at the 001 goethite surface plane; and GLP **M** motif (g) and GLP (2O + 2Fe) **B** motif (h) at the 100 goethite surface plane.

This journal is © the Owner Societies 2018

Finally, to elucidate the decisive role played by water as the solvating medium, the six GLP–goethite models without water have been investigated using quantum chemical geometry optimization. The optimized structures for all models are gathered in Fig. 5(a and d–h). For more details, relevant important bond lengths are summarized in Table S1 (ESI†). Here we will compare briefly the structural differences to the GLP–goethite–water models. In general, approach of the GLP carboxylate group to the goethite surface and their direct interaction has been observed for most cases, which is in contrast to the models including water (for details, see Fig. 5d and f–h). In addition to the covalent bond formation between GLP and the different goethite surface planes, several intermolecular HBs have been observed for all cases (see Fig. 5a and d–h). Moreover, proton transfer processes have been found from GLP to the 001 and 100 goethite surfaces (see Fig. 5e–h). The 010 goethite surface exhibits the same binding motifs (**M** and (2O + 1Fe) **B**) like to the case of including water. Similarly, the 100 goethite surface also exhibits the same binding motifs (**M** and (2O + 2Fe) **B**) as the case of including water. For the 001 goethite surface, two different stable **B** binding motifs (1O + 2Fe and 2O + 2Fe) have been formed between GLP and the surface. This indicates the stability of the (2O + 2Fe) **B** binding motif and the instability of the **M** one at the 001 goethite in vacuum compared to the case of including water.

4. Summarizing discussion and conclusions

There is a huge body of investigations discussing the GLP–goethite binding nature, formation of **M** *versus* **B** binding motif, and pH effect on this interaction with the aim to clarify the impact and fate of GLP in the environment. With a few exceptions, most of it is experimental work, which provides only indirect insight into the molecular level details. Direct insight comes from atomistic simulations, but the dynamics and mechanism of the overall GLP–goethite–water interactions and the individual GLP–goethite, GLP–water, and goethite–water interactions for different goethite surface planes had not yet been explored at the molecular scale. This gap has been filled by the present contribution, which aimed to investigate the mechanism and dynamics of the different GLP binding motifs at different goethite surface planes, intermolecular as well as intramolecular HBs, the competition between GLP and water molecules for goethite adsorption sites, effect of solution pH, and effect of water. For the first time, these objectives have been tackled using DFT-based MD *ab initio* simulations. The main results can be summarized as follows:

For all GLP–goethite–water models, MD simulations showed that neither the GLP amino group nor the carboxylate one contributes to the surface complexation, which is in good agreement with previous studies.[23,24] In addition, GLP was found to be stable against dissociation of its C–N and C–P bonds (their calculated distances vary in the range of 1.46–1.49 and 1.83–1.85 Å, respectively), which is in accord with experimental data indicating that these GLP bonds are highly stable and impervious to strong acid/base hydrolysis.[48]

Referring to the heterogeneity of goethite nanoparticles in real environmental systems containing different crystal planes, two binding motifs have been examined for the considered relevant crystal planes. They all exhibit **M** binding motifs and their binding stability to the goethite surface planes increases in the order 001 < 010 < 100 surface plane. Three stable **B** binding motifs have been investigated for the different surface planes with a binding stability increases in the order (2O + 2Fe) **B** at the 100 surface < (1O + 2Fe) **B** at the 001 surface < (2O + 1Fe) **B** at the 010 surface. Overall, the binding strength of GLP at the goethite surface increase in the order **M** at 001 < **M** at 010 < **B** at 100 < **M** at 100 < **B** at 001 < **B** at 010. Therefore, one can conclude that in general the binding motifs for GLP at the 010 goethite surface plane are more favoured than the corresponding ones at the 001 surface plane. This indicates to stronger binding for GLP at the 010 surface plane compared to the 001 surface plane. Moreover, both the 010 and 001 goethite surface planes prefer formation of the **B** binding motif to the **M** one. In contrast, the **M** binding motif is more favoured than the **B** one at the 100 surface. In addition, this **M** binding motif is more favourable than the corresponding ones at the 010 and 001 surface planes. One may attribute this observation to the saturation of the Fe atom participating in the **M** motif to its octahedral coordination for the 100 goethite surface plane, compared with the same **M** binding motifs at the 001 and 010 surfaces. Similarly, one can conclude that the **M** binding motif stability increases with increasing the coordination of its contributing Fe atom. This explains the increasing interaction energy between GLP and goethite for the **M** binding motifs at the goethite surface in the order of 001 < 010 < 100 surface plane.

The present study indicates that the most stable **M** and **B** binding motif occurs for the 100 and 010 goethite surface planes, respectively. Considering the fact that the 100 surface plane is the most abundant surface plane, one can conclude that the **M** binding motif is the most predominant species for the GLP adsorption on goethite. This is in good agreement with previous experimental[23] and theoretical[26] studies referring to the predominance of the **M** binding motif compared with the **B** one.

GLP forms dissociative complexes with the studied goethite surfaces by deprotonation and transfer of these protons to the surrounding water as well as to the surface. This process increases the interaction energies between GLP and the relevant surfaces as discussed in ref. 46. For most cases, some of the transferred protons stayed in contact with their original GLP donating O atoms *via* HB formation. The presence of these HBs between the GLP phosphonate group and the goethite surface enhances formation of the **M** binding motifs over the **B** one. The same effect has also been observed due to formation of intramolecular HB between the GLP phosphonate and amino groups. This confirms and explains the experimental outcomes by Sheals *et al.*[23] indicating that GLP adsorbs *via* predominantly **M** complexation in the presence of this intramolecular HB between the GLP phosphonate and amino groups. In addition,

considering the fact that the GLP deprotonation process takes place with increasing the solution pH, one can explain the predominance of the **M** binding motif at low pH and the predominance of the **B** one by increasing the pH up to around the neutral pH as found in ref. 23 and 24.

In addition to the strong interaction between GLP and the goethite surface, water also shows a strong interaction with the goethite surface. This interaction included formation of **M** and also **B** motifs between the water O atoms and the surface Fe atoms of different surface planes, dissociation of water at the surface, and formation of intermolecular HBs between water and the surface. But in comparison with the GLP–goethite-interaction, our results indicate that GLP can replace the competing water molecules at the goethite surface. In the same context, we have found that the presence of the OH^- can replace the adsorbed GLP at the goethite surface. This is a key point for explaining the experimental observation of the drastic drop in the GLP adsorption at high pH.[23,24,47]

To summarize, we have provided a molecular-level picture of the various interactions occurring at the goethite–water interface in the presence of GLP. The explicit consideration of water molecules has been found to be vital for any realistic simulation of GLP binding. The present systematic study of different binding motifs and surface planes using *ab initio* molecular dynamics will provide a benchmark and starting point for future investigations of the interactions of GLP and other phosphorus-containing compounds with soil constituents.

Conflicts of interest

There are no conflicts to declare.

Acknowledgements

This work belongs to the InnoSoilPhos-project, funded by the German Federal Ministry of Education and Research (BMBF) in the frame of the BonaRes-program (No. 031A558). This research was performed within the scope of the Leibniz ScienceCampus ''Phosphorus Research'' Rostock.

References

1 K. Z. Guyton, D. Loomis, Y. Grosse, F. El Ghissassi, L. Benbrahim-Tallaa, N. Guha, C. Scoccianti, H. Mattock and K. Straif, Carcinogenicity of Tetrachlorvinphos, Parathion, Malathion, Diazinon, and Glyphosate, *Lancet Oncol.*, 2015, **16**(5), 490–491.

2 J. P. Myers, M. N. Antoniou, B. Blumberg, L. Carroll, T. Colborn, L. G. Everett, M. Hansen, P. J. Landrigan, B. P. Lanphear, R. Mesnage, L. N. Vandenberg, F. S. vom Saal, W. V. Welshons and C. M. Benbrook, Concerns over Use of Glyphosate-Based Herbicides and Risks Associated with Exposures: A Consensus Statement, *Environ. Health*, 2016, **15**, 1.

3 R. H. Coupe, S. J. Kalkhoff, P. D. Capel and C. Gregoire, Fate and Transport of Glyphosate and Aminomethylphosphonic Acid in Surface Waters of Agricultural Basins, *Pest Manage. Sci.*, 2012, **68**(1), 16–30.

4 D. R. Van Stempvoort, J. W. Roy, S. J. Brown and G. Bickerton, Residues of the Herbicide Glyphosate in Riparian Groundwater in Urban Catchments, *Chemosphere*, 2014, **95**, 455–463.

5 W. Skeff, C. Neumann and D. E. Schulz-Bull, Glyphosate and AMPA in the Estuaries of the Baltic Sea Method Optimization and Field Study, *Mar. Pollut. Bull.*, 2015, **100**(1), 577–585.

6 G. A. Khoury, T. C. Gehris, L. Tribe, R. M. Torres Sánchez and M. dos Santos Afonso, Glyphosate Adsorption on Montmorillonite: An Experimental and Theoretical Study of Surface Complexes, *Appl. Clay Sci.*, 2010, **50**(2), 167–175.

7 B. Liu, L. Dong, Q. Yu, X. Li, F. Wu, Z. Tan and S. Luo, Thermodynamic Study on the Protonation Reactions of Glyphosate in Aqueous Solution: Potentiometry, Calorimetry and NMR Spectroscopy, *J. Phys. Chem. B*, 2016, **120**(9), 2132–2137.

8 R. J. Hance, Adsorption of Glyphosate by Soils, *Pestic. Sci.*, 1976, **7**(4), 363–366.

9 S. M. Carlisle and J. T. Trevors, Glyphosate in the Environment, *Water, Air, Soil Pollut.*, 1988, **39**(3), 409–420.

10 M. B. McBride, Electron Spin Resonance Study of Copper Ion Complexation by Glyphosate and Related Ligands, *Soil Sci. Soc. Am. J.*, 1991, **55**(4), 979.

11 C. N. Albers, G. T. Banta, P. E. Hansen and O. S. Jacobsen, The Influence of Organic Matter on Sorption and Fate of Glyphosate in Soil – Comparing Different Soils and Humic Substances, *Environ. Pollut.*, 2009, **157**(10), 2865–2870.

12 P. Gros, A. Ahmed, O. Kühn and P. Leinweber, Glyphosate Binding in Soil as Revealed by Sorption Experiments and Quantum-Chemical Modeling, *Sci. Total Environ.*, 2017, **586**, 527–535.

13 A. Piccolo, G. Celano, M. Arienzo and A. Mirabella, Adsorption and Desorption of Glyphosate in Some European Soils, *J. Environ. Sci. Health, Part B*, 1994, **29**(6), 1105–1115.

14 H. H. Hill, Competitive Sorption between Glyphosate and Inorganic Phosphate on Clay Minerals and Low Organic Matter Soils, *J. Radioanal. Nucl. Chem.*, 2001, **249**(2), 385–390.

15 P. Sprankle, W. F. Meggitt and D. Penner, Rapid Inactivation of Glyphosate in the Soil, *Weed Sci.*, 1975, **23**, 224–228.

16 R. L. Glass, Metal Complex Formation by Glyphosate, *J. Agric. Food Chem.*, 1984, **32**(6), 1249–1253.

17 W. E. Dubbin, G. Sposito and M. Zavarin, X-Ray Absorption Spectroscopic Study of Cu-Glyphosate Adsorbed by Microcrystalline Gibbsite, *Soil Sci.*, 2000, **165**(9), 699–707.

18 B. Nowack, Environmental Chemistry of Phosphonates, *Water Res.*, 2003, **37**(11), 2533–2546.

19 C. Jonsson, *Modeling of glyphosate and metal-glyphosate speciation in solution and at solution-mineral interfaces*, Department of Chemistry, Umeå Univ., Umeå, 2007.

20 M. Ramstedt, C. Norgren, A. Shchukarev, S. Sjöberg and P. Persson, Co-Adsorption of cadmium(II) and Glyphosate at the Water–manganite (γ-MnOOH) Interface, *J. Colloid Interface Sci.*, 2005, **285**(2), 493–501.

 This journal is © the Owner Societies 2018

21 J. S. McConnell and L. R. Hossner, pH-Dependent Adsorption Isotherms of Glyphosate, *J. Agric. Food Chem.*, 1985, **33**(6), 1075–1078.

22 G. M. Day, B. T. Hart, I. D. McKelvie and R. Beckett, Influence of Natural Organic Matter on the Sorption of Biocides onto Goethite, I. γ-BHC and Atrazine, *Environ. Technol.*, 1997, **18**(8), 769–779.

23 J. Sheals, S. Sjöberg and P. Persson, Adsorption of Glyphosate on Goethite: Molecular Characterization of Surface Complexes, *Environ. Sci. Technol.*, 2002, **36**(14), 3090–3095.

24 B. C. Barja and M. dos Santos Afonso, Aminomethylphosphonic Acid and Glyphosate Adsorption onto Goethite: A Comparative Study, *Environ. Sci. Technol.*, 2005, **39**(2), 585–592.

25 C. M. Jonsson, P. Persson, S. Sjöberg and J. S. Loring, Adsorption of Glyphosate on Goethite (α-FeOOH): Surface Complexation Modeling Combining Spectroscopic and Adsorption Data, *Environ. Sci. Technol.*, 2008, **42**(7), 2464–2469.

26 L. Tribe, K. D. Kwon, C. C. Trout and J. D. Kubicki, Molecular Orbital Theory Study on Surface Complex Structures of Glyphosate on Goethite: Calculation of Vibrational Frequencies, *Environ. Sci. Technol.*, 2006, **40**(12), 3836–3841.

27 F. Xiu, L. Zhou, S. Xia and L. Yu, Adsorption Mechanism of Water Molecule on Goethite(010) Surface, *J. Ocean Univ. China*, 2016, **15**(6), 1021–1026.

28 H. Guo and A. S. Barnard, Thermodynamic Modelling of Nanomorphologies of Hematite and Goethite, *J. Mater. Chem.*, 2011, **21**(31), 11566.

29 J. Rakovan, U. Becker and M. F. Hochella, Aspects of Goethite Surface Microtopography, Structure, Chemistry, and Reactivity, *Am. Mineral.*, 1999, **84**(5–6), 884–894.

30 R. M. Cornell and U. Schwertmann, *The Iron Oxides: Structure, Properties, Reactions, Occurrences, and Uses*, Wiley-VCH, Weinheim, 2nd completely rev. and extended edn, 2003.

31 K. W. Paul, J. D. Kubicki and D. L. Sparks, Sulphate Adsorption at the Fe (hydr)oxide–H_2O Interface: Comparison of Cluster and Periodic Slab DFT Predictions, *Eur. J. Soil Sci.*, 2007, **58**(4), 978–988.

32 J. D. Kubicki, K. W. Paul and D. L. Sparks, Periodic Density Functional Theory Calculations of Bulk and the (010) Surface of Goethite, *Geochem. Trans.*, 2008, **9**, 4.

33 J. D. Kubicki, D. Tunega and S. Kraemer, A Density Functional Theory Investigation of Oxalate and Fe(II) Adsorption onto the (010) Goethite Surface with Implications for Ligand- and Reduction-Promoted Dissolution, *Chem. Geol.*, 2017, **464**, 14–22.

34 A. Szytuła, A. Burewicz, Ž. Dimitrijević, S. Kraśnicki, H. Rżany, J. Todorović, A. Wanic and W. Wolski, Neutron Diffraction Studies of α-FeOOH, *Phys. Status Solidi B*, 1968, **26**(2), 429–434.

35 D. Van Der Spoel, E. Lindahl, B. Hess, G. Groenhof, A. E. Mark and H. J. C. Berendsen, GROMACS: Fast, Flexible, and Free, *J. Comput. Chem.*, 2005, **26**(16), 1701–1718.

36 J. VandeVondele, M. Krack, F. Mohamed, M. Parrinello, T. Chassaing and J. Hutter, Quickstep: Fast and Accurate Density Functional Calculations Using a Mixed Gaussian and Plane Waves Approach, *Comput. Phys. Commun.*, 2005, **167**(2), 103–128.

37 J. Hutter, M. Iannuzzi, F. Schiffmann and J. VandeVondele, CP2K: Atomistic Simulations of Condensed Matter Systems, *Wiley Interdiscip. Rev.: Comput. Mol. Sci.*, 2014, **4**(1), 15–25.

38 B. G. Lippert, J. Hutter and M. A. Parrinello, Hybrid Gaussian and Plane Wave Density Functional Scheme, *Mol. Phys.*, 1997, **92**(3), 477–488.

39 J. P. Perdew, K. Burke and M. Ernzerhof, Generalized Gradient Approximation Made Simple, *Phys. Rev. Lett.*, 1996, **77**(18), 3865–3868.

40 M. Krack, Pseudopotentials for H to Kr Optimized for Gradient-Corrected Exchange-Correlation Functionals, *Theor. Chem. Acc.*, 2005, **114**(1–3), 145–152.

41 J. VandeVondele and J. Hutter, Gaussian Basis Sets for Accurate Calculations on Molecular Systems in Gas and Condensed Phases, *J. Chem. Phys.*, 2007, **127**(11), 114105.

42 S. Grimme, S. Ehrlich and L. Goerigk, Effect of the Damping Function in Dispersion Corrected Density Functional Theory, *J. Comput. Chem.*, 2011, **32**(7), 1456–1465.

43 H. B. Jansen and P. Ros, Non-Empirical Molecular Orbital Calculations on the Protonation of Carbon Monoxide, *Chem. Phys. Lett.*, 1969, **3**(3), 140–143.

44 D. Laage and J. T. Hynes, A Molecular Jump Mechanism of Water Reorientation, *Science*, 2006, **311**(5762), 832.

45 A. J. A. Aquino, D. Tunega, G. Haberhauer, M. H. Gerzabek and H. Lischka, Acid–base Properties of a Goethite Surface Model: A Theoretical View, *Geochim. Cosmochim. Acta*, 2008, **72**(15), 3587–3602.

46 G. Xiang, Y.-G. Wang, J. Li, J. Zhuang and X. Wang, Surface-Specific Interaction by Structure-Match Confined Pure High-Energy Facet of Unstable TiO_2(B) Polymorph, *Sci. Rep.*, 2013, **3**, 1411.

47 E. Morillo, T. Undabeytia, C. Maqueda and A. Ramos, Glyphosate Adsorption on Soils of Different Characteristics, *Chemosphere*, 2000, **40**(1), 103–107.

48 D. P. Jaisi, H. Li, A. F. Wallace, P. Paudel, M. Sun, A. Balakrishna and R. N. Lerch, Mechanisms of Bond Cleavage during Manganese Oxide and UV Degradation of Glyphosate: Results from Phosphate Oxygen Isotopes and Molecular Simulations, *J. Agric. Food Chem.*, 2016, **64**(45), 8474–8482.

Electronic Supplementary Material (ESI) for Physical Chemistry Chemical Physics.
This journal is © the Owner Societies 2017

Supplementary Information:

Unravelling the nature of glyphosate binding to goethite surfaces by ab initio molecular dynamics simulations

Ashour A. Ahmed[1,2,*], Peter Leinweber[3], Oliver Kühn[1]

[1] University of Rostock, Institute of Physics, D-18059 Rostock, Albert-Einstein-Str. 23-24, Germany.

[2] University of Cairo, Faculty of Science, Department of Chemistry, 12613 Giza, Egypt.

[3] University of Rostock, Soil Science, D-18059 Rostock, Germany.

ashour.ahmed@uni-rostock.de

peter.leinweber@uni-rostock.de

oliver.kuehn@uni-rostock.de

Figures

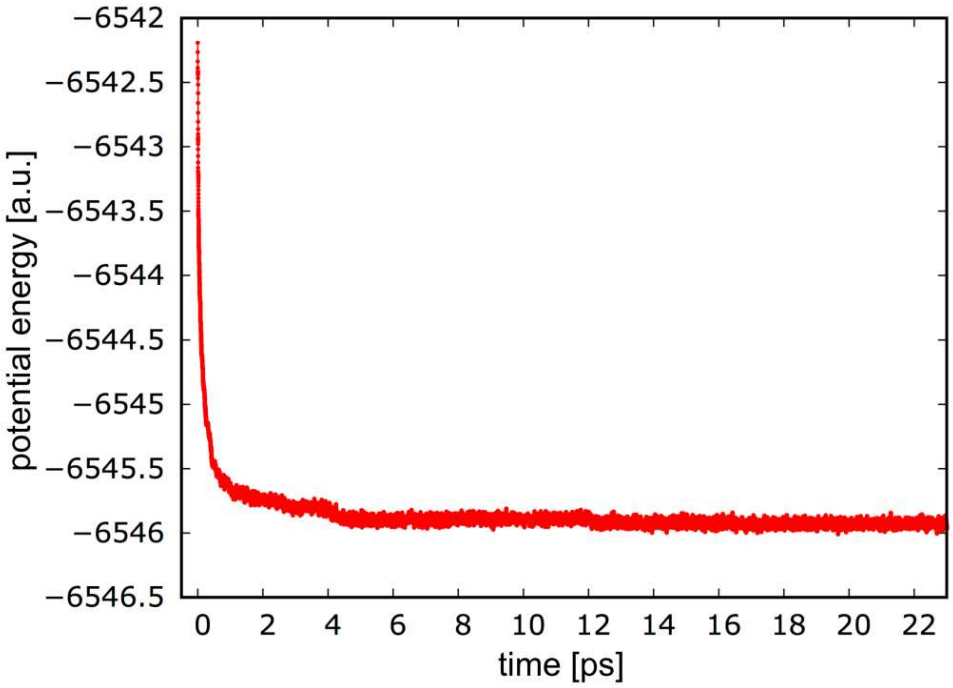


Figure S1. Potential energy of the GLP-goethite-water system along the MD trajectory of the monodentate binding motif at the 010 goethite surface plane.

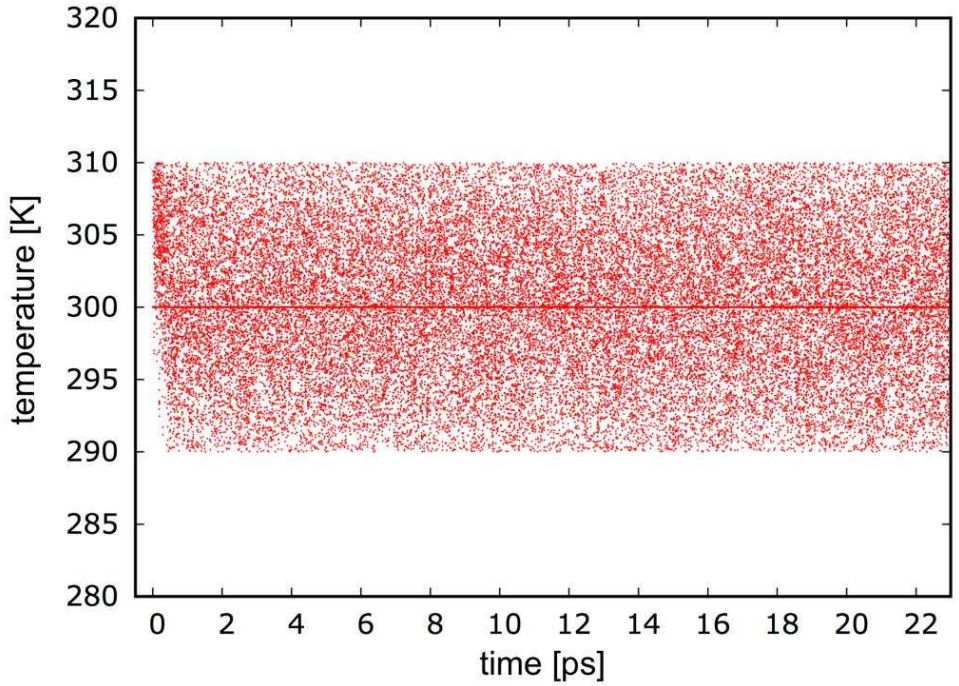


Figure S2. Temperature of the GLP-goethite-water system along the MD trajectory of the monodentate binding motif at the 010 goethite surface plane.

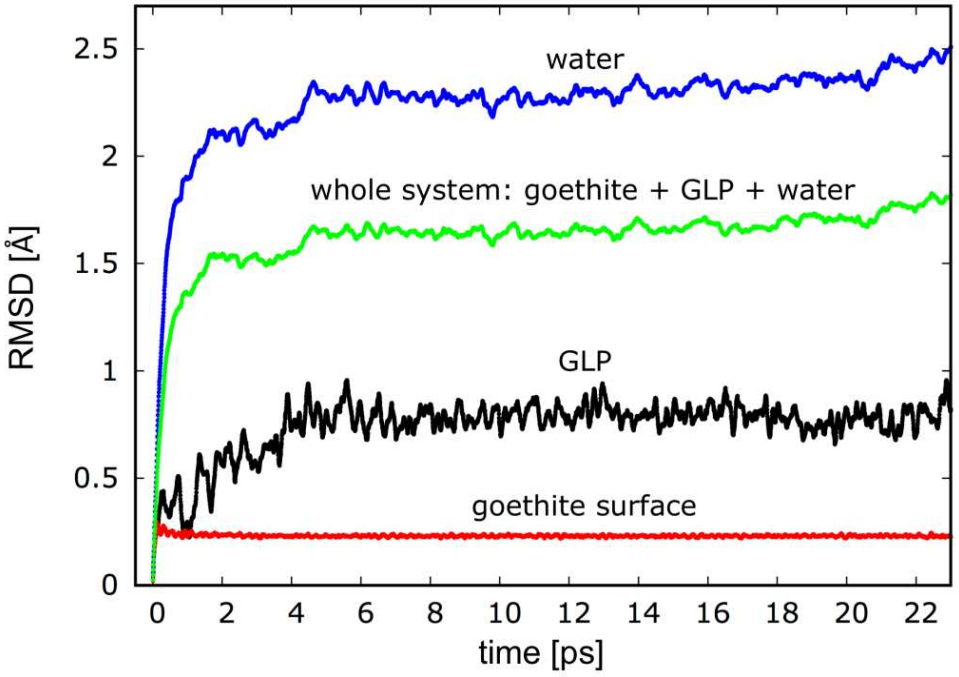


Figure S3. Root mean square deviation (RMSD) of the change in the spatial configurations of GLP (black), goethite (red), water (blue), and the GLP-goethite-water-system (green) along the MD trajectory of the monodentate binding motif at the 010 goethite surface plane. RMSD was calculated here with respect to the initial configuration of each subsystem as well as the whole system.

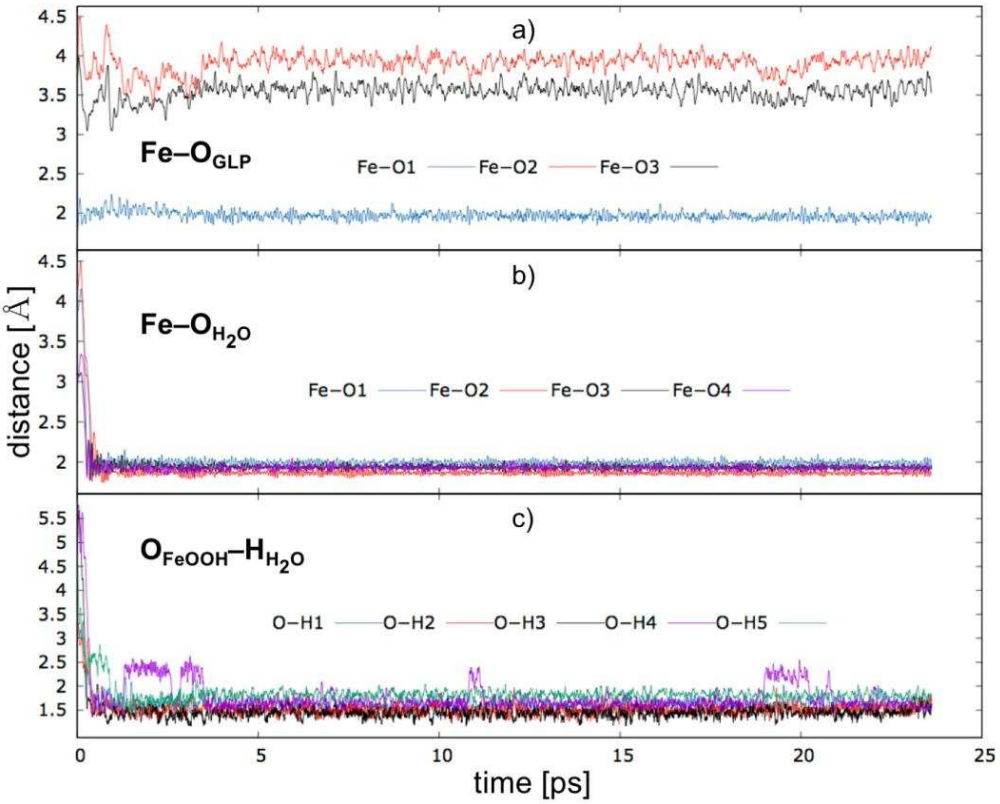


Figure S4. Intermolecular distance between the GLP phosphonate O atoms and surface Fe contributed to the monodentate binding motif (a), water O atoms and different surface Fe atoms (b), and water H atoms and different surface O atoms (c) along the MD trajectory of the monodentate binding motif at the 010 goethite surface plane.

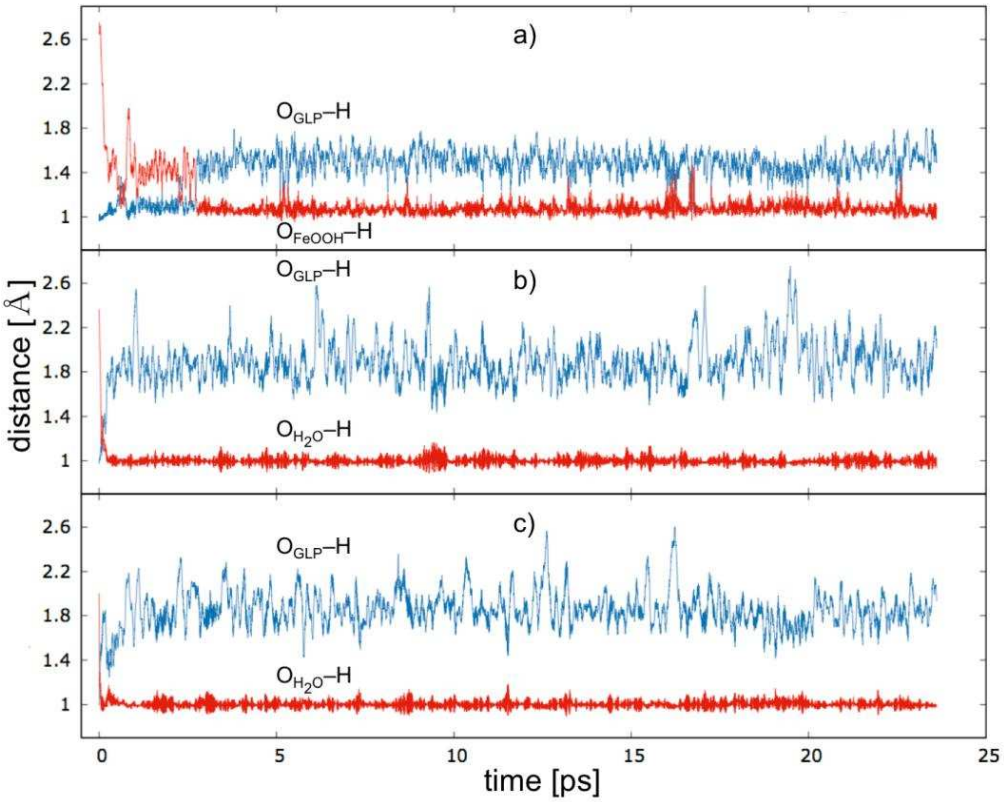


Figure S5. Intermolecular proton transfer from GLP to goethite surface (a), and water (b,c) along the MD trajectory of the monodentate binding motif at the 010 goethite surface plane.

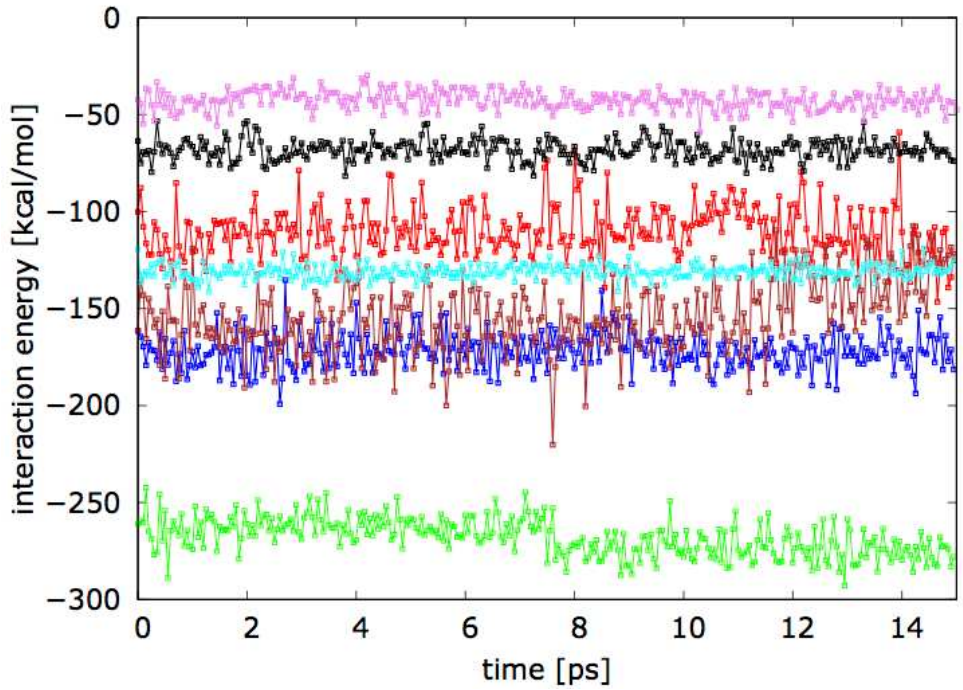


Figure S6. Interaction energy in kcal/mol along the production trajectory between GLP and the different goethite surface planes. Red, green, black, blue, brown, cyan, violet colours are corresponding to the monodentate at 0103, bidentate at 0103, monodentate at 0013, bidentate at 0013, monodentate at 1003, bidentate at 1003, and outer surface complex at 1003goethite surface plane, respectively.

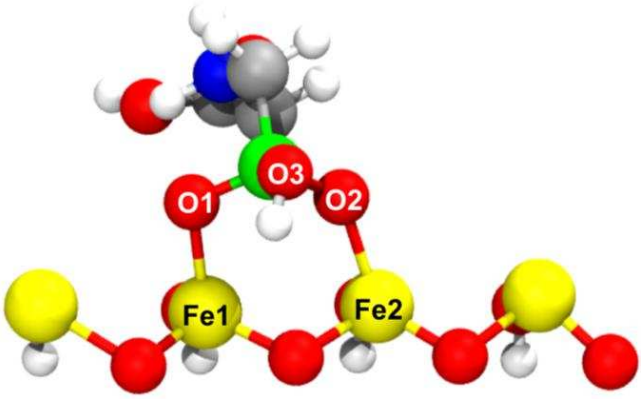


Figure S7. Spatial configuration of the starting bidentate binding motif for GLP at the 001 goethite surface plane. Here we only showed GLP with small part of the modelled surface. Labels of the GLP phosphonate O atoms and goethite Fe atoms will be used in the following figures to characterize the bidentate → monodentate transformation.

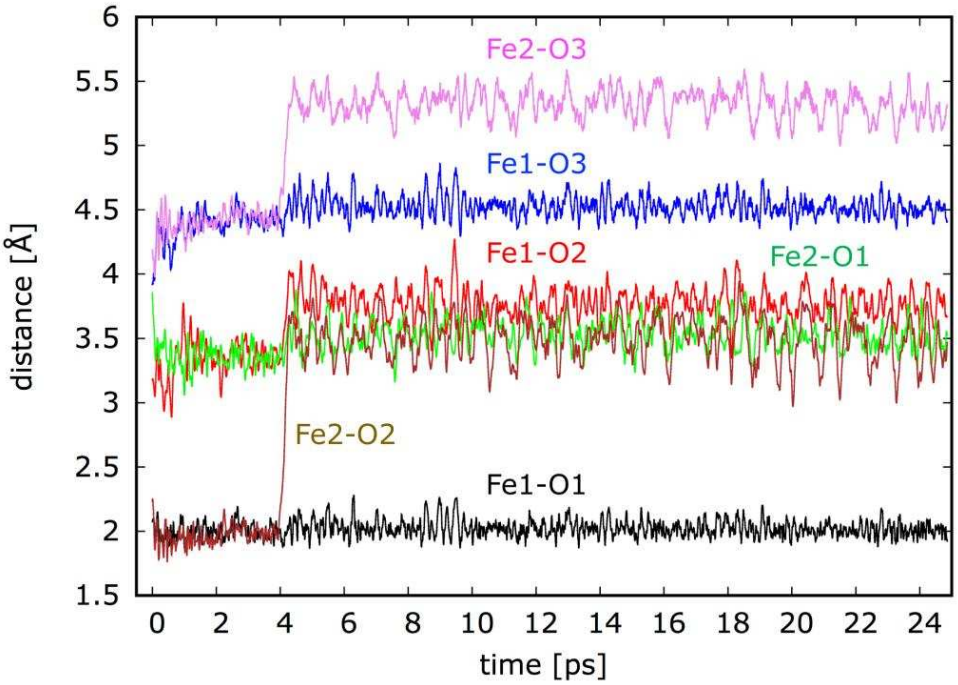


Figure S8. Intermolecular distance between all GLP phosphonate O atoms and the interacted surface Fe atoms showing the bidentate → monodentate transformation at the 001 goethite surface plane along the MD trajectory.

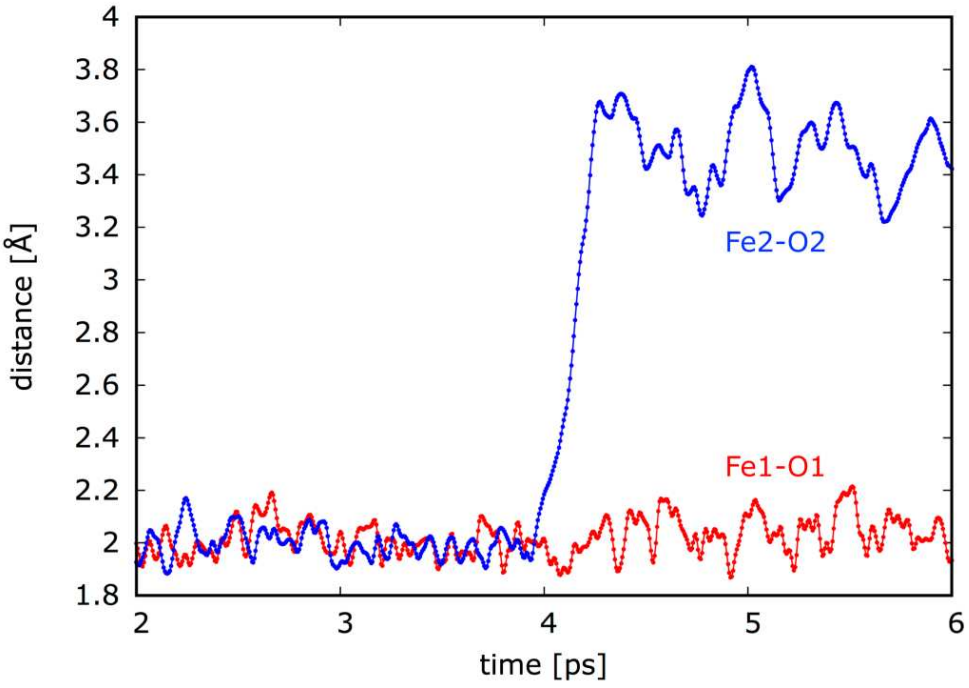


Figure S9. Focus on intermolecular distance between the GLP phosphonate O atoms (O1 & O2) and surface Fe atoms (Fe1 and Fe2) contributed to the bidentate → monodentate transformation at the 001 goethite surface plane around the transformation process9 period.

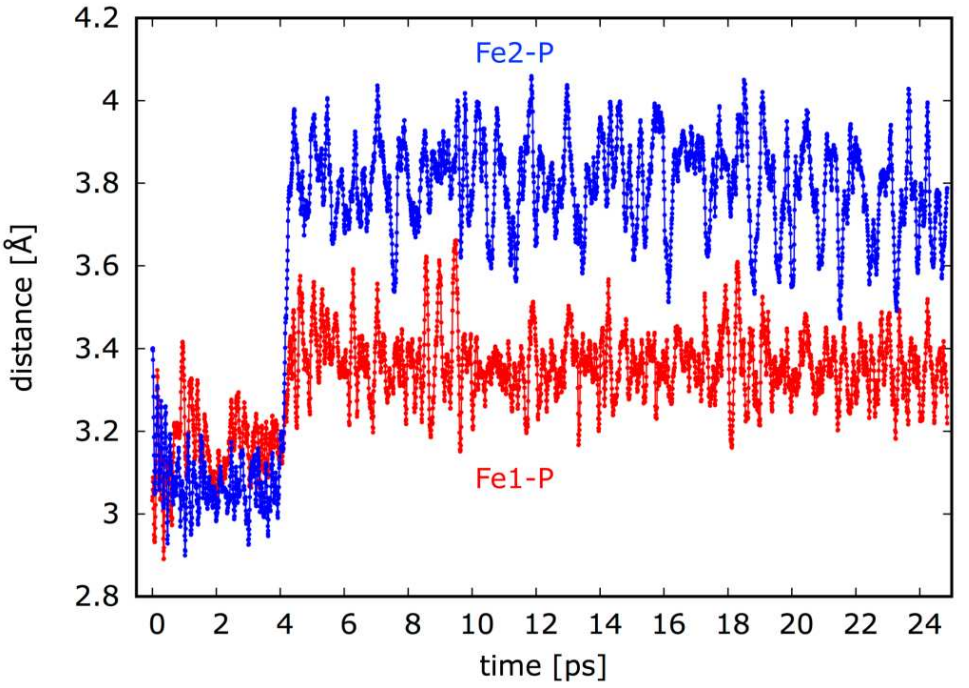


Figure S10. Intermolecular distance between the GLP phosphonate P atom and the interacted surface Fe atoms (Fe1 and Fe2) at the 001 goethite surface plane along the MD trajectory for the bidentate → monodentate transformation case.

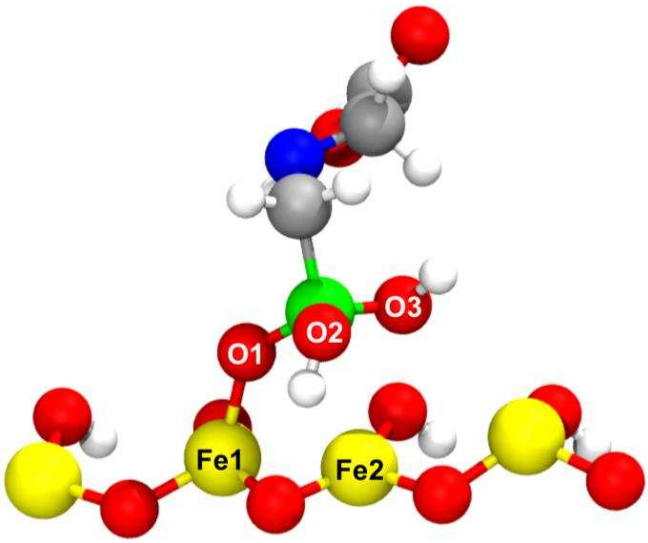


Figure S11. Spatial configuration of the starting monodentate binding motif for GLP at the 001 goethite surface plane. Here we only showed GLP with small part of the modelled surface. Labels of the GLP phosphonate O atoms and goethite Fe atoms will be used in the following figures to characterize the monodentate → bidentate transformation.

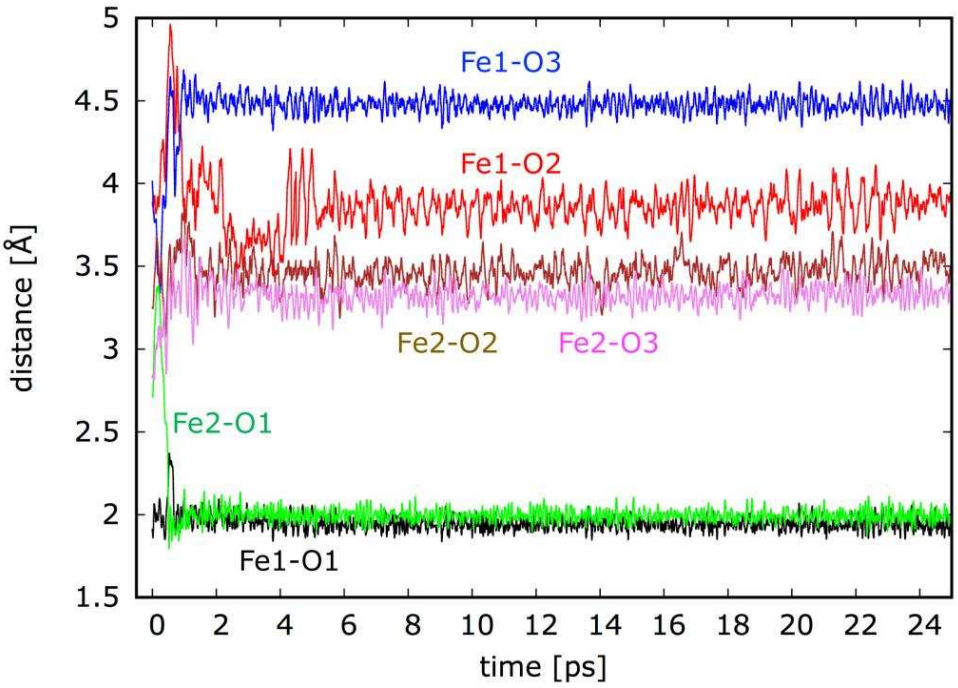


Figure S12. Intermolecular distance between all GLP phosphonate O atoms and the interacted surface Fe atoms (Fe1 and Fe2) showing the monodentate → bidentate transformation at the 001 goethite surface plane along the MD trajectory.

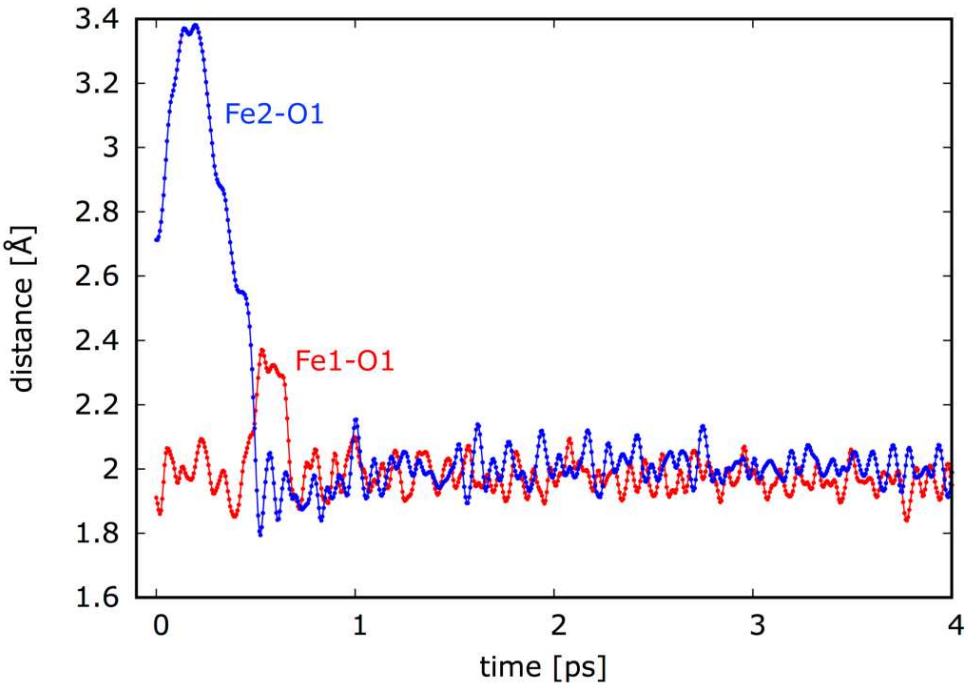


Figure S13. Focus on intermolecular distance between the GLP phosphonate O atom (O1) and surface Fe atoms (Fe1 and Fe2) contributed to the monodentate → bidentate transformation at the 001 goethite surface plane along the first 4 ps of the MD trajectory.

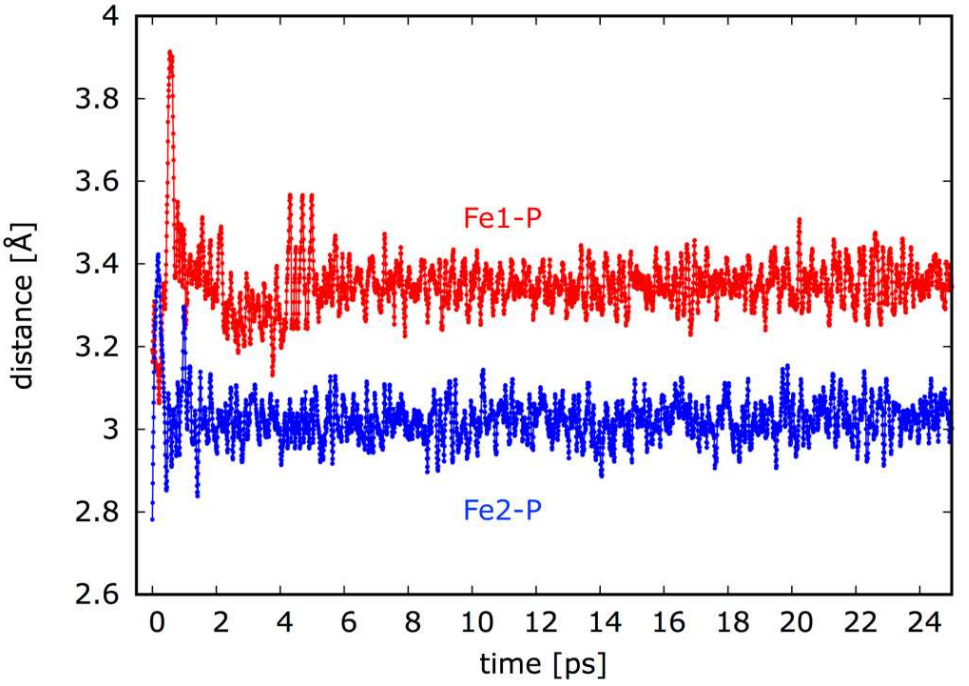


Figure S14. Intermolecular distance between the GLP phosphonate P atom and the interacted surface Fe (Fe1 and Fe2) at the 001 goethite surface plane along the MD trajectory for the monodentate → bidentate transformation case.

Table

Table S1. Selected bond lengths in Å for the geometry optimized binding motifs at the 010, 001, and 100 goethite surface planes.

surface plane	binding motif	distance [Å]			
		C3N	C3P	$Fe_{goethite}3O_{GLP}$	Fe3P
010	monodentate	1.45	1.82	1.96	3.00
	bidentate (2O+1Fe)	1.49	1.83	2.02 & 2.05	2.52
001	bidentate (1O+2Fe)	1.45	1.84	1.89 & 1.99	2.99 & 3.47
	bidentate (2O+2Fe)	1.47	1.84	1.90 & 1.91	2.76 & 2.87
100	monodentate	1.45	1.83	2.08	3.51
	bidentate (2O+2Fe)	1.49	1.84	2.02 & 2.03	3.20 & 3.20

Notes

1. Regarding Eq. 1 in the main article

In general, the effect of water on the GLP-goethite-interaction has been taken into account during the MD simulations due to the water-GLP-goethite-interactions based on the electronic and Van der Waals interactions. However, this effect has not been considered explicitly for computing the interaction energy in Eq. 1 at each snapshot. In practice, at every snapshot the molecular system is composed of three sub-systems (fragments) involving GLP (fragment1), goethite (fragment2), and water (fragment3). Within CP2K it is possible to calculate the pair interaction energy between two fragments. According to Eq. 1 ($E_{int} = E_{\mathrm{GLP-goethite-complex}} - (E_{\mathrm{GLP}} + E_{\mathrm{goethite\ surface}})$), we have defined GLP as the first fragment and goethite as the second fragment. The water enters only insofar as it determines the actual geometry of the interacting fragments. The interaction energy is calculated within the BSSE counterpoise correction philosophy, i.e. by performing five energy calculations as follows: total electronic energy of GLP including only the GLP basis functions (E_{GLP}^{GLP}), goethite including only the goethite basis functions ($E_{goethite}^{goethite}$), GLP including the basis functions of GLP and goethite ($E_{GLP}^{GLP+goethite}$), goethite including the basis functions of GLP and goethite ($E_{goethite}^{GLP+goethite}$), and finally GLP-goethite complex including the basis functions of GLP and goethite ($E_{GLP-goethite-complex}^{GLP+goethite}$). From these numbers one gets the interaction energy between GLP and goethite as $E_{int} = E_{GLP-goethite-complex}^{GLP+goethite} - (E_{GLP}^{GLP+goethite} + E_{goethite}^{GLP+goethite})$. Similarly, the interaction energies between GLP and water ($E_{int} = E_{GLP-water-complex}^{GLP+water} - (E_{GLP}^{GLP+water} + E_{water}^{GLP+water})$) and between goethite and water ($E_{int} = E_{goethite-water-complex}^{goethite+water} - (E_{goethite}^{goethite+water} + E_{water}^{goethite+water})$) have been calculated.

For a specific GLP-goethite-water-complex model, the same box dimensions for the complete model have been used for all energy calculations9processes whether for the individual fragments (GLP and goethite) or for the GLP-goethite-complex.

2. Regarding the average interaction energy between GLP and goethite

In the previous note, we showed how to calculate the interaction energy between GLP and goethite for one snapshot. For 25 ps MD simulation, snapshots are taken every 50 fs and the corresponding interaction energy for every snapshot has been calculated. The interaction energy values along the equilibrated production trajectory (last 15 ps, see Figure S6) are averaged giving rise to only one value. This average interaction energy value represents the binding strength between GLP and goethite for a certain GLP-goethite-model along the equilibrated MD trajectory. For our GLP-goethite-models with different binding motifs and different goethite surface planes, the corresponding average interaction energies have been calculated and inserted into Table 1 in the main article. For example, the interaction energy of -110 kcal/mol corresponds to the average interaction energy between GLP and goethite for M motif at the 010 goethite surface plane (see Figure 3a in the main article).

List of Publications

2023 – 2025

36. D. Makhmutov, B. Rungtaweevoranit, Ashour A. Ahmed, K. Faungnawak, M. Al-Yusufi, E. Salaya, S. Wohlrab, U. Armbruster, A. M. Abdel-Mageed. Insights from Catalytic and Kinetic-Isotope-Effect Studies during CO_2 Hydrogenation over Cu clusters supported on UiO-66 Catalysts. Applied Surface Science 2025, 688, 162323.
35. Y. Wu, Y. Zhu, Ashour A. Ahmed, M. Imran, S. Qiu, Y. Liu, X. Hu, Y. Hassan, Z. Sun, R. Deng, X. Li. Excitation-Dependent Anti-Thermal Quenching in Zero-Dimensional Manganese Bromides for Photoluminescence and X-ray Scintillation. Angewandte Chemie 2024.
34. L. F. Dettmann, O. Kühn, Ashour A. Ahmed. Automated parametrization approach for coarse-graining soil organic matter molecules. J. Chem. Theory Comput. 2024, 20, 23, 10684.
33. M. Meshhal, Ashour A. Ahmed, S. Aziz, M. Shibl, O. Kühn, K. Soliman. Two-dimensional antimonene as a potential candidate for dioxin capture. Phys. Chem. Chem. Phys. 2024, 26, 22539-22548.
32. Ashour A. Ahmed, M. Morshedizad, O. Kühn, P. Leinweber. Deciphering competitive interactions: Phosphate and organic matter binding on goethite through experimental and theoretical insights. Sci. Total Environ 2024, 940, 173510.
31. L. F. Dettmann, O. Kühn, Ashour A. Ahmed. A Martini-based coarse-grained soil organic matter model derived from atomistic simulations. J. Chem. Theory Comput. 2024, 20, 5291–5305.
30. Y. Luo, Y. Peng, Yimeng Li, Yage Li, C. Feng, R. Li, B. Gao, R. Xiao, X. Zhang, G. Qu, M. Li, Ashour A. Ahmed, S. G. Al-Solaimani, P. Ss Hooda, J. Rinklebe, Z. Zhang, S. S. Lee, S. M. Shaheen. Phosphorus removal from water using La-based absorbents: Insights into the impacts of crystal structure, surface area, and crystallinity on the removal efficiency and mechanisms. Sep. Purif. Technol. 2024, 330C, 125478.
29. A. I. Osman, Y. Zhang, Z. Y. Lai, A. K. Rashwan, M. Farghali, Ashour A. Ahmed, Y. Liu, B. Fang, Z. Chen, A. Al-Fatesh, D. W. Rooney, C. L. Yiin, P.-S. Yap. Machine learning and computational chemistry to improve biochar fertilizers: a review. Environ. Chem. Lett. 2023, 21, 3159–3244.
28. Ashour A. Ahmed, P. Leinweber, O. Kühn. Advances in understanding the phosphate binding to soil constituents: A Computational Chemistry perspective. Sci. Total Environ. 2023, 163692.

2012 – 2022

27. R. N. Aljawfi, S.M. Sherif, S. Akef, M. J. Alam, Ashour A. Ahmed, M. A.Swillam. Photon harvesting and light trapping in pentacene and PTCDI-C13H27 for organic solar cell application. Optik 2022, 258, 168931.
26. S. M. Shaheen, J. Wang, K. Baumann, Ashour A. Ahmed, L. Hsu, Y. Liu, S. Wang, O. Kühn, P. Leinweber, J. Rinklebe. Stepwise redox changes alter the speciation and mobilization of phosphorus in hydromorphic soils. Chemosphere 2022, 288, 132652.
25. L. F. Dettmann, O. Kühn, Ashour A. Ahmed. Coarse-grained molecular dynamics simulations of nanoplastics interacting with a hydrophobic environment in aqueous solution. RSC Adv. 2021, 11, 27734.
24. P. B. Ganta, M. Morshedizad, O. Kühn, P. Leinweber, Ashour A. Ahmed. The Binding of Phosphorus Species at Goethite: A Joint Experimental and Theoretical Study. Minerals 2021, 21, 323.

23. P. B. Ganta, O. Kühn, Ashour A. Ahmed. Ab Initio Molecular Dynamics Simulations of the Interaction between Organic Phosphates and Goethite. Molecules 2021, 26(1), 160.
22. Ashour A. Ahmed, S. Gypser, D. Freese, P. Leinweber, O. Kühn. Molecular level picture of the interplay between pH and phosphate binding at the goethite-water interface. Phys. Chem. Chem. Phys. 2020, 22, 26509-26524.
21. S. H. Mohamed, Y. M. Issa, S. A. Elfeky, Ashour A. Ahmed, N. S. Abdelkader. Spectroscopic, thermogravimetric studies and DFT calculations of pentoxyverine citrate ion-pairs with sulfonephthalein dyes. J. Mol. Struct. 2020, 1212, 128074.
20. P. B. Ganta, O. Kühn, Ashour A. Ahmed. QM/MM molecular dynamics investigation of the binding of organic phosphates to the 100 diaspore surface. Front. For. Glob. Change 2020, 3, 71.
19. P. B. Ganta, O. Kühn, Ashour A. Ahmed. QM/MM simulations of organic phosphorus adsorption at the diaspore-water interface. Phys. Chem. Chem. Phys. 2019, 21, 24316-24325.
18. P. Gros, Ashour A. Ahmed, O. Kühn, P. Leinweber. Influence of metal ions on glyphosate detection by FMOC-Cl. Environ. Monit. Assess. 2019, 191, 244.
17. Ashour A. Ahmed, S. Gypser, P. Leinweber, D. Freese, O. Kühn. Infrared spectroscopic characterization of phosphate binding at the goethite–water interface. Phys. Chem. Chem. Phys. 2018, 21, 4421–4434.
16. M. E. Salem, Ashour A. Ahmed, A. F. Darweesh, O. Kühn, A. H. M. Elwahy. Synthesis and DFT calculations of 2-thioxo-1,2-dihydropyridine-3-carbonitrile as versatile precursors for novel pharmacophoric hybrid molecules. J. Mol. Struct. 2019, 1176, 19–30.
15. S. H. Mohamed, A. I. Magdy, Ashour A. Ahmed. Exploring the Nature of Clopidogrel-Bromocresol Green-Interaction via Spectrophotometric Measurements and Quantum Chemical Calculations. RSC Adv. 2018, 8, 29104–29114.
14. Ashour A. Ahmed, P. Gros, O. Kühn, P. Leinweber. Molecular level investigation of the role of peptide interactions in the glyphosate analytics. Chemosphere 2018, 196, 129–134.
13. T. Stensitzki, Y. Yang, V. Kozich, Ashour A. Ahmed, F. Kössl, O. Kühn, K. Heyne. Acceleration of a ground-state reaction by selective femtosecond-infrared-laser-pulse excitation. Nature Chemistry 2018, 10, 126–131.
12. Ashour A. Ahmed, P. Leinweber, O. Kühn. Unravelling the nature of glyphosate binding to goethite surfaces by ab initio molecular dynamics simulations. Phys. Chem. Chem. Phys. 2018, 20, 1531–1539.
11. P. Gros, Ashour A. Ahmed, O. Kühn, P. Leinweber. Glyphosate binding in soil as revealed by sorption experiments and quantum-chemical modeling. Sci. Total Environ. 2017, 586, 527–535.
10. Ashour A. Ahmed, S. Thiele-Bruhn, P. Leinweber, O. Kühn. Towards a molecular level understanding of the sulfanilamide-soil organic matter-interaction. Sci. Total Environ. 2016, 559, 347–355.
9. G. M. Sukker, N. Wazzan, Ashour A. Ahmed, R. Hilal. Conformation and electronic structure of carbidopa. A QM/MD study. J. Theor. Comput. Chem. 2016, 15, 1650002.
8. Ashour A. Ahmed, S. Thiele-Bruhn, S. G. Aziz, Rifaat H. Hilal, S. A. Elroby, Abdulrahman O. Al-Youbi, Peter Leinweber, Oliver Kühn. Interaction of polar and nonpolar organic pollutants with soil organic matter: Sorption experiments and molecular dynamics simulation. Sci. Total Environ. 2015, 508, 276–287.

7. M. E. A. Salem, Ashour A. Ahmed, M. R. Shaaban, M. F. Shibl, A. M. Farag. Regioselective synthesis and ab initio calculations of fused heterocycles thermally and under microwave irradiation. Spectrochim. Acta A 2015, 148, 175–183.
6. Ashour A. Ahmed, O. Kühn, S. G. Aziz, R. H. Hilal, P. Leinweber. How soil organic matter composition controls hexachlorobenzene-soil-interactions: Adsorption isotherms and quantum chemical modelling. Sci. Total Environ. 2014, 476–477, 98–106.
5. Ashour A. Ahmed, R. H. Hilal, M. F. Shibl. Hydrogen bond coupling in sodium dihydrogen Triacetate. J. Mol. Model. 2014, 20, 2363.
4. Ashour A. Ahmed, P. Leinweber, O. Kühn. A computational study of hexachlorobenzene-soil organic matter interactions. J. Theor. Comput. Chem. 2014, 13, 1450009.
3. Ashour A. Ahmed, O. Kühn, R. H. Hilal, M. F. Shibl. Structure and cooperativity of the hydrogen bonds in sodium dihydrogen triacetate. Int. J. Quantum Chem. 2013, 113, 1394–1400.
2. S. A. K. Elroby, Ashour A. Ahmed, R. H. Hilal. Conformational preference and mechanism of decarboxylation of levodopa. A quantum dynamics/quantum mechanics study. Int. J. Quantum Chem. 2013, 113, 1966–1974.
1. Ashour A. Ahmed, O. Kühn, P. Leinweber. Controlled experimental soil organic matter modification for study of organic pollutant interactions. Sci. Total Environ. 2012, 441, 151–158.

Under review & In preparation

- Ashour A. Ahmed and A. M. Abdel-Mageed. Unveiling Catalytic Secrets: Integrated Experimental-Theoretical IR Analysis of Single-Site and Cu Clusters in UiO-66 Catalysts.
- S. Löbner, E. S.-Gerónimo, Ashour A. Ahmed, A. M. Abdel-Mageed. Diffuse Reflectance UV-vis spectroscopy - A facile tool for in situ and operando characterization of solid catalysts
- L. F. Dettmann, O. Kühn, Ashour A. Ahmed. Coarse-grained simulations of Sulfanilamide and Hexachlorobenzene interacting with soil organic matter.
- bin Jumah, Ashour A. Ahmed, A. Osman, A. S. Al-Fatesh, A. A. Garforth. Enhanced Hydrocracking Efficiency and Cost Reduction: Substituting Platinum with Nickel on Zeolite Catalysts for Post-Consumer Polymer Recycling.
- Ashour A. Ahmed, Unraveling the molecular-level effects of P loading on phosphate binding mechanisms at the goethite surface: Insights from MD simulations.
- M. Meshhal, O. Kühn, Ashour A. Ahmed. Graphene as a promising 2D material for capturing nanoplastics: Insights from molecular dynamics simulations.

Selected Talks

- Geometric H/D isotope effect and cooperativity of H-bonds in sodium dihydrogen triacetate, Theory Seminar, Institute of Physics, University of Rostock, **Rostock**, Germany, 28.04.2009.
- Interaction of soil organic matter with xenobiotics: pyrolysis field ionization mass spectrometry (Py-FIMS), X-ray absorption near-edge fine structure spectroscopy (XANES) and theoretical modeling, Spectroscopy-Detective in Science, **Rostock**, Germany, 17.06.2011.
- Binding of chlorinated organic pollutants to soils, 76th Annual Meeting of the DPG and DPG spring meeting, **Berlin**, Germany, 27.03.2012.
- Binding of chlorinated organic pollutants to soils, Physics Graduate Seminar, **Rostock**, Germany, 12.04.2012.
- Binding of hexachlorobenzene to soils: experimental measurement and theoretical modelling, Annual Meeting of the German Soil Science Society (DBG), **Rostock**, Germany, 11.09.2013.

- Advances in quantum chemical modeling of organic pollutants-soil interaction, Annual Meeting of the German Soil Science Society (DBG), **Munich**, Germany, 05.-10.09.2015.
- Binding of xenobiotics and P-compounds to the soil reactive surfaces: Computer simulations at the interface between Physics, Chemistry, and Soil Science, Physical Chemistry Seminar, University of Rostock, **Rostock**, Germany, 21.04.17.
- Towards a molecular level understanding of phosphorous-cycle, Symposium of Leibniz Science Campus Phosphorus Research: current projects and future perspectives, Leibniz-Institut für Ostseeforschung Warnemünde (IOW), **Rostock**, Germany, 08.-09.11.2017.
- Molecular-level picture of phosphorous binding mechanisms to soil constituents, BONARES Conference 2018: <Soil as a Sustainable Resource=, **Berlin**, Germany, 26.-28.02.2018.
- Fate of inorganic and organic P-compounds: new insights from quantum-chemical modeling, Leibniz conference on sustainable development goals, Leibniz Association, **Berlin**, Germany, 14.09.2018.
- Towards a molecular level understanding of Phosphorous-cycling in forest ecosystems, International Symposium of the Leibniz ScienceCampus Phosphorus Research Rostock, **Dummerstorf**, Germany, 20.11.2018.
- Fate of inorganic and organic P-compounds: new insights from quantum-chemical modeling, 83rd Annual Meeting of the DPG and DPG spring meeting, **Rostock**, Germany, 19.03.2019.
- Computer simulations at the interface between Chemistry, Physics and Soil Science, Colloquium of Soil, Water, and Air, University of Freiburg, **Freiburg**, Germany, 20.11.2019.
- Computer simulations at the interface between Chemistry, Physics and Soil Science, GdCh Colloquium, Chemistry Department, University of Rostock, **Rostock**, Germany, 22.10.2020.
- Advances in understanding and characterization of the P binding at the mineral/water interface using quantum chemical modeling, Closing SPP 1685 conference: Ecosystem Nutrition 2021", **Freiburg**, Germany, 26.10.2021.
- Advances in understanding the P binding in soil, P-Campus Symposium, **Rostock**, Germany, 06.-07.01.2022.
- Computer simulations at the interface between chemistry, physics, and soil science, Chemistry Department, King Abdul Aziz University, **Jeddah**, Saudi Arabia, 29.03.2022.
- Computational Chemistry: General overview, Arab molecular simulation community (AMSC), 23.04.2022.
- P binding in soil: Computational Chemistry perspective, Annual Meeting of the German Soil Science Society (DBG), **Trier**, Germany, 05.-08.09.2022.
- Advances in understanding the P binding in soil, European Workshop on Phosphorus Chemistry, **Rostock**, Germany, 14.-16.09. 2022.
- Application of Computational Chemistry in the Phosphorus research, LLM Department, University of Rostock, **Rostock** 27.01.2023.
- Computer Simulations at the Interface between Chemistry, Physics, and Soil Science: Advances in Understanding the Phosphorus Binding in Soil, Goldschmidt 2023, **Lyon, France** 12.07.2023.
- Molecular-level insights into phosphate binding in soil: Recent progress, P-Campus Symposium, **Rostock**, Germany, 09.-10.10.2023.
- Application of computational chemistry in water treatment technology, King Abdul Aziz University, **Jeddah**, Saudi Arabia, 27.12.2023.

Eidesstattliche Versicherung

Hiermit versichere ich, dass ich die vorliegende Arbeit selbstständig verfasst und keine anderen als die angegebenen Quellen und Hilfsmittel benutzt habe, alle Ausführungen, die anderen Schriften wörtlich oder sinngemäß entnommen wurden, kenntlich gemacht sind und die Arbeit in gleicher oder ähnlicher Fassung noch nicht Bestandteil einer Studien- oder Prüfungsleistung war.

Rostock, 30.01.2025

Dr. Ashour Ahmed